

Proceedings

MC 2025 Karlsruhe

Microscopy Conference

© kanpisut, SimpLine – Stock.Adobe.com

31 August–4 September 2025

www.microscopy-conference.de

DREILÄNDERTAGUNG

The MC 2025 is jointly organised by

DGE – German Society for Electron Microscopy e. V.

SSOM – Swiss Society for Optics and Microscopy

ASEM – Austrian Society for Electron Microscopy

This abstract e-book contains all abstracts submitted to the Microscopy Conference, which took place in Karlsruhe from 31 August to 4 September 2025.

The abstracts are first sorted by field. Within each field, the abstracts that were presented as talks (invited talks and oral presentations) are listed first, followed by the posters on the corresponding topic.

Inhalt

Plenary lectures 4
Materials Science (MS) 17
MS 1: Energy-related materials and catalysts 17
MS 2: Metals and alloys 116
MS 3: Disordered materials 208
MS 4: Low-dimensional and quantum materials 232
MS 5: Functional organics, carbon-based and hybrid materials 286
MS 6: Ceramics, composites and geoscience – In memory of Achim Kleebe 312
MS 7: Multi-scale and correlative in-situ/operando electron microscopy 349
MS 8: Beyond ideal 2D and van der Waals materials: Disorder, defects, adatoms and contamination 427
Life Sciences (LS) 447
LS 1: Structure and functions of cells and organelles – Cryo ET 447
LS 2: Structure and functions of cells and organelles – Imaging of large volumes and plastic section tomography 458
LS 3: Cryo-EM and image analysis of macromolecules and molecular assemblies 475
LS 4: Cryo-EM and image analysis of macromolecules and molecular assemblies 502
LS 5: Pathology, pathogens and diagnostics 537
LS 6: Advances in sample preparation 549
Instrumentation and Methods (IM) 573
IM 1: Progress in instrumentation and ultrafast EM 573
IM 2: Advanced spectroscopy 615
IM 3: SEM and FIB developments 675
IM 4: Emerging techniques and applications in 4D-STEM 743
IM 5: Beam shaping and analysis 808
IM 6: Big data and AI techniques 830
IM 7: Electron crystallography 866
Late Breaking Abstracts 888

Plenary lectures

ERL.02
Momentum-resolved STEM – A track in materials research with life science perspectives

K. Müller-Caspary[1]

[1]Ludwig-Maximilians University Munich, Chemistry, Munich, Germany

By recording a detailed diffraction pattern at each position of a scanning probe, the momentum-resolved STEM (MR-STEM) technique yields four-dimensional data combining real and momentum space information. Depending on the experimental acquisition parameters, MR-STEM can be used to

- map crystal lattice strain with precisions in the 10-4 range,
- quantitatively measure magnetic and electric fields,
- generate conventional STEM signals with dedicated detector geometries
- solve the inverse problem via various ptychographic methods
- image biological specimens under cryogenic conditions at low dose.

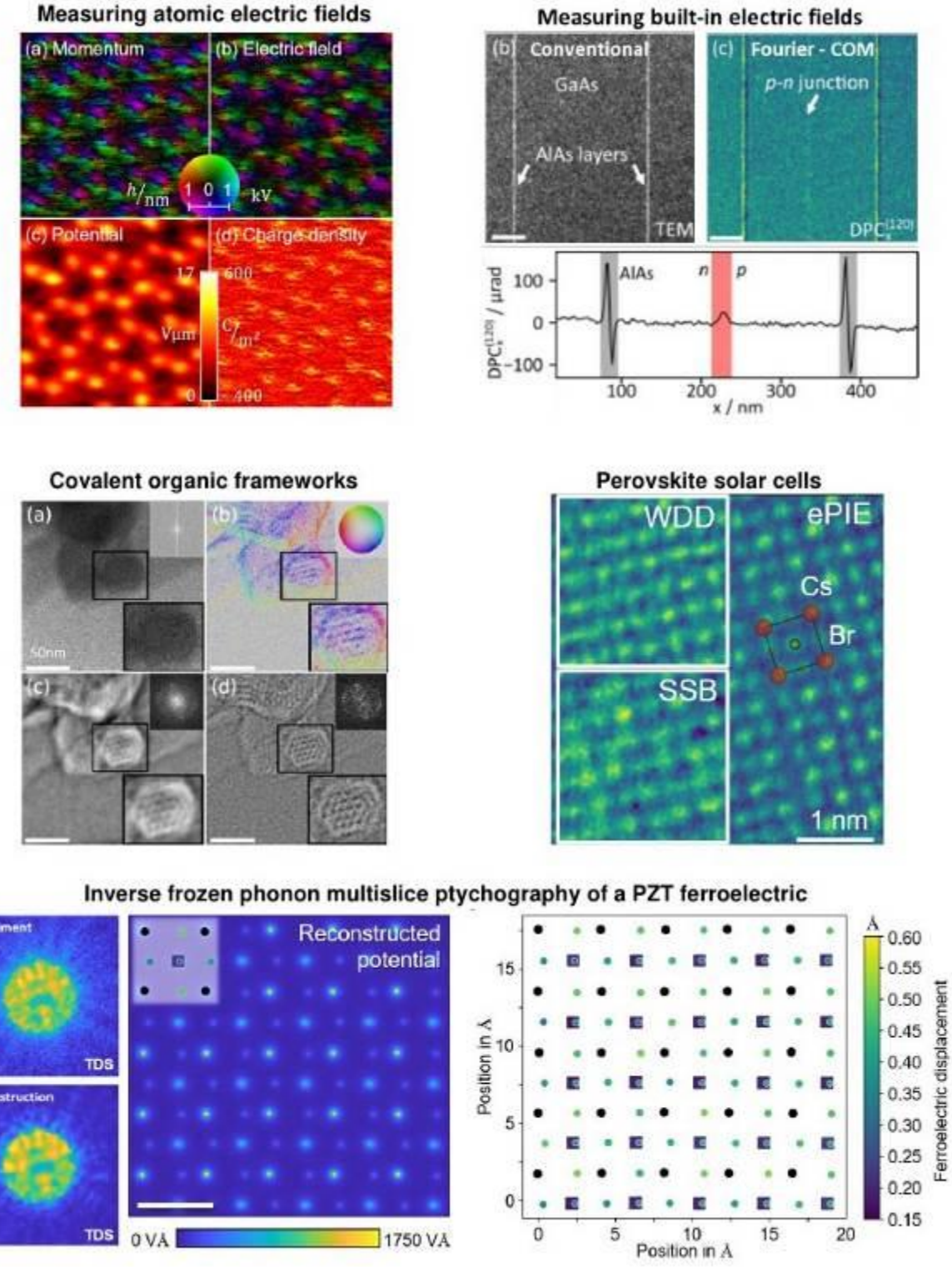
Due to the high demands on detector speed, the rise of MR-STEM coincided with the introduction of ultrafast diffraction cameras [1] more than a decade ago and is now an established standard setup in many laboratories.
The mapping of electric or magnetic fields involves two steps. First, the centre of mass (COM) of the whole diffraction pattern is calculated, also known as "COM-imaging". With a high sampling of the diffraction pattern provided by pixelated cameras, this represents the average lateral momentum <p> transferred to the probe. Second, Ehrenfest"s theorem can be used to derive proportionality between <p> and the projected electric field in thin specimens, cross-correlated with the probe intensity [2]. In this way, electric fields, charge densities and Coulomb potentials can be measured quantitatively down to the subatomic scale, e.g., in 2D materials [3]. COM-imaging can furthermore provide insights into polarisation-induced electric fields and the quantum-confined Stark effect in nanostructures under certain conditions [4]. MR-STEM can also be used to sense composition and structure via exploiting the characteristic fingerprints composition, thickness and strain leave in the angular dependence of the scattered intensity. This enables the simultaneous mapping of several elemental distributions as well as strain in semiconductor nanostructures [5].
COM-based imaging falls into the category of differential phase contrast (DPC) STEM and is not only dose-efficient but also provides high in-focus contrast for weak scatterers [6]. It can thus be applied to map the structure of proteins [7], covalent organic frameworks [8] or perovskite solar cells at doses well below 50 el/A².
Contemporary resources enable the solution of the inverse problem, such that thermal diffuse scattering and Z-contrast can be included in inverse multislice [9], and MR-STEM based phase retrieval can be implemented into single-particle workflows of cryo-STEM [10], where thousands to millions of particles are imaged. This contribution will close with putting interdisciplinary research on phase retrieval applications in Physical and Life Sciences into future perspectives.

Acknowledgements & References
I am thankful for the prestigious opportunities to work in and/or with the groups of A. Rosenauer, J. Zweck, S. Van Aert, J. Verbeeck, K. Volz, Frank Filbir, C. Sachse, H. Stahlberg. I thank all my former and current group members for their hard, creative work and outstanding motivation.

[1] APL 101, 212110 (2012)
[2] Nat Comm. 5, 5653 (2014)
[3] PRB 98, 121408 (2018)
[4] PRL. 122, 106102 (2019)
[5] Sci. Rep. 6, 37146 (2016)

[6] UM 2, 251 (1977)
[7] Nat. Meth. 19, 01586 (2022)
[8] Sci. Rep. 14, 1320 (2024)
[9] Nat Comm. 15, 101 (2024) & Phys. Rev. B 110, 064102 (2024)
[10] Nat Comm. 15, 1862 (2024)

Fig. 1



HRDL.02
Electron microscopical imaging using inelastically scattered electrons

H. Kohl[1]

[1]University of Münster, Institute of Materials Physics, Münster, Germany

The development of a scanning transmission electron microscope with a field-emission gun allowed to focus an electron beam to a spot with a diameter of a few Å [1], thus permitting to obtain images at almost atomic resolution. Attaching an electron energy loss spectrometer one can additionally record images using electrons having suffered a defined energy loss. The first images taken in this way of the edge of a thin carbon film [2] were rather blurry as compared with the corresponding annular dark field images. As there is no imaging lens beyond the specimen, this cannot be explained by the chromatic aberrations.

To understand this effect quantitatively, Rose developed a theory for the description of the imaging process using inelastically scattered electrons [3], which can be used for any excitation process. For single scattering processes he demonstrated that the object can be described by a mixed dynamic form factor thus generalizing the theory for scattering processes in a diffraction geometry. We shall discuss the basic concept of his description before turning to the numerous applications of these techniques in the course of time.

Soon after Roses pioneering paper, pictures were taken using volume and surface plasmon losses for oxidized Si [4,5] and Ga [6] spheres. In these images the bulk zones could be clearly distinguished from the surface. Furthermore it was demonstrated that the surface plasmons can be excited even from electrons passing the sphere at a distance. More recently the eigenmodes of plasmon excitations have been imaged [7].

To quantitatively measure this blurryness for inner-shell excitations in elemental maps, Mory et al. [8] used a cross-correlation technique to demonstrate, that the effect still exists but decreases with increasing energy loss. Nowadays elemental maps of crystalline specimens can be obtained with atomic resolution [9,10,11].

With the improvements in energy resolution of the spectrometers and the additional inclusion of monochromators in high-end microscopes, it became even possible to image vibrations. Krivanek et al. have shown that this can be used to identify molecular species. They demonstrated that one can obtain spectra from biological specimens using electrons passing far outside thus avoiding knock-on damage [12]. The excitation of phonon-polaritons in a MgO-cube is a further impressive example [13].

The scheme introduced by Rose decades ago [3] for the description of image formation with inelastically scattered electrons can be applied to all these types of excitations.

References

[1] Crewe, A., Wall, J., and Langmore, J. (1970) Science **168**, 1338

[2] Isaacson, M., Langmore, J. , and Rose, H. (1974) Optik **41**, 92

[3] Rose, H. (1976) Optik **45**, 139 and 187

[4] Batson, P. (1982a) Ultramicr. **9**, 277

[5] Batson, P. (1982b) Phys. Rev. Lett. **49**, 936

[6] Achèche, M., Colliex, C., Kohl, H., Nourtier, A., and Trebbia, P. (1986) Ultramicr. **20**, 99

[7] Rossouw, D. et al. (2011) Nano Lett **11**, 1499

[8] Mory, C., Kohl, H., Tencé, and Colliex, C. (1991) Ultramicr. **37**, 191

[9] Kimoto K. et al. (2007) Nature **450**, 702

[10] Bosman M. et al. (2007) Phys. Rev. Lett. **99**, 086102

[11] Muller D.A. et al (2008) Science **319**, 1073

[12] Krivanek, O. et al. (2014) Nature **514**, 209

[13] Lagos, M., Trügler, A., Hohenester, U., and Batson P. (2017) Nature **543**, 520

PL1.01
Extreme objective lenses for outlandish imaging

L. Jones[1,2,3], G. Motta Alves[2], T. Andrews[1,2,3], K. Gruver[4], D. Brittain[4], N. de Costa[4], C. Reid[4], P. McBean[4], F. Thompson[2], J. J. P. Peters[1,2,3]

[1]Trinity College Dublin, The University of Dublin, Advanced Microscopy Laboratory (AML), School of Physics, CRANN & AMBER, Dublin, Ireland
[2]turboTEM Limited, Dublin, Ireland
[3]Trinity College Dublin, The University of Dublin, School of Physics, Dublin, Ireland
[4]Allen Institute for Brain Science, Seattle, WA, United States

"The objective lens is the heart of the TEM" [1]. Perhaps unsurprisingly then, its design and performance dictate many of the operational capabilities and choices that are available to the operator. The range of pole-piece designs follows from the breadth of tasks these hugely valuable instruments are used for. Biological applications may favor high-contrast lenses (typically with higher Cs), while low-voltage EM benefits from lower chromatic aberration (Cc) designs with often very small pole gaps. Cryo-EM lenses often employ cryo-shields to reduce ice-build up, but this may exclude their use for x-ray spectroscopy (EDS). For EDS applications, sloping pole-gaps may be used to allow detectors to approach closely, reduce shadowing and improve collection angles, while for double-tilting, in-situ or tomography applications wide gaps are needed.

Previously we have reported on the design and manufacture of a "user adjustable pole-piece" or UAP [2]. The principle of the UAP is simple; the operators of a multi-user TEM should be able to optimize the objective lens to their individual experiments, specifically changing the gap size as they change beam voltage or imaging task with options spanning the range of 1.5mm to 6.5mm. The construction of the UAP is more involved with a gear mechanism being used to realize the physical adjustment while maintaining high vacuum. This adjustable gap capability can be used to design wholly unique experiments and we will report on one example from a UAP installed in Sandia National Laboratory relating to nuclear steels research. Imaging of a steel foil was performed with the UAP set to a high-resolution small gap position before the gap was expanded to its maximum height so that the sample could be tilted to 90degrees to enable ion implantation with a 1.4 MeV Fe2+ beam performed at room temp up to 5 DPA. The sample could then be reoriented, the lens gap closed and the post-exposure imaging performed.

Next, we report on a newly developed pole-piece geometry designed for single-particle cryoEM workflows. Previous efforts spearheaded by the Laboratory of Molecular Biology (Cambridge, UK) have advocated for lower cost cryoEM instruments [3,4,5]. Their work has shown that if a lens with Cc ≤1mm can be realized then a 70% improvement in contrast at 3Å could be expected. With this as a target specification for the design, a new genetic algorithm was developed to optimize the pole-piece geometry for this purpose. Following the design optimization, a prototype unit was manufactured before being tested at the LMB. Fig. 1b) shows the "first light" through our prototype lens achieved in November 2024. Subsequent imaging (c) and Fourier analysis revealed information transfer at the 1.23Å reflection from gold nanoparticles. We hope to report on more imaging results later in the year.

Neurological conditions are listed as a factor in more than 10 million deaths a year [6]. As such, mapping the brain is a rapidly growing area of research. One approach uses serial-section TEM to image a large number of thin sections which can then be reconstructed computationally back into the entire volume. Recently a workflow has been demonstrated that can extend to imaging one cubic millimeter (1mm3) [7]. However, for the connectomics community to move from a fly brain to a mammal brain (mouse), a leap to ≈1cm3, a factor of 500x or more in volume will be necessary. A typical 3.05mm TEM grid may have 2mm of usable width of travel. To enable a usable width of at least 10mm, a pole-piece was designed with an especially wide sample port (WSP). The dimensions of the opening in an original pole-piece of a JEOL-1200EXII is shown alongside our new design in Fig. 2. Preliminary testing has already delivered a 5mm width-of-view, achieved by montaging 65721 frames into a single image (approx. 256x256 tiles). The mappable width is now limited only by the width of the objective-lens"s sample insertion port and not by the pole-piece.

To move beyond our current 5mm width limitation, and to also handle the 10 times greater number of sections needed for 1cm3 imaging, we need to consider a drastically new approach. We are proposing a split pole-piece wafer handling stage objective lens. This will allow for samples of up to 100mm width to be imaged with extreme automation and potentially robotic sample handling and auto-loading. A preliminary design and visualization for such a system is shown in Fig. 3 and we hope to report on further results at the meeting.

Here we have described three innovative objective lens concepts for performing experiments at the extreme edges of what is possible in the TEM today. A fourth future concept is described for the high-throughput realization of peta-scale imaging pipelines on a 100mm wafer handling stage [8].

Fig. 1. a) Photograph of the modified JEOL1400 at the MRC LMB, image credit [5]. b) The first beam recorded using our retrofitted bespoke low-Cc pole-piece (photo from November 2024). c) Preliminary imaging of gold nanoparticles using the new low-Cc lens. Subsequent Fourier analysis showed information transfer at 1.23Å.

Fig. 2. a) Schematic of the sample insertion port from a ≈1990 vintage JEOL 1200EXII TEM and the relative width of our wide sample port (WSP). b) Using this new pole-piece, a 100x100 image montage data set was collected at 750x magnification covering a 5mm wide field-of-view. c) High-magnification performance was evaluated by capturing images at 3000x (right) and 10k x (not shown) magnification.

Fig. 3. Rendering of the proposed wafer imaging system, scaled and overlayed on a photograph of a JEOL-1200EXII TEM. Samples are loaded via the large vacuum door on the right-hand side of the column, while additional pumping and venting infrastructure is added to the left.

References:

1. Naoya Shibata, *personal communications* (November 2020).
2. Patrick McBean et al., *Micro. & Microanal.*, **29 (S1)**, p1885-1886, (2023). https://doi.org/10.1093/micmic/ozad067.973
3. K. Naydenova et al., *IUCr*, **6**, p.1086-1098 (2019). https://doi.org/10.1107/S2052252519012612
4. Greg McMullan et al., *PNAS*, **120**, (2023). https://doi.org/10.1073/pnas.2312905120
5. "Low energy cryo-EM to widen accessibility for fast and accurate structure determination", *Insight on Research*, https://www2.mrc-lmb.cam.ac.uk/low-energy-cryo-em-to-widen-accessibility-for-fast-and-accurate-structure-determination/, (November 2023).
6. "The Global Prevalence of Brain Disease", https://www.americanbrainfoundation.org/the-global-prevalence-of-brain-disease (accessed July 2024).
7. Wenjing Yin et al., *Nature Communications*, **11** (2020) https://doi.org/10.1038/s41467-020-18659-3
8. The authors would like to acknowledge the many contributions, discussions and advice from colleagues over the years including Maixent Cassagne, Khalid Hattar, Chris Smyth, Richard Henderson, Chris Russo, Greg McMullen, Ryusuke Sagawa and Yu Jimbo. LJ acknowledges funding from Research Ireland grants: URF/RI/191637 and 12/RC/2278_P2, and Enterprise Ireland grant: UAP-4-TEM. KG, DB, NDC and CR (WSP project) acknowledge NIH 5UM1NS132253-02.

Fig. 1

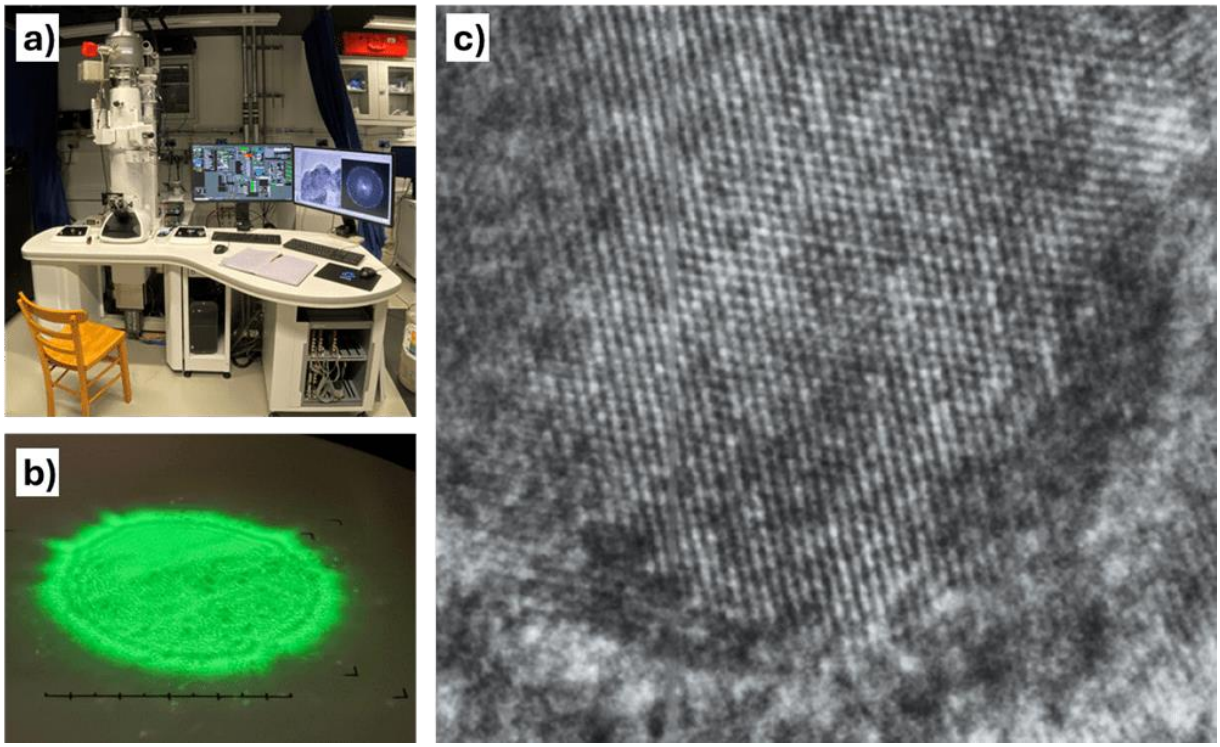


Fig. 2

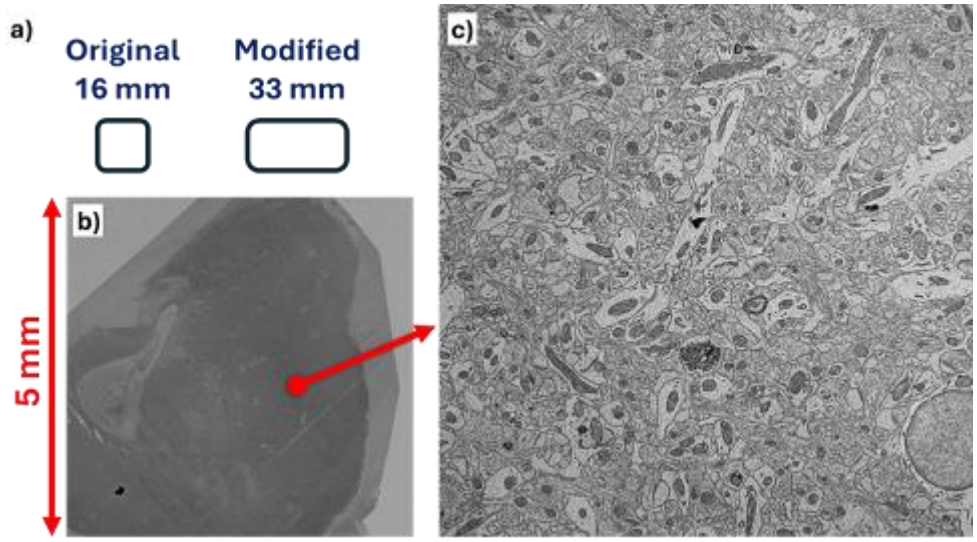


Fig. 3



PL2.02
From correlative microscopy to multimodal discovery: Connecting modalities, bridging scales, enabling insight

R. Wepf[1]

[1]The University of Queensland, Centre for Microscopy & Microanalysis (CMM), Brisbane, Australia

Correlative microscopy and multimodal imaging have evolved from specialist techniques into powerful, integrative platforms that bridge structural, chemical, and functional insights across life and material sciences. In this keynote, I will reflect on a personal journey through three decades of application and innovation—spanning foundational work in cryo-preparation, scanning probe, electron microscopy and CLEM, through to the development of high-throughput, 3D correlative workflows.

From early efforts in HR-TEM/FEGSEM/STM imaging of biological macromolecular structures, through instrument and method development at EMBL, Beiersdorf AG, ETH Zurich, and now at UQ"s Centre for Microscopy and Microanalysis, I will highlight personal key milestones—such as the VCT, HPM100, Shuttle & Find platform, OMNY, iCore, and the 2010"s seminal publications on CLEM workflows and flow-cell based correlation. These developments enabled us to correlate structures with different modalities and helped shape commercial systems now used globally, and catalysed community-wide adoption of CLEM as a standardised tool.

Alongside personal contributions, the lecture will showcase pioneering advances from other groups: from dynamic cryo-CLEM and lattice light sheet–guided ROI correlation, to multimodal microscopy, integrated mass spectrometry workflows, and federated FAIR data architectures. These examples illustrate how correlative imaging continues to push methodological and conceptual boundaries and AI-readiness for multimodal platforms.

The talk will conclude with a vision for the future—a "Google-Zoom"-like navigation of complex samples, where modalities and magnifications become software-linked layers of "meaning". Emerging instrumentation, real-time AI guidance, and data-centric microscopy are converging to unlock new forms of discovery—from hydrated cells to protein structures, from rocks to mineral interfaces, from atomic lattices to complex systems.

By connecting imaging modalities and bridging spatial and analytical scales, correlative and multimodal workflows are becoming more than a set of techniques—they are evolving into a **conceptual and technological bridge** (epistemological bridges) that enables new ways of seeing, understanding, and advancing science and our understanding of complex systems.

PL3.01
In situ studies of nanomaterials for spintronics with advanced electron probes

M. Varela del Arco[1]

[1]Universidad Complutense de Madrid, Facultad de CC. Físicas, Madrid, Spain

Our understanding of the properties of multifunctional nanomaterials relies on establishing the atomistic mechanisms responsible for functionality at the atomic scale. The success of aberration correction in the electron microscope has allowed electron probes to bear on this task with atomic resolution in real space both in imaging and spectroscopy. Recent years have also witnessed the development of specimen holders that allow tickling materials live, *in situ*. External stimuli, such as temperature or bias, can be used to modify systems of interest as we watch dynamics evolve, and this is a most important capability for nanomaterials. This talk will review examples of *in situ* investigations of point defects in the scanning transmission electron microscope (STEM) in materials of interest for fields as diverse as spintronics or energy. An example can be found in the study of single Bi dopants in Cu nanowires with very low doping levels. These are very interesting systems due to the giant spin Hall effect associated with the presence of Bi. However, the dopant size and the presence of defects such as grain boundaries may promote Bi segregation when the temperature is raised or electric polarization is applied, which may affect the electrical performance of future devices based on these wires. Density-functional theory calculations show that for Bi doping levels below 1% the most stable dopant configuration is sitting within a Cu lattice site. Larger doping levels result in a distribution of different types of defects, being the substitutional ones the less prone to react to temperatures of a few hundred degrees C. Other point defects of interest in functional materials are vacancies. We will again combine theory, experiment and simulation to quantify and detect small concentrations of O vacancies in complex oxides. Simulations show that virtual detector optimization in 4D-STEM techniques can, in fact, lead to vacancy detection for vacancy compositions below 0.7%. Experiments including *in situ* reduction processes will also be discussed.

PL4.01
Probing the molecular organization of cells and organelles using cryo-electron tomography

D. Nicastro[1]

[1]UT Southwestern Medical Center, Cell Biology, Dallas, United States

Cryo-electron tomography (cryo-ET) has opened a new frontier in structural cell biology by enabling three-dimensional imaging of macromolecular assemblies directly inside intact, rapidly frozen cells preserved in their native state. We use this powerful imaging technique in combination with cryo-focused ion beam (cryo-FIB) milling and subtomogram averaging to reveal cellular structures at molecular resolution. These approaches are further integrated with EM-visible protein labeling, correlative light and electron microscopy, comparative genetics, and proteomic analyses to investigate how molecular machines are spatially organized and regulated within the cellular environment. We focus on cytoskeletal assemblies and organelles, particularly motile cilia and flagella, which are essential for cilia-driven fluid flow, cell motility, and sensory signaling across a wide range of eukaryotes. Our cryo-ET studies have revealed how dynein motors interact with microtubules and transition between nucleotide states, and unexpectedly, how the inhibition—rather than activation—of specific dynein arms regulates the force asymmetry that underlies effective ciliary beating. Using cryo-FIB milling, we have gained access to previously inaccessible cellular regions and captured macromolecular complexes involved in active processes at molecular resolution. Comparative structural analyses across diverse species—from unicellular algae to humans—revealed both conserved protein complexes and species-specific adaptations in ciliary structures. Notably, our studies of the choanoflagellate *Salpingoeca rosetta*, a unicellular relative of animals, showed that key ciliary complexes more closely resemble those of metazoans than other protists, offering new insights into the evolutionary trajectory of cilia at the dawn of multicellularity. We have also extended our imaging approaches to other cellular systems, including the apical invasion complex of the parasite *Toxoplasma gondii* and cytoskeletal assemblies in yeast, uncovering structural principles that govern diverse cellular functions. Together, these findings demonstrate how cryo-ET defines the organization and regulation of macromolecular complexes and reveals conserved mechanisms that drive cellular motility, signaling, and host-pathogen interactions in both health and disease.

SP1.07
AI on the atomic edge – How autonomous microscopy is accelerating energy materials innovation

S. R. Spurgeon[1]

[1]Colorado School of Mines, Metallurgical and Materials Engineering Department, Golden, CO, United States

The global quest for an advanced energy future is intrinsically linked to our ability to innovate and deploy new materials at an unprecedented pace. Yet, navigating the vast, complex landscapes of material synthesis, characterization, and lifecycle performance often outstrips the capacity of traditional research methodologies. This plenary will address how "AI on the Atomic Edge"—the deep integration of artificial intelligence with state-of-the-art microscopy—is fundamentally transforming this challenge by powering autonomous microscopy systems to dramatically accelerate energy materials innovation. I will explore the core principles and practical implementations that allow autonomous microscopy to serve as a potent accelerator. This includes how multi-modal machine learning algorithms can intelligently interpret complex, high-dimensional data from atomic-scale imaging and spectroscopy in real-time, guiding experimental decisions without human intervention. Furthermore, I will detail how these AI-driven insights are translated into closed-loop, autonomous experimental workflows that can systematically explore material parameter spaces, inform optimal synthesis, and elucidate intricate degradation pathways far more efficiently than conventional approaches. Drawing on firsthand experiences, I will share insights into the design, deployment, and successful application of these intelligent systems to critical areas such as next-generation energy storage and microelectronics. This presentation will not only showcase the breakthroughs enabled by AI-powered autonomous microscopy but also discuss the practical strategies and lessons learned in bridging the gap between AI algorithms and real-world materials research. Ultimately, I will show how this paradigm shift is paving the way for a future where the innovation cycle for critical energy materials is measured in months, not years.

Fig. 1: Towards Autonomous Materials Experimentation: The development of the autonomous electron microscope hinges on bridging descriptive imaging with prescriptive, AI-driven control—a key challenge in accelerating materials discovery and understanding. Adapted under CC-BY license from [1].

Fig. 2: Automating Atomic-Scale Analysis in MXenes: Our Neural Network rapidly extracts atomic positions from STEM-HAADF images (left). By generating an intermediary mask (center), it precisely locates atoms (right), enabling the reproducible, scalable insights crucial for advancing 2D materials. Adapted under CC-BY license from [1].

References

[1] Guinan, G., Salvador, A., Smeaton, M. A., Glaws, A., Egan, H., Wyatt, B. C., Anasori, B., Fiedler, K. R., Olszta, M. J., & Spurgeon, S. R. (2025). "Mind the Gap: Bridging the Divide Between AI Aspirations and the Reality of Autonomous Microscopy." APL Machine Learning. In press. Preprint DOI: 10.48550/arXiv.2502.18604

Fig. 1

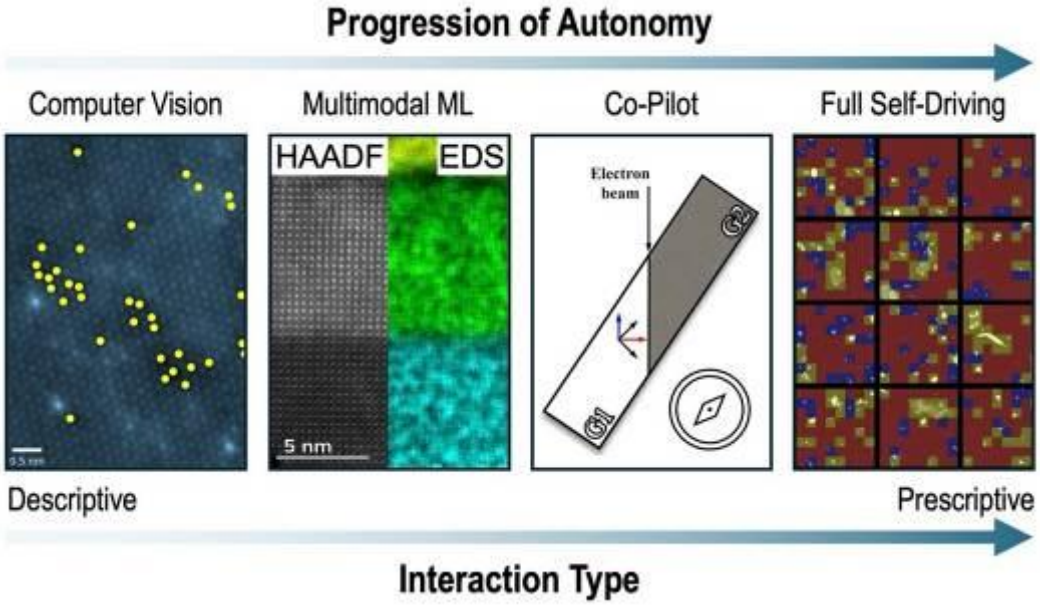
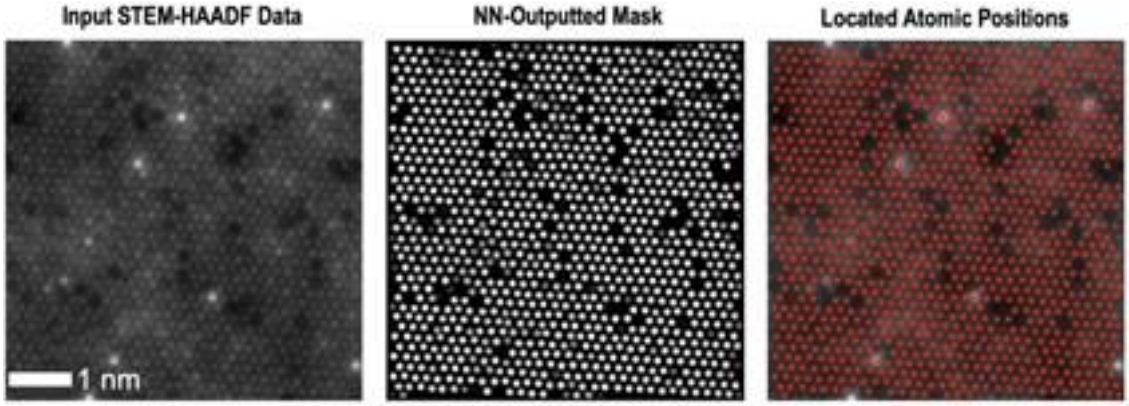

Progression of Autonomy
Computer Vision
Multimodal ML
Co-Pilot
Full Self-Driving
HAADF
EDS
5 nm
Electron beam
G2
G1
Descriptive
Prescriptive
Interaction Type

Fig. 2


Input STEM-HAADF Data
NN-Outputted Mask
Located Atomic Positions
1 nm

Materials Science (MS)

MS 1: Energy-related materials and catalysts

MS1.02(inv)
Electron microscopy advances in catalysis

S. Helveg[1]

[1]Center for Visualizing Catalytic Processes (VISION), Department of Physics, Technical University of Denmark, Kongens Lyngby, Denmark

Electron microscopy has emerged as a powerful tool in catalysis science. Advances in electron optics and image reconstruction algorithms enable visualizations of catalytic nanomaterials with three-dimensional atomic resolution. The advent of open and closed gas cells facilitates *in situ* and *operando* observations of catalysts immersed in chemical reaction environments, providing unprecedented insights into the labile behavior of catalysts as well as mechanistic and kinetic information on atomic processes unfolding during catalysis. Finally, new low-dose-rate and low-dose imaging concepts allow characterizing, quantifying and suppressing electron-beam induced alterations of catalyst surface structures and reaction pathways. In this presentation, I will showcase these advancements in atomic-resolution electron microscopy and highlight their impact on the understanding of catalytic active sites and their mechanistic roles, paving the way for innovative approaches in catalysis research, e.g. [1-11].

References

[1] S. Helveg, *J. Catal.* **328**, 102 (2015).

[2] S. Helveg et al., *Micron* **68**, 176 (2014).

[3] M. Ek et al., *Nat. Commun.* **8**, 305 (2017).

[4] M. Ek et al., *Nanoscale* **13**, 7266 (2021).

[5] F.-R. Chen et al., *Nat. Commun.* **12**, 5007 (2021).

[6] H.R. Ambjørner et al., *Nanoscale* **15**, 16896 (2023).

[7] E.S. Varo et al., *J. Am. Chem. Soc.* **146**, 2015 (2024).

[8] J.R. Jinschek et al., *MRS Bulletin* **49**, 174 (2024)

[9] C. Kisielowski et al., *Microsc. Microanal.* **31**, ozae107 (2025)

[10] I. Biran et al., submitted (2025)

[11] The Center for Visualizing Catalytic Processes is sponsored by the Danish National Research Foundation (DNRF146).

MS1.03
Microstructural studies of thin film all-solid-state batteries by STEM

V. Montanelli[1], J. Morzy[2], J. Casella[2], F. Töpperwien[2], Y. E. Romanyuk[2], M. D. Rossell[1]

[1]EMPA - Swiss Federal Laboratories for Materials Science and Technology, Electron Microscopy Center, Dübendorf, Switzerland
[2]EMPA - Swiss Federal Laboratories for Materials Science and Technology, Laboratory for Thin Films and Photovoltaics, Dübendorf, Switzerland

INTRODUCTION:

All-solid-state batteries (ASSBs) are considered a promising solution to the safety issues and energy density limitations of conventional Li-ion batteries (LIBs) containing liquid electrolytes. The employment of solid electrolytes with wider electrochemical windows allows the use of high-capacity Li-metal anodes and high-voltage cathode materials to achieve higher energy and power densities [1]. However, undesirable physical and chemical interactions at solid electrolyte/electrode interfaces lead to significant differences between predicted and actual ASSB performances hindering their large-scale commercialization [2]. These interfacial issues occur at the nanoscale, making scanning transmission electron microscopy (STEM) a powerful tool to study them.

OBJECTIVE:

To investigate the microstructural and compositional changes induced by electrochemical cycling in thin-film ASSB's cathodes.

MATERIALS & METHODS:

Thin-films ASSBs are used for this work because they offer easily accessible interfaces. Two cathode material systems are considered: the first system consists of batteries with NMC811 intercalation cathodes, while the second one includes batteries with Cu-Fe-LiF conversion cathodes in two different compositions.

A completely airless workflow is introduced for the sample preparation and analysis. TEM lamellas from the thin-film batteries are prepared by focused ion beam (FIB) on MEMS chips. The chips are then mounted on an air-free transfer TEM holder, which allows electrical biasing. The micro-batteries are then investigated using STEM imaging, diffraction (4D-STEM) and spectroscopy techniques (EDX and EELS).

RESULTS:

This work investigates the effects on the microstructure of flash lamp annealing (FLA) during the preparation of thin-film ASSBs with NMC811 cathodes. Compared to the non-annealed sample, the FLA-sample exhibits local delamination between the cathode and the current collector, along with the presence of vertical cracks in the cathode (Fig. 1). Diffraction experiments show that FLA-NMC811 generally has a higher crystallinity, which decreases near the interface with the solid electrolyte.

Fig. 1: *HAADF images of FLA and non-FLA samples. From bottom to top: Ti current collector, NMC811 cathode, and LiPON solid electrolyte.*

Additionally, the differences in the nanostructure of Cu-Fe-LiF cathodes before and after cycling are analysed. A combination of EDX and 4D-STEM reveals variations in the aggregation state of the small metal clusters within the LiF matrix.

CONCLUSIONS:

The microstructure of NMC811 cathodes is investigated using various STEM techniques to reveal the effects of the FLA process on the crystallinity of the material. The nanostructure of the Cu-Fe-LiF conversion cathode is also studied by *ex-situ* observations.

The established procedure for sample preparation and analysis will enable future studies on other battery types. Moreover, the experimental setup supports *in-situ* biasing experiments that can provide a deeper understanding of how, where and when degradation mechanisms and battery failure occur.

REFERENCES

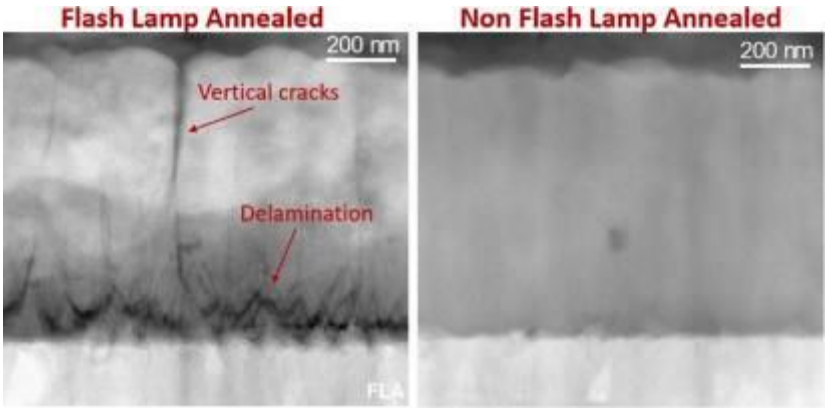
[1] Kravchyk et al, Chimia **78** (2024), p 403–414

[2] Pang, Y. et al, Electrochem. Energ. Rev. **4** (2021), p 169–193.

ACKNOWLEDGEMENTS:

This work has been funded by the SNF under Project No. 200021_219706.

Fig. 1



MS1.04
Decoding the structural complexity of technical ammonia synthesis catalysts

L. Sandoval-Diaz[1], J. Wang[1], K. Dembele[1], R. Blume[1,2], D. Kordus[1], F. Girgsdies[1], G. Koch[1], A. Hammud[1], Z. Gheisari[1], J. Folke[2], R. Eckert[3], S. Reitmeier[3], A. Reitzmann[3], H. Ruland[2], A. Knop-Gericke[1,2], J. Timoshenko[1], R. Schlögl[1,2], B. Roldan-Cuenya[1], T. Lunkenbein[1]

[1]Fritz-Haber-Institut der Max-Planck-Gesellschaft, Berlin, Germany
[2]Max Planck Institute of Chemical Energy Conversion, Mülheim a.d. Ruhr, Germany
[3]Clariant Produkte GmbH, Bruckmühl, Germany

Introduction

Ammonia is considered an important intermediate in a prospective hydrogen-based energy infrastructure.[1] Industrially, it is produced over Fe-based catalysts at high pressures (80-300 bar) and temperatures (300-550 °C).[2] Technically, multi-promoted wüstite ($Fe_{1-x}O$) is the most important iron oxide precursor that transforms upon suitable activation into a highly productive ammonia synthesis catalyst.[3] In view of its central role in the energy transition and for the development of prospective catalyst tailoring strategies it is important to explore the structural integrity of ammonia iron and to understand the genesis of the active material from the precursor oxides.

Objectives

Herein, we present a multi-modal and scale-bridging electron microscopy study paired with *operando* techniques, including X-ray photoelectron spectroscopy (XPS) and scanning electron microscopy (SEM), to unravel the structural complexity of the ammonia synthesis catalyst and correlate the structural evolution of this catalyst with its function.

Materials & Methods

The nanostructure of the technical catalyst was investigated with an aberration corrected transmission electron microscope (TEM, JEOL ARM 200F) operated at 200 kV. Post-catalytic analyses were accomplished after transfer of the sample under inert conditions. *Operando* studies have been conducted on catalyst platelets in an environmental scanning electron microscope (ESEM, FEI Quanta) and at the synchrotron facilities at BESSY II and DESY.

Results

Our analysis shows the presence of two additional cement phases and identifies seven different members of the ammonia iron family (Figure 1). *Operando* experiments inside the SEM conducted for almost 400 h unravel that each component has to fulfill a distinct role in ensuring highly active and stable ammonia synthesis catalysts. These experiments highlight that activation is the critical step in which the active catalyst structure is formed and decode the pivotal role of the promoters. The synergism between the different promoters contributes simultaneously to the structural stability, hierarchical architecture, catalytic activity, and poisoning resistance. We discuss that the confluence of these aspects is the key for the superior performance of technical catalyst formulations.

Conclusion

The study demonstrates that catalysis science can only proceed if we openly explore the full complexity of catalytic systems.

Figure 1. Summary of the ammonia iron family and cement phases with their hypothetic functions at different scales.

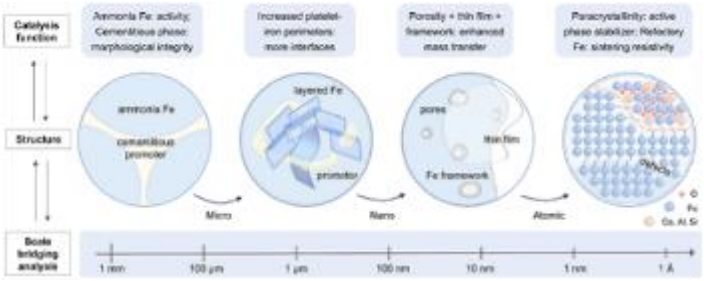
References

[1] R. Schlögl, *Angew. Chem. Int. Ed. 42* (2003) 2004-2008.

[2] H. Liu *Chinese Journal of Catalysis* 35 (2014) 1619–1640.

[3] J. Folke, et al. *Catalysis Today* 387 (2022) 12-22.

Fig. 1



MS1.05
Staging and defect limited intercalation in graphite electrodes

P. Schweizer[1,2], L. Vogl[1,3], C. Ophus[2,4], A. Minor[2,3]

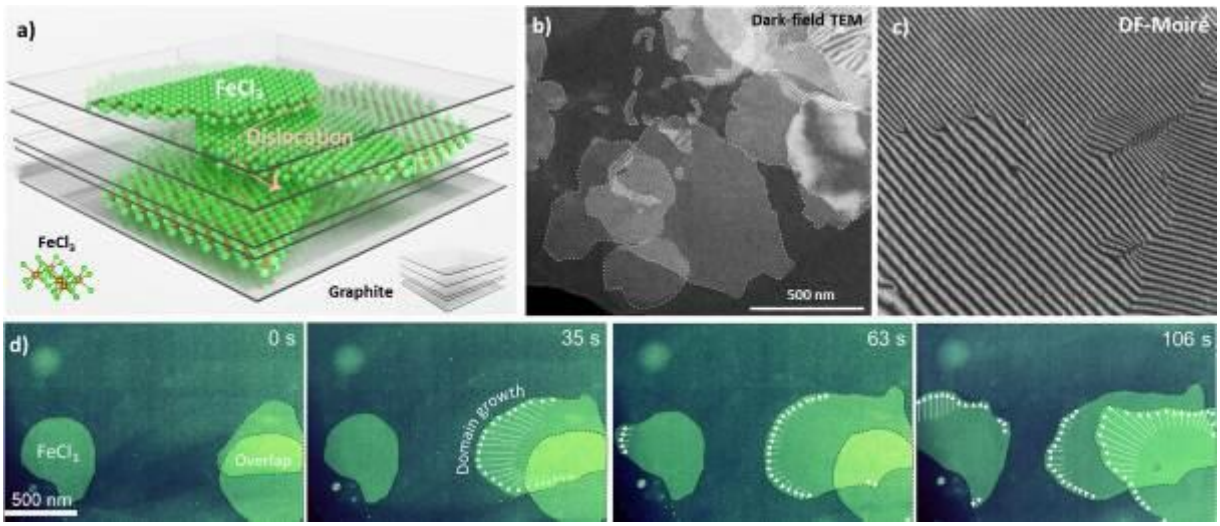
[1]Max-Planck-Institute for Sustainable Materials, Düsseldorf, Germany
[2]Lawrence Berkeley National Laboratory, Berkely, CA, United States
[3]University of California, Berkely, CA, United States
[4]Stanford University, Stanford, CA, United States

The need for sustainable mobility and renewable energy systems have been a major driving force for battery research in recent years. While ion batteries are in widespread application, there remain unsolved questions regarding fundamental processes occurring within batteries during use that ultimately limit their performance. The most important such process is intercalation, which describes the reversible incorporation of a guest species into a host lattice. In the case of graphite, the most important anode material, intercalation proceeds via insertion into the van-der-Waals gap of the host lattice. In the early stages of this process this leads to the formation of isolated 2D layers which are encapsulated inside the host material. To this day it is unclear how the initial intercalation reaction proceeds and how defects affect the process.

In this work we use advanced transmission electron microscopy to directly observe the structure, dynamics and host/guest interactions in a partially intercalated graphite model system. We show the structure and distribution of two-dimensional Iron Chloride ($FeCl_3$) layers inside a graphite host lattice (see Figure 1 a&b). Dark-field imaging and tomography enables us to show the spatial extent and three-dimensional layer occupancy. Moiré imaging (see Figure 1 c) is used to elucidate nanoscale defects within the intercalated layers. Using 4D-STEM we demonstrate how dislocations in the graphite host lattice crucially influence the spatial distribution of the intercalated species. Finally, using *in situ* heating we analyze the dynamic behavior of the guest species within the van-der-Waals gap of the host material (see Figure 1 d).

Figure 1: a) Schematic of the Iron-Chloride-Graphite model system. b) Dark-field image showing 2D intercalated layers within a graphite host lattice. The layers have complex shorelines and seem to be distributed randomly. c) DF-Moiré pattern showing defects in the intercalated layers. d) In situ heating experiment showing growth of intercaled domains.

Fig. 1



MS1.06
Revealing degradation of carbon-supported gold nanoparticles at the nanoscale during CO_2 reduction using identical-location scanning transmission electron microscopy

R. Zandonella[1], M. Heggen[1], P. Paciok[1], R. E. Dunin-Borkowski[1]

[1]Forschungszentrum Jülich GmbH, Ernst Ruska-Centre for Microscopy and Spectroscopy with Electrons, Jülich, Germany

Gold nanoparticles (AuNPs) have been successfully used as a catalyst in a variety of oxidative and reductive chemical reactions. In the process of electrochemical CO_2 reduction (CO2R), AuNPs exhibit high faradaic efficiency towards CO (FE_{CO}), which is used as a feedstock for subsequent reactions. While a high FE_{CO} is important for industrial application, catalyst stability is equally so. It has been shown that AuNPs detach or aggregate at oxidative potentials (1, 2). Stability and degradation mechanisms of supported AuNPs in a reductive environment such as during CO2R however are still unclear.

In this work we focus on the aspect of particle migration and aggregation through the application of identical-location (scanning) transmission electron microscopy (IL- (S)TEM) using dark-field (DF) and secondary electron (SE) imaging. By using a special finder grid (Plano, S147A9), this technique allows for the same sample location to be studied, prior and after ex-situ experiments. In contrast to conventional characterization with (S)TEM, information such as, but not limited to, migration and aggregation of a specific sub-set of particles can be drawn. Ex-situ electrolysis is performed using commercial AuNPs supported on Vulcan XC-72 (Premetek, P60N200) as a model system and samples were held at -1.1 V *vs* RHE for 10 minutes with 0.1 M $KHCO_3$ as the electrolyte. As conventional rotating disc electrode setups suffer from stationary gas bubbles impeding the reaction, an inverted tweezers setup was used instead (3). At potentials relevant to CO2R however, the carbon film frequently experiences rupture and delamination, resulting in sample loss. This issue was circumvented by physically stabilizing the carbon film using a nylon grid (SPI Supplies, 418CN-MB). Furthermore, a deep neural network was trained using Dragonfly® to perform automatic particle segmentation, providing a shortcut to quantifying statistically relevant amounts of particles (4).

From SE as well as DF images, migration and aggregation of small particles on the surface of the support can be seen, while large particles remained mostly stationary. Interestingly, small particles did not migrate towards larger ones, but for the most part formed small clusters of their own. A particle distribution analysis performed, reveals that approximately 40% of particles were lost which roughly translates to a probable maximum loss of electrochemically active surface area of ~ 4×10^4 nm for this catalyst, either due to aggregation or possibly detachment from the support. This lowers the cell potential during chronopotentiometry and can drastically change the selectivity of the catalyst leading to undesired product distributions. Through these insights at the nanoscale, a deeper understanding of the degradation of supported AuNPs was gained and the need to develop stabilization strategies for such catalysts is highlighted.

1. M. Smiljanić et al., Journal of Physical Chemistry C. 125, 635–647 (2021).

2. X. Meng, Z. Li, Y. Zhang, R. Yan, H. Wang, Catal Commun. 146 (2020).

3. M. Vega-Paredes, C. Scheu, R. Aymerich-Armengol, ACS Appl Mater Interfaces. 15, 46895–46901 (2023).

4. R. Makovetsky, N. Piche, M. Marsh, Microscopy and Microanalysis. 24, 532–533 (2018).

MS1.07
Atoms on the move – Understanding intraframe atomic dynamics in ADF-STEM

T. Stoops[1,2], K. Luyckx[1,2], A. de Backer[1,2], S. van Aert[1,2]

[1]University of Antwerp, EMAT, Department of Physics, Antwerp, Belgium
[2]University of Antwerp, Antwerp, Belgium

Introduction

The unique properties of catalytically active nanoparticles (NPs) depend strongly on their particular three-dimensional (3D) shape and size, which can be reconstructed from an annular dark field scanning transmission electron microscopy (ADF-STEM) image using atom counting [1]. While atomic diffusion has been studied through multiple ADF-STEM images in a time series [2,3], the effect of atomic diffusion at microscopic time scales has been neglected. Diffusion constant pre-factors [4] range from tens to hundreds of Å^2/ps while probe dwell times are of the order of microseconds [5], potentially resulting in significant atomic dynamics between pixel measurements in a single image.

Objectives

To better understand the effects of surface diffusion on ADF-STEM images and their 3D reconstruction, we have modelled dynamics at the time scale of probe measurements. Using this time series of atomic configurations of the NP, an ADF-STEM image containing the effects of surface diffusion is simulated. By performing atom counting on these images, we aim to better understand the quantitative effects on the atomic column integrated scattering cross-sections and relate the observed ADF-STEM image to a physically meaningful interpretation of the time series of simulated atomic structures.

Materials & methods

A platinum NP of approximately 3 nm is constructed based on a modified Wulff structure containing several surface features [6]. For this NP, a kinetic Monte Carlo algorithm [7,8] is applied to allow atomic hopping on lattice positions based on atomic configuration and empirical parameters. Using this algorithm, we constructed a time series of atomic configurations for each pixel scan position, which are then passed to a multislice simulation [9,10]. Atom counting is then applied to recover the thickness information [1] and the NP is reconstructed in 3D using a Bayesian genetic algorithm [6,11].

Results

The simulated ADF-STEM images visually show the effect of atomic dynamics in the form of intensity variations caused by the presence or absence of atoms in one pixel or line compared to the next. This results in a "streaking" effect in the atomic columns along the fast-scan direction. Since atoms are allowed to hop between atomic columns as the probe moves to different scan positions, atom counting may yield fractional atoms, which in turn affects the 3D reconstruction of the image. This raises the fundamental question of how to interpret a 3D reconstruction, given that the particle of interest may undergo significant structural changes during acquisition.

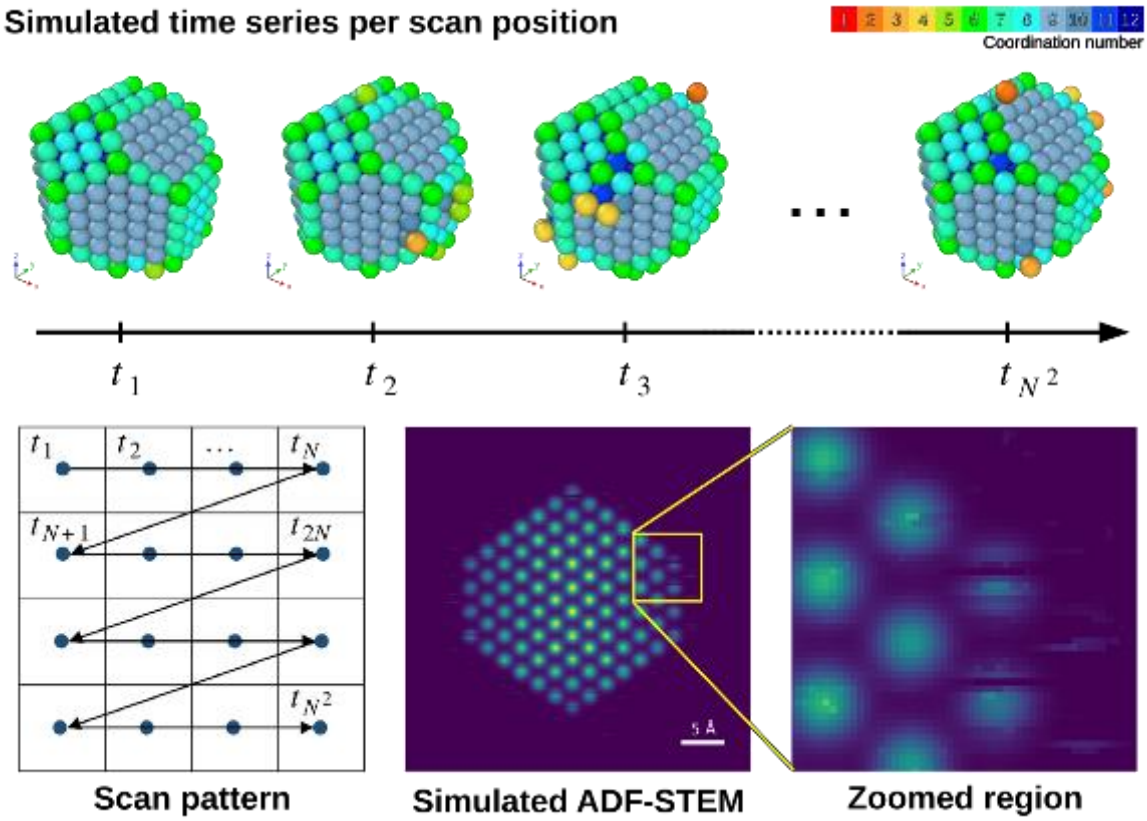
Conclusion

We simulated a time series of atomic surface dynamics for a catalytic platinum NP at the time scale of ADF-STEM pixel measurements. Using this data, an image was simulated and analysed both qualitatively and quantitatively. This allows us to relate the 3D reconstructed atom counting results to a time average of atomic configurations.

References

1. Van Aert et al, Nature **470** (2011) 374
2. Van Aert et al, Phys. Rev. Lett. **122** (2019) 066101
3. De wael et al, Phys. Rev. Lett. **124** (2020) 106105
4. Liu et al, Surf. Sci. **253** (1991) 334
5. Mullarkey et al, Microsc. Microanal. **28** (2022) 1428
6. De Backer et al, npj Comput Mater. **8** (2022) 216
7. Voter, Radiation Effects in Solids **253** (2007) 1
8. He et al, Sci. Rep. **6** (2016) 33128
9. Lobato et al, Ultramicroscopy **156** (2015) 9
10. Lobato et al, Ultramicroscopy **168** (2016) 17
11. Stoops et al, Microsc. Microanal. **31** (2025) ozae90

Fig. 1



MS1.P01
Cryogenic technology – A new era in energy materials

P. Jovicevic-Klug[1], M. Jovicevic-Klug[1], M. Amati[2], L. Tegg[3], L. Gregoratti[2], J. M. Cairney[3], M. Rohwerder[1]

[1]Max-Planck-Institute for Sustainable Materials, Interface Chemistry and Surface Engineering, Düsseldorf, Germany
[2]Elettra - Sincrotone Trieste, Trieste, Italy
[3]University of Sydney, Australian Centre for Microscopy and Microanalysis, Sydney, Australia

The new emerging technology - Cryogenic Treatment (CT) - offers great potential for improving materials and at the same time exploring new options for developing alternative materials with target properties for applications in various sectors, such as sustainable energy (including fusion), biomaterials, etc. Metallic materials used in applications for energy transition and sustainable energy, must hold an ensemble of unique properties (e.g. high corrosion resistance and surface durability) to sustain their functionality in extreme environments. CT is one of such methods that can improve both surface and bulk properties while providing an environmentally friendly and cost-effective solution.

The main objectives of this study were to determine the changes in microstructure and surface chemistry of selected martensitic stainless steels (AISI 431) after the application of CT. The selected properties and their relation to the CT conditions were analysed with scanning electron microscopy (SEM), transmission electron microscopy (TEM), atomic force microscopy (AFM), atom probe tomography (APT), X-ray photoelectron spectroscopy (XPS) and scanning photoelectron microscopy (SPEM).

The study reveals that CT modifies the microstructural evolution during tempering. During the conventional treatment, AISI 431 develops austenite reversion transformation (ART), whereas CT progresses the microstructure even further by retransforming the reverted austenite formed through ART into tertiary α-martensite, ε-martensite and carbides. This unique phenomenon is named the cryogenic austenite retransformation (CAR) effect that enables an alternative transformation route that yields novel set of properties of the same steel alloy system. Synchrotron-based SPEM provides insight into the agglomeration of carbon during exposure to CT that is correlated to the thermodynamical setting of the microstructure for supporting the CAR effect. Findings show that Mn and Cr play a crucial role in CT through its modification of chemical bonding states.

In conclusion, this study shows that CT is an effective route to modify the microstructural and final properties of alloys via a unique transformation phenomenon. The underlying mechanism of the newly discovered CAR effect is correlated with the alloying dynamics, initial microstructure and heat treatment parameters, enabling tailoring of the properties of stainless steels for future energy applications.

MS1.P03
Challenges and opportunities in the investigation of low content Cu on CeO_2 and ZrO_2 by STEM coupled with EDX and EELS

N. Rockstroh[1], C. R. Kreyenschulte[1], A. I. M. Rabee[1], J. Rabeah[1], A. Brückner[1]

[1]Leibniz Institute for Catalysis (LIKAT Rostock), Rostock, Germany

Introduction

Focus of current catalysis research is put on the discovery of catalysts that use abundant metals, prefeably in low amounts. Performance improvements are often achieved by the addition of small amounts of a second catalytically active metal or by tuning the electronic properties by the addition of alkali metals. Exemplarily, the reverse water-gas shift (RWGS) reaction that produces CO from CO_2 can be well-performed using Cu immobilized in low amounts, either with Fe on CeO_2 (0.43 wt% Cu)[1] or with Na on ZrO_2 (0.94 wt% Cu). While EDX was used to verify the presence of the supported elements, EELS was applied to prove the presence of the Ce^{4+}/Ce^{3+} couple.

Objectives

$FeCuCeO_2$ and $NaCuZrO_2$ (one-pot) showed the best activity and were characterized by in situ EPR and IR spectroscopy, XRD, STEM with EELS and EDX. Whilst EDX was used to verify the presence of the low-concentrated metals, EELS was used to spatially resolve potential differences in the oxidation state of Ce.

Materials and Methods

$CuCeO_2$ was prepared using a co-precipitation method, while $FeCuCeO_2$ was prepared by subsequent addition of Fe via wet impregnation. $NaCuZrO_2$ and $NaCu@ZrO_2$ catalysts were prepared by a one-pot procedure and by sequential addition of Cu and Na, respectively.

A probe corrected JEOL JEM-ARM200F (Schottky emitter) with a DRY SD60GV (JEOL) EDX spectrometer and a Gatan Enfinium ER EELS were used for electron microscopic investigation of the catalysts. A rather high beam current was applied to keep the acquisition time low. The FWHM of the zero-loss peak (ZLP) was about 1.2 eV and the lack of de-scan was compensated by the DualEELS mode. The spectra were recalibrated at each pixel by the position of the ZLP. Net count fitting was applied for the depiction of the EDX elemental maps.

Results

$FeCuCeO_2$ and $NaCuZrO_2$ show the best catalytic performance. In both materials, Cu is neither visible in the HAADF and BF images nor in the EDX spectra, implying either aggregation in bigger crystallites that escape STEM observation or a high dispersion. The latter has been proven by EPR and in-situ CO-DRIFTS. In contrast, $NaCu@ZrO_2$ clearly shows aggregation of Cu, which was also confirmed by EPR (Fig. 1). EELS of $FeCuCeO_2$ reveals the presence of Ce^{4+} and Ce^{3+} [2], whereby Ce^{4+} usually constitutes the inner parts and Ce^{3+} the outer parts of the CeO_x particles, with some crystallites at the outermost parts show exclusively Ce_{3+} (Fig. 2).

Figure 1. HAADF image and the corresponding EDX elemental mapping images of Cu and Na for $NaCu@ZrO_2$ (sequential) (top), and $NaCuZrO_2$ (one-pot) (bottom).

Figure 2. STEM ADF image of $FeCuCeO_2$ (left) with an overlaid false color elemental map. On the right, the distribution of two different cerium species (Ce-M (a) and Ce-M (b)) is shown independently as well as in a single-color elemental map. Adapted from ref [1], used under CC BY 4.0.

Conclusion

Using STEM coupled with EDX or EELS with these catalytic systems allows for the proof of small Cu-containing crystallites in $NaCu@ZrO_2$ and gaining information on the Ce oxidation state distribution in $FeCuCeO_2$, which is not possible with EDXS. The data underpin EPR and IR spectroscopic results, and Ce^{3+} can only be exactly localized by STEM-EELS.

Literature

[1] A. I. M. Rabee et al., *ACS Catal.* **2024**, *14*, 10913-10927.

[2] Y. Zhang, S. Bals, G. Van Tendeloo, *Part. Part. Syst. Charact.* **2019**, *36,* 1800287.

Fig. 1

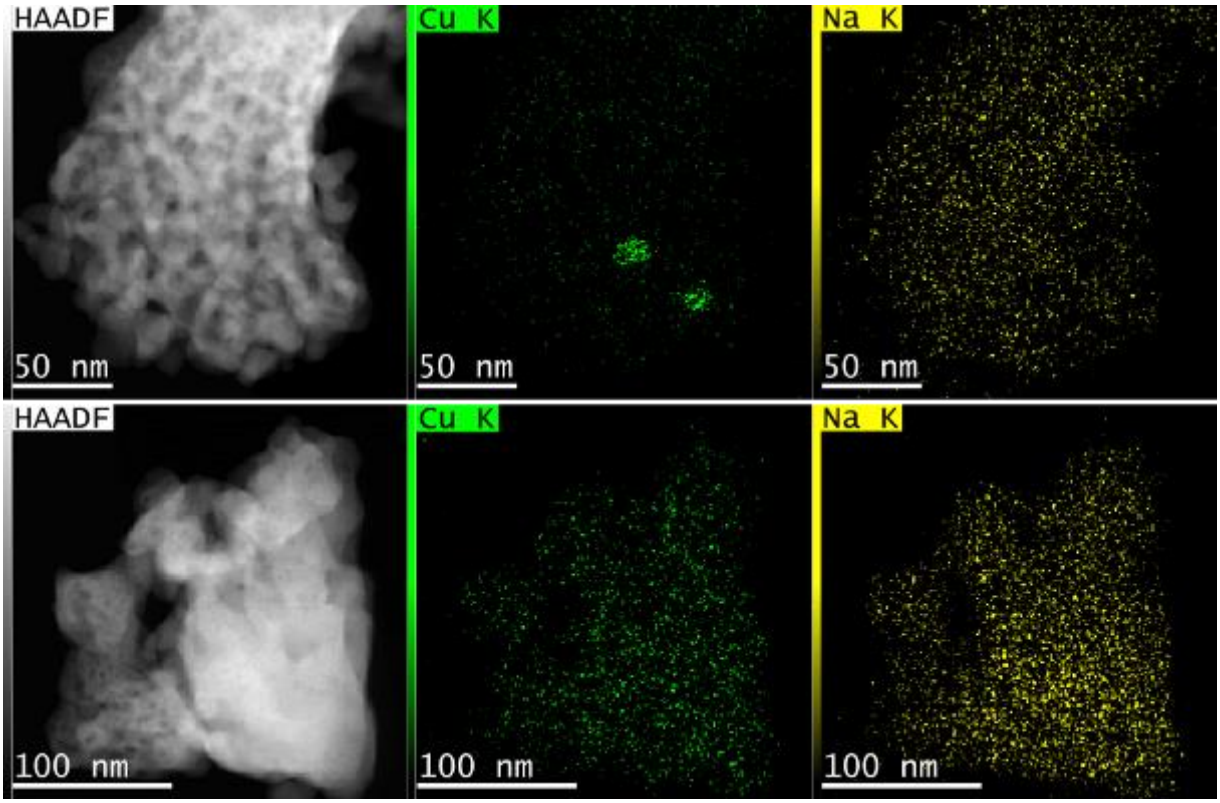
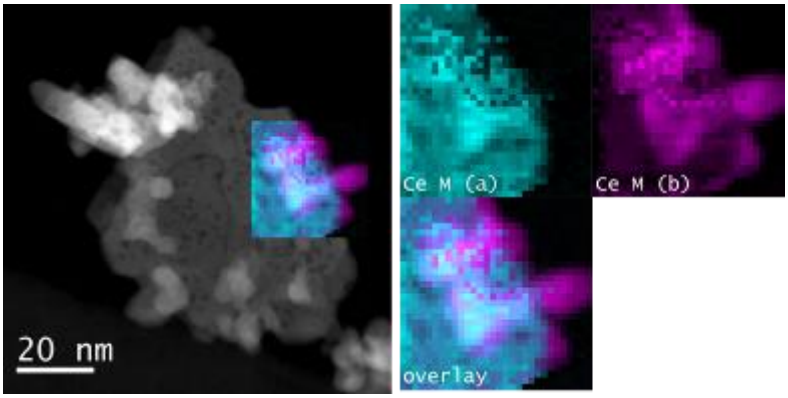


Fig. 2


20 nm
Ce M (a)
Ce M (b)
overlay

MS1.P04
Investigating the conversion reaction of the cathode active material FeS_2 in solid-state batteries via transmission electron microscopy

F. Hüppe[1], M. Pavan[2], S. Ahmed[1], J. Belz[1], J. Janek[2], K. Volz[1]

[1]Philipps-University Marburg, Department of Physics and Materials Sciences Center, Marburg, Germany
[2]Justus Liebig University Gießen, Institute of Physical Chemistry and Center for Materials Research, Giessen, Germany

Solid-state batteries are particularly promising for high-energy storage, as they potentially allow for the use of electrode materials with higher specific capacities compared to commercially available lithium-ion batteries. FeS_2 as cathode active material, for instance, has a theoretical specific capacity of 894 mAh/g[1], which is significantly higher than that of commonly used cathode materials in lithium-ion batteries like LCO or NCM.[2] Beyond its high capacity, FeS_2 offers additional advantages, including low cost and natural abundance.[3] However, FeS_2 is a conversion-type material that undergoes continuous compositional and structural changes during each cycling step. Its conversion reaction during (de)lithiation is not yet fully understood. In particular, the initial activation step - the first lithiation of the cathode material - plays a crucial role in determining the battery's long-term rechargeability. Therefore, characterizing these reactions at the micro- and nanoscale is essential for optimizing the battery performance. In this study, we use $Li_{5.5}PS_{4.5}Cl_{1.5}$ as solid electrolyte separator, and In/InLi as counter electrode alongside the FeS_2 cathode.

Scanning transmission electron microscopy (STEM) offers structural insights at atomic resolution. However, it requires a challenging sample preparation for sensitive battery materials. The plasma focused ion beam (PFIB) system Helios 5 Hydra CX (Thermo Fisher Scientific) is capable of an inert-gas transfer as well as sample preparation at temperatures around -190 °C. In the PFIB, the sample is thinned to electron-transparency, from where it is transferred to the glove box and mounted in a sealed transfer holder (Mel-Build) for further investigation in a STEM (JEOL JEM-2200FS). Electron imaging, STEM-PED (precession electron diffraction), STEM-EDX (energy dispersive X-ray spectroscopy), and STEM-EELS (electron energy loss spectroscopy) are performed at cryogenic temperatures.

The pristine, uncycled FeS_2-sheet exhibits a polycrystalline cubic structure, as revealed by STEM-PED. After the first discharge at 0.6 V vs. In/InLi (initial lithiation), the material becomes partially amorphous, and its composition becomes inhomogeneous, forming "flower-shaped" structures. A representative structure is depicted in Figure 1, where a STEM-EDX map of the first discharged sample reveals an iron enrichment in the center of the structure, an iron depletion area adjacent to it, and a more homogenous element distribution elsewhere. Lithium remains undetectable using EDX analysis, as its characteristic X-rays have too low energy and are absorbed by the detector's window. Hence, STEM-EELS measurements are performed to identify lithium components and their distribution.

The inert gas workflow and cryogenic temperatures during electron and ion beam exposure enable the investigation of the lithium-containing FeS_2 samples at the micro- and nanoscale. A comprehensive, multimodal STEM analysis - combining imaging, diffraction, and spectroscopy - reveals significant structural changes and the partial separation of iron and sulphur during lithiation, which will be discussed in detail during the presentation.

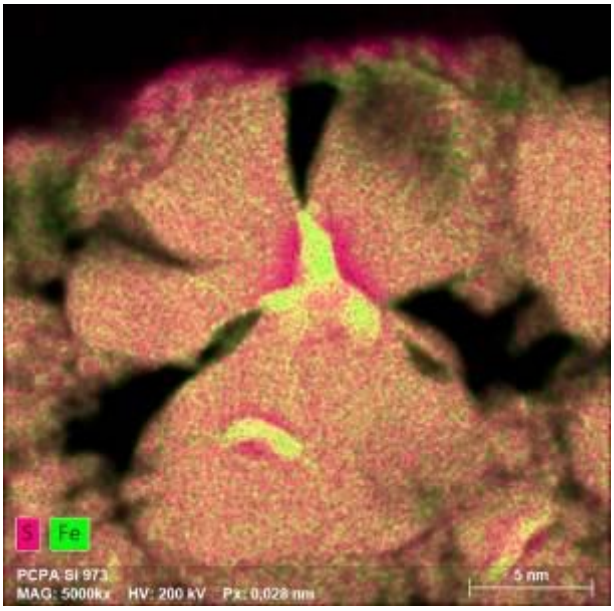
Figure 1: STEM-EDX map of a representative structure with an Fe-rich core, formed after the first lithiation of FeS_2.

[1] Dewald, G. F. et. al.: *Angew. Chem., Int. Ed.*, 2021, **60**, 17952

[2] Julien, C. M. et. al.: *Inorganics*, 2014, **2**, 132

[3] Chiu, K.-C. et. al.: *Molecules*, 2023, **28**, 4579

Fig. 1



MS1.P06
Local hydrogen concentration and distribution in Pd nanoparticles – An *in situ* STEM-EELS approach

S. Korneychuk[1,2,3], S. Wagner[4], D. Rohleder[5], P. Vana[5], A. Pundt[1]

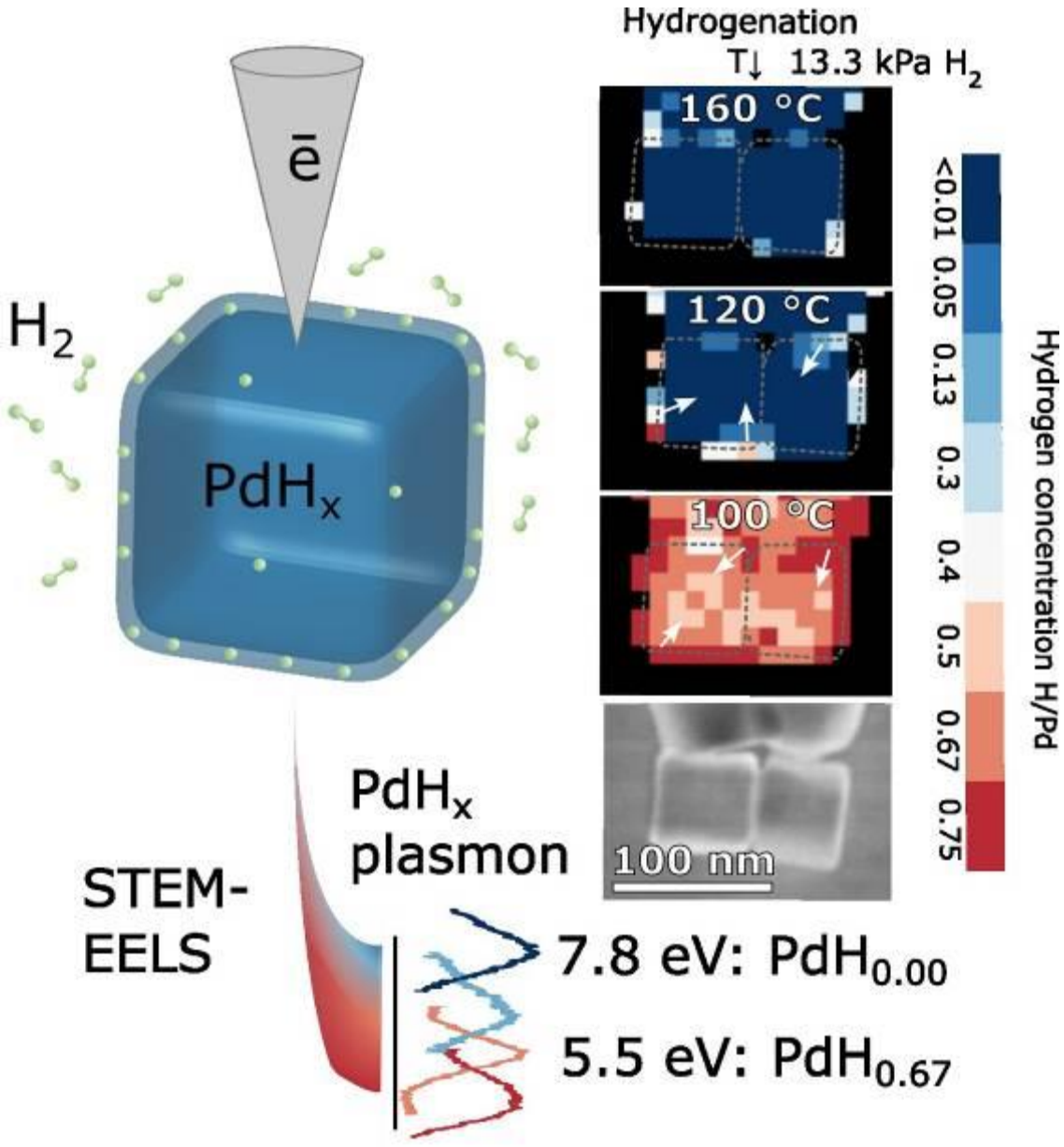
[1]Karlsruhe Institute of Technology, IAM-WK, Karlsruhe, Germany
[2]Karlsruhe Institute of Technology, Karlsruhe Nano Micro Facility (KNMFi), Eggenstein-Leopoldshafen, Germany
[3]Karlsruhe Institute of Technology, Institute of Nanotechnology, Eggenstein-Leopoldshafen, Germany
[4]Karlsruhe Institute of Technology, IAM-WK, Karlsruhe, Germany
[5]Georg-August-Universität Göttingen, Institute of Physical Chemistry, Göttingen, Germany

Local detection of hydrogen concentration in metals is of central importance for many areas of hydrogen technology, such as hydrogen storage, detection, catalysis, and hydrogen embrittlement. We demonstrate a novel approach to measure the hydrogen concentration in a model system consisting of cubic palladium nanoparticles (Pd NPs), with a lateral resolution down to 4 nm. By measuring the shift of the Pd bulk plasmon peak [1] with scanning transmission electron microscopy (STEM) combined with energy electron loss spectroscopy (EELS) during *in-situ* hydrogen gas loading and unloading, local detection of the hydrogen concentration is achieved in TEM [2]. The method offers a way to observe the hydrogenation and dehydrogenation processes from the early stages of hydrogenation while the NPs stay in solid solution phase, to the later stages when the NPs are fully transformed to the hydride phase, in great detail at the nanoscale. With this method, concentration changes inside the NPs at various stages of hydrogenation/dehydrogenation are observed with nanometer resolution. The versatility of *in-situ* TEM allows to link together microstructure, hydrogen concentration and local strain, opening up a new chapter in hydrogen research.

[1] A. Baldi, T. C. Narayan, A. L. Koh, J. A. Dionne, "In situ detection of hydrogen-induced phase transitions in individual palladium nanocrystals", *Nat Mater* 2014, *13*, 1143.

[2] S. Korneychuk, S. Wagner, D. Rohleder, P. Vana, A. Pundt, "Local hydrogen concentration and distribution in Pd nanoparticles: An *in-situ* STEM-EELS approach", *Small,* 2024, 2407092. https://doi.org/10.1002/smll.202407092

Fig. 1


Hydrogenation
T↓ 13.3 kPa H_2
160 °C
120 °C
100 °C
100 nm
<0.01 0.05 0.13 0.3 0.4 0.5 0.67 0.75
Hydrogen concentration H/Pd
ē
H_2
PdH_x
PdH_x plasmon
STEM-EELS
7.8 eV: $PdH_{0.00}$
5.5 eV: $PdH_{0.67}$

MS1.P07
Characterization of li-ion batteries – Correlating eds with raman, libs and sims

J. Blau[1], K. Geiger[1], L. Schon[1], J. Oehm[1], C. Weisenberger[1], V. Knoblauch[1], U. Golla-Schindler[1], G. Schneider[1]

[1]Hochschule Aalen (IMFAA), Aalen, Germany

The materials in lithium-ion batteries (LIBs) undergo aging due to complex reactions occurring simultaneously, complicating isolated studies. Understanding these mechanisms is vital for improving performance, sustainability, and recycling and can be achieved by advanced analytical technologies.

Two main aging mechanisms occur on the battery's anode: solid electrolyte interphase (SEI) growth and Li-plating. Distinguishing between these processes is crucial for understanding the reactions that cause aging and failure and the factors that trigger them. [1]

Anodes from two LIBs, specifically aged to induce Li-plating (sample: Li-P) and SEI growth (sample: SEI-g), respectively, were analyzed to gain insights into these phenomena. To achieve this, multiple methods, including computed tomography (CT), scanning electron microscopy (SEM), energy-dispersive X-ray spectroscopy (EDS), Raman spectroscopy, time-of-flight secondary ion mass spectrometry (ToF-SIMS), and laser-induced breakdown spectroscopy (LIBS), were used.

Upon conducting the CT analysis, it was noted that Li-P exhibits a crack in the anode, while the CT results for SEI-g appeared unremarkable. A SEM comparison revealed significant differences between the two anodes; the layer on SEI-g only covers a single particle, unlike the observed layer spread over multiple particles on Li-P. Additionally, the layer on SEI-g appears more uniform, with no elongated deposits present, just round and spot-like features. The EDS results show that Li-P has a layer mainly composed of carbon, while SEI-g contains lower carbon content and significantly higher oxygen proportions compared to the Li-P sample. The first results of Raman spectroscopy revealed that Li-P and SEI-g appear to have differences as can be seen in Figure 2. The spectra revealed varied carbon hybridizations in the active material. To determine the lithium content, we employed techniques like ToF-SIMS for Li-P and included LIBS results, illustrated in Figure 3 and Table 1.

Employing various analytical methods is essential to differentiate between the two aging phenomena in Li-P and the SEI-g, as each method focuses on different aspects like structure, elements, and compounds.

[1] Ghanbari, N.; Waldmann, T.; Kasper, M.; Axmann, P.; Wohlfahrt-Mehrens, M., J. Phys. Chem. C 2016, 22225–22234, DOI: 10.1021/acs.jpcc.6b07117

[2] The authors gratefully acknowledge the German BMBF (FKZ:03XP0317A) and BMWK (FKZ:16BZF320C) for financial support the Physical Electronics GmbH for the XPS and ToF-SIMS measurements and the following persons for scientific support: C. Wett, J. Haß, L. Billmann, B. Turan, H. G. Schweiger.

Figure 1 SEM images of the anodes. A) Li-P B) SEI-g

Figure 2 Raman images of anodes A) Li-P B) SEI-g

Figure 3 LIBS spectra of anodes A) reference B) Li-P. Li in reference is constant through all z-levels; Li in Li-P anode decreases continuously with z-level

Table 1 ToF-SIMS (positive polarity) of aged (Li-P) and reference anode. Change in Li-compounds: in aged anode more oxygen containing Li-compounds, reference mostly fluorine-lithium-compounds.

Fig. 1

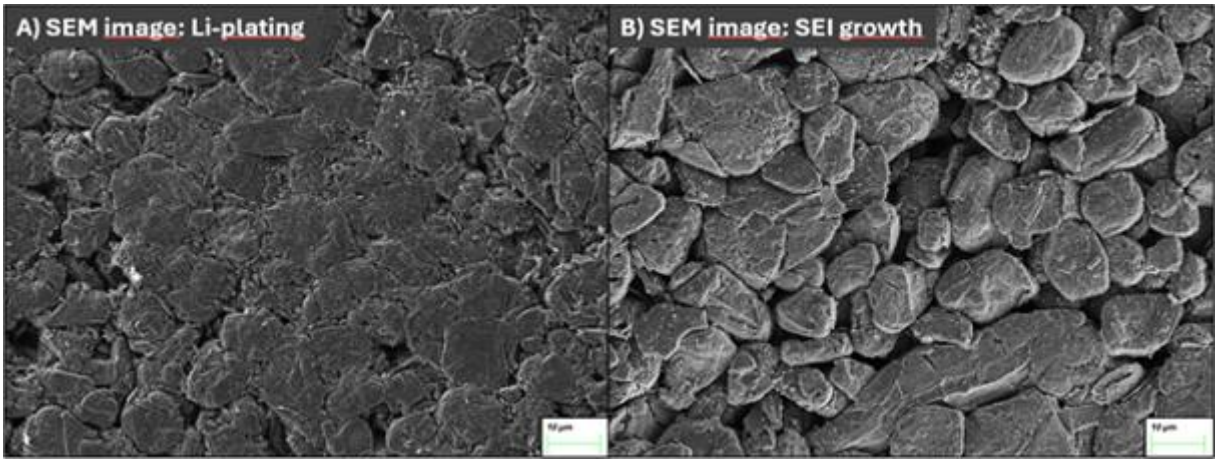


Fig. 2

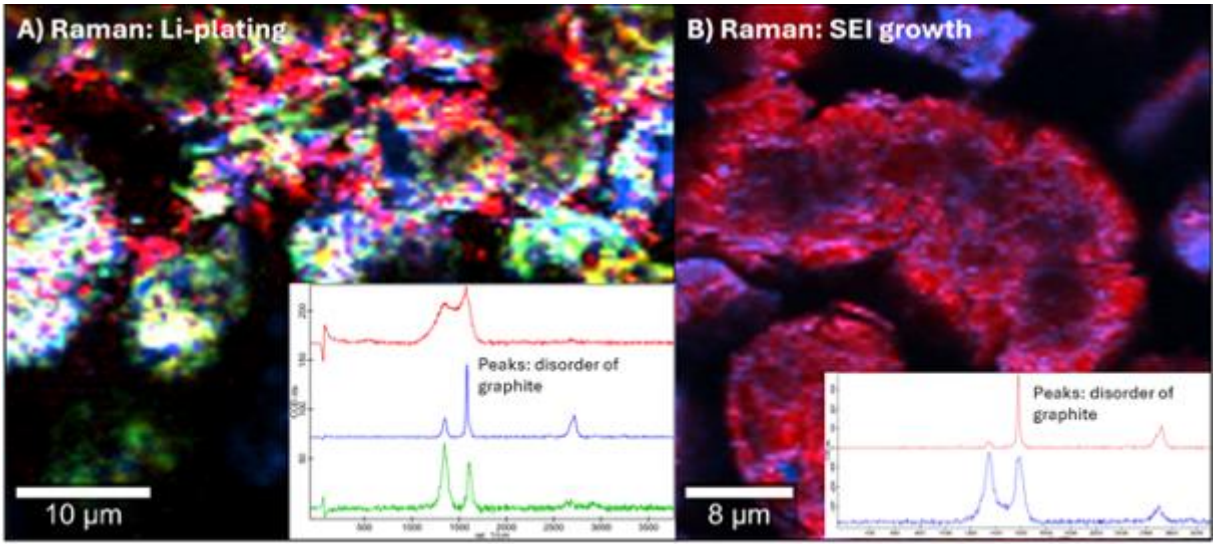


Fig. 3

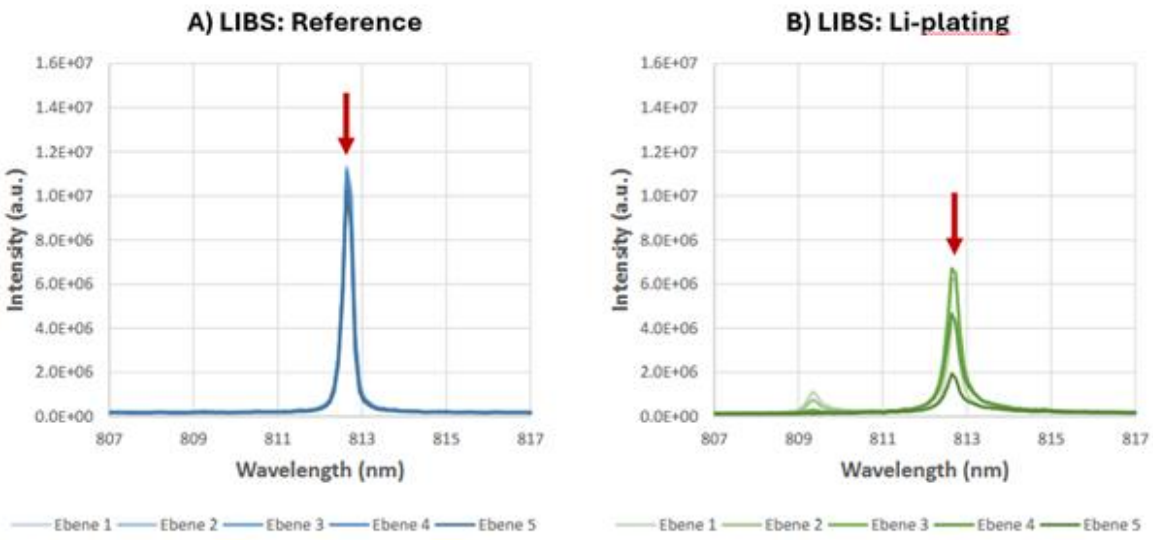


Fig. 4

Li-compounds	Reference	Li-plating
Li_2	6.13	6.65
$Li_2 + O + H$	1.33	2.56
$Li_2 + F$	11.00	3.25

MS1.P08
PEO block-co-polymers as high-conductivity electrolyte membrane materials for Li-batteries

B. Förster[1], A. Bharati[2], J. Allgaier[2], M. Dulle[2], S. Förster[2]

[1]Forschungszentrum Jülich GmbH, ER-C-1, Jülich, Germany
[2]Forschungszentrum Jülich GmbH, JCNS-1, Jülich, Germany

Introduction: Poly(ethylene oxide) (PEO) block-co-polymers have emerged as promising candidates for electrolyte membrane materials in batteries due to their unique ability to combine both ionic conductivity and mechanical stability.

Objectives: This study investigates the relationship between the structure and Li-ion conductivity of PEO block copolymer/LiTFSI systems at high Li:EO ratios. Therefore, we combined electron microscopy with small- and wide-angle X-ray scattering (SAXS/WAXS). Using cryo-ultramicrotomy, we aim to demonstrate that LiTFSI-filled PEO block copolymer membranes can be dry sectioned while maintaining moisture exclusion.

Materials & Methods: PEO block copolymers with added LiTFSI salt were prepared by mixing the PEO block copolymer in THF with LiTFSI in various Li:EO ratios and then drying. The polyelectrolyte membrane was sandwiched between aluminium sheets acting as electrical contacts. The assembly was either measured by SAXS/WAXS or sectioned by cryo-ultramicrotomy and examined by a JEOL F200 cryo-TEM.

Results: Using cryo-ultramicrotomy, we have obtained thin sections of LiTFSI-loaded PEO block copolymers approximately 80 nm thick. These sections can be imaged with STEM at high voltages of 200 kV. The thin sections were prepared under cryogenic conditions and transferred to the TEM using a cryo holder. Images of poled and unpoled samples can be compared to identify morphological changes. Electron microscopy provides crucial information about domain morphology, ordering and orientation within the membrane. Unlike most studies of PEO polyelectrolyte membranes [1], our approach uses LiTFSI in excess at Li:EO ratios of 3:1 or 4:1, resulting in significantly high conductivity values of 4×10-2 S/cm at room temperature. [2].

Conclusion: We demonstrate that ultramicrotomed thin sections of block copolymer polyelectrolyte membranes can be imaged with high contrast by STEM at 200 kV in TEM. This allows the visualisation of LiTFSI conduction paths across the block copolymer membranes, which is crucial for improving the conductivity of solid polymer electrolytes in Li-battery applications.

References

Sharon, D., Bennington, P., Webb, M. A., Deng, C., de Pablo, J. J., Patel, S. N., & Nealey, P. F. (2021). Molecular Level Differences in Ionic Solvation and Transport Behavior in Ethylene Oxide-Based Homopolymer and Block Copolymer Electrolytes. *Journal of the American Chemical Society, 143*(8), 3180-3190. DOI: 10.1021/jacs.0c12538

Krause, D. T., Förster, B., Dulle, M., Krämer, S., Böckmann, S., Mönich, C., Hansen, M. R., Schönhoff, M., Siozios, V., Grünebaum, M., Winter, M., Förster, S., & Wiemhöfer, H.-D. (2024). A Super-Ionic Solid-State Block Copolymer Electrolyte. *Small, 20*, 2404297. DOI: 10.1002/smll.202404297

MS1.P09
The effect of cobalt substitution into LLZTO on microstructure and electrochemical performance and mechanical properties

J. Ahmed[1], K. Kim[2], J. A. Barr[3], C. L. Tsai[1], Z. Qin[1], A. Windmüller[1], A. Domgans[1], J. Borowec[1], L. Wan[2], R. Schierholz[1], F. Hausen[1], H. Tempel[1], R. A. Eichel[1]

[1]Forschungszentrum Jülich GmbH, IET-1, Jülich, Germany
[2]Lawrence Livermore National Laboratory, Quantum Simulations Group, Livermore, CA, United States
[3]Washington State University, Washington D.C., United States

Introduction

The Cobalt interdiffusion between cathodes, such as $LiCoO_2$ (LCO), and solid-state electrolytes, such as $Li_7La_3Zr_2O_{12}$ (LLZO), at the cathode-electrolyte interface in all-solid-state batteries (ASSBs) poses a significant challenge on the long life stability of composite cathodes.[1,2] Macroscopically the Cobalt diffusion leads to discoloration of the separator and on the local scale it causes leaching of Al-into the LCO. Both impact mechanical and electrochemical properties through resistive interphase formation and structural degradation.

Objectives

This study aims to understand the influence of Co substitution in LLZO on its structure as well as on its electrochemical and mechanical properties and if Co-doping can reduce interdiffusion during cycling.

Materials and Methods

Two ways of doping $Li_{6.6}La_3Zr_{1.6}Ta_{0.4}O_{12}$ with Cobalt are compared. Sintering in an inert environment (argon), which leads to Co^{2+} and or in an oxygen-rich environment (air), which leads to Co^{3+}, with varying amounts of Co ($0.005 \leq x \leq 0.1$), which should lead to stoichiometry of $Co_xLi_{6.6-nx}La_3Zr_{1.6}Ta_{0.4}O_{12}$ (x-Co-LLZTO), with n being either 2 for Co_{2+} or 3 for Co^{3+}. We analyze the resulting microstructure and stoichiometry using STEM-EDS and correlative Raman spectroscopy and combine these results with x-ray powder diffraction and mechanical tests by Nanoindentation.

Results

The samples with different amounts sintered in Argon to stabilize Co^{2+} and oxidizing atmosphere (air) to stabilize Co^{3+} show a clear different optical appearance as shown in the optical photograph in Figure 1. SEM-EDS shows the formation of Co-rich secondary phases at triple-points in the microstructure, which can be confirmed by correlative Raman spectroscopy. This and EDS-analysis of the grain composition indicates that Co cannot be introduced into the LLZTO-structure up to the desired amount. The microcroscopic results agree with our other experiments like XRD and nanoindentation.

Conclusions

Our results show that pre-doping of LLZTO with Co is limited to a maximum amount lower than the reported solubility level of 0.16 per formula unit.[3]. Electrochemical tests will show, if the long-term stability can be enhanced nonetheless by the changes on the microstructure rather than Co-incoorparation into the LLZO structure.

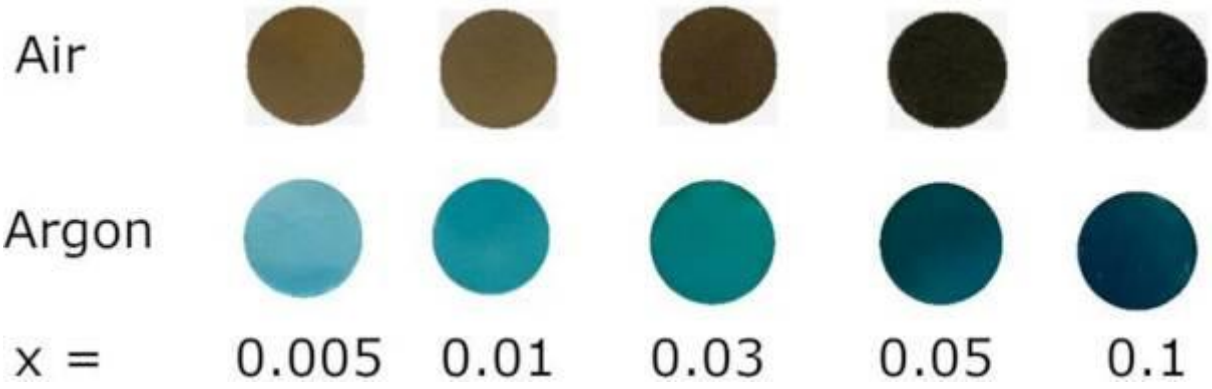
References

[1] Scheld, W. S., et al. "The riddle of dark LLZO: Cobalt diffusion in garnet separators of solid-state lithium batteries." *Advanced Functional Materials*, 33.43 (2023): 2302939.

[2] Ihrig, Martin, et al. "Study of LiCoO2/Li7La3Zr2O12: Ta interface degradation in all-solid-state lithium batteries." *ACS applied materials & interfaces* 14.9 (2022): 11288-11299.

[3] Din, Mir Mehraj Ud *et al.* "A Guideline to Mitigate Interfacial Degradation Processes in Solid-State Batteries Caused by Cross Diffusion" (2023) *Advanced Functional Materials* , Vol. 33, No. 42 p. 2303680.

Fig. 1



MS1.P10
Hydrothermal synthesis of spherical LNMO spinel particles and detailed phase and structural analysis using XRD, raman microscopy, EDX, and SEM

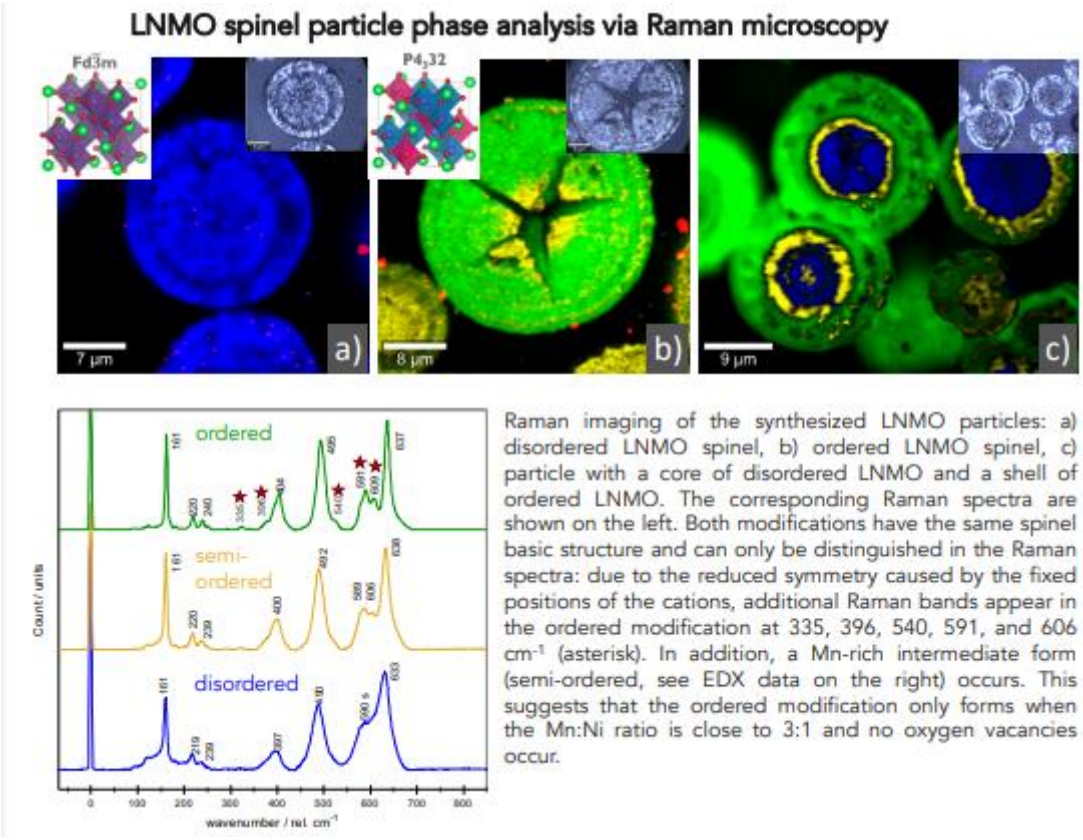
S. Schauer[1]

[1]Ulm University Medical Center, AC II, Ulm, Germany

Through a hydrothermal synthesis route, spherical carbonate precursors of Mn0.75Ni0.25CO3 were produced. These were converted into a LNMO spinel with the composition LiNi0.5Mn1.5O4 by calcination and lithiation while maintaining the morphology. Depending on the selected temperature program and atmospheric composition during the thermal treatment, the ordered or disordered modification of the spinel could be specifically synthesized with high phase purity (<1% by-product phase). Under appropriate conditions, core-shell particles could be produced, with an ordered shell and a disordered core. Differentiating between the individual modifications using XRD is extremely difficult due to the nearly identical crystal lattice. In contrast, differentiation using confocal Raman microscopy, even with spatial resolution, is possible.

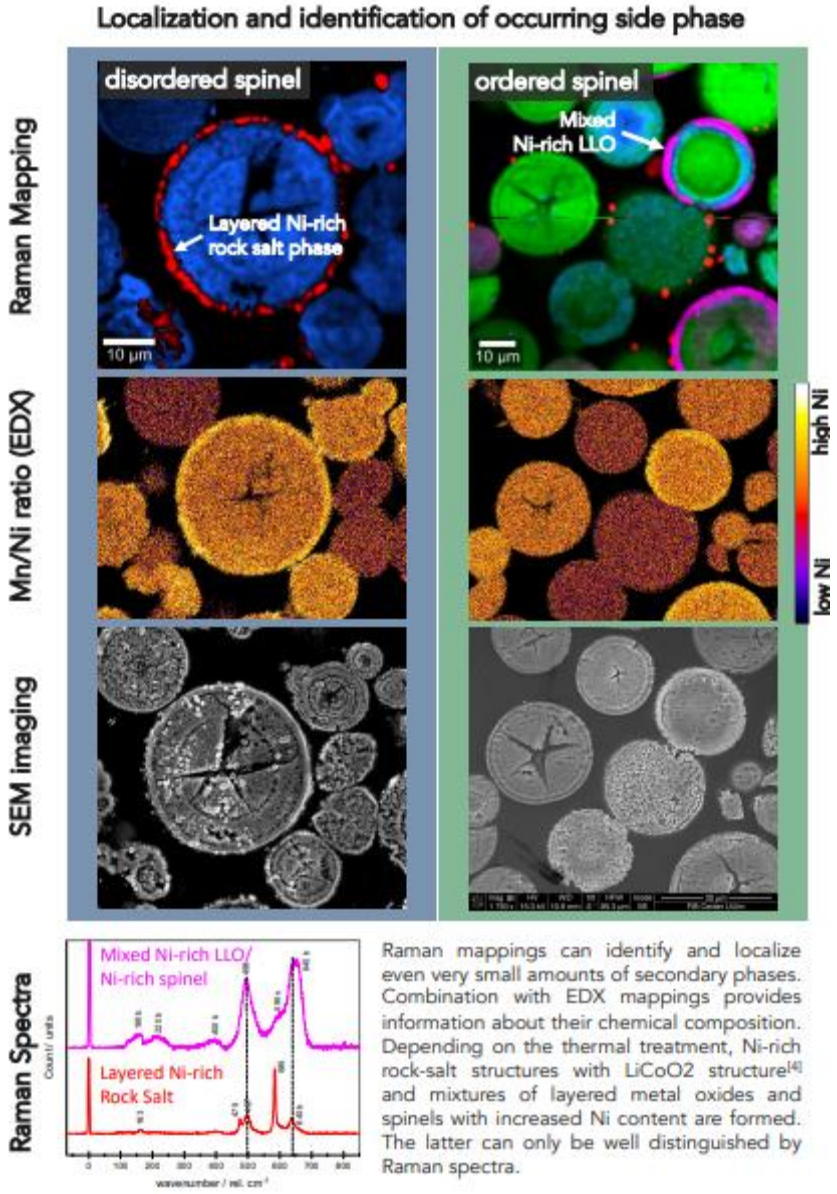
Furthermore, the identification and localization of emerging by-products, even in amall amounts, were possible. In combination with EDX mappings and high-resolution SEM images, spatially resolved determination of the elemental composition was also achieved. It was found that the frequently occurring rock salt by-product phase originates from Ni-rich deposits at the edge of the carbonate precursors. Additionally, the results show that the Ni-rich by-product phases are converted into different modifications (rock salt, bixbyite derivates) depending on the temperature program and oxygen saturation.

Fig. 1



Raman imaging of the synthesized LNMO particles: a) disordered LNMO spinel, b) ordered LNMO spinel, c) particle with a core of disordered LNMO and a shell of ordered LNMO. The corresponding Raman spectra are shown on the left. Both modifications have the same spinel basic structure and can only be distinguished in the Raman spectra: due to the reduced symmetry caused by the fixed positions of the cations, additional Raman bands appear in the ordered modification at 335, 396, 540, 591, and 606 cm^{-1} (asterisk). In addition, a Mn-rich intermediate form (semi-ordered, see EDX data on the right) occurs. This suggests that the ordered modification only forms when the Mn:Ni ratio is close to 3:1 and no oxygen vacancies occur.

Fig. 2


Localization and identification of occurring side phase
Raman Mapping
Mn/Ni ratio (EDX)
SEM imaging
disordered spinel
Layered Ni-rich rock salt phase
10 µm
ordered spinel
Mixed Ni-rich LLO
10 µm
high Ni
low Ni
Raman Spectra
Mixed Ni-rich LLO/ Ni-rich spinel
Layered Ni-rich Rock Salt
Raman mappings can identify and localize even very small amounts of secondary phases. Combination with EDX mappings provides information about their chemical composition. Depending on the thermal treatment, Ni-rich rock-salt structures with LiCoO2 structure[4] and mixtures of layered metal oxides and spinels with increased Ni content are formed. The latter can only be well distinguished by Raman spectra.

MS1.P11
High resolution 3D-Imaging of conductive networks in lithium-based batteries – Challenges and best practices

A. Lindner[1], M. Viornery[1], M. Mail[2], T. Scherer[2], C. Kübel[2], U. Krewer[1], W. Menesklou[1]

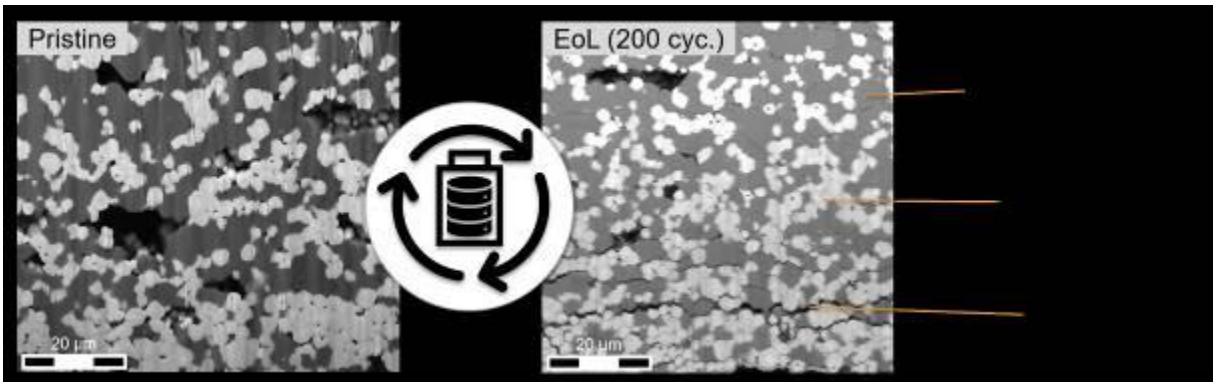
[1]Karlsruhe Institute of Technology, Institute for Applied Materials - Electrochemical Technologies, Karlsruhe, Germany
[2]Karlsruhe Institute of Technology, Karlsruhe Nano Micro Facility (KNMFi), Eggenstein-Leopoldshafen, Germany

Three-dimensional imaging of battery materials has become a convenient tool to elevate understanding of the complex structure-performance interactions occurring inside the cell. Additionally, the need for precise model parameterization established 3D characterization across the battery community. However, despite its broad use no common workflows and evaluations strategies exist and the precise 3D-imaging of electronicnnetworks remains challenging. Our contribution introduces strategies and best-practices for the high-resolution FIB-SEM tomography of battery materials. We show how to obtain high quality image data of the porous carbon-binder network present in all state-of-the-art lithium-ion-batteries. In addition, we image performance-critical crack formation in novel all-solid-state batteries *(figure 1)* and utilize advanced image processing techniques for processing and segmentation. Ultimately, we funnel 3D data into electrochemical continuum models to validate our workflows and quantify structure-property relations. In summary, we introduce suitable workflows and provide best-practices for the characterization and quantification of conductive networks in battery electrodes. This allows for precise parameterization and elevates our understanding of the systems at hand.

Figure 1: focused-ion-beam cross sections of garnet-type all-solid-state battery cathodes before and after electrochemical cycling. Crack formation is clearly visible after cycling.

Acknowledgements This work was funded by the German Ministry for Education and Research (BMBF) in the project CatSE2 under the reference number 03XP0510C. This work was carried out with the support of the Karlsruhe Nano Micro Facility (KNMF) a Helmholtz Research Infrastructure at Karlsruhe Institute of Technology (KIT) under reference number 2024-031031950.

Fig. 1



MS1.P13
Characterization of porous iron structures in the iron-steam process for indirect hydrogen storage

J. Kaltenbach[1], M. P. Kannengießer[2], F. P. Hagen[2], B. Stelzner[2], M. Seitz[2], K. Märkle[1], D. Trimis[2], Y. M. Eggeler[1]

[1]Karlsruhe Institute of Technology, Laboratory for Electron Microscopy, Karlsruhe, Germany
[2]Karlsruhe Institute of Technology, Engler-Bunte-Institute (EBI), Karlsruhe, Germany

Introduction

Climate-neutral hydrogen production is one of the keys towards achieving global climate goals. The oxidation of iron with steam enables the direct production of hydrogen. Subsequently, the oxides formed can be reduced with hydrogen to iron, enabling indirect hydrogen and energy storage through cyclic redox reactions. The structural properties of iron play a critical role in determining the efficiency, reactivity, and stability of these processes.

Objectives

This study aims to gain insights into the oxidation and reduction processes on the micron scale within porous iron structures for indirect hydrogen storage. By analyzing surfaces and cross-sections using scanning electron microscopy (SEM), we investigate the spatial distribution of iron oxide phases, redox progression, and morphological changes linked to high cyclic stability.

Materials & methods

In this work, various macroscopic porous iron structures, including iron foams, wools with different fiber diameters, granular packings, wire meshes, and iron shavings, are investigated for their effects on cyclic stability, morphological changes, and hydrogen storage capacity. Figure 1 shows SEM images of four exemplary structures. The redox cycles are conducted in a fixed bed reactor under well-defined reaction conditions.

Results

SEM analysis reveals that high cyclic stability correlates with minimal morphological changes after repeated redox cycles. While iron wools (Fig. 1 – B) exhibit high initial reaction rates due to their large specific surface area, they undergo significant structural degradation, limiting their cyclic stability. In contrast, iron foams (Fig. 1 – A) and wire meshes (Fig. 1 – D) maintain both their macroscopic and microscopic morphology, supporting superior stability over multiple cycles. In accordance with the stability limit of wüstite, FeO, described by the Baur-Glaessner diagram, a change in the oxidation and reduction mechanism is observed. Direct oxidation of iron to magnetite, Fe3O4, below 570 °C shows lower conversion than the indirect route via wüstite above 570 °C. These differences are attributed to variations in solid-state diffusion and growth-related morphological changes, as postulated by Wagner"s theory [1]. SEM images of the surfaces (Fig. 1 – C) and cross-sections of porous iron structures confirm these findings and provide detailed insights into redox processes on the micron scale.

Conclusion

This study provides fundamental insights into the redox and morphological stability of porous iron structures, contributing to the optimization of the steam-iron process for indirect hydrogen storage.

References

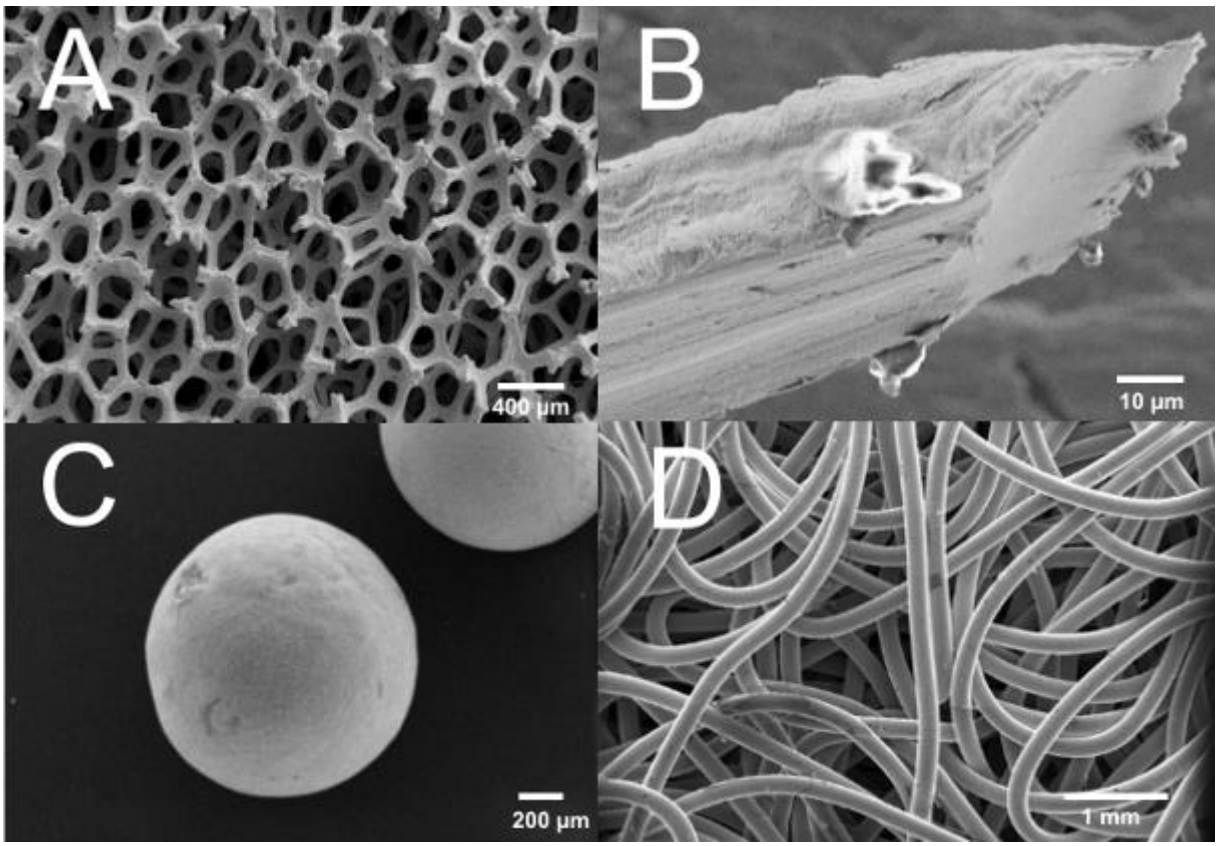
[1] C. Wagner, Z. Phys. Chem. 21 (1933), 25-41.

Acknowledgments

F.P.H. and B.S. gratefully acknowledge support from the Academy for Responsible Research, Teaching, and Innovation (ARRTI) at Karlsruhe Institute of Technology (KIT). This work was also supported by the Friedrich and Elisabeth Boysen Foundation within project BOY-200. Additionally, this research contributes to the Helmholtz Association's MTET program, specifically the Resource and Energy Efficiency, Anthropogenic Carbon Cycle (38.05.01) initiative.

Fig. 1. SEM images of porous iron structures: Iron foam (A), a single fiber of iron wool (B), an iron granulate particle (C), and iron mesh (D).

Fig. 1



MS1.P14
Cross-sectional reparation of complex energy devices and their characterization by advanced microscopic methods

M. Hepp[1], D. Stepien[2], D. Bresser[3], B. Butz[1]

[1]University of Siegen, Micro- and Nanoanalytics, Siegen, Germany
[2]Humboldt University of Berlin, Berlin, Germany
[3]Helmholtz Institute Ulm and Karlsruhe Institute of Technology, Ulm, Germany

Energy devices such as batteries, fuel cells, and solar cells are composed of multiple functional components with different material properties. To gain a deeper understanding of structure-property relationships, systematically contribute to performance optimization, and uncover degradation and failure mechanisms, it is essential to obtain high-quality cross-sections of entire devices or as large regions as possible.

Since devices like batteries contain not only different material classes but also liquid and/or air-sensitive components, working under cryogenic and/or inert conditions is crucial to preserve their pristine state. To enable scale-bridging cross-sectional characterization of these devices down to the atomic level, we employ different preparation tools. A novel glovebox integrated cryo-cutter enables rapid one-step preparation of cross-sections of entire pouch cells, including liquid components, for observation by OM even at the centimeter scale **(Fig. 1A)**. For smaller scales, a workflow from glovebox to cryo-ultramicrotome to cryo-TEM has been developed, allowing the preparation of large-scale lithium electrode cross-sections for investigation by (S)TEM(-EELS), as high-quality thin samples are provided **(Fig. 1B)**.

In this contribution, we demonstrate the scale-bridging capabilities of these preparation techniques when applied to batteries and their components, combined with advanced electron microscopic and spectroscopic methods. These techniques are well-suited not only for examining the integrity and morphology of such devices but also for locally resolving composition and chemical bonding states, e.g. before and after cycling.

Part of this work was performed at the Micro-and Nanoanalytics Facility (MNaF) of the University of Siegen.

Fig. 1

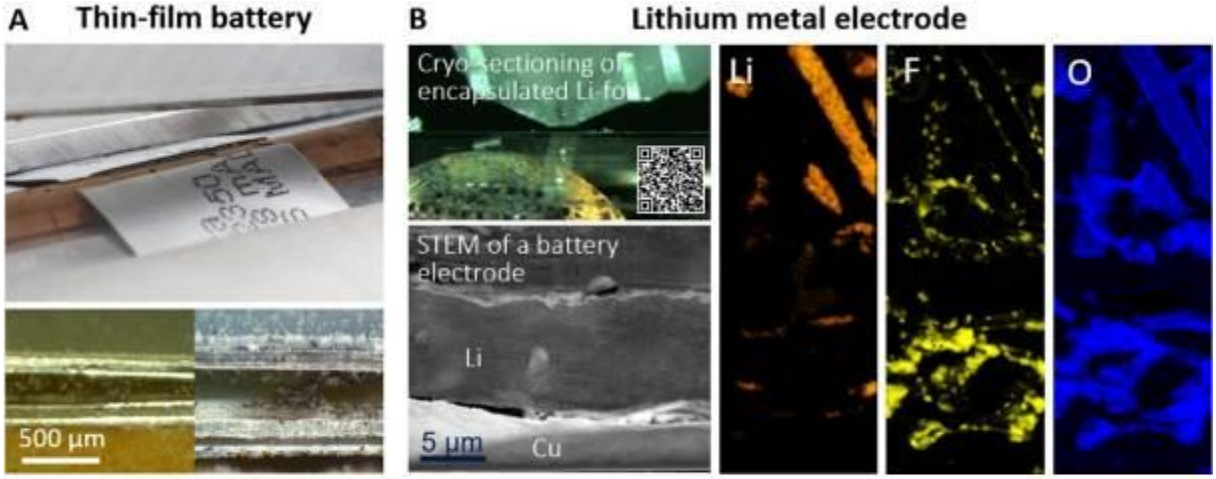


Fig. 1 A: Cross-sectional preparation of commercially available Li/MnO2 thin-film battery by self-built cryo-cutter tool. **B:** Cryo-ultramicrotomy of lithium metal electrode and EELS mapping for investigation of reaction products during cycling.

MS1.P15
Pt-decorated mesoporous transition metal foams for efficient electrocatalysis

J. Frohne[1], J. Kleine[1], J. Müller[1], J. M. V. Nsanzimana[1], B. Butz[1]

[1]University of Siegen, Siegen, Germany

Introduction & Objectives

Mesoporous materials are highly attractive for energy storage, catalysis, and sensing due to their tunable properties. Among them, mesoporous copper offers cost efficiency, accessibility, and great structural control. The pore structure of mesoporous transition metals strongly affects surface area, conductivity, catalytic activity and stability. A scalable fabrication approach was used to obtain hierarchical porous metals with tailored structural and functional properties.[1] Platinum is among the most active catalytic elements but faces severe supply limitations, making it unlikely to meet future global demand.[2] Alternatives are needed to either replace or optimize its use. In this study, we explore a strategy in which minimal platinum additions enhance the performance of mesoporous copper structures while reducing overall platinum consumption. Specifically, we investigate how subtle modifications affect the structure and catalytic performance—particularly in the hydrogen evolution reaction (HER)—and assess whether efficient noble metal utilization can help address resource scarcity.

Materials & Methods

Mesoporous Cu-based materials were fabricated under controlled conditions and selectively modified with trace amounts of platinum to study its impact on structural and catalytic properties. Advanced 3D imaging techniques, including micro-computed tomography (µCT) and electron microscopy, were used for multiscale structural characterization. Electrochemical performance was evaluated through HER and OER activity measurements.

Results & Conclusion

The modified structures exhibited systematic variations in pore characteristics, stability and platinum distribution. Even minimal compositional adjustments significantly influenced morphology and mechanical integrity, leading to enhanced catalytic performance. These findings demonstrate that strategically modified mesoporous Cu-based materials provide a promising platform for electrocatalysis, maximizing efficiency while minimizing material use. Multiscale structural analysis deepens our understanding of structure-property relationships, contributing to the sustainable design of high-performance catalytic materials.

Figure 1. (A) 3D rendering of a mesoporous copper foam obtained from micro-computed tomography (µCT). (B) surfaces of a mesoporous copper foam. (C) HER measurements with mesoporous copper-based electrodes. (D) Representative 2D slice from TEM tomography of a modified Pt-Decorated foam after 20 iterations of algebraic reconstruction technique (ART) algorithm.

Reference:

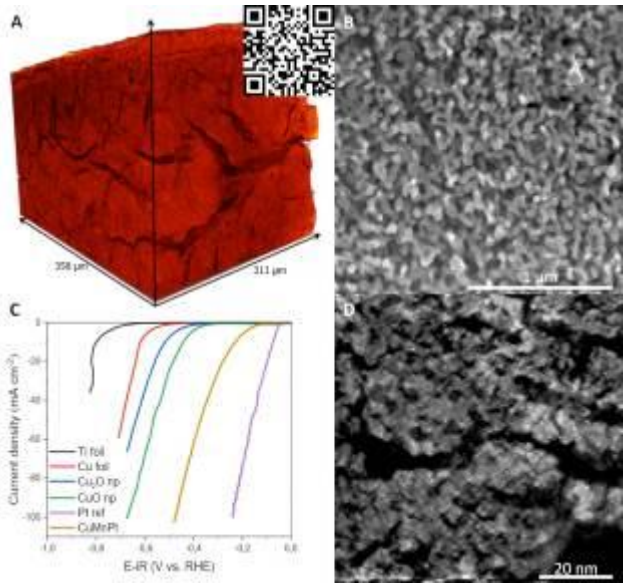
[1] McCue, I., Benn, E., Gaskey, B., & Erlebacher, J. (2016). Dealloying and Dealloyed Materials. Annual Review of Materials Research, 46(1), 263–286.

[2] Vesborg, P. C. K., & Jaramillo, T. F. (2012). Addressing the terawatt challenge: scalability in the supply of chemical elements for renewable energy. *RSC Advances*, *2*(21), 7933.

Acknowledgements

We acknowledge use of the DFG-funded Micro-and Nanoanalytics Facility (MNaF) at the University of Siegen (INST 221/131-1).

Fig. 1



MS1.P16
Scale-bridging analysis of a complex cobalt-boride-based hydrogen evolution electrocatalyst

C. O. Ogolla[1], J. M. V. Nsanzimana[1,2], N. Farahbakhsh[2], Y. Sakalli[3], M. Hepp[1], J. Frohne[1], W. S. Scheld[1], M. S. Killian[2], B. Butz[1]

[1]University of Siegen, Micro- and Nanoanalytics, Siegen, Germany
[2]University of Siegen, Chemistry and Structure of Novel Materials, Siegen, Germany
[3]University of Siegen, Micro- and Nanoanalytics, Siegen, Germany

Targeted phase engineering of nanomaterials through non-equilibrium synthesis strategies provides a suitable platform for the development and tuning of nanostructured catalysts with outstanding properties and life-time. Unconventional phases or even complex heterostructures play a crucial role in the performance of catalysts for efficient water electrolysis. Using a controlled, iterative reduction synthesis route, a tailored binder-free cobalt boride-phosphite electrode (CoxB-[0.2]P-O) with mixed crystalline-amorphous phases is developed. The tailored cobalt chemistry, hierarchical morphology and mixed phases synergistically enhance the catalytic activity for hydrogen evolution reaction (HER). Those electrodes exhibit platinum-like HER performance with an overpotential of 33 mV at the standard current density of 10 mA cm-2, with excellent intrinsic kinetics and enhanced electron transfer in an alkaline 1M KOH electrolyte (cf. Fig. 1 A).

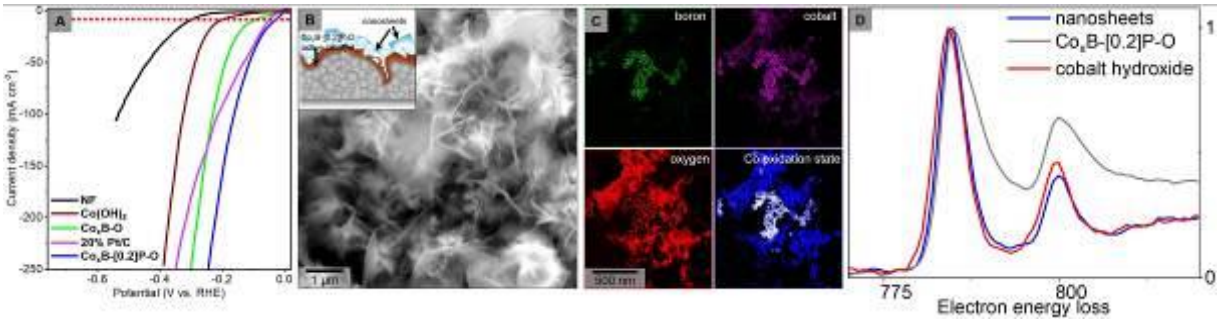
Comprehensive microstructural and spectroscopic analyses confirmed the success of the one-pot strategy to modulate cobalt chemistry through the incorporation of boron and phosphite. TEM analysis reveal nanostructures with locally varying morphology and unraveled the co-existence of amorphous and crystalline phases. Furthermore, distinct seed and active catalyst layer were identified as well as nanosheets (cf. Fig. 1 B). STEM-EELS elemental distribution maps clearly revealed variations in the chemical composition of the major elements -boron, cobalt and oxygen- particularly within the seed/active catalyst layer and the B-depleted nanosheets. Owing the local exothermic reaction during synthesis, distinct Co species corresponding to different oxidation states of Co are revealed by quantitative comparison to reference data (cf. Fig. 1 C, D).

The platinum-competitive performance of the synthesized catalyst is therefore linked to the modulation of the cobalt active site chemistry and ligand field from the incorporation of boron and phosphite species in conjunction with the interplay between the complex morphology, and crystal structure.

Figure 1: A) Linear sweep voltammetry curves of as-fabricated catalysts, B) SEM image of CoxB-[0.2]P-O active catalyst with typical B-depleted nanosheets (inset: model of catalyst structures), C) representative EELS maps showing B, Co and O distribution as well as Co oxidation state distribution, D) EEL spectra showing Co L2,3 white lines of nanosheets, CoxB-[0.2]P-O active catalyst and as-prepared Co(OH)2 reference.

Acknowledgements: We acknowledge funding from the European Union"s Horizon 2020 research and innovation program under the Maria Skłodowska-Curie grant agreement No 945422. Part of the study was performed at the DFG-funded Micro-and Nanoanalytics Facility (MNaF) of the University of Siegen (INST 221/131-1) by utilizing its major instrumentation (FEI Talos F200X TEM: DFG INST 221/93-1, DFG INST 221/126-1).

Fig. 1


A
B
C
D
Current density (mA cm⁻²)
Potential (V vs. RHE)
NF
Co(OH)2
CoxB-O
20% Pt/C
CoxB-[0.2]P-O
1 μm
boron
cobalt
oxygen
Co oxidation state
500 nm
nanosheets
CoxB-[0.2]P-O
cobalt hydroxide
775
800
Electron energy loss

MS1.P18
Unveiling the electrochemical stability of 2D bismuthene in Na-Ion batteries via S/TEM and EELS – Structural evolution and SEI formation

X. Guo[1], X. Du[1], V. Nicolosi[1]

[1]Trinity College Dublin, The University of Dublin, Dublin, Ireland

Bismuth (Bi) is a promising anode material for Na-ion batteries (NIBs), demonstrating exceptional electrochemical stability in ether-based electrolytes but suffering from low capacity and rapid degradation in ester-based electrolytes. To elucidate the underlying mechanisms, we employed two-dimensional (2D) bismuthene as a model system due to its flat structure and well-exposed facets, enabling a systematic investigation of its structural evolution and solid electrolyte interphase (SEI) formation using identical-location scanning/transmission electron microscopy (S/TEM) and electron energy loss spectroscopy (EELS).

Our study reveals that 2D bismuthene undergoes the same reaction pathways in both electrolytes, transitioning from a flake-like structure to a network morphology and from a single-crystal to a polycrystalline phase. However, the SEI characteristics differ significantly: in ether-based electrolytes, thinner, more uniform, and continuous SEI forms, facilitating fast ion transport while effectively passivating the electrode surface. This stable SEI prevents continuous electrolyte decomposition and excessive exposure of newly active surfaces, ensuring long-term cycling stability. In contrast, the SEI formed in ester-based electrolytes is less uniform and less effective in stabilizing the electrode.

These findings highlight the critical role of SEI properties in governing the electrochemical performance of 2D bismuthene anodes, providing insights for optimizing electrolyte formulations to enhance NIB stability.

MS1.P19
Correlating active catalyst states and oxygen evolution reactivity in *in situ* ETEM experiments by fabricating a local probe mass spectrometer

S. Firoozabadi[1], T. Ivanov[1], F. J. Stender[1], J. Grahl[2], S. Schulz[2], C. Jooss[1], T. Meyer[1]

[1]Georg-August-Universität Göttingen, Institut für Materialphysik, Göttingen, Germany
[2]University Duisburg-Essen, Institute of Inorganic Chemistry, Essen, Germany

Hydrogen production is crucial for renewable energy storage due to its high energy density, non-toxic nature, and environmental benefits [1]. However, the sluggish oxygen evolution reaction (OER) at the anode, driven by the four-electron transfer process and Gibbs energy differences between oxidation steps, remains a key challenge [2-4]. To address this, we are conducting atomic-scale analysis of the electrocatalyst-water interface using a differentially pumped environmental TEM (ETEM) and correlating the findings with reaction products detected by a local probe mass spectrometer (LPMS).

The setup includes a MEMS chip-based gas/liquid flow biasing holder and an MS. To enhance resolution, both the bottom and top membranes of the holder are open, and gas flow is regulated via the ETEM. We validated the system by introducing argon (Ar) and oxygen (O_2) into the ETEM chamber and successfully detecting them with the MS, showing a 12-second delay. The main challenge in correlating ETEM data with reaction products stems from gas flow dynamics. The large reaction environment, including a sizable sample chamber and differential pumping, dilutes reaction products as gases travel from the octagon to the MS. To address this, we are developing a localized MS probe near the electron-transparent sample for more precise OER product detection. A micro-scale capillary positioned near the holder"s counter electrode transfers reaction gases to the MS via one of the holder"s gas lines.

To develop a sample preparation workflow for nanoparticle studies combined with an LPMS setup, $LiMn_2O_4$ nanoparticles were initially transferred and positioned onto a MEMS chip using an FIB machine. The nanoparticles were first attached to a micrometer-sized conductive tip by poking it into the nanopowder, allowing adhesion to the lamella, which was then accurately transferred to the MEMS chip"s working electrode. However, this method had limitations, including the inability to orient the particles to the right crystal orientation, the presence of reactive materials due to FIB milling and welding, and the challenge of transferring large, uncountable clusters of particles, complicating correlation between reaction products and the catalyst's atomic-scale behavior.

To overcome these, we present a refined method for studying high-efficiency catalysts, such as Co_3O_4 nanoplates. The inherent electron transparency of the nanoplates eliminates the need for TEM lamella preparation, avoiding ion implantation and surface damage. Our approach involves drop-casting ultra-small nanoplates onto a micrometer-scale conductive gold film with open windows, referred to as a "micro shuttle." Afterwards, the shuttle is transferred to the MEMS chip without ion beam exposure or welding. The drop-casting process helps orienting the nanoplates in the correct crystal orientation and allows better control over the number of transferred particles, enabling a more accurate correlation between reaction products and the catalyst"s atomic-scale behavior. Moreover, we ensure that only gold is added to the reaction site, preventing the introduction of additional reactive materials.

[1] Sarmah, M. K., et al. (2023). RSC Adv., 13(36), 25253-25275.

[2] Krishtalik, L. I. (1986). Biochim. Biophys. Acta (BBA) - Bioenergetics, 849(1), 162-171.

[3] Rossmeisl, J., et al. (2007). J. Electroanal. Chem., 607(1-2), 83-89.

[4] Man, I. C., et al. (2011). ChemCatChem, 3(7), 1159-1165.

MS1.P21
State-of-the-art STEM characterization of lithium-ion battery cathodes

R. Egoavil[1], D. Krishman[1], P. Potocek[1,2], M. Ishimaru[3], M. Meledina[1]

[1]Thermo Fisher Scientific, Eindhoven, Netherlands
[2]Saarland University, Saarbrücken, Germany
[3]Thermo Fisher Scientific, Tokyo, Japan

Understanding of the battery cycling process, charging and discharging of a lithium-ion battery (LIB) is crucial to evaluate its performance, stability, and degradation over time. This process undergoes significant changes of the material at the nano- and atomic-scale, resulting in particle surface reconstruction attributed to cation intermixing and electrolyte decomposition with direct impact to the battery performance.

Advanced scanning transmission electron microscopy (STEM) techniques are therefore essential to study surface reconstruction of the cycling process providing deep insights into the atomic scale structural details. However, characterization of lithium-ion battery materials has been a difficult task in transmission electron microscopy due to their high electron-beam sensitivity, resulting in amorphization, decomposition, or phase changes under the electron beam.

To reduce the electron beam damage in lithium-ion battery materials, low voltage and low dose imaging are often used, although at the expense of poor spatial resolution and low yield signal limiting analytical techniques such as energy-dispersive X-ray spectroscopy (EDS) and electron energy loss spectroscopy (EELS).

This work shows the benefit of using unrivalled detection technologies such as Ultra X and Iliad EELS to retrieve state-of-the-art information from a layered lithium cathode sample with dose efficient budgets. Correlation from particle surface reconstruction, chemical distribution and electronic structure within the material is discussed to offer a better understanding of the battery cycling process.

Fig. 1. Fig 1. Atomic scale STEM imaging reveals particle surface reconstruction of a lithium nickel-cobalt-aluminum oxide (NCA) sample after charging.

Fig. 2. Fig 1. Atomic scale STEM EDS mapping of a lithium nickel-cobalt-aluminum oxide (NCA) performed at 60kV.

Fig. 1

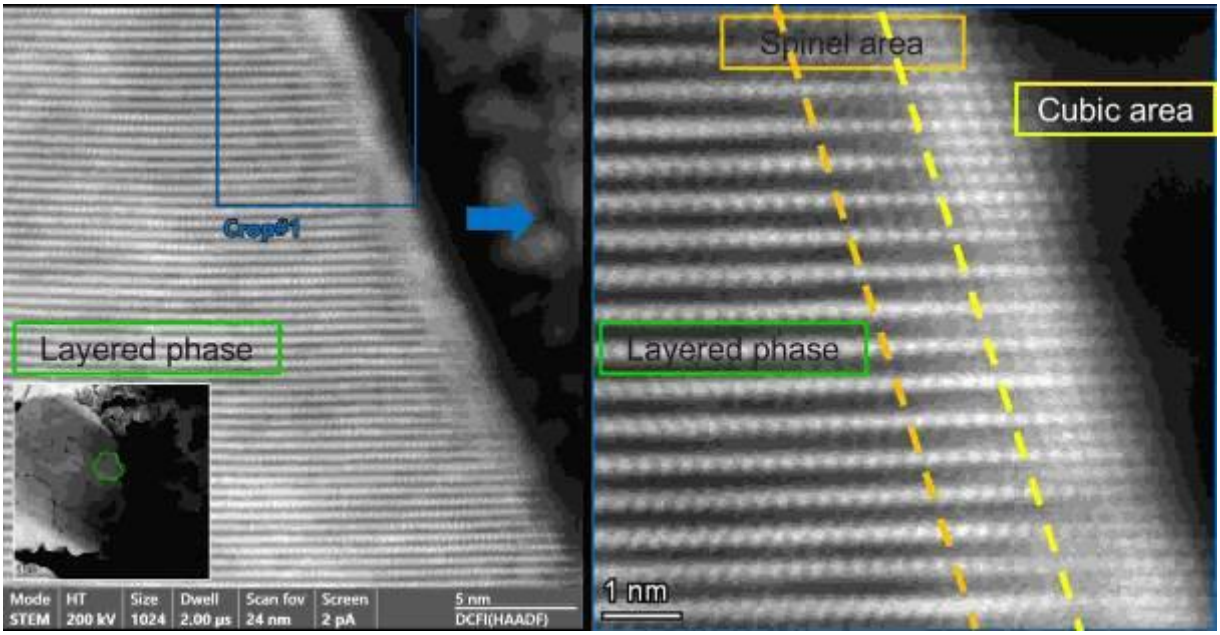
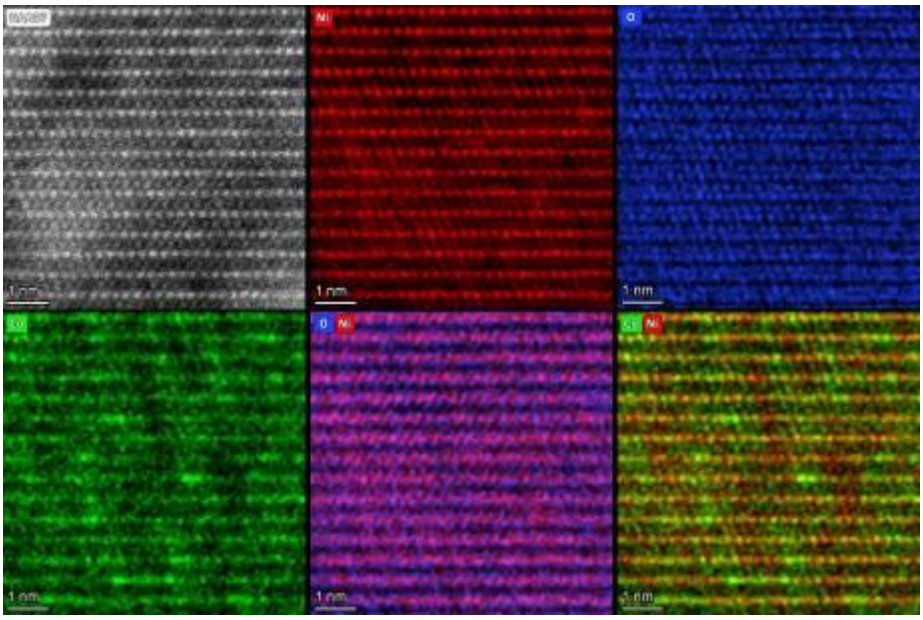

Crop#1
Layered phase
Mode STEM
HT 200 kV
Size 1024
Dwell 2.00 µs
Scan fov 24 nm
Screen 2 pA
5 nm DCFI(HAADF)
Spinel area
Cubic area
Layered phase
1 nm

Fig. 2


Ni
O
Co
O Ni
Co Ni
1 nm

MS1.P22
Atomic scale investigation of interface processes in perovskite solar cell heterostructures

E. Özmen[1,2], J. Loehr[3], R. Peibst[3], J. Schmidt[3], M. Seibt[1], T. Meyer[2]

[1]Georg-August-Universität Göttingen, IV. Physical Institute, Göttingen, Germany
[2]Georg-August-Universität Göttingen, Institut für Materialphysik, Göttingen, Germany
[3]Institute for Solar Energy Research, Hamelin, Germany

Introduction: Metal halide perovskite solar cells (MHPSCs) have emerged as promising candidates for next-generation photovoltaic technology due to their exceptional optoelectronic properties and low-cost fabrication [1]. However, their long-term stability and performance remain critical challenges, largely influenced by interface phenomena within the heterostructure [2]. Understanding these interface processes at the atomic scale is crucial for optimizing material properties and device performance. Advanced transmission electron microscopy (TEM) techniques provide unique insights into the nanoscale mechanisms governing degradation, charge transport, and interfacial reactions in these systems [3].

Objectives: This study aims to investigate the atomic-scale interactions at interfaces within MHPSC heterostructures using Environmental Scanning Electron Microscopy (ESEM) and Transmission Electron Microscopy (ETEM). Key objectives include:

- Identifying structural and chemical changes at critical interfaces under operational conditions.
- Understanding ion migration and phase evolution in response to external stimuli such as temperature, bias, and environmental exposure [4].
- Correlating observed atomic scale phenomena with macroscopic device performance to inform material and interface engineering strategies.

Materials and Methods: ESEM and ETEM will be utilized to study perovskite-based heterostructures in situ, enabling real-time observation of interfacial dynamics under controlled environmental conditions. High-angle annular dark-field scanning TEM (HAADF-STEM) will be employed for atomic-resolution imaging, enabling direct visualization of structural and compositional variations at the interfaces of perovskites-based heterostructures [5]. Various in situ techniques, including controlled heating, electrical biasing, and gas exposure, will be employed to replicate real-world operating environments and investigate their impact on material stability and device efficiency. Sample preparation will involve focused ion beam (FIB) milling to ensure site-specific analysis.

Results and Discussion: Our study will reveal critical insights into the stability and degradation pathways of perovskite-based heterostructures. Preliminary expectations include:

- Direct visualization of ion migration and phase segregation at perovskite interfaces [6].
- Identification of interfacial reactions leading to defect formation and charge trapping [7].
- Correlation between atomic-scale changes and macroscopic device degradation trends [8].

These findings will provide a deeper understanding of perovskite interface dynamics, contributing to the development of more stable and efficient solar cell architectures.

Conclusion: By leveraging atomic-resolution microscopy techniques, this study seeks to uncover fundamental interfacial mechanisms in MHPSCs, addressing key challenges related to device stability and performance. The insights gained will inform strategies for material and interface engineering, advancing the practical implementation of perovskite solar cells for sustainable energy solutions.

References: [1] H. Dong et al., *eLight*, 2023, **3**. [2] H. Snaith, *Nat. Mater.*, 2018, **17**. [3] C. Jooss et al., *Adv. Energy Mater.*, 2025. [4] A. M. Smith et al., *Nat. Mater.*, 2023, **22**. [5] J. P. Correa-Baena et al.,

Science, 2017, **358**. [6] Y. Wang et al., *Photonics Research*, 2020, **8**. [7] M. Saliba et al., *Joule*, 2018, **2**. [8] J. J. Choi et al., *J. Mater. Chem A*, 2019, **7**.

MS1.P23
An experimental procedure for heating battery materials *in situ* under atmospheric pressures in the (S)TEM

T. Demuth[1,2], S. Ahmed[1], P. Kurzhals[3,2], F. Gruber[1], J. Belz[1], A. Beyer[1], J. Janek[2], K. Volz[1]

[1]Philipps-University Marburg, Department of Physics, Marburg, Germany
[2]Justus Liebig University Gießen, Institute for Physical Chemistry, Giessen, Germany
[3]BASF SE, Ludwigshafen, Germany

Introduction
Due to the increasing demand for safe, high-capacity and high-power energy storage devices, battery research is a hot topic. However, despite great research efforts, many phenomena have not yet been fully understood. (Scanning) transmission electron microscopy ((S)TEM) allows for structural insights at the atomic level. However, the conditions battery materials are exposed to during manufacturing or cycling differ from the experimental conditions in a (S)TEM, where samples are typically measured *ex situ* in vacuum. Here, *in situ* measurements using special (S)TEM holders to replicate real-world conditions can yield new insights into processes on the nano scale

Objectives
As battery materials are often subjected to elevated temperatures during manufacturing, the goal of this work is to develop an experimental setup to investigate the battery material during heating at an atomic level under real-world conditions.

Materials & Methods
A custom-made *in situ* setup including a Protochips Inc. Atmosphere holder is developed. This holder comprises a micro electro-mechanical systems (MEMS) chips, which enables heating of up to 1000 °C, and can accommodate gas pressures in the tip of up to 1 bar. The gas is provided by a gas bottle, and the flow is controlled by valves located up- and downstream of the holder. We modified the holder with lockable valves so that an inert transfer over the whole experimental process from sample preparation to the experiment is possible, as depicted in the accompanying Figure.
To prove the functionality of our setup, thinned $LiNiO_2$ (LNO) secondary particles were chosen for investigation. To securely fix a thinned LNO particle with a diameter of 5 µm on top of a 9 µm wide electron-transparent Si_3N_4 window in the MEMS heating chip, a complex sample preparation routine was developed.
To examine both structural and morphological changes during the heating procedure, a scanning nanobeam mode is employed. The small semi convergence angle (1 mrad), results in a larger depth of focus, which is beneficial for high-angle annular dark-field (HAADF) STEM imaging during heating, where thermal movement can shift the sample out of focus. Moreover, in this mode, diffraction discs are not overlapping so that 4D scanning nanobeam diffraction (SNBD) can be recorded and indexed for structural analysis.

Results
Morphological and structural changes starting from 350 °C were detected using HAADF STEM imaging and 4D SNBD, respectively. These changes can be attributed to the phase transformation from the layered (R-3m) to a $Li_{1-z}Ni_{1+z}O_2$ rock-salt phase (Fm-3m). The onset temperature of 350 °C is significantly higher than previously reported for *in situ* TEM experiments conducted in vacuum,[1,2] highlighting the importance of replicating real-world experimental conditions.

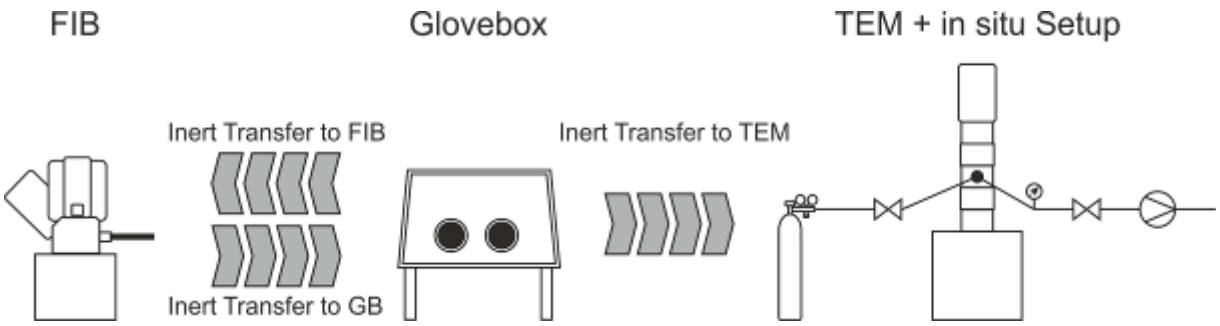
Conclusion
We have developed and tested an experimental setup, which enables *in situ* heating of materials in the (S)TEM in a gas environment at atmospheric pressures. During the whole procedure from sample preparation to investigation in the TEM, the sample can be transferred in an inert atmosphere, preventing degradation due to contact with air. Successful heating experiments using LNO secondary

particles in an oxygen atmosphere have been conducted. The setup can be readily adapted to use different gases and material systems.

References

[1] Wang et al, Matter 2021, 4, 2013
[2] Pokle et al, ACS Appl Mater Interfaces 2020, 12, 57047

Fig. 1



MS1.P24
In situ ESEM study of catalyst support dynamics under reaction conditions

B. Holtermann[1], M. Dortmund[1], A. J. Schwartz[1], E. Müller[1], Y. M. Eggeler[1]

[1]Karlsruhe Institute of Technology, Laboratory of Electron Microscopy (LEM), Karlsruhe, Germany

Supported noble metal nanoparticles (NPs), such as Pt, Pd, and Pt-Pd alloys on reducible and non-reducible supports, play a crucial role in heterogeneous catalysis. Due to the high cost of noble metals, it is essential to develop catalysts that maintain high activity over their lifetime. However, a major challenge is thermal deactivation through sintering, which reduces catalytic performance.

One effective strategy for stabilizing noble metal NPs at elevated temperatures is the strong metal-support interaction (SMSI). Traditionally, SMSI was thought to be limited to reducible supports like CeO_2, but recent studies have demonstrated similar effects in non-reducible supports as well [1]. To investigate sintering behavior and SMSI transmission electron microscopy (TEM) has been widely used [2]. However, the environmental scanning electron microscope (ESEM) has recently emerged as a powerful tool for studying catalyst systems under reaction conditions.

Our goal is to leverage electron microscopy to gain deeper insights into catalyst support dynamics under reaction conditions. To achieve this, we use an ESEM with a heating stage, a custom-built gas injection system for precise control of the gas atmosphere composition, and a residual gas analyzer for real-time monitoring of gas species.

This setup enables high spatial resolution imaging of morphological changes in catalyst nanoparticles throughout the experiment. The micrometer size field of view during experiments allows for robust statistical analysis. Furthermore, secondary electron contrast has been shown to be highly sensitive to changes in work function [3]. Recent results during one of our *in situ* model dewetting experiments of Pt on amorphous SiO2, also suggest that secondary electrons can effectively detect the *in situ* growth of an encapsulating layer during elevated temperature, see fig.1.

The dewetting transitions in fig.1 are observed along a vertical progression from top to bottom, as indicated in the marked area. After dewetting a localized transition in secondary electron contrast becomes apparent, see arrows in fig.1b. These darker regions gradually expand until they cover the entire specimen. While the exact mechanisms require further *ex situ* investigation, these observations demonstrate the potential of secondary electron contrast for studying *in situ* catalyst transformations under reaction conditions in the ESEM.

We will present experimental results obtained under both oxidation and reduction conditions across a range of temperatures for different nanoparticle species on reducible and non-reducible supports. Building on a previous study in which we analyzed the *ex situ* redispersion mechanism of Pt/CeO_2 under alternating oxidation/reduction cycles, we will now showcase the results of this redispersion experiment using our new ESEM setup.

The authors gratefully acknowledge funding from the DFG (German Research Foundation) under Project TrackAct (SFB 1441, Project-ID 426888090).

Figure 1: Sequential stages of *in situ* Pt thin film dewetting and secondary electron contrast transition. (a) The dewetting front (blue line) moves downward. (b) Dark spots appear post-dewetting (white arrows). (c) These regions grow and merge, leading to a uniform darker contrast in (d).

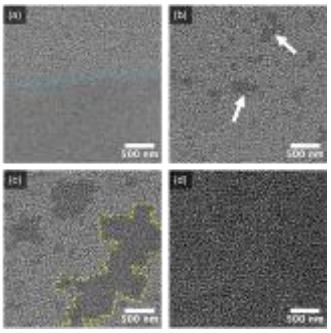
References:

[1] Luo et al., Adv. Energy Mater. 2022, 12, 2201395.

[2] Dai et al., Angew. Chem. 2024, 136(42), e202409673.

[3] Barroo et al., Nat. Catal. 3.1 (2020): 30-39.

Fig. 1



MS1.P25
Bridging the nanoscale gap – Multimodal electron microscopy for advancing electrolyzer technologies

S. Basak[1], P. K. Chakraborty[1,2], J. P. Poc[1,2], J. Park[1], E. Jodat[1], A. Karl[1], R. A. Eichel[1,2,3]

[1]Forschungszentrum Jülich GmbH, Institute of Energy Technologies - Fundamental Electrochemistry (IET-1), Jülich, Germany
[2]RWTH Aachen Universityy, Institute of Physical Chemistry, Aachen, Germany
[3]RWTH Aachen University, Faculty of Mechanical Engineering, Aachen, Germany

The transition to a sustainable energy future is inseparably linked to the development of efficient and reliable hydrogen production technologies. Electrolysis, encompassing both low-temperature (PEM/AEM) and high-temperature (SOFC/SOEC) approaches, holds immense promise [1,2]. However, a significant hurdle remains: a comprehensive understanding of the complex electrochemical processes at the nanoscale and how that translates to macro-scale performance and durability. This presentation shows how advanced electron microscopy can address this challenge.

Overall our research aims to correlate fundamental nanoscale mechanisms with device performance in both low- and high-temperature electrolysis by developing and implementing a comprehensive multimodal electron microscopy strategy. We emphasize visualizing nanoscale dynamics using *in-situ* transmission electron microscopy (TEM) and correlating these observations with the microstructural changes in lab or large-scale cells during long-term operation via a multimodal approach. Specifically, the low- and high-temperature electrolysis present distinct microscopy challenges. Beam-sensitive AEM and PEM electrolytes and catalysts necessitate low-dose TEM and cryo-sample preparation. Maintaining critical hydration states during imaging is crucial for accurate degradation mechanism analysis. Furthermore, the limitations of single-chamber MEMS-based *in-situ* TEM cells for gas/liquid phase reactions require careful consideration of electrochemical processes to maximize the information gained. Finally, the limited field of view and thin sample requirements of TEM necessitate careful consideration of broader relevance.

Thus, we combine laser scanning microscopy (LSM) for large-scale context, (cryo) plasma FIB for precise TEM sample preparation or obtaining high-resolution 3D information to construct a comprehensive picture of the material's structure and behavior. Then, employ well though in-situ TEM investigation in (environmental) TEM to obtain necessary nanoscale process information. This presentation will showcase unique degradation processes observed in PEM electrolysis and the nano-exsolution process and its long-term stability in high-temperature electrolysis [3]. These nanoscale insights are crucial for the rational design and optimization of next-generation electrolyzers, accelerating the transition to a hydrogen-based economy.

Acknowledgments

The authors acknowledge the funding provided by the BMBF (German Research Foundation) through the project DERIEL (03HY122C).

References

[1] A. Karl et al.., Electrochemical Science Advances (2025). https://doi.org/10.1002/elsa.202400041

[2] S.E. Wolf et al.., Journal of Materials Chemistry A (2023). https://doi.org/10.1039/D3TA02161K

[3] P.K. Chakraborty et al.., Nanotoday (2025). https://doi.org/10.1016/j.nantod.2025.102649

Fig. 1

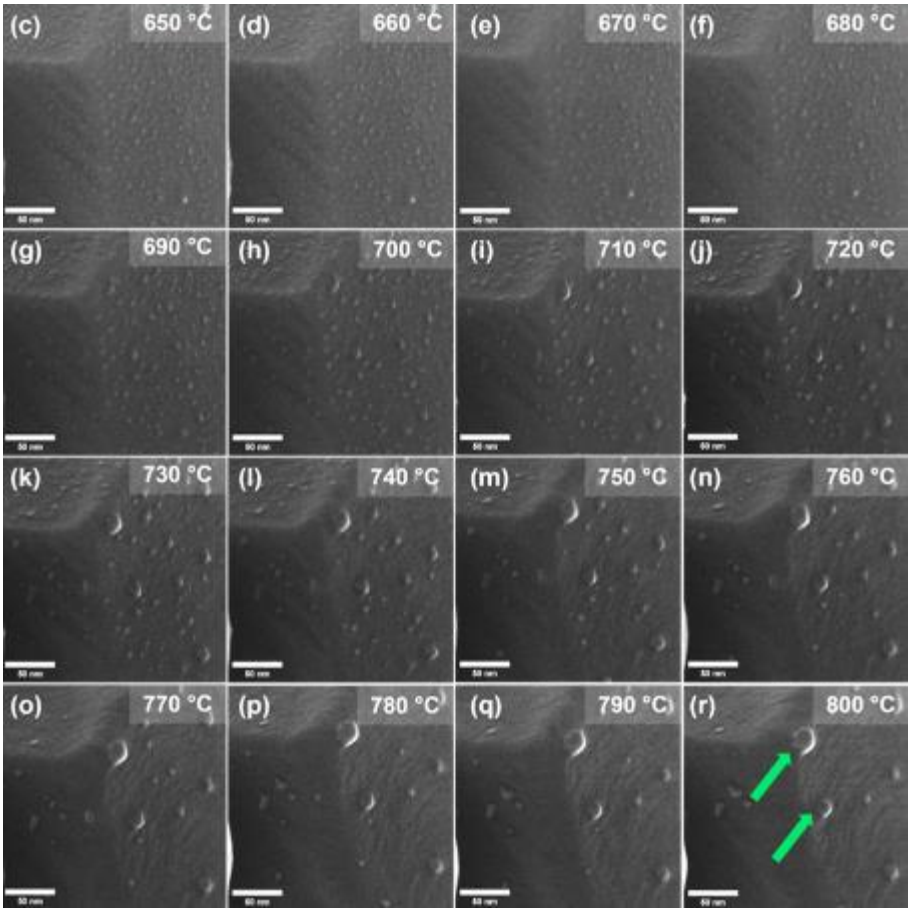
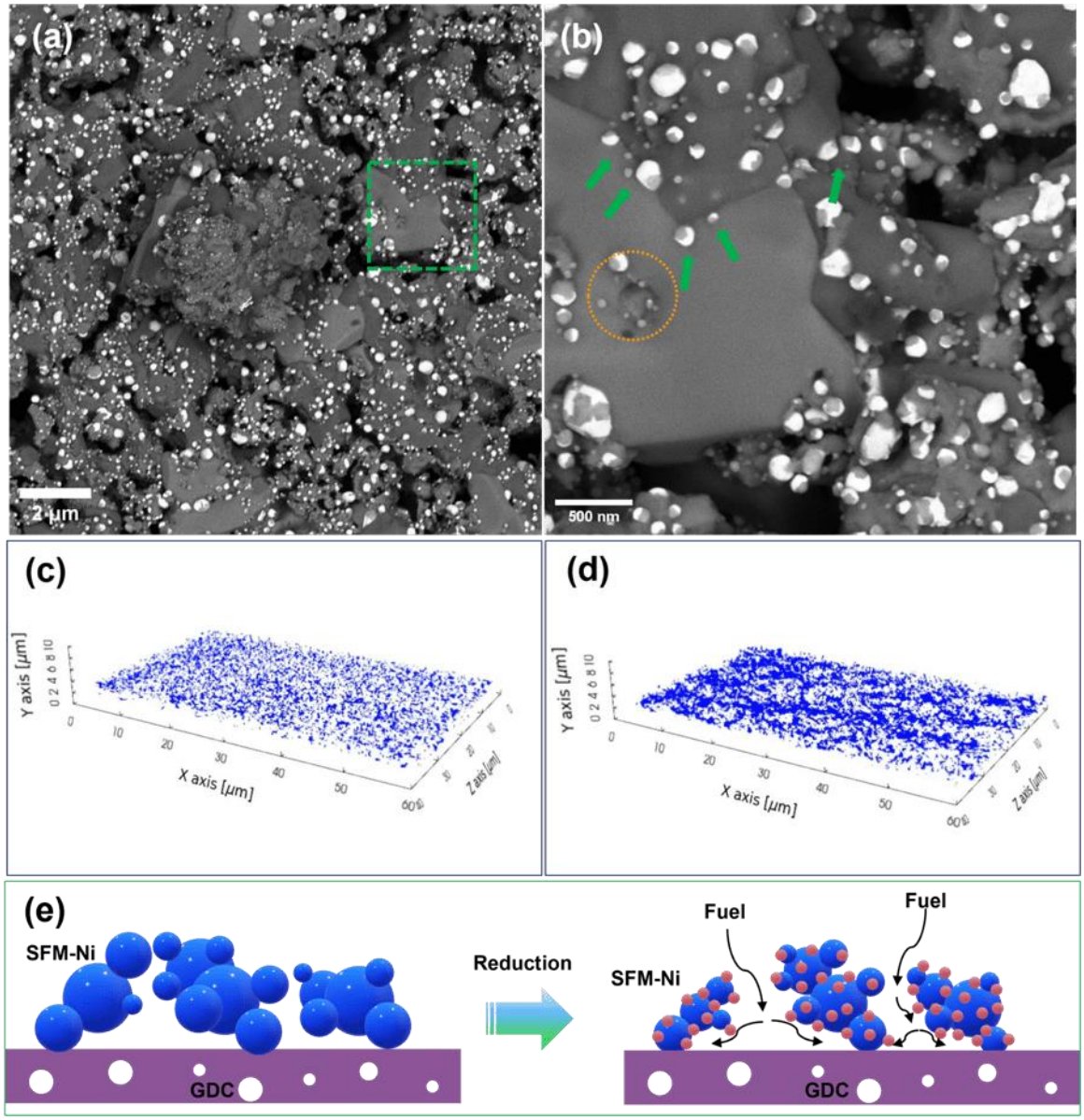

(c) 650 °C
(d) 660 °C
(e) 670 °C
(f) 680 °C
(g) 690 °C
(h) 700 °C
(i) 710 °C
(j) 720 °C
(k) 730 °C
(l) 740 °C
(m) 750 °C
(n) 760 °C
(o) 770 °C
(p) 780 °C
(q) 790 °C
(r) 800 °C

Fig. 2


(a)
2 μm
(b)
500 nm
(c)
Y axis [μm]
X axis [μm]
Z axis [μm]
(d)
Y axis [μm]
X axis [μm]
Z axis [μm]
(e)
SFM-Ni
GDC
Reduction
Fuel
Fuel
SFM-Ni
GDC

MS1.P26
Structure and texture of Sb2S3 and Sb2Se3 thin films investigated with precession-assisted 4D-STEM and EBSD

M. Wu[1], M. Dierner[1], M. Barr[1], P. C. Liao[1], J. Will[1], P. H. Lu[2], R. E. Dunin-Borkowski[2], J. Bachmann[1], E. Spiecker[1]

[1]FAU Erlangen-Nürnberg, Erlangen, Germany
[2]Forschungszentrum Jülich GmbH, Ernst Ruska-Centre for Microscopy and Spectroscopy with Electrons, Jülich, Germany

Antimony chalcogenides (Sb2S3, Sb2Se3 and their alloys), compounds of earth-abundant elements, triggered growing interest as a solar absorber material in photovoltaics due to their tunable and favorable band gap, high defect tolerance and recent progresses of performances [1]. A key aspect influencing their device performance is the orientation of the crystal and texture of thin films. Due to the highly anisotropic crystal structure, forming strong covalently bonded quasi-one-dimensional ribbons, charge transport is significantly more facile along the ribbon direction than in the perpendicular directions. Major efforts are focused on engineering the crystal orientation to coincide with the desired carrier collection directions and grain boundary and interface to minimize losses caused by defects. Challenges remain in achieving high-quality thin films with controlled crystal nucleation, growth, orientation and texture for optimal device performance.

Here, we showcase the use of precession-assisted 4D-STEM and SEM-EBSD for the analysis of the crystal grain orientation and texture of Sb2S3 and Sb2Se3 thin films, and highlight in situ TEM investigation to reveal phase transformation, nucleation and growth phenomena to derive deeper insights. The samples were deposited by atomic layer deposition and were annealed either in situ in the TEM (Sb2S3), or on hot plate (Sb2Se3).[2-3] Precession-assisted 4D-STEM was carried out using a TESCAN Tensor instrument, and other TEM studies on a ThermoFisher Scientific Titan Themis. EBSD were carried out on a Zeiss Gemini 560 with an EDAX Clarity Super EBSD detector and operated at 10 kV. EBSD data were analyzed with spherical indexing method in OIM Matrix (AMETEK) with pre-calculated master pattern using EMsoft.

The in situ observations reveal that the as-deposited amorphous films crystallizes at 243ºC, grown anisotropically and formed very large grains with dominated [100] out-of-plane texture. Introducing an ultra-thin ZnS interfacial layer increased nucleation density, resulted smaller, few micrometer sized, more uniform grains, while retain the overall texture. In situ observations and subsequent orientation analysis revealed that the grains grew faster along the ribbon direction and that the bare films underwent early-stage dewetting, forming holes in amorphous regions during annealing. The ZnS interlayer mitigated dewetting, stabilizing the films and improving their uniformity. In contrast, the Sb2Se3 films develop into much smaller, few hundred nm sized grains with overall [100] texture. In the fine-grained films, higher-index oriented grains ([201] and [301]) are identified, which were reported to be preferable for carrier transport in solar cell devices [4]. These studies offer valuable insights for solar cell device optimization.

1. Tang, R. et. al., *Nature Energy* (2020) **5** 587.
2. Büttner, P., et. al., *Nano Energy* (2022) **103** 107820.
3. Wu, M., et. al. *arXiv* (2025) arXiv: 2502:11247
4. Jin, X. et. al., *Advanced Materials* (2021) 33 e2104346.

Fig. 1

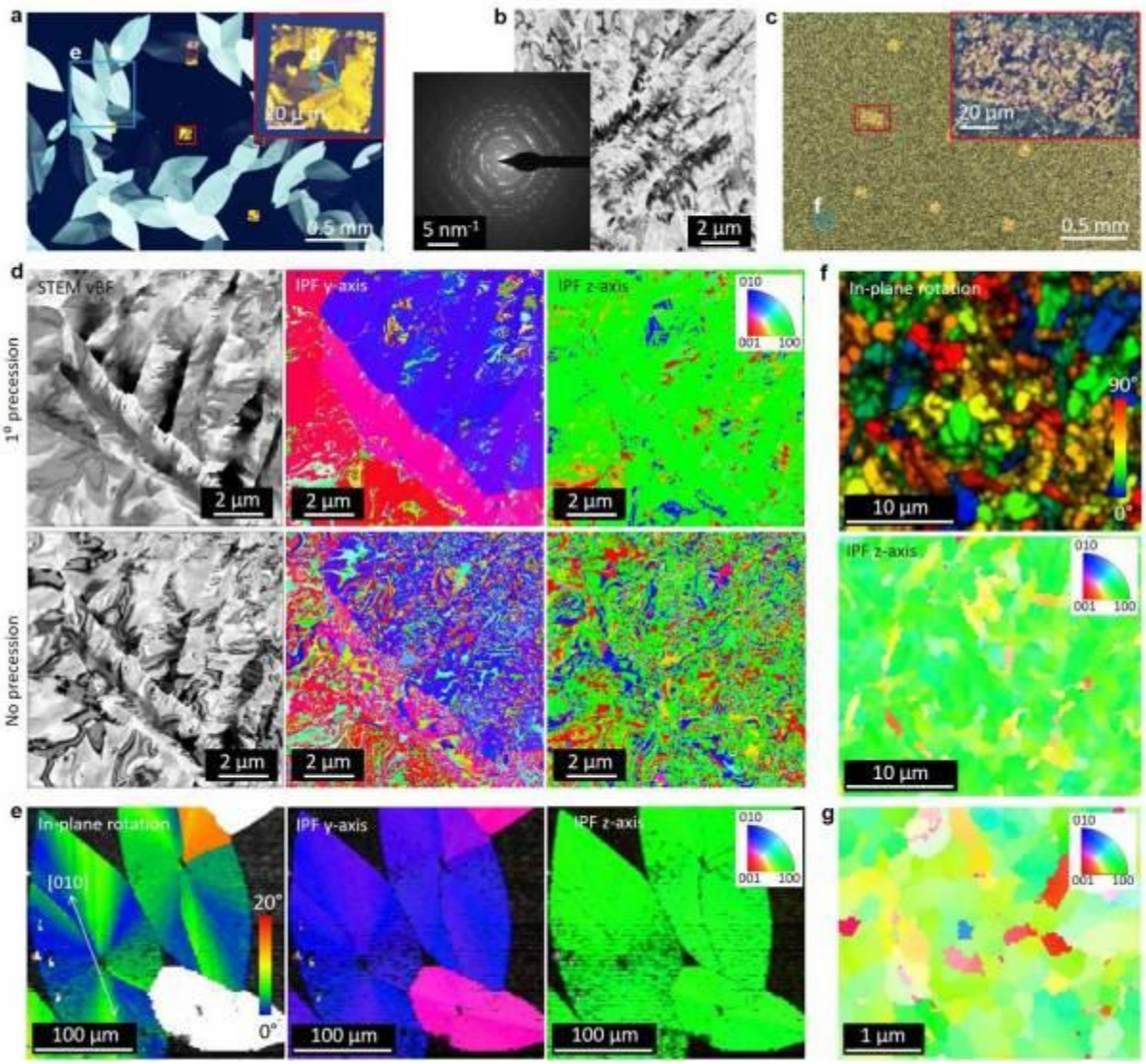
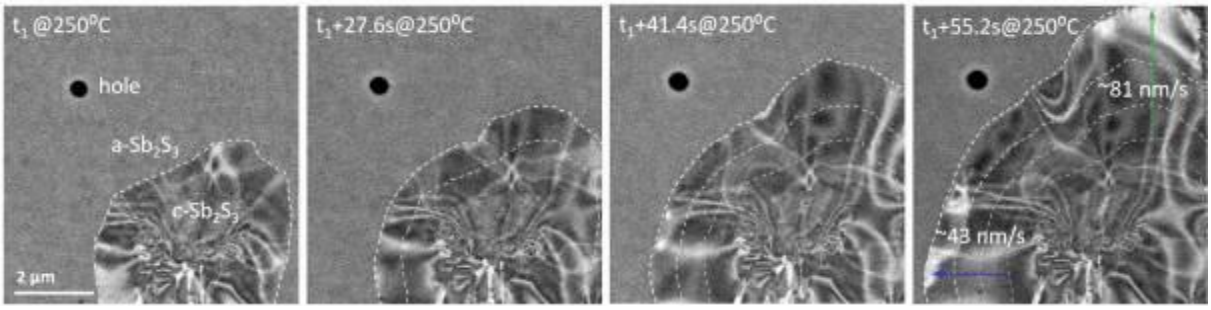

a
b
c
d
e
f
g
0.5 mm
5 nm⁻¹
2 µm
20 µm
STEM vBF
IPF y-axis
IPF z-axis
1° precession
No precession
In-plane rotation
90°
0°
10 µm
[010]
20°
100 µm
1 µm

Fig. 2


t1 @250°C
hole
a-Sb2S3
c-Sb2S3
2 µm
t1+27.6s@250°C
t1+41.4s@250°C
t1+55.2s@250°C
~81 nm/s
~43 nm/s

MS1.P28
Structural and chemical evolution of LSCF/GDC air electrodes in solid oxide cells with metallic interconnectors – A (S)TEM analysis

A. Makvandi[1], C. Grosselindemann[2], H. Stoermer[1], A. Weber[2], Y. M. Eggeler[1]

[1]Karlsruhe Institute of Technology, Laboratory for Electron Microscopy, Karlsruhe, Germany
[2]Karlsruhe Institute of Technology, Institute for Applied Materials - Electrochemical Technologies, Karlsruhe, Germany

In solid oxide cell (SOC) applications, ceramic single cells - comprising a fuel electrode, electrolyte, and air electrode - are assembled into a stack using metallic interconnectors. However, this integration can result in higher contact resistance and chromium poisoning.

A previous study [1] examined the electrochemical performance of 1 cm² single cells featuring stack-like metallic flow fields made from Crofer 22 APU steel, both with and without a cerium-cobalt (CeCo) protective coating. Performance metrics and loss mechanisms were evaluated using IV-characteristics, electrochemical impedance spectroscopy, and distribution of relaxation times (DRT) analysis. Building on these findings, this study investigates how uncoated and CeCo-coated metallic flow fields influence the structural and chemical evolution of LSCF/GDC composite air electrodes. This analysis was conducted using (scanning) transmission electron microscopy ((S)TEM). STEM imaging and energy-dispersive X-ray spectroscopy (EDX) were performed with a Tecnai OSIRIS ChemiStem TEM, while TEM sample preparation was carried out using a Helios G4 FX dual-beam instrument. Due to the relatively large TEM sample size, stabilization between layers was required, as illustrated in Figures 1(a) and 2(a).

Uncoated interconnectors experienced significant performance deterioration due to increased contact losses and air electrode polarization, primarily caused by Cr-oxide scale formation and Cr-poisoning. STEM-EDX analysis identified Cr-poisoning as the key factor behind $SrCrO_4$ formation in the air electrode, specifically within the LSCF layer (Figure 1). Additionally, Cr was detected in both LSCF and GDC (Figure 2). In contrast, CeCo-coated interconnectors exhibited improved performance by minimizing contact losses and effectively suppressing Cr evaporation, thereby reducing degradation and achieving notable enhancements in electrochemical performance [1].

References:

1. C. Grosselindemann, M.J. Reddy, H. Störmer, D. Esau, M. Dorn, F.M. Bauer, D. Ewald, L. Wissmeier, J. Froitzheim, A. Weber, *J. Electrochem. Soc.*, **171**, 054508 (2024).

Fig. 1

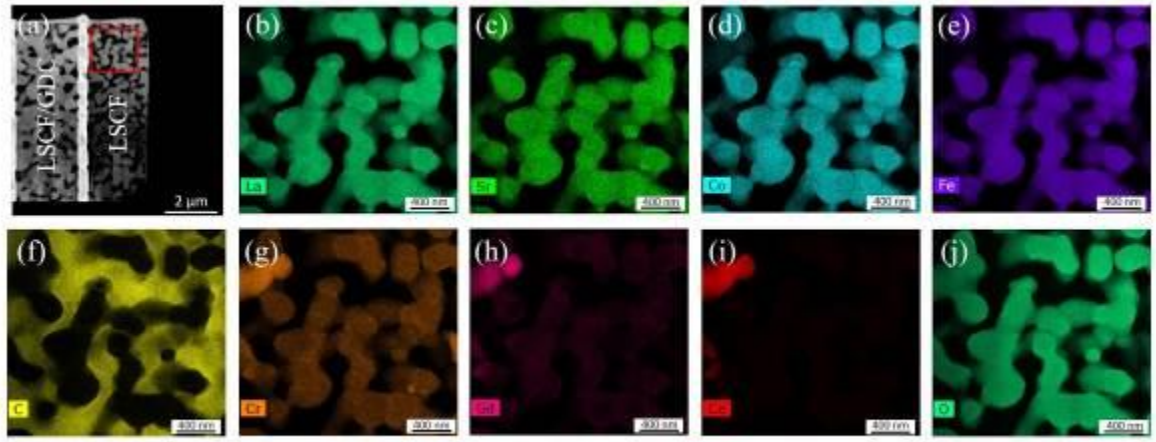


Figure 1. STEM-EDX of the LSCF-layer, (a) HAADF-STEM image, (b-j) EDX elemental map indicating that the concentration of Cr in GDC is higher compared to LSCF.

Fig. 2

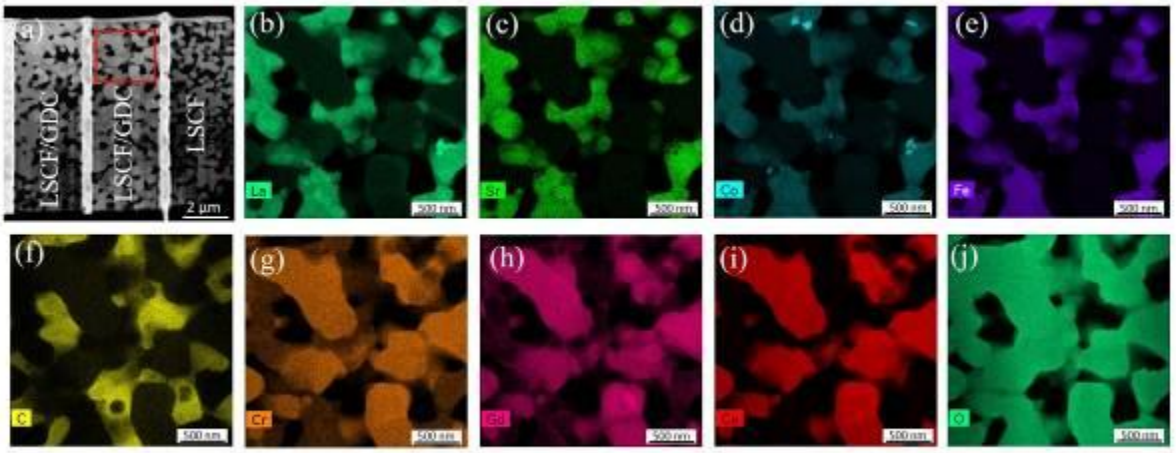


Figure 2. STEM-EDX of the LSCF/GDC layer, (a) HAADF-STEM image, (b-j) EDX elemental map showing that Cr is present in the form of $SrCrO_4$ which is due to Cr-poisoning.

MS1.P29
Role of microstructure in electrochemical processes – Insights from Al-ion Batteries

M. Velazquez-Rizo[1], A. Ahmadian[1,2], C. Kübel[1,3]

[1]Karlsruhe Institute of Technology, Institute of Nanotechnology, Eggenstein-Leopoldshafen, Germany
[2]Karlsruhe Institute of Technology, Helmholtz Institute Ulm for Electrochemical Energy storage, Eggenstein-Leopoldshafen, Germany
[3]Technical University of Darmstadt, Department of Materials Science, Darmstadt, Germany

Understanding the microstructure of electrode materials is crucial for improving battery performance, as it directly impacts electrochemical (EC) processes such as ion transport, reaction kinetics, and long-term cycling stability. This is particularly relevant in emerging battery technologies, where optimizing electrode stability is key to overcoming existing challenges.

Among these emerging technologies, Al-based batteries are promising candidates, as Al anodes present many potential benefits compared with current technologies. Despite this potential, the performance of these batteries is highly influenced by the purity of the material, surface topography, and microstructure.[1,2]

In this work, we systematically studied the EC plating and stripping of Al in symmetric Al/EMIMCl:$AlCl_3$/Al cells. High-purity (99.999%) electropolished Al samples were used, ensuring that any observed surface changes could be directly correlated with the underlying microstructure. The electrodes underwent either a single-step Al plating or stripping EC process at specific capacity values. Their surfaces were analyzed in both pristine and after the EC process, using identical location scanning electron microscopy (SEM) techniques, including backscattered electron detection (BSE) for imaging and electron backscattered diffraction for orientation mapping.

Our observations show that using a plating capacity of 10^2 mA•s•cm^{-2}, randomly distributed particles with diameters < 7 µm formed, showing no apparent relationship with the microstructure. As the plating capacity increased to 10^4 mA•s•cm^{-2}, the maximum diameter of the particles observed increased to ~40 µm, but they became more sparsely distributed. In addition to this phenomenon, a uniform Al layer covered the entire surface, suppressing the crystallographic contrast in BSE imaging.

In contrast, the stripping process exhibited a significant influence of the grain boundaries and grain orientation. At a capacity of $2.5x10^3$ mA•s•cm^{-2}, stripping resulted in pit formation and significant etching at high-angle grain boundaries (θ>15°). Certain crystallographic orientations, such as (001) planes displayed higher resistance to Al removal. At higher capacities (~10^4 mA•s•cm^{-2}), the surface topography varied depending on crystallographic directions. The (001) planes maintained a relatively smoother surface with circular pits, whereas other individual grain orientations presented a rougher surface morphology with grooves in specific directions.

This work demonstrates that the most influential part of the plating/stripping process in the formation of surface roughness in Al metallic electrodes is the stripping process. We expect our work to contribute to the design of more resilient Al electrodes for Al-ion batteries and to motivate solutions to the challenges identified in this study.

1. Rahide, F. et al., ChemSusChem e202301142 (2023).

2. Razaz, G. et al., ACS Appl Mater Interfaces **16**, 65725–65736 (2024).

Figure 1.- BSD imaging (left) before and (right) after Al plating at a capacity of 10^4 mA•s•cm^{-2}. The inset shows in detail the particles formed. Note that there is no crystallographic contrast after the plating.

Figure 2.- Left: BSE imaging of the sample after Al stripping at a capacity of 10^4 mA•s•cm^{-2}. Right: Inverse pole figure of the sample obtained before the EC stripping. Note that the topographic features left after the Al stripping strongly depend on the crystallographic orientation of the grains.

Fig. 1

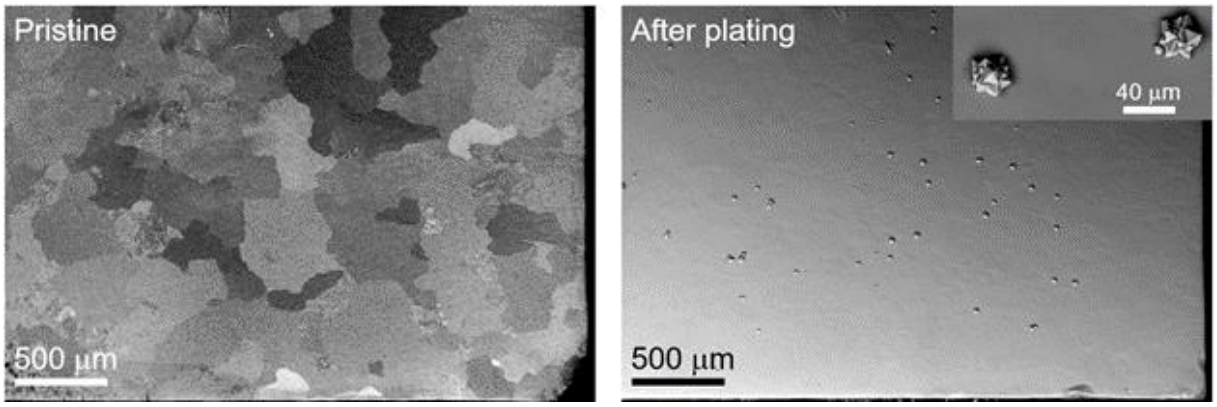
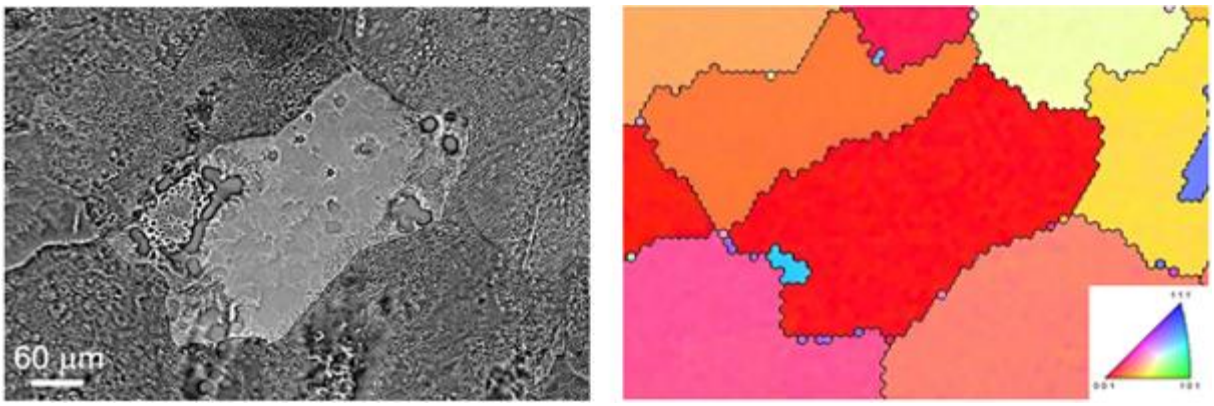


Fig. 2



MS1.P30
Combining 4DSTEM & EELS – Characterization and optimization of iron oxide thin films for sustainable applications

N. Kosian[1], S. Saood[1], P. Schweizer[1], M. Vega Paredes[1], J. P. Best[1], G. Dehm[1], L. Vogl[1]

[1]Max-Planck-Institute for Sustainable Materials, Department Structure and Nano-/Micromechanics of Materials, Düsseldorf, Germany

Green hydrogen is a crucial component of the global transition to sustainable energy, offering a clean alternative to fossil fuels. A major challenge in large-scale green hydrogen production is the development of efficient oxygen evolution reaction (OER) electrocatalysts. Iron oxides are abundant, inexpensive, and environmentally friendly alternatives to noble metal catalysts. Especially α-Fe2O3 has proved to be a good photoanode material for photoelectrochemical cells since its band gap allows the absorption of visible light[1]. Moreover, grain boundary engineering is a powerful pathway to improved OER electrocatalysis[2]. Studies conducted with metal oxide catalysts show that a higher grain boundary density can accelerate the overall OER kinetics[3] and increase the catalytic activity of the material significantly[4].

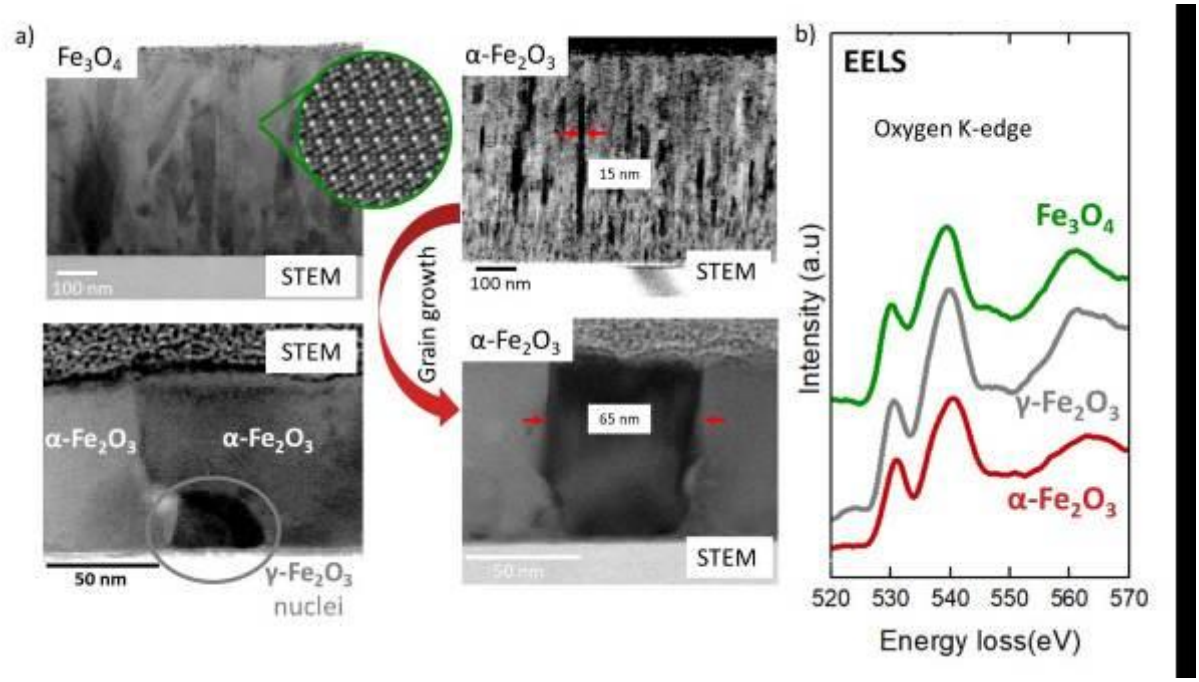
In order to systematically study the influence of the microstructure of iron oxides on their catalytic properties and thus determine the optimal film parameters, it is essential to be able to distinctly tune the microstructure during film deposition. In this work, we have adjusted the deposition parameters for reactive magnetron sputtering (growth rate, substrate heating, oxygen flow rate) to create different types of iron oxide thin films with varying oxide phases, grain size and shape. Following a scale-bridging approach, the films have been characterized using incident X-ray diffraction (XRD), scanning electron microscopy (SEM) and advanced transmission electron microscopy (TEM) techniques. To distinguish between the different iron oxide phases, electron energy loss spectroscopy (EELS) and nanobeam diffraction (4DSTEM) are used. Figure 1a shows some exemplary STEM images of deposited films in cross-section with different microstructures and Figure 1b shows the corresponding EELS data (oxygen K-edge).

As a next logical step, we will study structural changes induced during electrocatalysis, demonstrating the impact of the microstructure on the OER reaction. This will enable us to gain a comprehensive understanding of the structure-property relationship of iron oxide films and establish optimal conditions for sustainable applications. Overall, this work provides novel insights into the reactive sputtering process of functional iron oxide thin films with improved control over the phase and microstructure, showing promising properties for electrocatalysis. In the future, the deposition routine will be used to create functional thin films for water splitting applications such as photocatalysis.

Figure 1: Exemplary TEM characterization of iron oxide thin films with different phases, grain sizes, and shapes. a) STEM images (cross-section) of different samples achieved by tuning the deposition conditions during reactive magnetron sputtering. b) EELS: the oxygen K-edge is used to distinguish between the oxide phases.

1) Yatom, N.; et al. Settling the Debate on the Role of Fe2 O3 Surface States for Water Splitting. J. Phys. Chem. C 2015, 119 (44), 24789–24795.
2) Xu, X.; et al. Grain Boundary Engineering: An Emerging Pathway toward Efficient Electrocatalysis. InfoMat 2024, 6 (8), e12608.
3) Zhao, X.; et al. 2D Ruthenium–Chromium Oxide with Rich Grain Boundaries Boosts Acidic Oxygen Evolution Reaction Kinetics. Small 2024, 20 (29), 2311172.
4) Heo, Y.; et al. Symmetry-Broken Atom Configurations at Grain Boundaries and Oxygen Evolution Electrocatalysis in Perovskite Oxides. Adv. Energy Mater. 2018, 8 (34), 1802481.

Fig. 1


a)
Fe_3O_4
100 nm
STEM
α-Fe_2O_3
15 nm
100 nm
STEM
Grain growth
STEM
α-Fe_2O_3
α-Fe_2O_3
50 nm
γ-Fe_2O_3
nuclei
α-Fe_2O_3
65 nm
STEM
b)
EELS
Oxygen K-edge
Fe_3O_4
γ-Fe_2O_3
α-Fe_2O_3
Intensity (a.u)
520 530 540 550 560 570
Energy loss(eV)

MS1.P31
Optimization of the infiltration of meso-/macroporous materials and components with epoxy resin

S. Cordes[1], M. Hepp[1], J. Frohne[1], T. Zemke[1], C. Pritzel[2], M. S. Killian[2], B. Butz[1]

[1]University of Siegen, Micro- and Nanoanalytics, Siegen, Germany
[2]University of Siegen, Chemistry and Structure of Novel Materials, Siegen, Germany

Meso- and macroporous materials are found in many different areas of application, such as functional materials in batteries, fuel cells as well as catalysis, filtration or separation membranes, or structural materials for lightweight applications. Porous materials are thus of significance for an energy- and resource-efficient future. To characterize their scale-bridging microstructure and porosity, they are commonly examined using electron, ion and X-ray microscopy & tomography. Due to its porous morphology, those sample are susceptible to physical damage from mechanical preparation and beam exposure. The damage and the morphology result in image/data artifacts during the imaging process. Porous samples are particularly challenging for FIB milling and 3D analyses due to unwanted curtaining, redeposition or even collapse of the pore network. Mechanical stress may impede cross-sectional preparation by microtomy (collapse or severe compression of the porous structures). Another disadvantage of FIB-SEM tomography of noninfiltrated samples is that SEM imaging provides image information not only of the front-most (freshly cut) surface but from background surface beyond the intended cross-section, which complicates reliable data analysis and reconstruction.

To tackle these problems, one approach is to at least fill open porosity by, e.g., epoxy resin infiltration/ impregnation. Important influencing factors influencing the infiltration behavior and resulting quality are the viscosity of the respective resin, its surface tension and curing (time). Infiltration under vacuum conditions or deaeration after infiltration are beneficial (Fig. 3A). This study focuses on the investigation of the impacts of parameters like temperature and pressure during infiltration to facilitate a maximum degree of pore filling of mesoporous specimens with high/extreme aspect ratios at shortest curing time. For this purpose, reference silicon wafers and anodized aluminum samples with evenly distributed vertical µm-sized pore channels (diameters in the range of 150 nm – 5 µm) with lengths up to a few hundred µm are systematically infiltrated using different types of commercial epoxy resins (Fig. 1,2,3). To understand the flow and curing behavior of different resins, rheological measurements are performed. In addition, materials sciences samples from catalysis (mesoporous metal foams) and energy devices are prepared. The infiltration performance is determined by quantitative micro-CT (Fig. 1) and cross-sectional analyses employing SEM (Fig. 2,3). The aim of this work is to gain an understanding of the factors influencing the infiltration behavior in porous structures, to apply this knowledge to optimize the infiltration process and to provide guidance to the community by quantitatively comparing commercial and untypical embedding media.

Acknowledgements: We acknowledge use of the DFG-funded Micro-and Nanoanalytics Facility (MNaF) at the University of Siegen (INST 221/131-1)

Figure 1: incomplete infiltration under ambient conditions (µCT image; silicon wafer with 5µm wide dead-end pores); Figure 2: challenges like pores, due to trapped gas (SEM image; silicon wafer with 1µm wide dead-end pores); Figure 3: A) optimized vacuum infiltration (SEM image; silicon wafer with 1µm wide dead-end pores); B) carbon distribution inside the pore structure (EDS mapping; silicon wafer with 1µm wide dead-end pores)

Fig. 1

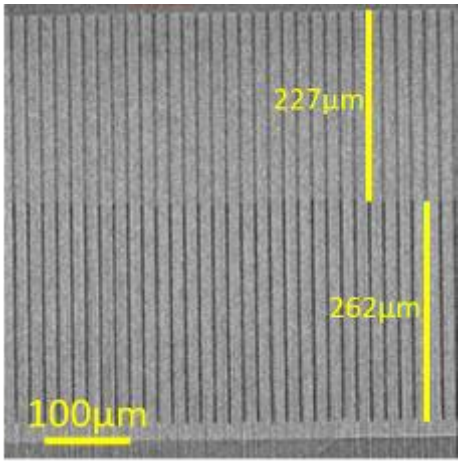


Fig. 2

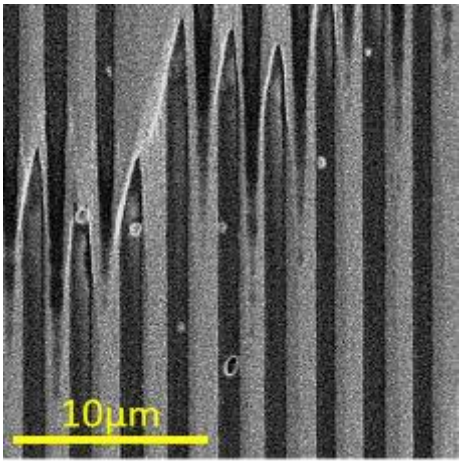
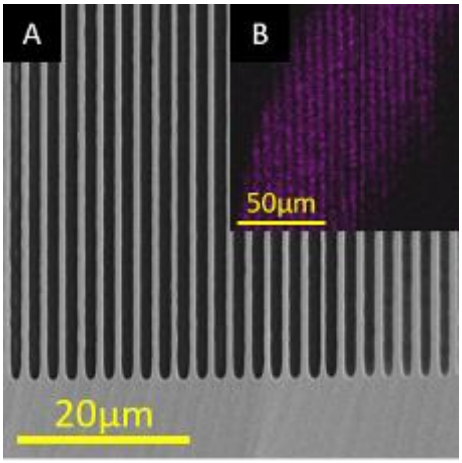


Fig. 3



MS1.P32
Dependency of SMSI effect of TiO2 supported Pt particles on Ti reduction state and pressure

N. Radde[1], A. Plucienik[1], A. Rinaldi[1], C. Sun[1], M. G. Willinger[1]

[1]Technical University of Munich, Chemistry, Garching, Germany

Background The concept of strong-metal-support-interaction (SMSI) was first proposed in 1978 by Tauster, who observed a decrease in hydrogen and carbon monoxide adsorption due to an interaction between noble metal and TiO2 due to encapsulation overlayers [1]. Since then, the SMSI effect has been investigated continuously, due to its relevancy to catalysis [2,3,4].

The aim of our work is to investigate how reduction state, as well as pressure of oxygen and hydrogen influences the SMSI effect and the catalytic activity of the TiO2 supported Pt particles.

Methods An Environmental Scanning Electron Microscope (ESEM) was used to observe the encapsulation of the Pt particles and their sintering behavior at pressures around 30 Pa. Gasses used were H2 and O2. An atomic force microscope (AFM) was used to measure the conductivity of different reductive states of the TiO2 support, which was a TiO2 Rutile single crystal with (110) surface orientation. The TiO2 crystals were reduced inside the ESEM using a commercial heating system and home-built gas feeding system.

Results TiO2 crystals, which were just lightly reduced showed a lower conductivity than the highly reduced ones. Additionally Pt particles on the highly reduced support were more easily encapsulated under high temperature treatment, and thus also showed less sintering than the Pt particles on the lightly reduced TiO2 crystals. Under 1 bar, the encapsulation of Pt particles under H2 could be reversed by changing to a H2/O2 mixture. Under 13.3 Pa, the encapsulation of the Pt particles could not be reversed by changing from O2 to H2 or UHV. Lastly, unsurprisingly, the reduction and re-reoxidation of the TiO2 crystals led to a considerable amount of surface roughening.

Keywords Catalysis, Titanium Oxide, SMSI, Operando Scanning Electron Microscopy

Reference

[1] S. J. Tauster, S. C. Fung, R. L. Garten, Strong Metal-Support Interactions. Group 8 Noble Metals Supported on TiO2, J. Am. Chem. Soc., 100, 170-175, 1978.

[2] F. Kraushofer et al. The influence of bulk stoichiometry on near-ambient pressure reactivity of bare and Pt-loaded rutile TiO2(110). Nanoscale, 16, 17825-17837, 2024.

[3] P. Petzoldt et al. Tuning Strong-Metal-Support Interaction Kinetics on Pt-Loaded TiO2(110) by Choosing the Pressure: A Combined Ultrahigh Vacuum/Near-Ambient Pressure XPS Study. J. Phys. Chem. C, 126, 16127-16139, 2024.

[4] H. Frey et al. Dynamic interplay between metal nanoparticles and oxide support under redox conditions. Science, 376, 982-987, 2022.

MS1.P33
Synthesis of Cu nanoparticle Co-Catalysts supported on Ga_2O_3 for visible-light-driven photocatalytic reactions

G. Hejime[1], O. Satoshi[1,2], K. Makoto[1,2]

[1]Nagoya University, Energy Engineering, Nagoya, Japan
[2]Nagoya University, Institute of Material and Systems for Sustainability (IMaSS), Nagoya, Japan

1. Introduction

The development of photocatalysts is crucial for applications in water purification, solar energy, and sustainable energy generation [1]. Metal nanoparticle-supported photocatalysts, particularly Cu and Cu alloy-based catalysts, show promise due to copper's high activity [2–4]. However, conventional methods mainly yield Cu/Cu_2O composites, reducing efficiency and affecting alloy formation [5]. To address this, we employed the solution plasma process (SPP), a rapid (~1 μs), non-equilibrium technique enabling stable Cu nanoparticle (CuNP) synthesis [6]. This study explores CuNP fabrication via SPP and their integration with Ga_2O_3 for CO_2 photoreduction, demonstrating SPP"s potential for advanced nanoparticle synthesis.

2. Experiment

Synthesis: CuNPs were successfully synthesized by SPP using hydrazine (N_2H_4) as an electrolyte solution and the reduction agent. The fabricated CuNPs were loaded on Ga_2O_3 powder by SPP and the CuNPs/Ga_2O_3 composite underwent calcination under H_2 atmospheres at 200–500 °C.

Characterization: Ultraviolet-visible absorption Spectroscopy (UV-vis) to investigate optical properties, Scanning Transmission Electron Microscopy (STEM) for particle size measurement, and X-ray Absorption Fine Structure (XAFS) for chemical state determination.

Catalytic Performance: Water splitting reaction was performed using GC system under UV and visible light.

3. Results and discussion

Fig. 1 presents STEM images of CuNPs synthesized in N_2H_4 aqueous solutions at concentrations of 70 mM (a) and 30 mM (b). The STEM image in Fig. 1(b) reveals smaller CuNPs with an average size of approximately 2.1 nm, whereas Fig. 1(a) displays larger CuNPs with an average size of 27.6 nm. The inset images in Fig. 1 further illustrate variations in the optical properties of nanoparticle solutions produced at different electrolyte concentrations.

Fig. 2 shows the XANES spectra of the CuNPs/Ga_2O_3 system and Fig. 3 presents the effects of calcination under different gas atmospheres and temperatures. The results indicate that samples calcined at 300°C in a hydrogen atmosphere achieved the highest degree of reduction.

4. Conclusion

To enhance semiconductor photocatalysts for CO_2 reduction, CuNPs were synthesized via the solution plasma process (SPP) in varying N_2H_4 concentrations. Characterization revealed that electrolyte concentration significantly affects CuNPs' chemical states, size, and morphology. Calcination above 300°C led to re-oxidation, likely due to Ga_2O_3 decomposition in a hydrogen atmosphere. UV and visible light driven water splitting tests showed that CuNPs as co-catalysts

significantly improved Ga_2O_3 performance, demonstrating their potential for CO_2 photoreduction applications.

References

[1] Schneider, J.et al., Chem Rev 114 (19) ,9919-9986, 2014.
[2] Schultz, D. et al., Science, 343 (6174), 2014.
[3] Zou, Z et al., Nature, 414 (6864), 2001.
[4] Manoj B et al., Chemical Rev 116 (6) (2016).
[5] M. Brust et al., J. Chem. Soc., Chem. Commun. 16, 1655 (1995).
[6] N. Saito et al., Thin Solid Films 518, 912 (2009).

Figure legends

Fig. 1 STEM images of (a) CuNPs (70 mM N_2H_4 aq) (b) CuNPs (30 mM N_2H_4 aq).
Fig. 2 XANES spectra of CuNPs/Ga_2O_3.
Fig. 3 Radial distribution function obtained from EXAFS spectra of CuNPs/Ga_2O_3 after H_2 calcination.

Fig. 1

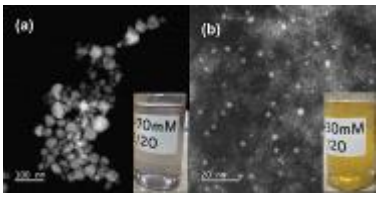


Fig. 2

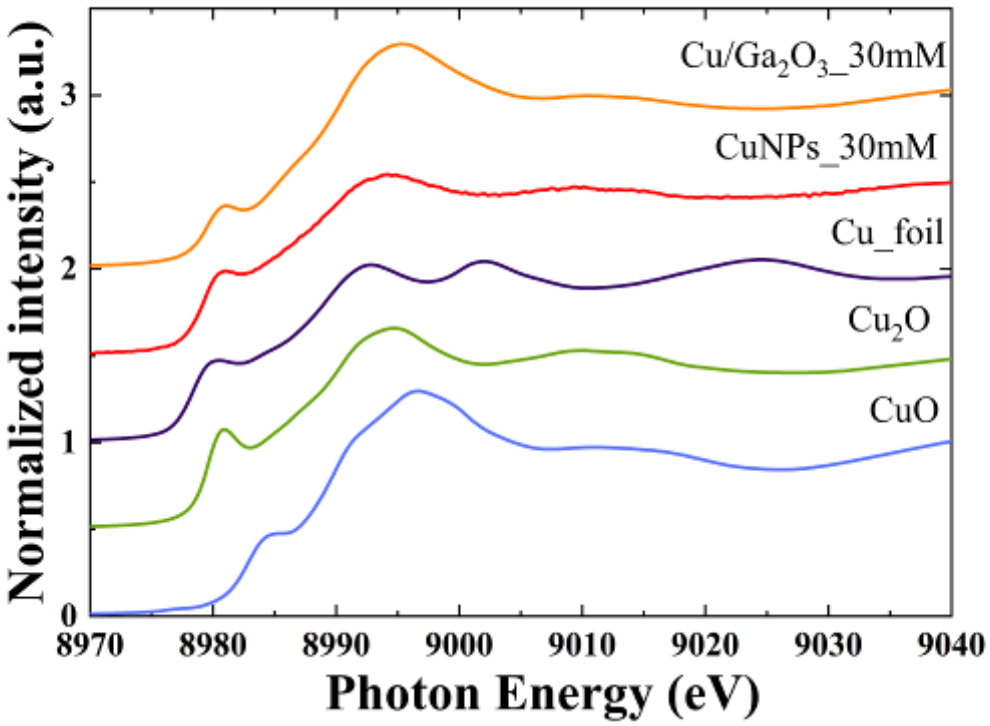
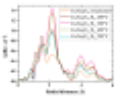

Cu/Ga2O3_30mM
CuNPs_30mM
Cu_foil
Cu2O
CuO
Normalized intensity (a.u.)
0
1
2
3
8970
8980
8990
9000
9010
9020
9030
9040
Photon Energy (eV)

Fig. 3



MS1.P34
New method of FIB TEM sample preparation for *in situ* heating and biasing MEMS chip used for investigation on Zn4Sb3 thermoelectric material

D. Mattlat[1], C. Jung[1], P. Ying[2], S. He[2], J. Li[2], A. Bahrami[2], S. Zhang[1], C. Scheu[1]

[1]Max-Planck-Institut für Eisenforschung, Düsseldorf, Germany
[2]Leibniz-Institut für Festkörper- und Werkstoffforschung, Dresden, Germany

INTRO: Thermoelectric devices generate clean energy by converting thermal energy into electrical power by using a temperature differential. The microstructure of thermoelectric materials is crucial for their conversion efficiency, as it determines their thermoelectrical properties. Transmission electron microscopy (TEM) is a powerful tool to characterize the microstructure from micrometer down to the atomic scale. However, the microstructure may be altered during operation at elevated temperatures and electrical biasing, which further leads to changes in thermoelectric properties.

OBJECTIVES: These modifications may cause degradation and instabilities in thermoelectric materials over time. To characterize these changes in situ in a TEM, MEMS-based microchips have been commercialized. Thermoelectric device conditions, like heat loads and electrical biasing, can be applied to the MEMS chips during TEM observation. In this work, a new procedure for preparing thin TEM samples on MEMS chips using focused ion beam (FIB) will be presented and the first results will be shown. This method differs from other method that are known from literature. In our technique, the sample is directly transferred to the MEMS chip and thinned on the chip while in literature, the TEM sample has been transferred first to a Cu-grid for thinning with a follow up transfer to the chip. Zn4Sb3, a material prone to Zn-whisker growth by Zn ion diffusion due to phase transitions at elevated temperatures, was used for testing this method.[1,2]

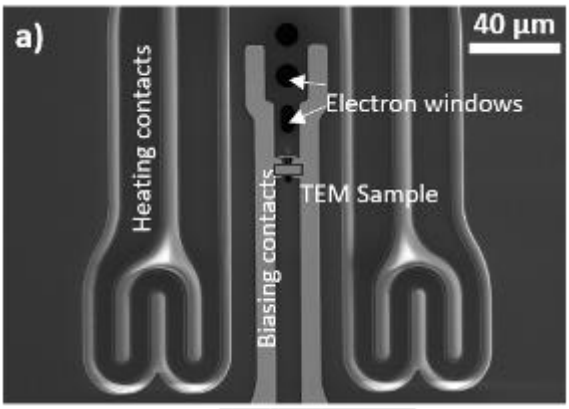
MATERIALS & METHODS: For this new procedure, the sample is lifted and transferred to the MEMS chip with a micromanipulator needle in a FIB device. There, it was contacted with the biasing contacts by ion beam deposition of a Pt-C composite. Finally, the TEM sample was thinned down directly on the MEMS chip to the defined dimensions. For the in-situ experiments, a TEM was used and a holder for heating and biasing that has been connected to an external setup.

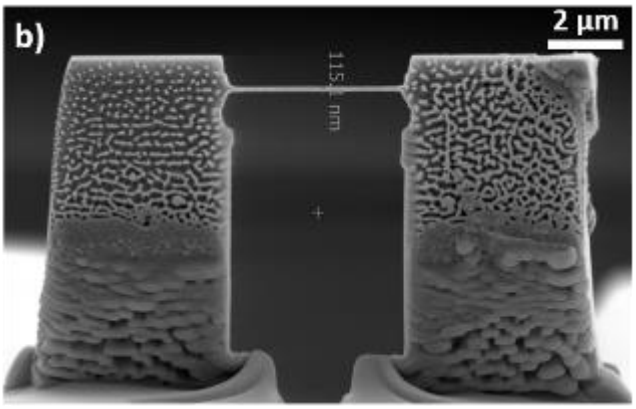
RESULTS: To measure the electrical properties of the TEM sample in situ, a voltage is applied between the electrodes, and the current is measured to derive the resistance from the current-voltage curve. The sample's resistivity is determined from the resistance and geometry. Biasing of 1mV and 5mVwith stepwise heating up to 200°C was applied in TEM. After initial stepwise heating with 1mV bias, the electrical resistivity followed the same trend as the bulk material. 5mV bias showed no more changes in electrical resistivity. This highlights the successful minimized contact resistance for this sample preparation method. The resistivity measurements for bulk, 1mV and 5mV biasing can be seen in figure 2 a-c below.

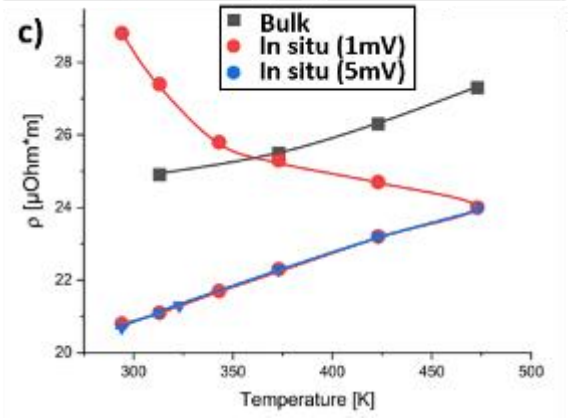
CONCLUSION: The preparation showed an efficient way of producing in situ TEM sample on heating and biasing MEMS chips. The method offers a fast way with side specific extraction by FIB without extra steps that would be required if thinning was done at a Cu-grid and afterwards being transferred to the MEMS chip. The biasing and heating experiments showed the reduction of contact resistance which offers direct measurements in the TEM of the electrical resistivity by heating the sample.

Figure 2: The MEMS chip with the heating and biasing contacts is shown in a). The thinned lamella with a thickness of about 110 nm can be seen in b) and the measured electrical resistivity for the bulk, 1mV and 5 mV biasing over the temperature range can be seen in c).

Fig. 1


a)
40 µm
Heating contacts
Electron windows
TEM Sample
Biasing contacts


b)
2 µm


c)
Bulk
In situ (1mV)
In situ (5mV)
ρ [µOhm*m]
Temperature [K]
20
22
24
26
28
300
350
400
450
500

MS1.P35
Electron beam effect on polymer thin films graphitization at elevated temperatures

C. Chemin[1], B. Rezaei[1], A. I. Bunea[1], S. Sylvest Keller[1], A. Bastos da Silva Fanta[1], T. W. Hansen[1]

[1]Technical University of Denmark, Nanolab - National Centre for Nano Fabrication and Characterization, Kongens Lyngby, Denmark

Pyrolytic carbon, which can be obtained by heating a polymeric carbon precursor at high temperatures in inert atmospheres, is a promising material for electrochemical energy storage, medical implants, sensing and other applications. However, an in depth understanding of the pyrolytic carbon graphitization process is needed to further optimize material properties. *In situ* transmission electron microscopy (TEM) is a highly suited technique for investigating graphitization at the nanoscale [1]. Nevertheless, possible structural modifications resulting from interactions between sample and high-energy electrons must be considered [2]. Understanding these beam-induced effects is essential when developing novel methods for *in situ* characterization.

In this study, *in situ* TEM imaging of a polymer film during pyrolysis is conducted and the electron beam effect on the graphitization and carbon structure arrangement is investigated.

Suspended polymer thin films are patterned on TEM heating chips by two-photon polymerization (2PP) 3D printing, followed by pyrolysis for *in situ* TEM graphitization studies. The design consists of a suspended ribbon with a central through-hole (Fig. 1a). The 700 nm-thick central ring (dark grey) is optimized for TEM imaging (Fig. 1c), while the 900 nm-thick surrounding ribbon (light grey) enhances structural stability [3]. TEM was performed with an FEI Titan 80–300 environmental transmission electron microscope (ETEM) operated at 300kV. The ribbon, printed on the imaging window, was pyrolyzed *in situ* in the TEM (Fig. 1b) using MEMS heating chips (Wildfire, DENSsolutions). The sample is heated to 1300°C and kept at this temperature for 5h.

Figure 2 shows a series of TEM micrographs obtained when the sample is at 1300°C, illustrating the structural evolution of pyrolytic carbon. Figure 2a–d and g–j, acquired from the monolayer membrane edge (Fig. 3f), compare two conditions: beam blanked between acquisitions (Fig. 2a–d) to minimize the influence of the beam on the carbon structure, and continuous beam exposure (Fig. 2g–j). Initially amorphous (Fig. 2a), carbon rearranged in laterally stacked graphene sheets as the temperature is held at 1300°C (Fig. 2b–d), confirmed by the 3.3 Å interlayer distance (Fig. 2e–f). In comparison, continuous beam exposure resulted in longer stacks of graphitic domains (Fig. 2k–l). The electron beam seems to provide additional energy for the atoms to rearrange in graphitic domains compared to purely thermally driven graphitization when the beam was blanked between acquisition.

Our experiments showed graphitization of the sample during pyrolysis, which was accelerated in the presence of the electron beam. To gain a better understanding of the interaction of the electron beam with the pyrolytic carbon we aim to investigate the influence of changing the electron beam energy and dose rate using *in situ* TEM.

[1] C. Kumar et al., Nanoscale 9 (2017) 12835-12842

[2] R.F. Egerton et al., Micron 35 (2004) 399-409

[3] C. Chemin et al., Nano Today 59 (2024) 102524

Figure 1: a) 3D design of the ribbon b) SEM micrograph of the ribbon after pyrolysis, c) TEM micrographs acquired during the dwell at 1300°C, showing the graphitic domains.

Figure 2: *In situ* TEM micrographs acquired on the edge of aperture ribbon design, during the dwell at 1300°C, from 1h10 to 1h25 of dwell: a-d) beam blanked between acquisitions, g-j) beam on between acquisitions. e,f,k,l) HRTEM images of graphitic domains.

Fig. 1

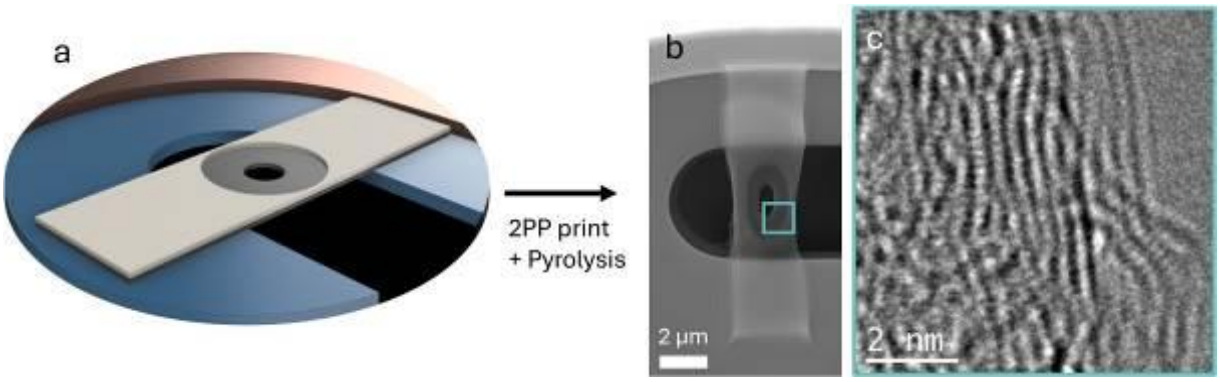
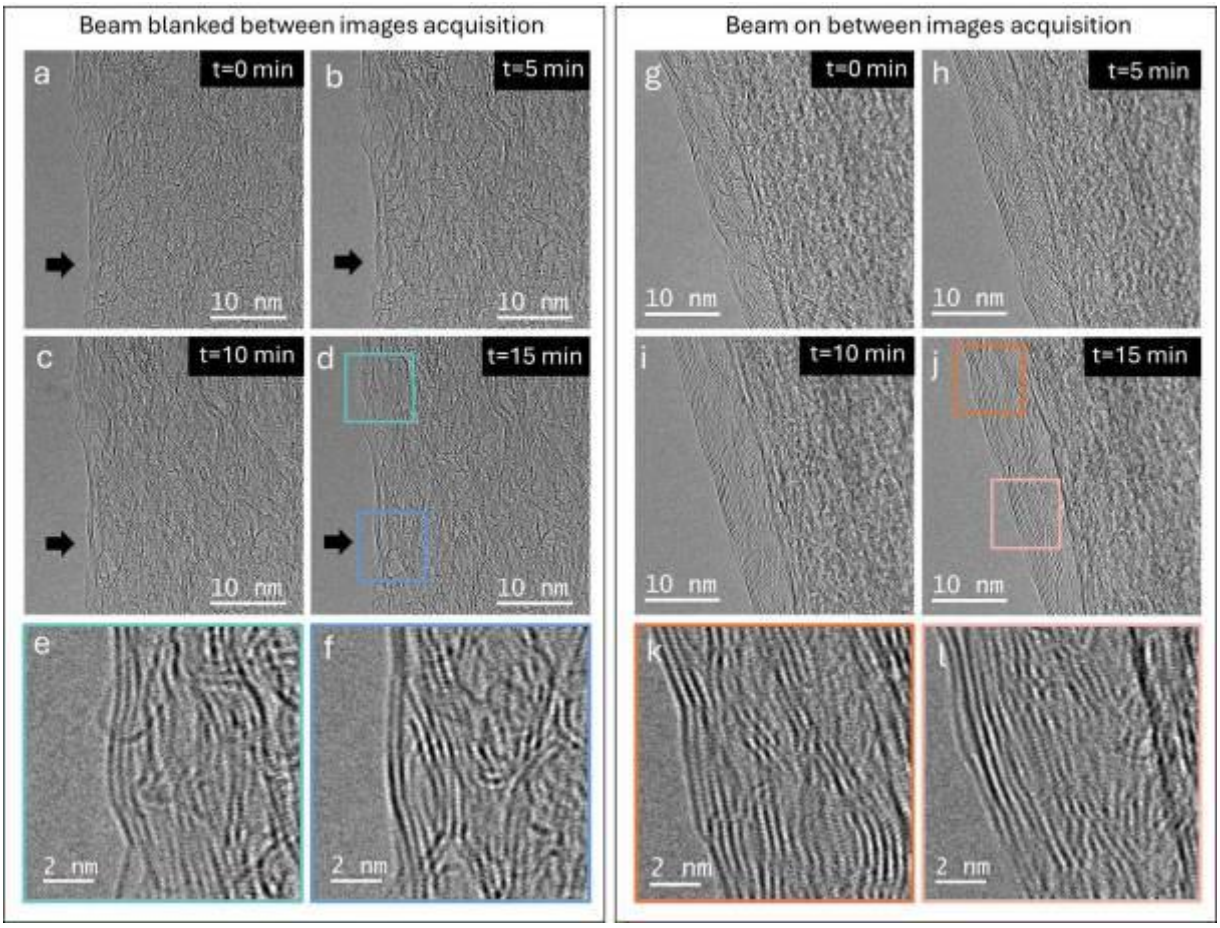


Fig. 2



MS1.P36
Operando (S)TEM on mass selected Pt_{200} clusters deposited on CeO_2 for CO oxidation catalysis

A. R. Lakshmi Nilayam[1,2,3], R. Shadkam[1,3], C. B. Maliakkal[1], H. Hahn[1,3,4], D. Wang[1,2], C. Kübel[1,2,3]

[1]Karlsruhe Institute of Technology, Institute of Nanotechnology, Karlsruhe, Germany
[2]Karlsruhe Institute of Technology, Karlsruhe Nano Micro Facility (KNMFi)., Karlsruhe, Germany
[3]Technical University of Darmstadt, Department of Materials and Earth Sciences, Darmstadt, Germany
[4]University of Oklahoma, School of Sustainable Chemical, Biological and Materials Engineering, Oklahoma City, OK, United States

Model catalyst systems with mass selected precious metal clusters on nanostructured metal oxide supports are employed to understand the fundamental processes in catalytic reactions in exhaust gas catalysis, to unravel the complex relationship between the structure and the catalytic properties. *In-situ* TEM can be of aid to track the dynamic intermediate stages corresponding to some local energy minimum involved, the structural or morphological changes of clusters under catalytic reaction conditions. In this work the behavior of size selected Pt clusters (50-200 atoms) deposited on CeO_2 support are studied using advanced scanning transmission electron microscopy (STEM) techniques, under pure gas environments (H2, Ar, O_2, CO, CO_2) and during CO oxidation. Size selected Pt clusters is deposited using an ultra-high vacuum (UHV) cluster ion beam deposition (CIBD) system on a CeO_2 thin film, which is grown on an *in-situ* TEM MEMS chip with pulsed laser deposition (PLD). The dynamics of the clusters, cluster-support interaction and cluster-gas interaction, have been studied in real-time in exhaust gas environments using *in-situ* STEM imaging & EELS/EDX spectroscopy. The CO_2 generation and the level of conversion at different temperatures have been monitored using a high sensitivity residual gas analyzer (RGA). In addition, identical location STEM experiments are also conducted to understand the effect of e- beam on the cluster dynamics and to deduce its effect on the catalytic process. Under oxidizing conditions with pure O_2 (100%, 1 atm), the Pt clusters on CeO_2 completely dissolve into single sites. Complete dissolution occurs at 800°C after heating for an hour. The active state of the catalyst is restored through a pretreatment process with H_2 (100%, 1 atm), where Pt clusters reform on the CeO_2 surface upon heating to 800°C in the presence of H_2. This reversible process, Pt dispersion into single sites in O_2 and reformation into clusters in H_2 at high temperatures, can be attributed to the strong metal-support interaction (SMSI) between Pt and CeO_2. The Ce oxidation states at both oxidized and reduced states have been analyzed using electron energy loss spectroscopy (EELS). After activation, the model catalyst is imaged close to catalytic reaction conditions (2% CO, 38% He, and 60% O_2, 1 atm). The underlying CeO_2 thin film also undergoes noticeable morphological changes, becoming more porous (Figure 1c). Residual gas analysis (RGA) detected CO_2 formation starting at approximately 460°C, indicating catalytic activity (Figure 2). However, as the temperature increases beyond 800°C, the catalyst loses activity, evidenced by a drop in the CO_2 signal and the dispersion of Pt clusters into single sites due to the oxygen-rich environment. Beam effects at elevated temperatures are minimal, with damage primarily limited to knock-on effects on the clusters under high-magnification scans, also confirmed with identical location STEM. Thus, ***operando*** TEM characterization is unduly helpful in directly observing the evolution of Pt clusters and their interactions with CeO_2 under realistic conditions. We gain valuable insights into catalyst stability, reactivity, and regeneration strategies, which are crucial for optimizing catalytic performance.

Figure 1: HAADF-STEM images of Pt_{200} on CeO_2 a) pretreatment with O_2 , b) followed by H_2, c) after CO oxidation till 800°C and d) reformation of Pt clusters again with H_2 at 800°C

Figure 2: RGA output showing the activity at ~460°C with a rise in CO2 signal

Fig. 1

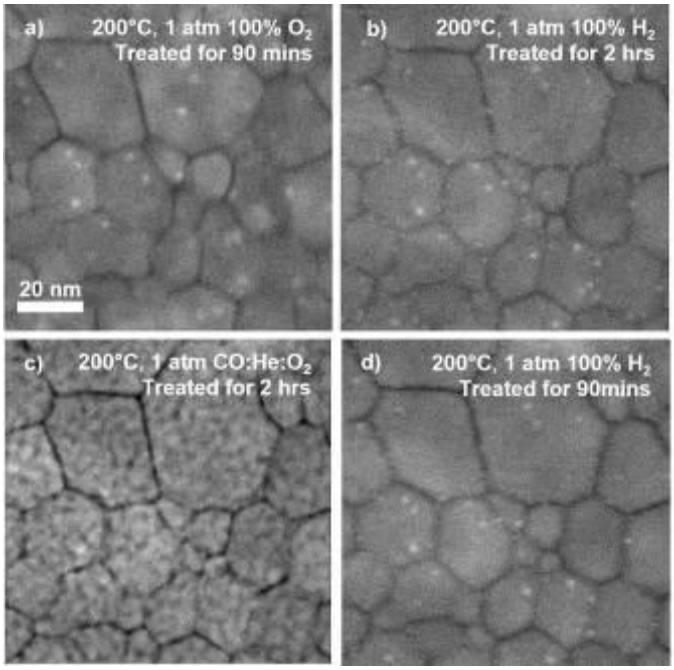
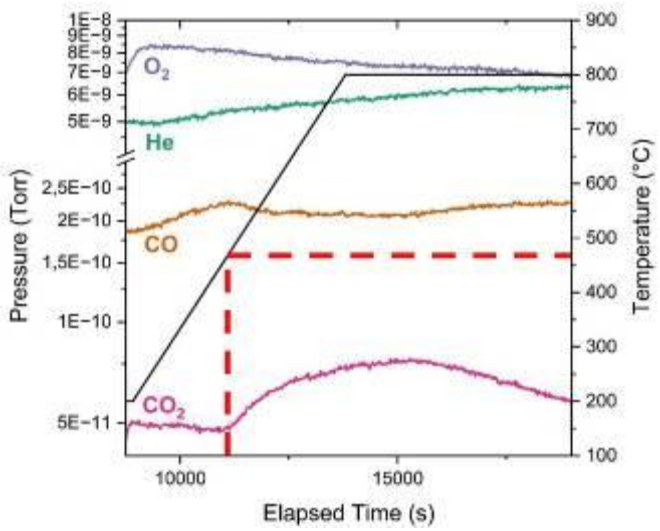

a) 200°C, 1 atm 100% O_2
Treated for 90 mins
20 nm
b) 200°C, 1 atm 100% H_2
Treated for 2 hrs
c) 200°C, 1 atm CO:He:O_2
Treated for 2 hrs
d) 200°C, 1 atm 100% H_2
Treated for 90mins

Fig. 2


Pressure (Torr)
Temperature (°C)
Elapsed Time (s)
O_2
He
CO
CO_2
1E-8
9E-9
8E-9
7E-9
6E-9
5E-9
2,5E-10
2E-10
1,5E-10
1E-10
5E-11
900
800
700
600
500
400
300
200
100
10000
15000

MS1.P37
Thin films of iridium-based catalysts for *in situ* electrochemical TEM OER study

E. Shcherbacheva[1], V. Tileli[1]

[1]Ecole Polytechnique Fédérale de Lausanne, Lausanne, Switzerland

Iridium-based catalysts, including amorphous and crystalline iridium oxides as well as metallic iridium, are widely recognized for their high activity and stability toward the oxygen evolution reaction (OER). Understanding the reaction mechanisms occurring on these materials' surface is crucial for the development of next-generation low-cost catalysts [1]. However, due to the reversible nature of intermediates formation, conventional *ex situ* methods often fail to capture key mechanistic insights. In contrast, *in situ* techniques such as electrochemical liquid-phase transmission electron microscopy (EC-LPTEM) enable direct nanoscale observation of catalyst evolution during OER. When coupled with electron energy loss spectroscopy, these methods can provide valuable insights into reaction product release [2].

However, *in situ* EC-LPTEM imposes certain limitations on the samples used. For example, commercially available iridium oxide particles can be too thick to take full advantage of this technique. Therefore, in this work, we aim to develop thin-film iridium-based electrodes on microelectromechanical (MEMS) chips optimized for *in situ* EC-LPTEM for detailed OER studies.

Thin films of iridium oxide (IrO_x, Ir(III) and Ir(IV)) and metallic iridium (Ir(0)) were deposited onto MEMS chips with transparent SiN_x membranes using DC magnetron sputtering. Calcination at 500° C for 8 hours was performed to transform sputtered oxide films into the rutile phase (IrO_2, Ir(IV)). Reference and counter electrodes were made of platinum with a titanium adhision layer. The electroactive area of electrodes was limited by SiO_2 passivation layer. Electrochemical characterization was performed using a Bio-Logic SP-300 potentiostat.

The fabricated thin films exhibited a homogeneous morphology with an average thickness of 15 nm, ensuring sufficient electron transparency for *in situ* EC-LPTEM studies. The sputtering process also provided strong adhesion to the MEMS chip surface, eliminating the need for additional adhesion layers. Electron diffraction analysis confirmed that the as-sputtered iridium oxide films were amorphous and transformed into a polycrystalline structure upon calcination. This phase transition was further validated electrochemically, as cyclic voltammetry revealed a redox peak at 1.4 V vs RHE in amorphous IrO_x, which disappeared in the polycrystalline IrO_2 samples. Additionally, a polycrystalline structure of metallic iridium films was demonstrated, undergoing amorphization under potential cycling.

In conclusion, thin iridium-based films were successfully fabricated on MEMS chips, providing a reliable platform for further *in situ* studies of OER mechanisms. Their optimal thickness and stability make them well-suited for use in liquid cells, enabling detailed investigations of catalytic behavior and intermediate formation during OER.

This work was supported by the Swiss National Research Foundation (SNSF) under award number 200020_204240.

References

[1] J. Murawski et al., Physical Johns. Matthey technol. rev. 68, 1 (2024)

[2] T.-H. Shen et al., J. Electrochem. Soc. 170, 5 (2023)

MS1.P40
Measurement of EELS standards and application on oxidation state determination and comparison of MeOH catalysts

D. Ramermann[1], E. H. Wolf[1], M. Poschmann[1], C. Göbel[1], L. Pielsticker[1], H. Ruland[1], W. Hetaba[1]

[1]Max Planck Institute of Chemical Energy Conversion, Mülheim a.d. Ruhr, Germany

Electron energy loss spectroscopy (EELS) is a powerful analytical technique providing information on the elemental composition, furthermore allowing investigation of electronic properties like chemical bonding and oxidation states. Most common for the analysis of EELS data are cross-section models, which are sufficient for determination of the elemental composition. A different analysis approach allows to extract information like oxidation states: Spectra of well-known reference materials (standards) improve the quantification results and allow fitting of the edge shapes to investigate and map oxidation states. These reference spectra can either be obtained by using EELS reference databases [1-2] or by measuring well-defined materials. Since the database content is mostly not exhaustive to provide a set of reference spectra for each element and oxidation state for a given material, the process of obtaining commercially available materials, evaluating them for their ability to be usable as standards and using the obtained set of standards to map and compare the oxidation states of two differently synthesized Cu-based MeOH catalysts [3, 4] post-catalysis is presented.

The investigated catalysts [3, 4] consist of Cu, ZnO and Al_2O_3, therefore, a commercially available sample of each Cu, Cu_2O, CuO, Zn, ZnO and Al_2O_3 has been obtained and investigated for its purity and oxidation state via XRD and TEM using EDX and EELS. Storage and sample transfer under inert conditions are considered mandatory for all samples that could oxidise further, as well as the catalysts. Standard spectra have been measured on suitable sample parts and imported into Gatan GMS3 as references. EELS maps of the MeOH catalysts [3, 4] after catalytic reaction have been acquired and evaluated for materials and oxidation states based on the measured standard spectra and the results compared with each other.

The XRD analysis showed two materials with deviations from the desired state: Cu showed ~5% oxidation, and ZnO exhibited an additional unknown phase. EDX maps of each material resulted in ~3-5% O in Cu, non-homogeneous oxidation and a substoichiometric O content in Cu_2O, while CuO was homogeneous as described. Some oxidation of ~5-7% O was found in the Zn sample, and additional O was present in the ZnO. The oxidation layer on the Zn appears to be XRD-amorphous. Trace elements in all cases were Al, Si, and Zn (for Cu-based materials) or Al, Si, and Cu (for Zn-based materials), with each amount < 0.2 at.%. The additional phase in the ZnO likely consists of zinc hydroxides.

From regions where the sample is in the desired state, EELS spectrum images have been acquired; and evaluated by composition to identify a suitable region for standard spectrum extraction. Using these standards, a concurrent standards fit on the spectrum image of the MeOH catalysts is able to differentiate between elements and oxidation state, resulting in a detailed, spatially resolved map for each. A detailed comparison shows common and different oxidation state features of the catalysts.

[1] Ewels et al. https://doi.org/10.1017/s1431927616000179

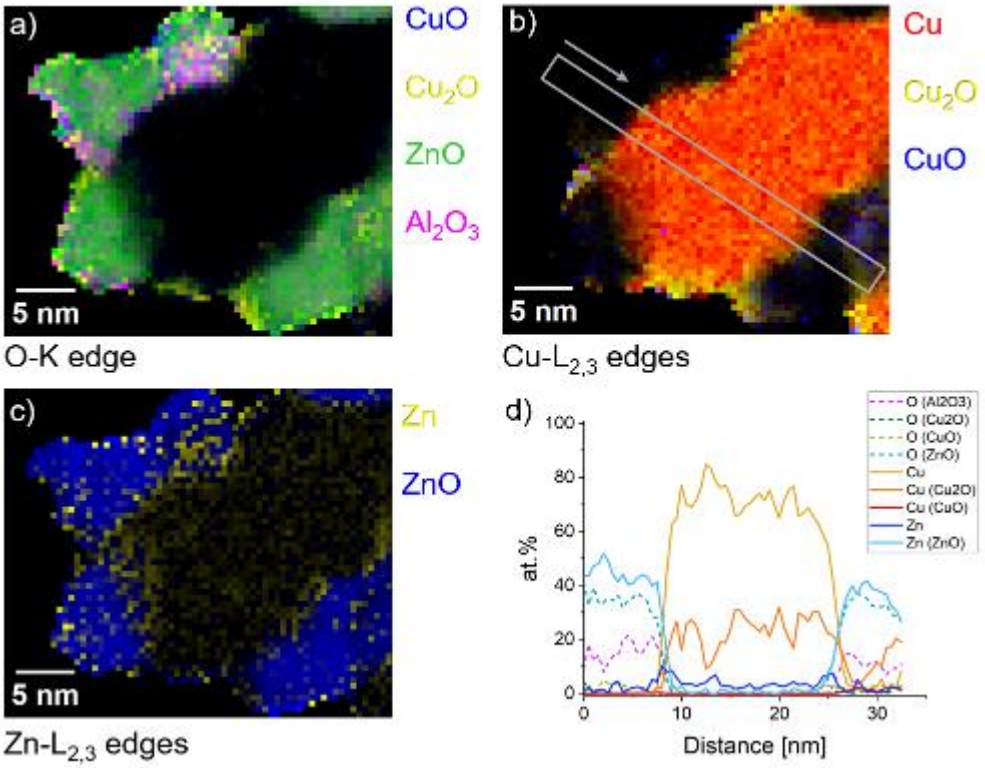
[2] https://eels.info/atlas

[3] Schumann et al. https://doi.org/10.1002/cctc.201402278

[4] Synthesis adapted from Dasireddy, Likozar https://doi.org/10.1016/j.renene.2019.03.073

Figure1: Evaluated EELS oxidation map of a MeOH catalyst a) O-map, b) Cu-map, c) Zn-map, d) line profile.

Fig. 1



MS1.P41
Real-time observations of Fe-Ni exsolution in perovskites – Implications for high-performance energy conversion applications

P. K. Chakraborty[1], S. Wolf[1], V. Vibhu[1], S. Basak[1], E. Jodat[1], A. Karl[1], R. A. Eichel[1]

[1]Forschungszentrum Jülich GmbH, Institute of Energy Technologies - Fundamental Electrochemistry (IET-1), Jülich, Germany

Introduction

The global shift toward clean energy has intensified research on solid oxide fuel cells (SOFCs) and electrolysis cells (SOECs).[1] The fuel electrode plays a key role in fuel interactions, but Ni/yttria-stabilized zirconia (Ni/YSZ), the widely used material, suffers from redox instability, Ni agglomeration, and coking.[2]

Perovskite-based alternatives, particularly Sr_2FeMoO_6-δ (SFM), have gained attention for their electrochemical stability and mixed electronic-ionic conductivity (MIEC).[3] A major advantage is **in situ** exsolution, where B/B′-site cations, doped with transition metals like Ni, Co, or Mn, undergo controlled exsolution upon reduction, mitigating agglomeration and coking.[4]

$Sr_2FeMo_{0.65}Ni_{0.35}O_6$−δ (SFM-Ni) exhibits superior performance due to Ni"s high catalytic activity.[5] However, the mechanism governing **in situ** $FeNi_3$ nano-exsolution remains unclear. Understanding this process is critical for optimizing material design and improving SOC performance.

Objectives

Using **environmental transmission electron microscopy (ETEM) and in situ TEM**, with precise temperature and gas pressure control via MEMS chips, this study provides real-time imaging of exsolution dynamics, informing material design for enhanced SOCs.

Materials and Methods

This study investigates **bimetallic $FeNi_3$ nanoparticle exsolution in SFM-Ni** under reducing conditions at both low and high gas pressures. ETEM with a secondary electron detector and **in situ TEM at 1 bar pressure** were utilized for analysis.

Results

Exsolution formation was examined through **in situ heating at ~10 Pa H_2 pressure** within 650–800 °C. Nucleation initiated at **650 °C**, progressing in **50 °C increments**. Preferential growth at **surface edges** aligns with nucleation theory, which attributes site preference to regions with **higher wetting angles** (e.g., edges) and **lower face angles** (e.g., concave surfaces), where reduced surface energy enhances stability and growth [Figure 1].

Figure 1. (a-d) SE images of SFM-Ni in H2 at ~10 Pa pressure between 650 °C-800 °C showing the evolution of Fe-Ni bimetallic nanoparticles around surface edges of SFM-Ni.

Under high-pressure reduction (4% H_2/Ar, 800 °C, 1 bar), **bright-field TEM (BF-TEM) images** revealed similar $FeNi_3$ growth dynamics [Figure 2]. Compared to ETEM-based reductions, these transformations occurred **more rapidly**, likely due to **higher pressure (~1 bar) in the MEMS chip assembly**.

Figure 2. Time series of BF-TEM images showing the evolution of Fe-Ni bimetallic nanoparticles around surface edges of SFM-Ni.

Conclusions

The **in situ** $FeNi_3$ exsolution mechanism follows a **multi-step process** influenced by **oxygen vacancy concentration, surface morphology, gas environment, and pressure**. Surface edges and concave regions **favor exsolution** and enhance adhesion via the **anchoring effect**. These findings guide the strategic design of **advanced double perovskites with controlled in situ exsolution**, advancing **high-performance energy conversion technologies**.

References

[1] S. He, Y. Zou, K. Chen, S.P. Jiang, *Interdisciplinary Materials*, 2 (2023) 111-136.
[2] Z. Du et al., *ACS Nano*, 10 (2016) 8660-8669.
[3] H. Lv et al., *Adv Mater*, 32 (2020) e1906193.
[4] Wolf SE et al., *Electrochemistry Communications*, 167 (2024) 107799.
[5] P. Chakraborty et al., *Nano Today* (2025) (https://doi.org/10.1016/j.nantod.2025.102649).

Fig. 1

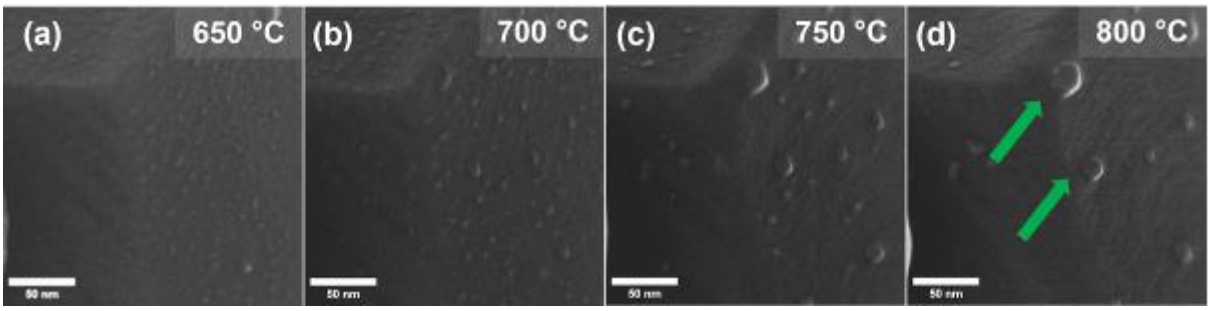
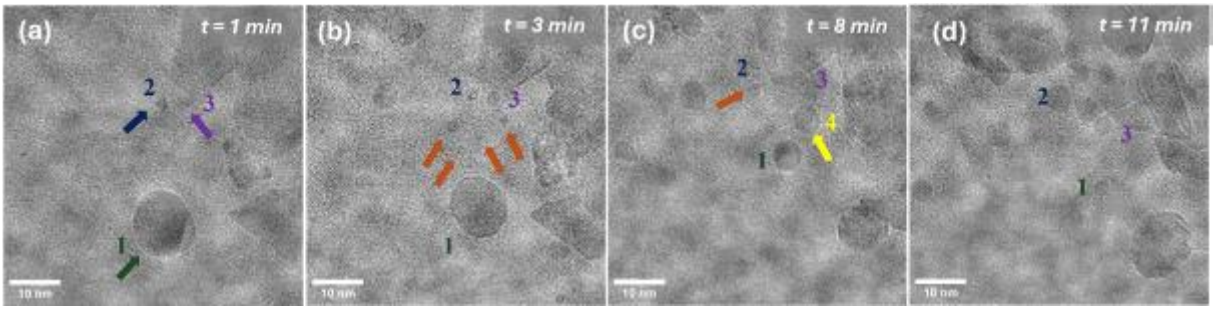


Fig. 2



MS1.P42
Modulating metal support interactions for durable and selective CO2 hydrogenation reaction – An operando transmission electron microscopy study

H. Sun[1], P. K. Chakraborty[2], R. Spruit[1], Y. Pivak[1], S. Basak[2], R. A. Eichel[2,3,4], H. Pérez Garza[1]

[1]DENSsolutions, Delft, Netherlands
[2]Forschungszentrum Jülich GmbH, Institute of Energy Technologies - Fundamental Electrochemistry (IET-1), Jülich, Germany
[3]RWTH Aachen University, Institute of Physical Chemistry, Aachen, Germany
[4]RWTH Aachen University, Faculty of Mechanical Engineering, Aachen, Germany

Carbon dioxide (CO2) hydrogenation is a promising route to generate clean high-value fuels and chemicals, for example CO, CH4, CH3OH, and C2+ hydrocarbons [1]. Heterogeneous metal-support catalysts have emerged as prime candidates for this reaction, effectively dissociating H2 to facilitate CO2 conversion [2]. While considerable effort has focused on tailoring the size, morphology, and composition of both supports and metal nanoparticles, achieving high activity, selectivity, and stability remains a significant challenge [3]. Crucially, metal-support interactions (MSI) are now recognized as playing a decisive role, as the interface provides active sites and oxygen vacancies that influence gas adsorption, activation, and product formation. Therefore, directly observing these dynamic MSI under realistic reaction conditions is essential for understanding catalytic mechanisms and designing advanced catalysts.

While various *in-situ* techniques have been employed to probe CO2 hydrogenation, recent advances in MEMS-based sample carriers and corresponding transmission electron microscopy (TEM) holders, coupled with residual gas analysis, have enabled *in-situ* TEM studies of near-atmospheric pressure reactions [4,5]. As TEM provides the opportunity to perform simultaneous high-resolution imaging, chemical composition mapping, and local electronic structure studies, in-situ TEM allows for real-time observation of MSI dynamics and correlation with reaction products, providing unprecedented insights into the catalytic processes [6].

In this work, by comparing different types of metal-substrate interaction, we will uncouple the effect of substrate during CO2 hydrogenation (Figure 1) [7]. Our study would contribute to deepen the understanding of high temperature (co)electrolysis processes, leading to the design of high-performance electrode materials.

Figure 1. Time series of TEM images showing the evolution of nickel nanoparticles around surface edges of the substrate.

References:

[1] R-P Ye et al., Nature Commun. **10** (2019), p. 5698.

[2] S Mirzakhani et al., ChemPlusChem **88** (2023), p. e202300157.

[3] A Álvarez et al., Chem. Rev. **117** (2017), p. 9804.

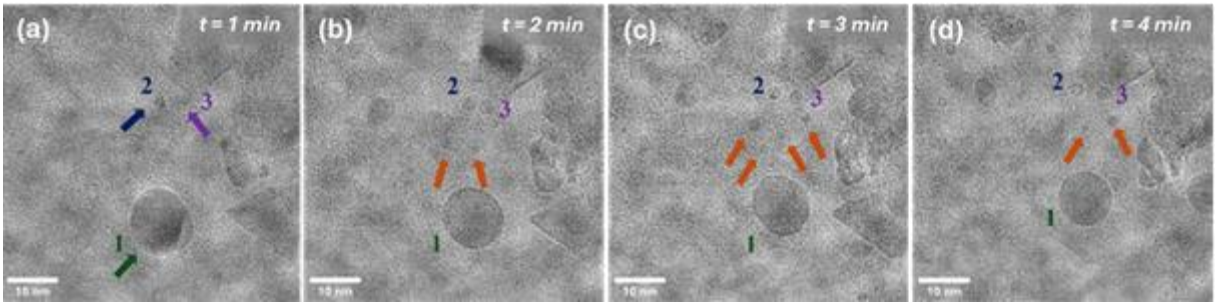
[4] YY Li et al., Catal. Today **420** (2023), p. 114029.

[5] R Singh et al., ChemPlusChem **89** (2024), p. e202300511.

[6] F Tao et al., Science **386** (2024) p. 865.

[7] P. Chakraborty et al., Nano Today (2025) accepted.

Fig. 1



MS1.P43
A systematic study on PtRu alloy composition for direct methanol oxidation reaction

T. Kloos[1], M. Vega Paredes[1], A. Saksena[1], M. Kim[2], W. Schuhmann[2], J. Schneider[3], C. Scheu[1,3]

[1]Max-Planck-Institute for Sustainable Materials, Nanoanalytics and Interfaces, Düsseldorf, Germany
[2]Ruhr University Bochum, Electroanalysis and Sensors, Bochum, Germany
[3]Rheinisch-Westfälische Technische Hochschule, Materials Chemistry, Aachen, Germany

Introduction

In order to reduce CO2 emissions in the areas of energy supply and consumption the use of fuel cells is inevitable. Since the availability of green hydrogen is still very limited and areas of application e. g. CO2 free steel production have a higher impact the use of direct methanol fuel cells (DMFC) become more and more important. The DMFC can directly oxidize methanol to generate electricity without any additional hydrogen producing step. For the methanol oxidation reaction on the anode side the system of PtRu catalyst nanoparticles is well studied. Until now just few compositions of the PtRu nanoparticles are investigated in terms of structure and their performance since it is challenging and time consuming to synthetize nanoparticles with different specific compositions.

Objectives

In this work we perform a systematic investigation on the different chemical compositions of PtRu alloys and the influence on their micro- and nanostructure using a thin film. Additionally, the local electrochemical performance of the catalyst is correlated to the composition and structure of the alloy. This approach offers a high throughput investigation method on the influence of chemical composition to the structure and the catalytic performance of the catalyst alloy

Materials and Methods

The thin film was deposited on a silicon wafer via combinatorial magnetron sputtering. With positioning the Pt target and the Ru target in an 180° angle to each other a geometrical concentration gradient is generated. The surface of the thin film was analyzed in a Scanning Electron Microscope (SEM) followed by Energy dispersive X-ray Spectroscopy (EDXS) to determine chemical composition and distribution of the elements. Scanning electrochemical cell microscopy (SECCM) experiments are performed to precisely corelate the electrochemical performance. Using a focused ion beam (FIB) lamellae were lifted out on specific targeted areas. Theses were analyzed with a Transmission Electron Microscope (TEM) to obtain the local structure and composition before and after the methanol oxidation reaction.

Results

The deposited thin film had a smooth surface with no macroscopic defects. The atomic concentration range goes from Pt:Ru 73:27 at % - 23:77 at % along different samples. The thickness of the thin film was determined to be 615 nm ± 5 nm based on TEM micrographs. Additionally, the TEM micrographs taken from cross sections of the thin film showed columnar grains with 35 nm ± 9 nm width and the height of the thin film. With lamellae from areas of targeted positions EDXS was performed in the TEM

to verify the validity of the calculated phase diagram. EDXS maps revealed that a two-phase material exists in regions where the calculation suggests a single phase material.

Conclusion

Combinatorial magnetron sputtering can be used to create thin films with a concentration gradient covering a brought composition range. A systematic study on the influence of the chemical composition on the structure was performed. Local electrochemical experiments were performed for better understanding the role of chemical composition in PtRu alloys regarding the methanol oxidation reaction. These results were correlated with the structure before and after the experiment to study the relationship of structure and performance. Correlation of structure and electrochemical experiments is key for future catalyst design.

MS1.P44
Improving electron tomography of mesoporous silica by Ga filling

J. Böhmer[1], A. Kichigin[1], M. Buwen[1], B. Apeleo Zubiri[1], M. Wu[1], J. Will[1], D. Drobek[1], A. Götz[1], N. Vorlaufer[2], J. Söllner[3], M. Thommes[3], P. Felfer[2], T. Przybilla[1], E. Spiecker[1]

[1]FAU Erlangen-Nürnberg, Institute of Micro- and Nanostructure Research (IMN) & Center for Nanoanalysis and Electron Microscopy (CENEM), Erlangen, Germany
[2]FAU Erlangen-Nürnberg, Institute of General Materials Properties, Erlangen, Germany
[3]FAU Erlangen-Nürnberg, Institute of Separation Science and Technology, Erlangen, Germany

Introduction
Mesoporous silica is widely used in heterogeneous catalysis as a carrier material [1]. A precise characterization of the pore network is crucial to improve the material´s properties. Electron tomography (ET) provides three-dimensional imaging to obtain local information about the porous material with nm spatial resolution. ET typically utilizes the high-angle annular dark-field (HAADF) detector in scanning transmission electron microscopy (STEM) mode. However, the contrast for light elements is poor because the detector intensity scales with the atomic Z-number of the material [1]. We developed a novel method (Figure 1) to infiltrate gallium (Z-number 31) into porous silica (Z-number ~10), significantly improving imaging contrast. This approach not only enhances contrast in the tomographic tilt series but also improves the quality and resolution of the 3D reconstruction, enabling more precise phase segmentation for quantitative analysis.

Materials & Methods
Ga is forced into the mesoporous silica (20 nm pore size) under high pressure. Filling degrees of 50% and 100% are achieved and compared to the unfilled case. From all filling states, pillar-shaped specimens are prepared onto tomography tips using a scanning electron microscope-focused ion beam device (Helios NanoLab 660 DualBeam SEM-FIB). 360° ET is carried out in a FEI Titan3 Themis at 300 kV using the HAADF-STEM mode.

Results
SEM imaging and FIB preparation of the unfilled sample is adversely affected by charging and image drift. The Ga filling mitigates these effects by forming a conductive path through the non-conductive silica pore network. The tilt series benefits from the gallium filling, as reflected in the increased contrast and detector intensity when comparing the unfilled sample to the fully filled one (Figures 2a-c). In turn, this significantly improves 3D reconstructions, as evidenced by the substantial reduction in noise in the tomograms of the filled samples (Figures 2d-f). As a result, the segmentation of the pore network becomes more reliable (Figures 2g-i), enabling more accurate quantitative analysis. During tilt series acquisition, carbon contamination accumulates on the sample, degrading the image quality. This effect is minimized by the Ga filling procedure due to the higher Z-number difference between Ga and C. Quantitatively, the contrast improves by a factor of ~5, aligning well with theoretical calculations. Furthermore, the interface sharpness in the reconstruction is enhanced by 49%. This is evaluated using the proximity histogram (proxigram), which calculates the grey value distribution along the Ga/silica (filled) or void/silica (unfilled) interface. The resolution of the tomographic reconstruction improved by 34% after Ga filling. The pore size distribution of the filled sample, assessed by the local thickness algorithm, is narrower than that of the unfilled sample, attributed to enhanced sharpness, contrast and resolution.

Conclusion
This study highlights the benefits of filling mesoporous silica with Ga for contrast enhancement between pore space and material in ET. Additionally, interface sharpness and resolution increase, which lead to better segmentation of the 3D data. Gallium filling might serve as a general method to improve ET not only of mesoporous silica but also of other light porous materials.

References

[1] D. Ozkaya, W. Zhou, J. M. Thomas, P. Midgley, V. J. Keast, and S. Hermans, Catalysis Letters 60 (1999), 113-120.

Fig. 1

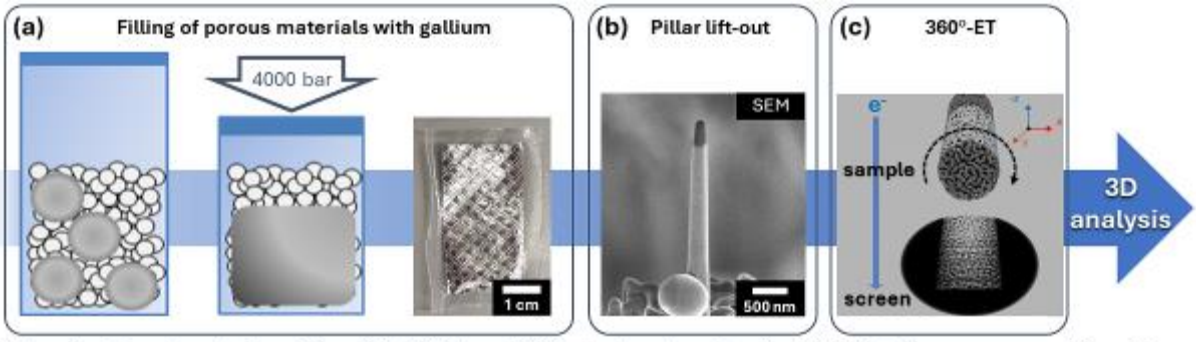


Figure 1: Experimental workflow of Ga filling and 360° electron tomography. (a) Filling of mesoporous silica with Ga. (b) Preparation of pillar-shaped specimen for (c) 360° electron tomography, followed by 3D data analysis.

Fig. 2

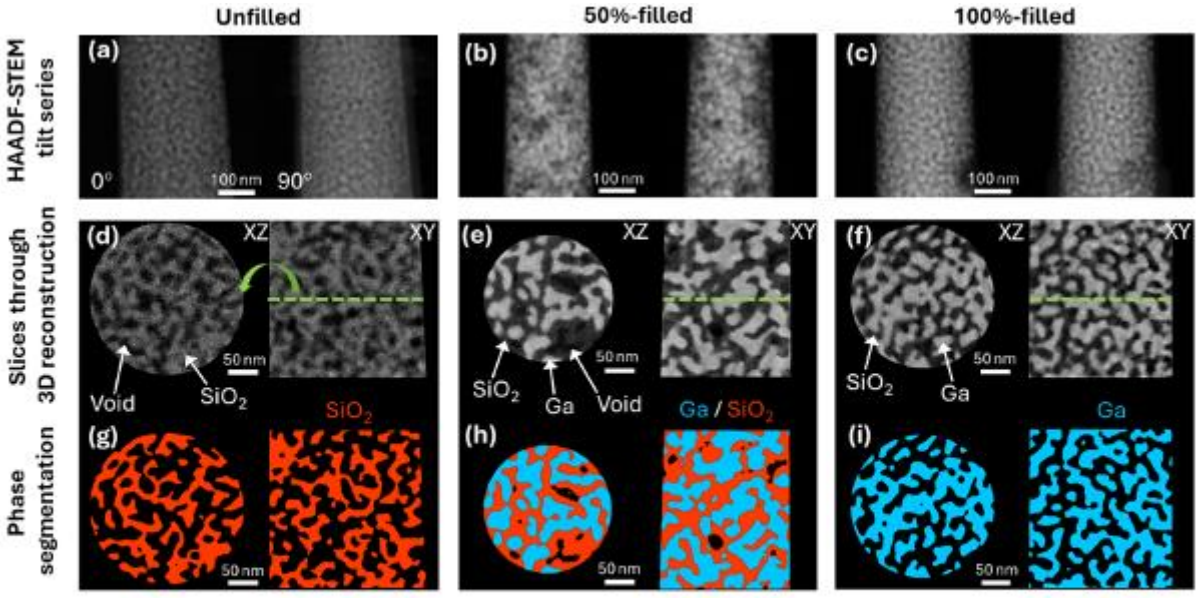


Figure 2: Overview of imaging and data analysis for the unfilled, 50% filled and 100%-filled mesoporous silica samples. (a–c) HAADF-STEM tilt series images acquired at 0° and 90°, showing variations in contrast and imaging quality. (d–f) 2D slices from the reconstructed ET volumes (XZ and XY slices), demonstrating improved contrast in the intruded samples. (g–i) Segmentation of the same reconstructed slices.

MS1.P45
Bridging structure and chemistry – Advancing nanoscale insights by correlating 360° electron tomography and atom probe tomography

A. Kichigin[1], M. Buwen[1], T. M. Schwarz[2], J. Seltsam[3], M. Dierner[1], N. Karpstein[1], J. Böhmer[1], B. Apeleo Zubiri[1], T. Przybilla[1], J. Will[1], J. Bachmann[4], B. Gault[2], P. Felfer[3], E. Spiecker[1]

[1]FAU Erlangen-Nürnberg, Institute of Micro- and Nanostructure Research (IMN) and Center for Nanoanalysis and Electron Microscopy (CENEM), Erlangen, Germany
[2]Max-Planck-Institute for Sustainable Materials, Düsseldorf, Germany
[3]FAU Erlangen-Nürnberg, Institute for General Materials Properties, Department of Materials Science, Erlangen, Germany
[4]FAU Erlangen-Nürnberg, Chemistry of Thin Film Materials, Department Chemistry and Pharmacy, Erlangen, Germany

1. Introduction

Advanced nanoscale characterization demands both precise spatial resolution and accurate chemical composition. 360° electron tomography (360°-ET) provides non-destructive, complete 3D imaging with nanometer-scale precision, free of the missing wedge artifact. In contrast, atom probe tomography (APT) yields highly accurate chemical data independent of ion mass, but its reconstructions suffer from spatial distortions. Moreover, APT is inherently destructive – allowing only one measurement per sample. Correlating these two techniques on the same sample promises a dataset that is both spatially precise and chemically accurate.[1]

2. Objectives

This study aims to develop and validate a correlative 360°-ET/APT method to:

- Establish a robust data registration protocol that leverages 360°-ET precision to correct APT spatial distortions.
- Combine non-destructive structural imaging with destructive, high-fidelity chemical mapping for comprehensive nanoscale characterization.
- Reveal subtle interfacial phenomena and heterogeneities that are difficult to detect otherwise.

3. Materials and methods

A model system (with potential use in energy materials) was prepared comprising small Pt particles (10–20 nm) on a Si wafer via Pt layer solid-state dewetting, subsequently covered with ~80 nm of ZnO and ~20 nm of Ni (designed to evaporate first during APT). Needle-shaped specimens were prepared by FIB lift-out and annular milling. As shown in Figure 1, the workflow begins with non-destructive 360°-ET, where a tilt series is collected over 180° using HAADF-STEM on needle-shaped specimens. This ensures complete coverage and nm-scale spatial accuracy via Z-number contrast. The specimen is then transferred to the atom probe, where ions are identified by their mass-to-charge ratios. Although APT yields precise chemical composition, chemical heterogeneities introduce spatial distortions. A bespoke registration protocol aligns the ET framework with the APT data, correcting these distortions to yield a composite dataset that is both spatially precise and chemically robust.

4. Results

The integrated 360°-ET/APT approach uniquely combines ET"s spatial precision with APT"s chemical accuracy. As shown in Figure 2, the complete 360°-ET tilt series enables a high-resolution 3D reconstruction that clearly delineates Pt particles in the ZnO matrix. ET-informed correction of the APT data reveals a thin (few nm) SiO_2 layer between the Si substrate and the Pt/ZnO region (likely due to atmospheric oxidation) and detects trace Au within the Pt particles, probably from residual

contamination in the e-beam vapor deposition system. These findings have important implications for materials processing and quality control.

5. Conclusion

Correlating 360°-ET and APT yields a dataset with nanometer-scale spatial accuracy and atomic-scale chemical detail. By using ET to correct APT distortions, this method reliably maps complex interfacial features, such as the SiO_2 layer and trace Au contamination, opening new avenues for optimizing materials processing and enhancing quality control in advanced nanoscale characterization.

6. Acknowledgements

We gratefully acknowledge the DFG for financial support within CRC1411 (Project ID 416229255).

7. References

[1] I. Arslan, E.A. Marquis, M. Homer, M.A. Hekmaty, and N.C. Bartelt, Ultramicroscopy **108**, 1579–1585 (2008).

Fig. 1

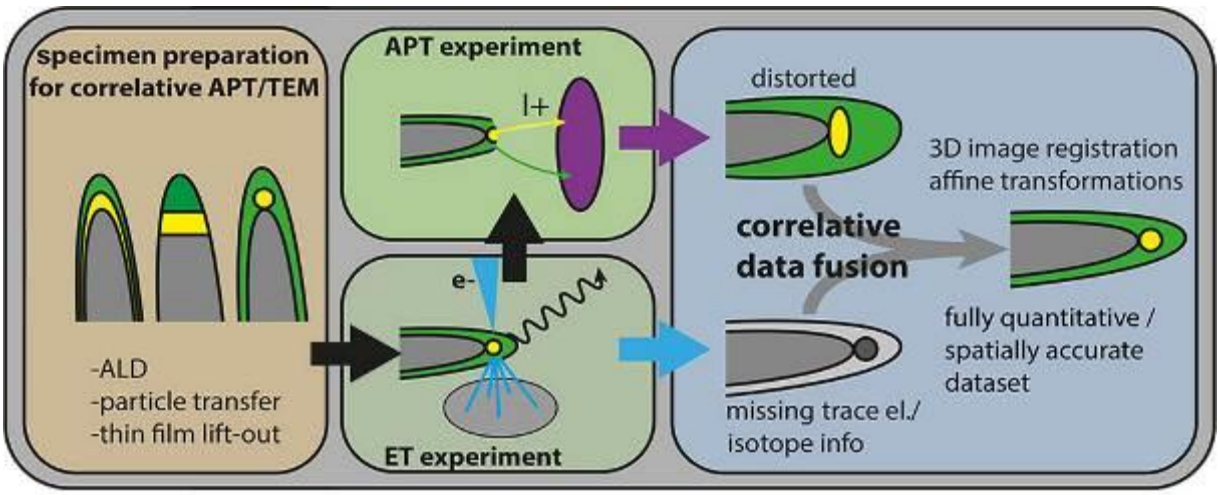


Figure 1. Scheme of the correlative workflow: non-destructive 360°-ET imaging on pillar specimens followed by destructive APT analysis, with ET data used to correct APT spatial distortions.

Fig. 2

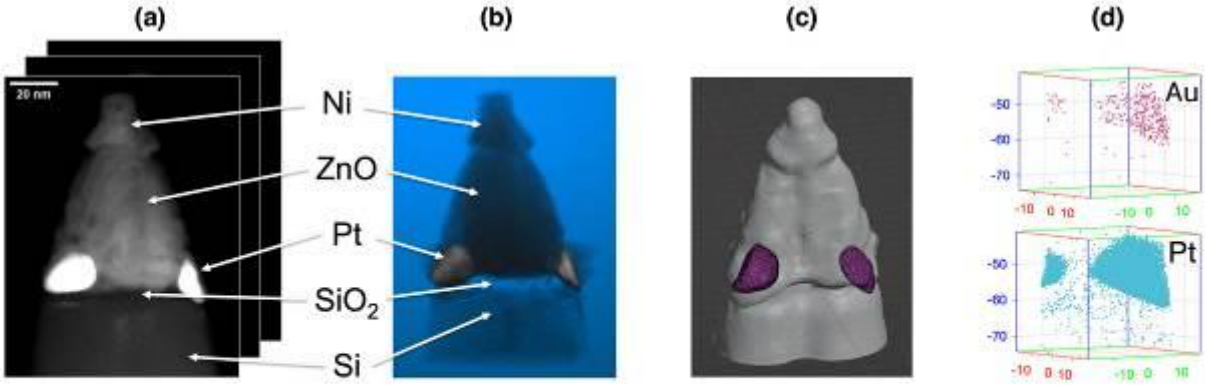


Figure 2. Correlative dataset overview: (a) 360°-ET tilt series; (b) Slice through 360°-ET reconstruction showing Pt particles covered in ZnO; (c) 3D isosurface with segmented Pt particles; (d) 360°-ET-corrected APT map revealing Pt particle content containing a trace of Au.

MS1.P47
Electron tomography at sub-nanometer resolution to uncover the nanoscale pore structure of carbon catalyst supports

R. Girod[1,2], V. Tileli[2]

[1]University of Antwerp, EMAT, Department of Physics, Antwerp, Belgium
[2]Ecole Polytechnique Fédérale de Lausanne, Institute of Materials, Lausanne, Switzerland

Introduction: Carbon black electrocatalyst supports are central components of proton exchange membrane fuel cells (PEMFCs). They provide a large surface for catalyst dispersion and tunable porosity for reactant diffusion. Pores may also be internal, hosting large fractions of the catalysts and reducing their mobility and degradation [1]. However, internal pores also limit accessiblity and mass-transport performance [2]. Characterization is highly needed to understand the structural origin of this tradeoff, but remains challenging due to the the partially-(dis)ordered, three-dimensional (3D) nature of carbon blacks, their beam-sensitivity, and their sub-nm dimensions.

Objective & Methods: Here, we aimed to characterize the pore structure of high-surface area supports in 3D using high-resolution, full-range electron tomography. We studied Ketjenblack carbons with 20 wt% Pt nanocatalysts (Pt/C, TEC10E20E, Tanaka, Japan). For sample preparation, tungsten microprobes where fabricated using electropolishing and primed with Nafion D2021 to facilitate adhesion of particles (**Fig.1**). Electron tomography was performed in low angle annular dark field (LAADF) scanning transmission electron microscopy (STEM) mode at a probe-corrected ThermoFisher Scientific (TFS) Titan Themis, and in high resolution (HR)TEM mode at a TFS F20. All acquisitions were done at 200 kV. Reconstructions were computed with the Astra toolbox and an in-house code for total-variation minimization (TVM).

Results: Optimization of the sample preparation showed that probes with ~µm-sized apex were ideal to obtain particles well positioned for acquisition of tilt-series spanning 180° (**Fig.1**). This, crucially, yielded 3D reconstructions with isotropic resolution in the directions perpendicular to the tilt-axis, i.e., without missing wedge (**Fig.2**). Comparison of acquisition modes showed that a tradeoff between resolution and beam-induced damage can be achieved for both TEM and STEM imaging, while TVM achieved better quality than conventional reconstruction algorithms. In the reconstructions, individual carbon walls are clearly visible, and the interior morphology of the supports could be studied in detail (**Fig.2**). Across five reconstructions, a core-shell morphology was typically observed, with pores up to > 10 nm in the center, and slit-shaped pores, on average < 1 nm in width, in the shell. Furthermore, openings between the interior pores and the exterior space were found to be rare, also around 0.8 nm in diameter. These findings show that the diffusion pathways to the interior catalysts are smaller and more complex than typically assumed, and describe a clear bottleneck to mass-transport in PEMFCs [3].

Conclusion: We have shown that full-range electron tomography achieves sub-nm resolution on carbon catalyst supports, clearly visualizing their 3D nanoporosity. This approach is transferable to a range of partially ordered and light materials including, but not limited to, all other nanocarbon-based supports for energy conversion electrocatalysts.

1. Lazaridis, T. & Gasteiger, H. A. *J. Electrochem. Soc.* **171**, (2024)
2. Girod, R., *et al*. *Nat Catal* **6**, (2023)
3. Girod, R. & Tileli, V. *Submitted* (2025)

Fig.1: a, Acquisition geometry. **b**, SEM micrograph of an electropolished probe for full-range electron tomography with Pt/C catalysts

Fig.2: a, HRTEM image and **b**, orthoslice through the corresponding 3D reconstruction of a Pt/C particle. **c,** Isosurface rendering of the segmented reconstruction

Fig. 1

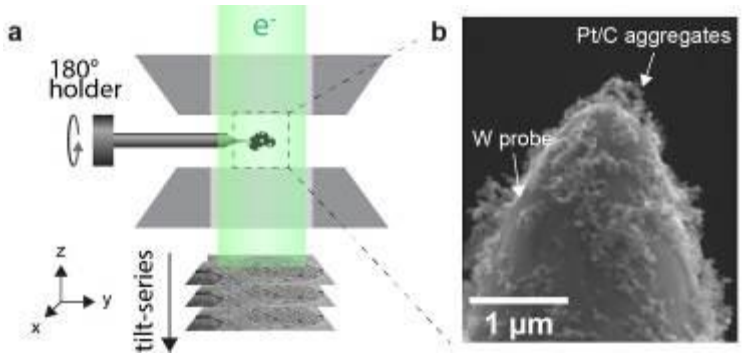
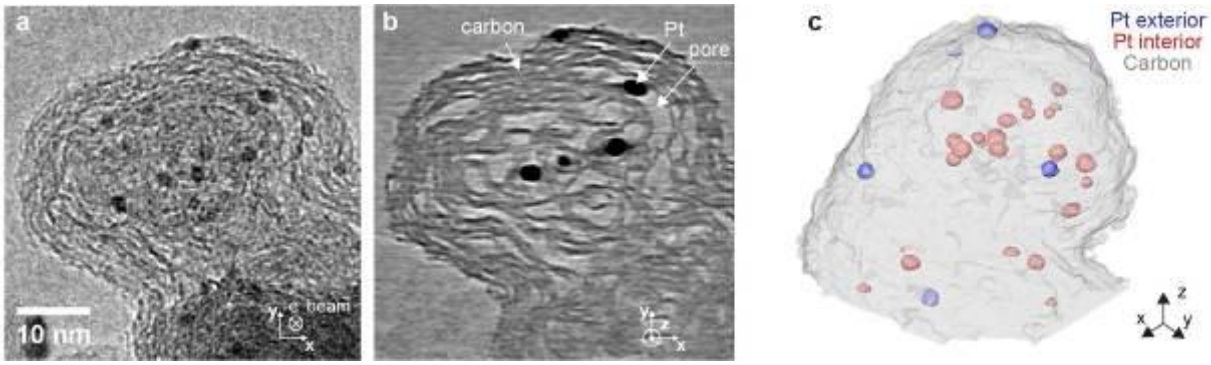


Fig. 2



MS1.P48
TiO_2 supported Ir catalysts – A strategy for improved stability and insights from SEM, TEM and EELS

Y. Bang[1], R. Aymerich Armengol[2], J. Bae[3], J. Lim[3], C. Scheu[1]

[1]Max-Planck-Institute for Sustainable Materials, Düsseldorf, Germany
[2]Technical University of Denmark, Kongens Lyngby, Denmark
[3]Kangwon National University, Chemistry, Gangwon-do, South Korea

Introduction
The transition to eco-friendly energy solutions, such as solar and fuel cells, is crucial to mitigate global warming. However, efficient energy carriers and storage systems are needed for the industry of these alternatives. Hydrogen stands out as an ideal energy carrier due to its ability to be stored, transported, and produced without carbon emissions.1) To generate hydrogen, the development of high-performance electrocatalysts is essential. Among them, Ir-based catalysts demonstrate exceptional oxygen evolution reaction (OER) performance but suffer from high costs and stability limitations.2) In this work, it is addressed to enhance the stability of Ir while reducing its loading for cost efficiency by employing TiO_2 as a support material.

Objectives
The development of cost-effective and durable Ir-based electrocatalysts is important for hydrogen industry. In this study, TiO_2 is used as a support material to enhance the stability and efficiency of Ir-based catalysts. TiO_2 plays a significant role in improving catalyst perspective by preventing Ir particle agglomeration and making high surface area via Ir dispersion, leading to an increased number of active sites for the OER. This improved dispersion enables a reduction in Ir loading. To get the insights of Ir/TiO_2 electrocatalyst and the Ir state, scanning electron microscopy (SEM), (scanning) transmission electron microscopy ((S)TEM), energy dispersive X-ray spectroscopy (EDS) and electron energy-loss spectrometry (EELS) are used.

Materials & methods
Ir/TiO2 catalyst was synthesized on fluorine doped tin oxide coated glass slide (FTO) using a facile hydrothermal approach with different amount of Ir precursor. After synthesis, films were prepared for SEM by using copper tape attached to an aluminium SEM holder. ZEISS merlin FE-SEM (field emission gun) was applied for examining the morphology of samples. For the (S)TEM analysis and EELS, the Ir/TiO_2 nanostructures were collected on a TEM holey carbon-copper (C/Cu) grid. An image Cs-corrected Titan Themis 80-300 and a probe corrected Titan Themis from Thermo Fisher was used for the (S)TEM and EELS examination.

Results
SEM images reveal that Ir/TiO_2 nanostructures form an assembly of faceted nanowires on the FTO substrate. Cross-sectional SEM analysis indicates that nanowire length increases with Ir content. High-resolution (S)TEM analysis confirms that the nanostructures exhibit a rutile crystalline structure, regardless of Ir concentration, and possess a Wulff shape with finger-like defects at the top of the nanowires. Additionally, EDS and EELS provide insights into the Ir/TiO_2 composition and chemical state.

Conclusion
To minimize the Ir content, TiO_2 was employed as a support material. The synthesis process revealed that the Ir content led to an increase in the nanowire length, indicating a influence of Ir loading on structural characteristics. However, all nanowires retained a rutile structure, regardless of Ir concentration. Advanced characterization techniques, such as EELS and TEM, provided deeper

insights into the structural and electronic interaction within the catalyst system, offering an understanding of Ir dispersion and its role in catalytic performance

Reference

1)Rosen, M.A. (2016). The prospects for hydrogen as an energy carrier. *Energ. Ecol. Environ.*, **1**, 10–29.

2)Kasian, O. (2021). Stabilization of an iridium oxygen evolution catalyst by titanium oxides. *J. Phys. Energy*, **3**, 034006.

MS1.P49
Low beam does analysis using quantitative backscatter electron imaging and EBSD on beam-sensitive lead-based mixed-halide perovskites

J. Mausz[1], R. de Kloe[2], Y. Gupta[3], O. Cojocaru-Mirédin[3], J. Borchert[3,4,5]

[1]Ametek GmbH, Gatan + EDAX, Weiterstadt, Germany
[2]Ametek GmbH, Gatan + EDAX, Tilburg, Netherlands
[3]University of Freiburg, Department of Sustainable Systems Engineering (INATECH), Freiburg i. Br., Germany
[4]Fraunhofer Institute for Solar Energy Systems ISE, Freiburg i. Br., Germany
[5]Cluster of Excellence livMatS @ FIT, Freiburg Center for Interactive Materials and Bioinspired Technologies, Freiburg i. Br., Germany

The overall efficiency of tandem photovoltaic devices is drastically influenced by the bandgaps of the individual layers in the tandem stack. A common method for tuning the bandgap in lead-based mixed-halide perovskites (LB-MHP) involves incorporating iodine and bromine ions at specific atomic sites. While this methods facilitates the bandgap optimization, it predisposes chemical instability and halide segregation, resulting in regions with various halide compositions. High beam dose measurements can alter or damage the sample and for that reason X-ray diffraction (XRD) and photoluminescence (PL) are often used instead [1],[2].

Linking local chemical and crystallographic information with these techniques alone has been a challenging task [1]. To overcome this gap, electron backscatter diffraction (EBSD) and quantitative backscatter electron (qBSE) analysis were used to correlate the chemical and structural information of LB-MHPs. This approach aims to facilitate the material characterization and interpretation of segregation processes in LB-MHPs.

The experiment focused on thin layers of $CsPb(Br_xI_{(1-x)})_3$ coated on Si and SiO_2 substrates. Both, fully intact coatings and samples with ongoing halide segregation were investigated. Phase identification and orientation measurements were obtained using a direct electron detection EBSD camera and Spherical Indexing in OIM Analysis 9. A dedicated low-dose backscattered electron detector with high dynamic range was employed to calibrate the electron backscatter signal with atomic number contrast.

EBSD and qBSE analysis were successfully performed on all samples. Each measurement was carried out under low beam current conditions off approx. 100 pA and 6 to 10 kV. For fully intact layers, qBSE confirmed the absence of halide segregation and indicated a Br:I ratio in agreement with the manufacturing process. Accordingly the re-indexing was carried out with the cubic $CsPb(Br,I)_3$ phase. These layers showed a grain size distribution in the order of 50 nm and a weak (111) fiber texture in the sample normal direction. During halide segregation, the grain size distribution increased to around 500 µm and distinct phases could be differentiated. EBSD patterns and spherical indexing enabled the identification of these phases as trigonal and orthorhombic. Halide redistributions were quantitatively observed through qBSE imaging and correlated with the different phase regimes.

The combination of these techniques provides a robust method for local characterization and phase identification of beam-sensitive LB-MHPs. The use of qBSE for compositional analysis using the average atomic number has great applicability for the understanding of LB-MHPs integrity and halide segregation. However, halide segregation must be handled carefully and further research is required to comprehend the details of the segregation process.

Fig. 1: Correlation index map after Spherical Indexing and NPAR

Fig. 2: Inverse pole figure map on correlation index grey scale map after Spherical Indexing

References:

[1] Knight, Alexander J., et al. "Halide segregation in mixed-halide perovskites: influence of A-site cations." *ACS Energy Letters* 6.2 (2021): 799-808.

[2] Ran, Junhui, et al. "Electron-beam-related studies of halide perovskites: Challenges and opportunities." *Advanced Energy Materials* 10.26 (2020): 1903191.

Fig. 1

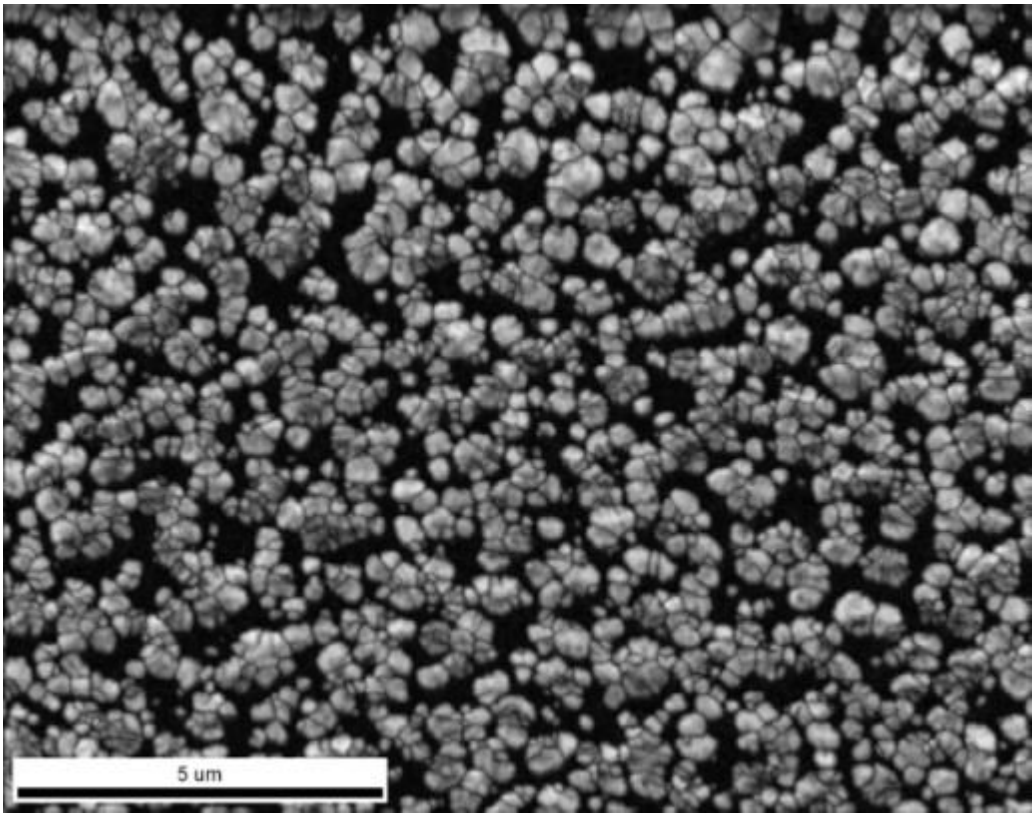
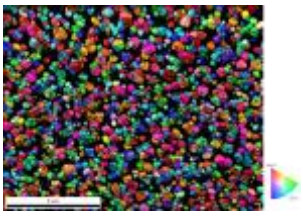


Fig. 2



MS1.P50
Influence of substrate topography on the formation of Pt nanoparticles on FTO via solid-state-dewetting

M. Dierner[1], S. Peters[1], M. Wu[1], C. Rubach[1], S. Harsha[2], R. K. Sharma[2], Z. Y. Siah[3], S. W. Ng[3], E. Spiecker[1], M. Altomare[2], J. Will[1]

[1]Fraunhofer Center for Silicon Photovoltaic, Institute of Micro- and Nanostructure Research (IMN) & Center for Nanoanalysis and Electron Microscopy (CENEM), Erlangen, Germany
[2]University of Twente, Department of Chemical Engineering, MESA+ Institute of Nanotechnology, Enschede, Netherlands
[3]Fraunhofer Center for Silicon Photovoltaic, Department of Chemistry and Pharmacy, Erlangen, Germany

Introduction

Recently, we demonstrated that Solid-State Dewetting (SSD) can be utilized to fabricate model, binder-free Pt nanoparticle (NP) electrodes on fluorine-doped tin oxide (FTO). Our findings revealed that the transformation of thin Pt films into nanoparticles influences the hydrogen evolution reaction (HER). Although this process reduces the electrochemical surface area (ECSA), the resulting Pt NPs exhibit significantly enhanced HER activity due to electronic metal-support interaction (EMSI). Charge transfer from the FTO substrate to the Pt NPs alters their electronic structure, particularly along the Pt-FTO contact line, thereby accelerating HER kinetics. Notably, smaller nanoparticles with an extended Pt-FTO contact line demonstrate even greater catalytic performance [1].

Objective

To maximize these advantages, a deeper understanding of the fundamental SSD mechanisms and NP formation on topographically structured FTO substrates is essential.

Materials and Methods

In this study, we introduce a methodology that combines plan-view sample preparation of rapid thermal annealed Pt-FTO heterostructures with in situ TEM analysis, offering detailed insights into the mechanisms and resulting morphologies of dewetted Pt particles on FTO (Fig.1).

Results

Our investigation provides a unique perspective on the early stages of the SSD process, capturing dynamic changes occurring within the first few seconds (Fig.2A). We identify a bimodal Pt particle distribution, where small nanoparticles rapidly form in the valleys, while larger particles emerge over an extended period, competing with Pt grain growth on the flat FTO facets (Fig.2B). The intrinsic FTO topography plays a crucial role in this process by: (i) inducing a shadowing effect during thin-film deposition, which leads to a reduced film thickness (<5 nm) in the valleys, and (ii) introducing local surface curvature through FTO grains, which directs Pt agglomeration into the valleys and toward the center of the flat grain facets (Fig.2B). Due to variations in the initial Pt reservoir—determined by the local Pt film thickness and the available area on valley sides versus flat terraces—the final particle size in the valleys is significantly smaller than in the flat FTO regions (Fig.3). This demonstrates that substrate topography can be strategically used to promote the formation of small nanoparticles on structured surfaces.

The presented methodology is highly versatile and can be applied to almost any dewetted system of interest. It provides insights into underlying mechanisms that remain inaccessible with conventional approaches traditionally used to investigate SSD.

[1] Harsha, Shreyas, et al. "Dewetting of Pt Nanoparticles Boosts Electrocatalytic Hydrogen Evolution Due to Electronic Metal-Support Interaction." Advanced Functional Materials 34.40 (2024): 2403628.

Fig. 1

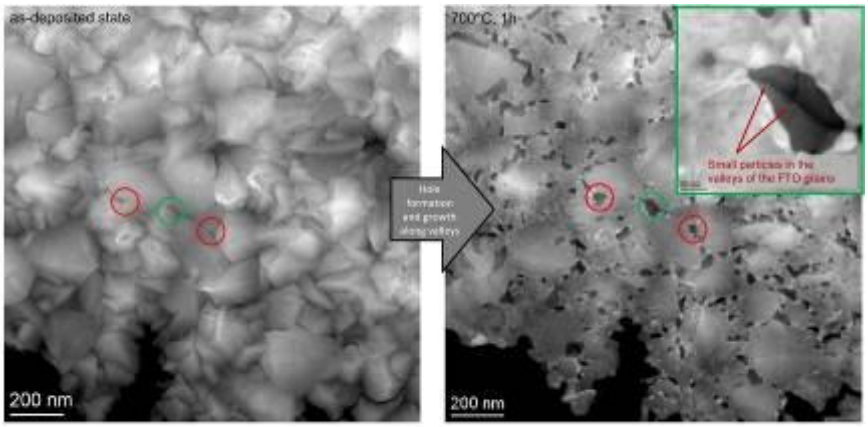


Fig.1: STEM in situ measurement showing that the hole formation and growth starts in the valleys of the FTO grains. After 1h at 700°C, directly at the valleys, already small Pt-NPs have formed.

Fig. 2

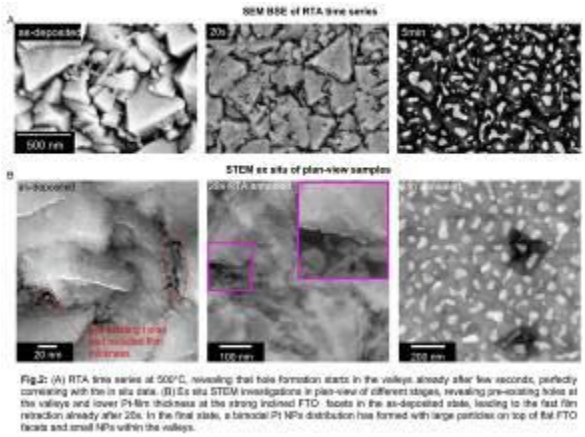


Fig.2: (A) RTA time series at 500°C, revealing that hole formation starts in the valleys already after few seconds, perfectly correlating with the in situ data. (B) Ex situ STEM investigations in plan-view of different stages, revealing pre-existing holes at the valleys and lower Pt-film thickness at the strong inclined FTO facets in the as-deposited state, leading to the fast film retraction already after 20s. In the final state, a bimodal Pt NPs distribution has formed with large particles on top of flat FTO facets and small NPs within the valleys.

Fig. 3

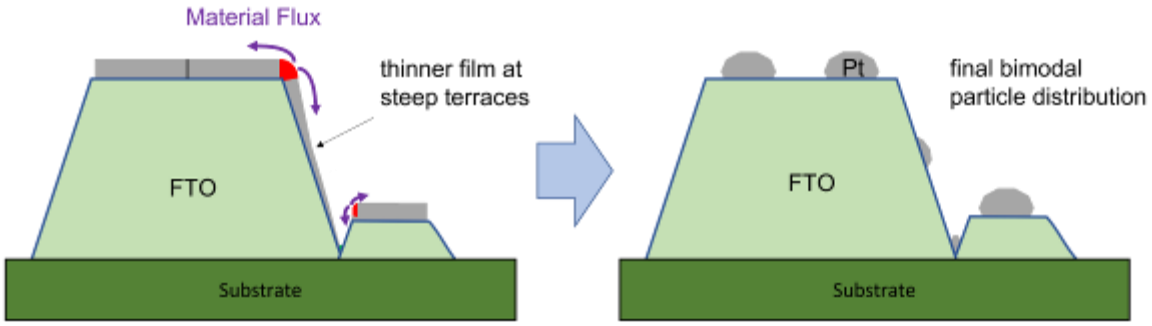


Fig.3: Model for the NP formation via Solid-state-Dewetting, extracted from the experimental in situ and ex situ plan-view investigations. The initial thinner film at the inclined FTO facets as well as topography induced surface curvatures lead to the final bimodal NPs size distribution.

MS1.P51
Insights on degradation pathways of Cu nanocubes during CO2 electroreduction with liquid-phase TEM

S. Toleukhanova[1], P. Albertini[1], R. Buonsanti[1], V. Tileli[1]

[1]Ecole Polytechnique Fédérale de Lausanne, Lausanne, Switzerland

Cu-based nanocatalysts with controlled shape and size have received considerable attention due to their ability to tailor selectivity of CO2 conversion into carbon-rich products1. However, Cu is known to rapidly deactivate and lose its selectivity during CO2 electroreduction (CO2ER) due to structural and morphological retsructuring2. Therefore, it is crucial to understand the catalyst degradation pathways under CO2ER conditions to aid in the further design and development of selective catalysts with improved stability and long-term activity. Herein, we use liquid-phase transmission electron microscopy (LPTEM) to obtain real-time insight into the structural and morphological evolution of Cu nanocubes (NCs) in neutral electrolyte under CO2ER-relevant potential.

We employed energy-filtered TEM along with direct electron imaging to obtain nanoscale insights into Cu NCs degradation processes occurring during CO2ER. Electrochemical chips with glassy carbon (GC) working electrode (WE) were fabricated in-house3. For the experiments, the bottom spacer and top electrochemical chips were air plasma treated. Cu NCs were drop-casted onto the electron beam transparent membrane region of the WE. The electrochemical chip was then assembled with the spacer chip and sealed with o-rings into the tip of TEM holder. CO2ER was driven in a CO2-saturated 0.1M KHCO3 electrolyte by applying -0.8 VRHE to the WE. In TEM, real-time recording was performed at 200 kV at a frame rate of 20 fps and an electron dose rate of 60 e-nm- 2s- 1. The obtained images were denoised and synchronized with electrochemical data to correlate the restructuring of the catalyst with the current profile.

The in situ TEM studies reveal that 40 nm Cu NCs undergo spontaneous oxidation under open-circuit conditions, forming a thin Cu2O layer on the surface before the start of CO2ER measurements. Synchronized image sequence and electrochemical data show that Cu NCs follow multiple degradation pathways in parallel, while segmentation reveals the kinetics of catalyst degradation. The most statistically prevalent mechanisms are dissolution and fragmentation. The majority of NCs exhibit mild dissolution, seemingly related to the reduction of surface oxide. This dissolution leads to more rounded outer corners of NCs and is accompanied by redeposition and growth of spherical-shaped secondary particles a few nanometers in size. Some of these redeposited particles tend to attach to the high-energy sites of the primary NCs, supposedly via an oriented attachment process. Meanwhile, some of the Cu NCs, consistent with previously reported bulk catalytic studies4, undergo fragmentation through the detachment of nanoclusters from the NCs' surface. Nanocubes with defects and cracks appear more prone to fragmentation. In addition to the two primary degradation pathways, we also observed that a minority of NCs undergo restructuring via dissolution followed by growth, while others remained stable.

In conclusion, LPTEM studies of Cu-based catalysts under CO2ER conditions provide meaningful insights into the degradation processes in accordance with earlier reported bulk catalytic system studies.

1. De Gregorio, G. L. *et al. ACS Catal.* **10**, 4854–4862 (2020)
2. Popović, S. *et al. Angew. Chem. Int. Ed.* **59**, 14736–14746 (2020)
3. Vavra, J. *et al. Angew. Chem. Int. Ed.* **60**, 1347–1354 (2021)
4. Huang, J. *et al. Nat. Commun.* **9**, 3117 (2018)

This work was supported by NCCR Catalysis funded by SNSF (grant number 180544)

MS1.P52
Performance degradation mechanisms of TiO_2 nanorod photoanode during the photoelectrochemical water splitting in different electrolytes process by *in situ* ICP-MS characterization

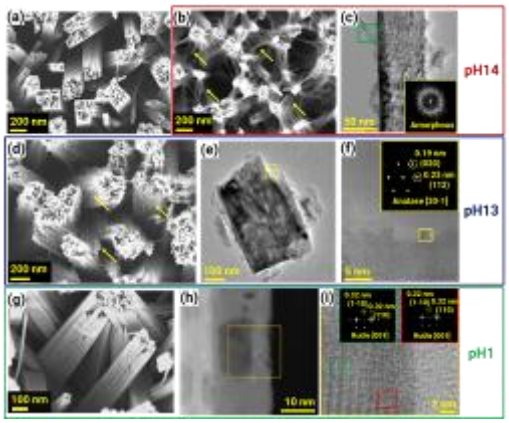
Y. Jiang[1], C. Scheu[1], S. Zhang[1]

[1]Max-Planck-Institute for Sustainable Materials, Düsseldorf, Germany

Introduction:
Hydrogen is one of the most desirable energy carriers due to its abundance, high energy density and reaction product of water. TiO_2 photoanodes have been widely used in photoelectrochemical water splitting and often considered stable during the reaction.
Objectives:
To reveal the performance degradation mechanism of TiO_2 photoelectrodes, we applied scanning electron microscopy (SEM) and transmission electron microscopy (TEM) to characterize their structural evolution after long term operation in different electrolytes. Moreover, by using an illuminated scanning flow cell (iSFC) coupled to inductively coupled plasma mass spectrometry (ICP-MS),[1] the stability of TiO_2 photoelectrode was investigated during photoelectrochemical water splitting.
Materials and methods:
Herein, we successfully prepared TiO_2 nanorod by hydro-thermal synthesis on a fluorine-doped tin oxide substrate.[2] Long-term photoelectrochemical measurements were conducted to measure the stability in alkaline electrolyte at pH14 and pH13, as well as acidic electrolyte at pH1. XPS, XRD, SEM, TEM and STEM/EDS are also employed to characterize the morphology and structure of the photoanode.
Results:
As shown in Fig. 1a, the photoanode is composed of TiO_2 nanorods with diameter of ~200 nm. After long-term measurement at pH14, the performance of TiO_2 is decreased and the surface of TiO_2 is formed with a layer of amorphous TiO_2 indicated by the yellow arrows in Figure 1b-c. New substance is also formed on the surface at pH13 and STEM result indicates that the formed substance is anatase TiO_2 nanoparticle explaining the stable performance as can be seen from Figure 1d-f (also indicated by the yellow arrows). iSFC results show no dissolution in alkaline electrolyte. While the morphology of TiO_2 photoanode is changed from smooth to porous structure at pH1 (Figure 1g) after above 60 hours measurement. The performance is degraded. The degradation rate is decreasing over time. iSFC result shows that TiO_2 suffers from dissolution at pH1 from the beginning and the dissolution rate is decreased with decreasing performance rate. No substance is formed on the surface as shown in Figure 1h-i.
Conclusion:
This study reveals the performance degradation mechanisms of TiO_2 photoanode in different electrolytes. At pH14 the performance of TiO_2 is degraded resulting from the redeposition of amorphous reduced TiO_2, at pH13, the performance of TiO_2 is stable due to the redeposition of anatase TiO_2 nanoparticles, and at pH1, TiO_2 suffers dissolution at the beginning because of the defective sites and keeps stable afterwards. . The mechanistic understanding is essential for the design and development of efficient and stable photoanodes.
Figure 1. SEM image of TiO_2 before (a) and after long-term measurement at pH14 (b), bright field (BF)-STEM image of TiO_2 after long-term measurement at pH14 (c), SEM image (d) and BF-STEM images (e, f) of TiO_2 after long-term measurement at pH13, SEM image (g) and BF-STEM images (h, i) of TiO_2 after long-term measurement at pH1.
References:
[1] J. Lim, S.-H. Kim, R. Aymerich Armengol, O. Kasian, P.-P. Choi, L. T. Stephenson, C. Scheu. Angewandte Chemie International Edition, 59 (2020) 5651-5655.

[2] N. Cheng, L. Kanzler, Y. Jiang, A. M. Mingers, M. Weiss, C. Scheu, S. Zhang. ACS Catalysis, 14 (2024) 10789-10795.

Fig. 1



MS1.P55
Microstructural influence of gold interlayer by inhomogeneous sodium deposition in anode-free all solid-state batteries via *in situ* TEM investigation

Z. Ding[1], T. Ortmann[2], M. Rohnke[2], J. Janek[2], C. Kübel[1,3,4,5]

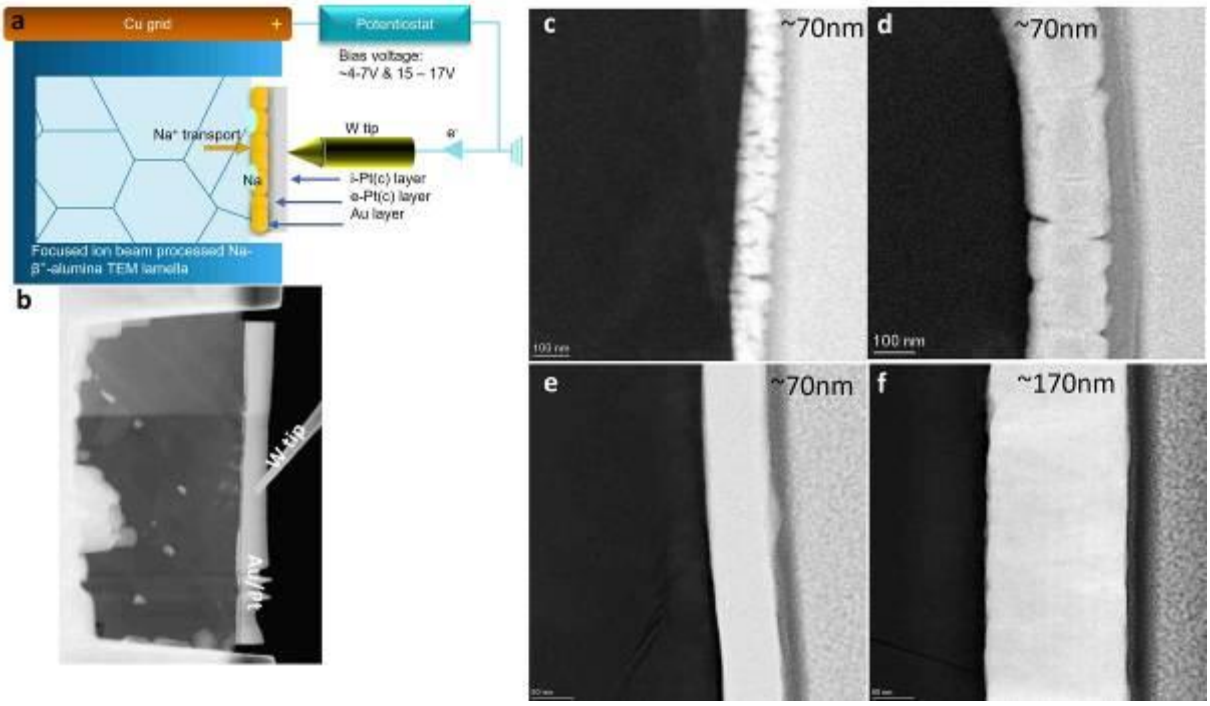
[1]Karlsruhe Institute of Technology, Institute of Nanotechnology, Eggenstein-Leopoldshafen, Germany
[2]Justus Liebig University Gießen, Institute for Physical Chemistry, Giessen, Germany
[3]Karlsruhe Institute of Technology, Karlsruhe Nano Micro Facility (KNMFi), Eggenstein-Leopoldshafen, Germany
[4]Technical University of Darmstadt, Darmstadt, Germany
[5]Helmholtz Institute, Karlsruhe, Germany

Anode-free solid-state batteries are a transformative energy storage solution, combining environmental compatibility with ultrahigh energy density and enhanced safety. Sodium is gaining additional commercial traction due to its natural abundance and low cost. To minimize the filament growth and achieve uniform sodium deposition at the electrolyte–current collector interface, a gold (Au) nano-interlayer has been introduced to reduce nucleation energy and enhance sodium diffusion. However, the impact of its microstructure and its evolution during sodium deposition remain unclear, particularly regarding its potential contribution to cyclic performance.

In this study, a TEM-compatible Cu | Na-β""-alumina | Au(Pt) multilayer system was fabricated using focused ion beam (FIB) milling (FEI Strata 400S, Zeiss Auriga 80). Sodium deposition at the Au interlayer was induced by applying an electric bias via a scanning tunneling microscopy (STM) nanotip (ZEPtools Technology Company), as illustrated in **Figure 1a–b**. The influence of Au interlayer microstructure—such as thickness, grain size, and porosity (as shown in **Figure 1c-f**) —on inhomogeneous sodium deposition was investigated. Additionally, high bias voltage was found to possibly disrupt the interlayer"s structural continuity, affecting its protective function and cyclic performance. This in-situ TEM study, coupled with spectroscopy techniques, highlights the critical role of interlayer engineering in optimizing anode-free solid-state battery performance.

Figure 1. a. illustration of the in-situ TEM setup; b. HAADF-STEM image of the overview of the setup; c-d; magnified HAADF-STEM image of the pristine Au nano-interlayer with different microstructure.

Fig. 1


a
Cu grid
+
Potentiostat
Bias voltage:
~4-7V & 15 – 17V
Na+ transport
W tip
e-
Na
i-Pt(c) layer
e-Pt(c) layer
Au layer
Focused ion beam processed Na-β''-alumina TEM lamella
b
W tip
Au/Pt
c
~70nm
100 nm
d
~70nm
100 nm
e
~70nm
f
~170nm

MS1.P56
In situ TEM-based selected area electron diffraction for determination of physicochemical catalyst properties

T. Zemke[1], B. Fritsch[2], D. Wang[3], R. Spruit[4], P. J. Lobpreis[1], A. Hutzler[5], B. Butz[1]

[1]University of Siegen, Engineering, Siegen, Germany
[2]Forschungszentrum Jülich GmbH, Jülich, Germany
[3]Karlsruhe Institute of Technology, Karlsruhe, Germany
[4]DENSsolutions, Delft, Netherlands
[5]Helmholtz Institute Erlangen-Nürnberg, Erlangen, Germany

Catalysis plays a pivotal role in modern chemical processes, enabling reactions to occur under milder conditions and with greater efficiency by lowering activation energies. This capability is essential not only for industrial synthesis but also for addressing critical energy and environmental challenges. In particular, platinum group metal catalysts have emerged as leading candidates in applications ranging from methane production to the mitigation of carbon monoxide (CO) pollution due to their exceptional activity and selectivity.1,2

In this study, we explore the dynamic local processes of platinum group metal catalysts under operational conditions to establish clear correlations between their physicochemical properties and catalytic performance. Our investigation is motivated by the recognition that a catalyst"s local structure and morphology are crucial determinants of its efficiency. To probe these aspects, we employ advanced in-situ Transmission Electron Microscopy (TEM) techniques, which provide real-time insights into the catalysts" behavior during gas-phase reactions. By integrating TEM with Selected Area Electron Diffraction (SAED), we capture subtle yet significant changes in reciprocal space, allowing us to monitor variations in the crystal lattice as they evolve in response to reaction conditions.3,4

The experimental framework is designed to systematically assess how structural dynamics influence the catalysts activity, particularly under exothermic reaction conditions that are typical in energy conversion processes. The in-situ TEM approach is uniquely suited for this task because it enables the direct observation of transient phenomena such as phase transformations, and surface reconstructions. By correlating these dynamic processes with the catalysts performance metrics, our study provides a comprehensive understanding of how structural and morphological changes can enhance or impede catalytic efficiency.

Our findings indicate that the local structural attributes—such as crystallographic evolution — significantly influence the kinetics and thermodynamics of the reactions under study. The high sensitivity and reproducibility of the in-situ TEM method allow us to link observable exothermic reaction events with corresponding alterations in the catalyst's structure. This correlation not only validates the robustness of our characterization technique but also offers valuable insights into the underlying mechanisms that drive catalytic activity in platinum group metals.

In summary, this work integrates catalysis with a detailed analysis of platinum group metal catalysts using state-of-the-art in-situ TEM techniques. Our systematic investigation reveals how local structural dynamics during gas-phase reactions impact catalyst performance, paving the way for the rational design of more efficient and durable catalysts. The insights gained from this study have broad implications for energy applications and environmental remediation, underscoring the importance of advanced, real-time characterization tools in the development of next-generation catalytic materials.

[1] Journal of Catalysis, Volume 98, Issue 1, 1986, Pages 166-177, ISSN 0021-9517
[2] Electrochimica Acta, Volume 47, Issues 22–23, 2002, Pages 3595-3609, ISSN 0013-4686
[3] Ultramicroscopy, Volume 176, 2017, Pages 161-169, ISSN 0304-3991

[4] Ultramicroscopy, Volume 235, 2022, 113494, ISSN 0304-3

MS 2: Metals and alloys

MS2.01(inv)
Expanding the capabilities of the scanning electron microscope – Diffraction, imaging, and *in situ* testing

D. S. Gianola[1]

[1]University of California Santa Barbara, Materials, Santa Barbara, United States

Defects in crystalline solids, as well as their atomic microenvironments, play a central role in plastic deformation. Evidence is also emerging of confined phases that remain anchored to crystalline defects including planar faults, grain boundaries and dislocations. Here, we highlight recent developments in defect characterization across a suite of electron microscopy modalities, including both TEM and SEM platforms, the latter of which offers versatility for in-situ testing. We further demonstrate how information encoded in diffraction patterns collected using SEMs is amplified by a new generation of direct electron detectors that enable acquisition of high-fidelity patterns that can be used for defect characterization. We will show how these techniques can be employed for experiments to study the nature of dislocations in structural metals and alloys, by way of transmission (both imaging and scanning diffraction) and electron backscattered diffraction (EBSD) modalities.

Using EBSD, we introduce a framework for characterizing dislocations across a range of microstructures using orientation-adaptive virtual apertures that enable the generation of virtual images tied to specific diffraction conditions. This approach facilitates the high-throughput determination of Burgers vectors owing to the anisotropic encoding of the defect strain and local orientational field within the diffraction patterns. We discuss these approaches in the context of developing a wide suite of characterization platforms to address the range of length scales that govern the properties, performance, and degradation of metals and alloys.

MS2.02(inv)
Unraveling ordering phenomena in alloys using advanced TEM techniques

L. Vogl[1], P. Schweizer[1], S. Chen[2], T. Li[2], D. Byrne[3], S. Mills[3], D. Liu[3], F. Allen[3], A. Sharma[4], J. Michler[4], G. Dehm[1], A. Minor[3]

[1]Max-Planck-Institute for Sustainable Materials, Structure and Nano- / Micromechanics of materials, Düsseldorf, Germany
[2]George Washington University, Washington D.C., United States
[3]University of California, Berkely, CA, United States
[4]Swiss federal laboratories for materials science and technology, Thun, Switzerland

The microstructure has a tremendous impact on the properties of alloys. With the increasing number of elements in combination with nanostructuring approaches, ordering phenomena in alloys are becoming more prominent. It has been shown that even slight microstructural inhomogeneities have a significant impact on the overall performance. Understanding atomic arrangements under different boundary conditions allows us, as a next logical step, to leverage this knowledge to tune materials properties through atomic scale manipulation.

In this talk, I will give a comprehensive overview of advanced Transmission Electron Microscopy (TEM) analysis to study ordering phenomena across different length scales: from short-range ordering (SRO) within solid-solution lattices to the formation of intermetallic phases. In order to cover the broad range of ordering phenomena, the analyzed material systems range from binary alloys to multicomponent systems with increasing compositional complexity.

For the dedicated TEM analysis, small scale model systems have been created to study the transition from solid-solution to the formation of ordered domains via *in situ* heating experiments. Advanced diffraction techniques (4DSTEM) allow us to characterize locally the microstructure, giving us the chance to analyze otherwise hardly detectable nano-domains. In combination with spectroscopy e.g. Energy-Dispersive X-ray spectroscopy (EDS) compositional inhomogeneities can be revealed and linked to microstructural differences. The gained insights into microstructural control can now be used to tailor the mechanical properties of nanostructures in respect to their intended applications. *In situ* mechanical TEM experiments of samples with varying degree of ordering demonstrate the transition from slip to twinning as a function of microstructure.

While long-range ordering describes an ordered atomic arrangement over extended lattice periods, SRO is referred to the next atomic neighboring and describes the formation of preferred pairs (first-nearest neighbor/second nearest neighbor). Diffuse intensities between sharp Bragg discs can be revealed by Energy Filtering (EF) 4DSTEM which opens up a unique strategy to analyze diffraction phenomena on an unprecedented scale. Based on atomistic structural models, virtual 4DSTEM datasets are acquired, that are used as guideline for interpretation as short-range ordering (SRO) motifs. Building on these results, distinct irradiation experiments have been conducted to provoke an atomic rearrangement.In future, correlative Electron Energy Loss Spectroscopy (EELS) measurements will be performed, focusing on the energy loss near edge structure to provide further information on the specific bonding environment.

Covering a broad range of ordering phenomena, these insights gained through advanced TEM analysis not only enhance our fundamental understanding of atomic arrangements in alloys but also open new pathways for the precise engineering of material properties at the atomic scale.

MS2.03
Advanced phase characterisation of galvanised high-strength steel coatings – Overcoming challenges with EBSD and PED

A. Minenkov[1], A. Brozyniak[1], M. Krenn[1], P. Kürnsteiner[1], H. Groiß[1]

[1]Johannes Kepler University, CD Laboratory for Nanoscale Phase Transformations, Center for Surface and Nanoanalytics, Linz, Austria

Zn-based coatings are highly relevant for the corrosion protection of modern high-strength steels. However, factors like temperature variations during production and the abundance of alloying elements in the steel can impact the Fe-Zn-phase structure during galvannealing and cause unfavourable precipitates, altering the desired material properties. Therefore, accurate identification of the phase structure at the nanoscale is vital for further advancement in material design but remains a significant challenge for sensitive Zn-Fe compounds.

To address this obstacle, we optimised TEM sample preparation, preserving the material's pristine properties [1]. Due to Zn-based phase sensitivity to Ga-FIB cutting, we suggest a low-temperature Xe-PFIB approach [2]. For industrial samples, TEM ensures accurate and site-specific insights but is not statistically representative. Conventional EBSD, in turn, provides statistical crystallographic information, but fails to distinguish structures with similar symmetry like the different cubic Fe-Zn phases Γ and Γ_1. We present an enhanced EBSD/TKD analysis by pattern matching to address this challenge, with the results refined by TEM.

This approach was applied to different Zn-coated steels, including nanoprecipitates in an Fe-Zn matrix. EBSD analysis, augmented with pattern matching, was applied to phase-map bulk samples and then extended to TKD mapping of thin lamellae, showing good agreement with complementary SAED, PED, HRTEM, and STEM EDXS. In particular, PED combined with zero-loss filtering improves the signal-to-noise ratio and the clarity of the obtained diffraction patterns and thus the phase identification at the micro- and nanoscale.

With our workflow it was possible to trace the phase evolution in low- and high-Si steels at different stages of galvannealing [2,3]. In contrast to low-Si samples, in high-Si steel, the δ phase is more prominent, while the formation of expected Γ/Γ_1 is suppressed. Additionally, Si oversaturation can trigger the appearance of Fe-Si-Al-based nanoprecipitates, identified as $AlFe_2Si$. In most cases, EBSD/TKD with pattern matching indexing showed remarkable results, reliably distinguishing phases with similar crystal structures. The validation of remaining difficult-to-identify regions via TEM revealed a high defect density as the reason for unreliable pattern matching.

In summary, low-temperature FIB preparation is crucial for accurate Zn-Fe coating characterization. EBSD/TKD pattern matching combined with TEM is a valuable tool for identifying the general coating microstructure. PED drastically enhances phase identification in such a complex system and provides deeper insights into structural orientation relationships. Our results show that advanced characterization techniques are essential for understanding phase interactions and improving material performance, which is relevant for both fundamental research and industrial applications.

[1] A. Minenkov et al., Towards a dependable TEM characterization of hot-dip galvanized steels with low and high Si content, Mater. Des. 227 (2023) 111684.

[2] A. Minenkov et al., Nanophase Identification via Correlative Transmission Electron Microscopy: A Case Study of Galvannealed Advanced High-Strength Steel, Mater. Des. 251 (2025) 113696.

[3] A. Minenkov et al., Interaction and evolution of phases at the coating/substrate interface in galvannealed 3rd Gen AHSS with high Si content, Mater. Des. 237 (2024) 112597.

MS2.04
Revealing extreme variations in local deformation via 4D-STEM-based strain mapping in nanocrystalline gold

L. Schretter[1], J. Eckert[1,2], C. Gammer[1]

[1]Austrian Academy of Sciences, Erich Schmid Institute of Materials Science, Leoben, Austria
[2]Montan University Leoben, Chair of Materials Physics, Leoben, Austria

Nanocrystalline (nc) materials are of great interest due to their high strength and enhanced ductility. However, as grain size decreases below a critical threshold, deformation shifts from dislocation-mediated processes to grain boundary (GB)-dominated mechanisms, resulting in mechanical softening. Advances in molecular dynamics simulations have shed light on these size-dependent behaviors. While in-situ transmission electron microscopy (TEM) allows for direct observation of GB migration, its utility is limited by alignment constraints. An alternative, 4D scanning transmission electron microscopy (4D-STEM) with automated crystal orientation mapping (ACOM), offers high-resolution visualization of grain rotation and sliding. Nevertheless, experimental data on nanoscale elastic strain fields at arbitrary grain boundaries, crucial for understanding deformation, remain limited.

This study aims to develop a new routine to map the nanoscale strain in polycrystalline materials, facilitating the measurement of strain fields and grain rotations during in-situ deformation of polycrystalline materials with a resolution of 2 nm.

To demonstrate the technique a 50 nm thick nanocrystalline gold (Au) thin film is used. The sample was produced by DC magnetron sputtering and subsequently underwent heat treatment at 360 °C to reduce the dislocation density present after deposition. In-situ tensile testing was conducted using a Hysitron PI 95 picoindenter capable of recording the load-displacement data during deformation. The tensile test was intermittently halted during deformation to acquire full 4D-STEM datasets. Precession electron diffraction was employed to enhance the quality of diffraction patterns: The utilization of a direct electron detector and an in-column energy filter further refines the dataset quality.

The results indicate an increase in elastic strain in the tensile direction, along with substantial grain rotations exceeding 6° within the nominally elastic regime. Deformation varies considerably among different grains, a phenomenon that cannot be solely explained by differences in grain orientation. By analyzing the acquired strain data, we traced the origin of these rotations to a combination of grain size, strain state, and initial material heterogeneities. Notably, the residual strains and dislocations present after annealing have a significant impact on grain rotation. After fracture, while global elastic strains are largely released, strong strain concentrations remain, and the grains remain rotated relative to the initial state. These results not only demonstrate the feasibility of mapping elastic strains with high precision and nanometer resolution across arbitrary grain boundaries, but they also highlight the importance of these strains for the overall deformation behavior.

In conclusion, we have developed a new routine for quantifying the deformation mechanisms in polycrystalline materials and have applied it to nc Au. The innovative combination of ACOM and 4D-STEM-based strain mapping provides a comprehensive understanding of deformation at the nanoscale. This method enables the tracking of grain rotations, local transient nanoscale strain, and grain boundary movements. The results highlight the significance of heterogenous strain states on the deformation behavior of nc metals, allowing to tune their mechanical properties.

We acknowledge support from the Austrian Science Fund (FWF) 10.55776/Y1236, 10.55776/TAI796.

Fig. 1

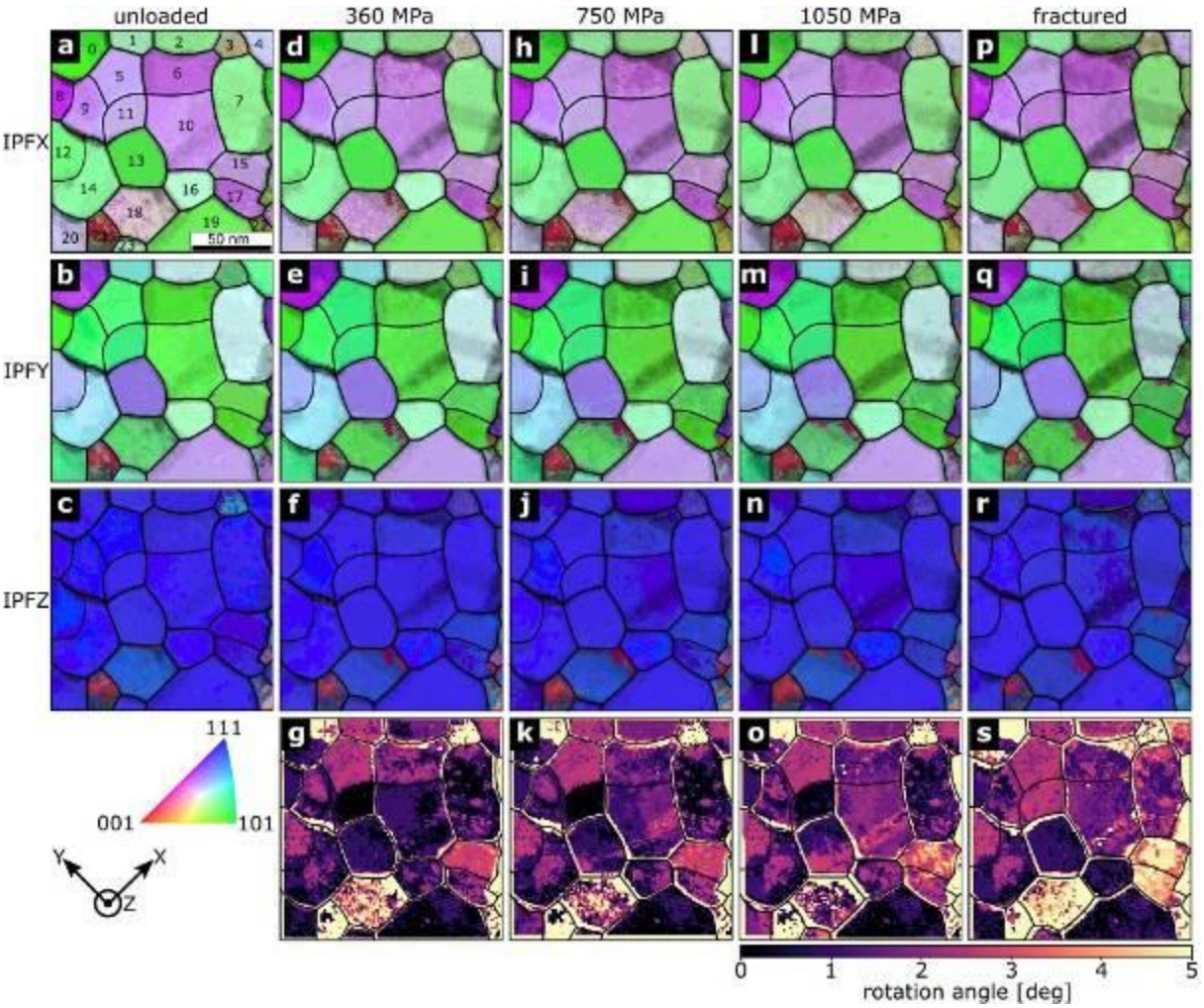
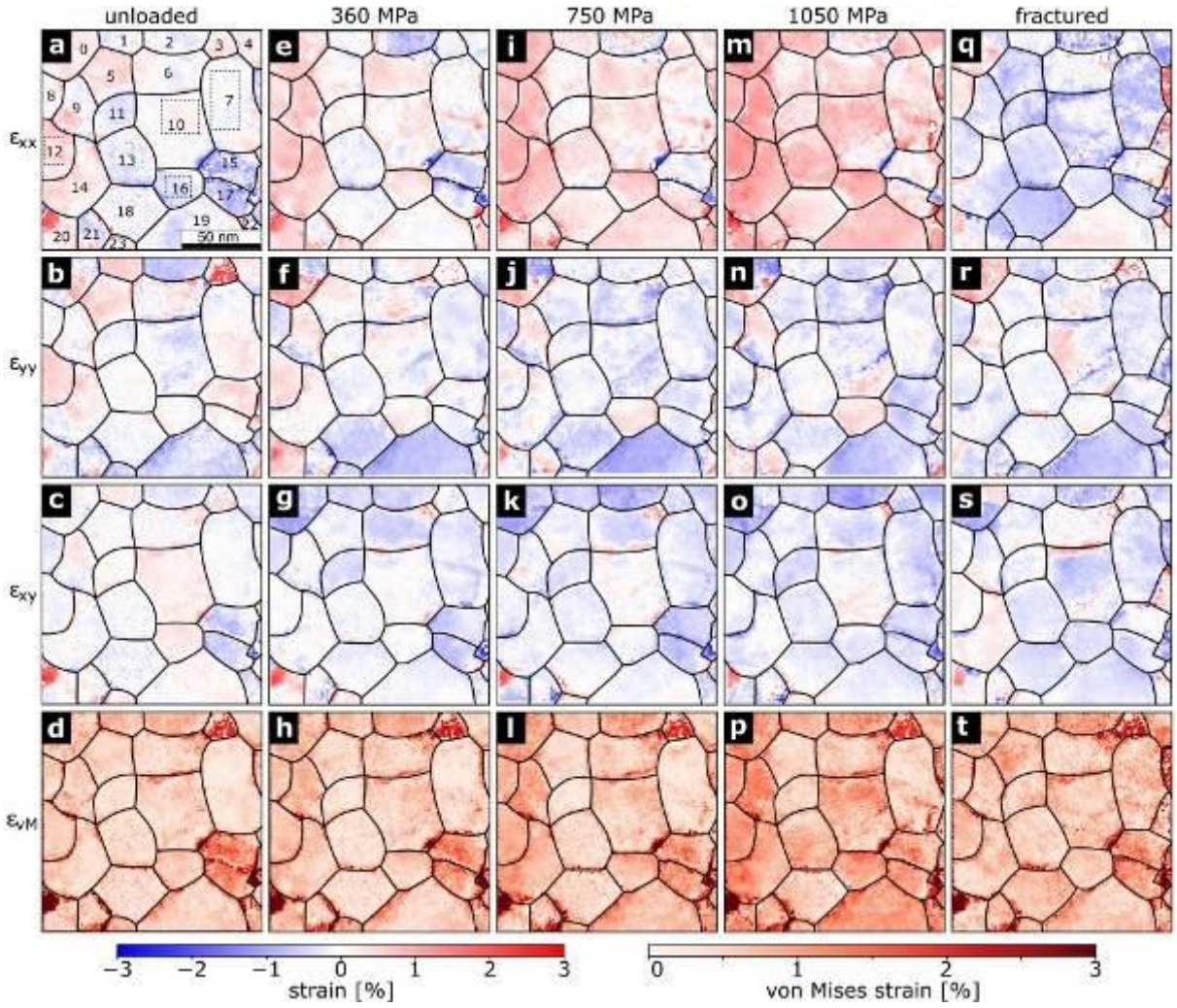

unloaded
360 MPa
750 MPa
1050 MPa
fractured
IPFX
IPFY
IPFZ
a
b
c
d
e
f
g
h
i
j
k
l
m
n
o
p
q
r
s
50 nm
111
001
101
Y
X
Z
0
1
2
3
4
5
rotation angle [deg]

Fig. 2


unloaded
360 MPa
750 MPa
1050 MPa
fractured
a
b
c
d
e
f
g
h
i
j
k
l
m
n
o
p
q
r
s
t
ε_{xx}
ε_{yy}
ε_{xy}
ε_{vM}
0
1
2
3
4
5
6
7
8
9
10
11
12
13
14
15
16
17
18
19
20
21
22
23
50 nm
−3
−2
−1
0
1
2
3
strain [%]
0
1
2
3
von Mises strain [%]

MS2.05
Mismatch design of $Au_xNi_{1-x}(111)/\alpha\text{-}Al_2O_3(0001)$ interfaces and their investigation by X-ray diffraction and electron microscopy

M. Dierner[1], J. Will[1], M. Landes[1], T. Yokosawa[1], T. Przybilla[1], S. Hübner[1], T. Zech[2], K. Götz[2], L. Lahn[3], O. Kasian[3], T. Unruh[2], E. Spiecker[1]

[1]Fraunhofer Center for Silicon Photovoltaic, Institute of Micro- and Nanostructure Research (IMN) & Center for Nanoanalysis and Electron Microscopy (CENEM), Erlangen, Germany
[2]Fraunhofer Center for Silicon Photovoltaic, Institute of Crystallography and Structural Physics, Erlangen, Germany
[3]Helmholtz Institute Erlangen-Nürnberg, Erlangen, Germany

Introduction

Metal/ceramic interfaces are of great scientific and technological importance, with applications in electroceramic devices, structural composites and catalysis [1]. In many cases, applications suffer from mechanical stresses due to a high lattice mismatch making the metal-ceramic interfaces the weak point in the device.

Objective

The usage of a binary metal alloy offers the possibility to tailor the mismatch (δ) via the alloy composition, potentially leading to a stress-free interface with improved mechanical stability.

Materials and Methods

Correlating X-ray diffraction (XRD) methods with electron microscopy techniques including SEM, EBSD, conventional TEM and high resolution (HR) iDPC-STEM, it is demonstrated how the type of interface, as well as the interface strain and chemistry can be adjusted by a compositional variation of the metal NPs on sapphire, produced via Solid-State-Dewetting of Au/Ni bilayers on Sapphire.

Results

XRD out-of-plane (OOP) scans confirmed the formation of AuNi alloy NP due to the systematic left-shift of the diffraction peaks with increasing Au concentration (Fig.1A). The spatially averaging XRD measurements are complemented by SEM-EBSD investigations of the local crystallographic texture, which are presented as orientation distribution functions (ODFs) (Fig.1B). They reveal, that (i) for a positive mismatch, the main epitaxial relation between NPs and substrate is AuNi (111)[1-10] || α-Al_2O_3 (0001)[10-10] (OR1) and (ii) switching to a negative mismatch leads to an increase of NPs with an epitaxial relation of AuNi (111)[1-10] || α-Al_2O_3 (0001)[11-20] (OR2). HRSTEM investigations of an OR2 oriented NP in plan-view, as well as HR-iDPC imaging in cross-section revealed, that a near-coincident site lattice likely constitutes an interface configuration with reduced energy and thus stabilizes OR2 (Fig.2).

To get a deeper understanding of the interface, surface sensitive XRD in-plane measurements were conducted in combination with cross-sectional HR iDPC imaging, revealing (i) a semi-coherent interface for a positive mismatch of 0.68% (55at%), indicated by a prominent diffuse background in IP XRD and moiré fringes in TEM plan-view images (Fig.3B) and (ii) a nearly coherent interface for reduced mismatch of 0.21%, marked by a decrease in diffuse background and an interface structure similar to that of lattice-matched Pd/α-Al_2O_3, as revealed by high-resolution STEM analysis (Fig.3D). Additionally, comparing the iDPC micrographs with simulated iDPC images confirmed the presence of an Al2 termination of the Al_2O_3 substrate for all samples.

Via STEM EDXS the interface chemistry was investigated, revealing that independent of the mismatch sign, interfacial Au segregation is present(Fig.4), demonstrating that in addition to stress effects [2] electrochemical interactions (Au-Al interplay) play an important role in determining the chemistry of AuNi-sapphire interfaces.

Overall, we demonstrate an elegant route to produce lattice matched supersaturated AuNi NPs on a ceramic substrate and provide insight into the structure and chemistry of the system by complementary scattering probes.

[1] Sinnott et al., Materials Science and Engineering: R: Reports 43.1-2 (2003): 1-59

[2] Herre et al., Acta Materialia 220 (2021): 117318

Fig. 1

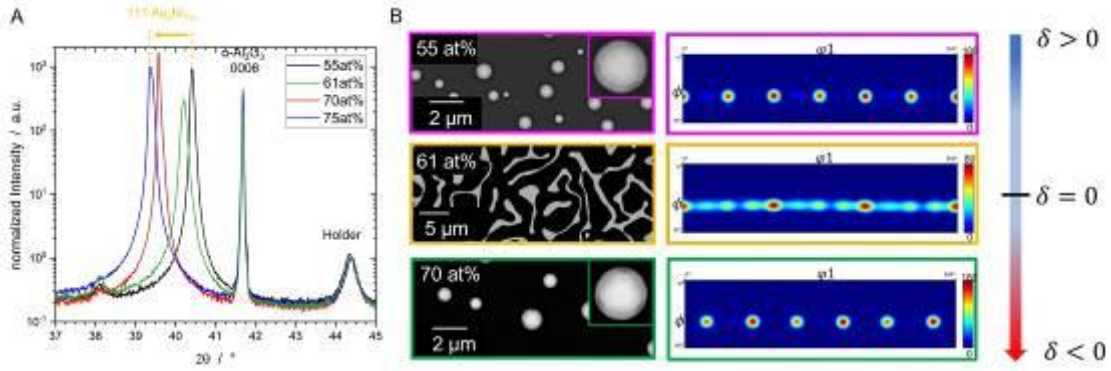


Fig.1: (A) XRD out-of-plane (OOP) measurements, showing the systematic left-shift of the Au 111 reflections, confirming the succesfull formation of AuNi alloy nanoparticles. (B) SEM-EBSD measurements revealing the local microstructure of the AuNi-Sapphire heterostructures. While OR1 is the predominant orientation relation for a positive mismatch and nearly no mismatch, a negative mismatch leads to a more pronounced OR2.

Fig. 2

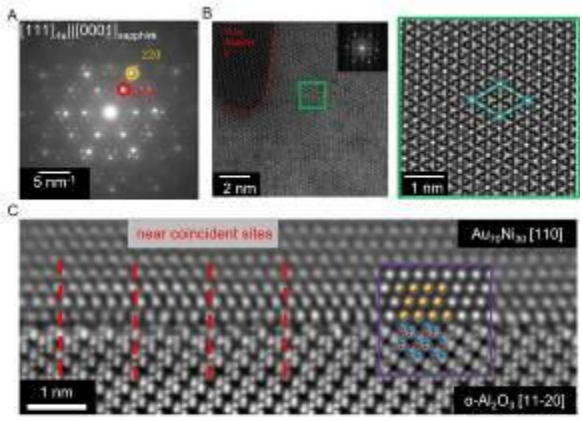


Fig.2: (A) Plan-view SAED pattern of the $Au_{70}Ni_{30}$ Sapphire heterostructure, confirming the OR1 relation between both crystals. (B) HR-STEM image recorded in plan view showing a rhomboidal cell corresponding to the unit cell of the projected near-coincidence site lattice (CSL). (C) HR iDPC cross-sectional view of the particle-substrate interface showing the interfacial near CSL as well as the Al_2 termination of the substrate.

Fig. 3

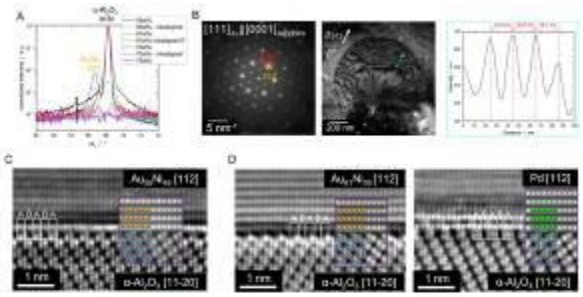


Fig.3: (A) In-plane XRD measurements. Beside the systematic shift of the 220 reflection with increasing mismatch, an increasing diffuse background occurs in particular for the 55% sample, hinting to the presence of dislocations and their strain fields at the interface. (B) SAED of a plan-view lamella from a particle with a nominal concentration of 55at%, showing the perfect alignment of the 220_{AuNi} and $30\text{-}30_{Sapphire}$ planes. On the right, a two-beam TEM DF image reveals periodic moiré fringes with an average spacing of 21 nm, consistent with a mismatch of 0.68%, as measured from IP-XRD. (C) iDPC-STEM analysis of the interface structure in cross-section, prepared via FIB milling for 55at% Au. Periodic units dividing the interface in repetitive coherent (A units) and incoherent units (B units) are detected. A closer look at the image shows that the contrast between the AuNi and sapphire planes shifts slightly from one side to the other side stemming from the residual mismatch. (D) iDPC-STEM analysis of the interface structure of 61at% and pure Pd. Here, no shift in the contrast can be detected, confirming the match of the $220_{AuNi/Pd}$ planes and the $30\text{-}30_{Sapphire}$ planes.

Fig. 4

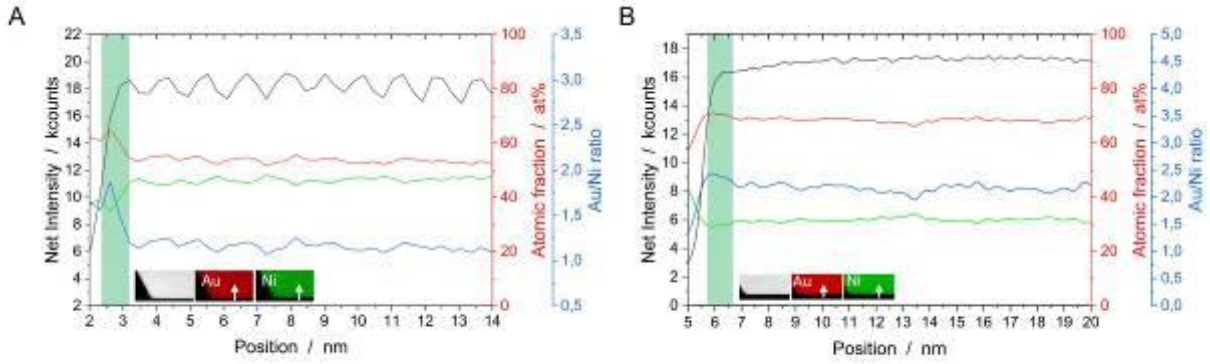


Fig.4: STEM-EDXS of (A) 55at% and (B) 70at%. For both, a positive and a negative mismatch, Au segregation is detected directly at the interface.

MS2.06
Unravelling the impact of microstructure and impurities using high-purity and recycled sources in FeTi Hydrogen storage alloys – A TEM and APT study

R. Bueno Villoro[1], Y. Shang[2], A. Saksena[3], A. Karami[3], C. Scheu[3], C. Pistidda[2], C. H. Liebscher[1]

[1]Ruhr University Bochum, Bochum, Germany
[2]Helmholtz-Zentrum Hereon, Geesthacht, Germany
[3]Max-Planck-Institute for Sustainable Materials, Düsseldorf, Germany

Hydrogen (H_2) is a promising energy carrier for a CO_2-neutral economy. However, one of the main challenges for the implementation of a large-scale H_2 economy is the difficulty to store H_2 efficiently. Solid-state hydrogen storage in metal hydrides offers several advantages over liquid or gas storage, such as higher energy density, lower explosion risk, low H_2 loss rates and potential for H_2 purification. Iron-titanium (FeTi) alloys are promising solid-state hydrogen storage materials for stationary applications due to their reversible phase transformation from FeTi to $FeTiH_x$ hydride at near-room temperature and pressure. The use of recycled source materials can reduce material costs and enable the large-scale production of FeTi. However, it may also introduce additional elements that affect the storage capacity and cyclability of the material. Understanding the impact of micro-/nanostructure and the presence of impurities in FeTi is essential for optimizing material properties and enabling large-scale, cost-effective implementation of solid-state hydrogen storage solutions. Transmission electron microscopy (TEM) and atom probe tomography (APT) provide critical insights into the structural evolution, phase transformations, and microstructural changes in FeTi during hydrogenation and dehydrogenation cycles. High-resolution scanning transmission electron microscopy (HRSTEM) enables the identification of phase transitions, while energy-dispersive X-ray spectroscopy (EDS), electron energy loss spectroscopy (EELS), and APT allow for the mapping of elemental distributions. We have used these techniques to study the impact of microstructural features such as defects, secondary phases, and grain boundaries in the properties of high purity FeTi alloys and in FeTi alloys using recycled Fe sources, thus providing insights into the microstructure evolution after hydrogenations and unravelling the role of impurities coming from the recycled sources. Our findings contribute to the development of improved FeTi-based materials for efficient and reversible hydrogen storage applications.

MS2.P01
Optimization of mechanical and electrical properties in age-hardened aluminum alloy through HPTE processing

V. Tavakkolisaiej[1], Y. Ivanisenko[1], A. Mazalkin[1], T. Scherer[1], T. Boll[1], C. Kübel[1]

[1]Karlsruhe Institute of Technology, Eggenstein-Leopoldshafen, Germany

Aluminum alloys are gaining significant attention in electrical applications due to their excellent conductivity, corrosion resistance, and cost-effectiveness. However, their low strength limits their service life and increases maintenance costs. To address this issue, a combination of severe plastic deformation (SPD) and post-aging treatment has been proposed as an effective strategy . This study explores high-pressure torsion extrusion (HPTE) , a relatively novel SPD technique, which offers promising opportunities for scaling up product sizes.

Aluminum alloy samples processed via HPTE and subsequently post-aged demonstrated enhanced strength along with significantly improved electrical conductivity. The results revealed distinct features, including defective precipitate structures induced by matrix defects, the formation of core-shell precipitate structures, and a new orientation relationship (OR) that has not been previously reported. Furthermore, the effects of stored strain on the crystal structure of precipitates were investigated, shedding light on the interactions between deformation-induced defects and precipitate behavior.

High-resolution imaging techniques such as high-resolution transmission electron microscopy (HRTEM), scanning transmission electron microscopy (STEM), and atom probe tomography (APT) provided a wealth of insights into the crystal structure of precipitates, contributing to a deeper understanding of the observed phenomena.

In conclusion, HPTE emerges as a promising method for simultaneously enhancing the mechanical and electrical properties of aluminum alloys from an industrial perspective. These findings highlight the potential of HPTE for developing high-performance aluminum alloys and provide new perspectives on precipitate structure and behavior.

MS2.P04
Investigation of phase formation at the Ni/Sn interface during the soldering process

S. Gaertner[1], H. Rösner[1], S. V. Divinski[1], G. Wilde[1]

[1]University of Münster, Institute of Materials Physics, Münster, Germany

Soldering is a well-established method for creating permanent bonds between metal parts, often resulting in the formation of intermetallic compounds. For the purpose of soldering, various elements like Sn, Pb, Bi, Sb, Ag and Cu, or their alloys, are utilized in different compositions based on the respective field of application. The shift towards lead-free solder, driven by environmental regulations, has increased interest in Sn-based solder alloys. However, the complex phenomena related to material transport, phase stability, phase formation, and kinetic aspects of phase transformation. [1, 2]

This study aimed to investigate the interdiffusion and diffusion-controlled phase formation to gain a deeper understanding of these intricate processes.

To achieve this goal, Sn-Sb solder alloy between a Ni-based layer with a small amount of Si and a Cu substrate were investigated using various electron microscopy techniques. Initial scanning electron microscopy analyses of cross-section samples provided an overview of the interfaces, including the Sn-Sb solder alloy. For detailed examination, focused ion beam techniques were employed to create electron-transparent samples for analysis using analytical transmission electron microscopy.

Examination of the untreated states of the Ni-based layer and the solder alloy enables differentiation between the initial microstructure and post-soldering changes. The Ni-based layer exhibited a lamellar-type structure with a uniform elemental distribution perpendicular to the soldered interface, while the raw solder alloy consisted of a tetragonal β-Sn phase as a matrix and a trigonal SbSn phase. After the soldering process, CuSnNi and SnCu intermetallic compounds are formed with various shapes, surrounded by the β-Sn matrix. The SbSn phase remained as small inclusions throughout the process. Moreover, the Ni-based layer initially shrank due to diffusive interactions with Cu and Sn, resulting in a residual film that displayed an increased Si content compared to its untreated counterpart, eventually leading to complete consumption of the Ni-based layer.

This study highlights the complex processes involved in Cu transport from the substrate through the solder material, emphasizing the significant role of Cu in forming intermetallic compounds. Alongside with Sn, Cu drives the transformation of the Ni-based layer, ultimately to its complete consumption. In addition to elemental influences, microstructures play a crucial role in the Ni consumption process.

References

1. K. N. Subramanian, *Lead-Free Solders: Materials Reliability for Electronics*, (John Wiley and Sons Ltd Registered, 2012).
2. G. Humpston and D. M. Jacobson, *Principles of Soldering* (ASM International, 2004).

MS2.P05
Advancing the understanding of gold nanoparticle formation in ionic liquids using variable temperature *in situ* liquid-phase scanning transmission electron microscopy (LP-STEM)

R. Butti[1], D. Keller[1]

[1]EMPA - Swiss Federal Laboratories for Materials Science and Technology, Electron Microscopy Center, Dübendorf, Switzerland

Gold nanoparticles (Au-NPs) exhibit tunable properties, making them relevant in catalysis, biosensing, and optoelectronics.[1] However, their nucleation and growth mechanisms remain insufficiently understood, limiting synthesis control.[2] Ionic liquids (ILs) provide an ideal medium due to their low vapor pressure, thermal stability, and dual role as solvents and stabilizers. We employed *in situ* variable temperature liquid-phase scanning transmission electron microscopy (VT LP-STEM) to investigate atomic-scale Au-NP formation in ILs, aiming to enhance size, morphology, and growth control.[3]

We synthesized Au-NPs in ILs such as 1-butyl-3-methylimidazolium chloride ([C_4mim]Cl) and tetrabutylammonium chloride ([TBAC]Cl), using metal precursors including $HAuCl_4 \cdot 3H_2O$ and AuCl, in combination with reducing agents such as citric acid and oxalic acid. A MEMS-based *in situ* heating holder enabled us to manipulate the temperature of our sample in the TEM from room temperature up to 250°C, leading to real-time observation of NP nucleation and growth (*Figure 1*). Complementary UV-Vis spectroscopy and NMR analyses assessed the influence of experimental parameters on NP formation.

Our findings reveal that [C_4mim]Cl facilitated localized, electron-beam-driven NP formation, with growth initiating in irradiated regions and transitioning from triangular to rounded shapes as temperature increased (*Figure 2*). In contrast, [TBAC]Cl showed limited NP formation, highlighting IL composition's role in nucleation and growth. The use of citric acid enabled gradual precursor reduction, enhancing NP uniformity and reproducibility compared to rapid reduction observed with other reducing agents.

Further analysis demonstrated that [C_4mim]Cl exhibited higher viscosity at lower temperatures, providing a confined nanoreactor environment that promoted controlled Au-NP growth. As the temperature increased, the viscosity of [C_4mim]Cl decreased, allowing for enhanced coalescence while maintaining stability within the IL matrix (*Figure 3*). In contrast, [TBAC]Cl, with lower viscosity and reduced confinement effects, exhibited limited NP formation under comparable conditions.[4]

By integrating *in situ* and *ex situ* methodologies, our study establishes [C_4mim]Cl as a superior medium compared to [TBAC]Cl for achieving controlled NP growth in ILs, and it underlines the critical role of the reducing agent for promoting Au-NP growth. These insights contribute to sustainable NP synthesis strategies, including core-shell structures and ternary quantum dots, advancing green nanotechnology and precision materials engineering.[5]

Figure Captions:

1.) Experimental set-up for IL preparation. **a)** *In situ* TEM holder tip with heating electrodes and **b)** mounted heating E-chip. **c)** E-chip with holey carbon foil on SiN, filled with IL via hair loop deposition. **d)** Active E-chip area with free-standing IL droplet, heated to initialize Au-NP growth.

2.) *In situ* STEM series depicting the growth of a triangular-shaped Au-NP in [C_4mim]Cl triggered by heat.

3.) STEM time series of Au-NP growth in [C_4mim]Cl at 60 °C, showing rapid, random dynamics within the IL, with NP coalescence as highlighted by dashed circles over a 15-minute timespan.

References:

[1] D. Keller et al., *Nanoscale* **12**(44), 2020.

[2] Khare et al., *Int. J. Precis. Eng. Manuf.* **13**(7), 2012.

[3] H. Zheng et al., *Science* 324(**5932**), 2009.

[4] X. Ji et al., *J. Am. Chem. Soc* **129**(45), 2007.

[5] M. A. Cotta, ACS *Appl Nano Mater.* **3**(6), 2020.

Fig. 1

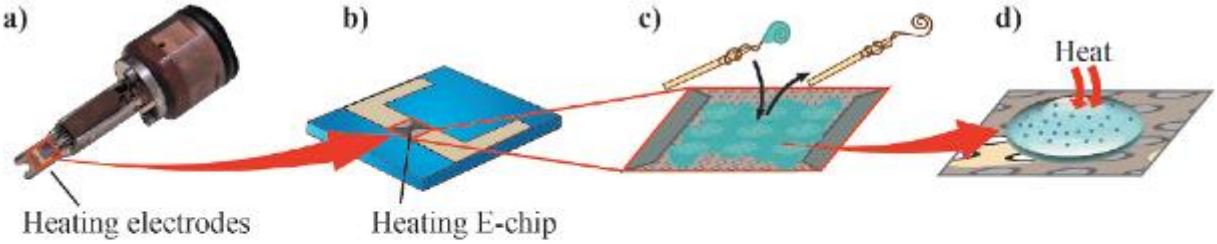


Fig. 2

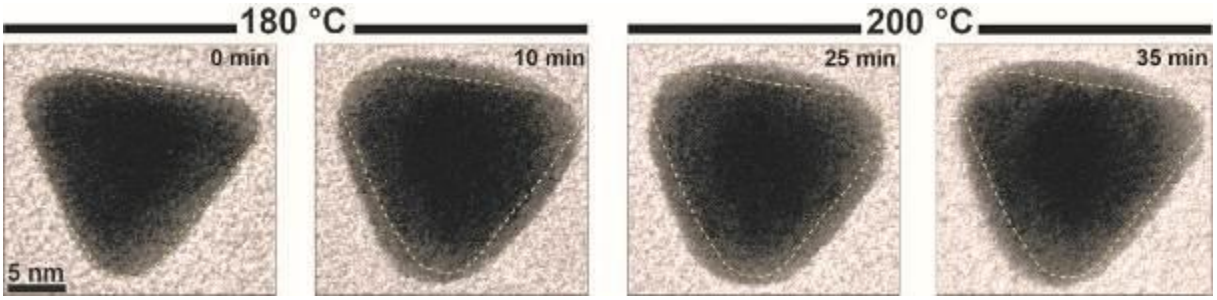
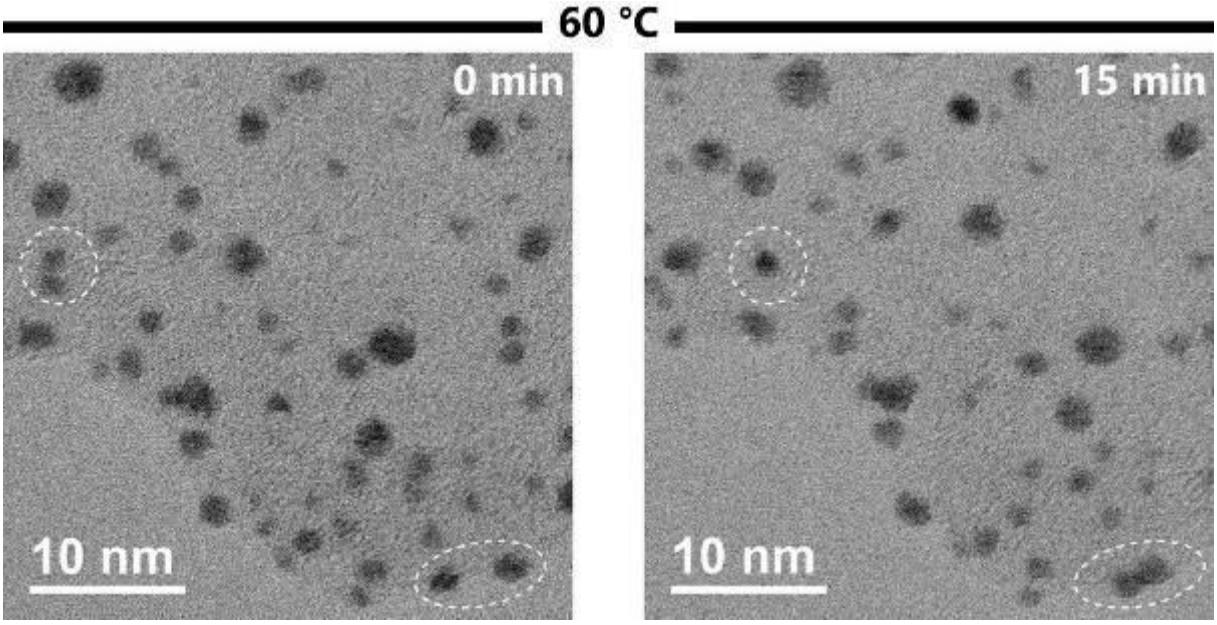


Fig. 3



MS2.P06
On the use of advanced SEM and (S)TEM techniques to study fine dislocation networks and their relation to the large- and small-scale heterogeneities in Ni-base single crystal superalloys (SXs)

G. Eggeler[1], A. Parsa[2], P. Thome[3], A. Mussi[4], S. Gamanov[5], L. Agudo Jácome[5], A. Dlouhy[6]

[1]Ruhr University Bochum, Institute for Materials, Bochum, Germany
[2]Siemens Energy, Large Gas Turbine Design, Mülheim a.d. Ruhr, Germany
[3]University of Arizona, Materials Engineering, Tucson, AZ, United States
[4]University of Lille, Unité Materiaux, Lille, France
[5]Bundesanstalt für Materialforschung, Berlin, Germany
[6]Institute of Physics of Materials, Brno, Czech Republic

Superalloy single crystals (SXs) are used to make turbine blades which operate in gas turbines of powerplants and aeroengines. In service they must withstand mechanical loads at temperatures close to their melting point. Large- and small-scale heterogeneities characterize their as-processed microstructure. Dendrites and interdendritic regions represent the large-scale microstructural heterogeneity of SXs (average dendrite spacing: 300µm). A fine γ/γ'-microstructure, on the other hand, with cuboidal γ'-particles (ordered L12-phase, average cube edge length: 0.3 µm, volume fraction: 70%) separated by thin γ-channels (fcc solid solution, average channel width: 50 nm, volume fraction: 30%), represents the small-scale heterogeneity of SXs.

Fine dislocations networks play a key role on both length scales. They separate dendrites and groups of a small number of parallel dendrites, and meander through the microstructure over mm-distances. On the small length scale, they enwrap all γ'-prime particles to accommodate misfit and to enforce a dynamic equilibrium between knitting in and knitting out dislocation reactions. Dislocations also affect the local morphology of γ/γ'-interfaces. We present methods which were developed and results which were obtained within SFB/TR 103, a collaborative research center on single crystal Ni-base superalloys, funded by the German Research Association (DFG) [1-5]. (S)TEM diffraction contrast studies are used to study dislocation networks and to reveal the elementary dislocation mechanisms. Electron tomography reconstructions help to appreciate the 3D morphology of a 0.5° dislocation network boundary which has formed during directional solidification. For high resolution orientation imaging in the SEM, the rotation vector baseline electron back scatter diffraction (RVB EBSD technique) was developed. It is shown how one can combine these techniques to contribute to a better understanding of elementary processes which govern the evolution of microstructures during processing and high temperature deformation of single crystal Ni-base superalloys.

[1] L. Agudo Jacomé, G. Eggeler, A. Dlouhy, Advanced scanning transmission stereo electron microscopy of structural and functional engineering materials, Ultramicroscopy, 122 (2012) 48-59

[2] A.B. Parsa, P. Wollgramm, H. Buck, A. Kostka, C. Somsen, A. Dlouhy, G. Eggeler, Ledges and grooves at γ/γ'-interfaces of single crystal superalloys, Acta Mater., 90 (2015) 105-117.

[3] P. Thome, S. Medghalchi, J. Frenzel, J. Schreuer, G. Eggeler, Ni-base superalloy single crystal (SX) mosaicity characterized by the Rotation Vector Base Line Electron Back Scatter Diffraction (RVB-EBSD) method, Ultramicroscopy, 206 (2019) 112817

[4] S. Gamanov, A. Dlouhy, D. Bürger, G. Eggeler, P. Thome, Evolution of local misorientations in the γ/γ'-microstructure of single crystal superalloys during creep studied with the rotation vector baseline (RVB) EBSD method, Microsc. Res. Tech., 87 (2024) 516-533

[5] A.B. Parsa, D. Burger, T.M. Pollock, G. Eggeler, Misfit and the mechanism of high temperature and low stress creep of Ni-base single crystal superalloys, Acta Mater., 264 (2024) article no. 119576

MS2.P07
In situ electron microscopy for analyzing recrystallization in the aluminum alloy AA2024

M. Theissing[1], G. Falkinger[2], V. Shah[2], K. Strobel[2], S. Mitsche[1]

[1]TU Graz, Graz, Austria
[2]AMAG rolling GmbH, Ranshofen, Austria

Introduction

The mechanical properties of wrought aluminum alloys depend heavily on the microstructure, crystallographic texture and the secondary phase particles. In industrial processing, thermomechanical treatments such as rolling or annealing are used to positively influence these properties. In many cases, annealing of a deformed material leads to recrystallization and texture changes, which then determines the new microstructure. Knowledge of recrystallization is important for predicting the microstructure after an annealing treatment. In this work, *in situ* electron backscatter diffraction (EBSD) is used to study recrystallization in AA2024 aluminum alloy, a typical aerospace material.

Objectives

The main objective of this work is to develop a measurement procedure to reliably investigate recrystallization in aluminum alloys. Accompanying phenomena like dissolution or precipitation of secondary phase particles should also be examined.

Materials & Methods

An AA2024 sheet alloy with different degrees of deformation was investigated. The main alloying elements are copper, magnesium and manganese. Samples were produced from the material by a combination of mechanical and electrochemical polishing. A heating stage in a scanning electron microscope in combination with EBSD was used for the recrystallization experiments. The heat treatments were carried out at different constant heating rates. During heating EBSD scans were performed to record the changes in microstructure and texture. Before and after the heating electron backscatter images were recorded to observe possible changes in the precipitation state. To improve the orientation determination of the EBSD scans, spherical indexing [1] was performed during post-processing.

Results

The described workflow was used to characterize recrystallization of AA2024 in dependence of degree of deformation and heating rate. By comparing the precipitation state before and after the heating treatment no significant change was found, only small particles got smaller or completely dissolved. Applying spherical indexing on the in situ scans the amount of non-indexed points was drastically reduced. This ensured a better evaluation of texture development during recrystallization. One interesting result was that no obvious advantage of cube grains during recrystallization, which is often found in various aluminum alloys, could be seen in the *in situ* experiments. With the optimized EBSD scans also inhomogeneous growth rates of the recrystallizing grains could be found.

Conclusion

The use of *in situ* EBSD provides insights into the mechanisms of the recrystallization process of AA2024 sheet alloy. The optimization in pattern indexing provided a superior evaluation of the texture.

[1] Lenthe, W. C., Singh, S., & De Graef, M. (2019). A spherical harmonic transform approach to the indexing of electron back-scattered diffraction patterns. *Ultramicroscopy*, *207*, 112841.

MS2.P08
Secondary phase measurements on a large scale in aluminum alloys

J. Prechtl[1], M. Theissing[1], G. Falkinger[2], V. Shah[2], K. Strobel[2], S. Mitsche[1]

[1]TU Graz, Graz, Austria
[2]AMAG rolling GmbH, Ranshofen, Austria

Introduction

Secondary phase particles are very important for the mechanical properties of wrought aluminum alloys. Some phases can ensure the hardening of the material or serve as nuclei for recrystallization. Detailed information about the type, size and distribution of precipitates within the sheet is therefore important. With sheet thicknesses of up to several millimeters, it is difficult to collect statistically relevant information, as an area of several square millimeters has to be measured. This work presents a method that can be used to generate meaningful particle statistics for an aluminum sheet alloy AA2024.

Objectives

A method for measuring secondary phase particles on a large scale should be implemented including optimized sample preparation for an artifact free surface.

Materials & Methods

An AA2024 aluminum sheet alloy with copper, magnesium and manganese as the main alloying elements was investigated. Mechanical and electrochemical polishing methods were used for sample preparation to obtain a large surface area (several mm2). As a final preparation step, Ar-ion polishing was used to remove preparation artifacts such as oxidation of secondary phase particles. The Oxford Instruments feature mode in the Aztec software was mainly used for automated particle measurement. First, a large backscattered electron (BSE) image is acquired, which is then segmented. Any segmented particle larger than a certain threshold is then measured using energy dispersive X-ray spectroscopy (EDX) by pointing the electron beam on the centroid of the particle. To scan even larger areas, the examined area is divided into several individual measurement sections, which are then stitched together. By optimizing the acquisition parameters, the total measurement time could be shortened and up to 150,000 particles were measured for the largest measured areas.

Results

After measuring a large area, one has very good chemical information about the measured particles. Size and shape on the other hand are prone to measurement and interpretation errors because grey color value segmentation which is used in the first place has strong limitations. To overcome this problem all BSE images were segmented afterwards again with the software ilastik [1] which uses AI assisted classifiers and provides much better results. The new segmentation was then combined with the chemical information with custom MATLAB scripts. From that as an example it was found that the S-phase (Al_2MgCu) in AA2024 seems to show no uniform distribution across the thickness of the sheet and has broad size distributions.

Conclusion

Automated particle analysis provides important information on secondary phase particles in statistically relevant numbers. With this technique, it is possible to characterize changes in the proportion depending on the position of the sheet.

MS2.P09
Electron microscopy of oxides formed at elevated temperature in high chromium ferritic cast iron containing silicon

A. Wiengmoon[1], K. Ruangchai[1], S. Nusen[2], T. Chairuangsri[2]

[1]Naresuan University, Department of Physics, Phitsanulok, Thailand
[2]Chiang Mai University, Department of Industrial Chemistry, Chiang Mai, Thailand

Introduction

The alloys to be used at elevated temperatures must have sufficient resistance to oxidation and high-temperature corrosion together with structural and dimensional stability. Alloys with Cr and Si are widely used to increase the oxidation resistance by forming protective oxidation layers such as Cr_2O_3, $FeCr_2O_4$, SiO_2 and Fe_2SiO_4 [1]. The 30-40wt.%Cr cast irons with 1-2wt.%C and stable ferritic matrix are used in applications that require heat resistance at elevated temperatures up to 1050°C such as sinter plants and furnace parts, and also have useful abrasion resistance [2]. The purpose of this work is to investigate the oxides formed at elevated temperature in a ferritic high-Cr cast iron by electron microscopy including SEM-EDS, SEM-EBSD and CTEM.

Materials and methods

A ferritic 31wt.%Cr-1.2wt.%C-0.3wt.%Si cast iron was used for high temperature oxidation experiment. The samples were prepared by grinding on the SiC paper and polished with 6 μm diamond paste, and placed in alumina crucibles. Oxidation testing was carried out at 1000°C for 2-48 h in air. The weight gain of the samples was measured at different times. The Apreo S, Thermo Fisher Scientific FE-SEM with EDS was used to observe the oxide layer and elemental distribution analysis in the oxide. To characterize the type of oxide, SAED in CTEM was performed using a JEOL JEM-2100plus TEM operated at 200 kV. SEM-EBSD was also performed to identify the type of oxides using a FEI NovaNano SEM 450 series equipped with a Bruker model e-Flash HR+series EBSD.

Results

The weight gain and the thickness of the oxide layer increased with increasing oxidation times. At short oxidation time, the external oxide with Cr-rich was formed on the surface. When the oxidation time exceeded 8 h, the external and internal oxidations were clearly observed. The external oxide layer has three different areas (Fig. 1). The outer oxide layer is denser and composed of Fe-rich. The thin oxide layer is composed of Cr-rich, while the beneath oxide has small pores and is composed of (Fe, Cr)-rich oxide. The thin Si-rich layer can be observed at the region between the Cr-rich and (Fe, Cr)-rich oxide layers. The internal oxide reveals a porous area composed of (Fe, Cr)-rich and Cr-rich oxides at the interface. The SADPs identified that the outer oxide is Fe_2O_3 and the thin Si-rich layer is SiO_2 (Fig. 2). The Si layer was identified as amorphous silica. Furthermore, Cr_5O_{12} and Cr_2SiO_4 oxides were also found. From EBSD results, the outer oxide can be Fe_2O_3, which have a larger grain size than the inner (Fe, Cr)-rich oxide.

Conclusion

In the first state of oxidation at elevated temperature of the ferritic 31wt.%Cr-1.2wt.%C-0.3wt.%Si cast iron, external oxidation of Cr was occurred forming a Cr-rich oxide layer on the alloy surface. At longer time, Fe diffused passing through the Cr-rich oxide layer and reacts with O_2 resulting in an outer Fe_2O_3 layer. Si diffused and formed the SiO_2 layer by internal oxidation beneath the Cr-rich oxide layer together with the (Fe,Cr)-rich oxide layer.

References

[1] Wu, Y. et. al., Metals, 2023, 13, 1670.

[2] Boyes, J.W., Iron and Steel, 1966, 39, 102-109.

Fig. 1

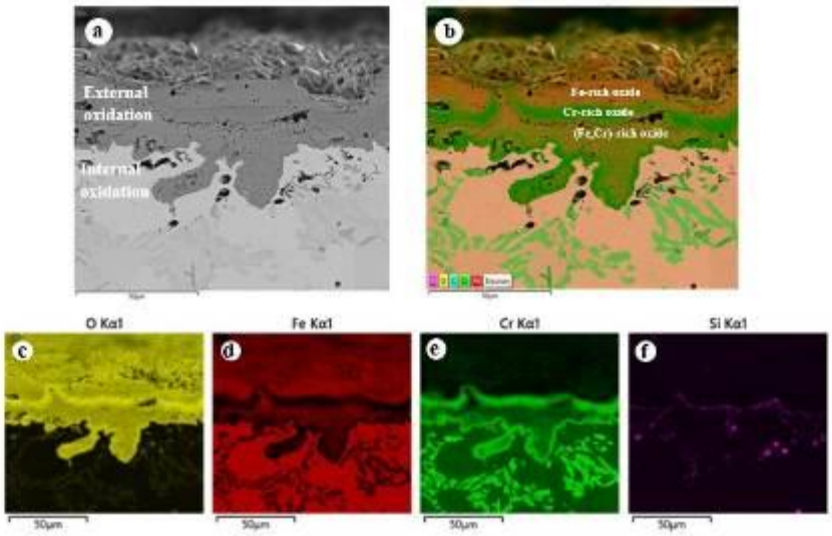


Fig. 1. (a) SEM-SEI shows a cross-section of the iron after oxidation testing at 1000°C for 48 h, and (b-f) Elemental maps by SEM-EDS.

Fig. 2

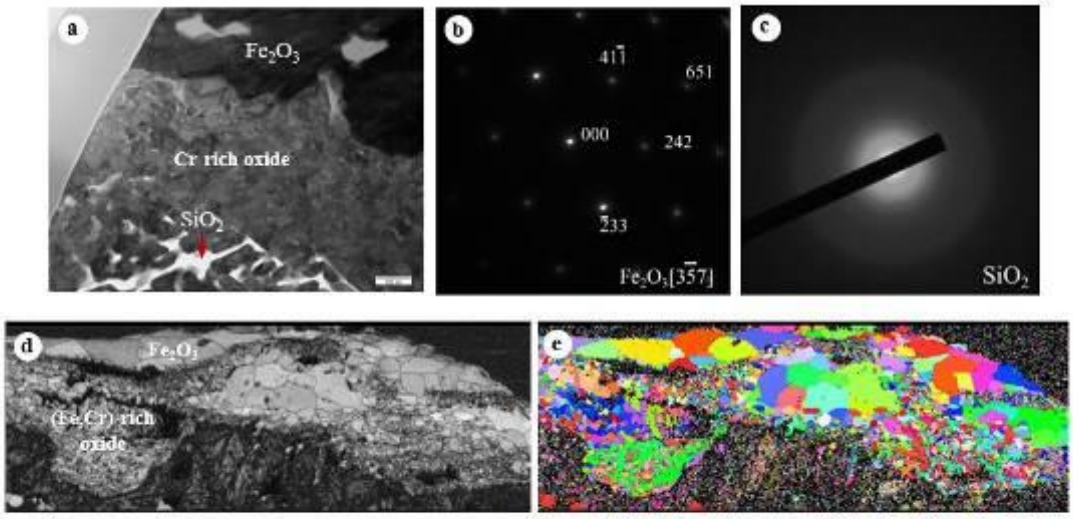


Fig. 2. (a) A BF-TEM image shows the oxide layer (b-c) corresponding SADPs from Fe_2O_3 and amorphous SiO_2 (d-e) Image quality and IPFZ images by SEM-EBSD.

MS2.P10
Correlation of *in situ* µDIC with EBSD for damage investigation in a three-point bending test of an AA6xxx

F. Zrim[1], G. Falkinger[2], A. Thum[2], S. Mitsche[1]

[1]FELMI-ZFE, Graz, Austria
[2]AMAG rolling GmbH, Ranshofen, Austria

Introduction

Electron backscatter diffraction (EBSD) and in situ digital image correlation (DIC) measurements were performed on an AA6xxx to investigate the relationship between microstructure and damage development during bending. An in situ three-point bending test was set up in a scanning electron microscope (SEM) to facilitate µDIC analysis and trace damage development. By correlating DIC strain maps with EBSD data, detailed insights were obtained on how microstructural features influence strain localization and crack initiation.

Objectives

This study aimed to understand the damage mechanisms in an AA6xxx during bending. The complex strain state inherent to the bending process is challenging to simulate computationally, necessitating experimental DIC measurements. A particular focus was placed on finding a suitable nanoscale surface pattern for µDIC and identifying key microstructural features—such as pores, precipitates, and shear bands—that contribute to strain localization and damage initiation.

Materials & Methods

Samples of an AA6xxx were subjected to solution heat treatment and rolled to a thickness of 1 mm. Initial microstructural characterization was performed using EBSD and conventional SEM on the unstrained samples. Subsequently, an in situ three-point bending experiment was conducted in the SEM to enable DIC analysis and monitor damage development.

To achieve high-resolution DIC analysis at the nanoscale, the sample surface was patterned using silica nanoparticles with an approximate size of 40 nm. The particles were applied via drop casting of OPS (oxide polishing solution) diluted with water at a 3:1–5:1 ratio, followed by an alcohol rinse. While this method provided a quick way to achieve sufficient particle distribution for DIC analysis, it also led to areas with particle agglomeration and multiple layers, especially near the sample edges. Alternatively, OPS was applied using a polishing cloth in a polisher, resulting in a more uniform particle distribution. However, this method was more sensitive to variations in preparation parameters, such as polishing pressure, OPS dilution, and polishing time, leading to lower reproducibility.

The DIC and EBSD data were correlated using the DefDAP Python package [1], which employs a polynomial transformation for alignment by identifying homologous points in both datasets. This enabled the analysis of strain and crystal orientation for each distinct grain.

Results

In situ measurements enabled successful DIC analysis at image widths of up to 400 µm, constrained by the pattern size and image resolution. Effective shear strain maps revealed shear bands extending across multiple grains, often coinciding with surface cracks or pores. Grain boundaries, evaluated with EBSD, and precipitates showed high strain localization, serving as an indication for subsequent damage in the respective areas.

Conclusion

Two surface patterning methods based on OPS were utilized, enabling μDIC analysis. The strain distribution obtained from the in situ three-point bending test with DIC proved to be a reliable indicator of damage onset, with strain localization primarily occurring along grain boundaries and precipitates. DIC analysis highlighted the significant role of shear bands in strain accommodation, providing valuable insights into damage development in an AA6xxx.

[1] M. Atkinson, R. Thomas, P. Crowther, D.T. Fullwood, J. Quinta da Fonseca, A. Harte. MechMicroMan/DefDAP: v0.93.4. 2022.

MS2.P11
Nanoscale investigation of 9Cr-ODS steels

M. Dürrschnabel[1], C. Bonnekoh[1], U. Jäntsch[1], S. Baumgärtner[1], M. Rieth[1]

[1]Karlsruhe Institute of Technology, Institute of Applied Materials/Applied Material Physics, Eggenstein-Leopoldshafen, Germany

Introduction

Optimal performance of power plants in general and future fusion reactors in particular relies on a carefully designed configuration and the highest possible operating temperature. In addition to structural steels such as for example EUROFER97, oxide-dispersion strengthened (ODS) steels can be utilized in components subjected to intense heat and neutron radiation, providing excellent neutron radiation resistance, enhanced high-temperature strength, and improved creep resistance. The exceptional material performance of ODS steels is determined by their micro- and nanostructure.

Objectives

The overall objective of this study is to scale up the production of ODS steels and to identify the process parameters that consistently yield desirable material properties. A key aspect of this effort is achieving a detailed understanding of the nanostructure.

Materials & methods

A batch of four powder samples was prepared for this study: two were conventionally milled in an argon (Ar) atmosphere, and two were milled in a hydrogen (H_2) atmosphere. All samples were subjected to hot isostatic pressing (HIP) at 1150°C, followed by rolling at 980°C. Microstructural characterization was performed using scanning electron microscopy (SEM) and transmission electron microscopy (TEM). Specifically, electron backscatter diffraction (EBSD) maps were acquired via SEM to extract matrix grain sizes, which were used to contextualize the TEM results, while energy-dispersive X-ray spectroscopy (EDX) and electron energy-loss spectroscopy (EELS) were conducted using TEM to analyze ODS particle sizes, particle densities, and composition. High-resolution phase-contrast imaging was additionally employed to examine the structure of individual ODS particles.

Results

Figure 1: STEM-EDX elemental mapping of a representative sample area of an H_2-milled sample.

Figure 2: STEM-EDX elemental mapping of a representative sample area of an Ar-milled sample.

Figure 3: (left) High resolution phase contrast image (HRTEM) of a $Y_2Ti_2O_7$ ODS particle oriented in [011] zone axis and (right) corresponding FFT.

Conclusion

The number density of ODS nanoparticles was consistently in the range of 10^{21} particles m^{-3} across all analyzed samples. However, an inhomogeneous distribution of ODS particles at the low-micron scale was observed, which was attributed to the powder preparation process. Additionally, samples milled under an Ar atmosphere contained nanosized Ar bubbles of a similar magnitude. The composition of the ODS nanoparticles was comparable across all samples, with the expected $Y_2Ti_2O_7$ nanoparticles observed alongside Si- and Al-containing particles. Since the base material is a 9Cr steel, $M_{23}C_6$ particles were also present, predominantly located at grain boundaries, with a number density of 10^{19} m^{-3}. The quantitative results obtained in this study will be used to further refine and scale up the ODS manufacturing process.

Fig. 1

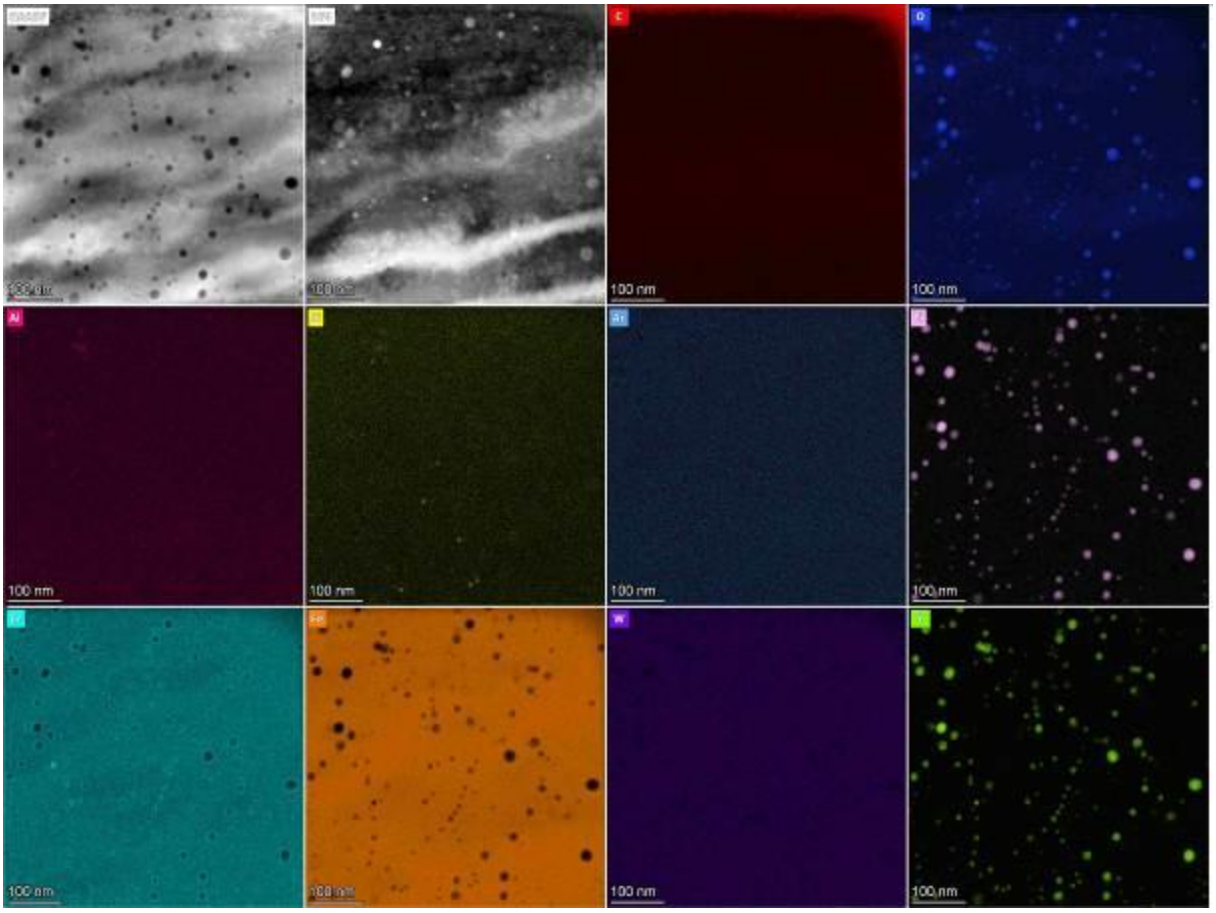

100 nm
100 nm
100 nm
100 nm
100 nm
100 nm
100 nm
100 nm
100 nm
100 nm
100 nm
100 nm

Fig. 2

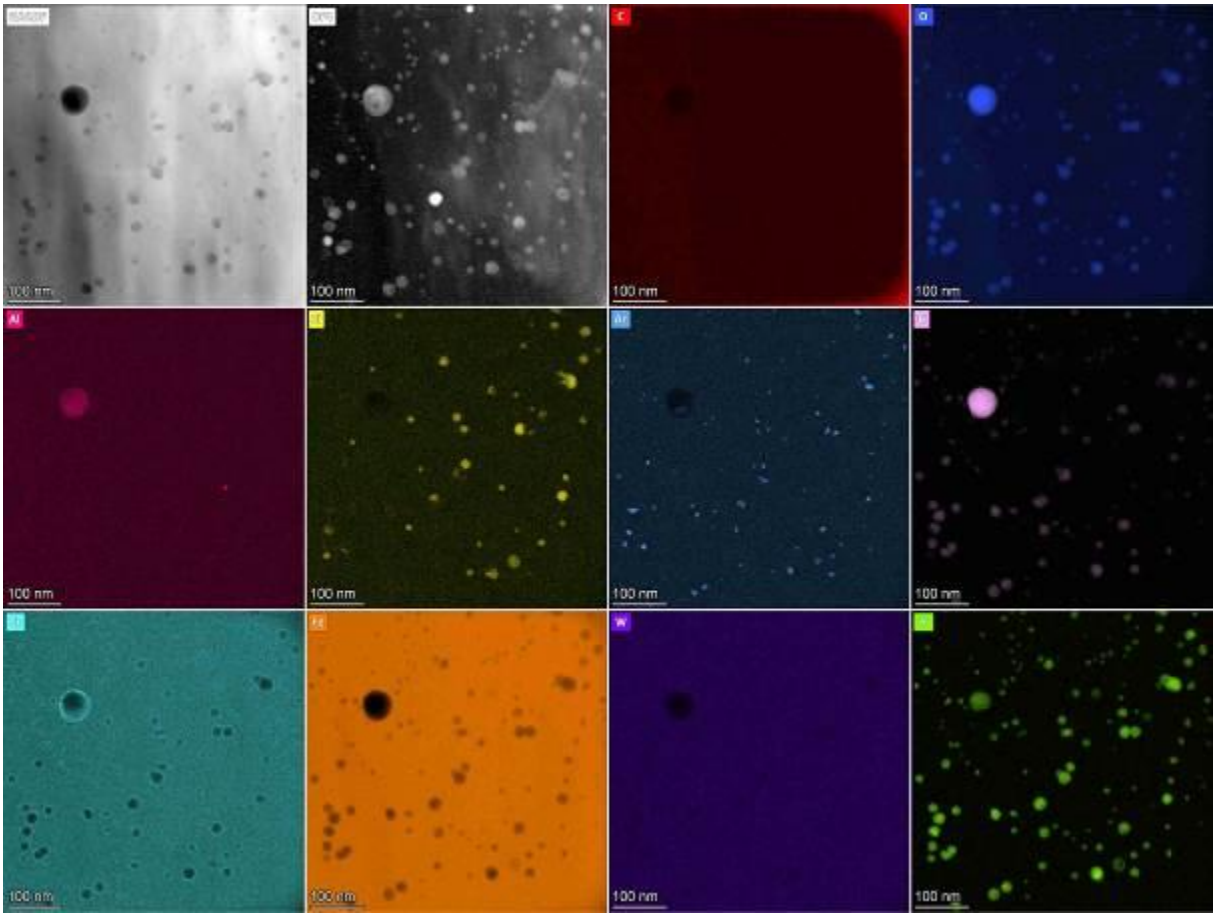
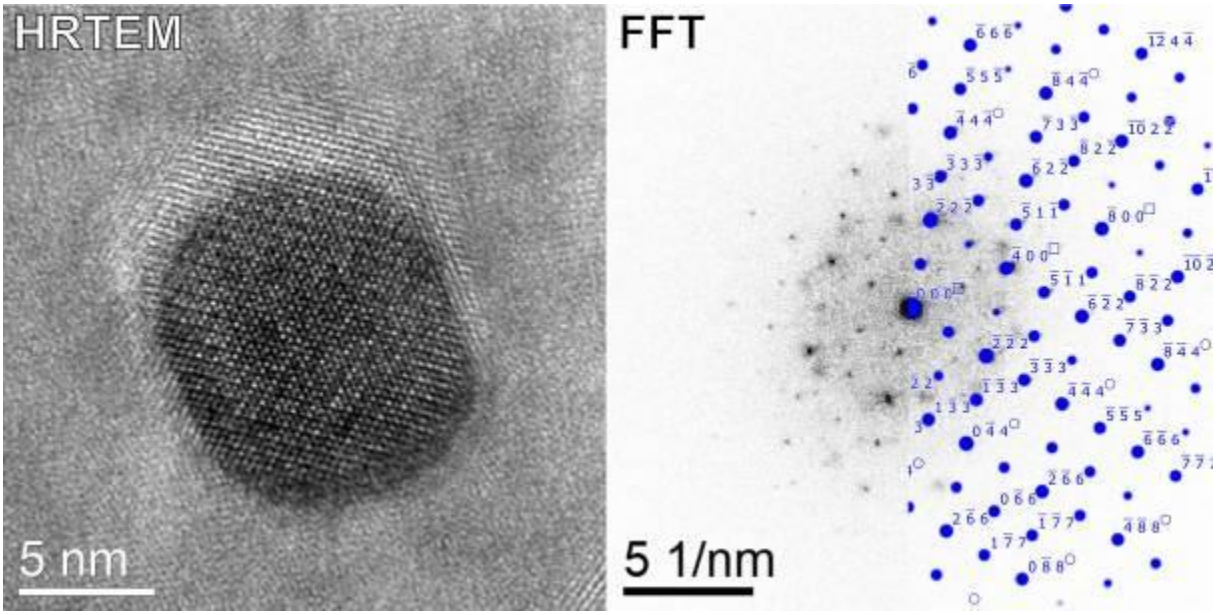


Fig. 3



MS2.P12
Understanding corrosion and decay in artifacts – How electron microscopy allows us to trace history

H. Groß[1], U. Schürmann[1], T. Boyadzhieva[2], M. A. Johns[3], L. Ræder Knudsen[2], J. Fiutowski[3], L. Kienle[1]

[1]Kiel University, Materials Science, Kiel, Germany
[2]Conservation Centre Vejle, Vejle, Denmark
[3]University of Southern Denmark, Mads Clausen Institute, Sønderborg, Denmark

Introduction

Each artifact that is discovered, originating from the Neolithic Era to the Renaissance, incorporates a unique history and with it, different processes of corrosion and change over time. To understand these processes and to gain insight into the artifacts" usage and manufacture, a synergistic approach of different methods of analysis, often as unique as the artifact itself, is required. This study highlights the importance and effectiveness of our multi-faceted approach of analysis, as well as the preparation of sensitive artifacts, minimizing damage and loss of material.

Objectives

This study aims to identify the materials and composition of historic artifacts from different time periods to understand the corresponding processes of corrosion and change over time. Analysing the surfaces of weapons in regard to metal traces and structure, insight into the original processing, finishing and processes during burial can be gained. By identifying the composition and crystal structure of mineral pigments, their history and provenance can be traced, facilitating period-correct restoration.

Materials & Methods

Suitable locations for sample acquisition are identified via Scanning Electron Microscopy (SEM), with sample preparation being performed through the Focused Ion Beam (FIB) technique. Obtained lamellae are investigated in the Transmission Electron Microscope (TEM). For pigment analysis, correlated microscopy and Energy-Dispersive X-Ray Spectroscopy (EDX) are used to identify individual layers and composition, with mineral analysis performed via X-Ray and Electron Diffraction (XRD/ED).

Results

Silver traces on the surface of Neolithic weapons were investigated and could be attributed to a corrosion process rather than an intentionally manufactured coating. Colour pigments from faded cladding decorations and a sarcophagus fragment could be identified chemically and structurally. This allowed a correlation to their provenance, while also facilitating a restoration with period-correct pigments.

Conclusion

This study highlights the effectiveness and possibilities of our multi-faceted approach, while also underscoring the importance of integrating modern scientific techniques in the preservation of historic artifacts. It further serves as an example on how common cultural heritage can be discovered, preserved and its stories told across borders.

Figure 1: (Left) TEM micrograph of a FIB lamella extracted from the corroded surface of a Neolithic copper axe (Top right). Particles marked with arrows indicate silver traces and particles, which could be identified via TEM-EDX. (Bottom right) EDX elemental mapping detailing a larger silver particle, marked with "Ag" and arrows in the micrograph, incorporated in the axe"s copper matrix.

Figure 2: SEM micrograph and corresponding EDX elemental mapping of a wood cladding decoration in cross section. From bottom (oldest) to top (youngest), a complex layering of different pigments is apparent, identifiable via the pigments" corresponding metal cation.

Fig. 1

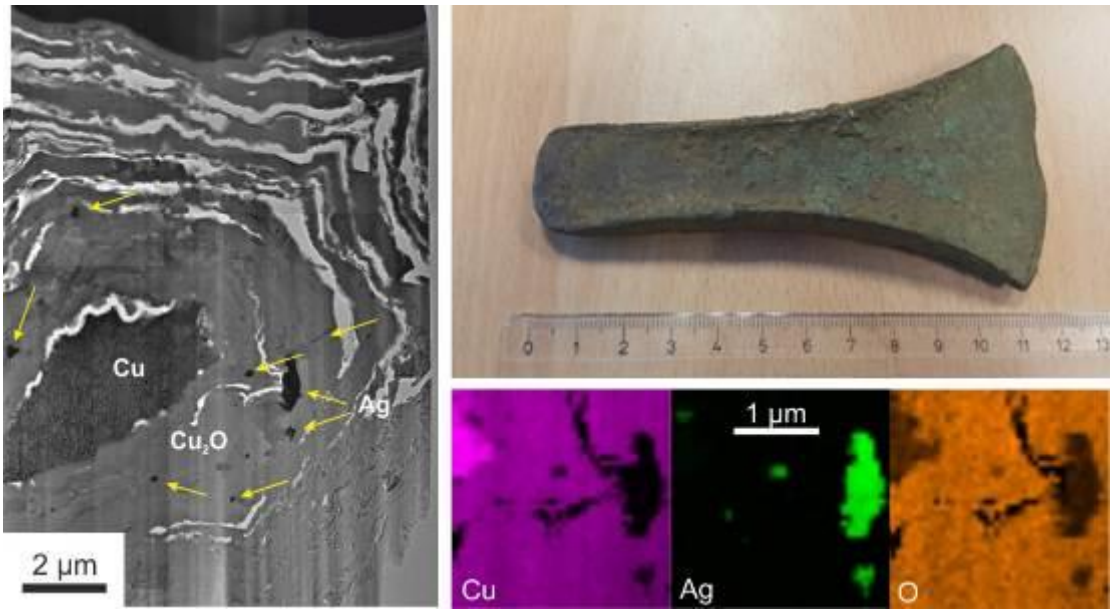
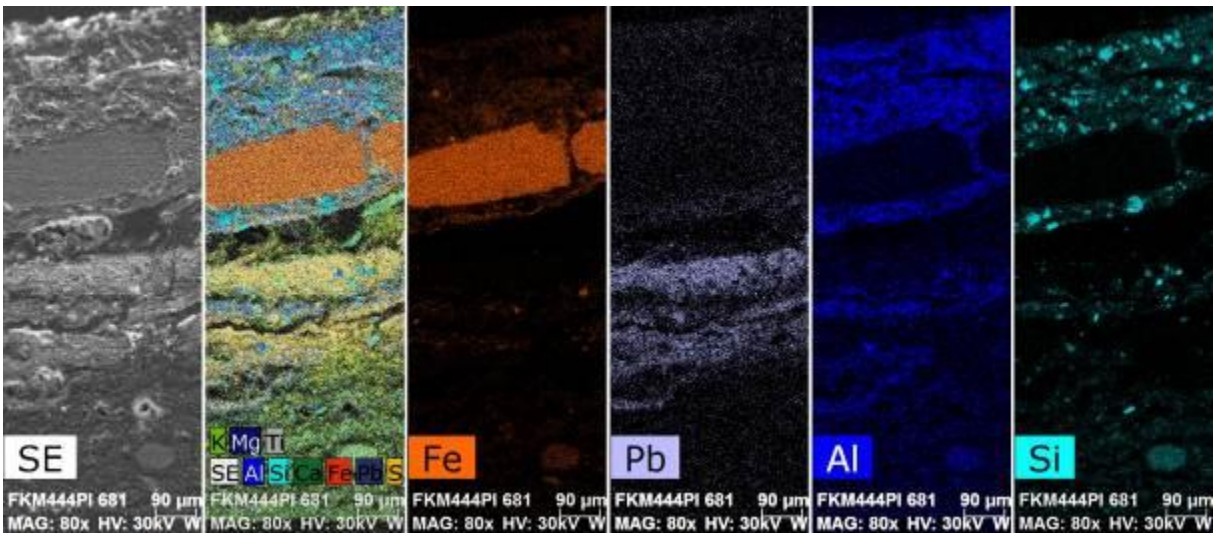


Fig. 2



MS2.P13
Irradiation tolerance of Co-free high entropy alloy

L. Chauhan[1], D. Litvinov[1], N. Meena[1], E. Gaganidze[1], C. Kaden[2], J. Aktaa[1]

[1]Karlsruhe Institute of Technology, IAM-MMI, Eggenstein-Leopoldshafen, Germany
[2]Helmholtz Research Center Dresden-Rossendorf, Dresden, Germany

Introduction

In the recent years, high entropy alloys (HEAs) have been extensively studied because of their attractive physical and mechanical properties, such as elevated temperature strength, ductility, wear resistance, corrosion, and oxidation resistance [1], which makes them a suitable candidate for structural applications in next-generation advanced nuclear reactor components subjected to harsh environments. Multiple studies on the irradiation tolerance of HEAs show a considerable reduction of the irradiation-induced void swelling, which is hypothesized to arise from enhanced recombination of interstitials and voids, high lattice distortion leading to slower diffusion, and lower thermal conductivity prolonging defect cascades [2].

The majority of the HEAs examined to date incorporate cobalt as a constituent element; nonetheless, the significant transmutation of ^{59}Co to ^{60}Co (a potent gamma radiation emitter) renders its utilization in nuclear reactors impractical. Consequently, it is imperative to explore cobalt-free HEAs that may exhibit comparable resistance to defects induced by irradiation.

Materials and Methods

A novel Co-free high entropy alloy was fabricated using vacuum arc melting followed by homogenization and cold rolling to realize a 50% reduction in thickness. To mitigate the cold-working-induced hardening, recrystallization was carried out at 950 °C for 15 minutes. The alloy was further irradiated employing 5 MeV Fe ions at 300 °C to a fluence of $9x10^{15}$ ions/cm² achieving a peak damage of ~8 dpa. The microstructural characterization was executed using scanning electron microscopy (SEM), electron backscattered diffraction (EBSD), and transmission electron microscopy (TEM).

Results

The TEM analysis of the pristine HEA reveals a single-phase face-centered cubic structure characterized by a heterogeneous distribution of dislocations, which arises from the dominance of local planar slip phenomena (refer to Fig. 1(a)). The occurrence of local planar slip may be correlated with the existence of short-range order within the material; however, we did not detect any diffuse reflections in the selected area diffraction (SAD) pattern. Figure 1(b) provides a comprehensive overview of the HEA after irradiation. The irradiated region extends to an approximate depth of 1.5 µm from the free surface. The SAD pattern obtained from the irradiated area indicates the emergence of additional {100} and {011} superlattice reflections, implying the development of ordered precipitates ($L1_2$). A further examination of the irradiated microstructure was conducted at a depth ranging from 500 to 600 nm from the free surface to mitigate any influence from the free surface. The analysis revealed the presence of both ½<110> type perfect loops and 1/3<111> type faulted loops, with an average dimension of approximately 20 nm. No void formation was detected at any depth, which can be ascribed to the relatively low irradiation temperatures (~0.2 T_m) and the sluggish diffusional pathways for vacancies and interstitials, which facilitate enhanced vacancy-interstitial recombination.

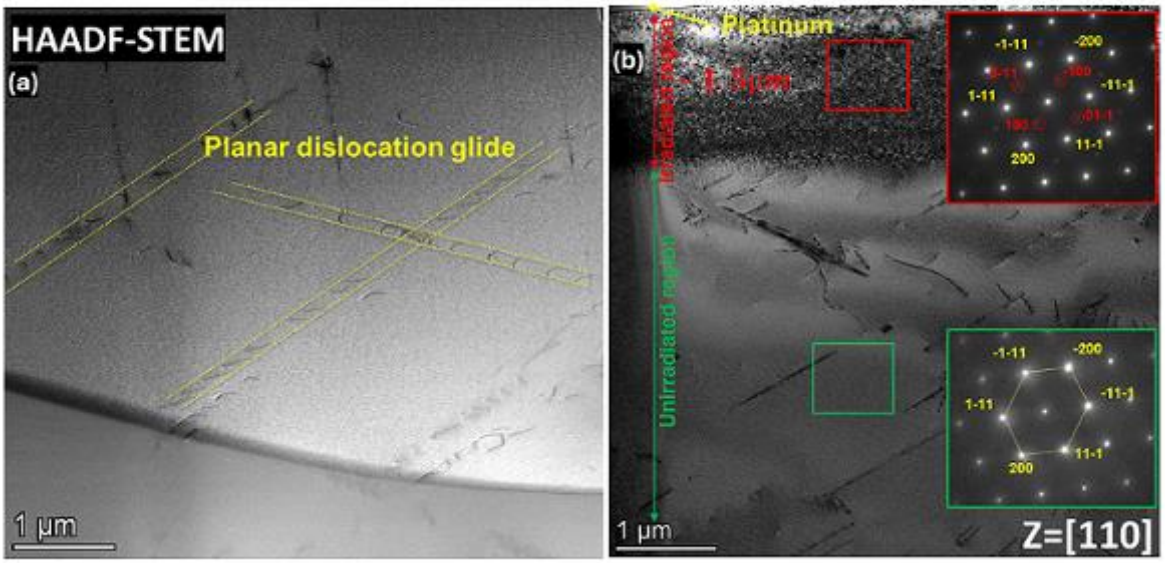
References

[1] A. Bastin et al. Adv Eng Mater 26 (2024) 2400650.

[2] C. Lu et al. Nat Commun 7 (2016). https://doi.org/10.1038/ncomms13564.

Fig. 1: (a) HAADF-STEM image of pristine HEA (b) On zone BF-TEM image of the irradiated HEA taken along [110] zone axis, insets correspond to the SAD pattern taken from the respective areas

Fig. 1



MS2.P14
Structure and composition of refractory Ni-contained CrMoNbTaVW high entropy alloy thin film

D. Litvinov[1], M. Stüber[1], S. Ulrich[1], J. Aktaa[1]

[1]Karlsruhe Institute of Technology, Eggenstein-Leopoldshafen, Germany

Refractory high entropy alloys have attracted attention due to their versatile properties, such as mechanical properties, excellent anti-oxidation performance, outstanding corrosion resistance, and thermal stability, indicating high application potentials. In this work, the structure and composition of complex high entropy alloy thin films, CrMoNbTaVW (HEA) with small portion of Ni (ca. 3.6 %), were investigated by electron microscopy. The thin film with a thickness of ca. 5 µm was grown by magnetron sputtering from a multiple-elemental compound target. Cross-section sample was prepared using focus ion beam. For the determination of the thin film composition, energy-dispersive X-ray (EDX) spectroscopy was used. For the crystallographic investigations, conventional transmission electron microscopy (TEM) with selected area diffraction and high resolution TEM imaging (HRTEM) with fast Fourier transformation (diffractogram) were applied.

It is found, that Ni-containing HEA thin film exhibits a single-phase body-centered cubic (BCC) crystal structure with a lattice parameter of a = 0.316 nm. Fig. 1 shows a HRTEM image of a HEA thin film with evaluated (left hand side) and simulated (right hand side) diffractograms from the area marked by the white square in the HRTEM image and the corresponding enlarged point pattern of the HRTEM image exact in [111]-zone axis (ZA) orientation. The grains in the HEA thin film are columns, extended in growth direction (as can be seen in the HAADF image in Fig.2). They are not always perpendicular to the substrate surface, have a texture and are elongated in <112> direction. The width of the grains slowly increases in the growth direction and reaches a few hundred nm.

An inverted HAADF STEM image of Ni-contained HEA thin film and elemental EDX maps are presented in Fig. 2. EDX measurements of the layer show almost equal atomic concentrations of Cr, Mo, Nb, Ta, V and W elements of around 16-17 % with uniform distribution. On the Ni-map, there are regions with decreasing Ni-concentration, which are indicated by arrows in Fig. 2. The local measurements of Ni-concentration in the layer are in range from 0.5 % to 4.5 %. Considering the thickness averaging in TEM samples along the electron beam, regions without Ni could exist. They may be either grains or grain boundaries. Note, that the elements Cr, Mo, Nb, Ta, V and W from which the investigated HEA thin film consists, have BCC crystal structures, while Ni has face-centered cubic crystal structure and may be not match to BCC crystal structure of the investigated HEA thin film. Moreover, the solubility of Ni may be low for such complex systems as HEA. These both factors may lead to inhomogeneity of Ni-distribution, which we observe in elemental EDX maps in Fig. 2. Different defects such as dislocations and stacking faults have been observed and analysed in this work.

Figure 1. HRTEM image of HEA thin film with evaluated (left) and simulated (right) diffractograms from the area marked by white square in the HRTEM image and corresponding enlarged point pattern of the HRTEM image.

Figure 2. Inverted HAADF STEM image of HEA thin film with elemental EDX maps. Arrows mark Ni-poor areas.

Fig. 1

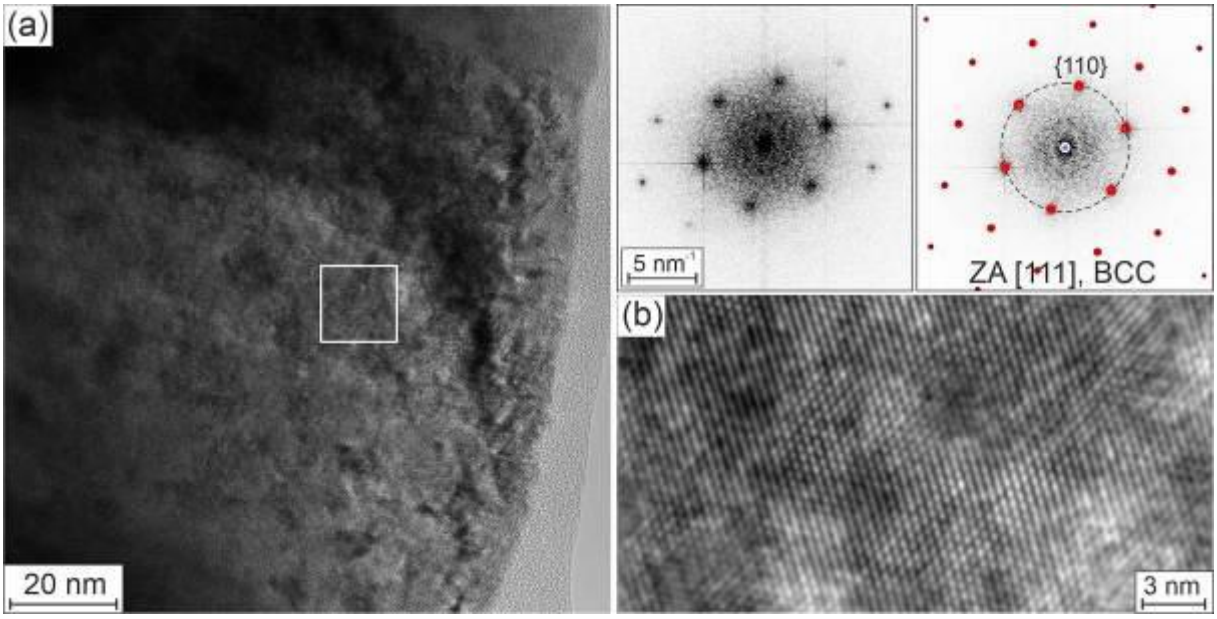
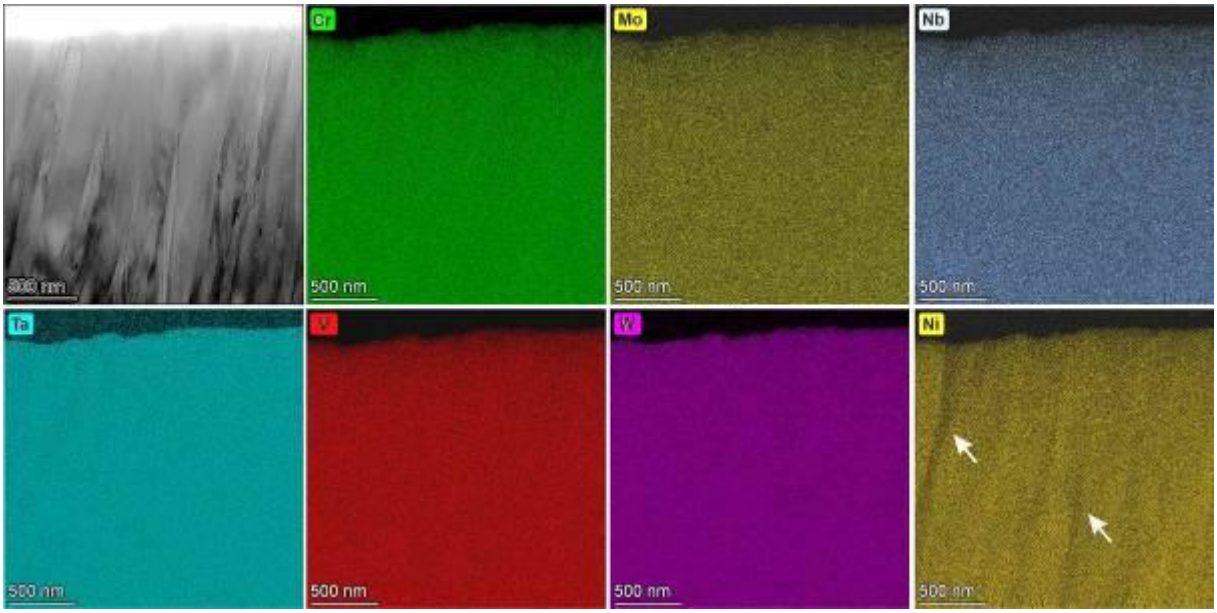


Fig. 2



MS2.P15
Microstructural response of Cu-based alloys to the neutron irradiation

M. Klimenkov[1], C. Bonnekoh[1], U. Jäntsch[1], M. Rieth[1], K. Iroc[2], D. Terentyev[2]

[1]Karlsruhe Institute of Technology, Karlsruhe, Germany
[2]Nuclear Materials Science Institute, Mol, Belgium

Pure copper (Cu) has high thermal conductivity but relatively low strength, which limits its application as a heat sink material. However, various strengthening mechanisms can enhance the strength of copper. Among these, precipitation hardening and dispersion strengthening are the most effective methods for improving copper"s strength while preserving its high electrical and thermal conductivities. This study examines two alternative alloys: precipitation-hardened CuCrZr-V and oxide-dispersion-hardened Cu-ODS alloys. The materials were irradiated in the BR2 reactor (Belgium) at 2.5 dpa and temperatures of 150°C, 350°C, and 450°C, followed by microstructural analysis of radiation defects using transmission electron microscopy (TEM).

The impact of neutron irradiation on the microstructure of Cu-based alloys can be classified into two effects: the formation of structural lattice defects, such as voids and dislocation loops, and the radiation-induced redistribution of alloying or transmutation-induced elements. Quantitative analysis of neutron radiation-induced defects, including voids (Figure 01) and dislocation loops (Figure 02), was performed. Dislocation loops of the a0½⟨110⟩ type formed in both alloys at all irradiation temperatures, while faulted a01/3⟨111⟩ loops were not observed. The determination of Burgers vector of dislocation loops in Cu-ODS alloy irradiated at 450 °C was performed using weak beam dark field imaging (WBDF) near the [100] zone axis (Figure 2). The applied method for materials with fcc structure, that based on based on the visibility criterion of dislocations. The images of dislocations in a grain that was oriented near [001] zone axis were obtained using [220], [2-20] and [002] and [200] g-vectors. The loops with a0½[110] and a0½[-110] Burgers vector are marked correspondingly with yellow and blue arrows in the images.

Neutron irradiation induced redistribution of Cr, Zr, and V in CuCrZr-V, leading to temperature-dependent coarsening of Cr-rich nanosized precipitates (Figure 3). Additionally, the analysis of Ni and Zn, generated by β^+ and β^- decay of ^{64}Cu, revealed segregation on precipitates and grain boundaries. It the present work, we were able to screen the distribution of Ni and Zn at the nanoscale level. In the CuCrZrV alloy, Ni was found to segregate on the Cr precipitates forming a shell around the Cr rich phase (Figure 3). At 450 °C, a shell of NiZr intermetallic phase forms around CrV precipitates. It is also found that at 350 °C about 30 % of Ni and at 450 °C about 80% Ni remains in solid solution. In the Cu-ODS alloy, Ni is homogeneously distributed within the grains. Only a very small fraction segregates at larger precipitates and grain boundaries. Segregation at structural defects such as dislocation loops or voids was not observed.

These insights contribute to the ongoing development of advanced heat sink materials for fusion applications, emphasizing the need for optimized microstructural stability and irradiation resistance in extreme environments.

Figure captions:

Figure 01: Bright-field TEM images showing voids in Cu-Y_2O_3 irradiated at 150 °C (a), 350 °C (b) and 450 °C (c).

Figure 02. DF-STEM images woth reversed contrast of the same region obtained with four different g-vectors near the [100] zone axis. The direction of g-vectors is indicated in the images. As an example, blue and yellow arrows indicate the loops with Burgers vector a0½[110] and a0½[1-10].

Figure 03: Elemental maps showing distribution of Cr, Zr, V and Ni obtained from CuCrZrV alloy irradiated at 350 °C (a) and 450 °C (b) temperatures.

Fig. 1

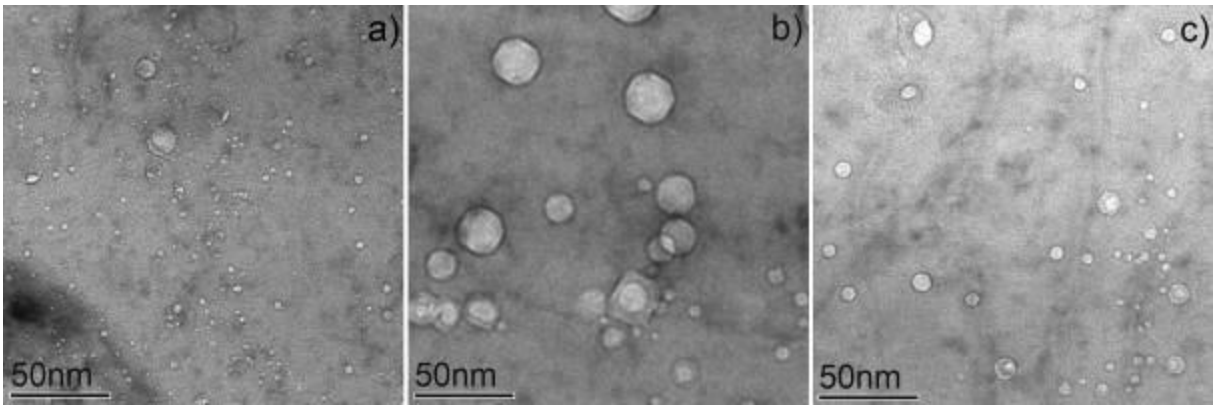


Fig. 2

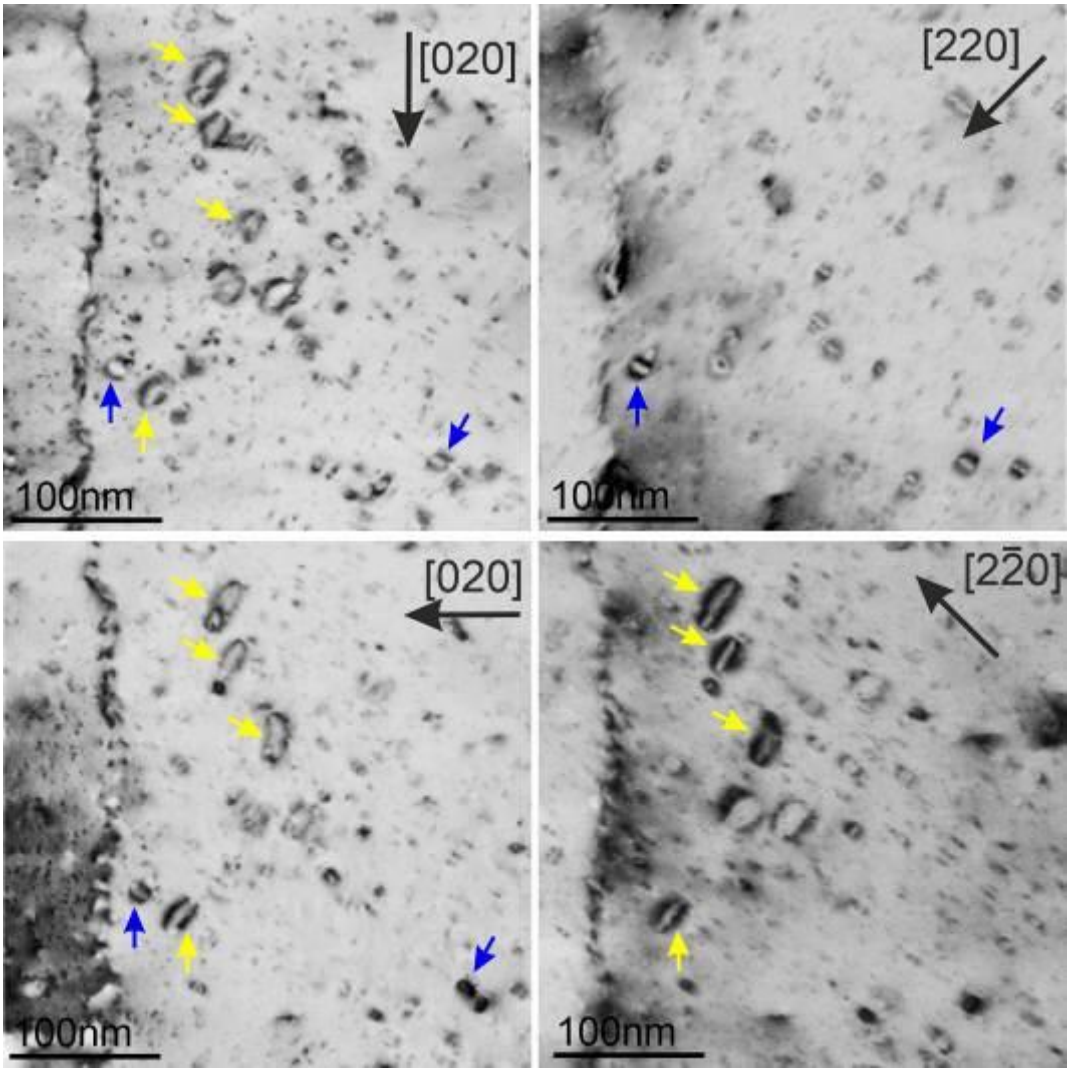
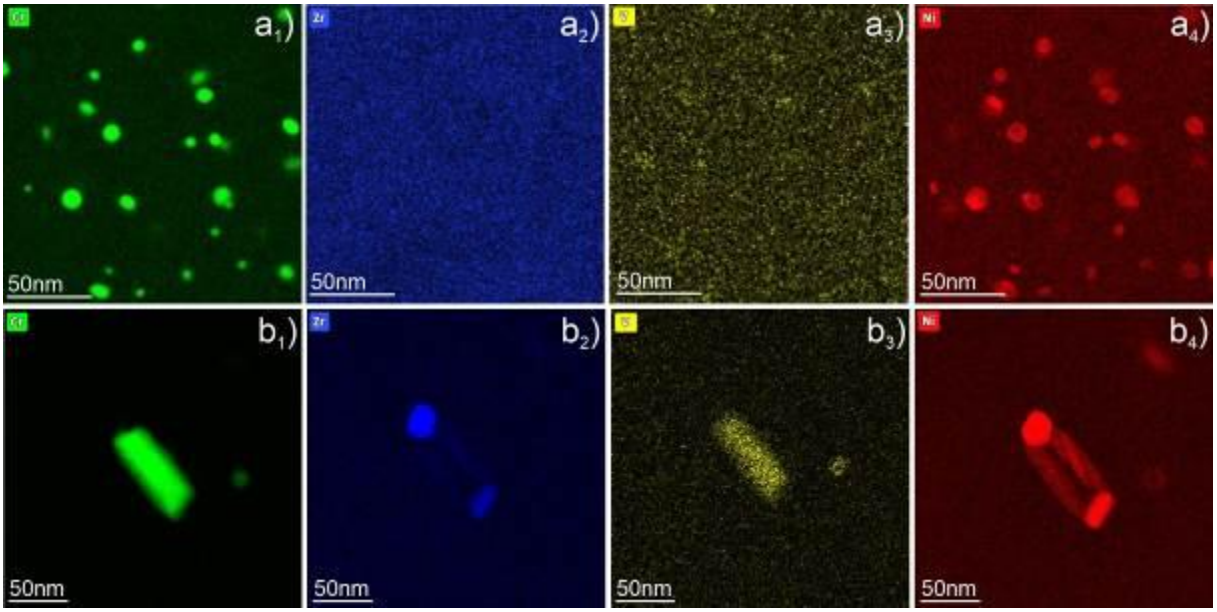


Fig. 3



MS2.P16
Crack growth and microstructure evolution in FIB-microcantilever bending fatigue – A case study on nanocrystalline nickel

C. Pauly[1], J. Luksch[2], G. Mohanty[3], F. Schäfer[2], C. Motz[2]

[1]Saarland University, Functional Materials, Saarbrücken, Germany
[2]Saarland University, Materials Science and Methods, Saarbrücken, Germany
[3]Tampere University, Materials Science and Environmental Engineering, Tampere, Germany

Introduction

Miniaturization of components, e.g. for MEMS and medical applications, poses challenges for materials testing. Established macroscopic fatigue testing procedures set boundary conditions for minimum sample dimensions depending on toughness and yield strength [1] resulting in rather macroscopic sample dimensions. Fatigue and fracture testing of smaller samples is not well-standardized and is an active area of research [3-9]. Of high interest is how intrinsic and extrinsic size effects ("smaller is stronger") affect micro- and mesoscale fatigue. Challenges for testing in the fields of instrumentation, sample preparation and testing procedures are discussed here in a case study on focused ion beam (FIB) fabricated nanocrystalline nickel (nc-Ni) microcantilevers.

Objectives

This presentation discusses practical considerations of microcantilever fabrication by FIB and shows a case study of fatigue in nc-Ni including post-mortem characterization. Limits and challenges in sample fabrication by Ga-FIB and Xe-FIB are discussed. A protocol for SEM in-situ fatigue-testing is developed and resulting da/dN curves are discussed in the context of size effects.

Materials & methods

Notched microcantilevers with square cross-sections of 5x5 to 50x50 µm² are made from electrodeposited nc-Ni coatings using Ga- and Xe-FIB. An in-situ nanoindenter in the SEM is used for crack initiation in tension-compression (-0.3<R<-0.2, Fig 1) followed by fatigue testing in tension (R=0.1). da/dN curves are calculated from the load-displacement data. Microstructure at the crack flanks after fatigue testing is investigated by FIB cross-sections and EBSD-tomography.

Results

Microcantilever fabrication by Ga-FIB beyond dimensions 10x10x50 µm³ is time-consuming due to beam current limitations. Larger cantilevers of 50x50x250 µm³ can be fabricated by high-current Xe-FIB at the expense of stronger curtaining artefacts in nc-Ni which may act as undesired crack nucleation sites. The da/dN curves show an increase of Paris exponent and data point scatter with decreasing cantilever size which points towards an extrinsic size effect. Finally, substantial grain growth at the crack flanks and transgranular crack growth is observed (Fig 2).

Conclusion

Current FIB microscopes enable sample preparation up to 50x50 µm² cross-section, but care must be taken to avoid negative effects of FIB artefacts. An extrinsic size effect in nc-Ni microcantilever samples is found. FIB-EBSD tomography exhibits significant grain growth at the crack flanks.

References

[1] ASTM E647, Standard Test Method for Measurement of Fatigue Crack Growth Rates

[2] K. Takashima et al., Mater. Trans. 42 (2001) https://doi.org/10.2320/matertrans.42.68

[3] J. Ast et al., Mater. Des. 173 (2019) https://doi.org/10.1016/j.matdes.2019.107762

[4] S. Wurster et al., Philos. Mag. 92 (2012) 1803–1825
https://doi.org/10.1080/14786435.2012.658449

[5] B.N. Jaya et al., J. Mater. Res. 30 (2015) https://doi.org/10.1557/jmr.2015.2

[6] K. Schmuck et al., JOM. 76 (2024) https://doi.org/10.1007/s11837-023-06348-7

[7] J. Luksch et al., Mater. Sci. Eng. A. 884 (2023) https://doi.org/10.1016/j.msea.2023.145452

[8] J. Luksch et al., Mater. Des. 241 (2024) 112880
https://doi.org/https://doi.org/10.1016/j.matdes.2024.112880

Figure 1: SEM image of microcantilever and -gripper for crack initiation (R<0).

Figure 2: EBSD tomography of microcantilever after fatigue test showing large grains at the crack flank.

Fig. 1

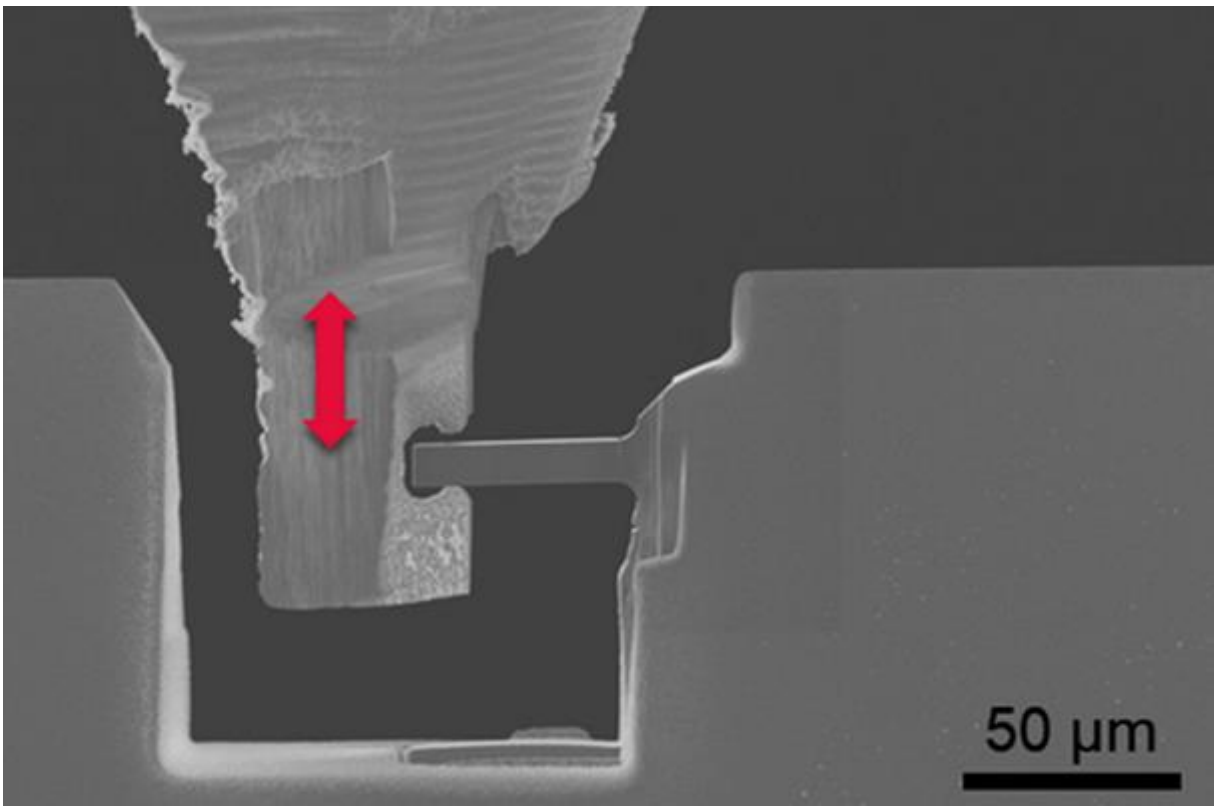
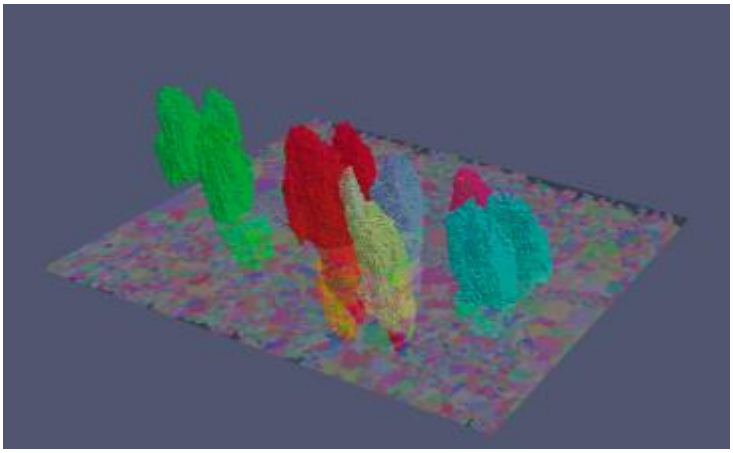


Fig. 2



MS2.P17
In situ atomic-scale TEM observation of structural transformations in $Ge_2Sb_2Te_5$ phase change memory alloys

A. Lotnyk[1], T. Dankwort[2,3], M. Behrens[1], L. Voß[2], S. Cremer[1], L. Kienle[2]

[1]Leibniz Institute of Surface Engineering (IOM), Leipzig, Germany
[2]Kiel University, Materials Science, Kiel, Germany
[3]Fraunhofer Institute for Silicon Technology ISIT, Itzehoe, Germany

Introduction

Ge-Sb-Te materials represent an outstanding class of functional materials. The materials can be used as non-volatile memory and thermoelectric materials as well as topological insulators. The alloys are distorted and contain a huge number of structural vacancies, which play important roles in structural and electronic transitions. Thus, control of disorder and understanding the structural transformations in GST materials are of great importance for the design and reliability of memory devices [1].

Objectives

In this work, structural transformations in $Ge_2Sb_2Te_5$ (GST) thin films prepared as membranes on carbon coated TEM Ni grids are studied by *in situ* heating TEM. The focus was on structural changes within <110>-oriented fcc-GST grains. In addition, in situ XRD heating was used as a complementary method to observe structural changes in epitaxial GST thin film [2].

Materials & methods

18 nm thick amorphous GST (a-GST) thin films were grown by pulsed laser deposition (PLD) on carbon coated TEM Ni grids. In situ heating TEM experiments were performed inside of a probe Cs-corrected Titan3 G2 60–300 microscope using a Gatan double-tilt heating holder. Complementary in situ XRD heating experiments were performed on Rigaku SmartLab diffractometer.

Results

At TEM holder temperatures ranging between 135°C and 150°C, the crystallization of a-GST resulted in the formation of fcc-GST grains with random distribution of vacancies. Starting from 160°C, the vacancies gradually accumulate into vacancy layers (Fig. 1). Further heating to 220°C and 240°C led to the formation of vacancy-ordered GST (vo-GST) grains and trigonal GST domains (possessing vdW-like gas) within the vo-GST grains as well as the formation of large <001>-oriented trigonal GST grains. This is in a good agreement with outcomes on in situ XRD heating of epitaxial vo-GST thin film. Moreover, vo- and fcc-GST structures can coexist with vdW t-GST structure in one grain. Full transformation to <11-20>-oriented t-GST grains occurs at 280°C. Unlike other grains, the <001> t-GST grains show abnormal grain growth behaviour, while the electron beam irradiation accelerates the growth. Detailed characterizations of vo-GST grains reveal transient structures that indicate shear transformation mechanism and different defects as well as chemical changes during the transformations (Fig. 2) [2].

Conclusion

Overall, this study provides new insights in understanding the phase transition mechanisms in thin Ge-Sb-Te layers and can be used for their microstructure optimization [2].

The authors thank to A. Mill for FIB lamellae preparation. German Research Foundation (DFG, project number 445693080) is acknowledged for financial support.

References

[1] A. Lotnyk, M. Behrens, B. Rauschenbach, Nanoscale Adv. 1 (2019) 3836-3857

[2] A. Lotnyk, T. Dankwort, M. Behrens, L. Voß, S. Cremer, L. Kienle, Acta Mater. 266 (2024) 119670

Fig. 1. (a), (b) and (c) HRTEM micrographs acquired at TEM holder temperatures of 150°C, 160°C and 220°C, respectively. Insets in (a) and (c) show simulated HRTEM images. VL shows a vacancy layer.

Fig. 2. HAADF-HRSTEM image acquired after thermal heating of GST thin film in TEM to a holder temperature of 240°C. Yellow and red strokes depict Te and GeSb layers, respectively. Green stroke marks the core of transition area and extra Te plane. The rectangles depict layered defects.

Fig. 1

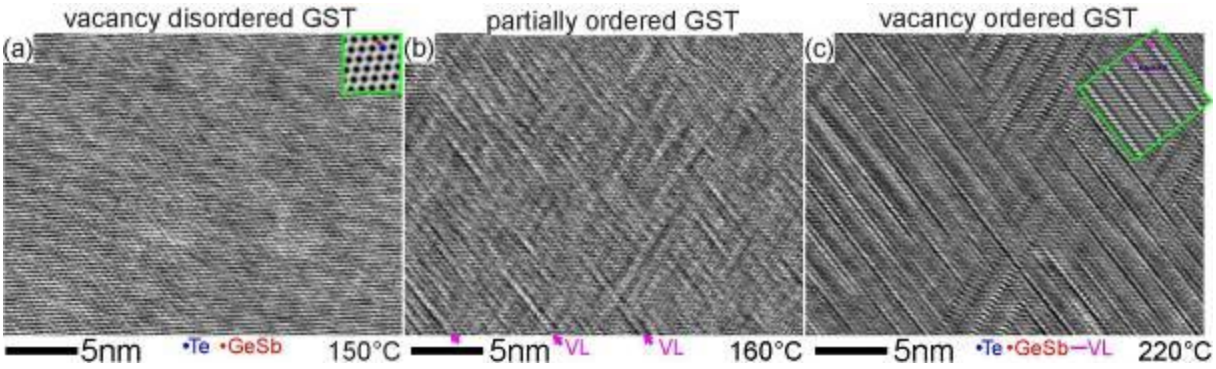
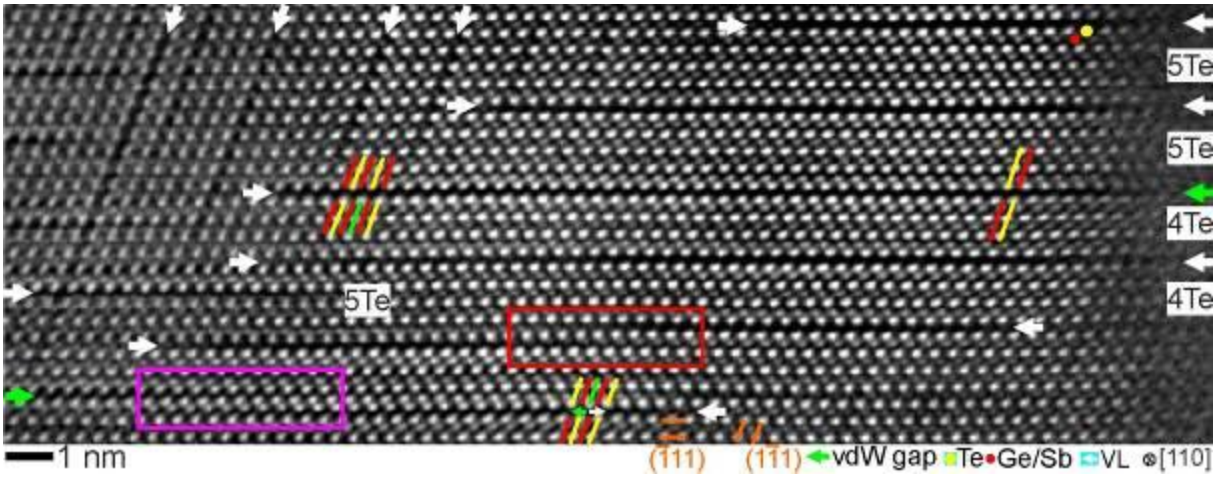


Fig. 2



MS2.P18
Strain mapping of a near Σ5(310) grain boundary in a pure and in an impurity-segregated Cu bi-crystal using 4D-STEM

A. Akbari[1], H. Ding[2], H. Rösner[1], E. Neelamegan[1], C. H. Liebscher[2,3,4], S. V. Divinski[1], G. Wilde[1]

[1]University of Münster, Institute of Materials Physicss, Münster, Germany
[2]Max-Planck-Institute for Sustainable Materials, Düsseldorf, Germany
[3]Ruhr University Bochum, Research Center Future Energy Materials and Systems, Bochum, Germany
[4]Ruhr University Bochum, Faculty of Physics and Astronomy, Bochum, Germany

Introduction

Grain boundaries (GBs) play an important role in determining the physical properties of materials. The presence of strain fields localized at GBs can alter the atomic transport characteristics. Our focus lies in elucidating the atomic structure of grain boundaries in pure copper, particularly in the presence of impurity segregation, and understanding the associated strain state along the GB on different scales.

Objectives

This study aims to investigate the evolution of strain fields along GBs in pure Cu and impurity-segregated regions, especially in relation to varying depths from a diffused surface. We utilized two distinct methodologies: Nano-Beam Diffraction Patterns (NBDPs) and Geometrical Phase Analysis (GPA). Our goal is to elucidate the correlation between impurity concentration, strain accumulation on GBs, and their impact on atomic transport properties, thereby linking microstructural features with the transport phenomena.

Materials & methods

A Cu bi-crystal featuring a near Σ5(310) GB was fabricated by a modified Bridgman method. A thin layer of Co was deposited and the sample was annealed at 800°C. To prepare electron-transparent specimens for examination, a Focused Ion Beam (FIB) was employed. Elastic strain measurements along and across the GB were conducted at both the nanometer and atomic scale. Using 4D-STEM, a stack of NBDPs was acquired with probe size of 1 nm, while maintaining the grains in zone axis orientations. A custom-written code [1] was employed to calculate the corresponding strain maps. For the atomic scale characterization, GPA was applied to high resolution STEM images, measuring lattice fringes displacement relative to a reference lattice.

Results

The reference strain state of the grain boundary structure of pure Cu was quantified using both NBDP and GPA methods [2]. NBDP measurements indicated relatively low strain levels approaching the GB, whereas the GPA method revealed pronounced localized strain fields associated with GB defects, evident through significant discontinuities in strain components. Strain mapping on the Co-diffused samples demonstrated a slight accumulation of Co atoms at the GB, as affirmed by STEM-EDX analysis. However, NBDP did not indicate any strain increase at the GB in these samples, prompting further strain analysis through GPA on the Co-deposited specimens.

Conclusion

The strain analysis of the GBs in pure and Co-diffused Cu-bicrystals was performed using GPA and NBDP methods. The GPA yielded localized strain information with atomic resolution, revealing strain fields influenced by atomic motif arrangements. In contrast, NBDP provided a broader strain

assessment over tens of nanometers, indicating an average elastic strain of zero in pure copper samples. The low concentration of diffused Co did not significantly alter the NBDP strain analysis results. Altogether, this work emphasizes the importance of strain fields in understanding GB diffusion mechanisms in metallic systems.

References

[1] Gammer, C., Mangler, C., Rentenberger, C., & Karnthaler, H. P. (2010). Quantitative local profile analysis of nanomaterials by electron diffraction. Scripta Materialia, 63(3), 312-315.

[2] Ding, H., Akbari, A., Chen, E., Rösner, H., Frolov, T., Divinski, S., Wilde, G., Liebscher, C.H. (2025). Hierarchy of defects in near-Σ5 tilt grain boundaries in copper studied by length-scale bridging electron microscopy. Acta Materialia. doi.org/10.1016/j.actamat.2025.120778

MS2.P21
Microscopic investigation of dissimilar welds in battery packs

T. Yallew[1], S. Cordes[1], F. Hashani[1], D. Schnug[2], Y. Janßen[2], B. Butz[1]

[1]University of Siegen, Mechanical Engineering; Micro- and Nanoanalytics Group, Siegen, Germany
[2]Omnitron Griese GmbH, Hilchenbach, Germany

The need for sustainable energy solutions is becoming a focus of scientific research. The rising demand is pressuring cost efficiency and process optimizations in battery packs manufacturing. Battery packs for machines and applications requiring a mobile and environmentally friendly energy source consist of multiple individual cells connected by a busbar. The interconnection creates an electrical and mechanical connection, which can be realized by means of different joining techniques. To join busbars to the batteries positive/negative terminals; laser beam welding, tungsten inert gas welding, and resistance spot welding techniques are generally used. The production of battery packs remains challenging because of the dissimilar metals" joint differences between their thermal, metallurgical properties and the resulting joint defects like pores, cracks and brittle connections. Another issue is the heat input into the battery electrolyte during the welding, caused by the different manufacturing processes. The adaption of the different joining techniques greatly influences the characteristics of the battery pack in terms of battery performance such as fatigue resistance, capacity and lifetime. Selection of a suitable joining technique, therefore, involves several requirements such as electrical, thermal, material and metallurgical requirements, and of course mechanical and economic requirements (suitability for mass production, costs and better possibility to be standardized). Therefore, cross-scale microscopic, tomographic and spectroscopic analyses are used to optimize the welding processes, improve the mechanical and electrical connection quality and ensure minimal impact on the battery interior.

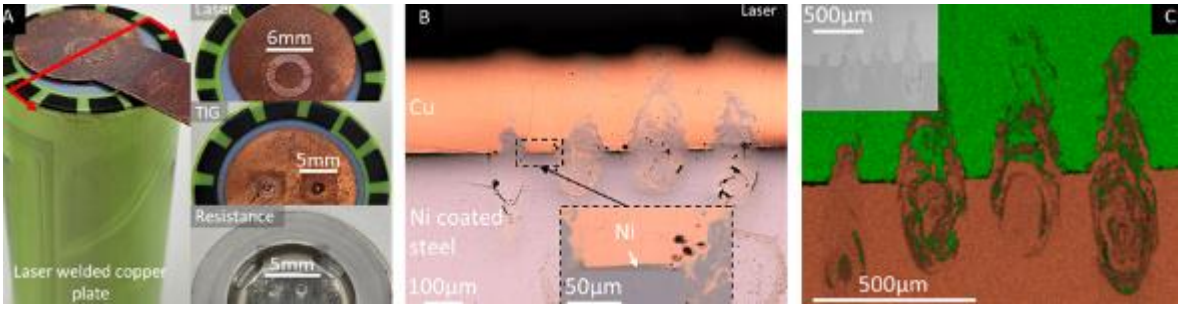
In this experimental work, the joints between the Cu/Ni and Cu/Ni coated steel of the batteries at the positive/negative terminals respectively, were made by laser beam welding, tungsten inert gas welding, and resistance spot welding techniques. The welded samples for metallographic analysis were site-specific sectioned perpendicular to the welding direction, then embedded, fine polished and finished with an Ar-ion cross-section polisher. Microstructure and phase/chemical analyses of the weld zone were conducted using SEM, including BSE (crystallographic contrast) imaging, EBSD, and EDS (Fig. 1). The three methods are then compared in terms of their welding quality and production and implementation costs.

This comprehensive approach provides valuable insights into the microstructure evolution of welds, paving the way to ensuring that welded parts meet stringent quality standards and reliability requirements. The analyzed welded microstructure in accordance with the defects generated shows laser beam welding as a viable alternative to the existing techniques of tungsten inert gas welding and resistance spot welding. Laser welding is a suitable alternative for welding dissimilar metals such as copper and nickel, as demonstrated in this work.

Fig 1: A) Top view of the different welding zones (Laser, TIG and Resistance welding); B) Light microscope image of the cross-section of a laser-welded sample (Cu on Ni coated steel); C) EDS of the welded zone

Acknowledgements: We acknowledge use of the DFG-funded Micro-and Nanoanalytics Facility (MNaF) at the University of Siegen (INST 221/131-1)

Fig. 1


A
Laser
6mm
TIG
5mm
Resistance
5mm
Laser welded copper plate
B
Laser
Cu
Ni coated steel
100µm
Ni
50µm
500µm
C
500µm

MS2.P23
TEM examinations of an Al diffusions coating on EUROFER97

U. Jäntsch[1], M. Dürrschnabel[1], M. Klimenkov[1], M. Rieth[1], J. Lorenz-Kleinert[1], C. Schroer[1], M. Yurechko-Hussy[1]

[1]Karlsruhe Institute of Technology, Institute for Applied Materials, IAM-AWP, Eggenstein-Leopoldshafen, Germany

The Reduced activation ferritic/martensitic (RAFM) steel EUROFER97 is regarded as a prime structural material for future fusion power reactors. In the breeding blanket design, EUROFER97 will operate at temperatures of up to 550°C while being in direct contact with liquid materials such as PbLi. However, RAFM steels exhibit significant corrosion under these conditions. To mitigate this, Al-based coatings are being explored as protective corrosion barriers. Examining the microstructure of these coatings is a critical step in assessing their effectiveness and suitability for use in these demanding environments. Understanding the structure of oxide layers and the Al-diffusion zone in EUROFER97 is crucial for evaluating its suitability for practical applications.

To produce cylinders, a thin Al layer (approx. 5µm) was deposited on the carrier substance EUROFER97 by means of an electroplating process (ECX process). Then, a three-stage heat treatment was conducted at 640°C, 980°C and 760°C, each in the presence of argon with intermittent cooling in the cold furnace section. The preparation and investigations of TEM (transmission electron microscopy) lamella were conducted using scanning electron microscopy (Crossbeam Auriga, ZEISS) and TEM in combination with energy-dispersive X-ray analysis (STEM-EDX in a ThermoFisher Scientific - Talos F200X).

The subject of the microstructure investigations was the approx. 50µm thick interdiffusion zone between an Al protective surface layer and the EUROFER97 substrate of the heat-treated sample. To be able to clearly assess the structural changes along this zone resulting from interdiffusion of Al and EUROFER elements, a TEM lamella at least 50µm long was cut out, Fig. 1. Finally, the foils for the TEM investigations were thinned out in a total of three areas of particular interest along the lamella.

Fig. 1: SEM/FIB picture showing the selected position of TEM lamella at sample material, defined target preparation.

The SEM/FIB image in Fig. 1 already clearly shows the existence of precipitates in the grains of the interdiffusion zone. As an example of the results of the TEM investigations, Fig. 2 shows a STEM-EDX element mapping of the Al/EUROFER97 interdiffusion zone along an area, located at the middle of the zone. This area is in 20µm to 35µm beginning from the still existing EUROFER structure.

The microstructure of EUROFER97 show a large grain of about 10µm size. The ferritic lath structure could not be recognized (Fig. 2). Dislocation lines, on which precipitates of the MX type (TaC) are located, are reminiscent of the previously existing EUROFER structure. The linearly oriented precipitations of type M23C6 suggest the former existence of a grain boundary. In addition, the presence of AlN particles with a length of several micrometers.

Fig. 2: STEM-EDX elemental maps after applying Three-stage heat treatment at first area of TEM lamella.

In summary, significant changes were observed in the three selected areas along the interdiffusion zone. These investigations on heat-treated sample material serve as a basis for assessing corrosion damage of the Al layer and the Al/interdiffusion zone interface. The effect of the existence of a 50µm wide interdiffusion zone with incorporated aluminum nitride particles on the stability of the steel EUROFER97 against the influence of liquid metals such as PbLi still must be evaluated in further experiments.

Fig. 1

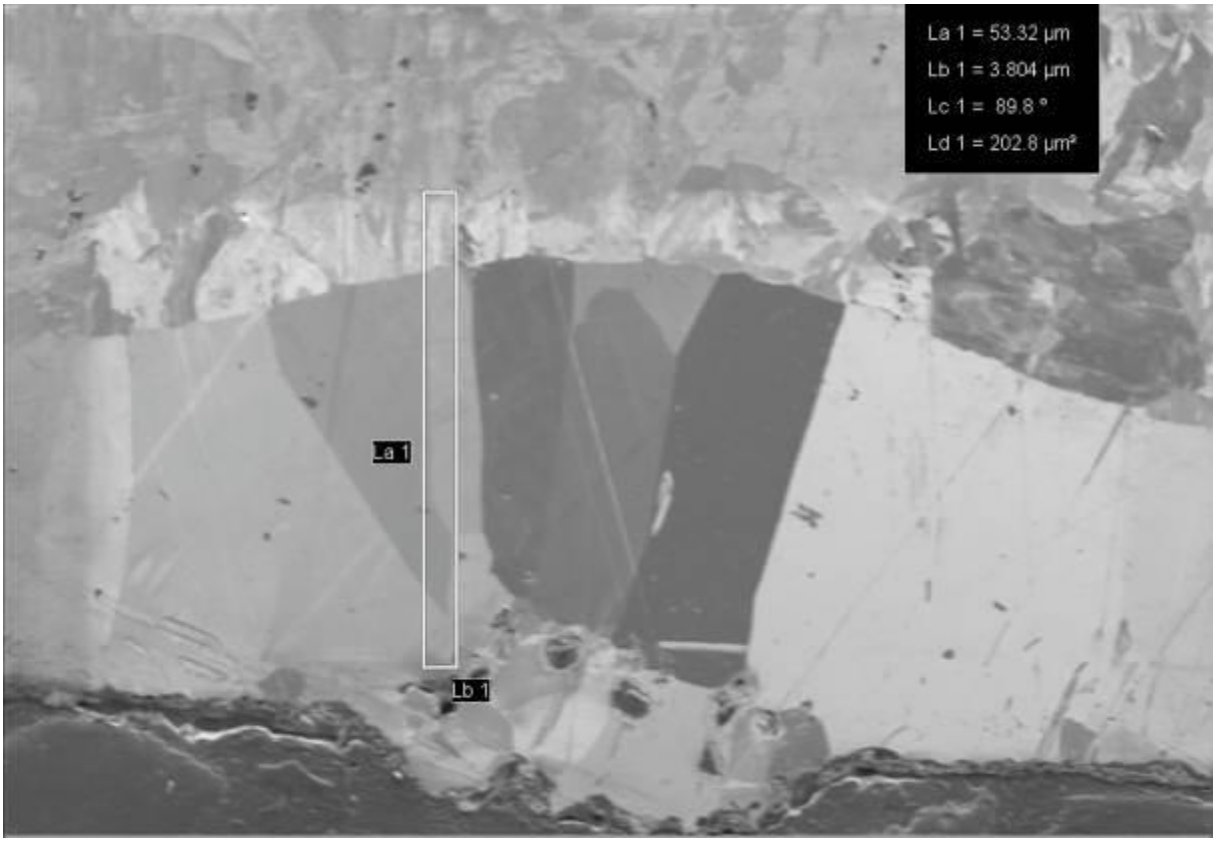
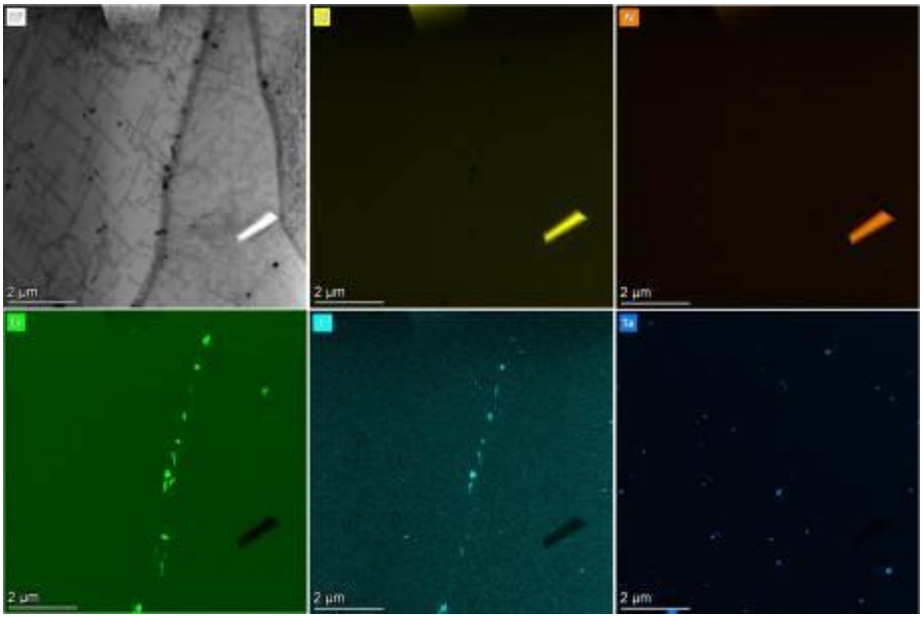

La 1 = 53.32 µm
Lb 1 = 3.804 µm
Lc 1 = 89.8 °
Ld 1 = 202.8 µm²
La 1
Lb 1

Fig. 2


2 µm
2 µm
2 µm
2 µm
2 µm
2 µm

MS2.P24
Preliminary *in situ* heating/cooling experiments in SEM investigating precipitation and dissolution in an AlZnMgCu alloy

C. R. Kreyenschulte[1], N. Rockstroh[1], F. Bigalke[2], B. Milkereit[2,3], O. Keßler[2,3]

[1]Leibniz Institute for Catalysis (LIKAT Rostock), Analytics, Rostock, Germany
[2]University of Rostock, Chair of Materials Science, Rostock, Germany
[3]University of Rostock, Competence Centre CALOR, Department Light, Life & Matter, Rostock, Germany

Aluminum alloys show a complex precipitation behavior during thermal treatment, which is utilized to steer the desired properties. For aluminum alloy (AA) 7068, Differential Scanning Calorimetry (DSC) was applied in combination with ex-situ Scanning Electron Microscopy (SEM) to understand relation between cooling rates and formation of different precipitation types [1].

As one drawback, DSC measures the sum of any heat event (during heating: endothermic dissolution and exothermic precipitation; during cooling: only exothermic precipitation). However, DSC cannot give any hint on the nature of the phases formed. After installation of a new heating stage in our SEM we aimed to establish procedures on how to acquire and evaluate data of in-situ heating experiments of materials. AA 7068 (AlZn7.5Mg2.5Cu2) was chosen as an Al alloy with a very high concentration of alloying elements showing relatively large precipitation effects [1]. The objective was now to correlate the precipitation events recorded with DSC (Fig. 1) with changes in the surface of the alloy imaged by SEM.

The material was initially solution annealed and rapidly cooled in order to form a supersaturated solid solution. For SEM preparation the raw material was cut into about 0.9 mm thin plates and polished in several stages to achieve sufficient smoothness of the surface. The resulting platelet was placed on a corundum platelet as an in-between layer onto the heater (Kammrath & Weiss, 1050°C Heating Transfer module) installed in the SEM (Thermo Fisher Scientific, Quattro S). Initially, the specimen was quickly heated to 200 °C. After a short annealing, the specimen was heated to 480 °C with 0.1 K/s. Following a short stabilizing phase, the heater was set to 200 °C without setting a defined ramp. This resulted in a cooling of the sample within about 1000 s, i.e. an averaged cooling rate of about 0.28 K/s. Images were recorded every 20 s with the secondary electron (SE) detector.

Selected images of the in-situ SEM experiments are presented in figure 2. The precipitation evolution could be followed correlating the current temperature with the different types of precipitate sizes forming on the surface of the specimen. During the heat treatment procedure, the brightness and especially the contrast had to be adjusted to compensate for the varying SE emission characteristics dependent on temperature.

The in-situ SEM experiments allowed to follow the formation and dissolution of different types of precipitates depending on the temperature. A key difference to the previous experiments was, that the in-situ data showed continuously the surface of the specimen, while for the ex-situ SEM data provides information from the bulk of the material. Within these limitations, in-situ SEM investigations of precipitation hardening seem worthwhile to be pursued further in order to gain additional knowledge on the temperature ranges of precipitation of specific phases.

Figure 1. Cooling curves of alloy 7068 after solution annealing: (a) DSC and (b) differential dilatometry, used with permission from [1].

Figure 2. SE images of AA 7068 at different stages in the in-situ temperature treatment procedure, a) at 200 °C, b) at 480 °C, and c) cooled to 200 °C again.

Literature

[1] Osten, J.; Milkereit, B.; Reich, M.; Yang, B.; Springer, A.; Nowak, K.; Kessler, O., *Materials* **2020**, 13, 918. https://doi.org/10.3390/ma13040918

Fig. 1

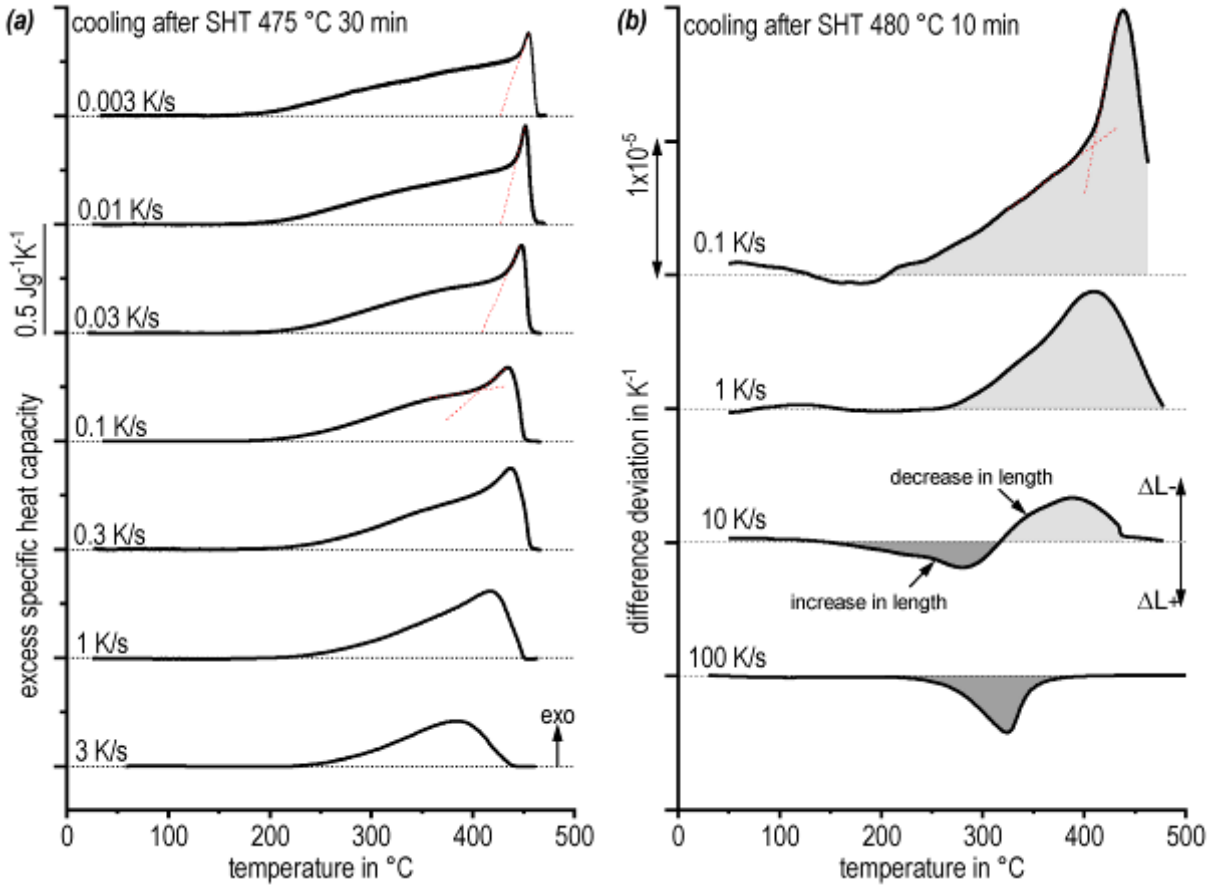
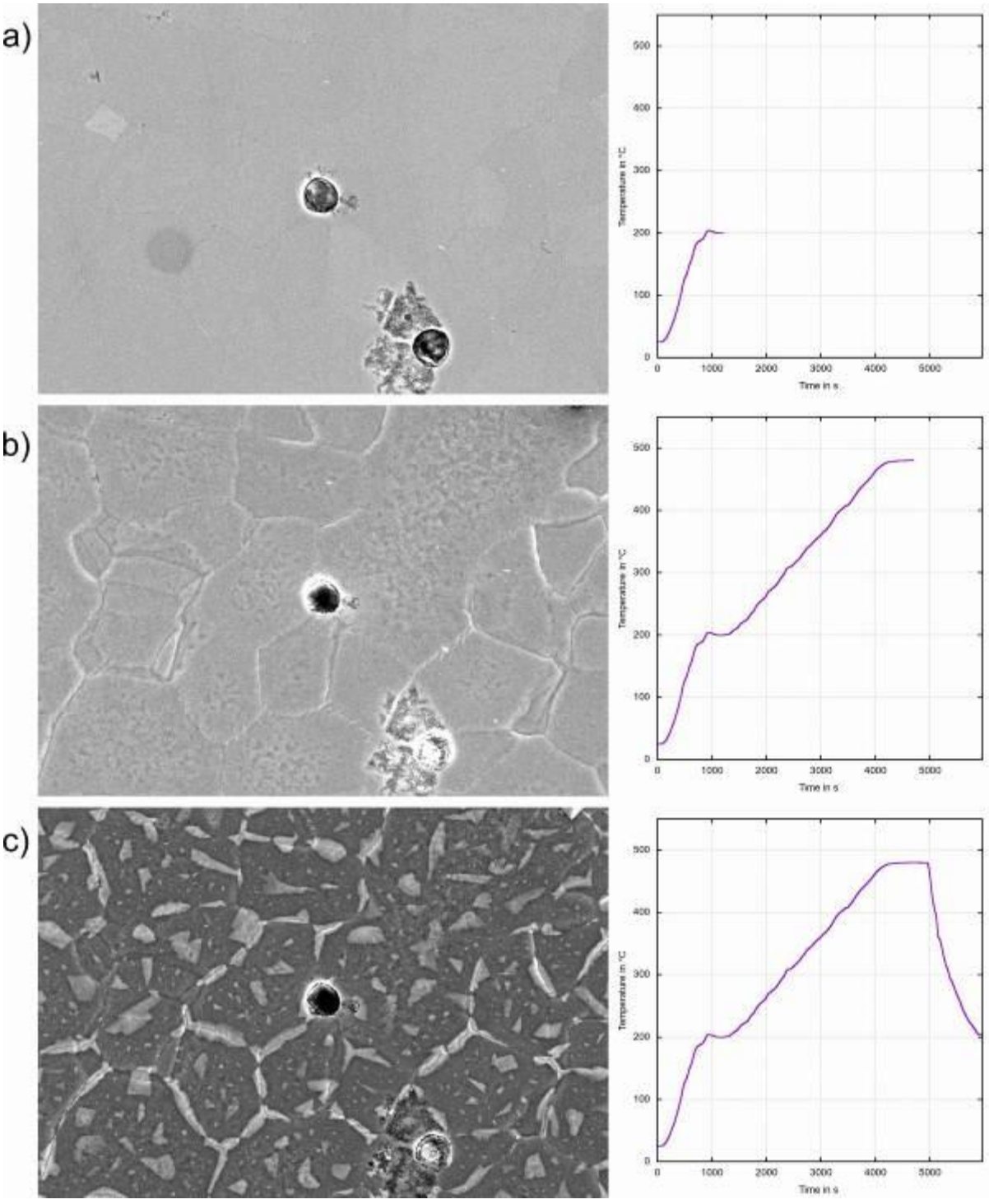


Fig. 2


a)
b)
c)
Temperature in °C
Time in s
0
100
200
300
400
500
1000
2000
3000
4000
5000

MS2.P25
Nano-structure modification of sputter-deposited WTaMoNiCr high-entropy alloy upon heat treatment and low-energy He^+ ion irradiation

H. Kirmse[1], K. Coogan[1], A. Gladyshev[1], P. Maragnoli[1], B. Haas[1], Z. Kochovski[2], M. Bilokur[3], C. T. Koch[1]

[1]Humboldt University of Berlin, Institute of Physics, AG SEM, Berlin, Germany
[2]Helmholtz Institute Ulm for Electrochemical Energy Storage, Institute for Electrochemical Energy Storage, Berlin, Germany
[3]Australian National University, Research School of Physics, Canberra, Australia

Introduction and objectives

In tokamak fusion reactors, the plasma-facing material (PFM) is exposed to high fluxes of low-energy helium (He) particles, fast neutrons (14.1 MeV) and a high heat-load (>10 MW/m2). The PFM has to exhibit high strength, excellent thermal conductivity and stability, and superior resistance to corrosion and radiation damage. Tungsten is the leading candidate as a PFM. However, W contamination of plasma [1], He bubble formation and enhanced surface nanostructuring, have been a common concern in pure tungsten [2-5]. As a potential alternative, high entropy alloys (HEAs) came into the focus of research [6,7].

Materials and Methods

HEA investigated in this work is composed of W, Ta, Mo, Ni and Cr. For studying the behavior upon fusion-relevant conditions, a 40 nm thin layer was sputter-deposited onto a Si substrate with native oxide. Three samples were compared: as-deposited HEA layer; two were exposed to 27 eV He+ ions and a fluence of 7.6·1024 ions/m^2, while heated to either 500°C or 700°C. For TEM investigations, samples were prepared in plan-view and in cross-section [8]. High-angle annular dark-field (HAADF) scanning TEM (STEM) imaging and electron diffraction patterns were recorded in a JEOL 2200FS. STEM-based electron energy loss spectroscopy (EELS) was performed in a NION HERMES dedicated STEM. Both microscopes were operated at 200 kV.

Results

Fig. 1 gives the morphology of the HEAs layer in plan-view. The pristine layer (a) exhibits amorphous islands (Fig. 2a) of an average lateral size of 7 nm. The 500°C sample (b) shows two distinct modifications. First, crystalline grains formed with random orientation (Fig. 2b) of an average size of 12 nm. Second, He bubbles formed appearing as dark spots of an average size of 5 nm. Their area density is ~10^{11} cm^{-2}. Upon heat treatment at 700°C (c), the nanocrystals grow to a size exceeding 20 nm. Thus, the number of crystals contributing to diffraction decreases resulting in a lower number of diffraction spots (Fig. 2c). The number of bubbles per area increases to $3 \cdot 10^{11}$ cm^{-2}. The average bubble size is 6 nm which is slightly larger than for the 500°C sample.

The presence of He within the bubbles is evidenced by STEM EELS (Fig. 3) for the sample treated at 700°C. Fig. a) gives EEL spectra recorded at the bubble (spectrum 1) and aside of it (spectra 2 and 3). The corresponding probe positions are marked in Fig. c). For improved visualization of the He-K peak at 23 eV, spectrum 2 is subtracted from spectrum 1 (Fig. b). The clearly visible He peak evidences that the bubble is filled with He.

References

[1] A.R. Field et al, Nucl. Fusion 63 (2023) 016028

[2] N. Yoshida, J. Nucl. Mat, 266 (1999) 197

[3] I. Ipatova et al, J. Nucl. Mat, 550 (2021) 152910

[4] S.H.B. Teo et al, Materialia, 35 (2024) 102110

[5] S. Kajita et al, Nucl. Mater. Energy 25 (2020) 100828

[6] H.W. Hsiao et al, Nat. comm., 13 (2022) 6651

[7] O. El-Atwani et al, Sci. Adv. 5 (2019) eaav2002

[8] Many thanks to K. Elsner for assistance in sample preparation.

Captions

Fig 1: HAADF STEM images of the differently treated HEAs layer.

Fig 2: Selected-area diffraction patterns of the differently treated HEAs layer (diameter of contributing area: 100 nm).

Fig 3: STEM EELS of HEAs (He+@700°C) in cross-section: a) EEL spectra taken at the bubble (1) and aside (2 and 3); b) difference signal between spectra 1 and 2; c) HAADF STEM image with markers of the probe position for spectra given in a).

Fig. 1

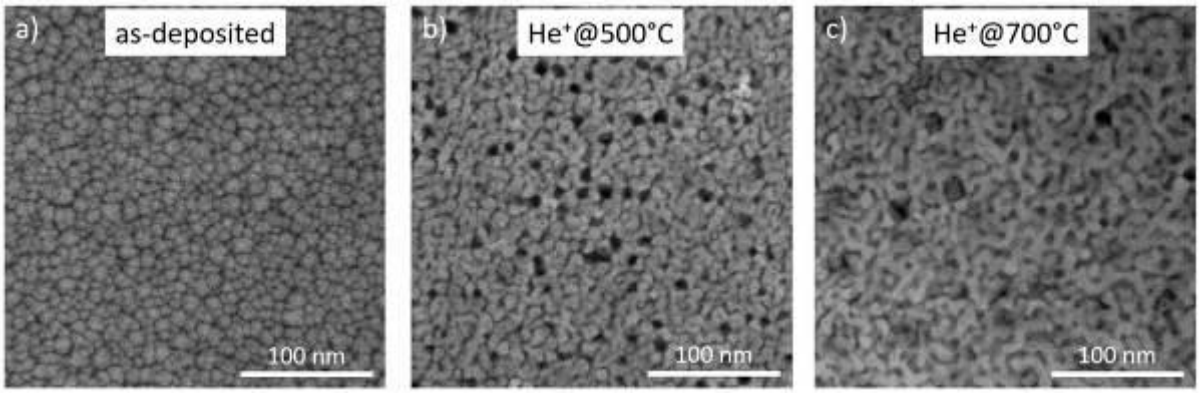


Fig. 2

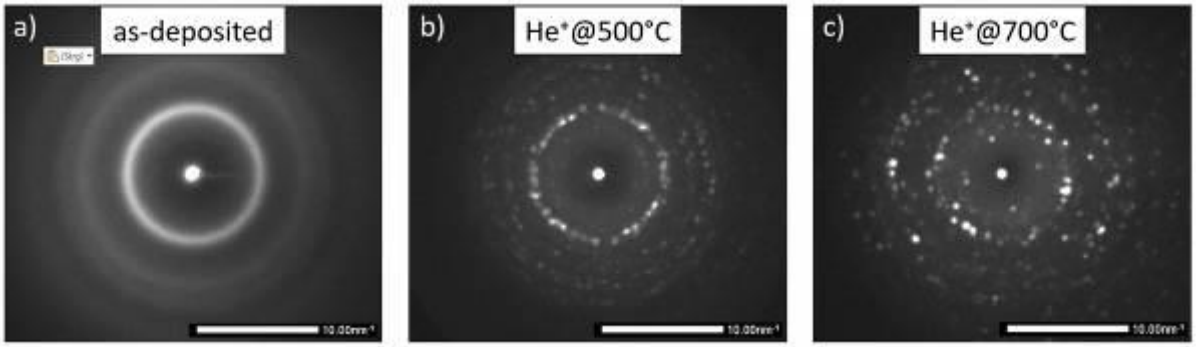
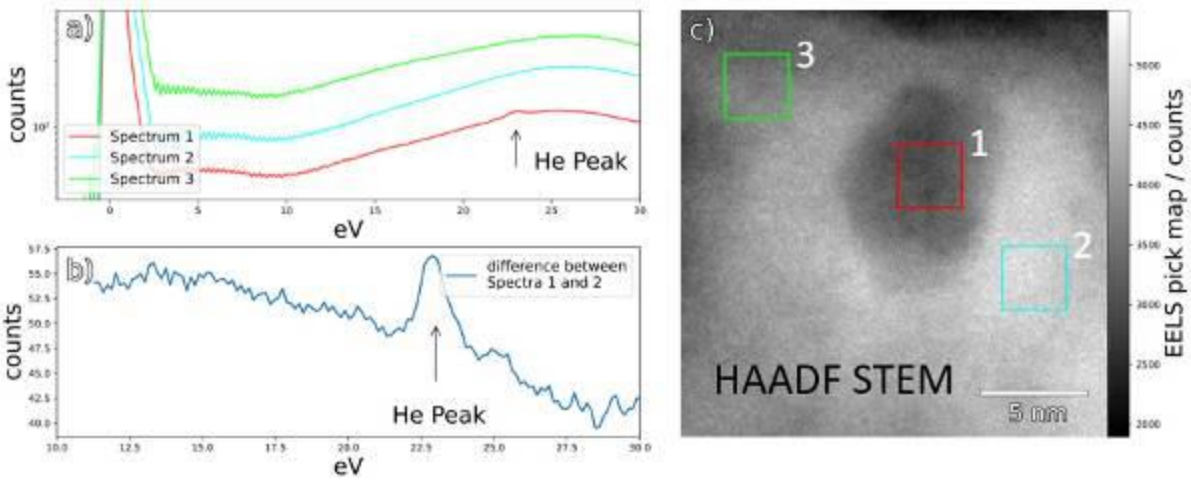

a)
as-deposited
b)
He⁺@500°C
c)
He⁺@700°C

Fig. 3


a)
counts
Spectrum 1
Spectrum 2
Spectrum 3
He Peak
eV
b)
counts
difference between
Spectra 1 and 2
He Peak
eV
c)
3
1
2
HAADF STEM
5 nm
EELS pick map / counts

MS2.P26
Hidden order – Revealing the rules of chirality in gold nanorods with electron tomography

R. Girod[1], V. G. Kyle[2], L. M. Luis[2,3,4,5], S. Bals[1]

[1]University of Antwerp, EMAT, Department of Physics, Antwerp, Belgium
[2]CIC biomaGUNE, Donostia-San Sebastián, Spain
[3]Centro de Investigación Biomédica en Red, Bioingeniería, Biomateriales y Nanomedicina (CIBER-BBN), Donostia-San Sebastián, Spain
[4]Ikerbasque, Basque Foundation for Science, Bilbao, Spain
[5]University of Vigo, CINBIO, Vigo, Spain

Introduction: Chiral gold nanocrystals with tailored shapes and optical properties have promising applications in fields such as bio-sensing, therapeutics or catalysis. Their seed-mediated synthesis with the recently proposed micelle-templated pathway, during which metal is reduced on achiral seeds, has seen strong interest for its large parameter space, shape uniformity, and interesting optical properties up to the infrared range [1]. In this approach, helical worm-like micelles would coil around the seed and template the growth of nm-sized chiral wrinkles (**Fig. 1**), which are preferentially oriented following a right-handed or left-handed helical morphology. Recent work by our groups has shown that the handedness can change following the choice of micelle enantiomer, but also depending on the single-crystalline (SC) or penta-twinned (PT) structure of the starting, achiral, seed [2]. However, a unifying mechanism of growth is lacking so that control of the produced morphologies remains difficult.

Objective: In this work, we aimed to understand the origin of handedness reversal during micelle-templated overgrowth on SC or PT nanorod seeds. Specifically, we hypothesized that wrinkle growth is influenced by the surface of the seeds, and used electron tomography to reveal correlations between the structure and morphology of the overgrowth products, and that of the seeds.

Materials and Methods: To uncover how winkles emerge, chiral gold nanorods were synthesized at incremental stages of growth with a novel "kinetic series" protocol [3]. Products were grown on SC and PT seeds, and were characterized with (fast) electron tomography. To reveal the structure and crystalline orientation of the wrinkles, additional electron tomography at atomic resolution was performed at selected timepoints. In both cases, imaging was performed in high angle annular dark field (HAADF) scanning transmission electron microscopy (STEM), and postprocessing for denoising and alignment was performed with Matlab routines developed in-house. Reconstructions were computed with the expected minimization algorithm implemented with the Matlab version of the Astra toolbox.

Results: Electron tomography show that chiral overgrowth on SC and PT occurs at different rate, but with common patterns (**Fig. 1**) [3]. Specifically, high resolution images and 3D reconstructions show that early growth occurs selectively in the <100> directions on both SC and PT achiral seeds. Upon further wrinkle development, morphological and structural data from atomic-resolution ET demonstrate that wrinkles are arranged in relation to the symmetry and structure of the underlying seed. Wrinkles are preferentially aligned along <100> crystal directions whenever available (**Fig. 2**), otherwise along <111>, and changes in direction preferentially occur at the interfaces between the seeds" facets. As a result, areas with and without helical inclination are seen to follow a 4-fold pattern around SC NRs and a 5-fold one around PT NRs. We will show how these observations are consistent with handedness reversal and demonstrate how electron tomography can support better control in chiral inorganic synthesis.

1.González-Rubio, G. *et al. Science* **368** (2020).

2.Van Gordon, K. *et al. Angew. Chem.* **63** (2024).

3.Van Gordon, K., *et al. Nano Letters.* **25** (2025).

Figure 1: Electron tomography overview of wrinkled growth

Figure 2: High resolution electron tomography of a SC particle after 30 seconds of growth

Fig. 1

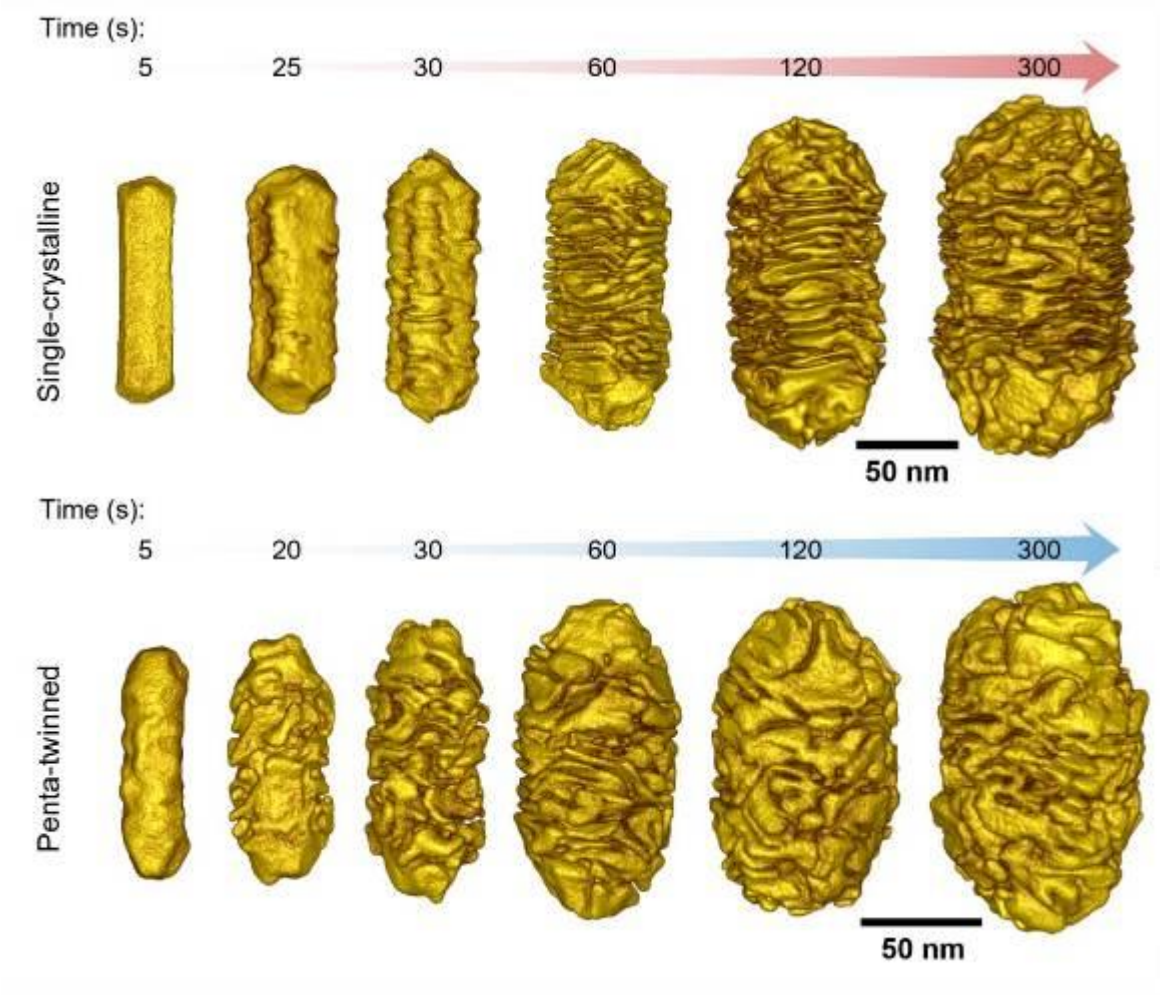
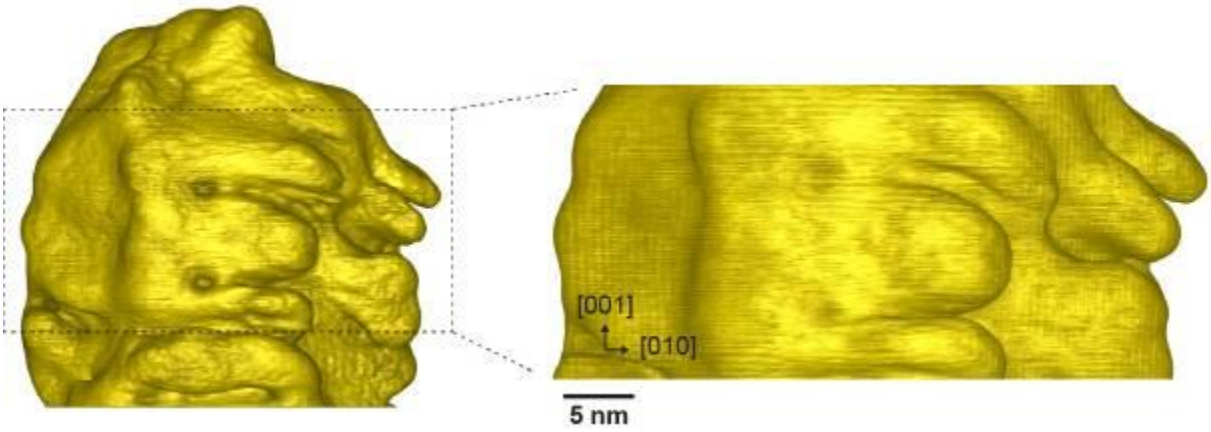


Fig. 2



MS2.P27
Origin of nanostructures in high-entropy alloys and their magnetic performance

A. Jelen[1], S. Vrtnik[1], P. Koželj[1,2], G. Kapun[3], J. Luzar[1], J. Petrović[1], G. Dražić[1,3], A. Meden[4], J. Dolinšek[1,2]

[1]J. Stefan Institute, Solid State Physics, Ljubljana, Slovenia
[2]University of Ljubljana, Faculty of Mathematics and Physics, Ljubljana, Slovenia
[3]National Institute of Chemistry, Ljubljana, Slovenia
[4]University of Ljubljana, Faculty of Chemistry and Chemical Technology, Ljubljana, Slovenia

Introduction

High-entropy alloys (HEAs) represent novel metals-based materials with complicated microstructures, where at least five different chemical elements, all in majority concentrations, are mixed on a simple crystal lattice. Likewise, the materials are usually comprised of more than one phase on different microscopic levels, ranging from a few nm to 1 mm.

Objectives

In order to interpret the physical properties as accurately as possible, the microstructure has to be known at different orders of magnitude (multi-spatial-scale), using different types of electron microscopes (correlative microscopy) that enable such magnifications.

Materials & methods

For complete microstructural investigation of HEAs, the following electron microscopes with corresponding techniques were used: Scanning Electron Microscope (SE and BSE imaging, EDS, EBSD), Transmission Electron Microscope (HAADF, EDS) and Focused Ion Beam (channelling contrast).

Magnetic measurements were conducted on a Quantum Design MPMS3 SQUID magnetometer equipped with a 7-T magnet, operating at temperatures between 1.8 and 400 K.

Results

With this contribution, I am showing the microstructures of 3 different HEAs, each of them presenting a special magnetic phenomenon. They all possess specific multi-phase nano to micro-structure, which influences the magnetic behaviour of the bulk HEA material accordingly. FeCoCrMnAl [1] is a single crystal with a two-phase structure that leads to two successive magnetic phase transitions above room temperature. This makes the material promising candidate for the application in magnetocaloric refrigeration. FeCoNiPdCu [2] is the first magnetically soft high-entropy alloy, which performs comparably to the best commercial soft magnets for static and low-frequency applications. AlCoFeNiCu [3] is a material that possess a combination of excellent magnetic softness and vanishing magnetostriction. This is beneficial for the applications that need supersilent (inaudible to a human ear) materials, like transformers, magnetocaloric coolers, and other "humming" electromagnetic machinery.

Recently, the investigations have shifted towards deeper understanding on the influence of the complex nano and micro-structure to the characteristics of the materials [4,5].

Figure1: Nanostructures of multi-phase magnetically diverse high-entropy alloys: a) BS FIB image of the FeCoCrMnAl HEA material [1], b) BS SEM image of the AlCoFeNiCu HEA material [3], c) HAADF STEM image of the FeCoNiPdCu HEA material [2] and d) TiZrHfSnFe superconducting High-entropy alloy [4].

Conclusion

The complex atomic and phase structure, together with the choice of the elements and their concentrations, determine the physical properties (magnetic, electric and thermal) of the HEAs, which are usually not just the compositional average of physical properties of the constituent phases.

References

1. Jelen, et al. *J. Alloys Compd*. **2021**, 864, 158115.

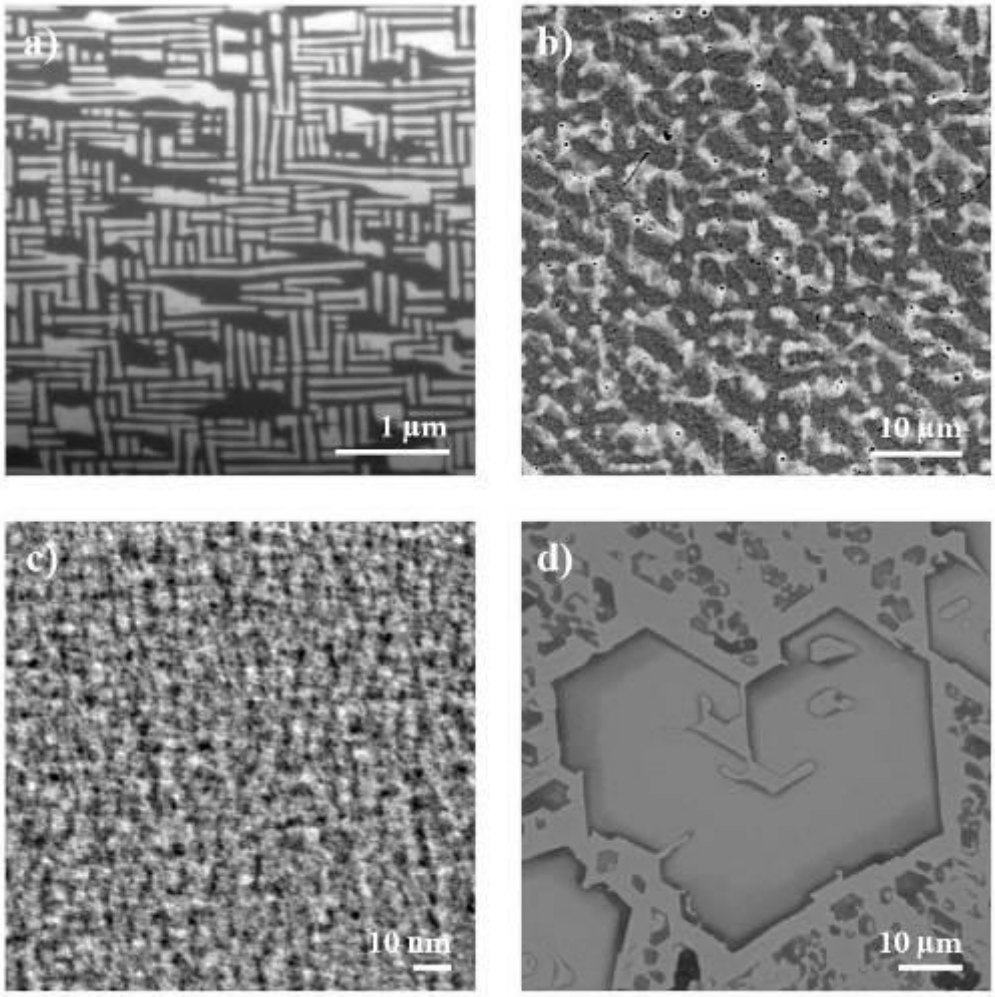
2. Koželj, S. Vrtnik, A. Jelen et al. *Adv. Eng. Mater*. 2019, 21, 1801055.

3. Luzar, P. Priputen, M. Drienovský, S. Vrtnik, P. Koželj, A. Jelen, et al. *Adv. Mater. Interfaces* **2022,** 9, 2201535.

4. Jelen et al., *J Mol. Liq*. **2024**, 415, 126275.

5. Luzar, A. Jelen et al., *Mat. & design*, **2024**, 247, 113396

Fig. 1



MS2.P28
Equiaxed microstructure design enables strength-ductility synergy in the eutectic high-entropy alloy

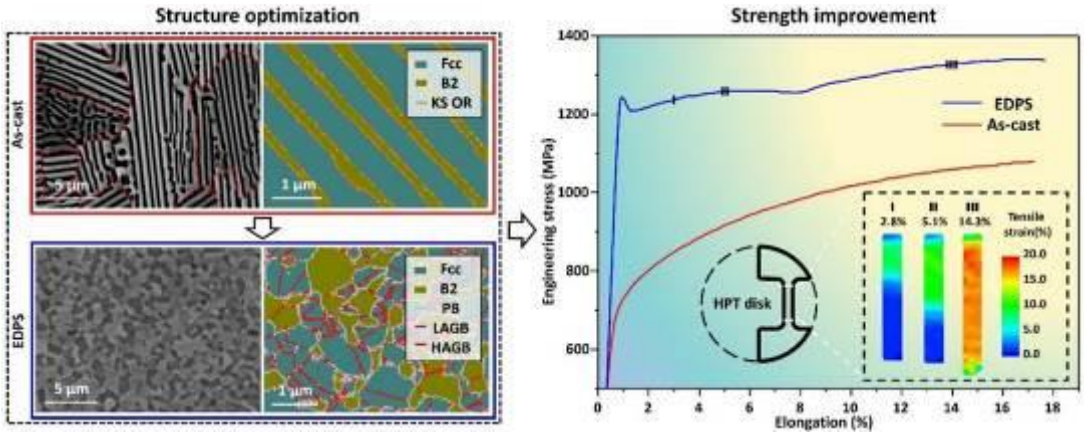
Z. Zhang[1], Y. Huang[1,2], Q. Xu[2], S. Fellner[1,2], A. Hohenwarter[2], S. Wurster[1], K. Song[3], C. Gammer[1], J. Eckert[1,2]

[1]Montan University Leoben, Erich Schmid Institute of Materials Science, Leoben, Austria
[2]Montan University Leoben, Department of Materials Science, Leoben, Austria
[3]Shandong University, Weihai, China

Eutectic high-entropy alloys (EHEAs) represent attractive candidate materials for overcoming the strength-ductility trade-off, which can be enhanced through the directional alignment of the lamellar structure along the loading direction. Methods include directional solidification, additive manufacturing and thermo-mechanical processing, etc. Although the microstructure adjustment using these approaches enhances strength and ductility simultaneously, it comes with a pronounced mechanical anisotropy and hence limits their use in potential engineering applications. Unexpected loading modes along weak directions during service could impair the safety and cause catastrophic failure of the structure. The safety concerns and the advancement of technologies call for a good combination of strength and ductility in EHEAs without orientation dependence.

Here, we put forward a new route to optimize the strength-ductility synergy without orientation dependence. Through a combination of severe plastic deformation and annealing, we convert the initially lamellar structure into a dual-phase structure comprised of ultrafine equiaxed grains. The significant grain refinement improves the yield strength from 703 MPa to 1199 MPa without sacrificing any ductility. During deformation, the localized softening resistance of the achieved dual-phase microstructure avoids necking, and the intrinsic microcrack-arresting mechanism effectively improves the fracture resistance. Grain boundaries and phase boundaries provide nucleation sites for dislocations and restrict dislocation transfer while the strain incompatibility is accommodated by geometrically necessary dislocations. This work demonstrates that dual-phase alloys comprised of ultrafine equiaxed grains provide a pathway for strengthening without loss of ductility.

Fig. 1



MS2.P29
Single-shot time-resolved Kerr microscopy for studying stochastic skyrmion nucleation

S. Wagner[1], D. Metternich[1], L. Seidel[1], C. von Korff Schmising[1], B. Pfau[1]

[1]Max Born Institut, B2: Imaging and Coherent X-rays, Berlin, Germany

Introduction

Magnetic skyrmions are topologically protected nanoscale spin textures that have gained significant interest for their potential applications in spintronic devices. Their small size, stability, and controllability via electric currents or optical pulses make them attractive candidates for memory and logic applications. While spin–orbit torques (SOTs) enable controlled displacement, creation, and annihilation of skyrmions, optical excitation provides an alternative means of nucleation. However, unlike SOT-induced processes, which can be influenced by material defects and pinning sites, light-induced skyrmion nucleation is inherently stochastic in unpatterned materials, as it is governed by thermal spin fluctuations [1]. This randomness poses a fundamental challenge for time-resolved studies, as conventional pump-probe techniques rely on signal averaging and assume a reproducible temporal evolution. As a result, direct imaging of individual nucleation events remains an open challenge.

Objectives

We developed a single-shot time-resolved Kerr microscopy setup to directly image skyrmion nucleation dynamics and overcome the limitations of ensemble-averaged techniques.

Materials & Methods

We employed a wide-field Kerr microscope [2] with a sub micrometer resolution. The system uses a femtosecond Yb fiber laser (λ=1030 nm, pulse duration 250 fs), with the probe pulse frequency-doubled to λ=515 nm. The pump-probe delay can be adjusted to up to 16 ns. Experiments were conducted on a CoPt-based multilayer system (Ta(3)/Pt(2.5)/ [Co(0.6)/Pt(0.8)]×12 /Ta(2), saturation field of 125mT) under varying pump fluences and external magnetic fields.

Results

We successfully demonstrated single-shot imaging of ultrafast magnetization dynamics in CoPt multilayers. Our setup captured the evolution from optically induced demagnetization to the nucleation of magnetic textures (Fig. 1). While individual skyrmions could not yet be optically resolved due to their high density in the investigated sample system it was nevertheless possible to access spatially and temporal resolved nucleation dynamics.

Conclusion

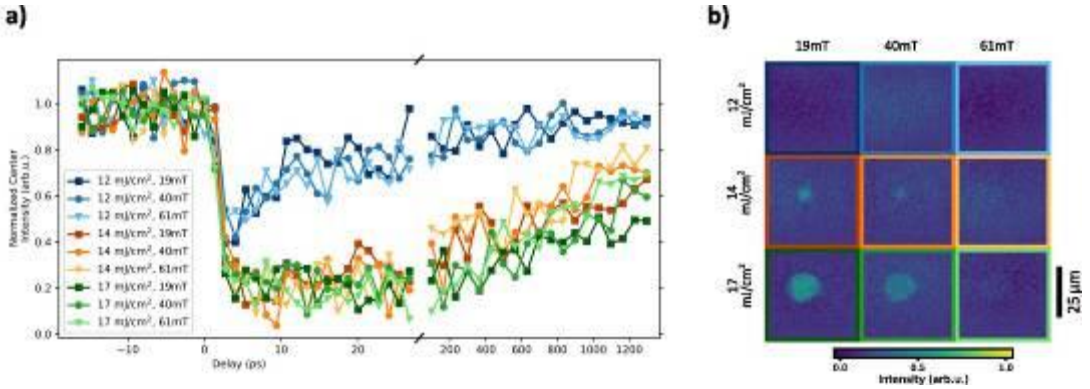
Single-shot Kerr microscopy is proving to be a powerful tool for capturing ultrafast magnetic dynamics in the laboratory. It allows time-resolved imaging of stochastic phenomena without averaging. By studying samples with increased skyrmion size and improving illumination stability, direct imaging of individual skyrmions during nucleation could be possible.

[1] F. Büttner et al., "Observation of fluctuation-mediated picosecond nucleation of a topological phase", Nature Materials 20 (1) (2021) 30–37, publisher: Nature Publishing Group. doi:10.1038/s41563-020-00807-1

[2] F. Steinbach et al., "Wide-field magneto-optical microscope to access quantitative magnetization dynamics with femtosecond temporal and sub-micrometer spatial resolution", Journal of Applied Physics 130 (8) (2021) 083905. doi:10.1063/5.0060091

Figure 1: (a) Normalized intensity in the center of the pump spot as a function of pump-probe delay for different excitation fluences (12, 14 and 17 mJ/cm2) and applied magnetic fields (19 mT, 40 mT, and 61 mT). (b) Map of the final states for each set of parameters.

Fig. 1



MS2.P30
Reevaluating the Brandon Criterion – Atomic-scale structure and properties of high-Σ grain boundaries in fcc-Al

A. Ahmadian[1,2], M. Velazquez-Rizo[1], C. Dösinger[3], L. Romaner[3], C. Kübel[1,4]

[1]Karlsruhe Institute of Technology, Institute of Nanotechnology, Eggenstein-Leopoldshafen, Germany
[2]Karlsruhe Institute of Technology, Helmholtz Institute Ulm, Ulm, Germany
[3]Montan University Leoben, Leoben, Austria
[4]Technical University of Darmstadt, Darmstadt, Germany

Grain boundaries (GBs) play a crucial role in determining the mechanical, electrical, and transport properties of polycrystalline materials. Based on the coincidence site lattice (CSL) model, GBs are classified as special or general (random) high-angle grain boundaries (HAGBs). Special GBs exhibit periodic atomic structures that contribute to lower interfacial energy, reduced solute segregation, lower diffusivity, enhanced resistance to corrosion and stress corrosion cracking [1]. However, defining what constitutes a special GB remains an open question. The Brandon criterion, which introduces a misorientation tolerance for near-CSL boundaries ($\Delta\theta = 15°/\sqrt{\Sigma}$), has been widely used to allowing certain GBs to still be considered special despite small misorientation offsets. Yet, this criterion is debated in the literature because it relies on a fixed tolerance, whereas experimental evidence suggests that GB stability, mobility, and segregation behavior vary significantly with atomic-scale structure. Alternative models, such as those by Pumphrey, Palumbo, and Ishida-McLean, propose different tolerances, further questioning the universal applicability of the Brandon criterion [2].

In this study, we use aberration-corrected STEM-HAADF imaging and 4D-STEM to investigate the atomic structure and local strain distribution of a 33.8° ⟨111⟩ tilt GB in fcc-Al. This misorientation closely aligns with the ∑7 (38.2° ⟨111⟩), ∑39 (32.0° ⟨111⟩), and ∑79 (33.6° ⟨111⟩) CSL boundaries, raising the question of whether it retains the structural characteristics of a special GB or exhibits the disordered nature of a general HAGB. From SEM-EBSD analysis, the macroscopic character of the GB was determined to be a symmetric boundary with a 33.8° misorientation between the neighboring grains (Figure 1a). While aberration-corrected STEM enables direct visualization of atomic configurations (Figure 1b), 4D-STEM provides a quantitative map of strain, lattice distortions, and local electric fields, offering deeper insight into GB behavior.

Emerging research suggests that certain high-Σ boundaries, while not classified as low-Σ special GBs, may still exhibit "special HAGB" behavior, characterized by reduced defect densities and improved stability compared to truly random GBs. By integrating atomic-resolution imaging with diffraction-based strain mapping, we assess the degree of structural periodicity, atomic relaxation, and potential solute segregation at this boundary. This work refines CSL theory for high-Σ boundaries by linking atomic-scale deviations to GB properties. By combining aberration-corrected STEM and 4D-STEM, we bridge structural classification with functional behavior, providing insights for optimizing GB stability and material performance.

1. Raabe, D., et al., *Grain boundary segregation engineering in metallic alloys: A pathway to the design of interfaces.* Current Opinion in Solid State & Materials Science, 2014. **18**(4): p. 253-261.
2. King, A.H. et al., *What does it mean to be special? The significance and application of the Brandon criterion.* Journal of Materials Science, 2006. **41**(23): p. 7675-7682.

Fig. 1

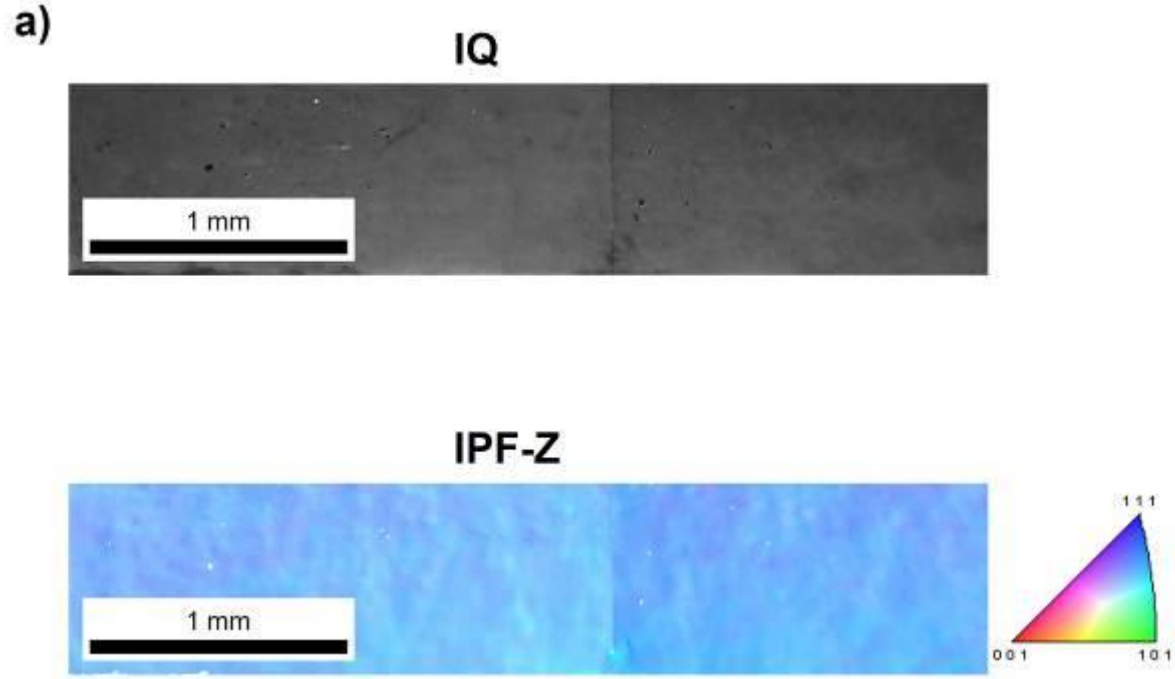
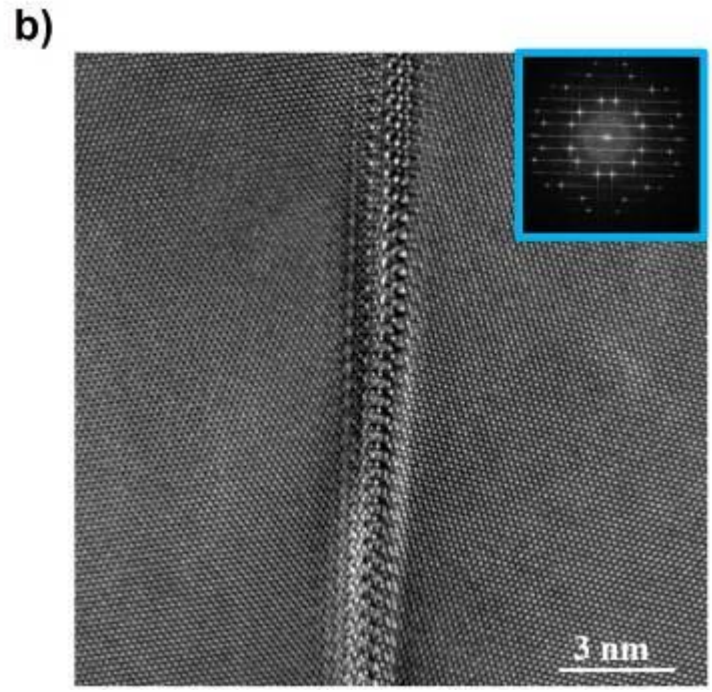


Fig. 2



MS2.P32
Creep-induced microstructural evolution of a eutectic Mo-Si-Ti alloy by correlative electron microscopy

H. Thota[1], D. Schliephake[2], A. Kauffmann[2], H. Wu[3], M. Heilmaier[2], A. Pundt[2], Y. M. Eggeler[1]

[1]Karlsruhe Institute of Technology, Laboratory for Electron Microscopy, Karlsruhe, Germany
[2]Karlsruhe Institute of Technology, Institute for Applied Materials (IAM-WK), Karlsruhe, Germany
[3]Forschungszentrum Jülich GmbH, Institute of Energy Materials and Devices IMD-1: Structure and Function of Materials, Jülich, Germany

The turbine blades in the current generation aero-engines are made up of single-crystal Nickel-based superalloys, precipitation strengthened by $L1_2$ γ' precipitates in a fcc γ matrix [1]. The operation temperatures are limited to 1100°C due to the solvus temperature of γ'. However, the thermodynamic efficiency of the turbine increases with higher operating temperatures [2]. Our goal is to design alternate high-temperature materials that can sustain higher operating temperatures without air cooling of turbine blades.

The Mo-Si-Ti system has been explored as an alternative to the existing high-temperature materials because of their lower density and high melting temperatures. A eutectic Mo-20Si-52.8Ti (at.%) alloy showed pesting resistance and optimal creep behavior. It has a two-phase microstructure: bcc solid solution consisting of Mo, Ti, and Si $(Mo,Ti,Si)_{ss}$ and hexagonal silicide $(Ti,Mo)_5Si_3$ [3]. Compressive creep tests performed at 1200°C and true stress of 100 MPa showed a characteristic creep minimum at 1.3% strain. To understand the related microstructural evolution, the samples were crept to true strains of 0.2%, 1.3%, 10%, 20%, and 40 % [4]. Transmission electron microscopy (TEM) is used for deciphering dislocation-precipitate interactions and other dislocation processes during creep.

TEM specimens of crept samples were prepared using electron backscatter diffraction (EBSD) for strain identification and subsequent focused ion beam (FIB) milling. The dislocations were imaged using scanning transmission electron microscopy (STEM) - bright field (BF) technique and the diffraction contrast of selected two-beam conditions was analyzed. The invisibility criterion was used to determine the character of dislocations in solid solution and acting slip planes in silicide respectively.

In the as-cast state, the high cooling rates during arc melting lead to Si supersaturation in solid solution and formation of silicide precipitates during cooling. During creep, precipitation occurred in both phases, which were semi-coherent with their respective matrices. The number density of precipitates per unit area is calculated from scanning electron microscopy (SEM)-backscattered electron (BSE) images in both phases covering a total area of 600 μm^2, with at least 20 grains.

At the creep minimum 1.3% strain, a number density of 15 ± 7 μm^{-2} was found for silicide precipitates in the solid solution. In contrast, at a later creep stage (10 %), the number density reduced by half to 7 ± 5 μm^{-2} in the solid solution. This indicates that precipitation strengthening leads to a creep minimum and, after that, precipitate coarsening, which reduces obstacle resistance and thus makes dislocation glide easier, thereby increasing the creep rate.

EBSD-kernel average misorientation (KAM) maps revealed that both phases deformed from 1.3% strain (creep minimum) onwards. Both phases contributed to creep deformation by dislocation accumulation. Two edge dislocations in the solid solution and two possible climb instances (shown in Fig. 2) were found in silicide. Hence, dislocation climb-controlled creep was confirmed.

References:

[1] Betteridge W, Shaw SWK. Materials Science and Technology. 3:682, 1987.

[2] Perepezko. Science, 326:1068,2009.

[3] Schliephake et al. Intermetallics,104:133, 2019.

[4] Thota et al. Advanced Engineering Materials, 2301909, 2024.

Fig. 1

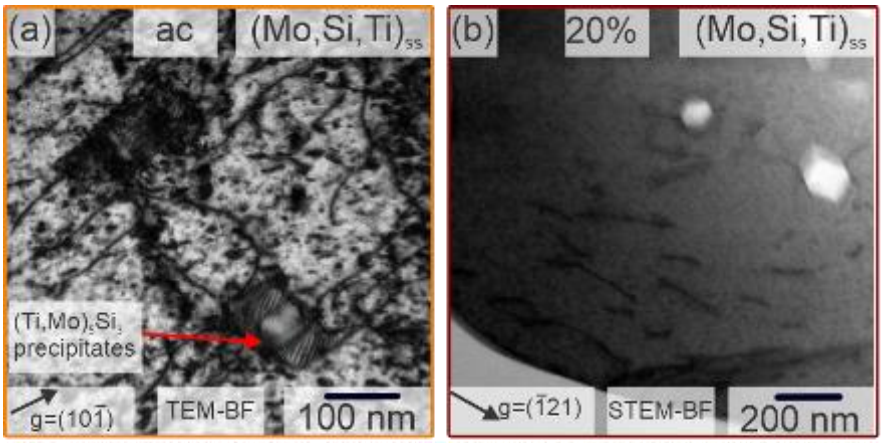


Figure 1: Two-beam condition imaging of dislocations in the solid solution of eutectic Mo-Si-Ti alloy a) TEM bright field (BF) image of silicide precipitate pinning the dislocations in as-cast (ac) state. *(Ti,Mo)$_5$Si$_3$* precipitates are semi-coherent, exhibiting Moiré contrast at the interface projection and b) scanning transmission electron microscopy (STEM)-BF image of dislocations in the 20% crept sample. The dislocations appear as dark lines in the BF images. The two beam condition STEM-BF images were annotated with g-vector on bottom left in all images.

Fig. 2

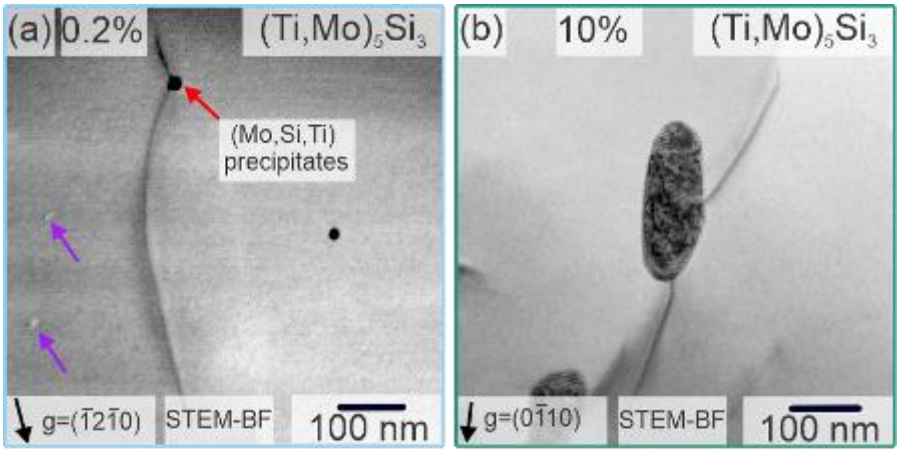


Figure 2: Two-beam condition imaging of dislocations in the silicide of eutectic Mo-Si-Ti alloy using STEM-BF technique. Solid solution precipitate pinning the dislocations in a) 0.2% true strained and b) 10% true strained sample state. Solid solution precipitates act as obstacles to the gliding dislocations, which can be overcome, either by precipitate shearing or by climb, as seen in Fig.2a. Purple arrows in Fig.2a indicate either dislocation loops or nanoprecipitates.

MS2.P33
4D-STEM and EDX characterization of grain boundary segregation in nanostructured CuSn5

Y. Dai[1], A. Ahmadian[2], K. Durst[3], C. Kübel[1]

[1]Karlsruhe Institute of Technology, Institute of Nanotechnology, Karlsruhe, Germany
[2]Helmholtz Institute Ulm for Electrochemical Energy Storage, Ulm, Germany
[3]Technical University of Darmstadt, Department of Materials and Earth Sciences, Darmstadt, Germany

Nanocrystalline metallic materials exhibit outstanding mechanical properties but suffer from grain growth-induced instability, particularly in pure nanocrystalline metals. Solute segregation engineering has emerged as a powerful strategy to mitigate this instability by stabilizing GBs and reducing their mobility [1]. However, recent studies have shown that not all grain boundaries are equally influenced by solute segregation. Segregation behavior is expected to depend strongly on the grain crystallographic character of the boundary. Selective segregation can significantly alter grain boundary energies, cohesion, and mobility, thereby influencing the overall thermal stability of nanostructured materials [2].

In this study, we employ 4D-Scanning Transmission Electron Microscopy (4D-STEM) with Energy Dispersive X-ray Spectroscopy (EDX) to resolve the nanoscale chemical and structural evolution of ultrafine-grained Cu-5 wt.% Sn during annealing. Furthermore, the correlation between 4D-STEM and EDX provided extensive statistical analysis of boundary character and segregation behavior. The results reveal that Sn preferentially segregates to HAGB, while LAGBs and low coincidence site lattice (Σ3-Σ13) boundaries show no or negligible amount of Sn enrichment (Fig. 1), which does not change noticeably during annealing up to 350 °C. Consequently, Sn segregation stabilizes HAGBs, suppresses grain growth and promotes thermally driven GB relaxation mechanism. This chemical modification and the resulting structural evolution directly correlate with the observed increase in hardness during annealing.

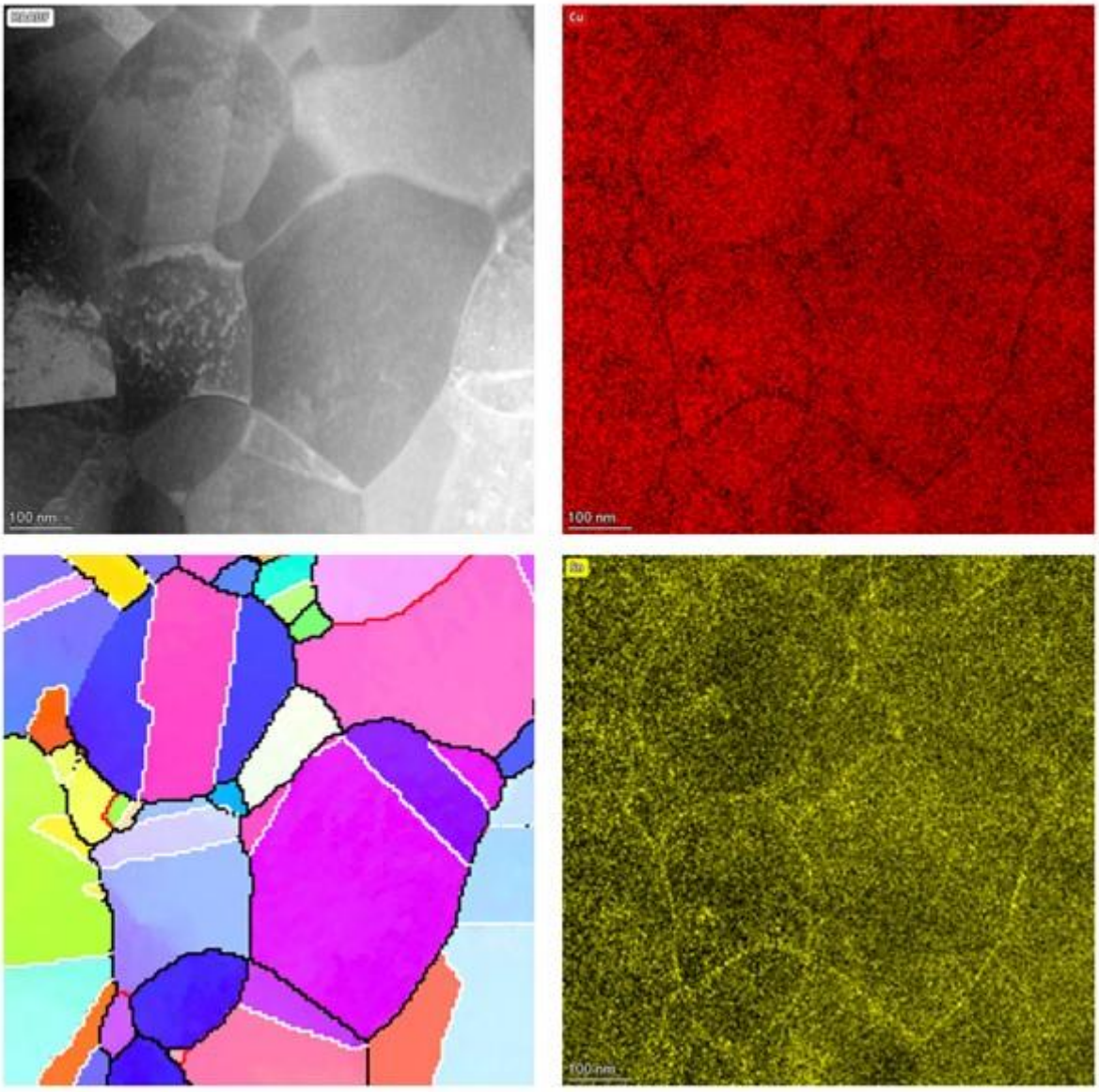
By elucidating the role of solute segregation in governing GB stability, this work provides new insights into the microstructural mechanisms underlying annealing-induced hardening in nanocrystalline Cu-based alloys. These findings contribute to the broader development of thermally stable nanostructured materials with enhanced mechanical performance.

Figure 1: Correlated STEM-EDX and ACOM maps of as-HPT CuSn5 after annealing at 350°C for 1 hour. High-angle grain boundaries (HAGBs) are represented by black lines, twin boundaries by white lines, and low-angle grain boundaries (LAGBs) by red lines.

[1] T. Meiners et al., Acta Materialia 190 (2020) 93-104.

[2] D. Raabe et al., Current Opinion in Solid State and Materials Science 18 (2014) 253-261.

Fig. 1



MS2.P34
Segregation to creep-induced stacking faults in Ni-base single crystal superalloys

Z. Long[1], D. Bürger[2], L. Grünewald[1], C. Dolle[1], Y. Dai[3], C. Kübel[3], K. V. Vamsi[4], Y. M. Eggeler[1]

[1]Karlsruhe Institute of Technology, Laboratory for Electron Microscopy, Karlsruhe, Germany
[2]Ruhr University Bochum, Institute for Materials, Bochum, Germany
[3]Karlsruhe Institute of Technology, Institute of Nanotechnology, Karlsruhe, Germany
[4]Metallurgical Engineering and Materials Science, Indian Institute of Technology Indore, Indore, India

Ni-based single crystal (SX) superalloys have long been essential for turbine blades in aerospace gas engines due to their exceptional creep resistance. This class of alloys possess the coherent γ/γ' microstructure, where γ' precipitates with an ordered $L1_2$ crystal structure are embedded within γ channels, which adopt a face centered cubic solid solution structure. Under extreme operating conditions, the mechanical behavior of SX superalloys is predominantly governed by precipitate shearing mechanisms, influenced by elemental segregation both toward and away from planar faults (PFs) within the γ' phase [1, 2].

Double shear creep experiments were carried out at 750°C and a constant stress of 250 MPa and interrupted after 1 % and 2 % creep strains. The samples were oriented such that the specific slip system [11-2](111) is activated and deformed along a [11-2] loading direction with a Schmid factor of 1 [3]. To study elemental segregation at PFs as a function of creep strain, we employed high-resolution energy dispersive X-ray spectroscopy(HREDX) in scanning transmission electron microscopy(STEM) mode combined with principal component analysis(PCA).

The 2% crept sample was characterized with a foil normal parallel to [1-10], where PFs lie edge-on. Figure 1(A) presents a dark field(DF) image under g(220), illustrating an inclined stacking fault that terminates the motion inside the γ' phase. HR high-angle annular DF(HAADF) micrograph in Figure 1(B) reveals that the nature of fault tip is a 3-nm complex intrinsic stacking fault(CISF), subsequently followed by a superlattice extrinsic SF(SESF) in its wake [2]. Figure 1(C) demonstrates that the elemental segregation at the CISF and SESF are completely different. While the intensity of elemental segregation at the CISF is very high and includes the enrichment of the γ formers like Cr, Co, Mo, and Re, γ' formers such as Al, Ni, Ta, Ti, and Hf are depleted as well as W. The intensity of segregation at SESF is lower and reveals depletion of γ' formers such as Ni and Al, and distinct enrichment with W, Ta, and Ti, known to be η phase formers, suggesting that η phase formation drives the SESF segregation.

The creep test of the superalloy was conducted at 750°C, which is 120°C lower than the pre deformation aging treatment of the sample. We proposed during the creep test, the bulk γ/γ' phases are adjusting their lower temperature compositional steady state [4]. Therefore, the creep-induced SFs in the γ' phase may act as favorable sites to attract γ formers that the γ' phase can no longer accommodate at low temperatures. The enhanced presence of γ formers including Re at the CISF, the precursor of SESF, can be explained this way. In contrast the segregation to the SESF seems to depend on its local hexagonal arrangement of the close packed planes, which is enriched by Ti, Ta and W. Furthermore, the segregation of the identical defect configuration of SESF and CISF in the 1% crept sample demonstrates that fault segregation is governed by partitioning behavior in the γ' phase and the corresponding fault crystal structure.

References:

[1] Y.M. Eggeler et al. Annu. Rev. Mater. Res. 51(1) (2021) 209-240.

[2] Z. Long et al. Microsc. Microanal. 30 (2024) ozae044.625.

[3] D.Bürger et al. Mater. Sci. Eng. A, 795 (2020) 139961.

[4] V. Yardley et al. Adv. Eng. Mater. 18(9) (2016) 1556-1567.

[5] Authors thank funding by DFG, RTG GRK 2561 MatCom – ComMat, and KNMFi at KIT for the access to Titan Themis Z.

Fig. 1

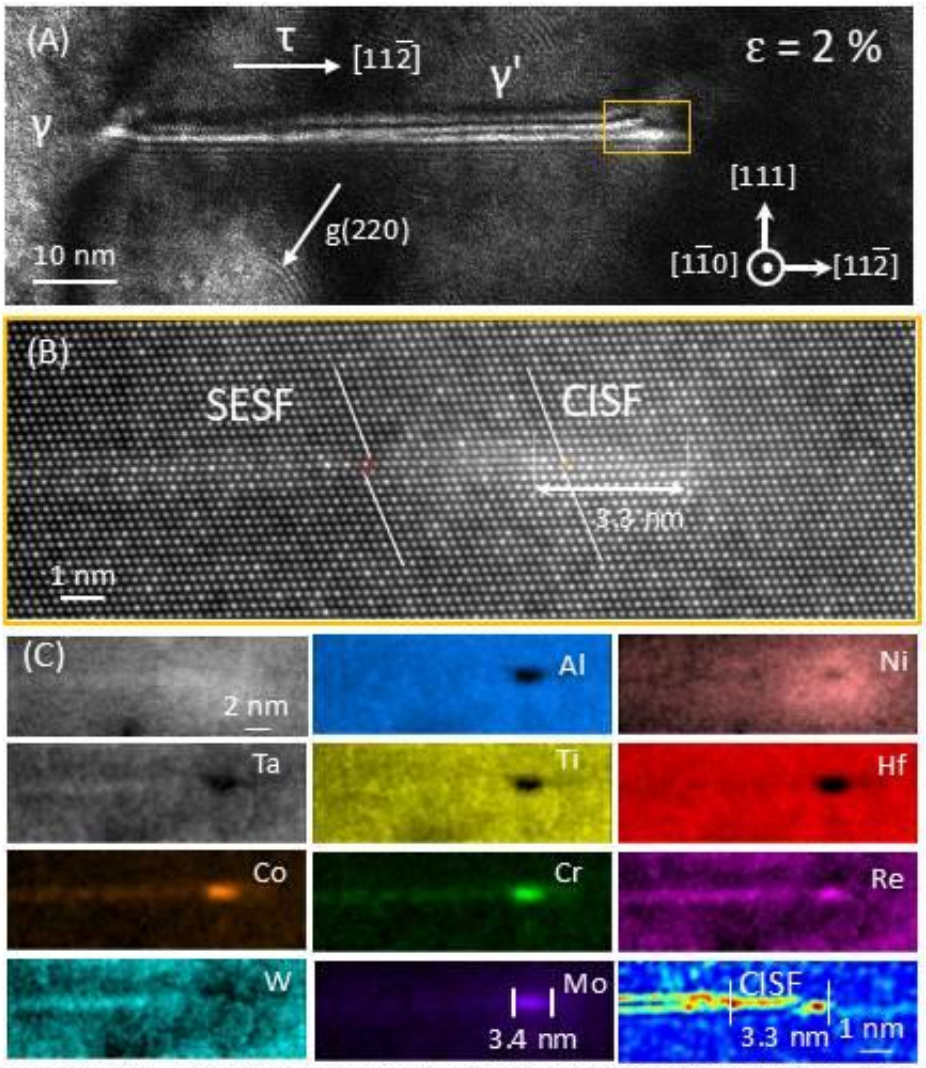


Fig. 1. Microstructural and chemical analysis of creep-induced SESFs after ε = 2% creep sample at 750° C and 250 MPa: (A) DF image with the two-beam condition of g(220). (B) HR-HAADF image shows the SESF and CISF. (C) The net intensity EDX maps of corresponding SESF and CISF after PCA processing.

MS2.P35
Structural investigation of B20 chiral compounds using high-resolution TEM

A. A. Biswal[1], D. Pohl[2], B. Rellinghaus[2], E. Lesne[1], C. Felser[1]

[1]Max Planck Institute for Chemical Physics of Solids, Topological Quantum Chemistry, Dresden, Germany
[2]Technical University Dresden, Dresden Center for Nanoanalysis (DCN), Dresden, Germany

Introduction

Topological chiral semimetals with a non-centrosymmetric cubic B20-type structure (space group $P2_13$) are notable for their chirality in crystal, magnetic, and electronic structures [1]. The chiral B20 compounds lack inversion and mirror symmetries but retain rotational symmetries. In magnetic B20 materials, broken inversion symmetry and strong spin-orbit coupling lead to the Dzyaloshinskii-Moriya interaction, enabling chiral magnetic excitations like Skyrmions. Nonmagnetic B20 compounds (e.g., CoSi, RhSi, PdGa, PtAl) exhibit multifold fermions due to topological band crossings, resulting in higher Chern numbers and larger Fermi arcs than Weyl or Dirac semimetals [2,3].

Each enantiomorph of B20 crystals has a right- or left-handed atomic arrangement. Structural transformations between opposite-handed domains involve subtle atomic rearrangements, creating grain boundaries with distinct structural motifs. Unlike the A and B enantiomorphs of CoSi, these regions contain an inversion center, enabling local enantiomorph transformations, though with slightly higher total energy due to multi-atomic bond reorganization [4].

Objectives

Identifying the absolute handedness (left or right) of crystals is essential, as chirality significantly affects their physical properties. Local Convergent Beam Electron diffraction (CBED) obtained through TEM or SEM are sensitive to local chirality, allowing for accurate determination of crystal handedness. Our analysis focuses on chirality-dependent features in CBED patterns and demonstrates how quantitative pattern matching can reveal the chirality of B20 crystals. Examining the enantiomorph conversion region offers insights into the mechanisms of transition between enantiomorphs and may uncover energy barriers, symmetry-breaking effects, and pathways for controlling these transformations in chiral materials.

Materials & methods

In this study, we analyze the structural properties of both single crystals and hetero-epitaxially grown films of a B20, synthesized using chemical vapor transport (CVT) and magnetron sputtering. We successfully grew B20 crystalline films by using suitable buffer layers by magnetron sputtering, which enabled the fabrication of epitaxial thin films.

Results

Structural analysis through high-resolution TEM reveals a thickness-dependent microstructure of the B20 films, attributable to a combination of strain relaxation of the films and formation of extended defects, which are under detailed investigation.

We further investigate high-quality bulk single crystals of CoSi and PdGa. For **high-resolution scanning transmission electron microscopy (HR-STEM)** studies, **focused ion beam (FIB) thin lamellae** are prepared in various orientation using a **Helios 5 FIB Dual Beam system (Thermo Fisher Scientific)** and analyzed using a **JEOL JEM-F200C Transmission Electron Microscope**.

Combining HR-STEM imaging with local CBED patterns will establish a general framework for **CBED-based chirality analysis** in crystalline samples of B20 crystals.

Conclusion

Successful fabrication and characterization of nonmagnetic B20 chiral topological semimetals marks a crucial step toward harnessing their topological surface states, enabling the development of chiraltronic devices with advanced optoelectronic and spintronic functionalities.

References:

1. B. Bradlyn, et al., Science **353** (2016).
2. D. S. Sanchez, et al, Nature **567** (2019).
3. Z. Rao, et al., Nature **567** (2019).
4. W. Carrillo-Cabrera, et al., Commun. Mater.**4**, (2023).

MS2.P36
Nanoscale characterization of AM316L stainless steel for hydrogen application

G. Palazzo[1], K. S. Lagemann[1], C. Kübel[2,3], S. Wagner[1], A. Pundt[1]

[1]Karlsruhe Institute of Technology, IAM-WK, Karlsruhe, Germany
[2]Karlsruhe Institute of Technology, Institute of Nanotechnology, Karlsruhe, Germany
[3]Karlsruhe Institute of Technology, Karlsruhe Nano Micro Facility (KNMFi), Karlsruhe, Germany

As hydrogen-based energy technologies gain prominence, understanding the impact of hydrogen on structural materials becomes increasingly crucial. High-pressure hydrogen management (in storage tanks or transport pipelines) requires specific properties in terms of embrittlement resistance, and one of the most considered candidates is austenitic stainless steel. The 316L grade, produced via additive manufacturing (AM) using selective laser melting (SLM), offers promising mechanical properties, but its susceptibility to hydrogen environmental embrittlement (HEE) remains poorly understood. This study aims to elucidate the atomic mechanisms driving HEE in AM 316L by examining its microstructural features and interaction with hydrogen.

We employed analytical (EELS, EDX) electron microscopy techniques, including scanning electron microscopy (SEM) and scanning transmission electron microscopy (STEM), are employed to provide insights into elemental distributions and information on electronic structure. In addition, the grain structure and deformation twins formed during mechanical deformation are investigated by EBSD and ACOM (see Figure 1).

Preliminary findings highlight the presence of characteristic SLM microstructures, including equiaxed and columnar cellular structure (see Figure 2), as well as silicon-manganese oxide nano-inclusions (see Figure 3, where an area with nano-inclusions present along the cell boundaries has been imaged via STEM, and Figure 4, where the respective STEM-EDX elemental map is reported). Preferential chromium and molybdenum segregation around these inclusions along with iron depletion and chromium enrichment around the cell boundaries in both untested and mechanically tested samples, has been observed. The characterisation and observation of microstructural defects and features is of interest, given their role to act as hydrogen trapping sites, which, in turn, can result in HEE, since local enrichment of this element may induce such mechanisms as hydrogen enhanced decohesion (HEDE) or hydrogen enhanced localized plasticity (HELP). The peculiar multi-scale AM microstructure accounts for the unique mechanical properties of AM316L in terms of resistance and ductile behaviour, compared to conventionally manufactured counterparts. It is therefore important to comprehend the role of hydrogen in the already observed hydrogen embrittlement phenomena, in order to be able to formulate strategies to preserve the superior mechanical properties of this steel.

Fig. 1

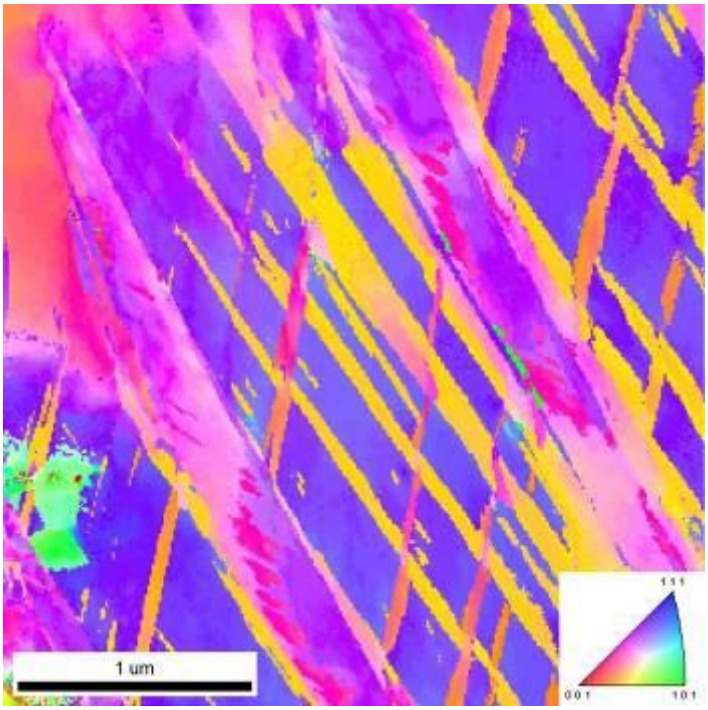


Fig. 2

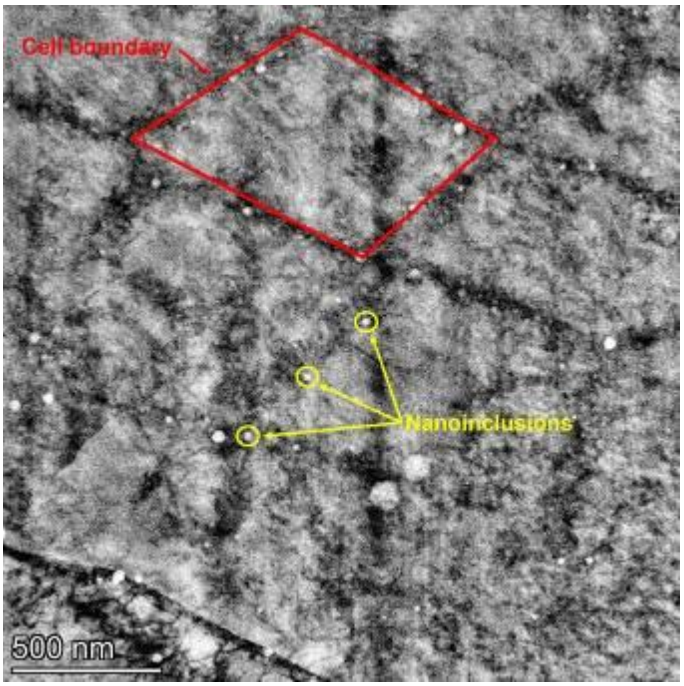


Fig. 3

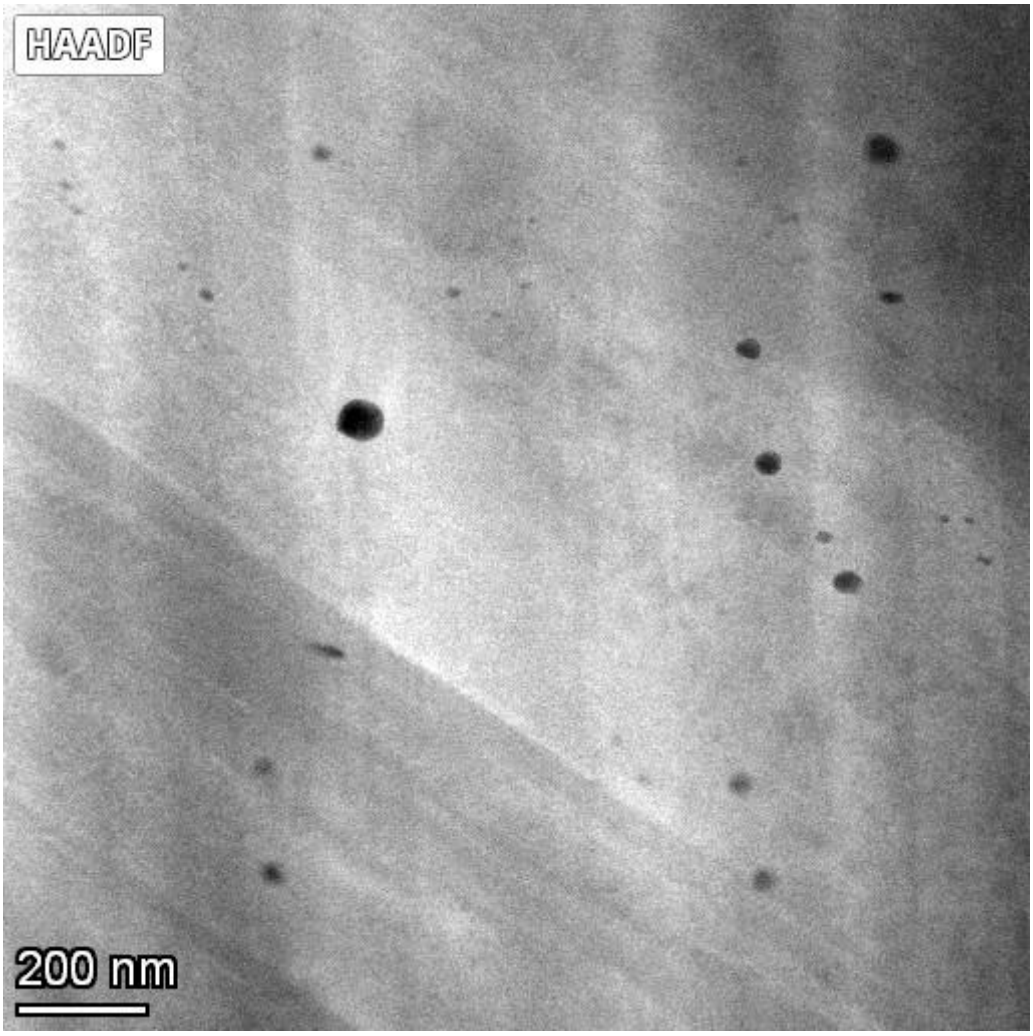
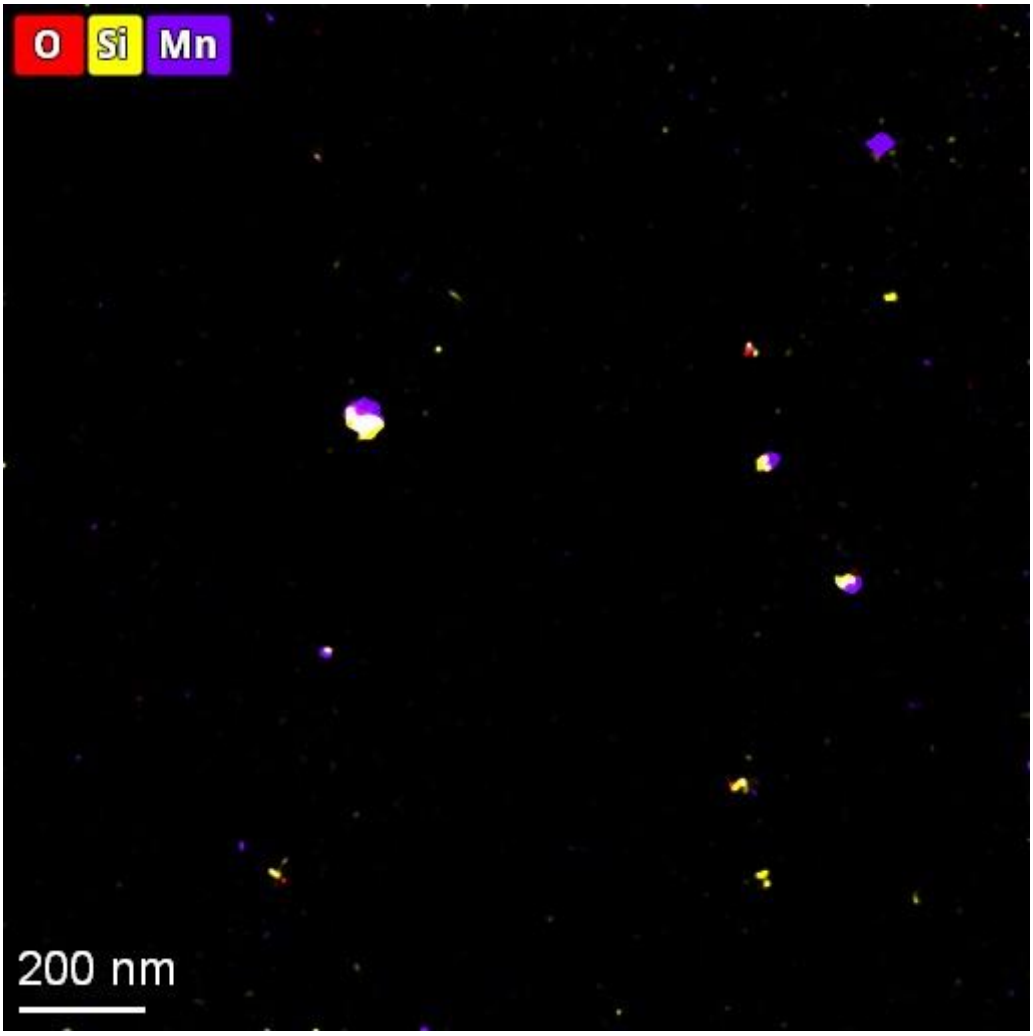


Fig. 4



MS2.P37
Influence of substrate polarity on thermal stability, grain growth and atomic interface structure of Au thin films on ZnO surfaces

M. Dierner[1], M. Landes[1], J. Will[1], A. Ziegler[2], S. Hübner[1], T. Przybilla[1], T. Zech[3], T. Unruh[3], B. Meyer[2], E. Spiecker[1]

[1]Fraunhofer Center for Silicon Photovoltaic, Institute of Micro- and Nanostructure Research (IMN) & Center for Nanoanalysis and Electron Microscopy (CENEM), Erlangen, Germany
[2]Fraunhofer Center for Silicon Photovoltaic, Interdisciplinary Center for Molecular Materials (ICMM) and Computer Chemistry, Erlangen, Germany
[3]Fraunhofer Center for Silicon Photovoltaic, Institute of Crystallography and Structural Physics, Erlangen, Germany

Introduction

Metal/oxide heterointerfaces are widely found in functional materials, where their microstructure significantly impacts macroscopic properties. In ceramics with a wurtzite lattice, such as zinc oxide, surface polarity is particularly important, as it can alter electronic properties [1] and affect the characteristics of deposited metal films [2].

Objectives

This study explores the impact of ceramic substrate polarity on the structural evolution of thin metal films during annealing at elevated temperatures, focusing on the competing mechanisms of solid-state dewetting (SSD) and grain growth, as well as the atomic structure of the epitaxial interface [3].

Materials and Methods

For this purpose, Au thin films on polar O-ZnO(000-1) and Zn-ZnO(0001) surfaces are annealed, varying temperature and time. The structures were analyzed via correlative X-ray diffraction and electron microscopy techniques, including SEM/EBSD, HR STEM and iDPC-STEM.

Results

Au deposited on O-ZnO shows faster SSD and thus lower thermal stability than Au on Zn-ZnO (*Fig.1*), coming from a reduction in adhesion strength of Au on O-ZnO at elevated temperatures as revealed by DFT calculations. Correlative texture analysis via XRD and EBSD revealed: i) for both substrate polarities, Au grains with Au(111)[110] || ZnO(0001)[11-20] (OR2) and Au(111)[110] || ZnO(0001)[10-10] (OR1) coexist up to 600°C due to similar interface energies of both ORs and kinetically hindered grain growth at low temperatures (*Fig.2*), while ii) at 800°C, at Au on Zn-ZnO a transition to a mazed bicrystal structure occurs consisting only of OR1, effectively lowering the thin films energy by eliminating high ∑ boundaries , while at Au on O-ZnO the mixture of OR2 and OR1 with slightly preferred OR2 is preserved (*Fig.3*).

Comparison of various atomic interface structures in density-functional theory (DFT) indicates that atomically sharp interfaces between the Au(111) films and the ideal bulk-truncated polar ZnO surfaces are energetically favored for both substrate polarities, in excellent agreement with atomically resolved scanning transmission electron microscopy (STEM) and integrated differential phase contrast (iDPC) STEM measurements of both interfaces, which show that the O and Zn termination, respectively, are fully preserved at the interface. Interfaces with OR2 exhibit a significantly larger coincidence site lattice (26.32 Å) compared to those with OR1 (5.70 Å). As a result, the OR2 interface appears semi-coherent, characterized by regularly spaced misfit dislocations, as confirmed by HR-STEM and iDPC-STEM measurements of the Au/O-ZnO OR2 interface (Fig.4 A,B). In contrast, the OR1 interface is largely incoherent. However, HR-STEM and iDPC-STEM analysis of the Au/Zn-ZnO OR1 interface reveal that

slight in-plane rotations between the film and substrate can induce an interfacial screw dislocation network, effectively rendering the interface semi-coherent (Fig.4 C,D).

[1] Rahman, Faiz. "Zinc oxide light-emitting diodes: a review." *Optical Engineering* 58.1 (2019)

[2] Dulub, Olga, Matthias Batzill, and Ulrike Diebold. "Growth of copper on single crystalline ZnO: surface study of a model catalyst." *Topics in Catalysis* 36.1 (2005): 65-76.

[3] Dierner, Martin, et al. "Influence of substrate polarity on thermal stability, grain growth and atomic interface structure of Au thin films on ZnO surfaces." Acta Materialia 284 (2025): 120531.

Fig. 1

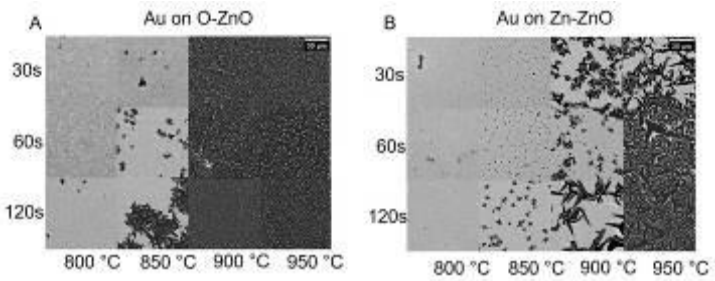


Fig.1: BSE-SEM images of Au on O-ZnO (A) and Zn-ZnO (B) annealed at different temperatures for different times. The ZnO substrates appear in black and the Au films in different shades of gray depending on the grain orientation. The higher coverage of Au at 900°C indicates higher thermal stability of Au films deposited on Zn-ZnO compared to Au deposited on O-ZnO.

Fig. 2

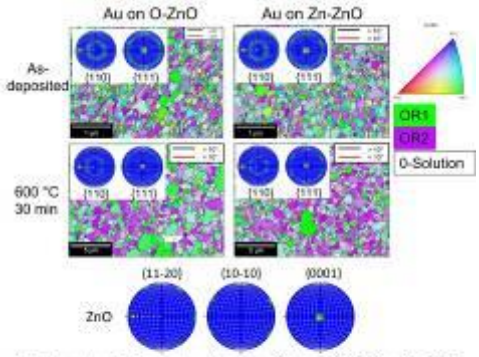


Fig.2: In-plane IPF maps in x-direction of Au on O-ZnO and Zn-ZnO. In the as-deposited state, Au exhibits a nanocrystalline texture with random in-plane orientation, independently from the substrate termination. Annealing at 600 °C leads to grain growth and the IPF coloring gives the impression of a dominance of OR 2 grains.

Fig. 3

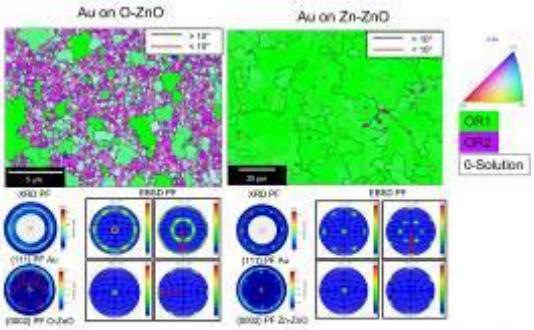


Fig.3: EBSD IPF maps of Au on O-ZnO and Zn-ZnO annealed at 800°C for 120s showing significant differences in the microstructural evolution dependend on the substrate polarity. While Au/O-ZnO preserves the OR 2 dominated texture, Au/Zn-ZnO consists almost exclusively of very large OR1 grains. Au{111} and ZnO{0002} XRD-PFs after annealing at 800 °C compared to the corresponding EBSD-PFs (B). The perfect agreement between XRD and EBSD confirms that the local information from EBSD is representative for the whole sample.

Fig. 4

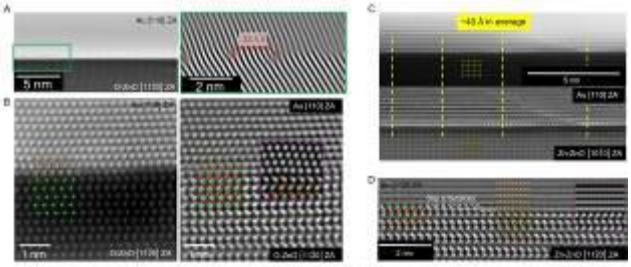


Fig.4: (A) HAADF-STEM image of the Au/O-ZnO interface equilibrated at 800 °C for 2 min (left) and FFT-filtered image showing the presence of periodic misfit-dislocations (right) with an average spacing of 23.3 Å. (B) HAADF-STEM image (left) with overlayed atomic columns of Au and Zn (Au: gold, Zn: green). The corresponding iDPC-STEM image (right) additionally reveals the O columns in the substrate (O: red) as well as at the very interface to the Au film, which is also confirmed by image simulation (purple framed image). The contrast fluctuation of the terminating Au layer in (B) is likely due to projection effects resulting from atomic steps of the interface in image direction. (C) HAADF-STEM image of the OR 1 Au/Zn-ZnO interface (top: unfiltered, bottom: high pass filtered) along the Zn-ZnO[1010] zone axis. The Au appears slightly rotated (~2°) from the perfect [110] ZA. The terminating Au layer shows a periodic contrast with a mean spacing of ~40 Å. This can be attributed to the presence of a screw dislocation network associated with the 2° layer twist (see text). (D) STEM-iDPC micrograph of the OR 1 Au/Zn-ZnO interface along the Zn-ZnO[1120] zone axis. The image clearly resolves the Zn and O columns (Zn: green, O: red), confirming the Zn-termination of the substrate. This can be additionally verified by comparing the experimental image with the simulated image (purple framed image).

MS2.P38
Simple aqueous-phase synthesis and structural characterization of PdCu solid-solution nanoparticles

A. E. Edvardsen[1], I. M. H. Olesen[2], G. Krishnan[1], G. di Palma[1], J. R. Jinscheck[1]

[1]Technical University of Denmark, Nanolab - National Centre for Nano Fabrication and Characterization, Kongens Lyngby, Denmark
[2]Technical University of Denmark, Department of Chemistry, Kongens Lyngby, Denmark

Palladium (Pd) nanoparticles are promising electrocatalysts for CO_2 reduction [1], but their scarcity and the high overpotential limit large-scale applications [1][2]. Copper (Cu) incorporation can reduce Pd usage and modify catalytic properties, yet its structural impact remains unclear. Developing a simple and sustainable synthesis route—avoiding toxic reducing agents—is also crucial for practical implementation.

This study aims to synthesize PdCu solid-solution nanoparticles using a straightforward aqueous-phase co-reduction method. Cu incorporation can be detected at the single nanoparticle level via facet and lattice parameter changes in solid solution. Structural changes associated with Cu incorporation were quantified by comparing PdCu nanoparticles of different sizes with Pd references and theoretical predictions.

Following the methodology in [3], PdCu nanoparticles (4.8 ± 0.3 nm) were synthesized via co-reduction of Pd and Cu precursors in an aqueous phase, using potassium bromide (KBr) as the capping agent. An initial KBr concentration of 0.315 M (300 mg in 8 mL) was used, with variations to study the effect on particle size and morphology. Reference Pd nanoparticles were synthesized under identical conditions. Samples for nanoscale characterization were prepared by ultra-centrifugation and drop-casting onto a standard gold TEM grid with ultrathin amorphous C support. Scanning transmission electron microscopy (STEM) was performed using Thermo Fisher Scientific Spectra Ultra-X at 300 kV to analyze particle morphology and size, while energy-dispersive X-ray spectroscopy (EDX) was employed to assess elemental Pd and Cu distribution inside individual nanoparticles. High-resolution TEM (HRTEM) and diffraction pattern analysis assessed lattice modifications, while X-ray diffraction (XRD) and X-ray photoelectron spectroscopy (XPS) provided additional crystallographic and surface composition insights.

STEM-EDX analysis confirmed the co-localization of Pd and Cu. Further structural characterization, including HRTEM and diffraction pattern analyses, clearly indicated lattice contraction upon Cu incorporation, confirming solid solution formation rather than phase separation or surface segregation. Comparisons with pure Pd reference nanoparticles and theoretical values predicted by Vegard"s Law provided further insight into the structural changes and exposed facets.

In conclusion, structural characterization confirmed co-localization of Pd and Cu and indicated changes in the lattice, and experimental-theoretical comparisons assessed Cu incorporation effects. This work demonstrates a straightforward approach to tuning Pd nanoparticle structure through Cu incorporation, contributing to the development of cost-effective and scalable nanocatalysts.

[1] D. Gao, H. Zhou, F. Cai, J. Wang, G. Wang, X. Bao, Pd-containing nanostructures for electrochemical CO_2 reduction reaction, ACS Catal. 2018, 8 (2), 1510–1519.

[2] P. C. K. Vesborg, T. F. Jaramillo, Addressing the terawatt challenge: scalability in the supply of chemical elements for renewable energy, RSC Adv. 2012, 2, 7933-7947.

[3] B. Cho, J. Lee, I. P. Roh, M. H. Lee, T. Yu, A facile aqueous-phase synthesis method for small PdCu alloy nanocatalysts to enhance electrochemical CO_2 reduction reactivity, J. Alloys Compd. 2022, 911, 164990.

MS2.P39
Combining bulge testing and 4D-STEM for observing fatigue damage in thin films

C. Gammer[1], D. Gebhart[1], A. Krapf[2], L. Schretter[1], A. Lassnig[1], B. Merle[2], M. Cordill[1]

[1]Montan University Leoben, Erich Schmid Institute of Materials Science, Leoben, Austria
[2]Fraunhofer Center for Silicon Photovoltaic, Erlangen, Germany

Cyclic bulge testing is a versatile technique for measuring fatigue properties of freestanding thin films and has given important insights into failure mechanisms of ultrathin metal films. The fundamental deformation mechanisms induced by the cyclic loading are, however still not fully understood. Therefore, it is of great importance to combine cyclic bulge testing with high-resolution structural characterization techniques. In the present work, we present a new experimental setup that allows to combine intermittent transmission electron microscopy (TEM) imaging with bulge testing. A special interchangeable holder is designed that allows to image the same location after different cycles. This allows to directly image the contribution of dislocation or grain boundary processes on the deformation and damage of the thin film and enables observing the influence of microstructure and film thickness on the overall fatigue properties. A combination of bright-field scanning TEM (STEM) for dislocation imaging and 4D-STEM for orientation mapping is used to reveal deformation mechanisms induced by cyclic loading of 150 nm freestanding gold films [1].
[1] D.D Gebhart, L. Schretter, A. Krapf, B. Merle, M.J. Cordill, C. Gammer. JOM (2025) https://doi.org/10.1007/s11837-025-07241-1
[2] We acknowledge support by the Austrian Science Fund (FWF) [TAI796, I 4384-N, Y Y1236-N37].

MS2.P40
Approaching microstructural hydrogen mapping and quantification in a binary system using quantitative backscattered electron imaging and energy dispersive spectroscopy

J. Mausz[1], R. de Kloe[2]

[1]Ametek GmbH, Gatan + EDAX, Weiterstadt, Germany
[2]Ametek GmbH, Gatan + EDAX, Tilburg, Netherlands

Hydrogen's relevance has increased in recent years due to its application in energy systems, including hydrogen storage and nuclear fusion reactors. Many of these applications are still material-limited and are actively being investigated [1],[2]. Currently, several microstructure-specific hydrogen mapping techniques are available, including secondary ion mass spectrometry (SIMS), neutron radiography (NR), and atom probe tomography (APT). However, these techniques are often applied in multi-scale approaches to mitigate their individual limitations [3]. The novel Cipher approach combines energy dispersive spectroscopy (EDS) and quantified backscattered electron (qBSE) detection to localize and quantify hydrogen in bulk samples.

While Cipher has demonstrated excellent capabilities in lithium mapping, its applicability to hydrogen has not been evaluated. To assess this, we conducted an initial study using a binary system. This simple system minimizes errors in composition determination, making it an optimal candidate for evaluating Cipher's potential for hydrogen mapping. The primary objective is to generate hydrogen distribution maps, evaluate the technique's ability to quantify hydrogen locally, and correlate the data with crystallographic results from electron backscatter diffraction (EBSD). This will support the interpretation of hydrogen diffusion and hydride formation processes.

Therefore the OnPoint qBSE detector and EDAX Octane Elite EDS from Gatan were applied to perform the Cipher method and complimented with Monte Carlo simulations at different acceleration voltages (at 5, 10, 15, and 20 kV) to determine the escape depths of backscattered electrons. Dynamic range optimization and atomic number calibration were performed on standards at 10 kV, followed by qBSE and EDS signal collection from the sample. EDS signals were recorded and aligned with the qBSE data to derive the hydrogen distribution maps. EBSD orientation measurements were obtained using an EDAX Velocity Super camera and analyzed with OIM Analysis 9 software to display the crystallographic orientation relationships.

The Cipher technique successfully discriminated between hydride formation and the matrix and effectively displayed hydrogen distribution in elemental maps. The hydride composition was quantified, and preferred locations for hydride formation were identified. The results were used to discuss hydrogen diffusion, and phases were correlated with EBSD phase analysis.

A large field of view could be analyzed in a matter of minutes, offering significant advantages, including its compatibility with SEM, low complexity, straightforward data interpretation, sub-micrometer lateral resolution, and the possibility to correlating it with crystallographic information. Future work needs to address the influence of orientation contrast and correction approaches.

Fig. 1: OnPoint qBSE calibration curve, using Si, Si_3N_4,Al, Cr_2O_3,Cu as standards

References:

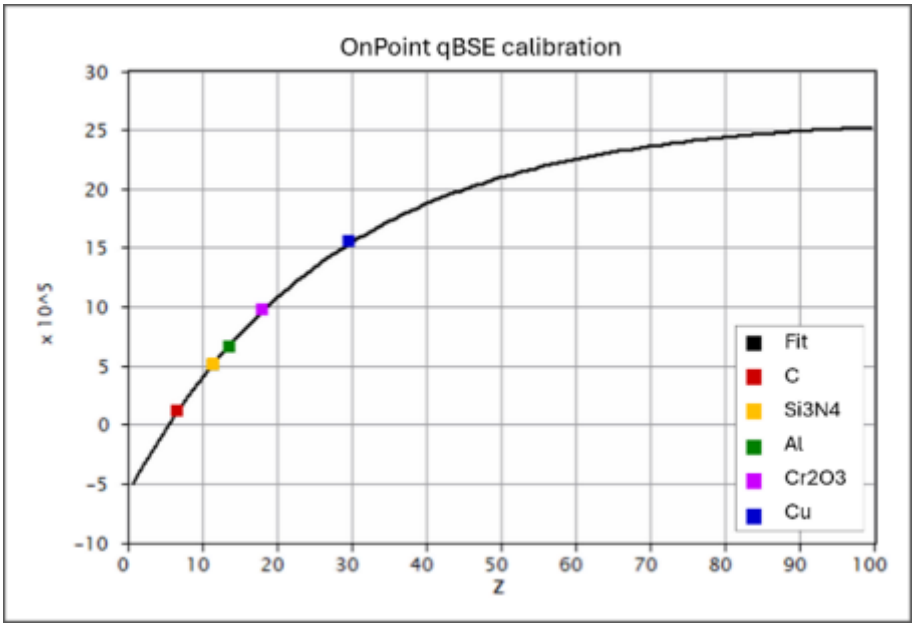
[1] Jung, Peter. "A hydrogen problem in fusion material technology." *Fusion technology* 33.1 (1998): 63-67.

[2] Meda, Ujwal Shreenag, et al. "Challenges associated with hydrogen storage systems due to the

hydrogen embrittlement of high strength steels." *International Journal of Hydrogen Energy* 48.47 (2023): 17894-17913.

[3] Wei, T. Y., et al. "A review on the characterization of hydrogen in hydrogen storage materials." *Renewable and Sustainable Energy Reviews* 79 (2017): 1122-1133.

Fig. 1



MS2.P41
Shorter aging cycle for additively manufactured inconel 718 with better mechanical performance avoiding detrimental phases

A. Shukla[1], H. Elangovan[1], G. Phanikumar[1]

[1]Indian Institute of Technology Madras, Metallurgical and Materials Engineering, Chennai, India

Selective solute segregation plays an important role in Ni based superalloys which are believed to showcase their high temperature performance. The goal of this study is to examine the heat treatment protocol for Laser Powder Bed Fusion (L-PBF) additively manufactured Inconel 718 alloy. Precipitation in the rapidly solidified microstructure forms γ', γ'', δ, and Lave phases at a very small length scale. The first two precipitates have an FCC structure, contributing to high strength between 630°C and 730°C. Later, δ phase, which forms due to Nb segregation and has an orthorhombic structure, is undesirable, as are the continuous Lave phases that develop at the grain boundaries. Additive manufacturing Inconel 718 typically exhibiting significantly smaller segregation sizes due to very fast cooling rate 106 K/s leading to more localized element clustering at grain boundaries and within the dendritic structure whereas conventional methods generally have larger segregation zones due to slower cooling rates 102–104 K/s and more time for element diffusion throughout. Modified heat treatment includes the solutnization at 850°C, 1050°C for 1 hour followed by water quenching approximately 200 K/s. The aging process begins with the first stage at 720°C for 4 hours, followed by heating at 55°C per hour. After furnace cooling, the second stage of aging is conducted at 620°C, followed by air cooling. Specifically short ageing time revealed good mechanical performance without losing the ductility. Microstructure observation with altered heat treatment conditions has direct impact of selective solute segregation (Al, Ti, Nb) at matrix and grain boundary with tensile strength at 700°C. Furthermore, the proposed heat treatment cycle employs a temperature of 1050°C, which exceeds the 1020°C solvus of the detrimental δ phase. This results in a small fraction of Ni3Nb forming at the grain boundary only after double aging. The observations mentioned above suggest that local selective elemental segregation can be tailored with a short heat treatment duration for various Ni-based alloys that are capable of withstanding high temperatures.

Keywords: Ni based superalloy, Additive Manufacturing, Solute Segregation.

Reference:

Yunhao Zhao, Kun Li, Matthew Gargani, Wei Xiong, A comparative analysis of Inconel 718 made by additive manufacturing and suction casting: Microstructure evolution in homogenization, Additive Manufacturing 36 (2020) 101404, https://doi.org/10.1016/j.addma.2020.101404

Fig. 1

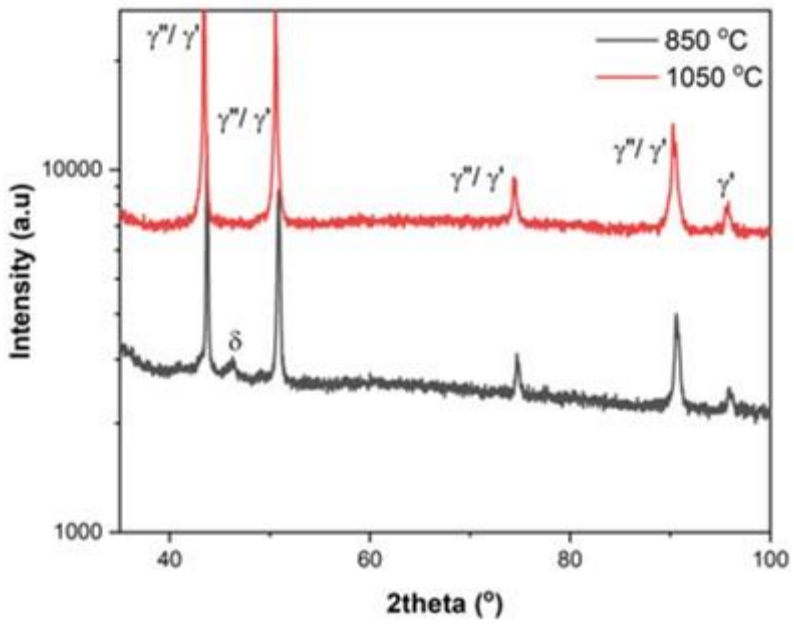

γ"/ γ'
γ"/ γ'
γ"/ γ'
γ"/ γ'
γ'
δ
850 °C
1050 °C
10000
1000
Intensity (a.u)
40
60
80
100
2theta (°)

Fig. 2

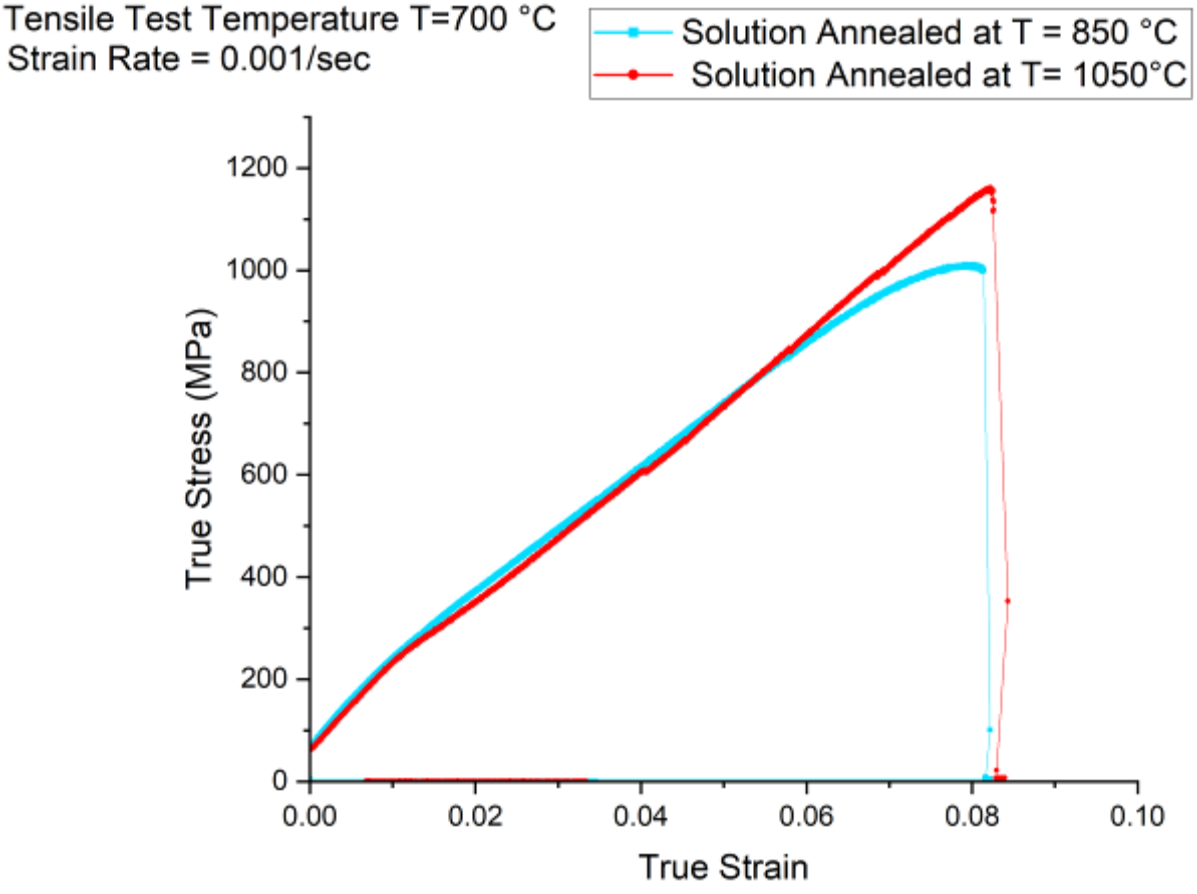

Tensile Test Temperature T=700 °C
Strain Rate = 0.001/sec
Solution Annealed at T = 850 °C
Solution Annealed at T= 1050°C
1200
1000
800
600
400
200
0
True Stress (MPa)
0.00
0.02
0.04
0.06
0.08
0.10
True Strain

Fig. 3

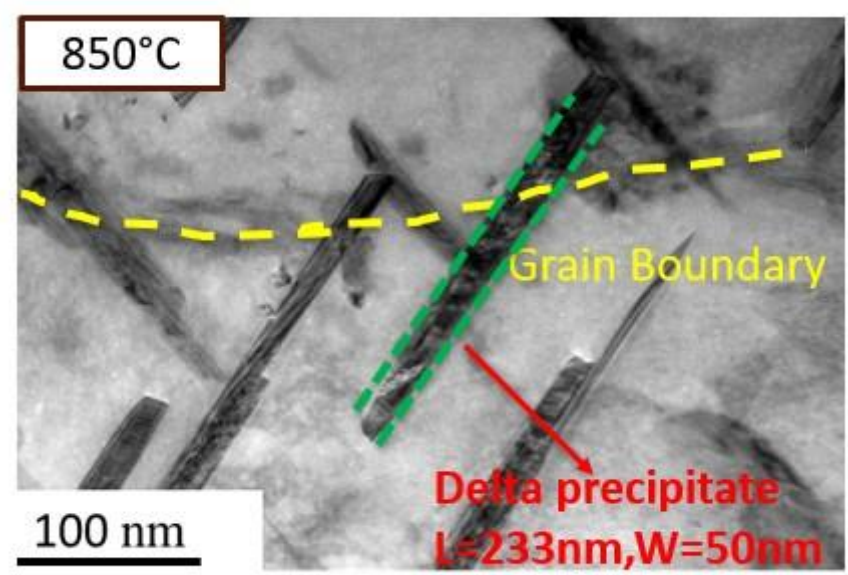
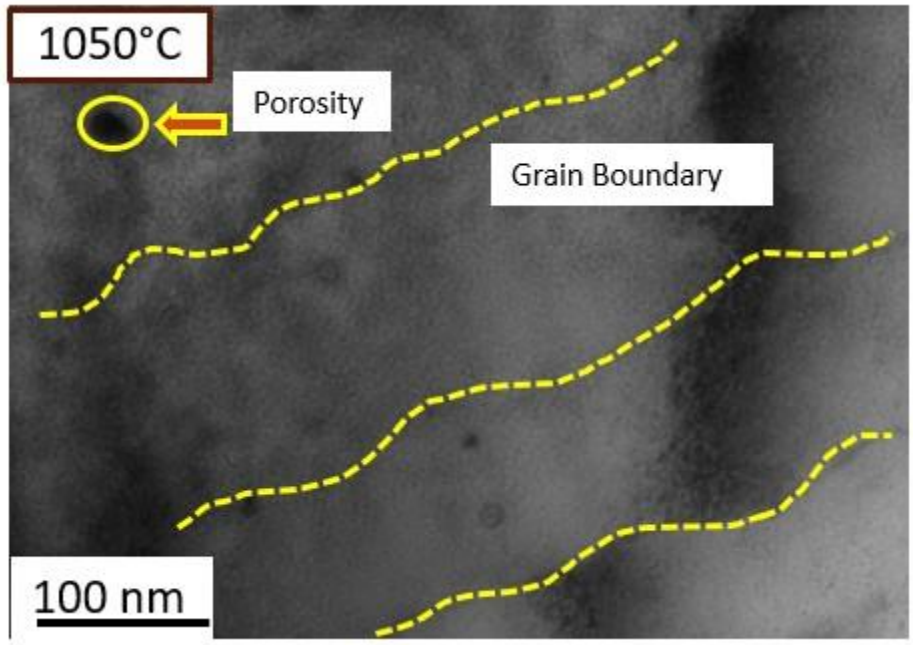

850°C
Grain Boundary
Delta precipitate
L=233nm,W=50nm
100 nm

Fig. 4


1050°C
Porosity
Grain Boundary
100 nm

MS2.P42
Fabrication and structural evolution of Al-Al_2Cu nanostructures via Magnetron sputtering with gas aggregation

L. Bajtosova[1], E. Chocholaková[1], N. Štaffenová[1], J. Hanuš[1], P. Minárik[1], M. Cieslar[1]

[1]Charles University, Faculty of Mathematics and Physics, The Department of Physics of Materials, Prague, Czech Republic

Nanofabrication techniques have enabled precise control over material microstructures, significantly impacting applications such as battery electrodes, where anode geometry influences ion diffusion and charging efficiency. Aluminum-based eutectic composites, particularly Al-Al_2Cu, are promising for electrochemical applications, such as aluminum-based batteries, due to their improved stripping/plating stability. This study explores the fabrication of branched Al-Al_2Cu nanostructures using magnetron sputtering combined with a gas aggregation source, providing a novel alternative to traditional eutectic solidification methods.

The primary goal of this research is to develop and characterize heterogeneous Al-Al_2Cu nanostructures with a high-density interconnected Al_2Cu phase inside an Al matrix, maximizing the surface area ratio for enhanced electrochemical performance. The study aims to investigate the structural evolution of Cu nanoparticles within the Al matrix during in situ annealing and to analyze the resulting phase formation, morphology, and orientation relationships.

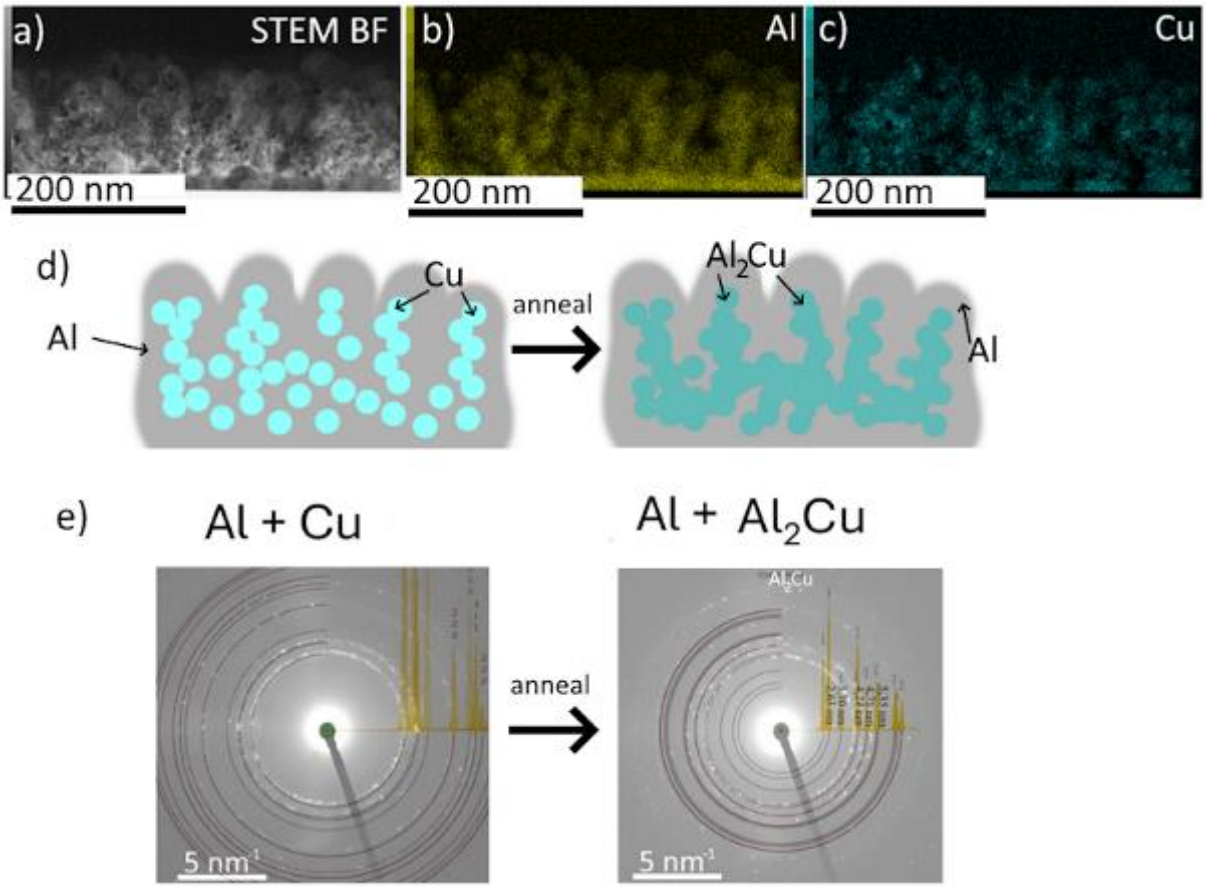
Al-Cu nanostructures were fabricated using a dual-chamber magnetron sputtering system, where a gas aggregation source generated Cu nanoparticles, which were subsequently coated with Al layers. The resulting specimens were annealed in situ in a transmission electron microscope (TEM). Structural and compositional analyses were conducted using scanning transmission electron microscopy (STEM) with bright field (BF), high annular dark field (HAADF) and secondary electron (SE) detectors, energy-dispersive X-ray spectroscopy (EDS), automated crystal orientation mapping (ACOM-TEM), and high-resolution TEM (HRTEM). Phase transformation was tracked using selected area electron diffraction (SAED), and the growth of Al_2Cu particles was analyzed through HAADF imaging.

The initial Al-Cu nanostructure consisted of Cu nanoparticles embedded within an Al matrix, forming columnar nanostructures. Upon in situ annealing, Cu nanoparticles gradually transformed into Al_2Cu. The phase evolution was confirmed through SAED. EDS and ACOM-TEM analyses verified the distribution and orientation of Al_2Cu within the Al matrix. Particle coalescence was observed with increasing temperature. The phase retained some coherency with the Al matrix with orientation relationships different from the ones most commonly formed under traditional eutectic solidification methods.

This study successfully demonstrated the fabrication of Al-Al_2Cu nanostructures using magnetron sputtering with a gas aggregation source, offering a controllable and scalable approach to their production. The transformation of Cu nanoparticles into Al_2Cu begins at 200°C, and Al_2Cu remains the dominant intermetallic phase. The findings provide valuable insights into the controlled synthesis of Al_2Cu-based nanostructures, paving the way for further optimization in electrochemical applications, particularly in aluminum-based batteries.

Figure 1: a-c) cross section of the sputtered nanostructure, a) STEM BF, b) EDS map Al, c) EDS map Cu, d) schematics of the annealing process, e) SAED of phase transformation.

Fig. 1


a)
STEM BF
200 nm
b)
Al
200 nm
c)
Cu
200 nm
d)
Al
Cu
anneal
Al2Cu
Al
e)
Al + Cu
Al + Al2Cu
anneal
5 nm-1
Al2Cu
5 nm-1

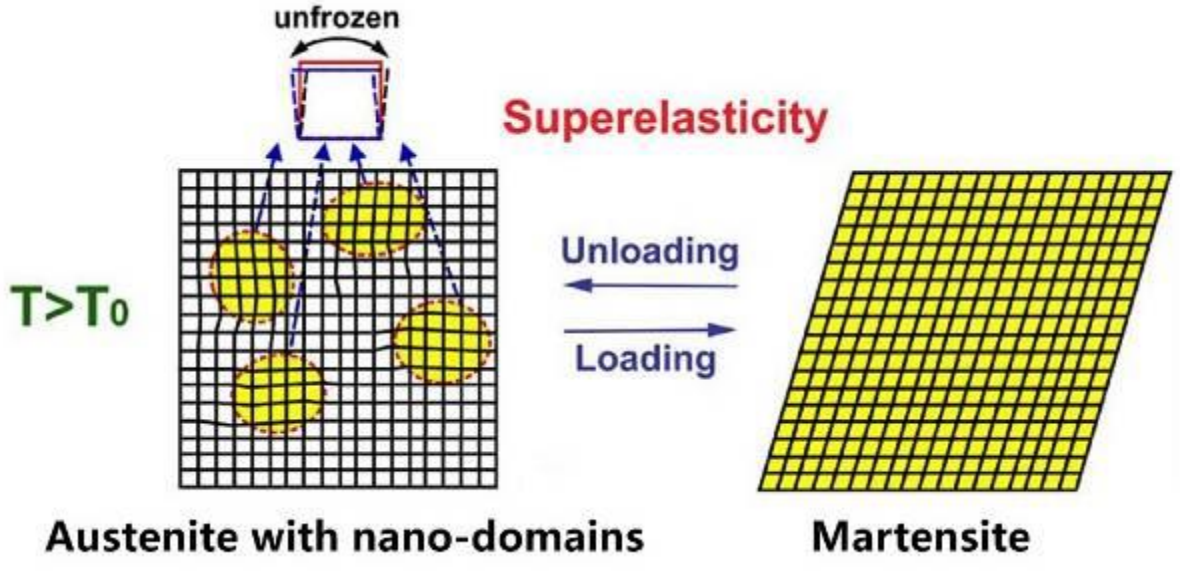
MS2.P43
Observing lattice strains in the strain glass alloy using 4D-STEM

Y. Guo[1], P. H. Lu[1], Y. Lu[1], L. Jin[1], R. E. Dunin-Borkowski[1]

[1]Forschungszentrum Jülich GmbH, Jülich, Germany

Strain glass is a new strain glassy state discovered recently in ferroelastic alloy systems, analogous to spin and polarization glass in ferromagnetic and ferroelectric systems respectively. It is a frozen state with short-range ordered lattice strains (nano-sized strain domains). Microscopically, it is characterized by many randomly distributed nano-sized strain domains embedded in austenite matrix, typically ranging in size around 10 nm. These domains can respond to stress, resulting in multifunctional properties such as the shape memory effect, superelasticity, and the elastocaloric effect. Such characteristics make strain glass materials highly promising for smart metal applications. Understanding the *in situ* dynamic behavior of lattice strain or nano-domains under stress is crucial for both fundamental research and practical applications of strain glass alloys. Transmission electron microscopy (TEM) is commonly used to characterize strain glass states. However, conventional TEM techniques often lack the necessary spatial resolution to observe short-range ordered lattice strains and the orientation of nano-domains. Recently, 4D-STEM has featured high-resolution data acquisition and dynamic process monitoring, making it possible to investigate strain glass states in greater detail. In this study, we employed 4D-STEM combined with precession electron diffraction to observe the *in situ* evolution of lattice strains distribution and nano-domains orientation in Ni-Ti strain glass alloys under loading and unloading conditions. The nano-domains in austenite can rotate and grow under stress, and upon unloading, they return to their original state, illustrating the process of superelasticity. In summary, our findings provide further insights into the physical properties of strain glass alloys.

Fig. 1



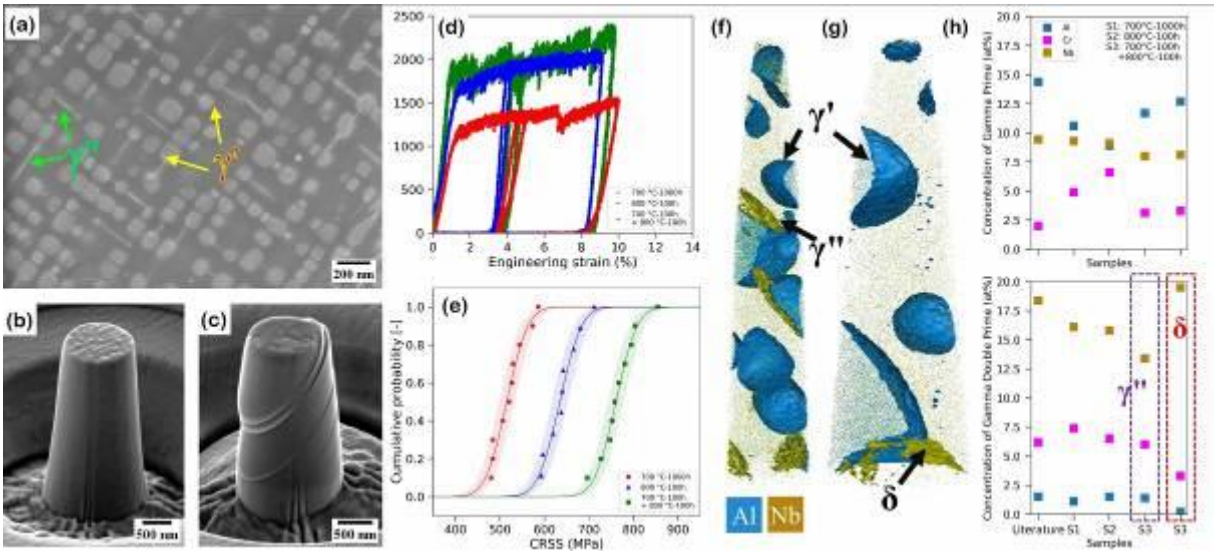
MS2.P44
Mechanistic insights into strengthening via precipitate assemblies using *in situ* micropillar compression of Ni-Cr-Al-Nb alloys

U. Bansal[1], S. Lee[1], Y. M. Eggeler[1], C. Kirchlechner[1]

[1]Karlsruhe Institute of Technology, IAM-MMI, Eggenstein-Leopoldshafen, Germany

Introduction: Ni-based superalloys, such as Inconel 718, are primarily strengthened by the metastable γ" phase (stable variant: δ-Ni_3Nb), and $L1_2$-ordered γ' phase [1]. Both precipitates co-exist within the γ matrix, where γ' phase is surrounded by plate-shaped γ" precipitates, forming a γ-γ'-γ" composite precipitate assembly, which have been proven effective in enhancing alloy"s strength [2]. However, the underlying strengthening mechanisms for the improvement in strength and the quantitative role of composite precipitate assembly to the overall strength have not yet been explored. Objective: In this study, we aim to enhance the mechanistic understanding of induced strengthening due to composite precipitate assemblies by examining the dislocation interactions with such assemblies. Materials & methods: The variations in the γ-γ'-γ" microstructure were induced through ageing of Ni-16Cr-4Al-6Nb (at.%) alloys. The composition of precipitates was analyzed using APT (LEAP 4000 HR, Cameca). Micropillars with a diameter 1 µm were fabricated using focused ion beam (FIB). Yield strength (YS) at RT was measured through in situ SEM micropillar compression test using diamond flat punch under displacement control mode at a strain rate of 10^{-3}. TEM investigations of deformed pillars were conducted using aberration-corrected STEM operated at 300 kV. Results: Fig. 1(a) shows the SEM image NiCrAlNb alloy aged at 700°C for 1000h, displaying γ-γ'-γ" microstructure. The micropillars before and after testing is shown in Fig. 1(b) and (c), respectively. The measured YS (2% offset) after 700 °C for 1000 h was ~ 1146 MPa, consistent with literature [4]. At 800°C for 100 h, there was a 1.4-fold improvement, while a short-duration annealing at 700°C for 100 h followed by 800°C for 100 h resulted in a strength enhancement of 1.5 times. A representative stress-strain curve from each set is shown in Fig. 1(d). The critical resolved shear stress (CRSS) was then calculated from the YS by considering the highest Schmid factor. A cumulative distribution function (CDF) of CRSS from different heat treated samples is presented in Fig. 1(e), elucidating the impact of microstructure post heat treatment. Given that the pillars were fabricated within the similar grain orientation, two potential strengthening mechanisms could have been activated: solid-solution strengthening and precipitate strengthening. The 3D-APT analysis in Fig. 1(f-g), suggests the presence of the δ-phase in addition to the γ-γ'-γ" microstructure in alloys annealed at 800°C. However, the matrix composition remains unchanged across all heat-treated conditions, indicating that the contribution of solid-solution strengthening is same. Therefore, the difference in yield strength can be directly attributed to precipitate strengthening. Conclusions: The γ-γ'-γ" microstructure with δ-phase contributes to increased yield strength, attributed to precipitate strengthening, as matrix composition remains constant across heat treatments. This talk discusses the impact of precipitate assembly, and δ-phase distribution on the strength of NiCrAlNb alloys. [1] M. Sundararaman, P. Mukhopadhyay, S. Banerjee, Metall. Trans. A 19A (1988) 453–465 [2] P.M. Mignanelli, N.G. Jones, et al., Scripta Mater. 136 (2017) 136–140 Figure 1 – SEM micrograph showing (a) γ-γ'-γ" microstructure in NiCrAlNb alloy after annealing at 700 °C-1000h, (b) micropillar before testing, and (c) after testing. (d) stress-strain curves and (e) a CDF of CRSS measured from in situ micropillar compression test at RT. APT 3D reconstruction of NiCrAlNb alloy heat-treated for (f) 700°C-1000h, and (g) 700°C-100h+800°C-100h. (h) Concentration (in at%) of Al, Cr and Nb elements in γ', γ", and δ precipitates.

Fig. 1


(a)
200 nm
(b)
500 nm
(c)
500 nm
(d)
Engineering strain (%)
(e)
Cumulative probability [-]
CRSS (MPa)
(f)
(g)
γ'
γ''
δ
Al
Nb
(h)
Concentration of Gamma Prime (at%)
Samples
Concentration of Gamma Double Prime (at%)
Literature
S1
S2
S3

MS 3: Disordered materials

MS3.01(inv)
Crystallization and atomic rearrangement events in supercooled metallic liquids from *in situ* 5D STEM

P. Voyles[1]

[1]University of Wisconsin-Madison, Department of Materials Science and Engineering, Madison, WI, United States

Time-resolved 4D STEM, which we call 5D STEM, with a high coherence, low convergence angle electron probe beam is well suited to studying phenomena in highly viscous, supercooled liquids. The nanometer-diameter probe size is well-matched to interesting structural length scales, and the higher coherence increases the contrast of the "speckles" that supplant the diffuse scattering rings observed in wide-area diffraction.

We have used 5D STEM with an ultrafast detector to study the crystallization of a Pd77.7Cu4Si16.3 liquid. In textbook classical nucleation, such a liquid would form a crystal embryo with the same internal structure as the first crystallizing phase and a sharp interface with the surrounding liquid. Many embryos would fluctuate in size by random attachment and detachment of single atoms until one embryo fluctuated above the critical size by a large enough margin to grow monotonically into a crystal.

We observe a different sequence of events: first, a poorly ordered precursor state forms. The precursors grows to a just-detectable area of a few square nanometers, but not larger. Then, inside the precursor, a more structural ordered phase nucleates. This ordered phase grows rapidly into a crystal, but it maintains a thin layer of less order material between itself and the liquid.

5D STEM can also be used to measure structural relaxation in the liquid itself without crystallization. We have previously used these data to measure the length scale of spatially heterogenous dynamics in a supercooled liquid and to separately the measure the dynamics of different elemental pairs in a multicomponent alloy. More recently, we have used topological data analysis (TDA), a method that quantifies the persistent homology of complex data sets, to demonstrate that 5D STEM data is consistent with dynamic facilitation in the supercooled liquid. Dynamic facilitation is a process by which rapidly rearrangement regions in the liquid (short relaxation time), speed up atomic rearrangements in neighboring regions. The potential for TDA to identify individual relaxation events in liquids will also be discussed.

MS3.02(inv)
Simultaneous assessment of structural and dynamical heterogeneities via 5D-STEM

K. Nakazawa[1], K. Mitsuishi[1], S. Kohara[1], K. Tsuchiya[1]

[1]National Institute for Materials Science, Tsukuba, Japan

Introduction

The glass transition occurs when materials such as metals, polymers, and ceramics are rapidly cooled, preventing crystallization and forming a disordered atomic structure. A key feature of this transition is the sudden change in viscosity near the glass transition temperature (Tg) despite little change in structure. This behavior is believed to be influenced by *dynamical heterogeneity* (differences in atomic motion). Although a heterogeneity in atomic structure (*structural heterogeneity*) is also found, their direct correlation remains unclear due to the lack of experimental techniques capable of capturing both simultaneously.

Objectives

This study aims to explore the relationship between dynamical and structural heterogeneities in metallic glass using five-dimensional scanning transmission electron microscopy (5D-STEM) [1]. 5D-STEM adds a time dimension to 4D-STEM by repeating 4D-STEM measurement, enabling observation of spatiotemporal diffraction pattern variations. By analyzing the spatiotemporal distribution of diffraction patterns in a metallic glass, we try to detect the correlation between dynamics and atomic structure and examine how temperature affects this relationship.

Materials & Methods

The Zr50Cu40Al10 metallic glass sample was used in experiment. The glass transition and crystallization temperature of the sample are 673 K and 750 K. Thin samples were prepared via focused ion beam milling. 5D-STEM imaging was performed at 200 kV using an aberration-corrected scanning transmission electron microscope (JEM-ARM200F; JEOL. Ltd.). Diffraction patterns are recorded by 4DCanvas camera (JEOL Ltd.). The experiment covered temperatures from 633 K to 673 K in 10 K increments. The local dynamics was assessed by the characteristic time (or relaxation time) of the decay of temporal correlation of diffraction patterns. The order of local structure was assessed via diffraction intensity fluctuations called speckles.

Results

Relaxation time maps showed spatial variation, with times ranging from 200 s to 5,000 s at 633 K. Thus, dynamical heterogeneity was directly visualized by 5D-STEM. At higher temperatures, heterogeneity was also observed and relaxation times decreased, indicating increased atomic mobility. Diffraction intensity fluctuations confirmed local variations in atomic order. These persisted at all temperatures but declined slightly with increasing temperature, suggesting a change toward more disordered structure near Tg. We measured the correlation between the heterogeneities by Spearman"s rank correlation. A positive correlation was found between relaxation time and structural order at all temperature. Higher-order regions had slower atomic motion, while less-ordered regions had faster dynamics. This suggests the ordered structures hinder rearrangements.

Conclusion

Using 5D-STEM, it successfully visualized these heterogeneities at the nanoscale and tracked their temperature evolution. This study experimentally links dynamical and structural heterogeneities in

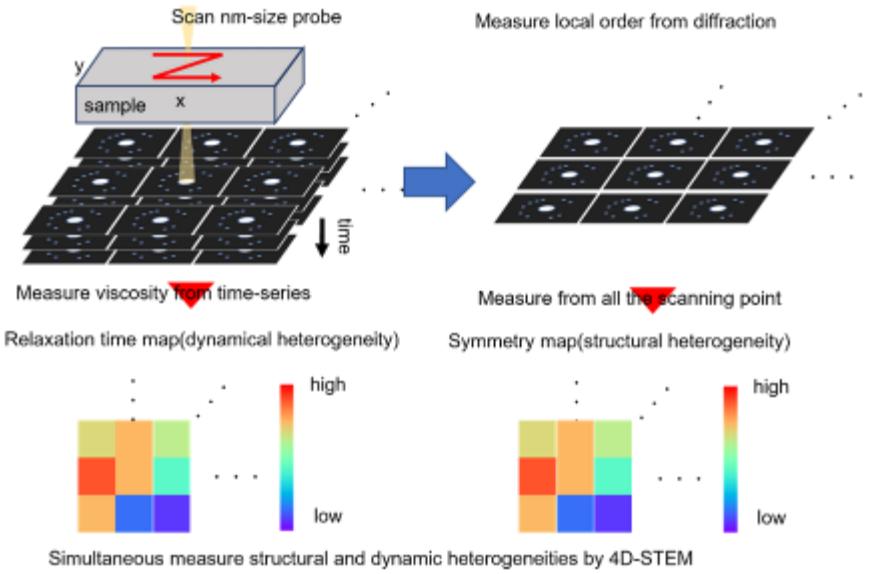
metallic glass, showing that atomic order slows atomic motion. The findings deepen our understanding of the glass transition and highlight the role of atomic structures in defining material properties [2].

Reference

[1] Katsuaki Nakazawa, Kazutaka Mitsuishi, Microscopy, 72, 5 (2023)

[2] Katsuaki Nakazawa et al., NPG Asia Materials. 16, 57 (2024)

Fig. 1



MS3.03
Time-resolved TEM study of disorder-order transition in laser excited Si

Y. Zou[1], J. Lei[1], P. H. Lu[1], R. E. Dunin-Borkowski[1]

[1]Forschungszentrum Jülich GmbH, ERC-1, Jülich, Germany

The disorder-order transition in solid materials plays a critical role in semiconductors, alloys and functional ceramics, directly impacting material properties and device performance. For example, in thin-film transistors (TFTs), amorphous silicon (a-Si) can be crystallized into crystalline silicon (c-Si) through laser-induced processes, significantly enhancing carrier mobility and enabling applications in high-resolution displays and flexible electronics [1-3]. Similarly, order-disorder transitions in alloys and functional ceramics regulate essential properties such as mechanical strength, ferroelectricity, and magnetoelectric coupling [4-6]. Achieving real-time insight into these transformations is crucial for both fundamental understanding and practical optimization of materials and devices. In this work, we use Si as a model system and apply time-resolved transmission electron microscopy (TEM) to understand the disorder to order process. The time-resolved TEM was performed in an image corrected FEI Titan Holo microscope equipped with Euclid UltraFast Pulser (UFP). The lamellar a-Si specimen used was prepared by focused ion-beam (FIB) milling with thickness less than 100 nm and excited by pulsed laser that can work from femtosecond to picosecond range. By synchronizing the laser excitation and diffraction pattern acquisition at controlled time delays, the intermediate phase transition states can be studied, following the analysis of fluctuation electron microscopy (Fluctuation EM), electron pair distribution function (ePDF) and/or crystal symmetry characterization [7-10].

References

[1] T. Y. Choi et al., Optical engineering 42, 3383-3388 (2003).

[2] N. Yamauchi and R. Reif, J. Appl. Phys. 75, 3235-3257 (1994).

[3] N. Farid et al., ACS Applied Materials & Interfaces, 13, 37797-37808 (2021).

[4] J. L. M. Rupp et al., Advanced Functional Materials 19, 2790-2799 (2009).

[5] P. Fratzl, Applied Crystallography, 36, 397-404 (2003).

[6] C. J. Gilbert et al., Applied Physics Letters 71, 476-478 (1997).

[7] P. M. Voyles and D. A. Muller. Ultramicroscopy 93, 147-159 (2002).

[8] T. E. Gorelik, Lecture Note, University of Ulm 1-18 (2018).

[9] J. B. Souza Junior et al., Matter 4, 441-460 (2021).

[10] S. Huang et al., Ultramicroscopy 232, 113405 (2022).

MS3.04
Direct observation of quadrupolar strain fields forming a shear band in metallic glasses

S. Kang[1,2,3], X. Mu[1,4], D. Wang[1,3], A. Caron[5], C. Minnert[2], K. Durst[2], C. Kübel[1,2,3]

[1]Karlsruhe Institute of Technology, Institute of Nanotechnology, Karlsruhe, Germany
[2]Technical University of Darmstadt, Department of Material- and Geosciences, Darmstadt, Germany
[3]Karlsruhe Institute of Technology, Karlsruhe Nano Micro Facility (KNMFi), Karlsruhe, Germany
[4]Lanzhou University, Department of Materials Science, Lanzhou, China
[5]KoreaTech, Department of Material Science, Cheonan, South Korea

The applications of metallic glasses are limited by their tendency to fail catastrophically at low strain due to shear banding. For decades, scanning/transmission electron microscopy (S/TEM) has been used to study shear bands, but conventional S/TEM lacks direct reciprocal space information, preventing characterization of key structural variations like local atomic configurations [1].

Recently, Gammer et al. introduced a method to measure local elastic strain in amorphous materials by quantifying elliptical deviations in diffraction patterns [2]. We advance this approach by implementing an algebraic singular value decomposition (SVD) method to fit an ellipse to the amorphous diffraction ring. This unbiased technique significantly improves precision while reducing computational demands by orders of magnitude compared to nonlinear or iterative methods [3]. From the ellipse's axes, we extract principal strains, which are then transformed algebraically into loading coordinates to obtain the strain tensor. By decomposing principal strains, we separate deviatoric strain, indicating true local distortion, from volumetric strain, capturing net volume changes due to hydrostatic stress. Additionally, we perform pair distribution function (PDF) analysis from the 4D-STEM dataset to gain insight into the local atomic structure of metallic glasses [4]. The 4D-STEM approach enables correlative visualization of nanoscale strain fields and atomic structures.

For this study, we analyzed a deformed Fe85.2Si0.5B9.5P4Cu0.8 metallic glass ribbon, chosen for its soft ferromagnetic properties (Figure 1). Our analysis reveals complex residual strain fields near shear bands, with quadrupolar shear strain fields concentrated around inclusions. These quadrupolar stress fields create vortex-like perturbations, influencing nearby inclusions and driving shear band formation. Our method expands possibilities for studying amorphous materials and understanding their

Figure 1: 4D-STEM-based strain and PDF mapping schematic. (a) A quasi-parallel electron probe scans the TEM lamella, recording spatially-resolved diffraction patterns. (b) Data processing: Principal strains are derived from diffraction ring distortion. For better visualization, the diffraction pattern is elongated along the principal direction. Strain tensors are calculated by projecting principal strains onto the reference coordinate system. For PDF analysis, diffraction patterns are azimuthally integrated into intensity profiles I(s). Structure factors, S(q), are extracted, and PDFs are obtained by Fourier sine transformation of S(q). (c) Results for deformed Fe85.2Si0.5B9.5P4Cu0.8 metallic glass ribbon show maps of volumetric strain (εVol), maximum shear strain (τmax). and strain components εxx, εxy, and εyy.

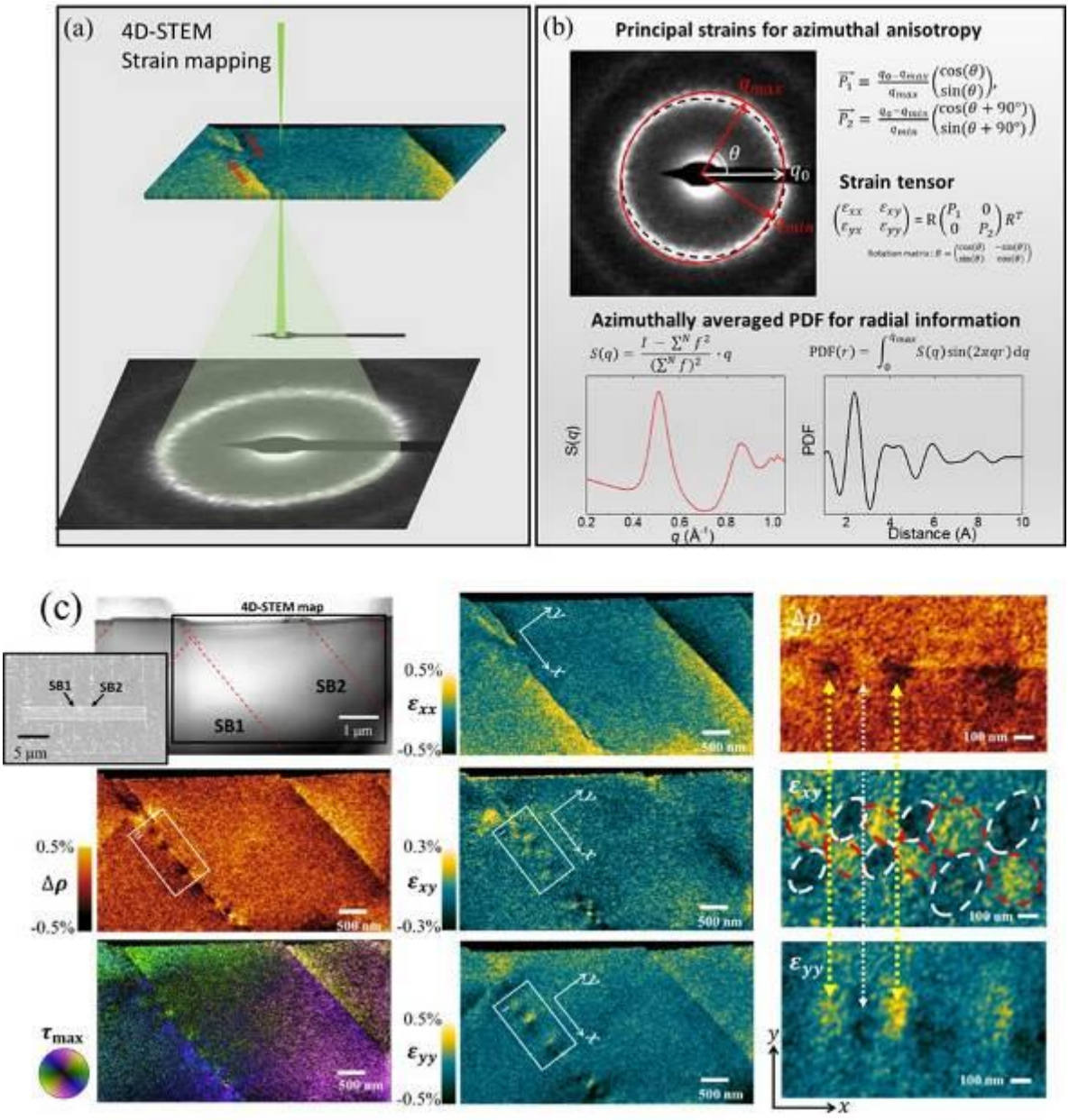
[1] D. Şopu, S. Scudino, X. Bian, C. Gammer, Eckert, Scripta Materialia 2020, 178, 57

[2] C. Gammer, C. Ophus, T. C. Pekin, J. Eckert, A. M. Minor, Applied Physics Letters 2018, 112, 171905

[3] S. J. Kang, D. Wang, A. Caron, C. Minnert, K. Durst, C. Kübel, X. Mu, *Advanced Materials*, 2023, 202212086

[4] S. J. Kang, V. Wollersen, C. Minnert, K. Durst, H. S. Kim, C. Kübel, X. Mu, Acta Materilla, 2024, 119495

Fig. 1


(a)
4D-STEM
Strain mapping
(b)
Principal strains for azimuthal anisotropy
Strain tensor
Azimuthally averaged PDF for radial information
S(q)
PDF
q (Å⁻¹)
Distance (A)
(c)
4D-STEM map
SB1
SB2
5 μm
1 μm
0.5%
-0.5%
0.3%
-0.3%
500 nm
100 nm

MS3.05
4D-STEM revealing structure-property relationships in bulk metallic glasses

H. Rösner[1], M. W. da Silva Pinto[1], G. Wilde[1]

[1]University of Münster, Institute of Materials Physics, Münster, Germany

Introduction:

Micro- or minor alloying of metallic glasses holds significant technological potential. We investigated a Pd-based monolithic bulk metallic glass ($Pd_{40}Ni_{40}P_{20}$), focusing on the effects of selective additions of Fe and Co. The results revealed strikingly different mechanical behaviors: Co addition enhanced ductility, while Fe introduction led to immediate catastrophic failure under uniaxial compression and 3-point bending tests [1].

Objectives:

To elucidate the mechanisms behind these contrasting deformability outcomes, we employed 4D-STEM for in-depth analyses of the amorphous structures. Traditional x-ray diffraction and selected area electron diffraction showed no discernible changes that could account for the observed differences. However, variable resolution fluctuation electron microscopy (FEM) [2] provided compelling evidence that minor alloying significantly influences the medium-range order of glassy structures, extending beyond the typically reported 2 nm range, consequently affecting material ductility.

Materials & Methods:

To achieve our objectives, we conducted statistical analyses of individual nanobeam diffraction patterns using variable resolution fluctuation electron microscopy [2]. This approach allowed us to reveal the medium-range order of the glassy structures, extending beyond the conventional 2 nm threshold. Furthermore, we applied angular symmetry analyses [3] to extract insights from the diffraction patterns of the micro-alloyed samples.

Results:

Our findings indicate that minor alloying has a profound impact on the correlation of glassy structures beyond the usual 2 nm range, influencing the ductility of the material (see Fig. 1). Moreover, angular symmetry analysis revealed a distinct 5-fold symmetry in $(Pd_{40}Ni_{40}P_{20})_{99}Fe_1$, whereas this symmetry significantly diminished in $(Pd_{40}Ni_{40}P_{20})_{99}Co_1$, approaching 4- and 6-fold symmetries (see Fig. 2). Thus, the diversity of the medium-range order, along with the crystal-like symmetries present in the Co-doped bulk metallic glass, appears to facilitate multiple shear banding, ultimately enhancing its deformability.

Conclusion:

These findings, achieved through advanced microscopic techniques, offer new insights into the role of minor alloying in the mechanical behavior of bulk metallic glasses. The ability to fine-tune properties through medium-range order engineering presents exciting opportunities for enhancing the performance of metallic glasses.

References

1. S. Hilke, H. Rösner, G. Wilde, *The role of minor alloying in the plasticity of bulk metallic glasses:* Scripta Materialia 188, 2020, 50-53.
2. P.M. Voyles and J. Hwang, *Fluctuation Electron Microscopy*: *Characterization of Materials (John Wiley, 2002,1-7)*
3. S. Huang et al., *Correlation symmetry analysis of electron nanodiffraction from amorphous materials:* Ultramicroscopy 232, 2022, 113405.

Figure legends:

Fig 1: FEM analysis of the amorphous structure using the normalized variance at k=4.8 nm^{-1} obtained by variable probe sizes. For better perception, the plots are vertically shifted. Plateaus are indicated by colored boxes.

Fig.2: Angular symmetry analyses of the amorphous structures through electron diffraction by utilizing local symmetry information extracted from individual nanobeam diffraction patterns of the micro-alloyed samples.

Fig. 1

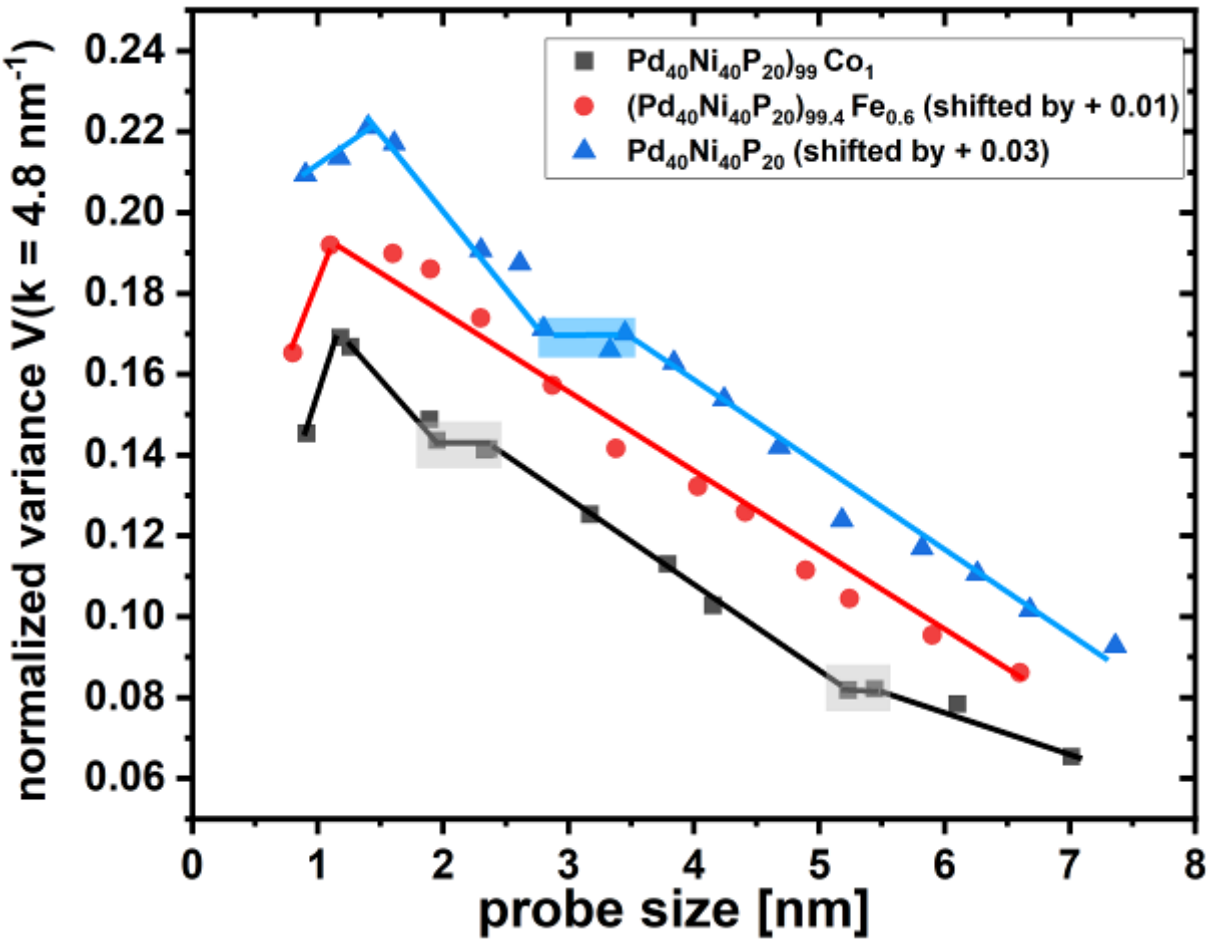
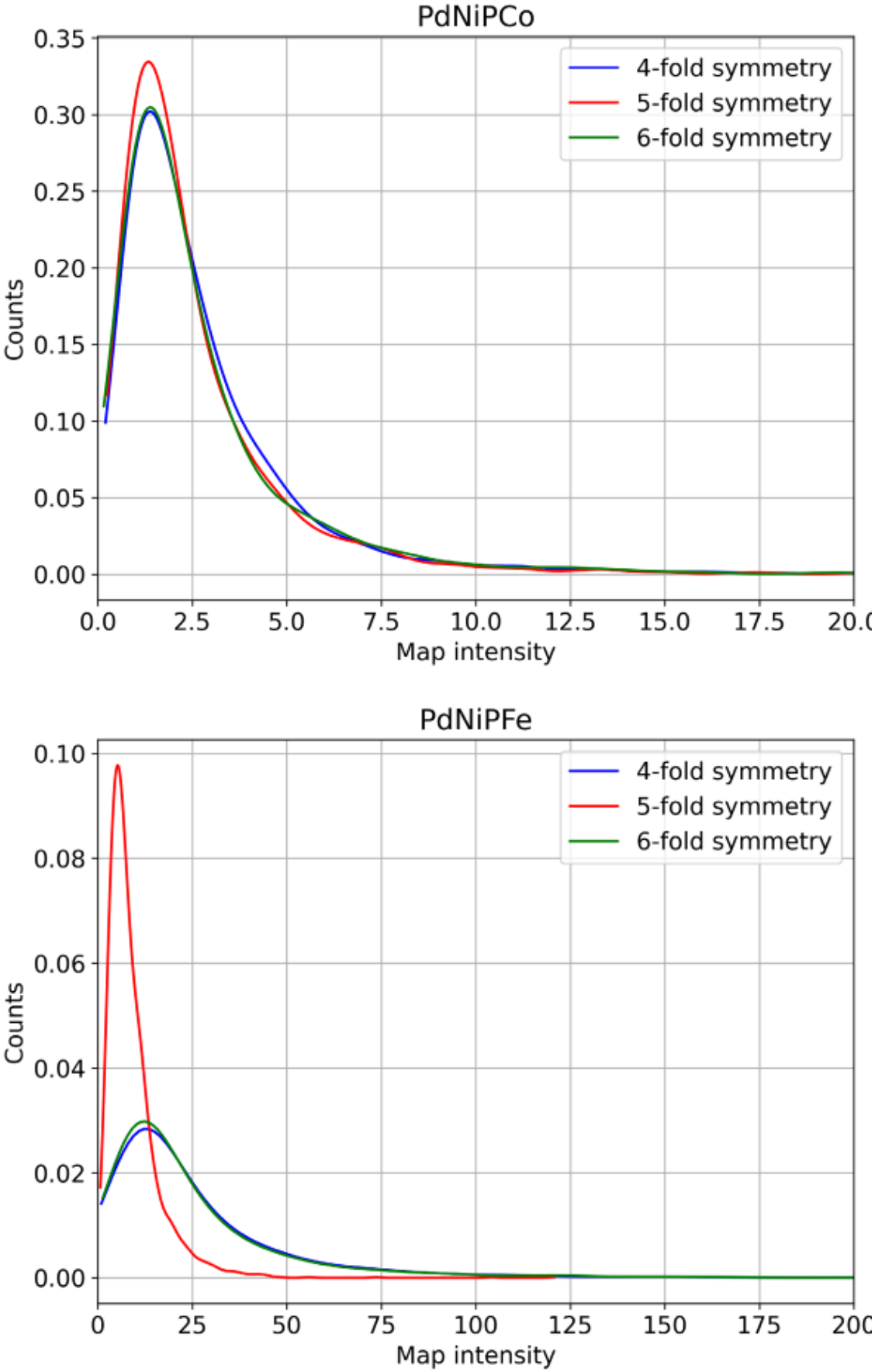


Fig. 2


PdNiPCo
4-fold symmetry
5-fold symmetry
6-fold symmetry
Counts
Map intensity
0.00
0.05
0.10
0.15
0.20
0.25
0.30
0.35
0.0
2.5
5.0
7.5
10.0
12.5
15.0
17.5
PdNiPFe
4-fold symmetry
5-fold symmetry
6-fold symmetry
Counts
Map intensity
0.00
0.02
0.04
0.06
0.08
0.10
0
25
50
75
100
125
150
175

MS3.06
Electron beam irradiation induced phase transformations in W-Ta-C ultrathin layers

S. M. Noisternig[1], U. Ludacka[2], H. P. Karnthaler[1], C. Rentenberger[1]

[1]University of Vienna, Physics of Nanostructured Materials, Vienna, Austria
[2]Norwegian University of Science and Technology, Department of Physics, Trondheim, Norway

By electron microscopy, we study beam induced structural changes in a system of tungsten tantalum carbide (W-Ta-C). In situ phase transitions, triggered by the electron beam enable controlled structural changes on a nanometer scale. W-C carbides have gained interest in connection with the challenges of the energy transition. Ongoing research focuses on the exchange or reduction of Pt for the hydrogen evolution reaction. W-C carbides are catalytically active plus, when used in combination with Pt, the system can even outperform pure Pt [1].

Ultrathin amorphous W-Ta-C layers of 6-7 nm are produced by electron beam physical vapor deposition (EB-PVD) from a W-Ta alloy target. In addition, an amorphous pure W ultrathin layer of 3 nm nominal thickness was deposited by EB-PVD; to check the long time stability of pure amorphous W, this sample was kept inside a vacuum chamber for more than 2 years.

Irradiation experiments of the ultrathin amorphous layers were carried out by TEM experiments in a FEI Titan 80-300 using 80 kV acceleration voltage (see Fig.) and by STEM experiments in a Nion UltraSTEM 100 using 60 kV acceleration voltage, respectively. In both cases a two step phase transformation of amorphous W-Ta-C was observed by electron beam irradiation: (i) A transition from the metastable amorphous phase to crystalline W-Ta carbide phases resulting in a local layer of nanocrystalline W-Ta-C at the area of electron beam irradiation. (ii) After further irradiation, the nanocrystals transform to the bcc W-Ta phase. W and Ta form a solid solution with a bcc crystal structure. The observed phase transformations show a clear dependency on acceleration voltage and electron flux. The crystalline phases of the W-Ta-C nanocrystals were identified by comparison of FFT patterns from HAADF and HRTEM images with known W-C phases in the literature. These results were then confirmed by HRTEM and HAADF image simulations.

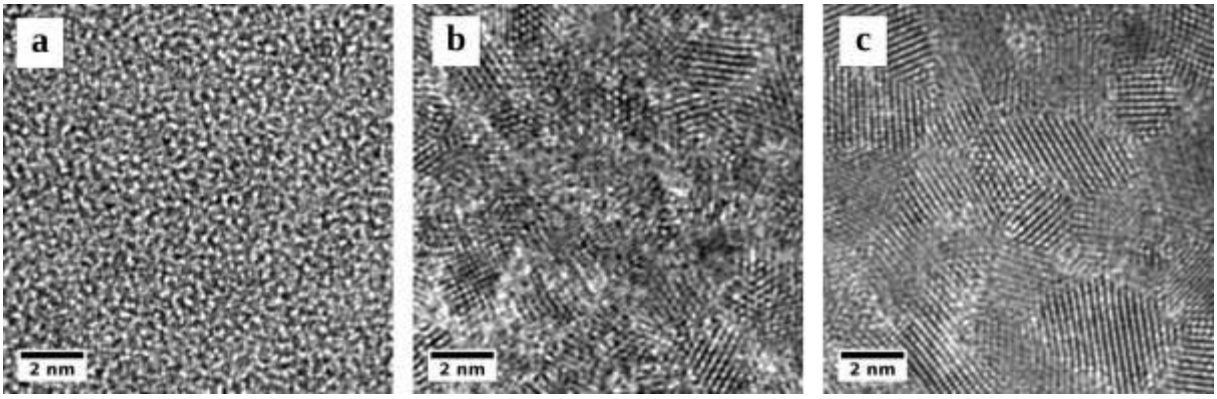
Afterwards we study the time dependency of the amorphous to crystalline transition by in situ STEM irradiation experiments at different electron fluxes. A routine was developed to obtain a quantitative parameter for the time of crystallization by analyzing the time dependency of the normalized variance on the first ring in the FFT patterns of HAADF image series. The emergence of crystalline reflexes on the amorphous ring leads to a change in the normalized variance.

For the deposited ultrathin layer of pure W, the irradiation experiments were also carried out. In this case, the layer stays still amorphous after a long storage time at high vacuum conditions. It is important that, in contrast to W-Ta-C, amorphous pure W does not crystallize at similar irradiation conditions. Finally, in combination with considerations regarding knock-on damage and crystal orientations, we propose that carbon displacement and sputtering play a significant role for the observed phase transitions.

[1] D. J. Ham, R. Ganesan, J. S. Lee, Tungsten carbide microsphere as an electrode for cathodic hydrogen evolution from water, Int. J. Hydrogen Energy, 33 (2008), 6865-6872

Fig.: HRTEM images of a W-Ta-C layer at different stages of electron irradiation. (a) was acquired at the start of electron irradiation and shows an amorphous structure, while after 10 minutes of irradiation, in (b) W-Ta carbide nanocrystals can be observed. In (c) after long time exposure for 60 minutes, the layer is completely crystallized and transformed to the bcc W-Ta phase.

Fig. 1



MS3.P01
In situ investigation of the structure and local dynamics in a Zr-based bulk metallic glass

O. Vaerst[1], H. Rösner[1], M. Peterlechner[2], G. Wilde[1]

[1]University of Münster, Institute of Materials Physics, Münster, Germany
[2]Karlsruhe Institute of Technology, Laboratory for Electron Microscopy, Karlsruhe, Germany

Metallic glasses are disordered materials in a thermodynamic non-equilibrium state that remain only partially understood. Ongoing research continues to explore their formation mechanism and the relationship between their unique structure with the properties that these materials exhibit. Thermal treatments of metallic glasses induce structural relaxation, which facilitates a transition in their thermodynamic state. Analyzing these states and the processes of structural relaxation is crucial for improving our understanding of the disordered structure and its connection to atomic processes occurring in metallic glasses.

In the present study, we investigate the structural changes and the mechanisms driving structural relaxation using advanced electron microscopy techniques to gain insights into the fundamental relaxation mechanisms of metallic glasses.

We adjust various thermodynamic states of a commercial Zr-based bulk metallic glass through annealing treatments conducted in a differential scanning calorimeter (DSC). Local structural analyses of the electron-transparent samples, prepared using a focused ion beam (FIB), are performed by 4D-STEM fluctuation electron microscopy (FEM) to explore the material"s state-specific characteristics. Additionally, local dynamics are investigated using electron correlation microscopy (ECM) in TEM mode, where changes of speckle intensities in dark-field images are correlated over time to yield spatially resolved dynamics. The experiments are carried out at room temperature on pre-set states and during *in situ* heating to investigate the structural changes during relaxation.

FEM analyses of normalized variances reveal medium-range order (MRO) correlation lengths and volume fractions. Interestingly, for the investigated Zr-based glass, the MRO correlation length remains unchanged after annealing, suggesting that the nature of MRO is not affected by structural relaxation. However, changes in MRO volume fraction with structural relaxation were observed in both, pre-annealed samples and during *in situ* heating FEM measurements, potentially linked to the material"s low fragility. ECM measurements provide deeper microstructural insights by monitoring local mobilities at various temperatures, including also elevated ones. The results indicate that ongoing structural relaxation results in a deceleration of dynamics.

In conclusion, our findings enhance insights into the amorphous phase and local relaxation dynamics of bulk metallic glasses. They suggest a correlation between fragility, as determined from macroscopically averaged measurements, local dynamics assessed spatially, and the local medium-range order structure.

Funding by DFG is acknowledged (research grants Wi 1899/47-1 and Pe 2290/2-2).

MS3.P02
Evaluating the local structure and thermal behavior of SiCN in hybrid bonding using ePDF and 4D-STEM

H. Cho[1,2], S. Kang[1,2,3], C. Kübel[1,2,3]

[1]Technical University of Darmstadt, The Department of Material- and Geosciences, Darmstadt, Germany
[2]Karlsruhe Institute of Technology, Institute of Nanotechnology, Eggenstein-Leopoldshafen, Germany
[3]Karlsruhe Institute of Technology, Karlsruhe Nano Micro Facility (KNMFi), Eggenstein-Leopoldshafen, Germany

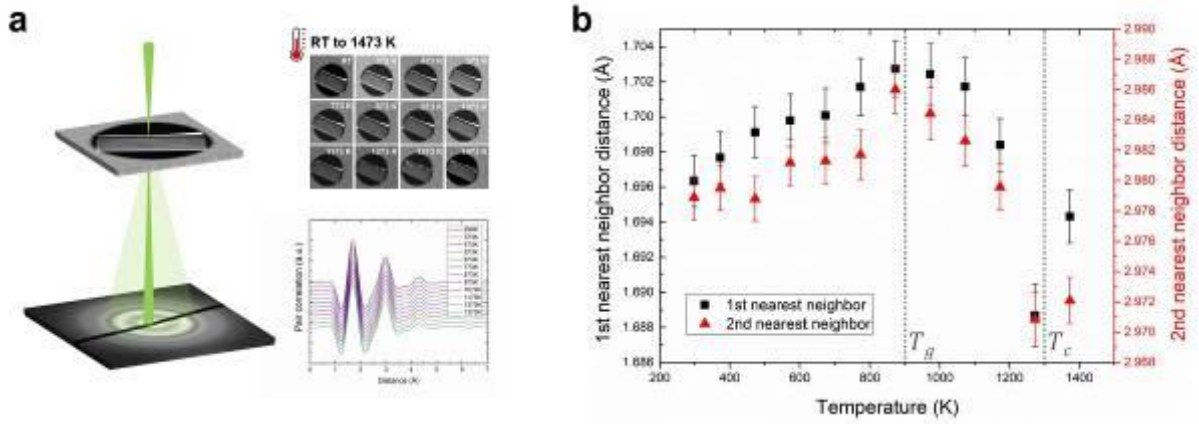
Hybrid bonding is a critical technology for high-density 3D semiconductor integration, particularly in high bandwidth memory (HBM) and advanced packaging applications [1]. Amorphous silicon carbo nitrides (SiCN) have emerged as a promising dielectric material owing to its high mechanical stability and strong interfacial bonding [2]. The structure of amorphous materials is typically studied by pair distribution function (PDF) analysis using X-ray and neutron scattering experiments. However, understanding its local atomic structure and thermal stability of SiCN remains challenging due to the limited spatial resolution of traditional PDF analysis using conventional scattering experiments. In this study, we applied electron pair distribution function (ePDF) analysis based on 4-dimensional scanning transmission electron microscopy (4D-STEM) to investigate the nanoscale structure and structural variations of the SiCN dielectric layer in hybrid bonding [3, 4]. The effect of electron dose on ePDF signal quality was systematically evaluated to ensure reliable structural analysis. Additionally, in-situ heating experiments were conducted to examine thermal structural evolution, with a focus on nearest-neighbor atomic distances to assess bonding stability and interfacial behavior. Our results identified optimal electron dose conditions for accurate ePDF measurements. We observed thermal expansion of atomic distances below the glass transition temperature (~900 K), followed by contraction due to structural relaxation. Furthermore, at 1373 K – 1473 K, cracks were detected along the Si-SiCN interface, highlighting potential reliability concerns for high-temperature applications. These findings provide new insights into the structural and thermal stability of SiCN, offering valuable guidelines for optimizing hybrid bonding conditions and enhancing the reliability of 3D integration technologies.

References

[1] F. Nagano et al., ECS J. Solid State Sci. Technol., 12, 033002 (2023).
[2] E. Beyne et al., 2017 IEEE International Electron Devices Meeting (IEDM), 32.4.1-32.4.4 (2017).
[3] X. Mu et al., Ultramicroscopy, 168, 1-6 (2016).
[4] S. Kang et al., Acta Materialia, 263, 119495 (2024).

Figure 1: (a) Schematic illustration of 4D-STEM-based in-situ heating and ePDF analysis of SiCN in hybrid bonding. (b) Temperature dependence of the first (black squares) and second (red triangles) nearest neighbor distances extracted from ePDF analysis. The glass transition temperature (Tg) and crystallization temperature (Tc) are indicated with dashed lines. Atomic distances exhibit thermal expansion below the glass transition temperature (Tg≈900 K), followed by contraction due to structural relaxation.

Fig. 1


a
RT to 1473 K
b
1st nearest neighbor distance (Å)
2nd nearest neighbor distance (Å)
1st nearest neighbor
2nd nearest neighbor
T_g
T_c
Temperature (K)

MS3.P03
Studying dark-field speckle contrast of amorphous matter as a function of time

M. Peterlechner[1]

[1]Karlsruhe Institute of Technology, Laboratory of Electron Microscopy (LEM), Karlsruhe, Germany

Amorphous materials are often in a thermodynamic non-equilibrium state. Since a few decades research focuses to explore the formation mechanisms of an amorphous phase and the relationship between the structure with the properties that these materials exhibit. Thermal treatments of metallic glasses induce structural relaxation, which facilitates a transition to a thermodynamically more stable state. Analyzing these structures and the processes of structural relaxation is crucial to understand disordered materials, their structure and its connection to atomic processes occurring in metallic glasses.

In the present study, we investigate the structural changes and the mechanisms driving structural relaxation using advanced electron microscopy techniques to gain insights into the fundamental relaxation mechanisms of metallic glasses or at least metallic amorphous structures.

Structural analyses on the nanometer scale was accomplished using thin electron-transparent foils. Samples were prepared using a focused ion beam (FIB), ion milling as well as electropolishing. Fluctuation electron microscopy (FEM) measurments were made to gain insight into the structure, and local dynamics is analyzed based on time series of dark-field (DF) images. Changes of speckle intensities in DF-images are quantified over time by calculating the intensity correlation function. This yields data on dynamics, with a very high spatial resolution. The experiments are typically carried out at room temperature and during *in situ* heating to investigate the relaxation dynamics and the corresponding structural changes.

The results of the DF-image analysis indicate, that ongoing structural relaxation results in a slower and slower dynamics. In agreement with earlier work it becomes clear, that the electron beam and its dose-rate increase the relaxation rate, however, do not generally change the type of dynamics. Moreover the convergence of the numerical values of relaxation time and kinetic stretching exponent (obtained by a Kohlrausch-Williams-Watts function fit) with increasing measurement time suggests, that a sweet spot for the practical measurement time window is already achieved after a few hours. However, comparing pure materials (as Si and Ge) with complex alloys (as PdNiP or FeNiP) there seems to be no general rule to deduce. It can be concluded, that dynamics is depending on the materials type and processing history.

In the present work it is shown, that beam driven relaxation in amorphous metallic structures and pure materials can accelerate relaxation dynamics in amorphous structures. In extreme cases even starting crystallization. Numerically there are sweet spots to run beam driven experiments to partly replace heating experiments by using the electron beam at room temperature as an external stimulus.

Funding by DFG is acknowledged (Pe 2290/2-2).

MS3.P04
Atomic and chemical structure characterization of nanocrystalline CrCoNi alloys using 4D-STEM pair distribution function mapping

A. R. Lakshmi Nilayam[1,2,3], S. Kang[1,2,3], G. Iankevich[3], H. Hahn[1,3,4], D. Wang[1,2], C. Kübel[1,2,3]

[1]Karlsruhe Institute of Technology, Institute of Nanotechnology, Karlsruhe, Germany
[2]Karlsruhe Institute of Technology, Karlsruhe Nano Micro Facility (KNMFi), Karlsruhe, Germany
[3]Technical University of Darmstadt, Department of Materials and Earth Sciences, Darmstadt, Germany
[4]University of Oklahoma, School of Sustainable Chemical, Biological and Materials Engineering, Oklahoma City, OK, United States

Nanostructured CrCoNi alloys, with its multi-principal element composition, high surface area, and active defect sites, shows enhanced catalytic activity and unique soft magnetic properties1. To obtain this MEA with control of the nanostructure, we used Cluster Ion Beam Deposition (CIBD), a physical vapor deposition (PVD) technique, where we can adjust the landing energy of the clusters on substrate: 25eV per cluster ion and 250eV per cluster ion. We aim to understand how varying deposition energies impact the atomic and microstructure of the material by analyzing the effect of different cluster ion impact energies during deposition. Due to lack of long-range order in the CIBD deposited CrCoNi alloy, we used 4D-scanning transmission electron microscopy (4D-STEM) based pair distribution function (PDF) analysis in combination with energy dispersive X-ray spectroscopy (EDX) maps to understand the local atomic arrangement, spatial distribution and the chemical state of the principal elements in the system. Using 4D-STEM data, we constructed a 3D PDF data cube where each channel contains a PDF corresponding to the specific position in the 2D image array. These PDFs represent a mixture of CrCoNi clusters, potential secondary phases, background contributions from the carbon substrate, and shot noise from data acquisition. Additionally, strong signal overlap from different phases and the carbon substrate can cause peak shifts, cancellations, or reinforcements, making a direct or averaged PDFs difficult to interpret. To address this, we apply matrix factorization techniques2 to decompose the mixed PDFs into individual component PDFs, enabling clear identification of the atomic and chemical structure of the specimen while distinguishing it from the substrate contribution. The average PDF signal from all probe positions in the 4D dataset is shown in figure 1a. The medium-range order reveals changes in atomic coordination, highlighting varying levels of oxidation in the specimens. Using techniques like non-negative matrix factorization (NMF) and MCR-ALS, we successfully separate the CrCoNi cluster core, chromium oxide and carbon substrate components in the PDF maps (figure 1b, 1c). This allows us to visualize the spatial distribution of oxidation within the specimens, which is otherwise hidden in the average PDF dataset. This can also be seen from the MCR-ALS analysis of EDX maps, which show that the 25eV deposition, with its softer cluster landing, results in a better distribution of oxidized Cr on the surface and at grain interfaces (figure 2a). Component 1 is rich in the CrCoNi with minimal contributions from C and O, component 2 has contributions from oxidized Chromium and from the C substrate. In contrast, the 250eV deposition creates a densely packed and regular CrCoNi network, with minimal Cr oxidation; leading to no distinct component of Chromium oxide. This work highlights the power of combining 4D-STEM PDF analysis with data decomposition techniques for precise atomic and chemical characterization, offering deep insights into oxidation behavior and structural characterization of amorphous/ nanocrystalline materials at the atomic scale.

Figure 1: a) average PDF from 4DSTEM, b) spatial map of NMF factorized PDF components and c) NMF components of 25eV deposition

Figure 2: MCR-ALS factorization of EDX maps: a) 25eV and b) 250eV

(1) Bajpai, S. et al. Materialia 2022, 24, 101476. https://doi.org/10.1016/j.mtla.2022.101476.
(2) Kang, S. et al. Acta Mater. 2024, 263, 119495. https://doi.org/10.1016/j.actamat.2023.119495.

Fig. 1

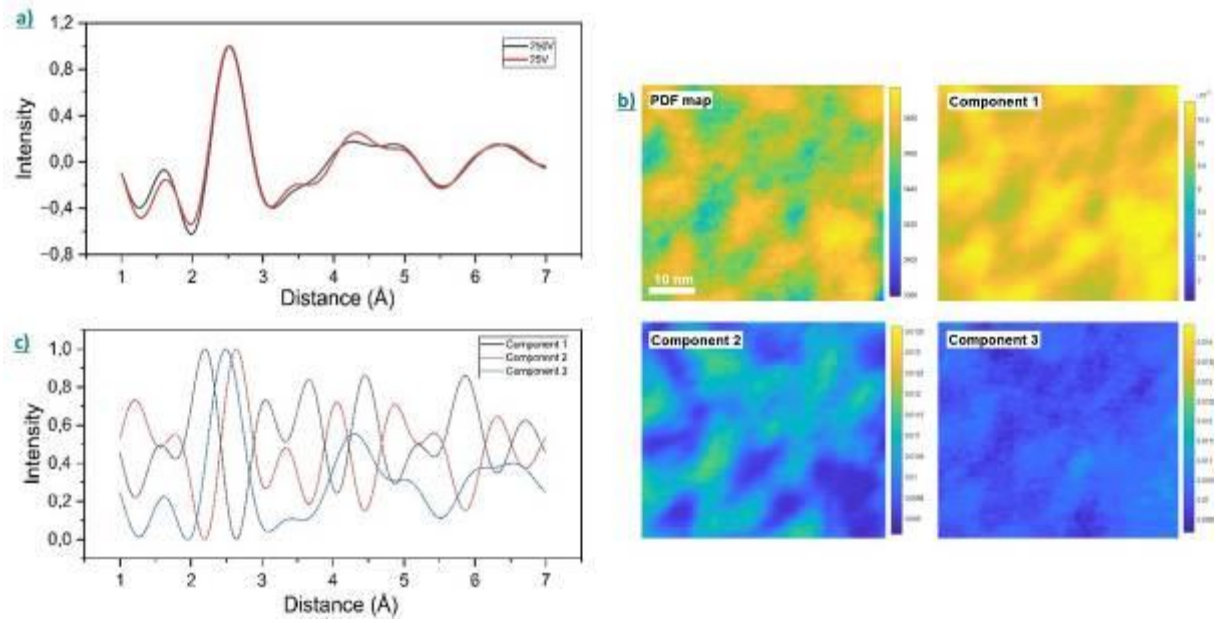
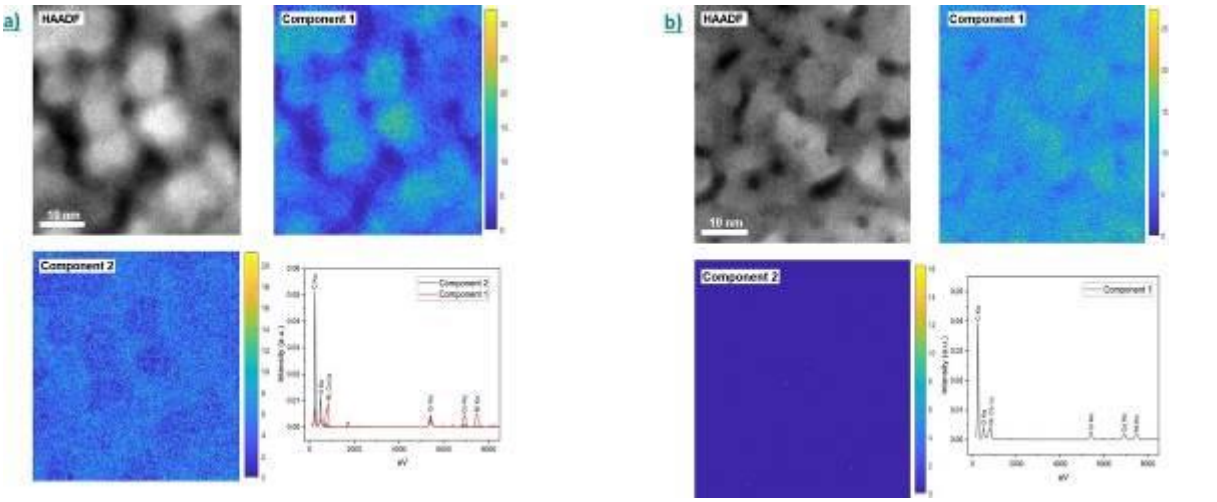

a)
Intensity
Distance (Å)
b)
PDF map
10 nm
Component 1
Component 2
Component 3
c)
Intensity
Distance (Å)

Fig. 2


a)
HAADF
Component 1
Component 2
b)
HAADF
Component 1
Component 2

MS3.P05
Geometry dependent localization of surface plasmons on random gold nanoparticle assemblies

M. F. Kalady[1], J. Schultz[1], K. Weinel[1], D. Wolf[1], A. Lubk[1]

[1]Leibniz Institute for Solid State and Materials Research Dresden, Dresden, Germany

Introduction

Plasmonic nanostructures exhibit unique optical properties driven by localized surface plasmon (LSP) resonances. LSP modes in ordered nanoparticle (NP) arrays hybridize into delocalized lattice resonances (plasmon bands), enabling efficient energy transport. However, disorder in the geometric arrangement of the NP lattice can induce spatial and spectral localization, significantly altering plasmonic behavior [1]. Understanding the interplay between disorder, geometry, and LSP localization is crucial for sensing, optoelectronics, and metamaterials applications.

Objectives

This study investigates the localization behavior of LSP modes in completely disordered assemblies of gold (Au) NPs, fabricated via electron beam synthesis [2]. The primary objective of our study is to analyze the influence of NP thickness on plasmon localization and identify the transition between localized and delocalized modes.

Materials & methods

Random Au NP assemblies with a wide range of thicknesses were fabricated using a focused electron beam in a scanning electron microscope (SEM) [2]. Their plasmonic properties were probed using electron energy loss spectroscopy (EELS) in a scanning transmission electron microscope (STEM) [3]. Numerical simulations were performed using a self-consistent dipole model based on discrete dipole approximation to complement the experimental findings. Localization behavior was analyzed through spectral and spatial mapping of LSP modes and quantified using the inverse participation number [4].

Figure 1. HAADF STEM image of Au NP assembly.

Results

The results reveal a strong dependence of LSP localization on NP thickness. For ultrathin NPs (thickness <0.4 nm), localization increases with higher energy, suppressing hybridized modes beyond 1.6 eV. In contrast, localization decreases at higher energies for thicker NPs (>10 nm), indicating a transition toward delocalized modes. This transition is driven by the thickness-dependent polarizability of individual NPs. Simulations confirm that disorder-induced localization is modulated by geometric parameters, with an intermediate thickness range exhibiting a distinct transition energy, where localization is minimized.

Conclusion

This study demonstrates that NP thickness is a key parameter in controlling LSP localization in disordered Au assemblies. The observed trends provide insights into designing plasmonic materials with tunable optical properties, particularly for applications requiring enhanced localization in specific spectral ranges.

References

[1] J. Schultz, K. Hiekel, P. Potapov, et al., Physical Review Research **6**, 10.1103 (2024).

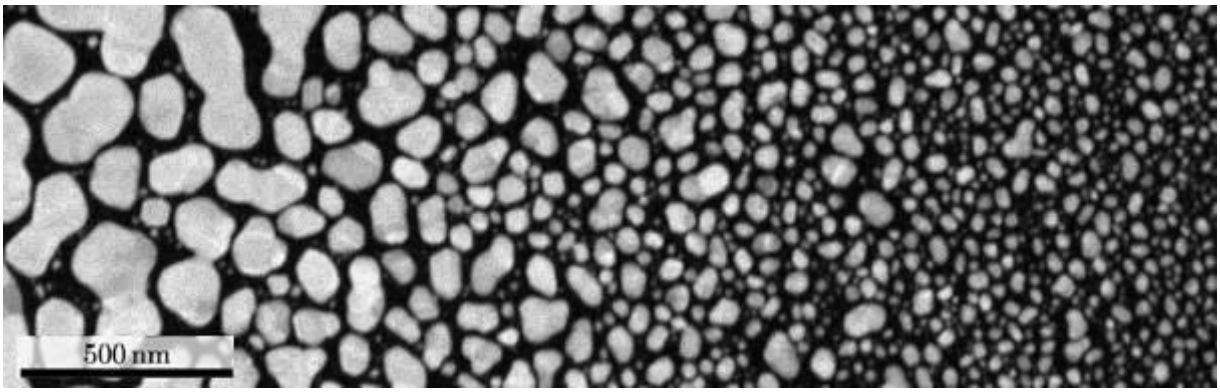
[2] K. Weinel, M. B. Hahn, A. Lubk, et al., arXiv:2408.02409 (2024).

[3] J. Nelayah, M. Kociak, O. Stéphan, et al., Nature Physics **3**, 348 (2007).

[4] V. A. Markel, Journal of Physics: Condensed Matter **18**, 11149 (2006).

[5] We acknowledge funding from the Deutsche Forschungsgemeinschaft (DFG), CRC-1415, 417590517, and the Leibniz association within the Leibniz competition funding program under project number K524/2023.

Fig. 1



MS3.P06
Unraveling the structure of porous glass for validation of sorption processes

D. Poppitz[1], D. Enke[1]

[1]Leipzig University, Instiute of Chemical Technology, Leipzig, Germany

Porous glass materials have emerged as versatile platforms for catalysis and sorption applications due to their high thermal and chemical stability, tunable pore structures and functional surface properties. Their well-defined porosity, combined with the ability to modify surface chemistry, makes them attractive for heterogeneous catalysis, gas separation and other applications. [1] Understanding the structure-property relationships of these materials is essential for optimizing their performance in catalytic transformations and sorption processes. However, due to their unordered and complex pore structure, there are only few insights into the actual structure of porous glasses in the literature, e.g. by Paufler et al. [2].

In this study, we will build a model system of mesoporous glass materials with unordered pore structures for the validation and characterization of sorption processes. Therefore, a precise understanding of the real structure of the complex mesoporous network is essential for accurate validation. Conventional characterization methods based on sorption, e.g. N_2, Ar, or intrusion, e.g. Hg, are widely used to determine average surface area, pore volume and pore size distribution, but provide only bulk data and lack local information about individual pores and their connectivity. TEM allows direct imaging of the mesoporous network at the nanometer scale and even three-dimensional (3D) data by using electron tomography. From this we can reconstruct the porous network, providing deeper insights into pore size distribution, tortuosity or connectivity. [3] These structural parameters serve as a basis for advanced computational modelling, allowing more accurate predictions of molecular transport and sorption dynamics. Simulation of molecular transport and adsorption behavior, allows us to validate conventional sorption characterization techniques by distinguishing between idealized model assumptions and the actual structural complexity of the material. The combination of high-resolution imaging, tomography, diffusion studies by NMR techniques and modelling improves the fundamental understanding of sorption mechanisms. and facilitates the rational design of porous glass materials for optimized performance in catalytic and separation applications.

By bridging the gap between electron microscopic imaging, experimental measurements, and theoretical modeling, this study provides a more comprehensive understanding of sorption processes in mesoporous glass materials, paving the way for their tailored optimization in catalytic and separation applications.

[1] B. Zhu, Z. Zhang, W. Zhang, Y. Wu, J. Zhang, Z. Imran, Di Zhang, J. Shanghai Jiaotong Univ. (Sci.) 24 (2019) 681-698.

[2] P. Paufler, S.K. Filatov, I.P. Shakhverdova, R.S. Bubnova, M. Reibold, B. Müller, A.A. Levin, D.C. Meyer, Glass Phys Chem 33 (2007) 187-198.

[3] S. Weber, R.T. Zimmermann, J. Bremer, K.L. Abel, D. Poppitz, N. Prinz, J. Ilsemann, S. Wendholt, Q. Yang, R. Pashminehazar, F. Monaco, P. Cloetens, X. Huang, C. Kübel, E. Kondratenko, M. Bauer, M. Bäumer, M. Zobel, R. Gläser, K. Sundmacher, T.L. Sheppard, ChemCatChem 14 (2022) e202101878.

MS3.P07
Mapping the complex deformation dynamics of metallic glasses during *in situ* deformation using 4D-STEM

S. Fellner[1], J. Eckert[1,2], C. Gammer[1]

[1]Montan University Leoben, Erich Schmid Institute of Materials Science, Leoben, Austria
[2]Montan University Leoben, Department of Materials Science, Leoben, Austria

Introduction:

Despite having unique attractive properties, disordered materials often suffer from catastrophic failure after reaching their yield strength. To overcome this limitation, heterogeneities need to be introduced. The ability to improve the mechanical and functional properties of metallic glasses (MGs) depends on understanding their inherent strain state. Recently, nanoscale strain mapping using transmission electron microscopy (TEM) was used to unravel shear band formation in a monolithic MG [1]. The effect of structural changes induced by the introduction of secondary crystalline phases, highly rejuvenated regions or other defects renders transformation mechanisms in MGs even more complex. Due to the emergence of novel dedicated specimen holders, *in-situ* TEM measurements are a powerful tool allowing to directly measure the deformation behavior of these tailored nanocomposites [2].

Objective:

In this work, we want to directly image the local elastic strain fields at heterogeneities in MGs using precession nanodiffraction mapping.

Materials & methods:

The study was carried out on a CuZr-based alloy, which is a well-known glass former. Thermal processing techniques and plastic deformation were used to introduce heterogeneities. Nanosized specimens were fabricated through focused ion beam milling. A Bruker Hysitron nanoindenter holder in combination with a push-to-pull device were used for *in-situ* tensile testing in the TEM. Precession nanodiffraction mapping using a TVIPS USG was combined with an in-column energy filter (JEOL 2200FS) and a direct electron detector from QuantumDetectors. This experimental approach enabled rapid acquisition of high quality diffraction patterns and allowed us to follow the structural response during *in-situ* deformation at the nanoscale.

Results:

The results of nanodiffraction mapping revealed local events of cooperative shear in MGs. From acquired in-plane atomic level strain maps the interaction between heterogeneities could be described quantitatively. Unraveling shear band mechanisms, demonstrated that the structure of disordered materials strongly depend on the processing history. It was shown, that high interfacial stresses between heterogeneities cause complex strain concentrations preventing strain localization in a single shear band. We were also able to show that crystalline phases strongly influence the stress field in the amorphous phase. As a result, a direct link could be established between the structure and properties of these tailored MG composites.

Conclusion:

We demonstrated the experimental measurement of local quantitative strain fields in heterogeneous MGs at the nanoscale. For this purpose, their structure was changed using controlled deformation or

thermal treatment. It could be shown how heterogeneities influence the nanoscale deformation behavior and thus the overall mechanical properties of heterogeneous MGs. These new findings will improve the understanding of the interplay between structural heterogeneities and carriers of plastic deformation. With these conclusions, our work contributes significantly to the development of new high-performance composite materials.

The authors gratefully acknowledge the financial support from the Austrian Science Fund (FWF): Y1236-N37.

[1] H. Sheng, D. Şopu, S. Fellner, J. Eckert, C. Gammer PHYSICAL REVIEW LETTERS 128 (2022) 245501;

[2] H. Sheng, et al. Materials Research Letters, 9 (2021) 190-195.

MS3.P08
Atomistic insight into the structural differences of the η- and γ-Al_2O_3 and the related catalytically active sites

E. Willinger[1], J. Meyet[2], M. G. Willinger[3], C. Coperet[2]

[1]Technical University of Munich, Physicss, Garching, Germany
[2]ETH Zurich, Department of Chemistry and Applied Biosciences, Zurich, Switzerland
[3]Technical University of Munich, Chemistry, Garching, Germany

Introduction

Transition aluminas, particularly η- and γ-Al_2O_3, are widely used in catalysis due to their high surface area and tunable acidity. While both phases are considered defective spinels, their exact structure and associated different surface properties are still debated. The transformation pathways from oxyhydroxide precursors (bayerite for η and boehmite for γ) significantly influence their microstructure. Consequently, this has a marked effect on the surface atomistic arrangement, which in turn defines the difference in their surface acidity.

Objectives

This study aims to provide an atomistic characterization of η- and γ-Al_2O_3, focusing on their symmetry, long-range and local order, and defect structures. By employing advanced electron microscopy techniques, we reveal the structural differences and investigate how they afffect catalytic properties.

Materials & Methods

High-resolution scanning transmission electron microscopy (HR-STEM), selected area electron diffraction (SAED), electron pair distribution function (ePDF) analysis, and energy-loss spectroscopy (EELS) were used to probe the structural features of η- and γ-Al_2O_3 at the atomic scale.

Results

This study provides direct atomistic insights into the structural differences between η- and γ-Al_2O_3, demonstrating that both phases exhibit orthorhombic rather than cubic symmetry, as evidenced by the distinct point symmetries (2 and 2mm) of their (110) planes. While η-Al_2O_3 possesses a more ordered sublattice of octahedrally coordinated aluminium (AlVI), γ-Al_2O_3 is characterized by significant stacking faults due to antiphase domain boundaries (APBs). Our findings reveals that γ-Al_2O_3 consists of η-phase domains that are interconnected by APBs along the (100) planes. Atomic-resolution imaging reveals that these APBs comprise alternating O-AlVI-O and O-AlVI-O-AlIV atomic rows, with tetrahedrally coordinated aluminium (AlIV) sites exhibiting nearly full occupancy at the APB. These direct-space structural observations are further supported by ePDF and EELS measurements, which confirm that the occupancy of tetrahedral AlIV sites is lower in η-Al_2O_3 than in γ-Al_2O_3.

Regarding the surface termination, we find that γ-Al_2O_3 predominantly exposes (111) and (100) planes, whereas η-Al_2O_3 is mainly terminated by (111) facets and nanosteps. Atomic-resolution ADF-STEM imaging further shows that the (100) surface of γ-Al_2O_3 structurally mirrors its APB boundaries but incorporates pentacoordinated aluminum (AlV) instead of the octahedrally coordinated AlVI. As a result, γ-Al_2O_3 exhibits Lewis acidity due to undercoordinated Al sites on its (100) surfaces, distinguishing it from η-Al_2O_3, which is exclusively (111)-terminated and shows oxygen-rich surfaces with predominant Brønsted acidity.

Conclusion

This study provides direct atomic-scale evidence of structural variations between η- and γ-Al_2O_3, linking precursor transformation mechanisms to long-range, short-range order structures and surface atomistic arrangement. The combination of local analytical STEM investigation and integral characterization (ePDF) add valuable new insights on structures that can not be fully charcterized based on integral methods.

MS 4: Low-dimensional and quantum materials

MS4.01(inv)
Disentangling structural responses in strain-stabilized superconducting thin films

L. Bhatt[1], A. Jiang[2], E. K. Ko[3,4], N. Schnitzer[1], G. Pan[2], D. Ferenc Segedin[2], Y. Liu[3,4], Y. Yu[3,4], E. Abarca Morales[5], C. Brooks[2], H. Hwang[3,4], J. Mundy[2], D. Muller[1], B. Hansen Goodge[5]

[1]Cornell University, Ithaca, NY, United States
[2]Harvard University, Cambridge, MA, United States
[3]SLAC National Accelerator Laboratory, Menlo Park, CA, United States
[4]Stanford University, Stanford, CA, United States
[5]Max Planck Institute for Chemical Physics of Solids, Dresden, Germany

Quantum materials are driven by rich interplay between atomic lattice, orbital, charge, and spin degrees of freedom which give rise to exotic and functional behaviors. This "from the atoms up" framework can be complemented by advanced synthesis and fabrication techniques to manipulate and engineer dimensionality, providing a route to tune materials properties "from the top down". The scanning transmission electron microscope (STEM) is a powerful tool to probe the span both of these fundamental frameworks, probing the relevant order parameters from sub-Angstrom to few-micron length scales.

The 2023 discovery of high-temperature superconductivity in bilayer Ruddlesden-Popper nickelates under high hydrostativ pressure led to an explosion of interest in their subtle structural responses [1], including raising of crystalline symmetry, straightening Ni-O bond angles, and compressed lattice constants. The stabilization of ambient-pressure superconductivity in epitaxially strained thin films of $La_3Ni_2O_7$ [2] provides a unique opportunity for direct investigations of atomic structure in the STEM. We study a series of $La_3Ni_2O_7$ films ranging from compressive to tensile strain and track the impacts on bond lengths, lattice symmetry, and oxygen octahedral distortions [3]. Multislice electron ptychography (MEP) provides access to both heavy ion and oxygen sublattices with unparalleled real-space precision [4].

Ptychographic 4D-STEM datasets are collected on a Thermo Fisher Scientific Spectra 300 X-CFEG at 300 kV equipped with EMPAD-G2 detector [5]. The probe convergence semi-angle is 30 mrad with outer collection angles of ~55 or 66 mrad, step sizes of 0.44 or 0.63 Å, probe overfocus of 5-15 nm, and dwell time of 100 µs per scan position. Iterative phase retrieval is performed using the maximum likelihood algorithm implemented in the fold-slice package [4, 6, 7] with position correction and multiple probe modes [8, 9]. A Bayesian optimization algorithm with data error as the objective function was used to optimize parameters such as defocus, convergence angle, and rotation angle [10]. Final reconstructions are carried out with 8 probe modes and slice thickness of 0.6-0.9 nm.

Compressive epitaxial strain raises the crystalline symmetry and induces oxygen octahedral distortions reminiscent of those reported in bulk crystals under high pressure conditions. While tensile epitaxial strain compresses the *c*-axis bond lengths to values approaching those reported under high pressure, no superconductivity is observed. With multiscale structural and chemical analysis by high-angle annular dark-field (HAADF)-STEM and electron energy loss spectroscopy (EELS), we reveal structural and stoichiometric inhomogeneities which provide insights for ongoing synthesis optimization. Together, these insights also help to guide theoretical understanding of the most relevant tuning parameters and their consequence for electronic properties in novel quantum materials.

1. Sun et al. *Nature* 621, 493–498 (2023).
2. Ko et al. *Nature* 638, 935–940 (2025).
3. Bhatt et al. *arXiv:2501.08204* (2025).

4. Chen et al. *Science* 372, 826 (2021).
5. Philipp et al. *Microsc. Microan.* 28, 425–440 (2022).
6. Thibault and Guizar-Sicairos. *New J. Phys.* 14, 063004 (2012).
7. Wakonig et al. *J. Appl. Cryst.* 53, 574 (2020).
8. Thibault and Menzel. *Nature* 494, 68 (2013).
9. Chen et al. *Nat. Comm.* 11, 2994 (2020).
10. Zhang et al. *Microsc. Microan.* 28, 3146 (2022).

MS4.02
Atomic-scale investigation of reverse phase transition in two-dimensional $Re_{0.5}Mo_{0.5}S_2$

R. Sahu[1], L. M. Brauch[1], A. Ahmadian[1,2], C. Kübel[1,3]

[1]Karlsruhe Institute of Technology, Institute of Nanotechnology, Karlsruhe, Germany
[2]Helmholtz Institute Ulm for Electrochemical Energy Storage, Ulm, Germany
[3]Technical University of Darmstadt, Department of Materials Science, Darmstadt, Germany

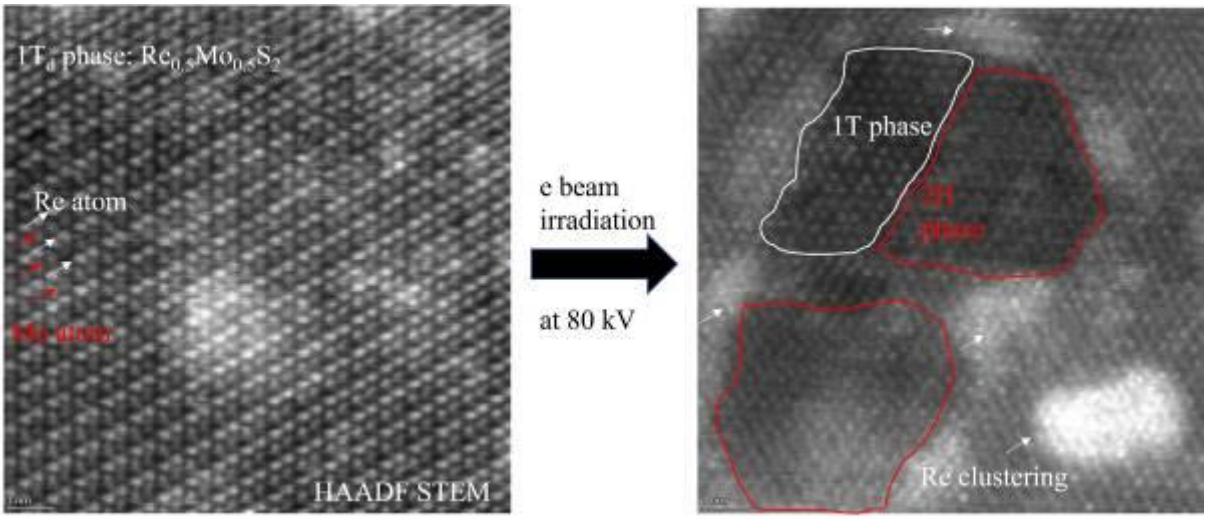
Atomically thin transition metal dichalcogenides (TMDs) are promising candidates for next-generation electronics, energy conversion, and storage applications due to their unique excitonic, spin, and valley properties[1-2]. MoS_2, with a stable 2H structure, has a monolayer band gap of 1.88 eV, while ReS_2 retains a direct band gap even in bulk due to weak interlayer coupling, crystallizing in a $1T_d$ structure with quasi-1D Re_4 clusters and a monolayer band gap of 1.55 eV[3]. The metastable 1T phase of MoS_2 offers metallic properties for carrier transport, stabilized by rhenium doping, while its modulated $1T_d$ phase shows excellent catalytic activity for hydrogen evolution reactions (HER)[4-5]. In its stable $1T_d$ form, MoS_2 adopts a 2a × a superstructure similar to ReS_2, with a band gap of 0.1–0.2 eV. Phase stability between 2H and 1T polytypes in $Re_{0.5}Mo_{0.5}S_2$ depends on local Re concentration, while spontaneous or externally induced 1T-to-2H transitions significantly impact physicochemical properties. However, atomic-scale insights into these phase modulations, particularly the role of local strain at interfaces, remain limited.

In this study, we investigate phase modulations of $Re_{0.5}Mo_{0.5}S_2$ under electron beam irradiation using in situ scanning transmission electron microscopy (STEM) experiment. We focus on the stability of the metallic (1T) and semi-metallic ($1T_d$) phases and elucidate the mechanism of the reverse phase transition (1T to 2H), predicted to occur via sulfur (S) plane gliding based on density functional theory (DFT) calculations. The phase, orientation and strain mapping were performed using 4D-STEM to capture local structural variations at the atomic scale. $Re_{0.5}Mo_{0.5}S_2$ alloys, consisting of mixed 1T and $1T_d$ phases, were synthesized using a solid-state reaction route[4]. Monolayer to few-layer flakes were obtained via probe sonication from the bulk material. In situ STEM experiments of electron beam induced phase transformation were conducted using a Thermo Fisher probe-corrected Titan ThemisZ operated at 80 kV. A convergence semi-angle of 23.8 mrad and a collection angle range of 78–200 mrad were used for high angle annular dark filed (HAADF) STEM imaging, with a beam current of 40 pA. The scan area was 1024 × 1024 pixels with a dwell time of 1µs. The 4D-STEM experiment was performed using a Nanomegas ASTAR system at 80 kV. Our findings reveal that under electron beam irradiation, Re clustering leads to sulfur plane gliding, facilitating the reverse phase transition from the metallic or semi-metallic phases to the 2H phase. Additionally, 4D-STEM analysis provides phase-specific orientation and strain distributions, offering deeper insights into the structural evolution and stability of these 2D materials. These results contribute to a better understanding of phase transformations in TMD alloys, which is critical for their application in electronic and energy-related technologies.

Figure 1: Phase modulation of $Re_{0.5}Mo_{0.5}S_2$ under electron beam irradiation at 80 kV accelerating voltage.

1. *Nat. Rev. Maters., 2017, 2, 17033*
2. *Energy Environ. Sci., 2020,13, 2684-2740*
3. *J. Appl. Phys., 2016, 119, 114309*
4. *J. Appl. Phys., 2017,121, 105101*
5. *Adv. Funct. Mater., 2024, 35, 2413720*

Fig. 1


1T$_d$ phase: $Re_{0.5}Mo_{0.5}S_2$
Re atom
Mo atom
HAADF STEM
e beam
irradiation
at 80 kV
1T phase
2H
phase
Re clustering

MS4.03
Nanobeam ultrafast electron diffraction of structural phase transformations in charge-density wave materials

T. Domröse[1], S. F. Schaible[1,2], C. Ropers[1,2]

[1]Max Planck Institute for Multidisciplinary Sciences, Department of Ultrafast Dynamics, Göttingen, Germany
[2]Georg-August-Universität Göttingen, 4th Physical Institute - Solids and Nanostructures, Göttingen, Germany

Introduction

Optical control over charge-ordered phases promises the tuning of macroscopic properties of quantum materials and the realization of metastable states. In many transition metal dichalcogenides (TMDCs), strong electron-phonon coupling favors the formation of charge-density waves (CDWs) [1]. Pulsed laser excitation has been shown to efficiently suppress this additional superperiodicity or induce transitions between different phases. The periodic lattice distortion (PLD) accompanying CDW formation is accessible in ultrafast electron diffraction (UED) and microscopy, elucidating the femtosecond evolution of lattice symmetries and phonon populations in laser-pump/electron-probe measurements [2].

Objectives

Here, we combine methodological advances in nanobeam UED with investigations of non-equilibrium structural dynamics in TMDC thin films. We characterize the photosensitivity of PLD phases, quantify transformation times and pathways on femtosecond time scales, and resolve transient PLD disorder.

Materials & methods

Our experiments are carried out in an ultrafast transmission electron microscope equipped with a field emission electron gun [3]. Photoemitting ultrashort electron pulses from this nanometric source yields high momentum resolution in collimated electron nanobeams. Thermally-optimized sample support structures enable reversible cycling of structural dynamics at unprecedented megahertz repetition rates [4]. The associated gain in coherent electron probe current enables tracing of optically-induced CDW transformations in 2*H*-$NbSe_2$, 1*T*″-$TaTe_2$, 1*T*-$TaSe_2$, and 1*T*-TaS_2.

Results

2*H*-$NbSe_2$ forms an incommensurate (IC) CDW phase below 33 K, recognizable by the appearance of additional CDW diffraction spots. In thermal equilibrium, increasing the laser excitation density leads to gradual spot suppression, and to the population of distinct phonon modes. On ultrafast time scales, the IC periodicities are rapidly melted within 1 ps. Similarly, in 1*T*″-$TaTe_2$, one-dimensional cooperative atomic motions completed after 500 fs connect the low-temperature 3x3 and the room-temperature 3x1 PLD [5]. We contrast this transition between two mutually commensurate structures with the emergence of incommensurate superperiodicities in 1*T*-$TaSe_2$ and 1*T*-TaS_2 after a strong optical quench, finding transient disorder encoded in characteristic three-dimensional CDW diffraction spot broadening. For 1*T*-TaS_2 in particular, we tomographically map out the generation and subsequent recombination of topological point defects, i.e., CDW dislocations, uncovering a transient dimensional crossover and a light-induced hexatic state within the first 10 ps of the dynamics [6].

Conclusion

All in all, nanobeam UED at megahertz repetition rates provides insights into non-equilibrium structural dynamics, exploring phase transformations in CDW materials. In the future, we expect the combination

of nanoscale probing, high-repetition-rate driving, and the versatility of ultrafast electron microscopy to widen the understanding of such processes in a broad range of compounds, heterostructures and functional devices.

References

1. K. Rossnagel, J. Condens. Matter Phys. **23(21)** 213001 (2011)
2. D. Filippetto, *et al.*, Rev. Mod. Phys. **94(4)** 045004 (2022)
3. A. Feist, *et al*. Ultramicroscopy **176** 63-73 (2017)
4. T. Domröse, *et al.*, arXiv:2410.02310 (2024)
5. T. Domröse, C. Ropers, PRB **110(8)** 085155 (2024)
6. T. Domröse, *et al.*, Nat. Mater. **22(11)** 1345-1351 (2023)

MS4.04
The added value of combining real and reciprocal space characterizations – Magnetic fans in a chiral magnet

M. Winter[1,2], A. Pignedoli[3], M. C. Rahn[4], A. Sukhanov[4], A. Tahn[1], S. Schneider[1], D. Pohl[1], M. Azhar[3], K. Everschor-Sitte[3], J. Geck[4], G. von der Laan[5], T. Hesjedal[6,5], P. Vir[2], C. Felser[2], B. Rellinghaus[1]

[1]Technical University Dresden, Dresden Center for Nanoanalysis (DCN), Dresden, Germany
[2]Max Planck Institute for Chemical Physics of Solids, Dresden, Germany
[3]University Duisburg-Essen, Faculty of Physics and Center for Nanointegration Duisburg-Essen, Duisburg, Germany
[4]Technical University Dresden, Institute for Solid State and Materials Physics, Dresden, Germany
[5]Diamond Light Source, Harwell Science and Innovation Campus, Didcot, United Kingdom
[6]University of Oxford, Department of Physics, Oxford, United Kingdom

1. Introduction

The Heusler compound $Mn_{1.4}PtSn$ is a chiral magnet with non-topological and topologically protected magnetic textures at room temperature [1-3] and well suited to study field-driven transformations between these states. Lorentz transmission electron microscopy (LTEM), resonant elastic X-ray scattering (REXS), and micromagnetic simulations are used to characterize in-situ the magnetic structures as function of external magnetic fields. A subtle interplay between perpendicularly oriented chiral soliton lattices (CSLs) and magnetic fan domains is found to lead to the nucleation of non-topological magnetic bubbles by providing the right and left-handed chiral "ingredients" to their texture and thus allows to unveil the mechanism of formation of anti-skyrmion lattices.

2. Objectives

While the various magnetic textures emerging in chiral magnets are usually well established, in-depth understanding of the kinetic pathways that render transitions specifically between non-topological and topologically protected states is often lacking. The latter are investigated here, and the role of intermediate magnetic fan states for such transitions is highlighted.

3. Materials & methods

$Mn_{1.4}PtSn$ single crystals were grown by the self-flux method [1]. A thin lamella with a c-axis surface normal was cut from it by focused ion-beam milling. Complementary LTEM and REXS were used to characterize the magnetic textures of one and the same sample in real and reciprocal space, respectively.

4. Results

The REXS patterns displayed in Fig. 1 reveal how upon increasing the in-plane magnetic field, one of two variants of a chiral soliton lattice with 180° domain walls (π-CSLs, not shown here) - the magnetic ground state in zero field - vanishes. The remaining periodic magnetic structure is periodic in a direction perpendicular to the applied field and thus defavors a CSL comprised of domains of alternatingly opposite spin direction energetically. Profiles of the in-plane magnetic induction obtained from TIE reconstructions [4] of LTEM images supported by micromagnetic simulations (Fig. 2) allow to solve this puzzle and reveal the fan-type nature of this field-induced magnetic state (cf. Fig. 3). The latter can be shown to be most essential for overcoming the topological barrier towards forming anti-skyrmions in $Mn_{1.4}PtSn$.

5. Conclusion

The combination of real-space LTEM and reciprocal-space REXS is shown to be essential for unveiling the nature of the transition between non-topological and topologically protected states in the chiral magnet $Mn_{1.4}PtSn$.

Financial support by MPG through IMPRS-CPQM and DFG through SPP 2137, project 403503416, is gratefully acknowledged.

[1] A.K. Nayak et al., Nature (2017). DOI: 10.1038/nature23466

[2] P. Vir et al., Chem. Mater. (2019). DOI: 10.1021/acs.chemmater.9b02013

[3] M. Winter et al., Comms. Mater, (2022). DOI: 10.1038/s43246-022-00323-6

[4] C. Zuo et al., Opt. Laser Eng. (2020). DOI: 10.1016/j.optlaseng.2020.106187

Fig 1. REXS measurements on a $Mn_{1.4}PtSn$ lamella as function of an in-plane field parallel to the a-axis. (a, b) Mixed state of π-CSLs aligned along the a and b axes at 0 mT and 150 mT and (c,d) of a single domain state above 250 mT.

Fig 2. (a) LTEM image of the lamella tilted by 30° in a magnetic field of 200 mT. In-plane magnetic induction as (b) deduced by TIE reconstruction and (c) obtained from micromagnetic simulation.

Fig 3. Model spin texture of the magnetic fan from micromagnetic simulations.

Fig. 1

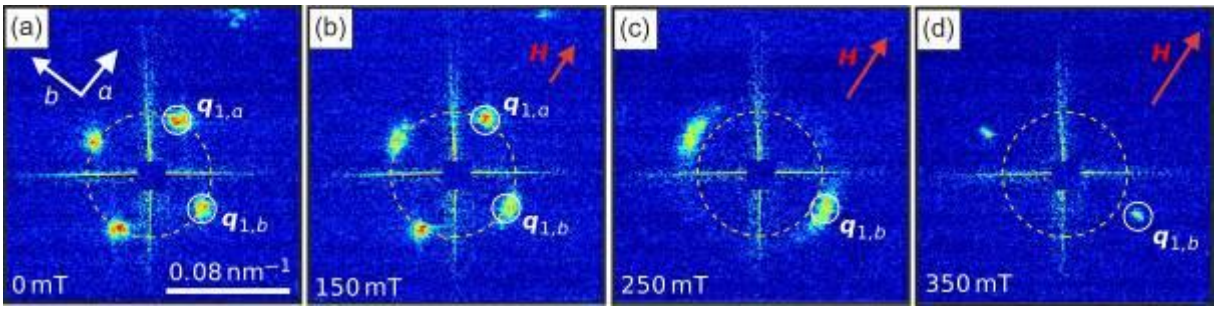


Fig. 2

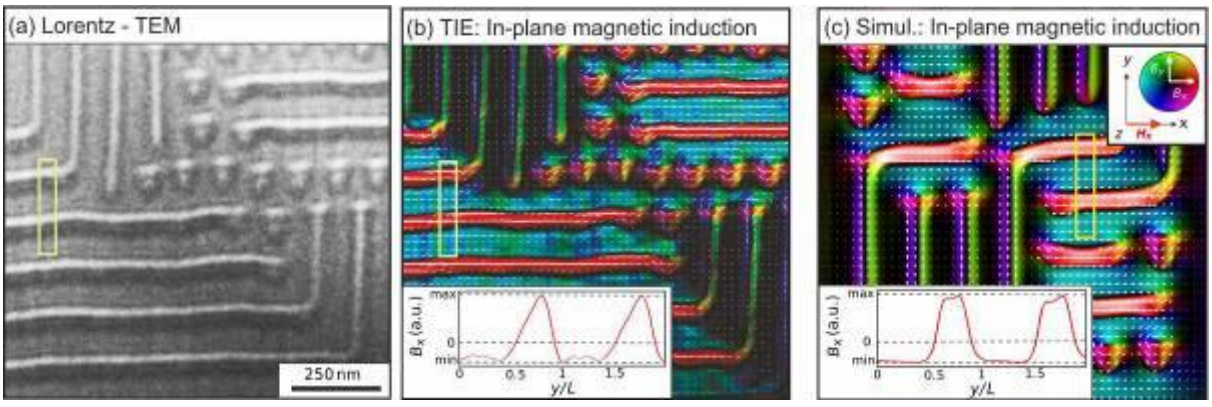
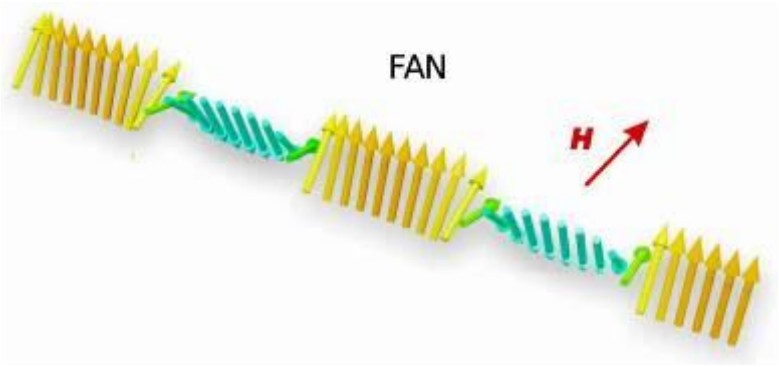


Fig. 3



MS4.05
High-resolution electron microscopy for the design and scalability of neuromorphic quantum photonics

S. Taheriniya[1], R. Xu[1], A. Varri[2], R. Bankwitz[1], S. Jo[2], R. R. Schröder[3], W. Pernice[1,2]

[1]Heidelberg University, Kirchhoff-Institute for Physics, Heidelberg, Germany
[2]University of Münster, Institute of Materials Physics, Münster, Germany
[3]Heidelberg University, BioQuant, Heidelberg, Germany

Future technology is being defined by breakthroughs around the concept of neuromorphic quantum photonics, where high-speed, low-power, and highly scalable platforms are set to revolutionize computing, communication, and information processing1–3. At the heart of these advancements lies the precise design and fabrication of integrated photonic structures, which must be engineered with nanometer-scale accuracy to ensure optimal performance4–6. To seamlessly transition from theoretical designs to real-world implementation, it is essential to ensure that fabricated devices precisely match their intended properties. Even minor deviations in design can significantly impact light-matter interactions, which are critical for the performance and reliability of quantum applications. This is where high-resolution characterization techniques, particularly Scanning/Transmission Electron Microscopy (S/TEM), play a transformative role by providing sub-nanometer insights into material properties, interface quality, and fabrication-induced imperfections. Incorporating S/TEM-based analysis into fabrication establishes a feedback loop that automates manufacturing, enables post-fabrication tuning, and optimizes material processing, ensuring scalable, stable, and high-performance photonic platforms for quantum applications. This work presents a systematic approach to photonic device analysis, emphasizing optimized sample preparation using Focused Ion Beam (FIB) milling with minimized artifacts for high-resolution imaging, spectroscopy (EDS, EELS), phase mapping, and microstructural analysis4,6,7. Applied across a diverse range of integrated photonic platforms, this methodology enhances fabrication precision, enabling highly tunable device properties. Additionally, it refines simulation parameters, paving the way for scalable solutions and models tailored for real-world applications.

(1) Ashtiani, F.; Geers, A. J.; Aflatouni, F. An On-Chip Photonic Deep Neural Network for Image Classification. *Nature* **2022**, *606* (7914), 501–506.

(2) Mehonic, A.; Kenyon, A. J. Brain-Inspired Computing Needs a Master Plan. *Nature* **2022**, *604* (7905), 255–260.

(3) Bai, Y.; Xu, X.; Tan, M.; Sun, Y.; Li, Y.; Wu, J.; Morandotti, R.; Mitchell, A.; Xu, K.; Moss, D. J. Photonic Multiplexing Techniques for Neuromorphic Computing. *Nanophotonics* **2023**, *12* (5), 795–817.

(4) Varri, A.; Taheriniya, S.; Brückerhoff-Plückelmann, F.; Bente, I.; Farmakidis, N.; Bernhardt, D.; Rösner, H.; Kruth, M.; Nadzeyka, A.; Richter, T.; Wright, C. D.; Bhaskaran, H.; Wilde, G.; Pernice, W. H. P. Scalable Non-Volatile Tuning of Photonic Computational Memories by Automated Silicon Ion Implantation. *Adv. Mater.* **2024**, *36* (8), 2310596.

(5) Brückerhoff-Plückelmann, F.; Feldmann, J.; Gehring, H.; Zhou, W.; Wright, C. D.; Bhaskaran, H.; Pernice, W. Broadband Photonic Tensor Core with Integrated Ultra-Low Crosstalk Wavelength Multiplexers. *Nanophotonics* **2022**, *11* (17), 4063–4072.

(6) Xu, R.; Taheriniya, S.; Varri, A.; Ulanov, M.; Konyshev, I.; Krämer, L.; McRae, L.; Ebert, F. L.; Bankwitz, J. R.; Ma, X.; Ferrari, S.; Bhaskaran, H.; Pernice, W. H. P. Mode Conversion Trimming in Asymmetric Directional Couplers Enabled by Silicon Ion Implantation. *Nano Lett.* **2024**, *24* (35), 10813–10819.

(7) S. Taheriniya; A. Varri; S. Jo; F. Lenzini; W. Pernice. Exploring Novel Photonic Platforms for Quantum Computing through Si Ion Implantation. In *2024 24th International Conference on Transparent Optical Networks (ICTON)*; 2024; pp 1–4.

MS4.06(inv)
Spin resonance spectroscopy with a transmission electron microscope

P. Haslinger[1]

[1]Technical University of Vienna, Atominstitut - USTEM, Vienna, Austria

- **Introduction**

Coherent spin resonance methods such as nuclear magnetic resonance and electron spin resonance spectroscopy have led to spectrally highly sensitive, non-invasive quantum imaging techniques. However, despite their spectral sensitivity, these techniques are limited in spatial resolution.

- **Objectives & methods**

Here, I will present a spin resonance spectroscopy approach developed for transmission electron microscopy [1,2] and will explain different techniques to sense with electrons for microwave manipulated spin states of the sample. Our approach utilizes microwave excitation at GHz frequencies, while employing the free-space electron beam as a signal receiver to sense spin precession [1]. Spin state polarization is achieved via the magnetic field of the TEM's polepiece, while a custom-designed microresonator (microwave antenna) integrated into a TEM sample holder drives spin transitions [2].

- **Results and Conclusion**

This could enable state-selective observation of spin dynamics on the nanoscale and indirect measurement of the environment of the spin systems, providing information on, for example, atomic structure, local chemical composition and neighbouring spins.

[1] P. Haslinger, S. Nimmrichter, and D. Rätzel, *Spin Resonance Spectroscopy with an Electron Microscope*, Quantum Sci. Technol. **9**, 035051 (2024).

[2] A. Jaroš, J. Toyfl, A. Pupić, B. Czasch, G. Boero, I. C. Bicket, and P. Haslinger, *Electron Spin Resonance Spectroscopy in a Transmission Electron Microscope*, arXiv:2408.16492 1 (2024).

MS4.P01
Characterization of bismuth plasmonic antennas by STEM-EELS

M. Foltýn[1], M. Horák[1]

[1]Brno University of Technology, Brno, Czech Republic

Although gold-based plasmonic applications show great potential, their widespread use is hindered by high fabrication costs and the limited plasmon energy range imposed by band transitions. These challenges could be addressed by the use of alternative metals such as bismuth, lead, and tin, which have been theoretically predicted to provide comparable plasmonic performance while offering broader plasmon energy ranges [1], [2].

The current studies on nanostructured non-noble metals are largely limited to optical spectroscopy of large ensembles of nanostructures. As a result, a direct correlation between plasmon energy and nanostructure size—crucial for evaluating their application potential—remains unexplored. In this work, we experimentally assess the plasmonic properties of bismuth plasmonic antennas using STEM-EELS and evaluate their feasibility as a gold substitute.

To investigate the plasmonic potential of bismuth, we sputtered polycrystalline thin bismuth films onto SiN_x substrates and fabricated bowtie- and bar-shaped plasmonic antennas of varying sizes using focused ion beam lithography [3], [4]. The plasmonic response of individual antennas was then characterized by STEM-EELS [5].

Although the fabricated bismuth antennas exhibit lower plasmon resonance intensity than gold ones, the nearly identical plasmon energies across the entire range of tested antenna sizes demonstrate bismuth"s potential as a viable alternative in plasmonic applications. Moreover, the experimentally verified wider interval of bismuth plasmon energies allows applications at shorter wavelengths as well.

The validated plasmonic performance of bismuth antennas highlights their potential as a viable substitute for gold. While their plasmon resonance intensity is lower, the broader plasmon energy range and comparable plasmon energies compensate for this drawback—particularly given bismuth"s significantly lower cost.

Figure 1: Dependence of the plasmon resonant modes' energy on the reciprocal antenna width for bismuth and gold antennas. Based on the observed overlap of the two dependencies, bismuth can serve as a cheaper plasmonic alternative to gold. The data for gold bowtie antennas were taken from [6].

References:

[1] McMahon, J. et al. Phys. Chem. Chem. Phys. 2013,15(15), p. 5415-5423 https://doi.org/10.1039/C3CP43856B

[2] Sanz, J. M., et al. The Journal of Physical Chemistry C. 2013, 117(38), p. 19606-19615. https://doi.org/10.1021/jp405773p

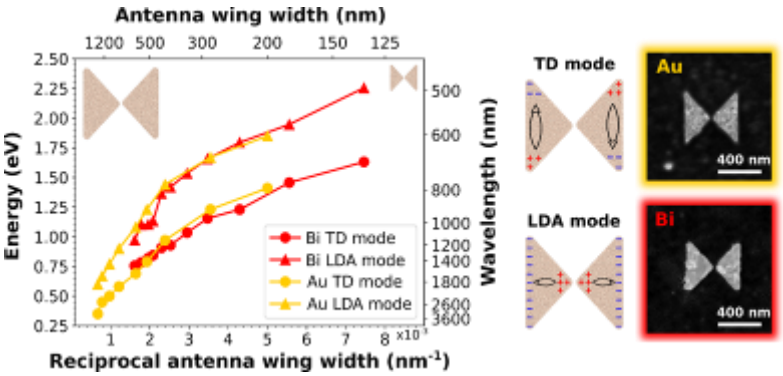
[3] Horák, M., et al. Scientific Reports. 2018, 8(1), 9640. https://doi.org/10.1038/s41598-018-28037-1

[4] Foltýn, M., et al. ACS Omega. 2024, 9(35), p. 37408-37416. https://doi.org/10.1021/acsomega.4c06598

[5] Horák, M., Šikola, T. Ultramicroscopy. 2020, 216, p. 113044. https://doi.org/10.1016/j.ultramic.2020.113044

[6] Křápek, V., et al. Nanophotonics. 2019, 9(3), p. 623-632. https://doi.org/10.1515/nanoph-2019-0326

Fig. 1



MS4.P02
Investigating nitrogen doped nanocarbon materials as potential carbon dioxide adsorbers

I. Musil[1,2], L. Rieger[1], V. Kannan[1], M. Kögel[2], J. C. Meyer[1,2]

[1]University of Tübingen, University of Tübingen, Tübingen, Germany
[2]NMI Natural and Medical Sciences Institute at the University of Tübingen, Reutlingen, Germany

The climate crisis, propelled by the continuous rise of CO_2 emissions, has spurred research to find technical solutions for this problem. One possibility is to directly capture CO_2 from the atmosphere via an adsorber and sequester it inside a suitable long-term storage. Naturally, high efficiency of the adsorber material is needed, which could be offered by nanocarbon materials such as graphene and carbon nanotubes due to their high surface area and stability. However, the catch is their unreactive nature. To enhance adsorption one could alter the chemical structure of the nanocarbons by inserting new elements through doping. Nitrogen is a promising candidate, as it can be exchanged with the carbon atoms inside the crystal lattice of the materials. It is known to be a crucial component in other CO_2 fixating mechanisms. One goal of this research is to find novel routes for nitrogen doping of these materials and try to understand and control the process of ion implantation. Another aim is to create an efficient CO_2 adsorber out of these materials.

Doping with nitrogen is realized by different methods of ion bombardment, like pure ion beam exposure, RF or DC plasma. An example of simple doping via DC plasma is shown in Fig. 1, where nitrogen plasma is created via arc discharge with the sample on top of the cathode. Graphene is used as a basic model and analysed via HRTEM combined with image simulation, allowing to gain in-depth knowledge about the nitrogen doping process. To investigate the potential for CO_2 adsorption, various kinds of carbon nanotube films (also called buckypaper) are produced, which are then doped with nitrogen afterwards. As this leads to quite complex structures, diverse analytical methods like HRTEM, SEM-FIB coupled with ToF-SIMS, EDX, AFM and XPS are used to study these samples. Finally, the nitrogen doped carbon nanotube films are evaluated for their performance as CO_2 adsorbers. For this purpose an experimental setup was built, which is able to simulate a large number of adsorption and desorption cycles, while simultaneously monitoring the amount and type of gaseous species being released from the sample. Through HRTEM it was found that all applied ion bombardment methods produced nitrogen doped graphene and rough estimates of doping levels were made. These doping techniques were successfully transferred to the carbon nanotube systems, confirming amount and depth of nitrogen doping via ToF-SIMS, EDX and XPS (example shown in Fig. 3). The evaluation of the CO_2 adsorption performance showed that nitrogen doping increases the capturing efficiency of the materials. Fig. 3 shows how the amount of extracted CO_2 differs between a doped and undoped sample when applying heat to the sample after adsorption (at 220 s).

This research shows how different and also simple methods can be used to dope nanocarbons with nitrogen. Through doping the materials CO_2 adsorption efficiency can be enhanced, offering new opportunities for mitigating climate change via CO_2 capturing.

Fig. 1

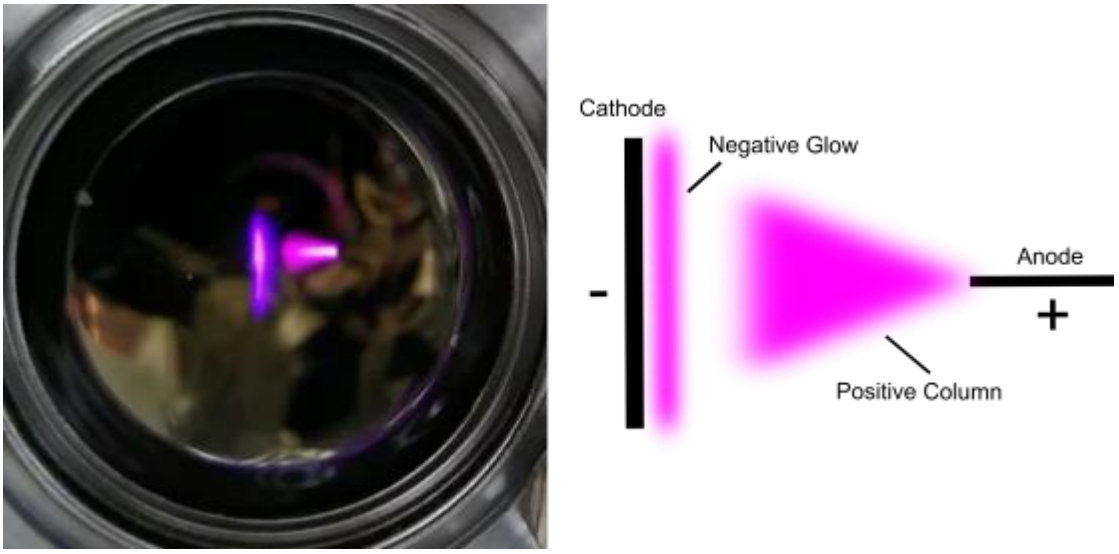

Cathode
Negative Glow
Anode
-
+
Positive Column

Fig. 2

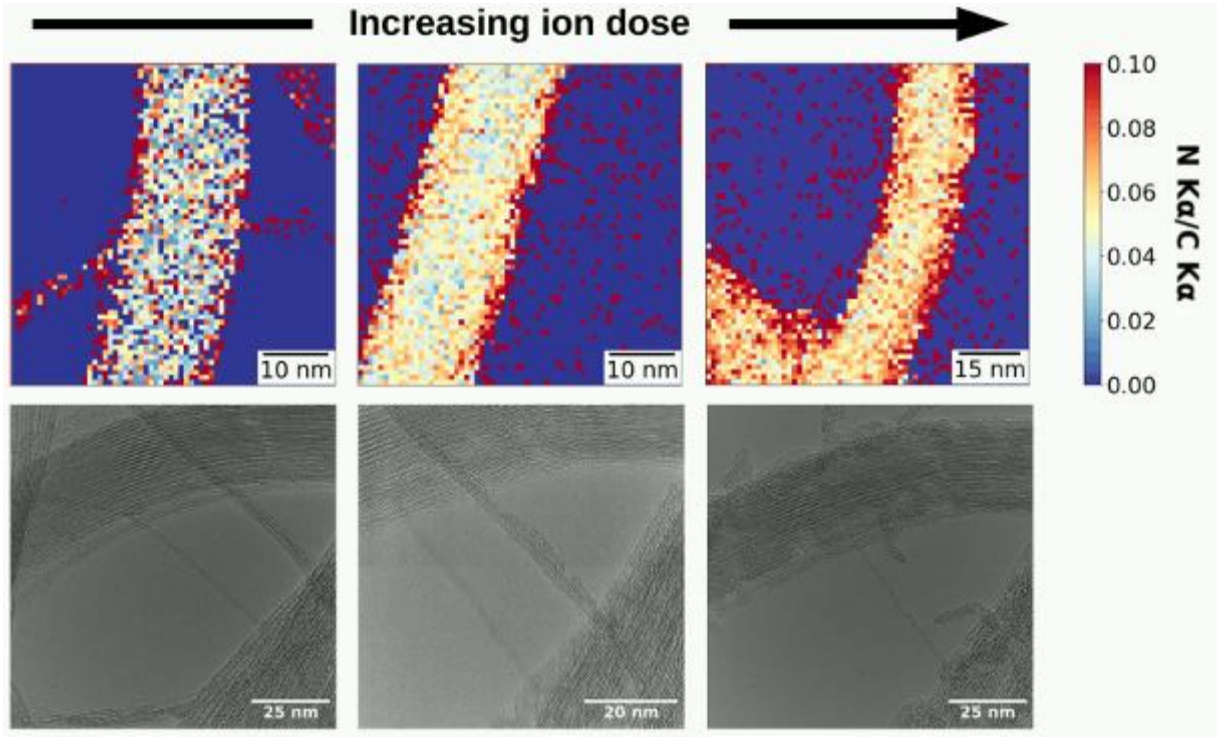
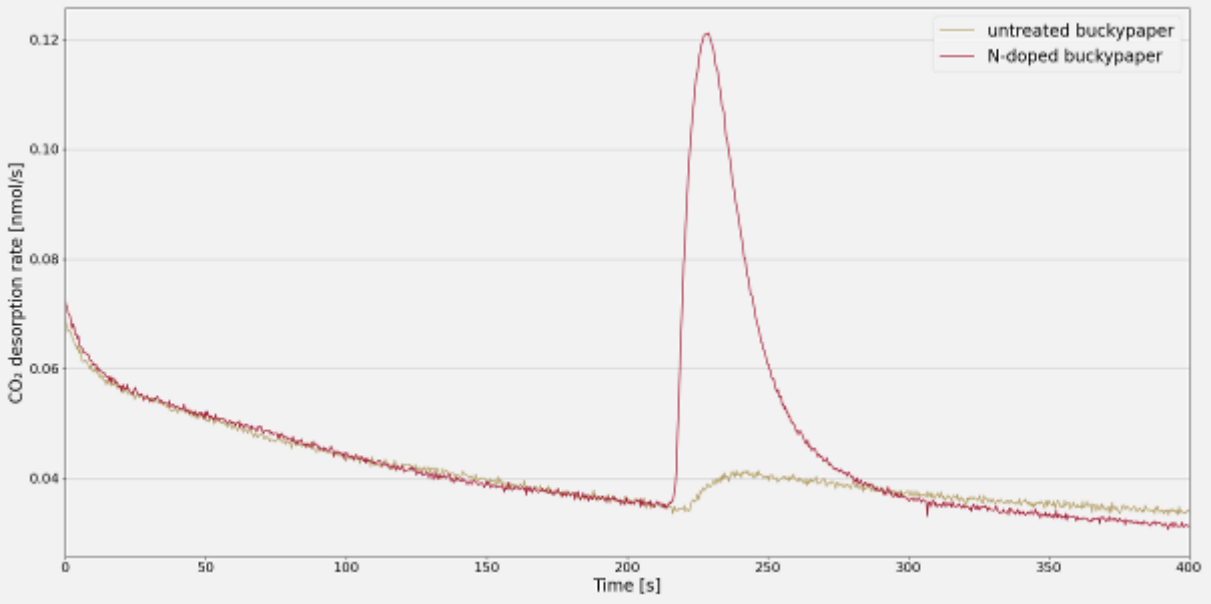

Increasing ion dose
10 nm
10 nm
15 nm
25 nm
20 nm
25 nm
0.10
0.08
0.06
0.04
0.02
0.00
N Kα/C Kα

Fig. 3


untreated buckypaper
N-doped buckypaper
0.12
0.10
0.08
0.06
0.04
CO2 desorption rate [nmol/s]
0
50
100
150
200
250
300
350
400
Time [s]

MS4.P03
High quality graphene TEM supports for *in situ* gas transmission electron microscopy

J. Verstraelen[1], N. Claes[1], M. Tang[1], S. Bals[1]

[1]University of Antwerp, Physics, Antwerp, Belgium

Introduction

Transmission electron microscopy (TEM) plays a critical role in the investigation of the atomic structure, morphology and chemical composition of nanomaterials. The field has significantly evolved during the last decade through the implementation of improved aberration correctors, novel detectors and the implementation of many new low dose techniques. However, further progress in spatial resolution and contrast can still be achieved with improvements in sample preparation, particularly from the optimization of the TEM sample support.

The ideal sample support would be as thin and clean as possible in order to avoid interference with the sample signal, resulting in background noise and a reduction of the contrast in the final (S)TEM image. Graphene-based TEM grids have recently appeared as a promising alternative to the regular carbon coated TEM grids. Graphene, a monolayer of tightly bound carbon atoms, possesses exceptional properties. The monoatomic thickness of graphene minimizes the background signal, significantly improving signal to noise ratio which is crucial for high resolution imaging. One area in which the graphene substrates would be highly beneficial is in in-situ gas TEM. Here, a sealed gas cell is made by closing two chips with electron "transparent" Si3N4 windows of ~50nm each. This adds around 100nm of sample substrate that significantly reduces the signal to noise ratio during experiments. Partially replacing both Si3N4 windows with graphene would reduce the thickness of the substrate with a factor 100.

However, applying suspended graphene on in-situ chips is challenging. Firstly, the graphene should remain structurally intact during the transfer to the Si3N4 windows, so that the gas-cell can be sealed. Secondly, the newly applied graphene windows on the top and bottom chips should align, so that the electron beam only travels through the graphene and avoids the Si3N4 on the top or bottom window.

Objectives

In this research, we drill holes in the Si3N4 windows of in-situ gas chips and reseal them with a graphene layer. We established a pattern that guarantees the alignment of the graphene windows and verified the improvement in contrast during an in-situ gas experiment.

Materials & methods

We modified the Si3N4 windows with focused ion beam milling. Afterwards, we transfered graphene on top of the holes, using an in house graphene wet transfer method and verified the quality with scanning electron microscopy. Utilizing TEM, we evaluated the improved contrast of the graphene gas-cell during an in-situ experiment.

Results

Preliminary results show that we can fabricate a closed graphene gas cell that retains H2 gas for several hours, facilitating an in-situ experiment on Pt nanoparticles. The increased signal to noise ratio on the graphene drastically reduces the electron dose necessary for quantification during in-situ experiments.

Conclusion

Current TEM in-situ devices contain relatively thick Si3N4 windows that severely limit the capabilities of these devices. We partially replaced the Si3N4 windows of in-situ gas chips with graphene, drastically improving the image quality and unlocking previously unfeasible in-situ experiments.

Reference:

[1] The authors acknowledge financial support by the ERC (Hypergraph - 101059468)

MS4.P04
Capturing *in situ* atomic scale insights into the growth of CdS quantum dots in aqueous environment

D. Keller[1], W. Dachraoui[1], R. Butti[1], R. Erni[1]

[1]EMPA - Swiss Federal Laboratories for Materials Science and Technology, Electron Microscopy Center, Dübendorf, Switzerland

CdS quantum dots (QDs) have gained great popularity in a wide range of technological fields such as electronic and biomedical applications. While the size-dependency and tunability of these QDs' optoelectronic properties bear an enormous potential for the design of complex QDs with new, specific properties, fundamental knowledge on how their formation can be manipulated is still limited. In order to design more systematic, efficient, and controllable fabrication processes in the future, an in-depth understanding of QD formation by wet chemistry processes is urgently required [1].

In situ liquid-phase transmission electron microscopy (LP-TEM) is a powerful tool to investigate the atomic QD formation processes in liquid environments. However, the highly reactive oxidative species created by radiolysis of water under electron beam irradiation etch CdS QDs during STEM analyses, and hamper the direct observation of CdS formation [2]. So far, several studies have reported and investigated CdS etching processes *in situ* in the TEM, while *in situ* triggering of CdS formation processes in contrast remains challenging [3,4].

Here, by tuning the chemical environment towards less acidic and less oxidative *in situ* conditions, we are able to enhance the stability of CdS crystals in aqueous solution under electron beam irradiation, and to provoke CdS nucleation and growth reactions *in situ*. Using thin graphene liquid cells (GLCs), allows us for observing at atomic scale the formation of CdS crystals by HAADF-STEM (Fig. 1).

The nucleation and growth of CdS QDs from two different precursor solutions (cadmium acetate and (a) thiourea resp. (b) thioacetamide) under electron irradiation, tracked by HAADF-STEM time series, is shown in Fig. 2a and b. The colored insets in (c) show individual CdS crystals of Fig. 2b at higher magnifications. Furthermore, we performed analytical and structural analyses of the CdS particles. Fig. 3a shows a *post mortem* EDS analysis of CdS particles previously formed *in situ*, and the fast Fourier transform (FFT) of a HAADF-STEM image of CdS QDs further confirms the presence of Wurtzite CdS QDs (Fig. 3b).

We here propose conditions that allow for growing and observing CdS QDs *in situ* under electron beam irradiation. Our results provide insights into the formation processes of CdS particles at the atomic scale, which is crucial to understand, control, and design new CdS synthesis reactions in the future. Furthermore, our studies demonstrate how an optimal design of the liquid environment can improve the stability of sensitive and complex QDs.

Figure Captions:

Figure 1: Experimental setup: Graphene liquid cell encapsulating an aqueous solution wherein the growth of CdS QDs is tracked *in situ* by HAADF-STEM.

Figure 2: *In situ* growth of CdS QDs in aqueous solution recorded by HAADF-STEM time series.

Figure 3: a) HAADF-STEM image of CdS QDs, with insets showing EDS Cd- and S-signal intensities within the indicated area. b) HAADF-STEM image of CdS crystals, with the corresponding FFT in the insets showing typical reflections of Wurtzite CdS.

References

1. 1. V. Lahariya et al., in *Quantum Dots*, N. Thejo Kalyani et al., Eds. (Woodhead Publishing, 2023), p. 235-266, DOI: 10.1016/B978-0-323-85278-4.00018-0.

2. J. Woehl, P. Abellan, J. Microsc. 265, 135 (2017).

3. C. Yan et al., Sci Adv. 8, eabq1700 (2022).

4. Y. Wu et al., New J. Chem. 43, 12548 (2019).

Fig. 1

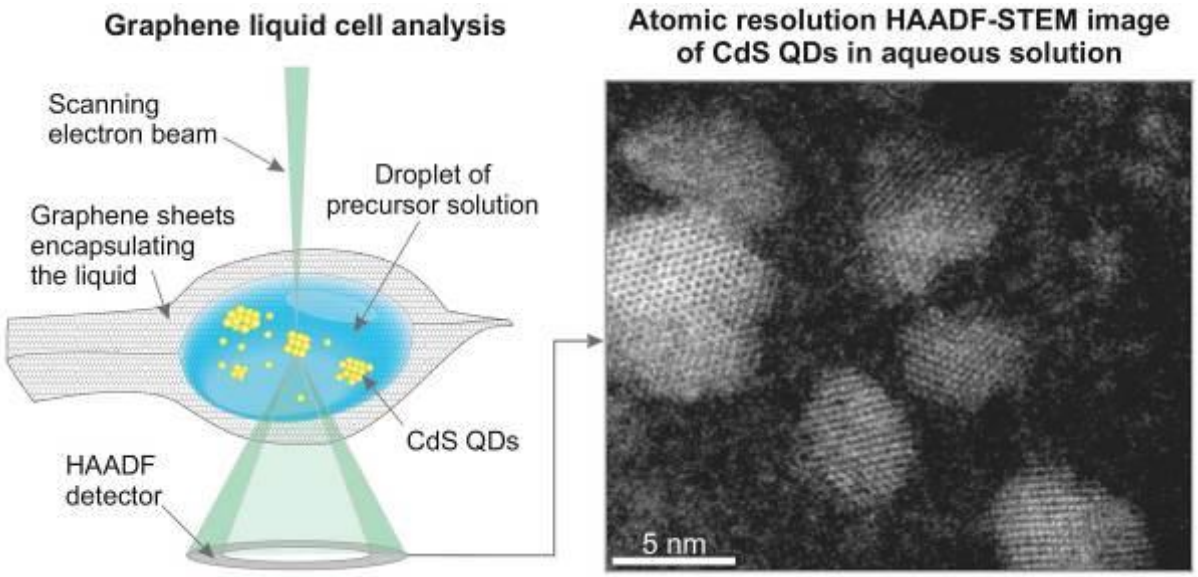


Fig. 2

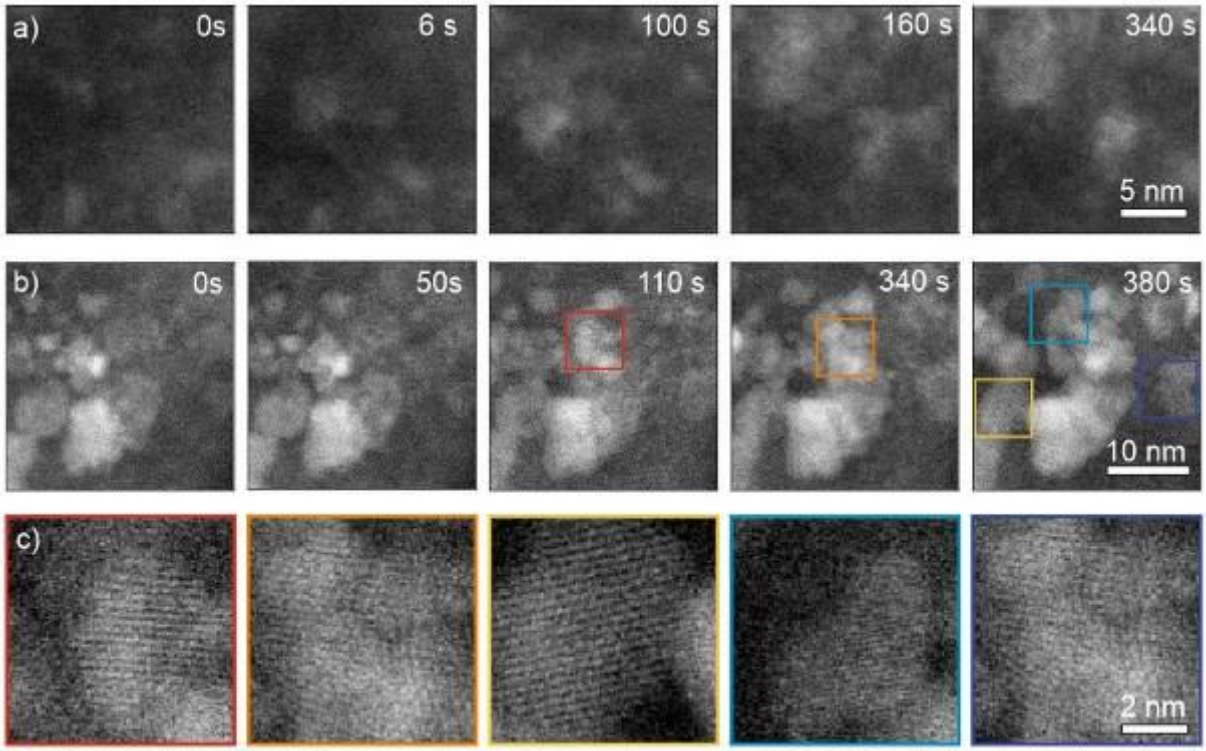
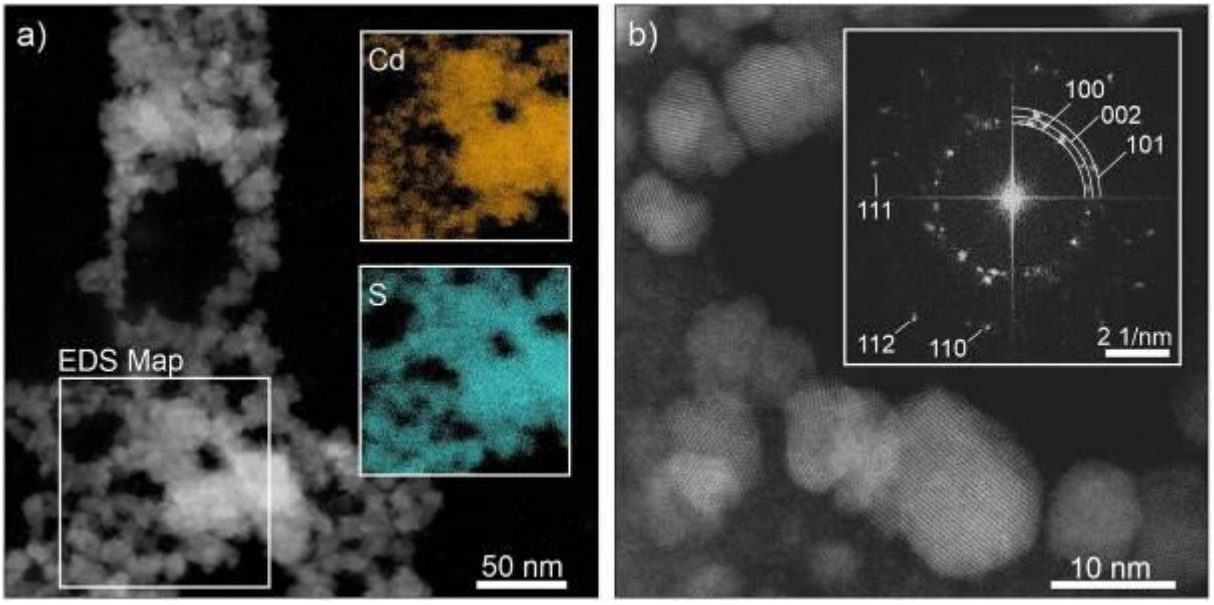

a)
0s
6 s
100 s
160 s
340 s
5 nm
b)
0s
50s
110 s
340 s
380 s
10 nm
c)
2 nm

Fig. 3


a)
Cd
S
EDS Map
50 nm
b)
100
002
101
111
112
110
2 1/nm
10 nm

MS4.P05
Symmetry-forbidden oxide interfaces with moiré-type reconstruction

H. Wang[1], V. Harbola[1], Y. J. Wu[1], P. A. van Aken[1], J. Mannhart[1]

[1]Max Planck Institute for Solid State Research, Stuttgart, Germany

Interfaces in oxide heterostructures often exhibit emergent electronic properties that are absent in their bulk counterparts [1, 2]. Traditionally, epitaxial growth has been the predominant method for fabricating high-quality interfaces in three-dimensional (3D) materials. However, this approach is fundamentally constrained by the need for lattice and symmetry compatibility. Recent advances in the fabrication of freestanding membranes of 3D materials provide an opportunity to overcome these limitations. This work explores a novel class of interfaces, termed symmetry-forbidden interfaces, which transcend epitaxial constraints, enabling new possibilities for interface engineering.

We fabricated interfaces between three-fold symmetric sapphire (Al2O3) and four-fold symmetric SrTiO3 using an oxide membrane transfer technique [3]. High-angle annular dark-field scanning transmission electron microscopy (HAADF-STEM) and electron energy-loss spectroscopy (EELS) were employed to analyze the structural and electronic properties at the atomic scale. The interfacial sharpness, homogeneity, and potential novel electronic configurations were systematically investigated.

HAADF-STEM imaging confirmed that the fabricated interfaces exhibit exceptional atomic sharpness and cleanliness, comparable to epitaxially grown structures (Figure 1). EELS analysis revealed an unconventional electronic structure localized at the interface, confined within a single monolayer. The structural and electronic properties of these interfaces demonstrate that symmetry-forbidden heterostructures can be realized with high precision, opening up new avenues for materials engineering.

Our results establish a new category of oxide interfaces beyond the constraints of epitaxial growth. The ability to integrate materials with disparate symmetries paves the way for the discovery of unprecedented interface-driven phenomena. This study highlights the potential for designing innovative electronic systems with tailored functionalities, offering a promising platform for future research in quantum materials and interface physics.

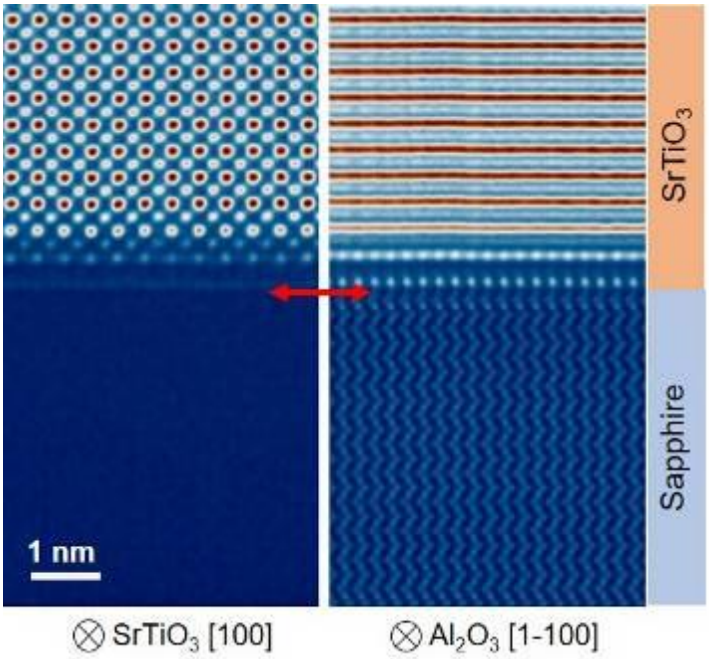
References

1. Hwang, H. Y., Iwasa, Y., Kawasaki, M., Keimer, B., Nagaosa, N., & Tokura, Y. (2012). Emergent phenomena at oxide interfaces. Nature Materials, 11(2), 103-113.

2. Mannhart, J., & Schlom, D. G. (2010). Oxide interfaces—an opportunity for electronics. Science, 327(5973), 1607-1611.

3. Wang, H., Harbola, V., Wu, Y. J., van Aken, P. A., & Mannhart, J. (2024). Interface Design Beyond Epitaxy: Oxide Heterostructures Comprising Symmetry-forbidden Interfaces. Advanced Materials, 36, 2405065.

Fig. 1



MS4.P06
Controlled formation of nanoribbons and their heterostructures via assembly of mass-selected inorganic ions

X. Zhang[1], V. Srot[1], X. Wu[1], K. Kern[1], P. A. van Aken[1], K. Anggara[1]

[1]Max Planck Institute for Solid State Research, Stuttgart, Germany

Control of nanomaterial dimensions with atomic precision through synthetic methods is essential to understanding and engineering of nanomaterials. For single-layer inorganic materials, size and shape controls have been achieved by self-assembly and surface-catalyzed reactions of building blocks deposited at a surface. However, the scope of nanostructures accessible by such approach is restricted by the limited choice of building blocks that can be thermally evaporated onto surfaces, such as atoms or thermostable molecules. We herein bypass this limitation by using mass-selected molecular ions obtained via electrospray ionization as building blocks to synthesize nanostructures that are inaccessible by conventional evaporation methods. As the first example, we show micron-scale production of MoS_2 and WS_2 nanoribbons and their heterostructures on graphene, generated by the self-assembly of asymmetrically-shaped building blocks obtained from the electrospray. We expect judicious use of electrospray-generated building blocks would unlock access to previously inaccessible inorganic nanostructures.

MS4.P07
Fabrication and high-resolution transmission electron microscopy characterization of nanopores in silicon nitride and 2D materials

T. Tang[1], M. Mierzejewski[1], M. Kögel[1], M. Schlegel[2], P. D. Jones[1], J. C. Meyer[1,2]

[1]University of Tübingen, NMI Natural and Medical Sciences Institute, Reutlingen, Germany
[2]University of Tübingen, Institute for Applied Physics, Tübingen, Germany

Introduction

Solid-state nanopores are an emerging technology for single molecule sensing of biomolecules including DNA, RNA, and proteins [1]. They provide a more resilient alternative to traditional biological nanopores, which are sensitive to temperature, pH, and other environmental factors. Specifically for solid-state nanopores, 2D materials provide a good foundation that is easy to modify, robust, and reusable [2,3]. 2D materials have unique properties that only appear when bulk materials are reduced to the nanoscale. Specific attributes can be generated in the 2D material and alter the dynamics of molecules travelling through the nanopores.

Objectives

Using various microscopy techniques, solid state nanopores are produced and analyzed. Materials of interest include graphene, hexagonal boron nitride (h-BN), and transition metal dichalcogenides (TMDCs).

Methods

Different techniques for manufacturing solid state nanopores are investigated. These include transmission electron microscopy (TEM), scanning transmission electron microscopy (STEM), and helium ion microscopy (HIM). From these microscopy methods, nanopores are created in SiNx membranes as well as in 2D materials.

Results

Pores in the range of tens of nanometres are milled into SiNx using the HIM. Single nanopores as well as arrays of nanopores were created to investigate various milling parameters (Figure 1. A, B). DNA translocations were observed by ionic current measurements, validating the presence and function of the nanopore. For 2D materials, a scaffold of SiNx must be used to create freestanding 2D materials. Graphene and h-BN are transferred onto HIM milled or gallium focused ion beam (FIB) milled holes in SiNx membranes. The resulting membranes are imaged with high resolution TEM (Figure 1.C).

Conclusion

Electron microscopy and ion beam milling are promising techniques for the production of solid-state nanopores. Various pore geometries will continue to be explored and methods will be developed to create novel nanopores in 2D materials. The combination of 2D materials results in unique properties in nanopore structures which would otherwise be difficult to achieve without the use of electron microscopy and nanostructuring.

Figures

Figure 1: (HR)-TEM images of various nanopores milled into SiNx membranes using HIM. A) A single nanopore of 15 nm diameter in SiNx, imaged with TEM. B) An array of 225 nanopores (15×15), used to compare dose and dwell time parameters. C) Monolayer graphene transferred onto a HIM-milled nanopore of 15 nm diameter. The lattice of the graphene can be seen, as well as traces of carbon contamination.

References

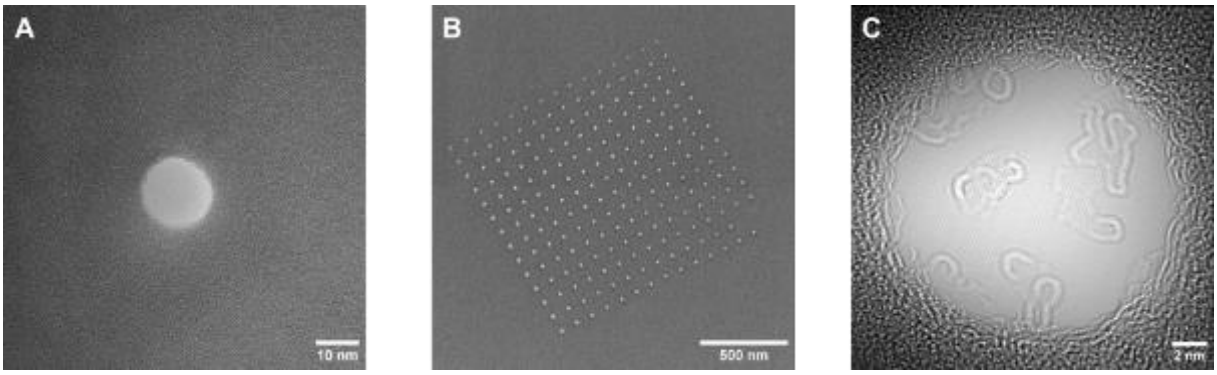
[1] Xue L et al. Nat. Rev. Mater 5, 931–51 (2020).

[2] Danda G, Drndić M. Curr. Opin. Biotechnol., 55, 124–33 (2019).

[3] M. Thakur et al., npj 2D Materials and Applications 7, Art.no. 11 (2023)

[4] This work has received funding from the Federal Ministry of Education and Research (BMBF), under project Nanodiag, 03ZU1208BG. This work received financial support from the State Ministry of Baden-Württemberg for Economic Affairs, Labour and Tourism.

Fig. 1



MS4.P08
Interfacial structure and charge-transfer in 3*d*/5*d* oxide heterostructures studied by atomically resolved spectroscopic imaging

D. Wang[1,2], A. K. Jaiswal[3], V. Wollersen[1,2], M. Le Tacon[3], D. Fuchs[3], C. Kübel[1,2]

[1]Karlsruhe Institute of Technology, Institute of Nanotechnology, Eggenstein-Leopoldshafen, Germany
[2]Karlsruhe Institute of Technology, Karlsruhe Nano Micro Facility (KNMFi), Eggenstein-Leopoldshafen, Germany
[3]Karlsruhe Institute of Technology, Institute for Quantum Materials and Technologies (IQMT), Eggenstein-Leopoldshafen, Germany

The combination of different transition metal (TM) oxide in thin films heterostructures not only results in the possibility of tuning their intriguing electronic transport and magnetic properties via lattice strain and symmetry change but can also generate new exotic phases at the interface between oxides. In 5d iridates the competition between strong spin orbit coupling and electron correlation, which facilitates the emergence of novel quantum states, can be tuned by combining with the 3*d* perovskites $LaMnO_3$ (LMO), $LaFeO_3$ (LFO) and $LaCoO_3$ (LCO) to form multilayer structures, which can be epitaxially grown with atomic precision by e.g. pulsed laser deposition. Characterizing the interface structure between different oxides at atomic resolution is essential for the understanding of electro-magnetic properties induced by confined interface charge transfer (ICT).

We studied systematically the ICT in 5*d* $SrIrO_3$ (SIO) heterostructures by HAADF-STEM, atomically resolved EDX and EELS spectrum imaging (SI). Figure 1 shows exemplarily the HAADF-STEM image of $[(SIO)_4(LFO)_4]_5$, indicating coherent epitaxial growth of pseudo cubic perovskite structures, suppressing the orthorhombic distortion in comparison to bulk SIO. Non-local PCA denoised STEM-EDX maps and the corresponding normalized intensity profiles along the growing direction (left to right) are shown in Figure 2. The SIO-LFO interface layers (arrows) show a mixture of Sr and La, however with Sr dominating. The last Ir monolayer (ML) in SIO and the first ML of Fe in LFO appeared very sharp at the either side of the interfaces, ensuring the ICT by alignment of oxygen states at the interface due to the continuity of the common oxygen in corner sharing Ir-O and TM-O octahedra [1]. ICT is well described by difference in electronegativity between SIO and TM oxides. With increasing number of *d*-electrons electronegativity of TMs decreases, suggesting more charge transfer from Ir to Co than to Mn.

Atomically resolved EELS SI was performed to identify the ICT at the SIO/LMO multilayers and compared to the previous result from SIO/LCO bilayer interfaces [2]. Mn L2,3 signals were integrated to construct the Mn map shown in Figure 3 together with the HAADF-STEM image. The LMO/SIO interface is atomically sharp as seen from the Mn map. EELS spectra were integrated from the four Mn MLs, as indicated in the Mn map. There is no distinguishable difference for Mn valence in the four MLs, suggesting the ICT from Ir to Mn is negligible. This result is in clear contrast to the previous study for SIO/LCO bilayer system, where both chemical shift towards lower energy and an increased L3/L2 ratio for Co L2,3 edges were identified in the two atomic layers at the SIO/LCO interface [2]. This finding is in agreement with the XANES experiment for Ir L edge, where the increase of number of holes from Mn to Co was evidenced. In summary, atomically resolved imaging and spectroscopic methods has been used to identify the characteristic charge transfer phenomena at 3*d*/5*d* oxide heterostructures to correlate to the electronic transportation property and induced changes in magnetism.

[1] Z. Zhong and P. Hansmann, *Phys. Rev. X* **7** (2017) 011023.

[2] A. K. Jaiswal, D. Wang, V. Wollersen, R. Schneider, M. Le Tacon, D. Fuchs, *Adv. Mater.* (2022) 2109163.

Figure 1. HAADF-STEM image of $[(SIO)_4(LFO)_4]_5$.

Figure 2. EDX maps and intensity profiles of $[(SIO)_4(LFO)_4]_5$.

Figure 3. Mn EELS map and L2,3 edge from four Mn MLs in SIO/LMO.

Fig. 1

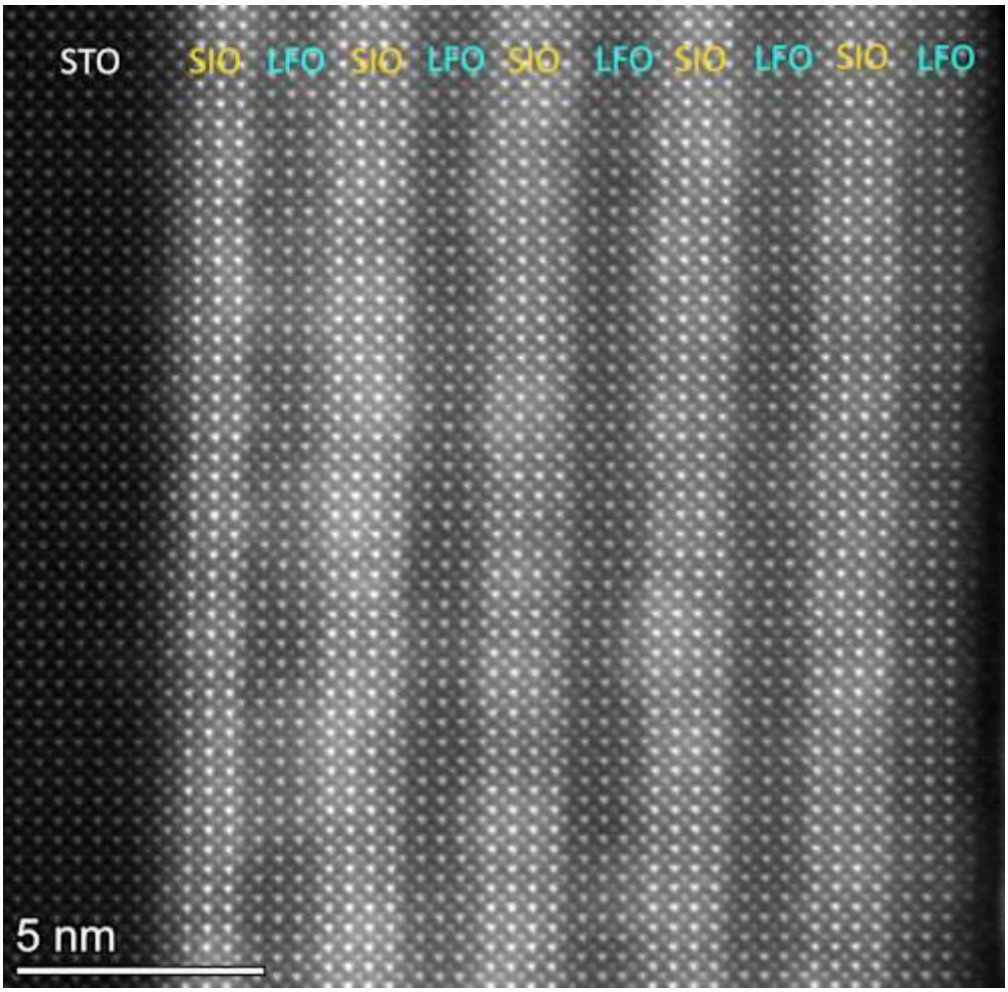


Fig. 2

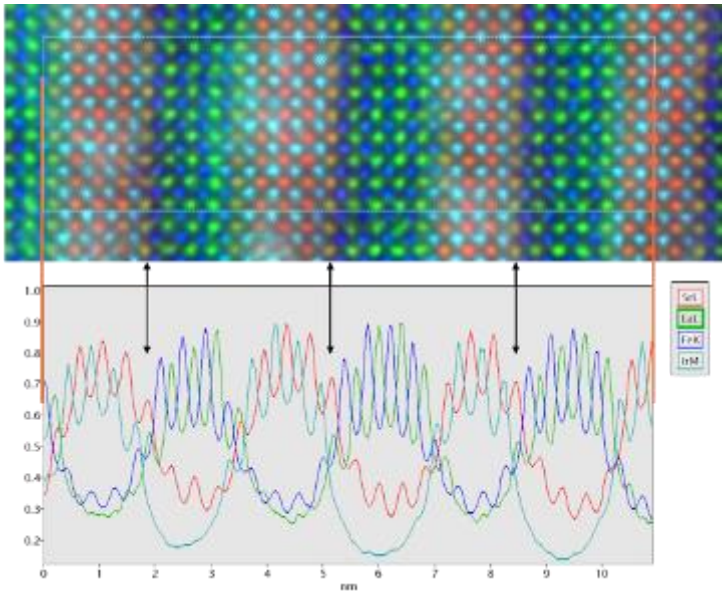
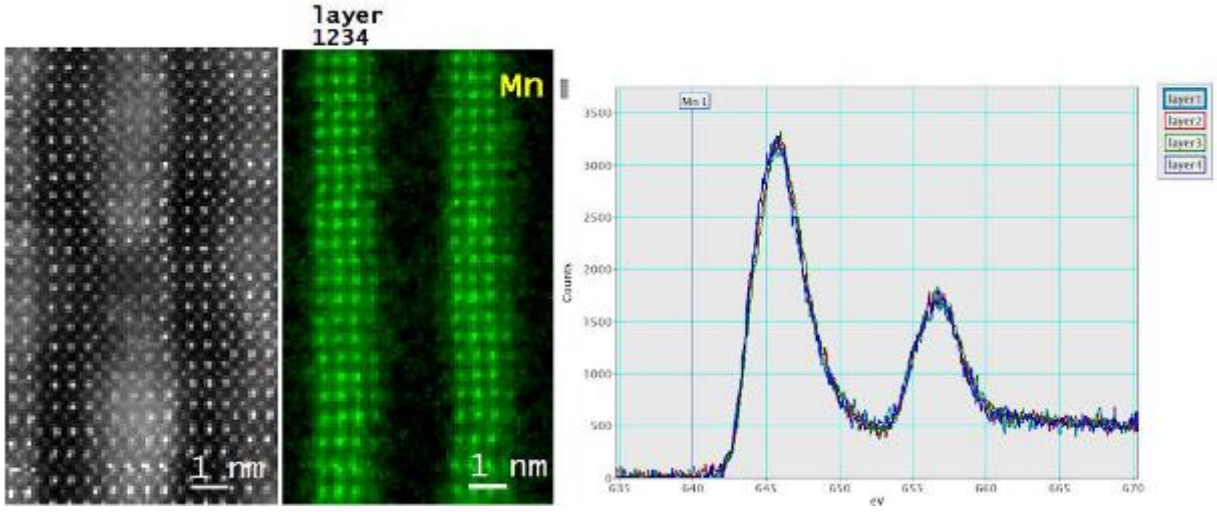


Fig. 3



MS4.P09
Microstructural evolution in Cu-Sb_2Te_3 thin films studied by atomic-resolution transmission electron microscopy

A. Lotnyk[1], N. Braun[1], V. Roddatis[2], S. Cremer[1], D. Kalanov[1], H. Bryja[1]

[1]Leibniz Institute of Surface Engineering (IOM), Leipzig, Germany
[2]GFZ Helmholtz Centre for Geosciences, Potsdam, Germany

Introduction

The increasing interest in thermoelectricity as a sustainable and renewable energy conversion technology has driven the development of solid-state thermoelectric. Telluride-based materials, such as Sb_2Te_3 (SBT), are well-established thermoelectric materials suitable for room-temperature applications. The thermoelectric performance of these materials can be enhanced through Cu doping and alloying, which can lead to the formation of Cu-Te secondary phases [1].

Objectives

While many studies have focused on bulk materials, this research investigates phase formation and microstructural changes in SBT thin films induced by magnetron sputtering of Cu and electrical switching of Cu-SBT system.

Materials & methods

SBT thin films were synthesized using pulsed laser deposition [2], while Cu and Pt thin layers were deposited via magnetron sputtering. Microstructural analysis was conducted using atomic-resolution Cs-corrected scanning transmission electron microscopy and electron energy loss spectroscopy (EELS).

Results

Microstructural investigations of the Cu/polycrystalline SBT thin film system revealed a reaction between the Cu and SBT layers during magnetron sputtering. This reaction resulted in the formation of $Cu_{7-x}Te_{4+x}$ grains, which exhibited layered Cu-Te structures with alternating two- and three-layer Te arrangements, as shown in Fig. 1(a). Similar phase formations were observed after Cu deposition onto epitaxial SBT thin films. However, in these films, Cu-Te structures formed layered intergrowths within SBT grains, as depicted in Fig. 1(b). More pronounced interdiffusion was detected in a resistive memory device consisting of Cu electrode/epitaxial SBT layers [3]. Switching the device to a low-resistance state led to Cu dissolution within the film, triggering an epitaxial transformation of SBT into layered Cu-Sb-Te structures comprising two- and three- Te layers, as shown in Fig. 1(c). Atomic-resolution EELS confirmed the presence of distinct Cu layers within these structures, with Sb and Te sharing atomic sites.

Furthermore, depositing a Pt layer onto Cu/ polycrystalline SBT thin film facilitated the formation of large $Cu_{3-x}Te_2$ grains, resembling the rickardite phase, as depicted in Fig. 1(d). In contrast, the use of epitaxial SBT thin films promoted the epitaxial growth of a triple-layered Cu_7Te_4 structure, identified as a novel $Cu_7(SbTe)_4$ phase.

Conclusion

This study provides valuable insights into the local structure and preferred Cu-Te phases that emerge during the solid-state reaction of Cu with SBT thin films. These findings contribute to a deeper

understanding of phase evolution in Cu-SBT systems, which is critical for optimizing their thermoelectric and electronic applications.

Reference

[1] Y. Xiao et al., J Am. Chem. Soc. 139 (2017) 18732−18738

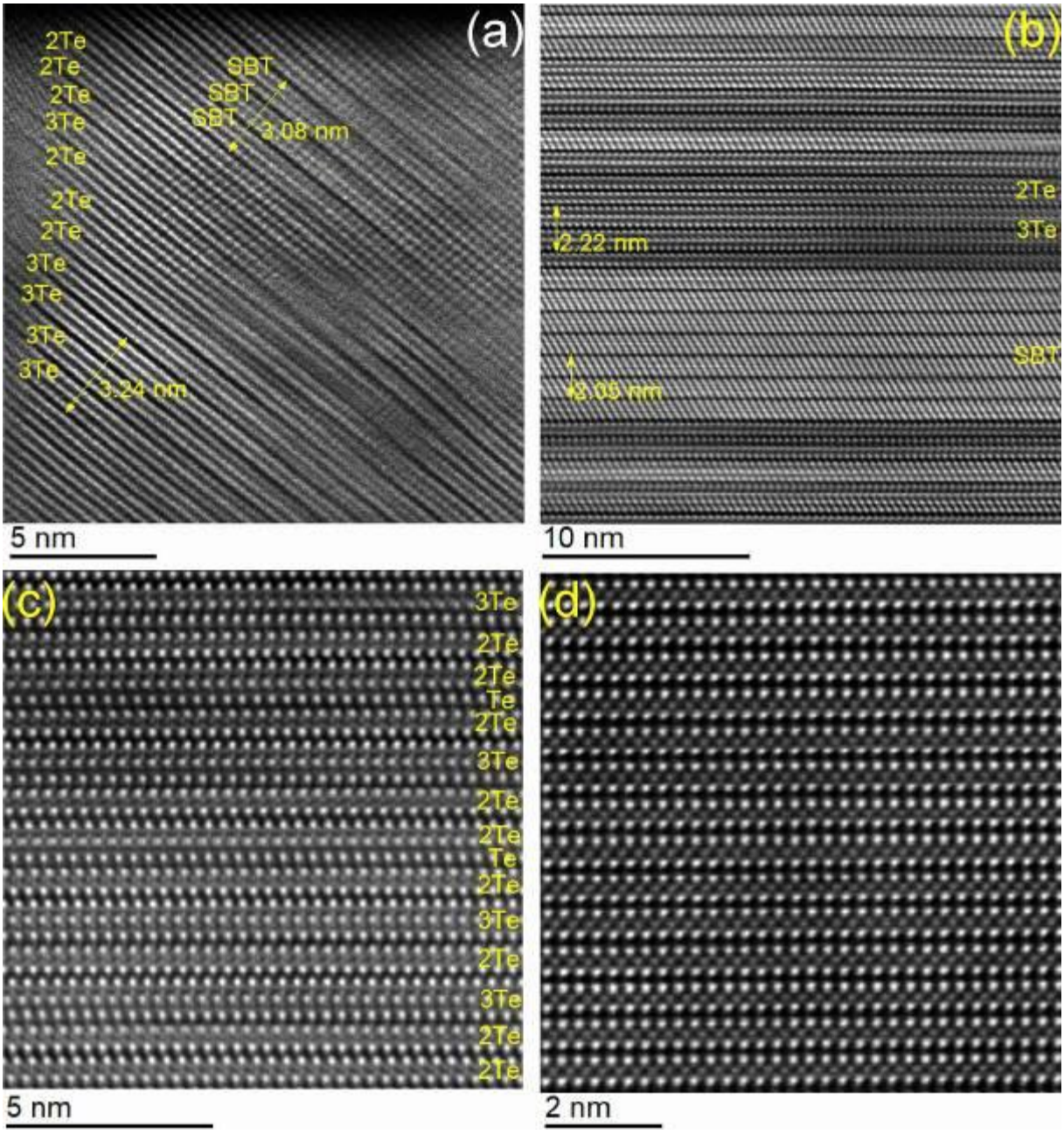
[2] S. Cremer et al., Applied Surface Science 655 (2024) 159679

[3] H Bryja et. al., 2D Materials 8 (2021) 045027

We acknowledge A. Mill, T. Pröhl and P. Hertel for their technical support and German Research Foundation (DFG, projects 448667535 and 445693080) for financial support of this work.

Fig. 1. Atomic-resolution HAADF-STEM images showing the microstructure of SBT thin films after (a) and (b) deposition of Cu onto the polycrystalline and epitaxial thin films, respectively, (c) electrical switching of Cu-SBT thin film system, and (d) deposition of Pt onto Cu/polycrystalline SBT system.

Fig. 1


(a)
2Te
2Te
2Te
3Te
2Te
2Te
2Te
3Te
3Te
3Te
3Te
SBT
SBT
SBT
3.08 nm
3.24 nm
5 nm
(b)
2Te
3Te
2.22 nm
SBT
3.05 nm
10 nm
(c)
3Te
2Te
2Te
Te
2Te
3Te
2Te
2Te
Te
2Te
3Te
2Te
3Te
2Te
2Te
5 nm
(d)
2 nm

MS4.P10
Correlating structures with local photophysical properties of quasi-2D halide perovskites via photoluminescence and raman microscopy

M. Sun[1], S. Kahmann[1]

[1]Chemnitz University of Technology, Physics, Chemnitz, Germany

Recently, 2D and quasi-2D metal halide perovskites have been attracting great attention for optoelectronic applications by virtue of their outstanding optoelectronic properties including broadly tunable bright and narrowband luminescence with high quantum yields. When used in optoelectronic devices, such as light-emitting diodes (LEDs), quasi-2D perovskites are cast as polycrystalline thin films – often comprising a mixture of different compositions and bandgap energies. The impact of these heterogeneous structures at different length scales on their optoelectronic properties and the general device performance is still underexplored.[1] Many studies involve macroscopic spectroscopy techniques unable to resolve properties of materials on a local scale. By contrast, multimodal microscopy techniques are powerful approaches to visualizing spatial heterogeneities and attaining inter-property relationships.[2]

This work aims to uncover working mechanism of quasi-2D polycrystalline perovskite thin films for use in LEDs by unraveling their photophysics on a local scale. To this end, we studied the effect of the phase purity on the local photophysical properties and degradation mechanisms by correlating the structural-chemical insights from Raman spectro-microscopy with the charge carrier dynamics accessed via PL microscopy.

Solution-processed quasi-2D Ruddlesden-Popper perovskite thin films with the average octahedral layer thickness of <n>=2 have been used in this work. Hyperspectral PL and non-resonant Raman mapping were conducted via a confocal stage scanning approach, whereas time-resolved PL microscopy was performed under widefield conditions. We considered both inter- and intra-grain variations in properties and applied state-of-the-art computational techniques to analyze these multidimensional datasets.

References

[1] E. M. Tennyson, T. A. S. Doherty, and S. D. Stranks, "Heterogeneity at multiple length scales in halide perovskite semiconductors", *Nat. Rev. Mater.*, vol. 4, no. 9, pp. 573–587, Sep. 2019, doi: 10.1038/s41578-019-0125-0.

[2] S. D. Stranks, "Multimodal microscopy characterization of halide perovskite semiconductors: Revealing a new world (dis)order", *Matter*, vol. 4, no. 12, pp. 3852–3866, Dec. 2021, doi: 10.1016/j.matt.2021.10.025.

MS4.P11
Atomic-scale insights into the Bi-directional growth of functional oxide heterostructures

N. Bonmassar[1]

[1]University of Stuttgart, Stuttgart, Germany

Typically, heteroepitaxial single crystalline thin films are grown along a single growth direction and the highest precision is reached with a *Frank-Van der Merwe*-type of growth, i.e. atomic layer-by-layer growth. Here, a method is presented, where the step-edges of substrates with high and precise offcuts along different crystallographic directions are used to grow along two directions simultaneously with atomic precision, cf. Figure 1. [1]

Figure 1: Schematic of the terrace-by-terrace (a) and layer-by-layer (b) type of growths. Reproduced with permission from N. Bonmassar et al., *Adv. Funct. Mater*, DOI: 10.1002/adfm.202314698, **2024**. [1]

Here, recent findings on the use of offcut substrates to achieve atomic precision in this specific growth-type along both in-plane and out-of-plane directions are presented. This is accomplished through *in situ* monitoring of reflected high-energy electron diffraction (RHEED) oscillations during the growth by molecular beam epitaxy (MBE) under an ozone atmosphere. The effectiveness of this approach is demonstrated with a bi-directionally grown superlattice of alternating $LaMnO_3$ and $SrMnO_3$ layers, exhibiting interfacial ferromagnetism. This system serves as a model to highlight the method"s versatility, supported by structural and functional characterization via scanning transmission electron microscopy (STEM), sheet resistance measurements, and magnetometry. To gain deeper insights into the structural and electronic properties, we employed geometric phase analysis (GPA) by evaluating high-angle annular dark field (HAADF) images to directly visualize the strain state of highly mismatching materials. It is revealed that localized strain states form at the step edges between two materials with highly different c-axis parameters and immediate strain relaxation occurs by the formation of a defective unit cell in direct proximity to the step edge. [2] Furthermore, we quantified the valence state of the Mn ions in the $LaMnO_3/SrMnO_3$ superlattice by analyzing the L_3/L_2 white-line ratio in electron energy loss spectroscopy (EELS) measurements, providing crucial information on charge transfer and interfacial electronic reconstruction, cf. Figure 2. [1] Additionally, this approach is applied to superconducting $La_{1.84}Sr_{0.16}CuO_4$ thin films on various offcut substrates, resulting in an anisotropic critical current emerging from two distinct substrate-induced mechanisms.

In this talk, I will discuss the challenges encountered during this project and how we overcame well-known issues such as the loss of *in situ* RHEED oscillations, terrace broadening, step bunching, 3D defect formation, and the associated degradation of functionalities like superconductivity. Finally, I will give an outlook about the future research regarding offcut substrates, for example the growth of 2D superconducting interfaces in $La_{1.55}Sr_{0.45}CuO_4/La_2CuO_4$ heterostructures [3] grown on offcut substrates to induce a reduction in dimensionality from 2D to quasi 1D terraces.

Figure 2: Structural and chemical analysis of the bi-directionally grown superlattice. Reproduced with permission from N. Bonmassar et al., *Adv. Funct. Mater*, DOI: 10.1002/adfm.202314698, **2024**. [1]

References

[1] N. Bonmassar et al., *Adv. Funct. Mater*, DOI: 10.1002/adfm.202314698, **2024**.

[2] N. Bonmassar et al., *Nano Lett.*, DOI: 10.1021/acs.nanolett.4c00832, **2024**.

[3] G. Logvenov, N. Bonmassar et a., *Condens. Matter*, DOI: 10.3390/condmat8030078, **2023**.

Fig. 1

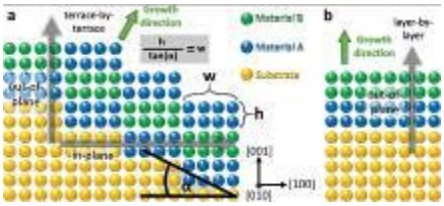
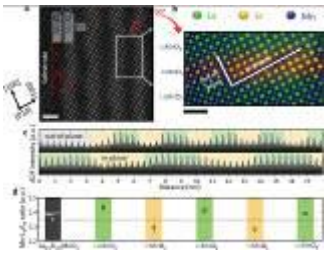

a
terrace-by-terrace
Growth direction
Material B
Material A
Substrate
w
h
[001]
[100]
[010]
b
layer-by-layer
Growth direction

Fig. 2



MS4.P13
iDPC-STEM imaging of monolayer graphene-based heterostructures

D. K. Dinkar[1], C. J. Humphreys[1]

[1]University of London, Queen Mary, School of Engineering and Materials Science, London, United Kingdom

Graphene-based heterostructures have emerged as a crucial platform for next-generation electronic and optoelectronic applications. High-resolution structural and compositional characterization of these materials is essential for understanding their interfacial properties, defects, and atomic-scale arrangements. Although high-angle annular dark-field scanning transmission electron microscopy (HAADF-STEM) is widely used for imaging heterostructures due to its atomic number (Z-contrast) sensitivity, it has limitations in detecting low-Z elements and light atomic structures, such as graphene and hexagonal boron nitride (hBN), with high contrast.

On the other hand, integrated differential phase contrast scanning transmission electron microscopy (iDPC-STEM) offers significant advantages for imaging graphene-based heterostructures. iDPC-STEM provides simultaneous imaging at atomic resolution of both light and heavy atoms with high contrast, enabling the direct visualization of weakly scattering materials like graphene while maintaining sensitivity to heavier elements. This capability is particularly beneficial for investigating van der Waals heterostructures composed of graphene, hBN, and transition metal dichalcogenides (TMDs), where high contrast atomic-scale imaging is required to determine the structure of interfaces and defects.

We have studied metal oxide layers deposited on MOCVD-grown graphene. Cross-sectional TEM specimens were prepared using a Dual Beam Focused Ion Beam/Scanning Electron Microscope (FIB/SEM) *via* the lift-out method. These specimens were then analyzed using aberration-corrected transmission electron microscopy (TEM) to assess structural integrity and composition. In my presentation, I will discuss the TEM specimen preparation process, along with the STEM HAADF and IDPC images, and energy-dispersive X-ray spectroscopy (EDS) results, providing insights into the material"s quality and potential for next-generation graphene-based devices.

References:

1. Xiaowen Yu et.al., Graphene-based smart materials, Nat. Rev. Mater. 2, 17046 (2017).
2. Ivan Lazic et al., Phase contrast STEM for thin samples: Integrated differential phase contrast, Ultramicroscopy, 160, 265 (2016).

MS4.P14
Atomic-scale investigation of symmetry-forbidden LaAlO3 (001)/La0.67Sr0.33MnO3 (111) interfaces

Y. Wang[1], V. Harbola[1], J. Mannhart[1], P. A. van Aken[1], H. Wang[1]

[1]Max Planck Institute, Stuttgart, Germany

Oxide interfaces are a fertile ground for emergent phenomena, including two-dimensional electron gases (2DEG), ferroelectricity, and ferromagnetism1. However, the exploration of novel electronic states has been historically constrained by the limitations of conventional epitaxy, which necessitates lattice symmetry and lattice constant matching between constituent materials2. This restriction has hampered the creation of interfaces exhibiting fundamentally different symmetries, potentially unlocking access to unprecedented electronic behavior. Recent advances in freestanding membrane transfer techniques3 have overcome this limitation, enabling the fabrication of atomically sharp interfaces between complex oxides with disparate crystallographic symmetries and lattice parameters, opening up a new frontier in interface engineering. This study investigates the atomic-scale structure and electronic properties of a symmetry-forbidden interface created by stacking a freestanding LaAlO3 (001) (LAO) membrane onto a La0.67Sr0.33MnO3 (111) (LSMO) film. Specifically, we utilize state-of-the-art aberration-corrected scanning transmission electron microscopy (STEM) to probe the interfacial region with atomic resolution. This approach allows us to directly correlate structural and electronic characteristics at this novel interface. High-angle annular dark-field (HAADF) STEM imaging revealed an atomically sharp LAO/LSMO interface, free from observable defects, dislocations, or stacking faults, confirming the efficacy of the transfer technique in creating high-quality interfaces. However, STEM and electron energy-loss spectroscopy (EELS) analysis demonstrated significant Mn/Al intermixing within the LAO layer, with Mn diffusing from the LSMO into the LAO and substituting for Al atoms in a non-uniform distribution. This Mn diffusion plays a crucial role in mediating both the atomic and electronic structures of the LAO in the vicinity of the interface. Furthermore, atomically resolved electron energy-loss near-edge structure (ELNES) analysis across the LAO/LSMO interface revealed variations in the Mn valence state and the presence of oxygen vacancies near the interface, highlighting the complex interplay between structure, chemistry, and electronic properties of this novel interface. Our findings demonstrate the successful fabrication of an atomically sharp, symmetry-forbidden interface between LAO (001) and LSMO (111), exhibiting unique structural and electronic characteristics distinct from conventional epitaxial interfaces. This work underscores the potential of exploiting symmetry-forbidden oxide interfaces to engineer novel interfacial states beyond the limitations imposed by traditional epitaxy. Further exploration of such interfaces is crucial for advancing the fundamental understanding of interface physics and for developing next-generation electronic devices with tailored functionalities. The ability to create and characterize such interfaces opens new avenues for designing materials with emergent properties, paving the way for breakthroughs in fields such as microelectronics, spintronics, and energy technologies. References 1.Hwang, H. Y.; Iwasa, Y.; Kawasaki, M.; Keimer, B.; Nagaosa, N.; Tokura, Y. Emergent phenomena at oxide interfaces. Nature Materials 2012, 11 (2), 103-113. 2.Lu, D.; Baek, D. J.; Hong, S. S.; Kourkoutis, L. F.; Hikita, Y.; Hwang, H. Y. Synthesis of freestanding single-crystal perovskite films and heterostructures by etching of sacrificial water-soluble layers. Nature Materials 2016, 15 (12), 1255-1260. 3.Wang, H. G.; Harbola, V.; Wu, Y. J.; van Aken, P. A.; Mannhart, J. Interface Design beyond Epitaxy: Oxide Heterostructures Comprising Symmetry-Forbidden Interfaces. Advanced Materials 2024, 36 (32).

MS4.P15
Atomically clean free-standing two-dimensional materials through heating in ultra-high vacuum

P. Irschik[1], D. Lamprecht[1,2], C. Mangler[1], S. Chokappa[1], J. Kotakoski[1]

[1]University of Vienna, Physics of Nanostructured Materials, Vienna, Austria
[2]Technical University of Vienna, Institute for Microelectronics, Vienna, Austria

Main abstract text:

As-grown two-dimensional (2D) materials such as monolayer graphene and hexagonal boron nitride (h-BN) usually suffer from adsorption of surface contamination during and after the synthesis process. In addition, transfer from the growth substrate onto another platform can introduce further contamination, obstructing the underlying structure and potentially degrading the material"s inherent properties.

Thermal annealing in ultra-high vacuum has been shown to effectively reduce the amount of carbonaceous surface contamination while inducing only a minimal amount of damage to the underlying material [1]. While the thermally-induced cleaning effect of adsorbed contaminants on graphene has been extensively studied, the desorption behavior of the hydrocarbon-rich contamination on free-standing monolayer h-BN has not yet been thoroughly reported. Additionally, there is no consensus regarding which temperatures and treatment durations are sufficient, in addition to a lack of information on how the local structure of the contamination changes on the atomic scale.

Here, we employ atomic-resolution scanning transmission electron microscopy to assess the reduction and removal of surface contamination down to the atomic level. Using thresholding-based digital image processing, we identify the amount of clean surface area before and after the thermal treatment, carried out in a custom-built ultra-high vacuum heating chamber integrated into the CANVAS system at the University of Vienna [2]. The samples are then transferred to the microscope while remaining in near-UHV conditions, ensuring that the effects of the annealing can be characterized without introducing airborne contaminants in the process.

First signs of desorption of carbonaceous contamination on free-standing monolayer h-BN and graphene are found above 250°C, while the cleaning effect starts to plateau at temperatures above 400°C. Heavily contaminated samples, with clean areas only on the nanometer scale, are transformed into samples where the majority of carbonaceous surface contamination has been removed, uncovering atomically clean regions that are hundreds of nanometers in size (see Figure). These increased sizes can facilitate engineering atomicscale features in 2D materials, such as defect engineering and impurity atom implantation [3], which require large clean areas to allow interacting with the material rather than the contamination.

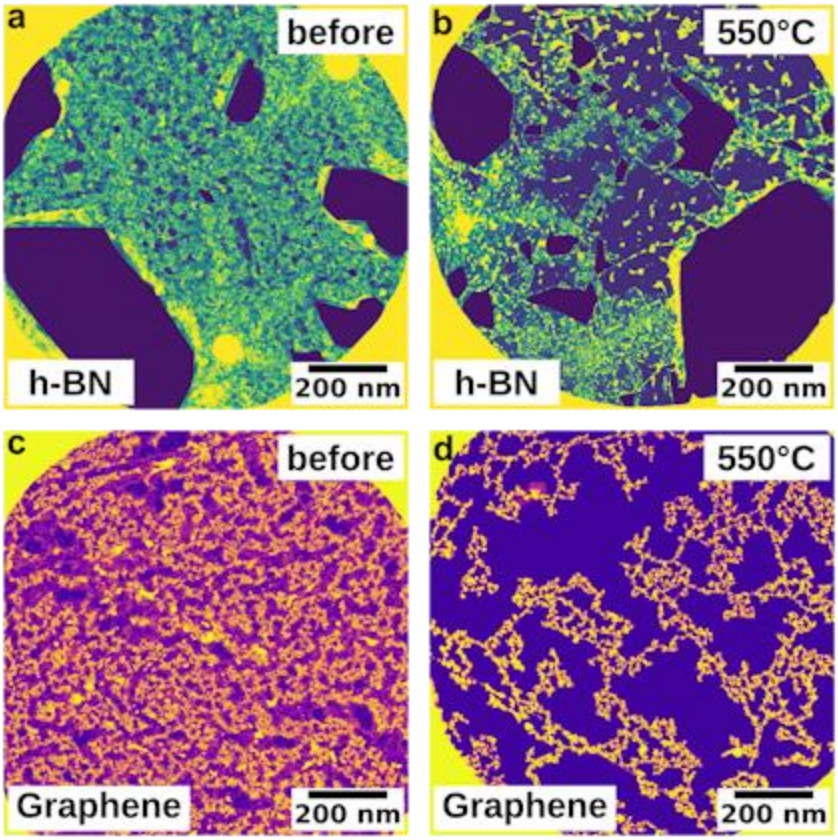
Figure caption:

Figure 1: Comparison of free-standing h-BN and graphene before and after heating in UHV. (a) As-prepared h-BN before the thermal treatment. (b) h-BN after thermal annealing at 550°C for 3h. The darkest contrast is holes in the material, the second darkest contrast is pristine monolayer h-BN. (c) For comparison, as-prepared monolayer graphene before heating. (d) Graphene after thermal annealing at 550°C for 3h. Here, the darkest contrast is monolayer graphene.

References:

[1] Tripathi et al., Phys. Status Solidi RRL 11, No. 8 (2017), 1700124
[2] Mangler et al., Microscopy and Microanalysis 28 (2022), 2940-2942
[3] Trentino et al., Nano Letters 21 (2021), 5179-5185

Fig. 1


a
before
h-BN
200 nm
b
550°C
h-BN
200 nm
c
before
Graphene
200 nm
d
550°C
Graphene
200 nm

MS4.P16
Local sublattice distortions in a high-pressure superconducting ruddlesden-popper nickelate

P. Sosa-Lizama[1], Y. M. Wu[1], P. Puphal[1], V. Sundaramurthy[1], M. Isobe[1], B. Keimer[1], M. Hepting[1], P. A. van Aken[1], Y. E. Suyolcu[1]

[1]Max Planck Institute for Solid State Research, Stuttgart, Germany

Recently, a renewed interest in Ruddlesden-Popper nickelates has developed after the discovery of unconventional superconductivity under high pressure in $La_3Ni_2O_7$ with the bilayer structure [1] and in a polymorph of alternating La_2NiO_4 (monolayer) and $La_4Ni_3O_{10}$ (trilayer) stacking [2]. These systems are characterized by their layered arrangement, hosting perovskite slabs with different numbers of blocks, separated by a rock-salt layer. In turn, this exact characteristic results in decoupled slabs, facilitating the emergence of short-range structural inhomogeneity in the different sublattices. In this work, we investigate the emergence of picometer-scale disorder in the Ni and O sublattices in the $La_3Ni_2O_7$ polymorph using scanning transmission electron microscopy (STEM).

The sample under study, $La_3Ni_2O_7$, was grown via the optical floating zone method under high oxygen pressure. The STEM lamellae were prepared by thinning the crystal specimens down to electron transparency via focused ion beam (FIB) milling with Ga ions on a Thermo Fisher Scios I FIB using the lift-out method. High-resolution imaging was performed with a JEOL JEM-ARM200F equipped with a cold field-emission electron source and a probe C_s-corrector (DCOR, CEOS GmbH). The acquisition was carried out with an acceleration voltage of 200 kV with a probe size of ~0.8 Å, and a beam current smaller than 70 pA. Collection angles for STEM high-angle annular dark field (HAADF) and annular bright field (ABF) images were 75 to 310 and 11 to 23 mrad, respectively. The analysis of the atomically-resolved images was performed employing tools from the Python package Atomap [3].

We initially employ STEM-HAADF imaging to focus on the Ni positions at the edges of the trilayer slabs and their related displacement patterns towards the rock-salt layers, which are found to involve shifts up to ~10 pm. In order to track the response of the O sublattice, STEM-ABF images – simultaneously acquired with STEM-HAADF – are used, on which the centers of masses of the apical O sites are determined. In these cases, distinct displacement patterns are observed. Our findings demonstrate two instances of picometer-scale displacements emerging over nanometer-sized regions in layered nickelates. Here, the decoupling between slabs allows the presence of different displacement patterns for the Ni and O sublattices.

References

[1] Sun, H. *et al.* Signatures of superconductivity near 80 K in a nickelate under high pressure. *Nature* (2023).

[2] Puphal, P. *et al.* Unconventional Crystal Structure of the High-Pressure Superconductor $La_3Ni_2O_7$. *Phys. Rev. Lett.* **133**, 146002 (2024).

[3] Nord, M., Vullum, P. E., MacLaren, I., Tybell, T. & Holmestad, R. Atomap: a new software tool for the automated analysis of atomic resolution images using two-dimensional Gaussian fitting. *Adv Struct Chem Imag* **3**, 9 (2017).

MS4.P17
3D structure determination of a twinned HfO_2 nanocrystal

H. Du[1], T. Ohlerth[2], U. Simon[3], J. Mayer[1,3]

[1]Forschungszentrum Jülich GmbH, Ernst Ruska-Centre for Microscopy and Spectroscopy with Electrons, Jülich, Germany
[2]RWTH Aachen University, Institute of Inorganic Chemistry, Aachen, Germany
[3]RWTH Aachen University, Central Facility for Electron Microscopy (GFE), Aachen, Germany

Transition metal oxides exhibit a wide variety of properties such as electronic and ionic conductivity and catalytic activity that are of technological importance for applications in advanced electronics and chemical catalyses. These properties are determined not only by the ideal crystal structure of the materials but also often by atomic-scale defects, which are particularly abundant in nanoscale materials. Consequently, quantitative three-dimensional (3D) characterization of nanocrystals at the atomic level recently attracts intensive research attention. Here, we quantitatively characterized twined HfO_2 colloid nanocrysals [1] using negative spherical aberration imaging (NCSI) in conventional TEM mode [2,3]. Quantitative interpretations were obtained through an optimization process to match the experimental with the simulated images [2]. We determined three dimensional (3D) atomic structure of a novel {011} twinned HfO_2 nanocrystal by matching between the multislice simulated and the experimental TEM images through an optimization procedure for minimal mean squared error. The presented 3D quantification method is based on the principles of TEM image formation physics and opens up opportunities for studying colloidal nanocrystals in three dimensions.

Fig. 1 Optimized 3D structure from which the multislice simulated TEM image matches the experimental TEM image with minimal mean squared error.

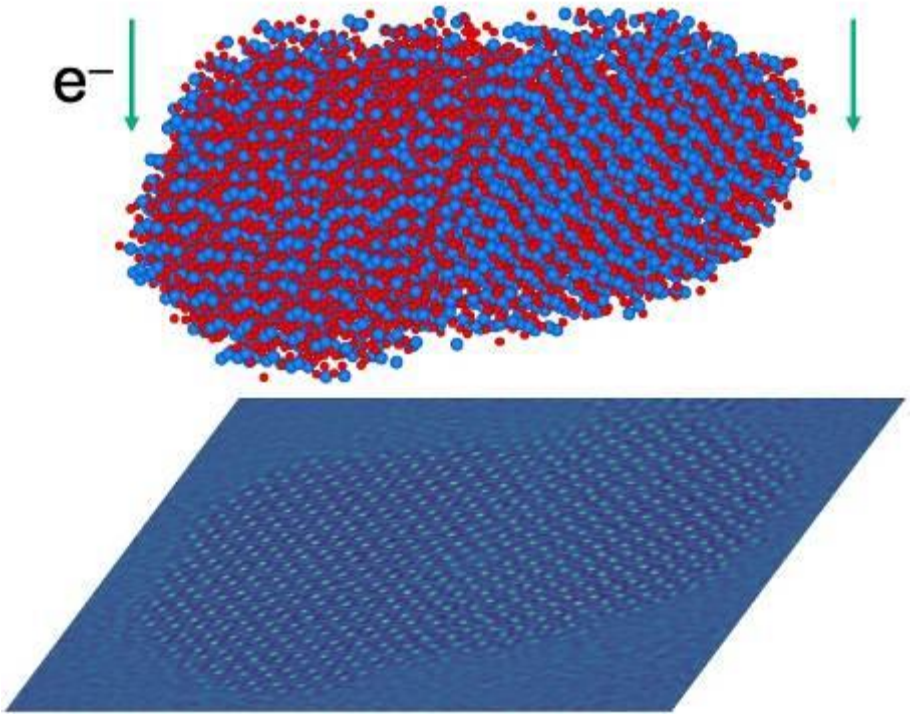
References

[1] T. Ohlerth, H. Du, T. Hammoor, J. Mayer, U. Simon, Tailoring of Colloidal HfO_2 Nanocrystals with Unique Morphologies and New Self-Assembly Features, *Small Science* 4 (**2024**) 2300209. https://doi.org/10.1002/smsc.202300209.

[2] H. Du, C. Groh, C.-L. Jia, T. Ohlerth, R.E. Dunin-Borkowski, U. Simon, J. Mayer, Multiple polarization orders in individual twinned colloidal nanocrystals of centrosymmetric HfO_2, *Matter* 4 (**2021**) 986-1000. https://doi.org/10.1016/j.matt.2020.12.008.

[3] H. Du, Structure of 180° ferroelectric domain walls in HfO_2 and ZrO_2, *arXiv* preprint, arXiv:2202.09663, **2022**. https://doi.org/10.48550/arXiv.2202.09663

Fig. 1



MS4.P18
Probingh high-pressure superconducting $La_3Ni_2O_7$ and topotactically reduced $LaNiO_2$ crystals at the atomic scale

Y. E. Suyolcu[1], Y. M. Wu[1], P. Sosa-Lizama[1], P. Puphal[1], P. Reiss[1], B. Keimer[1], M. Hepting[1], P. A. van Aken[1]

[1]Max Planck Institute for Solid State Research, Stuttgart, Germany

Rare-earth nickel oxides, known for their complex interplay between structure and properties, serve as a key platform for novel quantum phases and advanced applications. Topotactic transformations of perovskite nickelates have allowed precise control of oxygen vacancies, leading to the discovery of superconductivity in thin films of the infinite-layer (IL) nickelate $Nd_{0.8}Sr_{0.2}NiO_2$ (*1*). In addition, the discovery of high-temperature superconductivity – with a superconducting transition of ~80 K – in $La_3Ni_2O_7$ at elevated pressures (>14 GPa) has stimulated extensive research efforts (*2*). The fundamental properties of the superconducting phase have been the subject of controversial debates, including the interpretation of a possible filamentary character, whereas early investigations consistently postulated a crystal structure consisting of NiO_6 octahedral bilayers stacked along the *c*-axis in $La_3Ni_2O_7$.

Recently, we reported the unconventional structure of optical floating zone-grown high-pressure superconducting La3Ni2O7 single crystals and microstructural effects of topotactic reduction on undoped $LaNiO_3$ single crystals (*3*, *4*). Focusing on high-resolution scanning transmission electron microscopy (STEM) imaging and electron energy-loss spectroscopy (EELS), we reveal multiple crystallographic phases in $La_3Ni_2O_7$ crystals, where the main phase is dominated by alternating monolayers and trilayers of NiO_6 octahedra (*3*), different from the $La_3Ni_2O_7$ systems composed of bilayer structures. Additionally, we demonstrate that the reduction process leads to different types of structural deformations in topotactically reduced $LaNiO_3$ crystals (*4*, *5*).

References:

1. D. Li *et al.*, *Nature*. **572**, 624–627 (2019), https://doi.org/10.1038/s41586-019-1496-5.
2. H. Sun *et al.*, *Nature*. **621**, 493–498 (2023), https://doi.org/10.1038/s41586-023-06408-7.
3. P. Puphal *et al.*, *Phys. Rev. Lett.* **133**, 146002 (2024), https://doi.org/10.1103/PhysRevLett.133.146002.
4. Y.-M. Wu *et al.*, *APL Materials*. **12**, 091119 (2024) , https://doi.org/10.1063/5.0227732.
5. Y. E. Suyolcu *et al.*, *MRS Communications*, 1–12 (2025), https://doi.org/10.1557/s43579-025-00689-x.

MS4.P19
Correlating strain measurements, elemental mapping and high-resolution STEM of a quaternary III-V nanowire heterostructure

M. Döblinger[1], C. Doganlar[2], G. Koblmüller[2], K. Müller-Caspary[1]

[1]Ludwig-Maximilians University Munich, Chemistry, Munich, Germany
[2]Technical University of Munich, Walter Schottky Institute, Garching, Germany

Physical properties of III-V nanowire (NW) heterostructures strongly depend on composition, strain and defects to optimize their performance in optoelectronic devices. In turn, these parameters are related by the lattice matching of the participating layers in such NW heterostructures. We conducted a comprehensive STEM study of a quaternary radial core-shell III-V NW heterostructure, including compositional and strain mapping, as well as high-resolution (HR) imaging to characterize and correlate these properties.

GaAs-InAlGaAs/InGaAs core-shell NWs were grown along the Zinc Blende [111]B direction by molecular beam epitaxy on prepatterned SiO2/Si(111) [1]. This resulted in uniform, coaxial multi-quantum well NWs (length ~ 7.4 µm, width ~ 1.04 µm). STEM investigations of a FIB cross section (CS) were conducted at 300 kV with a probe-corrected FEI Titan, equipped with a Super-X EDX detector. For Nanobeam Electron Diffraction (NBED), a Quantum Detectors Medipix Quad detector was used. Reflection positions were optimized by radial gradient optimization [2].

Figure 1 a) shows an overview HAADF-STEM image of the CS, half-overlaid by an EDX map (Figure 1 b)). The core is made up of two GaAs(Sb) layers, followed by ten nominally 8 nm thick In0.25Ga0.25As0.5 quantum wells (QWs), each embedded in a 20 nm thick In0.16Al0.17Ga0.17As0.5 barrier, and finally a 5 nm GaAs capping.

The average measured layer compositions of the inner and outer core are Ga0.53As0.34Sb0.13 and Ga0.53As0.38Sb0.09, respectively. The average composition of barriers and QWs was Al0.13Ga0.20In0.16As0.51 and Al0.01Ga0.28In0.21As0.50, respectively. Assuming Vegard"s rule, these layer compositions would result in lattice constant variations of up to 1.6 %, with the maximum difference between outer core (574 pm) and QWs (583 pm). By HR-STEM and NBED, no defects were detected that could result in lattice relaxation, suggesting epitaxial coherence, and mostly radial strain. Furthermore, within all subsequent layers beyond the inner core, all corner directions are enriched by smaller atom species, as shown in Figure 1 c).

Strain measurements were conducted on two scales, by NBED for the whole CS at a 900x900 raster of scan pixels (Figure 2) and by HR-STEM for smaller regions (not shown). NBED strain maps were produced by locally evaluating the spacing of {02-2} Friedel pairs relative to their average in the outer core layer. Figure 2 a) shows a typical NBED pattern, the reflections marked in red were used for the color-coded strain map shown in Figure 2 b). The map reveals mainly tensile strain in the QWs normal to their layer facet (yellow) and compressive strain in the corner direction normal to that facet (black arrows). Figure 2 c) shows a 1 D line scan along the red line marked in Figure 2 b).

In summary, we present a detailed and consistent analysis of a NW CS, including structure, composition and strain, which we will discuss in conjunction with finite element strain calculations and with the excellent optoelectronic device performance.

Figure 1 a) HAADF-STEM image of the NW CS. b) Half-overlaid EDX map. c) Magnified detail along a corner direction.

Figure 2 a) Typical NBED pattern, the marked reflections are used for the strain map shown in b). c) Line scan along the red line marked in a), representing the strain normal to the (02-2) facet.

[1] P. Schmiedeke et al., Appl. Phys. Lett. 124, 071112 (2024).

[2] K. Müller et. al, Microsc. Microanal. 18, 995–1009 (2012).

Fig. 1

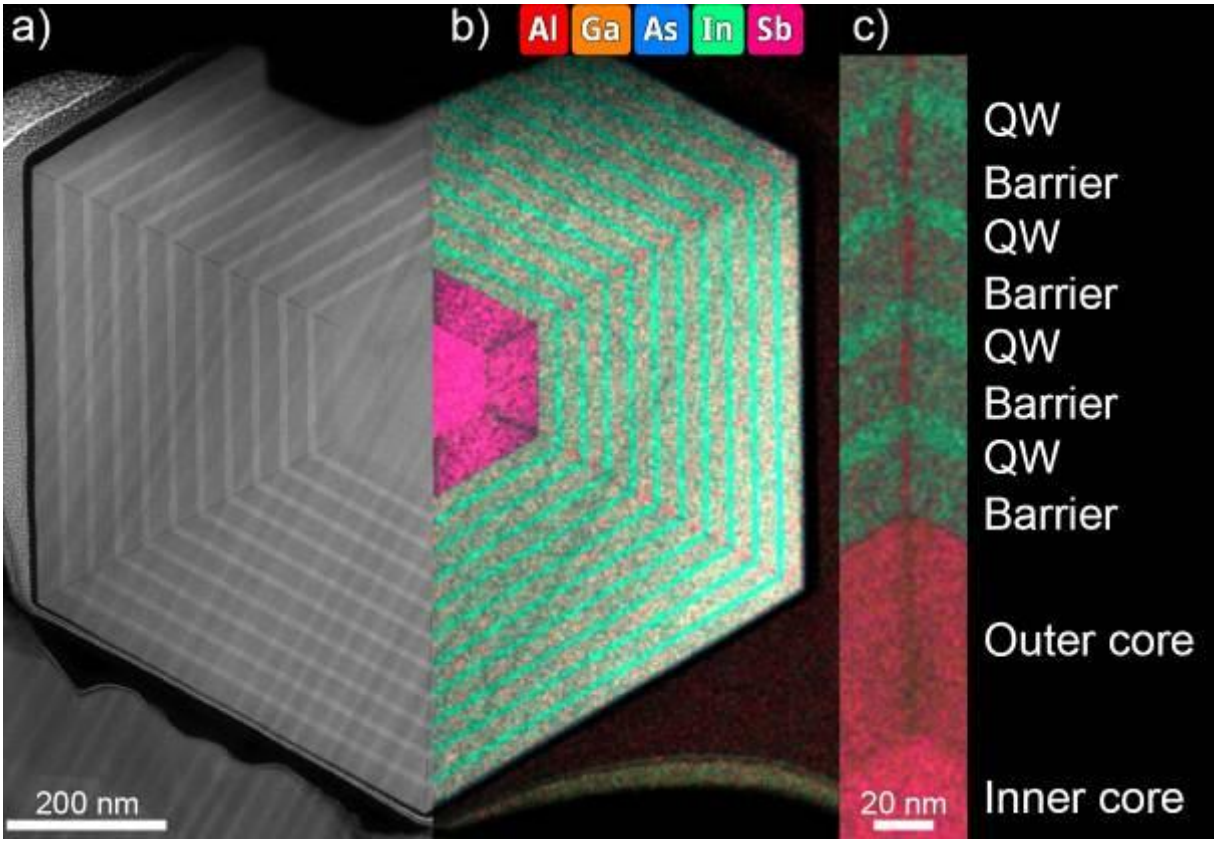
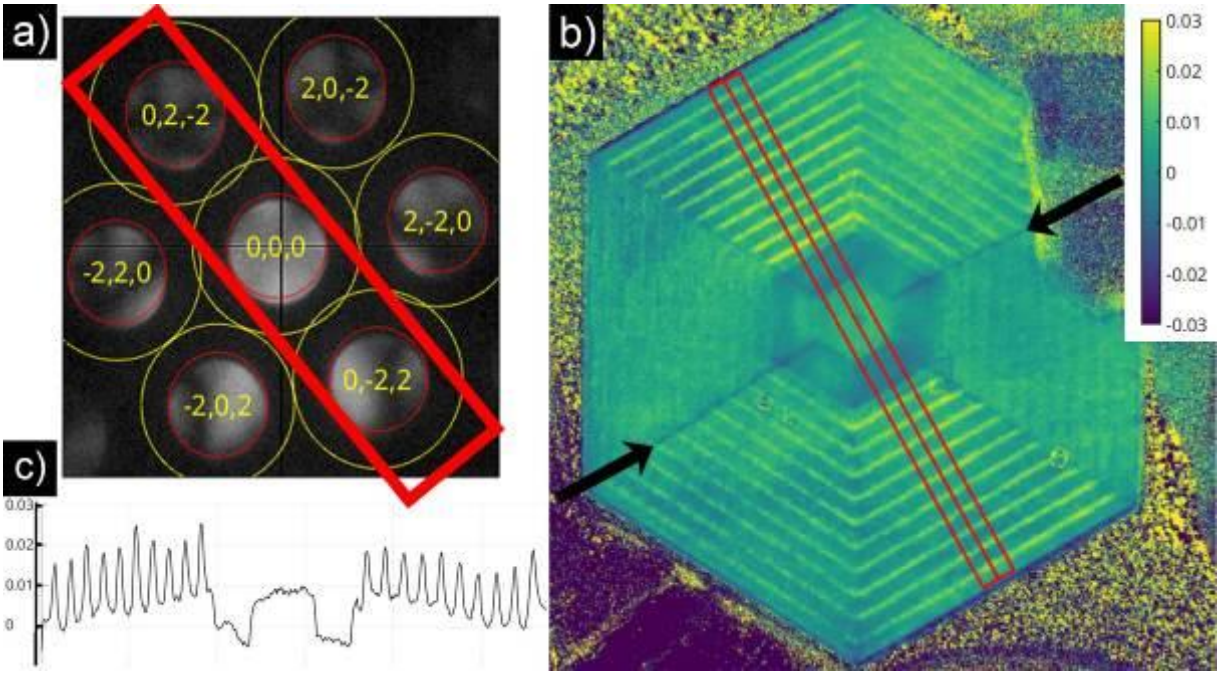


Fig. 2


a)
0,2,-2
2,0,-2
2,-2,0
0,0,0
-2,2,0
0,-2,2
-2,0,2
b)
0.03
0.02
0.01
0
-0.01
-0.02
-0.03
c)
0.03
0.02
0.01
0

MS4.P20
Atomic scale investigations of Sr_2RhO_4 single crystals

L. Kalaydjian[1], V. Zimmermann[2], A. Yogi[3], V. Srot[1], B. Keimer[2], M. Hepting[2], P. A. van Aken[1], Y. E. Suyolcu[1]

[1]Max Planck Institute for Solid State Research, Stuttgart, Germany
[2]Max Planck Institute for Solid State Research, Stuttgart, Germany
[3]UGC-DAE Consortium for Scientific Research (CSR), Indore, India

Transition-metal oxides (TMOs) offer a versatile platform for quantum phenomena, including exotic magnetic ground states, metal-insulator transition, and high-temperature superconductivity. Sr_2RhO_4 (SRO) is a Rh^{4+} strongly correlated 4*d*-electron TMO[1], which exhibits strong spin-orbit coupling (SOC)[2] that partially splits its filled t_{2g}-orbital manifold into separate bands with total angular momentum J = 1/2 and J = 3/2. Moreover, Ir-doped SRO, *i.e.,* $Sr_2Rh_{1-x}Ir_xO_4$, presents a wide plethora of electronic properties, ranging from a correlated metal phase (for $0 \leq x < 0.15$), an Anderson localized phase (for $0.15 \leq x < 0.75$), and paramagnetic metallic and insulating phases (for $0.75 \leq x < 1$)[3].

In this work, we explore the local structural and electronic properties of optical floating zone grown Ir-doped $Sr_2Rh_{0.6}Ir_{0.4}O_4$ (SRIO) and undoped SRO single crystals[4] using scanning transmission electron microscopy (STEM) techniques , including high-angle annular dark-field (HAADF) imaging, electron energy-loss spectroscopy (EELS), and energy-dispersive X-ray spectroscopy (EDXS). TEM specimens were prepared via a focused ion beam (FIB) using the lift-out method on a FEI Scios DualBeam system (Thermo Fisher Scientific, Inc.). A JEOL JEM-ARM200F STEM (JEOL Co. Ltd.) equipped with a cold field-emission electron source, a probe Cs-corrector (DCOR, CEOS GmbH), a Gatan GIF Quantum ERS spectrometer, and a large solid-angle JEOL Centurio SDD-type EDXS detector were used for atomic-resolution analyses.

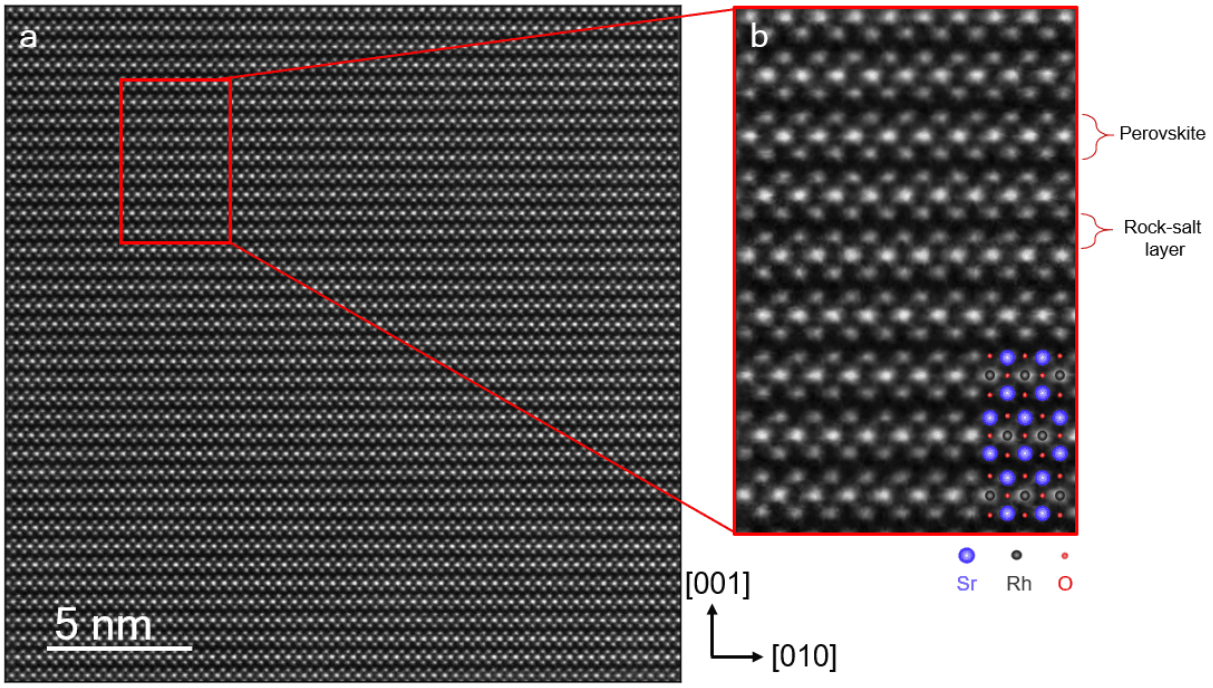
We initially revealed that the specimen is sensitive to the high-energy electron beam, akin to what was observed in the isostructural Sr_2RuO_4 system[5]. After experimental conditions are optimized for the beam-sensitive compound, the high crystal quality of both SRO and SRIO crystals is confirmed (Figure 1). By employing the STEM-EELS technique, the local electronic structure of the samples, including the O-*K* edge profiles, are revealed. In addition to STEM-EELS analyses, we utilized SEM-EDXS and STEM-EDXS measurements to determine the distribution of the dopants in the lattice. Our analyses confirm that the doped crystal exhibited a homogeneous distribution of dopants across the lattice, indicating uniform Ir substitution throughout the crystal structure.

References:

1. Wang, L. *et al.* Spin-Orbit Excitons in a Correlated Metal: Raman Scattering Study of Sr_2RhO_4. *Phys. Rev. Lett.* **132**, 116502 (2024).
2. Sandilands, L. J. *et al.* Spin-Orbit Coupling and Interband Transitions in the Optical Conductivity of Sr_2RhO_4. *Phys. Rev. Lett.* **119**, 267402 (2017).
3. Qi, T. F. *et al.* Spin-orbit tuned metal-insulator transitions in single-crystal $Sr_2Ir_{1-x}Rh_xO_4$ ($0 \leq x \leq 1$). *Phys. Rev. B* **86**, 125105 (2012).
4. Zimmermann, V. *et al.* Coherent propagation of spin-orbit excitons in a correlated metal. *Npj Quantum Mater.* **8**, 53 (2023).
5. Goodge, B. H. *et al.* Disentangling types of lattice disorder impacting superconductivity in Sr_2RuO_4 by quantitative local probes. *APL Mater.* **10**, 041114 (2022).

Figure 1. (**a**) High magnification STEM-HAADF image of Sr_2RhO_4 displaying the high quality and homogeneity of the crystal in [100] crystallographic orientation. (**b**) The higher magnification area extracted from the red box in (a) is overlayed with the structural model, where the red atoms correspond to O, the black corresponds to Rh, and Sr is purple. The alternating SrO_2 rock-salt layers and the perovskite blocks are indicated in (b).

Fig. 1



MS4.P21
Investigation of curved Bi0.5Sb1.5Te3 nano-doubleplatelets via HAADF STEM-tomography

S. Sturm[1], F. Hölzl[1], N. Goyal[2], N. Ravishankar[2], K. Müller-Caspary[1]

[1]Ludwig-Maximilians University Munich, Faculty Chemistry and Pharmacy, Munich, Germany
[2]Indian Institute of Science, Materials Research Center, Bangalore, India

Hexagonally shaped nano-platelets consisting of two layers of material (Bi2Te3 and Sb2Te3) with slightly different lattice parameters, grown on top of each other, result in a remarkable curved structure with expected radii of curvature in the order of few micometers.Investigating this bending in 3D with STEM Tomography [1] however, is not straight forward, as they naturally tend to lay flat on the surface of TEM-Grids. This preferred orientation fully exposes them to an incomplete tilt range, the so called "missing wedge" (MW) in Fourier space, in the most unfavorable way, impeding measurements of their slight curvature. Especially such extended, homogeneous and clean facets perpendicular to the MW direction are most difficult to reconstruct for state of the art algorithms.
Fig. 1 illustrates this problem with a simulated nano-platelet (Fig. 1a). After reconstruction with a WSIRT [2] algorithm (Fig. 1b), MW artifacts dominate in the direction perpendicular to the platelet. The effect strongly depends on sample pre-orientation, as seen in the 10°, 20° and 30° pre-tilted case (Fig. 1c, d,e).
In order to mitigate this MW problem in the experiment, several strategies have been prosecuted:
- Explicit selection of well pre-oriented specimen.
- Dual axis STEM Tomography [1] to reduce the MW to a missing cone.
- Gradient-based optimization of the tomogram, taking into account its total variation
- Pointwise 1D center of mass in MW direction and subsequent fitting of an ellipsoid to estimate the radii of curvature from the tomograms.
The experimental data in Fig. 2 was acquired using an FEI Themis operated at 300kV in STEM mode with an HAADF detector and tilt range of ca. -70° to +70° for the tilt series. The curvature of the nano-platelet shown in Fig.2a is confirmed by typical asymmetric bending contours under defocus (Fig. 2b). The tomogram (Fig. 2c) has been reconstructed using a state of the art WSIRT algorithm.
Afterwards the 1D center of mass in MW direction was calculated over the reconstructed area of the nano-platelet (Fig. 2d). A central slice through these points (indicated in black) is presented in Fig. 2e in side view, showing clear indication of bending.
Despite all challenges, estimation of a curvature radius of ca. 4µm was possible by fitting an ellipsoid to the extracted point-cloud.

Figure 1: Simulation: Influence of "missing wedge".
a..e) corresponding central slices through the original test object (a) and its tomograms (b, c, d, e) with same total tilt range, but differing sample pre-orientation.
f..h) Isosurfaces of original object (a) and its tomograms (g, h) corresponding to likewise sample pre-orientation of (b) and (e), respectively.

Figure 2: Experiment
a) Infocus HAADF STEM image of a Bi0.5Sb1.5Te3 nano-platelet (tomogram region indicated in yellow),
b) Defocused HAADF STEM images of the specimen,
c) Isosurface rendering of the tomogram, reconstructed via WSIRT.
d) Point-cloud of 1D center of mass, applied along missing wedge direction throughout the tomogram.
g) Central slice through the point-cloud in (d, indicated in black) in side view, exhibiting a bending radius of ca. 4µm.

References:
[1] MIDGLEY, et al. Nature materials, 2009
[2] WOLF, et al. Ultramicroscopy, 2014

S.S. and K.M.-C. acknowledge funding from the Bavarian Hightech Agenda (Germany) within the EQAP project, the German Academic Exchange Service (DAAD) of the German Federal Ministry of Education and Research (BMBF), project 57723688.

Fig. 1

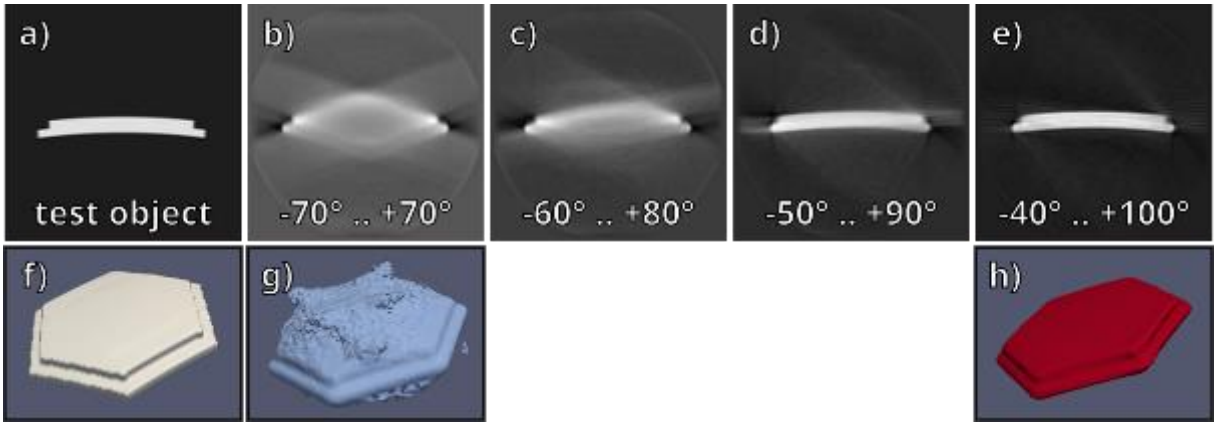
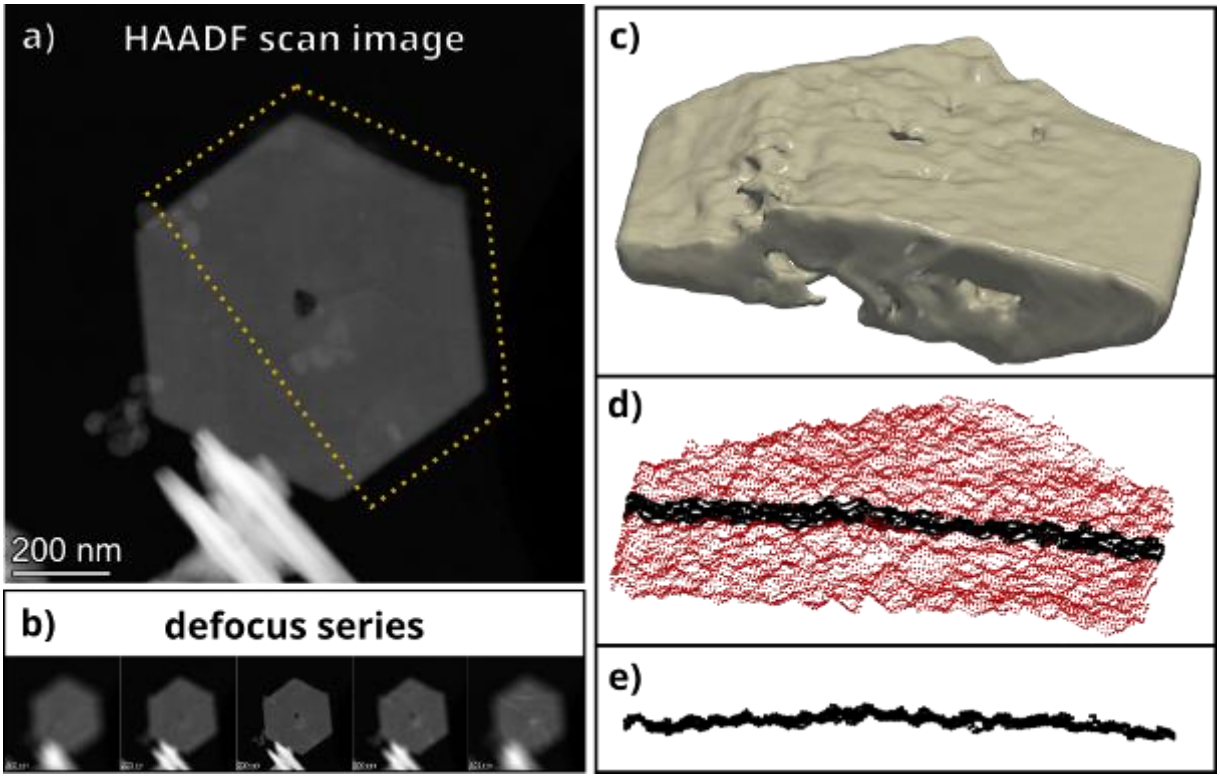


Fig. 2



MS4.P22
Imaging the three-dimensional morphology of granular superconductors with energy-filtered TEM tomography

L. M. Brauch[1,2], T. Reisinger[1], D. Wang[3,4], I. Pop[1,5], C. Kübel[2,3,4]

[1]Karlsruhe Institute of Technology, Institute for Quantum Materials and Technologies (IQMT), Eggenstein-Leopoldshafen, Germany
[2]Technical University of Darmstadt, Darmstadt, Germany
[3]Karlsruhe Institute of Technology, Institute of Nanotechnology, Eggenstein-Leopoldshafen, Germany
[4]Karlsruhe Institute of Technology, Karlsruhe Nano Micro Facility (KNMFi), Eggenstein-Leopoldshafen, Germany
[5]Karlsruhe Institute of Technology, Physikalisches Institut (PHI), Karlsruhe, Germany

Introduction and Objectives

This work aims to resolve the structure - property relationship in granular aluminum (grAl) thin films to advance the understanding of granular superconductors. GrAl is currently applied in microwave kinetic inductance detectors, parametric amplifiers, fluxonium qubits, resonators and filters. In order to resolve the Al particle network, energy-filtered TEM (EFTEM) tomography in combination with the Discrete Algebraic Reconstruction Technique (DART) was applied to resolve the morphology of the grAl.

Materials

GrAl is produced by physical vapor deposition of aluminum in the presence of oxygen partial pressure. The emerging granular aluminum nanostructure that is embedded in an amorphous aluminum oxide features tunable nonlinearity, kinetic inductance and low AC losses in its superconducting state.Tunability of the non-linear properties is achieved by adjusting the room temperature resistivity of the film and varying the number of tunneling junctions in the network by changing the volume of the grAl component..

Methods

Three samples have been investigated. Two PVD samples with 120 µΩcm and 25000 µΩcm resistivity and one sputtered sample with 100 µΩcm resistivity were investigated. Films of 20 nm thickness were deposited on lacey Carbon TEM grids for easy nanowire templating. The coated carbon laces were imaged by Plasmon EFTEM on a Thermo Fisher Scientific Titan Themis Z at 80 kV with a Gatan image filter equipped with a K3 camera. The EFTEM tilt series is aligned with the help of fiducial markers and reconstructed using DART.

Results

Image corrected HRTEM shows partially polycrystalline grains in projection. EFTEM at 14 to 16 eV shows good contrast for the aluminum volume plasmon. The sputtered and physical vapor deposited low resistivity samples are reconstructed as a network of interconnected aluminum particles. However, an oxide barrier fully separating neighboring grains is not observed within the tomography resolution. Pair distribution function analysis (PDF) of the particle distribution shows no difference in size and close-range order for the two low resistivity networks. The high resistivity sample shows many grains are still interconnected but there are oxide barriers separating clusters of grains from each other. PDF analysis shows a peak for the nearest neighbor distances and lower grain sizes. [CK1] [CK2] The [CK3] observed interconnected grains for the high resistivity grAl is clear evidence for a high non-uniformity.

Conclusion

This study provides novel insights into the 3D morphology of granular Aluminum (grAl) thin films, challenging previous assumptions about the structure-property relationship in these materials. The advanced electron microscopy analysis has revealed that the non-linear properties of grAl are more likely due to constrictions in the conductive path through the grains rather than full oxide barriers. PVD and sputtering result in comparable film morphologies. These findings pave the way for more accurate simulations and could potentially enhance the performance of devices utilizing grAl.

Fig. 1: 3D reconstruction of the aluminum particle network in PVD deposited grAl: (top) low resistive sample, (bottom) high resistive sample. The different colors indicate particles separated by skeletonization analysis.

Fig. 1

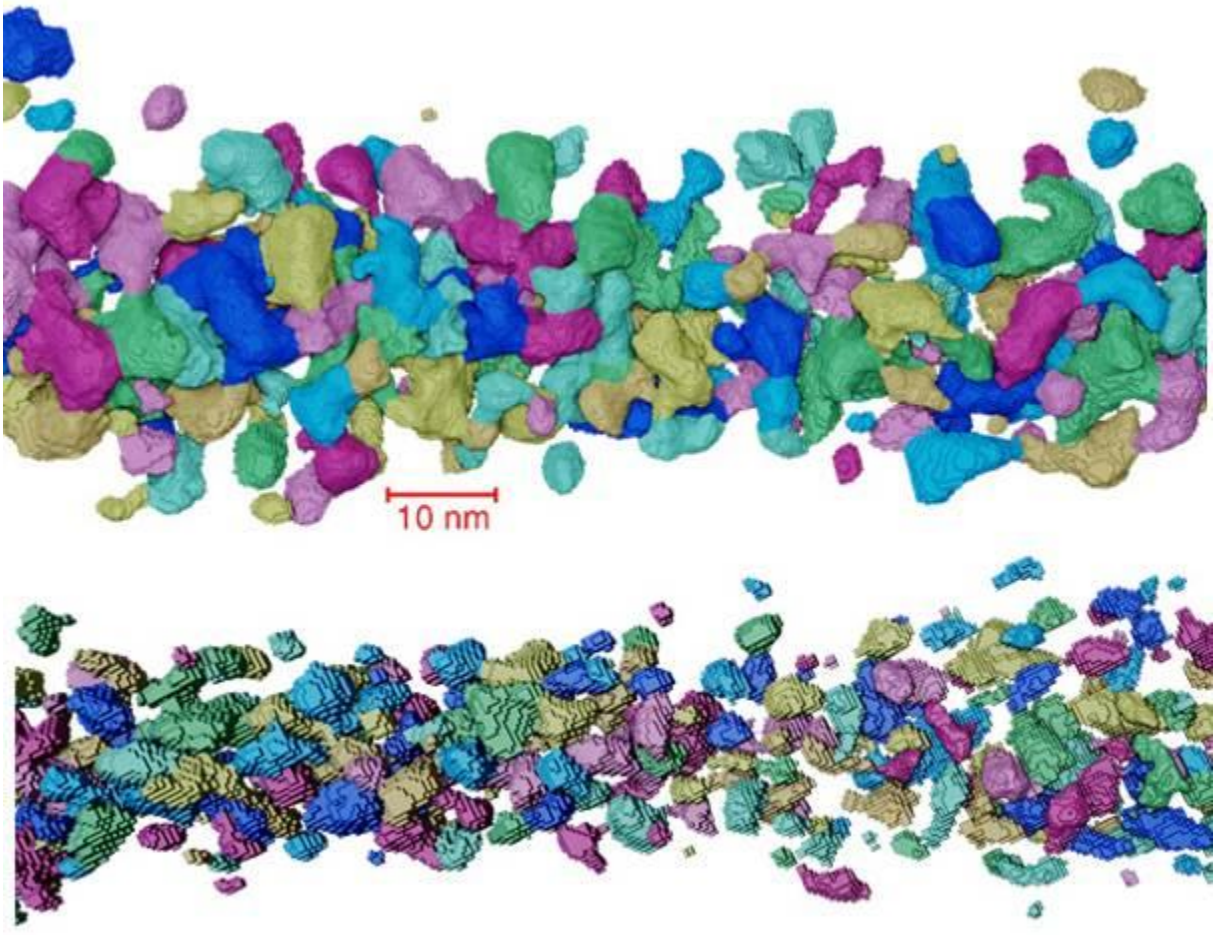
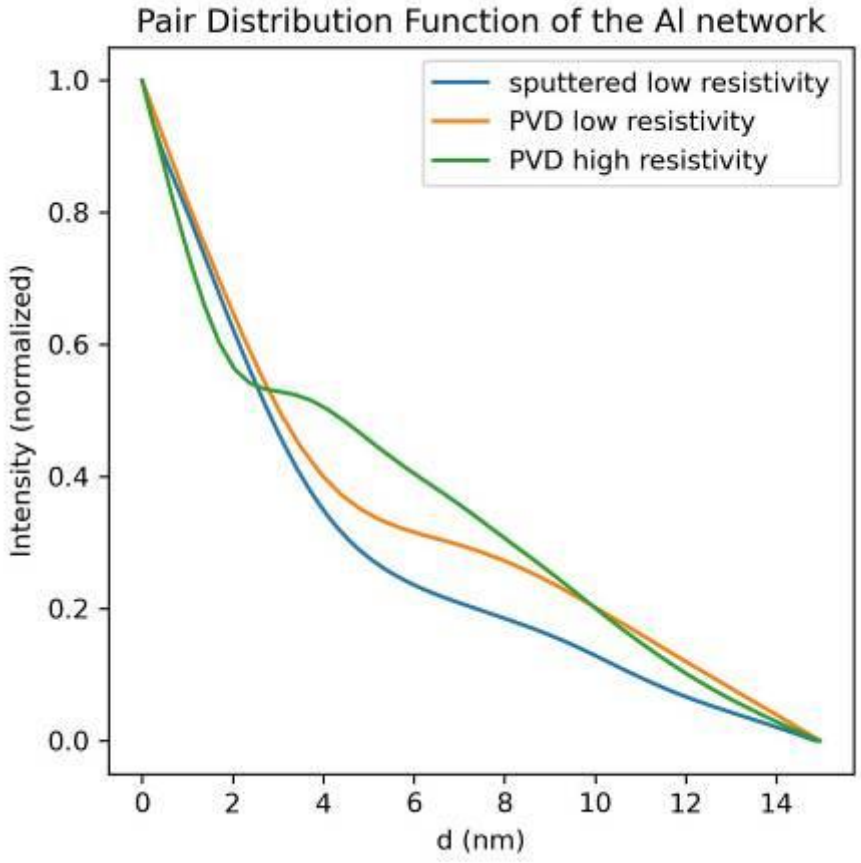


Fig. 2


Pair Distribution Function of the Al network
sputtered low resistivity
PVD low resistivity
PVD high resistivity
Intensity (normalized)
1.0
0.8
0.6
0.4
0.2
0.0
0
2
4
6
8
10
12
14
d (nm)

MS 5: Functional organics, carbon-based and hybrid materials

MS5.01(inv)
New developments in transmission electronmicroscopy for 2D and 3D investigations of organic and hybrid materials

S. Bals[1], S. Kavak[1], N. J. Schrenker[1], I. Skvortsova[1], T. Craig[1], N. Claes[1], A. Annys[1], T. Stoops[1], R. de Meyer[1], A. de Backer[1], J. Verbeeck[1], S. van Aert[1]

[1]University of Antwerp, EMAT, Department of Physics, Antwerp, Belgium

A local, high resolution characterization of organic and carbon based materials such as metal organic frameworks (MOFs)and organic-inorganic hybrid perovskite (OIHP) is of great importance for specific fields such as eg optoelectronics, where a precise shape control and understanding hereof is required. Transmission electron microscopy (TEM) is an excellent technique to investigate the structure and composition of nanomaterials. However, investigating MOFs and OIHP by TEM is extremely challenging due to their sensitivity towards the electron beam. Beam instability becomes increasingly problematic for techniques which demand high electron beam exposure. For instance, to accurately observe the 3D structure of nanomaterials, electron tomography can be used. However, the collection of a tomogram requires c.a. 150 images of the same structure at different specimen tilt-angles, which results in considerable beam irradiation, especially when using high angle annular dark field scanning TEM (HAADF STEM), the conventional mode for electron tomography in materials science. Here, we will present recent progress in the development of novel TEM techniques that will enable the two-dimensional (2D) and 3D investigation of MOFs and OIHPs at improved resolution and reduced electron dose.

At technique of interest is 4D STEM, for which a full 2D diffraction pattern is collected at every pixel of a STEM image. Hereby, all electrons collected by the detector are used to form an image, whereas in HAADF STEM only electrons scattered to relatively high angles are used. 4D STEM is therefore superior with respect to information richness and dose efficiency as compared to HAADF STEM. Through different examples, both for MOFs and MHPs, we will demonstrate the superior resolution and improved sensitivity of a recently developed 4D STEM based technique in comparison to HAADF STEM at low electron doses [1]. Another route to reduce the electron dose during an electron tomography experiment is "undersampling", where a balance is sought between the spatial resolution of the 3D reconstruction and the number of projection images, and therefore electron dose, required. Typically, this optimization is performed in a trial-and-error approach, which is inefficient and time consuming. We recently presented a novel method to optimize tilt undersampling during a single electron tomography experiment and will here demonstrate the benefits for 3D characterization of metal nanoparticle-MOF composites [2].

Finally, an emerging challenge is to fully understand the connection between the 3D structure and properties under realistic conditions, including high temperatures as well as in the presence of liquids and gases. We will therefore provide an outlook on the combination of in situ electron microscopy and electron tomography for MOFs and IOHPs, but also for the study of ligands at the surface of metal nanoparticles [3].

References

[1] C.P Yu, T Friedrich, D Jannis, S Van Aert, J Verbeeck, *Microscopy and Microanalysis* **2022**, 28, 1526-1527
[2] T Craig, A Anil Kadu, J Batenburg, S Bals, *Nanoscale* **2023**, 15, 5391-5402
[3] A Pedrazo-Tardajos, N Claes, D Wang, A Sánchez-Iglesias, P Nandi, K Jenkinson, R De Meyer, L.M Liz-Marzán, S Bals, *Nature Chemistry* **2024**, 16, 1278-1285

MS5.02(inv)
Understanding, mimicking and mitigating radiolytic damage to polymeric soft matter in LP-TEM

H. Wu[1], J. van Hest[1], H. Friedrich[1]

[1]Eindhoven University of Technology, Chemical Engineering and Chemistry, Eindhoven, Netherlands

Visualizing how polymers self-assemble in liquid media, how they interact with each other and how they respond to various environmental stimuli is important for the design of micro-nanoreactors, nanoparticles for drug delivery, and artificial systems with life-like behaviours. Advances in liquid phase transmission electron microscopy (LP-TEM) have made it possible to track assembly processes of polymeric soft matter in (organic) solvent mixtures [1], to measure and modulate liquid layer thickness [2] and to controllably replenish the liquid inside the observation window [3]. However, one of the biggest challenges still to date is to understand and mitigate the effects that the electron beam and confinement play in observed formation mechanisms and final structures.

In this contribution, I will present our recent work on understanding, mimicking, and mitigating radiolytic damage in functional polymers in LP-TEM [4]. We quantified polymer damage across all conceivable (LP-)TEM environments, focusing on understanding the key characteristics and especially the differences between polymer degradation in water vapor and liquid water. We demonstrated that the hydroxyl radical-rich environment in LP-TEM can be mimicked by UV light irradiation in the presence of hydrogen peroxide, allowing the use of bulk techniques to probe damage at the polymer chain level. In the last step we compared the protective effects of commonly used hydroxyl radical scavengers, revealing that the effectiveness of graphene"s protection is distance dependent.

This work provides a detailed view on polymer degradation in LP-TEM, paving the way for future studies that visualize shape transitions or drug encapsulation in polymeric assemblies.

[1] A. Ianiro, H. Wu, M. van Rijt, M. P. Vena, A. Keizer, A. C. C. Esteves, R. Tuinier, H. Friedrich, N.A.J.M. Sommerdijk, J.P. Patterson "Liquid–liquid phase separation during amphiphilic self-assembly" ***Nature Chemistry*** 11 (2019) 320-328.

[2] Hanglong Wu, Hao Su, Arthur D. A. Keizer, Laura. S. van Hazendonk, Maarten J. M. Wirix, Joseph P. Patterson, Jozua Laven, Gijsbertus de With, Heiner Friedrich "Mapping and controlling liquid layer thickness in liquid phase (S)TEM" ***Small Methods*** 5 (2021) 2001287.

[3] J. Tijn van Omme, Hanglong Wu, Hongyu Sun, Anne France Beker, Mathilde Lemang, Ronald G. Spruit, Sai P. Maddala, Alexander Rakowski, Heiner Friedrich, Joseph P. Patterson, H. Hugo Pérez Garza "Liquid Phase Transmission Electron Microscopy with temperature and flow control" ***Journal of Materials Chemistry C*** 8 (2020) 10781-10790.

[4] Hanglong Wu, Hongyu Sun, Roy van der Meel, Siyu Li, Jingxin Shao, Jianhong Wang, Rick R. M. Joosten, Xianwen Lou, Yingtong Luo, Yevheniy Pivak, Loai K. E. A. Abdelmohsen, H. Hugo Pérez Garza, Jan C. M. van Hest, Heiner Friedrich "On radiolytic damage to polymers in liquid phase transmission electron microscopy" ***Advanced Materials*** 36 (2024) 2402987.

MS5.03
Mechanisms of electron beam-induced damage in ZIF-8 MOF and its implications for *in situ* TEM studies

P. Banerjee[1], K. L. Kollmannsberger[2], R. A. Fischer[2], J. R. Jinscheck[1]

[1]Technical University of Denmark, DTU Nanolab, Kongens Lyngby, Denmark
[2]Technical University of Munich, Garching, Germany

Ultra-small, atom-precise metal nanoclusters (NCs) have gained great attention as (electro)catalysts due to their extensive surface area and abundant unsaturated active sites. However, their catalytic activity is hindered by surface ligands and a strong tendency to agglomerate. Zeolitic imidazolate frameworks (ZIFs), a subset of metal-organic frameworks (MOFs), emerge as excellent supports for NCs, offering controllable pore sizes (11.6 Å), pore apertures (3.4 Å), and high internal surface areas. Understanding the state and stability of NCs within ZIF pores under operating conditions is crucial for optimizing catalytic properties.

High-resolution TEM (HRTEM) experiments reveal that few-atom NCs are generally more stable than ZIF when exposed to electron beams. This poses challenges in studying structures like Pt_{27}@ZIF-8 nanocomposites, as ZIF-8 loses crystallinity well below the threshold for standard HRTEM imaging. The critical electron dose limit for real-time observations of ZIF-8 (and NCs@ZIF-8) under operating conditions remains unquantified, leaving these materials' structural and morphological integrity under electron beam exposure and the mechanism of crystallinity loss largely unexplored.

To address this, a systematic examination of the impact of accumulated electron dose on ZIF-8 crystallinity was conducted using selected area electron diffraction (SAED). The fading intensity of specific Bragg planes and their relative displacement were quantitatively measured as a function of total accumulated electron dose. Variables included TEM sample support (graphene vs. amorphous holey carbon) and TEM imaging parameters such as accelerating voltage (200 vs. 300 kV). ZIF-8 stability was assessed at temperatures ranging from -176°C to 550°C using a ThermoFisher Titan microscope with Gatan 626 and Inconel holders for cryo and heating experiments, respectively.

The study determined a critical accumulated dose of ~10 $e^{-}Å^{-2}$ for non-invasive structural characterization using HRTEM imaging. This provides insights into the fundamental mechanisms of electron beam-induced damage in ZIF-8. The influence of imaging conditions, substrate materials, and temperature on the critical dose was analyzed. Additionally, ZIF-8 stability under an oxygen atmosphere and elevated temperatures was investigated using a ThermoFisher Titan ETEM (300 kV) and a Gatan Inconel heating holder, with temperatures varying from 350°C to 550°C under constant O_2 pressure.

These findings have significant implications for developing NC@MOF hybrid nanocomposites in various applications, particularly catalysis. The study also addresses challenges and developments in in-situ gas experiments on beam-sensitive materials, using the ZIF-8 MOF to ZnO transformation as a reference. This comprehensive analysis provides valuable insights into the behavior of these materials under various conditions, contributing to the advancement of their applications in catalysis and related fields.

MS5.04
Pseudo-1D wave-like deformations in (Poly)-heptazine imide photocatalysts driven by sodium ion intercalation

D. Khaykelson[1], S. Cohen[2], T. Kashti[2], N. V. Tarakina[3], L. Houben[2], B. Rybtchinski[1]

[1]Weizmann Institute of Science, Chemistry, Rehovot, Israel
[2]Weizmann Institute of Science, Rehovot, Israel
[3]Max Planck Institute of Colloids and Interfaces, Potsdam, Germany

Poly)-heptazine imides (PHIs) are two-dimensional crystalline covalent organic frameworks renowned for their ability to act as photocatalysts in water-splitting reactions. Their rising prominence in green chemistry is underpinned by their sustainable catalytic properties without the need for rare metals. In this study, we unravel the intricate morphology and crystalline structure of sodium-poly-heptazine imides (Na-PHI), a PHI variant featuring Na^+ as a counterion. Employing a combination of advanced characterization techniques—including high-resolution TEM (HR-TEM), atomic force microscopy (AFM), tilted-STEM, 4D-STEM, multislice simulations, and ML based analysis—we demonstrate how Na^+ intercalation within the PHI lattice, coupled with island growth mechanisms, drives unique structural phenomena. Our findings reveal that sythesis on NaCl induces macroscopic curvature in Na-PHI films, along with Na^+ intercalation induced pseudo-1D wave-like deformations perpendicular to the stacking (001) direction, providing fresh insights into the structure–function relationships of these promising materials.

MS5.05
Chemical distribution of highly similar functional polymers from low-loss EELS signals and machine learning

J. A. Kammerer[1], F. Feist[2,3], D. Ryklin[2,4], I. Wacker[2,4], C. Barner-Kowollik[2,3,5], R. R. Schröder[2,4]

[1]Humboldt University of Berlin, Institute of Physics, Berlin, Germany
[2]3DMM2O, Cluster of Excellence, Karlsruhe, Germany
[3]Karlsruhe Institute of Technology, Institute of Nanotechnology, Karlsruhe, Germany
[4]Heidelberg University, BioQuant, Heidelberg, Germany
[5]Queensland University of Technology (QUT), Brisbane, Australia

Introduction: Complex morphologies, material combinations, and functionalization drive the advancement of organic functional materials and devices. However, similar composition and structure of the carbon-based materials manifest in a lack of contrast in most conventional imaging modalities and challenge the understanding of these materials and devices. **Objective:** To reveal the chemical distribution of functional polymers with as little compositional difference as three hydrogen atoms per repetition unit (Figure 1A), (**methods:**) we apply low-loss Electron Energy Loss Spectroscopy (EELS) and Energy Filtered Transmission Electron Microscopy (EFTEM) in combination with machine learning.[1,2]

Results: Specifically, we utilize EELS signals in the optical and UV light energy range to perform a segmentation (Figure 1C) by dimensionality reduction via Uniform Manifold Approximation and Projection (UMAP)[3] and clustering. When using the averaged spectra from this segmentation as a starting point for Multivariate Curve Resolution by Log-Likelihood Maximization (MCR-LLM),[4] we can further unmix these spectra (Figure 1D) and obtain pixelwise chemical compositions (Figure 1E). **Conclusions:** The achieved high analytical sensitivity is based on the sensitivity of the low-loss part of the EEL spectrum towards the electronic structure of the sample, rendering our workflow a potent method for the analysis of organic functional heterostructures beyond the investigated materials. Furthermore, we point out that advances in monochromation,[5] which enabled vibrational EELS carrying bond signatures, can significantly complement the obtained functional analysis with local chemical information.

References

1. J. A. Kammerer, F. Feist et al., *Advanced Materials* (2023), 2211074. https://doi.org/10.1002/adma.202211074
2. I. Wacker et al., *Advanced Functional Materials* (2023), 2302025. https://doi.org/10.1002/adfm.202302025
3. L. McInnes, J. Healy, *ArXiv180203426 Cs Stat* (2018). http://arxiv.org/abs/1802.03426
4. F. B. Lavoie et al., *Chemometrics and Intelligent Laboratory Systems*, ***153*** (2016), p. 40. https://doi.org/10.1016/j.chemolab.2016.02.006
5. O. L. Krivanek et al. *Nature*, **514** (2014), p. 209. https://doi.org/10.1038/nature13870
6. The authors acknowledge funding from the Deutsche Forschungsgemeinschaft (DFG, German Research Foundation) under Germany's Excellence Strategy for the Excellence Cluster "3D Matter Made to Order" (EXC-2082/1–390761711), by the Carl Zeiss Foundation and by the Helmholtz program "Materials Systems Engineering." J.A.K. acknowledges the Deutsche Forschungsgemeinschaft (DFG, German Research Foundation) for his WBP fellowship (DFG—500289223), and his WBP return grant (DFG—559314442). C.B.-K. additionally acknowledges continued support by the Australian Research Council (ARC) in the context of a Laureate Fellowship and support by QUT's Centre for Materials Science.

Fig. 1

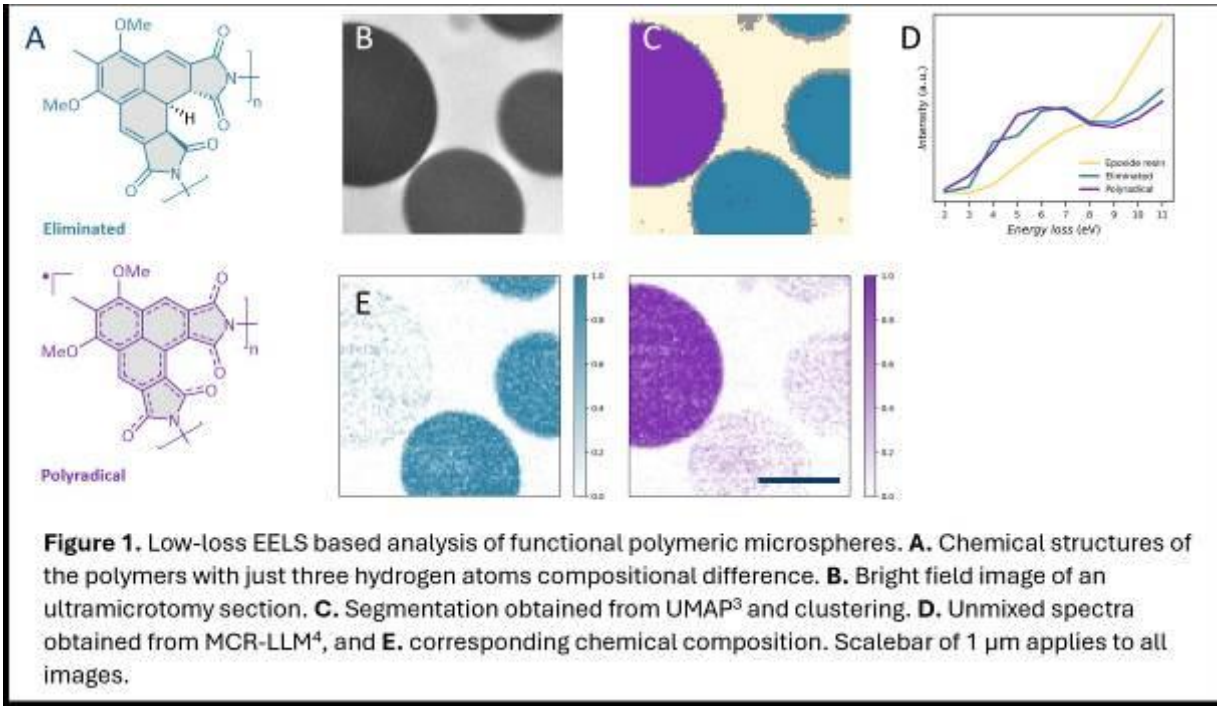


Figure 1. Low-loss EELS based analysis of functional polymeric microspheres. **A.** Chemical structures of the polymers with just three hydrogen atoms compositional difference. **B.** Bright field image of an ultramicrotomy section. **C.** Segmentation obtained from UMAP[3] and clustering. **D.** Unmixed spectra obtained from MCR-LLM[4], and **E.** corresponding chemical composition. Scalebar of 1 µm applies to all images.

MS5.06
In situ Pyrolysis of 3D printed building blocks for functional nanoscale metamaterials

Q. Sun[1], C. Dolle[1], C. Kurpiers[2], K. Kraft[1], M. Islam[3], R. Schwaiger[4], P. Gumbsch[2,5], Y. M. Eggeler[1]

[1]Karlsruhe Institute of Technology, Laboratory for Electron Microscopy, Karlsruhe, Germany
[2]Karlsruhe Institute of Technology, Institute for Applied Materials, Karlsruhe, Germany
[3]Karlsruhe Institute of Technology, Institute of Microstructure Technology (IMT), Eggenstein-Leopoldshafen, Germany
[4]Forschungszentrum Jülich GmbH, Institute of Energy and Climate Research, Jülich, Germany
[5]Fraunhofer Institute for Mechanics of Materials, Freiburg i. Br., Germany

The integration of 3D printing and pyrolysis techniques has revolutionized the fabrication of nanoscale carbon-based metamaterials with tunable properties [1]. Understanding the pyrolysis-induced structural and chemical changes in 3D-printed microstructures is crucial for precise control over their final properties [2]. However, key questions remain regarding the environmental dependencies of pyrolytic shrinkage in 3D-printed microarchitectures.

We aim to bridge this gap by exploring the real-time structural evolution of 3D printed building blocks under different atmospheric conditions, namely the laboratory high vacuum environment and industrial inert atmosphere with ambient or reduced pressure using an *in situ* heating environmental scanning electron microscope (ESEM) approach [3].

We highlight that 3D printed building block or so called microstruts were fabricated using two-photon direct laser writing (DLW) with IP-Dip photoresist directly on microelectromechanical system (MEMS)-based heating chips [3]. *In situ* isothermal pyrolysis experiments were conducted in an ESEM under high vacuum (10^{-5} mbar) and low vacuum (3 mbar with nitrogen) conditions. The heating temperatures of 450, 500, and 550 °C were determined based on two early heating experiments, as shown in Figure 1, to identify the onset of pyrolysis and morphological changes. For the first time, structural evolution was continuously monitored through secondary electron imaging (see Figure 2). A postmortem cross-sectional study was performed using scanning transmission electron microscopy (STEM) and electron energy loss spectroscopy (EELS) to examine morphology and elemental composition from the interior to the surface of the pyrolytic carbon materials.

The results reveal that shrinkage kinetics depend strongly on temperature and atmospheric conditions. By extracting the effective activation energy from pyrolysis kinetic data, we find that under high vacuum, shrinkage follows a predictable trend with an activation energy of approximately 2.6 eV. While in nitrogen atmosphere, the activation energy is much lower ranging from 0.5 to 0.9 eV, indicating different pyrolysis mechanisms. By analysing the element distribution in Figure 3, a subtle enrichment of oxygen was observed on the surface of the nitrogen-pyrolyzed samples, suggesting variations in gas-phase reactions. Furthermore, higher surface-to-volume ratios led to increased shrinkage rates in low vacuum conditions, while in high vacuum, shrinkage was more uniform across different microstrut geometries. By discussing the influence of different processing parameters, a degassing-based morphological mechanism is proposed.

As a results, this study provides critical insights into shrinkage kinetics of 3D-printed nanoarchitectures during pyrolysis. The findings pave the way to precise control and tailoring of final dimensions and resulting properties, essential for applications in carbon micro-electromechanical systems (C-MEMS).

References

[1] Y. M. Eggeler *et al.*, *Adv. Funct. Mater.* 2024, 34, 2302068.
[2] J. Bauer *et al.*, Nature Materials 15, 438-443, 2016.
[3] Q. Sun *et al.*, *Adv. Funct. Mater.* 2024, 34, 2302358.

[4] All authors acknowledge financial support by the German Research Foundation (Deutsche Forschungsgemeinschaft, DFG) under Germany"s Excellence Strategy via the Excellence Cluster 3D Matter Made to Order (EXC-2082/1-390761711).

Fig. 1

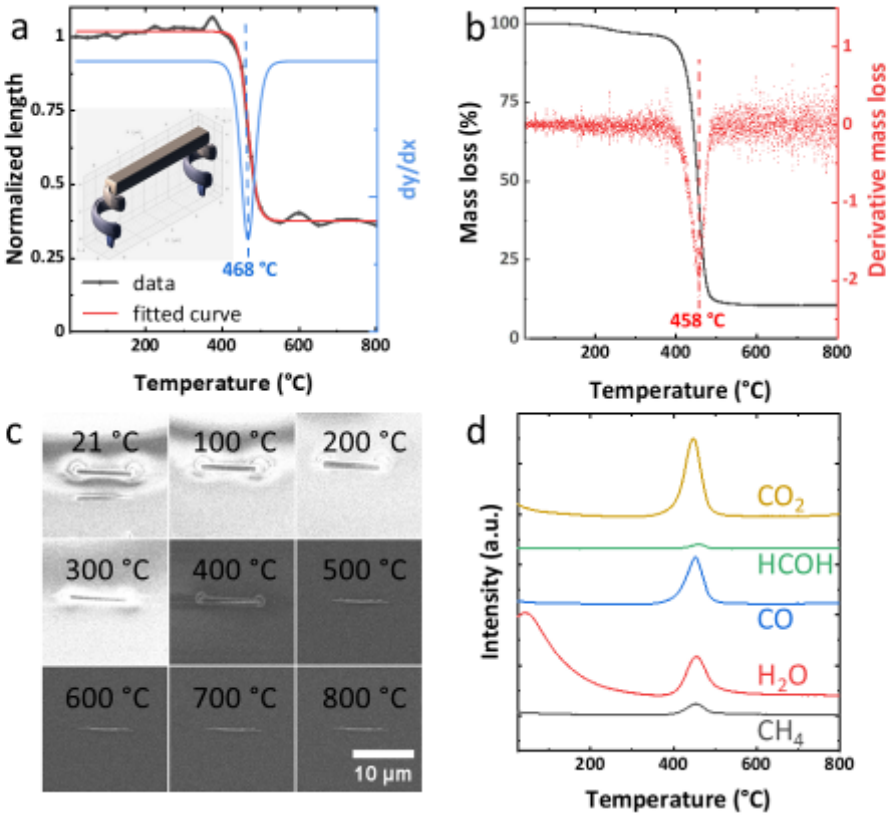


Figure 1 Two early heating experiments of IP-Dip polymer with increasing temperatures. (a) and (c) show an *in situ* he ating experiment in an ESEM with 25 °C stepwise ramping. (a) Shrinkage kinetics: the normalized length of the microst rut as a function of temperature, with the derivative curve indicating a maximum shrinkage at 468 °C. Inset in (a): the i nitial microstrut design, featuring two springs attached at both ends. (c) A selection of micrographs captured during th e heating process. (b) and (d) present thermogravimetric analysis coupled with mass spectroscopy (TGA-MS), perform ed from room temperature to 820 °C with a ramp rate of 5 °C s^{-1} in an Ar atmosphere. (b) The extreme of mass loss oc curs at 458 °C, with an onset at 385 °C. (d) In the same temperature range, pyrolysis-induced volatile byproducts such as CH_4, H_2O, CO, HCOH and CO_2 are detected. Figure adapted from [3].

Fig. 2

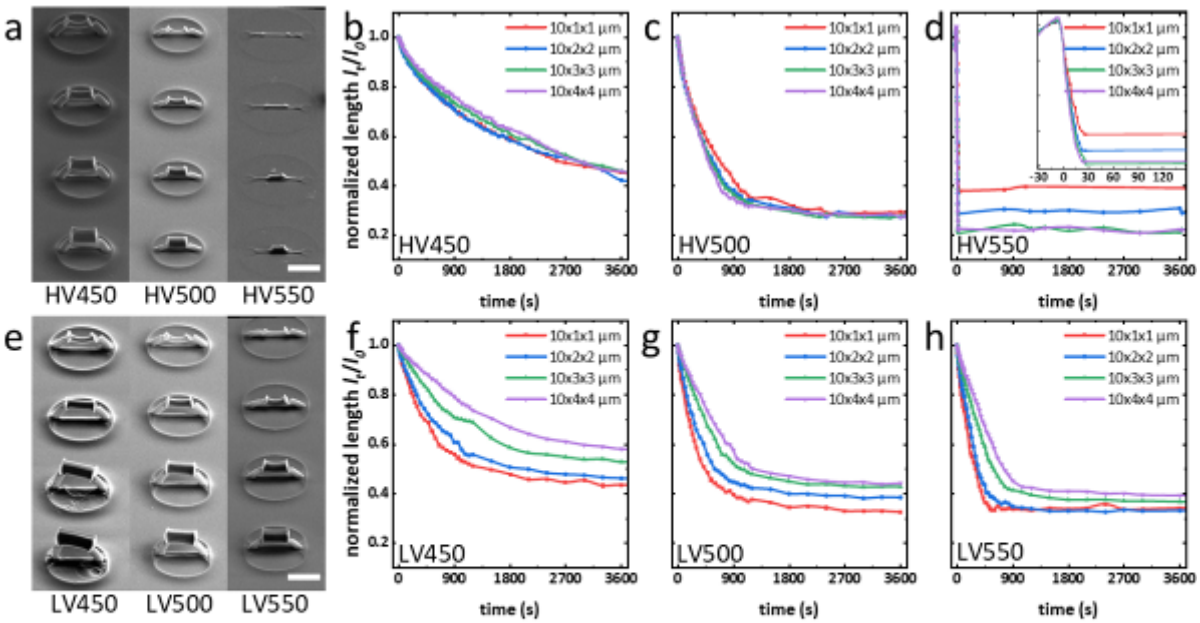


Figure 2 Comparison of microstrut shrinkage during isothermal pyrolysis under high vacuum (upper row) and low vacuum (lower row) conditions. Post-mortem micrographs of pyrolyzed microstruts at 450, 500, and 550 °C in high vacuum (a) and low vacuum (e) environments, observed from a perspective view (52°). Scale bars represent 5 µm. (b)-(d) Pyrolysis kinetics of *in situ* heating experiments in high vacuum for the three temperatures: normalized length of each microstrut with respect to heating time over one hour. (e)-(g) Corresponding pyrolysis kinetics for the *in situ* heating experiments conducted in low vacuum. Figure adapted from [3].

Fig. 3

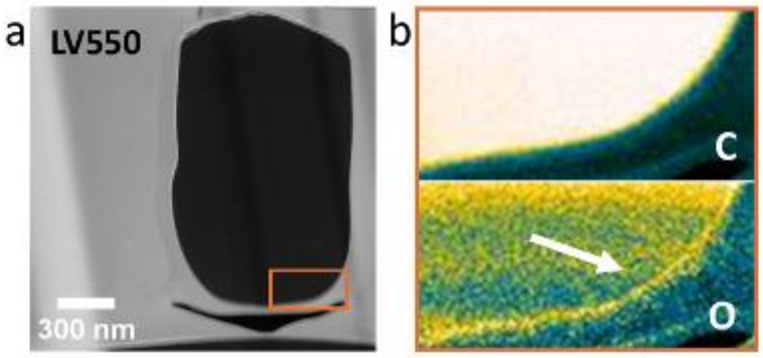


Figure 3 Cross-sectional investigation and local chemical analysis of a low-vacuum pyrolyzed microstrut at 550 °C. (a) Cross-section image of the pyrolyzed microstrut obtained through focused ion beam (FIB) lift-out technique, captured using annular dark-field scanning transmission electron microscopy (ADF-STEM). The initial dimensions of the microstrut were 10×3×3 µm. (b) Spectrum images acquired through STEM-EELS at the carbon (upper) and oxygen (lower) K edges, revealing an accumulated oxygen signal at the surface of the microstrut. Figure adapted from [3].

MS5.P01
(S)TEM-based characterization of DNA origami structures – Strategies, potentials and limitations

A. Ong[1], D. Pohl[1], T. Jeong[2,3], A. Heerwig[3], C. Hadlich[4], R. Seidel[4], M. Mertig[2,3], B. Rellinghaus[1]

[1]Technical University Dresden, Dresden Center for Nanoanalysis (DCN), Dresden, Germany
[2]Technical University Dresden, Physical Chemistry, Dresden, Germany
[3]Kurt-Schwabe-Institut für Mess- und Sensortechnik Meinsberg e.V., Waldheim, Germany
[4]Leipzig University, Peter Deybe Institute for Soft Matter Physics, Leipzig, Germany

1. Introduction

Due to their programmability and structural diversity, DNA origami nanostructures are versatile building blocks in nanotechnology [1]. Assembled from DNA strands, they mechanically robust and can be tailored for applications. A key feature of DNA origami is its high intrinsic negative charge. This makes it responsive to electric fields, enables their controlled manipulation and orientation on surfaces, and allows for their integration into electro-mechanical devices [2]. DNA origami can also be precisely folded into templates for advanced nanostructure synthesis [3, 4], enabling the products to accurately grow and replicate the template's shape.

2. Objectives

Two types of DNA origami including customized 6-helix-bundles (6HBs) [5] and 3D-DNA origami molds (3D molds) [4] are explored. Bare 6HBs, 6HBs attached to gold nanoparticles (6HB @ AuNPs), and 3D molds are investigated using (scanning) transmission electron microscopy, (S)TEM. Various (S)TEM techniques are explored for optimum visualization of these DNA origami structures.

3. Materials & methods

100 nm long 6HBs were synthesized by scaffolded self-assembly [5]: Long ssDNA (part of a *M13mp18*) is folded by oligonucleotides, partially extended by ssDNA, whose sequence is complementary to that on the AuNP-surface. 3D molds were synthesized from single-stranded scaffold DNA, followed by one-pot assembly reaction [4].

Ex-situ (S)TEM and in-situ liquid phase (S)TEM (LP-(S)TEM) were conducted on a *JEOL F-200* microscope at 200 kV. For LP-(S)TEM investigations, a *Protochips Poseidon Select* holder was used to keep the samples in a liquid environment that is sealed with SiN membranes against the high vacuum of the liner tube.

4. Results

Imaging 6HBs using (S)TEM is challenging due to the low atomic number of DNA components. Different imaging modes including TEM, defocused TEM (Fig. 1(a)) and STEM (Fig. 1(b)) were compared for visualizing negatively-stained 6HBs. Defocused TEM and STEM images are found to provide for enhanced contrast, thus enabling quantitative analyses.

Defocused TEM images (Fig. 2) confirm the attachment of 6HBs to AuNPs (d = 20nm). Statistical analyses reveal different length distributions for the 6HBs in their original state (94 nm) and after attaching them to AuNPs (69 nm). The shorter apparent length of the 6HBs when attached to AuNPs suggests that part of the 6HBs is obscured by the AuNPs or undergo bending along the z-axis.

Negatively stained 3D molds were imaged (Fig. 3(a)) to confirm their structural integrity. Unstained 3D molds were examined using TEM, defocused TEM, and STEM (Fig. 3(b)). The latter is identified as the optimal imaging technique as it provides for optimized contrast.

5. Conclusion

Defocused TEM and STEM imaging are found to allow for optimized visualization and quantitative analysis of 6HBs and 3D DNA origami molds. Effects of varying microscope parameters such as the camera length are discussed.

Financial support by DFG through RTG 2767 and EU"s Horizon 2020 Program (grant #964248) is acknowledged.

[1] P.W.K. Rothermund, Nature 440 (2006) 297.

[2] F. Kroener et al., J. Am. Chem. Soc. 139 (2017) 16510.

[3] J. Zessin et al., Nano Lett. 17 (2017) 5163.

[4] S. Helmi et al., Nano Lett. 14 (2014) 6699.

[5] A. Heerwig et al., Phys. Stat. Sol. A. 215 (2018) 1700907.

Fig 1. Negatively stained 6HB in (a) defocused TEM and (b) STEM mode.

Fig 2. Defocused TEM of 6HB@AuNPs.

Fig 3. STEM of (a) stained and (b) unstained 3D DNA molds.

Fig. 1

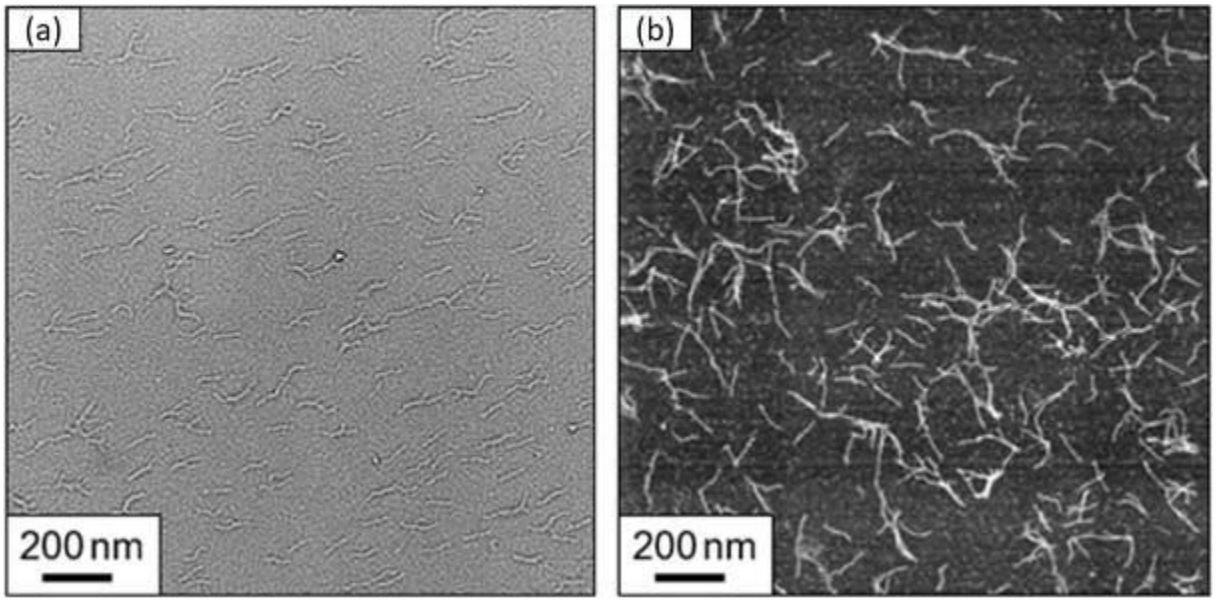


Fig. 2

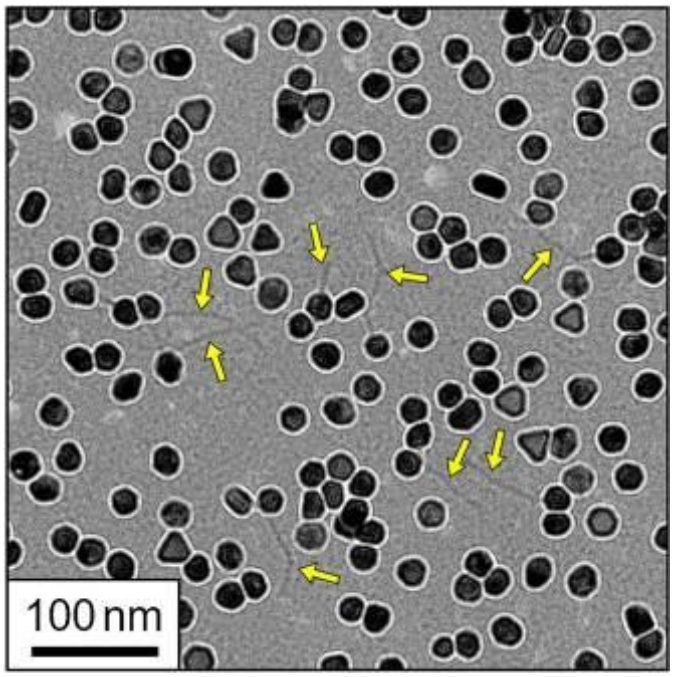
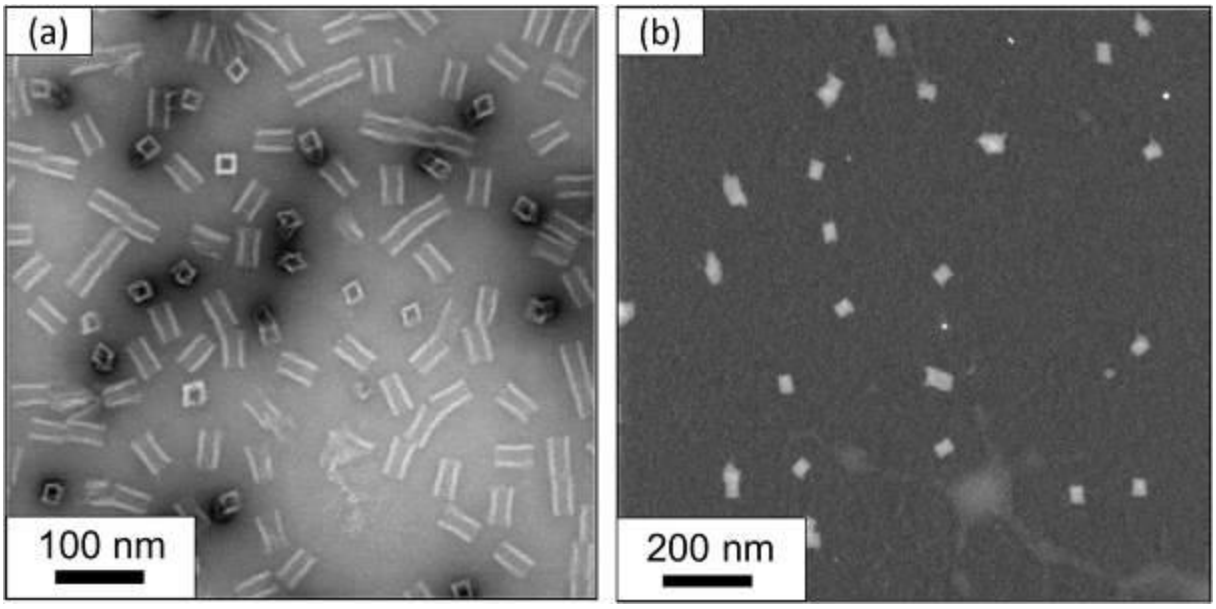


Fig. 3



MS5.P02
Ultrastructural analysis of hydrogels – Avoiding the macropore trap

I. Wacker[1], R. Curticean[1], W. Wagner[2], S. J. Mentzer[3], P. Mainik[4], T. Spratte[4], C. Selhuber-Unkel[4], E. Blasco[4], R. R. Schröder[1]

[1]Heidelberg University, BioQuant, Heidelberg, Germany
[2]Universitätsklinikum Heidelberg, Department of Diagnostic and Interventional Radiology, Heidelberg, Germany
[3]Harvard Medical School, Laboratory of Adaptive and Regenerative Biology, Boston, MA, United States
[4]Heidelberg University, Institute for Molecular Systems Engineering and Advanced Materials, Heidelberg, Germany

Correlation between functional properties of hydrogels and their morphology is often complemented by SEM images showing so-called "macropores" [1]. Upon examining the preparation route leading to such data it becomes clear that there must be a problem: The usually employed "flash freezing" – dumping millimeter-sized objects into liquid nitrogen - followed by lyophilization is hardly adequate to preserve the structural information of such delicate, highly hydrated samples. A thorough analysis of different cryo-preparation routes for cryo-SEM imaging was carried out on the matrix morphology of alginate hydrogels [2]. Depending on the freezing method, pore sizes varied by two orders of magnitude, from micropores (tens of nanometers) to macropores (micrometers). Even with high pressure freezing (HPF), the gold standard for analysis of cells and tissues, pore sizes were slightly different between central and peripheral sample locations. Since hydrogels are often used as scaffolds for 3D cell or organoid cultures HPF may not be a productive option: Limitation of the sample size that can be vitrified (ca 2x2x0.2 mm) and the need for rather sophisticated equipment hamper its utilization e.g. in high throughput screening experiments.

We therefore sought to develop an alternative, easily accessible workflow for preparation of both, bio-derived and synthetic hydrogels. One approach – used in the early days of cryo-preparation – is the replacement of freely diffusible water. This can be done by a number of reagents either leading to a gentle dehydration or preventing formation of ice crystals during suboptimal freezing.

We tested partial dehydration by low concentrations of ethanol (15% -40%) or tannic acid (0.2% -5%) on a number of different hydrogels, such as polyacrylamide (PAM) and Poly(N-isopropylacrylamide) (pNIPAM) hydrogels, pectin from different plant sources, and 2-photon-printed collagen scaffolds. After staining with OsO4 and further dehydration, samples were either lyophilized or air-dried for bulk analysis of fracture faces or resin embedded for ultramicrotomy and analysis of ultrathin sections.

Macropore formation is prevented by treatment of synthetic hydrogels with tannic acid before lyophilization as shown in figure 1. Fracture faces (Fig1 A, C) or ultrathin sections from resin-embedded samples (Fig. 1 B, D) show pore sizes below 100 nm. For pectin films a limited hydration with ethanol produced different morphological signatures – a more globular appearance for potato pectin (Figure 2A, B) or a highly branched network of carbohydrate chains for orange pectin (Figure 2C, D).

We have shown that partially hydrated hydrogels can be processed for ultrastructural analysis without the danger of artificial macropore formation. An additional asset of tannic acid incorporated into hydrogels as stabilizer is the fact that it readily reacts with OsO4. That helps to create contrast and combat charging even in hydrogels without reactive groups for binding of Osmium such as PAM, pNIPAM or the carbohydrate-based pectin films.

[1] Wen J. et al. Nature Mater 13, 979–987 (2014) https://doi.org/10.1038/nmat4051
[2] Aston R. et al. Eur Polym J 82, 1 (2016) https://doi.org/10.1016/j.eurpolymj.2016.06.025
[3] Research funded by DFG via the Excellence Cluster "3D Matter Made to Order" (EXC-2082/1-390761711) and by BMBF under Grant No. 13N14476.

Fig. 1

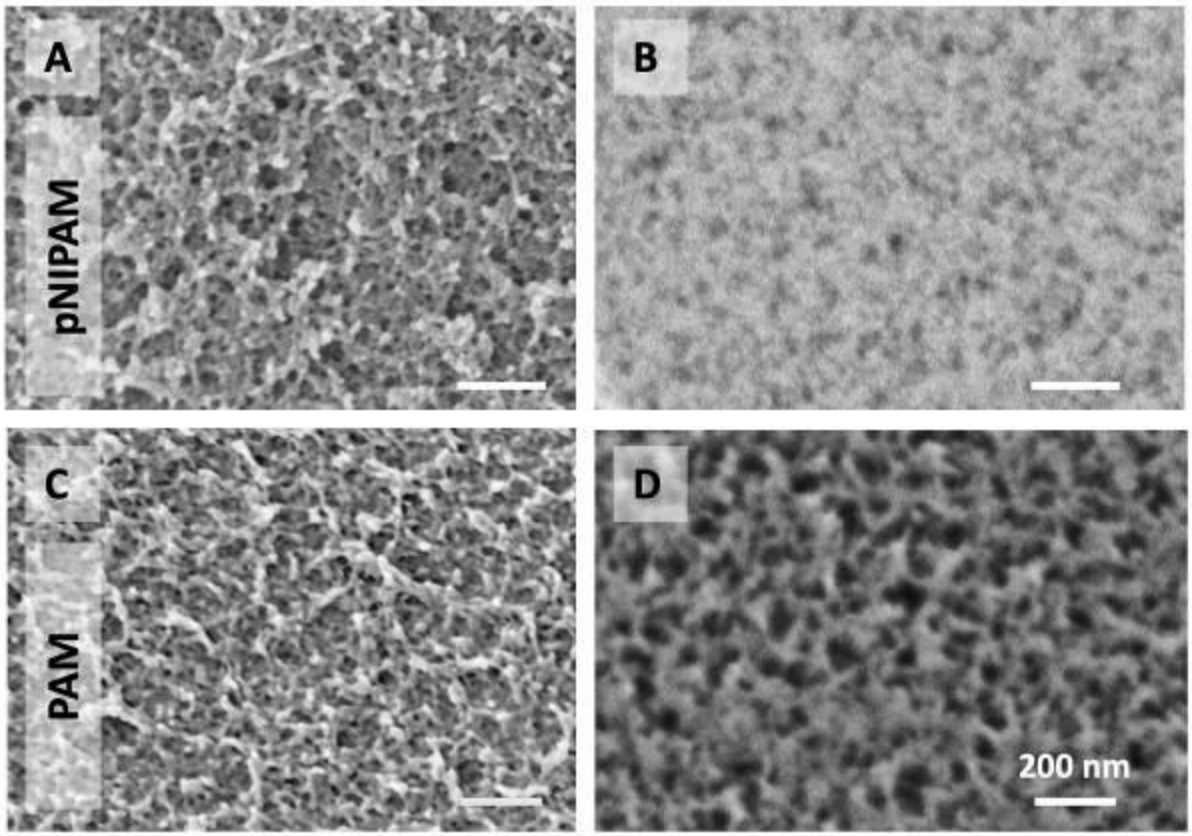


Figure 1 Ultrastructure of synthetic hydrogels. pNIPAM (A, B) or PAM (C, D) were treated with tannic acid and OsO_4, then either plunge frozen and lyophilized (A), air dried (C) or dehydrated with ethanol and acetone and embedded in Epon resin (B, D). Fracture faces, sputtercoated with PtPd (A, C) or 80nm thick sections (B, D) were imaged in an SEM. All scale bars 200 nm

Fig. 2

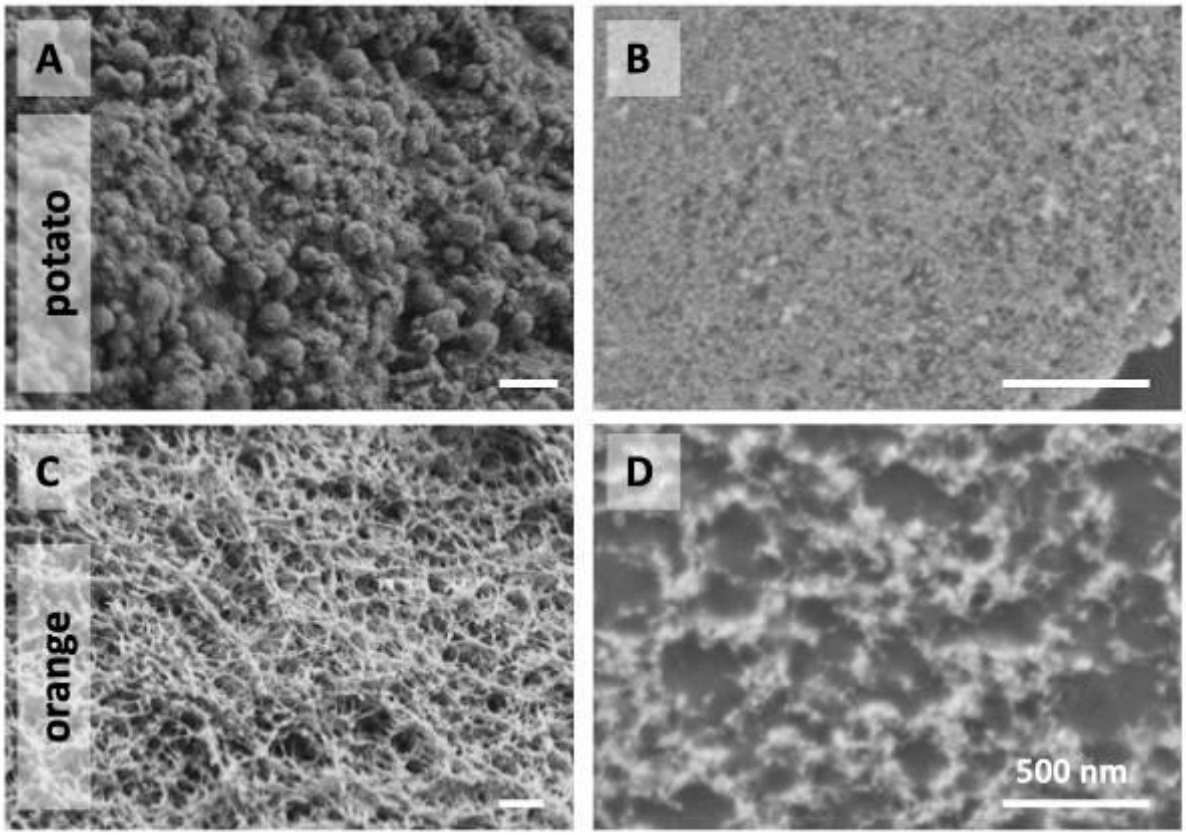


Figure 2 Ultrastructure of bio-derived hydrogels. Films fabricated from potato (A, B) or orange (C, D) pectin were treated with 40% (A, B) or 15% (C, D) ethanol and Ruthenium Red, followed by OsO_4, dehydrated with ethanol and acetone and either air dried (A, C) or embedded in Epon resin (B, D). Fracture faces (A, C) or 80nm thick sections (B, D) were imaged in an SEM. All scale bars 500 nm

MS5.P03
Nanoscale characterization of enzyme-MOF nanocomposites using advanced electron microscopy

S. Talebi Deylamani[1,2], Z. Bognar[2], P. Banerjee[1], G. di Palma[1], S. Helveg[2], J. R. Jinscheck[1,2]

[1]Technical University of Denmark, Nanolab - National Centre for Nano Fabrication and Characterization, Kongens Lyngby, Denmark
[2]Technical University of Denmark, Center for Visualizing Catalytic Processes, Kongens Lyngby, Denmark

Improving enzyme stability and long-term performance by trapping and immobilizing enzymes into support has gained significant attention, with metal-organic frameworks (MOFs) emerging as promising material for this application [1]. MOFs are advanced porous crystalline materials with very high chemical and thermal stability that find applications in separation technologies, gas storage, catalysis, and drug delivery. Their flexible architecture provides opportunities to design more suitable structures with specific functionalities for developing enzyme-MOF nanocomposites. The application of MOFs as enzyme support offers a promising strategy to enhance enzyme immobilization, stability and reusability in biocatalytic applications. However, precisely controlling enzyme distribution within MOFs and understanding enzyme-MOF interactions at the nanoscale remain major challenges [2]. Structural investigations using advanced electron microscopy techniques could therefore provide valuable insights into the complex structure of enzyme-MOF nanocomposites and reveal how structural modifications affect overall functionality.

Herein, a correlative study using X-ray-, electron-based imaging and spectroscopy methods was performed to gain a comprehensive understanding of how synthesis condition and enzyme concentrations can contribute to the distribution of enzymes in MOF crystals. In detail, by establishing correlations between the synthetic conditions of MOF with varying amounts of enzyme and loading strategies, we aim to understand how these parameters can affect the distribution of enzymes in the MOF crystal without compromising the structural integrity. We systematically synthesis the enzyme-MOF nanocomposite with different concentrations of enzymes and different immobilization strategies. For detailed structural characterization, Fourier-transform infrared spectroscopy (FTIR), scanning electron microscope (SEM), and X-ray diffraction (XRD) were used to confirm the incorporation of enzyme within the MOF crystal. Low-dose high-resolution scanning/transmission electron microscopy (S/TEM) techniques provide insight into the localization and the distribution of enzymes at the nanoscale. In addition, energy-dispersive X-ray spectroscopy (STEM-EDS) further elucidated the presence of immobilized enzymes within the MOF crystal.

Our results demonstrate that precise control over MOF morphology and enzyme concentration can significantly affect the enzyme distribution and arrangement within the MOF crystal. By unravelling the structural and chemical interactions between enzymes and MOFs using electron microscopy techniques, crucial insights into immobilization efficiency and stability have been gained. Our findings will contribute to a better understanding of rational design of functional enzyme-MOF nanocomposites, paving the way for more efficient and robust biocatalysts.

1. Wang, Xiaoliang, Pui Ching Lan, and Shengqian Ma., ACS Central Science (2020),6, 1497-1506. https://doi.org/10.1021/acscentsci.0c00687
2. R. Dhaoui, S. L. Cazarez, L. Xing, E. Baghdadi, J. T. Mulvey, N. S. Idris, P. J. Hurst, M. P. Vena, G. Di Palma and J. P. Patterson, Adv Funct Mater (2024), **34**, 2312972. https://doi.org/10.1002/adfm.202312972
3. The authors acknowledge support by the Novo Nordisk Foundation (Grant no. NNF21OC0072844 and NNF22SA0078767). DTU VISION was supported by the Danish National Research Foundation (DNRF146).

MS5.P04
In situ TEM insights into graphitization driven by metal-based catalysts

C. Chemin[1], P. Murugesan[1], M. Vadmand Adelmark[1], B. Rezaei[1], A. I. Bunea[1], S. Sylvest Keller[1], A. Bastos da Silva Fanta[1], T. W. Hansen[1]

[1]Technical University of Denmark, Nanolab - National Centre for Nano Fabrication and Characterization, Kongens Lyngby, Denmark

Pyrolytic carbon, with its excellent physical, chemical and electrochemical properties, is promising for applications in energy storage, electronics and biomedical technologies [1]. It can be obtained by heating a polymeric carbon precursor to high temperatures in inert atmospheres. While process parameters such as heating rate, dwell duration as well as cooling time significantly influence the final material properties, achieving well-defined graphitic domains typically requires high temperatures and extended dwell times [2], leading to considerable energy consumption [3].

In this work, we investigate catalyst-driven graphitization as a strategy to reduce the energy required for structural ordering in pyrolytic carbon.

Suspended polymer thin films are patterned on TEM heating chips by two-photon polymerization (2PP) 3D printing, followed by catalyst addition for *in situ* TEM graphitization studies. The optimized polymer thin film design, a suspended ribbon with a central through-hole (Fig. 1a), enables *in situ* TEM analysis of catalyst-driven graphitization [2]. The 700 nm-thick central ring (dark grey) is optimized for TEM imaging (Fig. 1d-f), while the 900 nm-thick surrounding ribbon (light grey) enhances structural stability. The 2PP process is optimized for High Temperature Yellow 5 (HTY5), a commercial resin from Boston Micro Fabrication (Fig. 1b-c). The catalyst is added by drop casting a solution of ferric chloride hexahydrate ($FeCl_3 \cdot 6H_2O$) on 2PP printed polymer structures. The structures are pyrolyzed in a furnace to a maximum temperature of 900°C for 3 hours.

Our tests confirmed that TEM chips are compatible with the salt immersion, as the chip contacts remained fully functional. To optimize catalyst addition and minimize TEM chip use, we introduced test structures printed on test chips. Scanning electron microscopy (SEM) analysis confirmed that the ribbon and hole are well-defined before (Fig. 2a-b) and after catalyst addition and pyrolysis (Fig. 2c-d). Energy-dispersive x-ray spectroscopy (EDS) mapping (Fig. 2e) revealed a homogeneous distribution of iron on the carbon structure, indicating successful iron impregnation. Finally, we conducted TEM imaging on a 3D-printed sample infused with iron precursor. We use a test chip with a suspended silicon nitride membrane and patterned holes, suitable for TEM imaging (Fig. 3a). Figures 3b and 3c show iron nanoparticles nearly encapsulated by graphitic carbon rings (Fig. 3d), confirming their catalytic activity.

Overall, these preliminary results show great potential to conduct *in situ* TEM studies of catalyst driven graphitization, using 2PP printed structures followed by iron precursor impregnation.

[1] M. Fu et al., Mater. Chem. Front. 5 (2021) 2320-2327

[2] C. Chemin et al., Nano Today 59 (2024) 102524

[3] S. Sharma et al., Sci. Rep. 8 (2018) 16282

Figure 1: a) 3D design of the ribbon. SEM micrographs of the ribbon: b) before and c) after pyrolysis. d) Pyrolysis profile. e) to f) TEM micrographs during the pyrolysis, showing the evolution of graphitization.

Figure 2: SEM micrographs of polymer: a-b) before pyrolysis, c-d) post catalyst addition and pyrolysis. e) EDS map showing the homogeneous distribution of iron (Fe).

Figure 3: a) SEM micrograph of 2PP printed structure post catalyst addition and pyrolysis. b-c) TEM image showing iron nanoparticles encapsulated in graphitic rings, with d) line scan showing the characteristic inter layer distance of graphite, 3.3Å.

Fig. 1

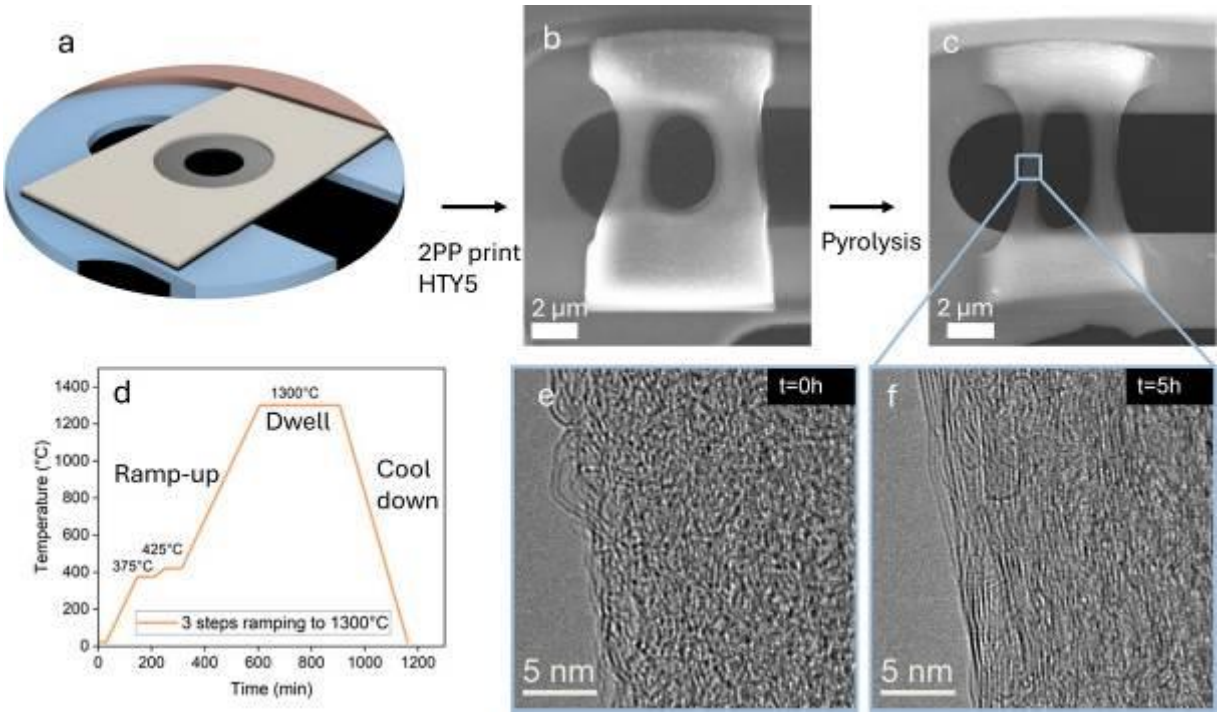


Fig. 2

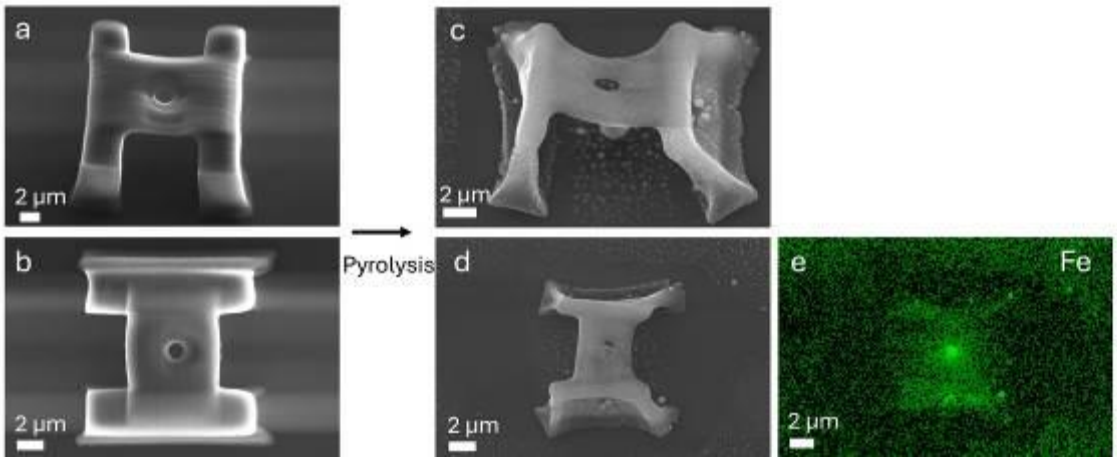
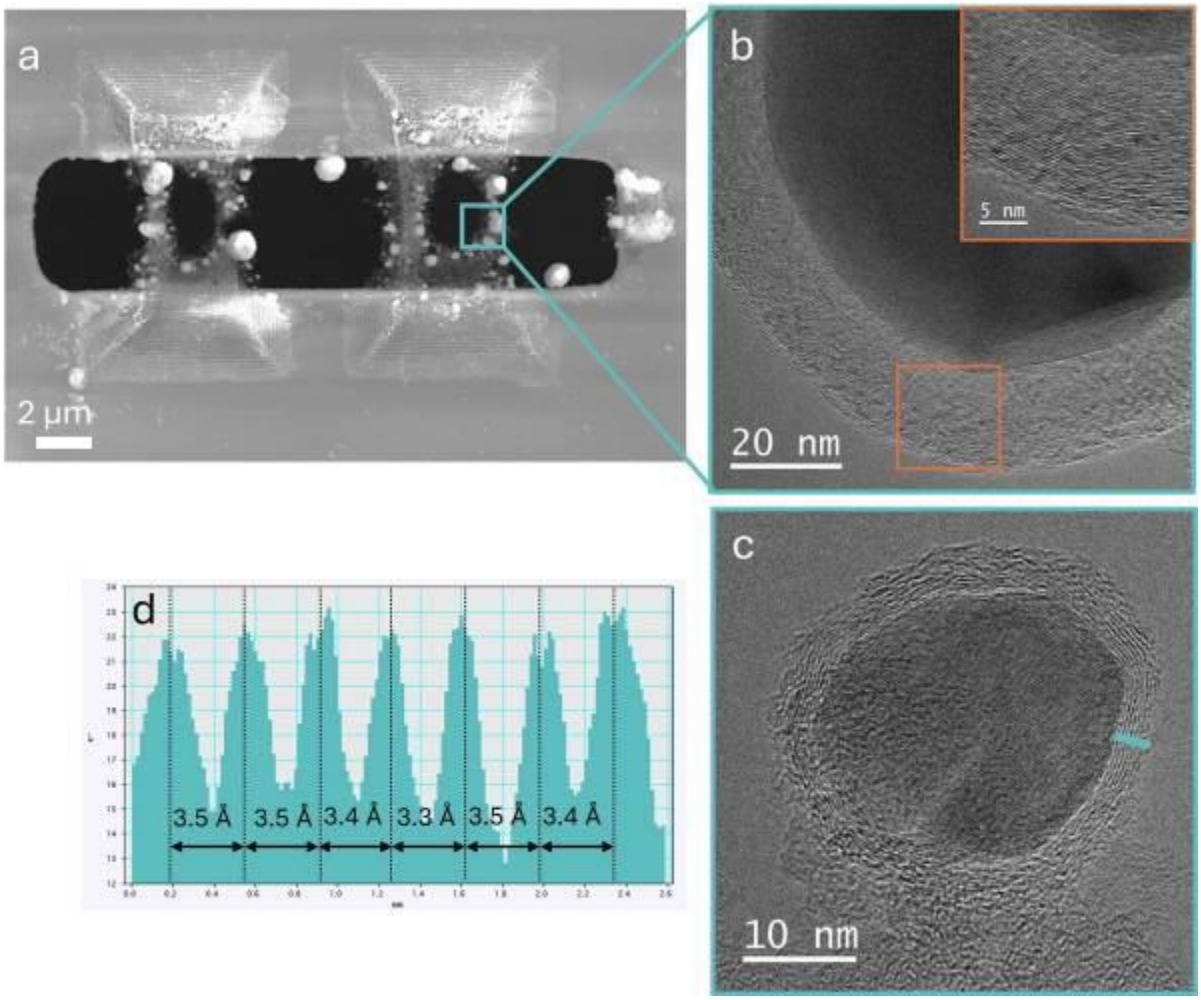


Fig. 3



MS5.P05
Swelling and de-swelling behavior of thermo-responsive polymers at phase transition

J. Michalska-Walkowiak[1], B. Förster[2], S. Hauschild[3], S. Förster[1,3]

[1]Forschungszentrum Jülich GmbH, JCNS-4, Jülich, Germany
[2]Forschungszentrum Jülich GmbH, ER-C-1, Jülich, Germany
[3]Forschungszentrum Jülich GmbH, JCNS-1, Jülich, Germany

Poly(isopropyl acrylamide) (PNIPAM), as a thermoresponsive polymer can change its state by varying the temperature across the phase transition temperature. PNIPAM-based polymers, with broad hysteresis for the volume phase transition between the swollen and de-swollen state, showed atypical behavior, such as bistability, remanence, write-read information storage, and memory function. The polymer behavior across the transition point and the long stability of swollen or collapsed polymer clusters at the temperature range of the hysteresis was investigated in detail by scattering and electron microscopy techniques.

The phase transition from swollen to collapsed state, and reverse, was studied by cryo-TEM imaging. Samples were prepared across the transition point with a small temperature step. The temperature of the solution and the grids during preparation was controlled inside the Vitrobot's climate chamber using the internal temperature controller and an additional temperature controller installed near the grid. When the temperature in the climate chamber was stable, the polymer solution was applied to the grid, then blotting and vitrification were proceeded. To measure hysteresis, great care must be taken not only with temperature control but with the direction of heating and cooling.

Our findings show that information can be thermally written on the polymer"s solution using a heated/cooled metal pen tip or laser pulse and stored intact for a long time. Furthermore, memory function was observed for the first time in the case of the PNIPAM-based polymer solutions. Broadening the application of this polymer allows a better understanding of the phase transition of stimuli-responsive polymers.

References:

J.Michalska-Walkowiak, B. Förster, S. Hauschild, S. Förster, Bistability, Remanence, Read/Write-Memory, and Logic Gate Function via a Stimuli-Responsive Polymer. *Adv. Mater.* 2022, 34, 2108833. https://doi.org/10.1002/adma.202108833

MS5.P06
TEM analysis of Porphyrin-Based 2D polymer films synthesized at the Air-Liquid interface

J. Belz[1], O. Maßmeyer[1], M. Bergmann[1], S. Kachel[1,2], A. Beliakouskaya[2], J. Herritsch[2], M. Gottfried[2], K. Volz[1]

[1]Philipps-University Marburg, Department of Physics & Structure & Technology Research Laboratory, Marburg, Germany
[2]Philipps-University Marburg, Department of Chemistry, Marburg, Germany

The synthesis of high-quality crystalline 2D conjugated polymer thin films (2DCPs) remains a key challenge in chemistry, requiring precise control over monomer assembly and polymerization. The liquid-interface growth strategy offers significant advantages over conventional solid-state synthesis, including minimized defect formation, enhanced crystallinity, and controlled molecular orientation [1]. The resulting conjugated polymer network exhibits a highly ordered structure, with promising applications in optoelectronics, catalysis, and molecular sieving [2]. Our findings provide new insights into interfacial polymerization mechanisms, contributing to the fundamental understanding of nanoscale film formation and structure-property relationships in 2D conjugated systems.

In this study, we focus on the surfactant-assisted liquid-interface polymerization of 5,10,15,20-tetrakis(4-aminophenyl)-21H,23H-porphyrin (TAPP) and 2,5-dihydroxyterephthalaldehyde (DhTAPDhTPA), forming an extended porphyrin-based 2D polymer across the liquid surface. Our TEM investigations span from (energy-filtered) conventional high-resolution TEM and electron diffraction to advanced techniques such as scanning nanobeam diffraction (sNBD), which, in combination with optimized and relaxed DFT supercell calculations, enables orientation mapping and structure determination using the Py4DSTEM package [3].

Additionally, we employ confocal Raman spectroscopy alongside DFT-based Raman calculations and electron energy loss spectroscopy (EELS) to investigate the chemical structure of the 2D polymer network. These methods support our observations of differences between experimental and simulated electron diffraction patterns (c.f. Figure 1).

Careful dose and exposure settings allowed successful measurements at 300 kV, though lower acceleration voltages and cryogenic temperatures could further improve material stability during STEM analysis. Nonetheless, we can show that diffractive imaging using sNBD and dose mitigation can help retain the pristine state of the material. We find that most synthesis runs show polycrystallinity (c.f. Figure 2) indicating a seed based nucleation similar to the observations of Qui et al. [4]. Our findings establish TAPP as a valuable model system for the wide field of 2DCPs, highlighting the challenges of analyzing such films.

This work lays the foundation for systematic quantitative investigations of 2D polymers synthesized at liquid-air interfaces via different approaches. Moreover, we show a workflow compatible with a systematic analysis of advanced functionalization studies, such as the incorporation of metal ions into the porphyrin structure, which provides a controlled method to tailor electronic properties.

References:

[1] H. Sahabudeen et al., Angew. Chem. Int. Ed. Engl., 59, 6028–6036 (2020).

[2] G. Fu et al., Adv. Mater., 36, 2311541, (2024).

[3] B.H. Savitzky et at., Microsc. Microanal., 27(4), 712−-743 (2021).

[4] H. Qi, et al., Sci. Adv., Vol. 6, No. 33 (2020).

Figure 1: a) Diffraction pattern generated from a DFT-relaxed supercell of the porphyrin-based 2D polymer and b) the corresponding diffraction pattern from selected area diffraction using TEM.

Figure 2: Orientation mapping highlighting the polycrystallinity of the film and its orientation. Each grain is shown in a different color based on its relative rotation. On the right side an averaged scanning nano-beam diffraction pattern and its corresponding location is shown.

Fig. 1

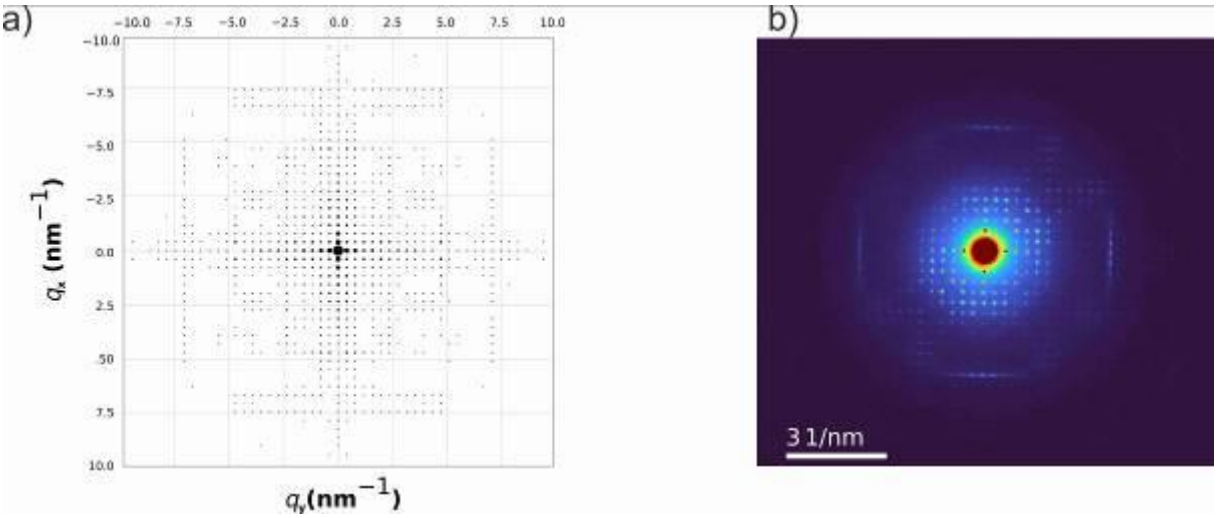
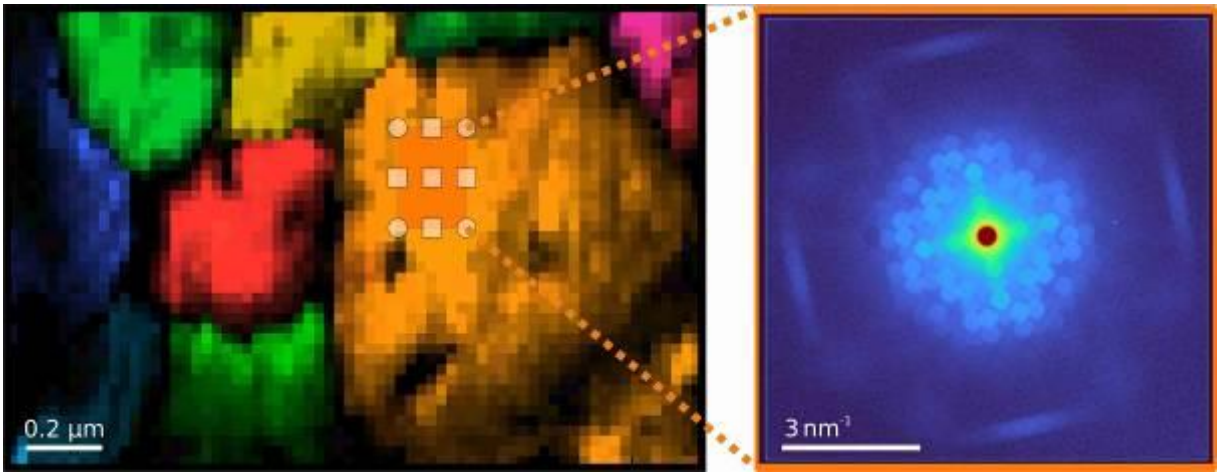


Fig. 2



MS5.P07
Investigation of SWCNT films by combined scanning electron microscopy (SEM) and atomic force microscopy (AFM)

M. Magg[1], T. Scherer[1], B. Flavel[1]

[1]Karlsruhe Institute of Technology, Institute of Nanotechnology, Eggenstein-Leopoldshafen, Germany

Single-Walled Carbon Nanotubes (SWCNTs) have been extensively studied as semiconductor materials for field- effect transistors owing to their excellent electron transport properties.[1]Nowadays, solution-based sorting techniques are available to separate semiconducting from metallic SWCNTs, e.g. by aqueous two phase separation (ATPE) or polymer-wrapping in Toluene solution.[2][3]Recently, precipitation by polymethacrylic acid (PMAA) has been shown to produce SWCNT dispersion with uniform length.[4] While these methods already constitute significant improvements to the performance of the devices, challenges remain with regard to the organization of CNTs into high density thin films over a large area. [5]In our contribution, we study films of semiconducting and metallic Carbon Nanotubes using a Nenovision Litescope, which combines scanning electron microscopy (SEM) with atomic force microscopy (AFM). Conductive maps are obtained by application of a bias voltage between the tip and the sample providing spatially resolved information. In addition we investigate the effect of encapsulation of redox active inorganic clusters inside the Carbon Nanotubes on the conductive maps.

References

[1] M. D. Bishop, G. Hills, T. Srimani, C. Lau, D. Murphy, S. Fuller, J. Humes, A. Ratkovich, M. Nelson, M. M. Shulaker, *Nat Electron* 2020, *3*, 492–501.

[2] H. Li, G. Gordeev, O. Garrity, N. A. Peyyety, P. B. Selvasundaram, S. Dehm, R. Krupke, S. Cambré, W. Wenseleers, S. Reich, M. Zheng, J. A. Fagan, B. S. Flavel, *ACS Nano* 2020, *14*, 948–963.

[3] A. Graf, Y. Zakharko, S. P. Schießl, C. Backes, M. Pfohl, B. S. Flavel, J. Zaumseil, *Carbon N Y* 2016, *105*, 593–599.

[4] P. Shapturenka, B. K. Barnes, E. Mansfield, M. M. Noor, J. A. Fagan, *RSC Adv* 2024, *14*, 25490–25506.

[5] C. Rust, H. Li, G. Gordeev, M. Spari, M. Guttmann, Q. Jin, S. Reich, B. S. Flavel, *Adv Funct Mater* 2022, *32*, DOI 10.1002/adfm.202107411.

MS5.P08
Determining the distribution of the different carbon based nano phases in the photoactive layer of semitransparent organic solar cells

K. Märkle[1,2], Y. Chen[1], S. Coen[1], E. Müller[2], Y. M. Eggeler[2], C. Sprau[1]

[1]Karlsruhe Institute of Technology, Light Technology Institute, Karlsruhe, Germany
[2]Karlsruhe Institute of Technology, Laboratory for Electron Microscopy, Karlsruhe, Germany

The narrow absorption range of organic semiconductors enables high semitransparency of organic solar cells (OSCs) in the visible spectrum. This property opens up a wide range of photovoltaic applications, such as in agricultural land, also referred to as agrivoltaics. Typically, the active layer of OSCs consists of an interpenetrating network of donor and acceptor materials known as a bulk heterojunction. The effective separation of carriers at the interfaces between the donor and acceptor materials and their subsequent transport to the electrodes is crucial for device performance. Therefore, the size and distribution of the material phases are essential to achieve a high power conversion efficiency.

For large-scale fabrication, transparent fillers are incorporated into the photoactive layer to increase its thickness and enable defect-free deposition. However, this additional component has a significant impact on the morphology. The aim is to use and develop advanced electron microscopy methods and sample preparation, which allow us to distinguish the different carbon-based nanoscale phases from each other and develop an understanding of the morphologies.

The material system investigated in this study consists of PTQ10 as the donor material and BTP-FTh as the acceptor material. This combination has a suitable absorption spectrum for semitransparency in agrivoltaic applications. The topography of the bulk heterojunction layer can be studied by AFM, see figure 1(a). However, this does not allow any information regarding material contrast. Due to the close density of the individual carbon-based material components within the photoactive layer, the method of low-energy STEM for high sensitive material contrast is applied[1]. For the measurements, the photoactive layer with a thickness of around 100 nm was deposited on a water-soluble layer of PEDOT:PSS by spin coating. The photoactive layer can then be transferred to a TEM grid by dissolving the layer of PEDOT:PSS with a drop of water. In a BF-STEM image at 15kV, see fig. 1(b), strongly defined features with high brightness can be observed. These already indicate a potential material contrast. In order to further reduce the influence of the topography, additional sample cross-sections are to be produced using ultramicrotomy for further investigations. This method should also enable the investigation of other material systems with additional filler materials within the photoactive layer.

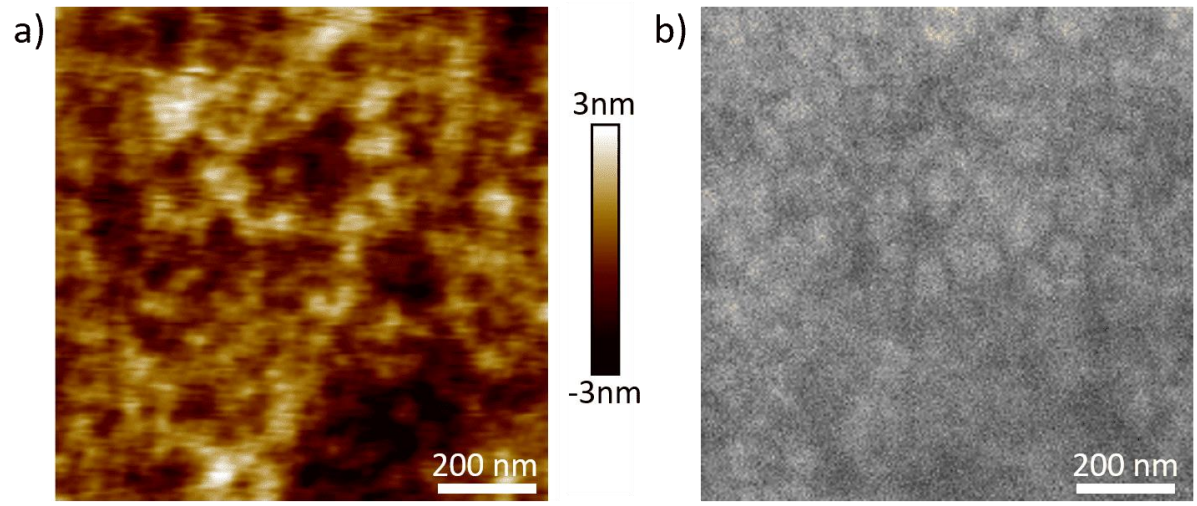
The morphological investigation of the photoactive layer in semitransparent OSCs is essential to understand the effect of the additional filler material, such as polystyrene, on the morphology and therefore also the functionality. In this work, the method of low-energy STEM on suitable electron transparent samples will be applied to enable a material contrast within the bulk heterojunction. The study of the morphology will enable the optimization of transparent solar cells suitable for large-scale fabrication.

References: [1] M. Pfaff, et al. *Microscopy and Microanalysis* 18.6 (2012): 1380-1388.

Acknowledgements: This research was supported by the German Federal Environmental Foundation (Deutsche Bundesstiftung Umwelt - DBU) through the DBU Ph.D. scholarship program and by the Vector Foundation through the young investigator group program.

Figure 1: Comparison of (a) the topography measured with the AFM and (b) a low-energy BF-STEM image at 15 keV of a thin film of PTQ10:BTP-FTh.

Fig. 1



MS 6: Ceramics, composites and geoscience – In memory of Achim Kleebe

MS6.01(inv)
Intergranular glassy films in silicon nitride – A tribute to Achim Kleebe

I. Tanaka[1]

[1]Kyoto University, Materials Science and Engineering, Kyoto, Japan

Achim Kleebe"s pioneering contributions to the understanding of intergranular glassy films (IGFs) in ceramics have left a profound impact on the field of electron microscopy. My talk will revisit the collaborative research conducted with Achim during my stay as an Alexander von Humboldt Fellow at the Max Planck Institute for Metal Research in Stuttgart (1992–1993). Under Kleebe"s leadership within Manfred Rühle"s group, extensive high-resolution electron microscopy (HREM) studies were undertaken to explore the grain boundary characteristics of silicon nitride ceramics.

Kleebe"s seminal works [1, 2] demonstrated that silicon nitride ceramics exhibit uniform IGFs with thicknesses ranging from 5 to 15 Å, maintaining remarkable consistency across grain boundaries regardless of the crystal orientation, with variations within ±1 Å. My own research [3] complemented these findings by producing additive-free silicon nitride ceramics via hot isostatic pressing (HIP), achieving high purity with minimal impurities aside from 1.3wt% oxygen in the starting powders.

Using HREM, we confirmed the presence of uniform IGFs even in these high-purity, additive-free ceramics (Fig. 1). Further studies [4] revealed a systematic dependence of IGF thickness on calcium doping levels (80–500 ppm Ca). Interestingly, the IGF thickness decreased with initial Ca additions but increased with higher concentrations. This behavior was attributed to a delicate balance among van der Waals forces, steric interactions, and electrostatic double-layer forces acting across the film.

EELS measurements by STEM dedicated for high special resolution further elucidated the IGF composition, revealing a Si-O-N network with calcium segregation at the grain boundaries [5]. This insight enabled the development of an atomic-scale model of the IGF structure [6]. Subsequent first-principles calculations [7] on the Si-*L*2,3 edge ELNES provided a deeper understanding of the local electronic environment within the IGF (Fig. 2).

This presentation will comprehensively explore these findings, emphasizing the structural and compositional nuances of IGFs in silicon nitride and their implications on material properties. Through this tribute to Achim Kleebe, I aim to highlight the enduring significance of his meticulous work in advancing our understanding of ceramics at the atomic scale.

References:

1. H.-J. Kleebe, M.J. Hoffmann, M. Rühle, *Int. J. Mater. Res.*, **83**, 610 (1992).
2. H.-J. Kleebe, M.K. Cinibulk, R.M. Cannon, M. Rühle, *J. Am. Ceram. Soc.*, **76**, 1969 (1993).
3. I. Tanaka, G. Pezzotti, T. Okamoto, Y. Miyamoto, M. Koizumi, *J. Am. Ceram. Soc.*, **72**, 1656 (1989).
4. I. Tanaka, H.-J. Kleebe, M.K. Cinibulk, J. Bruley, D.R. Clarke, M. Rühle, *J. Am. Ceram. Soc.*, **77**, 911 (1994).
5. H. Gu, R.M. Cannon, M. Rühle, *J. Mater. Res.*, **13**, 376 (1998).

6. M. Yoshiya, H. Adachi, I. Tanaka, *J. Am. Ceram. Soc.*, **82**, 3231 (1999).
7. I. Tanaka, *J. Ceram. Soc. Jpn.*, **109**, S127 (2001).

Fig.1 HREM image of IGF in HIPed high purity silicon nitride ceramics

Fig.2 Si-*L*2,3 edge ELNES of IGF in HIPed high purity silicon nitride ceramics.

Fig. 1

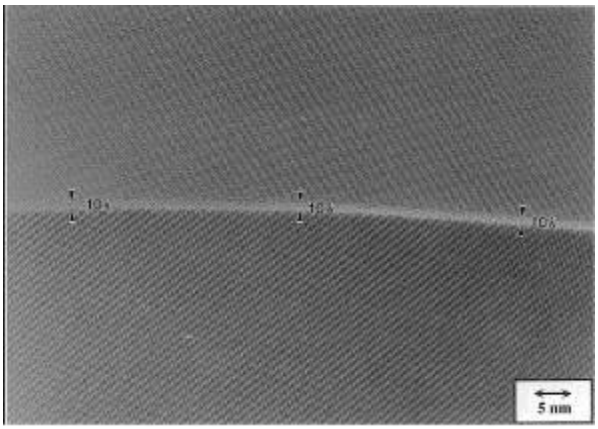
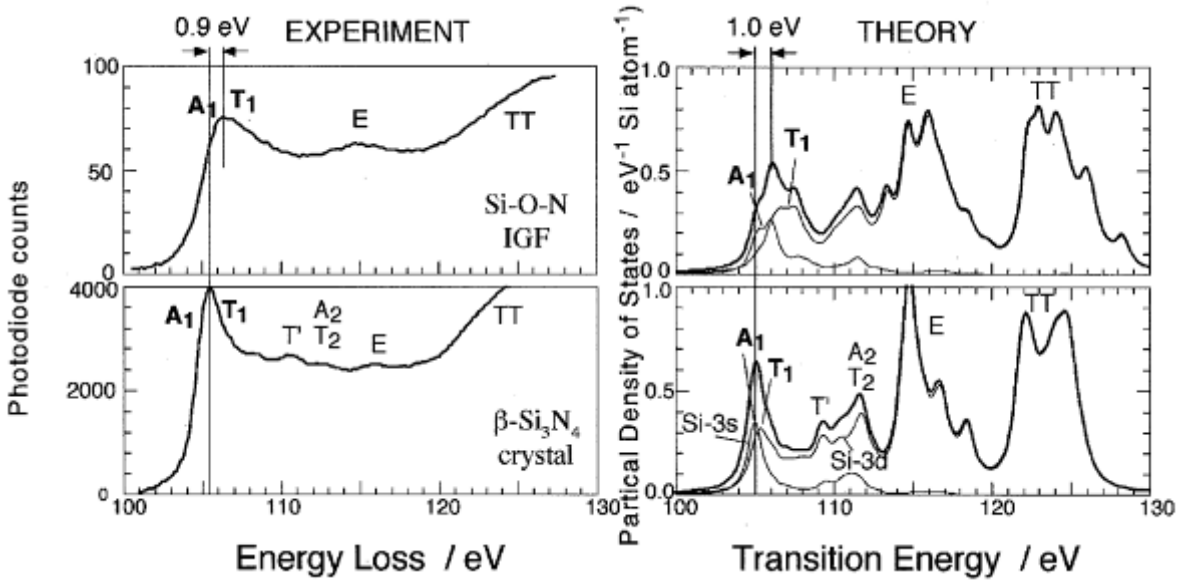


Fig. 2



MS6.02
Probing of dislocation-controlled domain nucleation and domain wall pinning in single-crystal $BaTiO_3$ by MEMS-based multi-stimuli *in situ* (S)TEM

T. Jiang[1], R. Winkler[1], A. Zintler[2], Y. Pivak[3], F. Zhuo[1], L. Molina-Luna[1]

[1]Technical University of Darmstadt, Department of Materials and Earth Sciences, Darmstadt, Germany
[2]University of Antwerp, Electron Microscopy for Materials Sciences, Faculty of Science, Antwerp, Belgium
[3]DENSsolutions, Delft, Netherlands

Introduction: Engineering domain walls at the nanoscale offers a promising avenue to enhance the macroscopic functional properties of materials, unlocking vast potential for advancements in electromechanics and electronics. This approach involves imprinting topological defects into functional materials, thereby presenting a significant opportunity to bolster material performance[1,2]. However, the current limited understanding of how these topological defects influence domain nucleation and domain wall motion in ferroelectrics impedes the development of this class of ferroelectric functional materials. Overcoming this knowledge gap is crucial for fully realizing the benefits of nanoscale domain wall engineering.

Objectives: We investigated the atomic and electronic structures of {100}<100>-type and {101}<101>-type dislocation cores in deformed single-crystal $BaTiO_3$ samples. The dislocation-mediated domain nucleation and evolution were characterized with respect to temperature variations.

Materials and methods: Through high-temperature uniaxial compression along [110] and [001] directions on single-crystal $BaTiO_3$ samples, we introduced well-aligned {100}<100>-type and {101}<101>-type dislocations, respectively. Employing MEMS-based multi-stimuli *in situ* scanning/transmission electron microscopy (S/TEM) with a Cs-corrected microscope, a broad temperature range, varying from -175 °C to 200 °C, was applied to the TEM specimens[3]. Electron energy loss spectroscopy (EELS) spectrum was acquired at two types of dislocation cores. Atomic-scale strain analyses at the dislocation cores were achieved by applying geometry phase analysis (GPA) algorithm to high angle annular dark field (HAADF-) STEM images.

Results: Using multi-stimuli *in situ* S/TEM, we observed the dislocation-controlled domain nucleation and dynamic interactions between domain walls and topological defects across all phases of $BaTiO_3$, from the rhombohedral phase at cryogenic temperatures to the cubic phase at high temperatures. HAADF-STEM images at two types of dislocation cores will be shown in the presentation, along with the corresponding polarization mapping and the strain mapping. These comprehensive perspectives offer detailed insights into the electro-mechanical behaviors of this ferroelectric material. We further examined how ferroelastic domain walls are pinned by these imprinted dislocations under various stimuli, a phenomenon driven by the stress fields emanating from the dislocations. Additionally, we analyzed differences in the local electronic structure between the {100}<100>-type and {101}<101>-type dislocation cores.

Conclusions: This provides us with a comprehensive understanding of the dislocation-controlled nucleation and the dynamic interplays between the domain wall and the topological defects, considering both the elastic lattice and space charge degrees of freedom. Our study not only deepens our understanding of domain wall engineering in ferroelectric materials but also introduces a novel approach suitable for advanced nanoelectronics and broad applications across diverse temperature ranges.

Reference:

(1) Zhuo, F. *et al*., *Adv. Mater.,* **2024**, 36 (52), 2413713.

(2) Jiang, T. *et al*., *Appl. Phys. Lett*., **2023**, 123 (20), 202901.

(3) Jiang, T. *et al*., *Microstructures,* **2024**, 4 (4), 2024058.

T.J. and L.M.-L. acknowledge the European Research Council (ERC) under Grant No. 805359-FOXON, 957521-STARE and 101088712-ELECTRON.

MS6.03
Toward enhanced measurement of electromagnetic fields using electron beam precession and advanced post-processing in 4D-STEM

S. Kang[1,2,3], D. Wang[1,3], D. Jennings[4], W. Rheinheimer[5], A. Klein[2], C. Kübel[1,2,3]

[1]Karlsruhe Institute of Technology, Institute of Nanotechnology, Karlsruhe, Germany
[2]Technical University of Darmstadt, Department of Material- and Geosciences, Darmstadt, Germany
[3]Karlsruhe Institute of Technology, Karlsruhe Nano Micro Facility (KNMFi), Karlsruhe, Germany
[4]Forschungszentrum Jülich GmbH, Institute of Energy and Climate Research, Jülich, Germany
[5]University of Stuttgart, Institute for Manufacturing Technologies of Ceramic Components and Composites, Stuttgart, Germany

Ceramic capacitors store and release electrical energy via an electric field [1]. Polycrystalline $BaTiO_3$ and $SrTiO_3$ are widely used for their reliable dielectric properties, compact size, and cost-effectiveness [2]. However, they degrade over time, with increased leakage current as resistance drops under high temperature and voltage stress. This degradation stems from oxygen vacancy migration, which accumulates at grain boundaries before reaching the cathode [3]. Doping with Fe and Mn modifies the space charge layer (SCL) at grain boundaries, influencing vacancy migration and degradation.

Understanding the electromagnetic field distribution at the SCL is crucial for many ceramic applications. Various techniques, including off-axis electron holography and differential phase contrast (DPC) imaging, have been explored to achieve high spatial resolution in mapping electromagnetic fields. However, these approaches often suffer from intrinsic limitations, such as phase-wrapping artifacts, electron dose constraints, and sensitivity to environmental noise. Moreover, in conventional 4D-STEM methodologies, diffraction contrast introduces significant orientation-dependent distortions, making it difficult to achieve reliable and reproducible field measurements.

To address these issues, recent research has focused on enhancing diffraction-based field measurements. Electron beam precession reduces diffraction contrast artifacts by averaging over multiple crystal orientations, improving accuracy. Machine learning-based feature extraction and SVD-based decomposition further refine diffraction pattern analysis and enhance precision.

In this study, we extend 4D-STEM electromagnetic field mapping to polycrystalline materials. By integrating electron beam precession with advanced post-processing, Sobel edge detection and SVD-based refinement [4, 5], we achieve high-precision field extraction in complex nanoscale structures. This approach surpasses conventional methods (Figure 1), expanding 4D-STEM applications in heterogeneous and polycrystalline systems. Combined with in-situ biasing TEM, we visualize SCRs under different biasing conditions and temperatures. Our findings enhance the understanding of ceramic capacitor performance and degradation under high voltage stress.

Fig. 1: Comparison of raw diffraction patterns with and without electron beam precession, highlighting improved uniformity. Precession-corrected images show enhanced disk stability and uniformity. In-situ biasing 4D-STEM analysis of electric fields at Fe-doped $BaTiO_3$ grain boundaries. The left column presents differential phase contrast (DPC) maps, with a color wheel indicating electric field directions. The middle and right columns show DPC maps along the X and Y directions under 0V and 50V biases. Results reveal space charge region (SCR) changes under applied bias, offering insights into grain boundary charge accumulation and capacitor degradation.

References

[1] K. Hong, T. H. Lee, J. M. Suh, S.-H. Yoon, and H. W. Jang, Journal of Materials Chemistry C, 7 (2019) 9782–9802

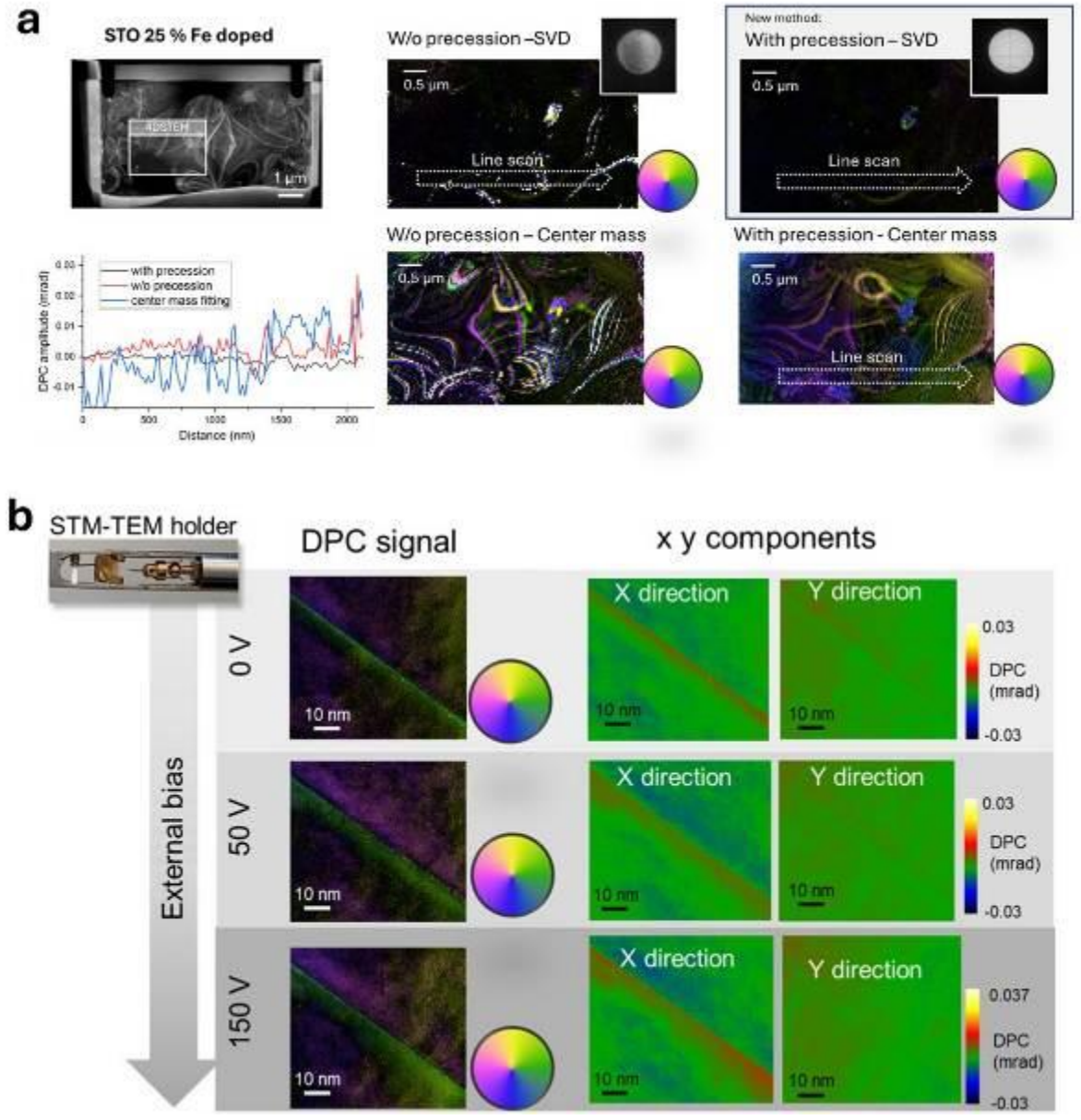
[2] Vijatović, M. M., J. D. Bobić, and Biljana D. Stojanović. Science of Sintering 40.3 (2008): 235-244.

[3] R. Giesecke, R. Hertwig, T. J. M. Bayer, C. A. Randall, and A. Klein, Journal of the American Ceramic Society, 100, 10 (2017) 4590–4601

[4] S. Kang, et al. Advanced Materials 35.25 (2023) 2212086.

[5] S. Kang et al. Nature Communications, (2025) 16, 1305

Fig. 1



MS6.04(inv)
The universe is my NanoFab – Electron microscopy for space exploration and materials discovery

R. Stroud[1]

[1]Arizona State University, School of Earth and Space Exploration, Tempe, AZ, United States

Our solar system formed from the gas and dust of many ancient dying stars gathered into a molecular cloud that gravitationally collapsed. Although most of the primordial raw ingredients of the solar system lost all signatures of their prior circumstellar or interstellar origins, a few dust particles (~1 nm to 10,000 nm) retained isotopic signatures that identify them as the products of stars of specific mass and metallicity (bulk elemental composition) distinct from our Sun. Coordinated nanoscale analysis of individual dust grains can providence evidence of the dust grain formation conditions, and subsequent astrophysical processing. Transmission electron microscopy (TEM) reveals the elemental compositions and crystal structures of the grains, which then constrains the ambient gas composition, pressure and temperature of the dust condensation. Secondary ion mass spectrometry (SIMS) provides isotopic composition information that constrains the time and place of formation, i.e., the outflows of a core collapse supernovae before the formation of the Sun. Example astromaterials include phases of technological interest, including doped nanodiamonds, SiC, Al_2O_3, Si_3N_4, graphene, and nanostructured carbons. The study of these materials with state-of-the-art electron microscopy allows us to explore the wide range of astrophysical conditions available across the Universe for materials synthesis over the last > 4.5 billion years, develop our understanding of how the rocky and organic components in our solar system formed, and potentially discover new, exotic phases.

MS6.05
Exploring extraterrestrial materials with surface techniques

P. Jovicevic-Klug[1], M. Jovicevic-Klug[1], B. Ambrožič[2], C. Kasdorf Giesbrecht[1], Z. Miłosz[3], E. V. Woods[1], M. Amati[3], L. Gregoratti[3], A. Vogel[1], C. Schwab[4], M. Rohwerder[1]

[1]Max-Planck-Institute for Sustainable Materials, Interface Chemistry and Surface Engineering, Düsseldorf, Germany
[2]Nanocenter, Ljubljana, Slovenia
[3]Elettra - Sincrotone Trieste, Trieste, Italy
[4]Forschungszentrum Jülich GmbH, Institute of Energy Materials and Devices, Jülich, Germany

Exploration of the extraterrestrial materials such as meteorites, asteroids and comets are of great interest to today's society for future industrial and research applications (magnetism, rare earth elements extraction etc.) and expansion of fundamental knowledge.

The different magnetic phases in meteorites have great potential as chronological markers due to their unique magnetic properties that can be correlated to the genesis/evolution of a meteorite through remanent geomagnetic fields imprinting. Thus, the history of the solar system can be studied by studying the paleomagnetism and chemical composition of meteorites. Another aspect of meteorite research is to gain a fundamental understanding of the tetrataenite phase, which is of great interest for the further development of new generation permanent magnets due to its naturally-occurring high uniaxial magneto-crystalline anisotropy coupled with high coercivity. However, it is difficult to artificially produce such a phase due to the kinetic limitations of its formation. For these reasons, exploration of meteorites and their different groupings (iron meteorites, stone meteorites and stony-iron meteorites) provides a rich avenue to explore the magnetic, geological, chemical and structural properties of the different phases found within them.

In this study, the Aletai meteorite (iron-nickel meteorite), Diablo meteorite (iron-nickel meteorite) and Northwest Africa pallasite are examined. Complementary spatially resolved imaging techniques (atom force microscopy - AFM) are used to better understand the unique phases within typical iron meteorites and the paleomagnetism. For correlative analysis, petrography with scanning electron microscopy - SEM, scanning transmission electron microscopy - STEM, time-of-flight secondary ion mass spectrometry (ToF-SIMS), X-ray photoelectron spectroscopy - XPS and synchrotron scanning photoelectron microscopy (SPEM) were carried out to investigate correlative surface-bulk chemical-structural-magnetism relationship.

New petrographic, mineral and paleomagnetism data reveal unique characteristics of the meteorites and also show the potential to use magnetic-based characterization coupled with microscopic analysis to further understand the history of meteorites and local properties of individual phases, maybe even of relevance for a better understanding of the evolution of the universe. Furthermore, this study provided fundamental understanding of meteorite paleomagnetism into the tetrataenite phase and its correlation with softer magnetic phases, which is of great interest for progressing the paleomagnetic field as well as possible deepening of the fundamental understanding of the said phases and structures for development of future magnetic materials.

MS6.06
A FIB-SEM protocol for high-resolution imaging combined with EDX analysis of cement-based materials with minimized damage

F. Kleiner[1], C. Rößler[1], H. M. Ludwig[1]

[1]Bauhaus-Universität Weimar, F. A. Finger-Institute for Building Material Science, Weimar, Germany

The application of focused ion beam-scanning electron microscopy (FIB-SEM) in materials science is a powerful tool for high-resolution three-dimensional imaging. However, similar to biological specimens, the use of FIB-SEM in combination with energy-dispersive X-ray spectroscopy (EDX) on water-containing mineral phases like calcium-silicate-hydrate (C-S-H) and portlandite (CH) presents unique challenges. At room temperature, the interaction between the electron beam and hydrated minerals can induce damage due to the prolonged irradiation time on a small surface, limiting the applicability of this technique for studying cement-based materials. However, the damage caused by the method is rarely mentioned in the literature.

This is highlighting the need for optimized preparation and application protocols with a focus to minimize specimen damage while achieving high-resolution imaging and EDX for chemical characterization. Furthermore, in the present study a larger volume of interest (VOI, 20 x 20 x 20 µm³) is investigated, representing a significant increase in scale compared to our previous FIB-SEM studies (10 x 10 x 10 µm³) [1,2].

Samples of cement paste and mortar were prepared from standard mortar mixture with a water-cement ratio of 0.5. The hydration was stopped after 28 days by immersion in isopropanol and subsequent drying. The specimen was then embedded in epoxy resin, polished and carbon coated. Using large area back scattered electron imaging, a site for the FIB-SEM-preparation was selected. After clearing the VOI from the site, it was lifted out and welded to a copper comb. Then the specimen was cut in 10 nm slices and mapped using EDX every 10 slices to identify key phases, such as alite, C-S-H, CH, pores, and aggregates.

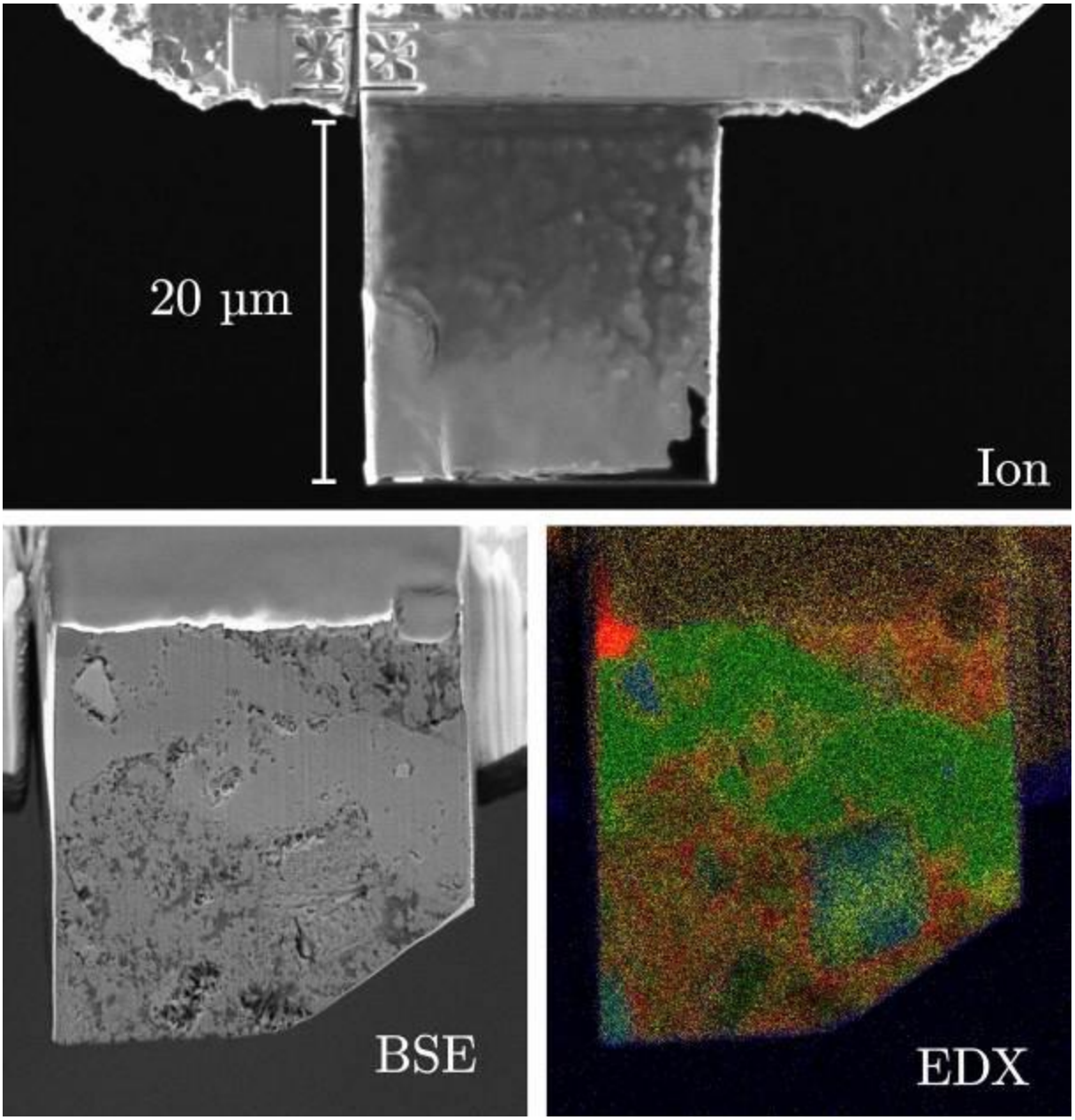
The FIB-SEM protocol produced high-resolution images of the cement microstructure without inducing significant visible damage (Fig. 1). Key features, including pores, C-S-H phases, and aggregates, were clearly resolved. EDX mapping enhanced phase differentiation and allows the segmentation of specific phases that are indistinguishable in the BSE dataset. The larger VOI demonstrated the scalability of the method for studying more representative volumes of cement-based materials. Additionally, the process was recorded and condensed into a detailed video documenting the workflow, from specimen preparation to imaging.

By optimizing the specimen preparation and imaging parameters, we achieved high-resolution imaging without inducing damage, which still can be found in the literature. The accompanying video tutorial ensures that this protocol can be adopted by other researchers, promoting best practices in FIB-SEM analysis for cement-based materials. The application to larger sample volumes enhances the method's versatility and applicability. This work underscores the importance of careful preparation and application of advanced microscopy techniques, enabling more accurate and reliable studies of concrete microstructures.

- [1] Kleiner, C. Rößler, *Nano-scale 3D reconstruction of C-S-H-phases using modern FIB/SEM technology,* 3. ICCCM, **2021**, doi: 10.13140/RG.2.2.32892.67207
- [2] Kleiner, Ch., F. Vogt, A. Osburg, H.-M. Ludwig, *Reconstruction of calcium silicate hydrates using multiple 2D and 3D imaging techniques: Light microscopy, µ-CT, SEM, FIB-nT combined with EDX*, J. of Microsc., **2021**, doi: 10.1111/jmi.13081

Fig 1: Ion-, BSE- and EDX- dataset of the generated dataset after the lift-out procedure.

Fig. 1



MS6.P01
Observation of disorder texture in crocidolite asbestos using low-dose STEM imaging techniques

I. Ohnishi[1]

[1]JEOL Ltd., EM Business Unit, Tokyo, Japan

Introduction: Asbestos has been utilized for many years as a building material due to its exceptional heat resistance properties. However, its extremely fine morphology, known as asbestiform, can easily infiltrate the human body and remain for long periods, potentially causing health risks such as lung cancer and mesothelioma. Asbestos is mineralogically classified into six types. Among them, crocidolite asbestos is considered the most toxic due to its elongated shape and its ability to survive in the lung environment [1]. Previous studies using high-resolution transmission electron microscopy (TEM) reported that crocidolite asbestos consists mainly of fine fiber aggregates, with numerous defects and sheet silicate minerals, suggesting that these structural features contribute to its tendency to fragment easily [2]. To elucidate the mechanism of asbestiform, we conducted more detailed observations using an aberration-corrected microscope for amphibole asbestos [e.g., 3]. Our investigation, employing a low-dose imaging technique known as optimum bright field scanning transmission electron microscopy (OBF-STEM) [4], revealed that the sheet silicate in crocidolite asbestos corresponds to talc-like silicate [3]. In this study, we attempt to observe the defects in crocidolite asbestos using OBF-STEM.

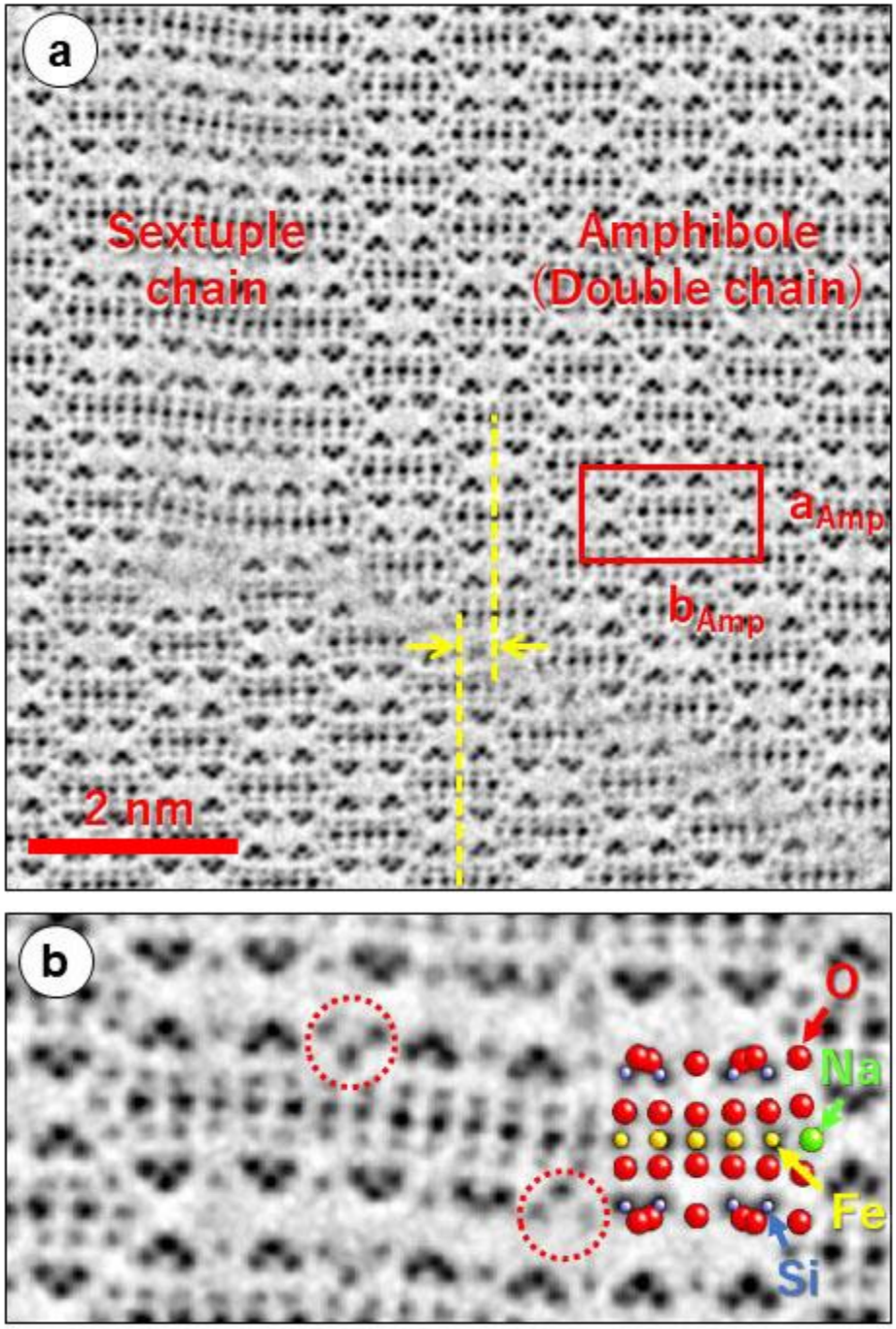
Method: OBF-STEM observations were applied to a cross-section specimen of crocidolite asbestos, prepared using an ion milling method. For the observations, we used an aberration corrected 300 kV microscope (JEM-ARM300F2) with an eight segment STEM detector and a probe current of ~4 pA at 300 kV.

Results and Discussion: Our observations confirmed that crocidolite asbestos is composed mainly of aggregates of many fine amphibole (double chain silicate) crystals, which contain intergrown wide-chain silicates such as triple, quadruple and so on, as reported previously [2]. The incoherent termination of a wide-chain silicate causes a variety of defects in amphibole crystals. For instance, an intergrowth of sextuple chain, which is slightly bent along the [100] direction, causes misfit and displacement of double chain periodicity along both the [100] and [010] directions of amphibole (Figure 1). Moreover, OBF-STEM also revealed the presence of extra atoms at the bending point in the sextuple chain, suggesting that the incorporation of extra atoms into a wide-chain is one of the reasons for the formation of defects in amphibole structure. The OBF-STEM observations in this study exhibited the detailed texture of defects in crocidolite asbestos. We hope that further investigation using this method might help to reveal the formation mechanism of asbestiform for amphibole asbestos.

Figure 1: OBF-STEM image showing the intergrowth of sextuple chain with amphibole (double chain) in crocidolite asbestos. Yellow arrows and dashed lines in (a) indicate the displacement of the double chain along the [010] direction of amphibole. Red dashed circles in (b) indicate the presence of extra atoms in the sextuple chain.

References: [1] Y. Murai, *Ganseki Koubutsu Kagaku* **35** (2006), 34-39 (Japanese with English abstract), [2] J. H. Ahn and P. R. Buseck, *American Mineralogist* **76** (1991), 1467-1478, [3] I. Ohnishi, *Microscopy and Microanalysis* **30** (Suppl 1) (2024), 1073, [4] K. Ooe et al., *Ultramicroscopy* **220** (2021), 113133.

Fig. 1


a
Sextuple chain
Amphibole (Double chain)
a_{Amp}
b_{Amp}
2 nm
b
O
Na
Fe
Si

MS6.P02
Unstained sample observation using segmented detector

Y. Segawa[1], H. Miura[1], A. Nakamura[1], Y. Kohno[1], H. Hirose[1], Y. Konyuba[1], S. Ohta[1], T. Seki[2], N. Shibata[2]

[1]JEOL Ltd., EM Research and Development, Akishima, Japan
[2]University of Tokyo, School of Engineering, Tokyo, Japan

Introduction & objectives

The use of a segmented detector has become standard in various STEM observations, particularly in Differential Phase Contrast (DPC) STEM [1] and Optimum Bright Field (OBF) STEM [2]. Especially, OBF STEM method has achieved noticeably better contrast during live imaging in low-dose experiments with beam-sensitive materials, such as zeolites and metal-organic frameworks (MOFs) [3]. The applications of a segmented detector are expected to further extend across a variety of material and life science fields. One such application is the observation of soft materials, including polymers, colloids, and biomaterials. In traditional S/TEM observations, polymer materials composed of light elements are often stained with heavy metals to enhance contrast. However, this staining process may cause artifacts such as the change of the sample's structure. Therefore, observation methods that provide clear contrast without staining are better for the structure analysis. This research shows the OBF observation results of unstained polymer sample under low-dose condition.

Materials & methods

The sample was a polystyrene-b-poly(2-vinylpyridine) (PS-b-P2VP) with lamellar structure and a thickness of about 40 nm. The experiment was performed using JEM-ARM300F2 (JEOL Ltd.), equipped with SAAF Octa detector (an eight-segmented detector, JEOL Ltd.). For the experiment, the following conditions were used: an accelerating voltage of 300 kV, a convergence semi-angle of 0.097 mrad (objective lens off), a camera length of 4,000 cm, a dwell time of 20 µsec, and a probe current of 1 pA (~21 e^- / nm^2).

Results

Figure 1 shows an OBF image of an unstained PS-b-P2VP lamellar sample. The lamellar structure, in which dark and light phases are stacked alternately, can be clearly observed. The contrast in OBF STEM is very sensitive to a projected potential, such as the density distribution in the direction of electron beam transmission. In this experiment, the contrast was defined so that the higher the density, the brighter the contrast. Since the density of P2VP is higher than that of PS, it can be determined that the dark phase is PS and the light phase is P2VP.

Conclusion

We acquired OBF image of an unstained PS-b-P2VP lamellar sample under low-dose conditions. OBF STEM is one effective way to provide clear contrast avoiding artifacts caused by staining reagents. On the day of the presentation, we plan to present detailed experimental methods as well as the results from observation of other unstained samples.

Figure 1.

The OBF image of an unstained PS-b-P2VP was acquired using the segmented detector (SAAF Octa). The magnified view of the white squared area is shown on the bottom right.

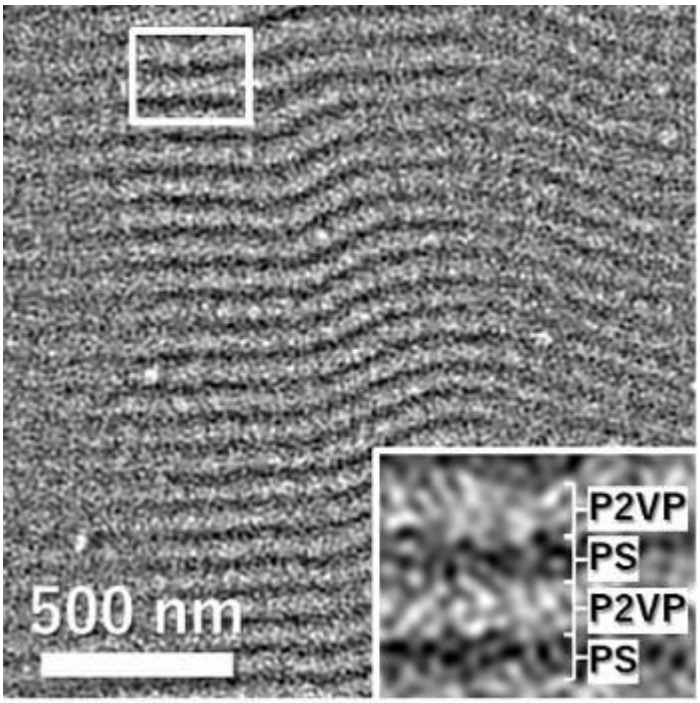
Reference:

[1]N. Shibata et al., Nature Physics, **8**, 611 (2012).

[2]K. Ooe et al., Ultramicroscopy, **220**, 113133 (2021).

[3]H. Hashiguchi et al., Vacuum and Surface Science, **66**, 695 (2023).

Fig. 1



MS6.P03
Forensic microscopy and microanalysis

I. Turková[1], M. Kotrlý[1], R. Šefců[2]

[1]Institute of Criminalistics, Prague, Czech Republic
[2]National Gallery Prague, Prague, Czech Republic

Forensic institutes and their expert examinations are accepted by the courts as a guarantee of seriousness, impartiality, and incorruptibility, and at the same time, it is assumed that their instrumental equipment, abilities, knowledge, and the hard work of their experts keep them one step ahead of illegal practices.

The development of the electron microscope and the introduction of electron microscopy, especially scanning, into forensic practice have pushed the identification and analysis of forensic traces forward to unprecedented levels. The possibility of displaying in the µm/nm range, analyzing and identifying various types of traces and materials from a crime scene, and comparing them at micro/nano levels is currently used by many forensic disciplines. These include in

particular the detection and analysis of thermogenetic particles, such as gunshot residue (GSR), post-blast explosive residue (PBR), metal fragments and scales, various fracture surfaces, analysis of soil, precious stones, etc. In addition to standard analyses, automatic screening systems are also being introduced, which significantly speed up and facilitate the work of an expert.

With microscopes equipped with an ion beam, it is possible to perform microsections and study the internal structure of particles or stratigraphy of layers, such as in thermogenetic particles, fibers, color-changing pigments, etc.

The Institute of Criminalistics of the Police of the Czech Republic (ICP) is also involved in the detection of forgeries in the field of fine arts. In these case the laboratory conducts scientific research on particularly controversial works by authors from the first and second half of the 20th century, which are very often tradable on the Czech market. When detecting counterfeits, knowledge of the artists' palette and also the dating of the creation of synthetic pigments is equally important. A wide range of analytical methods is used to verify the authenticity of a work of art, both from organic and inorganic analysis, but for works of art, one of the key analyses is the verification of originality by studying the color layer of pigment phases and thus imaging using optical microscopy, and the key analysis is SEM/EDX. ICP in cooperation with the National Gallery Prague, has been developing robust and proven procedures for identifying forgeries in the field of fine art, so that they can be fully defended in court. The correctness of the developed procedures and techniques has already been tested in many cases involving disputed works.

The knowledge of experts about the historical production processes of pigments that contain specific components also plays an indisputable role. In the laboratories of the University of Pardubice, pigments were synthesized according to historical recipes, which are compared with materials available on the market.

The wide range of scientific disciplines and instrumental possibilities catapult forensic institutes into top institutions that are capable of covering various scientific fields with their interdisciplinary capacity and thus producing well-founded, comprehensive expert opinions.

Interesting analytical moments from analysis of forensic objects are part of this paper.

This work has been financially supported by the project of the Ministry of the Interior of the Czech Republic VJ01010004 and VK01010153.

Fig. 1

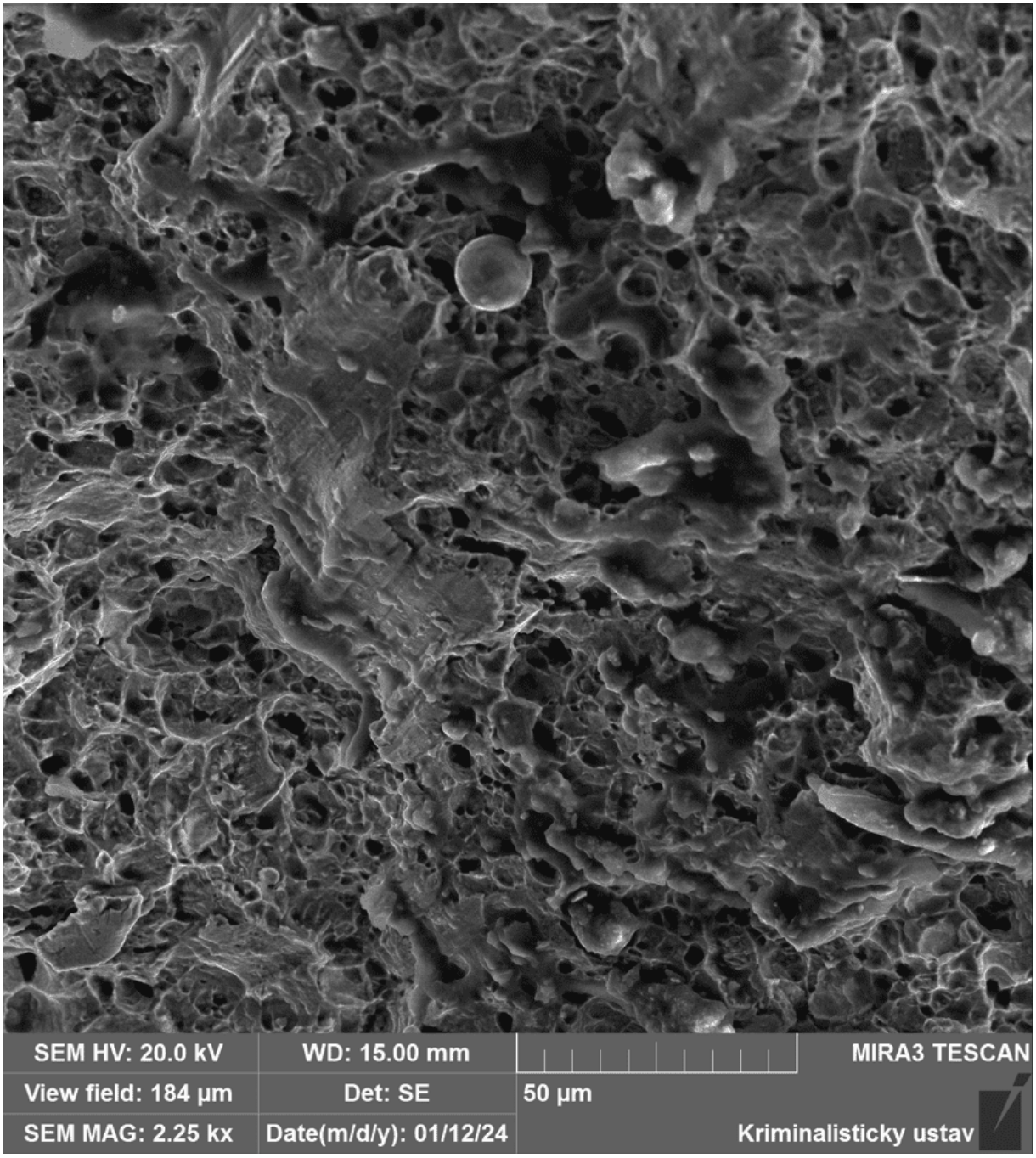
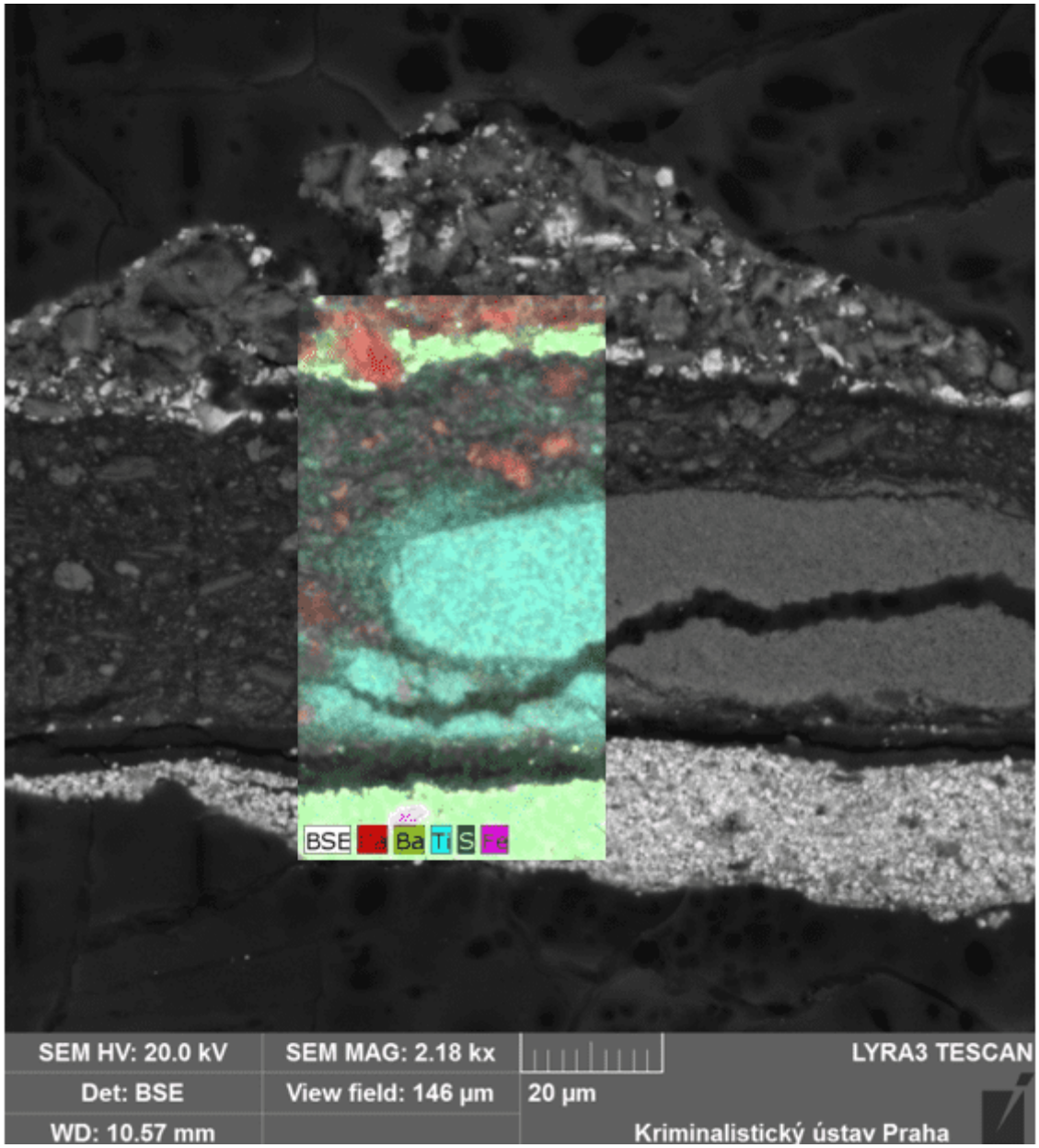

SEM HV: 20.0 kV
WD: 15.00 mm
MIRA3 TESCAN
View field: 184 µm
Det: SE
50 µm
SEM MAG: 2.25 kx
Date(m/d/y): 01/12/24
Kriminalisticky ustav

Fig. 2


BSE
Ba
Ti
S
Fe
SEM HV: 20.0 kV
SEM MAG: 2.18 kx
LYRA3 TESCAN
Det: BSE
View field: 146 µm
20 µm
WD: 10.57 mm
Kriminalistický ústav Praha

MS6.P04
Characterization of surface defects of piezoelectric $Ca_3TaGa_3Si_2O_{14}$ after high temperature heat treatment

M. Seifert[1], T. Gemming[1]

[1]Leibniz Institute for Solid State and Materials Research Dresden, Dresden, Germany

The piezoelectric $Ca_3TaGa_3Si_2O_{14}$ (CTGS) is a high-temperature stable crystal, which can be used e.g. as a substrate material in surface acoustic wave devices. Since it keeps its piezoelectric properties without any phase transition up to its melting temperature of 1350 °C, an application temperature close to this limit is expected. However, CTGS reacts with an oxidizable material at temperatures above 600 °C. A systematic analysis of the stability of CTGS crystals in different atmospheres at high temperatures is still missing.

500 µm thick CTGS substrates were annealed at 800 °C or 1000 °C in high vacuum (HV), pure O_2, N_2, Ar as well as in air for 48 h and in H_2 for 2 h. A part of the annealed substrates was covered by 100 nm RuAl and then annealed at 800 °C for 10 h in HV. SEM was used to analyze the surface of the samples. STEM and EDX of FIB cross sections of the samples were performed to study changes of the morphology or degradation. In addition, X-ray diffraction (XRD) was performed to check for new phases.

XRD measurements did not show any differences for the 800 °C annealed pure substrates as compared to the untreated CTGS. Still after annealing at 1000 °C, no differences were observed for the substrates annealed in air, O_2, Ar and N_2. In contrast to this, many additional peaks appeared in the X-ray diffractograms of the substrates annealed in HV or H_2 at 1000 °C, indicating a severe degradation.

For the 800 °C annealed substrates, SEM hardly showed any features at the substrate surface. Only in case of the sample annealed in HV, maze-like patterns were observed locally (Fig. 1(a)). Apart from these defects, EDX measurements revealed a lack of Ga close to the surface of the HV and more pronounced in case of the H_2 annealed substrate.

For the substrates annealed at 1000 °C, SEM revealed severe defects in case of the annealing in HV and H_2. TEM and EDX measurements showed the formation of an about 60 nm thick layer consisting of $CaSiO_3$ and $Ca_2Ta_2O_7$ grains in case of the HV sample (Fig. 1(b)). In contrast to this, the CTGS annealed at 1000 °C in H_2 showed defects and µm large pores across the whole thickness of the TEM lamella of about 8 µm (Fig. 1(c)).

The analysis of the substrates covered with the RuAl film, which were then annealed at 800 °C, did not show a reduction of the chemical reaction between the film and the substrate due to the pre-treatment.

In summary, the analyses showed a strong degradation of uncovered surfaces of the CTGS substrate in reducing (HV or H_2) atmospheres during annealing at 1000 °C. In contrast to this, hardly any changes were observed in oxygen or neutral atmospheres. The results demonstrated that a protection of uncovered surfaces of the CTGS is essential for high-temperature application.

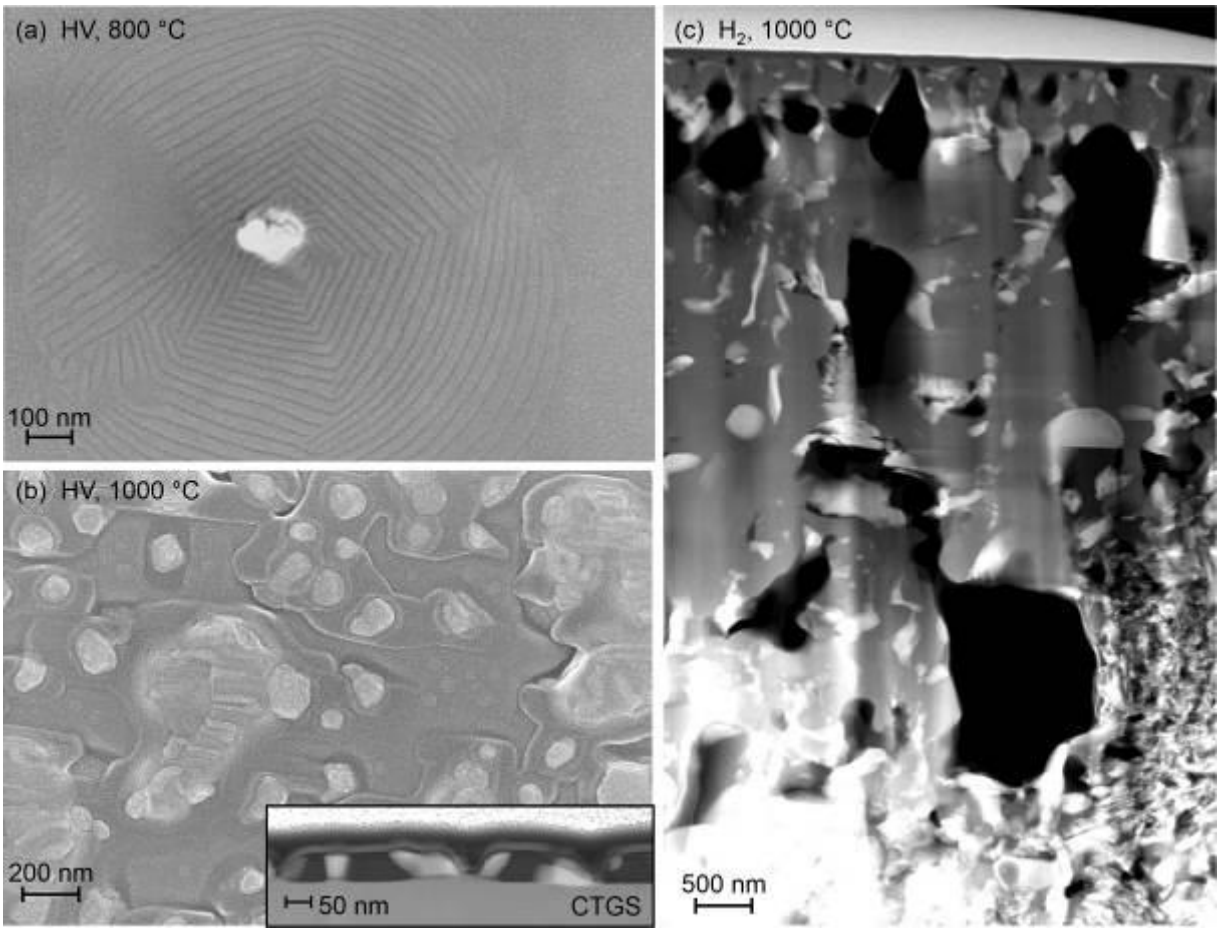
[1] Seifert, M., et al. (2016). TEM studies on the changes of the composition in LGS and CTGS substrates covered with a RuAl metallization and on the phase formation within the RuAl film after heat treatment at 600 and 800 °C; Journal of Alloys and Compounds 664: 510-517.

[2] Seifert, M., et al. High-temperature stability of $Ca_3TaGa_3Si_2O_{14}$ in various atmospheres up to 1000 °C; submitted to Surfaces and Interfaces (2024)

The authors gratefully acknowledge funding from German BMBF (03ET1589 A) and DFG (470028346).

Fig. 1: (a) SEM image of CTGS annealed at 800 °C in HV, (b) SEM and TEM image of CTGS annealed at 1000 °C in HV, (c) TEM cross section image (surface at top) of CTGS annealed at 1000 °C in H_2

Fig. 1



MS6.P05
Dependence of the structural and magnetic properties on the growth sequence in heterostructures designed by $YbFeO_3$ and $BaFe_{12}O_{19}$

B. Nergis[1], S. Bauer[1], X. Jin[2], R. Schneider[3], D. Wang[4,5], C. Kübel[4], P. Machovec[6], L. Horak[6], V. Holy[6], K. Seemann[7], T. Baumbach[1], S. Ulrich[7]

[1]Karlsruhe Institute of Technology, Institute for Photon Science, Eggenstein-Leopoldshafen, Germany
[2]Thermo Fisher Scientific, Rotherdam, United Kingdom
[3]Karlsruhe Institute of Technology, Laboratory of Electron Microscopy (LEM), Karlsruhe, Germany
[4]Karlsruhe Institute of Technology, Karlsruhe, Germany
[5]Karlsruhe Institute of Technology, Karlsruhe Nano Micro Facility, Karlsruhe, Germany
[6]Charles University, Department of Condensed Matter Physics, Prague, Czech Republic
[7]Karlsruhe Institute of Technology, Laboratory of Electron Microscopy (LEM)/ KIT, Karlsruhe, Germany

The structure and the chemical composition of individual layers as well as of interfaces belonging to the two heterostructures M1 ($BaFe_{12}O_{19}$/$YbFeO_3$/YSZ) and M2 ($YbFeO_3$/$BaFe_{12}O_{19}$/YSZ) grown by pulsed laser deposition on yttria-stabilized zirconia (YSZ) substrates are deeply characterized by using a combination of methods such as high-resolution X-ray diffraction, transmission electron microscopy (TEM), and atomic-resolution scanning TEM with energy-dispersive X-ray spectroscopy. The temperature-dependent magnetic properties demonstrate two distinct heterostructures with different coercivity, anisotropy fields, and first anisotropy constants, which are related to the defect concentrations within the individual layers and to the degree of intermixing at the interface. The heterostructure with the stacking order $BaFe_{12}O_{19}$/$YbFeO_3$, i.e., M1, exhibits a distinctive interface without any chemical intermixture, while an Fe-rich crystalline phase is observed in M2 both in atomic-resolution EDX maps and in mass density profiles. Additionally, M1 shows high c-axis orientation, which induces a higher anisotropy constant K1 as well as a larger coercivity due to a high number of phase boundaries. Despite the existence of a canted antiferromagnetic/ferromagnetic combination (T < 140 K), both heterostructures M1 and M2 do not reveal any detectable exchange bias at T = 50 K. Additionally, compressive residual strain on the BaM layer is found to be suppressing the ferromagnetism, thus reducing the Curie temperature (Tc) in the case of M1. These findings suggest that M1 ($BaFe_{12}O_{19}$/$YbFeO_3$/YSZ) is suitable for magnetic storage applications.

Fig. 1

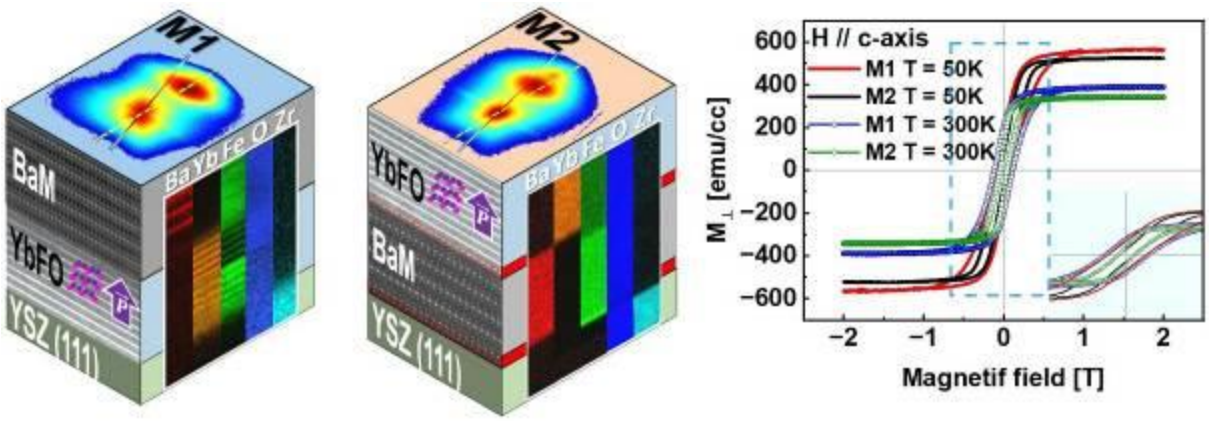
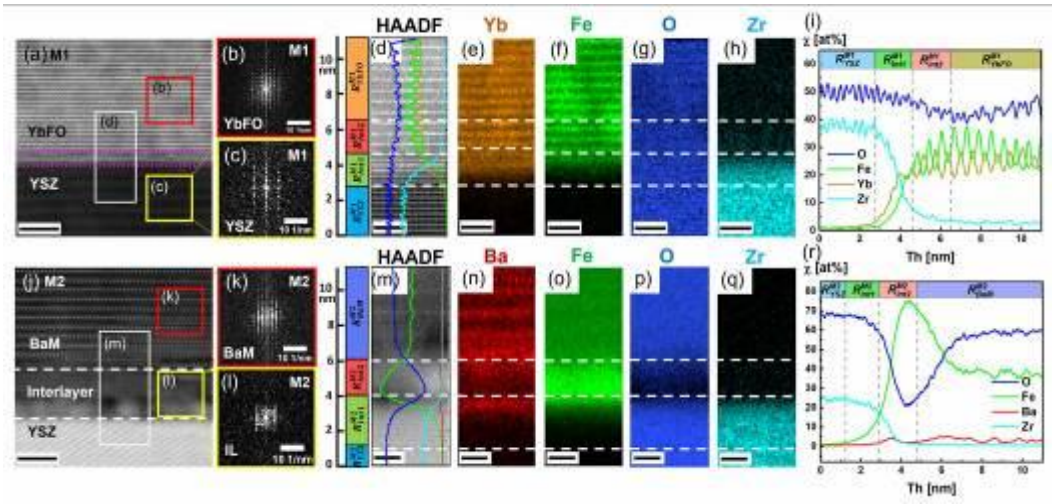


Fig. 2


(a) M1
YbFO
YSZ
(b) M1
YbFO
(c) M1
YSZ
HAADF
(d)
(e) Yb
(f) Fe
(g) O
(h) Zr
(i)
Σ [at%]
O
Fe
Yb
Zr
Th [nm]
(j) M2
BaM
Interlayer
YSZ
(k) M2
BaM
(l) M2
IL
HAADF
(m)
(n) Ba
(o) Fe
(p) O
(q) Zr
(r)
Σ [at%]
O
Fe
Ba
Zr
Th [nm]

MS6.P06
Evolution of ferroelectric domains in scandium alloyed aluminum nitride heterostructures

N. Wolff[1], G. Schönweger[1], Z. Ding[2,3], C. Kübel[2,3], S. Fichtner[1], L. Kienle[1]

[1]Kiel University, Material Science, Kiel, Germany
[2]Karlsruhe Institute of Technology, Institute of Nanotechnology, Karlsruhe, Germany
[3]Karlsruhe Institute of Technology, Karlsruhe Nano Micro Facility (KNMFi), Karlsruhe, Germany

Wurtzite-type materials, were previously thought to be polar but not ferroelectric. Recent research, however, has demonstrated that ferroelectric properties are indeed inherent in thin films of wurtzite-type materials with engineered structural and chemical properties. This is particularly true for solid solutions like AlScN [1], AlBN [2], ZnMgO [3], and GaScN [4]. These findings presented an unprecedented breakthrough for developing microelectronic devices that take advantage of the compatibility of wurtzite-based thin films with CMOS and nitride technologies. The ferroelectric characteristics of these materials - such as high spontaneous polarization and impressive scalability below 10 nm - make them ideal candidates for low-power memory devices and ferroelectric transistors.

While significant efforts have been made to understand the ferroelectric properties of wurtzite-type materials, further research is needed to fully understand the mechanisms of domain wall motion, switching pathways [5], and interface phenomena [6]. These studies aim to provide a fundamental understanding of the *structure-property relationships* in order to optimize ferroelectric properties. To better understand interface phenomena, local structures, and polarization states, solid solution thin film AlScN/GaN-based heterostructures were fabricated using magnetron sputtering and metal-organic chemical vapor (MOCVD) deposition. Aberration-corrected scanning transmission electron microscopy (STEM) was then used to examine these characteristics at an atomic scale.

The majority of the experimental STEM images were acquired using a JEOL NeoARM 200F microscope operated at 200 kV using the high-angle annular dark field (HAADF) and annular bright field (ABF) detectors. Chemical structure analyses were performed using energy-dispersive X-ray (EDX) and electron energy-loss spectroscopy (EELS). Crystallographic model structures were created for selected atomic structures using a supercell approach.

Comprehensive analyses of ferroelectric domain structures and both interfaces with the electrodes were carried out before and after *ex situ* polarization switching. The investigation revealed superior coherency between the functional AlScN layer and the n-GaN crystal lattice achieved for sputtered (see Figure 1) and MOCVD grown films. However, the observed ferroelectric domain structures and their switching mechanisms appear totally different in these films. Moreover, features of the electronic structure were examined as a possible tool to determine the variation of Sc concentration on the atomic scale.

The ferroelectric domain structures provide valuable insights for the engineering of materials with optimized ferroelectric properties and their applications.

[1] Fichtner, S.; et al. Journal of Applied Physics 2019, 125 (11), 114103. doi.org/10.1063/1.5084945.

[2] Hayden, J.; et al. Phys. Rev. Materials 2021, 5 (4), 044412. doi.org/10.1103/PhysRevMaterials.5.044412.

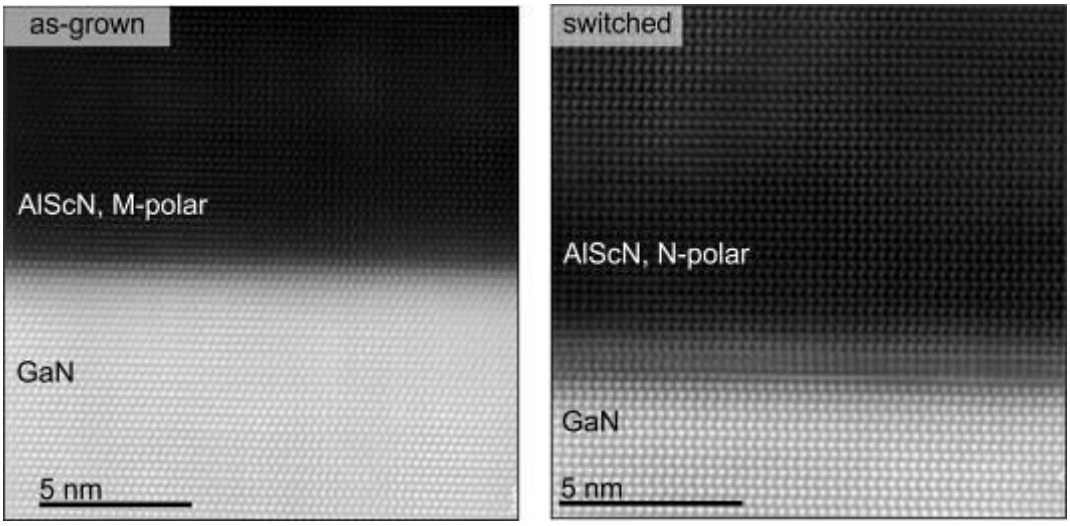
[3] Ferri, K.; et al. Journal of Applied Physics 2021, 130 (4), 044101. doi.org/10.1063/5.0053755.

[4] Uehara, M.; et al. Appl. Phys. Lett. 2021, 119 (17), 172901. doi.org/10.1063/5.0068059.

[5] Lee, C.-W.; et al. Science Advances 2024, 10 (20), eadl0848. https://doi.org/10.1126/sciadv.adl0848.

[6] Skidmore, C. H.; et al. Nature 2025, 637 (8046), 574–579. doi.org/10.1038/s41586-024-08295-y.

Fig. 1



MS6.P07
A comprehensive stem study on the role of surface structure and composition in photocatalysis of nanoceramic uv filters

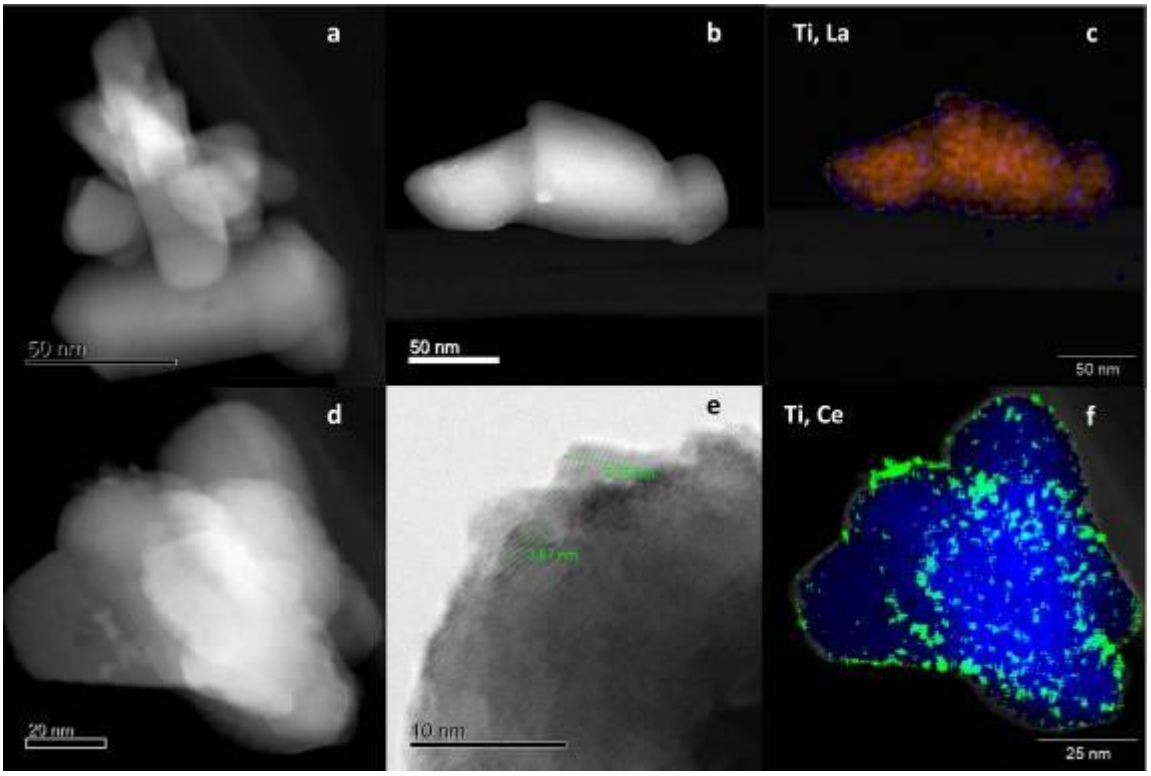
N. P. Cooray[1], L. A. Smillie[2], P. J. Barker[3], M. Lerch[4], J. H. Kim[1], K. Konstantinov[1]

[1]University of Wollongong, Institute for Innovative Materials, North Wollongong, Australia
[2]University of Wollongong, Electron Microscopy Centre, North Wollongong, Australia
[3]University of Wollongong, School of Chemistry and Molecular Bioscience, Wollongong, Australia
[4]University of Wollongong, Centre for Medical Radiation Physics, Wollongong, Australia

Titanium dioxide (TiO2) nanoparticles are one of the most used inorganic ultraviolet (UV) filters for broad-spectrum protection against UV radiation. However, upon exposure to UV radiation, these nanoparticles can generate reactive oxygen species (ROS), which can harm skin health and reduce the performance of the sunscreen formulations. This phenomenon, known as "photocatalytic activity", is an undesired property in sunscreens. The photocatalytic efficiency of TiO2 is known to be influenced by its surface structure, particularly at specific facets. For rutile nanoparticles, it is reported that (110) and (111) facets function as reductive and oxidative sites during photocatalysis. Furthermore, oxygen vacancies and titanium interstitials can act as trapping centres for photogenerated charge carriers and enhance ROS generation. Understanding the relationship between the structure, surface composition, and photocatalytic behaviour of nano UV filters is crucial for assessing their suitability as UV filters in sunscreens.

This study employs Scanning Transmission Electron Microscopy (STEM) techniques to investigate the structure and surface composition of TiO2 nanoparticles and nanocomposites with cerium oxide (CeO2) and lanthanum hydroxide (La(OH)3) quantum dots (QDs). High-angle annular dark-field (HAADF) imaging characterises nanoparticle morphology to understand the shapes and size distribution of the nanoparticles. Atomic resolution HAADF imaging examines the interfacial structure between the TiO2 core and the CeO2 and La(OH)3 QDs. Energy-dispersive X-ray spectroscopy (EDS) assesses the elemental composition and distribution of the elements within the nanocomposites. Electron energy loss spectroscopy (EELS) investigates the chemical bonding and oxidation states of the material interfaces. Suspensions of nanoparticles and composites mixed with 4-{Bis[4-(dimethylamino)phenyl]methylidene}-N,N-dimethylcyclohexa-2,5-dien-1-iminium chloride (crystal violet) organic dye is exposed to UV radiation to monitor the photocatalytic efficiency. Upon exposure to UV radiation, the generated reactive oxygen species by the nanoparticles and/or composites may degrade the organic dye via redox reactions. Analysis of these data demonstrates the influence of the structure and composition of the TiO2 nanoparticles and composites on photocatalytic activity, shedding light on how surface modification with CeO2 and La(OH)3 quantum dots affect photocatalytic efficiency. These findings will allow the development of safer and more effective UV filters for improved photoprotection.

Fig. 1



MS6.P08
An investigation into the relative thickness of TEM specimens for enhanced analysis

S. Drev[1], T. Gudžulić[1], M. Čeh[1]

[1]Jožef stefan Institute, Center for Electron Microscopy and Microanalysis, Ljubljana, Slovenia

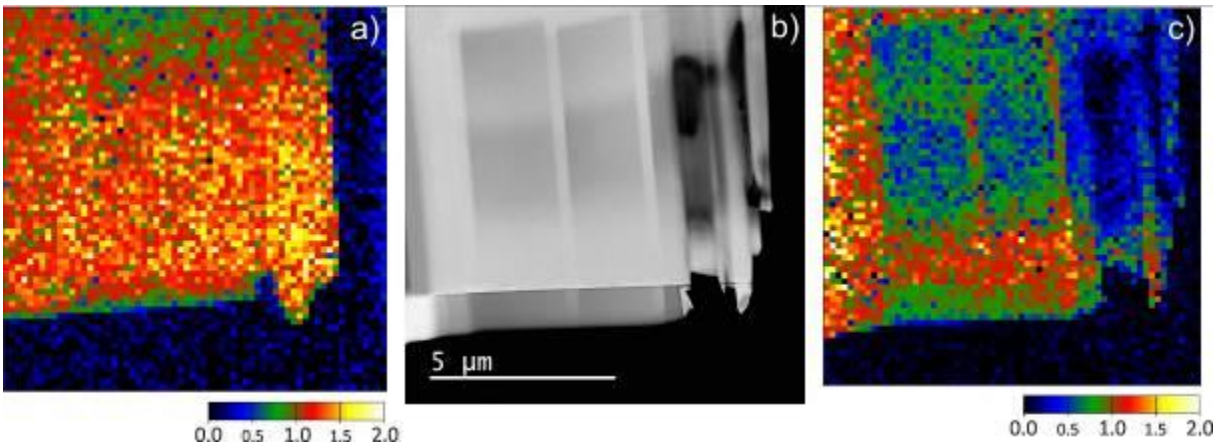
Investigating sample preparation methods is crucial in transmission electron microscopy (TEM). The emergence of new materials, such as ceramics, thin films, and composites, introduces unique properties that require precise treatment and often post-treatment. This presents ongoing challenges, necessitating continuous adjustments and improvements in advanced TEM preparation techniques like focused ion beam (FIB) sample preparation and conventional sample preparation.

In this comparison, we examine two of the most common TEM sample preparation techniques used today: conventional sample preparation and focused ion beam sample preparation. For both techniques, the samples were subsequently treated using the NanoMill® (model 1040, Fischione Instruments, Inc.) to achieve optimal results for further TEM/STEM analysis.

The first TEM sample was prepared using the FEI Helios NanoLab dual-beam Focused Ion Beam (FIB) system. This sample underwent final treatment (thinning and cleaning) with the NanoMill under specific conditions tailored for FIB-prepared samples. The second TEM sample was prepared conventionally. It was thinned and dimpled down to a transparent thickness using a Dimple Grinder (Gatan Inc.) and then ion-milled with a Precision Ion Polishing System (PIPS, Gatan Inc.) to create perforations. This sample was finally treated with the NanoMill under specific conditions suitable for conventional sample preparation.

We emphasize the significance of selecting the appropriate technique and conditions for TEM sample preparation.

Fig. 1



MS6.P09
Electron probe microanalysis of porous 3D nano-printed semiconducting ZnO nanoarchitectures

K. Kraft[1], L. Grünewald[1], E. Müller[1], A. Quintilla[1], Y. M. Eggeler[1]

[1]Karlsruhe Institute of Technology, Karlsruhe, Germany

Recently the writing of sub-micrometer semiconducting single-crystalline ZnO as wires for microelectronic devices have been achieved via photothermal 3D laser-printing on amorphous SiO_2 substrate using an advanced ink[1]. Intricate scanning electron microscopy (SEM) and transmission electron microscopy (TEM) analysis have revealed a single ZnO crystal with rotating lattice including the presence of a high number of interior nm-sized pores (Fig. 1) [2,3]. These nanopores influence material properties, which affects the overall material hence device performance. To better understand how porosity influences the device functionality, further local thickness, composition, and average density determination of porous ZnO in thin layer systems is performed, such as inkjet printed memristors[5]. Their performance depends on inner-structural details, which we analyze using an advanced non-destructive SEM method with energy dispersive X-ray spectroscopy (EDXS). In this work, we explore new paths to characterize the density of thin layers with nano-pores in the SEM, not resolvable with methods like nano-computed tomography (NanoCT), which typically achieve resolutions around 50 nm[4]. This allows us to correlate porosity with the performance of memristors which is crucial for optimizing.

Based on recorded EDX spectra, thin layer simulation, and TEM analysis we present a workflow (Fig. 2) to determine the average density of nano-pores in ZnO memristors, which are cross validated with focused ion beam (FIB)-SEM tomography and TEM.

For testing the proposed workflow, a model-multi-layer system with 20 nm Al, 50 nm Ti, and 50 nm on Si is prepared by EB-PVD. EDX spectra are acquired at different primary electron energies (Fig. 2a) and compared to spectra from reference samples. K-ratios are calculated from spectra using NIST DTSA-2 (Fig. 2b) and used in thin layer thickness simulation (BadgerFilm) to calculate the layer thicknesses. For determining the density of ZnO in memristors, k-ratios are calculated for different primary electron energies and thicknesses are measured by TEM imaging. This data is used to determine the average density of the inkjet printed memristor consisting of Au electrode, ZnO, and a top Ag electrode[6] (Fig. 2c).

In the first step, the layer thickness of the model-multi layer system is found by k-ratios fit (Fig. 3b) to be 20.4 nm for Al and 47.9 nm for Ti which meets in good agreement the layer thickness measured in cross-section samples with bright field (BF) scanning TEM (STEM)(Fig. 3a). For the Ag layer, a thickness of 55.7 nm was determined, which differs slightly from (52.2 ± 2.0) nm of TEM measurements (Fig. 3c). The small deviation of 2 nm is not significant and can be attributed to the uneven Ag top surface resulting from the deposition process. Investigating whether this method works consistently with other multi-layer systems would provide valuable insights.

As the next step, we will determine the layer thickness from STEM imaging of the inkjet-printed memristors. Using this data in combination with EDX spectra, we will calculate the density of the ZnO layer. This will allow us to better understand the material properties and optimize the printing process for improved device performance.

1. Steurer, M., et al. Advanced Science 2025
2. Kraft, K., et al. BIO Web of Conferences 2024
3. Grünewald, L., et al. Microscopy and Microanalysis 2024
4. Gou Q., et al. Fuel 2019
5. Hu H., et al. Advanced Functional Materials 2024
6. Hu H., et al. Applied Physics Letters 2021

Fig. 1

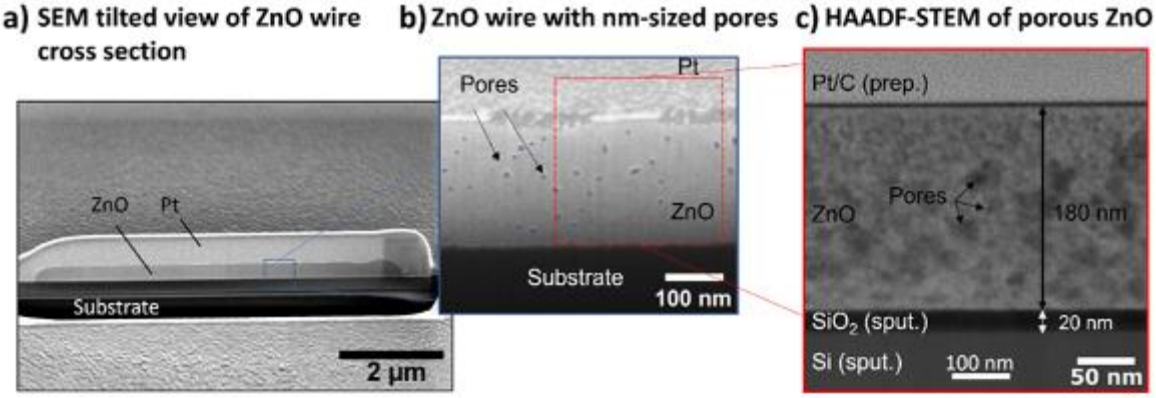


Figure 1. SEM and STEM images of porous ZnO wire. a) SEM tilted view of ZnO wire cross section cut using FIB. On top of the ZnO is Pt (FIB deposited) as a protection layer during cutting. **b)** Higher magnified SEM image of same ZnO wire showing nm-sized pores distributed in the ZnO layer. **c)** High-angle annular dark field (HAADF)-STEM image of ZnO wire with a high number of nm-sized pores, due to the projection through the whole structure (adapted from M. Steurer[1]).

Fig. 2

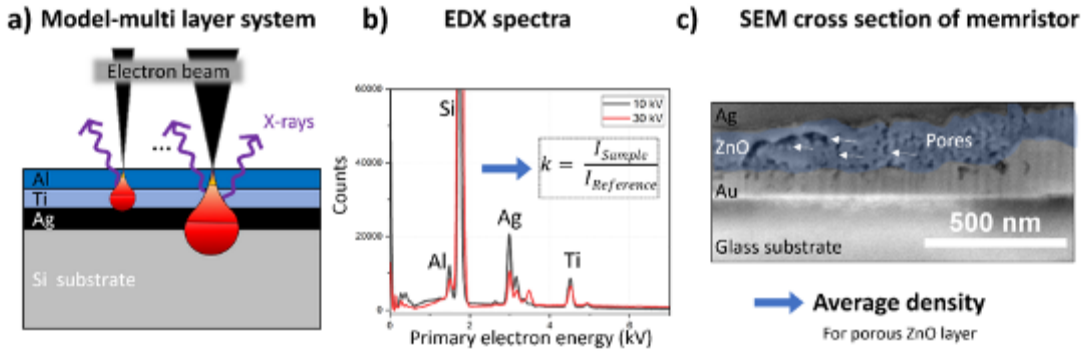
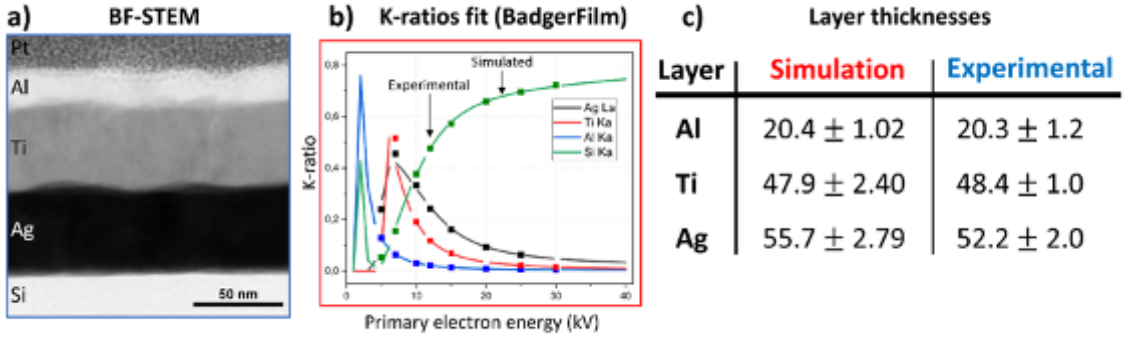


Figure 2. Workflow to determine the average density of porous ZnO in inkjet printed memristors. a) Schematic representation of the model-multi-layer system of Al/Ti/Ag on Si and interaction volumes for 2 different primary electron energies. **b)** X-ray spectra for 10 and 30 kV primary electron energy and the formula for calculating k-ratios from the multi-layer system and reference samples X-ray spectra. **c)** Cross section tilted SEM view of inkjet printed memristors with highlighted porous ZnO layer (pores marked with arrows).

Fig. 3



Layer	Simulation	Experimental
Al	20.4 ± 1.02	20.3 ± 1.2
Ti	47.9 ± 2.40	48.4 ± 1.0
Ag	55.7 ± 2.79	52.2 ± 2.0

Figure 3. Results for determining layer thicknesses from thin layer simulation and TEM. a) BF-STEM image of model-multi layer system with Pt deposited with FIB, acting as a protection layer during TEM lamella preparation. The model-multi layer is deposited with electron-beam physical vapor deposition (EB-PVD). **b)** K-ratio fit (from 5 to 30 kV) in thin layer simulation software BadgerFilm for the 4 elements containing in the model-multi layer system. **c)** Calculated layer thickness with standard derivation (in nm) for the k-ratios fit in **(b)** and TEM thickness measurements in **(a)**.

MS6.P10
Unraveling structure and properties of tubular structures made of quaternary misfit-layered compounds

S. Hettler[1,2,3], M. Furqan[2,3], M. Sreedhara[4], A. Khadiev[5], R. Tenne[6], R. Arenal[2,3,7]

[1]Karlsruhe Institute of Technology, Laboratorium für Elektronenmikroskopie, Karlsruhe, Germany
[2]CSIC-Universidad de Zaragoza, Instituto de Nanociencia y Materiales de Aragon, Zaragoza, Spain
[3]CSIC-Universidad de Zaragoza, Laboratorio de Microscopias Avanzadas, Zaragoza, Spain
[4]Indian Institute of Science, Solid State and Structural Chemistry Unit, Bengaluru, India
[5]Deutsches Elektronen-Synchrotron DESY, Hamburg, Germany
[6]Weizmann Institute of Science, Molecular Chemistry and Materials Science, Rehovot, Israel
[7]Araid Foundation, Zaragoza, Spain

- Introduction

Misfit-layered compounds (MLCs) are made up of alternating layers of two complementary materials that can be synergetically combined to create materials with unique properties.[1] The two subsystems exhibit a lattice mismatch in at least one direction generating misfit stress, which, combined with the removal of dangling bonds favors the formation of nanotubes (NTs). Recently, numerous MLCs with different compositions have been synthesized using the chemical vapour technique (CVT), including quaternary MLCs, were specific elements of the MLC are alloyed in a controlled way.[2-5]

- Objectives

The employed microscopy, spectroscopy and diffraction techniques aim for understanding structure and properties of the investigated MLC NTs.

- Materials & Methods

MLC NTs were synthesized using CVT, focusing on chalcogenide based MLCs MX-TaX_2 with M=La,Y,Sm and X=S,Se. Two aberration-corrected Titan microscopes were used for transmission electron microscopy (TEM), scanning (S)TEM, selected-area electron diffraction (SAED), energy-dispersive X-ray spectroscopy and electron energy-loss spectroscopy (EELS). Raman meaurements were conducted with an Alpha 300 M+ (WiTec) and synchrotron powder X-ray diffraction (SPXRD) was performed using the DESY beamline.

- Results

Figure 1 shows a SEM image of as-synthesized $Sm_{0.5}Y_{0.5}S$-TaS_2 revealing the tubular structures. The layered structure of the MLC is best visualized in STEM images, which allow to identify both subsystems as indicated exemplary for $Sm_{0.8}Y_{0.2}S$-TaS_2 in Figure 2. The image reveals that adjacent layers can show specific rotations of the lattice, which is seen in a SAED pattern from an individual $La_{0.1}Y_{0.9}S$-TaS_2 NT (Figure 3). These reveal the number of distinct orientations present in a single NT; two rotated by 30º in the case of Figure 3. The fine modifications of the MLC lattice upon alloying were traced in detail with SPXRD for the quaternary system $Sm_{1-x}Y_xS$-TaS_2.[5] Spectroscopy techniques such as Raman or EELS conducted on the individual NT level give insights into the electronic and vibrational properties of the MLC NTs. Figure 4 shows the comparison of Raman spectra of individual $Sm_{1-x}Y_xS$-TaS_2 NTs for different values of x revealing both small position and intensity modifications. When alloying S by Se in LaS-TaS_2, microscopic investigations revealed the exclusive bonding of Se with Ta forming LaS-$TaSe_2$ NTs.[3]

- Conclusion

Advanced microscopy, spectroscopy and diffraction techniques have been used to unravel the structure and properties of ternary and quaternary MLC NTs, revealing their potential for, e.g., thermoelectric applications.[6]

[1] Wiegers, *Prog Solid State Ch* **24**, 1996.
[2] Hettler et al, *ACS Nano* **14**, 2020.
[3] Sreedhara et al, *PNAS* **118**, 2021.
[4] Khadiev et al, *Acc Chem Res* **57**, 22, 2024.
[5] Hettler, Furqan, Sreedhara, Khadiev, Tenne, Arenal, *RSC Advances*, submitted, 2025.
[6] Funding by EU, Spanish MICIU and Gobierno de Aragón (DGA).

Figure 1: SEM image of SmS-TaS_2 MLC synthesized by CVT.
Figure 2: HAADF-STEM image of the outer walls of a $Sm_{0.8}Y_{0.2}S$-TaS_2 NT.
Figure 3: SAED pattern of an individual $La_{0.1}Y_{0.9}S$-TaS_2 NT with two different relative orientations of the subsystems as recognized from the two times 4 and 6 spots of the cubic (La,Y)S and the hexagonal TaS2 lattice, respectively.
Figure 4: Comparison of Raman spectra taken from individual $Sm_{1-x}Y_xS$-TaS_2 NTs for different alloying degree x with regions of the modes of the two subsystems marked.

Fig. 1

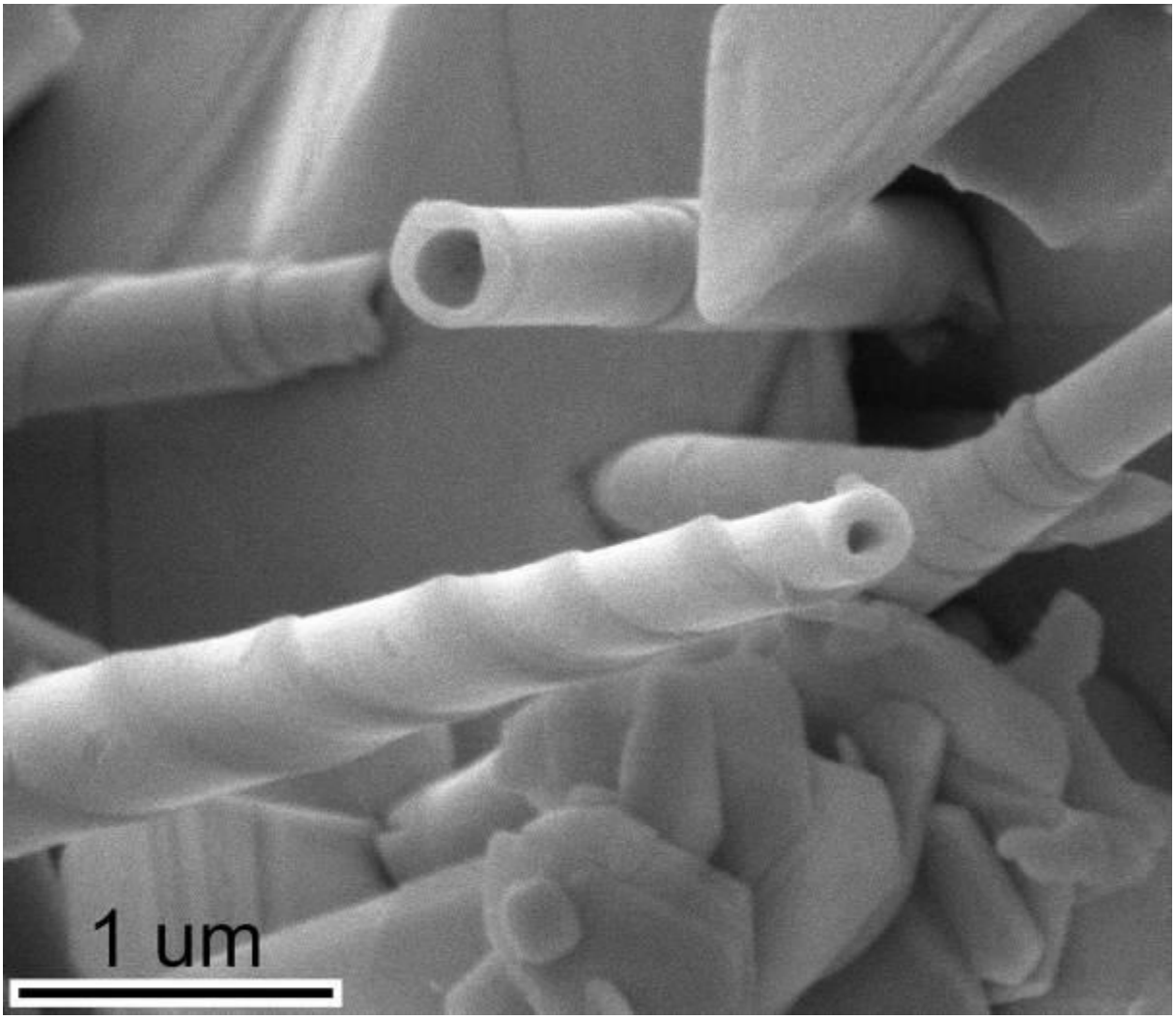


Fig. 2

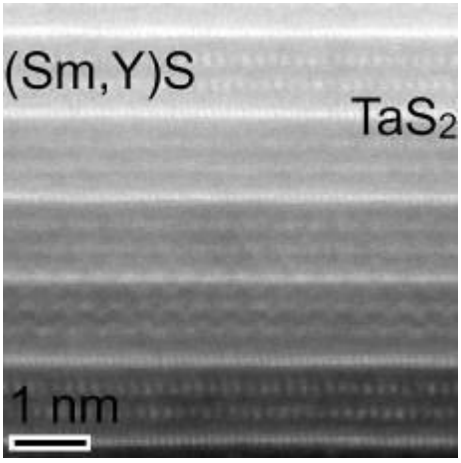


Fig. 3

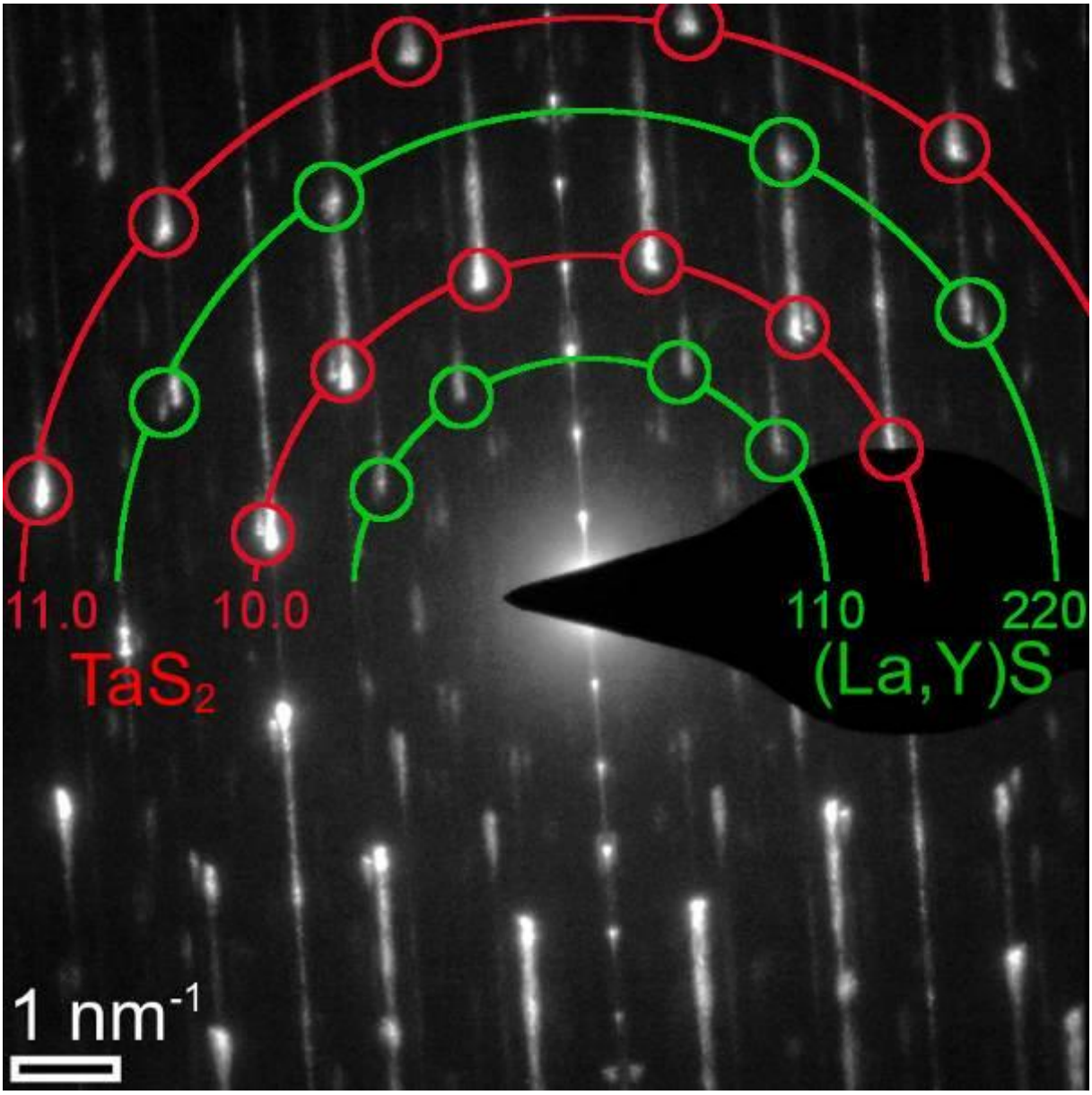
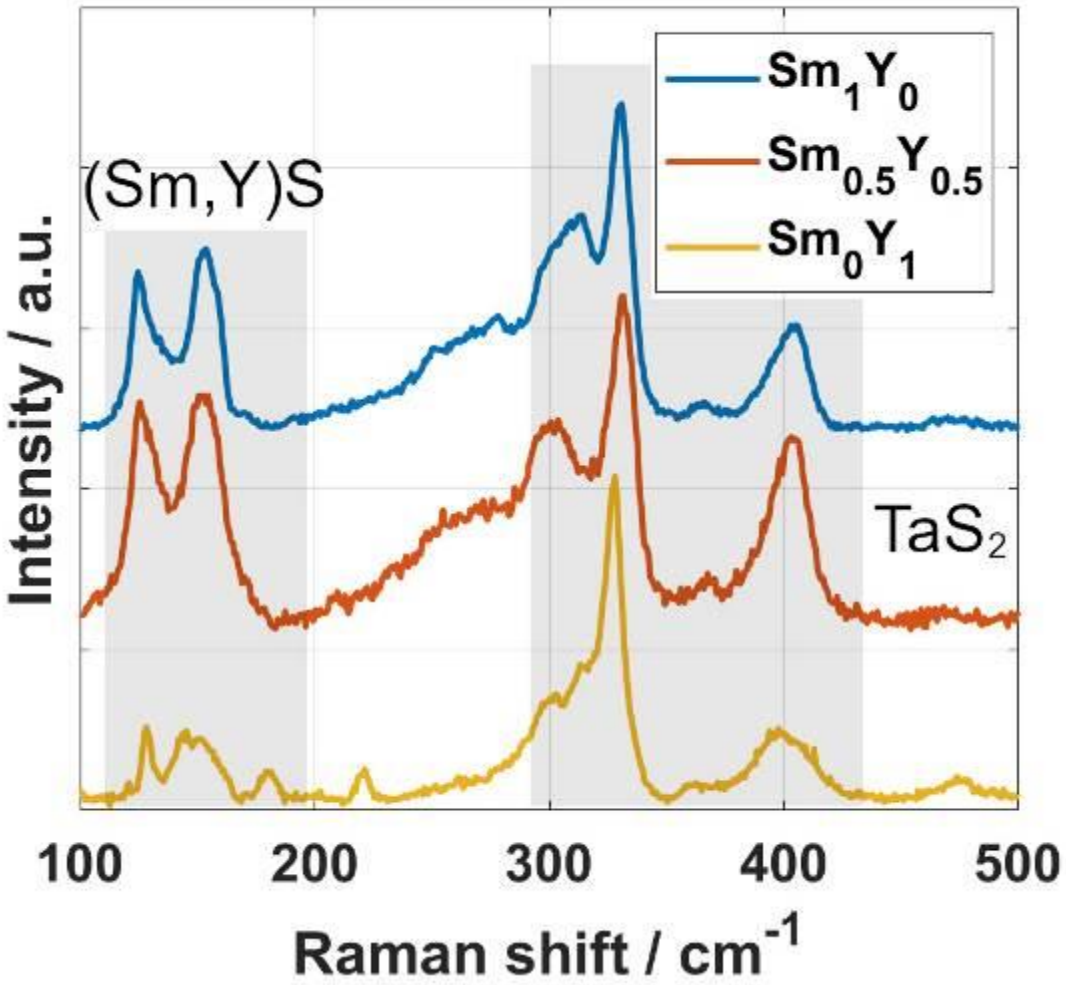


Fig. 4


Sm1Y0
Sm0.5Y0.5
Sm0Y1
(Sm,Y)S
TaS2
Intensity / a.u.
100
200
300
400
500
Raman shift / cm-1

MS6.P11
Interfacial reactions in multi-layered composite samples for high temperature application

I. S. R. Nurak[1], A. Pundt[1], Y. M. Eggeler[1], E. Ionescu[1], R. Riedel[1], D. Camacho Ramirez[1], S. Kredel[1], M. Galetz[1], L. Korell[1]

[1]Karlsruhe Institute of Technology, IAM-WK, Karlsruhe, Germany

The energy efficiency of thermal processes increases with temperature. To make use of this effect, structural materials are required that offer improved high- and ultrahigh-temperature performance. [1, 2]. Combination of refractory metal alloys and polymer-derived ceramic (PDC) nanocomposites (NCs) is considered as a promising new material for high temperature applications beyond .

Figure 1: BSE images and SEM-EDX elemental mapping of as prepared coated Mo-Si-Ti with Cr and one layer PDC

Fig. 1 shows the scanning electron microscopy (SEM) back scattered electron (BSE) image and individual Energy-dispersive X-ray spectroscopy (EDX) elemental maps for a sample with only one-layer PDC. In the BSE image different colors represent the different layers: green highlights the PDC, red visualizes the Cr bond coat layer, and yellow shows the Mo-Si-Ti substrate. The Cr bond coat layer (red) appears rough and uneven. The PDC layer appears only in the flat area between two Cr columns. There is no PDC detected on top of Cr column. This might result from the rotational movement during spin coating process. As illustrated in the Cr and Si map presented in the first row, the PDC layer on the right-hand side of the Cr hill is covered with Cr. This indicates Cr diffusion from Cr column. N enrichment is observed at the interface between the Mo-Si-Ti substrate and the Cr bond coat layer.

Figure 2: BSE images and SEM-EDX elemental mapping of as prepared coated Mo-Si-Ti substrate with Cr and 25-layer PDC

Fig. 2 illustrates the BSE images and individual elemental maps of a sample with -layers PDC at two different areas. The lower row elemental map shows chromium oxide, presumably Cr2O3 (visualized by combination of the red Cr and the purple O-signal) directly on top of the Cr bond coat layer. The element map from the upper row with Cr column shows chromium oxide next to the Cr column. This resembles the result observed in Fig. 1. Oxygen is present in the PDC coating and Cr bond coat, although the PDC precursor materials are oxygen-free. Oxygen is regarded to get into the PDC coating coating because the polymer preceramic get in contact with oxygen before its is converted to amorphous ceramic.

The results demonstrate the presence of oxygen contamination in the PDC-Coating, Nitrogen enrichment at the interface between Mo-Si-Ti Substrate and Cr bond coat layer, and Unevenness of the Cr bond coat layer.

References:

[1] High temperature materials for gas turbines: The present and future (Hiroshi Harada), 2003, Japan

[2] U.S.Energy Information Administration, Annual energy outlook 2023 (AEO2023)

Acknowledgment:

The authors gratefully acknowledge the financial support from DFG within the framework of GRK 2561.

Fig. 1

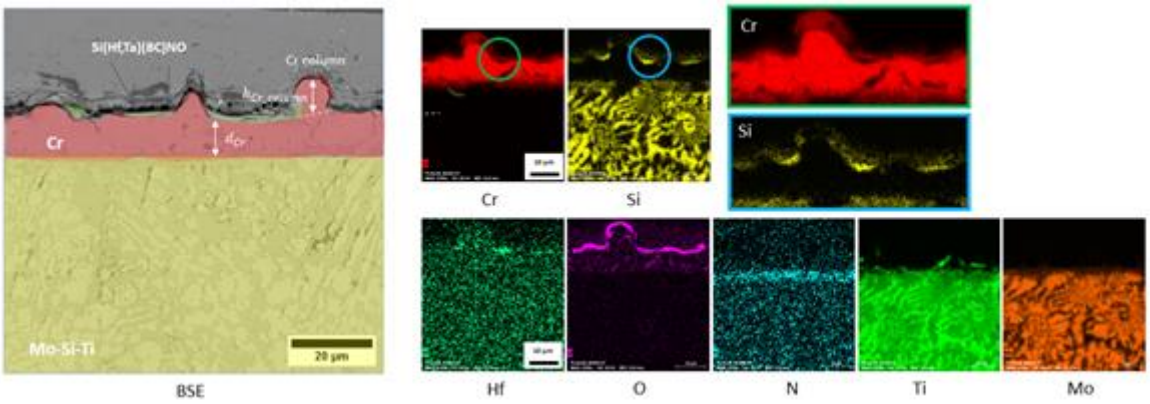
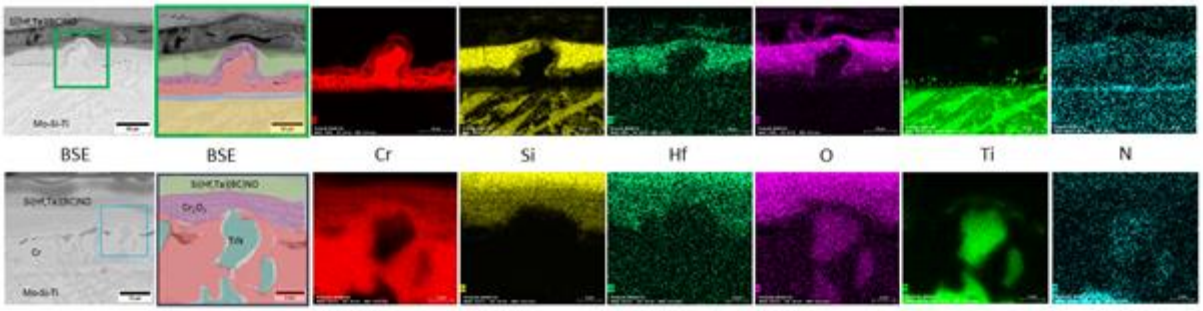

Si(Hf,Ta)(B,C)NO
Cr
Mo-Si-Ti
20 µm
BSE
Cr
Si
Hf
O
N
Ti
Mo

Fig. 2


BSE
BSE
Cr
Si
Hf
O
Ti
N

MS6.P12
Harvesting superior intrinsic plasticity in nitride ceramics with negative stacking fault energy

Y. Huang[1], Z. Chen[1], Z. Zhang[1]

[1]Austrian Academy of Sciences, Leoben, Austria

Introduction:
Ceramics are widely used in various structural and functional applications; however, their intrinsic brittleness at room temperature remains a critical challenge, often leading to early-stage catastrophic failures. This brittleness arises primarily due to the high critical-resolved shear stress required to initiate dislocation movement and the limited number of operational slip systems. Addressing this limitation is crucial for the development of ceramics with improved mechanical properties.

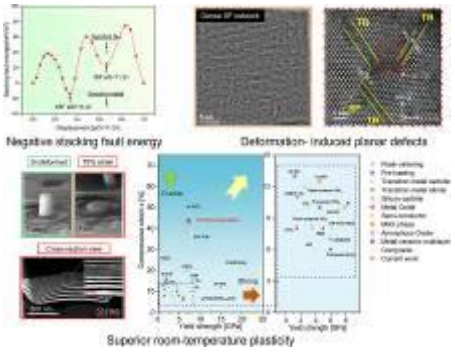
Objectives:
This study aims to develop a novel strategy for enhancing the deformability of ceramics by leveraging negative stacking fault energy (SFE). The approach seeks to reduce the energetic barriers to dislocation motion and expand the number of available slip systems, ultimately improving room-temperature plasticity while maintaining high strength and toughness.

Materials & Methods:
A TiN/TaN superlattice was fabricated and subjected to in-situ micro-mechanical testing to evaluate its mechanical response. Post-mortem transmission electron microscopy (TEM) was employed to analyze deformation mechanisms at the atomic scale, providing insights into the role of negative SFE in promoting dislocation activity, atomic plane faulting, and twinning.

Results:
The TiN/TaN superlattice exhibited remarkable room-temperature compressive plasticity (~43%), attributed to extensive atomic plane faulting and twinning facilitated by negative SFE. This behavior enabled an exceptional combination of plasticity, strength, and toughness, demonstrating the feasibility of overcoming the brittleness barrier in ceramics.

Conclusion:
This study successfully demonstrates a new paradigm for designing intrinsically ductile ceramics through negative SFE engineering. The findings provide a fundamental framework for the development of advanced ceramic materials with enhanced mechanical performance, paving the way for broader structural applications requiring both strength and deformability.

Fig. 1



MS 7: Multi-scale and correlative *in-situ/operando* electron microscopy

MS7.01(inv)
Nanocompression of 20 nm silver nanoparticles – *In situ* aberration-corrected TEM

P. Ferreira[1]

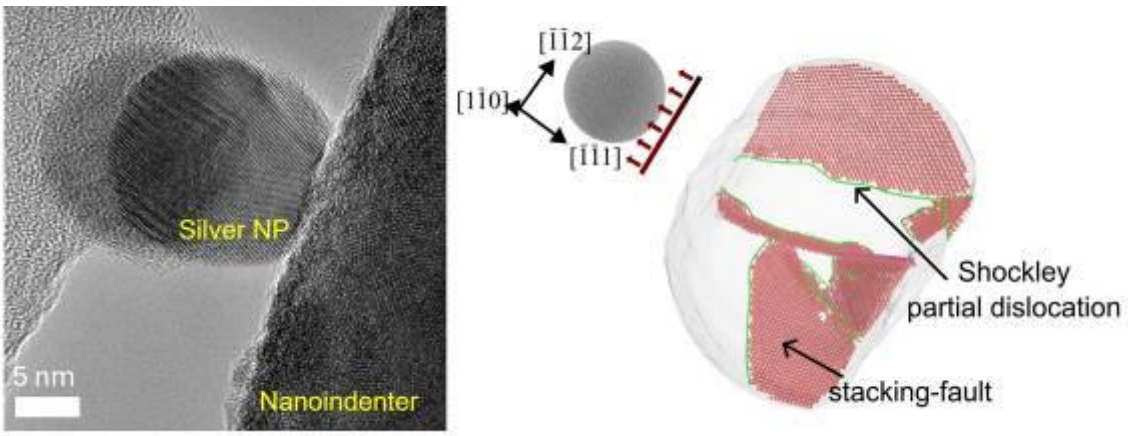
[1]University of Lisbon, International Iberian Nanotechnology/Laboratory, Braga, Portugal

Single-crystalline nanoparticles play an increasingly important role in a wide variety of fields including pharmaceuticals, advanced materials, catalysts for fuel cells, energy materials, as well as environmental detection and monitoring. Yet, the deformation mechanisms of very small nanoparticles are still poorly understood, in particular the role played by single dislocations and their interaction with surfaces. In this work, silver nanoparticles with particularly small dimensions (~20 nanometers in diameter) are compressed in-situ under phase-contrast in a transmission electron microscope (TEM). Two phase-contrast TEM experiments were done, one in a conventional TEM and the other in an aberration corrected TEM. During compression, the emergence of both dislocations and nanotwins were observed. However, these defects prove to be unstable and disappear upon removal of the indenter. Atomistic simulations confirm the role played by image stresses associated with the nearby surfaces and the reduction in dislocation line length as it approaches the free surface, thereby supporting experimental observations. These results provide justification for the frequent observation of the absence of dislocations in nanoparticles of a few nanometers size during in-situ experiments, even after significant deformation. This phenomenon contributes to the self-healing of samples through dislocation ejection towards the surfaces.

[1] C.E. Carlton, P.J.Ferreira, "In-situ TEM Nanoindentation of Nanoparticles", Micron, Special Issue, Vol. 43, pp. 1134-1139, (2012)

[2] Christopher Earl Carlton, Fátima Zorro, Maria José Caturla, Toshihiro Aoki, Yimei Zhu, Jonathan Amodeo, and Paulo Jorge Ferreira, "Nanocompression of 20 nm Silver Nanoparticles: In situ Aberration-Corrected TEM and Atomistic Simulations", Small, Volume 20, 2405292, (2024).

Fig. 1



MS7.02
Operando microscopy on thermoelectric materials – Measuring electrical and thermal transport on MEMS chips

S. Zhang[1], Y. Yu[2], P. Ying[3], C. Jung[1,4], D. Mattlat[1], C. Scheu[1]

[1]Max-Planck-Institute for Sustainable Materials, Düsseldorf, Germany
[2]RWTH Aachen University, Aachen, Germany
[3]IFW Dresden, TU Dresden, Dresden, Germany
[4]Pukyong National University, Busan, South Korea

Introduction: Thermoelectric materials use a temperature gradient to generate electrical energy. To benefit from a high Carnot efficiency, thermoelectrics operate across a wide range of temperatures, posing a challenge to optimize materials and microstructure design.

Objectives: Operando microscopy provides a unique opportunity to correlate the microstructure of materials with their transport properties. With advancing microelectromechanical systems (MEMS) technologies, samples with specific microstructure features can be prepared for microscopy observation at different temperatures, while their transport properties are measured.

Materials & methods: In this presentation, we examine 2-phase PbTe-Ag2Te thermoelectric materials that show a dynamic doping behaviour: Their carrier concentrations vary by an order of magnitude from room temperature to 500 °C. Samples from 2-phase regions were prepared by focused ion beam and mounted on a MEMS-based heating and biasing chip (DENSsolutions lightning).

Scanning transmission electron microscope (STEM) videos were recorded to observe the microstructural evolution during *in situ* heating, cooling and biasing. Spectroscopy and atom probe tomography (APT) were performed intermittently to study the compositional evolution of various microstructures.

Results: During heating, high angle annular dark field (HAADF)-STEM reveals the dissolution of Ag2Te precipitates into the PbTe matrix [1]. As shown in Fig. 1a-c, annular bright field (ABF)-STEM reveals dislocation nucleation at high temperatures accompanying the dissolution of precipitates, whereas APT confirms the segregation of Ag around the dislocations to form Cottrell atmospheres (Fig. 1e) [2].

During the *in situ* observations, I-V characteristics of the sample were measured *in operando* to evaluate the electrical transport properties (Fig. 1d). The continuous measurements on the electrical resistance was correlated to the *in situ* evolution of the sample microstructure, revealing the effect and mechanisms of dynamic doping. With considerations on the contact resistance, a numerical agreement of the electrical resistivity were reached between measurements from the micrometer-sized samples on *operando* MEMS chips and centimeter-sized bulk samples.

Conclusion: Combining the *in situ* STEM observation on the structural evolution of PbTe-Ag2Te with *operando* measurements on the electrical transport, we are able to propose the atomistic mechanisms behind dynamic doping [1, 2]. Furthermore, we investigate chip setups to measure other critical transport properties, such as the Seebeck coefficient.

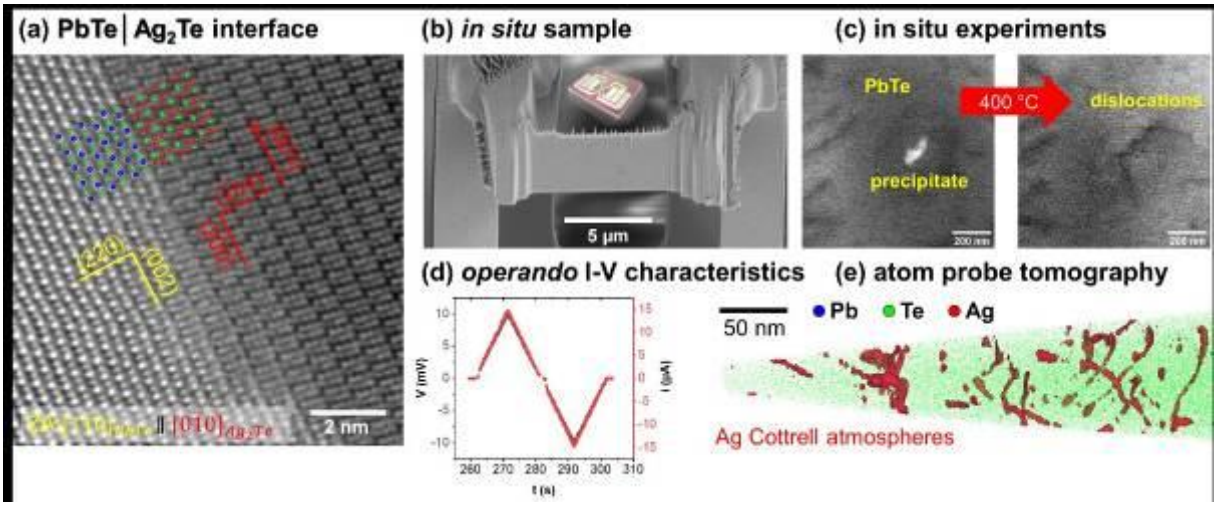
Figure 1. (a) HAADF-STEM image of the interface between PbTe and Ag2Te. 2-phase PbTe/Ag2Te thermoelectric materials and their interface. (b) In situ sample from FIB lift-out on a MEMS-based heating and biasing chip. (c) Schematic of dynamic doping revealed by in situ heating. (d) I-V characteristics of the sample. (e) Atom probe tomography of Ag Cottrell atmospheres around dislocations in PbTe [2].

References:

[1] Yu, Y., *et al.*, Dynamic doping and Cottrell atmosphere optimize the thermoelectric performance of n-type PbTe over a broad temperature interval, Nano Energy 101, 107576 (2022) https://doi.org/10.1016/j.nanoen.2022.107576

[2] Yu, Y., *et al.*, Ostwald ripening of Ag2Te precipitates in thermoelectric PbTe: Effects of crystallography, dislocations and interatomic bonding, Adv. Energy Mater. 14, 2304442 (2024) https://doi.org/10.1002/aenm.202304442

Fig. 1



MS7.03
Correlative *in situ* electrochemical TEM and electrochemistry coupled *in situ* Raman spectroscopy elucidation of mechanism of electropolymerization of 1,8-dihydroxynaphthalene derived allomelanin thin films

N. Sudheer[1,2,3], E. Maisonhaute[4], A. Tamayo[5], V. Ball[6], T. Ferte[7], C. Boissiere[4,8], P. Samori[4,5], O. Ersen[3,7], C. Sanchez[2,4,8]

[1]Karlsruhe Institute of Technology, Karlsruhe, Germany
[2]College de France, Paris, France
[3]University of Strasbourg, Strasbourg, France
[4]Sorbonne University, Paris, France
[5]Institut de Science et d´ingenierie supramoleculaires, Strasbourg, France
[6]Institut National de la Sante et de la Recherche Medicale, Strasbourg, France
[7]Institut de Physique et Chimie des Matériaux de Strasbourg (IPCMS), Strasbourg, France
[8]Laboratoire Chimie de la Matière Condensée de Paris, Paris, France

The electrochemical oxidative polymerization of 1,8-dihydroxynaphthalene (1,8-DHN) facilitates the creation of durable, melanin-like coatings with potential applications that include protective barriers and bio-inspired materials. We integrate in-situ transmission electron microscopy (TEM) within liquid cells, in-situ Raman spectroscopy, and cyclic voltammetry to clarify the mechanistic processes that dictate film nucleation, growth, and structural development under moderate aqueous conditions.

At potentials exceeding +0.3 V vs. Ag/AgCl, phenoxyl radicals and naphthoquinone intermediates are produced, resulting in the formation of distinct nuclei that attach to the electrode surface. Real-time TEM imaging demonstrates that these nuclei swiftly expand and merge, aligning with traditional nucleation-growth behavior. Simultaneously, in-situ Raman spectra exhibit significant fluorescence due to oxidized oligomers and radical cation species—an effect that is most evident in the initial phase of the reduction cycle. As potential sweeps progress, a consistent low-frequency Raman band (278–288 cm^{-1}) emerges, signifying reliable C–C connections between naphthalene rings, while the elevated fluorescence background progressively decreases. This history indicates a progressively crosslinked, conjugated network, wherein enlarged π-electron domains promote non-radiative deactivation rather than photon emission.

The presence of oxygen in the electrolyte facilitates supplementary oxidation pathways, resulting in localized bubble-templated structures identified using in-situ TEM. These H_2-bubble-driven microenvironments facilitate the modulation of film porosity and thickness, whereas oxygen-derived reactive species may sporadically overoxidize or restructure emerging oligomers. Notwithstanding these side reactions, the polymer film finally stabilizes into a melanin-like matrix characterized by heterogeneous aromatic domains containing several redox-active sites. Ex-situ profilometry and atomic force microscopy validate a cohesive covering, with its roughness and thickness adjustable through modifications in scan rate and cycle count.

Our comprehensive, multi-technique methodology elucidates the polymerization of 1,8-DHN into a resilient, redox-active thin film under electrochemical regulation. This research presents novel pathways for the development of "green" polyaromatic coatings with customizable attributes and underscores the need of employing in-situ spectroscopic and microscopic techniques to elucidate intricate electrochemical polymerization processes.

Fig. 1

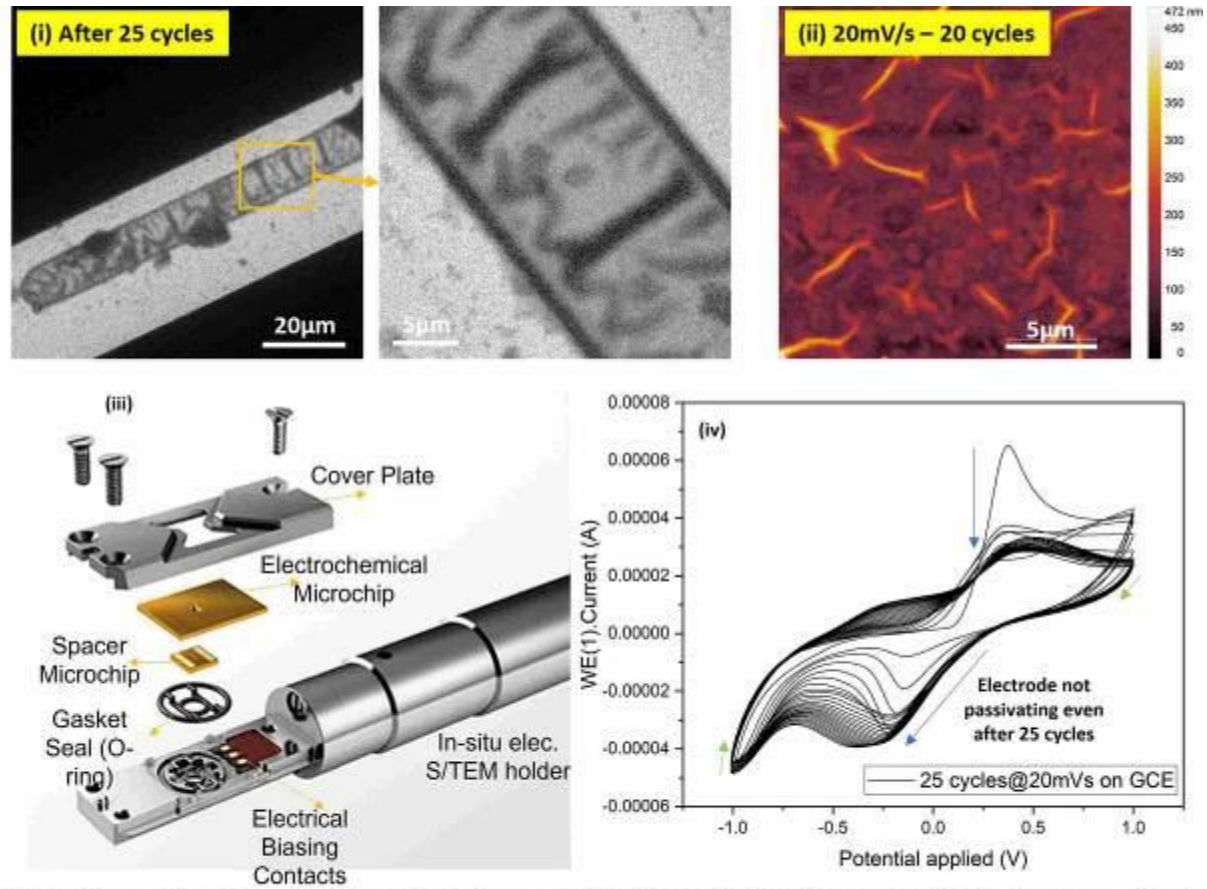


Fig.1. (i) Glassy carbon electron after 25 cycles in the in-situ cell; (ii) AFM image of 1,8 DHN films prepared in 20 cycles at scan rates of 20mV/s; (iii) In-situ liquid electrochemical Poseidon TEM holder from Protochips (the inset shows the tip of the holder where the miniaturized electrochemical cell is integrated. (iv) Successive CV curves for 1,8-DHN on an amorphous carbon electrode in the presence of 50mM sodium acetate buffer and at a potential sweep rate of 20mV.s-1.

Fig. 2

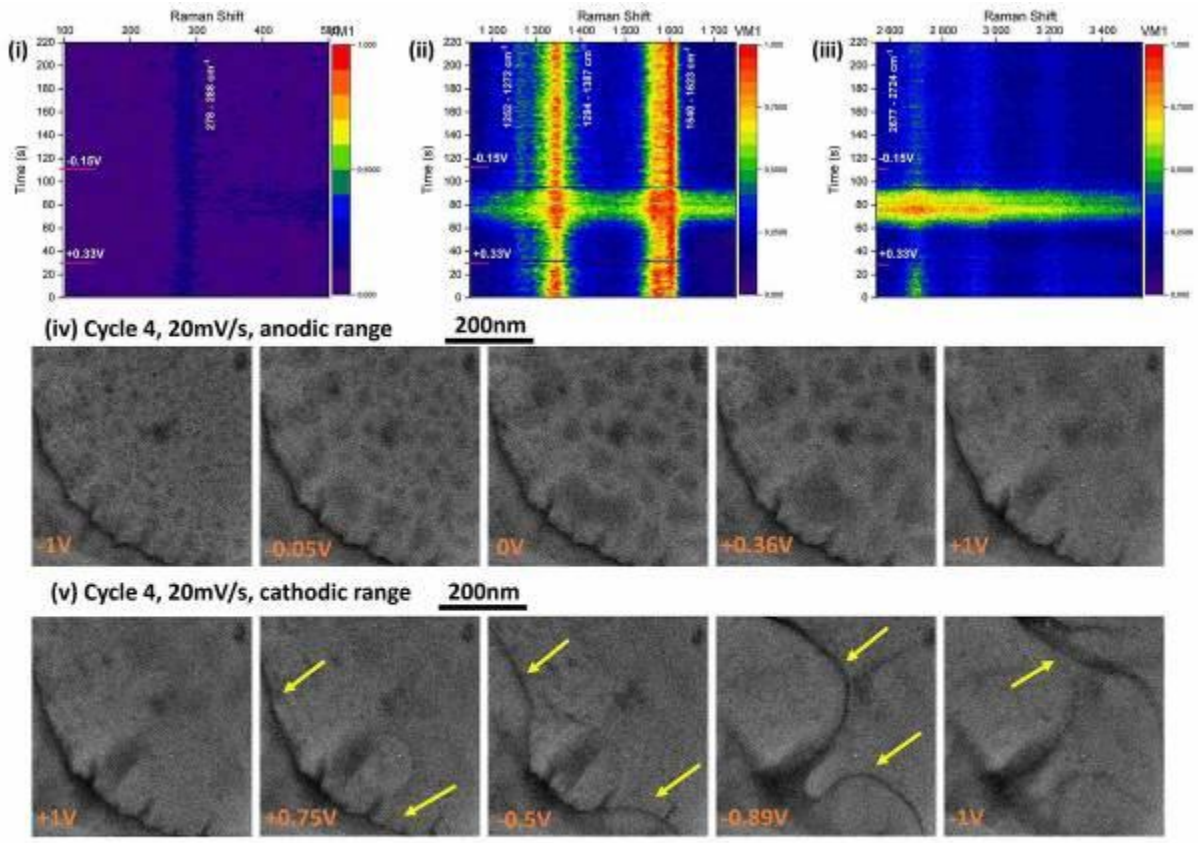


Fig.2. (i) (i) Time evolution of potential, current density and corresponding in situ Raman time maps of electropolymerization of 1,8 DHN in pH 5.6 on the [-1V; +1V] potential range at 20mV/s scan rate for the fourth cycle; data of the range 100cm-1 to 500 cm-1 . acquisition parameters; t_{acq} = 1s and λ = 473nm laser line. (ii) data of the range 1150cm-1 to 1750 cm-1 and (iii) data of the range 2550cm-1 to 3550 cm-1; Real time observation of the electropolymerization process of 1,8 DHN from -1V to +1V during the 4th anodic cycle at 20mV/s scan rate, and (iv) Real time observation of the electropolymerization process of 1,8 DHN from -1V to +1V during the 4th cathodic cycle at 20mV/s scan rate.

MS7.04
Tunneling field emission from plasmonic nanostructures under electron irradiation

K. Elibol[1], V. Srot[1], C. Yang[1], S. Satheesh[1], S. Arslan[2], M. Burghard[1], H. Giessen[2], P. A. van Aken[1]

[1]Max Planck Institute for Solid State Research, Stuttgart, Germany
[2]University of Stuttgart, Stuttgart, Germany

Field electron emission from plasmonic nanostructures has attracted significant interest due to its potential in various applications, including electron microscopy and plasmon-assisted electron sources [1-4]. Despite extensive studies in high-voltage and laser-driven systems, the realization of field electron emission from electron-beam-irradiated plasmonic nanostructures still faces challenges because of the experimental limitations and the lack of suitable emitter structures.

In this work, we aim to address these challenges by fabricating electron emitter arrays on electrical biasing chips and performing *in-situ* electrical measurements in transmission electron microscope (TEM), enabling the detection of field electron emission from plasmonics under electron irradiation.

The emitter arrays, consisting of gold (Au) nanoprisms, are fabricated on Au electrodes containing intrinsic Au grains using electron beam lithography. During *in-situ* electrical measurements in a TEM, the fabricated plasmonic emitter arrays are exposed to a 200 kV parallel electron beam to measure the electron-beam-driven field emission current.

Fig. 1a shows the schematic of the experiment used to measure the emission current from plasmonic nanostructures. The emitted electrons are driven under a static external electric field toward the collector for current measurement (Fig. 1b). Fig. 1c shows the bias dependence of field emission current which fits well to the Fowler-Nordheim (FN) field emission model. For an induced field estimated as E= 23.36 GV m-1, a tunneling ionization is favored since Keldysh parameter is smaller than 1 at this field strength. The tunneling emission is further confirmed by FN plot shown in Fig. 1d.

Fig. 1 (a) Schematic of the experiment displaying electron emitters under a parallel electron beam irradiation. (b) 3D AFM topography images of collector and emitter, respectively. (c) Emission current as a function of bias voltage. The red line is the fit for FN model. (d) FN plot generated from the raw data.

In conclusion, the fabricated nanostructures incorporate strong plasmonic hotspots that serve as efficient electron emission sites while also exhibiting significant surface-enhanced Raman scattering (SERS) activity due to localized field enhancement. The electron-beam-induced electric field distribution is mapped using four-dimensional scanning transmission electron microscopy (4D-STEM) and corroborated by finite element method (FEM) simulations revealing peak field intensities at the apex of emitter tips where field enhancement is maximized. *In-situ* TEM electrical measurements display a clear FN tunneling signature demonstrating a field emission process that significantly surpasses secondary electron emission. These findings establish a direct correlation between plasmonic field enhancement and electron-beam-driven field emission showing its potential for plasmon-assisted electron sources. The ability to map and control localized electron emission under electron beam could also enable advancements in attomicroscopy, scanning field emission electron microscopy, nanoscale vacuum electronics and high-resolution electron beam techniques.

References

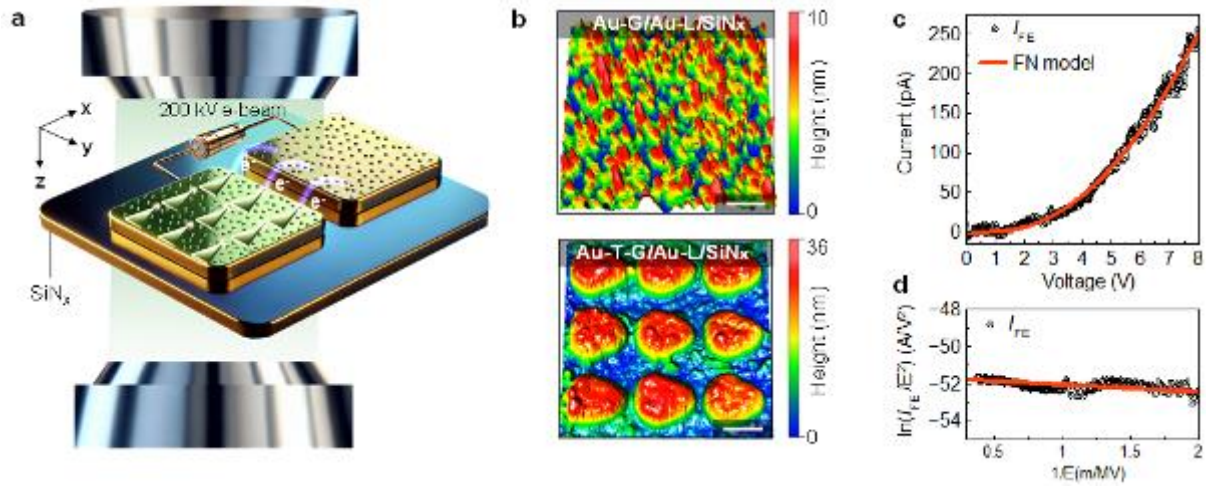
[1] F.S. Baker, *et. al*., Nature **239** (1972), 96-97.

[2] P. Dienstbier, *et. al*., **616** (2023) Nature, 702-706.

[3] H.Y. Kim, *et. al*., **613** (2023) Nature 662-666.

[4] X. Shao, *et. al*., **9** (2018) Nature Communications 1288.

Fig. 1



MS7.05
ILIAS – Identical Location Imaging And Spectroscopy – A low radiation damage and versatile alternative to operando electron microspectroscopy

F. P. Schmidt[1], T. Götsch[1], S. Najafishirtari[2,3], M. Behrens[2,3], C. Pratsch[4], S. Kenmoe[5], D. H. Douma[6], F. Girgsdies[1], J. Allan[1], A. Knop-Gericke[1,7], T. Lunkenbein[1]

[1]Fritz-Haber-Institut der Max-Planck-Gesellschaft, Berlin, Germany
[2]Kiel University, Institute of Inorganic Chemistry, Kiel, Germany
[3]Kiel University, Kiel Nano, Surface and Interface Science KiNSIS, Kiel, Germany
[4]Helmholtz Institute Ulm for Electrochemical Energy Storage, Berlin, Germany
[5]University Duisburg-Essen, Essen, Germany
[6]Université Marien Ngouabi, Brazzaville, Congo
[7]Max Planck Institute for Chemical Energy Conversion, Mülheim a.d. Ruhr, Germany

The correlation of structural features of a catalyst with its activity or selectivity is essential to understand complex processes in catalytic reactions, which is a pre-requisite to optimize catalysts. Nowadays, this task is approached by operando techniques, including operando electron or X-ray microscopy and spectroscopy [1]. But how to get access to local features without unwanted influence of the probing tools, i.e., X-rays or electron beams, and at relevant reaction conditions?

In our study we introduce ILIAS (identical location imaging and spectroscopy) in combination with a quasi in situ approach to separate the effect of heat and gas on the catalyst surface from the effect of the electron beam [2,3]. With this approach we allow high temperatures and pressures in any gaseous environment on the one hand, and atomic resolution imaging and spectroscopy on the other. As a proof of concept, we resolve the structural evolution of a Co_3O_4 spinel catalyst using ILIAS and track the oxidation state across the surface before and after heating in a reductive or oxidative environment with sub-nanometer resolution (Figure 1). The surface of the catalyst is then titrated using CO as a probe molecule to remove highly active oxygen species, providing unprecedented insight between pre-treatment and activity of the catalyst in CO oxidation. We thus provide an indirect but controlled and traceable correlation between product formation and catalyst structure.

The electron microspectroscopy results (STEM-EELS) are supported by complementary X-ray techniques (NAP-XPS, TXM, and XRD) and DFT simulations, confirming this approach as a promising way to follow the electronic structure of a catalyst experimentally and theoretically with atomic resolution.

Figure 1: (a) ILIAS before heating. TEM micrographs at different magnifications, from overview (left) to medium (center) to high (right) and EEL spectra (red) of the particle labelled "CoO". (b) ILIAS after heating in O_2 of the same regions as in (a) and the corresponding EEL spectra (blue) of the same particle after heating in O_2. The white arrows in the right image highlight the strong restructuring at the surface of the particles. The differences in peak ratio, energy difference and peak position are labelled 1, 2 and 3. (c) Evolution of the oxidation state across the surface (EELS). Peak ratios (pr) – extracted from Co^{3+}/Co^{2+} subpeak components of the Co-L3 peak – and oxidation states (os) before and after heating in N_2 (left) and before and after heating in O_2 (right). The vertical dotted lines indicate the surface position of the nanoparticle, the dashed lines are a guide to the eye.

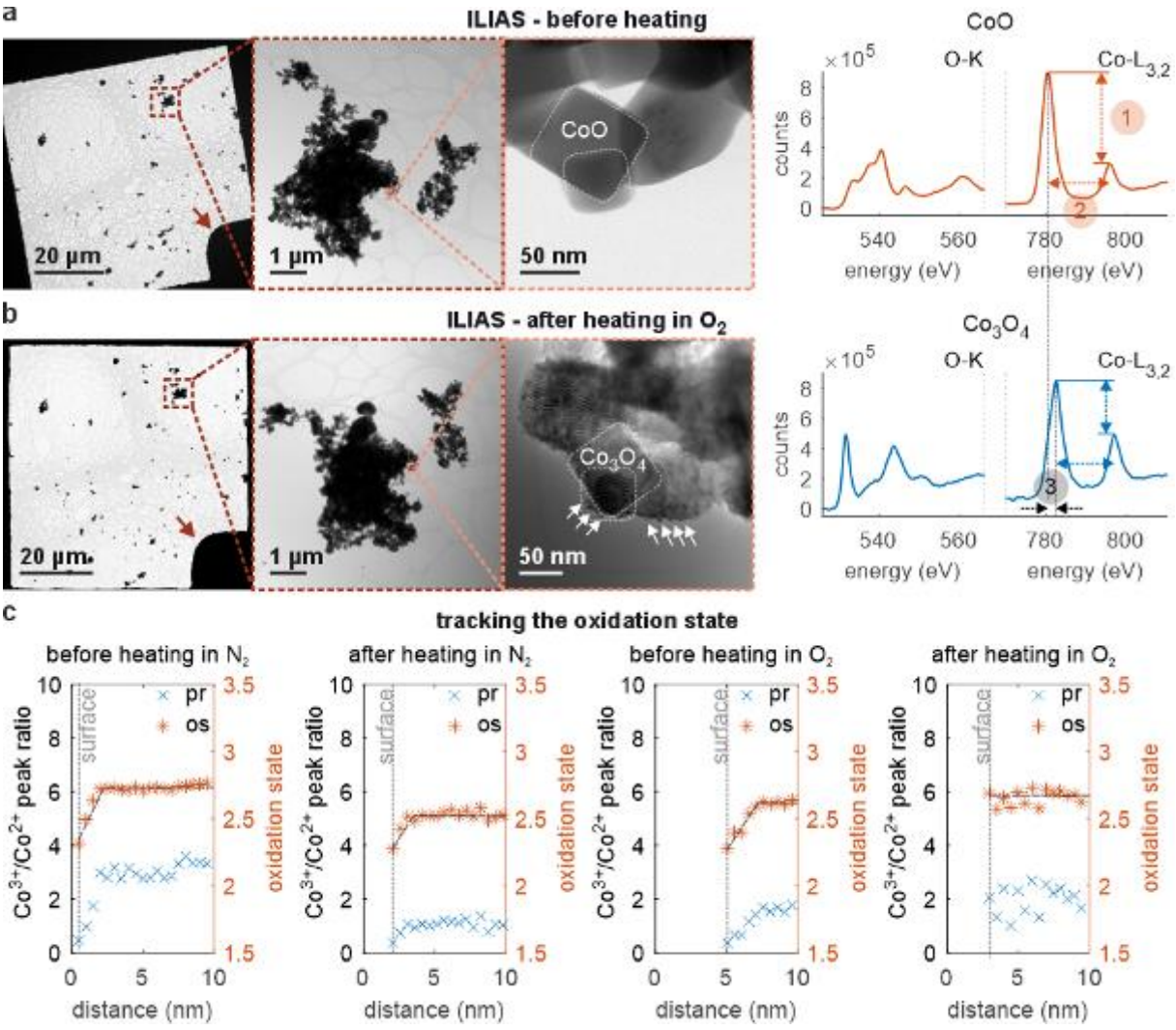
References:

[1] Chee, S. W.; Lunkenbein, T.; Schlögl, R.; Roldán Cuenya, B. Operando Electron Microscopy of Catalysts: The Missing Cornerstone in Heterogeneous Catalysis Research? Chemical Reviews 2023, 123, 13374–13418.

[2] Masliuk, L.; Swoboda, M.; Algara-Siller, G.; Schlögl, R.; Lunkenbein, T. A quasi in situ TEM grid reactor for decoupling catalytic gas phase reactions and analysis. Ultramicroscopy 2018, 195, 121–128.

[3] Schmidt, F.-P.; Götsch, T.; Najafishirtari, S.; Behrens, M.; Pratsch, C.; Kenmoe, S.; Douma, D.H.; Girgsdies, F.; Allan, J.; Knop-Gericke, A.; Lunkenbein, T. Subnanometer tracking of the oxidation state on Co_3O_4 nanoparticles by identical location imaging and spectroscopy. ACS Applied Materials & Interfaces 2025, 17, 9419–9430.

Fig. 1



MS7.06
Exact mechanisms of SEI formation and Li metal growth in Li-Ion batteries investigated by operando electrochemical liquid cell scanning transmission electron microscopy

W. Dachraoui[1], R. S. Kühnel[1], R. Pauer[1], C. Battaglia[1], R. Erni[1]

[1]EMPA - Swiss Federal Laboratories for Materials Science and Technology, Dübendorf, Switzerland

In lithium-ion batteries (LIBs), interfacial processes at the electrode-electrolyte boundary, such as the formation of the solid electrolyte interphase (SEI) and the growth of Li dendrites, are critical to performance and safety.[1] The SEI stabilizes the anode-electrolyte interface, reducing capacity loss, decreasing impedance, and inhibiting Li dendrite formation. The uncontrolled growth of Li dendrites particularly under fast charging or low-temperature can pose severe safety risks, as their extension from the anode to the cathode can cause a short circuit.[2] Additionally, Li dendrite formation accelerates capacity loss by generating dead Li.[3] Therefore, a deeper understanding of the mechanisms governing the nucleation, growth, and evolution of both the SEI and Li dendrites, as well as dead Li formation and the interplay between them, is crucial for improving the performance and cycling stability of LIBs. Despite extensive experimental and theoretical efforts by researchers to understand these processes, they remain elusive. Therefore, targeted experiments capturing the early stages of Li dendrite nucleation and evolution are essential for developing improved experimental methods and theoretical models capable of predicting its formation and progression to dead Li. Due to the sensitivity of the SEI and Li metals, it is essential to use a technique that provides high-spatial and temporal resolution while allowing real-time battery operation during analysis.

In this study, we utilize operando electrochemical liquid cell scanning transmission electron microscopy (ec-LC-STEM) to directly observe nanoscale processes at the anode-electrolyte interface of Li-ion batteries in real-time during (dis-)charge, using a classic electrolyte consisting of 1 M $LiPF_6$ in ethylene carbonate/ethyl methyl carbonate (EC/EMC). Our results reveal that the SEI formation is a multi-step process (figure 1.a)[4] and that Li metal dendrites initially nucleate as spherical Li nanoparticles beneath the SEI before growing into dendritic structures. During discharge, these dendrites undergo incomplete dissolution, leading to the formation of electrically isolated dead Li. Notably; the SEI layer plays a crucial role in both the growth and dissolution of Li dendrites. We identify three distinct growth stages: (i) nucleation, (ii) root growth, and (iii) tip growth. Furthermore, we demonstrate that the formation of dead Li is strongly influenced by the initial dendrite morphology and the structural characteristics of the SEI. Specifically, inhomogeneous thinning of Li whiskers results in root contraction before tip dissolution, ultimately leading to the detachment of Li metal (Figure 1.b).[5]

This study highlights the potential of combining in situ electrochemical liquid cells with advanced STEM techniques to investigate complex mechanisms within batteries, thereby challenging established theoretical and experimental models.

Figure 1. Time-lapse annular dark-field STEM images showing: (a) SEI formation and (b) Li dendrite growth (Reproduced from refs. 4 and 5)

References

1Harlow et al. *J. Electrochem. Soc.* **2019**, *166* (13), A3031.

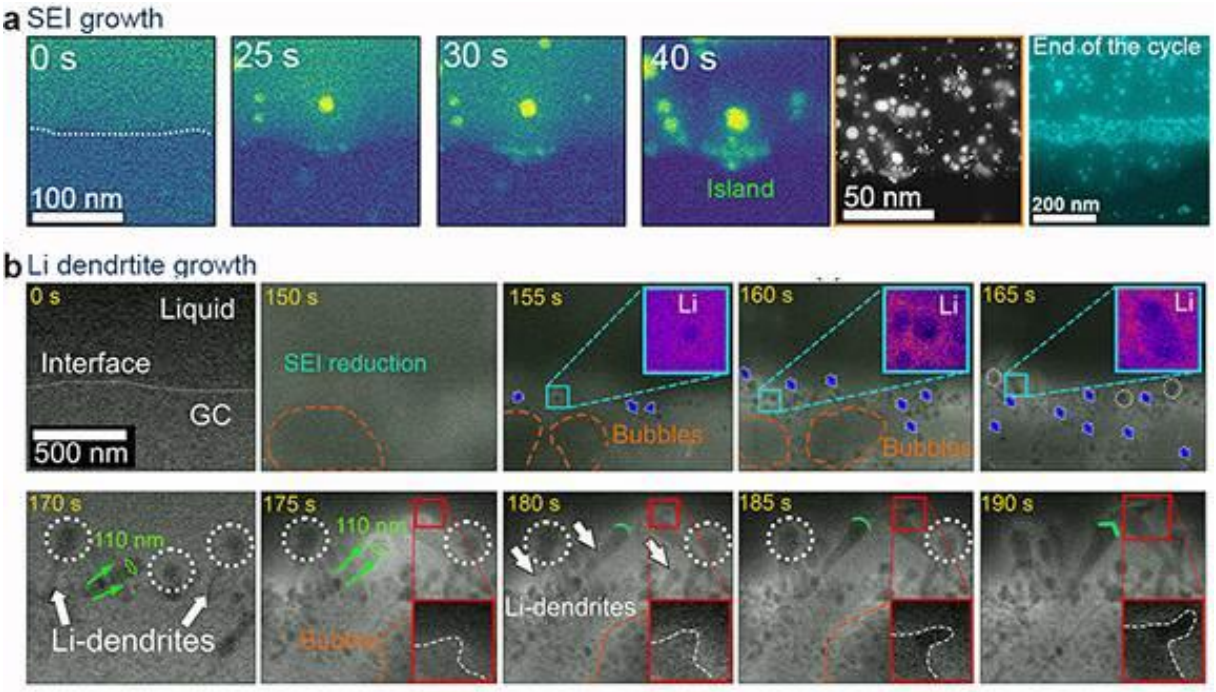
2Wood et al. *ACS Energy Lett.* **2017**, *2* (3), 664–672.

3Peled et al. *J. Electrochem. Soc.* **2017**, *167* (16), A1703–A1719.

4Dachraoui et al. *ACS Nano* **2023**, *17* (18), 20434–20444.

5Dachraoui et al. *Nano Energy* **2024**, *130*, 110086.

Fig. 1



MS7.07
Validating electrocatalysts (in-)stability – Correlating *in situ* electrochemical liquid phase transmission electron microscopy to operando electrochemical techniques

R. Aymerich Armengol[1], L. M. Kaas[1], A. Juul Nielsen[2], F. Wu[2], A. Bech Larsen[1], M. Birkedal Norby[1], A. M. Mingers[3], S. Zhang[3], C. Danvad Damsgaard[1,4], P. C. Kjærgaard Vesborg[1,2], J. Kibsgaard[1,2], S. Helveg[1]

[1]Technical University of Denmark, Center for Visualizing Catalytic Processes, Kongens Lyngby, Denmark
[2]Technical University of Denmark, Surface Physics and Catalysis, Kongens Lyngby, Denmark
[3]Max-Planck-Institute for Sustainable Materials, Düsseldorf, Germany
[4]Technical University of Denmark, Nanolab - National Centre for Nano Fabrication and Characterization, Kongens Lyngby, Denmark

Understanding the stability of electrocatalysts is key for the development of durable green energy harvesting and storage technologies. Stability characterization is however not straightforward and consequently it is oftentimes overlooked[1]. This knowledge gap prevents further advances in the application of materials with promising potential to substitute expensive state-of-the-art noble electrocatalysts, such as manganese oxides (MnO_2). Recently, the advent of electrochemical liquid phase transmission electron microscopy (ec-LPTEM) has enabled real-time and real-space investigations of electrochemical processes in the microscope. While this technique has the potential to ease the process of establishing structural-property relationships of electrocatalysts, its pitfalls including beam damage and radiolysis processes make a strong validation protocol a requirement to correctly interpret stability results[2].

Herein, we combine *in-situ* electron microscopy and *operando* electrochemical techniques to investigate the debated existence of a potential window of stable operation of MnO_2 electrocatalysts for the oxygen evolution reaction (OER) in acid media. For this purpose, we first study the growth of MnO_2 nanocatalysts by electrodeposition by ec-LPTEM and subsequently lower the pH to 1 by electrolyte exchange. Our *in-situ* findings suggest that the acid induces a fast dissolution of the MnO_2 catalyst at open circuit potential. To validate this result, *operando* scanning flow cell coupled to a mass spectrometer (SFC-ICPMS) measurements are conducted in a bulk MnO_2-GC electrode. These SFC-ICPMS measurements reveal the presence of a stability window narrower than the thermodynamic prediction of the MnO_2 Pourbaix diagram, which is further demonstrated by complementary imaging and spectroscopy imaging performed at identical locations before and after tests (IL-STEM).

This combined methodology of ec-LPTEM, identical location electron microscopy characterization, and *operando* electrochemical measurements allows to correlate and validate the results with data acquired from samples at different scales and techniques. Furthermore, it highlights the advantages and limitations of the ec-LPTEM technique to consider when applying it to study the stability of electrocatalysts. Overall, the results show that an inherent acid instability of MnO_2 calls for high pH environments for OER applications.

Ref.

[0]The Center for Visualizing Catalytic Processes (VISION) is funded by the Danish National Research Foundation (grant no. DNRF146).
[1] *ACS Energy Lett.* **2023**, *8,* 1607−1612
[2] *Acc. Chem. Res.* **2023**, *56, 21,* 3023–3032

MS7.P01
In situ ESEM analysis of platinum dewetting behaviour on different oxide supports under reactive atmospheres

M. Dortmund[1], B. Holtermann[1], E. Müller[1], Y. M. Eggeler[1]

[1]Karlsruhe Institute of Technology, Laboratory of Electron Microscopy (LEM), Karlsruhe, Germany

Noble metal nanoparticles(NPs) supported on oxide structures are highly effective for heterogeneous catalysis due to their small size and high surface-to-volume ratio. Optimising dispersion and stability is key to maximise catalytic and economic efficiency. Sintering, where larger NPs grow at the expense of smaller ones, reduces the surface-to-volume ratio, thus catalytic efficiency. Hence, understanding sintering processes and controlling reaction conditions is essential[1]. Our goal is to gain insight into dynamic sintering processes under realistic conditions using electron microscopy.

Previous *in situ* experiments using transmission electron microscopy(TEM) provided valuable insights[2], but were limited by number of NPs, lacking tools to explore the influence of interactions on a larger scale. The environmental scanning electron microscope(ESEM) has emerged as promising method, enabling the study of hundreds of NPs simultaneously under controlled gas conditions and elevated temperatures on a broad micrometre scale[3]

This work investigates *in situ* dewetting processes as a model system to understand Pt thin film dynamics on oxide supports. The experimental setup combines a heating stage with a controlled gaseous atmosphere inside the ESEM, realising temperatures/pressures up to 1000°C/10 mbar. This enables studying dewetting processes while independently adjusting pressure, gas and temperature. The studied supports include amorphous and crystalline SiO2, Al2O3 and CeO2, Al2O3 further classified as (non-)reducible.

The dewetting behavior of two Pt thin film thicknesses(7.3/4.4 nm) on amorphous SiO2 exposited to a heating profile up to 900°C in 0.7 mbar H2O atmosphere is shown in Fig 1. The NPs show different size distribution and morphological properties, compare Fig 1a-b. The mean NPs surface area was 519µm²/1719nm² for the Pt film thickness of 7.3/4.4nm, displayed in Fig 1c-d.

Different dewetting characteristic is revealed for 7.3nm Pt on α-Al2O3 [0001] in Fig 2. Post dewetting analysis in Fig 2a shows Pt in net-like structures, showing contrast edges highlighted by arrows in Fig 2b, suggesting dynamic changes in crystal orientations[4],[5]. Electron Backscatter Diffraction(EBSD) analysis reveals various crystal orientations, shown in Fig 2c-e. Those are not randomly distributed, as evidenced by the stereographic projection, instead a specific crystallographic path is followed as evidenced by the inverse pole figure along the z-direction in Fig 2f.

This work will present with *in situ* dewetting experiments of Pt thin films of varying thickness on oxide supports with different crystallographic orientations: SiO2, α-, γ-Al2O3, and CeO2. The *in situ* experiments will be complemented by SEM-EBSD analysis and cross-sectional *post mortem* TEM-EDX and HRTEM analysis to provide insights of the orientation relationship between Pt and its supports as well as its composition details.

The authors gratefully acknowledge funding from the DFG(German Research Foundation) under Project TrackAct(SFB 1441,Project-ID 426888090)

[1]Thompson,C.V.Annu.Rev.Mater.Res.2012,42(1),399–434.DOI:10.1146/annurev-matsci-070511-155048

[2]Simonsen,S.B.;et al.,Catal.2011,281(1),147–155.DOI:10.1016/j.jcat.2011.04.011

[3]Barroo,C.;et al.,Nat.Catal.2019,3(1),30–39.DOI:10.1038/s41929-019-0395-3

[4]Lee,J.-M.;Kim,B.-I..Mater.Sci.Eng.A2007,449-451,769–773.DOI:10.1016/j.msea.2006.02.403

[5]Niekiel,F.;et al.,Acta Mater.2016,115,230–241.DOI:10.1016/j.actamat.2016.05.026

Fig. 1

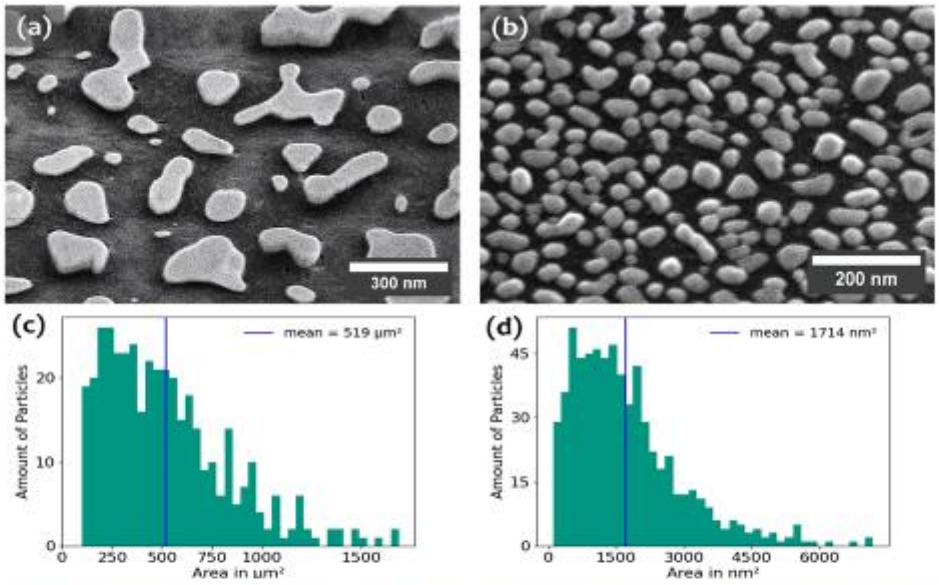


Figure 1: Dewetting of sputtered Pt thin film on amorphous SiO_2 substrate in 0.7 mbar H_20 exposited to a temperature profile up to 900°C results in island shaped Pt NPs. Post SEM analysis reveals difference in size and shape of Pt islands originating from thin film thickness of (a)7.3 nm – sample tilt by 45° - and (b) 4.4 nm - sample tilt by 52° - corresponding area size distributions of Pt islands (c,d).

Fig. 2

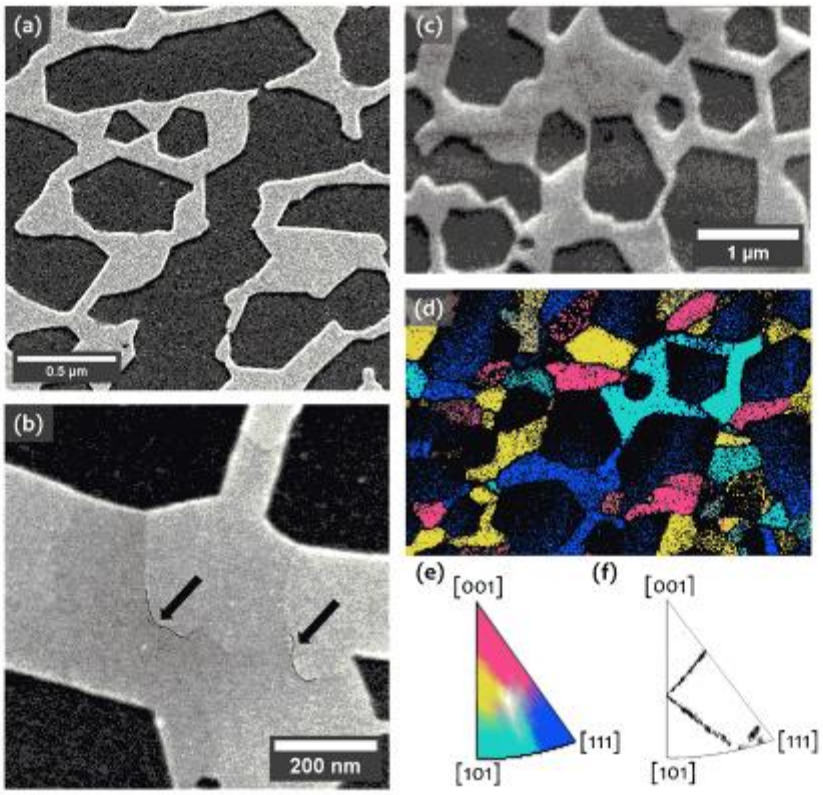


Figure 2:(a) Dewetting of platinum thin film of 7.3 nm thickness in 0.7 mbar H_2O exposited to temperature profile up to 900°C results in net like structured surface on Al_2O_3 in post SEM image with sample tilt of 44.6°. (b) Untilted analysis shows contrast edges in Pt structure suggesting different crystal orientations, supported by EBSD measurements. (c) SEM representation of area studied with EBSD. (d) Inverse pole figure in z-direction shows a variety of orientations of Pt, (e) presents colour interpretation of (d). (f) Stereographic representation shows preferred crystallographic orientation distributions.

MS7.P02
In situ scanning transmission electron microscopy to determine the photovoltaic properties of a pn junction at cryogenic temperatures

C. Flathmann[1], A. Dehning[2], B. Kressdorf[2], C. Jooss[2,3], M. Seibt[4], T. Meyer[2]

[1]Ruhr University Bochum, Research Center Future Energy Materials and Systems & Faculty of Physics and Astronomy, Bochum, Germany
[2]Georg-August-Universität Göttingen, Institute of Materials Physics, Göttingen, Germany
[3]International Center for Advanced Studies of Energy Conversion (ICASEC), Göttingen, Germany
[4]Georg-August-Universität Göttingen, 4th Physical Institute - Solids and Nanostructures, Göttingen, Germany

Introduction

One of the major challenges for developing future devices is to establish correlations between atomic/electronic structure and functional properties of materials. In recent years, new developments in scanning transmission electron microscopy (STEM) and in situ methods have enabled significant progress in this regard [1]. However, correlating structure and electrical properties, especially at cryogenic temperatures, remains a major challenge.

Objectives

In this contribution we use in situ cooling and biasing STEM to study the influence of a phase transition on the photovoltaic response of a manganite-titanate heterojunction. In a multimodal approach, we combine electrical characterization of TEM lamellae with different STEM techniques to get access to structural, electrical and electronic properties at different temperatures and bias conditions. We use the measured data to establish the structure-property relationships and to determine important photovoltaic parameters at the nanoscale.

Materials & methods

The samples we investigate are calcium doped praseodymium manganite (PCMO) thin films on niobium doped strontium titanate (STNO) substrates. The strongly correlated PCMO exhibits a hot polaron photovoltaic effect [2], where the charge carrier lifetime is expected to increase at low temperatures due to a structural and electronic ordering phase transition [3].

To access the electrical properties of the samples in the temperature range between 100K-300K, we use a DENSsolutions Lightning Arctic holder. We apply STEM electron beam induced current (STEM-EBIC) to probe the electrical response of the sample at the nanoscale [4] and combine this with 4D-STEM and electron energy loss spectroscopy to get a comprehensive picture of the samples.

Results

Fig. 1 a) shows an overview of the investigated TEM lamella. The corresponding IV-curve of the lamella is shown in Fig. 1 b), demonstrating that the lamella is strongly rectifying. Thus, the STEM-EBIC signal obtained at the PCMO/STNO interface probes the electrical properties of the junction. Comparing the STEM-EBIC signal obtained at room temperature (RT) with the signal at liquid nitrogen

(LN2) temperature shown in in Fig. 1 c), one sees a slower decay of the signal on the PCMO side at LN2 temperature, confirming the hypothesis of an increased lifetime of minority charge carriers. Further comparison of the STEM-EBIC signals with the plasmon energy obtained from EELS scans, shown in Fig. 1 d), shows that the maximum STEM-EBIC signal shifts from STNO at RT to the interface at LN2 temperature, indicating changes in the charge carrier separation process.

Conclusion

In conclusion, this contribution shows that a multimodal, in situ STEM approach can be used to obtain a comprehensive picture of electrical transport in functional materials at low temperatures. The presented approach has great potential for other applications, such as the characterization of quantum materials, and the ongoing improvement of TEM hardware will extend its applicability to lower temperatures and more stimuli in the future.

References:

[1] M. A. Smeaton et al., *ACS Nano*, 18(52) **2024**.

[2] B. Kressdorf et al., *Adv. Energy Mater.*, 14(45) **2024**.

[3] C. Flathmann et al., *APL Materials*, 21(6) **2024**.

[4] T. Meyer et al., *J. Phys.:Conf. Ser.*, 1190(1) **2019**.

Fig. 1

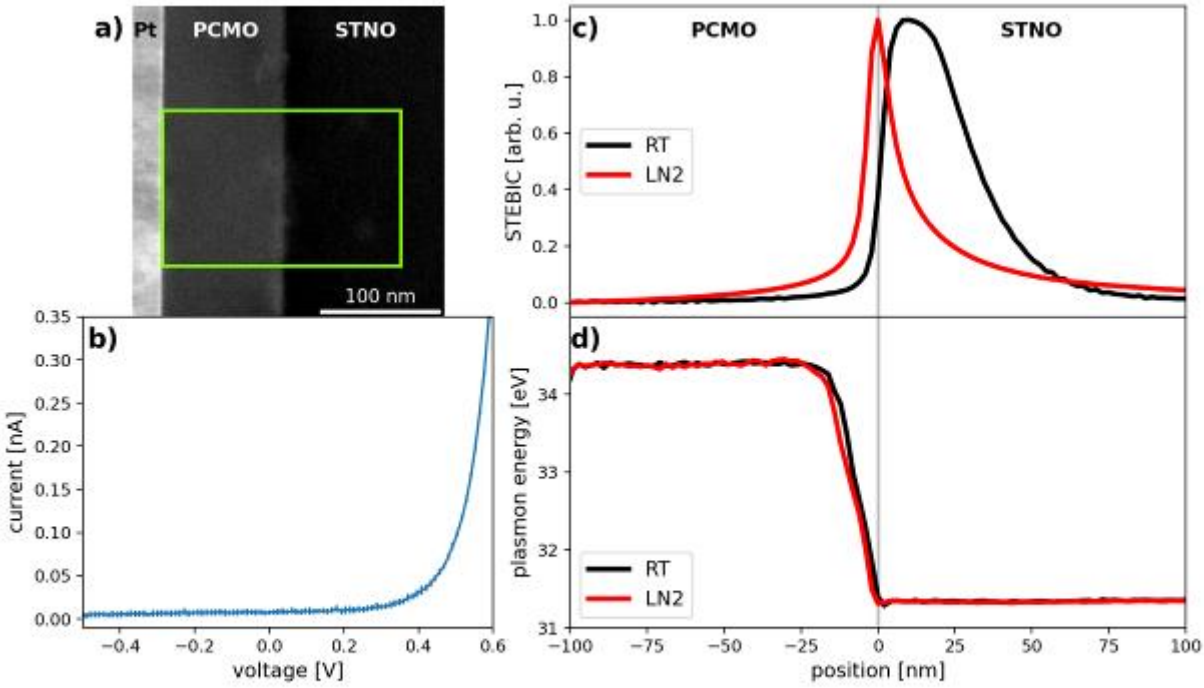


Fig. 1 : a) Shows an overview of the lamella with the area of the STEBIC scan indicated. b) The IV-curve obtained from the lamella shown in a). c) Normalized STEBIC signal, averaged along the interface direction, for RT and LN2 temperature. d) Energy of the first plasmon peak across the interface.

MS7.P04
Atomic-scale control of pore edges in 2D hexagonal boron nitride

U. Javed[1,2], M. Längle[1], V. Zobac[1], A. Markevich[1], C. Kofler[1,2], C. Mangler[1], T. Susi[1], J. Kotakoski[1]

[1]University of Vienna, Faculty of Physics, Vienna, Austria
[2]University of Vienna, Vienna Doctoral School in Physics, Vienna, Austria

Electron irradiation of hexagonal boron nitride (hBN) during (scanning) transmission electron microscopy ((S)TEM), even at energies lower than 80 keV, has been shown to lead to the formation of triangular pores with nitrogen-terminated edges [1]. In general, damage during electron microscopy is known to be a combination of knock-on damage [2], radiolysis [3] and chemical etching due to residual gases in the microscope column [4]. Knock-on damage caused by electron-nucleus scattering is the best known of such damaging mechanisms. The other mecanisms are both conceptually more complicated and also more difficult to directly address experimentally. Nevertheless, displacement cross-sections of boron and nitrogen atoms have been measured to be very similar at energies of 80 keV and lower [5], which does not explain how the triangular pores are formed. Here, we address this question by carrying out experiments with different acceleration voltages and at varying low-pressure oxygen and nitrogen atmospheres.

The Nion UltraSTEM 100 in Vienna with a base pressure of 1e-10 mbar was used for imaging. Due to modification to its column, it is possible to introduce a controlled gas atmosphere around the sample during microscopy [6]. In our experiments, electron-beam-induced pore growth was studied at oxygen partial pressures from 1e-10 mbar to 3e-8 mbar at 60 keV and 80 keV.

It was found that in ultra-high-vacuum (1e-10 mbar) electron irradiation leads to round pores with no preference to boron or nitrogen terminated edges. Experiments in nitrogen atmosphere show no difference. However, at oxygen partial pressure of ca. 1e-9 mbar, pore growth accelerates by ca. a factor of three, and the shapes remain circular. At ca. 1e-8 mbar, the pores turn into triangles while the growth further accelerates. Example image series recorded at 60 keV are shown in the figure. Although pore growth at 60 keV is generally slower than at 80 keV, at the highest pressure the growth rate appears independent of the electron energy. This indicates, that at higher pressures, the pore growth is dominated by a beam-assisted chemical process rather than direct electron-beam damage.

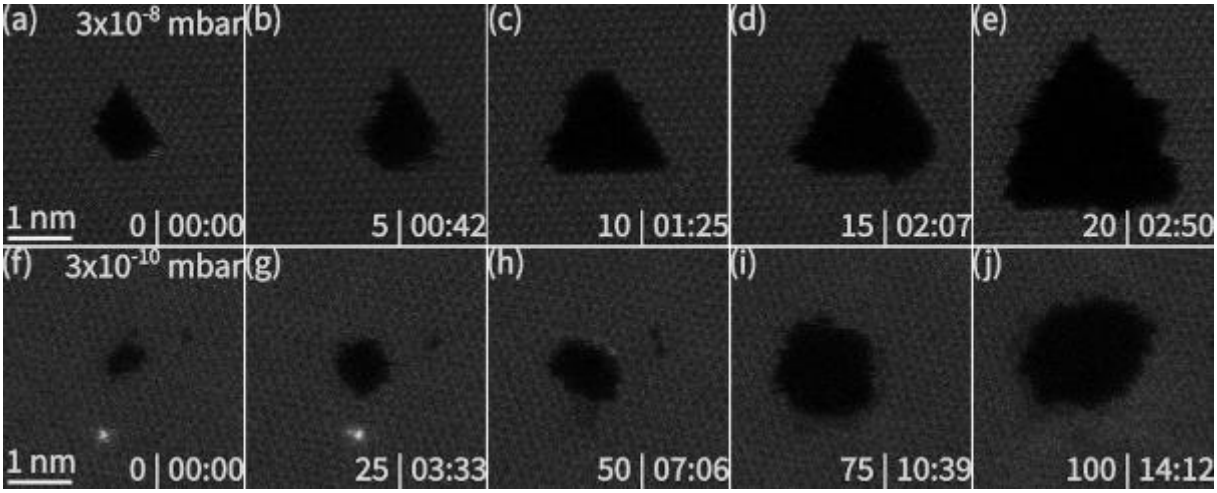
We turn to *ab initio* simluations to elucidate the underlaying reasons for this observation. They show that oxygen atoms, created from O_2 by the electron beam, attach preferentially on B at pore edges. From this configuration, it is easier to remove the O and B together rather than just O with the electron beam, whereas the opposite is true for N atoms at the edge. This explains the prevalence of nitrogen edges at higher oxygen pressures, and therefore also the observed triangular pores.

Our observations show that damage in hBN under electron irradiation is a combination of physical damage caused by electrons in the form of knock-on damage or radiolysis, and chemical damage caused by oxygen radicals, which affect boron significantly more than nitrogen. This opens up the possibility for defect-engineering of materials with desirable edges or atomics-scale defects by controlling both physical and chemical effects during particle irradiation.

References

[1] Meyer et al, Nano Lett. 9, 2684 (2009)
[2] Kotakoski et al, Phys. Rev. B 11, 113404 (2010)
[3] Cretu et al, Micron 72, 21 (2015)
[4] Gilbert et al, Sci Rep 7, 15096 (2017)
[5] Bui et al, Small 19, 2301926 (2023)
[6] Leuthner et al, Ultramicroscopy 203, 76 (2019)

Fig. 1


(a) 3x10^{-8} mbar
(b)
(c)
(d)
(e)
1 nm
0 | 00:00
5 | 00:42
10 | 01:25
15 | 02:07
20 | 02:50
(f) 3x10^{-10} mbar
(g)
(h)
(i)
(j)
1 nm
0 | 00:00
25 | 03:33
50 | 07:06
75 | 10:39
100 | 14:12

MS7.P06
Quantification of nanometer bulk minority carrier diffusion lengths via electron beam induced current in the presence of surface recombination

T. Meyer[1], C. Flathmann[2], D. A. Ehrlich[2], P. Paap-Peretzki[2], J. Lindner[1], C. Jooss[1,3], M. Seibt[2]

[1]Georg-August-Universität Göttingen, Institute of Materials Physics, Göttingen, Germany
[2]Georg-August-Universität Göttingen, 4th Physical Institute, Göttingen, Germany
[3]International Center for Advanced Studies of Energy Conversion (ICASEC), Göttingen, Germany

Keywords

Electron beam induced current, in situ, biasing, oxides, photovoltaics

Introduction

The shrinking size of electronic devices like transistors or thin film solar cells demands for an increased spatial resolution of related characterization methods. For those using focused electron beams as a probe, nanometer resolution can typically be achieved in a scanning transmission electron microscope (STEM). Consequently, STEM based electron beam induced current (STEM-EBIC) was proven to be a suitable method to characterize electronic devices on the nanometer or even Ångström scale [1,2]. However, since confined geometry usually leads to deviations from the electric behavior of bulk materials, e.g., due to interfaces, the high spatial resolution of STEM-EBIC needs to be combined with appropriate physical models to yield a quantitative interpretation of resulting signals [3,4].

Objectives

The study presented focuses on disentangling the effect of bulk and surface recombination of excess minority charge carriers to determine bulk diffusion lengths in STEM-EBIC experiments. To achieve this goal, sample positions with different thicknesses are investigated and the decay lengths of corresponding STEM-EBIC profiles are analyzed. The experimental results are compared to numerical simulations and analytical models.

Materials & methods

A rectifying junction consisting of a calcium doped praseodymium manganite (PCMO) thin film grown on niobium doped strontium titanate (STNO) substrate via ion beam sputtering is used as a model system with nanometer bulk minority carrier diffusion lengths. A cross-sectional STEM sample is extracted via focused ion beam (FIB) and investigated via STEM-EBIC using a DENSsolutions Lightning holder. In addition, finite element (FEM) simulations are used in conjunction with analytical considerations.

Results

Fig. 1a) shows an ADF-STEM image of the sample investigated via STEM-EBIC and including a PCMO-STNO interface. An intentional thickness gradient along the rectifying PCMO-STNO junction enables the extraction of profile decay lengths as a function of the sample thickness. Fig. 1b) demonstrates that the IV curve of the extracted lamella matches that of the macroscopic sample up to a scaling factor. Fig. 1c) presents the decay length in STEM-EBIC profiles on the STNO side with respect to the sample thickness as well as a model fit including bulk and surface recombination contributions.

Conclusion

Our contribution shows that the effects of surface and bulk recombination of excess minority charge carriers can be disentangled successfully enabling the quantification of nanometer bulk diffusion lengths in STEM-EBIC experiments. Furthermore, it paves the road for quantitative models accounting for different recombination centers, which is a prerequisite to describe the effects of defects or electric junctions.

References

[1] Meyer, Tobias, et al., *Journal of Physics: Conference Series* 1190 (2019)

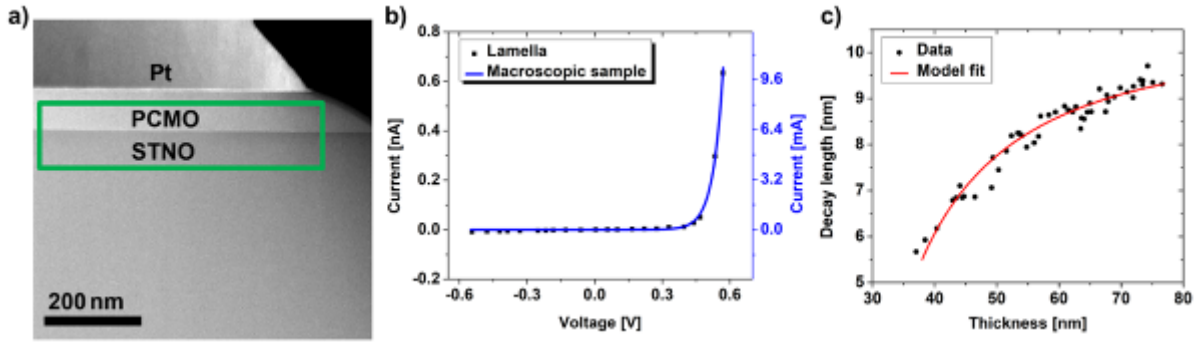
[2] Mecklenburg, Matthew, et al., *Ultramicroscopy* 207 (2019)

[3] Peretzki, Patrick, Dissertation (2019), http://dx.doi.org/10.53846/goediss-7223

[4] Meyer, Tobias, Dissertation (2021), http://dx.doi.org/10.53846/goediss-8815

Fig. 1: a) ADF-STEM overview of the STEM-EBIC lamella including a PCMO-STNO interface. b) IV curve of the lamella and the macroscopic sample. c) Thickness dependent decay length of STEM-EBIC profiles on the STNO side and corresponding model fit. Reproduced from [4].

Fig. 1



MS7.P07
Tracking (thermo-)electric properties during crystallization of an aGe thin film by *in situ* TEM

S. Hettler[1,2,3], R. Arenal[2,3,4]

[1]Karlsruhe Institute of Technology, Laboratorium für Elektronenmikroskopie, Karlsruhe, Germany
[2]CSIC-Universidad de Zaragoza, Instituto de Nanociencia y Materiales de Aragon, Zaragoza, Spain
[3]CSIC-Universidad de Zaragoza, Laboratorio de Microscopias Avanzadas, Zaragoza, Spain
[4]Araid Foundation, Zaragoza, Spain

- Introduction

In-situ transmission electron microscopy (TEM) provides a unique tool to study dynamic effects down to the atomic level. These dynamic processes can be triggered by a variety of different forces or environments. In the field of electrical forces, electrical voltages (*in-situ* biasing), e.g. [1], and electrical currents, e.g. [2], can be employed. Thermoelectricity is important for green energy production. However, the interplay between material structure and thermoelectric (TE) properties is complex. Therefore, the combination of the capabilities of TEM with the characterization of TE properties is promising to reveal fundamental relationships between structure and composition and TE properties.

- Objectives

The objectives of this study were to demonstrate a TE characterization of materials by *in-situ* TEM.

- Materials & methods

A novel *in-situ* chip with differential heating, capable of performing TE characterizations of materials by *in-situ* TEM was developed (Figure 1).[3] Several materials were chosen to demonstrate the functionality of the chip. Among others, an amorphous (a)Ge thin film was fabricated by electron-beam evaporation on a mica substrate and floating on a holey SiN TEM chip. A piece of the film was subsequently transferred to an *in-situ* chip using a FIB.[4] The *in-situ* TEM experiments were performed using a probe-corrected Titan low-base operated at 300 keV.

- Results

Figure 2 illustrates the used routine for TE characterization shown for a Si test specimen. I-V curves were applied for different applied differential heating currents I_H, which create a temperature gradient along the device and induce a TE voltage. The TE voltage offset V_O is given by the shift along the x axis (black circles), which increases approximately proportional to I_H^2. The setup was tested on different specimens and the results agree with the behavior expected from their TE properties.[3] Figure 3a shows a scanning (S)TEM image of the aGe thin film after transfer to the *in-situ* chip and the inset diffraction pattern (DP) reveals its amorphous nature. The application of electrical current sweeps with increasing maximum current led to a crystallization of the film as seen from Figure 3b. A non-linear decrease in resistivity is observed in dependence of the applied current.[3] Figure 4 shows a comparison of V_O determinations at three stages of the experiment and the increase in induced V_O with the degree of crystallinity is clear. This increase is linked to an increase of the Seebeck coefficient of the device. Raman spectroscopy performed on the crystallized device confirm the crystallization.[3] The challenges met during performing the experiments led us to design an improved layout of the chip that should facilitate a fullly quantitative TE characterization.[3]

- Conclusion

We demonstrated the general feasibility of combining TEM with TE measurements and the results obtained on tracking the TE properties during crystallization of an aGe thin film can give an indication of the potential of the method.[5]

References
[1] Zhang et al, *Nature Commun*. **8** (1), 2017.
[2] Hettler et al, *2D Mater.* **8** (3), 2021.
[3] Hettler et al, *Ultramicroscopy* **268**, 2025.
[4] Hettler et al, *Small Methods* **8** (12), 2024.
[5] Funded by EU, Spanish MICIU and Government of Aragón (DGA).

Figure 1: SEM image of *in-situ* chip.
Figure 2: TE characterization of Si device.
Figure 3: (S)TEM images (a) before and (b) after crystallization.
Figure 4: V_O for various degrees of crystallization.

Fig. 1

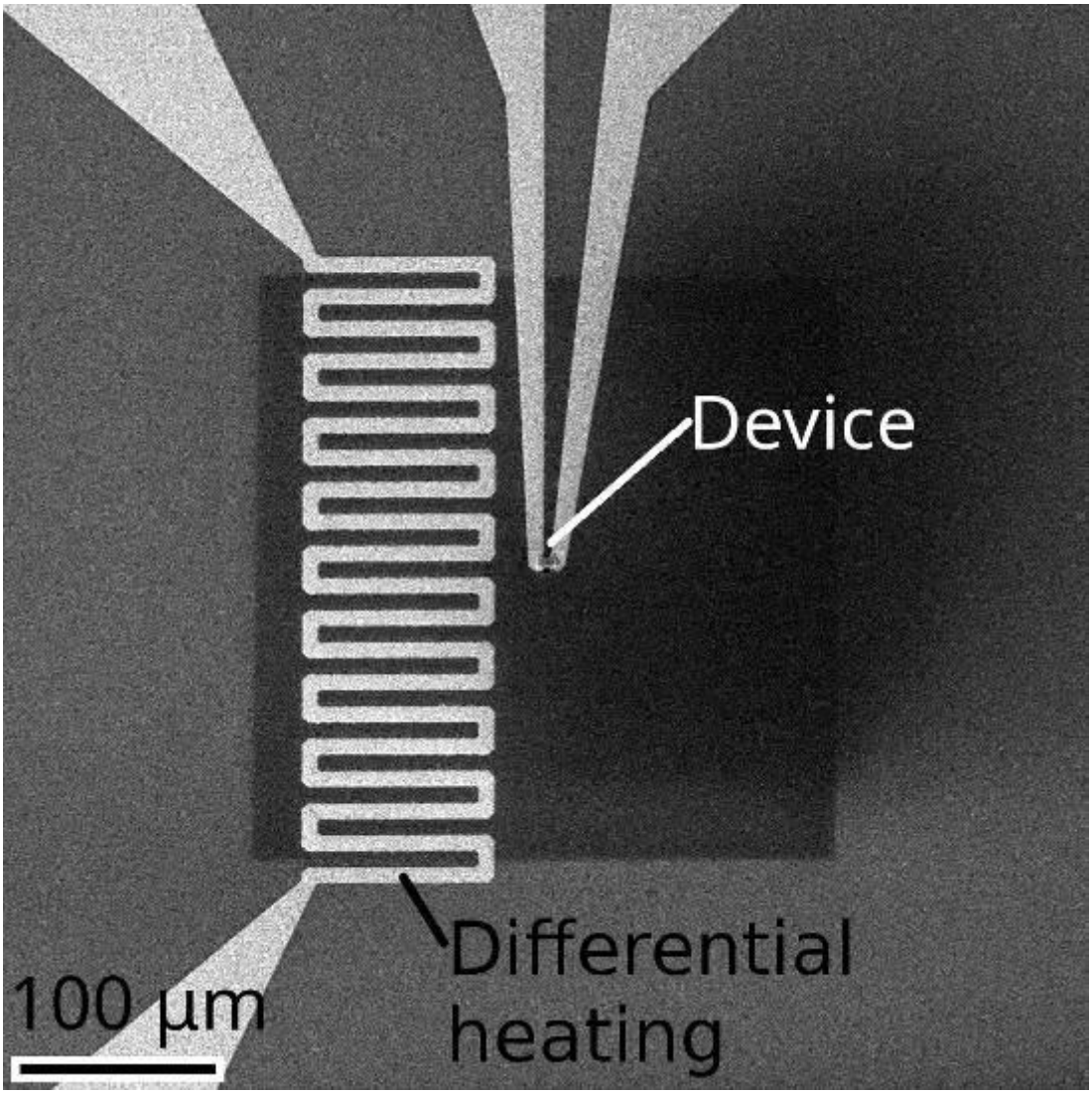


Fig. 2

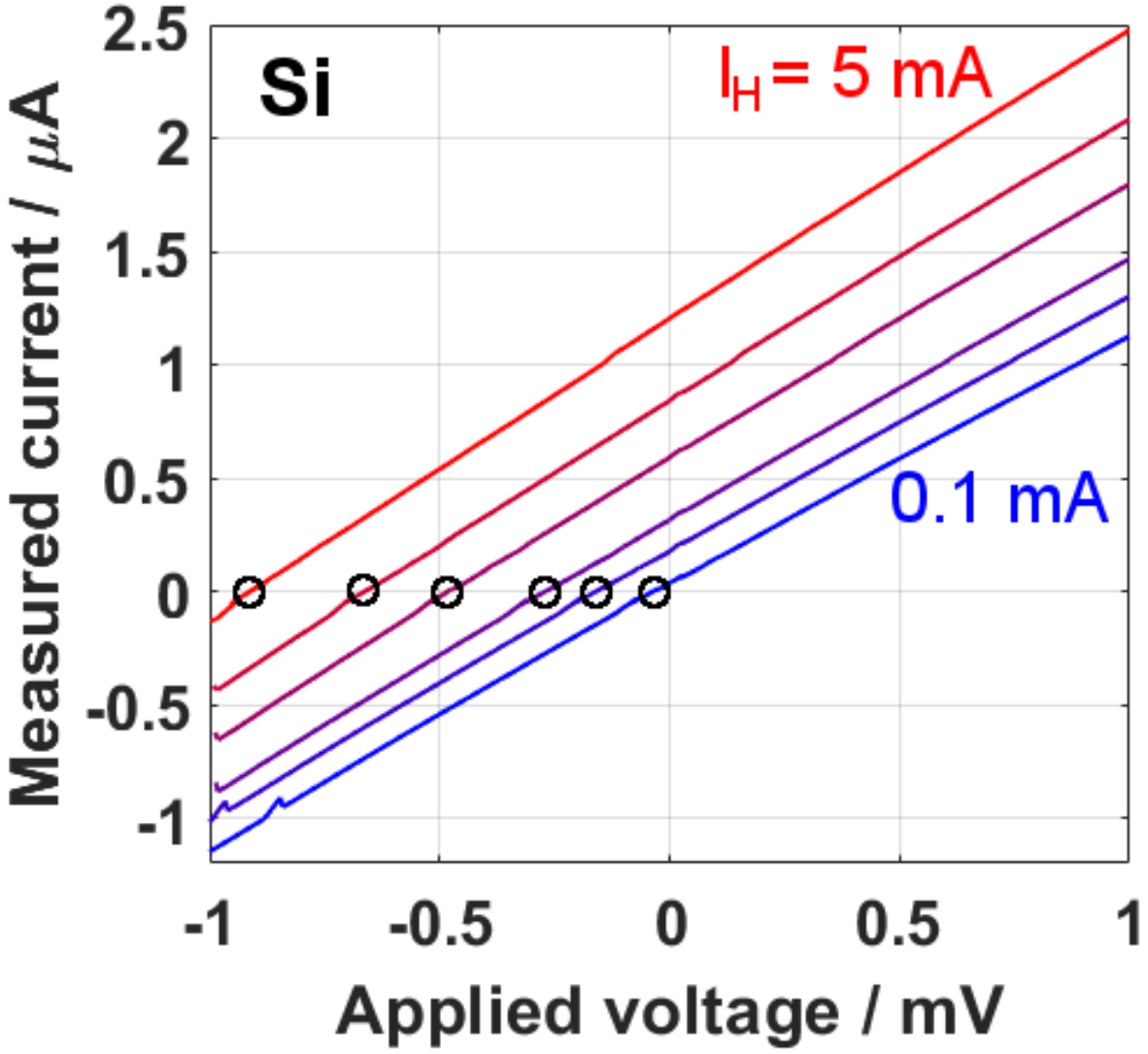

Si
I_H = 5 mA
0.1 mA
Measured current / μA
Applied voltage / mV
2.5
2
1.5
1
0.5
0
-0.5
-1
-1
-0.5
0
0.5
1

Fig. 3

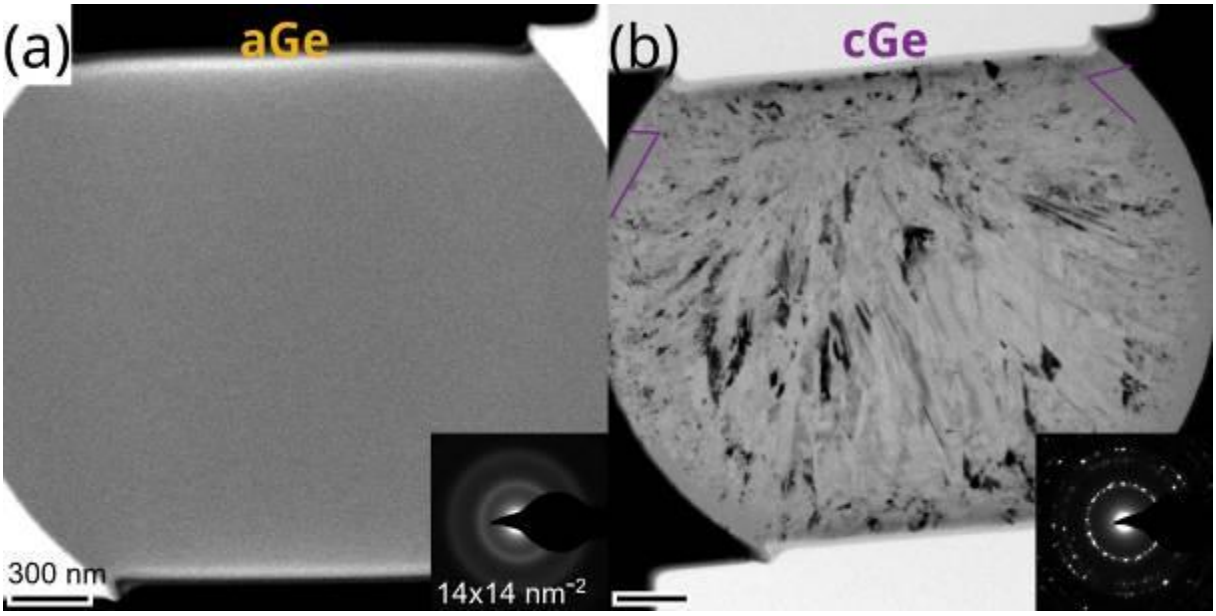
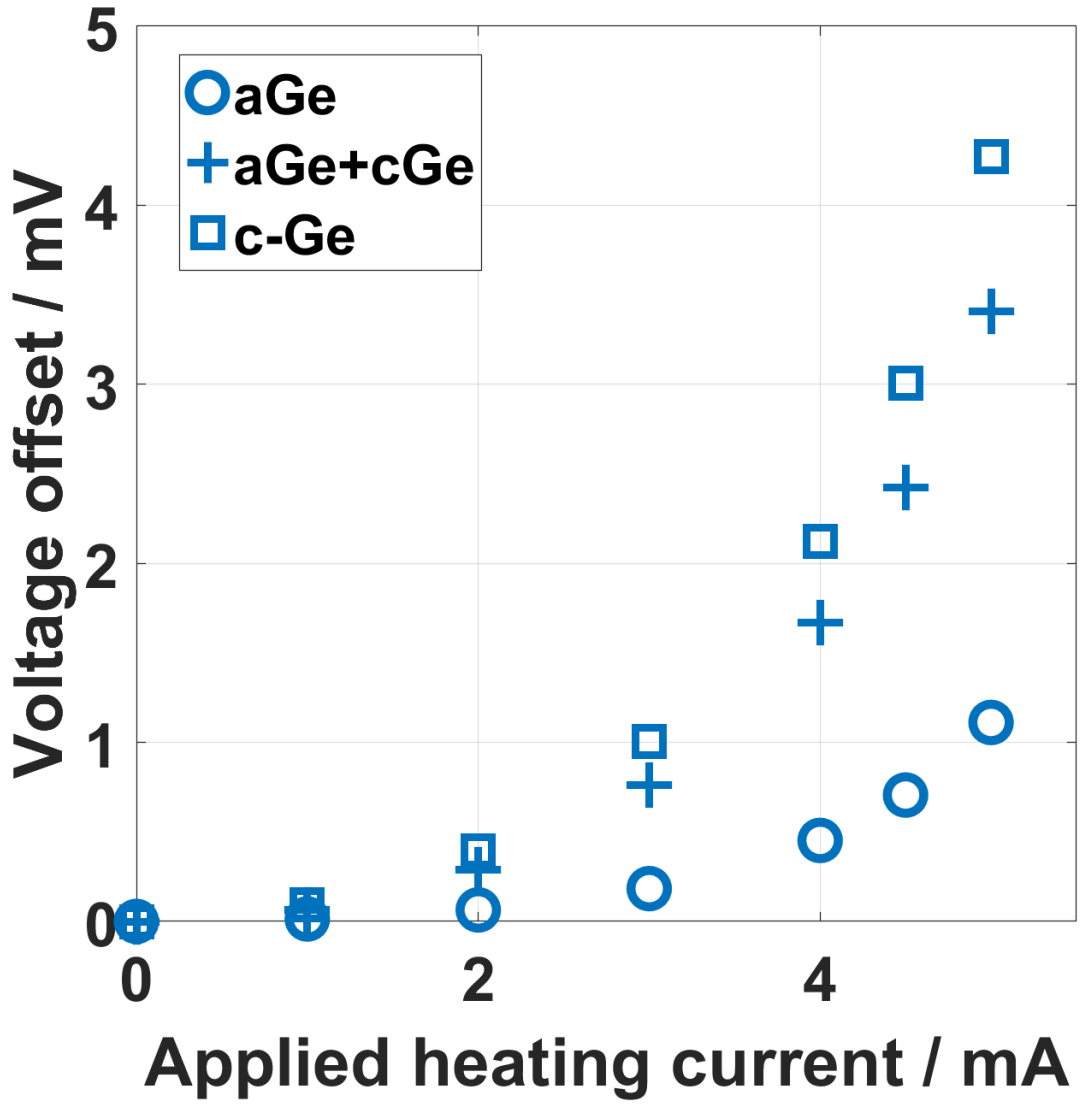


Fig. 4


aGe
aGe+cGe
c-Ge
Voltage offset / mV
Applied heating current / mA
0
1
2
3
4
5
0
2
4

MS7.P08
Rapid multi-scale modeling of real-world *operando* nanodevices in TEM

H. Çelik[1], T. Wagner[2], S. Gaebel[3], R. Fuchs[4], I. Häusler[2], C. T. Koch[2], M. Lehmann[1]

[1]Technische Universität Berlin, Institute of Optics and Atomic Physics, Berlin, Germany
[2]Humboldt University of Berlin, Institute of Physics & CSMB, Berlin, Germany
[3]Max-Born-Institut, B2: Imaging and Coherent X-rays, Berlin, Germany
[4]Technische Universität Berlin, Institute of Theoretical Physics, Berlin, Germany

Introduction

The functional properties of electronic nanodevices are highly dependent on their behavior under operational conditions. Multi-scale analysis, spanning from atomic to micron scales, is essential to understanding these behaviors, particularly when complex phenomena such as long-range electrostatic effects and sample-preparation-induced artifacts come into play (Fig. 1). However, traditional modeling techniques are computationally intensive and require detailed knowledge about the microscopic charge carrier distribution, thereby limiting their applicability to real-world operando TEM-samples.

Objectives

This study aims to develop and validate a computationally efficient framework for reconstructing the multi-scale electrostatic potential distributions in electronic nanodevices (Fig. 1b), with a focus on improving experimental workflows and enhancing the accuracy of in situ/operando TEM-investigations.

Materials & Methods

A convolution-based approach is introduced, solving a diffusion equation through a heat kernel, to model the potential distribution inside and around electronic nanodevices [1, 2]. The presented method requires only a single projection (e.g. electron hologram or DPC image) to map 3D distributions across scales. Samples, including FIB-fabricated p-n junctions, were systematically prepared under varying parameters to evaluate the impact of FIB-induced artefacts. Correlative experimental results from systematic EH (Fig. 2a) and DPC investigations are compared with FEM-simulations to validate the self-developed method.

Results

The proposed model demonstrates excellent agreement with both FEM-simulations and experimental EH (Fig. 2b) and DPC, achieving similar accuracy at significantly reduced computational costs (i.e. ~1000x faster with ~1/1000th of the memory usage at ~5000x more nodes). Additionally, the model effectively resolves the impact of FIB-preparation, such as ion implantation and surface amorphization, on the electrostatic potential distribution, highlighting its multi-scale implication.

Conclusion

This rapid multi-scale modeling approach provides a robust, efficient tool for studying operando nanodevices, enabling faster, more accessible TEM-investigations. By addressing both computational and experimental challenges, it paves the way for improved preparation strategies and deeper insights into the real-world behavior of semiconductor devices.

[1] H. Çelik et al., Ultramicroscopy **267**, 114057 (2024).

[2] T. Wagner, H. Çelik et al., Electronics **14**(1), 199 (2025).

Figure 1: Schematic of a FIB-prepared p-n junction and its simulated electrostatic potential. (a) Cross-sectional schematic showing the effects of FIB preparation—surface amorphization, implantation damage, and thinning—on the potential distribution in p-Si and n-Si. (b) Simulated potential map illustrating the complex multi-scale behavior and long-range electrostatic effects beyond the junction"s core.

Figure 2: Experimental validation of the convolution-based modeling. (a) Electron holography phase image of a p-n junction under reverse bias (U_{ext} = 3V), highlighting the phase difference. (b) Comparison of phase profiles from experiments (dashed) and simulations (solid) at U_{ext} = 0–3V. The model accurately reproduces the phase difference, confirming its robustness for multi-scale operando analysis.

Fig. 1

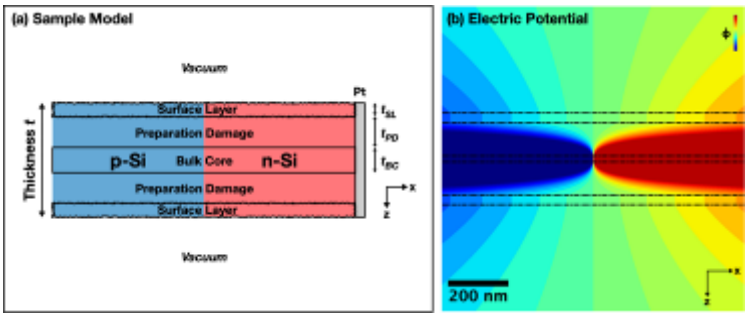
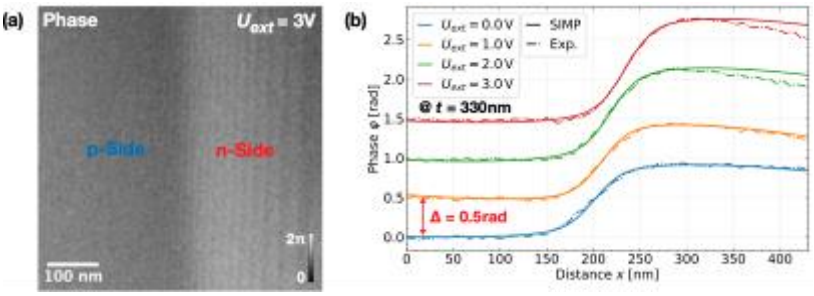


Fig. 2



MS7.P09
In situ insights into multivalent metal energy storage: A model system for calcium sulfur batteries

M. Kögel[1], J. C. Meyer[1,2]

[1]University of Tübingen, NMI Natural and Medical Sciences Institute, Reutlingen, Germany
[2]Eberhard-Karls-Universität, Institut für Angewandte Physik, Tübingen, Germany

Introduction

As we globally realize large-scale electrical energy storage coupled with the rapid increase in global electromobility, the challenge of securing a consistent supply of critical raw materials utilized in lithium-ion batteries (LIB) continues to grow. Consequently, the search for alternative systems delivering comparable energy densities has become an important topic. Multivalent metals, renowned for their long-term stability, emerge as promising candidates in this regard.

Objectives

The combination of calcium and sulfur represents a potent alternative, attributed to their abundant availability and recent research delineating the appreciable stability of their electrolyte system. [1] Nevertheless, to enhance fabrication efficiency, performance, and stability, a deeper understanding of the electrochemical dynamics at the anode surface, where the electrolyte interfaces with calcium, is essential. The work in the Casino project [2] aims for an understanding and optimization of key aspects towards its application.

Materials & methods

The electrochemistry happens at the surface between the electrodes and electrolyte system. Understanding the details is what makes improvements possible. A novel in-situ model system is developed to mimic the behaviour of the macroscopic symmetric Ca-Ca battery system while allowing atomic-level observations.

Results

The geometry of the Ca Anodes is shown in Figure 3. Direct transfer of 2D materials enables the formation of liquid pockets (Fig. 2) and therefore high-resolution studies. [3,4] Calcium and electrolyte solution is encapsulated between 2D materials, and In-situ investigations are employed combined with EELS and EDX to uncover key mechanisms.

Conclusion

In-situ investigations are made possible by the alignment of the 2D liquid cells with the structured anodes, as shown in the scheme of Figure 1. (Dis-)charging mechanisms of Calcium batteries are therefore experimentally accessible by TEM.

The project was financially supported by the Bundesministerium für Bildung und Forschung (BMBF), under project CaSino, Grant number (Förderkennzeichen) 03XP0487D.

Figure 1. Scheme of the Ca-Ca model system sealed with graphene on a MEMS Chip. The +/- poles refer to the wires, as shown in MEMS Chip schemes. The yellow beam indicated the scanning direction of the TEM.

Figure 2. TEM image of water liquid cells between graphene monolayers.

Figure 3. ADF Image of Ca "islands" on a Graphenea TEM grid®. FOV 35µm.

[1] Li, Z et. al., Energy Environ. Sci. 12, 3496–3501 (2019)

[2] https://www.dlr.de/tt/en/desktopdefault.aspx/tabid-14027/7108_read-80787/ , https://www.nmi.de/projekte-1/projektdetail/casino

[3] Jong et al., Science, 335(6077):61–64, 4 2012.

[4] Martin Textor and Niels de Jonge, Nano Letters 2018 18 (6), 3313-3321

Fig. 1

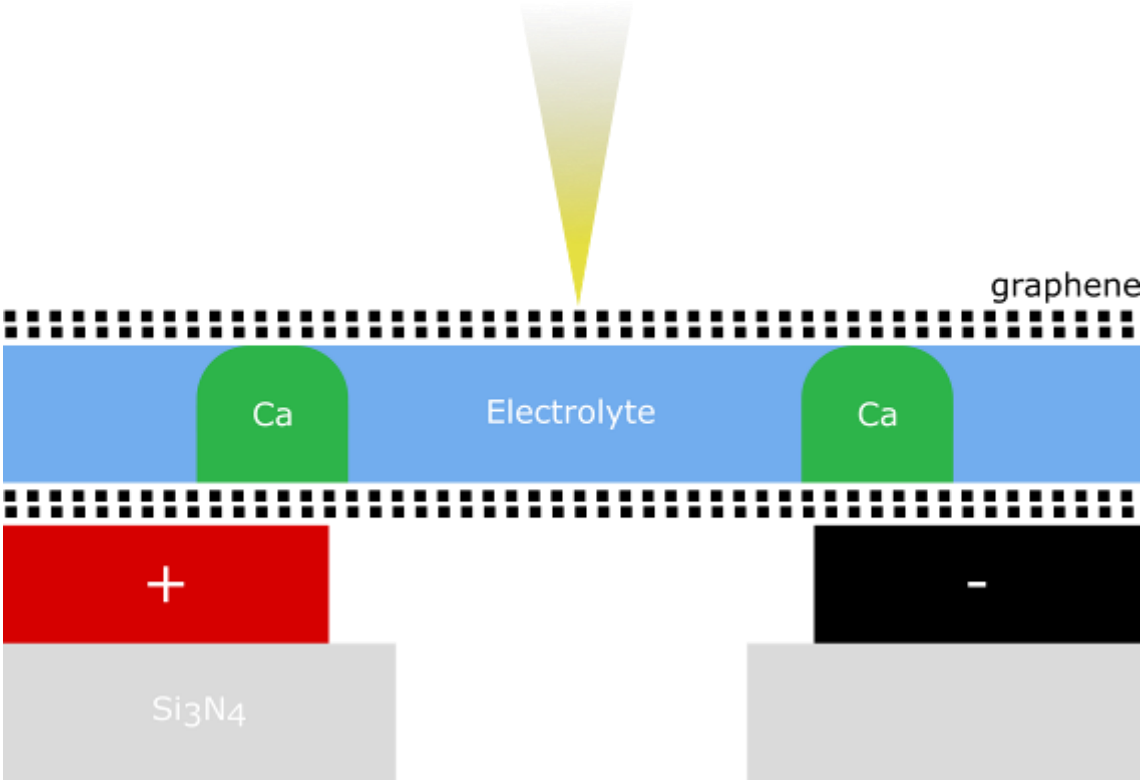


Fig. 2

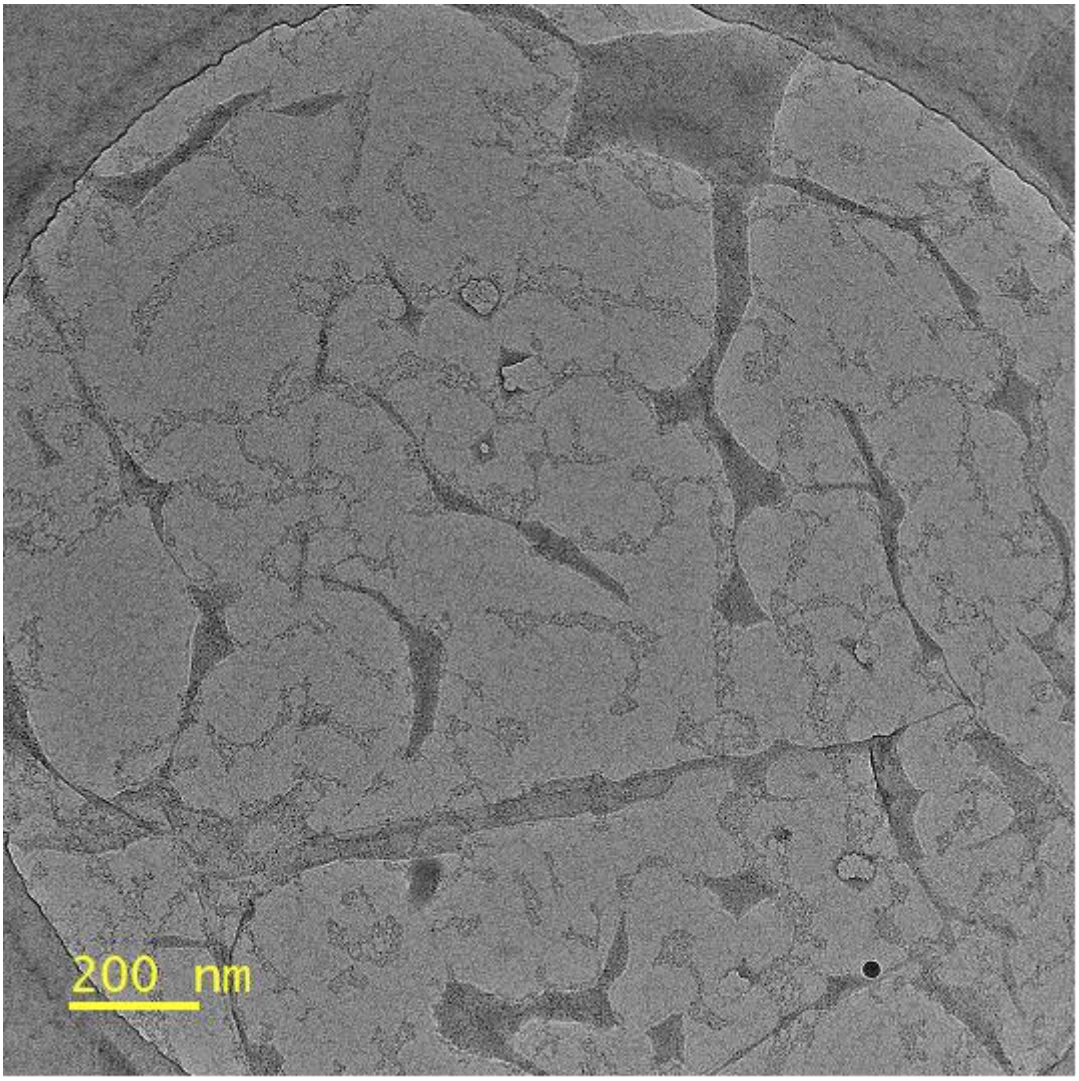
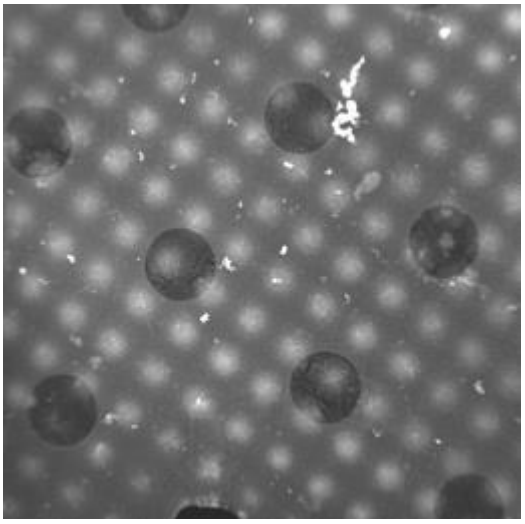


Fig. 3



MS7.P10
In situ TEM investigation of the 2:17 to 2:14:1 phase transformation in the Nd-Fe-Cu-Mo-B system

E. Adabifiroozjaei[1], O. Recalde-Benitez[1], L. Schäfer[1], F. Maccari[1], T. Jiang[1], K. Skokov[1], O. Gutfleisch[1], L. Molina-Luna[1]

[1]Technical University of Darmstadt, Advanced Electron Microscopy, Darmstadt, Germany

Introduction: In recent decades, significant efforts have been directed towards enhancing the magnetic properties of Nd-Fe-B magnets through microstructural engineering. The primary objective is to obtain a refined microstructure of Nd2Fe14B grains surrounded by an ultra-thin (nanoscale) Nd-rich grain boundary. This plays a crucial role in magnetically decoupling the Nd2Fe14B grains, thereby preventing the propagation of reverse magnetic domains and leading to enhanced coercivity. The traditional techniques to obtain fine microstructures are rapid solidification (e.g., melt spinning) and hydrogen gas-solid reaction hydrogen decrepitation (HD) and hydrogenation, disproportionation, desorption and recombination (HDDR), each of these processes having its own advantages and limitations. Recent studies have demonstrated an alternative approach, using insights from the Fe-Nd phase diagram to produce fine-grained Nd2Fe14B magnets via solid state transformation of an Nd2Fe17 precursor containing Mo, Cu, and Co. This method enables the attainment of high coercivity without requiring complex powder metallurgical processes typically used for conventional Nd-Fe-B magnets [1].

Objective: This study aims to understand the transformation pathway of the 2:17 to the 2:14:1 phase – fundamental to coercivity enhancement by using *in-situ* electron microscopy (TEM).

Materials & Methods: An *in-situ* TEM experiment was conducted from room temperature up to 1075 °C. At each temperature step, the sample was held for 30 minutes followed by low- and high-resolution TEM imaging, high-angle annular dark field (HAADF) imaging and chemical analysis.

Results: Room temperature TEM, including HAADF imaging revealed that the 2:17 precursor consists of 2:17 and 1:5 phases along with Mo-, Nd-, and Cu-rich precipitates within the nanostructure. At 300 °C, the 2:17 remained structurally intact, but fine grains of a secondary phase begin to emerge within the 2:17 matrix. These grains were found to be rich in Fe and Co, while being more Nd-deficient compared to the matrix. As the temperature increases the density of these secondary grains grew throughout the sample. At 600 °C, Fe,Co- and Fe,Mo-rich precipitates appear and continue to grow with further heating. The critical transformation of the 2:17 phase into the 2:14:1 was observed at 750 °C, leading to the formation of a refined nanostructure. Beyond this temperature, further heating resulted in only grain coarsening of the existing phases, without additional phase transformations.

Conclusion: based on our experimental findings, we conclude that the transformation of the 2:17 phase into the 2:14:1 phase occurs as a one-step process at 750 °C. When the initial composition is carefully optimized, this transformation route could serve as a viable approach for producing NdFeB magnets with a tailored nanostructure and enhanced magnetic properties.

[1] L. Schafer, K. Skokov, F. Maccari, I. Radulov, D. Koch, A. Mazilkin, E. Adabifiroozjaei, L. Molina-Luna, O. Gutfleisch, A novel magnetic hardening mechanism for Nd-Fe-B permanent magnets based on solid-state phase transformation, Adv. Funct. Mater. 33 (2022), 2208821.

All authors acknowledge the financial support of German Science Foundation (DFG) in the framework of the Collaborative Research Centre Transregio 270 (CRC-TRR 270, project number 405553726).

MS7.P11
Correlative characterization by X-ray tomography, SEM/FIB and TEM using reference markers – Bridging imaging with micro-structuring

A. Boubnov[1], C. Neidiger[1], R. Debastiani[1], T. Scherer[1], M. Mail[1], D. Wang[1], C. Kübel[1]

[1]Karlsruhe Institute of Technology, Institute of Nanotechnology, Karlsruhe, Germany

Introduction

Correlative characterization is the spatial registration of several imaging modalities aiming to combine complementary information on the same region of interest (ROI) [1]. The imaging modalities are supplemented by micro-structuring tools including focused-ion beam (FIB) technology for extraction of the ROI, and laser-milling for material removal.

Within the same length scale, combining several modalities on the same ROIs is well-established in electron microscopy, e.g. STEM imaging modalities (BF, DF, HAADF) with EELS and EDX spectroscopy, or the combination of APT and TEM. Across length-scales, the analysis of identical ROIs requires combination of different instruments. Without a correlative approach, the characterization of the full length-scale hierarchy relies on statistically random sample extracts, which only provides a good representation for very homogeneous samples, with similar ROIs uniformly distributed within the sample. However, for macroscopically inhomogeneous samples, such as heterogeneous catalysts, a correlative approach is indispensable to characterize the individual components of the sample. Therefore, for linking the local micro-structure to the macroscopic level of the sample, a full correlation of all applied techniques on the ROI is desired.

Objectives

We present a correlative workflow, which allows the combination of 3D analysis across several length scales from the bulk sample with defined laser pre-structuring for micro-CT at the sub-mm level, identification of regions of interest on the 10-100 µm scale in a FIB, for 2D/3D surface and tomography visualization by SEM/EDX/EBSD and light microscopy, followed by defined sample extraction and transfer to nano-CT and TEM.

Materials & methods

For this purpose, we developed a dedicated sample carrier, enabling large tilt angles for FIB work, and flexibility for direct transfer to micro-CT. The carrier is equipped with three-dimensional global reference markers for accurate determination of the rotation and tilt of the sample. Additionally, local markers, in the form of Pt-deposited or FIB-milled patterns, are placed directly on the sample in the vicinity of the ROI. These facilitate accurate translational positioning around the ROI for FIB-extraction, after the rotation and tilt has been aligned using global markers.

Results

The workflow, using the correlative sample carrier, global and local markers, and a series of geometrical calculations, gave a two-fold result. Firstly, once the ROI position was located with a few µm accuracy, FIB projection images were generated for real-time overlap with the FIB image, guiding the FIB-extraction of the ROI for nano-CT and/or TEM. Secondly, an accurate image correlation in 3D was enabled, overlapping 3D tomographic and 2D projection images virtually in common image-processing software. We verified this workflow on samples from metallurgy [2] and catalysis [3].

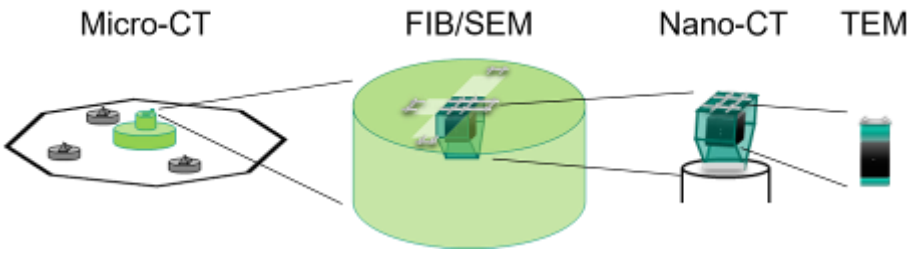
Conclusion

Using global and local reference markers, and tracking them at different length scales, we achieved accurate ROI-targeting for FIB-extraction, and covering multiple length scales and imaging techniques. The workflow is aimed at routine multi-scale, multi-modal correlative investigations on samples from materials science, targeting specific ROIs, thereby gaining local chemical and structural information from bulk samples.

References

[1] Sci. Reports 4 (2014)4711, [2] Metals 9 (2019) 1081, [3] Cat. Sci. Tech. 8 (2018) 4626.

Fig. 1



MS7.P13
Preparation of large and wide Cross-Sections using a Femtosecond laser– A crystal oscillator application example for SEM, EDX, and X-ray microscopy imaging and analysis

M. Heller[1], O. Vertsanova[1], R. Mitchell[2]

[1]Carl Zeiss Microscopy, Oberkochen, Germany
[2]Carl Zeiss Microscopy, Cambourne, United Kingdom

Introduction & Objectives

Crystal Oscillators are used in our daily life as part of mobiles, tablets and laptops. These small electronic devices are used for processor clock generators. They consist of different layers of materials stacked together. This results in challenging sample preparation as the materials show different mechanical properties. A large cross-section with a sufficient quality of a crystal oscillator can show defects (e.g. voids) or reveal structural features, which are determined by further analysis.

Methods

A unique solution is to prepare large cross-sections (>2 mm) fast using the ZEISS LaserSEM. A scanning electron microscope (SEM) is combined with a femtosecond laser for high-resolution imaging and fast material removal. The laser is attached to the SEM microscope in a dedicated chamber to prevent contamination within the main microscope chamber. Sample transfer between both chambers is performed using a motorized transfer rod enabling a fast and easy transfer and a continuous workflow for the user. All kinds of detectors can be attached to the microscope due to the modularity of the system.

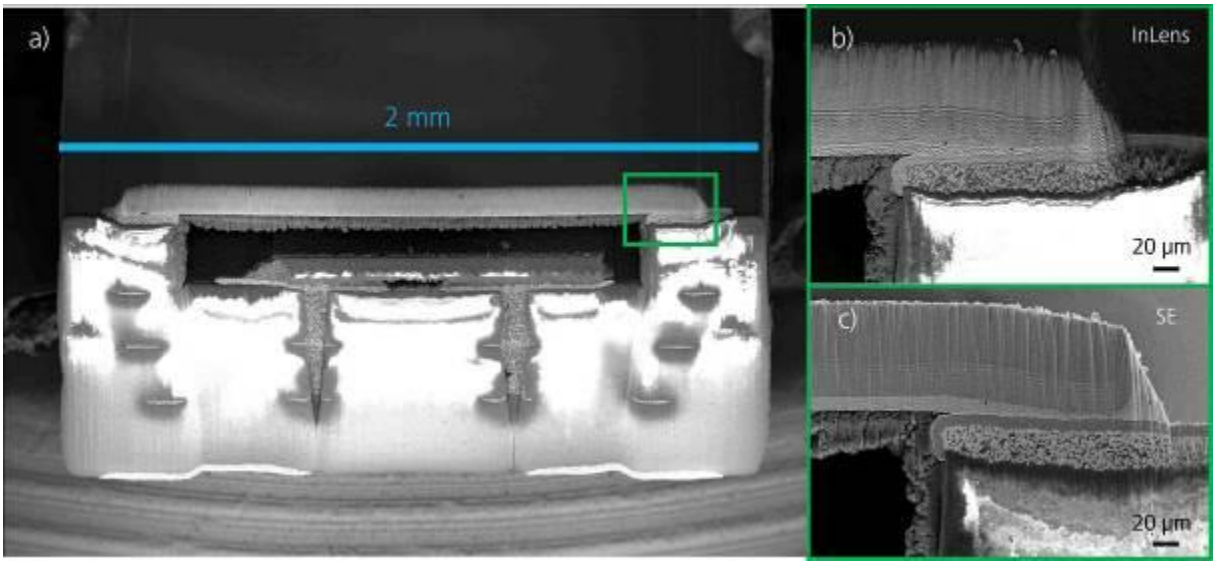
To get more insights and information about the structure of the crystal oscillator, firstly a non-destructive 3D overview scan using a ZEISS Versa X-ray microscope (XRM) is performed. Additional high resolution targeted region of interest scans are possible. Defects (e.g., voids) are located using this multi-scale scanning approach in the XRM, and are then ready for exposure using the LaserSEM for further investigation.

Results & Conclusion

The laser prepared surface is ready for SEM imaging and Energy-dispersive X-ray spectroscopy (EDX). Figure 1 displays a cross-section of a crystal oscillator. The prepared surface has a width of 2 mm and shows structures and pores in the material. This image is acquired with the large field of view of the ZEISS Gemini II column and captures the entire cross section. The highlighted green region in figure 1a) is magnified in figure 1b) and 1c) and imaged with the InLens detector (figure 1b)) and the Secondary Electron detector (figure 1c)). Both detectors show the different material layers stacked together in the crystal oscillator. This talk will highlight the benefits of a LaserSEM in combination with a Versa XRM and the possibilities of investigating electronic devices using this unique workflow.

Figure 1: The image in a) shows a huge cross section of a crystal oscillator prepared with a LaserSEM. More detailed images acquired with the InLens and SE detector are displayed in b) and c) showing the different layered structure.

Fig. 1



MS7.P14
Correlative AFM-in-SEM characterization of next-gen batteries

J. Kramář[1,2], T. Scherer[3], V. Hegrova[1], J. Neuman[1], R. Zhang[3]

[1]Nenovision, Microscopy Development, Brno, Czech Republic
[2]Brno University of Technology, University, Brno, Czech Republic
[3]Karlsruhe Institute of Technology, Institute of Nanotechnology, Karlsruhe, Germany

The growing demand for safer, more efficient, and higher-capacity energy storage systems is driving the advancement of battery technologies. In recent years, battery production capacity has expanded significantly, a trend expected to continue. The simultaneous reduction in battery cell costs and the expansion of global manufacturing highlight their crucial role in future energy storage [1,2].

Current research explores a variety of electrode and separator materials, each with unique advantages and challenges. However, new materials often introduce complexities in understanding their microstructure. Traditional electrochemical methods lack the lateral resolution needed for local electrical property analysis. While Scanning Electron Microscopy (SEM) - based techniques provide insights into structural, chemical, and crystallographic properties, they cannot directly image electrical properties [3,4].

A promising approach is Atomic Force Microscopy (AFM), where a sharp tip interacts with the sample surface to acquire various data maps of topography for height and roughness analysis. Additionally, applying a bias to the tip enables electronic property investigation [5,6].

Conventionally, SEM and AFM operate as separate devices under different conditions, making direct correlations difficult. Our approach integrates AFM within an SEM platform (AFM-in-SEM) using the LiteScope microscope. This setup enables simultaneous in-situ nanoscale electrical measurements alongside SEM-based structural and chemical insights. Such correlative characterization is essential for understanding chemical, structural, and electronic interactions in batteries [7,8].

One critical challenge in battery performance is particle contact loss in the cathode. This occurs when particles lose connection with the conductive matrix, leading to trapped electrons and reduced energy density. Some particles remain in charged or partially charged states, limiting active material utilization and degrading battery performance. Addressing this issue is key to improving energy capacity and cycle life [9,10].

Our project employs nanoscale characterization to investigate particle contact loss and its impact on battery efficiency. Conductive AFM (CAFM) probes local conductivity at the cathode level, identifying contact loss areas. We identify key degradation factors by analyzing particle size distribution, state of charge, and contact behavior.

This methodology is demonstrated on an ion beam-polished NMC cathode (Fig.1), where a) SEM image, b) local conductivity, and c) topography of the same region are shown. In the conductivity map, contrast variations indicate different electrical contacts among cathode particles.

Integrating these techniques within an AFM-in-SEM platform enables correlative in-situ characterization, combining electrical, structural, and chemical data. This comprehensive approach provides deeper insights into degradation mechanisms, helping optimize battery design and advance next-generation energy storage solutions.

Fig. 1

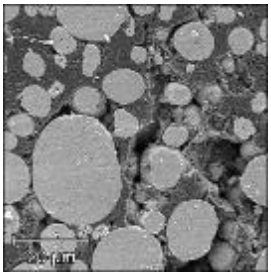


Fig. 2

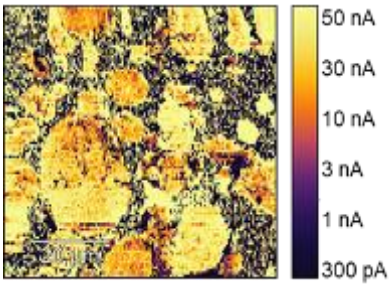
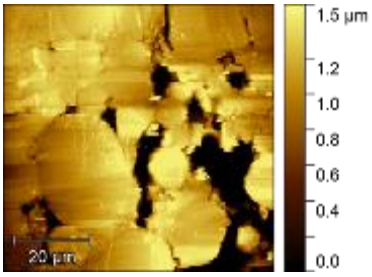


Fig. 3



MS7.P15
Multi-modal *in situ* gas cell electron microscopy and spectroscopy at pressures above 10 bar

G. Hollyer[1], E. Stach[1], D. Zakharov[2], D. H. Alsem[3], C. Parkin[3]

[1]University of Pennsylvania, Philadelphia, PA, United States
[2]Brookhaven National Laboratory, Upton, NY, United States
[3]Hummingbird Scientific, Lacey, WA, United States

Introduction

We present a high-pressure gas cell platform for the transmission electron microscope (TEM), scanning electron microscope (SEM), and X-ray synchrotrons, extending the operable pressure range of these in-situ systems up to 30 bar. In-situ gas cell TEM has enabled investigation of morphological changes to nanoscale catalyst materials during gas exposure, revealing structure-property relationships and mechanisms affecting catalytic performance. On-chip heating and temperature sensing for in-situ sample holders have enabled highly localized specimen heating, improving heating time and sample stability up to >1000 °C. To reproduce the intended operational conditions for the catalyst system at hand, experimental pressures above 10 bar are needed for in-situ hardware.

Objectives

Gas cell operation far above atmospheric pressure was demonstrated using a novel in-situ gas TEM holder and custom microfabricated gas-heating cell. The burst pressure and gas release during burst were investigated for safe usage in an ETEM system. Imaging and diffraction quality and stability were demonstrated using 2-beam TEM and selected area electron diffraction (SAED) on cobalt particles and deposited platinum. The strict drift, resolution, and vacuum requirements of the TEM make the gas cell also transferable to SEM and Xray synchrotron systems, enabling multi-modal investigation of catalyst evolution.

Materials & Methods

Burst pressures were determined in a high vacuum chamber by increasing the pressure until rupture. Operation of the holder was demonstrated in a Titan 80-300 Environmental TEM (ETEM) at the Center for Functional Nanomaterials at Brookhaven National Laboratory, wherein the deliberately burst viewing windows were tested to ensure the differential pumping system could safely handle cell rupture and the escaping gas volume.

Results

The chip membranes withstood up to 90 bar in rupture tests and the holder was successfully operated in the ETEM up to 30 bar. Co nanoparticles (15-20 nm and ~200 nm) and deposited Pt were used to assess imaging and diffraction quality at elevated pressure. Resolution of ~1.5 nm was achieved on Pt at a broad range of pressures. SAED patterns with distinguishable rings were also obtained at pressure. A greater sensitivity to contamination evolution under the electron beam was observed for elevated pressure and was ultimately the limiting factor in imaging resolution in these early experiments. Correlative imaging of 200 nm Co nanoparticle clusters was performed using scanning transmission X-ray microscopy (STXM) at 20 bar O2 at the Advanced Light Source at Berkeley Lab. This system will be used to study the morphological, microstructural, and microchemical evolution of heterogeneous CuZn catalysts at 10-20 bar of experimental gas and 200-300 °C.

Conclusion

Although the system can be operated up to 30 bar in the TEM, further qualification is needed to determine the appropriate maximum pressure rating for various imaging conditions. Ultra-high purity gases are required to mitigate beam-induced contamination at high pressure, and long purge times at startup are recommended. On-chip heating elements enable in-situ imaging of transformations in heterogenous catalysts under typical operational conditions. The full high-pressure gas heating system for TEM, SEM and synchrotron chambers will enable full multi-modal and multiscale characterization of nanocatalyst evolution mechanisms in industrial applications.

MS7.P16
Miniaturized material testing devices for multimodal *in situ* microscopic studies

M. Weber[1], R. Steinheimer[1], B. Engel[1], M. Möller[1], B. Butz[1]

[1]University of Siegen, Siegen, Germany

To contribute to the understanding of failure and fatigue, we examine the local microstructural strain/stress peaking as well as crack initiation/propagation by in situ methodology. We aim at two complementary goals. One is to contribute to alloy development and to optimize microstructure of selected alloys determining the macroscopic mechanical properties.

The second is to validate modern microstructure-based FEM simulations and to develop termination criteria for classical FEM simulations at microscopic scales which include unwanted microstructural changes leading to fatigue or crack initiation. Therefore, the Mechanical Engineering Department develops in situ testing machines for static and dynamic tests. Latest developments are a portable, miniaturized 3-point bending machine for use in FIB/SEM/XRD (Fig. 1 a). Thos enable the direct observation of microstructural changes like crack initiation/propagation, as well as phase transformations, e.g. in steels. As an example, the bending machine (750g, 100x100x50mm) with independent load/displacement sensors allows for massive plastic deformation at loads up to 4kN. Our solution includes a user-friendly interface to lower the entry barriers for beginners (Fig. 1 c). In this contribution, we highlight the possibilities to observe dynamics of crack initiation/propagation, phase transformations, and the local evolution of the microstructure during testing of materials like Al alloys and austenitic steel. Electron backscatter diffraction (EBSD) is employed to in detail understand the crystallographic structure adjacent to the crack (Fig. 1 b). Direct image correlation was used to examine local strain peaking. A key innovation is the use of AI-driven optical flow workflows to extract dynamic plastic deformation from SEM time-series images. This technique quantifies spatial deplacement across frames, enabling precise tracking of strain localization and crack propagation dynamics. By integrating AI-enhanced analysis, multimodal characterization, and in situ testing, this work refines failure analysis, microstructure simulation and material design.

Fig. 1



MS7.P17
On-Chip calorimetry in *in situ* TEM

D. Zhou[1], H. Ma[1], M. G. Willinger[2], M. Albrecht[1]

[1]Leibniz-Institut für Kristallzüchtung, Berlin, Germany
[2]Technical University of Munich, Chemistry, Munich, Germany

Introduction

Recent advances in microelectromechanical systems (MEMS)-based in situ TEM have opened new frontiers for investigating various material processes, including phase transformations, material growth, corrosion, and catalytic reactions. By dynamically and simultaneously visualizing multimodal material information—from the atomic to the microscale—these techniques provide deeper insights into complex phenomena. However, thermal analysis has long been absent from this multimodal approach.

In this work, we will briefly present examples, technical capabilities, and challenges related to the detection of heat flow during *in situ* TEM experiments. Using on-chip calorimetry, thermal analysis of an active model catalysts and phase-changes in a semiconductor material were detected while, at the same time, associated structural dynamics and changes in properties were followed through TEM observation coupled with on-line mass spectroscopy or other property measurements.

Material and Methods

DENSsolutions Climate TEM holder, gas and heating nano-reactor, and an FEI Titan TEM operating at 300 kV were used. Pd nanoparticles, serving as catalytic material, were dispersed in ethanol and drop-cast onto the Climate nano-reactor. The semiconductor material, Ga_2O_3 amorphous thin film, was deposited onto the Climate nano-reactor via MBE at approximately 100°C.

Real-time thermal measurements were achieved using the integrated set-measure-adjust feedback loop of the heating control system,1 allowing direct assessment of heat flow stabilization, temperature fluctuations due to endo-/exothermic reactions, and beam-induced thermal variations.

Results

Figure 1 presents the local-to-global dynamic oscillations of Pd nanoparticles during methane oxidation at 650°C, captured with synchronized multimodal data: structural evolution from HAADF STEM imaging, reaction status from mass spectrometry, and heat transfer dynamics from on-chip calorimetry.2

Figure 2 illustrates the heat transfer dynamics involved in the disorder-to-order phase transformation of Ga_2O_3, specifically from as-deposited amorphous to γ-phase, and subsequently to β-phase. This transformation is demonstrated through simultaneously acquired selected area electron diffraction (SAED) data, presented with radial integration.

Technical considerations—including chip design, characterization, and experimental workflows for achieving reliable calorimetry—along with ongoing challenges in advancing quantitative analysis, will be presented on-site.

Conclusion

The development and application of on-chip calorimetry provide higher temporal resolution and multimodal insights into structural and reaction properties, surpassing traditional thermal analysis methods. This advancement enhances the reliability of material process and heat transfer correlation

analysis. However, further hardware and workflow improvements are needed to achieve fully quantitative analysis.

Figure 1 Synchronized HAADF STEM imaging, mass spectrometry, and on-chip calorimetry for the characterization of Pd-catalyzed methane oxidation.

Figure 2 (a) Radially integrated profiles of in situ SAED patterns acquired over temperature ramping process. (b) 1st and 2nd derivative of heating power presenting corresponding phase transformation and heat transfer information.

References:

1. Zhang, F. *et al.* Data synchronization in operando gas and heating TEM. *Ultramicroscopy* **238**, 113549 (2022).

Fig. 1

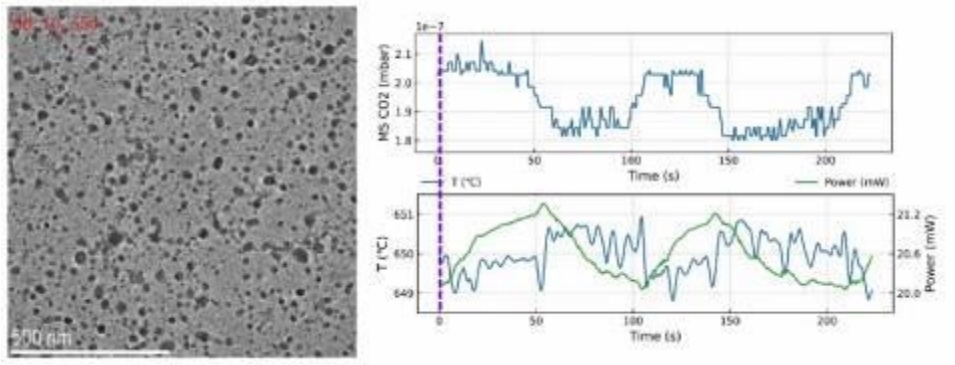
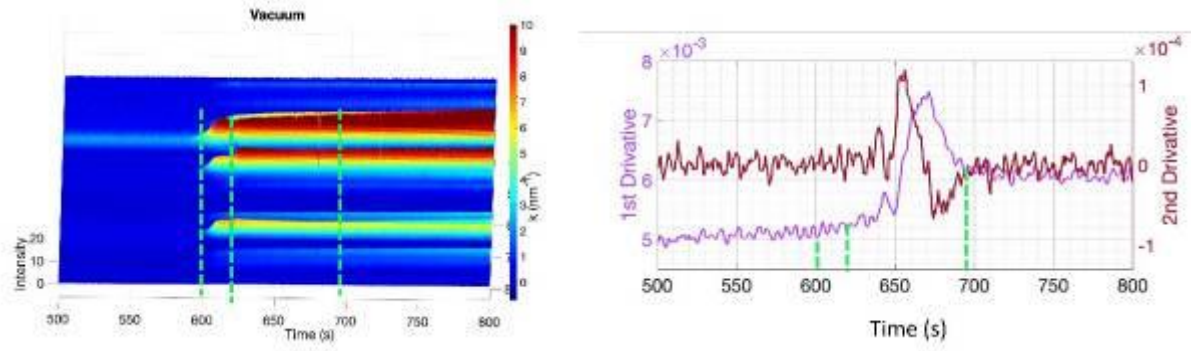


Fig. 2



MS7.P18
Advancing transmission electron microscopy with an open gas cell and sub-0.5 Å resolution

I. Biran[1], F. Dam[1], S. Kargo Kaptain[1], R. Bueno Villoro[1], C. Kisielowski[2], M. Wirix[3], D. Cats[3], N. Shastri[3], W. Haasnoot[3], P. C. K. Vesborg[1], J. Kibsgaard[1], T. Bligaard[4], C. Danvad Damsgaard[1,5], J. R. Jinscheck[5], S. Helveg[1]

[1]Technical University of Denmark, Department of Physics, Kongens Lyngby, Denmark
[2]Electron Scattering Solutions, Piedmont, CA, United States
[3]Thermo Fisher Scientific, Eindhoven, Netherlands
[4]Technical University of Denmark, Energy Conversion and Storage, Kongens Lyngby, Denmark
[5]Technical University of Denmark, Nanolab - National Centre for Nano Fabrication and Characterization, Kongens Lyngby, Denmark

Introduction:

Over the last decades, transmission electron microscopy (TEM) has achieved significant advancements in visualizing matter at the atomic level, especially by implementing aberration-corrected electron optics, monochromatizing the electron source, and stabilized lens systems. Hence, spatial resolution has been enhanced to exceed 50 pm in both broad and and focused beam modes, marking a shift from instrument-limited resolution to object-limited imaging resolution.[1–3] This progress enabled single-atom sensitivity imaging across the Periodic Table of Elements and the determination of the three-dimensional atomic structure of nanostructured materials.[4,5]

Objectives:

Because surfaces of most nanomaterials dynamically adapt to their environment which modulates their function, developing single-atom-sensitive TEM with high spatiotemporal resolution under controlled environmental conditions is key to understand the role of gas-surface interactions in catalysis, energy conversion, and crystal growth.

Materials & Methods:

We report on the design of the VISION PRIME microscope, based on an ultra-stable Thermo Fisher Scientific SPECTRA ETEM platform, designed to operate in reactive gas environments at pressures of up to 10-20 mbar. Key elements in the microscope design are (i) a new 5th-order aberration-corrector for the objective lens in broad-beam mode (CETCOR PRIME), (ii) a four-stage differential pumping system for confining a reactive gas environment in the mbar range close to the sample (iii) a monochromator setup to extend the information limit and (iv) a direct electron detection acquisition (Falcon 4i) for low-dose-rate imaging to suppress electron-beam-induced sample alterations.

Results:

Here we examine the new microscope's ultimate imaging capabilities in reactive gas environments. We demonstrate that the inherent information limit of the microscope measured by Young Fringes is ca. 50 pm without and with N_2 pressure of a few mbar. We also document the strong benefit of Nelsonian illumination for suppressing electron-beam-induced excitations of the gas-sample system,[6] consistent with expectations.[7] Finally, we directly measure the achievable resolution in real space images from an exit wave phase image of an Au sample oriented in a low-index zone axis. A resolution of less than 50 pm in real space was achieved also at 1 mbar of N_2.

Conclusions:

The VISION PRIME offers an image resolution that is limited by the atoms" electrostatic potentials and their vibrations in high vacuum and environmental conditions. Combined with channeling theory, it allows new ways to address three-dimensional atomic structures and their dynamic behavior while exposed to relevant reaction conditions.

Fig.1. Phase of reconstructed exit wave image of Au nanoparticle. The line scan shows the ability to obtain sub-50 pm resolution by measuring the width of the atomic columns.

References:

1.Kisielowski, C. *et al.*, *Microsc Microanal* **14**, 469–477 (2008).

2.Haider, M. *et al.*, *Nature* **392**, 768–769 (1998).

3.Jin, L., Barthel, J., Jia, C.-L., Urban, K. W., *Ultramicroscopy* **176**, 99–104 (2017).

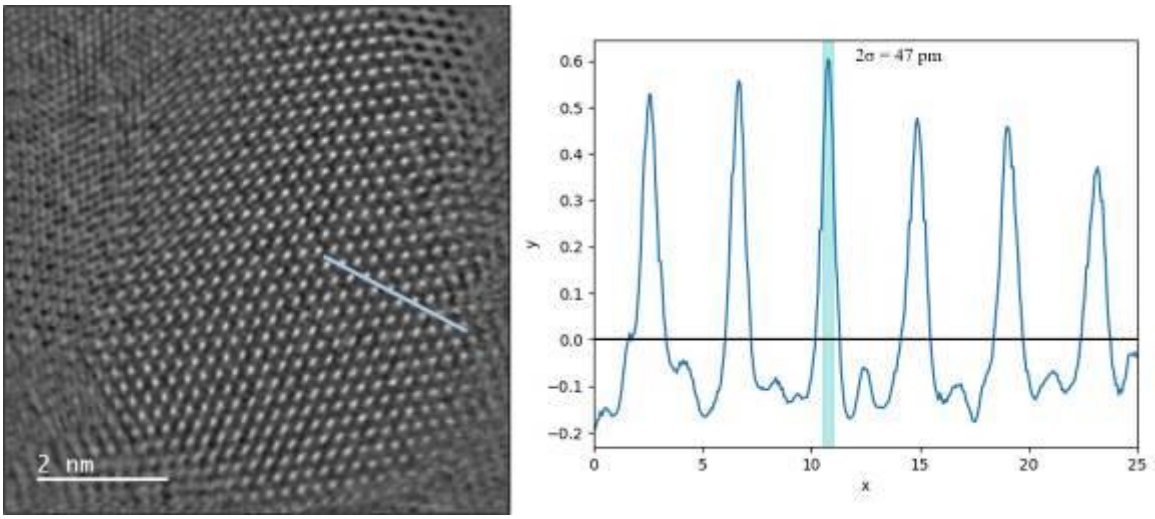
4.Chen, F.-R. *et al., Nat Commun* **12**, 5007 (2021).

5.Chen, F.-R., Van Dyck, D., Kisielowski, C., *Nat Commun* **7**, 10603 (2016).

6.Tiemeijer, P. C. *et al., Ultramicroscopy* **114**, 72–81 (2012).

7.Helveg, S. *et al., Micron* **68**, 176–185 (2015).

Fig. 1



MS7.P19
A unique correlative microscopy platform for combined AFM, SEM, EDS, and nanoprobing

C. Schwalb[1], H. Frerichs[1], D. Jangid[1], S. Seibert[1], L. Stühn[1], M. Wolff[1]

[1]Quantum Design Microscopy GmbH, Pfungstadt, Germany

Combining different complementary analytical methods into one instrument is a powerful technique for the contemporaneous acquisition of both structural and functional sample properties. Especially the combination of atomic force microscopy (AFM), scanning electron microscopy (SEM), and electrical nanoprobing can yield completely new insights for the study of various materials and nanostructures.

In this work, we introduce a highly integrated correlative microscopy platform – The FusionScope – that seamlessly combines AFM and SEM within a unified coordinate system (see Figure 1). In addition, a three-axis sample stage and a trunnion provide unique experimental capabilities such as profile view – an 80-degree tilt of the combined sample stage and AFM giving full SEM access to the cantilever tip region. This microscopy platform can easily be combined with a nanoprobing system that enables precise electrical characterization of nanoscale structures, offering insights into device functionality and performance [1-2].

We present a variety of novel case studies to highlight the advantages of this new tool for interactive, correlative, in-situ nanoscale characterization of different materials and nanostructures. Initial results will focus on the analysis of mechanical and electrical properties of individual nanowires. The combination of SEM and nanoprobes enables easy manipulation and positioning of individual nanowires, whereas the in-situ AFM allows the characterization of topography, surface roughness, mechanical and electrical properties of the nanowire [3-4]. Using the SEM"s high-resolution the AFM cantilever tip can be precisely positioned on an individual nanowire that is attached to the nanoprober and the topographical and mechanical properties can be determined.

In addition, we will show results for electrical nanoprobing of semiconductor devices in combination with conductive AFM and electrostatic force microscopy (EFM) measurements. A semiconductor device can be electrically probed by simultaneous use of two microprobers while the AFM provides detailed information on the 2D conductance map and the EFM signal of the device itself (see Figure 2).

Based on the broad variety of applications regarding the inspection and process control of different materials and devices, we anticipate that this new inspection tool will be one of the driving characterization tools for correlative analysis on the nanoscale.

Figure 1: The FusionScope analysis platform, combining AFM, SEM, EDS, and nanoprobing capabilities.

Figure 2: (Top) SEM image of two microprober needles(green) in combination with AFM cantilever (purple) positioned on an electrode structure. The microprober needles are used for biasing of the electrodes, whereas the cantilever measures the EFM signal of the structures. (Bottom) Correlative EFM on topography data during bias flip.

[1] Dukic M 2015 *Scientific Reports* **5 (1)** 16393
[2] Prohinig J M 2022 *Scripta Materialia* **214** 114646
[3] Alipour A 2023 *Microscopy Today* **6** 17-22
[4] Reisecker V 2023 *Advanced Functional Materials* **34 (7)** 2310110

Fig. 1

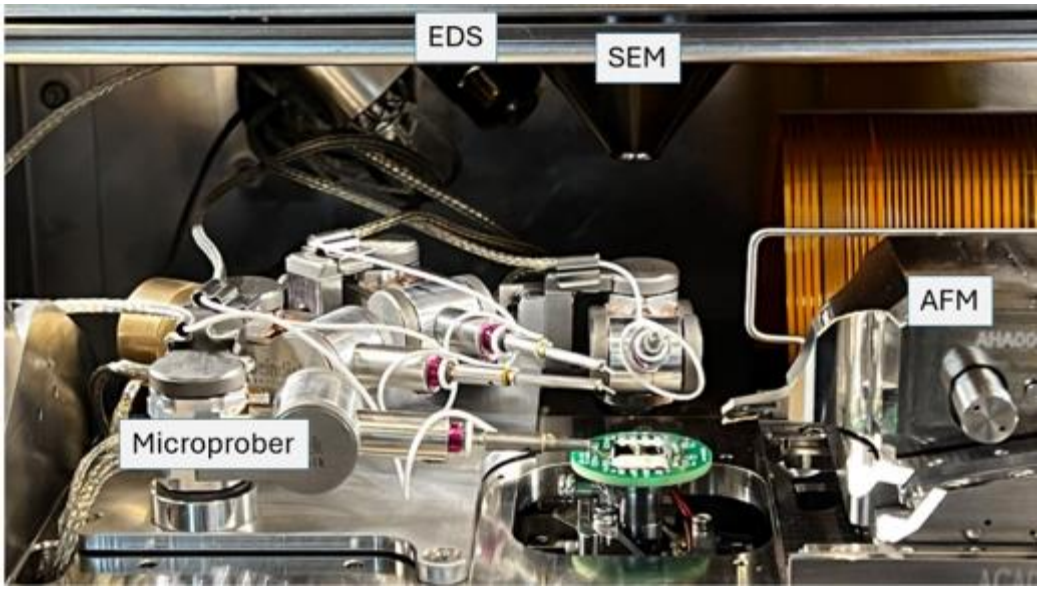
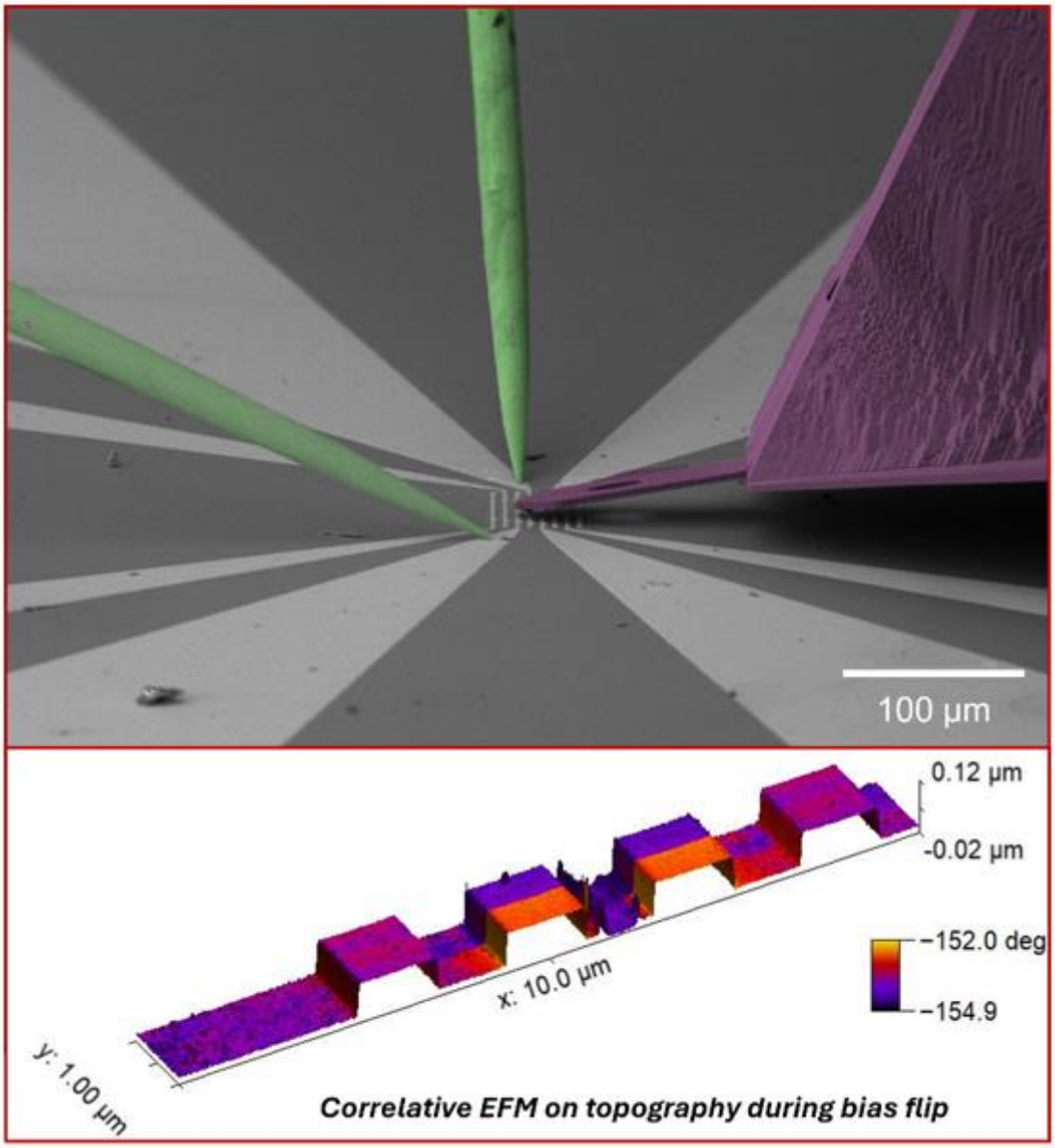


Fig. 2


100 µm
0.12 µm
-0.02 µm
−152.0 deg
−154.9
x: 10.0 µm
y: 1.00 µm
Correlative EFM on topography during bias flip

MS7.P20
Exploring nanoscale magnetism – *In situ* magneto-transport in a TEM

D. Pohl[1], S. Schneider[1], D. Kriegner[2], M. Garbrecht[3], M. Winter[1,4], A. Thomas[5,6], B. Rellinghaus[1]

[1]DCN, TU Dresden, Dresden, Germany
[2]Academy of Sciences of the Czech Republic, Prague, Czech Republic
[3]The University of Sydney, Sydney, Australia
[4]Max Planck Institute for Chemical Physics of Solids, Dresden, Germany
[5]Leibniz Institute for Solid State and Materials Research Dresden, Dresden, Germany
[6]Technical University Dresden, Dresden, Germany

Introduction

Non-trivial magnetic textures, such as skyrmions, are – besides others – typically characterized by measurements of the anomalous Hall effect and imaged using Lorentz TEM (LTEM). Frequently, however, these investigations are conducted on different samples, which may impede a direct correlation of transport and imaging data.

Objectives

We have therefore developed an advanced in-situ magneto-transport measurement setup in a transmission electron microscope, which for the first time allows for the direct correlation of the imaged magnetic textures with the Hall voltage [1]. This approach enables simultaneous magnetic imaging and four-probe electrical measurements supported by high-resolution structural and chemical characterization of the same sample.

Materials & methods

In-situ Lorentz-TEM (L-TEM) investigations were conducted on a JEOL F-200 microscope (200 kV, cold FEG) equipped with a Gatan OneView camera. A Protochips Fusion Select holder with gold-plated spring contacts connected to electrical feedthroughs is used to measure the anomalous Hall effect. TEM lamellas from various magnetic single crystals ($Mn_{1.4}PtSn$, $Co_8Zn_9Mn_3$ and CrSb) are cut using a focused ion beam system (FIB), deposited on a measurement chip with a Si_xN window, and soldered to the pre-defined contact pads by W deposition in the FIB.

A magnetic field perpendicular to the sample plane is applied by the objective lens. Acquisition of L-TEM images and concurrent measurements of the Hall voltage as function of the magnetic field were conducted automatically utilizing a Python scripting. The magneto-transport measurements are performed either in DC mode or using Lock-In technique.

Results

Fig. 1 highlights the variety of different samples and techniques that can be measured and combined with our new setup. Beyond simply measuring the hysteresis loop of materials such as $Mn_{1.4}PtSn$, the system also enables the controlled manipulation of specific magnetic textures (e.g., Fig. 1a–c) by tilting the sample, allowing real-time monitoring of their Hall voltage response. This capability facilitates the measurement of topological Hall voltage in (anti-)skyrmions (Fig. 1d) [2]. Additionally, diffraction analysis (Fig. 1e) can be integrated with magneto-transport measurements in a TEM, providing straightforward access to hysteresis loops along different crystallographic directions (Fig. 1f).

Conclusion

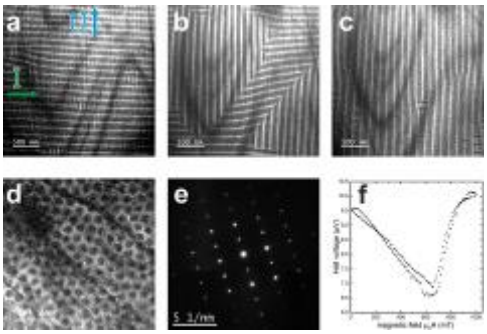
Our new setup allows us for the first time to follow in detail the field dependence of the Hall voltage while simultaneously monitoring the magnetic phases in several magnetic materials e.g. $Mn_{1.4}PtSn$, thereby providing valuable insights into the existence and nature of an intensely debated electrical signature of skyrmionics structures.

[1] D. Pohl et al., Scientific Reports (2023) https://doi.org/10.1038/s41598-023-41985-7

[2] A. Thomas et al., Small Methods (2025) https://doi.org/10.1002/smtd.202401875

Fig. 1: In-Situ magneto-transport of various magnetic samples: LTEM images of the helical phase in different variants in $Mn_{1.4}PtSn$ (a-c), Skyrmions at RT in $Co_8Zn_9Mn_3$, diffraction pattern and anomalous Hall voltage of CrSb.

Fig. 1



MS7.P21
In situ backside hydrogen charging cell for nanoscale imaging of hydrogen-materials interaction – A correlative microscopic approach based on SIMS

A. Suresh Kumar[1,2], S. Eswara[1], T. Wirtz[1]

[1]Luxembourg Institute of Science and Technology, Scientific Instrumentation and Process Technology, Belvaux, Luxembourg
[2]University of Luxembourg, Physics and Materials Science, Esch sur Alzette, Luxembourg

Hydrogen entering materials can have both beneficial and detrimental effects. Due to its low mass, high mobility, and low detection sensitivity, studying hydrogen behaviour at the nanoscale remains a challenge for conventional microscopic techniques. Secondary Ion Mass Spectrometry (SIMS) is a highly sensitive chemical analysis technique with an excellent detection limit, enabling high-resolution hydrogen mapping in materials[1]. When combined with conventional microscopic techniques, SIMS provides a holistic understanding of hydrogen-induced modifications in materials[2]. However, hydrogen"s rapid diffusion can lead to a loss of critical information when samples are charged outside the analysis setup. To address this, we present an in-situ backside electrochemical hydrogen charging system, integrated into a hybrid Focused Ion Beam (FIB)-Scanning Electron Microscope (SEM)-SIMS instrument, allowing real-time visualization of hydrogen-induced changes in materials.

The objective is to develop an in-situ backside hydrogen charging cell for real-time analysis of hydrogen distribution in materials, addressing key challenges in hydrogen-related applications.

The FIB-SEM-SIMS instrument integrates a high-vacuum commercial FIB-SEM (Thermo Fisher Scientific Scios) with an in-house developed double-focusing magnetic sector Secondary Ion Mass Spectrometer[1]. The SIMS detector, utilizing a continuous focal plane detector based on microchannel plates and delay-line detector, achieves high mass resolution ($M/\Delta M > 400$) and can simultaneously acquire a full mass spectrum for each scanned pixel. The in-situ backside hydrogen charging cell consists of an electrolyte compartment (~600 µl capacity), with the sample clamped on top so that only its bottom surface contacts the electrolyte, leaving the top surface clean for analysis. In this study, a 50 nm thick pure titanium (Ti) thin film (analysis surface) coated on a 1 mm thick ferritic stainless-steel substrate was used to demonstrate hydrogen-induced changes on the Ti film during in-situ backside charging.

Backscattered Electron (BSE) imaging and SIMS analysis were conducted every 30 minutes during in-situ hydrogen charging. BSE images confirmed the formation of titanium hydride phases, while corresponding SIMS hydrogen maps revealed signal intensity variations, providing insights into local variations in hydrogen diffusivity, hydride nucleation and growth dynamics in the sample.

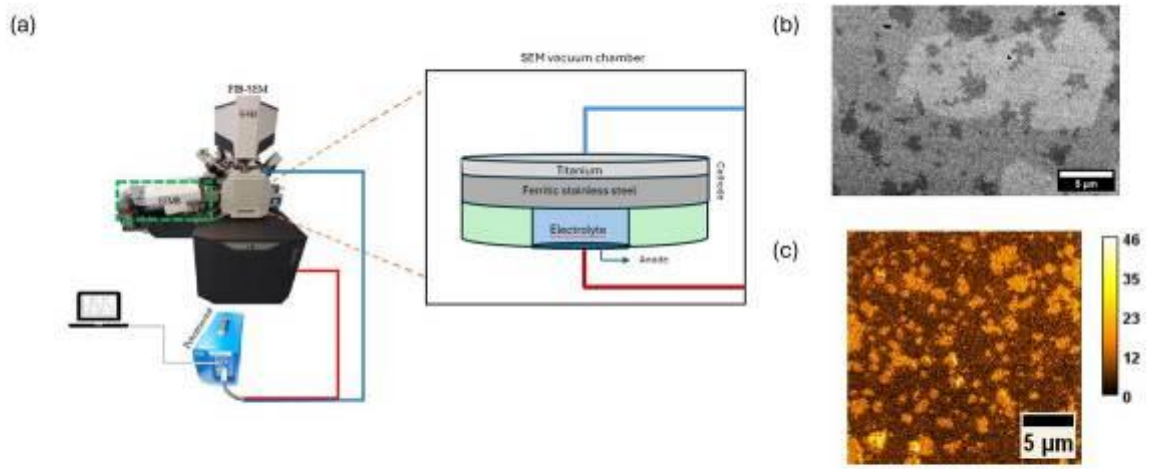
Figure 1: (a) Schematic of the FIB-SEM-SIMS instrument with an in-situ hydrogen charging setup (b) BSE image showing titanium hydride formation. (c) SIMS 1H- map showing increased hydrogen signal intensity from hydride phases.

To mitigate hydrogen loss due to diffusion during analysis, an in-situ electrochemical charging holder was developed for real-time hydrogen charging in the FIB-SEM-SIMS instrument. Results from the backside hydrogen charging of Ti thin films demonstrate the potential of this setup for correlative SIMS-based microscopy, enabling nanoscale visualization of hydrogen-metal interactions

[1] O. De Castro *et al.*, "Magnetic Sector Secondary Ion Mass Spectrometry on FIB-SEM Instruments for Nanoscale Chemical Imaging," *Anal Chem*, vol. 94, no. 30, pp. 10754–10763, Aug. 2022, doi: 10.1021/acs.analchem.2c01410.

[2] D. Andersen *et al.*, "Correlative high-resolution imaging of hydrogen in Mg2Ni hydrogen storage thin films," *Int J Hydrogen Energy*, Apr. 2023, doi: 10.1016/j.ijhydene.2022.12.216.

Fig. 1



MS7.P22
Quantifying carbon site switching dynamics in GaN by electron holography

K. Ji[1], M. Schnedler[1], Q. Lan[1], J. F. Carlin[2], R. Butté[2], N. Grandjean[2], R. E. Dunin-Borkowski[1], P. Ebert[1]

[1]Forschungszentrum Jülich GmbH, Ernst Ruska-Center, Jülich, Germany
[2]Ecole Polytechnique Fédérale de Lausanne, Institute of Physics, Lausanne, Switzerland

The understanding of the role of carbon in electronic properties and long-term stability of nitride devices remains limited: On the one hand, C is believed to play a central role in the degradation processes of, e.g., laser diodes. On the other hand, C is intentionally used to achieve semi-insulating layers, intended for reducing drain leakage currents and enhancing breakdown voltages in high-electron-mobility transistors. However, information about dynamic processes and point defect reactions of C is scarce, although being of paramount importance to understand degradation as well as explore paths towards extended durability of group-III nitride devices.

Off-axis electron holography (EH) in a transmission electron microscope (TEM) is utilized to investigate C point defect reactions and quantify their dynamics by probing the time and temperature dependence of the Fermi-level pinning upon annealing. We identify that the atomic process lifting the Fermi-level pinning in C-implanted GaN has a jump length in the range of a single lattice constant and a charge reversal in line with a site switching of C from substitutional to interstitial sites. The process has an activation barrier energy of 2.27±0.26eV.

Our work establishes EH in a TEM as a methodology to probe the dynamics and reactions of charged point defects in GaN and assess the thermal physical processes governing semiconductor device stability.

MS7.P23
In situ and *ex situ* thermal evolution, crystallization and optical properties of Amorphous $(In,Ga)_2O_3$

J. García Fernández[1], A. Pokle[1], M. Andreassen[1], Ø. Prytz[1], M. Grundmann[2], H. von Wenckstern[1,2]

[1]University of Oslo, Oslo, Norway
[2]Leipzig University, Leipzig, Germany

Solid solutions of In_2O_3 and Ga_2O_3 hold great potential for developing new transparent n-type electrodes or active materials for optoelectronic applications. This is due to their tunable bandgap energies (2.9 to 4.7 eV), adjustable by varying the relative cation concentration [1, 2]. In optoelectronic device applications, a common approach in thin film deposition and solid-state epitaxy involves growing amorphous materials at low temperatures on a crystalline substrate, followed by post-deposition processing [3]. Therefore, monitoring and controlling the crystallization process from high free-energy states (such as the amorphous phase) is crucial for achieving high-purity crystalline films with low defect density in a reproducible manner. This work investigates the crystallization of an amorphous alloy with a composition of 63% In_2O_3 – 37% Ga_2O_3 during annealing on a crystalline r-plane sapphire substrate, using *in-situ* transmission electron microscopy (TEM) under vacuum. Additionally, we examine the effects of sample surface-to-volume ratio on the annealing process, we conducted *ex-situ* annealing under vacuum on a bulk sample with same composition and measured the optical properties.

For thin film growth a combinatorial pulsed laser deposition (C-PLD) approach based on the ablation of radially-segmented targets [4]. Annealing of bulk sample was conducted from RT up to 800 °C with ramp rates 10 °C /min under high vacuum. At every 50 °C the temperature was maintained for 30 minutes. TEM lamellas were prepared by a focused ion beam (FIB) using a JEOL JIB 4500. High-resolution scanning transmission electron microscopy (HRTEM/STEM) and selected area electron diffraction (SAED) were conducted using a Thermo Fisher Scientific Cs-corrected Titan G2 60–300 kV microscope operated at 300 kV and equipped with a Gatan GIF Quantum 965 spectrometer.

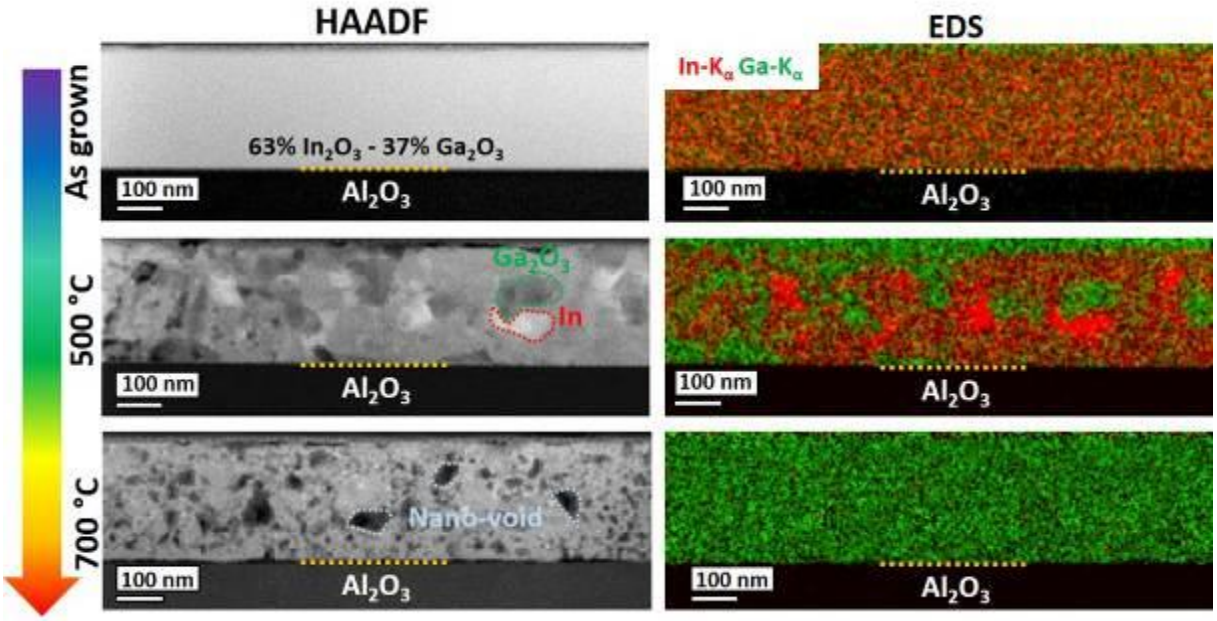
Initial XRD and TEM analyses confirmed the amorphous nature of the as-grown sample. Upon annealing at 400–500 °C by *in-situ* TEM, crystallization is initiated, forming a heterogeneous polycrystalline mixture of indium, β-Ga_2O_3, and a minor fraction of c-In_2O_3. As the temperature increased, progressive evaporation of indium was observed, leading to the dominance of β-Ga_2O_3 at 700 °C, accompanied by the formation of nano-voids as a consequence of the indium evaporation. Figure 1 shows, as a summary of all the *in-situ* TEM annealing process, the HAADF STEM image (left-hand side column) and corresponding cationic EDS maps (right-hand side column) using the In-Kα (red) and Ga-Kα (green) lines. The *in-situ* TEM results were consistent with *ex-situ* bulk annealing, confirming the transformation to c-$(In,Ga)_2O_3$ and the emergence of β-$(Ga,In)_2O_3$ at the surface. These findings provide a comprehensive understanding of the phase evolution and thermal stability of the material, offering valuable insights for its potential applications.

Figure 1. Left-hand side: Low magnification HAADF STEM images of as-grown sample (upper) and after annealing at 500 °C (middle) and 700 °C (lower). Right-hand side: Corresponding cationic STEM EDS maps using the In- Kα (red) Ga-Kα (green).

References

[1] H. von Wenckstern, Adv. Electron. Mater. 3, 1600350 (2017)
[2] D. Kaur at al. Adv. Optical Mater. 9, 2002160 (2021)
[3] M. A. Herman, Solid Phase Epitaxy. In: Epitaxy. Springer Series in materials science, vol 62. Springer, Berlin, Heidelberg, (2010)
[4] S. Montag et al. Phys. Rev. Mater. 7, 094603 (2023)

Fig. 1


HAADF
EDS
As grown
500 °C
700 °C
63% In_2O_3 - 37% Ga_2O_3
In-K_α Ga-K_α
100 nm
Al_2O_3
Ga_2O_3
In
Nano-void

MS7.P24
Stability of gold nanorods under tunable ps-pulsed laser illumination – An *in situ* TEM study

L. Monin[1], W. Albrecht[1]

[1]AMOLF, Amsterdam, Netherlands

Dynamic and resonant plasmonic photocatalysis is a new and exciting field that can overcome the classic Sabatier limit in catalysis. The underlying idea is to actively modify the catalyst at fast timescales through pulsed laser excitation. However, GNPs have been shown to be morphologically unstable under laser excitation, even for temperatures below the bulk melting temperature of gold severely limiting their application in this new field of catalysis [1,2]. This project aims at investigating the structural stability of gold nanoparticles (GNPs) under pulsed light excitation. This is studied in situ inside the transmission electron microscope (TEM). In particular, we investigate how different laser pulse conditions and pulse train sequences influence the stability of GNPs.

We use a JEOL NEOARM TEM equipped with the IDES light in coupling unit. This configuration allows us to directly fiber couple a ps pulsed laser into the column (Figure 1). The laser wavelength, fluence and repetition rate can thereby be tuned while keeping the laser beam (spot size of about 50um) and electron beam spatially overlapped.

Figure 1. Scheme of the TEM with the fiber coupled laser through the column.

In this work, we demonstrate that the laser excitation scheme plays a crucial role for the structural stability of GNPs (Figure 2). Varying the fluence and the cooling time between the heating cycles provides insights about the kinetics of the reshaping of GNPs. We correlate these in situ observations to single particle optical spectroscopy and heat dissipation simulations.

Figure2. Demonstration of the structural changes of gold nanorods on a lacey carbon grid before (left) and after (right) laser excitation at resonance. The GNPs were illuminated at a wavelength of 680nm with a fluence of 2.1 x 10^{-3} mJ cm^{-2}.

In conclusion, coupling light directly into the electron column allows us to observe how catalytic GNPs behave in real conditions. This research paves the road for the design of GNPs that would be stable under dynamic and resonant catalytic conditions. Future steps include the use of a holder equipped with a small reactor allowing to mimic the operational conditions of a light driven catalytic reactor.

References

[1] Albrecht et al., Adv. Mater. 33, 2100972 (2021)

[2] González-Rubio et al., Science 358, 640–644 (2017)

Fig. 1

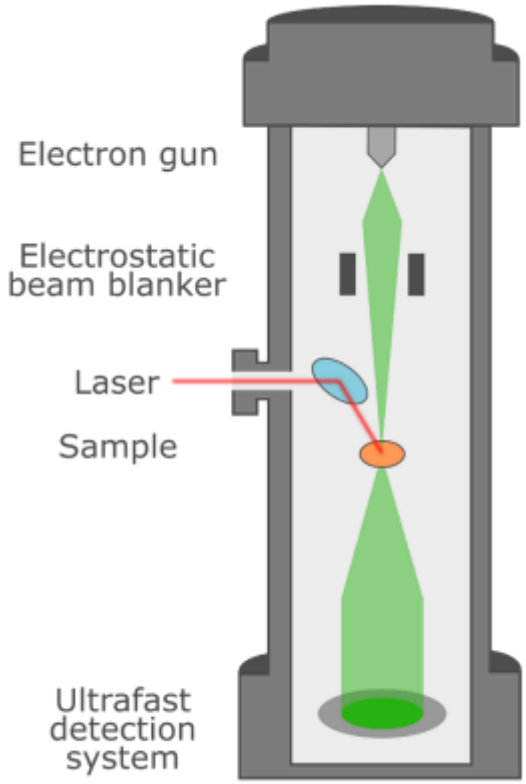
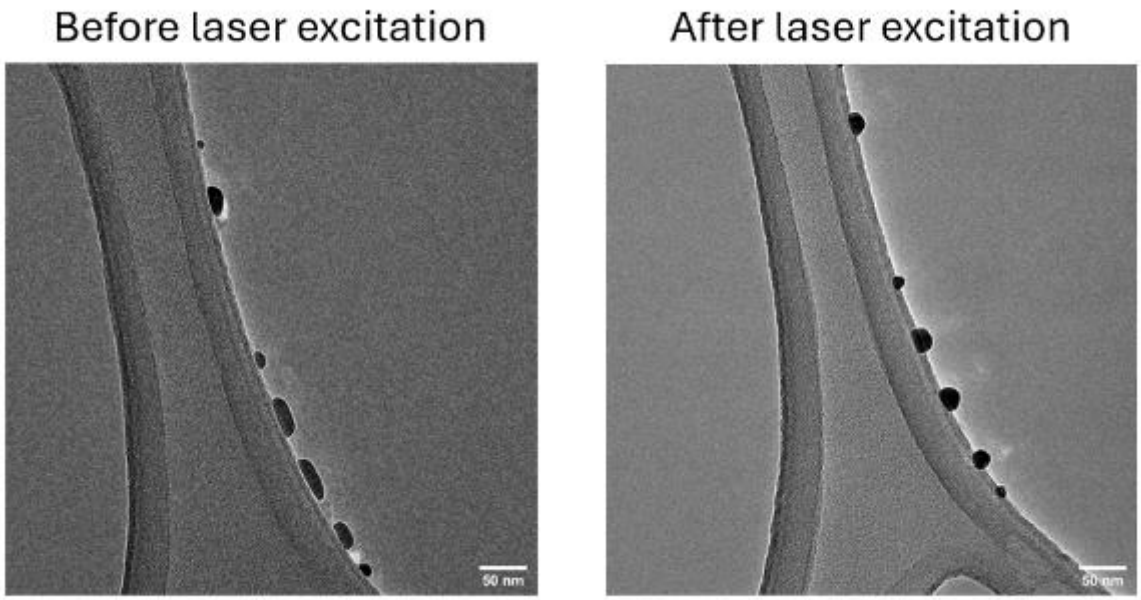

Electron gun
Electrostatic beam blanker
Laser
Sample
Ultrafast detection system

Fig. 2


Before laser excitation
After laser excitation
50 nm
50 nm

MS7.P25
A multi-scale *Operando* electron microscopy approach for understanding the interface evolution in Li-Argyrodite-based solid-state batteries

R. Tripathi[1], E. Reisacher[2], P. Kaya[2], V. Knoblauch[2], B. Linn[3], D. Lysenkov[1], M. Boese[3], R. Zarnetta[1]

[1]Carl Zeiss, IMT, Oberkochen, Germany
[2]Aalen University, Materials Research Institute Aalen (IMFAA), Aalen, Germany
[3]Carl Zeiss, RMS, Oberkochen, Germany

Introduction

Continuous innovation in battery technology has led to the discovery of new materials, advanced chemistries and next generation technologies such as solid-state batteries (SSBs) which have the potential to significantly enhance energy density and safety. However, a major challenge in SSBs is the poor interfacial contact between the electrode-electrolyte interface, leading to higher charge transfer resistance and consequently poor cyclability.

Objectives

Applying high temperature and stack pressure by encasing the SSB cells in custom-made set-ups improves the performance but makes it impossible to investigate the progressive aging processes during operation (i.e., during charging/discharging). As a result, the mechanisms leading to failure remain largely unknown. Additionally, these custom-made cells are not standardized and show disparity in post-mortem analysis results of similar cells. Therefore, efficient multi-scale characterization approaches such as *operando* investigations, are essential for accelerating advancements in the field.

Materials & Methods

To address these challenges, we present the development and application of an *operando* SSB testing technique for scanning electron microscope (SEM). This method integrates focused-ion-beam (FIB) milling for accessing the deeper regions and an energy dispersive x-ray spectroscopy (EDS) for chemical composition analyses. The system includes an integrated battery cycler for fully automated cycling and impedance measurements, enabling real-time observation of microstructural changes in SSB components under an electron beam. A vacuum transfer shuttle enables an inert atmosphere workflow for handling air and moisture-sensitive samples. Additionally, precise pressure control (up to 125 MPa) and temperature regulation (-100 to +100 °C) allow systematic investigations. The Li_6PS_5Cl-NMC-based SSB cells used in the study were fabricated using the pelletized cell process, in which composite cathode and solid separator pellets were prepared via uniaxial pressing under controlled pressure, followed by the addition of the metal anode layer.

Results

The chemo-mechanical aging, interfacial stability, and cycling effects were examined. Preliminary results show reduced impedance with increasing pressure, indicating lower internal resistance. However, beyond a critical pressure, excessive strain compromises mechanical integrity, as observed under the electron beam and reflected simultaneously in the cycling performance. EDS analysis provides insights into chemical stability. FIB cross-sections revealed delamination and crack formation in the composite cathode and solid separator after electrochemical loading. Prolonged pressure led to Li-metal anode creep, ultimately causing short circuits.

Conclusion

Testing these SSBs in custom-made cells made it impossible to identify the cause of failure because dismantling the cells for imaging released the pressure, which caused the existing cracks to spread. Overall, the present work combines a novel battery testing technique in a user-friendly and automated inert workflow, to study the aging behavior and identify the associated failure mechanism of the SSBs, which will aid the researchers in understanding their material characteristics and in faster achieving the targets for commercialization of SSBs.

MS7.P26
STEM EBIC for semiconductor characterization – Potential and pitfalls

S. Schneider[1], D. Pohl[1], B. Rellinghaus[1]

[1]Technical University Dresden, Dresden Center for Nanoanalysis (DCN), Dresden, Germany

Introduction

The continuous miniaturization of semiconductor devices necessitates characterization techniques with nanometer-scale resolution to probe their electronic properties. Scanning transmission electron microscopy (STEM) combined with electron beam-induced current (EBIC) measurements has emerged as a powerful tool for analyzing semiconductor materials, crucial for both fundamental research and industrial device optimization.

Objectives

This study aims to investigate the potential of STEM EBIC measurements for characterizing the electronic properties of a commercial Si photodiode. In particular, we assess the impact of sample thickness [1] and focused ion beam (FIB)-induced Ga implantation [2] on EBIC signal strength and electrical conductivity.

Materials & Methods

A 500 nm thick TEM lamella was prepared from a commercial Si photodiode using FIB milling. The lamella was positioned on a commercial MEMS chip and soldered to the contact pads in the FIB. It was then cut to ensure that the n- and p-type Si regions, separated by the depletion region, remained electrically connected to only one side of the chip respectively. STEM EBIC measurements were conducted in a JEOL Jem F-200C microscope equipped with a point electronic electrical analysis system. Additionally, a sample prepared using Plasma-FIB will be presented, and its results will be compared to those of Ga-FIB samples.

Results

The EBIC measurements revealed the depletion region of the photodiode as a bright contrast feature (cf. red rectangle in **Fig. 1**), with signal strength strongly influenced by the lamella thickness. Thinner samples exhibited a reduced interaction volume for charge carrier generation, as well as increased surface recombination, leading to a diminished EBIC contrast. Additionally, Ga implantation during FIB milling introduced defect surface layers that resulted in metallic-like behavior, as observed in the current–voltage characteristics (cf. **Fig. 2**). This effect can lead to misinterpretations in electrical analyses of FIB-prepared samples.

Conclusion

As semiconductor devices become increasingly complex, advanced characterization methods are essential for understanding nanoscale charge transport and optimizing device architectures. To improve the interpretation of STEM EBIC data, experimental results from complementary techniques such as differential phase contrast (DPC) imaging and off-axis electron holography will be discussed. The correlation of these methods enables a more comprehensive understanding of semiconductor device performance at the nanoscale.

References:

[1] Aidan P. Conlan et al., J. Appl. Phys. 129 (2021), 135701, https://doi.org/10.1063/5.0040243.

[2] William A. Hubbard, EDFA Technical Articles 26 (2024), 27–34, https://doi.org/10.31399/asm.edfa.2024-4.p027.

Fig. 1. *Superposition of EBIC measurement and ADF image of a Si photodiode. The EBIC signal of the depletion region is marked with a red rectangle.*

Fig. 2. *Current–voltage characteristic of the TEM sample in* ***Fig. 1****.*

Fig. 1

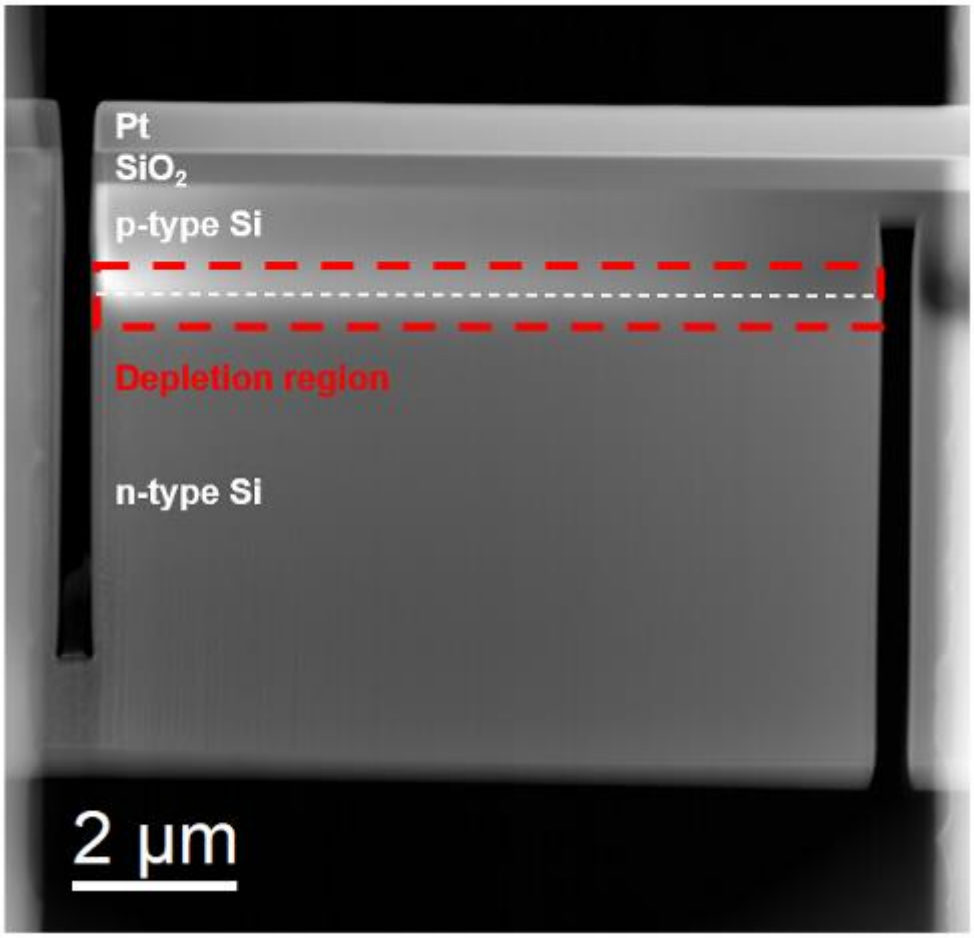
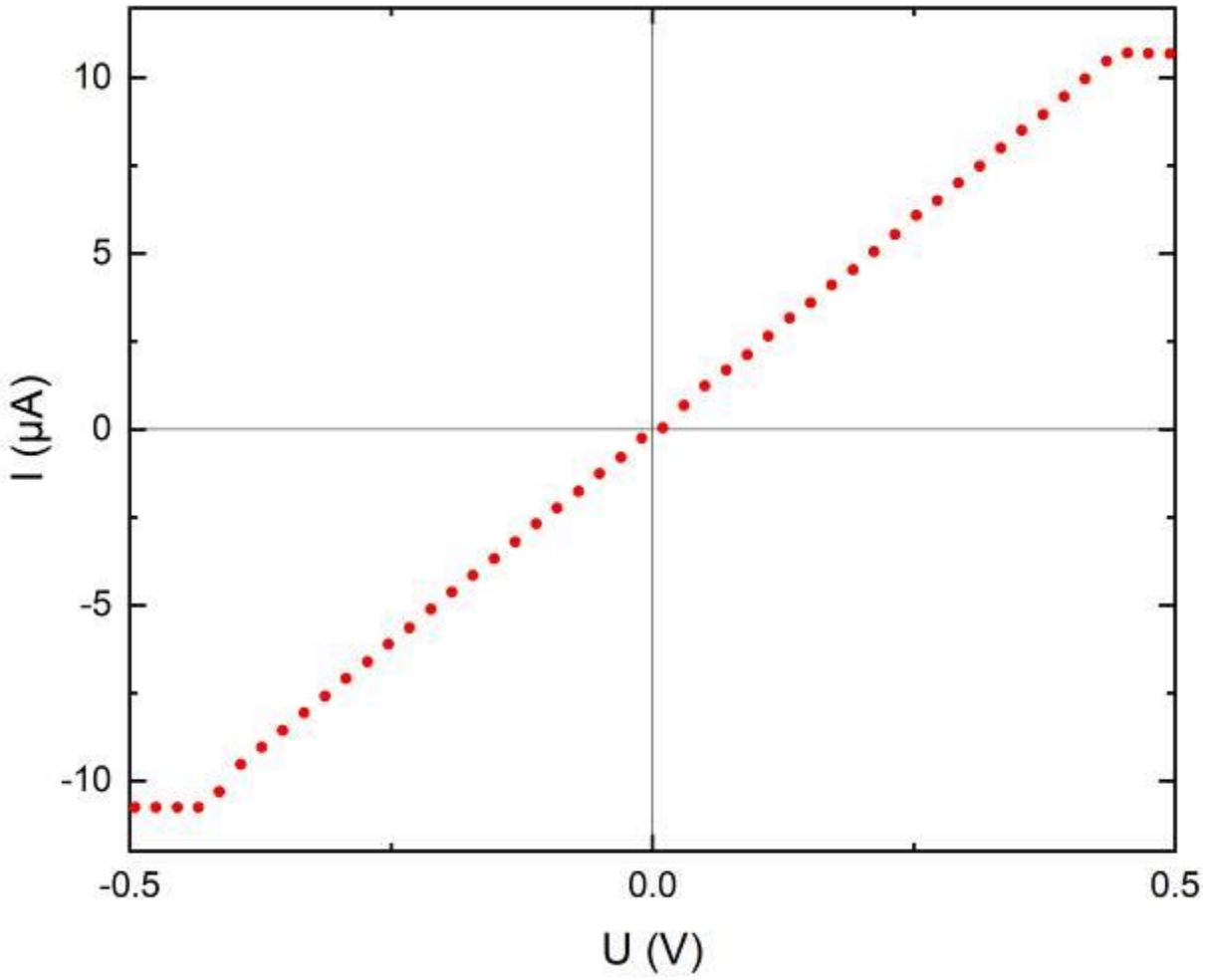


Fig. 2



MS7.P28
Advancing nanoscale material dynamics – Bridging *in situ* liquid phase SEM and TEM

A. Bo[1], H. Sun[1], C. Deen-van Rossum[1], M. Pen[1], S. Basak[2], R. A. Eichel[2,3,4], Y. Pivak[1]

[1]DENSsolutions, Delft, Netherlands
[2]Forschungszentrum Jülich GmbH, Institute of Energy Technologies - Fundamental Electrochemistry (IET-1), Jülich, Germany
[3]RWTH Aachen University, Institute of Physical Chemistry, Aachen, Germany
[4]RWTH Aachen University, Faculty of Mechanical Engineering, Aachen, Germany

Liquid phase electron microscopy (LP-EM) techniques have greatly enhanced research across various fields, including nanomaterial growth dynamics, electrochemical reactions in batteries, corrosion mechanisms, biological interactions, and phase transformations, enabling real-time insights at the nanoscale [1].

Integrating a liquid electrochemical cell into scanning electron microscopy (SEM) enhances materials science research, particularly in corrosion and battery studies. Like in-situ transmission electron microscopy (TEM) techniques, this approach enables real-time observation of electrochemical processes and material dynamics at the electron-transparent window [2,3]. Although not as widely adopted as LP-TEM, LP-SEM offers a relatively low-cost and potentially more convenient characterization method [4]. Notably, it does not impose strict limitations on liquid thickness for imaging, allowing a closer resemblance to a bulk liquid environment and, consequently, real-life applications [5].

In this study, we present the development of an SEM-compatible cell that enables real-time observation of electrochemical reactions within the SEM imaging environment (Figure 1a). Among many other applications, the SEM electrochemical cell can be used to study the growth of Cu dendrites upon cyclic voltammetry measurements using an electrolyte solution of 20 mM $CuSO_4$ and 10 mM K_2HPO_4. A key feature of this setup is the ability to accommodate bulk reference (e.g., Ag/AgCl) and counter (Pt wire) electrodes within the SEM environment, which ensures stable and accurate electrochemical measurements, which are essential for battery research and corrosion studies.

A MEMS-based nano-chip with on-chip electrodes (WE, RE, and CE) in the SEM electrochemical cell is identical to the one used in the in-situ electrochemical TEM holder (e.g., Stream). This cross-platform approach enables seamless integration of SEM and TEM methodologies, allowing complementary data acquisition from both techniques (Figure 1b). Additionally, the presence of bulk electrodes in the SEM cell allows for on-chip reference electrode calibration against a standard reference electrode such as Ag/AgCl. The SEM liquid cell has a volume of approximately 0.5 mL—up to 10^5 times larger than that of the TEM Nano-Cell—providing a unique opportunity to study the effects of liquid confinement on in-situ TEM electrochemical results.

In summary, in-situ LP-SEM enhances real-time nanoscale studies, offering detailed insights into material behaviour, electrochemical reactions, and biological processes under conditions that closely resemble real-world environments.

Figure 1. Images of Cu dendrite growth recorded during in-situ cyclic voltammetry (CV) measurements using Quanta 200 SEM (a) and JEM-200F TEM.

References

[1] U Mirsaidov et al., *MRS Bull.* 45 (2020), p. 704.

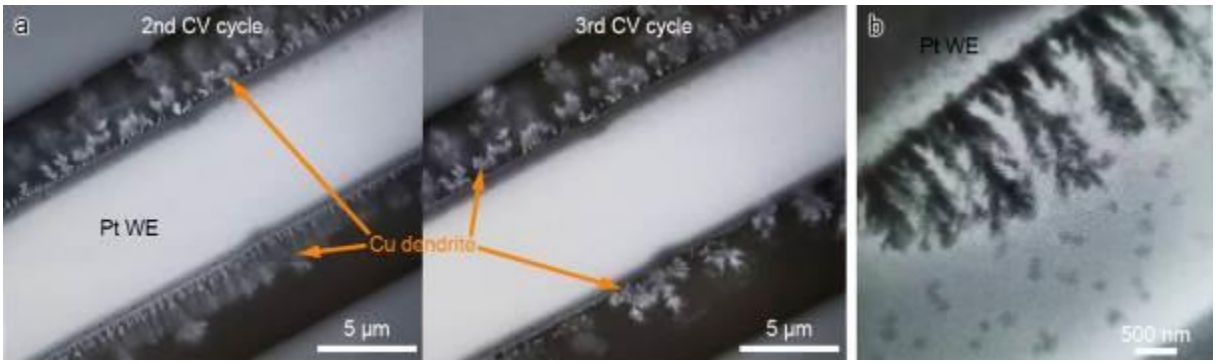
[2] JH Um et al., *Acc. Chem. Res.* 56 (2023), p. 440.

[3] M Golozar et al., *Commun. Chem.* 2 (2019), p. 131.

[4] X Chen et al., *Microsc. Res. Tech.* 86 (2023), p. 1057.

[5] G Rong et al., *Adv. Mater.* 29 (2017), p. 1606187.

Fig. 1



MS7.P29
In situ and operando electron microscopy investigation of Pt surface dynamics under H_2 and O_2 environments

M. Wang[1], A. Plucienik[1], F. Gollmann[1], G. Moldovan[2], J. Mausz[3], M. G. Willinger[1]

[1]Technical University of Munich, Chemistry, Garching, Germany
[2]Point electronic GmbH, Halle (Saale), Germany
[3]Gatan+EDAX, AMETEK GmbH, Munich, Germany

The catalytic oxidation of ammonia (NH_3) to nitric oxide (NO) over Pt/Rh catalysts is a key step in nitric acid production via the Ostwald process. However, long-standing challenges remain regarding catalyst selectivity and stability. In a consortium project funded by the German Federal Ministry of Education and Research (BMBF), we collaborate with the Fritz-Haber-Institute of the Max-Planck Society, the Technical University of Hamburg, and industrial partners to develop new catalysts and optimized process conditions aimed at mitigating nitrous oxide (N_2O) emissions—a potent greenhouse gas—and reducing platinum loss due to catalyst degradation.

To elucidate the relationship between catalyst restructuring and activity under reaction conditions, we employ operando scanning electron microscopy. Investigating gas-phase and temperature induced surface transformations in a microscope at up to 900°C in an ammonia and oxygen containing atmosphere is quite challenging, since ammonia and some of the reaction products are potentially harmful to the components of the environmental SEM (FEI Quanta) used in this project. To circumvent these issues, we initiate our studies using hydrogen (H_2) and oxygen (O_2) as model reactants, with nitrogen (N_2) serving as an imaging and buffer gas. Real-time monitoring via secondary electron, electron beam absorbed current, and backscattered electron (BSE) imaging allows us to track grain orientation-dependent restructuring and surface dynamics in Pt across varying H_2/O_2 ratios and temperatures (600–900°C). Simultaneous gas-phase composition analysis provides direct insight into the correlation between structural evolution and catalytic performance. Surface roughness and morphology changes are quantified via topographic reconstruction using a segmented high-temperature BSE detector. Additionally, electron backscatter diffraction (EBSD) is employed to map grain orientations, investigating the relationship between crystallographic texture and observed restructuring dynamics.

Preliminary results show that Pt surface restructuring is strongly orientation-dependent, with grain boundaries acting as preferential sites for corrosion initiation. The observed surface transformations involve the formation of thin polyhedral structures exposing {111} and {100} facets of Pt, resembling the "cauliflower" structures found on industrially used Pt/Rh gauzes [1]. The dynamics strongly depend on the H_2:O_2 ratio, pressure, and temperature and indicate a substantial mass transport from the polycrystalline foil, most likely via volatile PtO_2 species that are reduced and eventually re-deposited, thereby forming polyhedral structures that grow on the surface (Figure 1). The grown polyhedrons undergo etching, leading to a net loss of platinum.

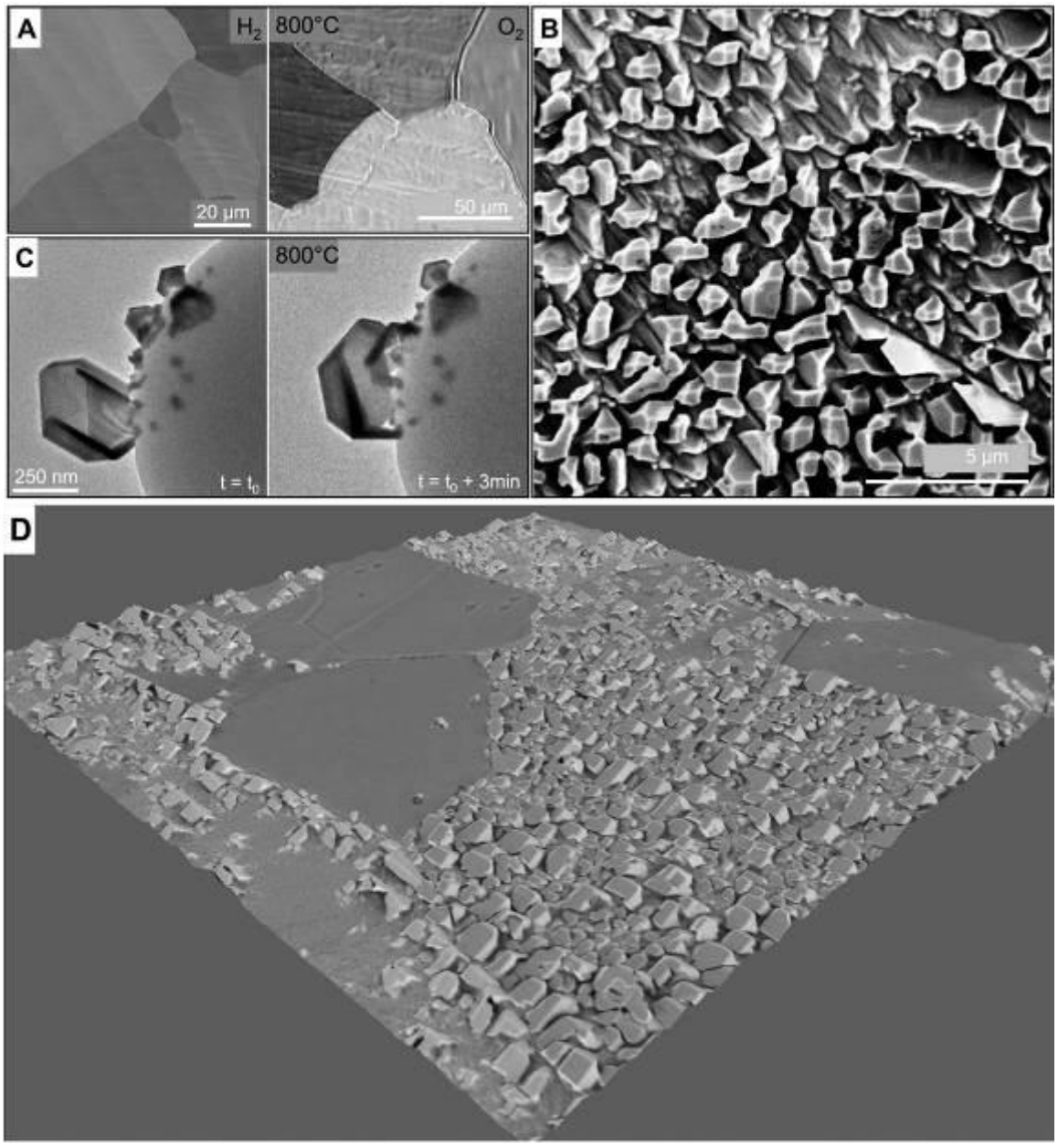
In the next step, the role of Rh addition in modifying these restructuring dynamics will be studied, followed by a stepwise transition from H_2 to NH_3 oxidation environments. This work will help to understand whether structural dynamics and volatile species formation are directly linked to catalytic function or represent a side effect that can be mitigated through improved catalyst formulations and process conditions.

Figure 1: The surface of a polycrystalline Pt foil does not substantially reconstruct in pure H2 and only slowly in O2 atmosphere **(A)**, but gets very dynamic in an atmosphere containing H2 and O2 at a ratio that is balanced with respect to Pt redox reactions **(B)**. TEM shows that the polyhedral structures are formed by thin Pt sheets **(C)**. A topography map can be reconstructed based on the signals from a segmented high-temperature BSE detector **(D)**.

References:

[1] Srashtasrita Das *et al.* J. Phys. Chem. *C* **2024** *128* (12), 5053-5063, DOI: 10.1021/acs.jpcc.4c00041

Fig. 1



MS7.P30
Multi-Ion PFIB Lamella-On-Chip preparation with nanoprobing and (SE)EBIC for tracking filament formation in transition Metal Oxide RRAM

A. Fakiner[1], R. Winkler[1], D. Vasquez[1], A. W. Shakib[1], L. Molina-Luna[1]

[1]Technical University of Darmstadt, AEM, Darmstadt, Germany

Alexander Fakiner1, Robert Winkler1, Daniel Vasquez1, A. Wahab Shakib1 and Leopoldo Molina-Luna1,*

*1*Advanced Electron Microscopy, Institute of Materials Science, Department of Materials- and Earth Sciences, Technical University of Darmstadt, Germany

*Corresponding author: leopoldo.molina-luna@aem.tu-darmstadt.de

Introduction: In transition metal oxide (TMO) resistive random-access memory (RRAM), conductive filaments (CFs) govern resistive switching by forming and dissolving under electrical stimuli [1]. Visualizing these CFs in a thin, biasable lamella device remains challenging due to the random and difficult-to-pinpoint nature of their formation sites. Nanoprobing approaches on half-grids attempt to isolate individual "island" devices in a lamella but can introduce mechanical strain and ion-induced damage, risking artificial short-circuit pathways [2].

Objective: To circumvent these limitations, we prepare a lamella-on-chip device that preserves the original vertical metal–insulator–metal (MIM) stack [3]. Grain boundary (GB) engineering in both the electrode and the dielectric are leveraged to guide CF formation to known locations [4–6], enabling targeted nanometer-scale probing for operando biasing. Because standard imaging does not reliably reveal CFs at the required scale [7], we use secondary electron-electron beam induced current (SEEBIC) mapping to monitor local conductivity changes under active bias.

Materials and methods: A TiN/HfO_2 MIM stack was deposited on *c*-cut sapphire via reactive molecular beam epitaxy (RMBE). Cross-sectional lamellae devices were prepared using a Thermo Fisher Helios Hydra UX PFIB and mounted on membrane-free chip carriers. Nanoprobing needles provided localized electrical contact at targeted GBs. During operando biasing, SEEBIC measurements were acquired to visualize conductive filament pathways, with particular attention paid to surface smoothness and lamella thickness to ensure reliable signal contrast.

Results: Preliminary data indicate that CFs appear preferentially at engineered GBs under device operation. Smooth lamella surfaces reduced spurious edge effects, which allowed SEEBIC to highlight genuine current pathways instead of artifacts.

Conclusion: This multi-ion PFIB lamella-on-chip approach shows promise for revealing how GB networks affect CF formation and propagation in TMO RRAM. By providing direct access for localized biasing and SEEBIC imaging, the method can link device architecture to switching performance. Future studies will explore extended bias cycles to clarify the long-term stability of GB-directed filaments in next-generation memory applications, thus enabling the design of more reliable RRAM devices.

References:

[1] F. Zahoor, T. Z. Azni Zulkifli, and F. A. Khanday, Nanoscale Res Lett **15**, 90 (2020).

[2] Y. Zhang, C. Wang, and X. Wu, Nanoscale **14**, 9542 (2022).

[3] O. Recalde-Benitez *et al.*, Ultramicroscopy **260**, 113939 (2024).

[4] R. Winkler *et al.*, Advanced Science **9**, 2201806 (2022).

[5] R. Winkler *et al.*, Nano Lett. **24**, 2998 (2024).

[6] R. Winkler *et al.*, Microscopy and Microanalysis **30**, ozae044.528 (2024).

[7] W. A. Hubbard *et al.*, Advanced Functional Materials **32**, 2102313 (2022).

The authors acknowledge funding from the ERC "HORIZON.1.1" Program under Grant Nos. 101088712-ELECTRON and 101189511-BED-TEM and funding from the research field "Matter and Materials" at TU Darmstadt under Project No. 40101746.

MS7.P31
Unraveling metal hydride phase transformation mechanisms of Magnesium thin films using *in situ/ex situ* STEM EELS

G. Krishnan[1], H. Schreuders[2], N. Balaji V.I.[3], L. Bannenberg[2], C. Danvad Damsgaard[4,1], B. Dam[2], J. R. Jinscheck[4]

[1]Technical University of Denmark, Physics, Kongens Lyngby, Denmark
[2]Delft University of Technology, Faculty of Sciences, Delft, Netherlands
[3]TESCAN Group, Brno, Czech Republic
[4]Technical University of Denmark, DTU Nanolab, Kongens Lyngby, Denmark

Introduction

Hydrogen (H2) is an effective solution to our present and future energy demands with its attractive non-zero emission capability1. However, achieving compact hydrogen storage remains a significant challenge, especially in safe, solid forms such as metal hydrides2, i.e., Magnesium (Mg). Moreover, enhancing storage efficiency requires a deeper understanding of phase transformation kinetics and mechanisms in Mg and Mg-based alloys at the nano/atomic scale. Therefore, we adopt scanning transmission electron microscopy (STEM) and low-loss plasmon EELS to pay the way for detailed understanding.

Objectives

In this work, we evaluate the phase transformation dynamics of Mg thin film in MgH2 formation via STEM. Our main objective is to understand the influence of external parameters, such as temperature and H2 pressure, on the phase transformation mechanism, e.g., H2 diffusion-controlled nucleation and growth. Also, how do morphology changes affect the hydrogenation mechanism and phase transformations after hydrogenation/dehydrogenation cycles?

Materials and Methods

Magnesium (Mg) is regarded as an archetypal framework for exploring metal-hydride formation. The Mg films were synthesized using a DC magnetron sputtering. The film consists of a stack with a Mg thickness of 400 nm, a 12 nm adhesion layer of Titanium (Ti), and a catalyst layer of Palladium (Pd) of 100 nm. A ThermoFisher Hydra plasma-focused ion beam (PFIB, Xe, 30kV) was used to prepare the TEM lamellas. Structural investigations were performed using a ThermoFisher Spectra Ultra and a Gatan Image Filter (GIF) Continuum HR. These phase transformations were studied under ex-situ and in-situ conditions to understand the effect of external hydrogenation parameters followed by STEM and (EELS) analysis. 4DSTEM was employed using a TESCAN Tensor STEM to investigate grain orientation.

Results

We observe contrasting hydrogenation mechanisms between our previous results in in-situ STEM experiments and the present ex-situ results. While in ex-situ studies, hydrogenation follows an H2 diffusion-controlled mechanism, in in-situ studies, a combination of H2 diffusion-controlled nucleation and growth mechanisms occurs at identical external H2 pressure and temperature conditions. In contrast, dehydrogenation under both ex-situ and in-situ conditions shows an H2 diffusion-controlled growth mechanism.

Our analysis indicates the same behavior in samples after repeated hydrogenation/dehydrogenation cycling, irrespective of the change in morphology. Moreover, Mg grain orientation tends to play a crucial role in the propagation and growth of MgH2.

Conclusion

In-situ and ex-situ STEM and EELS experiments allow us to follow the hydrogenation and dehydrogenation processes via a cross-section view in thin films. Alternative mechanisms that control hydrogenation kinetics have been identified that affect the hydrogen storage capacity of Mg thin films. Our results indicate asymmetry in the hydrogenation and dehydrogenation mechanism.

References.

1.Klopčič, N.; Grimmer, I.; Winkler, F.; Sartory, M.; Trattner, A. A Review on Metal Hydride Materials for Hydrogen Storage. *Journal of Energy Storage*. 2023. https://doi.org/10.1016/j.est.2023.108456

2. Yartys, V. A. et al. Magnesium Based Materials for Hydrogen Based Energy Storage: Past, Present and Future. *Int J Hydrogen Energy* **2019**, *44* (15), 7809–7859. https://doi.org/10.1016/j.ijhydene.2018.12.212.

MS7.P33
Technological advances for temperature dependent liquid and electrochemical studies using *in situ* TEM

Z. King[1], J. McConnell[1], D. Nackashi[1], K. Stephens[1], S. Walden[1], J. Damiano[1]

[1]Protochips, Morrisville, NC, United States

Introduction

Transmission electron microscopy (TEM) is a powerful technique used to characterize materials at the nano- and atomic scale. No other method achieves the same level of structural and chemical resolution, making TEM indispensable for understanding the atomic and chemical makeup that governs material behavior. However, because TEM operates in a high-vacuum environment, observing materials in their native state is traditionally impossible. This challenge has been addressed with *in situ* TEM holders, which create a sealed environment within the TEM, isolating samples from vacuum while allowing the controlled introduction of liquids, gases, and external stimuli such as temperature, voltage, and pressure. With this capability, researchers can now directly observe nanoscale phenomena, including electrocatalytic surface area loss[1], corrosion propagation in steel[2], nucleation and growth of nanomaterials[3], and battery shorting[4,5].

Objectives

For materials subjected to electrochemical stress during operation, temperature also plays a crucial role in overall performance. However, until now, no *in situ* TEM system has provided the broad temperature range needed for most applications. A breakthrough in temperature-controlled liquid systems for *in situ* TEM now enables experiments from -50°C to 300°C, simultaneous with electrochemical testing. This advancement allows researchers to replicate real-world conditions experienced by fuel cell catalysts and electric vehicle batteries, as well as achieve the high temperatures required for nanomaterial synthesis, such as high-entropy alloys. Additionally, these temperature capabilities can accelerate slow reactions, decelerate fast ones, and reduce dose damage—making it possible to visualize otherwise challenging processes and materials.

Materials & Methods / Results

In this presentation, examples of how the temperature, both below and above room temperature, affect the kinetics of electrochemical reactions as well as the morphological structures of the maerials will be showcased (Figure 1). In addition, examples of temperature-dependent phenomena, such as the crystallization of water to ice and the nucleation and growth of gold (Figure 2) will be discussed, with diffraction, energy-dispersive X-ray spectroscopy (EDX), and electron energy loss spectroscopy (EELS) analyses as a complement.

Conclusion

Temperature has a major impact on material behavior and, until now, it has been impossible to study materials at more extreme yet realistic temperatures *in situ* in a liquid environment within the TEM. Now, it is possible to study temperature dependence on batteries that will operate in cold climates, electrocatalysts at elevated temperatures, and the formation of different nanomaterials that at high temperatures.

Figure 1: (a) Chemical redox cycling of 50 mM ferric and 50 mM ferrous chloride at room temperature (blue), 40 °C (orange) and 70 °C (red) within a closed-cell TEM system (b) TEM micrograph of silver dendrites formed in real time on the platinum working electrode by chronoamperometry.

Figure 2. Demonstrating the effect of temperature on morphology as gold nucleates and grows in a solution of gold chloride.

[1] A. Impagnatiello, et al., ACS Appl. Energy Mater. 2020, 3, 3, 2360–2371

[2] D. Kovalov, et al., Corrosion Science 2022, 199, 110184

[3] K.A. Vailonis, et al., J. Am. Chem. Soc. 2019, 141, 10177−10182

[4] J. Poulizac, et. al., Microscopy and Microanalysis, 2023, 29, 105–117

[5] W. Dachraoui, et al., ACS Nano, 2023, 17(20), 20434-20444

Fig. 1

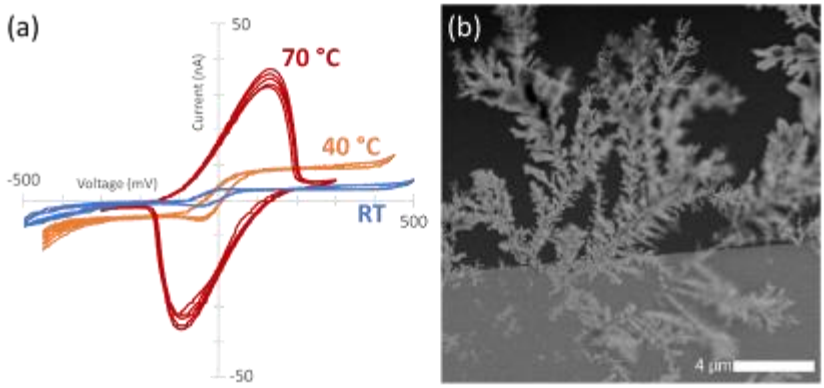
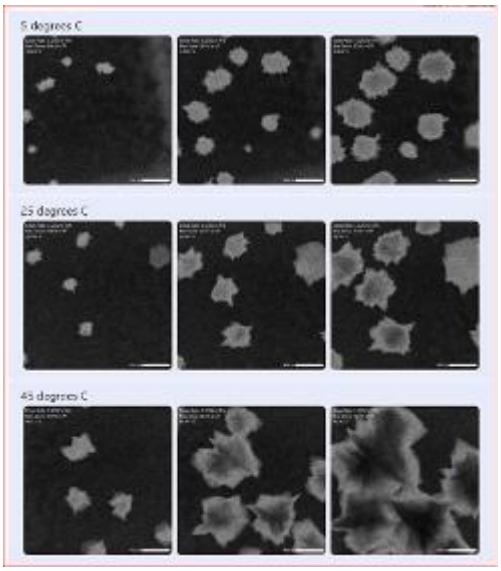


Fig. 2



MS7.P34
Real-time observation of electrostatic potential distribution in individual TiO_2 nanoparticles during resistive switching

J. Jo[1], V. Migunov[1,2], D. Schmidt[3], H. Soltner[4], U. Simon[3], M. Kim[5], R. E. Dunin-Borkowski[1]

[1]Forschungszentrum Jülich GmbH, Ernst Ruska-Centre for Microscopy and Spectroscopy with Electrons, Jülich, Germany
[2]RWTH Aachen University, Central Facility for Electron Microscopy (GFE), Aachen, Germany
[3]RWTH Aachen University, Institute for Inorganic Chemistry, Aachen, Germany
[4]Forschungszentrum Jülich GmbH, Central Institute of Engineering, Electronics and Analytics, Jülich, Germany
[5]Seoul National University, Department of Materials Science and Engineering and Research Institute of Advanced Materials, Seoul, South Korea

Introduction

Resistive switching phenomena in complex metal oxides have attracted great interest for applications in next-generation non-volatile memory devices. Recently, nanoparticles have been adopted as switching materials, both for use in smaller devices and as model systems for understanding resistive switching mechanisms in nanoscale materials [1,2].

Objectives

We investigate the origin of resistive switching behavior in individual TiO_2 nanoparticles that have an electrical bias applied to them *in situ* in the transmission electron microscope (TEM).

Materials and Methods

TiO_2 nanoparticles were synthesized using a sol-gel method and then vacuum annealed. Current-voltage (I-V) measurements were employed in the TEM using a Nanofactory STM-TEM holder to study resistive switching mechanisms in real time, while simultaneously applying off-axis electron holography to the same particles. The technique allows projected electrostatic potential distributions in materials to be recorded with nm spatial resolution [3], providing information about the role of heterointerfaces and conducting nanofilaments during switching processes.

Results

TiO_2 nanoparticles have close-to-spherical morphologies with a mean diameter of 79 ±14 nm and exhibit mostly single crystalline anatase phase. We observe reproducible forming-free bipolar switching in individual nanoparticles that are contacted electrically in the TEM using a moveable electrical probe. I-V curves obtained from single nanoparticles are correlated with electrostatic potential measurements. Comparisons with simulations suggest that a local conducting path is created and annihilated inside the nanoparticle during the resistive switching, while its subsequent formation and annihilation is primarily responsible for SET and RESET processes.

Conclusion

Non-volatile bipolar resistive switching of individual TiO_2 nanoparticles is observed, including soft forming followed by repeated SET and RESET. Comparisons between changes in electron phase shift measured using off-axis electron holography and projected electrostatic potential simulations confirm that resistance changes of individual nanoparticles are localized inside the nanoparticle during the resistive switching processes. Site-specific resistance changes are attributed primarily to the drift of oxygen vacancies and to their accumulation and depletion near the interfaces.

References

[1] E. Goren *et al.*, *Appl. Phys. Lett.*, **105,** 143506 (2014)

[2] D. O. Schmidt *et al.*, *Small*, **11,** 6444 (2015)

[3] M. R. McCartney *et al.*, *Annu. Rev. Mater. Res.*, **37,** 729 (2007)

MS7.P35
Tensile-strain-induced magnetic texture evolution in FeRh by off-axis electron holography

N. Wang[1], Q. Lan[1], M. Schnedler[1], A. Aubert[2], O. Gutfleisch[2], P. Ebert[1], R. E. Dunin-Borkowski[1]

[1]Forschungszentrum Jülich GmbH, Ernst Ruska-Center, Jülich, Germany
[2]Technical University of Darmstadt, Department of Materials Science, Darmstadt, Germany

FeRh has attracted great attention due to its first order antiferromagnetic (AFM) to ferromagnetic (FM) transition near room temperature (~300 K)[1], making it a promising candidate for applications in magnetic refrigeration, spintronics and memory devices. Strain plays a crucial role in modulating the AFM-FM transition temperature and magnetocaloric performance by altering the material's magnetic and structural properties. FeRh thin films grown on substrates with different lattice parameters have been used to investigate strain effects. However, it is then challenging to quantify or separate substrate or interface-induced phenomena from the intrinsic behaviour of FeRh.

Here, we apply tensile strain directly to a FeRh lamella *in situ* in the transmission electron microscope (TEM) and study the evolution of its magnetic texture in real time using off-axis electron holography. The ordered B2 phase $Fe_{50}Rh_{50}$ sample used in this study was prepared by arc melting, followed by annealing and water quenching[2]. TEM lamellae were prepared on a chip using focused ion beam milling in a dual beam scanning electron microscope. Tensile strain was applied using a double tilt (INSTEMS-MET) straining holder.

Our results show that $Fe_{50}Rh_{50}$ contains high-angle magnetic domains with a closure texture in the absence of strain. When a 2% tensile strain is applied along the [-211] $Fe_{50}Rh_{50}$ crystal orientation, the magnetic field lines turn to form 180° magnetic domain walls oriented parallel to the tensile strain axis. We also measure the dependence of magnetic domain wall width on the magnitude of the strain for different angles between the strain direction and the crystal orientation.

Such measurements can be used to provide a quantitative understanding of the effect of strain on the magnetic properties of FeRh alloys, which is essential for optimizing FeRh-based devices.

References:

1. Fallot and R. Hocart. "Sur l"apparition du ferromagnétisme par élévation de température dans des alliages de fer et de rhodium", Rev. Sci. 77 (1939): 498.

2. Aubert et al. "Residual ferromagnetic regions affecting the first-order phase transition in off-stoichiometric Fe–Rh", ACS Applied Materials & Interfaces 16 (2024): 62358-62370.

MS 8: Beyond ideal 2D and van der Waals materials: Disorder, defects, adatoms and contamination

MS8.01(inv)
Targeted disruption of the pristine flatlands of 2D hBN

F. Allen[1,2], D. Byrne[2,3], L. Tizei[4], J. C. Idrobo[5,6], D. Kepaptsoglou[7,8], Q. Ramasse[7,9]

[1]University of California, Department of Materials Science and Engineering, Berkely, CA, United States
[2]Lawrence Berkeley National Laboratory, Molecular Foundry, Berkely, CA, United States
[3]University of California, Department of Chemistry, Berkely, CA, United States
[4]Université Paris-Saclay, CNRS, Laboratoire de Physique des Solides, Orsay, France
[5]University of Washington, Materials Science and Engineering, Seattle, WA, United States
[6]Pacific Northwest National Laboratory, Physical and Computational Sciences Directorate, Richland, WA, United States
[7]SuperSTEM Laboratory, SciTech Daresbury Campus, Daresbury, United Kingdom
[8]University of York, School of Physics, Engineering and Technology, York, United Kingdom
[9]University of Leeds, School of Chemical and Process Engineering, Leeds, United Kingdom

Gazing out across the open savanna, it is the occasional "anomaly", like a tree punctuating the landscape, that catches the eye. So too with 2D materials. Without a doubt, the pristine 2D lattice already exhibits remarkable properties, as has been widely shown. But increasingly, it is the controlled interruption of this atomic perfection that captures our attention. This punctuation can take various forms, including single-atom vacancies, dopants and adatoms. The atomic flatlands can also be reshaped in a more undulating manner, through periodic modulations of the potential energy landscape induced by heterostructure moirés.

In the case of 2D hexagonal boron nitride (hBN), this material has attracted significant interest as a wide bandgap semiconductor that also exhibits exceptional thermal and chemical stability. Introducing defects into the lattice opens up a wealth of new opportunities, enabling functionalities beyond the material's intrinsic characteristics. One of the most exciting discoveries is that atomic-level defects in hBN can emit antibunched photons with high efficiency, even at room temperature [1]. This single-photon emission under ambient conditions holds great promise for quantum computation and cryptography outside of the controlled laboratory environment.

To turn these possibilities into reality, electron microscopy plays a pivotal role, not only by providing atomic-level insights into the engineered disruptions, but also by directly correlating structure with function—in fact, electron microscopes can even be used to fabricate the targeted modifications themselves. Low-voltage aberration-corrected scanning/transmission electron microscopy (S/TEM) [2], direct electron detection [3], monochromated electron energy-loss spectroscopy (EELS) [4], and in-situ measurements such as cathodoluminescence [5] are driving advancements in this field.

In this talk, we explore how cutting-edge electron microscopy and spectroscopy can be employed to engineer and characterize targeted modifications in 2D hBN. By combining in-situ electron irradiation with ion seeding and thermal treatments [6], we fabricate vacancy defects and dopant-vacancy complexes in monolayers. Additionally, through moiré-engineering [7], we investigate interlayer coupling effects in bilayers. With atomically resolved core-loss EELS, we fingerprint the chemistry of individual defects, while low-loss EELS allows us to probe defect-induced midgap states and Coulomb confinement. Ultimately, by shaping and analyzing at the single-atom level, we aim to unlock novel functionalities that will drive the technologies of the future.

[1] Tran TT *et al. Nature Nanotechnology* (2016) **11**, 37–41

[2] Krivanek OL *et al. Nature* (2010) **464**, 571–574

[3] Krivanek OL *et al. Nature* (2014) **514**, 209–212

[4] MacLaren I *et al. APL Materials* (2020) **8**, 110901

[5] Tizei LHG and Kociak M. Physical Review Letters (2013) **110**, 153604

[6] Byrne DO and Allen FI. *ACS Applied Nano Materials* (2025) **X**, XXX-XXX

[7] Sursala S *et al. Science* (2022) **378**, 1235–1239

This work was funded by NSF Award No. 2110924. Work at the Molecular Foundry was supported by the Office of Science, Office of Basic Energy Sciences, of the U.S. Department of Energy under Contract No. DE-AC02-05CH11231. SuperSTEM is the U.K. National Research Facility for Advanced Electron Microscopy, supported by the Engineering and Physical Sciences Research Council (EPSRC, UK) via grant numbers EP/W021080/1 and EP/V036432/1.

MS8.02
Electron-beam-induced carbon doping of hexagonal boron nitride

B. M. Mayer[1], M. Längle[1], J. Kotakoski[1]

[1]University of Vienna, Physics of Nanostructured Materials, Vienna, Austria

Hexagonal boron nitride (hBN) is a two-dimensional material structurally similar to graphene but distinguished by its wide bandgap and alternating boron and nitrogen atoms instead of carbon. Recently, hBN has gained significant interest, because some of its defects have been shown to serve as single-photon emitters at room temperature. The most common defects are single-atom vacancies and substitutional atoms, where defects with carbon impurities especially show promise for quantum technology applications [1].

This study investigates carbon doping in hBN based on electron-beam induced deposition. It is inspired by similar research by X. Wei et al. [2] on boron nitride nanotubes, in which carbon incorporation converted the material from an insulator to a conductor. Here, the high-energy electrons used for imaging in a scanning transmission electron microscope are used to create vacancies in the hBN lattice. At the same time, methane (CH_4) is introduced into the column, where the electron beam dissociates the molecules, releasing carbon atoms that migrate into the vacancies to form carbon-based structures. Time-resolved image sequences at various pressures (6^{-9} - 1^{-7} Torr) are recorded to monitor this process. After the experiment, a neural network is used to analyze these images to assess carbon incorporation. Electron energy-loss spectroscopy (EELS) is used to verify the elemental composition.

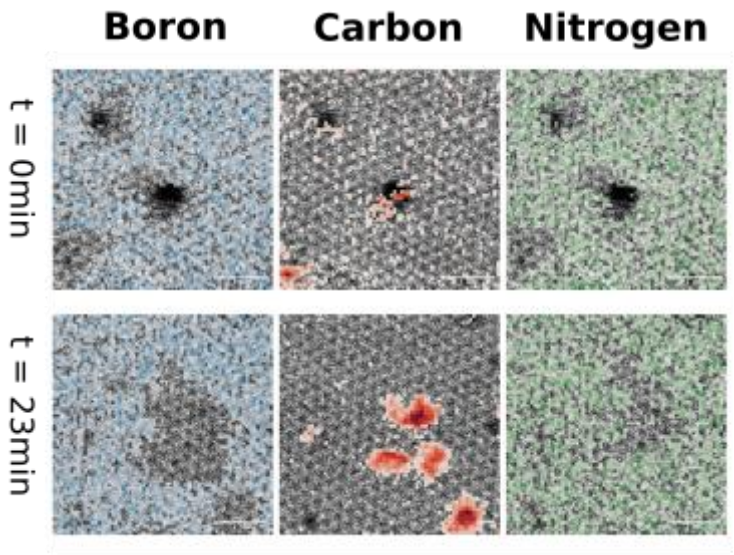
The results show that boron and nitrogen atoms are gradually replaced by carbon, which becomes more prominent at higher methane pressures (Fig. 1). Surprisingly, increased carbon concentration also slows the growth of nanopores during the experiment. At the highest studied pressures, carbon incorporation may even eventually lead to the reduction of the pore size. Finally, carbon substitution at the edges of pores results in a new type of defect–triangular carbon-terminated pores–that have not been reported before.

Overall, our results provide a new way to create carbon-containing structures within the hBN lattice. These structures can be further studied for their properties and applicability to quantum information technology.

Fig. 1: HAADF image overlaid with an EELS map integrated over the B, C, and N core loss peaks. More intense colors indicate a higher abundance of the element. The data in the second row was collected 23 minutes after the data in the first row.

[1] Chacón, I., Echeverri, A., Cárdenas, C. & Munoz, F. Carbon-based light emitting defects in different layers of hexagonal boron nitride. arXiv:2412.17457 (2024).
[2] Wei, X., Wang, M. S., Bando, Y. & Golberg, D. Post-synthesis carbon doping of individual multiwalled boron nitride nanotubes via electron-beam irradiation. Journal of the American Chemical Society 132, 13592–13593 (2010).

Fig. 1



MS8.03
In situ heating and growth studies of a copper–benzenehexathiol coordination polymer via high-resolution (liquid-phase) transmission electron microscopy

D. Mücke[1], B. Liang[1], Z. Wang[2,3], I. Cooley[4], E. Besley[4], S. Park[3], R. Dong[3,5], X. Feng[2,3], U. Kaiser[1]

[1]Ulm University, Ulm, Germany
[2]Max Planck Institute, Halle (Saale), Germany
[3]Technical University Dresden, Dresden, Germany
[4]University of Nottingham, Nottingham, United Kingdom
[5]Shandong University, Jinan, China

Two-dimensional polymers such as conjugated metal-organic frameworks (2D c-MOFs) and conjugated coordination polymers (2D c-CPs) are of growing interest due to their structure-dependent physical properties[1]. By connecting diverse organic linkers with metal atoms, a wide range of architecture and corresponding functionalities can be achieved. In this study, we investigate heat-induced transformations and growth mechanisms of the hydrogen-free c-CP Cu_3(BHT) (BHT = benzenehexathiol). Using in-situ high-resolution transmission electron microscopy (HRTEM), we study the thermal evolution of Cu_3(BHT). Additionally, we employ in-situ liquid-cell transmission electron microscopy (LC-TEM) to observe the material"s growth dynamics in real time. Cu_3(BHT) exhibits exceptional resistance to electron beam damage, which we attribute to its high electrical conductivity[2]. This robustness enables detailed HRTEM studies of heat-induced structural changes[3]. During LC-TEM experiments, we observed the formation of Cu_4(BHT) instead of the expected Cu_3(BHT), which we ascribe to radiolysis effects caused by electron beam interactions with the solution in the liquid cell[4].

[1] Wang, Zhiyong, et al., *Nature Reviews Materials* 10.2 (2025): 147-166. [2] Mücke, David, et al., *Nano Letters* 24.10, 3014-3020 (2024). [3] Mücke, David, et al., *Micron* 184, 103677 (2024). [4] Mücke, David, et al., *Crystal Growth & Design* 25.5, 1622-1627 (2025).

MS8.04
Correlative identification of the polytypes and their dislocations in bilayer MoS2 using TEM and Raman spectroscopy

X. Zhou[1], T. Dierke[1], M. Wu[1], S. You[1], P. Pelz[1], J. Maultzsch[1], E. Spiecker[1]

[1]FAU Erlangen-Nürnberg, Erlangen, Germany

Stacking orders and dislocations in 2D van der Waals materials governed by the relative sliding (lateral displacement) and rotation between atomically thin layers are fundamentally essential for understanding and tuning the properties of intrinsic materials and their artificially assembled structures. Among these scanning probe microscopy, Raman spectroscopy, and transmission electron microscopy (TEM), several techniques have been successfully developed to characterize the stacking order and topological defects. However, key challenges, including the lattice similarities between the different polytypes, waviness, minute scale of dislocations, strain, and contamination residue often limit the effectiveness of single characterization techniques and call for correlative approaches. In the present work, we reliably differentiate the 2H and 3R polytypes and their dislocations in bilayer MoS2 (Fig. 1a and b) using correlative TEM and Raman spectroscopy.

Basal-plane dislocations, characterized by the respective unique Burgers vector **b**, are closely tied to the atomic stacking sequence. Fig. 1c depicts a series of DF TEM images, revealing a perfect dislocation with **b**= ±(1/3) determined by the invisibility criterion (**g**·**b**=0). Fig. 1d presents the DF TEM images of a partial dislocation with **b**= ±(1/3), associated with 3R stacking in region #2. The careful dislocation analysis indirectly indicated the 2H and 3R stacking in the different areas, which is further confirmed by rocking curve analyses in TEM (Fig. 2a) and Raman spectroscopy. Fig. 2b compares the rocking curves along the qz direction and the kinematic simulations. For relrod, the central peak appears at *qz*=0 for 2H stacking, while the central peak shifted to *qz*= -0.07 Å-1 for 3R stacking. This shift results from the displacement of the top layer towards the crystalline orientation relative to the bottom layer. The Raman spectra depicted in Fig. 2d show the low-frequency range, with the shear mode (S) at a frequency of ~23 cm-1 and the layer-breathing mode (LB) at ~40 cm-1. The amplitude ratio of LB/S in 2H-stacking (~ 0.4) is lower compared to 3R-stacking (~ 1.4) due to the difference in the interlayer coupling from 2H- to 3R-stacking configuration.

In conclusion, we demonstrate a correlative TEM-Raman method to distinguish the 2H and 3R polytypes, as well as the dislocations in bilayer MoS2. This approach can be extended to other 2D materials, paving the way for property alternation via stacking and defect engineering.

(1) Butz, B., et al. Nature, 505 (2014), 533.
(2) Zhou, et al. arXiv:2502.11977.

Fig. 1 (a and b) Light microscopy images MoS2 flake on Si substrate and gold-coated TEM grid. (c and d) Series of DF TEM images acquired from the marked regions #1 and #2, respectively. The insets of (c) and (d) depict the top view of the crystal structure for 2H and 3R stacking; the red and blue arrows indicate the corresponding Burgers vectors.

Fig. 2 (a) Schematic illustrating the tomographic 4D STEM acquisition and the reconstructed 3D ED data. (c) Rocking curves of (red dots) and (black dots). (c) Low-frequency Raman spectra of the 2H and 3R bilayer MoS2, the peaks were fit using Lorentzians (dashed curves).

Fig. 1

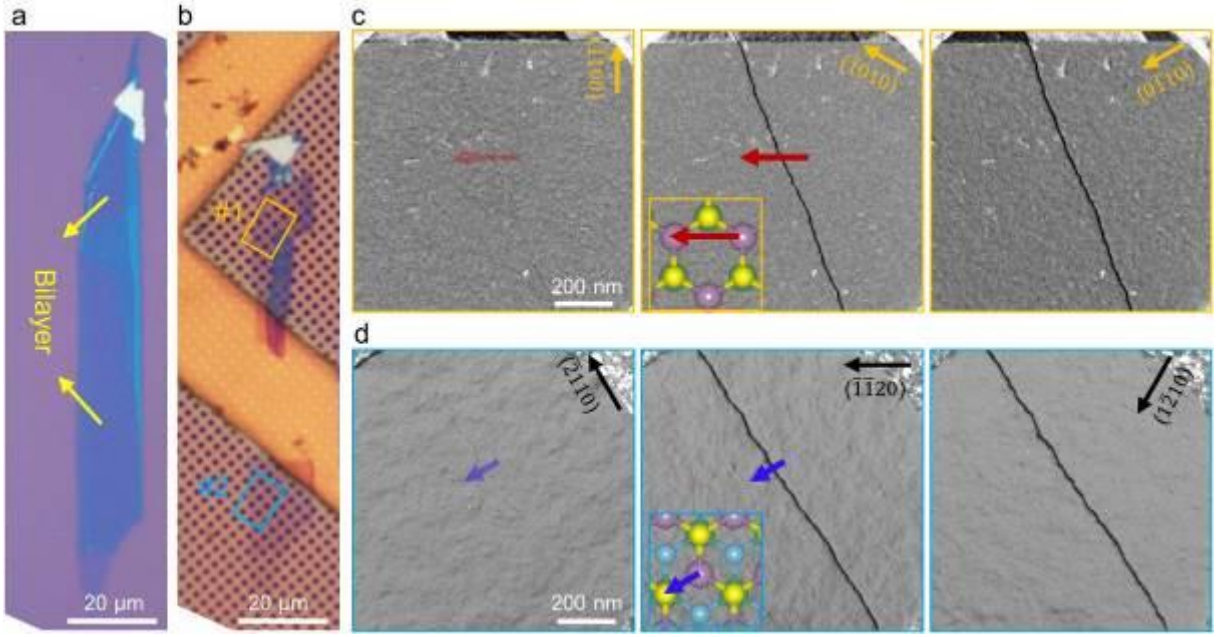
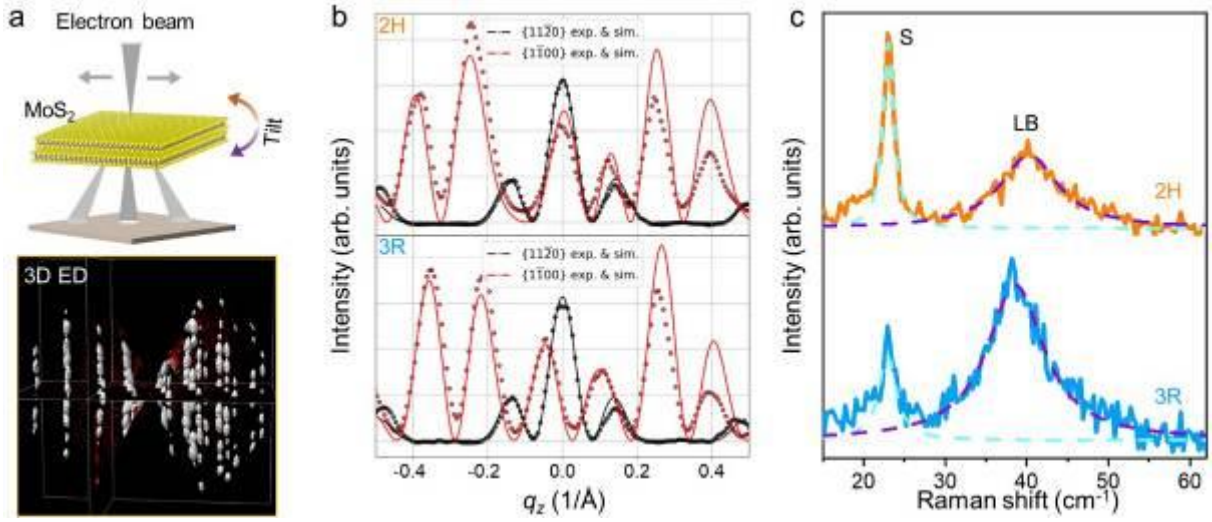

a
b
c
d
Bilayer
20 µm
20 µm
200 nm
200 nm

Fig. 2


a
Electron beam
MoS2
Tilt
3D ED
b
2H
3R
Intensity (arb. units)
qz (1/Å)
c
S
LB
2H
3R
Intensity (arb. units)
Raman shift (cm-1)

MS8.05
Uncovering the atomic structure of substitutional platinum dopants in MoS_2 with single-sideband ptychography

D. Lamprecht[1], A. Benzer[1], M. Längle[2], M. Capin[1], C. Mangler[2], T. Susi[2], L. Filipovic[1], J. Kotakoski[2]

[1]Technical University of Vienna, Institute for Microelectronics, Vienna, Austria
[2]University of Vienna, Physics of Nanostructured Materials, Vienna, Austria

MoS_2 has emerged as a promising material for a wide range of future applications, particularly in the fields of catalysis and gas sensing. However, its practical uses are hindered by the chemical inertness of its pristine basal plane, which limits adsorption and catalytic activities [1]. Substitutional doping with heteroatoms has been shown to introduce active sites and enhance reactivity. While the heteroatom replacement of Mo and S atoms has been explored for various elements, many studies lack unambiguous atomic-scale evidence, mostly due to surface recontamination between modification and imaging steps [2]. Due to the unique layout of our ultra-high vacuum (UHV) system, we are able to introduce defects in monolayer-MoS2 via helium plasma irradiation, repopulate the defective sites with heteroatoms via evaporation and subsequently analyze the resulting structures with scanning-transmission-electron microscopy (STEM) without exposition to ambient conditions [3].

For structural analysis, we employ high-angle annular dark field (HAADF) imaging and single-side-band (SSB) phase reconstruction ptychography. HAADF imaging offers insights into the elemental composition of the samples, but is limited by the beam-sensitivity of defective MoS_2. In contrast, aberration-corrected SSB reconstruction of 4D-STEM data gathered by a direct electron detector allows for atomic-resolution images at significantly lower doses than needed for HAADF and opens the door for simultaneous imaging of high and low Z elements [4,5]. By applying these techniques we gain insight into the defect structures produced by He ion irradiation as well as into the local structure of Pt atoms substituting Mo and S atoms. We show that with SSB we can reliably destinguish between Pt atoms trapped in sulfur mono- or divacancies, Mo vacancies and adatoms, see Fig. 1 [6]. We support these results with quantitative phase analysis and DFT calculations. Furthermore, our combined implantation and analysis methods open the way for systematically introducing controlled dopants into MoS_2. By tuning the ion beam parameters and incorporating a resulfurization step to heal remaining sulfur vacancies, this may in the future be adapted for larger-scale applications allowing for precise control over dopant placement.

[1] Filipovic et al., Nanomaterials 12, 20, 3651 (2022)

[2] Sovizi et al., Surface Science Reports 77, 3 (2022)

[3] Zagler et al., 2D Mater. 9, 035009 (2022)

[4] Jiang et al., Nature 559, 343–349 (2018)

[5] Hofer et al., arXiv:2301.04469 (2024)

[6] Lamprecht et al. submitted

Fig. 1

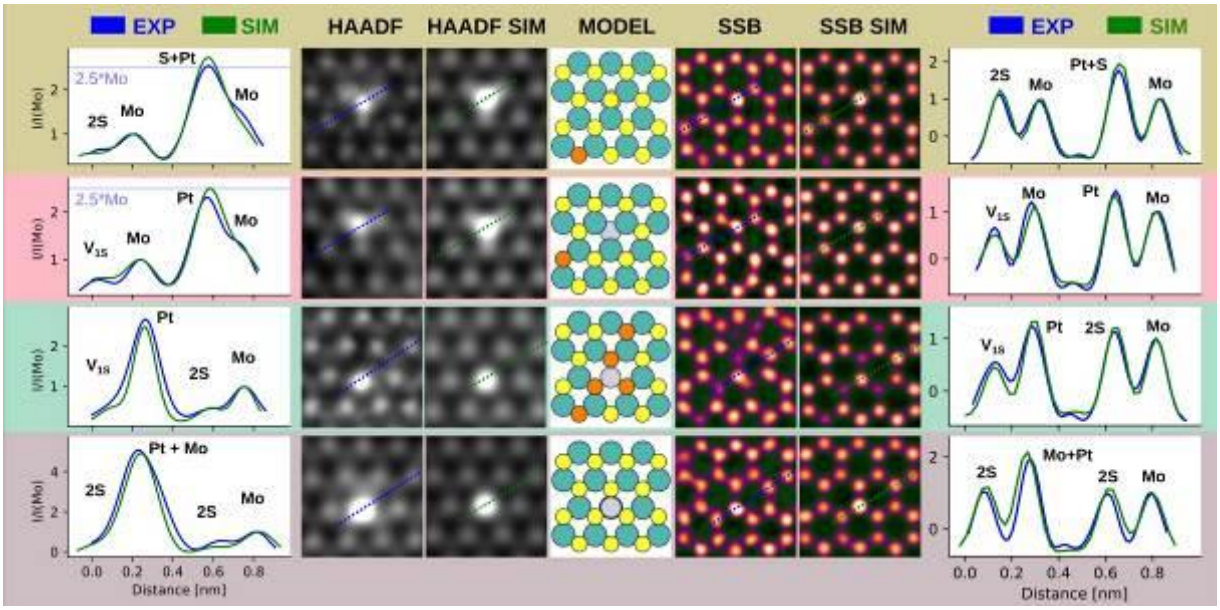
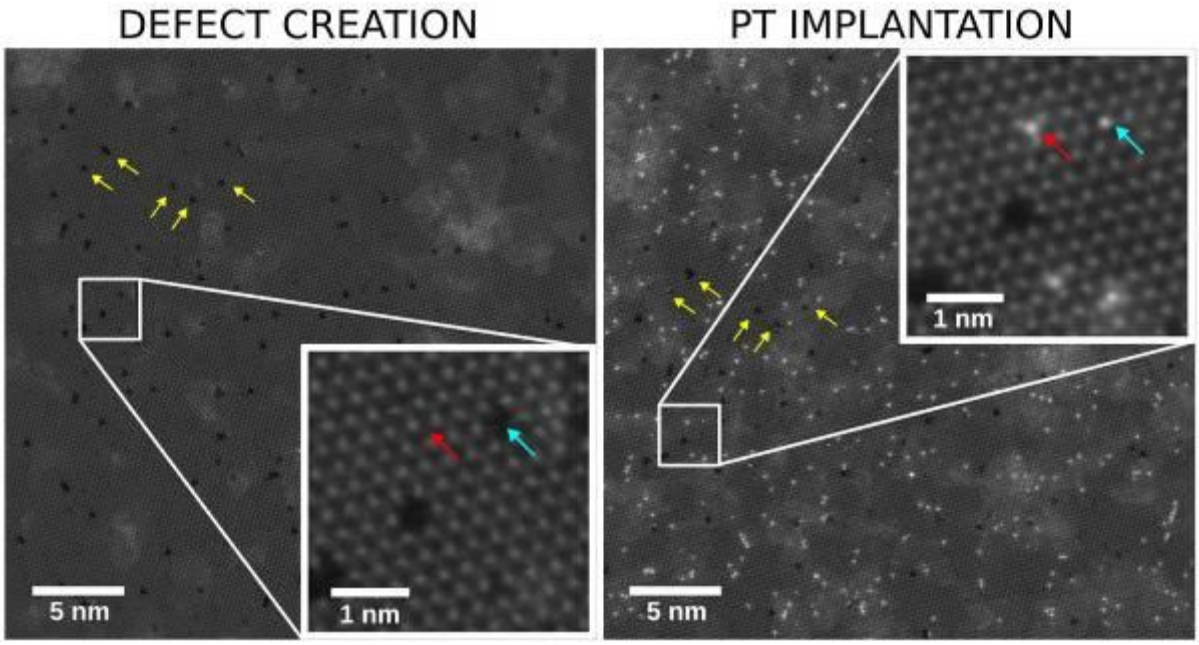

EXP
SIM
HAADF
HAADF SIM
MODEL
SSB
SSB SIM
EXP
SIM
S+Pt
2.5*Mo
2S
Mo
Mo
Pt+S
Pt
V1S
Pt + Mo
Mo+Pt
Distance [nm]

Fig. 2


DEFECT CREATION
PT IMPLANTATION
5 nm
1 nm
1 nm
5 nm

MS8.06
Van der Waals heterostructures of nanopatterned 2D materials for novel device geometries

M. Schlegel[1,2], J. Haas[1,2], K. Strobel[1,2], P. Santra[3], A. V. Krasheninnikov[3], J. C. Meyer[1,2]

[1]University of Tübingen, Institute for Applied Physics, Tübingen, Germany
[2]NMI Natural and Medical Sciences Institute at the University of Tübingen, Center of Nanoanalytics, Reutlingen, Germany
[3]Helmholtz Research Center Dresden-Rossendorf, Institute of Ion Beam Physics and Materials Research, Dresden, Germany

Introduction

As Moore's Law starts to stagnate and the continuous pursuit of smaller and faster devices persists, there is a growing need for new approaches to further push the boundaries of nanofabrication. The modification and stacking of two-dimensional (2D) materials has significant importance in this context. High precision structuring tools, such as a focused electron beam, can be employed to mill a wide range of structures into 2D materials to modify their properties.

Objectives

The work aims to better understand the behavior of 2D materials during the structuring process and to improve the process itself. Ultimately, by stacking customized sheets of 2D materials, it is possible to produce almost any three-dimensional (3D) structure with properties that have been finely tuned to suit desired requirements [1].

Materials and Methods

The 2D materials are structured by using scanning transmission electron microscopy (STEM). Clean samples are essential to the quality of the resulting structures. Therefore, to minimize contamination on the sample, a micro-electro-mechanical system (MEMS) chip is used for its ability to provide in situ heating. Investigation of the manufactured structures is done by transmission electron microscopy (TEM).

Results

Atomically clean graphene samples have been successfully produced using the in-situ heating of the MEMS chip. Furthermore, a wide range of structures using different STEM patterning parameters have been investigated. Clean nanostructuring was achieved on areas up to 500nm in diameter.

For example, bilayer graphene has been structured into nanoribbons which, when slim enough, transformed into carbon nanotubes. To change the electrical properties of graphene, large areas with small holes with a diameter of only 2-3 nm and a periodicity of 5-8 nm have been patterned. Theoretical calculations were done to estimate the band gaps introduced by these patterns, which however depend sensitively on the edge configuration and possibly strain.

Conclusion

The ability to work with contamination free 2D materials and the consequent high patterning resolution of the structures is very promising. Smaller and more complex structures will be in reach soon and thus, the possibility of larger bandgaps or connected nanotube networks will become available. Ultimately, novel van der Waals heterostructures will be created by stacking modified layers of various 2D materials.

Figure 1: *TEM image of atomically clean graphene in which a periodic array of holes has been milled into by STEM.*

Figure 2: *Three parallel carbon nanotubes which have been produced by cutting bilayer graphene into nanoribbons, which then convert into nanotubes.*

[1] *J. Haas et al., ACS Nano 2022, 16, 1836–184*

Fig. 1

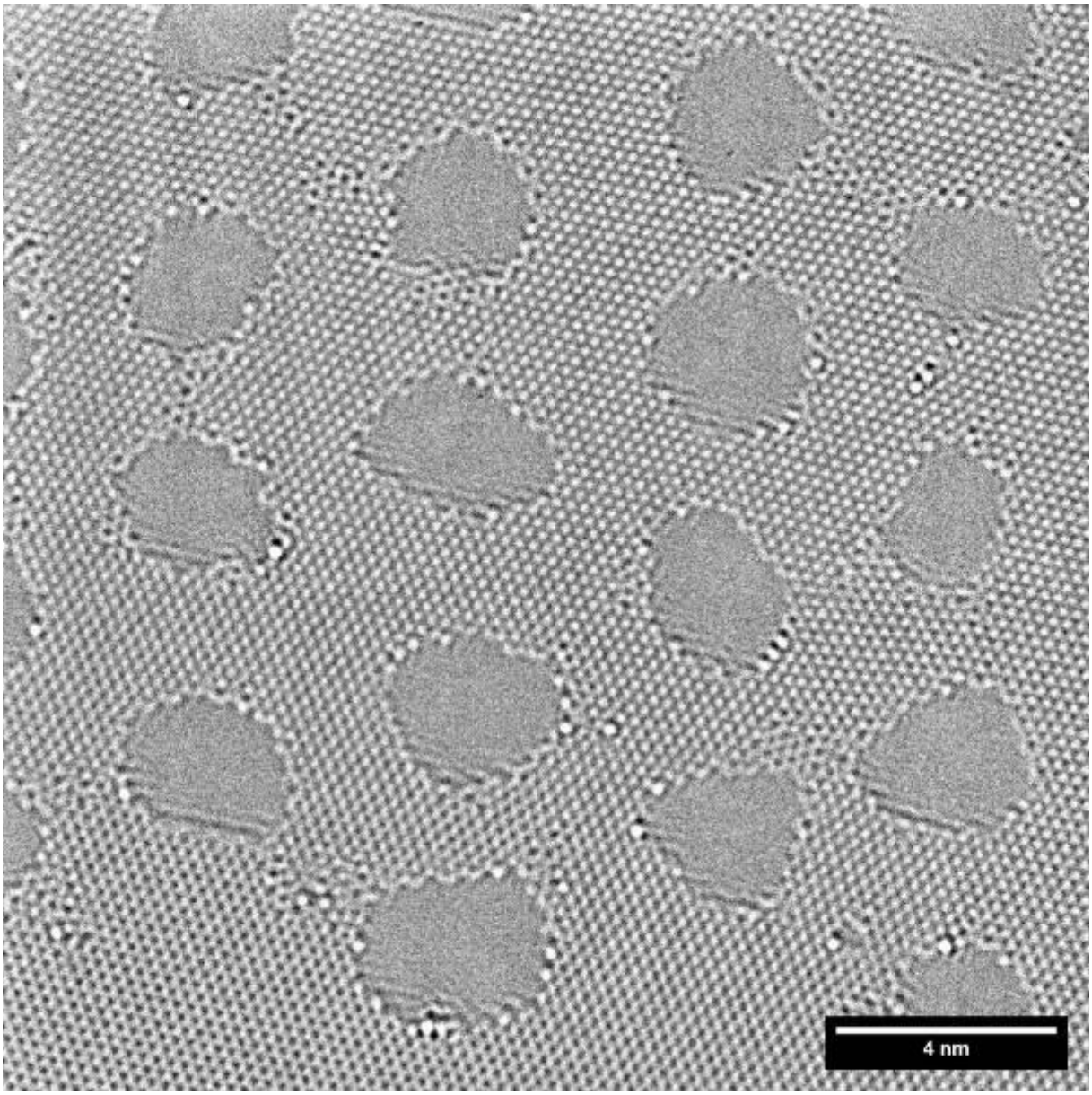
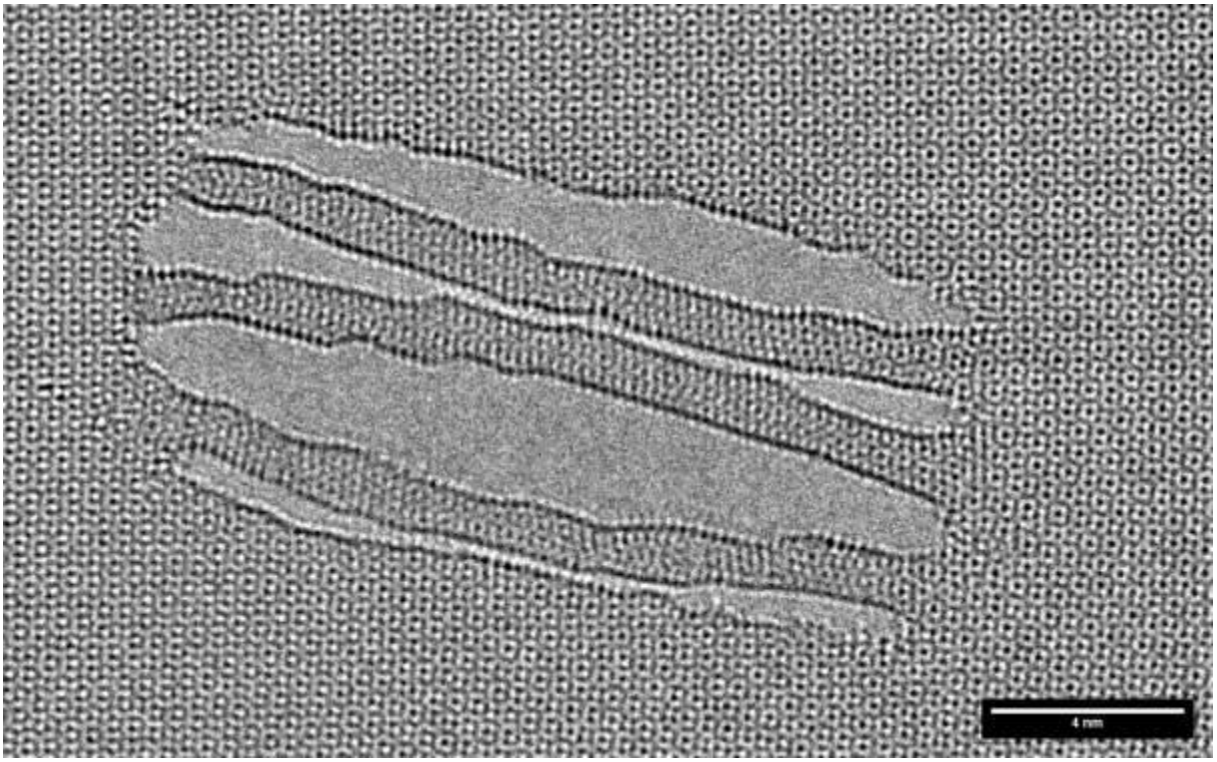


Fig. 2



MS8.07
Etching and carbon contamination dynamics on thin carbon films

A. J. Schwartz[1], E. Müller[1,2], Y. M. Eggeler[1,2]

[1]Karlsruhe Institute of Technology, Laboratory for Electron Microscopy, Karlsruhe, Germany
[2]Karlsruhe Institute of Technology, 3DMM2O - Cluster of Excellence (EXC-2082/1 – 390761711), Karlsruhe, Germany

Introduction

High-energy imaging techniques face the challenge of beam induced etching and carbon contamination. This issue becomes particularly critical when investigating dynamic processes in heterogeneous catalysis, where contamination can directly impact these processes. Therefore, it is crucial to study and comprehend these damages. This work focuses on two types of beam-induced damage: carbon contamination and etching.

Objectives

This study aims to better understand the dynamic interplay between substrate etching and carbon contamination under electron beam irradiation. Both processes are influenced by various factors, such as the concentration of hydrocarbons on the substrate, the composition of residual gases, the dose and energy of the primary electron beam. Material etching through electron irradiation occurs via several mechanisms. Gases such as N_2 and O_2 [1,2] can induce etching of the sample exposed to electron radiation. Additionally, adsorbed water (H_2O) contributes to substrate etching through the formation of reactive radicals such as H* and OH* [3]. Interestingly, carbon contamination may form a protective layer that suppresses substrate etching.

Materials & Methods

Thin carbon films were illuminated by a steady, defocused electron beam in a FEI DualBeam Strata 400S microscope to obtain homogeneously irradiated discs. The initial density of surface contaminants was varied by plasma cleaning to study their contribution to the contamination process. To analyze the volatile compounds in the microscope chamber, a Pfeiffer Prisma Pro residual gas analyzer (RGA) was used. For the extended illumination area, surface contaminant diffusion is the predominant effect for contamination at the edge of the irradiated region, while in the inner region, the main contribution comes from volatile compounds from the residual gas of the instrumental chamber. Thickness measurements are performed using calibrated intensities of high-angle-annular-dark-field (HAADF) images (Fig. 1). The thickness variations of the sample and contamination respectively were tracked *in situ* in distinct time steps, enabling the study of contamination and etching dynamics [4,5].

Results

Figure 4 shows the thickness variation of the carbon film after 20 minutes of irradiation. Etching of the substrate, of approximately 4.5 nm per hour at 20 kV and 120 pA, is found in the inner region of the illuminated disk. Different volatile compounds as well as water are detected by an RGA (Fig. 2) in the chamber hinting to be responsible for etching of the carbon film. At the edge of the irradiated disk carbon contamination is grown, driven by the diffusion of surface contaminants.

Conclusion

Etching of the substrate as well as the formation of carbon contamination is analyzed in a SEM. Carbon contamination growth is found at the edges of the irradiated disk due to the supply of contaminants by surface diffusion. In the inner region of the disk, less contamination is formed due to

the reduced availability of contaminants, enabling etching of the substrate by the impact of reactive compounds from the residual gas.

References

[1] Cleland et al. Physics Procedia (2015).

[2] Martin et al. Applied Physics Letters (2015).

[3] Schneider et al. The Journal of Physical Chemistry (2014).

[4] Müller et al. Ultramicroscopy (2024).

[5] Schwartz et al. BIO Web of Conferences (2024).

We acknowledge funding from TrackAct (SFB1441, Project-ID 426888090).

Fig. 1

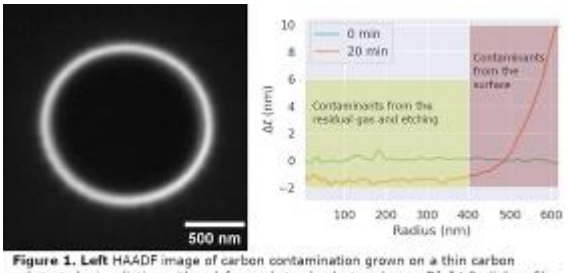


Figure 1. Left HAADF image of carbon contamination grown on a thin carbon substrate by irradiation with a defocused steady electron beam. **Right** Radial profile of thickness difference before and after 20 min of irradiation.

Fig. 2

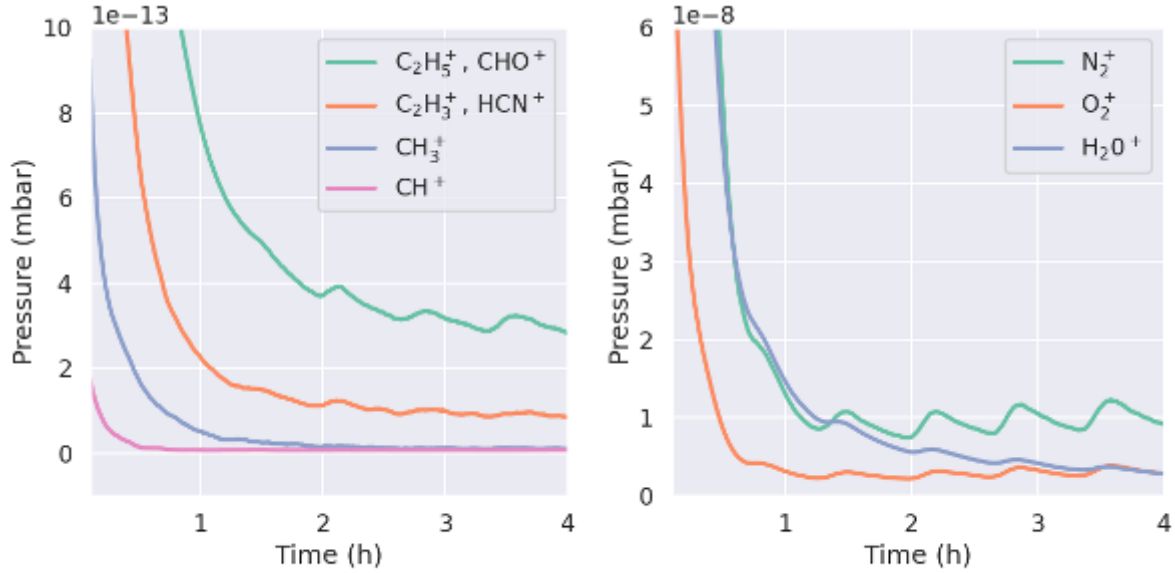


Figure 2. Partial pressure of residual gas components during pumping of the microscope chamber.

MS8.P01
Temperature-dependence of beam-driven dynamics in graphene-fullerene sandwiches

K. Strobel[1,2], M. Schlegel[1,2], M. Jain[3], S. Kretschmer[3], A. V. Krasheninnikov[3], J. C. Meyer[1,2]

[1]University of Tübingen, Institute for Applied Physics, Tübingen, Germany
[2]NMI Natural and Medical Sciences Institute at the University of Tübingen, Reutlingen, Germany
[3]Helmholtz Research Center Dresden-Rossendorf, Dresden, Germany

Aberration-corrected high-resolution transmission electron microscopy was used to investigate C60 fullerenes encapsulated between graphene sheets [1,2] at different temperatures (ca. 93K, 293K, and 773 K), along with molecular dynamics simulations. Cryogenic and heated conditions were reached using a custom in situ MEMS heating system. The study focused on the beam-induced dynamics of the C60 fullerenes and the encapsulating graphene, measuring the critical doses for the initial damage to the fullerenes and following the beam-induced polymerization. We observe that the doses for the initial damage are not significantly affected by temperature. However, the clusters formed by subsequent polymerization exhibit more tubular shapes at lower temperatures, while sheet-like structures are generated at higher temperatures. These experimental findings are supported by the results of first-principles and analytical potential molecular dynamics simulations. The merging of curved carbon sheets is promoted at higher temperatures and occurs rapidly over segments of only a few nanometers.

Fig. 1: First principle simulation of a low and high density C60 Fullerene Graphene sandwich. The simulation fits with experimental HRTEM observations at varying temperatures. The polymerization process is shown in a larger field of view on the bottom.

Fig. 2: Cryogenic and heated HRTEM observation show C60 in a rotating motion and fixed orientation. The Images are compared to HRTEM simulations, created with parameters similar to the imaging condition of the experimental data, using abTEM[3]

1. K. R. Strobel, M. Schlegel, M. Jain, S. Kretschmer, A. V. Krasheninnikov, J. C Meyer: Temperature-dependence of beam-driven dynamics in graphene-fullerene sandwiches, Micron 184, 103666 (2024). https://doi.org/10.1016/j.micron.2024.103666
2. Mirzayev, R., Mustonen, K., Monazam, M. R. A., Mittelberger, A., Pennycook, T. J., Mangler, C., Susi, T., Kotakoski, J., & Meyer, J. C. (2017). Buckyball sandwiches. Science Advances, 3(6), e1700176. https://doi.org/10.1126/sciadv.1700176
3. 1. Madsen, J., & Susi, T. (2021). The abTEM code: transmission electron microscopy from first principles. Open Research Europe, 1, 24. https://doi.org/10.12688/openreseurope.13015.1

Fig. 1

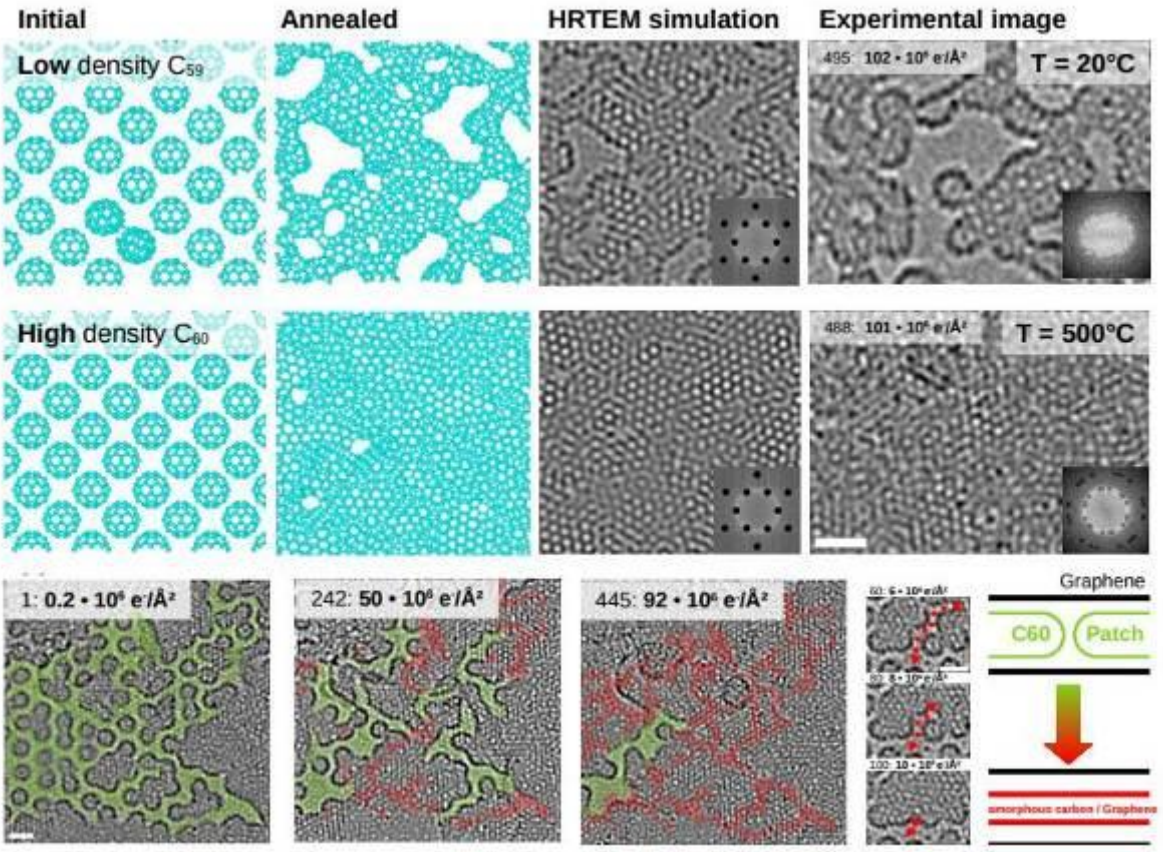
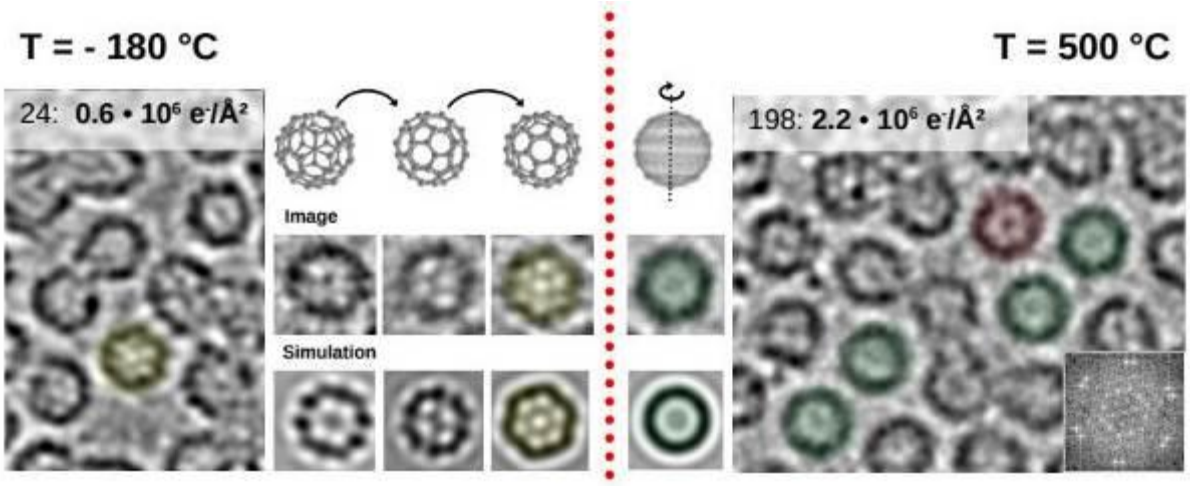

Initial
Annealed
HRTEM simulation
Experimental image
Low density C59
High density C60
T = 20°C
T = 500°C
1: 0.2 • 10⁶ e⁻/Å²
242: 50 • 10⁶ e⁻/Å²
445: 92 • 10⁶ e⁻/Å²
Graphene
C60
Patch
amorphous carbon / Graphene

Fig. 2


T = - 180 °C
T = 500 °C
24: 0.6 • 10⁶ e⁻/Å²
198: 2.2 • 10⁶ e⁻/Å²
Image
Simulation

MS8.P02
AI-Driven recognition of atomic structures in transition-metal dichalcogenides

T. Fan[1], D. Huang[1], P. A. van Aken[1], H. Wang[1]

[1]Max Planck Institute for Solid State Research, Stuttgart, Germany

Transition metal dichalcogenides (TMDs) have attracted significant attention due to their tunable magnetic, electrical, and optical properties, which are closely linked to their structural characteristics, such as stacking configurations [1]. Aberration-corrected Scanning Transmission Electron Microscopy (STEM) techniques allow for direct observation of TMD structures at the atomic scale. However, identifying structural features like grain boundaries, stacking polytypes, and intercalations in STEM images remain challenging due to subtle differences among similar structures, this challenge is further amplified when analyzing large STEM datasets. Advanced deep learning techniques present a powerful solution for precise and efficient recognition of these structural features, in this work, we present a U-Net neural network for the autonomous identification of stacking orientation, grain boundaries, and stacking polytypes in STEM images of $Nb_{1+x}Se_2$ films. This model enables accurate atomic positioning and provides insights into the structural configuration of the epitaxial $Nb_{1+x}Se_2$ film.

$Nb_{1+x}Se_2$ thin films were grown on c-cut sapphire substrates using a hybrid pulsed laser deposition (hPLD) technique [2]. High-Angle Annular Dark-Field (HAADF) STEM was employed to analyze the atomic-scale structure of the as-grown $Nb_{1+x}Se_2$ thin films, revealing multiple stacking polytypes. To analyze these HAADF images, we utilized a U-Net model for image segmentation [3]. The U-net model was trained on simulated HAADF datasets generated using an in-house developed code based on the frozen phonon approximation.

By applying the U-Net-based image segmentation model trained on simulated HAADF images, we were able to accurately map stacking orientations in real-space HAADF images of $Nb_{1+x}Se_2$ films. The model efficiently identifies atomic-scale grain boundaries within 2D layers and stacking configurations between adjacent 2D layers. This work demonstrates the effectiveness of the U-Net neural network for detailed image segmentation and structural recognition in TMD materials. Additionally, we show that simulated ADF images can be effectively used to train the model, addressing dataset limitations and enabling successful segmentation of real ADF images.

References

1. Wang, H., Yuan, H., Sae Hong, S., Li, Y. & Cui, Y. Physical and chemical tuning of two-dimensional transition metal dichalcogenides. *Chem. Soc. Rev.* **44**, 2664–2680 (2015).
2. Wang, H., Zhang, J., Shen, C. *et al.*Direct visualization of stacking-selective self-intercalation in epitaxial $Nb_{1+x}Se_2$ films. *Nat Commun* **15**, 2541 (2024).
3. Ronneberger, O., Fischer, P. & Brox, T. U-Net: Convolutional networks for biomedical image segmentation**.** *Med. Image Comput. Comput. Assist. Interv.* **9351**, 234–241 (2015).

MS8.P05
Graphene beyond ideal – Mechanical softening by vacancy creation and the role of contamination

W. Joudi[1,2], R. Windisch[3], A. Trentino[1,2], D. Propst[1,2], J. Madsen[1], T. Susi[1], C. Mangler[1], K. Mustonen[1], F. Libisch[3], J. Kotakoski[1]

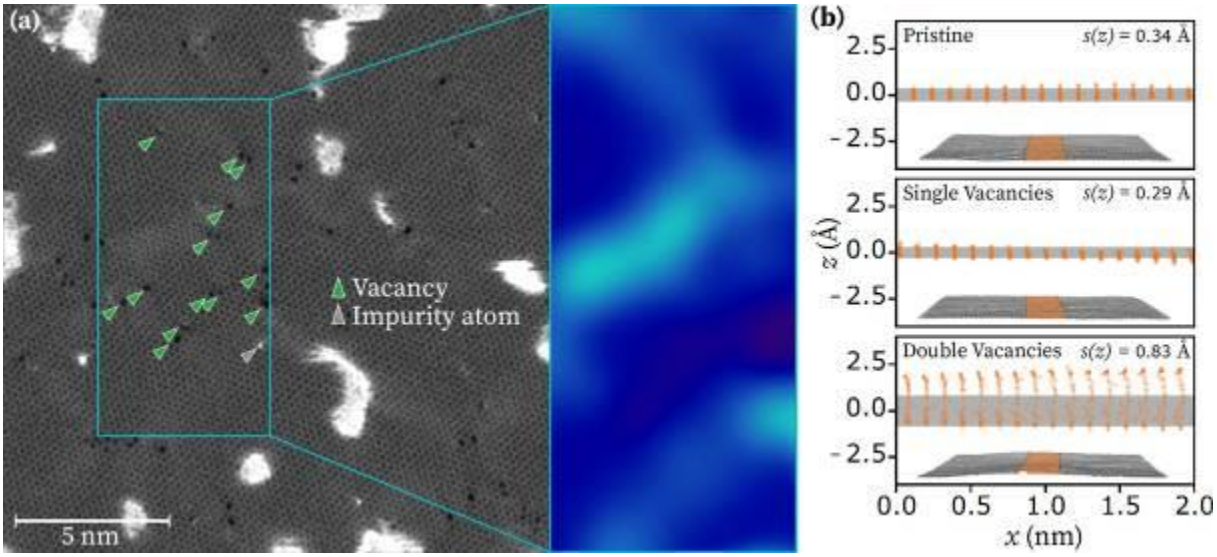
[1]University of Vienna, Faculty of Physics, Vienna, Austria
[2]University of Vienna, Vienna Doctoral School in Physics, Vienna, Austria
[3]Technical University of Vienna, Physics, Vienna, Austria

The two-dimensional elastic modulus E^{2D} of defective graphene is correlated to its vacancy density and vacancy type distribution, enabled by an interconnected ultra-high vacuum system including all instruments used [1]. The graphene surface is cleaned at a mm scale by laser light illumination. The vacancies are introduced into the exposed atomic lattice by irradiating pristine graphene with low energy (< 200 eV) Ar ions. The atomic structure of the irradiated graphene is imaged via aberration-corrected medium angle annular dark field (MAADF) scanning transmission electron microscopy (STEM). Specifically, in a semi-automated process, areas in the order of 10^4 nm² are imaged at atomic resolution and then analysed by a convolutional neural network in terms of atomic structure. Throughout multiple samples we find a total of 5865 vacancies and assign them to their corresponding types. The vacancy type distributions reveal single and double vacancies to be the most abundant. Subsequent atomic force microscopy nanoindentation measurements reveal a steep decrease of E^{2D} with increasing vacancy density. This is in contrast to what has been observed in Ref. [2]. We link this drastic drop in stiffness to vacancy-induced corrugation, which is observable in atomic resolution STEM images (Fig. 1(a)). According to atomistic simulations (Fig. 1(b)), these corrugations are caused by vacancies with two or more missing atoms, while single vacancies have no visible impact on the morphology. Based on this, we present an analytical model describing the decrease of E^{2D} as a function of the areal density of vacancies with at least two missing atoms. Lastly, we demonstrate that the opposite effect similar to Ref. [2], can be achieved by not removing the surface contamination prior to the irradiation, which also in our measurements leads to a similar increase of E^{2D}.

Figure 1: (a) MAADF STEM image of irradiated graphene, where the corrugation is visible as small intensity gradients across the graphene lattice. The magnification of the area within the turquoise box with Gaussian blur highlights the morphological roughness. (b) Cross-sectional view of simulated structures of graphene containing no vacancies (pristine), single vacancies and double vacancies. The orange dots represent carbon atoms within a 2x12 nm² cutout (orange area within the inset), while the grey overlay corresponds to their standard deviation $s(z)$ in terms of vertical position z. Each inset displays the corresponding complete 12x12 nm² structure. From Ref. [3]

[1] C. Mangler et al., Microscopy and Microanalysis 28 (S1), 2940 (2022)
[2] G. López-Polín et al., Nature Physics 11, 26 (2015)
[3] W. Joudi et al., arXiv (2025), https://arxiv.org/abs/2412.05194

Fig. 1


(a)
Vacancy
Impurity atom
5 nm
(b)
Pristine
s(z) = 0.34 Å
Single Vacancies
s(z) = 0.29 Å
Double Vacancies
s(z) = 0.83 Å
2.5
0.0
-2.5
z (Å)
0.0
0.5
1.0
1.5
2.0
x (nm)

Life Sciences (LS)

LS 1: Structure and functions of cells and organelles – Cryo ET

LS1.01(inv)
Molecular architecture of bacterial biofilms revealed by cryo-ET

Z. (. Wang[1], A. Tarafder[1], N. Dierlamm[1], G. LuTheryn[2], D. Carugo[2], T. Bharat[1]

[1]MRC Laboratory of Molecular Biology, Structural Studies, Cambridge, United Kingdom
[2]University of Oxford, Nuffield Department of Orthopaedics, Rheumatology and Musculoskeletal Sciences, Oxford, United Kingdom

Biofilms are a ubiquitous multicellular lifestyle adopted by many bacterial species including the important human pathogen, *Pseudomonas aeruginosa.* Infections caused by *P. aeruginosa* biofilms are challenging to treat as the bacterial cells are protected against antibiotics by an extracellular matrix (ECM), composed of a complex mix of extracellular polymeric substances. Despite its importance, direct visualisation of bacterial biofilms at high resolution has remained elusive, resulting in a gap in our knowledge regarding the molecular architecture of the biofilm ECM and how it links to antibiotic tolerance.

Here, we employ cryo focused-ion-beam (cryo-FIB) milling and electron cryo-tomography (cryo-ET) to visualise the *in situ* molecular architecture of *P. aeruginosa* biofilms formed under flow. We also correlate high-resolution cryo-ET data with cryo-volume EM and confocal imaging to illustrate the architecture of bacterial biofilm at multiple scales. Using this pipeline, we have obtained the first high-resolution pictures of the bacterial biofilm, revealing organisational details of the extracellular polymeric substances comprising the ECM. Notably, we identified an extensive meshwork of filamentous structures as key components of the ECM, contributing to the biofilm"s overall organisation and stability. Our structural data also depict distinct cellular states of bacteria in the biofilm lifestyle compared to the planktonic lifestyle, showing the adaptation strategies of cells within the biofilms.

Our molecular landscape of native bacterial biofilms provides unprecedented insights into their structural complexity and functional organization. Our findings on the undisrupted biofilms will pave the way for elucidating the molecular mechanism of antibiotic tolerance provided by bacterial biofilms.

LS1.02(inv)
Protein structure within human brain by fluorescence-guided – In-tissue cryo-electron tomography

R. A. Frank[1], M. Gilbert[1], N. Fatima[1], J. Jenkins[1], T. O'Sullivan[1], Y. Halfon[1], A. Schertel[2], M. Wilkinson[1], T. Morrema[1,3], N. Ranson[1], S. Radford[1], J. Hoozemans[3]

[1]University of Leeds, Leeds, United Kingdom
[2]Carl Zeiss Microscopy, Oberkochen, Germany
[3]VU Amsterdam, Amsterdam, Netherlands

A defining pathological feature of most neurodegenerative diseases is the assembly of proteins into amyloid that form disease-specific structures. I will present how using cryo-fluorescence microscopy (cryoFM)-targeted cryo-sectioning, cryo-focused ion beam scanning electron microscopy (cryoFIB-SEM) liftout and cryo-electron tomography (cryoET), we determined in-tissue molecular architectures in mouse model and post-mortem human tissues. Tomographic maps showed the architecture of β-amyloid and tau pathology. Subtomogram averaging of a microscopic region of pathology revealed the structure of a cluster of tau filaments from a single tomogram. These *in situ* structural approaches may be applied to address a broad range of neurodegenerative disease and neuroscience questions.

LS1.03
Visualizing the (ultra-)structural architecture of the Golgi-associated cytoskeletal filaments by cryo-electron tomography

D. Nazari[1,2,3,4], T. Stoll[1,2], C. Weber[1,2,3,4], F. Faessler[1,2,3,4]

[1]IGBMC, Integrated structural Biology, Illkirch, France
[2]University of Strasbourg, IGBMC, Illkirch, France
[3]Inserm, Illkirch, France
[4]CNRS, Illkirch, France

The Golgi apparatus plays a vital role in membrane trafficking and intercellular communication. In mammalian cells, individual cisternae stacks of the Golgi are connected laterally to form a prenuclear ribbon, important for proper cell polarity and migration. Studies show cytoskeleton filaments are key in maintaining Golgi architecture and positioning during cell polarization. Golgi-derived microtubules(MT) can induce cell asymmetry, facilitating transport in a specific direction. MT nucleating and stabilizing factors accumulate at Golgi membranes and act as molecular scaffolds. Their defects have been shown to induce Golgi disassembly and turn it into individual stacks of cisternae. The actin cytoskeleton is also emerging as a key factor in assembling and maintaining the Golgi architecture. In addition, the Golgi apparatus is a hub for a wide array of actin regulatory proteins, localized at the Golgi apparatus and the trans-Golgi network. Depletion of different F-actin nucleators can either lead to its dispersal or compaction. A distinct connection between Golgi membranes, actin filaments, and Golgi-derived MTs coordinates dynamics during Golgi ribbon formation. Consequently, the position and morphology of the ribbons depend upon interactions with them. In contrast to MTs and actin, less is known about the association of the Golgi complex with another cytoskeleton element, the intermediate filaments(IF). For instance, Septin-1 knock-down causes a dramatic alteration to the shape of Golgi cisternae. A commonality among these three cytoskeleton types and their assemblies at the Golgi, has not been well described at the structural and ultrastructural levels. A key to understanding how various cytoskeleton components impact the Golgi ribbon lies in examining the spatial organization of the filaments and the directions in which they may exert forces on cisternal membranes or facilitate transport processes. Here, vitreous hRPE1 cells tagged with Man2A-cis, mGat1-middle and GalT-trans Golgi markers (Fig.1B) were thinned by cryo-focused ion-beam milling (Fig.1D), and visualized by CLEM and cryo-electron tomography to study cytoskeleton in the context of the Golgi in situ. Quantitative ultrastructural information was derived from tomograms acquired on adherent cells combined with segmentation, vectorization, and geometrical analysis, with a pipeline being established for this aim, which guides to employ subtomogram averaging for detailed characterization of abundant cytoskeletal organizers (Fig.2B) The present data highlights our capability to prepare grids with suitable cell counts, the visibility of the marker in cryo-FM (Fig. 1B) and of cells in SEM/FIB-imaging, the potential to mill usable lamellae from the specimen (Fig.1D), and the success of correlation using the selected markers, we identified membrane structures with TGN identity (judged by shape and presence of densities representing a flat clathrin coat) surrounded by F-actin, IFs and MT(Fig.1EF). To further investigate filament tracing (Fig.2B), was done to find filament coordinates, so we can reconstruct individual filament subunits, allowing us to do classification and subtomogram averaging (Fig.2B). Finally, through the establishment of an optimized pipeline, we visualized the Golgi apparatus and its associated cytoskeletal elements. We aim to combine the acquired ultrastructural information into a model of the Golgi ribbon and the cytoskeleton surrounding it.

Fig. 1

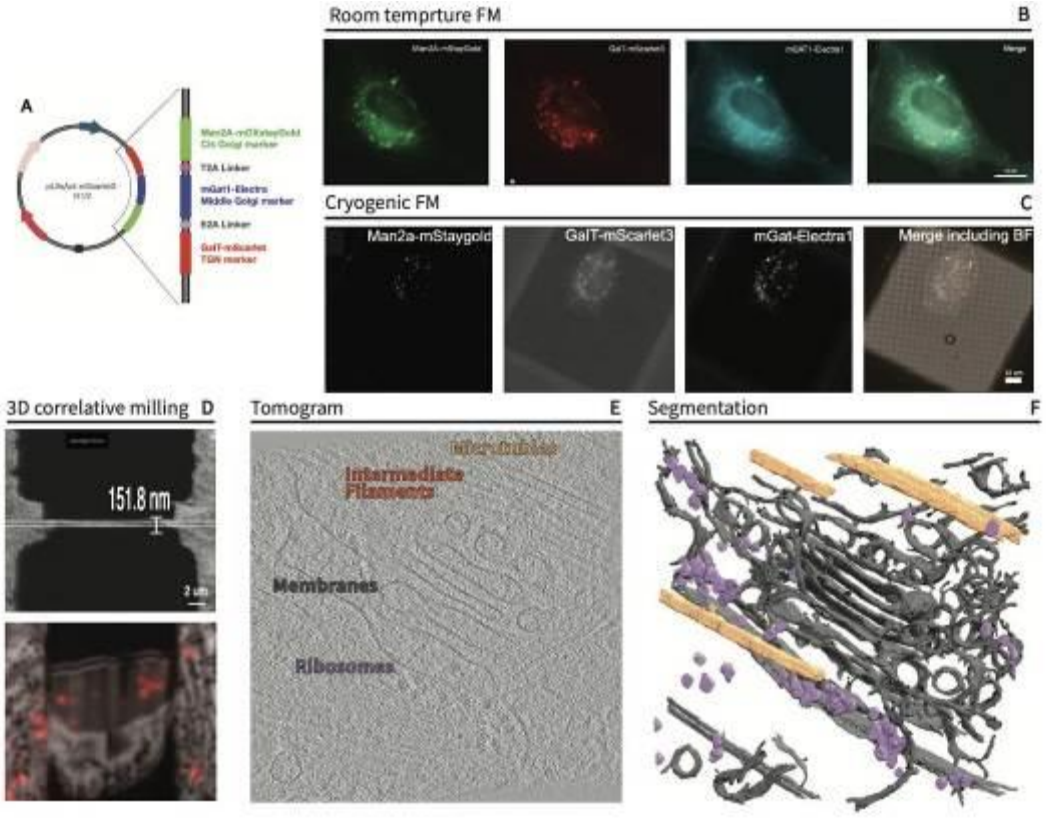


Figure 1: A, Schematic of plasmid and Golgi markers. B, room temperature fluorescent images of transfected hRPE1 cells labelled with Man2A-mStayGold (green), GalT-mScarlet (red) and mGat-Electra1 (blue). Scale bar 10 um. C, cryo fluorescent images of transfected hRPE1 cells labelled with Man2A-mStayGold, GalT-mScarlet, and mGat-Electra1. Scale bar 10 um. D, Illustration of 3D correlative cryoFIB milling workflow. Golgi markers were used for the correlation, and a fluorescence image of the targeted Golgi after rough milling. Scale bar 2 um. E, A representative tomographic slice of an acquired tomogram. Scale bar = 100 nm. F, The segmented volume of (E), shown as an overview. Ribosomes (Violet), membranes (gray) and microtubules (orange) are segmented with the indicated colours.

Fig. 2

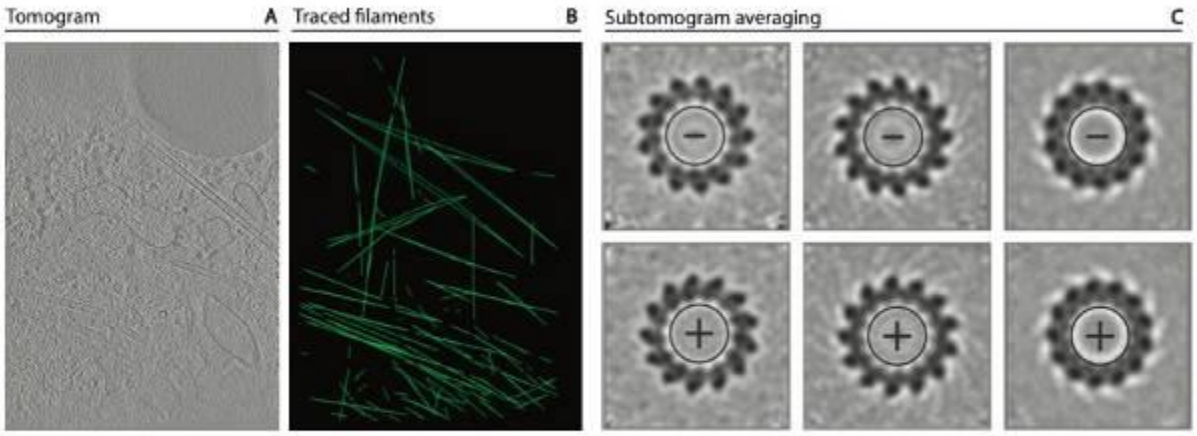


Figure 2: A, A representative tomographic slice of an acquired tomogram. Scale bar = 100 nm B, Traced filaments of the same tomogram (A). C, Subtomogram of one traced filament allows finding the plus and minus end of the microtubule, shows the polarity of the microtubule.

LS1.05
A correlative workflow streamlines synaptic imaging by cryo-electron tomography

T. T. Do[1], A. Siegert[1], F. Domart[1], F. Hahn[1], C. Zeising[2], S. Muth[3], C. Pape[3], K. Kusch[4], T. Dresbach[5], S. Rizzoli[2], A. Petrovic[1], R. Fernández-Busnadiego[1]

[1]University Medical Center Göttingen, Institute of Neuropathology, Structural Cell Biology Group, Göttingen, Germany
[2]University Medical Center Göttingen, Department of Neuro- and Sensory Physiology, Göttingen, Germany
[3]Georg-August-Universität Göttingen, Institute of Computer Science, Göttingen, Germany
[4]University Medical Center Göttingen, Institute for Auditory Neuroscience and InnerEarLab, Göttingen, Germany
[5]University Medical Center Göttingen, Institute of Anatomy and Cell Biology, Göttingen, Germany

34. Despite decades of intense research, the molecular organization of the synapse is not well understood. To address this issue, we sought to develop a method for systematic imaging of synapses by cryo-electron tomography (cryo-ET), a technology capable of mapping cellular architecture at molecular resolution. Thinning of cellular samples by cryo-focused ion beam milling is a prerequisite for high-quality cryo-ET imaging, but this process needs to be guided to the structures of interest. To allow robust synaptic targeting, we established a correlative cryo-light/electron microscopy approach by which synapses are fluorescently labeled in a minimally invasive manner, using a synthetic binder of the postsynaptic scaffold PSD-95 and antibodies against the presynaptic protein Synaptotagmin-1. Cryo-ET imaging at sites of colocalization consistently revealed excitatory synapses. Our method allows structural studies of synaptic protein complexes in situ, facilitating investigations of the molecular architecture of synapses.

LS1.06
Ribosomes hibernate on mitochondria during cellular stress

H. Rosa[1], O. Gemin[1], M. Gluc[2], M. Purdy[2], M. Niemann[1], Y. Peskova[2], A. Jomaa[2], S. Mattei[1]

[1]EMBL, Molecular Systems Biology Unit, Heidelberg, Germany
[2]University of Virginia, Department of Molecular Physiology and Biological Physics and Center for Cell and Membrane Physiology, School of Medicine, Charlottesville, VA, United States

Cell survival under nutrient-deprived conditions relies on cells" ability to adapt their organelles and to rewire their metabolic pathways.[1] In fission yeast, nutrient depletion is an unfavorable condition for protein synthesis and triggers a response characterised by mitochondrial fragmentation and the sequestration of cytosolic ribosomes on mitochondria.[2] The molecular mechanism underlying this sequestration remains elusive. In this study, we performed in situ cryo-electron tomography to elucidate the molecular details of this adaptive response. Our analysis indicates that upon glucose depletion protein synthesis is halted, causing ribosomes to enter an inactive state. Our data reveal the presence of oligomeric arrays of hibernating ribosomes tethered to the mitochondrial surface. Surprisingly, ribosomes bind to the outer mitochondrial membrane via the small ribosomal subunit, an interaction facilitated by the ribosomal protein RACK1-orthologue Cpc2. This study broadens our understanding of the cellular adaptations triggered by nutrient scarcity and the underlying molecular mechanisms that regulate cell quiescence.

References

[1] Efeyan, A. et al. (2015) Nature 517, 302-310.

[2] Liu, M. et al. (2019) *Biol Open 8*.

LS1.P01
Structural characterization of p62 helical filaments in their role as selective autophagy cargo receptor

L. Jungbluth[1,2], C. Sachse[2,3]

[1]RWTH Aachen University, Institute for Molecular and Cellular Anatomy, Aachen, Germany
[2]Forschungszentrum Jülich GmbH, Ernst-Ruska Centre 3: Structural Biology, Jülich, Germany
[3]Heinrich-Heine-Universität Düsseldorf, Biology, Düsseldorf, Germany

Autophagy describes the process of digesting cellular material and recycling of nutrients by degradation of cargo in autolysosomes. For selective autophagy the cargo gets specifically marked for digestion e.g. by labeling with polyubiquitin and the interaction with the selective autophagy receptor p62. p62 bridges the cellular machinery for degradation with the cargo by possessing a binding site for autophagy key player ATG8 proteins like LC3B as well as ubiquitinated cargo. Due to homo oligomerization of multiple p62 entities, p62 can create a spatial proximity of autophagy machinery and cargo. Additionally, p62 is able to crosslink cargo into so called phase separation droplets and induce autophagy on-site. *In vitro*, purified p62 forms helical filaments. Here we investigate how p62 filaments interact with model autophagy phagophores and model cargo. First, we investigate the interaction of p62 filaments with the autophagy machinery by recording cryo electron tomograms on p62 filaments mixed with SUVs decorated with LC3B. The reconstructed tomograms were segmented and the segmentation analyzed in regard to p62 filament morphology and membrane properties at interaction sites. Second, we studied p62 filaments in a cargo rich environment by adding soluble GST-4xUbiquitin in excess molar ration and imaging the emerging droplets with cryo electron tomography. In these tomograms it can be seen how p62 is organized in *in vitro* phase separation.

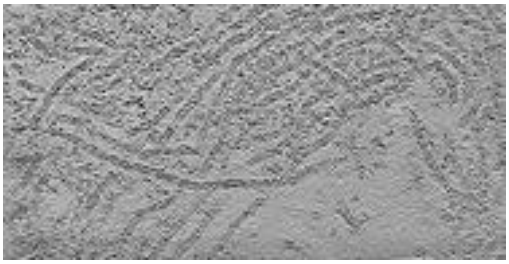
Fig. 1: Segmentation of a cryo electron tomogram of p62 filaments (yellow) with LC3B decorated SUVs (grey)

Fig. 2: Exemplary slice of a tomogram of p62 filaments in a phase separation droplet induced by excess of GST-4xUbiquitin

Fig. 1



Fig. 2



LS1.P02
Employing Xe plasma FIB for fast and precise sample preparation

S. Záchej[1], M. Zánová[1], M. Uher[2], J. Šmídová[3]

[1]Tescan GmbH, R&D, Brno, Czech Republic
[2]TESCAN Group, Applications, Brno, Czech Republic
[3]Tescan GmbH, Product Marketing, Brno, Czech Republic

Cryo-electron tomography is becoming increasingly accessible for a wide range of samples, from single cells to complex tissues, paving the way for new discoveries in structural biology. While focused ion beam (FIB) instruments utilizing Gallium ion sources are widely employed for high-resolution and precise milling, their slower processing speed can hinder throughput in large volume applications. Modern Xe-based plasma FIB offers a fast and comparably precise alternative for the demanding workflows.

This study explores optimized workflows for cryo-TEM sample preparation using the Xenon-based plasma FIB-SEM. Fast and precise ion beam milling with Xenon plasma not only accelerates sample preparation, but also enables the analysis of larger specimen volumes, enhancing our understanding of biological structures in a broader context. Additionally, we present novel approaches to the existing cryo-FIB workflows, inspired by related materials science techniques, such as the use of different materials as protective layers for FIB milling and 3D volume imaging, or the use of low-energy ion beams for sample processing.

LS1.P03
A correlative workflow streamlines synaptic imaging by cryo-electron tomography

T. T. Do[1], A. Petrovic[1], R. Fernández-Busnadiego[1]

[1]University Medical Center Göttingen, Institute of Neuropathology, Structural Cell Biology Group, Göttingen, Germany

Despite decades of intense research, the molecular organization of the synapse is not well understood. To address this issue, we sought to develop a method for systematic imaging of synapses by cryo-electron tomography (cryo-ET), a technology capable of mapping cellular architecture at molecular resolution. Thinning of cellular samples by cryo-focused ion beam milling is a prerequisite for high-quality cryo-ET imaging, but this process needs to be guided to the structures of interest. To allow robust synaptic targeting, we established a correlative cryo-light/electron microscopy approach by which synapses are fluorescently labeled in a minimally invasive manner, using a synthetic binder of the postsynaptic scaffold PSD-95 and antibodies against the presynaptic protein Synaptotagmin-1. Cryo-ET imaging at sites of colocalization consistently revealed excitatory synapses. Our method allows structural studies of synaptic protein complexes *in situ*, facilitating investigations of the molecular architecture of synapses.

LS 2: Structure and functions of cells and organelles – Imaging of large volumes and plastic section tomography

LS2.01(inv)
Myelin phenotypes analyzed using the focused ion beam – Scanning electron microscope

A. M. Steyer[1]

[1]European Molecular Biology Laboratory, Imaging Centre, Heidelberg, Germany

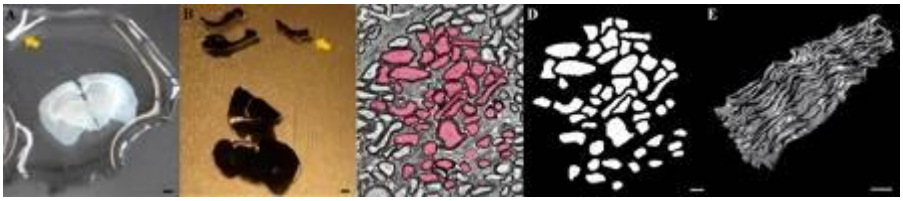
Traditionally to get a better understanding of the ultrastructure of the nervous system this was done using transmission electron microscopy (TEM). In the last years more research has been done on different 3D volume acquisition methods being developed further for neuroscientific questions. For all volume SEM methods; array tomography, serial block-face scanning electron microscopy (SBEM) and focused ion beam-scanning electron microscopy (FIB-SEM) the sample preparation is one of the most important parts. Driven by the wish to be able to look at bigger specimen e.g. the full Drosophila brain or even larger the sample preparation as well as the data processing/analysis become crucial parts. The combination of 2D TEM images to do statistics on e.g. Myelin phenotypes in combination with a better understanding of the 3D architecture based on volume SEM can be pivotal to understand new or already described phenotypes at nm resolution. Here I would like to give a better understanding of different sample preparation methods to be able to do 3D myelin imaging using the focused ion beam – scanning electron microscope, as well as different tools for postprocessing and analysis from manual to automated segmentation.

Figure 1: A) Freshly extracted *N. opticus* (yellow arrow) and brain slice of a wildtype mouse. B) Heavy metal treated nerves (*N. opticus* yellow arrow) and brain slices of a wildtype mouse (scale bar 2 mm). C) Semi-automated segmentation of axons in the optic nerve based on a focused ion beam-scanning electron microscopic dataset and D) binarized mask (scale bar 500 nm). E) 3D rendering of the 50 segmented axons (scale bar 4 µm).

Reference:

1. Steyer et al. 2019 Methods in Cell Biology, FIB-SEM of mouse nervous tissue: Fast and slow sample preparation
2. Steyer et al. 2019, JoVe, "Biological Sample Preparation by High-Pressure Freezing, Microwave-Assisted Contrast Enhancement, and Minimal Resin Embedding for Volume Imaging."
3. Steyer et al. 2020, Journal of Structural Biology, "Pathology of Myelinated Axons in the PLP-Deficient Mouse Model of Spastic Paraplegia Type 2 Revealed by Volume Imaging Using Focused Ion Beam-Scanning Electron Microscopy."
4. Steyer et al. 2022 Glia, "Focused Ion Beam-scanning Electron Microscopy Links Pathological Myelin Outfoldings to Axonal Changes in Mice Lacking Plp1 or Mag."

Fig. 1



LS2.02(inv)
Volume electron microscopy to elucidate structural features of beta cell function

A. Müller[1], N. Klena[2], S. Aurrecoechea[1], S. Pang[3], D. Schmidt[4], H. Hess[5], T. Kurth[6], F. Jug[2], M. Weigert[6], C. S. Xu[3], G. Pigino[2], M. Solimena[1]

[1]Paul Langerhans Institute Dresden, Dresden, Germany
[2]Human Technopole, Milan, Italy
[3]Yale School of Medicine, New Haven, CT, United States
[4]Max Delbrück Center, Berlin, Germany
[5]Janelia Research Campus, Ashburn, VA, United States
[6]Technical University Dresden, Dresden, Germany

Pancreatic beta cells produce, store and secrete insulin, the blood-glucose-lowering hormone of the body. They are part of the islets of Langerhans, clusters of endocrine cells surrounded by exocrine tissue. Proper insulin secretion is orchestrated by sub-cellular components including insulin secretory granules and cytoskeletal elements as well as paracrine signals from neighboring islet cells and systemic factors such as islet innervation. Failure of beta cells to provide a sufficient amount of insulin leads to diabetes.

Investigating subcellular features of beta cells together with their connectivity to islet and non-islet cells can help us to better understand their function. In my talk I will present our recent work on the reconstruction of insulin-microtubule interactions as well as the structure and connectivity of beta cell primary cilia.

We applied enhanced focused ion beam electron microscopy (eFIB-SEM) to image islets and pancreas at high resolution. We then performed organelle-specific segmentation, spatial analysis and 3D rendering of complete beta cells to investigate organelle-microtubule interactions. We furthermore applied our analysis workflow to primary cilia to elucidate their structure and interaction with the neighboring tissue.

With these tools we found that beta cell microtubules are non-centrosomal and not connected to the Golgi apparatus. Independent from glucose stimulation microtubules interact with insulin secretory granules close to the plasma membrane. We furthermore demonstrate that beta cell cilia have disorganized underlying microtubule structure characteristic of non-motile primary cilia. In the tissue context we observed numerous interactions of cilia with neighboring islet cells, with exocrine tissue and blood vessels. Most remarkably, we found connections between beta cell cilia and axons that had characteristic presynaptic features.

Our data provide novel insights into beta cell structure and define a novel role of beta cilia as a compartment for receiving not only islet intrinsic, but also extrinsic signals. These results also highlight to exploratory potential of eFIB-SEM and volume EM in general.

LS2.03
Pushing the limits of volume EM

S. Rey[1], L. Lab[1], P. Katz[2], J. Lichtman[1]

[1]Harvard University, Department of Molecular & Cellular Biology, Cambridge, MA, United States
[2]UMass Amherst, Neuroscience and Behavior Graduate Program and Department of Biology, Amherst, MA, United States

The brain is a highly powerful computer that defines how we perceive our environment and react to it. Deciphering its circuitry is the aim of many neuroscientists. Connectomics approaches this endeavour by acquiring image data sets with synaptic resolution. This can only be achieved using electron microscopy (EM). Traditionally, EM provides 2D information taken from ultrathin sections of a specimen. Volume EM techniques image consecutive sections which are subsequently aligned and merged to visualize the 3D specimen architecture. The development of volume EM started on the nematode *C. elegans*. The amount of manual labour involved made connectomes of larger animals seem to be an impossible task. However, the limits of volume EM have been pushed ever since.

Diffusion rates of fixatives limit the tissue depth that can be well preserved. Filling the tissue with mannitol maintains the extracellular space and allows fixatives to penetrate the tissue quickly into deep layers. Manual serial sectioning of plastic embedded specimen is prone to individual sections getting lost. Assistance of the automated tape collecting ultramicrotome (ATUM) decreases the risk of information loss. Image acquisition on a single-beam scanning electron microscope (SEM) is a time limiting step. The introduction of multi-beam SEMs which acquire up to 91 field-of-views simultaneously speeds up imaging considerably. Finally, machine learning supports the scientists in analysing the overwhelmingly large data sets.

Pushing the limits of volume EM is not only advancing large scale connectomics but also enabling quantitive and developmental analysis of small brains. I am introducing high pressure freezing to the lab"s connectomics pipeline to obtain high quality tissue preservation of the small sea slug *Berghia stephanieae*. I will collect connectomic data from multiple juvenile stages to elucidate how neuronal circuits grow.

The newest developments in pushing the limits of volume EM are iBEAM and SmartEM. iBEAM combines serial thick section collection with surface milling. Milling increases the z-resolution. In conjunction with a multi-beam SEM, milling and imaging can alternate on two wafers which speeds up the data collection. SmartEM is a software that optimizes imaging time on a single-beam SEM. Here, images are taken at short pixel dwell times, evaluated on the run and re-scanned at appropriate pixel dwell times if necessary. The final image is a composite of images taken at various pixel dwell times.

In summary, EM has evolved from focussing on sub-cellular details in small samples to the analysing large volume tissue architectures.

LS2.04
Data sharing, sample processing and benchmarking for optical STEM-based multibeam imaging – Sharing multibeam optical STEM data in life sciences

B. H. P. Duinkerken[1], A. J. Kievits[2], A. H. G. Wolters[1], D. V. B. Bergen en Henegouwen[1], J. Kuipers[1], J. P. Hoogenboom[2], B. Giepmans[1]

[1]University Groningen, University Medical Centre Groningen, Dept. Biomedical Sciences, Groningen, Netherlands
[2]Delft University of Technology, Imaging Physics, Delft, Netherlands

Electron microscopy (EM) is an indispensable technique to visualize biological ultrastructure in health and disease. Automated EM acquisition is pioneered by several labs moving towards sample imaging following analysis instead of analysis at the microscope, which we term nano-anatomy [1, 2], like in digital light microscopy used in pathology. The acquired big data is well suited for re-analysis of features that may not have included in the original studies [3], and data sharing is being pioneered via several platforms [4; and references therein]. In this lecture I will report on (i) faster high-throughput imaging using Delmic"s FAST-EM and (ii) discuss the challenges and opportunities in data sharing and reuse. High-throughput EM further enables larger scales and volumes to be recorded within feasible timeframes. Multibeam optical scanning transmission EM (OSTEM) utilizes multiple beamlets and optical separation of the transmitted electrons to increase imaging throughput with transmission-based imaging. However, the compatibility of multibeam OSTEM with routine sample preparation protocols and the effect of machine settings on image quality remains largely unknown. Here we show multibeam OSTEM to be an order of magnitude faster than (scanning) transmission EM while yielding comparable high-quality images of tissue processed with standard high-contrast staining protocols. Multibeam OSTEM benefits from embedding approaches that introduce high contrast, but is flexible in the type of stain used. Optimal results are obtained using an acceleration voltage of 5 kV, where section thickness and pixel dwell time require a balance between throughput and image quality [5]. Sharing of data globally can be via our initiative nanotomy.org, but increasing options are via bioimage archive [BIA; 6] and the image data repository [IDR; 7]. Access, pro"s and con"s of these repositories will be highlighted. Thus, high-throughput EM with imaging quality comparable to commonly used transmission-based modalities, enables biological ultrastructure analysis across larger scales and volumes. Sharing this data, like Google earth, in an open access format for reuse of biobanks were data of donors can easily be accessed: EM is only a mouse click away!

[1] http://nanotomy.org/

[2] de Boer P, Pirozzi NM, Wolters AHG, Kuipers J, Kusmartseva I, Atkinson MA, Campbell-Thompson M, Giepmans BNG. Large-scale electron microscopy database for human type 1 diabetes. Nat Commun. 2020;11:2475. doi:10.1038/s41467-020-16287-5

[3] Muralidharan C, Conteh AM, Marasco MR, Crowder JJ, Kuipers J, de Boer P, Linnemann AK. Pancreatic beta cell autophagy is impaired in type 1 diabetes. Diabetologia. 2021;64:865. doi: 10.1007/s00125-021-05387-6

[4] Giepmans BNG, Taatjes DJ, Wolstencroft KJ. In focus: data management and data analysis in microscopy. Histochem Cell Biol. 2023;160:165. doi:10.1007/s00418-023-02226-0

[5] Duinkerken BHP, Kievits AJ, Wolters AHG, van Beijeren Bergen en Henegouwen D, Kuipers J, Hoogenboom JP, Giepmans BNG. Sample processing and benchmarking for optical STEM-based multibeam imaging. 2025 Microscopy and Microanalysis (in press). DOI:10.1093/mam/ozaf024

[6] https://www.ebi.ac.uk/bioimage-archive/

[7] https://idr.openmicroscopy.org/

Keywords

Electron microscopy, optical STEM, FAST-EM, multibeam STEM

Competing interests

JPH is co-founder and shareholder of Delmic BV, which commercializes the FAST-EM. The NWO-ENPPS.LIFT.019.030 grant contains contribution of Delmic BV. All other authors declare no competing interests.

LS2.05
Mechanisms regulating mitochondrial morphology and ultrastructure implications in mitochondrial function

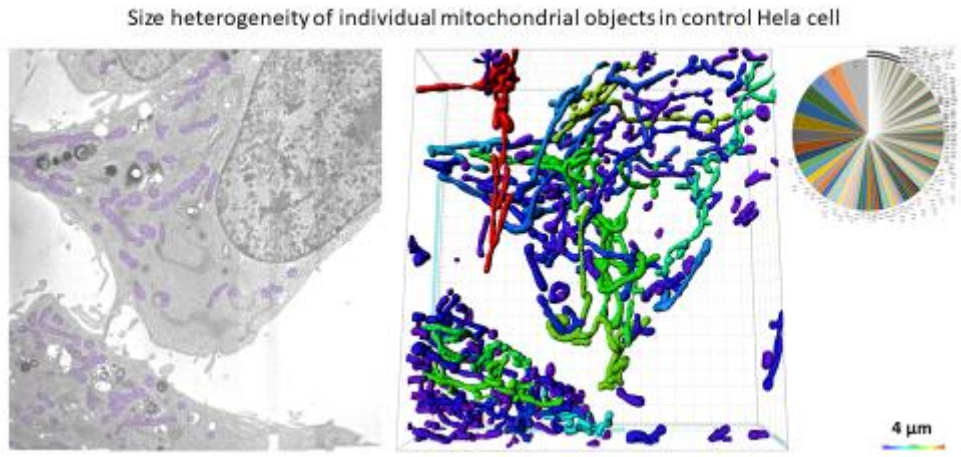
D. Puchkov[1]

[1]Leibniz Institute for molecular pharmacology (FMP), Cellular Imaging Facility, Berlin, Germany

Mitochondrial morphology reorganization is broadly reported in multiple cellular physiological conditions. Some of those mitochondrial shape reorganizations are regulated by shifts in mitochondrial fusion/fission dynamics whereas others involve individual mitochondrial shape and volume changes as well as inner membrane reorganizations.

As an electron microscopy facility, we have successfully provided our FIBSEM technology for our cooperation partners and investigated mitochondrial network ultrastructure under different conditions that include changes in mitochondrial potential modulation, hypoxia and nutrient deprivation challenges. Although our data derive from different labs and different model systems (namely Hela cells, human fibroblasts and yeast cells), we try to compare those versatile experiments and model systems to see how morphology per ce can affect mitochondrial function and cellular physiology.

Fig. 1



LS2.06
Thapsigargin-induced caspase-independent programmed cell death in innate immune- and cancer cells – Exploring non-apoptotic structure and function

P. A. Steiner[1], K. Melek[2], A. Andosch[3,4], L. Wiesbauer[1], A. Madlmayr[1], H. Kerschbaum[3], S. Zierler[1,5]

[1]Johannes Kepler University, Institute of Pharmacology, Linz, Austria
[2]University of Bern, Institute of Biochemistry and Molecular Medicine, Bern, Switzerland
[3]Paris Lodron University Salzburg, Department of Biosciences and Medical Biology, Salzburg, Austria
[4]Johannes Kepler University, Core Facility Imaging, Center for Medical Research, Linz, Austria
[5]Ludwig-Maximilians University Munich, Walther Straub Institute of Pharmacology and Toxicology, Munich, Germany

Thapsigargin (TG), a powerful inhibitor of the sarco/endoplasmic reticulum Ca^{2+}-ATPase (SERCA), has been widely used to investigate intracellular Ca^{2+} regulation and has shown promise as a potential anticancer agent, along with derivative compounds [1]. However, the conventional view that TG induces cell death primarily through caspase-dependent apoptosis [2] is being challenged by our research. Using a combination of advanced imaging techniques, including 2D and 3D transmission electron microscopy (TEM) and live-cell fluorescence imaging, along with cell death assays, we examined the effects of TG on immune- and cancer cells. Our findings revealed that TG does not cause the typical signs of apoptosis, such as nuclear fragmentation or apoptotic body formation. Instead, cells exhibited unique morphological changes, including ballooning of the perinuclear space, extensive vacuolization, mitochondrial enlargement and degradation and structural anomalies of the endoplasmic reticulum (ER, see Figure 1). Importantly, our cell death assays confirmed that TG triggers a form of programmed cell death that does not rely on caspase activation. These results suggest that TG induces a type of cell death more akin to autosis, a non-apoptotic process characterized by vacuolization and perinuclear space ballooning. This discovery has considerable implications for the development of TG and its derivatives as potential anticancer agents and highlights the need for a deeper understanding of cell death mechanisms in biomedical research.

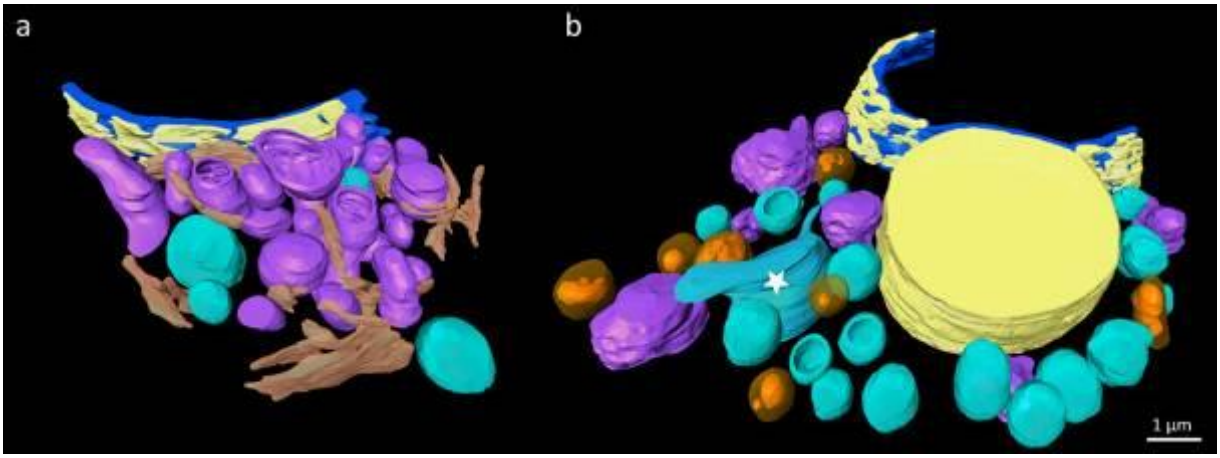
Figure 1: 3D ultrastructural analysis of control and TG-treated RBL-1 cells. (a) 3D TEM tomogram of an untreated RBL-1 cell, illustrating the typical morphology and spatial organization of cellular components, including mitochondria (purple), ER (melon), vesicles (mint), nucleus (blue) and perinuclear space (yellow). (b) 3D TEM tomogram of an RBL-1 cell 30 minutes after treatment with 2 µM TG, showing pronounced ultrastructural changes: mitochondria appear enlarged, fewer in number and exhibit irregular surface morphology; the ER is absent in thick tomography sections; vesicles are more numerous, occasionally displaying irregular shapes (asterisk); there is increased cellular vacuolization, a higher prevalence of autophagolysosomes (orange) and noticeable ballooning of the perinuclear space. The scale bar (1 µm) applies to both tomograms.

References:

[1] J.T. Isaacs, W.N. Brennen, S.B. Christensen, S.R. Denmeade, Molecules. 2021, 26 (24)

[2] A. Jaskulska, A.E. Janecka, K. Gach-Janczak, Int J Mol Sci. 2020, 22 (1)

Fig. 1



LS2.P01
Volume immuno-EM based morphological and molecular characterization of Kv4.3 expressing interneurons in layer CA1 of mouse hippocampus

L. K. Parajuli[1], M. Helmstadter[2], M. Ross[1], S. Durgvanshi[3], N. Sethumadhavan[1], C. Elgueta[3], A. Kulik[1]

[1]University of Freiburg, Institute of Physiology II, Faculty of Medicine, Freiburg i. Br., Germany
[2]University Hospital Freiburg, EM Core, Renal Division, Faculty of Medicine, Freiburg i. Br., Germany
[3]University of Freiburg, Institute of Physiology I, Faculty of Medicine, Freiburg i. Br., Germany

Volume EM (vEM) based techniques, such as Serial Block-Face Scanning Electron Microscopy (SBF-SEM), Focussed Ion Beam SEM (FIB-SEM) and SEM Array Tomography (SEM-AT) have been extensively applied for the structural investigation of neuronal tissues and revolutionized our understanding of neuronal connectomics. However, revealing neuronal connections alone cannot provide a complete picture of the neuronal physiology *per se* as the precise three-dimensional (3D) distribution of molecules are also crucial determinants of neuronal functions. Although volume immuno-EM (viEM) data remains indispensable in neuroscience, there are hardly any reports on the combination of vEM and pre-embedding immunogold labelling in the neuronal tissues. Several practical challenges regarding the structural preservation of the tissue due to weak fixation, lack of enough contrast from the tissue for SEM imaging, difficulty in automated alignment and segmentation of immunogold labelled micrographs poise bottleneck for the successful application of viEM methods in a reproducible and high-throughput manner. Here we used pre-embedding immunogold labelling in combination with SEM-AT for volumetric reconstruction of immunopositive neurons. Roughly, 400-500 serial ultrathin sections were cut from the tissue block containing the particular neurons of interest that were identified at the light microscopic level. The section ribbons that were collected on glow-discharged silicon wafer from the target neurons were counterstained with lead citrate to increase tissue contrast and imaged using SEM with imaging parameters that were optimized to achieve the best picture quality. Through 3D reconstruction of complete neuronal cell body and partial reconstruction of dendrites that protrude from the target neuron in the hippocampal CA1 pyramidal cell layer, we show that Kv4.3 subunit of the voltage-gated potassium channel shows unique, compartmentalized distribution pattern in subcellular compartments of interneurons (INs). These Kv4.3 macro-compartments can only be realized by the large volume reconstruction of soma and could be easily missed by short serial reconstruction of ultrathin sections. Quantification of immunogold particles showed the enrichment of the channel in the vicinity the synaptic inputs. The channel density was relatively low at the somatic plasma membrane portion of the interneuron that was in direct contact with the plasma membrane of the surrounding cells. This is not a general distribution pattern of the voltage-gated potassium channel subunits as the Kv2.1 subunit was rather enriched at the plasma membrane contact sites with the surrounding cells. We further developed a protocol for the double labelling with peroxidase and immunogold marker to demonstrate the neurochemical identity of the axonal inputs that contact the Kv4.3 labelled INs and estimate the ratio of excitatory and inhibitory inputs over the surface of cell bodies. In summary, using volume reconstruction we reveal the neuronal connectivity of Kv4.3 expressing INs and importantly provide precise 3D distribution pattern as well as the number and density of Kv4.3 in the perisomatic plasma membrane of hippocampal CA1 INs. As viEM offer possibilities to simultaneously acquire information on the ultrastructure and the molecular characteristics of target neurons, we believe that scaling up this approach can be a way forward towards understanding the structure-function relationship in neurons.

LS2.P02
Comparison of transmission electron microscopy images and backscattered electron images obtained by scanning electron microscopy

T. Haruta[1], R. Kawano[1,2]

[1]JEOL Ltd., Solution Development Center, Akishima, Japan
[2]JEOL Ltd., EP Business unit, Akishima, Japan

Introduction and Objective

The principle of backscattered electron (BSE) image formation by scanning electron microscope (SEM) reflects the average atomic number of the elements contained in the sample, similar to the transmission electron image by transmission electron microscope (TEM). Therefore, BSE images taken by SEM of ultrathin section samples stained with heavy metals are difficult to distinguish from TEM images. SEMs are smaller and cheaper than TEMs, there are an increasing number of cases where SEMs are used as a substitute for TEMs. Especially, in three-dimensional observation using electron microscopes called volume EM, it is typical to use SEM for observation of serial section surfaces. On the other hand, as the number of observation cases using SEM has increased, reports of differences with TEM images have been increased, but these have not been shared among researchers, and the cause of the differences has been unknown because the samples, sample preparation methods, and observation conditions vary depending on the observer. Therefore, we observed the same sample and the same field of view with TEM and SEM to investigate the cause of the differences.

Results and conclusion

In this study, ultrathin sections were mounted on a copper grid mesh, observed with TEM, and then observed the same field of view with SEM. As a result, knife marks that occur when slicing with an ultramicrotome were noticeable in TEM images but were not noticeable in SEM images. This result was suggested to be because in TEM images, electrons pass through the section, making the image highly sensitive to not only the heavy metals contained in the section but also the thickness of the section, which is why scratches on the surface of the section are noticeable. On the other hand, BSE images had low sensitivity to surface irregularities, but high sensitivity to heavy metals contained within the section.

Since it was thought that the difference between TEM and BSE images was related to the difference in electron penetration, the penetration of electrons was calculated using a Monte Carlo simulation, and then observations were performed by changing the section thickness and accelerating voltag . As a result, as with the simulation results, it was found that for a 100 nm section, all electrons remained within the section at an accelerating voltage of 2 kV, and some electrons were transmitted at an accelerating voltage of 5 kV. It was suggested that the difference in the section area used for this imaging also contributed to the difference in the acquired images.

Fig. 1

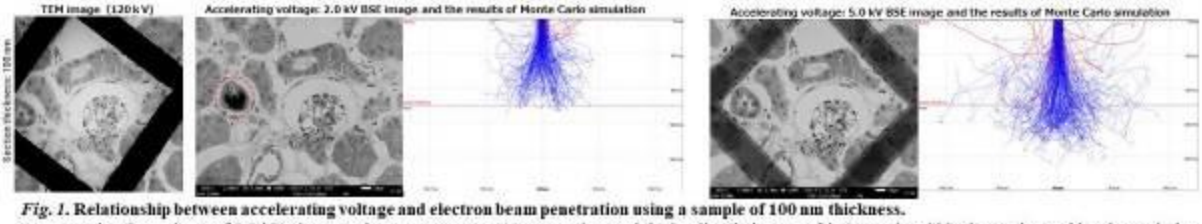


Fig. 1. **Relationship between accelerating voltage and electron beam penetration using a sample of 100 nm thickness.**
At an accelerating voltage of 2.0 kV, electrons do not penetrate a 100 nm section, and the irradiated electrons (blue) remain within the section and barely reach the mesh area. The backscattered electrons (red) that contribute to the image emerge at a depth of 40 to 50 nm. As a result, the mesh on the back of the slice is not visible in the observed image, and charge up area is observed in some areas. At the accelerating voltage to 5.0 kV, most of the irradiated electrons pass through the 100 nm section area and reach the mesh area. Backscattered electrons are also generated from some of the mesh area. The mesh structure on the back side becomes visible. No charge up is observed because the irradiated electrons can reach the conductive copper mesh.

Fig. 2

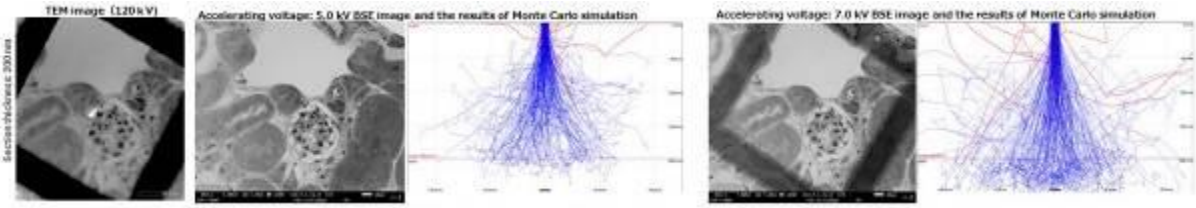


Fig. 2. **Relationship between accelerating voltage and electron beam penetration using a sample of 200 nm thickness.**
When observing a specimen with a section thickness of 200 nm at an accelerating voltage of 5.0 kV, most of the irradiated electrons reach the mesh region, but backscattered electrons are generated in the 100 to 150 nm region and almost none are generated from the mesh region. At an accelerating voltage of 7.0 kV, backscattered electrons are also generated from the mesh area.

Fig. 3

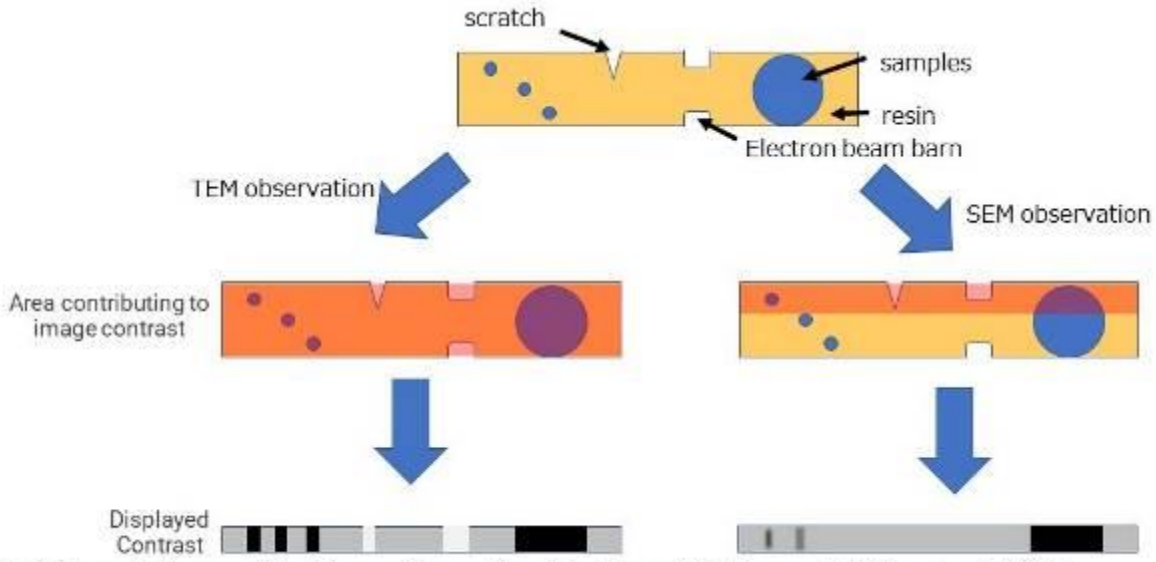


Fig. 3. **Schematic diagram of the difference in image formation between TEM image and BSE images with SEM.**

LS2.P03
1-UP – SEM with multi-ion-species focused-Ion-Beam column is next level for life sciences sample preparation and volume EM

T. Franke[1], A. Rigort[1], C. Tomova[1]

[1]Thermo Fisher Scientific, Planegg-Martinsried, Germany

Dual-beam instruments combine scanning electron microscopy (SEM) with a Focused-Ion-Beam (FIB) milling for integrated sample preparation and imaging as well as 3D volume-imaging (slice&view). Thermo Fisher Scientific Hydra Bio is a dual-beam SEM with a switchable multi-ion-species plasma FIB column that gives the choice between Argon, Xenon, Nitrogen, and Oxygen. Each ion-species has unique properties for milling and imaging. The higher milling currents of plasma-FIB allow faster milling and larger excavations compared to traditional Gallium-FIB milling, for example for cryo-TEM lamella preparation or serial-lift-out from HPF samples. Additionally, plasma-FIB can open up larger areas for slice&view, either using the classical cross-section geometry or the novel spin-milling method.

Large volume data acquisition is sped up by a new AI-based adaptive scanning function in the AutoSlice&View software. In the first image of the 3D data set, the user can outline cells or organelles which will be recorded at full resolution. Everything else will be recorded at a selectable, reduced resolution. The method can greatly reduce imaging times especially in sparse samples like cell culture, plant-, or lung-tissue, and avoid charging effects the can occur when scanning empty areas at large electron flux.

A related function makes cryo-slice&view acquisition in vitrified cells and tissues more robust: Adaptive focus-tracking re-positions the area for auto-functions execution on every new block face. It makes sure that there is enough high-frequency contrast in the area used for auto-functions, and that the area stays close to the area of high-resolution imaging without overlapping it.

Last but not least, Maps with Correlative Workflow functionality and Array Tomography allows the Hydra-user to run any correlative microscopy and serial-section imaging workflow.

LS2.P04
Developmental connectomics becomes feasible in the small sea slug *Berghia stephanieae*

S. Rey[1], R. Schalek[1], P. Katz[1], J. Lichtman[1]

[1]Harvard University, Cambridge, MA, United States

The nervous system is an intricate network of neurons that allows information collection, transmission and processing. Mapping all neurons and their synaptic connections, termed a connectome, to understand the mind of an animal is the goal of many neuroscientists. This endeavour started by acquiring a whole-body electron microscopy (EM) data set of the worm *C. elegans*. Since than protocols from tissue processing to data analysis have been developed to scale up feasible sample size in volume EM. While the generation of connectomes of bigger and bigger brains comes into reach, the newly developed techniques also allow to increase sample number of small nervous systems and applying connectomics to address neuro-developmental questions.

I"m set out to acquire four connectomes of the small sea slug *Berghia stephanieae*, a new model in neuroscience, throughout its juvenile development. This will unravel how nervous systems grow. The data sets with synaptic resolution will uncover how circuits expand to cope with animal growth and how new circuits are established to broaden the behavioural repertoire.

The small body size of early juveniles is within the size limit of high pressure freezing. Cryo-fixation of entire animals promises high quality tissue preservation. Well-fixed plasma membranes are crucial for machines to reliably detect cell boundaries, hence for automated segmentation of the data sets. Frozen specimen will be freeze substituted and resin embedded for serial-section SEM. I will employ the automated tape-collecting ultramicrotome which facilitates to obtain many consecutive sections. The tape holding the sections will be mounted on wafers for image acquisition using SEM.

First tests to high pressure freeze and freeze substitute whole-body *Berghia* resulted in promising tissue quality. *En-bloque* heavy metal stain in the freeze substitution cocktail gives sufficient contrast for single-beam SEM. Even processing of multiple specimens at once might be feasible.

In conclusion, connectomics pushes the limits of volume EM and opens the field to address new questions. Answering neuro-developmental questions comes into reach using the new and small model *Berghia*.

LS2.P05
The ultrastructure of symbiosomes – Insights into *Lotus japonicus* root nodules cells

I. Gantner[1], K. Parys[2], A. Klingl[1]

[1]Ludwig-Maximilians University Munich, Plant development and electron microscopy, Planegg-Martinsried, Germany
[2]Ludwig-Maximilians University Munich, Institute of Genetics, Planegg-Martinsried, Germany

In natural habitats, plants are colonized by a rich diversity of bacteria. While epiphytic bacteria reside on plant surfaces as leaves, stems, and roots, endophytic bacteria live inside plant tissues. A well-known example of mutualistic endophytes are root nodule forming rhizobacteria, which live intracellularly in the root tissue of legumes and supply the plant with essential nutrients by fixing atmospheric nitrogen. Inside the infected plant cell the bacteria are surrounded by a plant derived peribacteroid membrane, a plant-microbe interface (PMIs) also known as symbiosome. This PMI enables signal and nutrient exchange between host and microbe and leads to a successful symbiotic interaction. Knowing the ultrastructural details of this PMI is central for the biological and functional understanding of this specific plant-microbe interaction. This project aims to generate sample preparation methods for TEM and FIB/SEM techniques, visualize PMIs in 2D electron microscopy images and identify their 3D structure.

Lotus japonicus root nodules, were prepared for TEM and FIB-SEM by chemical fixation and embedding in epoxy resin blocks. Samples were cut in ultra-thin sectioning for 2D images generated with TEM. Furthermore, an image stack was generated by FIB/SEM to enable 3D modeling of the PMI region of interest by structure segmentation.

TEM images of infected root nodule cells confirmed the presence of symbiosomes, where rod shaped bacteroids of *Mesorhizobium loti* are enclosed by a peribacteroid space and surrounded by a plant derived peribacteroid membrane. The 3D model of these compartments visualized the orientation of bacterial cells in the peribacteroid space, as well as the tight spatial arrangement of the symbiosomes to each other and other plant cell organells. With regard to the TEM images, the model revealed further, that the number of bacteroids in one symbiosome can be much higher than it was previously assumed by 2D image data of this symbiosis. Ultrastructural details of plant-microbe interfaces visible in 2D TEM images were verified and analysed by 3D structure construction using FIB/SEM, which gives insight in the complex arrangement of microbes within infected plant cells.

Keywords

Plant-microbe interaction, TEM, FIB/SEM

LS2.P06
Application of STEM tomography to investigate smooth ER morphology under stress conditions

V. Heinz[1], R. Rachel[1], M. G. Madej[1], C. Ziegler[1]

[1]University of Regensburg, Biophysics II, Regensburg, Germany

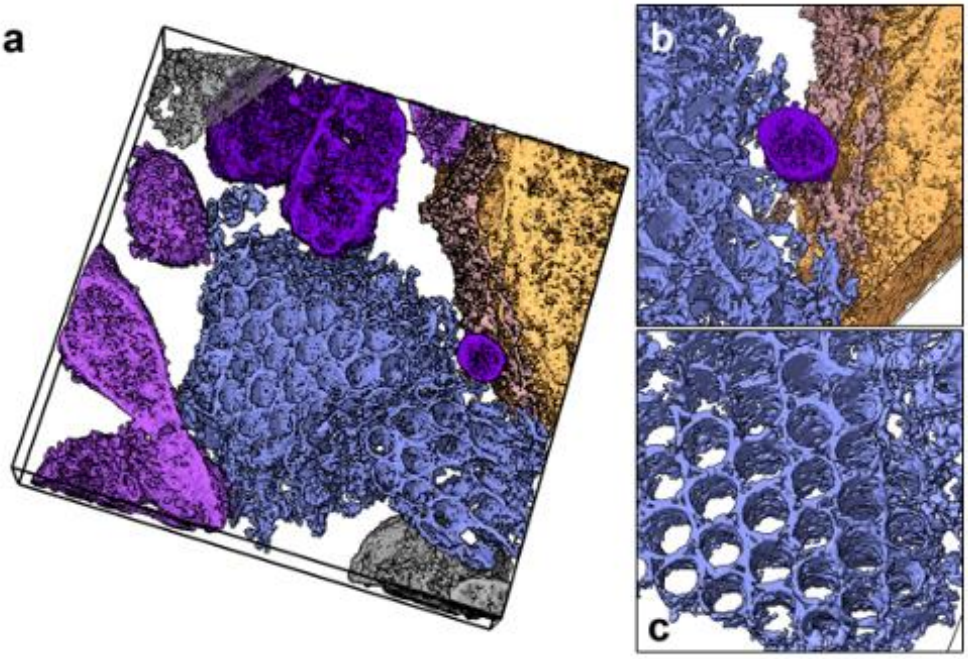
The endoplasmic reticulum (ER) plays a crucial role in various cellular processes and adapts its structure to meet the demands placed on cells, particularly under stress conditions. Such adaptations can lead to the formation of distinct structures, including ER whorls and crystalloid-ER. Traditionally, studying these complex formations has been challenging due to the limitations of conventional transmission electron microscopy (TEM), which cannot provide comprehensive three-dimensional (3D) data essential for understanding the intricate details of these structures. In this study, we aimed to overcome these limitations by employing electron tomography in scanning transmission electron microscopy (STEM) mode to explore the 3D morphology and interactions of crystalloid-ER and ER whorls in stressed human embryonic kidney (HEK) cells. Our focus was also on detailing the membrane architecture of these smooth ER (sER) morphotypes in greater detail than previously achieved.

To achieve this, HEK293S cells overexpressing the cation TRP channel polycystin-2 (PC-2) were used to induce ER stress, facilitating the formation of the structures of interest. The cells were prepared employing high-pressure freezing and freeze substitution techniques, which are crucial for maintaining the ultrastructural integrity of cellular components. We performed dual-axis STEM tomography on thick cell sections (800 nm), generating 3D reconstructions.

The results of this study provide an unprecedented view of the structural complexities of ER whorls and crystalloid-ER. We observed that while these structures are distinct, characterized by lamellar and tubular formations respectively, they can coexist within the same cell. Spatially separated, these morphotypes maintain their unique features; however, instances of direct membrane contact were also documented, indicating potential functional interactions. Even under stress-induced morphological alterations, the vital intracellular interaction networks with other organelles such as mitochondria and vesicles were preserved. Specifically, the tubular networks of the crystalloid-ER suggested structural connectivity, while ER whorls exhibited characteristic terminal turns in their stacked membranes.

This investigation underscores the effectiveness of dual-axis STEM tomography as a robust method for examining organellar morphology within large cellular volumes. The 3D reconstructions provided pivotal insights into the ultrastructure of sER, revealing intricate details about membrane architecture and tissue interactions under stress in HEK cells. This study not only advances our understanding of ER morphologies like the crystalloid-ER and ER whorls but also highlights the potential for employing these advanced imaging techniques in studying cellular stress responses and organelle dynamics at an ultrastructural level.

Fig. 1



LS 3: Cryo-EM and image analysis of macromolecules and molecular assemblies

LS3.01(inv)
A (male) Na^+/H^+ exchanger with potential – The case of the voltage-gated sperm-specific SLC9C1

C. Paulino[1]

[1]Heidelberg University, Heidelberg Biochemistry Center BZH, Heidelberg, Germany

The newly characterized sperm-specific Na+/H+ exchanger stands out by its unique tripartite domain composition. It unites a classical solute carrier (SLC) unit with regulatory domains usually found in ion channels, namely a voltage-sensing domain (VSD) and a cyclic-nucleotide binding domain (CNBD), making it a mechanistic chimera (molecular lego) and the first reported secondary-active transporter activated strictly by membrane voltage. Our structures of the sea urchin SpSLC9C1 in the absence and presence of ligands reveal the overall domain arrangement and new structural coupling elements. They allow us to propose a new gating model, where movements in the voltage sensor indirectly cause the release of the exchanging unit from a locked state through long-distance allosteric effects transmitted by the newly characterized coupling helices. We further suggest that modulation by its ligand cAMP occurs via disruption of the cytosolic dimer interface, which lowers the energy barrier for S4 movements in the VSD. Since SLC9C1 is essential for male fertility, including mammals, our structure represents a potential new platform for the development of novel non-hormonal on-demand male contraceptives.

LS3.02
Cryo-EM reveals the compositional diversity of mammalian respirasomes

I. Vercellino[1,2], L. Sazanov[2]

[1]Forschungszentrum Jülich GmbH, Jülich, Germany
[2]Institute of Science and Technology Austria, Klosterneuburg, Austria

Introduction

The mitochondrial respiratory chain is a set of four membrane-embedded complexes (complex I -CI-, complex II -CII-, complex III -CIII2-, complex IV -CIV-) that generate the electrochemical gradient necessary to produce ATP, the universal energy currency in cells.

Objectives

These complexes are functional in isolation but assemble in the membrane into supercomplexes of various composition and conformations: despite the consistent observation of supercomplexes in mitochondria across eukaryotes, their physiological role remains hotly debated.

Materials and methods

Structural biology plays a crucial role in the study of supercomplexes as a "**visual biochemistry**" tool to identify and characterize their assembly, composition and conformation, forming the basis to investigate their function.

Results

We previously (Vercellino and Sazanov, Nature 2021) used cryo-EM to describe the assembly mechanism of the mammalian supercomplex CIII2CIV, dependent on the specific assembly factor SCAF1 and combined the structures with biochemical assays to show that CIII2 and CIV gain catalytic advantage when assembled in the supercomplex.

In a new study (Vercellino and Sazanov, NSMB 2024), we expanded towards the "respirasomes" of murine mitochondria, supercomplexes that contain CI, CIII and CIV (i.e. are compositionally identical), but migrate as multiple bands on native electrophoresis (i.e. have different molecular weights), which make them impossible to characterize biochemically.

We identified two new forms of the respirasome, called the A-respirasome and the CS-respirasome, differing in the position and oligomeric state of complex IV when compared to the known canonical CICIII2CIV. The CS-respirasome features two copies of CIV, one bound in the canonical position and one linked to CIII2 via SCAF1. The A-respirasome features one copy of CIV, like the canonical respirasome, but this is bound to the "back" of complex I instead of the "heel".

Conclusion

The relevance of these structures, solved using SPA from solubilised membranes, is multifold.

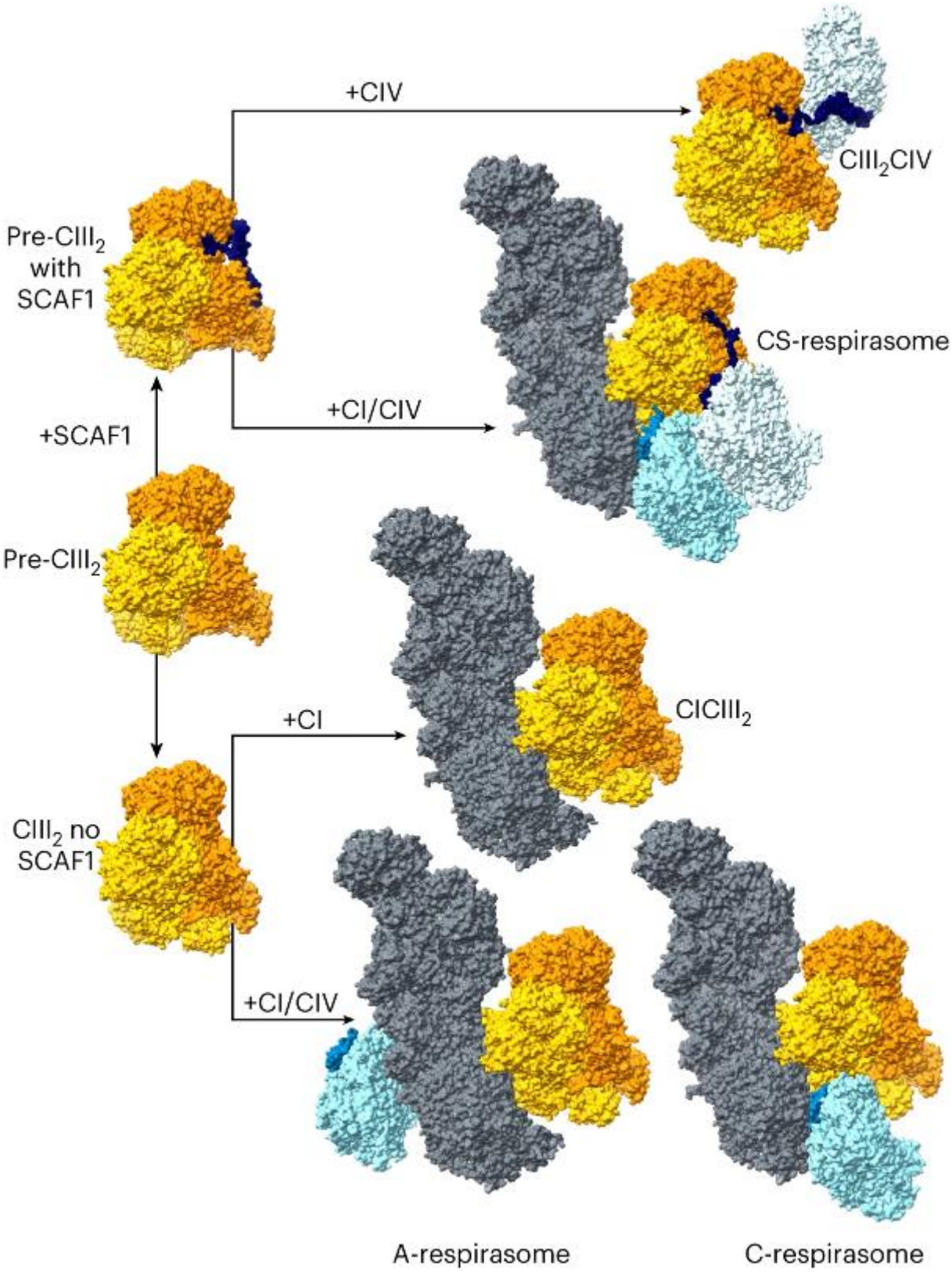
1) The CS-respirasome finally settled the debate between biochemists, who could detect SCAF1 in a "respirasome", and structural biologists, who never observed SCAF1 in the canonical respirasome structures.

2) The A-respirasome represents a new alternative conformation of the canonical respirasome, interestingly similar to the arrangement of CIV later reported for in situ mitochondrial complexes from Chlamidomonas (Waltz et al, biorxiv 2024). This strongly suggests that despite the isolation from the membrane the A-respirasome is a native species present in mitochondria and points towards its evolutionary conservation. Conversely, neither the CS- nor the A-respirasomes were identified in recent respirasome structures solved from isolated pig heart mitochondria (Zheng et al, Nature 2024), most likely because in mammals the C-respirasome is more abundant than the other two: this underscore the importance of single particle analysis to solve structures of low-populated species, which cannot be identified in situ.

3) From the perspective of bioenergetics, our work reveals the SCAF1-driven compositional landscape of mammalian supercomplexes (Fig 1) and forms a basis to hypothesize how conformationally and compositionally diverse supercomplexes can fine-tune mammalian metabolism.

Fig 1: Scheme of the SCs observed in the mouse mitochondrial membranes. From Vercellino and Sazanov, NSMB, 2024.

Fig. 1


+CIV
CIII2CIV
Pre-CIII2 with SCAF1
CS-respirasome
+CI/CIV
+SCAF1
Pre-CIII2
CICIII2
+CI
CIII2 no SCAF1
+CI/CIV
A-respirasome
C-respirasome

LS3.03
Architecture of the centriolar A-C linker

M. Wieczorek[1]

[1]ETH Zurich, Biology, Zurich, Switzerland

Centrioles are massive protein assemblies at the cores of centrosomes and basal bodies. A hallmark of centriolar architecture is the A-C linker, which connects the A- and C-tubules of neighbouring microtubule triplets. Despite its identification over 50 years ago, the composition and structural details of the A-C linker are not known. Here, we report cryo-electron microscopy (cryo-EM) reconstructions of the native A-C linker bound to centriolar microtubule triplets in *T. thermophila* basal bodies. We discovered that the A-C linker adopts two distinct conformations: an extended form in the proximal centriolar microtubule triplet region, and a narrow form in the distal portion. These conformations are distinguished by unique A- and C-tubule-binding proteins and an alpha-helical bundle that protrudes from the proximal A-C linker into the cell body. We identified core A-C linker components, which repeat every 8 nm along the centriole axis via a fishbone-like alpha-helical lattice. The structure of adjacent A and C-tubules shows that the A-C linker forms a bridge with novel triplet-specific B-C junction proteins, allowing us to build the first molecular model of a centriolar microtubule triplet pair. Our results uncover surprising structural and biochemical heterogeneity in centriole-associated complexes and suggest how the A-C linker could confer mechanical properties to centrioles in motile cells.

LS3.04
Bringing colour to cryo-EM with reconstructed electron energy loss analysis

B. Murphy[1], O. Pfeil-Gardiner[1], H. Rosa[1], D. Riedel[2], Y. S. Chen[3], D. Schäfer[1], C. Ho[1], D. Lörks[4], P. Kükelhan[4], M. Linck[4], H. Müller[4], F. van Petegem[3]

[1]Max Planck Institute of Biophysics, Frankfurt a.M., Germany
[2]Max Planck Institute for Multidisciplinary Sciences, Göttingen, Germany
[3]University of British Columbia, Vancouver, Canada
[4]CEOS GmbH, Heidelberg, Germany

Currently, no techniques exist for spatial mapping of elements within biological complexes, except in crystalline samples. Analytical techniques in the electron microscope, including electron energy loss spectroscopy (EELS) and energy dispersive X-ray spectroscopy (EDX), typically require very high electron doses to yield useable signal-to-noise ratios (SNR), while biological samples break down quickly in the beam. In biological single-particle analysis, high-SNR structural maps of biological complexes are obtained by three-dimensional reconstruction from many low-SNR images of different copies of the biological complex, helping to mitigate the limitations of dose sensitivity. Using a correlated approach, we have applied a similar strategy to data acquired in STEM-EELS mode, allowing for reconstruction of elemental information for cryopreserved complexes. I will discuss our proof-of-principle data, challenges, and next steps in the development of this technique.

LS3.05
Structural architecture of AcMNPV nucleocapsid and its implications for DNA portal organization and circular dsDNA packaging

E. Kandiah[1], M. Pelosse[2], G. Effantin[2,3]

[1]European Synchrotron Radiation Facility, Structural Biology, Grenoble, France
[2]EMBL, Grenoble, France
[3]Institut of Structural Biology, Grenoble, France

Introduction

Autographa californica multiple nucleopolyhedrovirus (AcMNPV) is a model baculovirus widely used in biotechnology, including biopesticides and recombinant protein production (Rohrmann, 2019). Despite its applications, the molecular details of its nucleocapsid assembly and DNA packaging mechanisms remain poorly understood. Structural insights into dsDNA virus packaging have been extensively studied in herpesviruses and bacteriophages (Sun et al., 2015), but similar studies on baculoviruses are lacking. Understanding AcMNPV"s nucleocapsid organization is crucial for improving baculovirus-based applications.

Objectives

This study aims to elucidate the structural organization of the AcMNPV nucleocapsid, focusing on the DNA portal complex and its role in the packaging of circular double-stranded DNA (dsDNA).

Materials and Methods

AcMNPV virions were purified and subjected to cryo-electron microscopy (cryo-EM) for high-resolution structural analysis. Extensive modeling studies were performed using new AI-based algorithms such as ModelAngelo (Jamali et al., 2023) and AlphaFold (Jumper et al., 2021) to refine protein structures and predict interactions within the DNA packaging machinery. Comparative analyses with known dsDNA packaging systems were conducted to identify conserved and unique structural features.

Results

Cryo-EM revealed a helical nucleocapsid with a DNA portal complex at one vertex, featuring an external C14 structure enclosing a C2-fold DNA portal, a C21 ring above, and a basal C14 complex enclosing a C7 plug. While resembling bacteriophage and herpesvirus systems (Dai & Zhou, 2018), it also exhibits unique features. AI-driven modeling (ModelAngelo, AlphaFold) identified seven new proteins, providing insights into key structural interactions. Motor-like proteins, including Ac66, suggest an active DNA translocation role, highlighting adaptations for circular genome packaging in AcMNPV.

Conclusion

This study provides the first detailed structural insights into the nucleocapsid organization of AcMNPV, highlighting the architecture of its DNA portal and packaging apparatus. We propose the C21 ring to be the DNA packaging apparatus, aiding the transport of the viral genome into the nucleocapsid. Alternatively, as the mature BV structure shows the genome fully packaged, with the translocase complex likely responsible for this step at the virogenic stroma, the C21 ring could simply be the reminiscent of this apparatus. Although the exact mechanism of genome incorporation into the nucleocapsid remains unclear, the 3D architecture presented here offers valuable insights for future studies and potential advancements in biotechnology and pest control applications.

References

Rohrmann, G. F. (2019). Baculovirus Molecular Biology. 4th edition. Bethesda (MD): National Center for Biotechnology Information (NCBI).

Sun, S., Gao, S., Kondabagil, K., Xiang, Y., Rossmann, M. G., & Rao, V. B. (2015). Proceedings of the National Academy of Sciences, 112(36), 11344-11349.

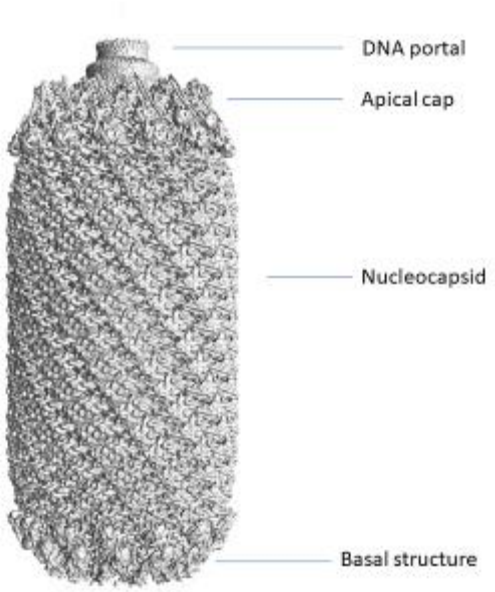
Dai, X., & Zhou, Z. H. (2018). Science, 360(6384), eaao7298.

Jamali, N., Kimanius, D., & Scheres, S. H. (2023). Nature Methods, 20(5), 689–696.

Jumper, J., Evans, R., Pritzel, A., et al. (2021). Nature, 596(7873), 583–589.

Figure1: A composite 3D map of the full baculovirus showing the nucleocapsid, the apical complex including the DNA portal and the basal complex.

Fig. 1



LS3.06(inv)
Insights into mechanisms of chromosome segregation from kinetochore structures

D. Barford[1]

[1]MRC Laboratory of Molecular Biology, Division of Structural Studies, Cambridge, United Kingdom

My laboratory is interested in understanding the mechanisms of chromosome segregation in mitosis. Over the past few years we have focussed on defining the structure and mechanism of kinetochores, large protein complexes that assemble onto centromeric chromatin and attach chromosomes to microtubule filaments of the mitotic spindle. I will discuss how using a combination of structural biology (mainly cryo-electrom microscopy), biophysical, and genetic approaches we have defined: (1) how the inner kinetochore recognises CENP-A nucleosomes and acts a load bearing element to tightly attach to centromeres, and how this is conserved within eukaryotes, (2) how the outer kinetochore attaches to microtubules and is regulated by the error correction mechanism to ensure sister chromatids pairs achieve biorientated attachment to the mitotic spindle prior to anaphase onset.

I will also present our approaches and preliminary results to use cryo-electron tomography to visualise the kinetochore structure in situ.

LS3.P01
Peptidomimetics with full antagonistic effect stabilize insulin receptor in novel conformation

M. Polak[1], I. Selicharova[2], M. Grzybek[3], U. Coskun[3], J. Jiracek[2], J. Novacek[1]

[1]Masaryk University, Cryoelectron Microscopy and Tomography Core Facility, Brno, Czech Republic
[2]Czech Academy of Sciences, Institute of Organic Chemistry and Biochemistry, Prague, Czech Republic
[3]Technical University Dresden, Center of Membrane Biochemistry and Lipid Research, Dresden, Germany

The human insulin receptor (IR) is one of the most studied receptor tyrosine kinases (RTKs). Binding of the signal molecule to the extracellular part of RTKs initiates receptor dimerization which triggers autophosphorylation on the intracellular part of the receptor. Unlike most RTKs, IR forms a disulfide bond stabilized dimer already in the apo-form. Therefore, an inhibitory mechanism must exist to prevent non-receptor activation of the signaling pathway.

We used single particle electron cryo-microcopy (cryo-EM) to describe the structural changes leading to insulin receptor inhibition. Instead of insulin we used three peptidomimetics: adamantane-derived mimetic (Ada), trimesic acid-derived mimetic (Trim) and S661. These proved to be full insulin antagonists.

Our cryo-EM maps reveal that the studied antagonists cross-link L1 and FnIII-1" domains of the insulin receptor, therefore stabilizing the Π shape structure in which membrane proximal regions of FnIII-3 and FnIII-3" are separated by 115 Å. This prevents autophosphorylation in the intracellular domains of the receptor. The head of the dimer (L1 to FnIII-1" and L1" to FnIII-1) is wider than in the case of insulin-IR and forms a shape resembling goggles. Remarkably, we do not observe α-CT helix densities in our maps. This helix is important for insulin binding.

LS3.P03
Dynamical scattering in ice-embedded proteins in conventional transmission electron microscopy

M. L. Leidl[1], J. Zivanov[1], C. Sachse[2,3], K. Müller-Caspary[1]

[1]Ludwig-Maximilians University Munich, Chemistry, Munich, Germany
[2]Forschungszentrum Jülich GmbH, Ernst Ruska-Centre for Microscopy and Spectroscopy with Electrons, Jülich, Germany
[3]Heinrich-Heine-Universität Düsseldorf, Biology, Düsseldorf, Germany

Introduction
For apoferritin, near-atomic resolution has been achieved in recent years [1,2]. However, obtaining atomic or near-atomic resolution continues to pose challenges for other proteins. Given their physical dimensions, the question arises whether the projection (PO) and weak phase object (WPO) approximation utilised in single-particle reconstructions are limiting factors.

Objectives
Both WPO and PO were compared with a full multislice simulation of various proteins embedded in low-density amorphous ice. The complex-valued exit waves were then compared using the Fourier ring correlation (FRC). The first meaningful zero crossing was employed as a resolution criterion, to which the single-slice models demonstrated a directly interpretable contrast compared to the multislice simulations.

Materials & methods
Eight different atomic models from the European Protein Data Bank are considered covering a range from 6.0 nm (haemoglobin) to 97.5 nm (rotavirus). These were embedded in low-density amorphous ice from molecular dynamics simulations using binary masks that account for the hydration radius [3]. The atomic models were then sliced into sections with a thickness of 0.375 nm, and multislice simulations were performed to calculate the wave function at the exit face of the specimen, which were compared to the single-slice models WPO and PO. To consider an additional defocus effect, the single-slice models were propagated by half the specimen thickness to the exit face and referred to as WPO_{exit} and PO_{exit}. Figure 1 summarises all scattering models. To separate multiple scattering from propagation, we also calculated the thick WPO (tWPO) for each protein [4], defined by a single scattering event of the plane wave with each slice and a coherent summation at the exit surface.

Results
The FRCs for the WPO_{exit} and tWPO are illustrated in Figure 2. All FRCs, except that from the 48-nm doublet microtubule, exhibit a positive contrast up to the first zero, which trends towards lower spatial frequencies as the specimen thickness increases. When comparing the tWPO model with the multislice simulation, only the FRCs of the two thickest proteins show zero crossings before reaching a resolution of 0.1 nm.
Figure 3 illustrates the resolutions for various proteins achieved by the single-slice models. The exit waves were directly compared through the FRCs using complex values, amplitudes (superscript A), or phases (superscript P). For all models, with a few minor exceptions, a reduction in resolution can be observed with an increase in specimen thickness, fitting linearly as a function of the square root of the thickness.

Conclusion
Our results demonstrate that in order to achieve atomic resolution, it is crucial to account for propagation and multiple scattering during single-particle reconstructions for thicker proteins. Figure 2 also shows that the contrast inversions are complex, protein-dependent and cannot be easily integrated into the single-particle workflow as an addition to the single-slice models. This conclusion refers solely to the constraints of the employed scattering model, whereas further aspects, such as dose and protein dynamics, are considered relevant in practice.

References
Funding: European Research Council Synergy Grant (No. 101118656: 4D-BioSTEM)
[1] Herzik J., Mark A. *Nature* 587, 39-40 (2020): 39-40.
[2] Yip, K. M., et al. *Nature* 587.7832 (2020): 157-161.
[3] Leidl, M.L. et al. *IUCrJ* 10.4 (2023) 475-486

Fig. 1

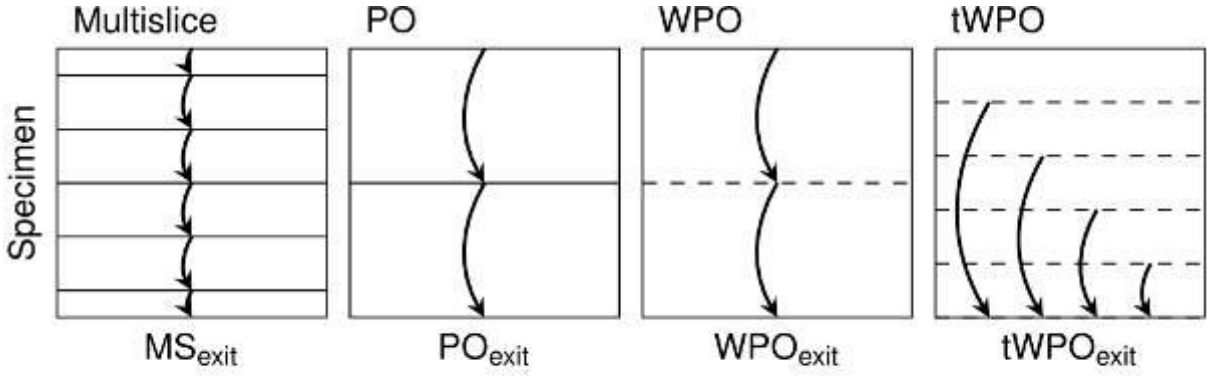


Figure 1: The different scattering models from left to right and their corresponding model at the exit surface: Multislice, PO, WPO and tWPO.

Fig. 2

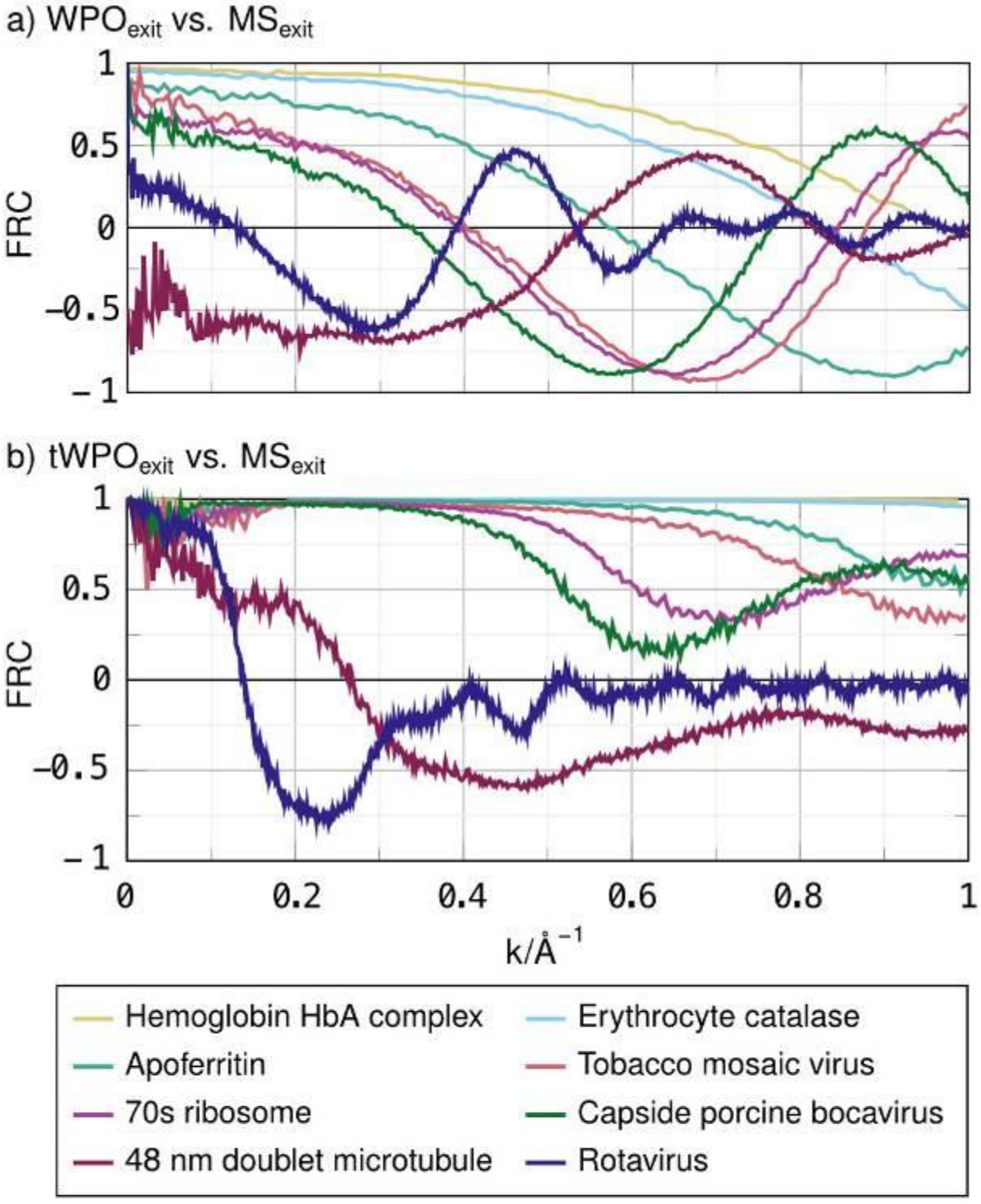


Figure 2: a) FRCs between the complex valued WPO$_{exit}$ and the multislice simulation for the different proteins. b) FRCs between the complex valued tWPO$_{exit}$ and the multislice simulation.

Fig. 3

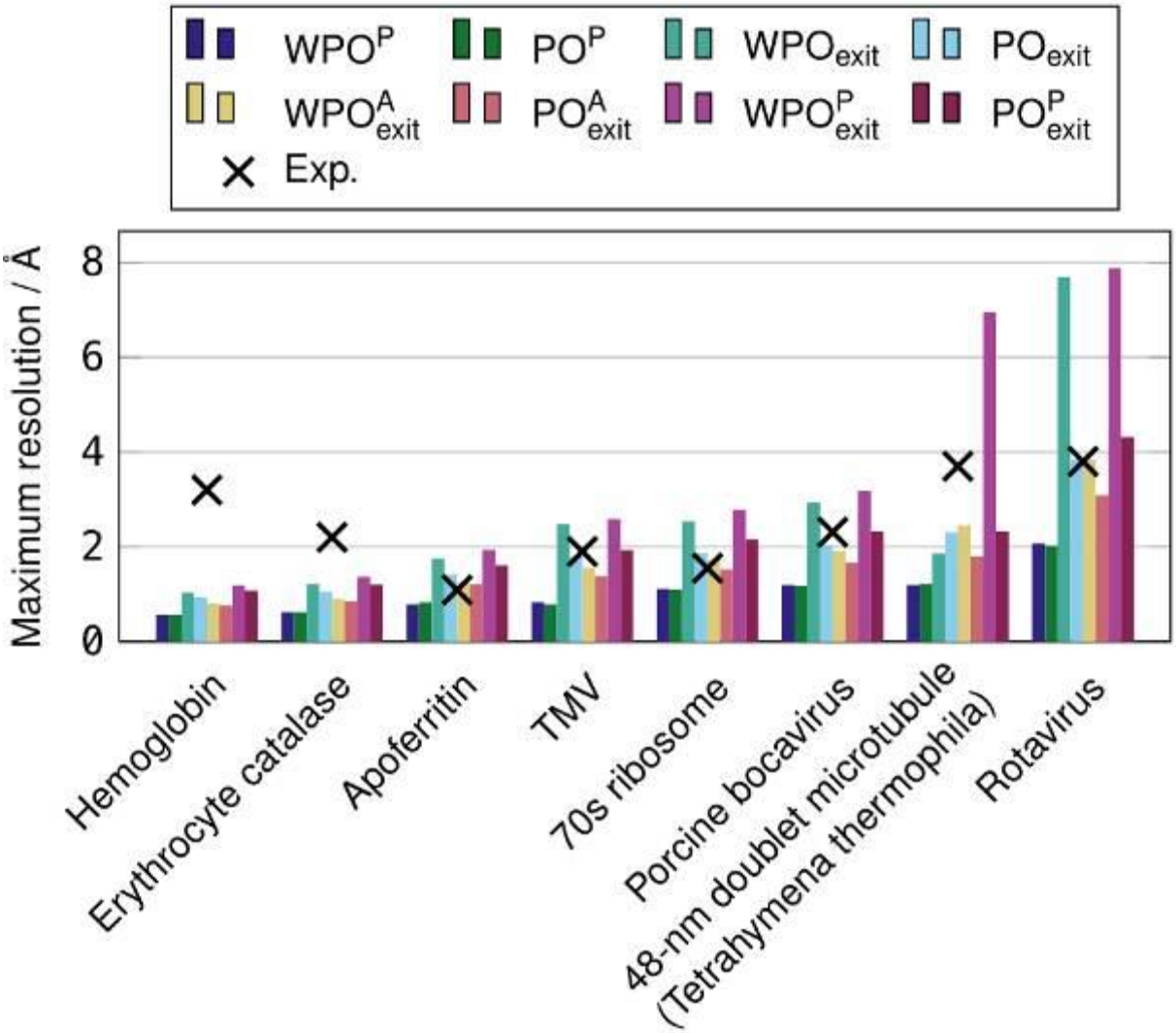


Figure 3: Resolution criterion as a bar chart for the different single-slice models and proteins and the highest published resolution on the PDB for the 3D map.

LS3.P04
The effect of fringe-free imaging on phase contrast cryo-STEM

M. L. Leidl[1], A. Jehle[1], D. Mann[2], C. Sachse[2,3], K. Müller-Caspary[1]

[1]Ludwig-Maximilians University Munich, Chemistry, Munich, Germany
[2]Forschungszentrum Jülich GmbH, Ernst Ruska-Centre for Microscopy and Spectroscopy with Electrons, Jülich, Germany
[3]Heinrich-Heine-Universität Düsseldorf, Biology, Düsseldorf, Germany

Phase contrast cryo-scanning TEM (STEM) recently achieved resolutions below 10 Å in single-particle reconstructions of several proteins [1,2] and near-atomic resolution for tobacco mosaic virus (TMV) [2]. In conventional cryo-TEM, fringe-free imaging (FFI) [3] optimises the number of acquisitions per grid hole by eliminating Fresnel fringes at the rim of the illuminating beam. Conversely, the probe-forming aperture in STEM is usually optically displaced from the focal plane of the probe-forming lens. As shown in Fig. 1, this leads to Fresnel fringes in diffraction patterns with crucial impact on STEM, and 4D-STEM ptychography in particular

The impact of FFI on STEM ptychography is worked out in detail based on simulations and experimental data. A method is developed to accurately incorporate the FFI effect in 4D-STEM reconstructions.

First, a multislice simulation study of TMV in low-density amorphous ice [5] is shown. Ptychographic reconstructions via self-consistent deconvolution of specimen and FFI-affected data are performed via the extended iterative ptychographic engine (ePIE). Additionally, the FFI effect is parametrised as Fresnel propagation in Fourier space and implemented in gradient-based ptychography [4]. Second, these benefits are elucidated using experimental 4D-cryo-STEM data of TMV, leading to higher contrast of the reconstructed phase and significantly higher resolution.

Fig.2a shows a gradient-based reconstruction assuming a normal STEM in the absence of the FFI mode for reference. In contrast, reconstructions Figs.2b-e rely on simulated 4D-STEM data, including the FFI setup. Importantly, Figs.2b,d ignore the FFI during the reconstructions with ePIE and using gradients, clearly deteriorating the result in comparison to Fig.2a. Enabling self-consistent STEM probe optimisation in ePIE leads to a significantly more reliable structure in Fig.2c, and the correct probe in Fig.2h (inset). Similar conclusions hold for the gradient-based result in Fig.2e, being quasi-identical to Fig.2a, with the probe optimised using our parametrised model for the FFI effect. Figs.f-j depict the corresponding power spectra with artificially enhanced low spatial frequencies if the FFI effect is ignored (Figs.2g,i).

Fig.3 shows a fully analogous study, however, including counting noise according to a realistic dose of 13.25 $e^{-}/Å^{-2}$. The TMV is barely picked by the algorithms in Figs.3b,d, where the FFI effect was neglected. Whereas ePIE tends to yield the coarse TMV structure (Fig.3c) and probe (Fig.3h) correctly, the parametrised gradient-based ptychography (Fig.3e) significantly stabilises the reconstruction, which resembles the reference in Fig.3a accurately up to the 3rd layer line, as seen in the power spectra below.

Operating a TEM equipped with fringe-free imaging in STEM mode can introduce severe artefacts in recorded diffraction patterns and subsequent ptychographic reconstructions. Here, a remedy was presented in Fresnel-propagating the probe-forming aperture in Fourier space, yielding accurate phase images in low-dose 4D-cryo-STEM.

References

Funding: European Research Council Synergy Grant (No. 101118656: 4D-BioSTEM)

[1] Küçükoğlu, B. et al. *Nat. Comm.* 15.1 (2024): 8062.
[2] Lazić, I. et al. *Nat. Methods* 19.9 (2022): 1126-1136.
[3] Konings, S. et al. *Microsc. & Microanal*. 25.S2 (2019): 1012-1013.

[4] Leidl, M.L. et al. *Micron* 185 (2024): 103688.
[5] Leidl, M.L. et al. *IUCrJ* 10.4 (2023).

Fig. 1

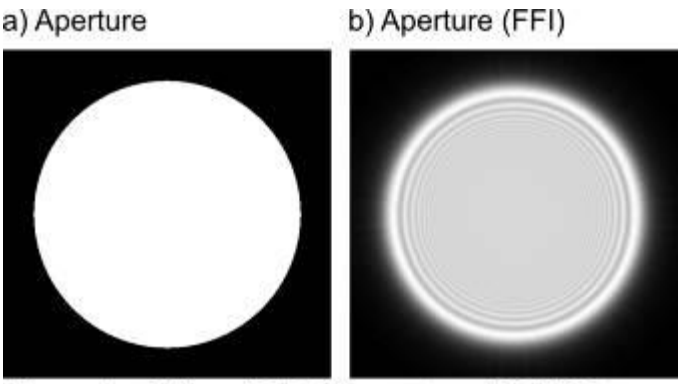


Figure 1: a) Normal STEM aperture. b) STEM aperture for the fringe-free setting.

Fig. 2

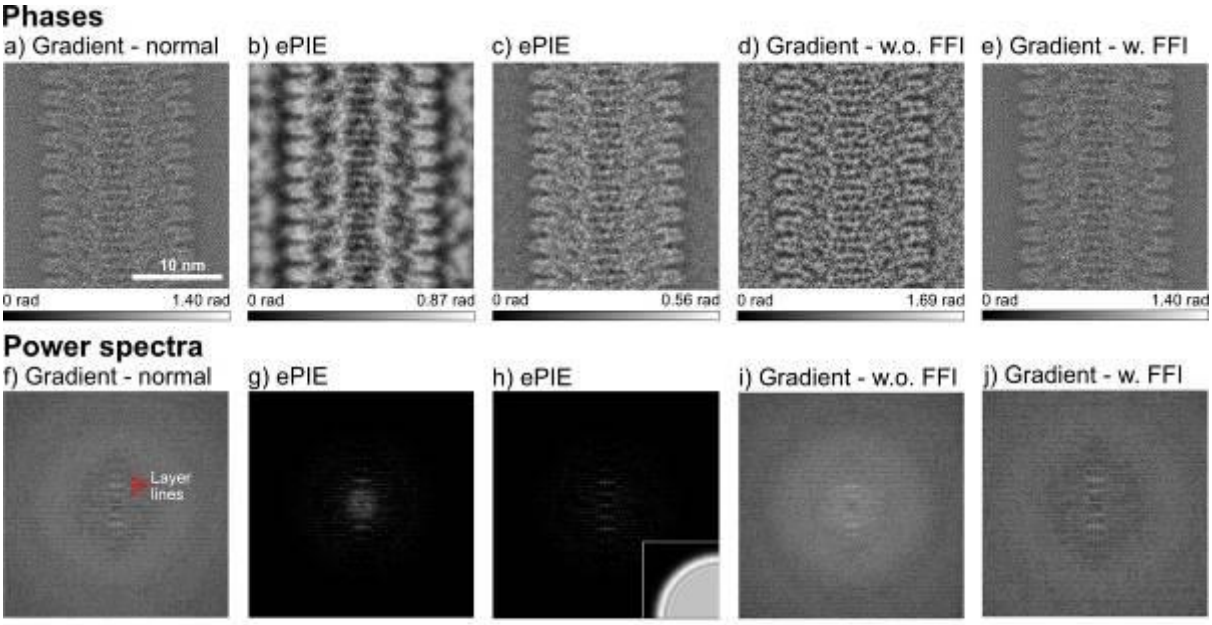


Figure 2: Reconstructions of a simulated TMV data set with a dose of 2650 $e^-/Å^{-2}$. a) Phase of a gradient based reconstruction without FFI. b) Phase of ePIE reconstruction - no probe optimisation. c) Phase of ePIE reconstruction - probe and specimen optimisation. d) Phase of the gradient based optimisation - without FFI. e) Phase of the gradient based optimisation - with FFI. f) - j) Corresponding power spectra. Inset h) Quarter of the reconstructed ePIE aperture.

Fig. 3

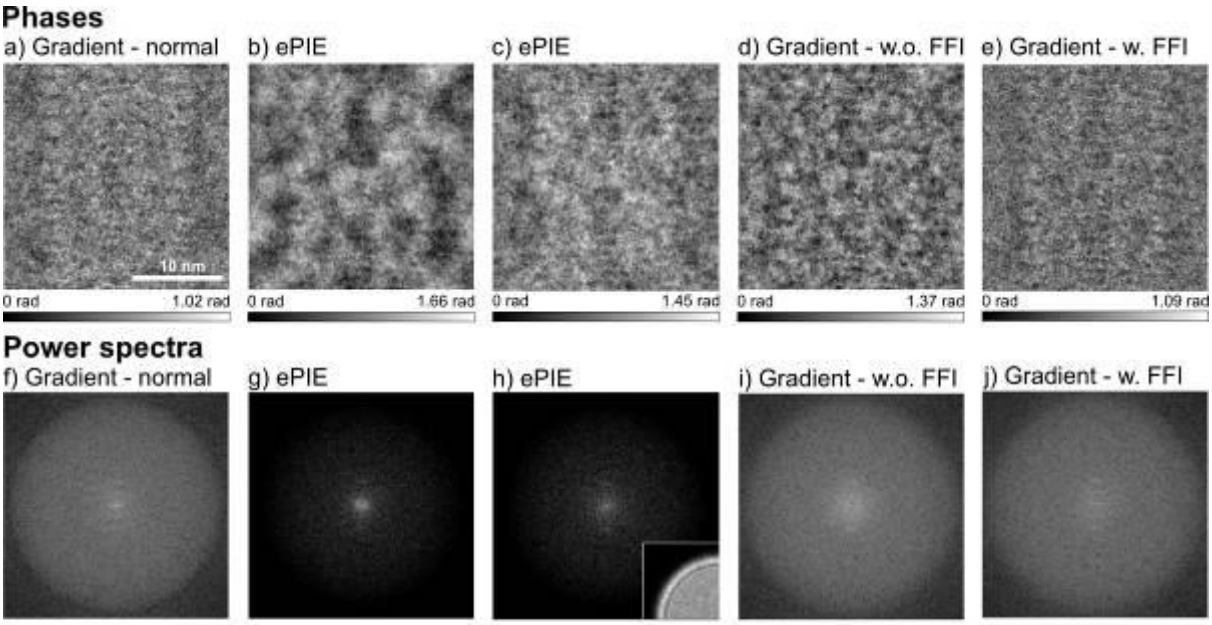


Figure 3: Reconstructions of a simulated TMV data set with a dose of 13.25 e⁻/Å^{-2}. a) Phase of a gradient based reconstruction without FFI. b) Phase of ePIE reconstruction - no probe optimisation. c) Phase of ePIE reconstruction - probe and specimen optimisation. d) Phase of the gradient based optimisation - without FFI. e) Phase of the gradient based optimisation - with FFI. f) - j) Corresponding power spectra. Inset h) Quarter of the reconstructed ePIE aperture.

LS3.P06
Thermo scientific smart EPU and tomo live – Automation to facilitate high-throughput structural biology

F. Grollios[1], R. Boer Iwema[2], M. Comet[3], J. Ortiz[4], E. Pryor[5]

[1]Thermo Fisher Scientific, Eindhoven, Netherlands
[2]Thermo Fisher Scientific, Brno, Czech Republic
[3]Thermo Fisher Scientific, Bordeaux, France
[4]Thermo Fisher Scientific, Dreieich, Germany
[5]Thermo Fisher Scientific, Hillsboro, OR, United States

The Cryo-EM community needs software automation to simplify workflows for single particle analysis (SPA) and cryo-electron tomography (cryo-ET) [1]. This automation would enable researchers to study demanding samples with heterogeneous compositions or dynamic macromolecular structures, regardless of their expertise in cryo-electron microscopy. Data acquisition and processing are often significant bottlenecks for users of both workflows.

We aim to automatize the sample screening process in cryo-EM, which traditionally involves tedious manual tasks such as selecting grid squares and foil holes, curating initial selections, and analyzing data to determine favorable conditions for data acquisition. Thermo Scientific's Smart EPU now offers a fully unattended workflow for SPA screening of multiple grids by leveraging a new session type for autonomous screening. The automatic execution of the session uses AI/ML decision algorithms (Smart Plugins).

With the introduction of a minimal number of parameters, a fully automated sequence of steps creates grid overviews (Atlases) and selects squares and representative foil holes with varied ice thickness to acquires corresponding high-resolution images. The monitoring of the entire process is new, and the screening results are accessible in real-time via the CryoFlow web portal, allowing users to trace image origins on the grid. This screening flow significantly reduces operator time and enhances microscope yield. This implementation enriches the previously available functionalities of multigrid batch acquisition, quality image monitoring, and the quality sample evaluation provided by Embedded CryoSPARC Live.

For cryo-ET workflows, we have developed an integrated solution that combines Thermo Scientific Tomography 5 acquisition software with Tomo Live, the processing software for automated, parameter-free alignment and on-the-fly reconstruction of tilt-series.

Here, we highlight our latest advancements in a parallelized microscope setup for cryo-ET and present the extension of the batch capabilities of Tomography 5 from single to multiple grids. This enhances productivity with optimal microscope time usage and more flexible time management for the microscopist during setup activities. Additionally, we demonstrate our innovative hierarchical data visualization tool in CryoFlow, which allows users to contextualize recorded tilt-series by tracing the position of each tomogram in the corresponding grid area (i.e., lamella). Quality metrics such as alignment accuracy, number of deleted tilts, astigmatism, sample thickness, and devitrification metric are provided, allowing users to filter and export only the highest quality data for subsequent processing steps. These developments provide a comprehensive solution for in situ dynamic structural biology.

Legends:

Fig 1. The Smart EPU Software enables fully automated SPA screening of multiple grids. After setting a few parameters, the execution of acquisition of representative areas on the grid proceed fully automatically and can be monitored in a dedicated new user interface.

Fig 2. Tomo Multigrid further enhances time savings by consolidating the setup time for multiple grids into a single session. Gains become substantial for high-throughput cryo-ET using a full autoloader (12 grids).

References:

Comet, M., et al. (2024) *Acta Cryst.,* D80, 247-258

Fig. 1



Fig. 2


Session Type
Single Grid
Multi Grid
thermoscientific
Multigrid
Multishot
Start
Batch
Stop
Multisite

LS3.P08
Comparative study of tannic acid diffusion as a micromolecular tracer in the meninges of the spinal cord and peripheral nerve sheaths – An electron microscopic investigation

S. Huseynova[1], E. Gasimov[1], L. Yildirim[1], S. Israfilova[1], I. Sadigi[1], N. Guliyeva[1]

[1]Azerbaijan Medical University, Cytology, embryology and histology, Baku, Azerbaijan

Introduction. Tannic acid (TA) enhances biomaterial properties [1] and penetrates cells with compromised plasmolemma [2], allowing precise ultrastructural analysis of collagen fibers [3]. While macromolecular transport in CSF and endoneural compartments has been studied, the diffusion of micromolecular tracers like TA across spinal meninges and peripheral nerve sheaths remains unclear. Understanding these diffusion patterns is essential for elucidating neural sheath function.

Objectives. This study investigates TA diffusion within spinal meninges and sciatic nerve sheaths. By comparing TA distribution via electron microscopy, we aim to identify key ultrastructural components that facilitate or restrict movement, providing insight into neural sheaths as selective molecular barriers.

Materials and Methods. Ten mature white laboratory rats (200–260 g) were used. Under deep anesthesia, spinal meninges and sciatic nerve fragments were extracted, fixed in 2.5% glutaraldehyde (pH 7.4), and postfixed in 1% osmium tetraoxide. Samples were incubated for two hours in a 1% TA solution in 0.5 M cacodylate buffer (pH 7.4). Standard electron microscopy procedures followed, including ethanol dehydration, embedding in Araldite-Epon and Spur resins, ultrathin sectioning (70–100 nm), staining with uranyl acetate and lead citrate, and imaging under a JEM-1400 transmission electron microscope.

Results. TA diffusion primarily followed collagen fibers within spinal meninges and peripheral nerve sheaths. The tracer selectively bound to glycosaminoglycan-rich extracellular matrix regions, forming osmophilic granules, while hyaluronic acid-rich areas remained unstained. At the meningeal level, TA diffusion was halted by a single inner layer of interconnected arachnoidal cells, confirming the arachnoid membrane as a selective barrier. In the sciatic nerve, TA migration was restricted at the inner layer of the perineurium, where perineural barrier cells prevented further diffusion into the endoneurium. These findings suggest that both the arachnoid and perineural sheaths function as physiological barriers regulating micromolecular transport.

Conclusion. This study highlights the selective diffusion properties of TA within neural sheaths, demonstrating that collagen fibers and glycosaminoglycan-rich extracellular matrix components play key roles in micromolecular transport. The findings reinforce that meninges and perineural sheaths act as dynamic barriers influencing molecular exchange. The accumulation of osmotic-active ions at these interfaces may affect CSF and endoneural fluid transport. Further research is needed to explore barrier permeability in pathological conditions and potential therapeutic applications.

Keywords. Cerebrospinal fluid, meninges, arachnoid membrane, perineural sheath, tannic acid, electron microscopy.

References:

1. Moghaddam SYZ, Biazar E, Esmaeili J, et al. Tannic Acid as a Green Cross-linker for Biomaterial Applications. Mini-Reviews in Medical Chemistry, 2023; 23(13):1320-1340.

2. Núnez-Durán H. Tannic acid as an electron microscope tracer for permeable cell membranes. Stain Technol. 1980; 55(6):361-5. doi: 10.3109/10520298009067265.

3. Meek KM. The use of glutaraldehyde and tannic acid to preserve reconstituted collagen for electron microscopy. Histochemistry. 1981; 73(1):115-20. doi: 10.1007/BF00493137.

LS3.P09
Structural investigation of amyloid fibril formation in medical insulin by cryo-EM

S. Sommerhage[1,2], F. Peralta Reyes[3], G. Schröder[1,2], L. Gremer[3,4]

[1]Forschungszentrum Jülich GmbH, Ernst Ruska-Centre for Microscopy and Spectroscopy with Electrons, Jülich, Germany
[2]Heinrich-Heine-Universität Düsseldorf, Physics, Düsseldorf, Germany
[3]Heinrich-Heine-Universität Düsseldorf, Physikalische Biologie, Düsseldorf, Germany
[4]Forschungszentrum Jülich GmbH, Institute of Biological Information Processing (IBI-7), Jülich, Germany

Insulin is a critical hormone for blood glucose regulation and diabetes treatment. However, it is prone to forming amyloid fibrils, which compromises its effectiveness. This **aggregation** poses challenges for insulin storage and stability, particularly in warmer climates and in low- and middle-income countries. Using cryo-electron microscopy (**cryo-EM**), we investigated insulin fibril formation at a molecular level to provide a foundation for developing strategies to prevent aggregation. This article reports novel cryo-EM structures of fibrils aggregated from recombinant human (RH) insulin and from **insulin glargine**, one of the most widely used modified insulin formulations in medical practice. Our analysis revealed that RH insulin produced primarily two fibril types, while glargine exhibited four distinct polymorphs (structural variants). We resolved the structures of two glargine fibrils and one of the two RH insulin fibrils to approximately **3.2 Å** resolution (Fourier shell correlation). Notably, the four glargine polymorphs differed significantly from both RH insulin fibril types in their protofilament structure and arrangement, presumably due to glargine's modified amino acid sequence. Additionally, the morphology of RH insulin fibrils differed substantially from previously reported structures, highlighting the strong influence of specific buffer conditions on the aggregation process. Our work provides valuable structural insights to address the challenge of insulin aggregation, potentially contributing to improved insulin formulations and storage methods. These findings may have significant implications for enhancing the stability and efficacy of insulin-based treatments, particularly in challenging environmental conditions.

LS3.P10
Cryo-EM analyses of the conformational spectrum of an ABC transporter in various membrane mimics

L. Hoffmann[1], A. Baier[1], L. Jorde[1], M. Kamel[1], J. H. Schäfer[1], K. Schnelle[1], A. Scholz[1], D. Shvarev[1], J. E. M. Wong[1], K. Parey[1], D. Januline[1], A. Moeller[1]

[1]Osnabrück University, Structural Biology, Osnabrück, Germany

Membrane proteins and especially ATP binding cassette (ABC) transporters play a major role in nature. ABC transporters are involved in numerous physiological processes and utilize ATP to translocate various compounds through the lipid bilayer. This process requires large-scale conformational changes and is highly dynamic. Therefore, structure determination is fundamental to understanding these transient proteins' function and mode of action.

Cryo-electron microscopy enables structure determination of proteins in solution to high-resolution and is, therefore, ideally suited to investigate such structural dynamics. However, particles must be extracted from the membrane and stabilized in artificial environments to facilitate cryo-EM sample preparation. To mimic the native environment, components such as detergents or lipid-based systems that form nanodiscs can be used.

In this study, we investigated the impact of various hydrophobic environments on the archetypical ABC transporter MsbA which translocates the precursor of Lipopolysaccharide through the inner membrane of gram-negative bacteria.

In addition, to different activity intensities, measured by phosphate release during ATP hydrolysis, we notice a strong bias of the observed conformational spectrum to the respective membrane mimic which complicates the accurate determination of the protein"s behavior.

We hope our experiments can serve as a blueprint for calibrating reconstituted membrane protein systems and highlight the importance of selecting the appropriate membrane mimic.

LS3.P11
Transport regulation in trimeric secondary transporters studied by cryo-EM SPA

K. Urbansky[1], T. Hermann[1], M. G. Madej[1], C. Ziegler[1]

[1]University of Regensburg, Biophysics II, Regensburg, Germany

Our comparative structural investigations highlight the trimeric state as a pivotal element that connects secondary transporters of different families, unveiling similarities in how subtle modifications in trimeric architecture, influenced chiefly by lipid-protein interactions, predominantly affect the binding properties of coupling sodium ions. Trimeric transporters are a vital class of membrane proteins that facilitate the transport of various substrates across biological membranes. Their unique trimeric structure is essential for their function and response to cellular signals. The primary objective of our studies was to obtain high-resolution structures of different trimeric transporters, such as those from the Betaine-Choline-Carnitine Transporter (BCCT) family and the Solute Carrier Family 1 (SLC1). We explored the mechanistic parallels between BetP, a stress-regulated betaine transporter, and excitatory amino acid transporters (EAATs), focusing on the role of potassium ions (K^+) in destabilizing the inward occluded state to facilitate substrate release. This destabilization appears to be a crucial step in the transport process of both transporters. BetP is an exemplary model for understanding cellular stress adaptation mechanisms, primarily due to its robust coupling of betaine and sodium (Na^+) binding. GltPh, a prokaryotic homolog of mammalian EAATs, plays a similar role by transporting L-aspartate along with three Na^+ ions. Through new cryo-electron microscopy (cryo-EM) structural analyses, we demonstrated that betaine and Na^+ binding in BetP is intricately regulated by lipid interactions. These interactions significantly impact the trimeric structure of the transporter, highlighting the importance of the trimeric assembly in the function of both BetP and GltPh. An intriguing finding is the dual role of betaine in BetP function. While betaine serves as the primary substrate, it also acts as a folding agent for the sensory domain of BetP, effectively downregulating the transporter. Conversely, K^+ maintains the active state of BetP, suggesting a collaborative role between K^+ and Na^+ in transporter regulation. Specifically, the coordination of Na^+ in the Na2 site is closely linked to the overall trimeric architecture, as evidenced by the latest structure of a heterotrimeric BetP.

These findings enhance our understanding of the fundamental principles governing transport mechanisms in both prokaryotic and eukaryotic systems, offering insights into the evolutionary strategies employed to optimize transporter function under various physiological conditions.

LS3.P12
Structural investigation of agonist-dependent ion-selectivity of human Two-Pore Channel 2

B. Mayer[1], T. Specht[1], M. G. Madej[1], C. Ziegler[1]

[1]University of Regensburg, Biophysics II, Regensburg, Germany

Human Two-Pore Channel 2 (*Hs*TPC2) serves as an endolysosomal ion-channel integral to various physiological functions by regulating the intravesicular pH, organelle trafficking, and excitability through the conductance of sodium and calcium ions. *Hs*TPC2 demonstrates an intriguing agonist-dependent ion selectivity switch between these cations. The lipid $PI(3,5)P_2$ within the endolysosomal membrane induces sodium selectivity, whereas the second messenger NAADP facilitates calcium conductance. Recently, synthetic agonist that mimic the effect of PI(3,5)P2 and NAADP have been developed. Given HsTPC2's critical role in various diseases, including viral infections like Ebola and Sars-CoV-2, cancer progression, and neurological disorders such as Parkinson"s disease, these synthetic agonists are emerging drug candidates. Consequently, structural investigations into the interactions of potential drug candidates with *Hs*TPC2 are essential. We have solved several cryo-EM structures of *Hs*TPC2 in complex with a NAADP-mimicking, lipophilic agonists unveiling molecular insights into the unique selectivity switch mechanism of *Hs*TPC2 and highlighting the significant role of lipids in the functionality of this highly pathophysiologically relevant endolysosomal ion-channel.

LS3.P13
New insights into the palisade layer of the poxvirus core

J. Liu[1], S. Schaefer[2], S. Lehnung[2], S. Welsch[3], K. Bahrami[2], J. Krijnse-Locker[2,4], B. Turoňová[1]

[1]Max Planck Institute of Biophysics, Department of Molecular Sociology, Frankfurt a.M., Germany
[2]Paul Ehrlich Institute, Electron Microscopy of Pathogens Unit, Langen, Germany
[3]Max Planck Institute of Biophysics, Central electron microscopy facility, Frankfurt a.M., Germany
[4]Justus Liebig University Gießen, Giessen, Germany

The Mpox outbreak has raised a public health concern since 2022. the World Health Organization declared a Public Health Emergency of International Concern (PHEIC) in 2022 and in 2024. This underscores the urgent need for studying the virus structure. Vaccinia Virus (VACV), the prototype poxvirus, was studied extensively throughout the 20th century, and these findings ultimately contributed to the successful eradication of smallpox in the late 1970s. However, despite the extensive studies, the structure of the mature virus (MV) remains poorly understood. The asymmetric shape, size and compactness of the VACV causes a significant challenge for electron microscopy (EM) analysis, including cryoEM and cryo-electron tomography (cryoET). To address these limitations, we devised an optimized workflow for precise particle localization in tomograms and subsequent subtomogram averaging (STA). We built a semi-automate particle picking pipeline using template matching, deep-learning based surface segmentation and oversampling. By automatically segmenting the virus core, we significantly sped up the particle localization process and enhanced particle curation by removal of outlier particles and misaligned particles based on virions" surface curvature. We demonstrate our workflow on membrane-free cores obtained by detergent-stripping mature virions, both untreated and treated under different conditions to initiate transcription. We obtained structures constituting the palisade layer of VACV at sub nanometer resolution. By incorporating the AlphaFold2 and 3 predictions into the experimentally determined maps we identified the molecular composition of the palisade layer of VACV core for the first time.

LS 4: Cryo-EM and image analysis of macromolecules and molecular assemblies

LS4.02(inv)
Fluorescence and X-ray targeted volume electron microscopy

P. Ronchi[1]

[1]EMBL, Electron Microscopy Core Facility, Heidelberg, Germany

Although many volume electron microscopy (vEM) workflows have been developed, precise targeting of small volumes remains challenging. Here, we show 2 easy and reliable approaches to target vEM acquisition based on fluorescence or morphological features.

For the first one, the region/cell of interest is labelled with a fluorescence tag (a fluorescent protein expressed in a cell, for example). The strategy relies on fluorescence preservation during sample preparation and targeting based on confocal acquisition of the fluorescence signal in block. Trimming of the block exposes the cell of interest and laser branding of the surface after trimming creates landmarks to precisely position the Focused Ion Beam - SEM (FIB-SEM) acquisition.

If the cell of interest in a tissue cannot be identified with fluorescence, the second strategy takes advantage of X-ray imaging to identify anatomical features in the embedded sample. This imaging modality provides good contrast for EM-prepared samples and allows the visualization of morphological features that can be used as fiducials to predict the position of the ROI to be acquired by FIB-SEM or Serial Block Face - SEM.

LS4.03
From routine histology to electron microscopy – Pragmatic use of what is in stock

S. Kretschmar[1], S. Weiche[1], D. Wittig[2], M. Carido[2], P. Schäfer[2], J. Benjamin[2], M. Ader[2], T. Kurth[1]

[1]Technical University Dresden, Technology Platform, Core Facility Electron Microscopy and Histology, Dresden, Germany
[2]Technical University Dresden, Center for Regenerative Therapies Dresden (CRTD), Dresden, Germany

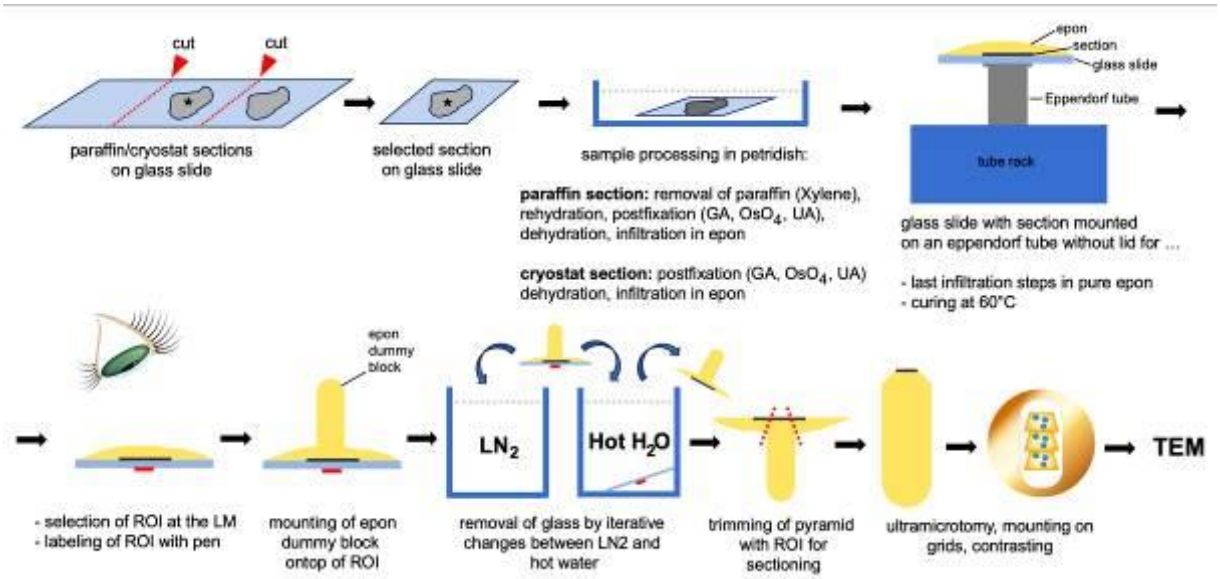
Sample preparation for electron microscopy normally involves sophisticated chemical fixation or cryopreservation followed by complex methods to preserve the ultrastructure of cells and tissues as close as possible to nature. Routine histology methods such as paraffin embedding or embedding for cryostat sectioning are different and usually not suitable for EM inspection. Especially the fixation is weaker and optimized for histology stains, immunohistochemistry or immunofluorescence. Therefore, EM preparation usually is performed on separate samples using EM specific methods (1-3). However, some samples are extremely rare, or the EM-analysis was not considered during the planning phase of a given project, or one would like to directly correlate imaging data from paraffin/cryostat sections to the corresponding ultrastructure. In this case, paraffin or cryostat sections could be further processed for EM (4,5). Here, we describe methods to process 2 um paraffin sections and 10 um thick cryostat sections mounted on microscope slides for TEM. The subcellular ultrastructure of paraffin sections is substantially obscured just leaving the shapes of the cells, the nuclei and a mostly coagulated cytoplasm with no membrane preservation whatsoever. Hence, paraffin sections are only of limited use for subsequent EM analysis. In contrast, the subcellular ultrastructure of cryostat sections can be quite comparable to routine EM preparations with nice membrane and organelle preservation. We tried different conditions: samples with and without immunofluorescence labeling (IF), or the use different detergents during IF. Indeed, most structures (mitochondria, ER, cell contacts etc.) were well preserved, if the samples were either not immunolabeled before the EM-preparation or if they were labelled using saponin as a detergent. Therefore, cryostat sections with stunning findings may still be further processed for ultrastructural analysis, rendering them suitable for a direct correlation of routine histology and EM using one and the same sample. This correlative approach is a versatile workflow to analyse tissue samples across scales.

Figure 1: Workflow to process histology sections mounted on glass slides for subsequent EM-analysis.

References:

1. Kurth T, Berger J, Wilsch-Bräuninger M, Kretschmar S, Cerny R, Schwarz H, Löfberg J, Piendl T, Epperlein HH (2010) Electron microscopy of the amphibian model systems *Xenopus laevis* and *Ambystoma mexicanum*. *Methods Cell Biol.* 96, 395-423
2. Tranfield EM, Fabig G, Kurth T, Müller-Reichert T (2024) How to apply the broad toolbox of correlative light and electron microscopy to address a specific biological question. *Methods Cell Biol.* 187, 1-41
3. Völkner M, Wagner F, Steinheuer LM, Carido M, Kurth T, Yazbeck A, Schor J, Wieneke S, Ebner L, Del Toro Runzer C, Taborsky D, Zoschke K, Vogt M, Canzler S, Hermann A, Khattak S, Hackermüller J, Karl MO (2022) HBEGF-TNF induce a complex outer retinal pathology with photoreceptor cell extrusion in human organoids. *Nat. Commun.* 13, 6183
4. Sousa AL, Rodrigues Loios J, Faisca P, Tranfield EM (2021) The Histo-CLEM workflow for tissues of model organisms. *Methods Cell Biol.* 162, 13-37
5. Carido M, Zhu Y, Benkner B, Cimalla P, Postel K, Karl MO, Kurth T, Paquet-Durand F, Koch E, Münch T, Tanaka E, Ader M (2014) Characterization of a mouse model with complete RPE loss and its use for RPE cell transplantation. *Invest. Ophthalmol. Vis. Sci*. 55, 5431-5444

Fig. 1


cut
cut
paraffin/cryostat sections on glass slide
selected section on glass slide
sample processing in petridish:
paraffin section: removal of paraffin (Xylene), rehydration, postfixation (GA, OsO4, UA), dehydration, infiltration in epon
cryostat section: postfixation (GA, OsO4, UA) dehydration, infiltration in epon
epon
section
glass slide
Eppendorf tube
tube rack
glass slide with section mounted on an eppendorf tube without lid for ...
- last infiltration steps in pure epon
- curing at 60°C
- selection of ROI at the LM
- labeling of ROI with pen
epon dummy block
mounting of epon dummy block ontop of ROI
LN2
Hot H2O
removal of glass by iterative changes between LN2 and hot water
trimming of pyramid with ROI for sectioning
ultramicrotomy, mounting on grids, contrasting
TEM

LS4.04
Optical near-field electron microscopy – A novel non-invasive widefield technique for prolonged super-resolution dynamic imaging

I. Zykov[1], H. Jafarian[1], W. G. Stam[2], P. Neu[2], A. Moradi[2], R. M. Tromp[3], M. Amaro[4], S. J. van der Molen[2], T. Juffmann[1]

[1]University of Vienna, Vienna, Austria
[2]Leiden University Medical Center, Leiden, Netherlands
[3]IBM, New York, NY, United States
[4]J. Heyrovsky Institute of Physical Chemistry, Prague, Czech Republic

Electron microscopy enables atomic-scale resolution in both dry and liquid environments. However, it has limitations due to the high energies the electrons transfer to the sample, which can induce structural damage. In contrast, light microscopy offers a non-destructive imaging tool but is limited in temporal or spatial resolution.

Optical Near-field Electron Microscopy (ONEM) [1] is a novel imaging technique that combines non-invasive visible light probing with a nanoscale resolution electron microscopy readout. In ONEM light interacts with the sample placed in the near-field proximity to the flat photocathode. The emitted electrons' flux corresponds to the local electric field intensities at the photocathode plane. These photoelectrons are subsequently imaged using an aberration-corrected Low Energy Electron Microscope. We present the first implementation of ONEM and benchmark its resolution capabilities on the sub-second scale. We then demonstrate proof-of-principle experiments in vacuum and environmental chamber. Measurements of nanophotonics samples show spatial resolution better than 30 nm. Electrochemistry measurements and live-cell imaging show ONEM's ability to image sample dynamics in a native environment over hours without damaging the system of interest. Being able to non-destructively image samples in situ, our new method can be applied to studying sensitive systems, e.g. protein dynamics in a lipid bilayer.

[1] Marchand, R. et al. Optical Near-Field Electron Microscopy. Physical Review Applied 16,014008 (2021).

LS4.05
Integrated correlative light-sheet and X-ray microscopy for multi-scale imaging of small and large organisms

N. Fuchs[1], J. Mayer[2], K. Kairiss[1], V. Weinhardt[1]

[1]Centre for Organismal Studies Heidelberg, Heidelberg, Germany
[2]Bruker Luxendo, Barcelona, Spain

Biological systems are of extreme complexity, spanning multiple scales from single cells to organisms. Understanding both structures and molecular compositions across various sample sizes is crucial. Light-sheet fluorescence microscopy enables low-phototoxicity imaging of targeted molecules, while X-ray microtomography (microCT) provides 3D structural information. Integrating these techniques, we develop a correlative imaging pipeline for high-resolution analysis and apply it to the teleost fish *Oryzias latipes* (medaka).

The aim is to develop a light-sheet and X-ray microscopy workflow for imaging of medaka embryos and larvae. To address laser penetration limitations in larger samples, we incorporate tissue-clearing methods.

Fluorescently labeled medaka was imaged using a light-sheet miltiview microscope (MuVi SPIM). To enhance optical penetration, we tested clearing protocols, including CUBIC[1], FOCM[2], and DeepClear[3]. Their compatibility with phosphotungstic acid[4] (PTA) staining for microCT was evaluated. After fluorescence imaging, samples were dehydrated, stained with PTA, and scanned using microCT.

Previously, we visualized developmental markers in small medaka embryos without tissue clearing[5]. Our results show tested clearing protocols were compatible with PTA staining, allowing workflow integration (Fig. 1). Using this approach, we visualized vasculature, postmitotic neurons, and mitotic cells in medaka upon clearing.

The new light-sheet and X-ray microscopy pipeline enables multimodal imaging of medaka across developmental stages. By applying tissue-clearing techniques, we overcame optical limitations and improved molecular marker visualization in larger specimens. This approach expands correlative imaging applications in developmental biology, and disease modeling, bridging high-resolution cellular imaging with whole-organism structural analysis.

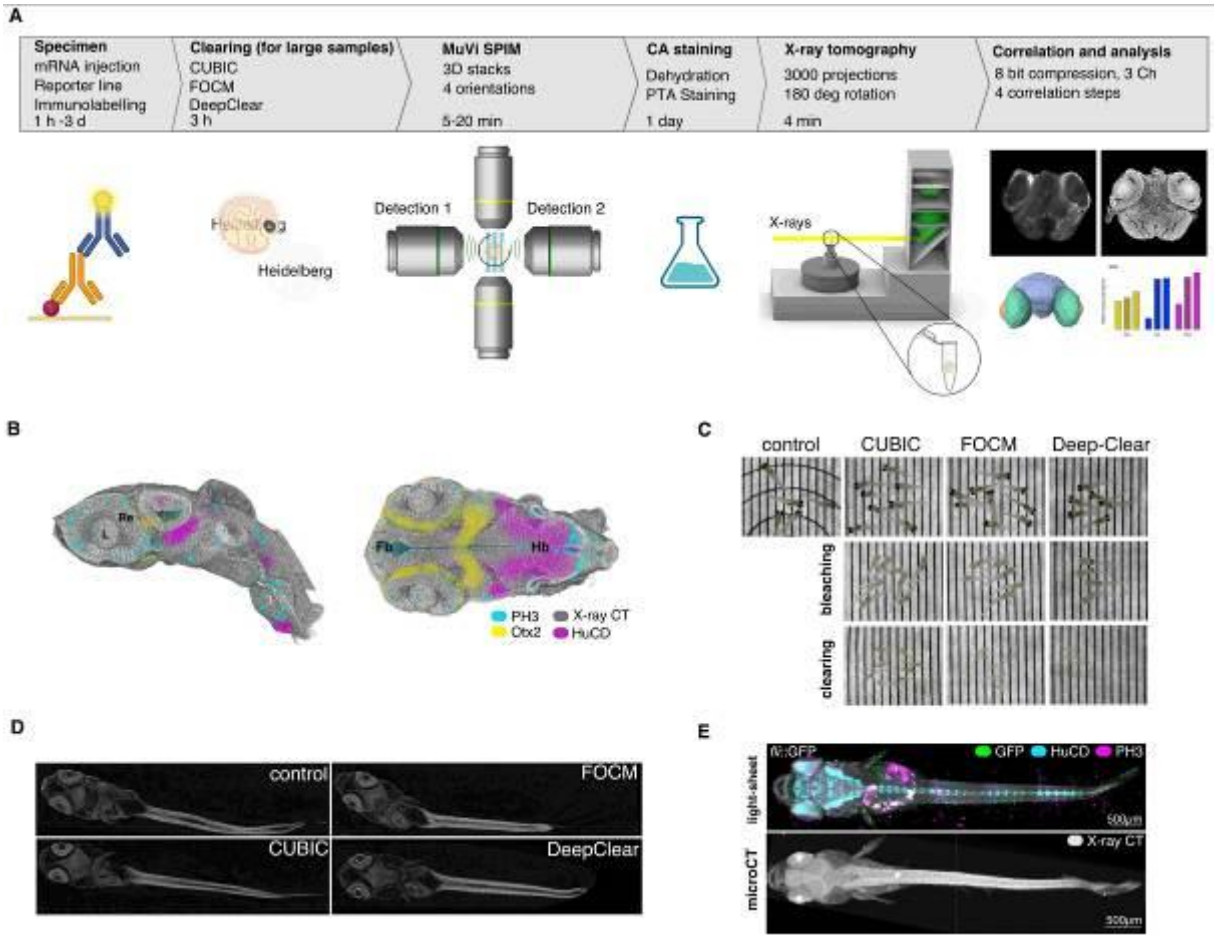
Figure 1. (A) Workflow: labeled specimens are cleared, imaged with MuVi SPIM, dehydrated, stained with PTA, and scanned with microCT. **(B)** Neuronal markers Otx2, HuC/D, and mitotic marker PH3 in a medaka embryo. **(C)** Evaluation of tissue-clearing solutions and **(D)** PTA staining in medaka larvae. **(E)** Imaging of fluorescence and X-ray microCT on *fli::GFP* larva[6].

References

1. Susaki EA, Tainaka K, Perrin D, Yukinaga H, Kuno A, Ueda HR. Advanced CUBIC protocols for whole-brain and whole-body clearing and imaging. *Nature Protocols 2015 10:11*. 2015;10(11):1709-1727. doi:10.1038/nprot.2015.085
2. Zhu X, Huang L, Zheng Y, et al. Ultrafast optical clearing method for three-dimensional imaging with cellular resolution. *Proc Natl Acad Sci U S A*. 2019;166(23):11480-11489. doi:10.1073/pnas.1819583116
3. Pende M, Pende M, Vadiwala K, et al. A versatile depigmentation, clearing, and labeling method for exploring nervous system diversity. *Sci Adv*. 2020;6(22). doi:10.1126/sciadv.aba0365

4. Metscher BD. MicroCT for developmental biology: A versatile tool for high-contrast 3D imaging at histological resolutions. *Developmental Dynamics*. 2009;238(3):632-640. doi:10.1002/DVDY.21857
5. Kairišs K, Sokolova N, Zilova L, et al. Visualisation of gene expression within the context of tissues using an X-ray computed tomography-based multimodal approach. *Sci Rep*. 2024;14(1). doi:10.1038/s41598-024-58766-5
6. Schaafhausen MK, Yang WJ, Centanin L, et al. Tumor angiogenesis is caused by single melanoma cells in a manner dependent on reactive oxygen species and NF-κB. *J Cell Sci*. 2013;126(Pt 17):3862-3872. doi:10.1242/JCS.125021

Fig. 1



LS4.06
Correlated cryo-EM and cryo-FIB-SIMS imaging enables sub-cellular chemical mapping in bacteria

H. Ochner[1], B. Isbilir[1], Y. Zhang[1], S. Blasche[2], D. Scheidweiler[2], Z. (. Wang[1], K. Patil[2], T. Bharat[1]

[1]MRC Laboratory of Molecular Biology, Cambridge, United Kingdom
[2]University of Cambridge, MRC Toxicology Unit, Cambridge, United Kingdom

Electron cryomicroscopy (cryo-EM) provides high-resolution images detailing the spatial structure of biological samples [1], however, there is no direct way of inferring the chemical composition of objects observed in an electron micrograph. As such information is highly relevant for the identification and localization of specific components within cells, a correlative approach providing both chemical and spatial information is needed [2]. To integrate spatial and chemical analysis into a single workflow at cryogenic temperatures, we combine spatial imaging by cryo-EM with focused ion beam (FIB) milling and chemical imaging by secondary ion mass spectrometry (SIMS) of the ions created during the FIB milling process [3]. Using bacterial cells as a test system, we were able to correlate and overlay cryo-EM and FIB-SIMS data, showing that the technique allows the mapping of elemental and small-molecule ions within a cellular sample prepared in a near-native state by vitrification. Specifically, we could show that the method can be used to study the uptake of fluorinated compounds by bacterial cells. To target larger molecules of biological interest, such as specific proteins, we are employing metal-based labelling strategies of cellular macromolecules to aid localisation in SIMS imaging. As the technique provides access to the three-dimensional sample volume and is widely applicable to a variety of samples, ranging from single cells to tissue-like samples such as FIB-milled lamellae, it is a promising approach for studying the spatial and chemical properties of biological specimens within an integrated workflow.

[1] Nogales, E. & Mahamid, J. (2024) Nature, 628: 47-56.

[2] Ochner, H. & Bharat, T.A.M. (2023), Structure, 31: 1297-1305.

[3] Pillatsch, L. et al. (2019), Progress in Crystal Growth and Characterization of Materials 65: 1–19.

LS4.P02
Enhanced ROI detection and accurate correlation in cryo-lamella preparation using integrated FLM in cryo-FIB/SEM

S. Záchej[1], D. Pinkas[2], J. Šmídová[3], V. Filimonenko[2,4], M. Smeets[5], W. Teunisse[5]

[1]Tescan GmbH, R&D, Brno, Czech Republic
[2]Institute of Molecular Genetics of the Czech Academy of Sciences, Prague, Czech Republic
[3]TESCAN Group, Product Marketing, Brno, Czech Republic
[4]Department of Biology of the Cell Nucleus, Institute of Molecular Genetics, Czech Academy of Sciences, Prague, Czech Republic
[5]Delmic, Delft, Netherlands

Cryo-lamella preparation for cryo-electron tomography (cryo-ET) demands precise and efficient workflows to generate ultrathin specimens while preserving regions of interest (ROIs) within the sample. Traditional workflows often face challenges due to sample transfer steps between fluorescence microscopy (FLM) and cryo-focused ion beam (cryo-FIB) systems, introducing risks of ice contamination, devitrification, and mechanical stress. These steps can result in loss of targeted regions or sample degradation, impacting the quality and reproducibility of results.

A challenge in cryo-FIB milling is accurately targeting regions of interest (ROIs), which can be difficult to locate, particularly in complex or heterogeneous samples. While fluorescence labeling and cryo-fluorescence light microscopy (cryo-FLM) can aid in targeting ROIs, conventional standalone FLM setups introduce handling steps that increase the risk of ice contamination, devitrification, and mechanical damage.

The novel combination of the TESCAN AMBER cryo- FIB/SEM with a fully integrated high quality FLM Delmic"s METEOR system allows smooth and accurate 3D correlation of FLM, FIB and SEM data. Furthermore, the integration of the FLM significantly reduces handling and ice contamination. Additionally, a full collision model allows safe control of the microscope ensuring novel users can adapt the technique quickly. The high-end fluorescent light microscope provides excellent resolution and brings background noise to an absolute minimum allowing researchers to image and mill challenging samples.

LS4.P03
Correlative light, EDX and electron microscopy of the p62 autophagy cargo receptor

S. Berkamp[1], P. H. Lu[2], L. Jungbluth[1], A. Katranidis[1], S. Mostafavi[1], A. Brech[3], R. E. Dunin-Borkowski[2], C. Sachse[1]

[1]Forschungszentrum Jülich GmbH, ER-C-3, Jülich, Germany
[2]Forschungszentrum Jülich GmbH, ER-C-1, Jülich, Germany
[3]Oslo University Hospital, Oslo, Norway

Introduction:

When cells have aggregated proteins, excess lipid droplets or malfunctioning organelles, they can be recycled via selective autophagy. This cargo is marked with a poly-ubiquitinated tag and subsequently recognized by cargo receptors which in turn recruit a double phospholipid bilayer, also called autophagosome, and fuse this with the lysosome for degradation. The most studied cargo receptor is called p62/SQSTM1. In our lab we have solved the single particle structure and described that it forms polymers *in vitro* and phase-separates to form biological condensates.

Objectives:

We aim to understand the formation of these intracellular structures by comparing the *in vitro* structure of p62 as well as the *in situ* structural organization of p62 with cellular cargo.

Materials and Methods:

To characterize these protein condensates inside the context of the cell, we have used correlative light and electron microscopy, super resolution confocal microscopy as well as energy-dispersive X-ray spectroscopy.

Results:

mCherry-p62 was expressed in human RPE-1 cells. Next, the cells were positioned on an EM grid and thinned to ~150nm with a cryo-FIB-SEM machine and tilt series recorded on areas positive for p62 in a cryo-TEM. When we reconstructed 3D volumes of the regions of the cell where p62 was present with cargo, and observed perfectly spherical cellular structures of approximately 520 nm in diameter. These p62 structures all had a homogeneous core and a very electron-dense coat of varying in thickness between 4 - 27 nm. Next, the elemental composition of the core and coat of this previously uncharacterized structure was analyzed by energy-dispersive X-ray spectroscopy, in a correlative manner. These structures had a core that was carbon enriched over the nearby cytosol and nitrogen and oxygen depleted. Based on this elemental signature, it is highly likely that the core is a cellular lipid droplet. The coat had a significant amount of calcium, phosphorus and magnesium, well beyond that of the cytosol. Using super resolution confocal microscopy, we showed that p62 was present surrounding this structure. Analysis of purified p62 filaments in the presence of calcium ions shows that the p62 filaments bundle, the function and cellular origin of these calcium ions is unknown.

Conclusion:

We were able to study the *in situ* cargo recognition of the p62 autophagy cargo receptor. We observed the protein enwrapping a cellular lipid droplet. This lipid droplet was also surrounded by a thick layer of calcium, phosphorus and magnesium. The function of these ions is unknown, but their importance in autophagy initiation had been observed before. Additionally, we were able to establish a correlative light, EDX and electron microscopy pipeline that allows observation of a fluorescent protein marker,

elemental analysis and a high-resolution 3D reconstruction of the cell, all in a correlative manner, giving an extra dimension to previously described workflows.

LS4.P04
Integrating CARD-FISH and SEM for characterizing Patescibacteria in complex environmental microbial communities

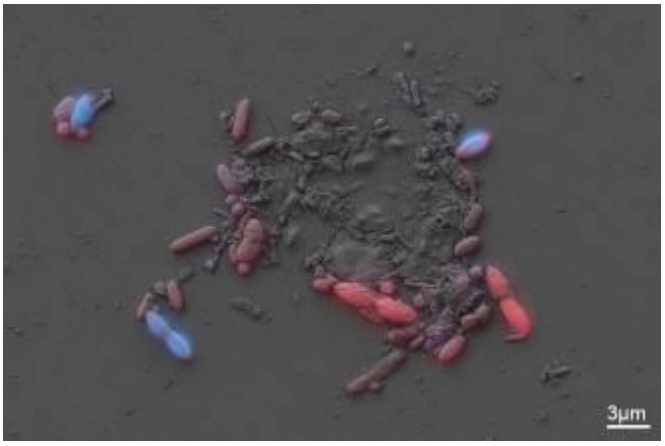
I. Banas[1,2], A. R. Soares[1,2], E. Baka[3], A. Táncsics[3], A. J. Probst[1,2,4]

[1]University Duisburg-Essen, Environmental Metagenomics, Essen, Germany
[2]University Duisburg-Essen, Centre of Water and Environmental Research, Essen, Germany
[3]Hungarian University of Agriculture and Life Sciences, Department of Molecular Ecology, Gödöllő, Hungary
[4]University Duisburg-Essen, Center of Medical Biotechnology, Essen, Germany

The majority of microorganisms escape isolation in pure cultures and remain largely understudied in their physiology. Patescibacteria, a highly diverse bacterial phylum that represents a major portion of prokaryotic life"s diversity, are hypothesized to thrive in symbiotic or parasitic lifestyles, given their genome and cell sizes, paired with limited metabolic capacities (Parks et al. 2017, Brown et al. 2017). Recent studies suggest that Patescibacteria are entangled in community-wide metabolic processes and can act as carbon sinks in highly productive ecosystems such as hydrocarbon-contaminated groundwater (Figueroa-Gonzalez et al, 2020). Here, we investigate a hydrocarbon-contaminated groundwater site in Hungary, which is highly enriched in Patescibacteria, as model a site for studying patescibacterial physiology via metagenome-informed microscopy approaches.
This study aims at identifying Patescibacteria hosts in environmental samples using fluorescence *in situ* hybridization (FISH), thus light microscopy, correlated with scanning electron microscopy (CLEM) for taxonomic identification paired with physiological characterization. By integrating CLEM with metagenome-recovered 16S rRNA FISH probes, we aim to shed light on possible cell-cell interactions between Patescibacteria and their hosts. These interactions will provide key insights into ecological roles of Patescibacteria and their potential metabolic interactions. The main challenges to overcome include: Low cell concentrations in environmental samples, background interference from sediment particles and weak signal intensity due to low ribosomal content within Patescibacteria cells.
To label microorganisms of interest, 16S rRNA CARD-FISH was employed as the primary method. Protocol optimization was performed using the general bacterial probe (EUB338). To address sediment background and improve labeling efficiency, our protocol included sonification for sediment removal, followed by chemical permeabilization. Once FISH data acquisition was complete, samples underwent SEM preparation involving osmium staining, acetone dehydration, and critical point drying. SEM imaging was then correlated with fluorescence microscopy data to evaluate microbial cell sizes more accurately and to identify ultra-small cells (<800 nm).
Sonification significantly improved the detection of prokaryotic cells under the microscope, with minimal impact on cell morphology. Using the EUB338 probe, we successfully labeled cells with sizes below 800 nm, consistent with CPR characteristics. These ultra-small cells were frequently observed in close spatial proximity to larger microbial cells, suggesting potential symbiotic, parasitic or syntrophic interactions. Additionally, SEM imaging provided detailed structural characterization, enabling assignment of fluorescence signal to individual cells, precise validation of cell sizes, and spatial arrangements.
Metagenomically-informed microscopy studies are an effective tool for investigating environmental cell-to-cell interactions. This study demonstrates the power of CLEM in resolving microbial community interactions, even for ultra-small bacteria. Our results open the gate for groundbreaking correlative microscopy in studying cell-cell interactions and physiology of Patescibacteria, the most enigmatic phylum on our planet.

Figure 1: CLEM image of a hydrocarbon-contaminated sample. Red: CARD-FISH EUB338 probe (Alexa 594); blue DAPI stain.

Fig. 1



LS4.P05
Development of a cryo-workflow for the preparation of the lubricated hinge-joints of beetles and other intricate biological samples

C. F. Pichler[1], M. Mail[2,3], H. Hölscher[1,4], T. Scherer[2,4]

[1]Karlsruhe Institute of Technology, Institute of Microstructure Technology (IMT), Eggenstein-Leopoldshafen, Germany
[2]Karlsruhe Institute of Technology, Institute of Nanotechnology, Eggenstein-Leopoldshafen, Germany
[3]Tescan GmbH, Dortmund, Germany
[4]Karlsruhe Institute of Technology, Karlsruhe Nano Micro Facility (KNMFi), Eggenstein-Leopoldshafen, Germany

The common multistep process for the preparation of biological samples for the electron microscope, including the stabilization of the sample in ethanol, critical point drying and sputtering of the sample, represents an enormous invasion into the biological system. In specific cases, this process can lead to information loss. In a recent study [1], we presented the tribological properties of the joint cuticle and lubricant, which can be found in beetle joints with the help of an intricate friction force microscopy method. The limited amounts of lubricant make the analysis with established methods quite challenging. Due to the open nature of the insect joints, the lubricant easily gets detached, dissolved and lost during the common sample preparation, making it impossible to detect and analyze. In our work, the beetle"s hinge-joint and lubricant were examined in their freshly frozen state with a multi(cryo)modal approach preserving the natural state of the sample. We present a detailed look into the joint tissue with the Cryo-FIB and manipulation of the lubricant with the *in-situ* nanomanipulator.

[1] Pichler, C.F.; Thelen, R.; van de Kamp, T.; Hölscher, H.; Friction Coefficient Evolution of Drying Lubricant in the Joints of Beetles by Friction Force Microscopy. *Tribol Lett* **73**, 31 (2025). https://doi.org/10.1007/s11249-025-01963-8

LS4.P06
NanoCT and SEM for 3D structural and mechanical characterization of lightweight seed samples

R. Debastiani[1], I. Tesari[1], T. Scherer[1]

[1]Karlsruhe Institute of Technology, Eggenstein-Leopoldshafen, Germany

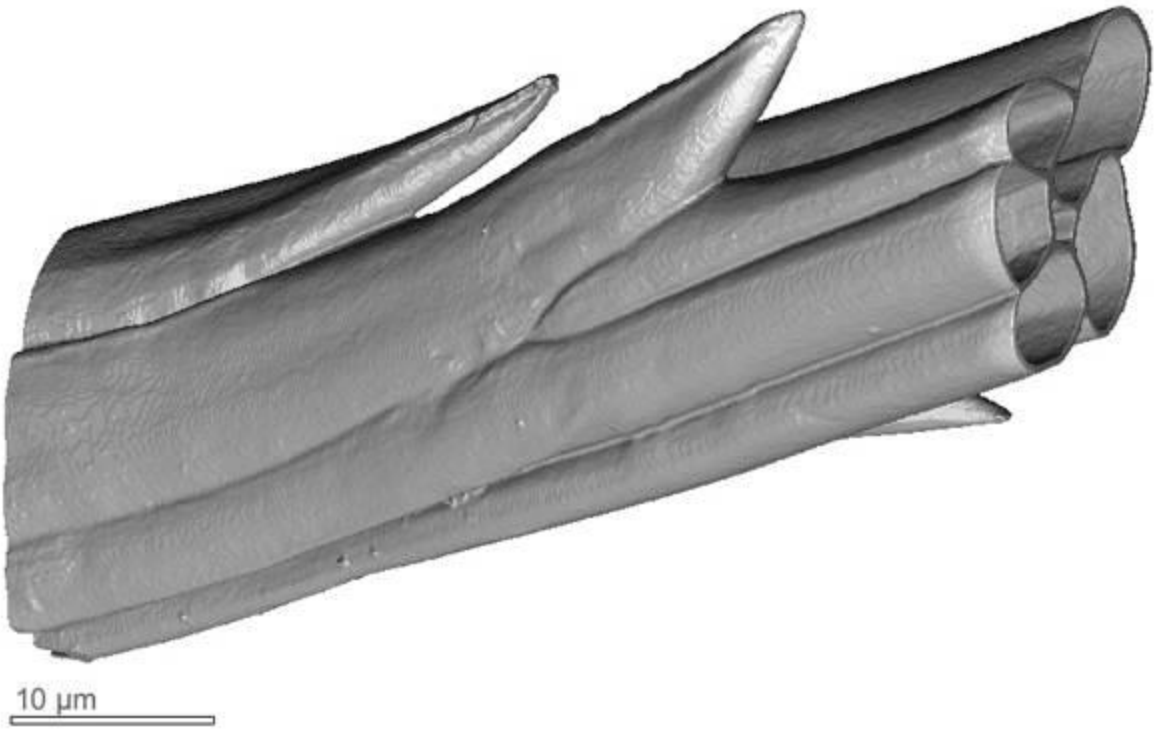
Lightweight seeds are characterized by their low density and specialized adaptation for wind dispersal. By analyzing their structural features, such as porosity, cell wall thickness and materials distribution and orientation, it is possible to understand the influence on their mechanical properties. These findings can encourage the development of novel bioinspired materials.

With an intermediate resolution between light and electron microscopes, the commercial lab-based nanoCT (Xradia Ultra 810) is a versatile new tool for the 3D structural characterization of samples. With its low energy X-ray source (Cr source, 5.4 keV) and Zernike phase contrast, the setup is ideal for analyzing low-density samples, such as polymers and biological samples, with resolution down to 50 nm. In addition, a mechanical in situ testing setup can be used during the experiments, allowing for the observation of microstructural changes as a function of time and mechanical load.

Combining scanning electron microscopy (SEM) with X-ray nanotomography (nanoCT), the surface and inner structural characterization of the samples was carried out with pixel size up to 10 nm for 2D and 64 nm for the 3D images (Figure 1). NanoCT images were acquired in phase contrast due samples low absorption, over 180° with an exposure time and number of projections varying for each sample. The reconstructed and segmented 3D data is then used for mechanical simulation and Finite-Element Analyses with ANSYS.

Figure 1: Volumetric reconstruction of the lightweight seed sample.

Fig. 1



LS4.P08
Application of multimodal techniques for assessing fruit sticker alteration during composting

M. Groß[1], M. Mail[2,3], O. Wrigley[1], R. Debastiani[2,3], T. Scherer[2,3], W. Amelung[1], M. Braun[1]

[1]Universität Bonn, Institute of Crop Science and Resource Conservation, Bonn, Germany
[2]Karlsruhe Institute of Technology, Institute of Nanotechnology, Eggenstein-Leopoldshafen, Germany
[3]Karlsruhe Institute of Technology, Karlsruhe Nano Micro Facility (KNMFi), Eggenstein-Leopoldshafen, Germany

Plastic contamination in compost is a known entry pathway for plastics into soil, often resulting from improper waste disposal. A lesser-known source is plastic fruit and vegetable stickers, which remain in organic waste despite sorting processes in composting plants. However, little is known about their alteration during industrial composting, particularly regarding surface degradation, structural changes, and microbial colonization.

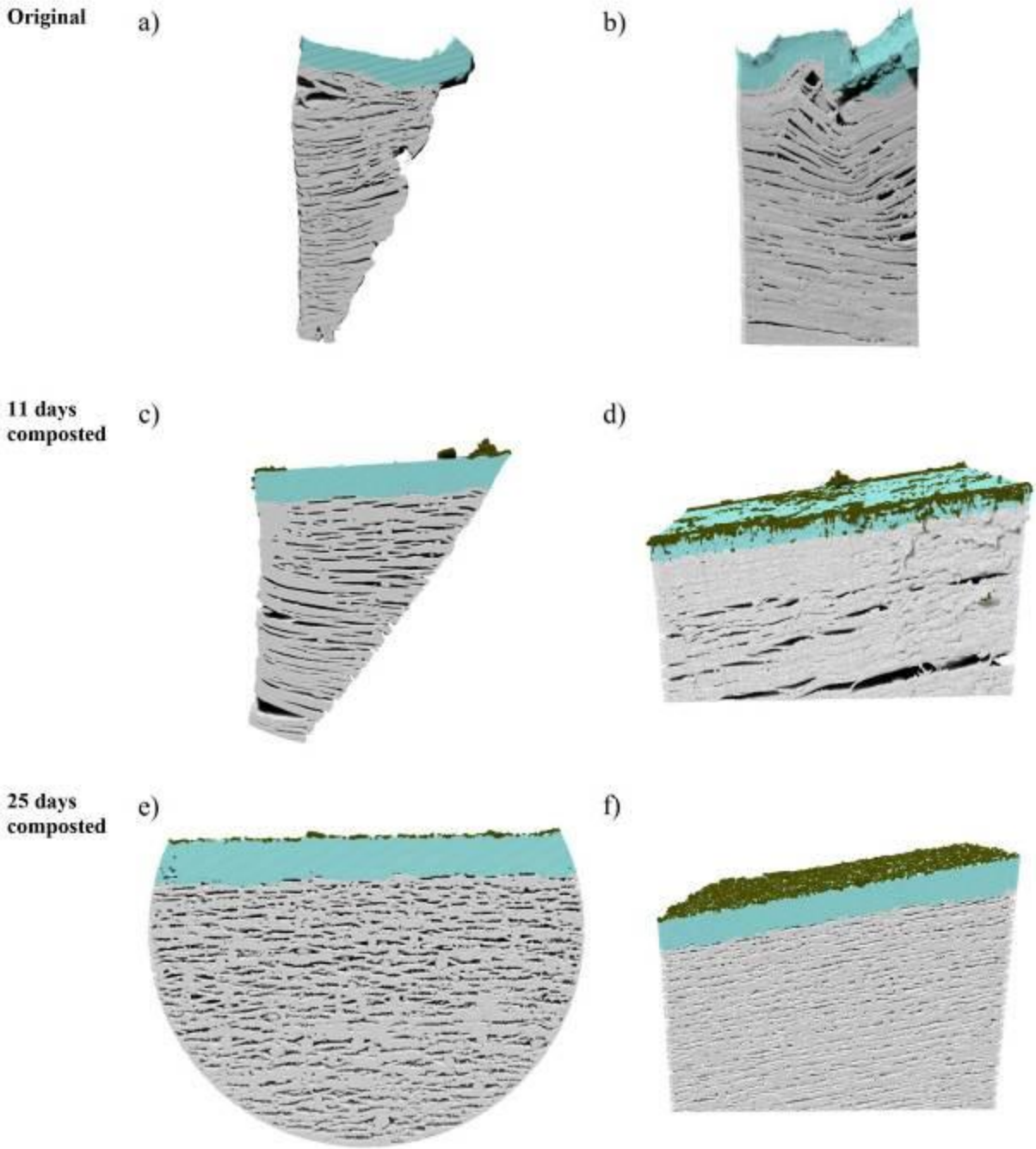
This study aimed to (i) assess surface and structural changes in fruit stickers during composting, (ii) determine when these changes and microbial colonization occur, and (iii) investigate the formation and detachment of smaller plastic fragments.

Polypropylene fruit stickers were placed on banana peels in an industrial composting plant and sampled after pre-rotting (11 days) and main rotting (25 days), alongside non-composted controls. Samples were analysed for surface and structural modifications using scanning electron microscopy (SEM), Fourier-transform infrared spectroscopy (FTIR), and micro- and nano-X-ray computed tomography (CT) combined with deep learning approaches.

All composted stickers exhibited surface degradation, including cracks, irregularities, and microbial colonization on both sides, visible from day 11. Structural analysis revealed an increase in pore volume from 16.7% to 26.3% and a rise in the carbonyl index, indicating chemical changes. Micro-CT imaging further showed large adhesions penetrating the sticker surface. By day 25, delamination was observed, suggesting sticker degradation and the potential release of microplastic fragments.

Figure:Orthographic 3D projections of the data obtained by nano-CT (scale bar: 10 µm). Cross section of the segmentation results of the original (a,b), the 11 day composted (c,d), and the 25 day composted (e,f) sticker. Dark green, turquoise, and white colors refer to the attachments, the upper part, and the lower part of the sticker, respectively.

Fig. 1



LS4.P09
Correlative multimodal approaches for evaluating microplastic weathering in european agricultural soils

M. Groß[1], W. Amelung[1], R. Debastiani[2,3], L. Hennig[1], R. Hurley[4], M. Mail[2,3], V. Martínez-Hernández[5], L. Nizzetto[4], P. E. Redondo-Hasselerharm[5], T. Scherer[2,3], S. Selonen[6], H. Soinne[7], M. Braun[1]

[1]Universität Bonn, Institute of Crop Science and Resource Conservation, Bonn, Germany
[2]Karlsruhe Institute of Technology, Institute of Nanotechnology, Eggenstein-Leopoldshafen, Germany
[3]Karlsruhe Institute of Technology, Karlsruhe Nano Micro Facility (KNMFi), Eggenstein-Leopoldshafen, Germany
[4]Norwegian Institute for Water Research (NIVA), Oslo, Norway
[5]IMDEA Water Institute, Madrid, Spain
[6]Finnish Environment Institute, Helsinki, Finland
[7]Natural Resources Institute Finland, Helsinki, Finland

Soils are considered to be a major sink for microplastics (MPs) in the environment, with the application of agricultural mulch films being one of the most important pathways to enter soil. Once in the soil, plastic particles are exposed to various environmental factors leading to MP ageing, characterised by morphological and structural changes. Soil aggregates can play a crucial role for these degradation processes, potentially preserving MP within them.

Therefore, the aim of this study was to investigate the degradation differences between MPs originating from mulching films inside and outside of soil aggregates over a two-year exposure period in European agricultural topsoils.

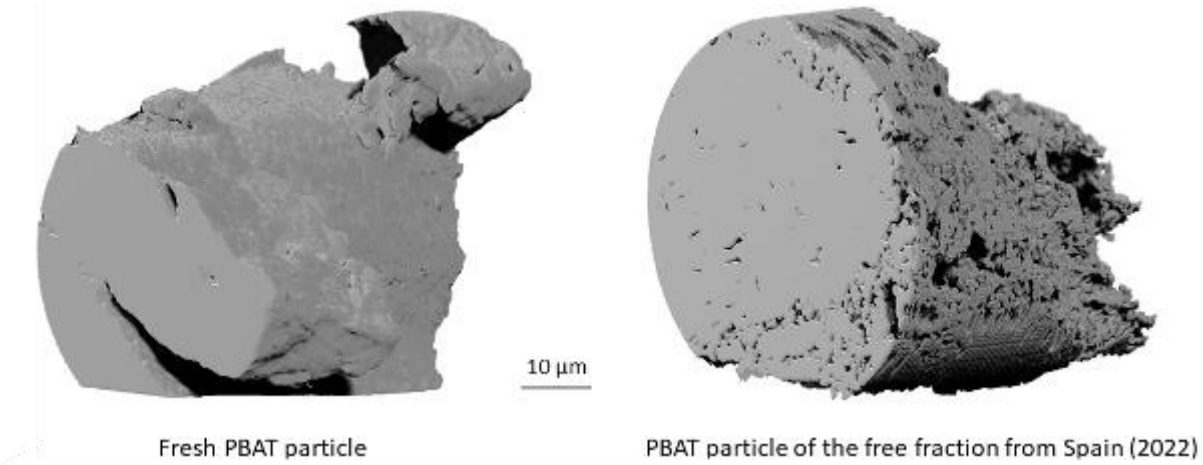
To do so, we analysed samples from field plot trials in Finland, Spain and Germany where MPs (< 1 mm) derived from recycled low-density polyethylene and starch - polybutylene adipate terephthalate (PBAT) films were incorporated into topsoil (0-10 cm) at a concentration of 0.05%. Barley was grown there in two consecutive years and soil samples were taken immediately after harvest.

Free MP and MP which was embedded in soil aggregates were separated using a combination of plastic extraction and aggregate separation techniques, ensuring that these methods did not alter the surface or structure of the MPs. The degradation state was assessed using a correlative multimodal approach, including scanning electron microscopy coupled with energy dispersive X-ray spectroscopy (SEM-EDX), nano-computed tomography (nano-CT) and Fourier transform infrared spectroscopy (FTIR).

Exposure to soil resulted in significant ageing effects of MPs, such as surface cracking, increased oxygen content and the formation of new functional groups, a higher proportion of pores, and the attachment of microorganisms. Notably, the ageing effects were more pronounced for MPs outside the aggregates compared to those embedded in the aggregates. In addition, differences were observed that were influenced by the specific conditions in each country. The results of this study reflect the complexity of environmental ageing, which depends on the soil conditions in each country. In conclusion, aggregates protect MPs from degradation, favouring plastic accumulation in the soil.

Figure: Orthographic 3D projections of the data obtained by nano-CT. Segmentation results of the fresh starch-PBAT particle (left) and the one-year-old starch-PBAT particle of the free soil fraction (right).

Fig. 1



Fresh PBAT particle

PBAT particle of the free fraction from Spain (2022)

LS4.P10
Advancing integrated cryo-fluorescence imaging for fast, reliable and high throughput cryo-ET lamella production

M. Smeets[1], D. Daviran[1], W. Teunisse[1]

[1]Delmic, Delft, Netherlands

Correlative cryo-FIB milling is a powerful sample preparation technique for in situ cryo electron tomography (cryo-ET). Using this technique, vitrified cells can be thinned down and cellular components can be directly visualized in their native context at near-atomic resolution. In recent years several solutions have been proposed to simplify the technique by integrating fluorescent microscopes in the cryo-FIB [1-4]. However, it remains challenging to accurately target the region of interest (ROI) while maintaining a high throughput workflow. Here we present a novel version of Delmic"s high-quality integrated fluorescent microscope, called METEOR 2.0, designed to sustain high throughput while enabling precise targeting of the ROI.

The field of view was expanded to over 8 times of the original, resulting in a 266 µm by 266 µm field of view with a 50x objective (see Figure 2). This allows the user to see more context in a single frame and significantly speeds up overview mapping of the sample while maintaining excellent resolution and image quality. We also optimized the optical path providing 44% higher power density at the sample location and 3 times higher signal intensity in the final image (see Figure 1). Additionally we redesigned the filter wheel providing 2 additional filter slots and significantly reducing the time needed to switch between filter positions.

Using workflow examples, we will showcase how the new features of METEOR 2.0 aid high-throughput workflows such as on-grid lamella preparation from plunge frozen cells and serial lift-out sectioning of high-pressure frozen organisms. Taken together, we show that METEOR 2.0 is a significant leap forward to facilitate groundbreaking research in structural biology and gain deeper insights into the organization and function of cellular architecture.

1. Smeets et al. (2021). Micros Today, vol. 29, no. 6, pp. 20–25.

2. Boltje et al. (2022). eLife, vol. 11

3. Wang et al. (2023) Nature Methods, Vol. 20 no. 2 pp. 276-283

4. J. Yaeng et al. (2023) Microscopy and Microanalysis, vol. 29, no. 1, pp-1055-1057

Fig. 1

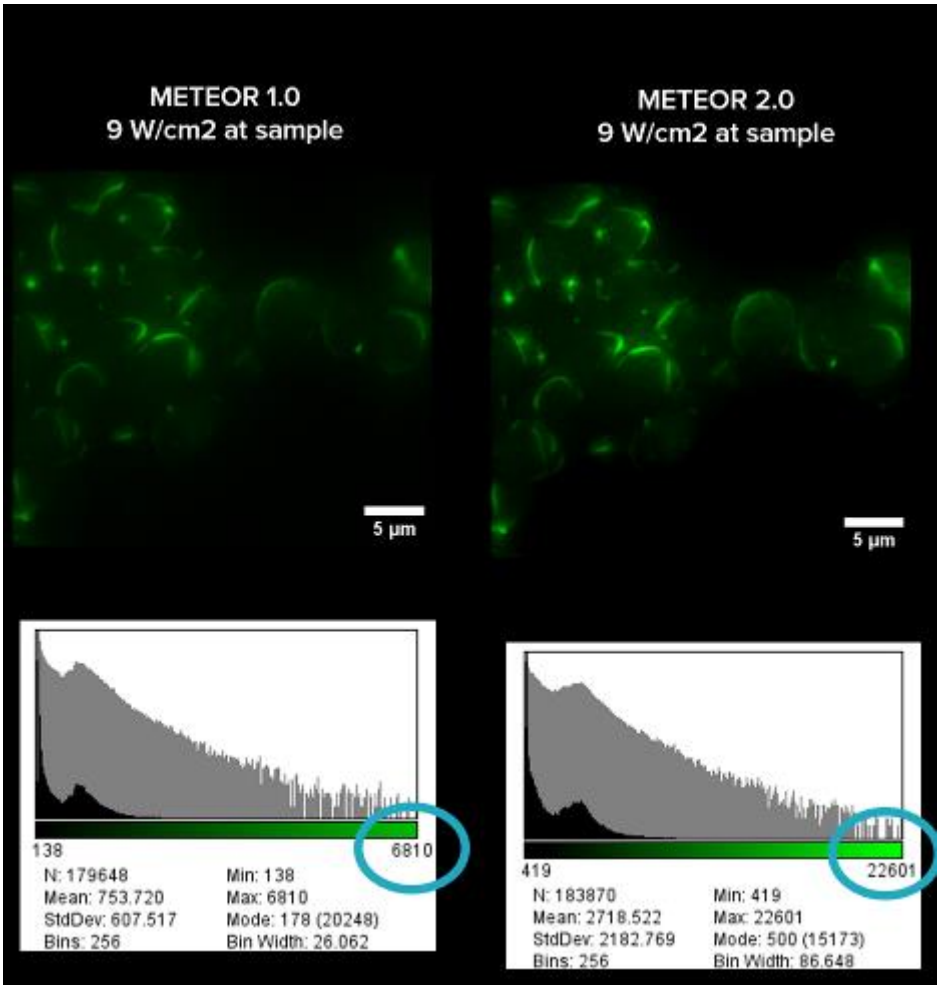
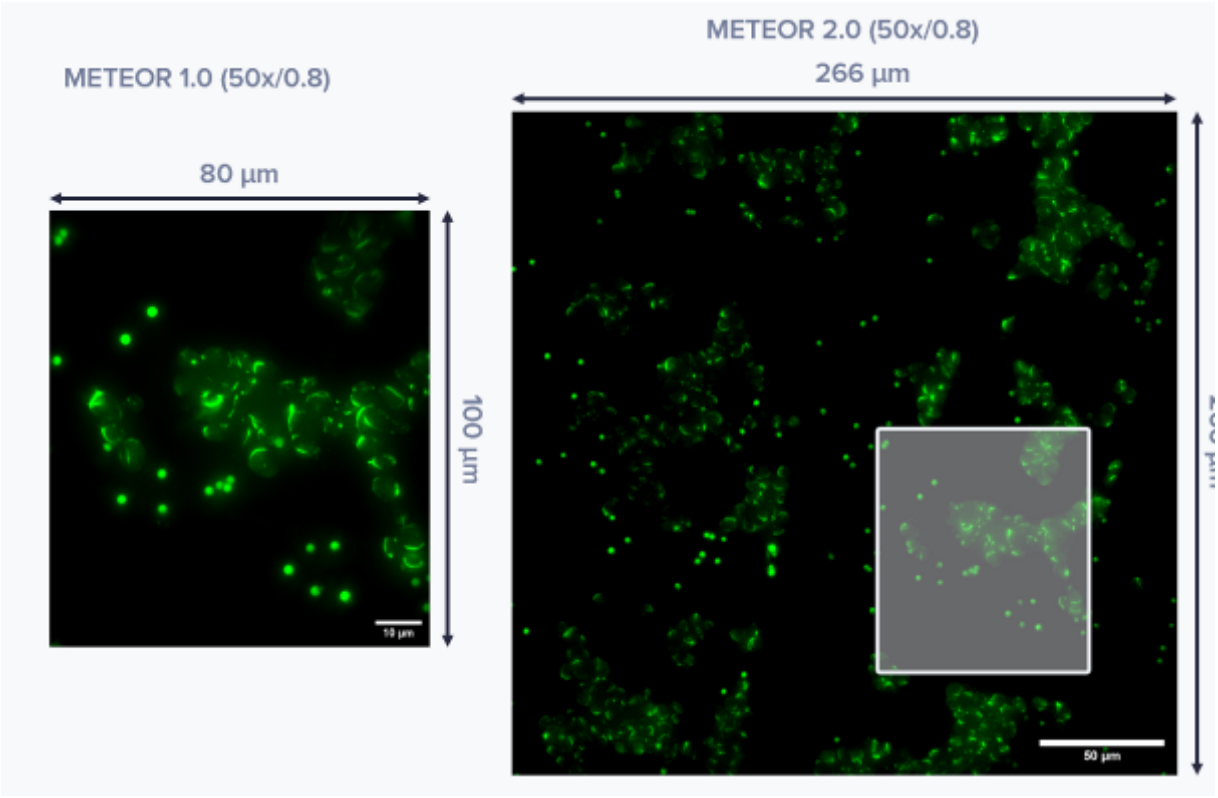

METEOR 1.0
9 W/cm2 at sample
5 µm
138
6810
N: 179648
Mean: 753.720
StdDev: 607.517
Bins: 256
Min: 138
Max: 6810
Mode: 178 (20248)
Bin Width: 26.062
METEOR 2.0
9 W/cm2 at sample
5 µm
419
22601
N: 183870
Mean: 2718.522
StdDev: 2182.769
Bins: 256
Min: 419
Max: 22601
Mode: 500 (15173)
Bin Width: 86.648

Fig. 2



LS4.P11
Towards a correlative microscopy workflow to identify and image virus particles in aerosol samples

M. Schmidt[1], D. Eckstein[1,2], R. Kallies[1,3], A. Bernstein[1], H. H. Richnow[1], A. M. Nasrabadi[4], H. Herrmann[4], M. Maier[2], N. Ghanem[1]

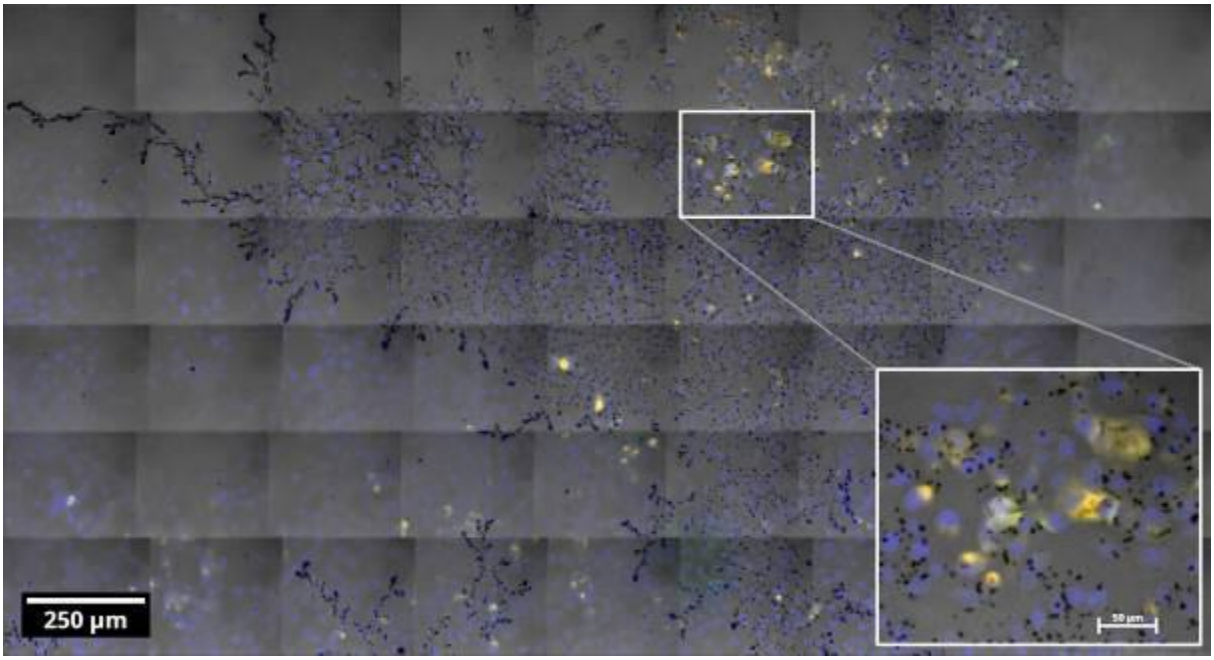
[1]Helmholtz-Centre for Environmental Research, Technical Biogeochemistry, Leipzig, Germany
[2]Universitätsklinikum Leipzig, Institut. f. Med. Mikrobiologie und Virologie, Leipzig, Germany
[3]German Environment Agency, Section Microbiological Risks, Berlin, Germany
[4]Leibnitz-Institute for Tropospheric Research, Atmospheric Chemistry, Leipzig, Germany

COVID-19 has highlighted the impact of airborne infectious particles on daily life which has motivated us to explore UV-light-based methods for indoor air disinfection. For that, we have tested their efficiency against bacteriophage- and feline coronavirus-loaded aerosols as surrogates by exposing them to UV-A and UV-C radiation in a controlled aerosol chamber [1]. After the irradiation, the aerosols are sampled and subsequently quantified by (RT)-qPCR to determine genome equivalents. As expected, a clear reduction in genome equivalents is observed after UV-C irradiation even at a low dose of mere 8.93 J/cm² based on qPCR measurements for both types of viruses. Surprisingly, also a reduction in genome equivalents is observed with UV-A light (53.15 J/cm²) proving the disinfection capabilities of less harsh UV-radiation.

While qPCR is an excellent tool for the quantification of genetic material in the sample it does not allow to make statements about the structural integrity, and in turn infectivity, of the viruses. To address this limitation microscopic analysis is required in order to (1) identify the locations of virus particles in the salt and protein containing matrix of the sampled aerosols and (2) to investigate their structural integrity. To detect feline corona viruses we use a commercial RNAscope™ ACD kit with adapted amplifiers to fluorescence-label the viruses. The accompanying image is a composite of different fluorescence channels on a bright-field microscopy and demonstrates the effectiveness of this approach: in an infected culture of CRFK cells (DAPI-stained nuclei in blue) feline corona appear in yellow. Building on that approach, we are currently optimising the sample preparation protocol to establish a correlative microscopy workflow that links fluorescence imaging with high-resolution helium-ion microscopy. We will outline how this integrated approach enables us to easily identify and investigate virus particles in the complex matrices that can be expected in environmental samples with regard to their abundance and structural integrity.

[1] Mohamadi Nasrabadi, A.; Eckstein, D.; Mettke, P.; Ghanem, N.; Kallies, R.; Schmidt, M.; Mothes, F.; Schaefer, T.; Gräfe, R.; Bandara, C.; Maier, M.; Liebert, U.; Richnow, H.-H.; Herrmann, H.: "*A Virus Aerosol Chamber Study: The Impact of UVA, UVC, and H_2O_2 on Airborne Viral Transmission*", Environment & Health (2025)

Fig. 1



LS4.P12
Dose-fractionated EELS spectrum imaging of cryogenically frozen biological samples

A. Thron[1], L. Spillane[1], G. H. Wu[2], R. Twesten[1], C. Booth[1], W. Chiu[2]

[1]Gatan Inc., Pleasanton, CA, United States
[2]Stanford University, Bioengineering, Stanford, CA, United States

Electron Energy Loss Spectroscopy (EELS) in the TEM has been widely applied across materials science due to it"s ability to acquire chemical information at or below the nanometer length scale. To achieve high spatial resolutions the TEM is operated in scanning TEM (STEM), and a single EELS spectrum is acquired at each pixel of the STEM image forming a matrix of spectra with a specific spatial location, known as a spectrum image. The total dose needed to achieve a spatial resolution ~nm or below, in an EELS spectrum image, is on the order of 106-107 e-/Å2. For extremely dose-sensitive materials such as polymers and biological samples, whose total dose threshold is between 40-100 e-/Å2, the spatial resolution ranges from 10"s to 100"s of nm since the dose needs to be spread over a larger area to prevent sample damage. This has limited the application of STEM-EELS to biological samples which are fixed in resin, and not cryogenically frozen [1]. However, with the advent of direct detection cameras, the increase in detector quantum efficiency (DQE) reduces the total dose needed to acquire a spectrum. This has allowed researchers to push the resolution of EELS spectrum imaging, enabling the investigation of soft-mater interfaces on the nm scale [2]. In this presentation we will show that the implementation of direct detection technology for acquiring EELS spectrum images enables sufficient resolution to spatially locate Ca granules inside cryogenically frozen mitochondria of human retinal ganglion cells (RGCs).

For this study we used a multimodal imaging approach to locate and analyze mitochondria of interest. Bright-Field TEM imaging together with Gatan"s Latitude-S software allowed for surveying the TEM grid for possible regions of interests. Once a region of interest was identified the STEM-EELS spectrum images were acquired, in the same microscope, to locate the position of Ca with in the Mitochondira. EELS spectrum images were acquired using dose-fractionated spectrum imaging, where a series of spectrum image passes are rapidly acquired rather than one long, single pass. Does fractioned spectrum images spread the total dose over time and extends the sample integrity over the course of the acquisition [3]. During the acquisition, the series of spectrum image passes are saved individually, which allows the removal of any compromised set of passes. Drift correction can also be measured and applied post-acquisition since each pass is saved individually. This is especially important since the contrast in the STEM images are weak due to the thickness of the samples, the low dose needed to preserve the integrity of the samples, and the small variation in atomic weight of each element in the sample.

During this presentation we will show that the sensitivity of direct detection in combination with dose-fractionated spectrum imaging enabled this multimodal approach. The ability to confirm the presence of dark granules in Bright Field TEM were Ca granules enabled further insights into optic disc drusen pathology through calcification in mitochondria of RGCs [4].

[1] Aronova M.A., Leapman R.D., *MRS Bulletin*, **37** (2012) DOI: 10.1557/mrs.2011.329.

[2] R. Colby et. al, *Ultramicroscopy* **246**, (2023) DOI: 10.1016/j.ultramic.2023.113688.

[3] Jones L. et. al., Microscopy, **67** (2018) DOI: 10.1093/jmicro/dfx125.

[4] Gong-Her Wu et. al., *bioRxiv, submiited for prereview* (2024) DOI: 10.1101/2024.12.17.628994.

LS4.P13
Unlocking new functionalities – The hybrid capabilities of combined SEM-AFM systems

F. Hitzel[1], G. M. Johnson[2]

[1]DoubleFox GmbH, Braunschweig, Germany
[2]Zeiss Microscopy, Poughkeepsie, NY, United States

The integration of Scanning Electron Microscopy (SEM) and Atomic Force Microscopy (AFM) into a single system has gained momentum, with multiple companies now actively marketing solutions in this area. One relevant commercial SEM-AFM system to use standard AFM cantilevers with optical beam deflection, the Binnig-Rohrer-Ruska (BRR) Microscope, was developed by me 14 years ago, demonstrating the potential of combining SEM and AFM for advanced nanoscale characterization. We named it BRR to commemorate the 80th and 25th anniversaries of the Nobel Prizes awarded to the pioneers of both techniques in the same year. Today, this technology is commercially available as the AFM-Option for ZEISS FE-SEMs, now in its second generation. The system supports a vast range of AFM probes, enabling diverse applications.

Still, the SEM-AFM is a niche technology. When it comes to real hybrid experiments, utilizing the physical effects of an electron beam together with the mechanical and electrical detection capability of an AFM, the field seems to be in its early stages. The electron beam manipulates the local carrier density and temperature. Both effects generate information that can be accessed using AFM. Using a modulated beam together with lock-in techniques on the AFM side, the influence of the beam can be isolated from other effects and detected by the AFM. In this way, the AFM can create an image that contains information about effects caused by the electron beam. The other way around is also possible: Scanning with an electron beam and generating the image not from secondary electrons but from the information coming from the AFM, i.e. using the AFM tip as SEM detector. In this way, the SEM can not only create an image from electrical information like e.g. work function, but even from mechanical information like thermal waves. This opens up a huge amount of combination possibilities. Even though there has been research in this field in the past 20 years, no real breakthrough has been achieved leading to "The" hybrid operation mode.

Recently, we organized a set of semiconductor samples featuring SRAM structures across different technology nodes down to 3 nm and conducted extensive experiments leveraging the hybrid functionalities of SEM and AFM. These studies highlight the unique advantages of real-time AFM tip navigation within the SEM, multimodal correlative imaging, force-controlled manipulations, and AFM-based tomography, where material is selectively milled and analyzed in situ. This talk will provide an overview of the latest capabilities enabled by this hybrid technology, demonstrating its potential for advanced semiconductor analysis and beyond.

Fig. 1

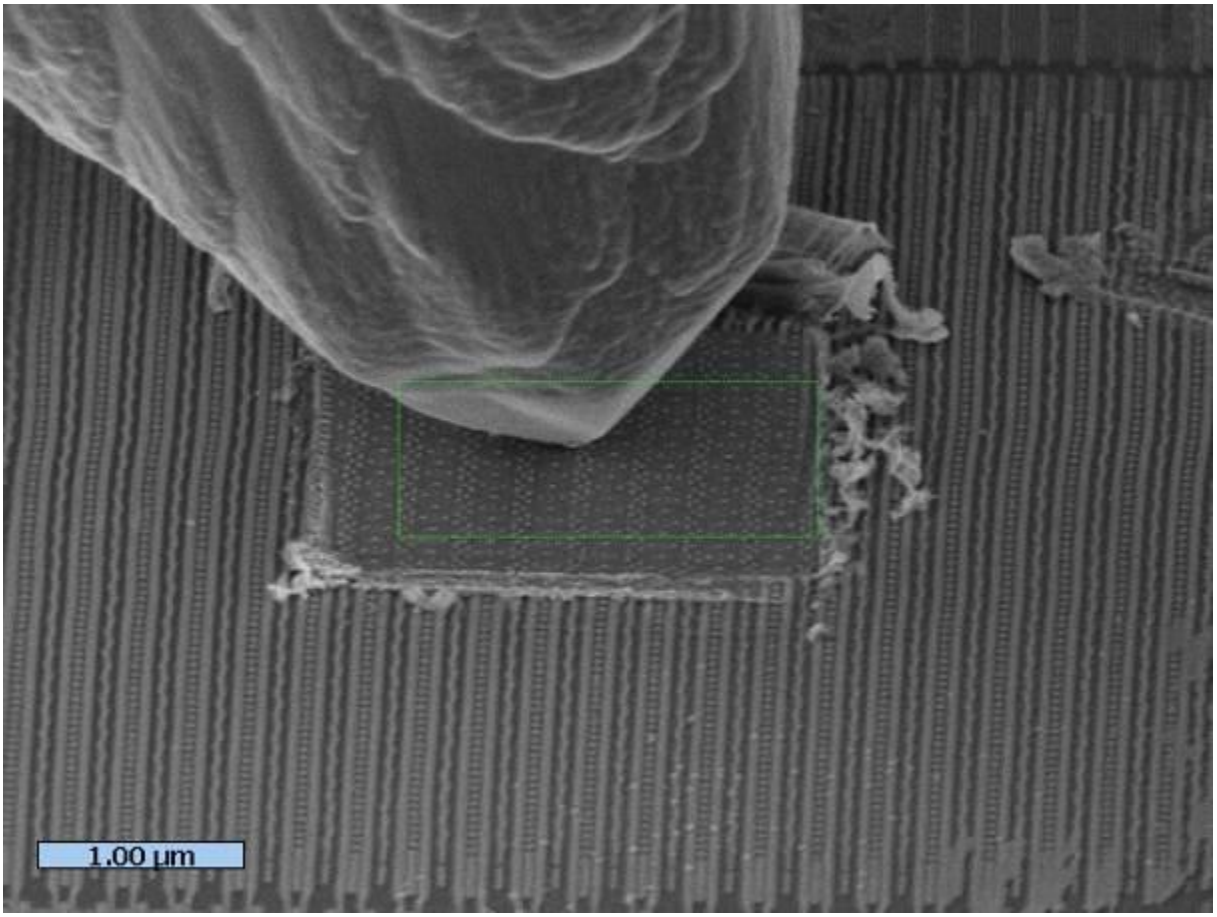


Fig. 2

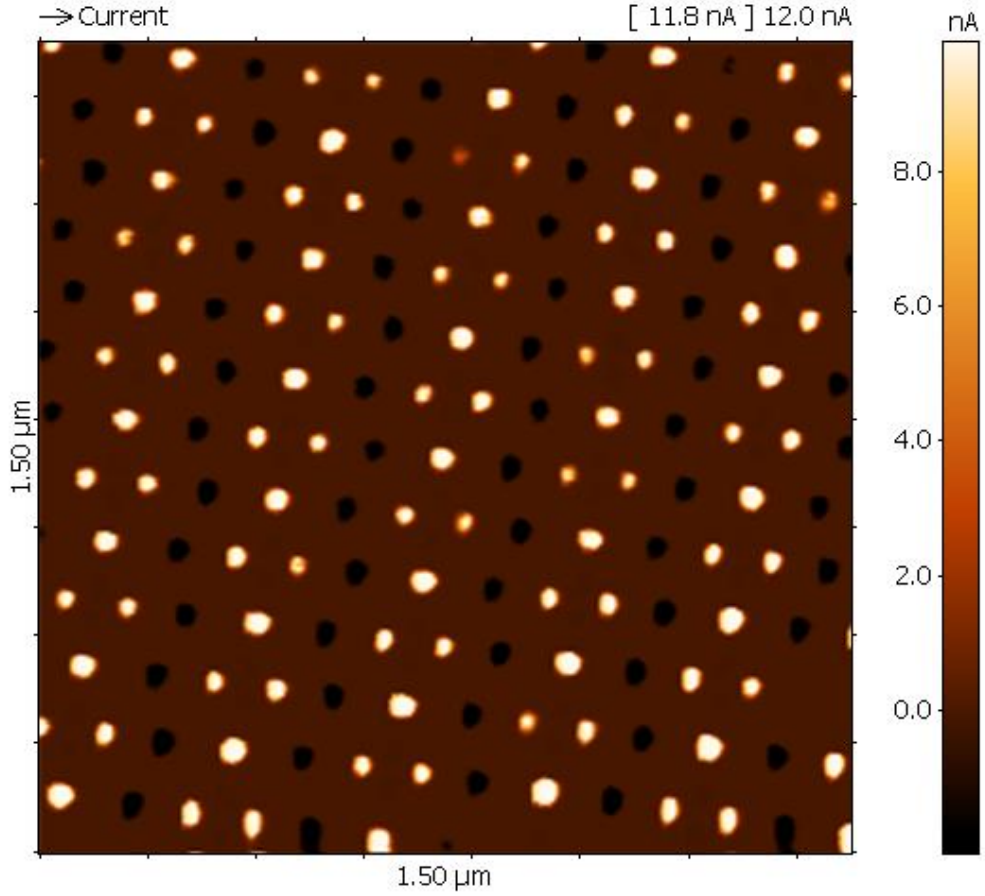
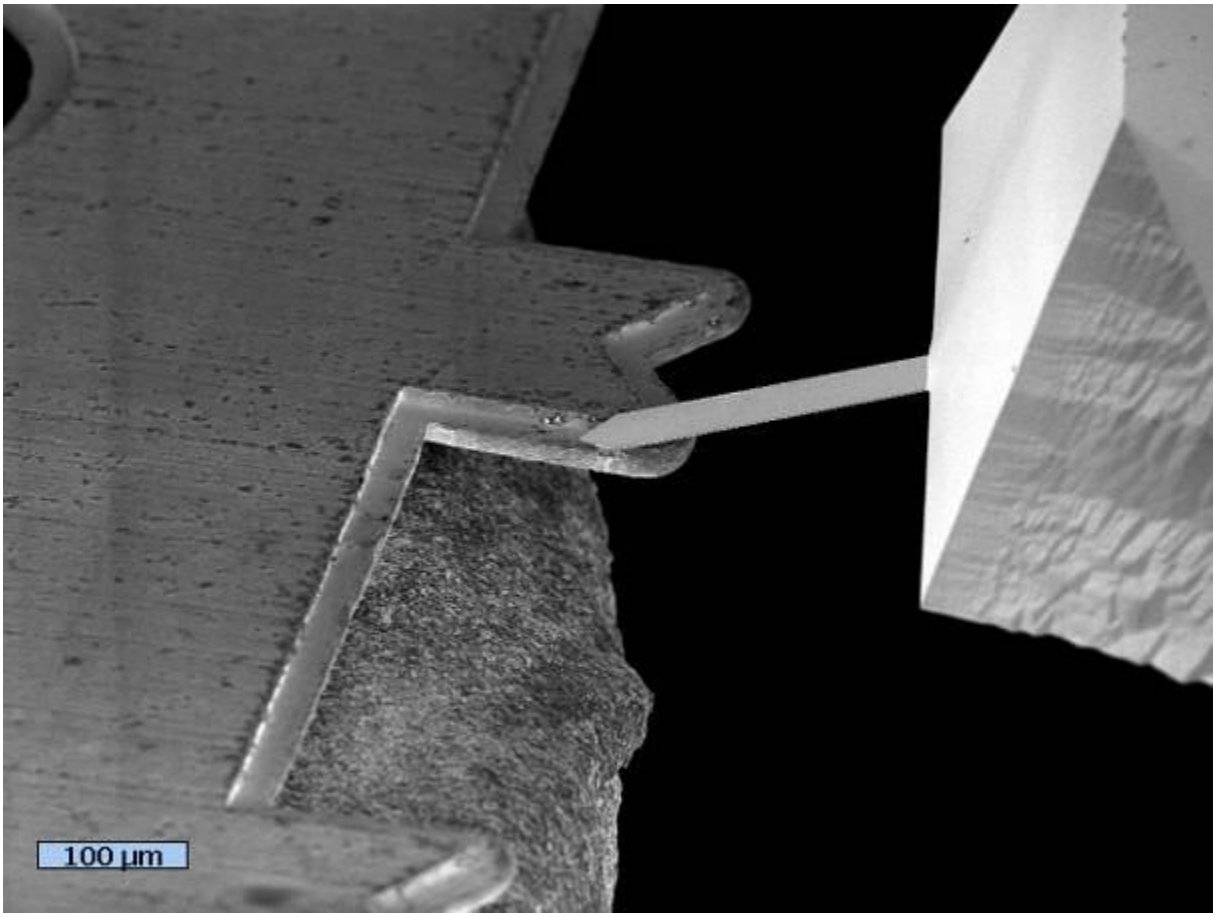


Fig. 3



LS4.P14
Correlative cryo soft x-ray tomography and fluorescent microscopy of biological samples in the laboratory

K. Fahy[1], P. Sheridan[1], W. Fyans[1], T. McEnroe[1], F. O'Reilly[1,2], S. Kapishnikov[1]

[1]SiriusXT Limited, Dublin, Ireland
[2]University College Dublin, Physics, Dublin, Ireland

Introduction Soft x-ray tomography (SXT) uses low energy x-rays to image frozen-hydrated biological specimens such as entire mammalian cells or thick tissue slabs with a few tens of nanometers of spatial resolution1. The technique takes advantage of the biological water window whereby water is relatively transparent to x-rays from 284 to 543 eV (2.34 to 4.4 nm) but carbon-based organelles are absorbing. This native contrast imaging allows high resolution imaging of bulk specimens with minimal sample preparation. While SXT has traditionally been confined to synchrotrons the recent development of a laboratory scale SXT microscope opens the possibility of integrating this novel technique into light and electron imaging workflows2. The SXT microscope features an integrated light microscope for overview imaging and fluorescence targeting, allows for swift acquisition of 2D and 3D x-ray images covering extensive areas on the specimen, and enables efficient and rapid identification of cells of interest.

Objectives The utility of the microscope is currently being demonstrated through 2 EU-funded consortia (https://cocid.eu/ and https://clexm.eu/). Recent case studies have included correlative imaging of whole, virus infected cells treated with anti-viral drugs; imaging the 3D distribution of therapeutic-laden nanoparticles in whole cells; and the development of correlative workflows for tissue imaging across scales. An alternative sample carrier in the form of a thin-walled glass capillary was also developed, further enhancing the novelty of the lab-based microscope.

Methods Integrated cryo fluorescence was used to screen an entire EM grid for cell selection and correlation with SXT. Low magnification/large field of view 2D x-ray mosaics were then acquired over large areas of the grid before acquiring tilt series from ±60° on selected targets. Data from both modalities were then overlaid to provide the location of fluorescent proteins in the context of whole cell ultrastructure. For cells suspended in glass capillaries the tilt series was acquired over ±90°.

Results Resulting cryo-SXT tomograms and fluorescent light images of cellular organelles and nanoparticles provide proof of concept for the lab-based microscope and associated workflows.

Conclusion Workflows of correlative light, electron and soft x-ray microscopy combines the strengths of each modality. The recent availability of a compact soft x-ray microscope will accelerate the development of novel workflows and biological imaging applications that can benefit from this technique. We will present our microscope workflows and application data.

References

1. Maria Harkiolaki, Michele C. Darrow, Matthew C. Spink, Ewelina Kosior, Kyle Dent, Elizabeth Duke; Cryo-soft X-ray tomography: using soft X-rays to explore the ultrastructure of whole cells. *Emerg Top Life Sci*20 April 2018; 2 (1): 81–92. doi: https://doi.org/10.1042/ETLS20170086
2. Stephen O"Connor, David Rogers, Maryna Kobylynska *et al*., Demonstrating Soft X-Ray Tomography in the lab for correlative cryogenic biological imaging using X-rays and light microscopy bioRxiv 2024.12.23.629889; doi: https://doi.org/10.1101/2024.12.23.629889
3. The authors acknowledge funding from the European Union"s Horizon 2020 Research and Innovation programme under grant agreements No. 101017116 and 101120151, and the Irish Research Council grant EBPPG-2020-278.

LS4.P16
Platform for cryo-fluorescence with high stability and improved ease of use

M. van Nugteren[1], M. Schwertner[1], N. Hosny[1], T. Marrable[1], H. Vader[1], K. Verduin[1], C. Ko[1], A. Kamp[1]

[1]Linkam Scientific Instruments Ltd., Salfords, United Kingdom

Keywords

Fluorescence imaging of vitrified biological samples, cryo-fluorescence microscopy (cryo-FM), cryo-EM, cryo-CLEM, cryo-EM tomography, cryo-super-resolution (SR), improved imaging stability, cryo-SR-CLEM

Introduction

Cryo-imaging of biological samples embedded in vitrified ice is of great interest recently - driven by applications such as particle cryo-EM (a technique used to investigate the molecular structure of smaller bio-molecules [1]), guided FIB-milling [2] and CLEM (Correlative Light and Electron Microscopy [3]). Cryo-fluorescence is used during such workflows to identify events or regions with well-established labelling techniques complementing EM. The biological cryo-sample remains in a fully hydrated state with superior preservation down to ultra-structural level.

The cryo-FM stages developed at Linkam deliver contamination-free imaging for longer periods because they use liquid nitrogen in the sample chamber acting as a cold trap. The latest CMS196V4 is compatible with most upright fluorescence microscopes and also supports transmitted light illumination with the integrated LED system for sample navigation. In the presentation we discuss new workflow options and the design changes and improvements in the CMS196V4 compared to the widely used CMS196V3 predecessor. Special emphasis for the new design was on improved drift stability (XYZ) because of more demanding requirements for super-resolution techniques.

Materials and Methods

The CMS196V4 cryo-stage is shown in Fig.1 while the touch-panel joystick is shown in Fig 2 and the Autofill unit in Fig.3. An example for the configuration of the sample chamber is depicted in Fig. 4 where the new cryotransfer container for the JEOL CRYOARM cartridge is also shown.

Improved drift stability of the new stage was achieved by multiple measures including:

- Continuous sample chamber fill mechanism
- Lens heater system (closed loop) to reduce sample drift in Z / focus stability
- Autofill dewar (3L) for long cryo runs supporting fast fill or slow drip-feed operation with minimal disturbance

To further improve ease of use the CMS196V4 features:

- New user interface: touch-panel and joystick in addition to USB control
- Cryo-bridge interchangeable by user for better flexibility of sample mounting interfaces
- Better cable – management / simplified topology: only one connector on stage
- Quick-release system for microscope mounting
- "Wireless" magnetic heated lid
- Support for JEOL CRYOARM cartridges and Silicon Nitride X-ray holders
- Revised AutoFill with multiple operation modes
- Modular Imaging Platform (MIP, option) to simplify sample loading

Conclusion

The updated CMS196V4 cryo-stage offers improved drift stability and better ease of use for typical applications:

- Screening of cryo-grids after sample preparation
- CLEM (Correlative Light and Electron Microscopy)
- Targeting of sample locations for FibSEM lamella preparation
- Cryo-Super-Resolution imaging
- Cryo-Spectroscopy

References

[1] https://www.nature.com/news/cryo-electron-microscopy-wins-chemistry-nobel-1.22738

[2] Rigort, A., et al. (2010) Micromachining tools and correlative approaches for cellular cryo-electron tomography. J. Struct. Biol. 172(2), 169–179.

[3] A. Sartori et al., "Correlative microscopy: Bridging the gap between fluorescence light microscopy and cryo-electron tomography", *J. of Structural Biology* 160 (2007) 135–145

Fig. 1



Fig. 2

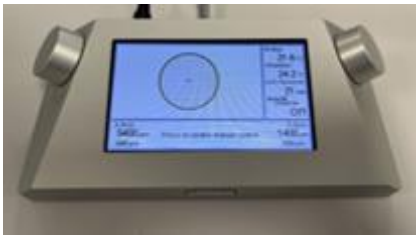
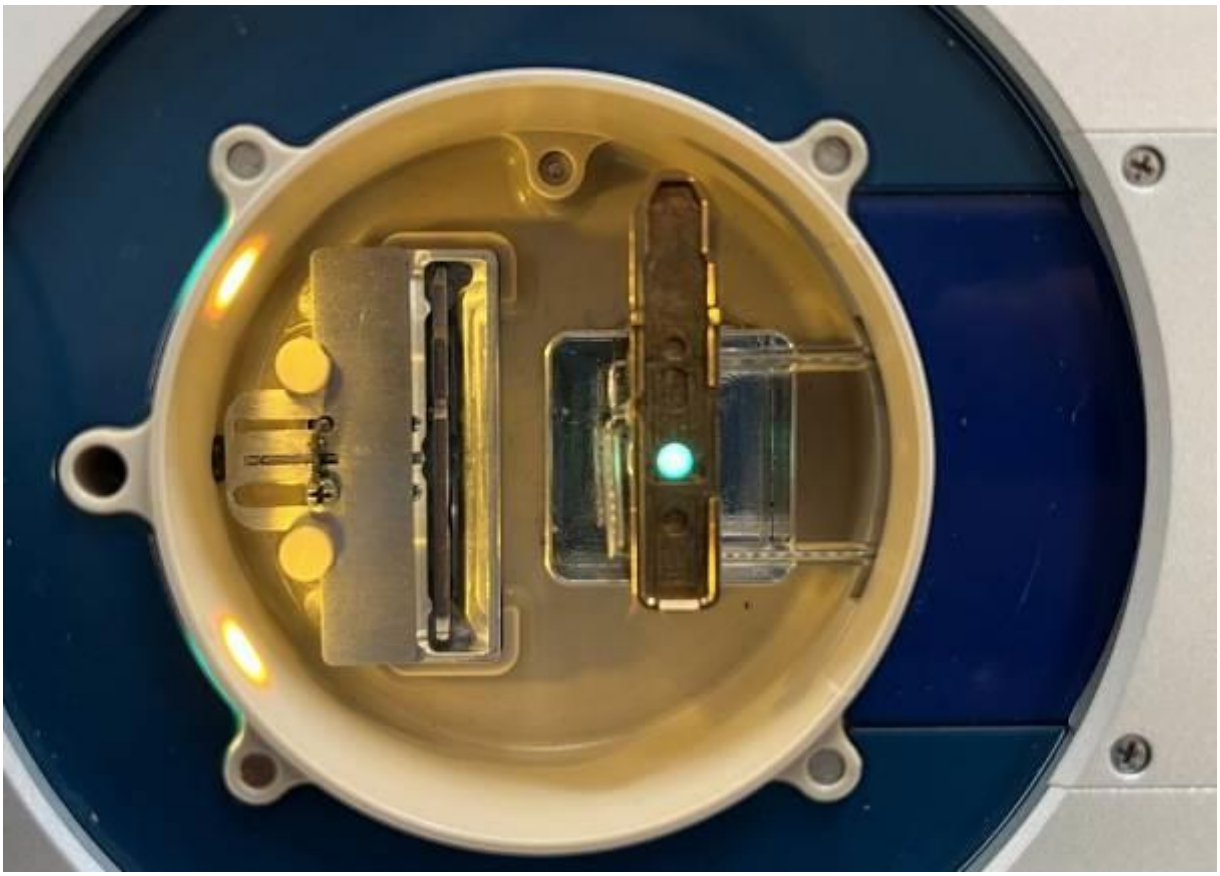


Fig. 3



Fig. 4



LS4.P17
Enhanced context preservation and targeting by integrating cryo soft X-ray tomography with *in situ* structural biology workflows

C. Kaiser[1], O. H. Schiøtz[1], S. Kapishnikov[2], P. Sheridan[2], W. Fyans[2], F. O'Reilly[2,3,4], K. Fahy[2], T. McEnroe[2], J. Plitzko[1]

[1]MPI of Biochemistry, KryoEM Technolgy, Planegg-Martinsried, Germany
[2]SiriusXT Limited, Dublin, Ireland
[3]University College Dublin, School of Physics, Dublin, Ireland
[4]University College Dublin, School of Biology and Environmental Sciences, Dublin, Ireland

Cryo-electron tomography (Cryo-ET) allows the cellular structural biology landscape to be charted in context with cellular ultrastructure in a close to native, fully hydrated cryogenically preserved, i.e. the vitrified state. Cryo-focused ion beam (Cryo-FIB) milling has become the standard method to thin biological specimens to allow for such *in situ* structural biology studies, as it introduces much less mechanical distortions than classical sectioning. While in prior FIB-milling approaches most of the subvolume studied must be ablated, the recently pioneered Serial Lift-Out technique [1] increases the spatial sampling density and hence the amount of obtainable contextual information as well as throughput for high pressure frozen samples by preparing multiple sections from a single sample subvolume.

Soft X-ray tomography (SXT) is a unique X-ray imaging modality which enables label-free imaging of vitrified biological samples up to about 10 µm thick, revealing ultrastructural details of entire cells or tissue slabs with a few tens of nanometers spatial resolution and minimal sample preparation [2]. In this study we introduce laboratory SXT [3] as an additional step in the cryo-ET workflow to provide for label-free targeting for downstream cryo-FIB milling and cryo-ET. Adding SXT to the workflow should also preserve a major fraction of biological information, albeit at lower resolution, otherwise lost during thinning. This allows for more reliable data annotation and a more consistent documentation of microanatomy context for large volume cryo-ET samples.

We exploit the fact that high-pressure frozen samples, *C. elegans* larvae in our study, usually too thick to be imaged by SXT, are sectioned into consecutive slabs in the process of Serial Lift-Out. These slabs were imaged by SXT and thinned down to electron translucency. We could segment and assemble the SXT data, preserving lower resolution information on about 90% of the sample. The study assesses how SXT can bring additional insights to, and facilitate, correlative workflows in cryo-ET. We also assess the impact of SXT on subsequent cryo-EM by subjecting samples of model proteins to differing levels of soft X-ray dose and probing the loss of molecular information by the pre-exposure to ionizing radiation using cryo-EM single particle analysis.

Our proposed workflow combines light, soft X-ray and electron imaging to reveal extended sample information across multiple size scales and levels of complexity. We highlight the potential of cryo soft X-ray tomography as an important tool to improve information content and targeting efficiency in *in situ* structural biology workflows, which in the future may prove particularly relevant for cryo-ET samples that are, when the native state is to be preserved, non-trivial to fluorescently label for correlative imaging approaches, such as human pathology or environmental samples.

1. Schiøtz, O.H., Kaiser, C.J.O., Klumpe, S. *et al.*Serial Lift-Out: sampling the molecular anatomy of whole organisms. *Nat Methods* **21**, 1684–1692 (2024).
2. Maria Harkiolaki, Michele C. Darrow, Matthew C. Spink, Ewelina Kosior, Kyle Dent, Elizabeth Duke; Cryo-soft X-ray tomography: using soft X-rays to explore the ultrastructure of whole cells. *Emerg Top Life Sci*20 April 2018; 2 (1): 81–92.
3. O"Connor et al., Demonstrating Soft X-Ray Tomography in the lab for correlative cryogenic biological imaging using X-rays and light microscopy bioRxiv 2024.12.23.629889

LS4.P18
Multimodal and correlative imaging approaches to study early stages of SARS-CoV 2 infection

J. Groen[1], A. Brelot[2], J. Enninga[2], A. Sartori-Rupp[1]

[1]Institut Pasteur, Structural Biology and Chemistry, Paris, France
[2]Institut Pasteur, Cell Biology and Infection, Paris, France

In this work we aim to investigate SARS-CoV-2 entry mechanisms (1) using cutting edge cryo-methodologies to obtain structural insights in the mechanism of infection. SARS-CoV-2 is the causative agent for the recent Covid pandemic and as such has been the centre of both scientific and public attention over the past few years. While much has been published on the viral replication and spread within a cell population (>12 hours post infection), little is know about the very first contact between host and pathogen (

Here we are using correlative and multimodal imaging in cryogenic conditions to study the viral entry within the very first hour, at a time that the cell-population is basically unaware of an ongoing infection. We want to describe the endocytic entry pathway of SARS-CoV-2; to map it and to visualize the host reaction towards viral entry. To achieve this, we are utilizing a cryo- correlative light and electron microscopy (cryo-CLEM) approach (2).

For this, VeroE6 cells were cultivated on top of EM grids and infected with a UV-inactivated version of the virus, which is able to fuse and enter the host, but lacks the ability to replicate. 40 minutes post infection the samples were plunge-frozen and cryo-fluorescence maps were acquired to localize potential areas of interest and assess the quality of the grid. From here on, we either went for cryo-soft X-ray tomography (3), or for cryo-electron tomography, with the latter doing both cryo-ET on cryo-FIB-lamellae (4), and at cell-peripheries without lamellae preparation.

By cryo-ET we were able to observe the Virus in the vicinity of the host cell periphery, and within endocytic vesicles. Using cryo-SXT we were able to confirm some of the phenotypes that we observed by cryo-ET, and it allowed us to put it into perspective of a larger area of the cell. It was possible to compare cellular morphologies, and the changes thereof over the course of the first hour of infection.

Here we use 3 complementary modalities that allow us to look at the SARS-CoV-2 infection process with complementary imaging methods at low (cryo-confocal), medium (cryo-SXT) and high (cryo-ET) resolution. While this approach is very time-consuming, it gives a more complete multiscale overview of the complex mechanism of virus-host interaction.

[1] Jackson, C. B., Farzan, M., Chen, B., & Choe, H. (2022). Mechanisms of SARS-CoV-2 entry into cells. Nature reviews Molecular cell biology, 23(1), 3-20.

[2] Bykov, Y. S., Cortese, M., Briggs, J. A. G., & Bartenschlager, R. (2016). Correlative light and electron microscopy methods for the study of virus–cell interactions. In FEBS Letters[AS1] .

[3] Collinson, L. M., Domart, M.-C., Carzaniga, R., Razi, M., Guttmann, P., Schneider, G., Pereiro, E., Tooze, S. A., & Duke, E. (2017). Soft X-Ray Tomography: Filling the Gap Between Light and Electrons for Imaging Hydrated Biological Cells. Microscopy and Microanalysis.

[4] Klein, S., Wachsmuth-Melm, M., Winter, S. L., Kolovou, A., & Chlanda, P. (2021). Cryo-correlative light and electron microscopy workflow for cryo-focused ion beam milled adherent cells. In Methods in Cell Biology (Vol. 162).

LS 5: Pathology, pathogens and diagnostics

LS5.01(inv)
Electron microscopy of the human lung

M. Ochs[1]

[1]Charité - Universitätsmedizin Berlin, Institute of Functional Anatomy, Berlin, Germany

In humans, the alveolar region of the lung is the site of gas exchange. A continuous epithelium consisting of two cell types covers the alveolar surface: type I alveolar epithelial cells (AEC1) with thin cell extensions and cuboidal type II alveolar epithelial cells (AEC2). While the main function of AEC1 is to provide a thin epithelial layer as part of the air-blood barrier for gas exchange, AEC2 serve two main functions as progenitors of the alveolar epithelium and as producers of surfactant. The surfactant system is essential for normal lung function due to its biophysical (surface tension lowering) and immunomodulatory properties.

A variety of EM techniques is available to study the ultrastructure of the human lung under physiological and pathological conditions, both qualitatively and quantitatively. This presentation will review these approaches and demonstrate how EM contributed and continues to contribute to our understanding of the functional architecture of the human lung, in particular its alveolar epithelium and surfactant system.

LS5.02(inv)
Leveraging hyperspectral electron microscopy towards data-driven segmentation of cellular ultrastructure

B. Giepmans[1]

[1]University Groningen, University Medical Centre Groningen, Groningen, Netherlands

Cellular electron microscopy (EM) was recently revolutionized by automation and digitalization allowing routine capture of large areas and volumes at nanoscale resolution. Analysis of the resulting large data volume is however hampered by the greyscale nature of electron images, often requiring laborious manual annotation. A major advance in segmentation has been the use of correlated fluorescence light microscopy and electron microscopy (CLEM; [1,2]) that successfully aids in analyzing targeted structures. However, CLEM-mediated segmentation targeting is typically limited to three probes per sample and further complicated by the resolution mismatch between both microscopy modalities. Furthermore, sample preparation for CLEM typically compromises fluorescence microscopy, like targeting efficiency or fluorescent yield, and/or preservation of ultrastructure for electron microscopy [1]. To overcome these limitations we explored the use of elemental analysis to help to classify subcellular structures in large-scale EM datasets in a data-driven manner [3].

Here we demonstrate unsupervised and automated extraction of biomolecular assemblies in conventionally processed tissues using large-scale hyperspectral energy-dispersive X-ray (EDX) imaging. First, we discriminated biological features in the context of tissue based on selected elemental maps. Next, we designed a data-driven workflow based on dimensionality reduction and spectral mixture analysis, allowing the visualization and isolation of subcellular features with minimal manual intervention [4]. Given the potential of guidance by elements, our ongoing work shows that probes equivalent to fluorescent dyes (quantum dots, diaminobenzidine, gold), targeting structures of interest, that can be specifically be shown in their respective abundant maps. Likewise, elemental stains with specific affinity for certain structures, conceptually equivalent to DAPI or hematoxylin and eosin (HE) in fluorescence microscopy, uniquely identifies other structures as we will show for tungsten and neodymium where synapses and other subcellular structures are highlighted. Broad implementations of the additional multimodal imaging workflows and fully exploiting the stains and probes as presented here will accelerate the understanding of biological ultrastructure by automated segmentation based on the multimodal microscopy.

1: de Boer P, Hoogenboom JP, Giepmans BN (2015) Correlated light and electron microscopy: ultrastructure lights up! Nat Methods. 12:503.

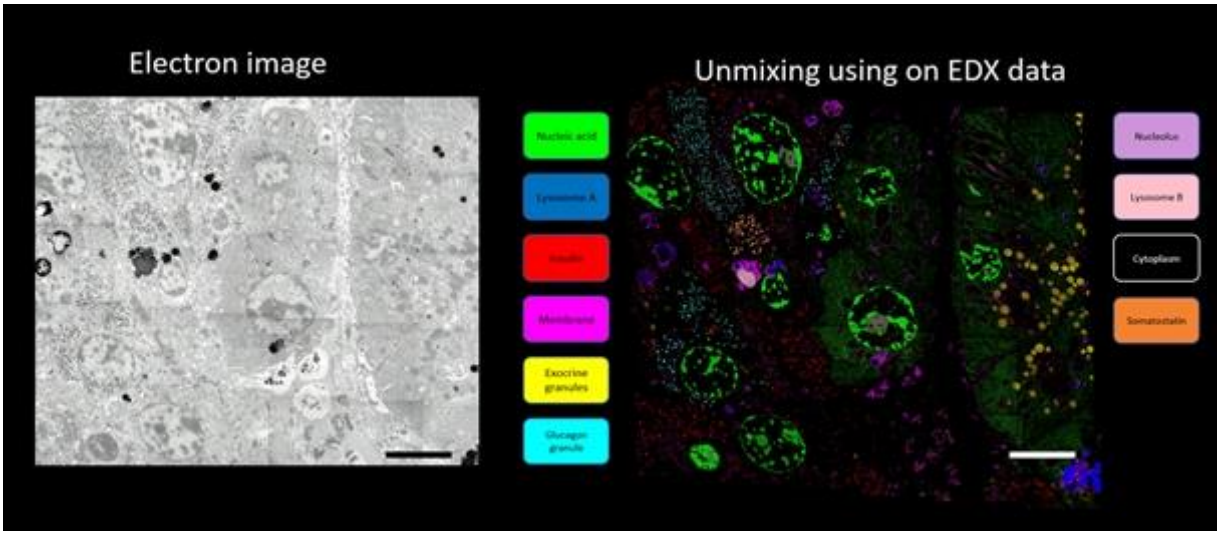
2: Ando T et al. (2018) The 2018 correlative microscopy techniques roadmap. J Phys D Appl Phys.51:443001.

3: Pirozzi NM, Hoogenboom JP, Giepmans BN. ColorEM: analytical electron microscopy for element-guided identification and imaging of the building blocks of life (2018). Histochem Cell Biol. 150:509.

4: Duinkerken BH, Alsahaf AM, Hoogenboom JP, Giepmans BN (2024). Automated analysis of ultrastructure through large-scale hyperspectral electron microscopy. npj Imaging2, 53.

Fig. 1. Large-scale EM image of a partial islet of Langerhans (left) and spatial representation of the unmixing result with the color representing the endmember with the highest abundance and the intensity scaled accordingly (right). Bar: 10 um. Reproduced and slightly modified from [4]. For the complete dataset and full resolution nanotomy.org/OA/Duinkerken2024NPJI.

Fig. 1



LS5.03(inv)
Diagnostic electron microscopy in human infectious diseases

M. Laue[1]

[1]Robert Koch-Institut, Spezielle Licht- und Elektronenmikroskopie (ZBS 4), Berlin, Germany

Infectious diseases are a major health threat for humans. Therefore, disease prevention and treatment are important to reduce the overall burden of disease which requires ample knowledge about the pathogen and the host reaction caused by infection. Diagnosis of infectious diseases is based on disease symptoms and the identification of the pathogen usually by the detection of specific molecular signatures of the pathogen such as protein or nucleic acid. Diagnostic electron microscopy (DEM) was one of the major diagnostic methods in the past and is still relevant in special non-routine cases of infectious diseases today. The reasons for its ongoing application are variable and case dependent, such as speed of detection or the capability to detect a pathogen without any distinct hypothesis ("open view"). This presentation will provide some examples to demonstrate the actual scope of DEM application in infectious diseases.

Besides supporting the diagnosis of infectious diseases, DEM plays an important role in understanding disease pathogenesis. At least for small pathogens, DEM is the only method available that is able to detect the infectious unit directly without using reporters or other indirect methods. For understanding diseases pathogenesis, it makes a difference if the pathogen is intact and propagates or if the pathogen has been cleared from the patient and only traces of the pathogen remain which are deposited somewhere. This presentation will give a few examples and document how important it is to actually see the infectious unit and how it performs in the host.

The general sample preparation methods used for DEM remain almost constant for the last five to six decades. While negative staining electron microscopy (EM) is used for the detection of small pathogens in suspensions, thin plastic section EM is used for the analysis of more compact material, such as tissue or cells. One advantage of this rather conservative usage of methods is that the literature contains a huge amount of reference data processed with roughly the same methods. Moreover, the methods are robust, reliable and are compatible with a wide range of samples, e.g. tissue type, sample size and form, that are commonly available with infectious diseases. The presentation will give an overview on the methods and important preparation steps.

Changes to the application of DEM in the near future will be expected by the introduction of more automation of the imaging and of the object detection. For instance, by using large-field imaging of thin sections, huge amounts of data can be recorded almost without any supervision. While this part is already available and constantly improving in speed and quality, fast and reliable automated object detection is still in its infancy. The number of studies on machine learning of pathogen recognition is still limited and far from being useful in practical approaches. The presentation finally will discuss these developments and provide an outlook to future needs.

Literature:

Laue M. Diagnostic electron microscopy in human infectious diseases - Methods and applications. J Microsc. 2024 Nov 19. doi: 10.1111/jmi.13370.

LS5.04
Plant virus structures and forms in symptomatic and asymptomatic plants

K. Richert-Pöggeler[1], C. Maaß[1], J. Ponath[1], R. Ilyas[1], M. Schipper[1], V. Maiberg[1]

[1]Julius Kuehn Institute, Federal Research Centre for Cultivated Plants, Institute for Epidemiology and Pathogen Diagnostic, Braunschweig, Germany

Introduction

Viruses coexist with their host depending on its ribosomes to produce viral proteins. Virus presence is not necessarily associated with a symptomatic phenotype. Recently, a number of viruses and viroids that do not develop symptoms upon infection of horticultural plants have been identified. Knowledge about their impact on the host cellular ultrastructure and induced modifications is still missing.

Objectives

Investigation of virus related structures, such as virions and RNA molecules and their interactions with organelles and membranes in infected cells of asymptomatic plants.

Materials & methods

Virus presence was confirmed in homogenized symptomatic and asymptomatic plant material using negative staining with 1% UAc. Embedding of plant material comprising leaf and root tissues in Epon resin followed by ultra-thin slicing using the Leica Ultramikrotom LM_UC7RT. The sections which are 70nm thin, are placed on a nickel grid and stained with 2% UAc. Sections were monitored in a Fei Tecnai Spirit G2 Twin at 80 kV and imaged using a Veleta 2k x 2k CCD camera. Immuno-electron microscopy with viral capsid specific polyclonal antibodies was used to determine virus identity and localization in the plant tissue.

Results

In asymptomatic plants, the ultrastructure of virus infected cells was clearly modified. The impact on the host and presence of virus related structures depended on the virus-host system investigated. In potyvirus systemically infected phylloclades of garden asparagus the viral cylindrical inclusion protein (CI) a core factor in viral replication, localized within the cytoplasm and adjacent to the plasmodesmata. Such CI bundles were perpendicular to the cell wall and were observed at both ends of the plasmodesmata, indicating cell-to-cell spread of asparagus virus 1. Despite the abundance of CI no virions were detectable in infected cells. In case of the latent hoya tobamovirus 2, infected cells contained small arrays of virions that reacted with antibodies against the serologically related youcai mosaic virus using immuno-gold labeling. In mixed infected *Solanum jasminoides*, the abundance of carlavirus particles was influenced by the co-infecting viroid.

Conclusion

In symptomless plants systemic spread of viruses and viroids occurs and typical signs of virus replication are visible in infected cells.

LS5.05
Comparison of transduction enhancing peptide nanofibrils and their interaction with virus-like particles and cells assessed by electron microscopy (SEM, TEM & STEM tomography)

J. La Roche[1], L. Rauch-Wirth[2], K. Kaygisiz[3], L. Zimmermann[2], T. Weil[4], J. Münch[2], C. Read[1]

[1]University of Ulm, Central Facility for Electron Microscopy (GFE), Ulm, Germany
[2]Ulm University Medical Center, Institute of Molecular Virology, Ulm, Germany
[3]Massachusetts Institute of Technology, Department of Chemistry, Cambridge, MA, United States
[4]Max Planck Institute for Polymer Research, Department Synthesis of Macromolecules, Mainz, Germany

Introduction:

The chimeric antigen receptor (CAR) T-cell therapy is a gene therapy approach to treat cancer. But low transduction efficiency caused by low retroviral titers and electrostatic repulsion between negatively charged viral and cellular membranes can hamper effectiveness and increase therapy costs. To enhance viral transduction by promoting virion attachment and reducing repulsion, positively charged peptide nanofibrils (PNFs) were developed. Vectofusin-1 (Vect-1), is a peptide consisting of 26 amino acids forming PNFs and a commonly used transduction enhancer [3]. More recently, we developed an 8-mer peptide forming PNF, termed D4, that enhance retroviral transduction as efficiently as Vect-1 [4]. Another class are the peptide amphiphiles PA1 and Pat10, which compromise a fatty acid and a peptide domain, that also form positively charged nanostructures [2].

Objectives:

The aim of this study was to elucidate the mechanisms by which the different PNF interact with viral particles and cells. For this, complementary EM techniques were applied to analyze PNF morphologies and their interaction with virus-like particles (VLPs) and cells.

Materials & methods:

To characterize the morphology of PNFs before and after binding of non-infectious VLPs, negative staining and transmission electron microscopy (TEM) was performed. Scanning electron microscopy (SEM) after critical point drying was used to analyze the binding of PNFs and virions to cells. For a deeper understanding of morphological characteristics of transduction enhancing PNFs bound to cells, high-pressure frozen and freeze-substituted samples were analyzed using TEM and STEM tomography [1].

Results:

The results showed that D4, Vect-1, and Pat10 PNFs form small spherical units or nm-long fibrils, which assemble into networks independent of the presence of VLPs (Fig. 1). In contrast, PA1 PNFs exhibited only µm-long fibrils in the absence of VLPs, and also nm-long fibrils upon addition of VLPs, while for D4 PNFs, the opposite effect was observed. Furthermore, VLP binding reduced the density of Vect-1 and D4 PNF networks, suggesting that VLP interactions influence both fibril morphology and the overall organization of fibril networks.

When analyzing the VLP binding pattern of µm-long fibril networks, we observed for D4 PNFs binding of VLPs exclusively to the network surface. In contrast, VLPs bound within the loosely packed network of µm-long PA1 fibrils, indicating that the VLP binding pattern is dependent on the morphology of the fibril network.

Furthermore, VLPs bind directly to the plasma membrane in close proximity to D4 and Pat10 networks. Moreover, VLPs near Pat10 networks had short Pat10 fragments attached to their surface, which may explain the high transduction efficiency associated with these fibrils.

Conclusion:

We used complementary EM techniques to analyze the morphology of different PNFs to better understand their transduction enhancing properties. We found that fibril morphology and fibril network structure influence the VLP binding pattern and provide a structural explanation about why Pat10 and D4 are such potent transduction enhancers. This understanding is important for the further development of these PNFs for clinical applications.

Figure 1: SEM of PNFs on cells

References:

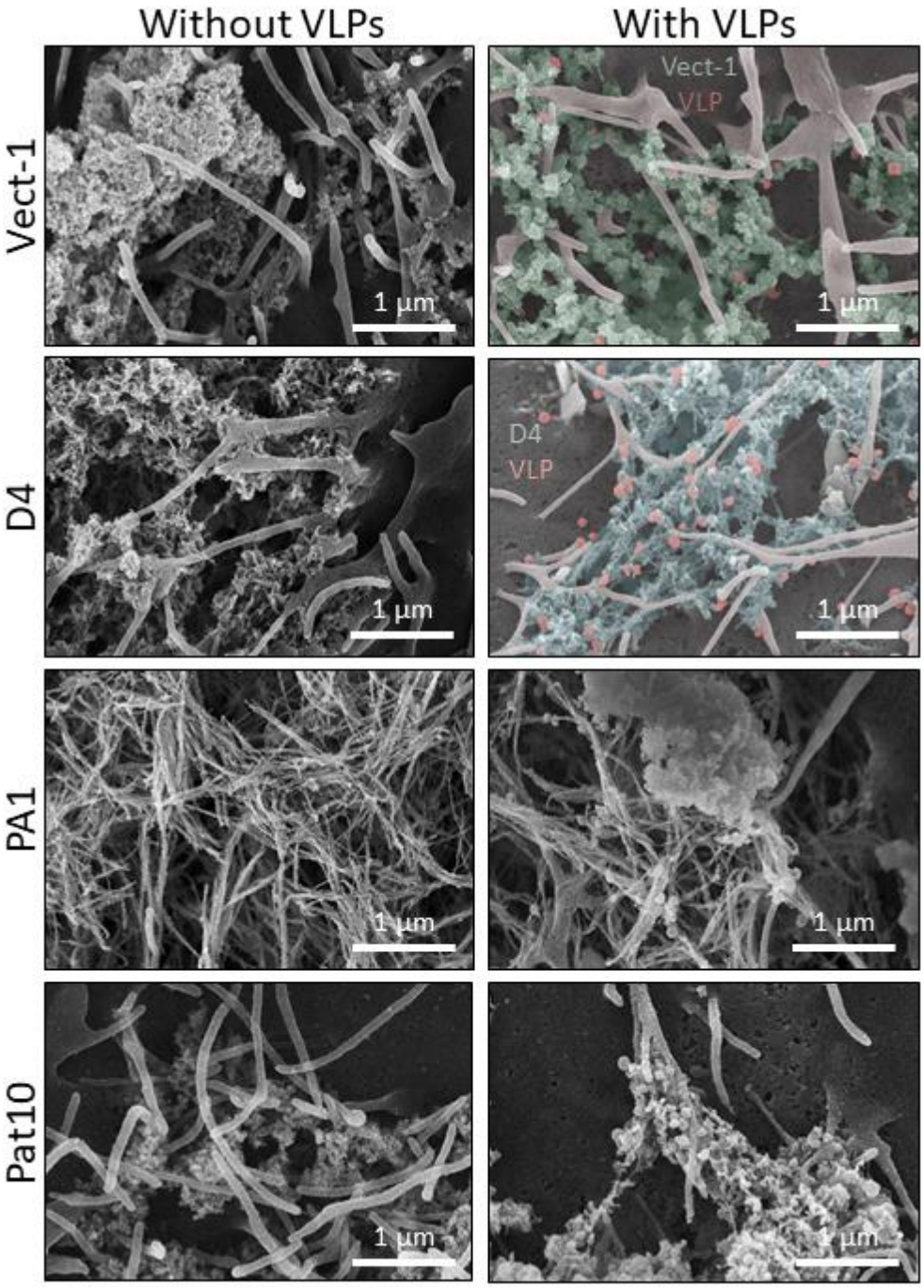
[1] Bergner *et al*., 2022 *Viruses*

[2] Kaygisiz *et al*., 2024 *Adv Healthc Mater*.

[3] Radek *et al*., 2019 *Hum. Gene Ther.*

[4] Rauch-Wirth *et al*., 2023 Front. *Immunol.*

Fig. 1


Without VLPs
With VLPs
Vect-1
D4
PA1
Pat10
Vect-1
VLP
D4
VLP
1 µm

LS5.P01
Imaging the efficacy of silver-decorated PLGA nanoparticle formulations against *Staphylococcus epidermidis* biofilms and evaluation of bacterial detoxification threshold to these nanoparticles

C. Takahashi[1], K. Moriguchi[2]

[1]National Institute of Advanced Industrial Science and Technology, Nagoya, Japan
[2]Wakayama Professional University of Rehabilitation, Department of Rehabilitation, Wakayama, Japan

We have designed various types of polymer particles for drug delivery systems [1]. Silver nanoparticles, known for their strong antibacterial properties, are increasingly being incorporated into polymeric formulations. Recent studies have demonstrated that polymeric systems containing silver nanoparticles are highly effective in combating biofilm infections, which are notoriously difficult to treat with conventional drugs alone [2]. However, the temporal and dose-dependent antibacterial effects of silver nanoparticles within polymer composites remain poorly understood. Furthermore, the detoxification mechanisms of bacteria against silver nanoparticles have not been elucidated. Thereby, we employed SEM and TEM to assess the antibacterial activity of silver-decorated poly (DL-lactide-co-glycolide) (Ag PLGA) nanoparticles against *Staphylococcus epidermidis* biofilms at various treatment durations. PLGA is a biodegradable polymer that breaks down into CO2 and H2O within the human body. Therefore, we selected PLGA due to its high biocompatibility, aiming to minimize cytotoxicity.

In this study, we utilized SEM and TEM for imaging. To examine a broad area of bacteria treated with Ag PLGA nanoparticles, FE-SEM (JXA-8530FA; JEOL Co., Japan) was used with an accelerating voltage of 10.0 kV. We applied an ionic liquid for sample pretreatment of SEM. For TEM observations, we applied the ultrathin section method to prepare samples. TEM images were acquired using a JEOL JEM-1400 Plus at an accelerating voltage of 80.0 kV, while STEM images were obtained using a JEOL JEM-ARM200F at an accelerating voltage of 200.0 kV. We performed time-dependent imaging of Ag PLGA nanoparticles on the biofilms up to 6 h after administration. Additionally, bacterial assays, cytotoxicity evaluations, and silver nanoparticle release characteristics were also assessed.

The antibacterial assay indicated that approximately 85% of the bacteria within the biofilms were eradicated after 6 h of exposure to Ag PLGA nanoparticles [3]. The formulation demonstrated both high efficacy and low cytotoxicity. SEM and TEM results suggest that bacterial cell detoxification was effective for up to 4 h of treatment. However, after 6 h of treatment, the antibacterial activity of the silver nanoparticles outweighed the detoxification effects on the bacteria (Figure 1). This study demonstrated that a specific dose and duration is necessary for silver ions to produce antibacterial effects and induce bacterial cell death, as evidenced by the relationship between the silver ion release rate from Ag PLGA nanoparticles and bacterial cell viability. Based on these findings, we propose a potential mechanism for the time-dependent antibacterial activity of silver nanoparticles, incorporating the detoxification capabilities of bacterial cells. The findings from this study are expected to contribute significantly to research in the fields of pharmacy, bacteriology, and biology.

References:

[1] C. Takahashi, T. Yamada, S. Yagi, T. Murai and S. Muto, Mater. Sci. Eng. C Mater. Biol. Appl., 2021, 121, 111718.

[2] F. Chen, J. Han, Z. Guo, C. Mu, C. Yu, Z. Ji, L. Sun, Y. Wang and J. Wang, Materials, 2023, 16, 3895.

[3] C. Takahashi, T, K. Moriguchi, Nanoscale Adv., 2024, 6, 4971–5210.

Figure 1: STEM images of *S. epidermidis* biofilms without any treatment (a), after treatment of Ag PLGA nanoparticles for 30 min (b), 2 h (c), 4 h (d), and 6 h (e).

Fig. 1

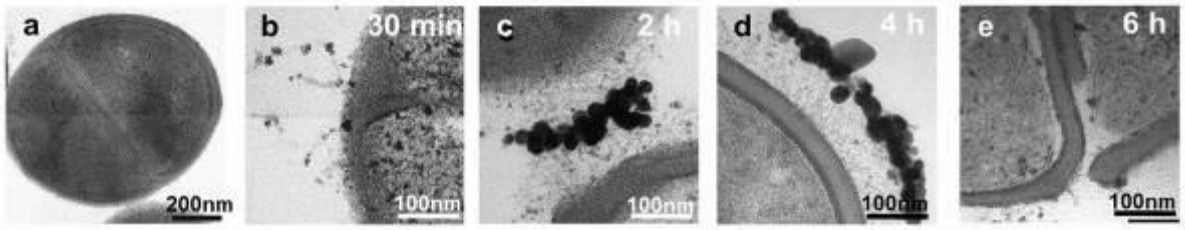


Figure 1: STEM images of *S. epidermidis* biofilms without any treatment (a), after treatment of Ag PLGA nanoparticles for 30 min (b), 2 h (c), 4 h (d), and 6 h (e).

LS5.P02
Possible effects of arsenic(III) oxide on histological structure and estrogen receptor expression in mouse ovaries

M. Marin[1], A. Birinji[1], M. Čakić-Milošević[1], A. Radovanović[2], D. Lalošević[3]

[1]University of Belgrade, Faculty of Biology, Belgrade, Serbia
[2]University of Belgrade, Faculty of Vetrinary Medicine, Belgrade, Serbia
[3]University of Novi Sad, Faculty of Medicine, Novi Sad, Serbia

Introduction: Arsenic is considered a serious environmental and health problem worldwide 1. As a reproductive toxin and endocrine disruptor, arsenic poses a serious threat to female reproductive health. **Objectives**: The aim of this study is therefore to analyze the possible histological changes in the structure of the ovaries of mice treated with arsenic(III) oxide.

Materials & methods: Female mice (*Mus musculus*, strain NMRI) aged 0-6 months were used for this experiment. The control group of mice received water from the water supply system, while the experimental group received a concentration (106 mg/l) of dissolved arsenic(III) oxide. After sacrifice the ovaries were removed and fixed in buffered formalin (pH=7.4). They were then dehydrated at ethanol and the paraffin-embedded tissue samples were cut into 5µm thick-sections for histological examination using a Leica microtome. The sections were stained with hematoxylin-eosin (H&E), periodic acid-Schiff (PAS), Azan and Masson's trichrome to observe the structure of the ovaries under a Leica Dc100 light microscope. For immunohistochemical localization of Erα in the ovaries, the sections were incubated with rabbit monoclonal anti-human Erα primary antibody, according to manufacturer's instruction. For negative control, primary anti- Erα antibody was omitted. After hematoxylin counterstaining, slides were analyzed with a Leica DMLB microscope.

Results: The control group was characterised by the preserved structure of the surface epithelium of the ovary, under which numerous follicles of varying degrees of development were located and numerous *corpora lutea* and stromal cells were visible (Fig. 1A). Our results showed slight damage in the structure of the stromal cells, zona *pellucida,* granulosa cells and dilated blood vessels in the experimental group. Azan blue staining of collagen fibers in the experimental group was observed in *theca* layers and area of granulosa cells (Fig. 1B). An intensive positive reaction in the zona *pellucida* were observed by PAS (Fig. 1C). Masson staining showed intense positive reaction in the granulosa cells of the follicles (Fig. 1D). Estrogen receptor expression results showed a positive response in the *corpus lutea* and a negative response was observed in the stromal cells (Fig. 1F).

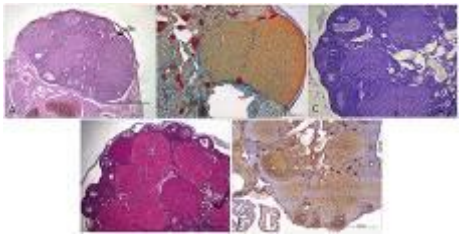
Conclusions: The histological analysis revealed a normal structural organization of the ovaries in the control group. In contrast, slight damage to the ovarian structure was found in the experimental group. The increased presence of collagen fibers was consistent with results previously reported by others 2, while slight changed to the zona *pellucida* was detected using the PAS. Strong expression of estrogen receptors in the *corpus lutea* was found in the experimental group. The different histological staining methods were useful to show that arsenic consumption caused minor but significant histopathological changes in the ovaries of the mice.

References:

1. Hughes MF, Kenyon EM, Kitchin KT. (2007). Toxicol Appl Pharmacol, 222:399–404.
2. Khalaf, H.A., Elmorsy, E., Mahmoud, El-H.M., Aggour, A.M., Amer, S.A. (2019). Cell and Tissue Research, 378: 371–383.

Fig. 1. A) H&E stainig of control group. (B-D) Experimental group: B) Azan, C) PAS, D) Masson, E) Estrogen receptor immunostaining. Surface epitel (Se), *corpus lutea* (Cl), stromal cells (Sc), primordial follicles, (Pf), secundary follicles (Sf), antral follicles (Af).

Fig. 1



LS 6: Advances in sample preparation

LS6.01(inv)
SOLIST – Towards a biopsy at the nanoscale

P. S. Erdmann[1]

[1]Human Technopole, Structural Biology, Milan, Italy

Deciphering molecular processes within complex biological systems requires imaging techniques that combine nanoscale resolution with mesoscale context. To address this need, we developed Serialized On-Grid Lift-In Sectioning for Tomography (SOLIST)[1], an innovative cryo-lift-out method that overcomes key limitations in cryo-electron tomography (cryo-ET) of high-pressure frozen samples, such as low throughput, ice contamination, and sample instability, which have historically restricted cryo-ET to simpler systems such as single cells.

SOLIST introduces a tenfold increase in the number of lamellas generated per lift-out compared to traditional methods, significantly streamlining the workflow and reducing the time required for sample preparation. With SOLIST, we achieve subnanometer resolutions within just one day of sample preparation and data acquisition. This efficiency is critical for optimizing the use of precious biological specimens, including patient-derived tissue biopsies and iPSC-derived organoids.

Our method also improves the consistency and quality of cryo-ET datasets by reducing ice contamination and enhancing sample stability. These advances enable the detailed visualization of cellular structures in their native environment. With SOLIST, we, for example, reveal the architecture of phase-separated chromatin droplets in NUT carcinoma, map the structural organization of neuronal precursor cells in human brain organoids, and resolve ribosome-rich regions in native mouse liver tissue. Additionally, we observe sarcomeric thin and thick filaments in native mouse heart muscle from just a handful of tomograms, demonstrating SOLIST"s broad applicability.

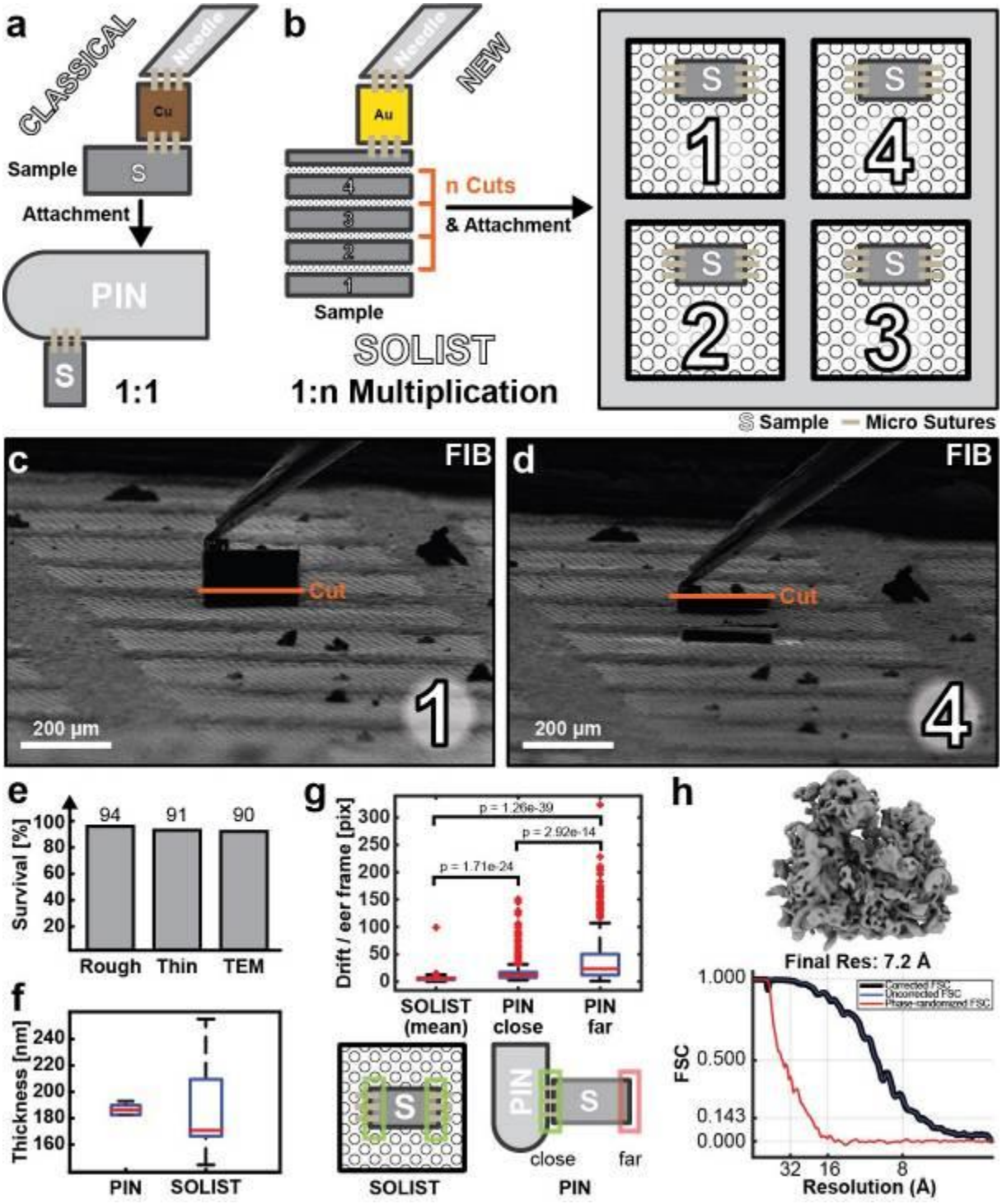
By bridging the gap between nanoscale resolution and mesoscale context, our method extends the reach of cryo-ET to medically relevant systems, for example, providing insights into human brain organoids, an important model system for neurodegenerative disorders. SOLIST, therefore, facilitates studies of human disease mechanisms and structural biology at an unprecedented complexity and scale.

With its serialized approach, our method maximizes data yield from every sample while minimizing waste and preserving the native molecular and structural integrity of complex biological systems. SOLIST, therefore, pushes the boundaries of cryo-electron tomography, offering a robust platform for high-resolution, in situ imaging and bringing us closer to achieving a "Biopsy at the Nanoscale."

[1] Nguyen, H. T. D. *et al.* Serialized on-grid lift-in sectioning for tomography (SOLIST) enables a biopsy at the nanoscale. *Nat. Methods* **21**, 1693–1701 (2024).

Figure 1. Concept and key features of Serialized On-grid Lift-In Sectioning for Tomography (SOLIST). a, Schematic of the classical lift-out procedure using pin grids. **b,** By dividing the sample into multiple sections, SOLIST multiplies the number of lamellas obtained. **c-d,** FIB view images of the first and the last *piece* of a four-lamella SOLIST session being attached to the grid. **e,** Success rates of each step of the SOLIST procedure: section attachment (Rough), fine milling (Thin), and transfer to the transmission electron microscope. **f,** Lamella thickness box plots for the classical lift-out (PIN) and the yeast test data set (SOLIST). **g**, Comparison of beam-induced motion in SOLIST and classical lift-out attached to pin grids. **h**, Resolution potential of SOLIST exemplified by a S. cerevisiae ribosome average obtained from 65 tomograms

Fig. 1


a
CLASSICAL
Needle
Cu
Sample
S
Attachment
PIN
S
1:1
b
NEW
Needle
Au
4
3
2
1
n Cuts
& Attachment
Sample
SOLIST
1:n Multiplication
S
1
S
4
S
2
S
3
S Sample
Micro Sutures
c
FIB
Cut
200 µm
1
d
FIB
Cut
200 µm
4
e
Survival [%]
100
80
60
40
20
94
91
90
Rough
Thin
TEM
f
Thickness [nm]
240
220
200
180
160
PIN
SOLIST
g
Drift / eer frame [pix]
300
250
200
150
100
50
0
p = 1.26e-39
p = 2.92e-14
p = 1.71e-24
SOLIST (mean)
PIN close
PIN far
S
SOLIST
PIN
S
close
far
PIN
h
Final Res: 7.2 Å
FSC
1.000
0.500
0.143
0.000
32
16
8
Resolution (Å)

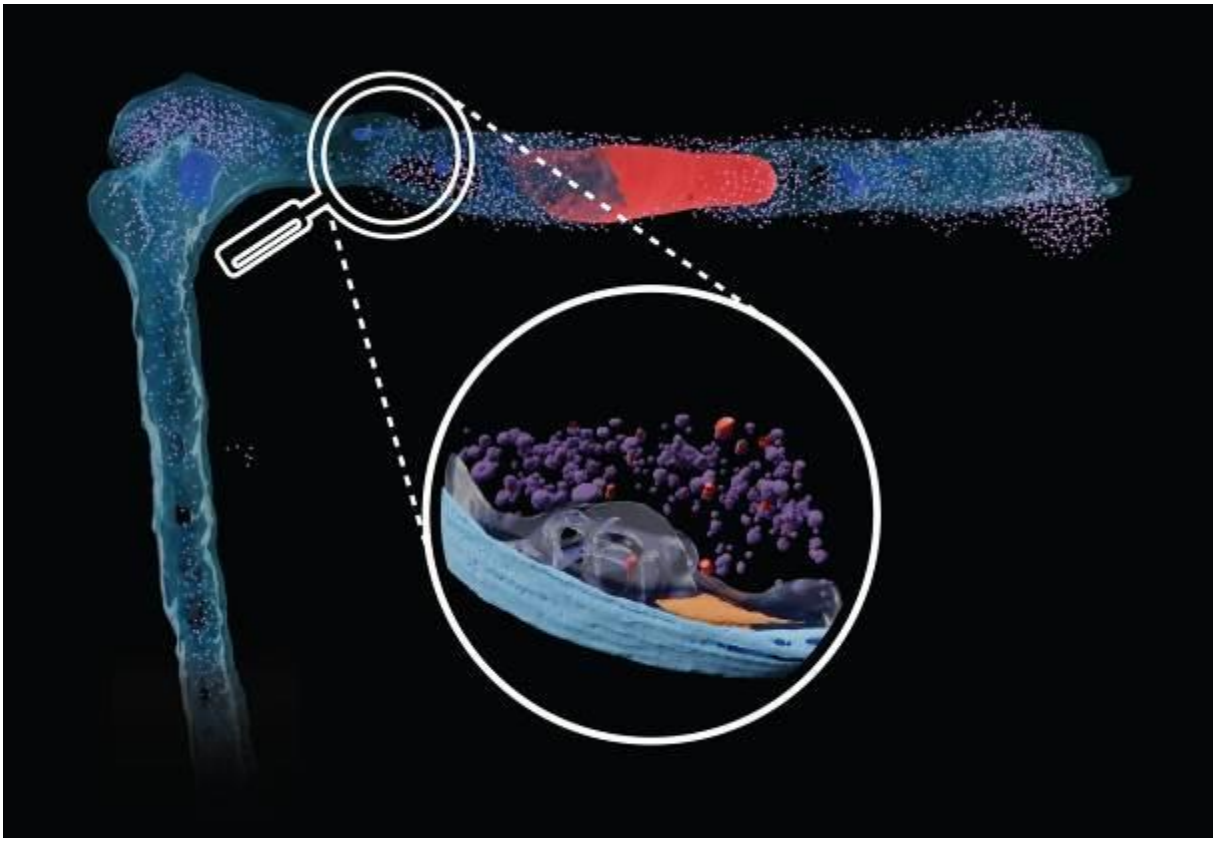
LS6.02(inv)
Combining array tomography with electron tomography provides insights into leakiness of the blood-brain barrier in mouse cortex

M. Schifferer[1]

[1]German Center for Neurodegenerative Diseases, Munich, Germany

Like other volume electron microscopy approaches, automated tape-collecting ultramicrotomy (ATUM) enables imaging of serial sections deposited on thick plastic tapes by scanning electron microscopy (SEM). ATUM is unique in enabling hierarchical imaging and thus efficient screening for target structures, as needed for correlative light and electron microscopy. However, SEM of sections on tape can only access the section surface, thereby limiting the axial resolution to the typical size of cellular vesicles with an order of magnitude lower than the acquired xy resolution. In contrast, serial-section electron tomography (ET), a transmission electron microscopy-based approach, yields isotropic voxels at full EM resolution, but requires deposition of sections on electron-stable thin and fragile films, thus making screening of large section libraries difficult and prone to section loss. To combine the strength of both approaches, we developed "ATUM-Tomo, a hybrid method, where sections are first reversibly attached to plastic tape via a dissolvable coating, and after screening detached and transferred to the ET-compatible thin films. As a proof-of-principle, we applied correlative ATUM-Tomo to study ultrastructural features of blood-brain barrier (BBB) leakiness around microthrombi in a mouse model of traumatic brain injury. Microthrombi and associated sites of BBB leakiness were identified by confocal imaging of injected fluorescent and electron-dense nanoparticles, then relocalized by ATUM-SEM, and finally interrogated by correlative ATUM-Tomo. Overall, our new ATUM-Tomo approach will substantially advance ultrastructural analysis of biological phenomena that require cell- and tissue-level contextualization of the finest subcellular textures.

Fig. 1



LS6.03
Novel embedding resins with enhanced resistance to E-Beam damage

J. Nebesářová[1,2], E. Pavlova[3], B. Strachotova[3], A. Strachota[3], M. Slouf[3], V. Krzyzanek[4]

[1]Biology Centre of CAS, Laboratory of EM, Ceske Budejovice, Czech Republic
[2]Charles University, Faculty of Sciences, Prague, Czech Republic
[3]Institute of Macromolecular Chemistry, CAS, Polymer Morphology, Prague, Czech Republic
[4]Institute of Scientific Instruments, CAS, Microscopy for Biomedicine, Brno, Czech Republic

Electron microscopy (EM) is one of the key techniques for characterizing soft and sensitive biological materials, such as tissues, cells, and their components. A crucial step before analysis is selecting an appropriate sample preparation method that ensures effective protection and fixation of the biological specimen"s structure. One well-established approach involves embedding samples in synthetic polymer resins. Commercially available embedding resins are optimized for transmission electron microscopy (TEM), which relies on detecting high-energy transmitted electrons. However, they are not well-suited for the increasingly popular volume EM visualization techniques that employ scanning electron microscopy (SEM). This limitation arises because SEM microscopes use lower primary electron energies and higher electron doses, leading to issues such as charging and electron beam damage in conventional embedding resins.

To address these challenges, we have developed two types of polymer resins with enhanced resistance to electron beam damage: (a) Commercial resins modified with different types of chemical stabilizing agents. (b) Novel resins based on more e-beam-resistant polymers, specifically siloxane resins.

Various mouse tissues, including the brain, liver, kidney, and other tissues, were prepared following the Hua protocol (1) for SBF-SEM analysis. These samples were embedded using both commercially available resins modified with different stabilizing agents and newly developed siloxane-based mounting resins. The laboratory-prepared siloxane resins were systematically optimized through minor chemical modifications to enhance adhesion to biological samples, improve cuttability in microtomes and ultramicrotomes, and simplify the preparation process, making them more accessible for use in standard biological laboratories. All prepared blocks were characterized using SEM, STEM, and TEM microscopy to evaluate their homogeneity, cuttability, mechanical properties, stability under electron beam exposure, and contrast of embedded test specimens. The obtained data were then statistically analyzed.

Our results demonstrate that both the modified carbon-based embedding resins and the newly developed siloxane-based resins outperform conventional, unmodified, commercially available resins. In this study, we present multiple examples showcasing the improved e-beam resistance, reduced charging, and enhanced contrast achieved with both types of newly developed resins.

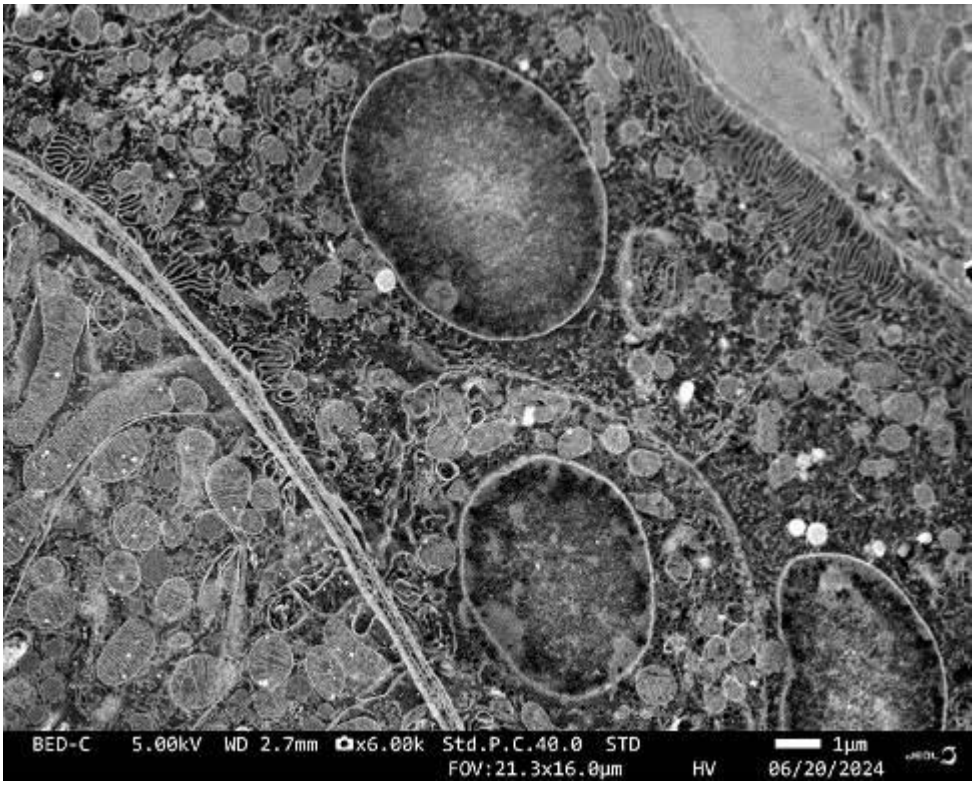
References:

Hua et al.(2015) *Nature Communications*, *6*(1), 7923. https://doi.org/10.1038/ncomms8923

Acknowledgement:
Financial support through grant TN02000020 (TA CR) is gratefully acknowledged.

Fig.: BSE image of the ultrastructure of mouse kidney cells embedded in Siloxane resin.

Fig. 1


BED-C 5.00kV WD 2.7mm x6.00k Std.P.C.40.0 STD
FOV:21.3x16.0µm HV
1µm
06/20/2024

LS6.04
Imaging beyond Uranyl – A systematic evaluation of safer stains for high-quality negative- and positive-staining TEM of organic specimens

V. M. Kissling[1], S. Eitner[1], D. Bottone[1], G. Cereghetti[2], P. Wick[1]

[1]EMPA - Swiss Federal Laboratories for Materials Science and Technology, Materials Meet Life, St. Gallen, Switzerland
[2]University of Cambridge, Department of Chemistry, Cambridge, United Kingdom

Introduction

Negative- and positive-staining transmission electron microscopy (ns/psTEM) is an essential cornerstone of research and diagnostics, enabling the rapid, cost-effective nanometer-resolution characterization of organic specimens from nanoparticles like proteins or viruses to thin sections of cells and tissues. Negative- or positive-staining provides the necessary contrast to organic samples for immediate EM imaging at room temperature. Thus, negative- or positive-staining is a gold-standard sample preparation technique that is not only key for ns/psTEM, but also for other room-temperature EM analyses across scientific fields, including serial-section array tomography, volume EM and scanning EM[1–3].

Objectives

For nearly 70 years, uranyl salts like uranyl acetate (UA) have been the gold-standard stains for negative-/positive staining[4]. However, mounting safety concerns due to their high toxicity and radioactivity have led to stricter regulations and expensive licenses, limiting access for many laboratories[1–3]. Thus, there is a global and urgent need for safer, more sustainable stains that deliver uranyl-comparable, high-quality imaging results.

Materials & Methods

In this recent study, we systematically assessed the eight stain-alternatives UranyLess, UAR, UA-Zero, PTA, STAIN 77, Nano-W™, NanoVan™ and lead citrate against UA. These stains were selected based on their lower toxicity and lack of radioactivity compared to uranyl salts, and their accessibility to users due to their commercial availability and ready-to-use packaging. They were evaluated regarding their contrast, resolution, stain-distribution, ease-of-use and when applicable, size measurement accuracy, in ns/psTEM on a diverse set of samples, including polymethylmethacrylate-nanoplastics, phosphatidylcholine-liposomes, Influenza-A viruses, globular ferritin, fibrillar pyruvate kinase amyloids, and human lung-carcinoma cell-sections[5].

Results

Based on our extensive screening using a safe and standardized workflow with common ns/psTEM equipment, we show that for this variety of samples, several stain-alternatives are commercially available that perform comparably or even better than UA, suggesting them as suitable UA-replacements for many samples of interest of ns/psTEM users in research and clinics without compromises in imaging quality, speed or ease-of-use of the staining protocol. In order to support ns/psTEM users in their transition to UA-alternative stains, we developed the multi-dimensional platform *GUIDE4U* for the fast identification of the appropriate uranyl-replacements for each sample of interest coupled with an efficient staining protocol, saving ns/psTEM-users time and costs while ensuring high-quality imaging results for ultrastructural analysis, thereby further catalyzing the use of safer stains[5].

Conclusions

Our key findings demonstrate a reduced necessity of UA in ns/psTEM and encourage a more widespread use of stain-alternatives in EM that are safer for the users and the environment. This work thus represents a significant advancement and important milestone on the path to UA-replacement, encouraging the EM community to also shift to safer and greener chemistry[5].

[1] H. Sasaki *et al.* (2022), *Sci Rep*.

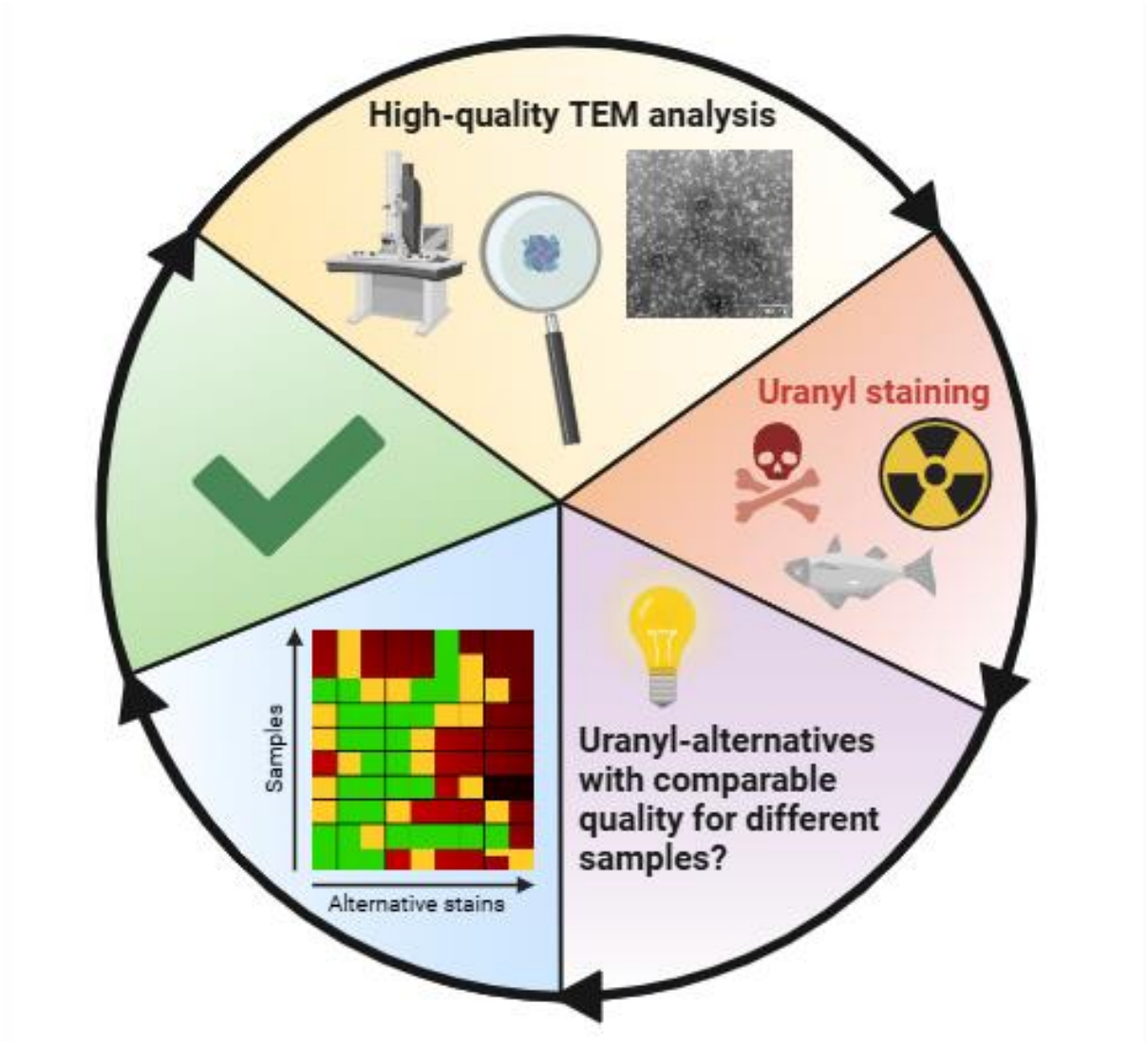
[2] N. Ishii *et al.* (2023), *Microscopy and Microanalysis*.

[3] A. L. Pinto *et al.* (2021), *Diagnostics*.

[4] M. L. Watson (1958), *J Cell Biol*.

[5] V. M. Kissling *et al.* (2025), *in revision*.

Fig. 1



LS6.05
Optimized cryo-FIB milling for dual-axis cryo-ET and modeling of lamella stability

M. Wachsmuth-Melm[1,2], S. Gomez Melo[3,2], C. Mense[3,2], L. Zimmermann[1,2], U. Schwarz[3,2], P. Chlanda[1]

[1]Heidelberg University, Department of Infectious Diseases-Virology, Heidelberg, Germany
[2]Heidelberg University, BioQuant, Heidelberg, Germany
[3]Heidelberg University, Institute for Theoretical Physics, Heidelberg, Germany

The combination of cryo-electron tomography (cryo-ET) and cryo-focused ion beam (cryo-FIB) milling has enabled the study of cellular architecture in 3D under near-native conditions with nanometer-scale resolution. However, this technique only allows for single-axis tomography and thus suffers from missing wedge artifacts.

Here, we present an optimized cryo-FIB milling procedure that produces lamellae enabling dual-axis tomography. Using a trapezoidal milling pattern instead of the conventional rectangular design allowed for a wider opening of the cell body. We can show that this milling strategy allows for dual-axis tomography, which reduces the missing wedge to a pyramidal shape.

We demonstrate that dual-axis tomograms improve the segmentation of cellular structures due to enhanced resolution along the tilt axis. Furthermore, we compare dual-axis tomography data with deep learning-based missing wedge reconstruction methods. Additionally, we apply calculations of the Von Mises stress, a commonly used metric in material physics. Here, presented models indicate that round lamella joints provide a more evenly distributed stress pattern and thus enhance lamella stability, reducing sample loss.

This work establishes that dual-axis tomography is feasible for cryo-FIB-milled samples and significantly improves the analysis of cellular structures. Moreover, it suggests refined cryo-FIB milling strategies to enhance lamella stability and overall imaging quality.

LS6.06
Need for speed – Cryo-plasma focused ion beam technology for faster cryo-electron tomography sample preparation

T. Taubitz[1,2], E. Lisicki[1], S. Raunser[1], S. Tacke[1]

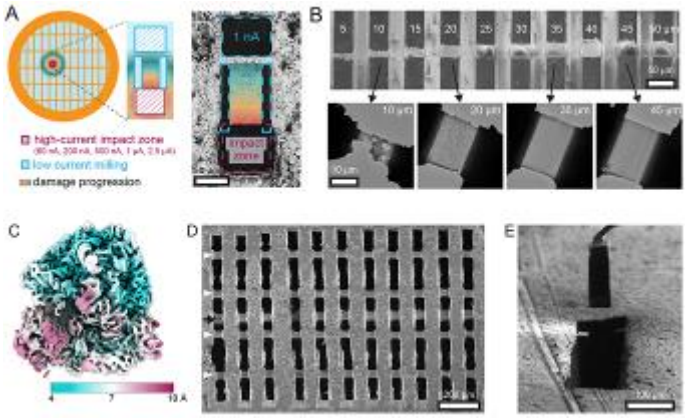
[1]Max Planck Institute of Molecular Physiology, Structural Biochemistry, Dortmund, Germany
[2]Thermo Fisher Scientific, Brno, Czech Republic

Introduction: Cryo-electron tomography (cryo-ET) is a powerful tool for studying cellular ultrastructure and resolving protein structures *in situ*. Biological samples must be thinned to less than 300 nm to enable tomography, usually by cryo-focused ion beam (FIB) milling. Single cell systems are routinely subjected to cryo-ET, but multicellular systems, e.g. 3D cell cultures, organoids and tissues, suffer from low sample preparation throughput, since FIB offers only limited sputter yields and low currents, limiting their study. Cryo-PlasmaFIB (PFIB) offers higher sputter yields and currents, possibly greatly reducing sample preparation times. However, the potential damage caused by high current milling is not yet understood. Objectives: We characterize the damage caused by high Xe PFIB currents. Based on the results, we developed milling strategies using high currents while maintaining sample integrity. Materials & methods: For the damage study, S. cerevisiae cells were high-pressure frozen according to the waffle method1 to yield 20 µm thick samples. A serial lift-out volume2 with one side exposed to a high Xe current (60 nA to 2.5 µA, triplicates, Fig. A) was created and sliced so each slab had an increasing distance from the high-current impact zone (Fig. B). Slabs were milled into lamellae, subjected to cryo-ET and yeast ribosome structures were obtained by subtomogram averaging. Lamella vitrification was evaluated by a custom script based on Brag reflections in tilt-series in Fourier space. To show how high currents can be applied for bulk sample preparation, 70 µm thick waffle-type yeast samples and high-pressure frozen mouse heart samples were milled using Xe currents up to 2.5 µA. Results: For the damage study, a total of 4788 tilt-series were acquired on 148 lamellae from 15 lift-outs created with 5 different currents. High Xe currents caused a current- and distance dependent devitrification: While 60 nA did not cause devitrification, 2.5 µA devitrified the sample up to 50 µm from the impact zone. However, at distances not affected by devitrification, samples prepared with 2.5 µA still gave high-resolution molecular structures (Fig. C). Based on these results, we developed milling strategies that allow the use of currents up to 2.5 µA for bulk sample preparation. Thus, it is possible to prepare a pre-lamella volume ready for automatic lamella fabrication in 30 minutes (Fig. D) and to extract a 140 µm long serial lift-out volume from a tissue sample in less than 30 minutes (Fig. E). Conclusion: High PFIB currents cause local devitrification, but do not affect the structural resolution in non-devitrified areas. Currents up to 2.5 µA can be used for sample preparation if the milling strategy is carefully designed, thus reducing sample preparation times.

References: **1** Kelley, K. *et al. Nat. Commun.* 13, 1857 (2022) **2** Schiøtz, O. H. *et al. Nat. Methods* 21, 1684 (2024)

Figure: A) High Xe currents create an impact zone from which potential damage spreads. Low currents were used to prepare a lift-out volume for damage analysis. B) Slabs were created from lift-outs (here: 2.5 µA) and milled into lamellae to study the damage progression as a function of distance. C) Local resolution of a ribosome reconstruction obtained from lamellae prepared at 2.5 µA that were not affected by devitrification. D + E) Staggered milling schemes (2.5 µA, 500 nA, 60 nA) can be used to prepare tightly packed lamellae (D) or serial lift-out volumes (E)

Fig. 1


A
high-current impact zone
low current milling
damage progression
1 nA
impact zone
B
5
10
15
20
25
30
35
40
45
50 µm
10 µm
30 µm
40 µm
C
4
7
10 Å
D
E

LS6.P01
Automated reordering of randomly arranged serial sections for array tomography

M. Suga[1], K. Shibayama[2], S. Suga[2], Y. Hirabayashi[2]

[1]JEOL Ltd., Solution planning center, Akishima, Japan
[2]University of Tokyo, School of Engineering, Tokyo, Japan

Introduction

Array tomography is a serial-section electron microscopy technique that involves preparing a ribbon of ultrathin sections and imaging them sequentially. This method does not require specialized equipment and is widely applicable. However, mastering the preparation of well-ordered serial sections requires significant skill and effort, creating a substantial barrier to its adoption and widespread use. To address this challenge, a computational approach leveraging image recognition to reorder sections collected in a randomly scattered arrangement is under investigation [1–3].

Objectives

The objective of this study is to develop an efficient workflow for reordering randomly arranged serial sections by integrating the following key steps:

1. Automated recognition of individual sections from optical microscope images using AI.

2. Automated determination of imaging locations and angles for low-magnification SEM.

3. Accelerated reordering of randomly acquired low-magnification SEM images into the correct sequence.

4. Evaluation of accuracy metrics for assessing reordering reliability.

Materials & Methods

Ultrathin sections of various resin-embedded biological samples were prepared using an ultramicrotome and randomly placed on a silicon substrate without the use of an eyelash. Optical microscope images were used for AI-based section detection, and low-magnification SEM imaging was automatically performed on the detected sections. The images were reordered computationally based on similarity measures. The computation time was reduced using two step calculation. The similarity measure was also used for reliability evaluation.

Results

Applying the proposed method to randomly scattered sections, we successfully reordered mouse brain sections (128 and 194 sections) and cultured cell sections (93 sections) purely through computational analysis. For mouse kidney sections (759 slices), reordering was validated by manually verifying and adjusting only one incorrectly ordered section, significantly reducing the need for human intervention.

Conclusion

This method enables array tomography without the use of an eyelash tool, thereby eliminating the requirement for advanced technical expertise. Additionally, it improved efficiency and reduced human effort of the entire workflow. Furthermore, for the case of serial sectioning process, it serves as an effective countermeasure for addressing irregularities that may arise during the process.

[1] Hanslovsky *et al*., Bioinformatics, **33**, 1379 (2017).

[2] Templier, eLife **8**, e45696 (2019).

[3] Fulton et al., Cell Reports Methods **4**, 100720 (2024).

LS6.P02
Sodium phosphotungstate and ammonium molybdate as non-radioactive negative staining agents for single particle analysis

M. Gunkel[1], E. Behrmann[1], A. Macha[1]

[1]University of Cologne, Chemistry/Biochemistry, Cologne, Germany

- **Introduction:** The most often used negative stains for single particle analysis are based on the radioactive element uranium. Due to their radioactive character, these stains are difficult to purchase and to dispose.
- **Objectives**: In order to make negative staining a method that can be used in any lab, also if it is not a dedicated EM-lab, we wanted to establish negative staining agents that are not radioactive and therefore are easier to purchase and dispose in contrast to uranyl acetate or formate. There are others contrast agents cited in literature, but most are developed to stain tissues. We tested sodium phosphotungstate (SPT) and ammonium molybdate (AMo) if they are suitable for single particle analysis. We specially tested if they can produce comparable contrast and protein preservation as uranyl formate (UF).
- **Materials and Methods**: Negative staining of apoferritin and beta-galactosidase was performed with UF, SPT and AMo on conventionel continuous carbon grids. For SPT and AMo an additional fixation step with paraformaldehyde was performed. Data sets were acquired with a TalosL120C (ThermoFisher). Overall structure preservation was evaluated for both proteins. The beta-galactosidase data were processed with cryoSPARC according to our standard single particle processing workflow and rigid-body fitting was used to fit the atomic model into the resulting density maps.
- **Results**: Initial structure evaluation of apoferritin showed that SPT and AMo required an on-grid fixation step to preserve particle integrity. Without fixation, particles appeared fuzzy, but fixation improved staining quality, revealing well-defined circular particles. Beta galactosidase was used to assess the suitability of SPT and AMo for SPA applications. All three stains (UF, SPT, AMo) allowed differentiation of β-galactosidase tetramers from smaller contaminants, though SPT and AMo resulted in slightly fainter images and lower particle densities. Despite differences in contrast, all three stains produced high-quality 2D class averages and comparable 3D reconstructions that allowed rigid body fitting of a β-galactosidase crystal structure.
- **Conclusion**: SPT and AMo turned out not only as good replacements for UF for single particle analysis but due to their chemical properties: higher pH and being anionic, they open up as real alternatives where UF fails. In combination with a chemical grid hydrophilization step with alcian blue, negative staining can be done in every lab without any special requirements with the non-radioactive stains.

Figure1: structure preservation of apoferritin

Apoferritin was stained with (a) UF, (b) SPT and (c) AMo. All three stains show good structure preservation. Scale bars 100 nm

Figure2: β-galactosidase stained with SPT and reconstructed with cryoSPARC

From the collected micrographs the high-quality micrographs were selected based on good CTF scores and low astigmatism. Particles were picked and classified in 2D, and afterwards in 3D by ab-initio reconstruction. All particles that showed clear 4 subunits were combined and used to create the final 3D volume.

Fig. 1

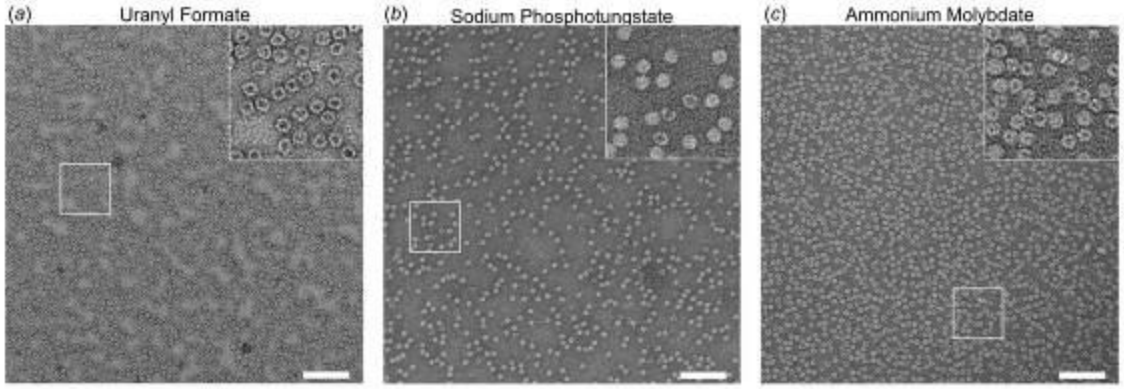
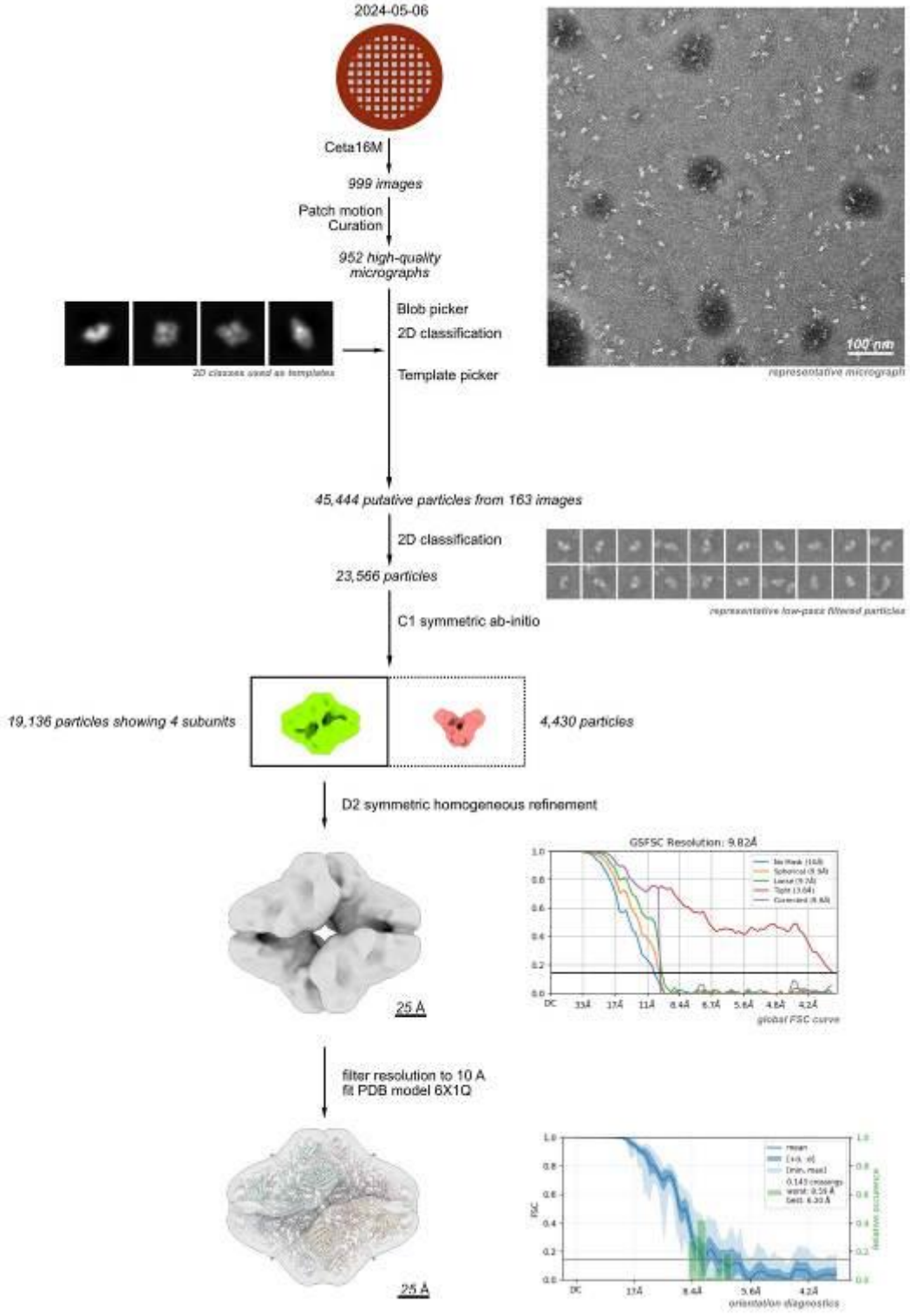

(a)
Uranyl Formate
(b)
Sodium Phosphotungstate
(c)
Ammonium Molybdate

Fig. 2


2024-05-06
Ceta16M
999 images
Patch motion
Curation
952 high-quality
micrographs
Blob picker
2D classification
Template picker
2D classes used as templates
100 nm
representative micrograph
45,444 putative particles from 163 images
2D classification
23,566 particles
C1 symmetric ab-initio
representative low-pass filtered particles
19,136 particles showing 4 subunits
4,430 particles
D2 symmetric homogeneous refinement
GSFSC Resolution: 9.82Å
25 Å
global FSC curve
filter resolution to 10 Å
fit PDB model 6X1Q
25 Å
orientation diagnostics

LS6.P03
Exploring dimethylacrylamide-based gels in Expansion Microscopy (ExM) with alternative solvents

M. Izidoro Santos[1], T. Hedtke[2], C. Schmelzer[2], R. B. Wehrspohn[1], J. Martins de Souza e Silva[1,2]

[1]Martin Luther University Halle-Wittenberg, Institute of Physics, Halle (Saale), Germany
[2]Fraunhofer Institute for Microstructure of Materials and Systems IMWS, Halle (Saale), Germany

Expansion microscopy (ExM) is a powerful super-resolution imaging technique that relies on the physical expansion of biological specimens within a hydrogel matrix to enhance optical microscopy"s magnification capabilities. [1] Traditional ExM methods utilize acrylamide (AA) and sodium acrylate (SA)-based hydrogels, which are limited to expansion in water. Developing alternative formulations that enable expansion in alternative solvents can expand the range of ExM applications.

This study aims to develop a dimethylacrylamide (DMAA)-based hydrogel formulation capable of expanding in multiple solvents, including ethanol, isopropanol, and acetone.

A series of hydrogel formulations were synthesized without SA, incorporating varying concentrations of DMAA and AA, along with different levels of the crosslinker bisacrylamide (MBA), to optimize expansion and mechanical properties across solvents.

Our findings indicate that excluding AA from the formulation enables the DMAA-based gel to maintain robust mechanical integrity while achieving moderate expansion (up to 2.2×) in various solvents (Fig. 1). Using eosin-stained tropoelastin fibers as a model system, we demonstrate that this gel preserves structural integrity and significantly enhances fluorescence microscopy resolution. Notably, expansion in ethanol yielded similar linear expansion and improved imaging contrast compared to water (Fig. 2), highlighting its potential advantages for applications that require reduced aqueous exposure.

These results suggest that DMAA-based hydrogels provide a flexible and effective alternative for ExM, broadening its applicability in diverse expansion and imaging conditions. Future studies will aim to enhance the expansion factor beyond current values, thereby further enhancing resolution and adaptability for advanced imaging applications. This work lays the groundwork for addressing limitations in traditional aqueous-based ExM, potentially enabling new experimental paradigms in high-resolution microscopy.

Figure 1. Expansion of DMAA-based gels across different solvents (scale bars: 0.5 cm).

Figure 2. Expansion of tropoelastin fleece embedded in a DMAA-based gel. Fluorescence micrographs of an eosin-stained fleece A) prior to gel treatment; expanded in B) water; and in C) ethanol. Two regions of interest (i and ii) are enlarged, and line profiles are shown below (red scale bars: 1000 µm; white scale bars: 100 µm).

[1] F. Chen, P.W. Tillberg, E.S. Boyden, Science, 347 (2015) 543-548.

Fig. 1

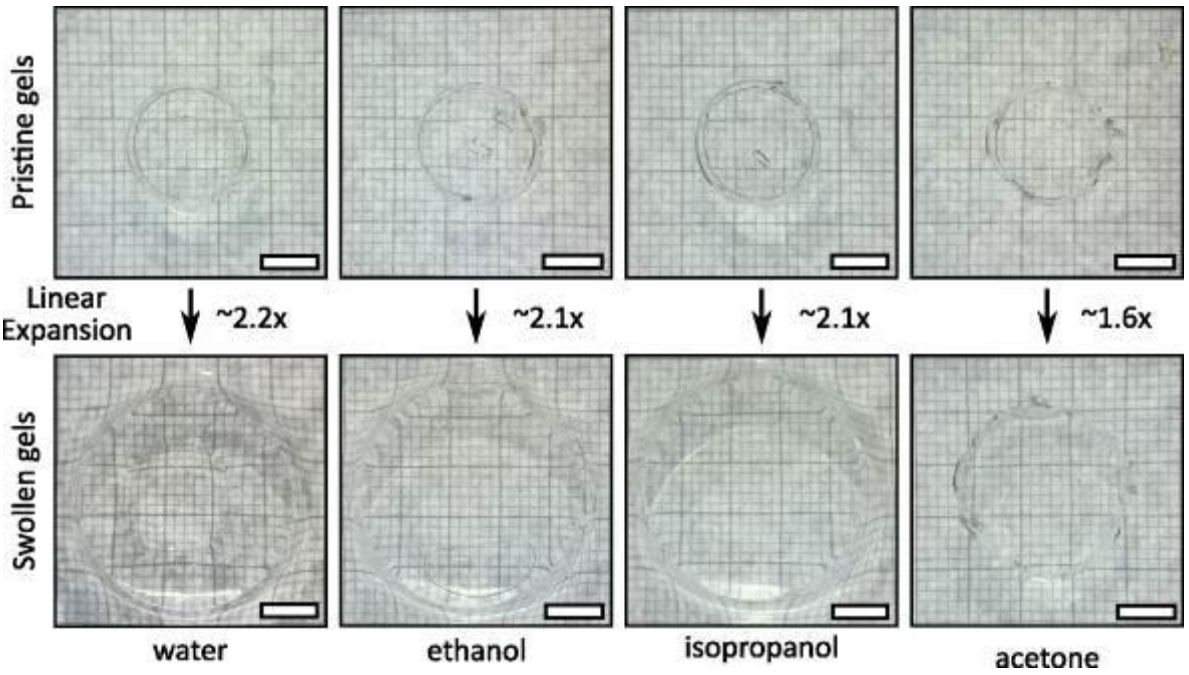
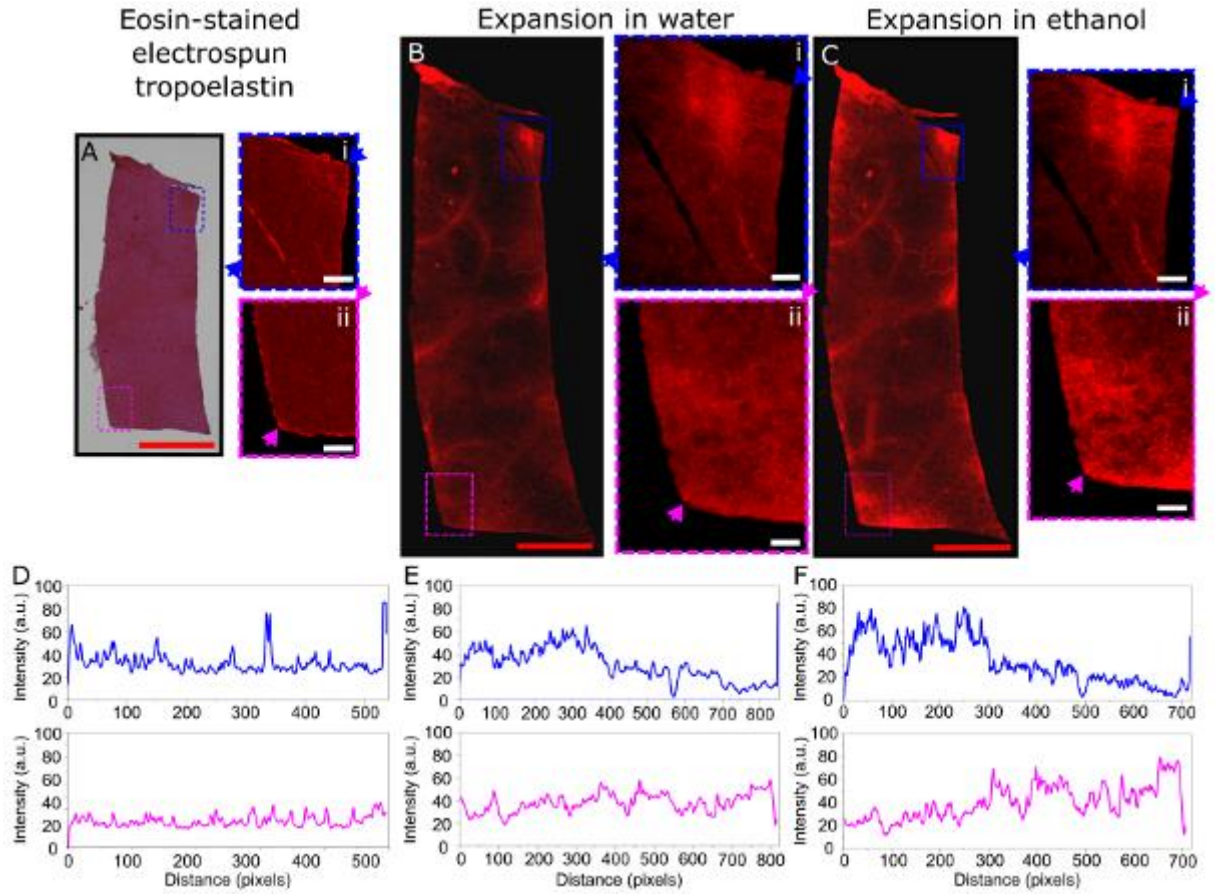

Pristine gels
Linear Expansion
~2.2x
~2.1x
~2.1x
~1.6x
Swollen gels
water
ethanol
isopropanol
acetone

Fig. 2


Eosin-stained electrospun tropoelastin
Expansion in water
Expansion in ethanol
A
B
C
i
ii
D
E
F
Intensity (a.u.)
Distance (pixels)

LS6.P04
CryoGenium – A robotic blot-free plunge freezing system to prepare CryoEM samples for SPA and cryo-ET

M. Schwertner[1], R. I. Koning[2], M. van Nugteren[1], T. Smit[1], H. Vader[1], L. Alexander[1], K. Verduin[1], C. Ko[1], A. Kamp[1], N. Hosny[1]

[1]Linkam Scientific Instruments Ltd., Salfords, United Kingdom
[2]Leiden University Medical Center, Leiden, Netherlands

Keywords

Vitrification of biological samples, blot-free ethane plunging, sample preparation robot, cryo-Electron Microscopy (cryo-EM), Single Particle Tomography (SPT), cryo-ElectronTomography (cryo-ET)

Introduction / Summary

Vitrification of biological samples is a method that offers superior preservation of the sample down to a molecular level. When cooling rates are sufficiently high, the sample is transformed into a glass-like vitrified state that is also naturally compatible with the conditions required for EM. In this work we explore plunge freezing in an automated machine based on a new principle to control the film thickness of the ice. In contrast to conventional blotting techniques a suction principle is deployed where small nozzles remove fluid from the edge of the EM grid. This procedure can be observed and controlled in real-time using the integrated optical microscope, before the plunge action is triggered. The imaging step delivers control as well as valuable information on sample quality at the time of plunging. Methods and workflows are discussed relating to Single Particle Tomography (SPT) as well as Cryo-ET.

Objectives

While SPA and Cryo-ET have been established as standard workflows in recent years, the sample preparation is still mostly manual or semi-automated, sometimes leading to trial-and-error especially for new users. Typical challenges in the preparation of cryo-samples are discussed in [1]. With CryoGenium we like to simplify sample preparation though automation, while also saving resources and time in typical facility environments by optical sample pre-screening at the time of plunge-freezing.

Materials and Methods

We have designed and built a robotic plunge freezer-system, CryoGenium, that uses a patented blot-free technique to adjust liquid film thickness on the EM sample grid [2]. For SPA the workflow is compared with a conventional blotting technique in Fig 1. Typically the EM grids are glow-discharged before use to make them hydrophilic. For CryoGenium a glow-discharge unit is integrated avoiding additional sample transfers to separate instruments. The sample is then applied by dipping into a small (12 uL) cup. After interactive film thickness adjustment using suction nozzles and the integrated optical microscope for visual feedback, the user triggers plunging of the sample into a cup of temperature-controlled liquid ethane. The sample is then stored in a cryo-cartridge that is ready for transfer to other cryo-devices.

The exterior of CryoGenium is shown in Fig. 2: the automated tweezers can be seen behind the transparent lid, there are two sections, a humidity-controlled drawer on the right and a cryo-section on the left. More details are shown in Fig. 3 where both drawer sections are open.

Results and Conclusion

CryoGenium delivers optical data to assess sample quality, offers direct control over parameters and enables the pre-selection of the best samples for EM screening. This saves time and cost while minimising manual handling. Vitrification of multiple sample types has been demonstrated including single particles, vesicles, cells and bacteria. In our presentation we will discuss how CryoGenium can simplify sample preparation workflows for cells, SPT and more.

References

[1] Nature Methods, VOL 18, May 2021, 463–471, P. J. Peters, et al.
[2] Nature Communications, (2022) 13:2985, https://doi.org/10.1038/s41467-022-30562-7

Fig. 1

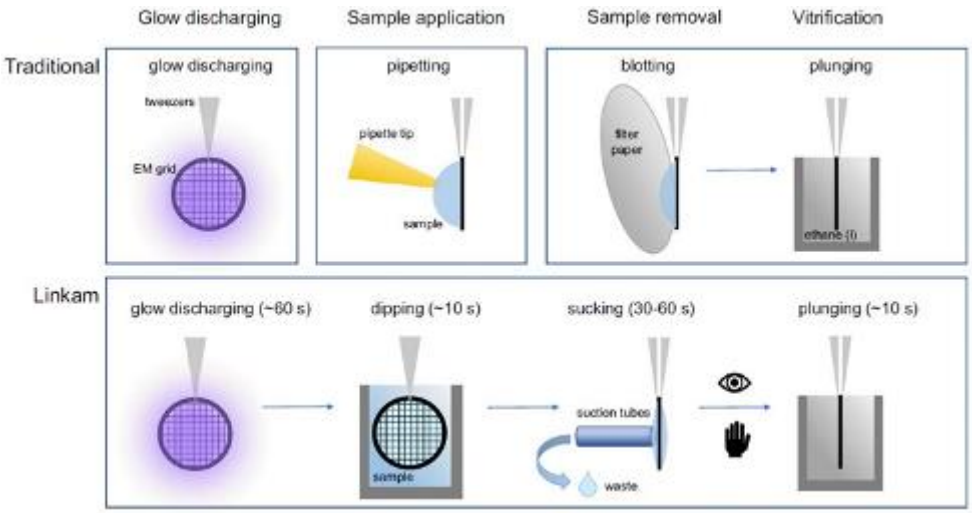
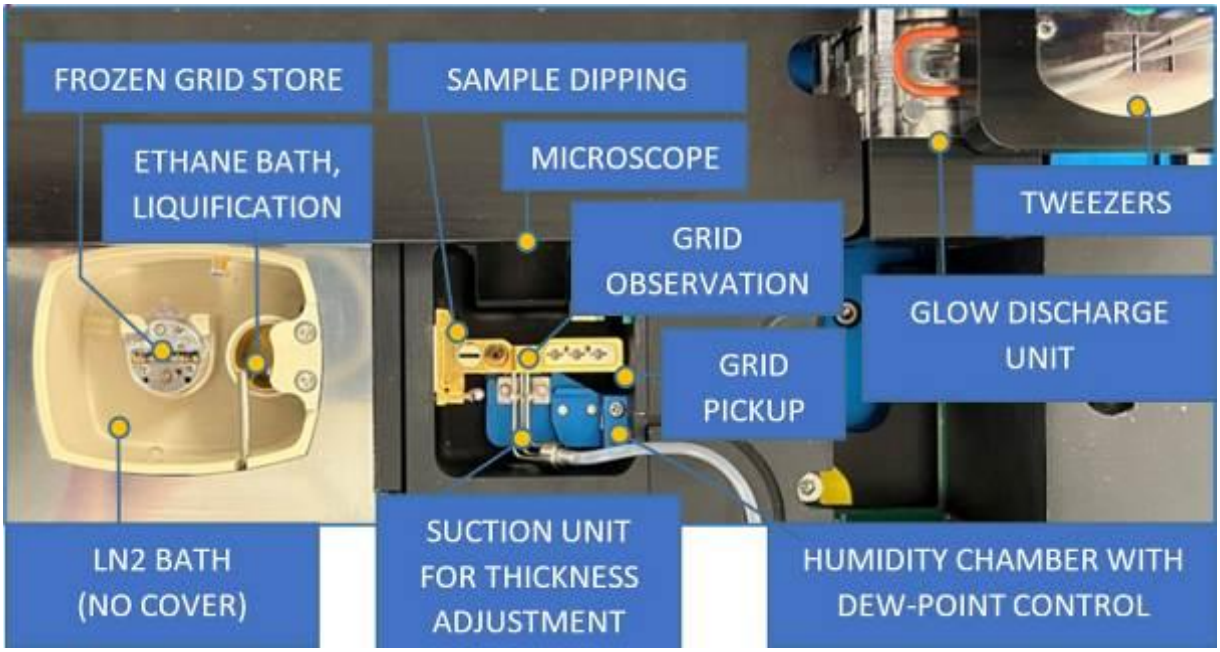


Fig. 2



Fig. 3


FROZEN GRID STORE
SAMPLE DIPPING
ETHANE BATH, LIQUIFICATION
MICROSCOPE
TWEEZERS
GRID OBSERVATION
GLOW DISCHARGE UNIT
GRID PICKUP
LN2 BATH (NO COVER)
SUCTION UNIT FOR THICKNESS ADJUSTMENT
HUMIDITY CHAMBER WITH DEW-POINT CONTROL

LS6.P05
Novel sample preparation technique for Soft X-ray imaging of *Physcomitrium patens*

F. M. Annesha[1,2], S. S. Tamanna[3], S. J. Müller-Schüssele[3], V. Weinhardt[2,4]

[1]Heidelberg University, HGSMathComp,, Faculty of Engineering, Heidelberg, Germany
[2]Heidelberg University, Centre for Organismal Studies (COS), Heidelberg, Germany
[3]RPTU Kaiserslautern-Landau, Molecular Botany, Kaiserslautern, Germany
[4]Lawrence Berkeley National Laboratory, Molecular Biophysics and Integrated Bioimaging Division, Berkely, CA, United States

Soft X-ray tomography (SXT) has emerged as a powerful imaging technique for studying cellular morphology and organelle organization at high resolution. This study introduces a sample preparation method for the model moss *Physcomitrium patens*, enabling high-resolution 3D imaging using SXT while addressing challenges in positioning cells within narrow capillaries.

SXT leverages carbon and nitrogen absorption edges to provide natural, quantitative contrast for cellular organelles in their near-native state. It offers several advantages, including spatial resolution down to 25-50 nm, the ability to image samples up to 15 µm thick, and quantitative analysis through linear absorption coefficient (LAC) measurements. These features make SXT particularly valuable for investigating plant cell biology, including organelle dynamics and metabolic processes.

Physcomitrium patens, a model organism in plant cell biology, displays considerable variability in cell size during its protonema stage, with caulonema cells being thinner than chloronema cells, do not have explicitly reported width measurements, but they are generally narrower than 20 µm [1]. These large cell dimensions present a challenge for capillary-based imaging since SXT capillary tips typically range from 6 to 12 µm in diameter. To overcome this limitation, we enzymatically digested the cell walls, facilitating cell entry into the capillaries, thereby promoting filamentous protonema growth inside capillaries with appropriate growth media and optimal light intensity. Unlike mechanical disruption methods such as pipetting, which induce stress and cause cell and organelle rupture, this enzymatic approach preserves cellular structures.

Our protocol preserves the native cellular architecture of *P. patens*, enabling high-resolution 3D reconstructions that capture subtle structural variations under different conditions, laying the groundwork for further studies on changes in organelle morphology and distribution under stress conditions in *P. patens* cells. This approach opens new possibilities for studying plant cell biology at high resolution, potentially applicable to other plant species and cellular systems where specimen size has been a limiting factor for SXT imaging.

References:

1. Tang, H., Duijts, K., Bezanilla, M., Scheres, B., Vermeer, J.E.M. and Willemsen, V. (2020), Geometric cues forecast the switch from two- to three-dimensional growth in *Physcomitrella patens*. New Phytol, 225: 1945-1955. https://doi.org/10.1111/nph.16276

LS6.P06
Innovations in the Arctis WebUI – Enhancing cryo-lamella preparation through the integration of multigrid workflow and sparse optical tileset

V. Vrbovská[1], R. Spurný[1], R. Kříž[1], P. Tomášek[1], R. Tichý[1], L. Chvíla[1], L. Červinka[1], L. Král[1], M. Müllerová[1], A. Kasáková[1], M. Hovorka[1], J. Mitchels[1], A. Rigort[1]

[1]Thermo Fisher Scientific, Brno, Czech Republic

Cryo-electron tomography is an essential technique for visualising proteins and protein complexes in their native cellular environment. To achieve high-resolution imaging, the preparation of thin cryo-lamellae from cells containing the region of interest is a critical step. Conventional lamella preparation methods often require multiple software applications, which can be a challenge for users inexperienced in the cryo-electron tomography workflow.

The Arctis cryo-plasma focused ion beam (PFIB) system plays a key role in the automated preparation of cryo-lamellae from cells. Supported by WebUI, a novel web-based software interface, the Arctis streamlines the creation of cryo-lamellae with minimal user input in a data-driven workflow. WebUI serves as a centralised platform for mapping and navigating cellular samples using three modalities: electron, ion, and optical imaging. The integration of a fluorescent light microscope enables in-situ targeting of specific labelled cellular structures. Additionally, its automatic sample loading system (Autoloader) provides a direct connection between the Arctis and the cryo-transmission electron microscope (cryo-TEM), enhancing both user experience and efficiency.

This presentation will provide a comprehensive overview of the application workflows for lamella preparation facilitated by Arctis WebUI. The key advancements are a multigrid workflow utilising tomogrids and the implementation of a sparse optical tileset. Tomogrids prevent grid rotation between loading events, which is important for maintaining the tomographic tilt axis. Users can create overview images and tilesets, conduct depositions, and set lamella sites on multiple grids, allowing them to be processed asynchronously rather than one by one. This approach enhances throughput and ensures efficient cryo-lamella preparation with maximum microscope utilisation. A sparse optical tileset complements the whole-grid optical tileset by allowing users to manually select specific regions for optical data collection. Once the lamellae are milled, they are transferred to a cryo-TEM and utilised for cryo-electron tomography data collection.

With the capability to simultaneously process up to 12 grids in a multigrid workflow, the Arctis WebUI streamlines the preparation of cryo-lamellae for tomography, enhancing efficiency and productivity in the field of cryo-electron microscopy. By providing a more accessible and efficient workflow, the Arctis WebUI enables researchers to focus on biological research while automating the sample preparation process.

Instrumentation and Methods (IM)

IM 1: Progress in instrumentation and ultrafast EM

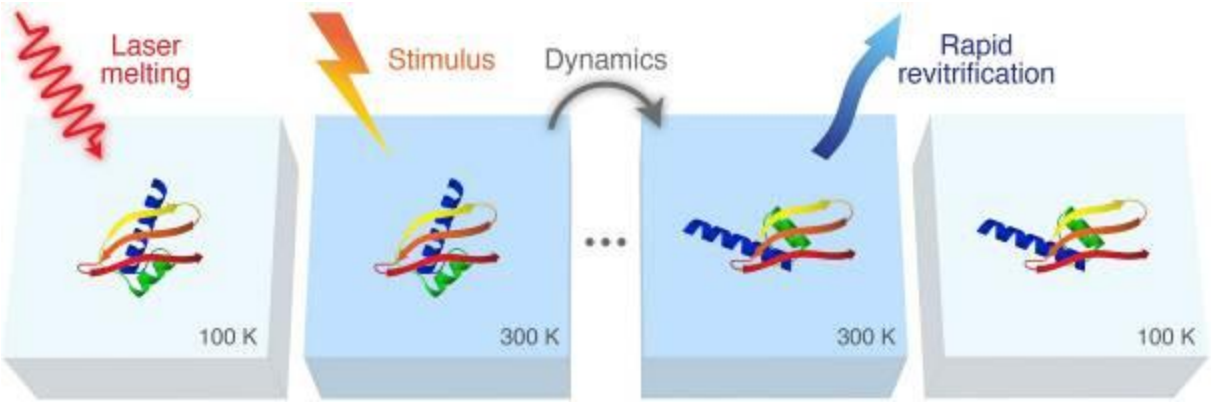
IM1.01(inv)
Advances in microsecond time-resolved Cryo-EM

U. J. Lorenz[1]

[1]Ecole Polytechnique Fédérale de Lausanne, Lausanne, Switzerland

Protein structure determination and prediction have made stunning progress. In contrast, it is generally not possible to observe proteins as they perform their tasks, which leaves our understanding of these nanoscale machines fundamentally incomplete. My group has recently introduced a novel approach to time-resolved cryo-EM that improves its time resolution by about 3 orders of magnitude, making it fast enough to observe the microsecond dynamics of proteins that are frequently associated with function. Our method involves melting a cryo sample with a laser beam, which allows dynamics of the embedded particles to occur in liquid if a suitable stimulus is provided. When the heating laser is switched off, the sample rapidly revitrifies, trapping the particles in their transient configurations, in which we can subsequently image them. As I will illustrate, this makes it possible to watch protein dynamics that were previously unobservable. Our method therefore promises to fundamentally advance our understanding of protein function. We also demonstrate that laser melting and revitrification of cryo samples can be used to overcome preferred particle orientation, an issue that still causes many cryo-EM projects to fail. Finally, I will show a new approach that significantly expands the utility of our method by extending its temporal observation window. This allows us to follow the structural evolution of conformational ensembles in a temperature jump experiment on a timescale of hundreds of microseconds.

Fig. 1



IM1.02
Does pulsed-electron beam illumination reduce beam damage in biological specimens?

V. Kumar[1,2], J. Radecke[1,2], P. Roth[3], D. Fotiadis[3], H. Stahlberg[1,2]

[1]Ecole Polytechnique Fédérale de Lausanne, Lausanne, Switzerland
[2]University of Lausanne, Lausanne, Switzerland
[3]University of Bern, Bern, Switzerland

Cryo-electron microscopy has revolutionized our fundamental understanding of biological processes by probing the structure of biological machinery at the atomic scale. Technological advancements in sample preparation, electron optics, improved cameras, and data analysis have enabled the resolution of protein structures close-to-native state. However, cryo-electron microscopy performance is limited by the inherent damage caused by high-energy electrons, which destroy high-resolution information in the sample even at very low electron fluences (~a few e⁄Å²).[1,2] The primary damage mechanism in organic macromolecules, i.e., radiolysis, rapidly destroys chemical bonds under continuous electron beam exposure. Recently, several groups have introduced the application of pulsed-electron sources in order to attempt to reduce beam damage in organic specimens.[3-6] Here, we have used a radio-frequency (RF) deflection cavity system operating at a 75 MHz frequency,[7] mounted on a cold field emission gun (FEG)-equipped Thermo Fisher Scientific Titan Krios, to produce pulsed electron beam illumination. To compare the critical electron dose (the dose at which an electron diffraction spot intensity falls to 1/e of the original spot intensity) using pulsed *vs*. continuous electron-beam illumination, we used model organic biomolecules: paraffin and bacteriorhodopsin (bR) 2D crystals in both electron diffraction and real-space imaging modes at cryogenic temperatures. Quantitative evaluations of the beam damage in different resolution ranges under different illumination conditions will be presented.

References:

1. Naydenova, Katerina, et al. "On the reduction in the effects of radiation damage to two-dimensional crystals of organic and biological molecules at liquid-helium temperature." Ultramicroscopy 237 (2022): 113512.
2. Peet, Mathew J., Richard Henderson, and Christopher J. Russo. "The energy dependence of contrast and damage in electron cryomicroscopy of biological molecules." Ultramicroscopy 203 (2019): 125-131.
3. VandenBussche, Elisah J., and David J. Flannigan. "Reducing radiation damage in soft matter with femtosecond-timed single-electron packets." Nano letters 19.9 (2019): 6687-6694.
4. Babayan, Nelly, et al. "Dose-rate effect of ultrashort electron beam radiation on DNA damage and repair in vitro." Journal of radiation research 58.6 (2017): 894-897.
5. H. Choe et al., "Mitigation of radiation damage in macromolecules via tunable ultrafast stroboscopic TEM," bioRxiv, p. 2020.05.15.099036, 2020, doi: 10.1101/2020.05.15.099036.
6. Kisielowski, Christian, et al. "Discovering hidden material properties of MgCl2 at atomic resolution with structured temporal electron illumination of picosecond time resolution." Advanced Functional Materials 29.11 (2019): 1807818.
7. Van Rens, J. F. M., et al. "Dual mode microwave deflection cavities for ultrafast electron microscopy." Applied Physics Letters 113.16 (2018).

IM1.03
Dynamic TEM using nanosecond electron pulses in the study of photoswitchable nanomaterials

H. Mba[1], Y. Hu[1], H. Zhang[1], M. Picher[1], G. Chastanet[2], P. Rabiller[3], M. Lorenc[3], F. Banhart[1]

[1]University of Strasbourg, IPCMS, Strasbourg, France
[2]Université de Bordeaux, ICMCB, Bordeaux, France
[3]Université de Rennes, ICR, Rennes, France

Nanomaterials are subjected to laser pulses in an ultrafast TEM. Electronic excitations, acoustic waves and thermal effects appear at timescales from femto- to microseconds. The size of the system determines the timescales of phase transitions when the laser-induced excitation (e.g., a sound wave or thermal diffusion) propagates through the system. The different approaches of ultrafast or dynamic TEM give access to fast transformations in nanomaterials that are detectable by imaging, electron diffraction or EELS. Reversible transitions are studied by the stroboscopic [1] and irreversible by the single-shot technique [2, 3]. In this contribution, thermal effects in nanomaterials occurring at the nanosecond timescale are described. In a dedicated setup, two coupled nanosecond lasers are used to induce transitions of the specimen and to create photoelectron pulses (Fig. 1).

Here we use the stroboscopic mode for studying photoswitchable materials that undergo reversible phase transitions under electronic excitation or temperature changes. Results on spin-crossover (SCO) materials [4, 5] and trititanium pentoxide (Ti_3O_5) crystals [6] are shown, where phase transitions at the nanosecond timescale occur. By measuring the time interval between the pump pulse and the onset of structural changes, the characteristic switching time of the materials is determined. Due to the high temporal resolution and spatial selectivity, the time-dependent behavior of individual nanocrystals can be studied.

Spin crossover nanoparticles undergo a phase transition where they change their size under laser irradiation. By encapsulating gold nanoparticles, plasmonic heating is achieved. The size changes are measured (Fig. 2), showing an expansion within tens of nanoseconds [4, 5]. In the same way, a phase transition in Ti_3O_5 nanoparticles is induced by laser pulses, and phase changes are detectable by electron diffraction. It is found that the switching dynamics of Ti_3O_5 depends strongly on the size and shape of the system [6].

The work was funded by the Agence Nationale de Recherche under contracts ANR-11-EQPX-0041 and ANR-22-CE09-0033-01, the Interdisciplinary Thematic Institute ITI-QMAT and the METSA Network (FR CNRS 3507).

[1] K. Bücker, M. Picher, O. Crégut, T. LaGrange, B. W. Reed, S. T. Park, D. J. Masiel, F. Banhart, *Ultramicroscopy* **171**, 8 (2016).

[2] M. Picher, K. Bücker, T. LaGrange, F. Banhart, *Ultramicroscopy* **188**, 41 (2018).

[3] S. K. Sinha, A. Khammari, M. Picher, F. Roulland, N. Viart, T. LaGrange, F. Banhart, *Nature Comm*. **10**, 3648 (2019).

[4] Y. Hu, M. Picher, N. M. Tran, M. Palluel, L. Stoleriu, N. Daro, S. Mornet, C. Enachescu, E. Freysz, F. Banhart, G. Chastanet, *Adv. Mater.* **33**, 2105586 (2021).

[5] Y. Hu, M. Picher, M. Palluel, N. Daro, E. Fresz, L. Stoleriu, C. Enachescu, G. Chastanet, F. Banhart, *Small* **19**, 2303701 (2023).

[6] Y. Hu, M. Mba, M. Picher, H. Tokoro, S.-I. Ohkoshi, C. Mariette, R. Mandal, M. Alashoor, P. Rabiller, M. Lorenc, F. Banhart, *J. Phys. Chem. C* **128**, 13991 (2024).

Figure 1. Schematic setup of the ultrafast TEM working with nanosecond electron pulses.

Figure 2. (a): A laser pulse heats SCO particles by plasmonic excitation of embedded Au nanorods. The SCO particles expand. (b): images of an SCO particle with 7 ns electron pulses before (t = 0) and 20 ns after the laser pulse. (c): Length measurements as a function of time. A pure SCO particle is compared with SCO particles where one or three Au nanorods are embedded.

Fig. 1

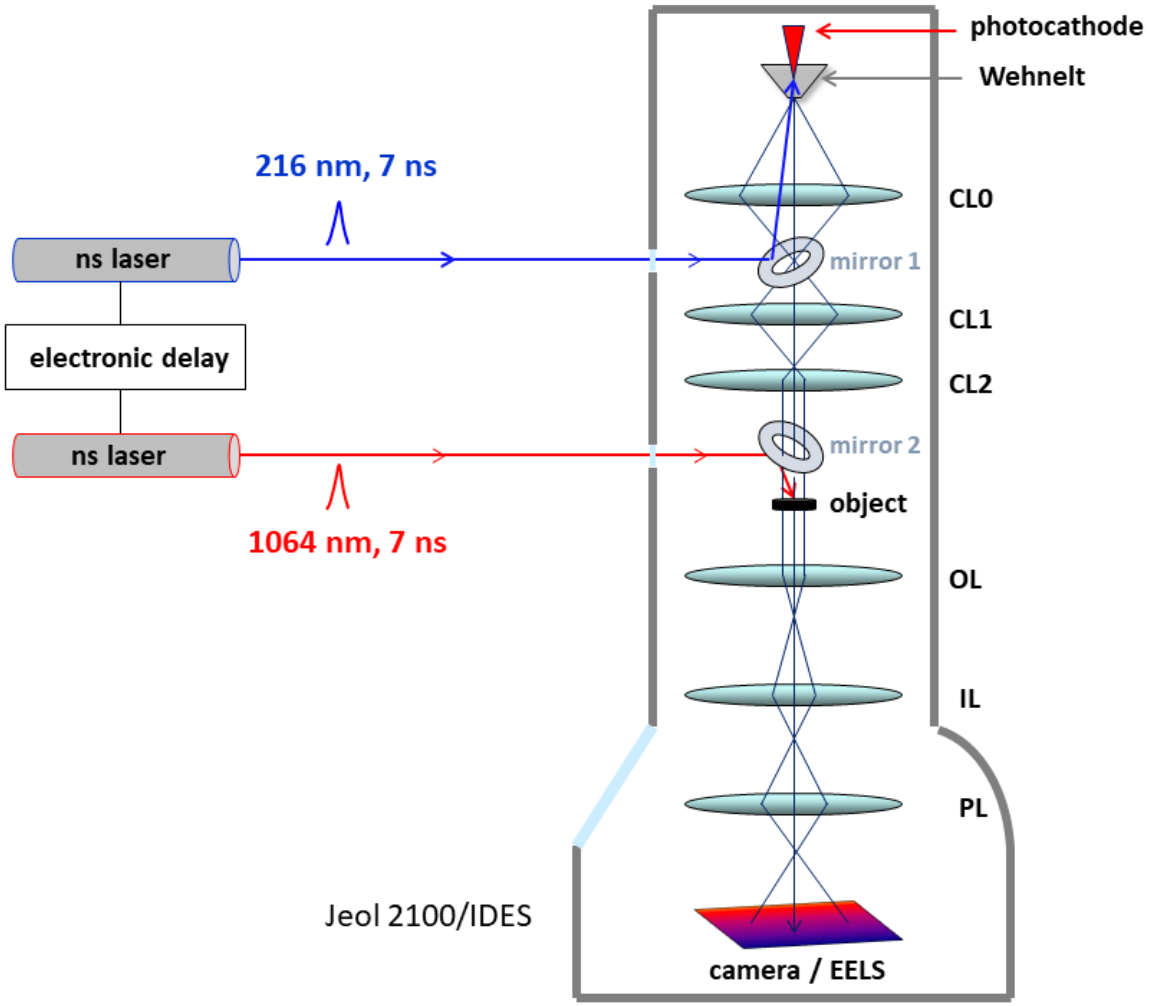
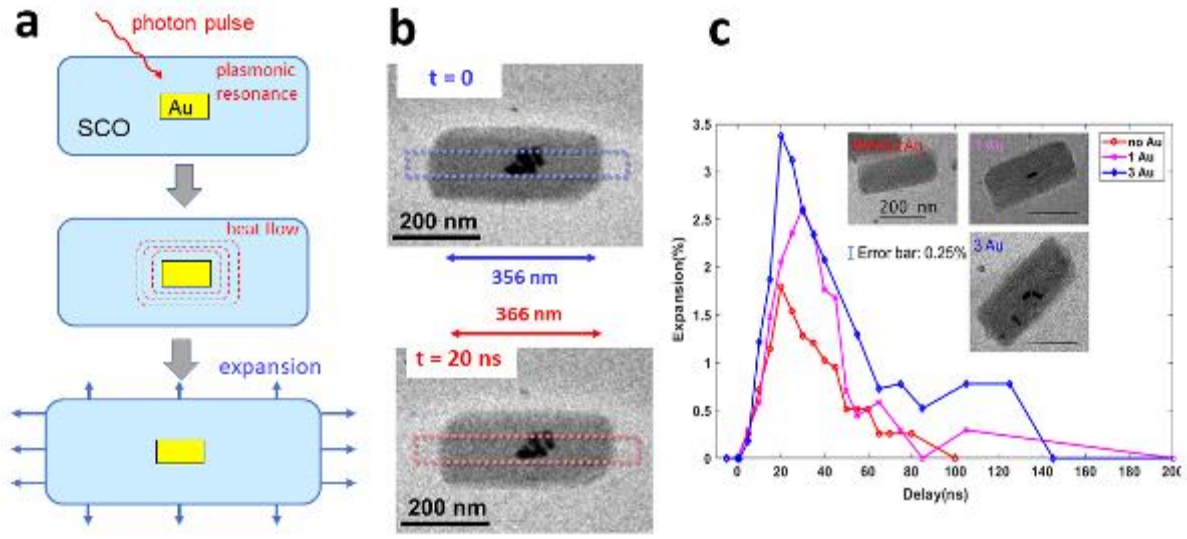


Fig. 2


a
photon pulse
plasmonic resonance
Au
SCO
heat flow
expansion
b
t = 0
200 nm
356 nm
366 nm
t = 20 ns
200 nm
c
Expansion(%)
Delay(ns)
no Au
1 Au
3 Au
Error bar: 0.25%
200 nm

IM1.04
Laser-driven cold-field emission source for ultrafast transmission electron microscopy

A. Wendeln[1], A. Schröder[1], J. Weber[1,2], M. Mukai[3], Y. Kohno[3], S. Schäfer[1,4]

[1]University of Regensburg, Department of Physics, Regensburg, Germany
[2]Carl-von-Ossietzky University Oldenburg, Department of Physics, Oldenburg, Germany
[3]JEOL Ltd., Tokyo, Japan
[4]Regensburg Center for Ultrafast Nanoscopy (RUN), Regensburg, Germany

Ultrafast transmission electron microscopy (UTEM) utilizing pulsed electron sources, is a powerful and versatile technique that enables the study of nanoscale dynamics with femtosecond temporal resolution by using a pump-probe approach. Recent developments of laser-driven Schottky emitters enables the use of electron pulses with high temporal and spatial coherence, achieving temporal widths below 200 fs and electron spot sizes as small as 1 nm [1]. Further improving the spatio-temporal resolution requires femtosecond photoelectron sources with a higher degree-of-coherence, which can be achieved by using a laser-driven cold-field emitter. However, previous approaches for laser-driven cold-field emitter UTEM sources utilized a multi-photon regime [2] severely limiting the tunability of this kind of pulsed electron source.

Here, a novel laser-driven cold-field emitter based on linear photoemission is implemented into a state-of-the-art UTEM. By measuring the characteristic transverse and longitudinal electron pulse properties, the achievable spatial and temporal coherence of the emitter is determined [3] and discussed with respect to applications in aberration-corrected UTEM.

The femtosecond electron source is based on a JEOL cold-field emitter. Localized linear photoemission is enabled by the Schottky-reduced workfunction at the tip apex [4]. The influence of different experimental parameters on the femtosecond electron pulse properties are determined.

As part of the implementation, the photoemission process was characterized by using CW lasers. At electric extraction fields on the order of 1 kV, we observe photoemission without continuous field emission (Fig. 1a). The emission current scales linearly with light intensity (Fig. 1c) and has a half-life of about 25 hours (Fig. 1d), demonstrating the long-term stability of the apex workfunction.

For the following experiments, the emitter is operated as part of the Regensburg JEOL F200 UTEM, using ultrashort laser pulses with a duration of 169 fs and a central wavelength of 343 nm. The longitudinal beam properties are determined by energy resolved measurements, leading to a minimum electron energy width down to 360 meV (Fig. 1b) and a pulse duration of 220 fs, as determined by an electron-photon cross correlation.

To characterize the transverse beam properties a CW laser is used to generate photoemission. Photoelectron beams with a minimum focal spot size down to 2.1 Å and a relative degree of coherence of up to 54 % were demonstrated. Using femtosecond optical pulses for photoemission, a normalized peak brightness of 6.7×10^{13} A/m^{2}sr is achieved (Fig. 1e), comparable to continuous field emission sources. Whereas the currently achieved photoelectron current in high-coherence pulses is limited to the 0.1 fA to 1 fA range, we expect a substantial improvement when combing our novel source with a probe aberration corrector.

In conclusion, we demonstrate the successful development of a stable, laser-driven cold-field emitter source for UTEM applications. The high coherence of the emitter could lead to increased spatial and spectral resolution in ultrafast high-coherence and energy-resolved measurements, paving the way for high-coherence UTEM experiments like holography.

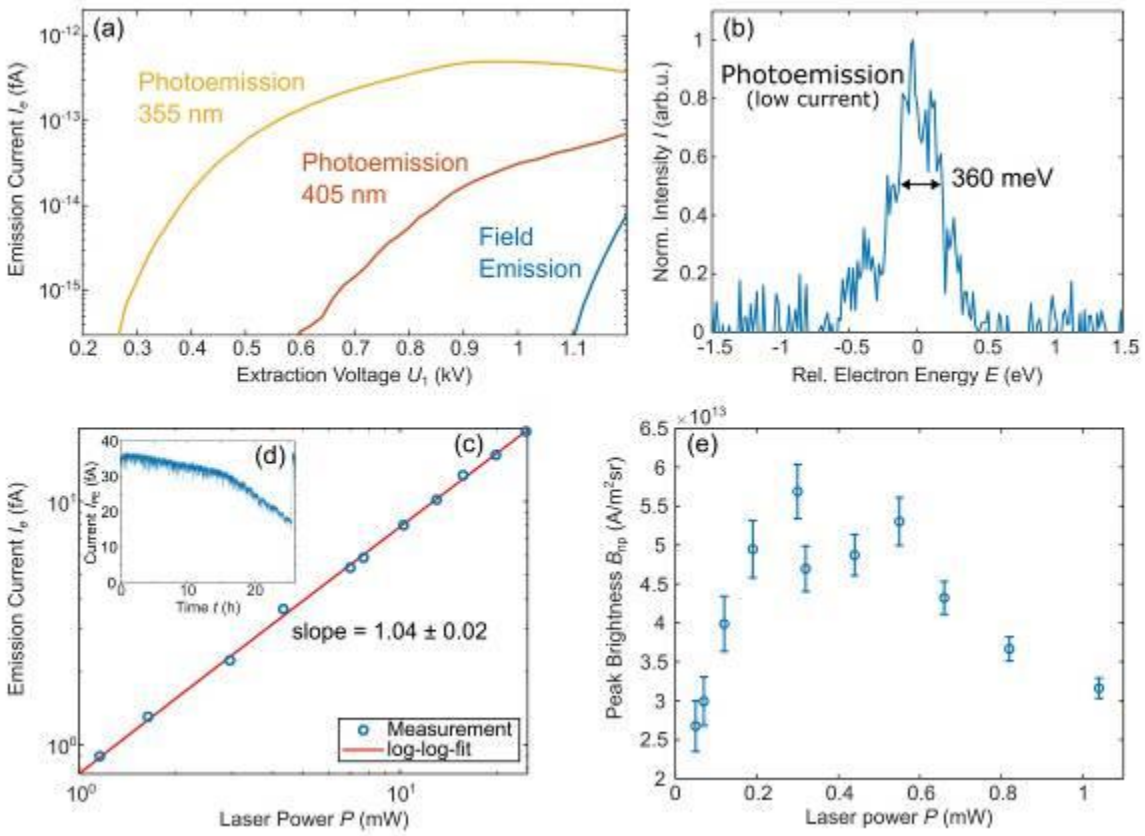
[1] A. Feist et al., Ultramicroscopy 176, 63 (2017).

[2] F. Houdellier et al., Ultramicroscopy 186, 128 (2018).

[3] Schröder et al., arXiv:2410.23961, (2024).

[4] Hommelhoff et al., Phys. Rev. Lett. 96, 077401 (2006).

Fig. 1



IM1.05
Development state of the CEOS ground-potential monochromator

F. Börrnert[1], S. Uhlemann[1], H. Müller[1], V. Gerheim[1], K. Hessenauer[1], H. Schulz[1], U. Löbau[1], P. Stiegler[1], M. Haider[1]

[1]CEOS GmbH, Heidelberg, Germany

Electron energy loss spectroscopy (EELS) is a long established analytical method to investigate the chemistry as well as the electronic and optical properties of materials. EELS often is integrated into an electron microscope adding spatial information to the spectroscopic signal.

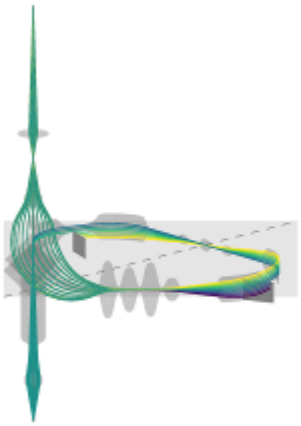
In spectroscopy using electrons, the energy distribution of the primary electron beam ΔE_0 is a major limiting factor for the energy resolving power of the spectrometer. Reducing ΔE_0 by means of a monochromator can enhance the energy resolving power of the system accordingly. Additionally, in (S)TEM, ΔE_0 in conjunction with the chromatic aberration of the imaging system C_c is one of the limiting factors for the maximum spatial information transfer. Therefore, a monochromator can also help to enhance the spatial resolving power of (S)TEM instruments.

To date, four different types of electron monochromators for (S)TEM instruments have been commercialised. First, the simple single-stage Wien filter [1] and second, the more advanced double-stage Wien filter [2], both employing crossed electric and magnetic multipole fields and a straight optical axis. Third, the purely electro-static Ω-monochromator using sector fields bending the optical axis into an Ω-shape [3] and fourth, the purely magneto-static ground-potential monochromator combining magnetic sector fields in such a way that the optical axis follows an α-shaped trajectory [4]. For the first three cases the monochromator is added in front of the accelerator at low electron energies or at high potential whereas in the fourth, it is added after the accelerator at high electron energies or at ground potential. In the latter case, only the interaction with the specimen causes energy differences and disturbing effects from instabilities of the accelerator can be neglected.

In this contribution, we present the development state of our novel design of a ground-potential monochromator based on magnetic prisms in a three-dimensional arrangement. This design abandons the energy selection at the central symmetry plane and the optical axis is not only curved in one section but the axis is curved in both, the xz section and the yz section. This allows for a highly symmetric and compact design with a variable energy window without the necessity for mechanically adjustable energy-filtering slit. Fixed blocking blades reside at two distinct planes with energy dispersion making the system in combination with optical deflectors robust and flexible. The practical design fits primary electron energies from 30 keV up to 300 keV and is expected to provide an energy resolving power of better than $2 \cdot 10^{-7}$ with respect to the primary electron energy. Also, the resulting beam cross-over after the monochromator is free of residual spatial or angular dispersion. Very importantly, the new monochromator is designed to be potentially retro-fittable to existing microscopes, adding only about 34 cm to the total height of the microscope column.

[1] Mook & Kruit (2000) Ultramicrosc. 81, 129.
[2] Mukai et al. (2014) Ultramicrosc. 140, 37.
[3] Kahl & Rose (2000) Proc. EUREM-12 3, 1459.
[4] Krivanek et al. (2009) Phil. Trans. R. Soc. A 367, 3683.

Fig. 1



IM1.06
Towards an experimental entanglement witness between a swift electron and a cathodoluminescent photon

I. C. Bicket[1,2], A. Preimesberger[1,2], S. Bogdanov[1,2], P. Rembold[1], P. Haslinger[1,2]

[1]Technical University of Vienna, Atominstitut - USTEM, Vienna, Austria
[2]Technical University of Vienna, University Service Center for Transmission Electron Microscopy, Vienna, Austria

Introduction

Entanglement [1, 2] lies at the heart of quantum mechanics and is key to many quantum optics experiments. The high resolution and flexibility of transmission electron microscopy (TEM), mitigated by challenges regarding electron beam damage of sensitive specimens [3], motivate the development of free electron quantum optics to bring quantum imaging techniques into electron microscopy. Coherent cathodoluminescence (CL) photons [4] provide a promising avenue towards demonstrating and utilizing quantum entanglement phenomena in the TEM [5].

Objectives

We aim to demonstrate a viable entanglement witness experiment between CL photons and primary electrons in a transmission electron microscope.

Materials and Methods

We use an FEI Tecnai F20 microscope equipped with a custom CL set-up and a Gatan GIF 2001 energy filter (see figure). 200 keV electrons are transmitted through a 50 nm thick silicon membrane and collected on a Timepix3 camera, where their time of arrival is stamped with 50 ns accuracy. CL radiation from the electron"s interaction with the specimen is collected by a parabolic mirror and directed out of a window in the TEM. Photons are then focused and steered to a single photon counter capable of time stamping individual photons for coincidence matching with the originating electrons.

Results

Using our coincidence-counting set-up, we are able to detect energy and momentum transfer between single electron-photon pairs [6]. We take advantage of these direct correlations for our entanglement witness experiments. We place a line grating in the photon path, in either the image plane or the Fourier plane, to establish mutually unbiased bases [5] and experimentally determine the joint probability distribution for our electron-photon coincidence pairs. If the joint uncertainty measurement resolution violates bounds set by Heisenberg"s uncertainty principle, then we can confirm that the electron-photon pairs are entangled. We will present preliminary results on electron-photon pair correlations, and discuss the probability of entanglement given the position and momentum resolution limits we achieve.

Conclusion

We demonstrate an experiment suitable for witnessing entanglement between a free electron in a TEM and a coherent CL photon. Using the resolution obtained in each bases, we rigorously quantify the joint uncertainty product required to confirm or deny the entanglement witness requirements.

References

[1] Einstein, Podolsky, & Rosen, *Phys. Rev.*, **47**, *10*, 1935.

[2] Horodecki, *et al.*, *Rev. Mod. Phys.*, **81**, *2*, 2009.

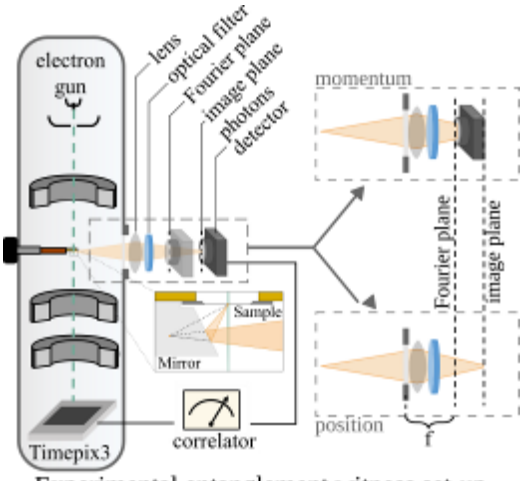
[3] Ilett *et al.*, *Phil. Trans. R. Soc. A*, **378**, *2186*, 2020.

[4] García de Abajo, *Rev. Mod. Phys.*, **82**, *1*, 2010.

[5] Rembold *et al.*, 2025; arXiv:2502.19536.

[6] Preimesberger *et al.*, Phys. Rev. Lett., **134**, 2025.

Fig. 1



Experimental entanglement witness set-up, performing coincidence counting between free electrons and photons

IM1.07
Charge particle optics simulation utilizing hamiltonian mechanics perturbation expansion and boundary elements field computation

A. Lubk[1,2], F. Houdellier[3], H. Müller[4], S. Uhlemann[4]

[1]Leibniz Institute for Solid State and Materials Research Dresden, Institute for Solid State Physics, Dresden, Germany
[2]Technical University Dresden, Institute of Solid State and Materials Physics, Dresden, Germany
[3]CEMES-CNRS, Toulouse, France
[4]CEOS GmbH, Heidelberg, Germany

Introduction

Advanced charge particle optics (CPO) requires fast and accurate computation of particle trajectories including aberrations that handle both arbitrary electrics and magnetic fields, bend optical axis, symmetries, and the optimization of geometric design parameters (e.g.,pole piece diameters). Such a tool should be available under open source licenses to facilitate widespread use and a sustainable distributed development. Despite the enormous level of available CPOsoftwares, they often lack a subset of the above functionalities, hampering the use of advanced CPO for, e.g., Transmission Electron Microscopy or Photo Electron Spectroscopy.

Objectives

Here, we provide an update on our development of an open source CPO framework[1] that allows for accurate and fast trajectory calculation. It utilizes a modular combination of fast electric and magnetic field computations via Boundary Element Method (BEM) and perturbation series expansion of Hamiltonian equations of motion implemented through a combination of freely available open source software packages.

Materials & Methods

(A) We use BEM computation of electric and magnetic fields, yielding smooth and accurate potentials, fields and higher-order derivatives at optical axis at arbitrary sampling, while reducing the meshing effort to surfaces of the CPO device. Herein, single layer representations of both electric and magnetic scalar potentials are most efficient. (B) We employ semianalytical solution of perturbation series of Hamiltonian equations of motion[2] in order to provide computationally effective and accurate built-up of aberrations along particle trajectories. (C) We integrate the fast field and particle trajectory computation with non-linear minimizersyielding optimalCPO parameters (e.g., electrode potentials, pole piece gap) with respect to certain target functionalities. This tool chain is written in Python and makes use of advanced open source libraries (OpenCascade for CAD, gmsh for meshing, BEMPP for BEM computation, SymPy for Hamiltonian mechanics perturbation expansion including automatic code generation, SciPy for solving equations of motion and non-linear optimization) in a modular way, which are partly adapted to the specifics of CPO.

Results

We demonstrate the above tool chain with the help of several electrostatic and magnetostatic optical elements (e.g., Fig. 1), touching implementation, numerical, and CPO aspects. Further development aims at general enhancement of functionality and user friendliness in order to support development of advanced CPO across the community.

Fig. 1: CPO of electrostatic quadrupole – aperture assembly (building block of low-voltage aberration corrector[3]): Computer aided design (CAD) modeling, meshing, and BEM field computation including axial multipoles.

References:

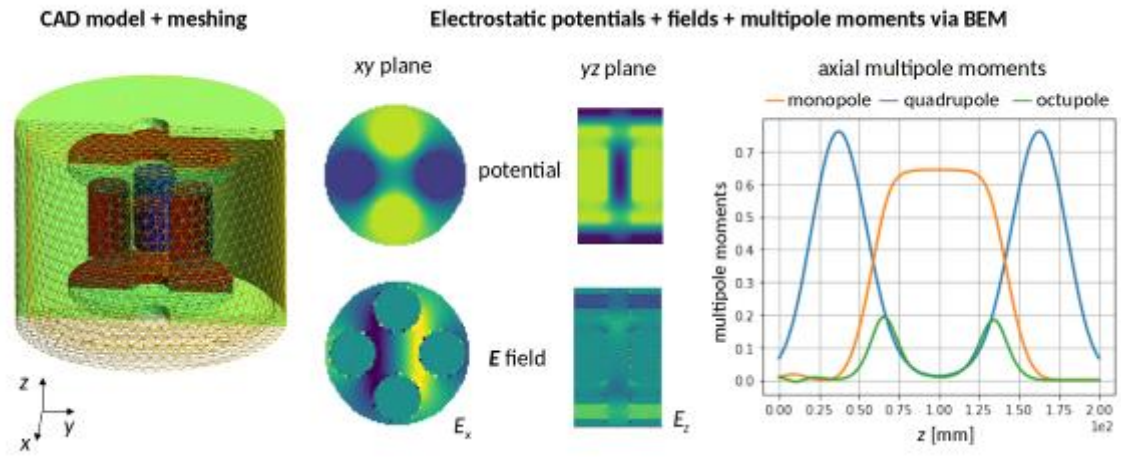
[1] https://gitlab.math.tu-dresden.de/amem-group/efly

[2] Kern, F., Krehl, J., Thampi, A., Lubk, A. "A Hamiltonian mechanics framework for charge particle optics in straight and curved systems", *Optik,* **2021***, 242*, 167242

[3] Tamura, K., Okayama, S., Shimizu, R. "Third-order spherical aberration correction using multistage self-aligned quadrupole correction-lens systems", *Journal of Electron Microscopy,* **2010***, 59*, 197

[4] We acknowledge financial support by the European Union's Horizon Europe framework program for research and innovation under grant agreement n. 101094299 (IMPRESS project).

Fig. 1



IM1.P01
Methods for dynamic re-focussing of an electron energy-loss spectrum

H. Müller[1], P. Kükelhan[1], J. Raju[1], G. Guzzinati[1], M. Linck[1], S. Uhlemann[1]

[1]CEOS GmbH, Heidelberg, Germany

Fast methods to shift the spectral region of interest have been successfully combined with multiple exposure techniques [1, 2] to record low-loss and core-loss signals simultaneously. While modern spectrometers with low-dispersion settings and hybrid-pixel detectors with large dynamic range allow to capture a spectral range of several keV with only one exposure [3, 4], dual- or multiple-range EELS techniques are still useful to collect information from several regions with high dispersion and energy resolution [5].

A bias voltage applied to the bended linertube inside the magnetic prism is used to shift the energy within sub-milliseconds. Unfortunately, an energy-shift depended defocus can impair the energy resolution. The first-degree effect is due to the chromatic aberration of the objective lens" post-field and chromatic aberration from the TEM and spectrometer projective optics. A second-degree effect due to the lensing effect of the fringing fields of the biased linertube is relevant for large energy shifts only. The effects from the post-specimen TEM optics become most severe for small camera length and large spectrometer acceptance angle. Both is very releveant for probe-corrected analytical STEM.

Commercially available spectrometers implement a fast electro-static stigmator adjusted simultaneously with the energy-shift to compensate for the defocus in the dispersive section. For spectrometers employing a tapered magnetic prism [6, 7, 8] we propose an alternative solution using a weak electro-static deflector outside the prism. Both the excitation of the linertube bias and the electro-static deflector cause an effective shift of the energy at the spectrum plane. We show that a combination of both exists where the total shift-induced defocus with repect to the dispersive section happens to vanish and the EELS stays in focus while the energy is shifted by a large amount. An additional focussing element is not necessary. This can be understood rather easily from the fact that for the tapered sector magnet quadrupole and hexapole fields are present along the curved optical axis as depicted in Fig. 1. The weakly excited electro-static deflector causes the electron trajectory for the selected energy to slightly deviate from the ideal optical axis inside the prism. Proportionally to the path deviation inside the magnetic prism an addional quadrupole field is induced due to the axial hexapole field. It can be adjusted to exactly compensate for the previously described deleterious chromatic effect by choosing the right combination of linertube bias and weak electro-static deflection as shown in Fig. 2. The excitation of the electro-static deflector must be dynamically coupled to the linertube bias.

Fig. 1. Geometry of a tapered prism (sector magnet) with axial quadrupole and hexapole strength [6].

Fig. 2. Combination of a linertube bias and a weak electro-static deflection operated such that a quadrupole field is generated to dynamically re-focus the EELS.

References:

1. Tencé, M. et al. In Proc. IMC 16 Sapporo, Japan (2006) 824-825

2. Scott, J. et al. Ultramicroscopy 108 (2008) 1586-1594
3. Plotkin-Swing, B. et al. Ultramicroscopy 217 (2020) 113067

4. Caridad, A. et al. Micron 160 (2022) 103331
5. Tiemeijer, P. et al. In Proc. EMC 17 Copenhagen, Denmark (2024) 05015
6. Uhlemann, S. et al. Optik 96 (1994) 163-178
7. Gubbens, A. et al. Ultramicroscopy 110 (2010) 962-970
8. Kahl, F. et al. Advances in Imaging and Electron Physics 212 (2019) 35-70

Fig. 1

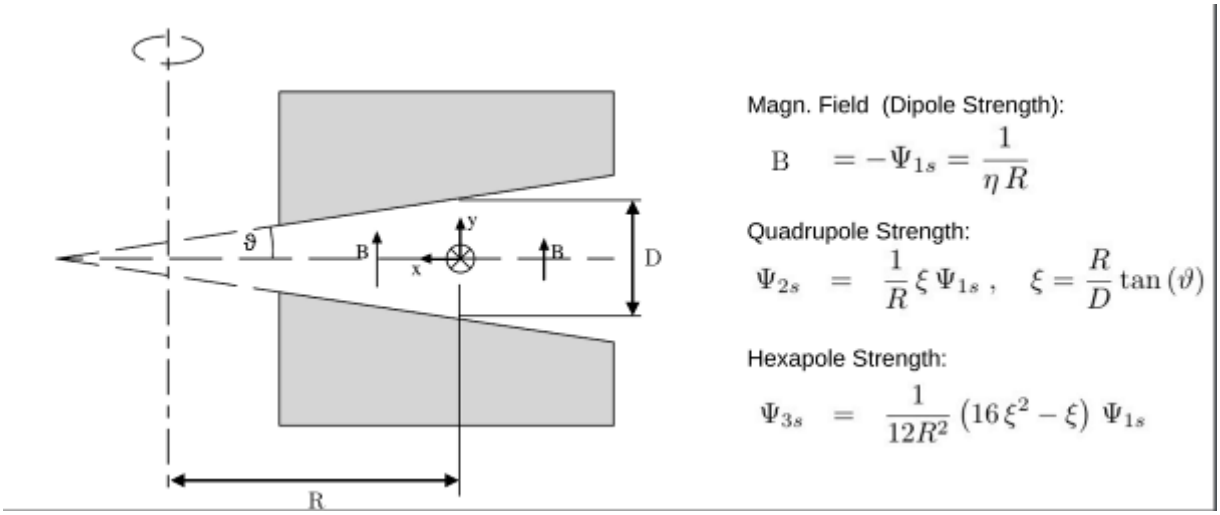
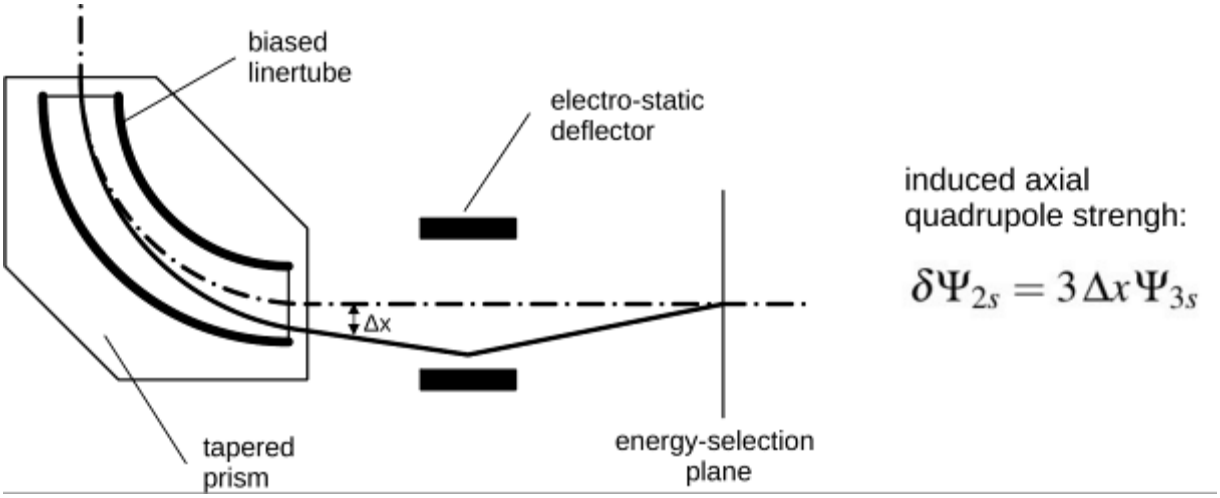


Fig. 2



IM1.P02
Phase contrast tuning via scanning transmission electron microscopy using semicircular aperture illumination

A. Yasuhara[1], F. Hosokawa[2], S. Asaoka[3], T. Akiyama[3], T. Iyoda[4], C. Nakayama[1], T. Sannomiya[5]

[1]JEOL Ltd., EM Business Unit, Tokyo, Japan
[2]FH electron optics, Tokyo, Japan
[3]Kyoto Institute of Technology, Kyoto, Japan
[4]Doshisha University, Kyoto, Japan
[5]Institute of Science Tokyo, Yokohama, Japan

[Introduction] Scanning transmission electron microscopy (STEM) techniques are widely used in material research, enabling visualization of structures from nm to atomic scale. However, interpreting STEM bright-field images is often challenging because the images are intricately affected by the defocus value. In the context of contrast enhancement using phase imaging in transmission electron microscopy (TEM), phase plates have successfully enabled phase retrieval in biological research. Recently, phase reconstruction techniques using segmented detectors in STEM differential phase contrast (DPC) has gained attention. In this study, we explore a newly developed low-cost phase imaging technique using semicircular-aperture illumination (SCI) STEM[1]. The bright-field (BF) image in SCI-STEM combines a standard BF image with sinus type response to potential and a derivative phase image obtained through the Hilbert transformation of a cosine type phase-plate image across the semicircular aperture. Consequently, SCI-STEM BF is expected to represent both low-frequency and high-frequency contrast transfer in the specimen.

[Objectives] We demonstrate SCI-STEM BF images of various specimens and use numerical calculations to simulate images and FFT patterns, evaluating its advantages.

[Materials & Methods] A semicircular aperture was fabricated using the focused ion beam (FIB) method on a gold film and installed in a probe-forming spherical aberration-corrected TEM (JEM-ARM200F). SCI-STEM BF images of biological and block-copolymer samples were acquired at 200 kV. The convergence angle was controlled by selecting the illumination lens settings and combining the SCI aperture with an additional condenser lens aperture. STEM image simulations were performed using Elbis software.

[Results] SCI-STEM BF and conventional STEM BF images of the block-copolymer sample[2] are shown in Figures 1a-d. The convergence semi-angle was set to 1 mrad, and the detection semi-angle to 30 μrad for efficient low-frequency contrast acquisition. The SCI-STEM BF image (Fig.1a, b) clearly reveals the hexagonal array structures of the block-copolymer, which are difficult to discern in the conventional BF image (Fig. 1c, d).

[Conclusion] We successfully demonstrated SCI-STEM BF imaging and reproduced original STEM images through numerical simulations. SCI-STEM BF imaging offers sine and cosine curves in the contrast transfer function (CTF), enabling contrast enhancement at low frequencies. This approach provides significant advantages over conventional phase plate methods, eliminating issues such as charge accumulation, material degradation, and unwanted background noise. Additionally, compared to DPC or ptychography techniques, the semicircular aperture is a far more cost-effective solution.

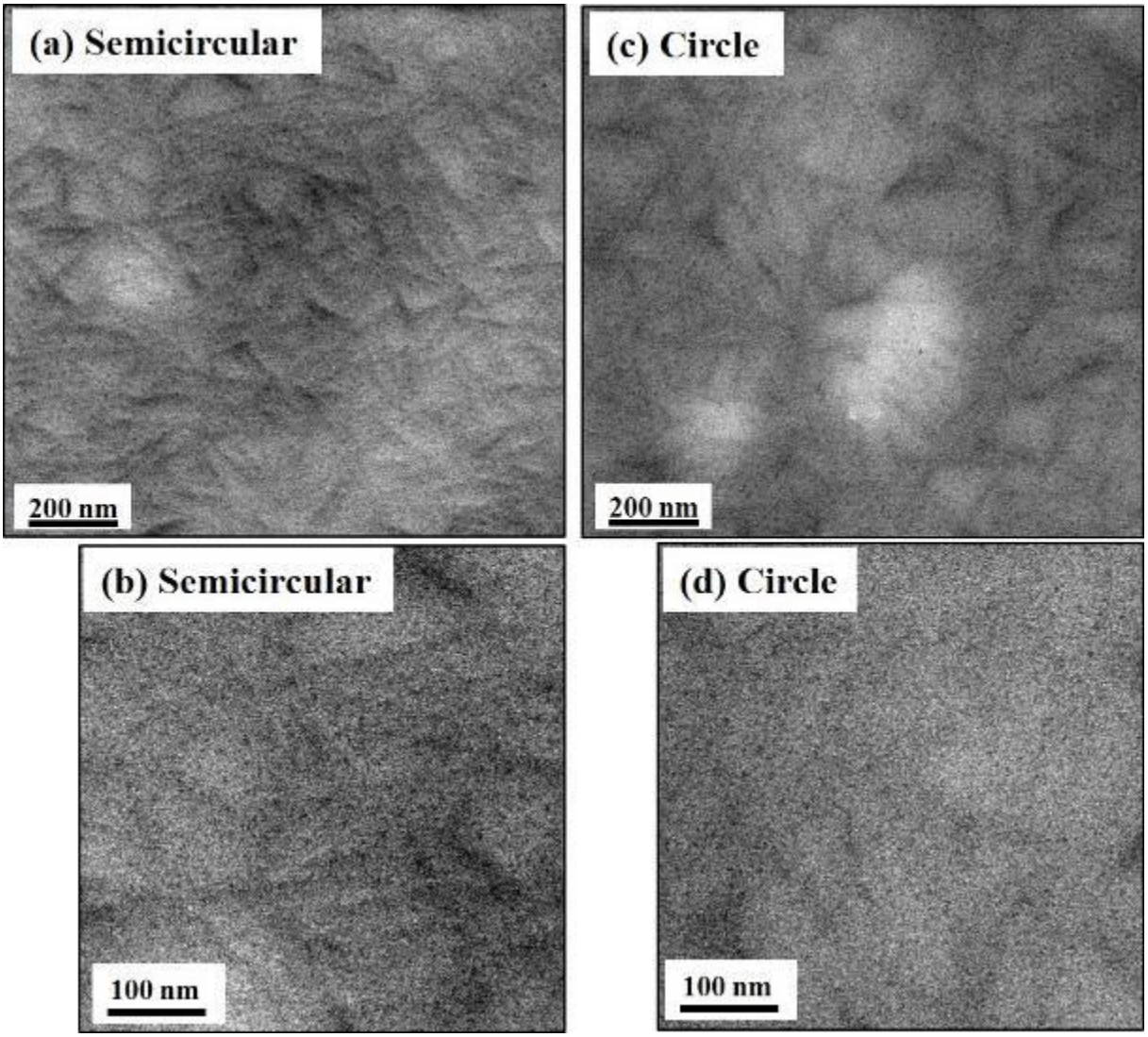
[Reference]

[1] Yasuhara, A., et.al, *Ultramicroscopy*, 2025, 114103.

[2] Asaoka, S., et.al, *Macromolecaules*, 2011, 44, 7645–7658.

Figure. SCI-STEM BF image and conventional STEM BF image of a block copolymer. Image (a) shows an SCI-STEM BF image with semicircular apertures, while image (b) is an enlarged image of (a). Images (c) and (d) display a STEM BF image and its enlarged version, obtained using a standard circular aperture

Fig. 1



IM1.P03
Enhanced time resolution with a room-temperature energy dispersive X-ray PIN photodiode detector for improved EDX-EELS coincidence measurements

L. Serafini[1,2], M. Gijbels[1,2]

[1]University of Antwerp, Electron Microscopy for Materials Science (EMAT), Antwerp, Belgium
[2]NANOlab Center of Excellence, Physics, Antwerp, Belgium

Although energy dispersive X-ray spectroscopy (EDX) and energy electron loss spectroscopy (EELS) can be acquired simultaneously with a TEM, it is not a common practise. Most users do one at the time despite that the two data streams complement each other very well allowing to have both the high selectivity of EDX with the high energy resolution of EELS. By time correlating simultaneously acquired X-ray events to electron events one can distinguish actual scattering-process correlated electron-X-ray events from unrelated background events [1]. This is extremely useful to improve sensitivity of EELS to trace elements in a matrix (e.g. nitrogen vacancies in diamond) as the subtle edges of the trace elements are otherwise buried in the background noise.

Currently coincidence measurements are however limited to low signal to noise ratios by the limited time resolution of the commercial silicon drift detectors (SDDs) used to detect the X-rays [2]. Those are column-mounted and evolved to large sizes to maximise collection efficiencies at the cost of time resolution due to long unsystematic drift times of the signal charge carriers created upon X-ray detection [3]. In order to improve this we are building a proof-of-concept detector for this application. Our approach consists of having a small fully-depleted Si-PIN photodiode detector mounted on the sample holder itself. Its small size ensures neglectable drift times, low capacitance and therefore high acquisition rates and high temporal resolution. Lastly having the sample close to the photodiode preserves collection efficienc

So far several prototypes have been made and tested in a scanning electron microscope (SEM). Over the different iterations the signal amplifying electronics, noise levels and form factor have been improved. The latest version (see picture) has a low-noise charge-sensitive amplifier circuit with a reverse biased, low capacitance Si-PIN photodiode that is commercially available and inexpensive to replace. The front end has already physical dimensions that would later fit a TEM holder. A theoretical noise analysis has been made and matches nicely to corresponding experimental measurements. Due to relatively high thermal energy of the photodiode, a dc leakage current is formed that substantially increases the dead time of the detector due to an increased reset rate of the charge-sensitive preamplifier. In order to solve this while preventing tedious cooling (cryogenic or peltier cooling) a precisely controlled compensating current is used that proved to work well without elevating noise levels. When irradiating with Cu X-rays the measured pulses exhibit sub-50ns rise times suggesting already a tenfold improvement in time resolution. Initial EDX spectra show an energy resolution of around 1,6keV at 8,05keV (Cu K-α) which we are now trying to improve further to be useful for EDX.

In conclusion, we present the development of an in-house build room-temperature PIN photodiode X-ray detector to improve time resolution and allow for advancements in EDX and EELS coincidence experiments that so far have been hampered by the slow drift mechanism in SDD setups.

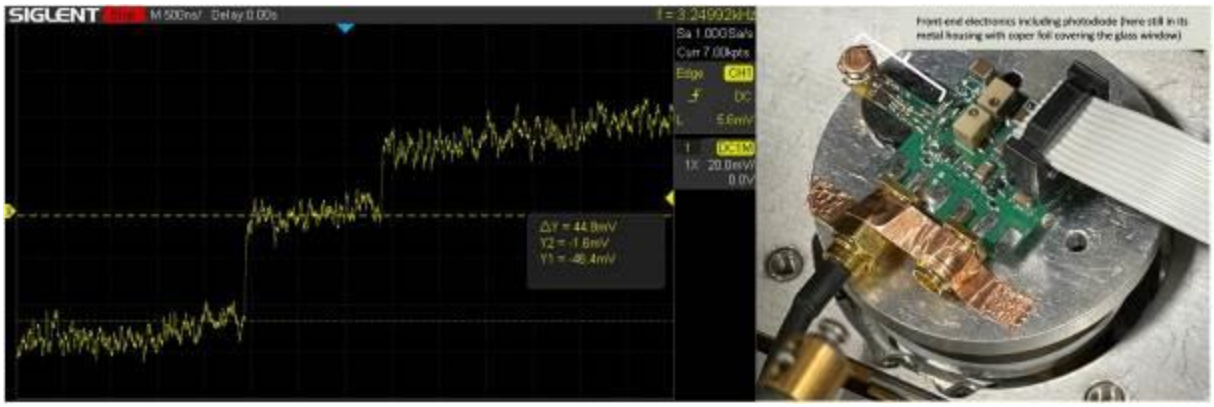
This work received funding from the Horizon 2020 research and innovation programme (European Union), under grant agreement No 101017720 (FET-Proactive EBEAM).

[1] P. Kruit et al. ; Ultramicroscopy, **13** (1984)

[2] G. F. Knoll, *Radiation Detection and Measurement*, 2010

[3] D. Jannis et al. ; Appl. Sci. **11**, 9058 (2021)

Fig. 1



IM1.P04
Physical limits of the detection of X-rays and electrons in SEM and TEM applications

M. Huth[1], B. Eckert[1], A. Fram[1], P. Majewski[1], L. Strüder[2,3], A. Niculae[1], H. Soltau[1]

[1]PNDetector GmbH, Munich, Germany
[2]University of Siegen, Physics, Siegen, Germany
[3]PNSensor GmbH, Munich, Germany

Silicon is a widely used material for the detection of X-rays and electrons due to its favorable properties. Continuous development of simulation tools and manufacturing equipment primarily driven by the semiconductor industry has significantly enhanced silicon-based detector designs and performance. In several key areas, silicon detectors have reached their fundamental physical limits dictated by material properties and ionization statistics. Optimizing silicon-based detectors for energy, position, and time-resolved detection requires an in-depth understanding of these constraints, particularly in electron microscopy applications, where precise detection of electrons defines the quality of quantitative results.

The detection of X-rays and electrons in silicon follow different fundamental mechanisms. Electromagnetic radiation (photons, X-rays) with energies below 30 keV mainly interact with the silicon atoms through the photoelectric effect with highly localized energy deposition.

In contrast, electrons undergo multiple inelastic scatter events starting with the interaction with the first atomic layer of the sensor material. If the energy is larger than the binding energy of the surrounding electrons it can continue to ionize until its energy is below the threshold of the weakest bound electron. In some cases a fraction can be back-scattered without leaving the full energy in the silicon. These combined effects result in a delocalized energy deposition profile along the particle trace in the sensor.

To quantify these effects, we have simulated energy deposition of energetic electrons (500 eV to 30 keV) and X-rays (200 eV to 30 keV) across various dielectric and conductive layer configurations on the radiation entrance window. A partially sensitive layer in silicon was considered in terms of charge collection efficiency [1]. Using Monte Carlo simulations, we determined the maximum achievable energy resolution and detection efficiency, incorporating all relevant physical interactions in silicon, silicon dioxide, silicon nitride, and aluminum. Our study also evaluates charge carrier generation and statistical fluctuations due to Fano noise.

Fano statistics impose a fundamental limit on energy resolution (Fig. 2a), with low-energy photons being particularly susceptible to additional degradation from electronic noise.

For electron detection, the detective collection efficiency (DCE) measures the ratio between the measured energy by the detector and the incident energy and directly affects the image contrast for a fixed electron dose on the sample (Fig. 2b).

We will present the physical limits over a wide range of energies and a variety of different entrance windows.

[1] S. Granato et al., "Characterization of eROSITA PNCCDs," in IEEE Transactions on Nuclear Science, vol. 60, no. 4, pp. 3150-3157, Aug. 2013, doi: 10.1109/TNS.2013.2269907.

Fig. 1: Cross-sectional view of different entrance window geometries [1]. For each entrance window electron traces for 5 keV (left) and 10 keV (right) are displayed. The straight lines that leaving the detector volume display backscattered particles.

Fig. 2: (a) Energy resolution as function of the photon energy. An equivalent noise charge (ENC) of zero describes the physical limit. Additional ENC caused by the readout electronics decreases the energy resolution. (b) DCE as a function of electron energy displayed for a selection of different radiation entrance windows. Layer thicknesses are taken from [1].

Fig. 1

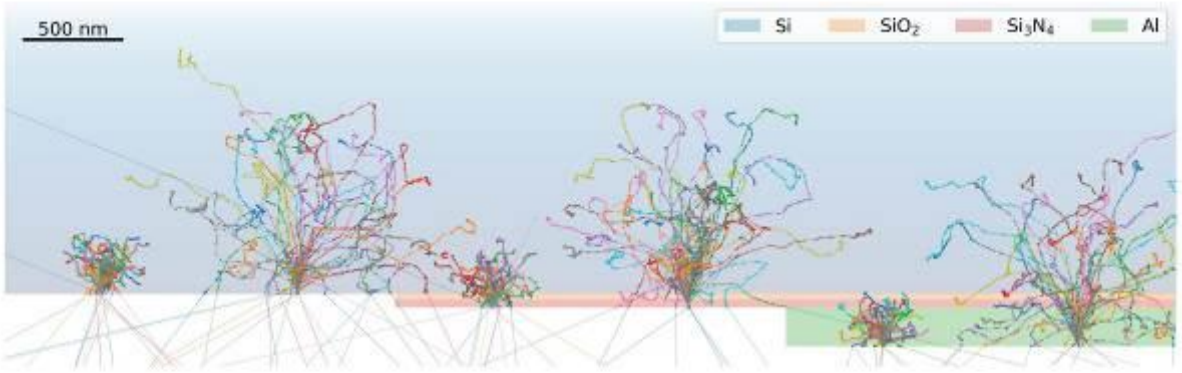
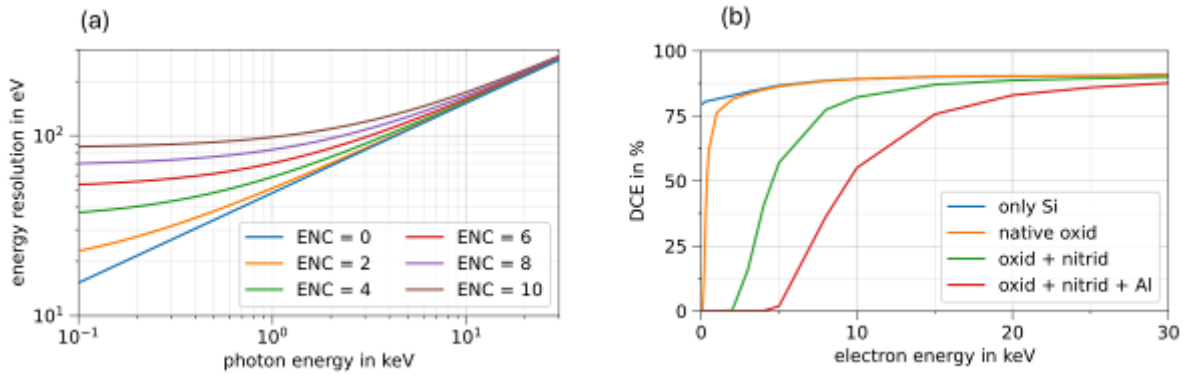


Fig. 2


(a)
energy resolution in eV
10^2
10^1
10^{-1}
10^0
10^1
photon energy in keV
ENC = 0
ENC = 2
ENC = 4
ENC = 6
ENC = 8
ENC = 10
(b)
DCE in %
100
75
50
25
0
0
10
20
30
electron energy in keV
only Si
native oxid
oxid + nitrid
oxid + nitrid + Al

IM1.P05
Fundamental limits on ultrafast transmission electron microscopy of time-dependent potentials

W. Schaap[1,2], C. Mechel[2], R. Ruimy[2], A. Niedermayr[2], Y. Israel[2,3], A. Gorlach[2], R. E. Dunin-Borkowski[1], J. Luiten[4], I. Kaminer[2]

[1]Forschungszentrum Jülich GmbH, Ernst Ruska-Centre for Microscopy and Spectroscopy with Electrons, Jülich, Germany
[2]Technion - Israel Institute of Technology, Solid State Institute and Faculty of Electrical & Computer Engineering, Haifa, Israel
[3]Tel Aviv University, Raymon & Beverly Sackler Faculty of Exact Sciences, Tel Aviv, Israel
[4]Eindhoven University of Technology, Faculty of Applied Physics, Eindhoven, Netherlands

The ultrafast transmission electron microscope (UTEM) offers the capability to image dynamic phenomena with femtosecond temporal resolution and sub-nanometer spatial resolution [1]. Techniques like photon-induced nearfield electron microscopy (PINEM) enable the study of optical excitations such as photons, plasmons, and phonon-polaritons by relying on *inelastic* electron-light interactions. Alternatively, conventional phase imaging methods like off-axis electron holography rely on *elastic* interactions to enable the direct visualization of structures such as skyrmions and superconducting vortices [2]. Current frontier research aims to integrate the UTEM with conventional phase imaging techniques to track the real-time dynamics and phase transitions of such phenomena [3].

This work aims to develop a theoretical framework for ultrafast off-axis electron holography and to define the fundamental limitations of phase imaging of time-dependent electric and magnetic potentials. Specifically, we aim to address the key challenge of phase decoherence stemming from the *inherently* inelastic interaction of time-dependent potentials and electrons.

We construct a theoretical model to explore the conditions necessary for successful phase imaging in ultrafast off-axis holography. The model examines the relationship between the fringe pattern, the electron pulse duration and the electron's peak phase value. Simulations are performed using dynamic Gaussian potentials to capture the guiding principles, which are subsequently applied to study ultrafast phase imaging of drifting vortices in type-II superconductors.

Our findings reveal two primary limiting factors for ultrafast phase imaging: (I) phase blurring due to transverse motion of the potential and (II) contrast reduction due to inelastic electron scattering. Each limiting effect occurs over a characteristic timescale, which we call the blurring timescale and contrast reduction timescale. Phase blurring dominates for weak phase values while contrast reduction becomes significant at higher phase values. For dynamic vortices in type-II superconductors, the electron phase shift depends on the tilt angle of the superconducting sample. At common experimental tilts (around 45 degrees), phase blurring is the dominant limitation, with electron pulse durations shorter than the bluring timescale being sufficient for effective imaging. For tilt angles exceeding 60 degrees, contrast reduction becomes increasingly important.

To conclude, we establish a theoretical framework that outlines the fundamental limits of ultrafast off-axis holography of dynamic electric and magnetic potentials. This work provides critical insights into optimizing experimental parameters, such as the electron pulse duration and sample tilt, to enhance phase imaging capabilities for ultrafast systems such as drifting vortices in type-II superconductors. These results offer a foundation for future experimental designs aiming to capture dynamic phenomena with high temporal and spatial resolution.

References:

[1] A. Feist, N. Bach, N. Rubiano da Silva, T. Danz, et al., Ultramicroscopy **176**, 63 (2017).

[2] J.E. Bonevich, K. Harada, T. Matsuda, et al., Phys. Rev. Lett. **70**, 2952 (1993).

[3] L. Embon, Y. Anahory, Z.L. Jelić, E.O. Lachman, et al., Nat. Commun. **8**, 85 (2017).

IM1.P06
Measurement of self-coherence in the Transmission Electron Microscope (TEM) by detecting time-dependent coherent-inelastic electron scattering in the Heisenberg limit

C. Kisielowski[1], P. Specht[2], J. R. Jinscheck[3,4], S. Helveg[4]

[1]Electron Scattering Solutions, Piedmont, CA, United States
[2]University of California, Department of Materials Science and Engineeringg, Berkely, CA, United States
[3]Technical University of Denmark, DTU Nanolab, Kongens Lyngby, Denmark
[4]Technical University of Denmark, VISION, Department of Physics, Kongens Lyngby, Denmark

It is established practice to describe the scattering of electron ensembles by either a particle picture or a wave picture. In spite of calls for solving Schrödinger"s time dependent equation, the static Schrödinger equation for wave functions is almost exclusively used to reliably simulate the image formation process using multislice calculations for coherent-elastically scattered electron ensembles [e.g. 1]. Moreover, the Copenhagen convention of quantum mechanic is adopted, which emphasizes the importance of an observation for the collapse of wave functions.

In order to foster further insight into fundamental quantum-mechanical aspects we pursue a series of experiments with low electron dose rates that guarantee the presence of single electrons in the microscope column at any given time. Consequently, we address the scattering of single electrons and build up intensities from electron ensembles over time. Recent energy filtered TEM experiments revealed the presence of image intensity at sample/vacuum interfaces that cannot be simulated using the established (static) calculation tools [2]. In contrast, they can be explained by the time-dependent Schrödinger equation assuming that an energy exchange ΔE occurs during any interaction of the electron with the sample in the Heisenberg limit $\Delta E = \hbar/2\ \Delta t^{-1}$ (coherent-inelastic scattering). In this process a wave package is formed by the superposition of partial waves and a decoherence phase of 0.5-1 radian [2]. The time-dependent Schrödinger equation yields two parameters that characterize the static and the dynamic behavior of any wave function $\psi(r, t) = \psi(r)\ \phi(t)$, namely $x_{static} = \hbar/(2m\Delta E)^{1/2}$ and $x_{dynamic} = \hbar c/\Delta E$. The former is the de Broglie wavelength if ΔE is a kinetic energy and the latter becomes an expression for self-coherence if the scattering process is coherent-inelastic in the Heisenberg limit. In these circumstances, the product of Planck"s constant and the speed of light hc is given by the product of the expression for temporal self-coherence $\lambda^2/\Delta\lambda$ and the energy loss ΔE ($hc = (\lambda^2/\Delta\lambda)\ \Delta E$). The validity of the relation is experimentally verified [3].

[1] e.g. Total Resolution, https://www.totalresolution.com.

[2] C. Kisielowski et al. Nanomaterials (2023) 13, 971.

[3] C. Kisielowski et al. Microsc. Microanal. (2024) ozae107.

IM1.P07
Extreme low-dose atomic resolution EELS mapping at cryogenic temperature

L. Spillane[1]

[1]Gatan Inc., Pleasanton, CA, United States

Atomic resolution imaging and electron energy-loss spectroscopy (EELS) in the scanning transmission electron microscope (STEM) has become routine, due to the widespread commercial availability of aberration-corrected high-brightness probes, fast scan systems and efficient EELS spectrometers. However, achieving this resolution with beam sensitive materials that cannot withstand the high probe currents (10s to 100s of pA) typically used in an analytical STEM remains challenging.

Multiframe spectrum image (SI) summation was successfully proposed and demonstrated as a means of improving STEM image resolution and signal-to-noise ratio [1]. While summation is effective for STEM imaging, it is ineffective for low dose EELS using traditional scintillator detectors such as CCD technology, due to the finite noise floor of a CCD sensor which is added to the total signal with every readout. This finite noise typically accumulates faster than the desired. Single electron counting and thresholding hybrid pixel detectors are capable of nearly noise-free readout so are less affected by this limitation, making them more suitable for multiframe summation. Here we explore the suitability of these detectors for acquiring atomic res. EELS SI time series under cryogenic conditions at low probe current.

All data were acquired at 200 kV using a 20 pA probe, and GIF Continuum IS equipped with Gatan K3 single electron counting and Stela thresholding hybrid pixel detectors. Data were acquired at room and cryogenic temperatures (-170 C) using a Gatan double tilt cooling holder. Strontium ruthenate (SRO) grown on [110] dysprosium scandate (DSO) was used as a model system to characterize dose fractionation as a method for performing atomic res. EELS analysis on radiation hard (DSO) and beam sensitive (SRO) materials simultaneously at low temperature.

Fig. 1 shows a 352 x 89 pixel 2D array acquired from SRO/[110]DSO. SI were acquired with a 110 ?s dwell time. Each SI pass was acquired in 3.4 s. 55 passes were summed to give a total dwell time of 6.1 ms per pixel. The survey image, SI capture and pre-drift measurement regions are shown on the left, in addition to summed ADF and principal component analysis (PCA)-denoised EELS elemental maps for the Dy-M4,5, Sr-L2,3 and Ru-L2,3 ionization edges. A comparison between the ADF, raw EELS areal density maps and denoised EELS areal density maps is shown in fig. 2. Line profiles extracted from identical regions show periodic contrast with spacing ~ 4Å with the exception of the raw Ru-L2,3 map. ADF intensity minima and maxima in both the DSO and SRO extraction region are in good agreement with intensity maxima in EELS maps, as expected.

EELS SI have been acquired under cryogenic conditions. Dose fractionation with electron counting cameras enabled the atomic resolution EELS mapping of ionization edges up to 3000 eV with accumulated dwell times of ~6 ms and probe current of 20 pA.

[1] Jones, L., et al. *Microscopy* 67.suppl_1 (2018): i98-i113.

Fig 1: EELS SI from SRO/[110]DSO. Survey image with target (green box) and pre-drift regions (orange box) are shown to the left. Summed ADF and EELS maps following PCA denoising are shown to the right.

Fig 2: Comparison of spatial resolution achieved in ADF and EELS maps. A single pixel line integral is shown for the ADF (grey). Line integrals averaged over several unit cells are shown for EELS data. PCA-denoised(solid) and raw areal density(glyph) are overlaid.

Fig. 1

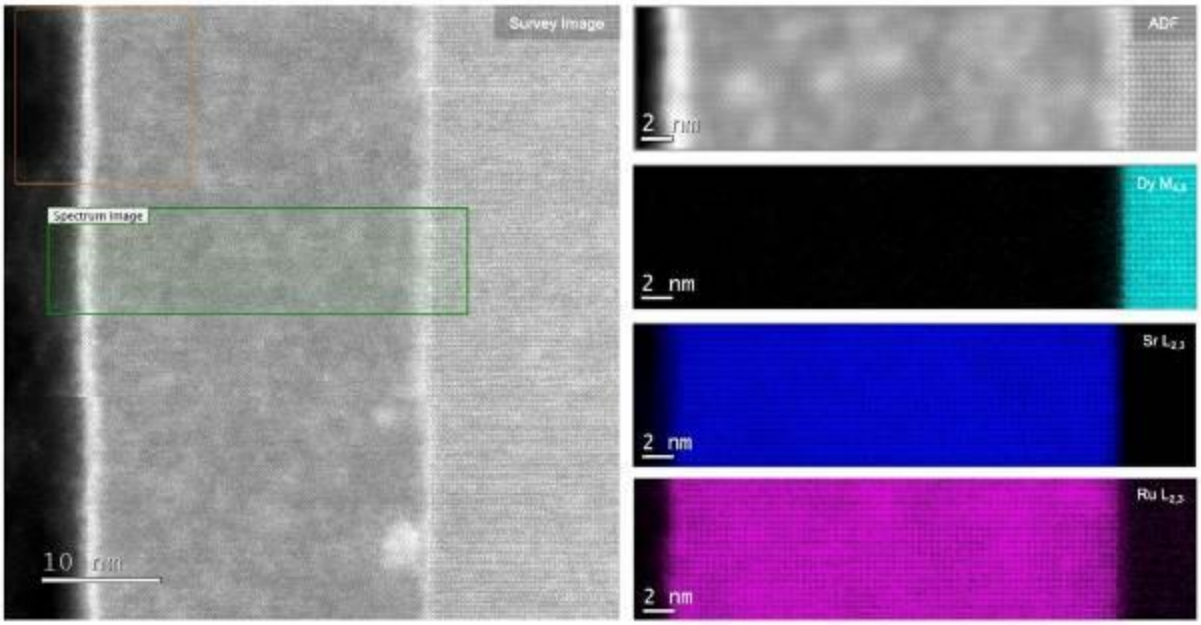
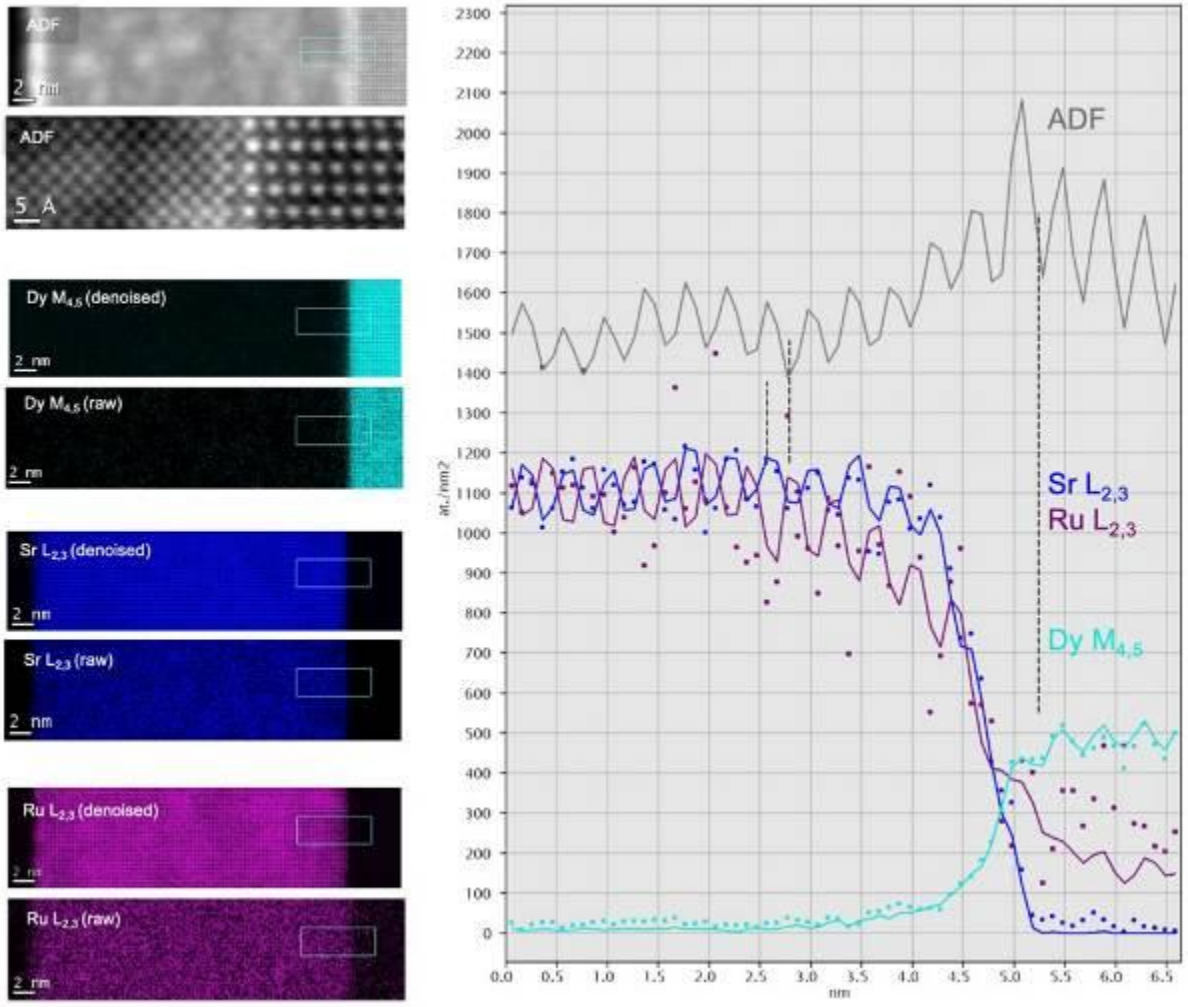

Survey Image
Spectrum Image
10 nm
ADF
2 nm
Dy M4,5
2 nm
Sr L2,3
2 nm
Ru L2,3
2 nm

Fig. 2


ADF
2 nm
ADF
5 A
Dy M4,5 (denoised)
2 nm
Dy M4,5 (raw)
2 nm
Sr L2,3 (denoised)
2 nm
Sr L2,3 (raw)
2 nm
Ru L2,3 (denoised)
2 nm
Ru L2,3 (raw)
2 nm
ADF
Sr L2,3
Ru L2,3
Dy M4,5
at./nm2
nm

IM1.P08
Advantages of an electrostatic beam blanker in STEM

R. Egoavil[1], P. Potocek[1,2], E. van Cappellen[3], M. Meledina[1], M. Wirix[1], B. Freitag[1], D. Jannis[1]

[1]Thermo Fisher Scientific, Materials & Structural Analysis, Eindhoven, Netherlands
[2]Saarland University, Saarbrücken, Germany
[3]Thermo Fisher Scientific, Materials & Structural Analysis, Hillsboro, OR, United States

Mitigation of radiation damage in scanning transmission electron microscopy (STEM) is essential to secure sample integrity for obtaining high quality information [1]. Especially beam sensitive materials such as biological specimens, zeolites, metal-organic-frameworks (MOFs) and lithium-battery electrodes, among others require rethinking the scan strategies in STEM. Structural degradation is a two-step process of excitation and relaxation processes with different time intervals in different materials [2]. By changing scan parameters and/or fast beam blanking in STEM these effects can be influenced to maximize the quality of the measurement [3,4].

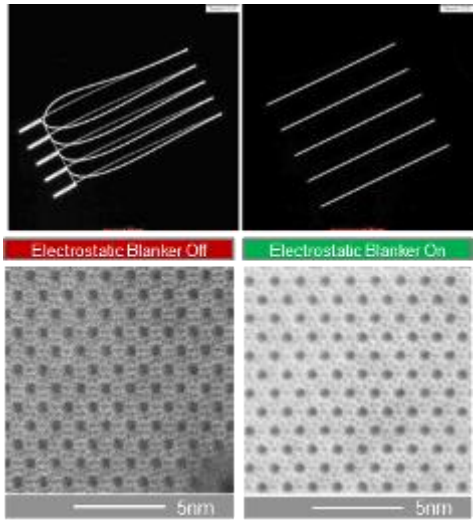
This work discusses damage mitigation advantages of using a fast electrostatic beam blanker to have a precise control over the electron dose(rate) in STEM to avoid damage due to flyback contributions of scan coil hysteresis. The blanker technology is tested on a Zeolite material (Figure 1). A semi-automated workflow is enabled via AutoScript TEM interface [5] accessible on the ILIAD TEM platform, which allows flexibility to set-up unconventional experiments via Python scripting. Here the shortest unblank time used is 25ns and the dwell time is varied from 1µs to 20µs level to explore the effect on beam damage.

Fig. 1. Effect of beam blanking on the conventional raster scan on the sample. Upper part shows the improvements in electron dose on the coil flyback when the electrostatic beam blanker is switched OFF (Upper left) and switched ON (Upper right). Bottom part shows the corresponding STEM ADF image of a zeolite structure with and without the beam blanking. Radiation damage is clearly visible if beam blanking is not used (bottom-left). Images recorded under equivalent conditions: scan size = 128x128, and dwell time = 10us, estimated electron dose ~ 7.85kel/A2.

References:

5. R.F. Egerton, Microscopy research and technique (2012), **75**, 1550–1556. https://doi.org/10.1002/jemt.22099
6. C. Kisielowski *et al*. Advanced functional materials (2019), **29**, 1807818. https://doi.org/10.1002/adfm.201807818
7. A. Velazco *et. al.* Ultramicroscopy (2022), **232**, 113398. https://doi.org/10.1016/j.ultramic.2021.113398
8. D. Jannis *et. al.* Ultramicroscopy (2022), **240**, 113568. https://doi.org/10.1016/j.ultramic.2022.113568
9. https://www.thermofisher.com/order/catalog/product/AUTOSCRIPT-TEM

Fig. 1


Electrostatic Blanker Off
Electrostatic Blanker On
5nm
5nm

IM1.P09
Time-resolved cryo-EM applications with the *SPITROBOT* plunger

M. Schröder[1], G. Göc[2], H. Schikora[3], J. P. Leimkohl[3], F. Tellkamp[3], E. C. Schulz[1,2], P. Mehrabi[1]

[1]University of Hamburg, Institute of Nanostructure and Solid State Physics, Hamburg, Germany
[2]University Medical Center Hamburg-Eppendorf, Institute for Biochemistry and Signal Transduction, Hamburg, Germany
[3]Max Planck Institute for the Structure and Dynamics of Matter, Hamburg, Germany

Understanding the relationship between protein structure and function requires not only high-resolution static structures but also insights into the dynamic processes that drive conformational changes. Techniques like time-resolved crystallography (TRX) or TR-single particle analysis (SPA) cryo-electron microscopy (cryo-EM) have become indispensable tools in structural biology, allowing to capture metastable states and mechanistic intermediates that are crucial for biological function. By bridging the gap between static snapshots and functional dynamics, these methods provide a more comprehensive understanding of molecular mechanisms at near-atomic to atomic resolution.

However, several challenges prevent routine application of time-resolved experiments. A main difficulty lies in reproducible sample preparation and precise time-delays. Our recently developed *SPITROBOT*[1] crystal plunger, in conjunction with the liquid application method for time-resolved analysis (LAMA)[2], streamlines sample preparation for TRX applications. To this end samples are mounted on standard micromeshes within a humidity and temperature-controlled environment. Reactions are initiated either via *in-situ* mixing with the LAMA method, or via optical laser excitation. Subsequently, reaction intermediates are trapped by rapid vitrification with a minimal delay time of 25 ms.

Now we aim to expand the *SPITROBOT*-application, to time-resolved MicroED (poster 1) and time-resolved SPA (poster 2). MicroED enables structure determination from crystals as small as 100 nm, overcoming the limitations of XRD, which requires larger crystals, while also allowing rapid ligand diffusion (~1 µs)[3], making it ideal for studying fast reaction kinetics and dynamic conformational changes. Cryo-EM on the other hand enables high-resolution structure determination without the need for large crystals, overcoming the limitations of XRD, which makes it ideal for studying large macromolecules that are difficult to crystallize such as membrane proteins or dynamic macromolecular complexes.

For compatibility with these cryo-EM applications, we have developed custom tools to mount and vitrify default 3-mm TEM grids within the *SPITROBOT*. Picolitre sample deposition via the LAMA method onto self-wicking grids[4] circumvents the blotting process, reduces subjectivity during sample preparation and minimizes sample consumption.

With these applications, we aim to establish the *SPITROBOT* as a user-friendly, cost-efficient tool for time-resolved Electron Microscopy to explore protein-ligand interactions and catalytic mechanisms at high resolution, advancing our understanding of protein dynamics and function.

Graphical abstract:

The graphical abstract illustrates the application of time-resolved cryo-EM techniques (TR-MicroED or TR-SPA) with the SPITROBOT plunger. The initial phase encompasses sample preparation and the vitrification of samples deposited on self-wicking grids at designated time points using SPITROBOT with LAMA nozzles. Subsequently, the data is collected by using Talos and Arctica, followed by data processing.

References:

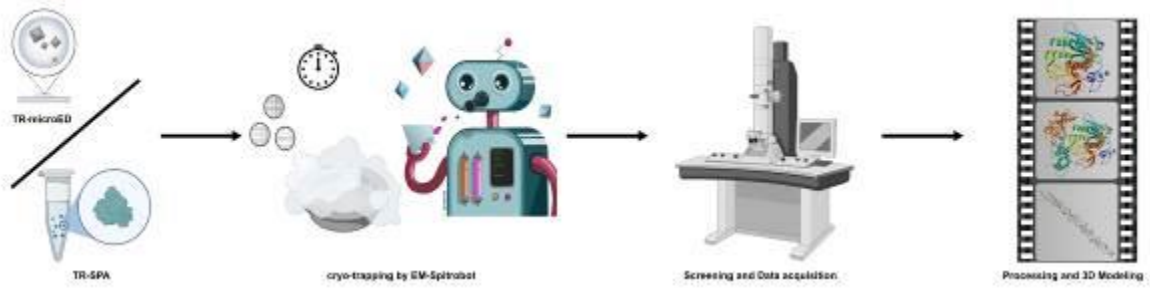
[1] P. Mehrabi, S. Sung, D. von Stetten, et al., Nat. Commun. 14, 2365 (2023).

[2] P. Mehrabi, E.C. Schulz, M. Agthe, et al., Nat. Methods 16, 979–982 (2019).

[3] M. Schmidt, Adv. Cond. Mat. Phys. (2013).

[4] H. Wei, et al., Journal of Structural Biology 202, 170 (2018).

Fig. 1



IM1.P10
Enhancing the spatial resolution of hybrid pixel detectors with GaAs:Cr sensors for use in transmission electron microscopy

K. Paton[1], J. P. Abrahams[2,3], S. Fernandez[4], E. van Genderen[2,3], D. Greiffenberg[1], U. Kolb[5,6], J. Mulvey[1], M. Stampucci[5], B. Schmitt[1], A. Bergamaschi[1], M. Brückner[1], M. Carulla[1], R. Dinapoli[1], S. Ebner[1], K. Ferjaoui[1], E. Fröjdh[1], S. Hasanaj[1], J. Heymes[1], V. Hinger[1], V. Gautam[1], T. King[1], V. Kedych[1], S. Li[1], C. Lopez Cuenca[1], D. Mezza[1], K. Moustakas[1], A. Mozzanica[1], C. Ruder[1], P. Sieberer[1], S. Silletta[1], D. Thattil[1], X. Xie[1], J. Zhang[1]

[1]Paul Scherrer Institute, Center for Photon Science Detector Group, Villigen, Switzerland
[2]Paul Scherrer Institute, Center for Life Sciences Nanodiffraction Group, Villigen, Switzerland
[3]University of Basel, Center for Molecular Life Sciences, Basel, Switzerland
[4]DECTRIS Ltd., Baden-Dättwil, Switzerland
[5]Johannes Gutenberg University Mainz, Centre for High Resolution Electron Microscopy, Mainz, Germany
[6]Technical University of Darmstadt, Institute of Applied Geosciences, Darmstadt, Germany

Hybrid pixel detectors (HPDs) are now a well-established technology in transmission electron microscopy, having enabled new insights in a range of fields. They have kHz frame rates and large, linear dynamic ranges, making them well-suited for diffraction-based modalities [1]. However, their imaging performance is limited by their large (typically ≥ 55 µm) pixels as well as the long-range scatter of electrons in Si sensors sufficiently thick to protect the readout electronics from incident electrons [2].

High-Z sensors, e.g. GaAs:Cr and CdZnTe, have been shown to improve the imaging performance of HPDs in terms of modulation transfer function (MTF) and detective quantum efficiency (DQE) at higher electron energies (≥ 120 keV) [3,4]. Their greater stopping power reduces the lateral scatter of incident electrons, improving device point spread function (PSF). In standard Si sensors, for smaller ratios of electron energy to pixel pitch, the electron entry point can be reliably identified using adaptations of interpolation routines that are used to identify the entry point of incident X-rays in photon science [5,6]. The reduced PSF of high-Z sensors should make this approach viable with higher electron energies for devices with comparable pixel pitches (i.e. for greater ratios of electron energy to pixel pitch). This would avoid the need for more computationally intensive machine-learning based approaches that have been developed for devices with Si sensors at higher energies [6,7].

We are currently characterizing a new variety of GaAs:Cr, supplied by DECTRIS, using the 75 µm pitch JUNGFRAU charge-integrating HPD [8]. JUNGFRAU has previously been used for electron crystallography [1], and earlier studies have confirmed its spatial resolution can be improved by using a high-Z sensor in place of a Si one [9]. This new variety of GaAs:Cr is available in large areas, such that single 0.5 Mpixel detector modules spanning an area of 4 × 8 cm^2 are possible. Reducing the effective pixel pitch and thereby increasing the number of pixels per unit area via interpolation should yield a highly versatile detector suitable for both high-resolution imaging and diffraction studies.

Our evaluation of this new material´s basic properties indicate it is similiar in quality to previously available varieties of GaAs:Cr [10], while our initial electron measurements confirm the expected reduction in lateral scatter of the primary electrons (Fig. 1). We will present the results of MTF and DQE measurements, currently in progress, which will be used to quantify the degree of improvement in spatial resolution possible via interpolation for electron energies up to 300 keV.

Fig. 1: Distributions pixel cluster sizes due to individual 300 keV electrons recorded by JUNGFRAU devices with 500 µm thick GaAs:Cr and 450 µm thick Si sensors.

[1] E. Fröjdh et al., Crystals, 10(12) (2020)

[2] G. Tinti et al., IUCrJ, 5(2), 190 (2018)

[3] K. A. Paton et al., Ultramicroscopy, 227, 113298 (2021)

[4] P. Zambon et al., NIMA, 1048, 167888 (2023)

[5] S. Cartier et al., Journal of Instrumentation, 9(5), C05027 (2014)

[6] X. Xie et al., Journal of Instrumentation 19(01), C01020 (2024)

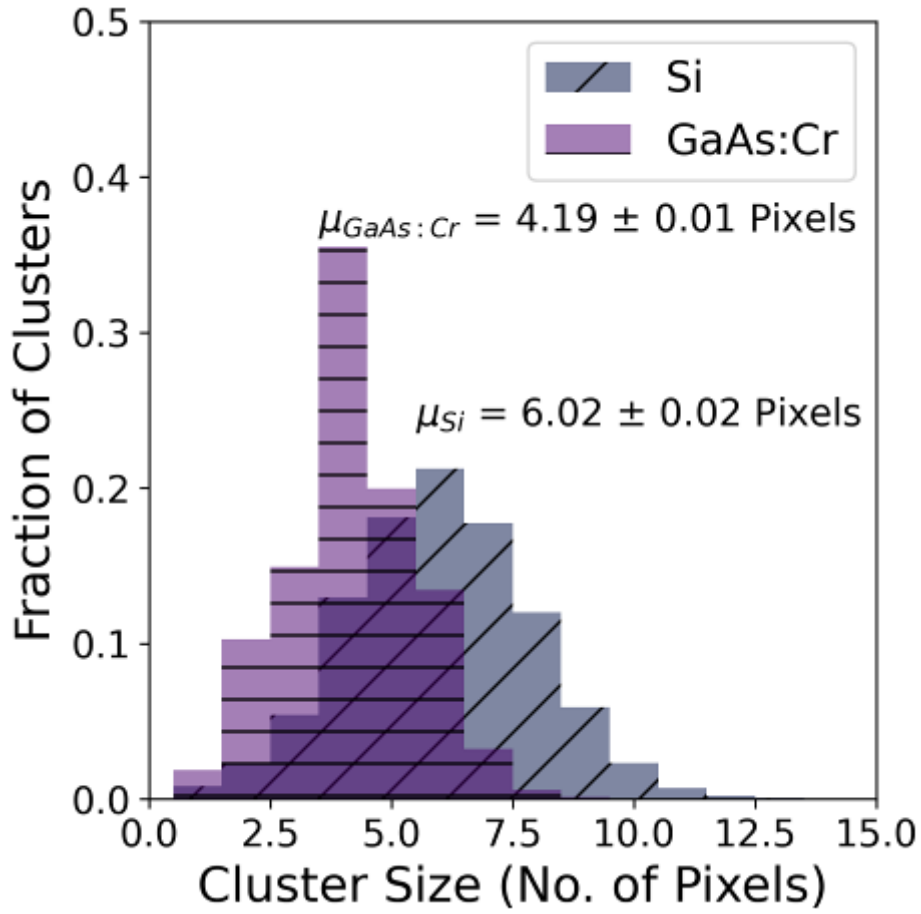
[7] P. van Schayk et al., Ultramicroscopy, 218, 113091 (2020)

[8] A. Mozzanica et al., Journal of Instrumentation, 9(5), C05010 (2019)

[9] E. Fröjdh et al., Journal of Instrumentation 17, C01020 (2022)

[10] D. Greiffenberg et al., Sensors, 21(4), 1550, (2021)

Fig. 1



IM1.P11
Driving spin states with the non-radiative near-field of a modulated electron beam

M. Kolb[1], T. Spielauer[1], T. Weigner[1], D. Rätzel[2], G. Boero[3], P. Haslinger[1]

[1]Technical University of Vienna, Atominstitut - USTEM, Vienna, Austria
[2]University of Bremen, ZARM, Bremen, Germany
[3]Ecole Polytechnique Fédérale de Lausanne, ZARM, Lausanne, Switzerland

The Franck-Hertz experiment was the first to demonstrate the quantization of atomic energy levels using electrons, leveraging inelastic scattering. We want to demonstrate coherent interactions between electrons and two-level systems using the non-radiative near-field of a spatially deflected electron beam. I will discuss recent progress on the our setup, which consists of an adapted Philipps XL30 Scanning Electron Microscope.
The electron beam is electrostatically deflected and passes by a spin ensemble to perform steady-state Electron Spin Resonance (ESR), which is read out inductively using a microcoil and a combination of heterodyne and lock-in detection. This could pave the way for coherent manipulation of quantum systems utilizing electrons, higher spatial resolution, non-destructive analytics by combining ESR and electron microscopy, using custom painted potentials from modulated electron beams.

IM1.P12
Sensing spin systems with Pico-Radian sensitivity

M. S. Seifner[1,2], A. Jaroš[1,2], J. Toyfl[1,2], B. Czasch[1,2], I. C. Bicket[1,2], P. Haslinger[1,2]

[1]Technical University of Vienna, USTEM, Vienna, Austria
[2]Technical University of Vienna, Atominstitut - USTEM, Vienna, Austria

Introduction

The spin is a fundamental quantum property of matter. Spin states are coupled to the chemical environment and can be coherently manipulated using microwave radiation. Spectroscopic techniques such as electron spin resonance (ESR) and nuclear magnetic resonance have been used to obtain deep insights into spin systems [1,2]. However, conventional techniques typically sense the global response of spin systems and are therefore not suitable for obtaining local information about the specimen.

Objectives

This work aims to develop spin-sensitive techniques for transmission electron microscopy (TEM) to study spin systems on the nanoscale.

Materials & methods

The magnetic field $\mathbf{B_0}$ created at the pole piece of the TEM is utilized for polarizing the spins in the specimen. A custom-built TEM holder with an integrated microresonator allows for coherent manipulation of spin states by the supply of microwaves (excitation field $\mathbf{B_1}$), leading to a collective spin precession **M** in the specimen [3]. The electron probe, positioned in aloof-mode, interacts with the precessing spins, resulting in beam deflections. These deflections can be extracted by acquiring images in momentum space and subsequent image processing. The setup and the basic concept of the experiment is illustrated in Figure 1.

Results

Extracting deflections from the modulated electron beam allows for obtaining signals that are similar to absorption and dispersion spectra observed in conventional ESR spectroscopy. The signals vary with the position of the electron probe relative to the specimen, showing the potential of the developed technique for collecting local information about the sample. Moreover, frequency and magnetic field sweeps confirm the expected Zeeman splitting of spin states. The concept is further optimized by incorporating different electron microscopy modes to enhance both sensitivity and spatial resolution.

Conclusion

Our study proves the feasibility of performing ESR measurements within a TEM by analyzing spin-induced modulations of the electron beam. The developed technique allows us to sense beam deflections with pico-radian sensitivity and can potentially lay the foundation for studying spin system with high sensitivity on the atomic scale.

References

[1] Bienfait, A.; et al. *Nat. Nanotechnol.* **2016,** *11*, 253.

[2] Callaghan, P. T. *Principles of Nuclear Magnetic Resonance Microscopy*; Clarendon Press: Oxford, 1993.

[3] Jaroš, A.; et al. Electron spin resonance spectroscopy in a transmission electron microscope. *arXiv Preprint* arXiv:2408.16492 (2024).

Fig. 1

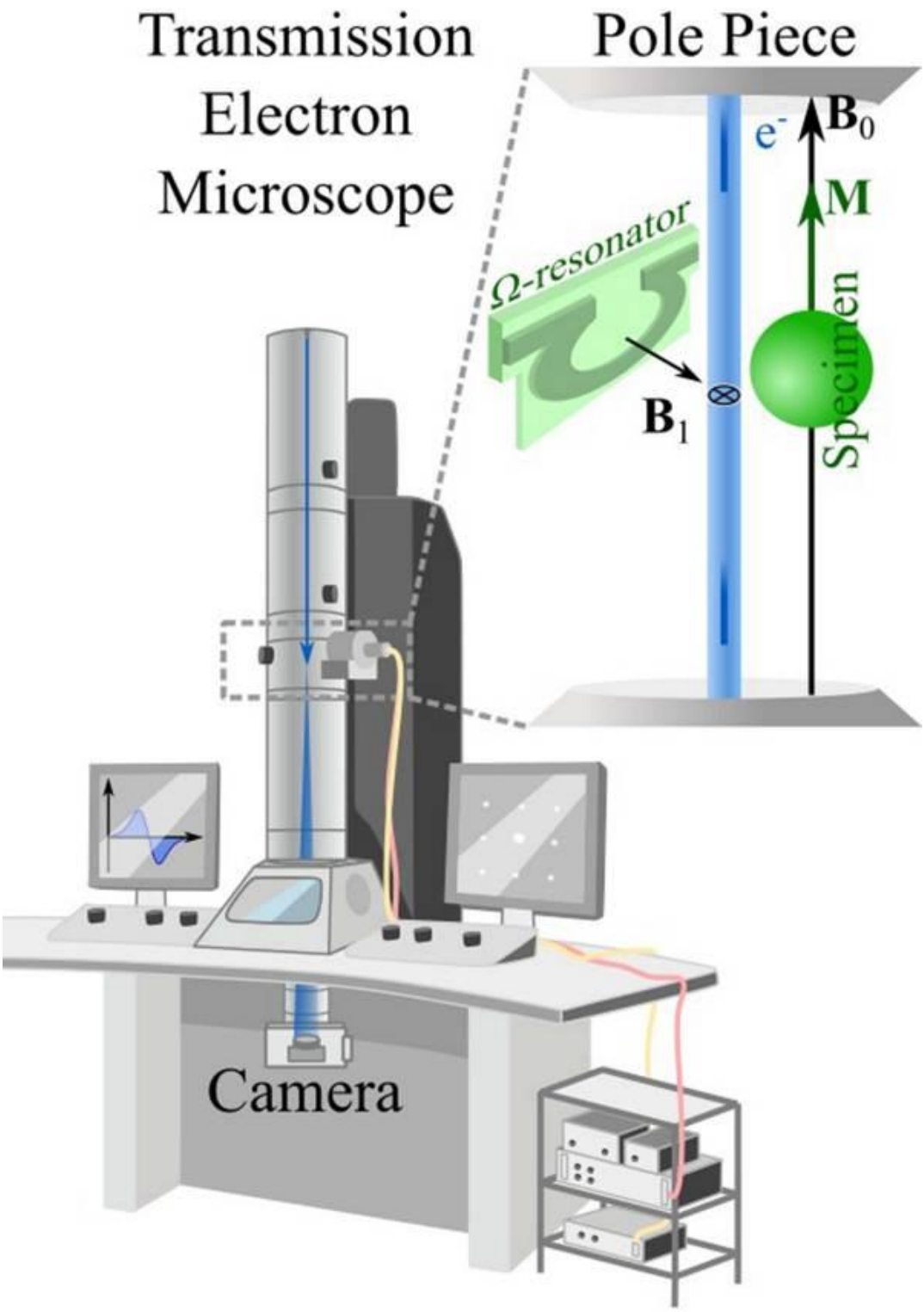


Figure 1. Schematic illustration of the used setup. The pole piece generates a magnetic field $\mathbf{B_0}$ that polarizes the specimen, leading to the sample magnetization **M**. The Ω-shaped microresonator applies an oscillating $\mathbf{B_1}$ field that excites the spin states and modulates the electron probe. The excitation initiates a spin precession, causing additional electron beam deflections upon interaction. The modulated electron beam with imprinted spin signatures is recorded with a camera and further analyzed.

IM1.P13
Optimizing spin detection in TEM – From imaging to quantum metrology

S. S. Beltrán Romero[1,2], M. Gaida[3], S. Löffler[1,2], S. Nimmrichter[3], D. Rätzel[1,4,2], P. Haslinger[1,2]

[1]Technical University of Vienna, Vienna, Austria
[2]Technical University of Vienna, University Service Centre for Transmission Electron Microscopy, Vienna, Austria
[3]University of Siegen, Siegen, Germany
[4]University of Bremen, ZARM, Bremen, Germany

Introduction: Transmission Electron Microscopy (TEM) has revolutionized nanoscale research by enabling unprecedented simultaneous spatial and temporal resolution thanks to advancements such as aberration correction as well as cryogenic and ultra-fast techniques. However, the ability of TEM to probe spin dynamics—essential for understanding quantum materials—remains limited. Recent innovations in microwave spectroscopic tools [1,2] suggest new possibilities for overcoming these limitations.

Objectives: We present a study on spin imaging capabilities in time-resolved TEM and methods for their enhancement. Specifically, we investigate the feasibility of imaging many-spin samples under parallel illumination with an unpolarized beam, optimize measurement conditions using Quantum Metrology, and explore the fundamental limits of spin detection through imaging and diffraction analysis.

Materials & Methods: We employ a framework based on scattering theory to model spin sample probing with time-resolved TEM. Our approach accounts for both elastic and inelastic processes, including electron backaction on the spin [3]. Using the Classical Fisher Information (CFI), we optimize measurement conditions for spin detection, comparing imaging and diffraction modes, as well as different defocus planes. An optimized image analysis pipeline is applied to maximize the CFI, and we discuss the attainability of the Quantum Fisher Information (QFI) limit for single magnetic dipole imaging.

Results: Our simulations reveal how the choice of measurement setup influences the magnetic dipole detection precision. We identify optimized conditions that enhance Signal-To-Noise Ratio (SNR) and contrast, significantly improving the sensitivity of TEM-based spin imaging. In particular, diffraction mode provides a major advantage, as the cumulative deflection from multiple spins enhances the detectable signal, especially at low deflection angles.

Conclusion: Our work establishes a theoretical foundation for integrating spin resonance techniques with advanced microscopy analysis tools. By optimizing imaging strategies and exploring the fundamental metrological limits of spin detection, we pave the way for breakthroughs in atomic-scale spin imaging and manipulation.

References

[1] P. Haslinger, S. Nimmrichter, and D. Rätzel, *Spin resonance spectroscopy with an electron microscope*, Quantum Science and Technology 9, 035051 (2024).

[2] Antonín Jaroš, Johann Toyfl, Andrea Pupić Benjamin Czasch, Giovanni Boero, Isobel C. Bicket, and Philipp Haslinger, *Electron spin resonance spectroscopy in a transmission electron microscope*, arXiv:2408.16492 (2024).

[3] D. Rätzel, D. Hartley, O. Schwartz, and P. Haslinger, *Controlling Quantum Systems with Modulated Electron Beams*, Phys. Rev. Research 3, 023247 (2021).

IM1.P14
AI-guided time resolved cryo-EM Single particle analysis to study dynamics in membrane proteins

J. Schuster[1], M. G. Madej[1], V. Heinz[1], N. Archipowa[1], C. Ziegler[1]

[1]University of Regensburg, Biophysics II, Regensburg, Germany

Time-resolved cryo-electron microscopy (cryo-EM) is a powerful technique for capturing transient conformational states of macromolecular complexes. This approach employs a light-coupled plunge freezing device, enabling time resolution from 10 milliseconds to several seconds. The device facilitates ex situ excitation of the sample prior to vitrification, allowing controlled initiation of structural transitions. Excitation occurs either through direct absorption of light by the photoactive component of the sample or via irradiation of caged compounds with mid-to-high quantum yield, which can induce pH changes or ionic imbalances. This approach is particularly relevant for membrane transporters embedded in membrane-like structures, such as proteoliposomes, where rapid perturbations are essential for studying functional dynamics. By integrating a revitrification strategy, the achievable timescales are anticipated to extend into the microsecond regime, significantly expanding the scope of time-resolved structural studies.

The inherently stochastic nature of sample excitation, achieved through highly focused LED irradiation, results in populations of targets at different excitation durations on a single cryo-EM grid. To address this heterogeneity, data collection is performed across multiple grids to generate sufficiently large datasets for each discrete time point. Automated workflows, developed in-house and inspired by previous implementations, have been integrated into the facility-owned JEOL CryoARM200 microscope. These workflows facilitate high-throughput data acquisition and ensure quality control through real-time preprocessing of micrograph data, allowing immediate feedback on session performance. Furthermore, the presence of diverse excitation states within the dataset necessitates machine-learning-based classification for effective sorting of collected 2D and 3D classes. Refinements to these classification strategies will be achieved by comparing classification results to AI-generated excited-state maps derived from adaptations of the AlphaFold machine-learning model, implemented on a dedicated in-house modeling server.

Future advancements will incorporate image analysis and machine learning techniques to optimize cryo-EM data collection, which will improve sample preparation by providing critical data to refine purification and concentration strategies.

IM1.P15
Towards cinematic STEM – Fast frame rates with scan shaping

J. J. P. Peters[1], G. Moldovan[2], L. Jones[1]

[1]Trinity College Dublin, The University of Dublin, School of Physics, Dublin, Ireland
[2]Point electronic GmbH, Halle (Saale), Germany

Higher scanning speed in STEM has long been desired to mitigate the effects of specimen drift [1], to capture dynamic events [2] or to control dose [3]. Until recently, STEM speed was limited to ~0.1 fps for typical images of 512x512 pix, as each line was synced with mains electrical frequency to minimize distortions from external fields. In more recent years, ~2 fps imaging has been developed in combination with multi-frame diagnose and distortion removal [1], yet the main roadblock was flyback efficiency.

As scan speed was increased, flyback hysteresis distortion was increased also, thus a larger proportion of time had to be allocated to line wait and pre-scan, leading to poor time and dose efficiency. Whilst limited distortions could be mitigated with computational post-processing [4], higher speed required higher efficiency, which was finally possible with a new generation of scan controllers capable of arbitrary scans strategies [5, 6, 7] without flyback.

These new controllers can also generate faster scans with pixel times on the order of 10 ns, however the inductive nature of scan coils and limited bandwidth in amplifier electronics present the present barrier to greater speeds. New coil designs can reduce scan coil inductance [2], though with a limited field of view and not existing columns. A new approach is now needed to achieve the highest speed on existing STEMs and at low magnification, which must mitigate distortions from the scan system.

We propose the serpentine scanning pattern where alternating lines are scanned in opposite directions. This removes the large discontinuities in beam position and velocity of conventional flyback scanning. A fast serpentine scanning pattern will still present distortions due to the imperfect deflection system, principally as the beam cannot change direction instantaneously. To account for this, we propose overdrive to shape the scan to the desired output, for this case by slowing down and "overstepping" at line ends to force the beam into the desired positions.

To measure necessary scan shaping, we record beam positions in a confocal configuration with a camera (Fig. 1), measure motion and then apply an iterative correction to account for the non-linear response of the beam (Fig. 2). We can show progress towards imaging at ~50 ns per pixel and frame rates of 50 fps with fully sampled images.

Fig. 1. Setup (a) and recorded serpentine motion (b) at 1 µs/pixel (blue), 200 ns/pixel (green), 100 ns/pixel (yellow), and 50 ns/pixel (red).

Fig. 2. Pre (a) and post (b) corrected deviation of measured beam position (dashed black) from desired beam position (solid orange).

References

1. Jones L et al Adv Struct Chem Imaging (2015) 1, 8
2. Ishikawa et al Microscopy (2020) 69, 240–247
3. Ilett M et al Philos Trans R Soc (2020) A 378, 20190601
4. Mullarkey T et al Microsc Microanal (2022) 28, 1428–1436
5. Velazco A Nord et al Ultramicroscopy (2020) 215, 113021
6. Peters JJ al Microsc Microanal (2023) 29, 1373–1379
7. Li Xet al Microsc Microanal (2018) 24, 623–633

Acknowledgement

J.J.P.P. and L.J. acknowledge SFI grant 19/FFP/6813 and URF/RI/191637

Fig. 1

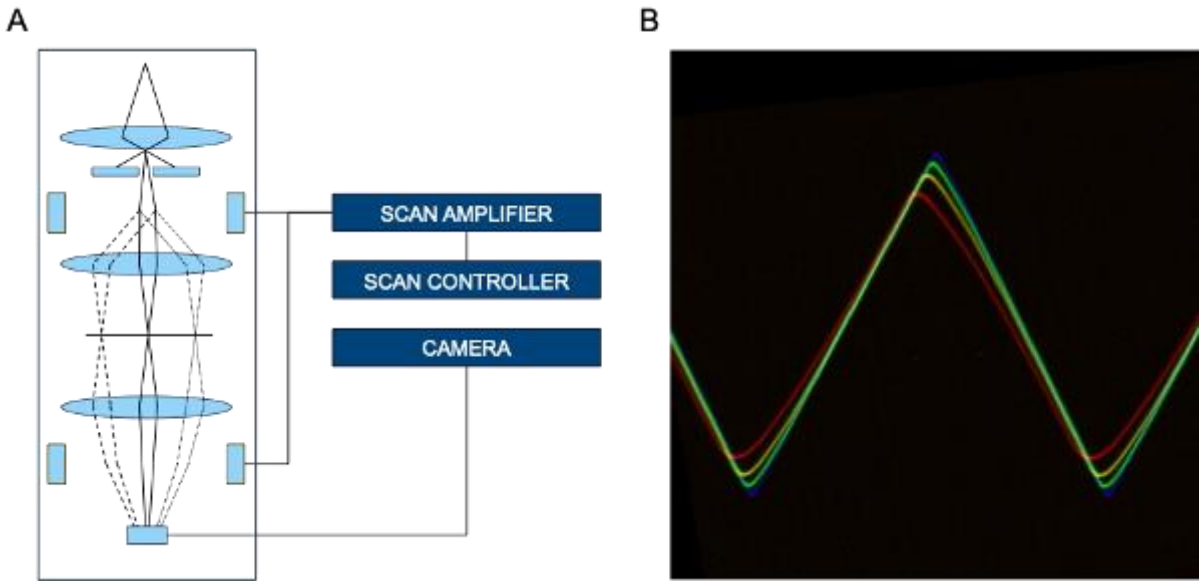
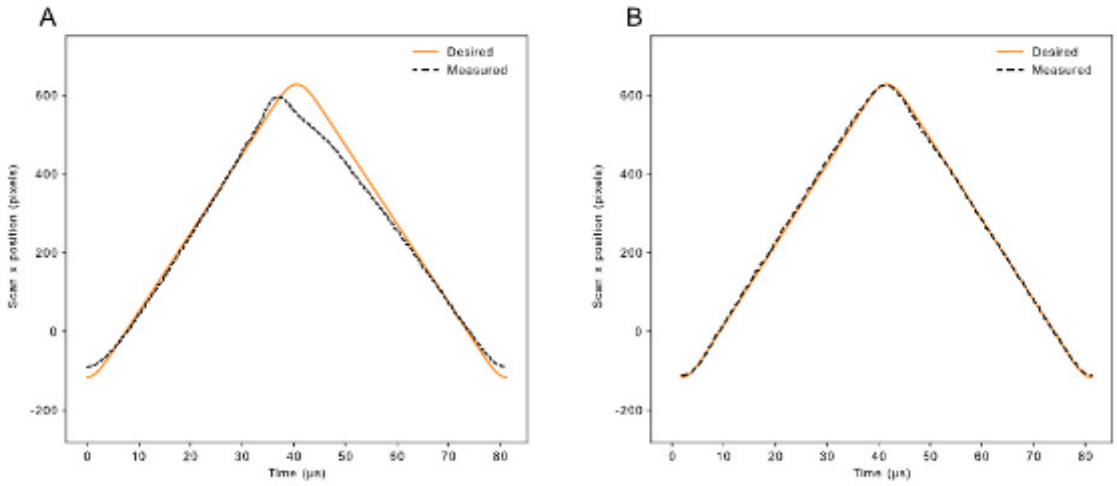


Fig. 2



IM1.P16
Design and fabrication of a custom TEM holder for *in situ* optical excitation – Combining light and free electrons for advanced transmission electron microscopy

M. R. Nielsen[1,2], M. N. Yesibolati[1], M. S. Seifner[1,2,3], S. Kadkhodazadeh[1,2]

[1]Technical University of Denmark, Nanolab - National Centre for Nano Fabrication and Characterization, Kongens Lyngby, Denmark
[2]Technical University of Denmark, NanoPhoton - Center for Nanophotonics, Kongens Lyngby, Denmark
[3]Technical University of Vienna, University Service Center for Transmission Electron Microscopy, Vienna, Austria

Introduction
Transmission electron microscopy (TEM) is a well-established technique for atomic-resolution imaging and diffraction analysis. However, its integration with optical excitation remains relatively underexplored in conventional TEM[1]. The incorporation of light into the TEM typically requires substantial modifications to the TEM column, which can be both expensive and potentially detrimental to the instrument[2]. This work presents the design and fabrication of an optical TEM holder. Different from previous work[3,4], our design incorporates a dedicated optical pathway for delivering light directly to the sample region by coupling the fibers directly to a silicon chip itself.

Objectives
The primary objective of this work is to design and fabricate a custom optical TEM holder capable of combining optical excitation with electron imaging inside the TEM. The holder was specifically designed to couple directly with a photonic silicon chip, which then guides light onto the sample area through an integrated waveguide network. By leveraging this chip-based light delivery, the need for high precision alignment within the TEM column is eliminated, enabling reliable coupling between the fiber-coupled laser and the grating coupler leading the light over the sample. Ultimately, this platform aims to establish a robust experimental basis for direct investigations of light-electron interactions at the atomic scale.

Materials & methods
The optical TEM holder was designed using SolidWorks[5], integrating fiber-coupled light delivery into the sample area through optical fibers embedded within the holder itself. These fibers, comprising of input, output, and reference channels, directly coupled to a photonic silicon chip mounted in the custom-made tip. Light is coupled into the chip using a grating coupler, which efficiently transfers the light into an on-chip waveguide network. This configuration guides the light toward a tailored nanocavity, designed to enhance photon-electron coupling in the presence of the electron beam. The structural components of the holder, hollow rod and base, were bought through InsightChips[6]. The light-compatible tip was fabricated in-house. Prior to final assembly, the optical path was pre-tested using confocal microscopy to verify that the focused laser spot aligned precisely with the grating coupler on the silicon chip, ensuring optimal coupling efficiency upon insertion into the TEM column.

Results and
With this holder, an initial proof-of-concept experiment was performed combining fiber-coupled laser illumination with 4D-STEM imaging. These experiments illustrate the holder"s potential for investigating photo-induced structural dynamics and plasmonic near-field effects.

Conclusion
By incorporates an optical pathway through a custom optical holder coupling directly yo the silicon chip, this work paves the way for correlative light-electron microscopy, uniting complementary modalities into a single, coherent experimental platform. This represents a significant step toward the realization of a photon-electron laboratory inside the electron microscope.

References

[1] M. Kociak, et. Al., *Ultramicroscopy* **176** (2017) 112-131.
[2] B.K. Miller et al., Microsc. Microanal. **19** (2013) 461-469.
[3] F. Cavalca et. al., Nanotechnology **23** (2012) 075705.
[4] J. Martis et al., Microscopy Today **29** (2021) 40–44.
[5] https://www.solidworks.com/ (March, 2025)
[6] https://www.insightchips.com/ (March, 2025)

IM 2: Advanced spectroscopy

IM2.01(inv)
Machine learning-enhanced EELS analysis

D. del Pozo Bueno[1], V. Costa-Ledesma[1], L. Yedra[1], S. Estradé[1], F. Peiró Martinez[1]

[1]Universitat de Barcelona, Electronics and Biomedical Engineering, Laboratory of Electron Nanoscopy (LENS-MIND-IN2UB), Barcelona, Spain

Introduction

The advancement of Scanning Transmission Electron Microscopy (STEM) coupled with Electron Energy Loss Spectroscopy (EELS) has significantly improved elemental and chemical characterization at the nanoscale. However, the exponential growth in data complexity calls for robust and efficient analytical tools. In this scenario, machine learning (ML) algorithms have opened new possibilities for efficient, automated, and accurate EELS data interpretation.

Objectives

In this work we will review some examples of ML enhanced EELS spectral classification using supervised and unsupervised strategies combined with novel data augmentation techniques to mitigate the challenges of limited labeled datasets for supervised ML algorithms. Some of these tools are being implemented as new functionalities in the software WhatEELS 2.0 and applied to nanomaterials including transition metal oxides nanoparticles and solid-state battery materials.

Materials and methods

First, the performance of soft-margin Support Vector Machines (SVMs) and Artificial Neural Networks (ANNs) on Electron Energy Loss (EEL) spectra for spectra classification, specifically targeting iron and manganese oxides is evaluated. Both models were trained to identify key spectral features, including white lines and the oxygen K edge, and were tested on data with induced energy shifts and noise to assess their robustness to spectral variability. Next, we employ Generative Adversarial Networks (GANs) for data augmentation, generating synthetic EEL spectra from a limited set of experimental samples. This significantly enhances the diversity and volume of the training data, improving model generalization without the need for extensive new measurements. Finally, we integrate several machine learning techniques to analyze the low-loss region of EELS, focusing on plasmonic resonances. This involves dimensionality reduction using Uniform Manifold Approximation and Projection (UMAP), clustering with Hierarchical Density-Based Spatial Clustering of Applications with Noise (HDBSCAN), and classification of clustering outliers using trained SVMs.

Results

The experimental validation of these approaches is proved on several materials. Our results show that GANs capture the variability and complexity of real spectra, enabling effective training of both SVMs and ANNs with fewer original samples in front of the task to classify spectra from iron-manganese oxide core-shell nanoparticles. The combination of UMAP and HDBSCAN with SVM for outliers classification successfully identifies plasmon resonances in Au/Si nanowires. Finally, by applying these dimensionality reduction and clustering algorithms, oxidation state changes and lithium signatures in solid state battery materials ($Li_{1.3}Al_{0.3}Ti_{1.7}(PO_4)_3$ and $LiFePO_4$) have been revealed, offering insights into degradation mechanisms.

Conclusions

By combining advanced machine learning strategies with open-source tools like WhatEELS, this work demonstrates a powerful framework for EELS data analysis. From oxidation state classification to plasmon detection in nanostructures and battery degradation assessments, these methods enhance precision, reduce manual effort, and open new avenues for high-throughput materials characterization.

IM2.02(inv)
Merging advanced photonics with time-resolved electron microscopy

A. Feist[1,2]

[1]Max Planck Institute for Multidisciplinary Sciences, Department of Ultrafast Dynamics, Göttingen, Germany
[2]Georg-August-Universität Göttingen, 4th Physical Institute, Göttingen, Germany

Electron beam probing offers unique insights into nanophotonic systems [1], with recent advances utilizing stimulated gain scattering [2] to study plasmonic and dielectric cavities in ultrafast electron microscopes [3,4]. Meanwhile, light optics features powerful techniques largely unexplored for electrons, including coherent spectroscopy, super-resolution, and correlation-enhanced imaging. Transferring these concepts requires novel schemes to couple and detect electrons and photons at the single-particle level.

In my talk, I will review the latest progress in coupling free electrons and photons using inelastic scattering at high-Q optical modes. Incorporating electron energy gain spectroscopy (EEGS) and correlated single-particle detection, we implement high-precision photonic mode imaging and establish a novel free-electron-driven quantum light source.

In the first experiment, an optically pumped high-Q integrated photonic microresonator facilitates highly efficient continuous-wave optical phase modulation, resulting in spectral sidebands in the electron energy distribution, here, using only a few μW of optical power [5]. Furthermore, high-frequency detuning of the exciting laser and nanosecond detection of electron spectra enables μeV-electron spectroscopy and imaging the buildup of dissipative Kerr solitons (DKSs) within a photonic chip–based microresonator [6].

In a second line of experiments, using a low-current stream of electrons, spontaneous scattering at the empty cavity creates electron-photon pair states [7]. The single photons generated in the waveguide (1550-nm wavelength) and corresponding electron energy loss (0.8 eV) are detected in coincidence, which enables strongly noise-suppressed imaging. In analogy to spontaneous parametric down-conversion, this mechanism enables the heralded generation of single-electron or multi-photon states [8], which is directly verified by measuring the quantum statistics of the generated light in a Hanbury Brown and Twiss experiment [9].

Ultimately, tailored electron-light interactions and the ability to induce highly correlated multi-electron/photon states may provide new avenues in electron microscopy, including new contrast mechanisms and enhanced sensitivity. Establishing single-particle coupling is pivotal for the emerging field of free-electron quantum optics, promising hybrid quantum technology that fuses free electrons and light.

References

[1] A. Polman et al., *Nat. Mater.* **18**, 1158–1171 (2019).
[2] B. Barwick et al., *Nature* **462**, 902–906 (2009).
[3] K. Wang et al., *Nature* **582**, 50–54 (2020).
[4] J. H. Gaida et al., *Nat. Photonics* **18**, 509–515 (2024).
[5] J.-W. Henke *et al., Nature* **600**, 653–658 (2021).
[6] Y. Yang et al., *Science* **383**, 168–173 (2024).
[7] A. Feist *et al., Science* **377**, 777–780 (2022).
[8] X. Bendaña et al., *Nano Lett.* **11**, 5099–5103 (2011).
[9] G. Arend et al., arXiv:2409.11300 (2024).

IM2.03
Imaging local magnetic moments with atomic-scale electron vortex beams via EMCD in $BaFe_{11}TiO_{19}$

D. Pohl[1], H. Makino[1], S. Schneider[1], R. Erni[2], A. Ernst[3], J. Rusz[4], D. Negi[5], B. Rellinghaus[1]

[1]DCN, TU Dresden, Dresden, Germany
[2]EMPA - Swiss Federal Laboratories for Materials Science and Technology, Electron Microscopy Center, Dübendorf, Switzerland
[3]Johannes Kepler University, Linz, Germany
[4]Uppsala University, Uppsala, Sweden
[5]Indian Institute of Technology Jodhpur, Jodhpur, India

Introduction

Electron magnetic circular dichroism (EMCD) allows the element specific measurement of spin and orbital magnetic moments with up to nanometer resolution in transmission electron microscopy [1]. Recently discovered electron vortex beams (EVBs), which carry quantized orbital angular momentum (OAM), are envisioned to be used in combination with EMCD measurements to determine the magnetic properties of a material in transmission electron microscopes [2]. Since EVBs can be easily focused down to sub-nanometer diameters, this novel technique has enormous potential for quantifying spin and orbital magnetic moments with unrivaled lateral resolution.

Objectives

For the measurement of magnetic properties down to the atomic scale using electron vortex beams, three prerequisites can be formulated: (i) single EVBs must be prepared with a well defined OAM to avoid a concurrent superposition of OAM, (ii) the EVBs need be to be of atomic size and (iii) electron energy loss spectra need to be measured from individual magnetic atomic columns [3].

Materials & methods

The generation of EVBs is achieved by the implementation of a 50 µm dislocation-type apertures into the condenser lens system. A special setup allows for scanning TEM investigations (STEM) with vortex beams, whose OAM is selected by means of an additional discriminator aperture in the C3 aperture plane. Although this selection of OAM and thus the limitation in total beam current results in a decrease of the signal-to-noise ratio, this novel technique still allows for atomic resolution EELS measurements [4].

Fig. 1a shows the HAADF image of the anisotropic ferrimagnet BaFe11TiO19 in [001] zone axis. The large lattice spacing between the Fe columns allows atomically resolved Fe-L edge maps.

Results

Spectrum images have been acquired with electron vortex probes carrying OAM of L = ±1 ħ. To overcome the low signal, a direct electron detector ELA from DECTRIS was used for the acquisition of fast spectrum images which are averaged by post-processing. By applying advanced fitting routines to the Fe-L edges, atomic maps of the EMCD signal of the ferrimagnetic sample are resolved. Fig 1b shows the extracted EMCD signal of the two magnetic sublattices. Besides the visualization of the ferrimagnetic arrangement in agreement with inelastic scattering simulations, local variation induced by Ti doping are observed. The role of the Ti doping on the magnetic super exchange of the Fe atoms will be supported by DFT calculations.

Conclusion

High quality vortex EMCD measurements allow for the necessary resolution to resolve the local ferrimagnetic order. Vortex EMCD therefore promise to open the door for future quantitative measurements of magnetic properties with ultimate spatial resolution and their local correlation with structural features at the very same position within the identical sample.

[1] P. Schattschneider et al., Ultramicroscopy 136 (2014), p. 81-85.

[2] J. Verbeeck et al., Nature 467 (2010), p. 301-304.

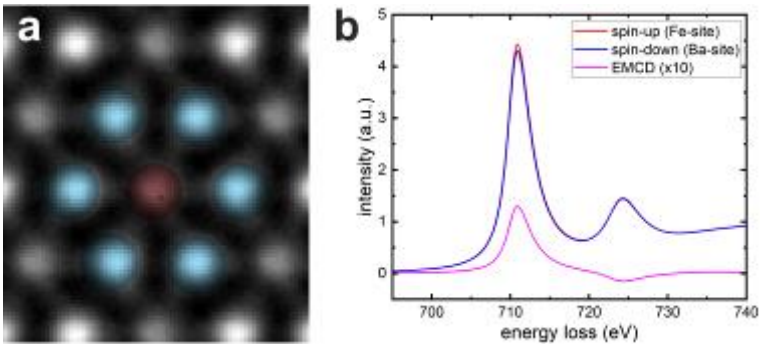
[3]J. Rusz and S. Bhowmick, Phys. Rev. Lett. 111 (2013), 105504.

[4] D. Pohl et al., Sci. rep. 7, (2015).

Financial support by the DFG project Vortex-EMCD (project number 504660779) is gratefully acknowledged.

Fig. 1: Vortex HR-STEM EMCD measurements. **a**, HAADF image of BaFe11TiO19 (overlay: magnetic sublattices) **b**, Fe-L edge and EMCD spectra acquired with L=+1ħ electron vortex beam extracted from the two Fe sublattice positions.

Fig. 1



IM2.04
EELS Compton scattering and the electronic structure of materials

A. Talmantaite[1], Y. Xie[2], A. Cohen[3], P. Mohapatra[3], A. Ismach[3], T. Mizoguchi[2], S. Clark[1], B. Mendis[1]

[1]Durham University, Dept of Physics, Durham, United Kingdom
[2]University of Tokyo, 2. Institute of Industrial Science, Tokyo, Japan
[3]Tel Aviv University, 3. Dept. of Materials Science and Engineering, Tel Aviv, Israel

Electronic structure is fundamental to a large class of materials phenomena, including mechanical, optical, magnetic and electronic transport properties. Momentum based spectroscopies such as angle resolved photoemission spectroscopy (ARPES), electron-positron annihilation and Compton scattering are traditionally used to measure the electronic structure. Compton scattering in the transmission electron microscope (TEM) was first explored in the 1980s using electron energy loss spectroscopy (EELS). Despite early success it did not achieve widespread use, largely due to the limitations in EELS spectrometer detector efficiencies, and artefacts arising from Bragg scattering within a crystalline specimen. However, with modern advances in EELS spectrometers as well as computational techniques for modelling dynamical scattering artefacts many of the challenges facing EELS Compton scattering are arguably now resolved. EELS Compton scattering in the TEM provides several benefits over standard X-ray and gamma-ray Compton measurements, such as a higher spatial resolution and the ability to extract useful information from even poly-crystalline materials.

In EELS Compton scattering the incident electron beam undergoes an inelastic collision with individual electrons in the solid. The Compton signal appears as a broad peak in an EELS spectrum acquired at large scattering angles (i.e. high momentum transfer). The width of the Compton profile, which can be as large as several hundred eV, is due to the intrinsic momentum spread of the solid-state electrons. The Compton profile shape is therefore directly related to $J(p_z)$, i.e. the density of solid-state electrons with momentum component p_z along the scattering vector direction. $J(p_z)$ provides a 1D projection of the electronic band structure in reciprocal space. We have applied EELS Compton scattering to examine the electronic structure of bi-layer WS_2, with a twist angle of 18^o between the two layers. EELS Compton scattering is particularly suitable to this problem, since the low dimensional nature of the WS_2 flakes make it difficult or impossible to analyse using conventional methods. Furthermore, the twist angle is known to control the optical, vibrational and electrical properties of TMD bilyares.

The $J(p_z)$ acquired along the 10-10 reciprocal direction indicates that the electrons are more delocalised in the bi-layer compared to monolayer WS_2. Comparison with density functional theory (DFT) simulations reveal that the delocalization is due to a small amount of electronic charge (i.e. 0.1%) accumulating in the inter-layer region. The inter-layer charge accumulates between overlapping W atoms, thereby screening the "wrong" bonds generated by the twist angle. The charge accumulation is also accompanied by a local dilation of the inter-layer spacing. The results uncover the precise nature of twist angle on the electronic and structural properties of bi-layer TMDs.

IM2.05
Closing the gap between simulation and experiment in plasmonics – Incorporating substrate effects in electron energy-loss spectroscopy and cathodoluminescence

A. Kichigin[1], G. Melis[1], B. Apeleo Zubiri[1], M. Wu[1], M. Yurkin[2], E. Spiecker[1]

[1]FAU Erlangen-Nürnberg, Institute of Micro- and Nanostructure Research (IMN) and Center for Nanoanalysis and Electron Microscopy (CENEM), Erlangen, Germany
[2]Université Rouen Normandie, INSA Rouen Normandie, CNRS, CORIA UMR 6614, Rouen, France

1. Introduction

Electron energy-loss spectroscopy (EELS) and cathodoluminescence (CL) are powerful techniques for probing plasmonic excitations in metallic nanoparticles. By irradiating a specimen with relativistic electrons (e.g., 100 keV) in a transmission electron microscope (TEM), one can collect the electron energy-loss spectrum and simultaneously measure photon emission (CL) arising from electron–matter interactions. Unlike far-field optical methods, EELS and CL offer nanometer-scale spatial resolution for mapping plasmonic modes, enabling deeper insights into structure–property relationships.

2. Objectives

We aim to extend the discrete dipole approximation (DDA) to accurately simulate EELS and CL for nanoparticles on substrates. Substrate-mediated effects often redshift and modify plasmonic resonances; these must be included to achieve quantitative agreement between simulations and experiments.

3. Methods

We built upon our previously published DDA framework for particles in an infinite medium [1], adapting it to handle semi-infinite (infinitely thick) substrates. By incorporating the substrate into the dipole–dipole interaction term and modifying the electron-induced field, we avoid discretizing the substrate volume and thus greatly reduce computational cost.

4. Results

Figure 1 compares simulated EELS spectra for a gold nanodisk (50 nm diameter, 10 nm thick) at various distances from a Si33N44 substrate. Placing the disk directly on the substrate (h/2) yields a pronounced redshift relative to the vacuum reference. Lifting the disk progressively farther (2h, 4h, 6h) shifts the resonance back, converging with the vacuum case at large separation (50h). Even modest changes in nanoparticle–substrate geometry thus significantly affect the plasmonic response.

Figure 2 shows experimental and simulated EELS maps of a triangular gold nanoparticle (180 nm side, 15 nm thick) on a Si33N44 membrane. Our extended DDA reproduces the redshifted plasmon energies and spatial EELS probability distributions measured experimentally. In contrast, vacuum-only simulations deviate noticeably from observed resonances and plasmon maps. These findings underscore the necessity of including substrate effects in EELS/CL simulations to achieve both qualitative and quantitative agreement.

5. Conclusion

By further extending the DDA theory to include semi-infinite substrates, we have achieved accurate EELS and CL simulations for plasmonic nanoparticles in experimentally relevant configurations. The resulting spectra and plasmon maps align closely with measurements, offering a robust framework to study substrate-induced effects and interpret experimental data. A brief theory overview, along with additional experiment–simulation comparisons for both EELS and CL, will be presented at the conference.

6. Acknowledgements

We gratefully acknowledge the DFG for financial support within the framework of CRC1411 (Project ID 416229255).

7. References

[1] A.A. Kichigin and M.A. Yurkin, J. Phys. Chem. C 127, 4154–4167 (2023).

Fig. 1

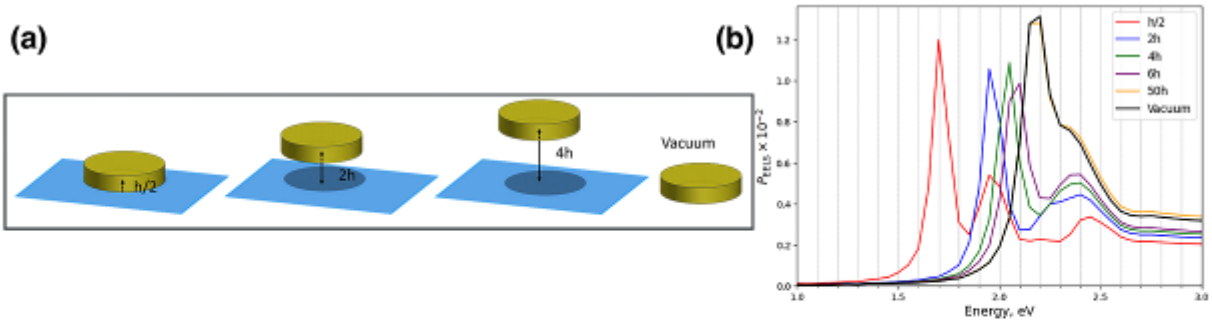


Figure 1. Simulated EELS spectra for a 50 nm diameter, 10 nm thick gold nanodisk at various distances from the substrate. h/2 indicates contact with the substrate; 2h, 4h, 6h are intermediate separations; 50h approaches the vacuum reference case.

Fig. 2

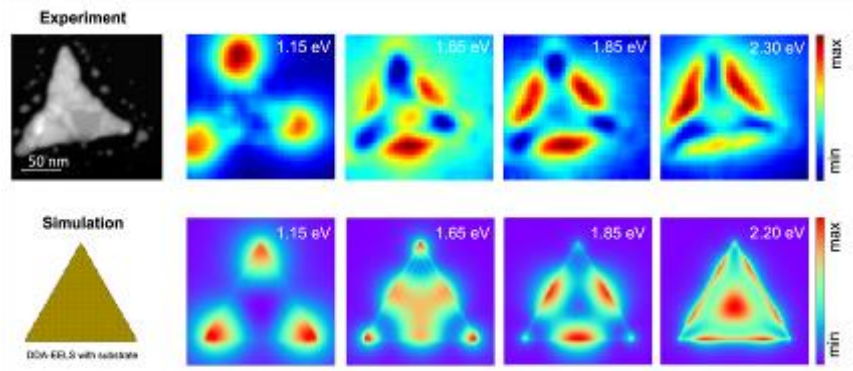


Figure 1. Experimental (top row) and simulated (bottom row) EELS maps of a triangular gold nanoparticle on a thin Si3N4 membrane. The extended DDA approach accurately reproduces the redshifted plasmon modes and spatial field distributions observed in experiment.

IM2.06
TACAW – A unified framework for phonon and magnon spectroscopy in STEM-EELS

J. Á. Castellanos-Reyes[1], P. Zeiger[1,2], J. Rusz[1]

[1]Uppsala University, Physics and Astronomy, Uppsala, Sweden
[2]University of Washington, Materials Science and Engineering, Seattle, WA, United States

Introduction

Understanding phonon and magnon dynamics at the atomic scale is critical for advancements in quantum materials, nanoscale heat transport, and spintronics. Recent developments in scanning transmission electron microscopy (STEM) with monochromated electron energy-loss spectroscopy (EELS) [1] have enabled unprecedented access to vibrational [2] and magnetic excitations [3]. However, theoretical approaches struggle to accurately capture critical physical phenomenon present in experiments including multi-phonon/magnon processes, multiple scattering effects, and temperature dependencies within a single, computationally efficient framework.

Objectives

Here, we present the Time Autocorrelation of Auxiliary Wavefunctions (TACAW) method [4] as a robust tool for momentum-resolved phonon and magnon EELS simulations.

Materials & Methods

TACAW incorporates molecular dynamics and atomistic spin dynamics-driven correlation functions to model temperature-dependent spectroscopy, detailed balance, and multiple inelastic scattering effects, offering a significant improvement over conventional perturbative methods

Results

We validate TACAW by reproducing reported experimental phonon EELS spectra, including the case of hexagonal boron nitride (hBN), and showcase its applicability to magnon excitations.

Conclusion

By unifying phonon and magnon simulations in a single framework, TACAW establishes a computationally efficient and theoretically versatile approach for next-generation STEM-EELS studies.

References

[1] O L Krivanek *et al.*, Nature **514**, 209 (2014).

[2] B. Haas, C. T. Koch, and P. Rez, Appl. Phys. Lett. **125**, 150502 (2024)

[3] D. Kepaptsoglou and J. Á. Castellanos-Reyes *et al.*, arXiv.2410.02908 (2024).

[4] J. Á. Castellanos-Reyes, P. M. Zeiger, and J. Rusz. Phys. Rev. Lett. **134**, 036402 (2025).

IM2.P01
A new approach for quantification of EELSpectra

P. Potapov[1,2], G. Guzzinati[3]

[1]IFW Dresden, TU Dresden, Dresden, Germany
[2]TEMDM, Dresden, Germany
[3]CEOS GmbH, Heidelberg, Germany

Introduction

The methods for quantifying Electron Energy-Loss Spectra (EELS) have been intensively developed over the last half-century [1]. However, recent advances in instrumentation introduce new challenges: 1) the large size of data in modern EELS spectrum-imaging necessitates automated quantification procedures with no or minimal user interaction. 2) EELS data are now available over wide energy ranges, up to several keV, where common assumptions of the standard quantification may no longer hold.

Objectives

The EELS background can be reasonably modelled by the power law $A\,E^{-r}$ within a given narrow energy region [1]. However, the simple power law becomes inaccurate over larger ranges, up to several thousand eV. To address this issue, increasingly complex fitting models have been proposed. While early models included a single power law term [2,3], recent models introduce between two [4] to five [5] such terms. We propose an alternative approach: a *smooth variation* of a power law exponent *r*.

Results

The algorithm begins by identifying an appropriate energy range for fitting. Higher-energy edges require wider ranges for accurate quantification. We fix the fitting width for all edges in the logarithmic scale at 0.6 ln(eV). For example, this width corresponds to 230eV for the C K edge (onset 283eV) but 1600eV for Sr L3 edge (onset 1940eV). Fitting regions for edges of different elements often overlap, then they are merged into a continuous fitting patch. We first identify the region preceding the first edge in the patch and evaluate the power law exponent *r0* in that region (Fig. 1a). This serves as the starting exponent for background fitting. Each edge is then fitted sequentially to the theoretical atomic cross section [6], progressing from left to right. This typically generates a misfit, which is most pronounced at the right end of the spectrum (Fig. 2b).

For subsequent iterations, two additional fitting parameters are introduced: the background value y_{fin} and the exponent r_{fin} at the right end of the fitting patch. The modelled background is schematically illustrated in Fig. 1a. The simple power law is represented by the straight line, while the deviations from it are approximated using a cubic spline with initial point (y_0, r_0) and final point (y_{fin}, r_{fin}). This approach ensures that 1) the pre-edges background matches the previously evaluated simple power law and 2) within any narrow region, the background behaves as a power law with a given local exponent *r*. Further iterations optimize the parameters (y_{fin}, r_{fin}) and the fractions of all edges to minimize the least squares difference with the experimental spectrum. Despite the non-linear nature of optimization, the computational cost remains low as it uses very simple and quick linear fits as elemental blocks.

Conclusion

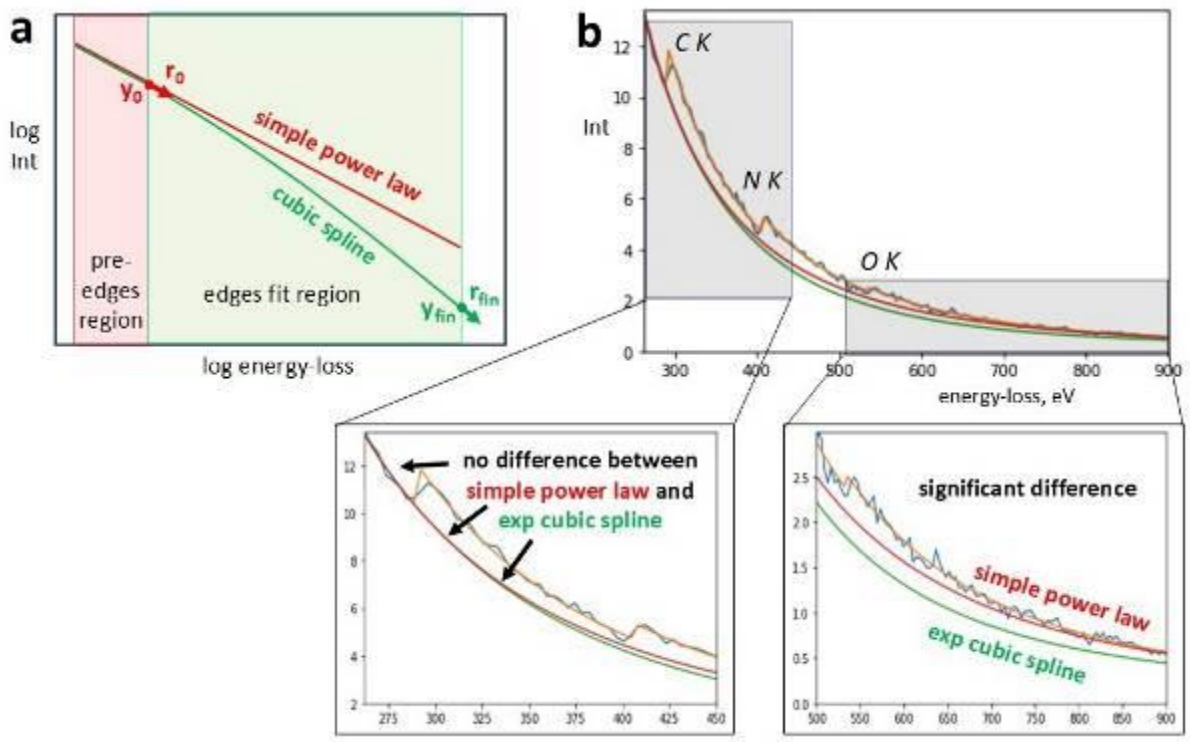
This approach was tested on over a hundred spectra with highly variable composition and background characteristics. In most cases, the resulting fits clearly outperformed the existing methods.

Fig.1 Simple Power Law and smooth cubic spline in log scale. The former has a constant inclination r, while the latter shows a gradual increase or decrease of r. (b) Example spectrum consisting of C, N and O, where a simple Power Law intersects the spectrum at high energies, but a cubic spline provides a reasonable background.

References

1. Egerton R.F. *Electron Energy-Loss Spectroscopy in the Electron Microscope*, NY: Springer; 2011.
2. Verbeeck J. *et al*. *Ultramicroscopy* (2008) **108**, 74-83.
3. EELS info, https://eels.info/how/quantification/extract-signal (accessed Jan. 27, 2025).
4. Cueva P. *et al*. *Microsc. Microanal.* (2012) **18(4)**, 667-675.
5. Van den Broeck W. *et al*. *Ultramicroscopy* (2023) **254**, 113830.
6. Segger L.G. *et al*., Generalised Oscillator Strengths, https://zenodo.org/records/7645765 (accessed Jan. 27, 2025).

Fig. 1



IM2.P02
Extraction of chi spectra from XEELS measurements

W. van den Broek[1], D. Jannis[1], Z. Zhang[2], C. S. Schnohr[3], S. Lazar[1], P. Tiemeijer[1]

[1]Thermo Fisher Scientific, Eindhoven, Netherlands
[2]AI for Science Institute, Beijing, China
[3]Leipzig University, Leipzig, Germany

Background

Recent advances in hardware have enabled the recording of extreme EEL spectra (XEELS) of K-edges with ionization energies of up to ~30 keV [1], while maintaining focus and the ability to record the low-loss spectrum. Like in x-ray absorption spectroscopy (XAS), this allows retrieval of the chi spectrum and its Fourier transform from the extended energy-loss fine structure (EXELFS). In EELS, multiple scattering of the primary electrons hinders reliable estimation of the chi spectrum. Furthermore, the electrons' inherently stronger interaction with matter necessitates limited exposure times leading to relatively noisier measurements.

Methods

We extract the EXELFS with pyEELSMODEL, a model-based EELS processing software package [2] that makes use of state-of-the-art atomic cross sections [3] and of an advanced background model [4], ensures the fine structure obeys the Bethe sum rule [5], and accounts for multiple scattering. The approach's superior noise properties compared to conventional deconvolution techniques lead to a relatively low-noise and single scattering EXELFS. This EXELFS is divided by the atomic cross section and a bandwidth-limited background is subtracted. Multiplication with the square of the wavenumber yields the weighted chi spectrum.

Results

Figure 1. displays the EELS spectrum of a Cu K-edge at 8979 eV recorded at 300 keV, with a convergence and collection semi-angle of 21 and 34 mrad, respectively. Furthermore, the final fit, the background and the single scattering atomic cross section and fine structure are shown as well.

The chi spectra multiplied with the square of the wavenumber are displayed in Figure 2 (left) for XAS (from [1]) and a 90 s and 900 s EELS exposure. Note that the 90 s exposure has a better resolution than the 900 s exposure. For the Fourier transforms in Figure 2 (right) a rolling-off window was applied, and for both EELS recordings they agree well with that of XAS, featuring maxima that are close to those of XAS.

Conclusions

The use of state-of-the-art EELS processing helps overcoming the multiple scattering and shot noise inherent in EELS, yielding a low-noise and well-resolved chi spectrum that is comparable to XAS data.

[1] S. Lazar et al., Physical Review Applied, accepted for publication

[2] D. Jannis et al., https://pyeelsmodel.readthedocs.io/en/latest/index.html

[3] Z. Zhang et al., https://zenodo.org/record/7729585

[4] W. Van den Broek et al., Ultramicroscopy 254 (2023) 113830

[5] D. Jannis et al., Ultramicroscopy 269 (2025) 114084

Figure 1. EELS spectrum of a Cu K-edge at 8979 eV recorded at 300 keV, with a convergence and collection semi-angle of 21 and 34 mrad, respectively. Furthermore, the final fit, the background and the single scattering atomic cross section and fine structure are displayed as well.

Figure 2. *Left*: Chi spectra multiplied with the square of the wavenumber for XAS and a 90 s and 900 s EELS exposure. *Right*: Absolute value of the Fourier transform of the chi spectra on the left as function of the radial distance *R*.

Fig. 1

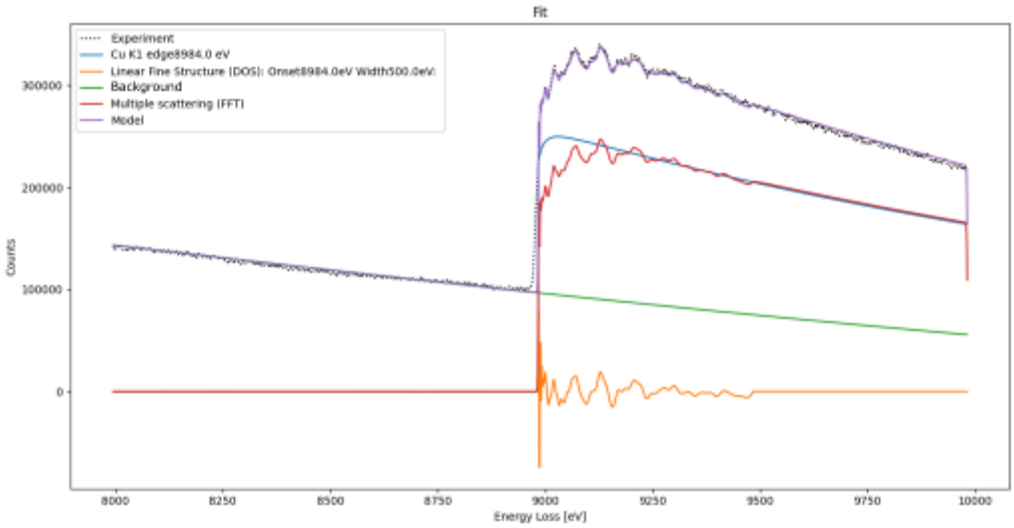
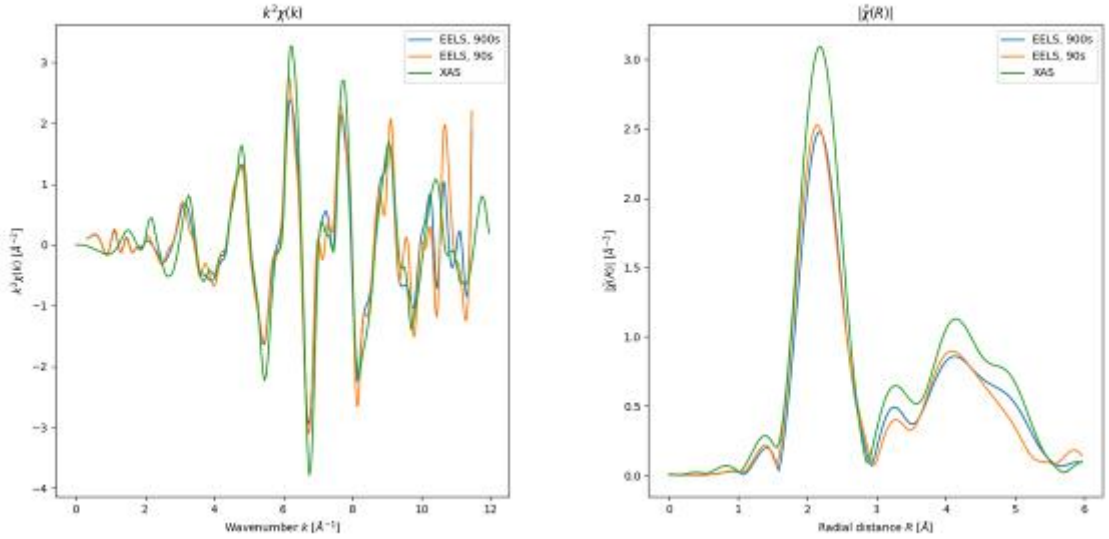


Fig. 2



IM2.P03
Iliad – The next generation integrated EELS solution

M. Meledina[1], R. Egoavil[1], I. Iatrakis[1], D. Klenov[1], D. Krishman[1], S. Lazar[1], P. Longo[1], P. Tiemeijer[1], M. Wirix[1]

[1]Thermo Fisher Scientific, Eindhoven, Netherlands

EELS is well established technique for expert users, but is demanding in setting up optimum experimental conditions, lacks integration and reproducibility of the entire optical system and often misses partly metadata documentation for quantitative offline analysis. . EELS experiments demand the precise setting and stability of both the TEM and the EELS filter optics for the reliable way to produce high quality data. In the experiments a broad range of electron energies must be simultaneously transferred through the microscope and through the spectrometer, from specimen and down to detector, minimizing chromatic blur or chromatic distortions which are degrading the performance. When optimizing the experiment the operator is constantly switching the setting of both the microscope (like high tension , camera length, beam current size & convergence angle, area of interest) and the spectrometer (energy loss&dispersion, dwell time) . introducing the extra challenges to maintain the accurate transfer and keep track of important metadata information influencing the quality of the result.

To ensure the superior performance and the high quality of the EELS data, we deeply integrated the TEM column and the EELS filter in hardware and software. The close integration of the optics of EELS filter and the TEM broadens the possibilities for the multimodal use of the advanced TEM techniques, such as for example simultaneous EELS and EDX [1]. A new Zebra EELS (Figure 1) detector, dedicated for the EELS data collection was developed. All the workflows and modalities are smoothly integrated into our Velox (Figure 2) software ecosystem, allowing the data collection for the operators with various backgrounds.

We will present the advances of deep integration of the TEM column and the EELS filter, Always-in-Focus technology, and highlight it with several practical examples covering the broad range of the applications of the new Iliad STEM platform. The application of both MultiEELSTM mode [2] and XEELSTM mode [3] will be presented.

Fig. 1. EELS Zebra detector.

Fig. 2. Velox software ecosystem for the collection of all the data modalities.

Acknowledgements:

Bas Cornelissen, Terry Dennemans, Sander Henstra, Sjaak Thomassen, Wouter Verhoeven

References:

1. M. Meledina et. al., Microscopy and Microanalysis, Volume 29, Issue Supplement_1, 1 August 2023, Pages 1983–1984, https://doi.org/10.1093/micmic/ozad067.1027F
2. D Jannis et al., Microscopy and Microanalysis, Volume 29, Issue Supplement_1, 1 August 2023, Pages 367–368, https://doi.org/10.1093/micmic/ozad067.171
3. S. Lazar et al., Microscopy and Microanalysis, Volume 29, Issue Supplement_1, 1 August 2023, Pages 369–370, https://doi.org/10.1093/micmic/ozad067.172F

Fig. 1

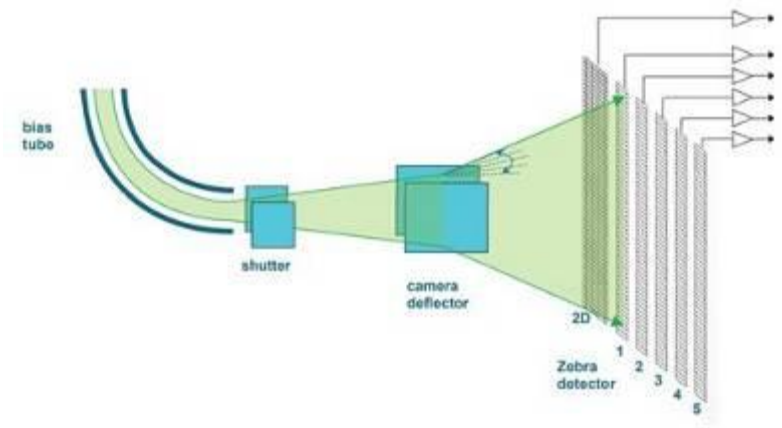

bias
tube
shutter
camera
deflector
2D
Zebra
detector
1
2
3
4
5

Fig. 2


Area #1
2 µm
Spectra from Area #1
Spectrum
Background
Modeled
Intensity (kCounts)
Energy (keV)
Mg
Magnesium
Experiment conditions
Quantification

IM2.P04
Battery material analysis with annular SEM/EDS detector

I. Németh[1], P. Soni[1], J. Aubourg[1]

[1]Bruker Nano GmbH, Berlin, Germany

Introduction, objectives

Since inhomogeneity, contamination and trace elements of battery electrode components (i.e. NCM precursors) affect the device performance, their pre-screening is important. For conclusive SEM/EDS elemental analysis flat, polished sample surfaces are ideal but cannot always be realized due to time constraints or because the materials must be analyzed in an "as received" manner. As these materials exhibit high surface topography, energy dispersive X-ray spectroscopy in an SEM can be challenging for such samples. Furthermore, samples having low electrical conductivity or high electron beam sensitivity can only be investigated using low beam currents, which in turn results in a low X-ray signal. Under such conditions, trace elements cannot be analyzed using EDS within reasonable measurement times.

Materials & Methods

We present a solution for maximizing X-ray signal collection: an annular EDS detector, inserted between the pole-piece and the sample. High count rates can be achieved even at low beam currents as the four separate X-ray detector segments cover a large solid angle (up to 1.1sr). Due to the high count rates, element distribution mapping (including trace elements) with this system is orders or magnitudes faster than using conventional EDS detection geometry. This configuration is also ideal for the analysis of samples with high topography as shadowing effects are minimized by X-ray detection from all spatial directions.

Results

Li-ion battery components (anode and cathode particles), NCM precursor grains or black mass material can be mapped with high spatial resolution without the need of any meticulous sample preparation. Contaminants and inhomogeneities in the submicron range can be visualized within the micrometer-sized particles (see Zr-distribution on Figure 1). We will demonstrate that the annular EDS detector is capable of identifying and mapping contaminants in the range of only a few tens of ppm within a few minutes of measurement time.

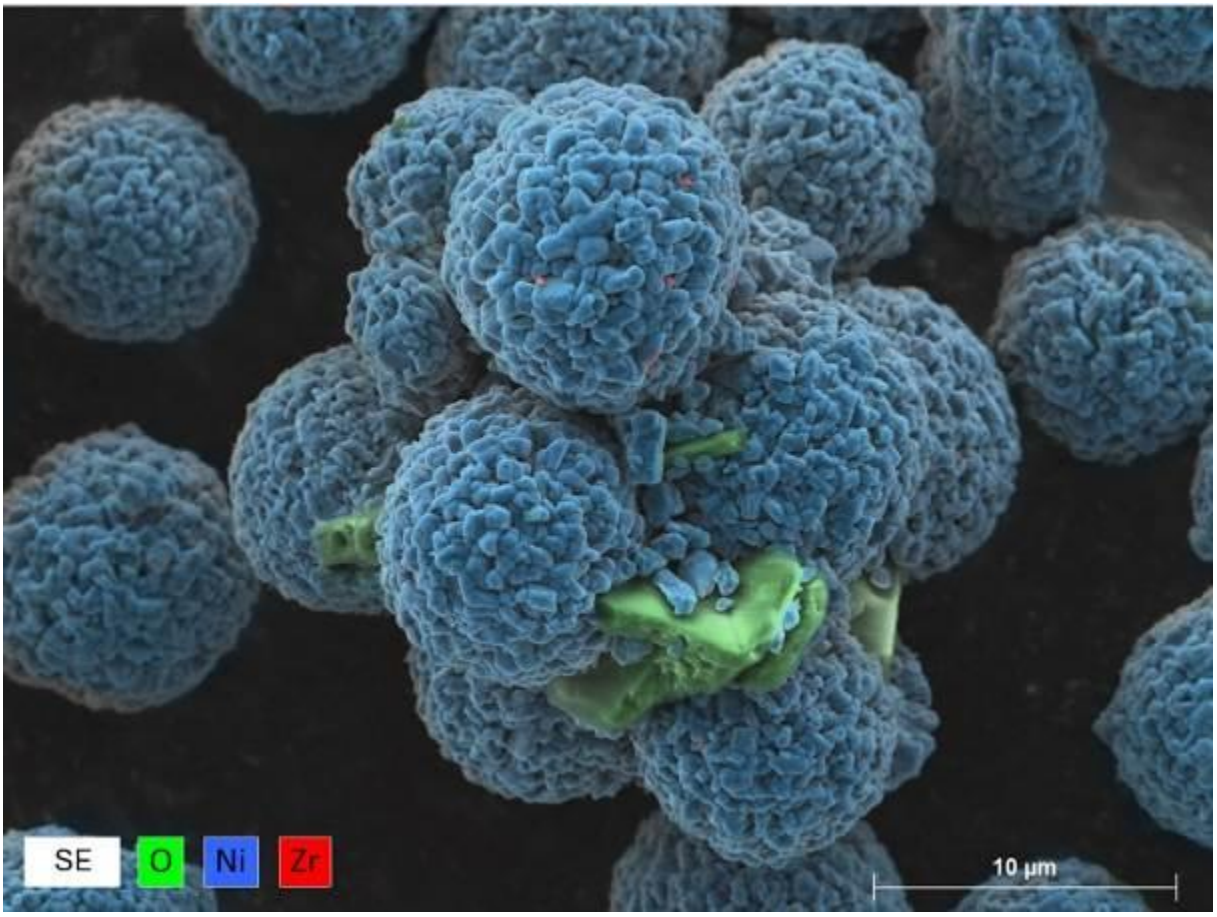
Conclusion

The annular EDS detector in an SEM has proven to be an ideal instrument for challenging elemental analysis of unprepared samples with high topography and low conductivity in the emerging field of battery materials. Due to its maximized collection solid angle, this type of detector yields significantly higher count rates compared to conventional EDS detectors and thus considerably reduces the necessary electron dose or measurement time. EDS using annular detectors is an analytical method capable of detecting and mapping contaminants in the sensitivity range of X-ray fluorescence methods maintaining the high spatial resolution of SEM/EDS analysis.

Figure 1:

NCM cathode particles (native, without sample preparation) mapped with annular EDS detector. The elemental distribution maps are covering the entire surface of the particles, minimized shadowing effect is visible. Trace elements or elements of contaminants (Zr) are mapped within a few minutes.

Fig. 1



IM2.P05
Pushing the limits of SEM EDS – 2 nm spatial resolution for advanced semiconductor characterization

P. Soni[1], I. Németh[1], M. Falke[1]

[1]Bruker Nano GmbH, Berlin, Germany

Introduction:

To meet the demands of next-generation computing, semiconductor fabrication facilities continue to enhance processing speeds by optimizing the structure and materials of advanced 3D devices such as FinFETs and GAAFETs. Characterizing these devices is crucial but challenging, as their smallest features measure below 1 nm. Traditionally, transmission electron microscopes (TEM) equipped with elemental analyzers like energy-dispersive X-ray spectroscopy (EDS) and electron energy loss spectroscopy (EELS) are used for this purpose.

Objectives:

In this study, we highlight the capabilities of scanning electron microscopy-based EDS (SEM EDS) for high-resolution chemical mapping of complex semiconductor structures in both bulk and electron-transparent specimens. We present ultra-high-resolution chemical maps of FinFET devices, demonstrating that spectral quality and spatial resolution remain intact even at extreme magnifications. This is achieved through Bruker ESPRIT software, which integrates an optimized detector design, high collection efficiency, and a precise drift correction algorithm. Additionally, overlapping X-ray peaks—such as Si-Kα (1.74 keV), W-Mαβ (1.802 keV), Hf-Mαβ (1.671 keV), and Ta-Mαβ (1.737 keV) needs to be deconvoluted for accurate elemental analysis.

Materials & Methods:

XFlash Oval7100 windowless: An oval-shaped, 100 mm² windowless detector that provides a large solid angle of up to 0.4 sr, ensuring high collection efficiency for SEM EDS analysis. XFlash FlatQUAD: An annular detector with a unique sample-detector geometry with an even larger solid angle of up to 1.1 sr low-probe current with highsest sensitivity for EDS measurements in SEM.

Results:

Ultra-high resolution SEM EDS map of a 25 nm thin FIB/TEM lamella showing the elemental distribution of a FinFET structure. The overlapping peaks of Si-K, W-M and Hf-M X-ray lines are deconvoluted automatically in the map (some elements are not displayed in the composite map for clarity).

Conclusion:

These results demonstrate that EDS in SEM, can routinely achieve sub-5 nm EDS spatial resolution which is comparable to EDS in S/TEM. This advancement establishes SEM EDS as a powerful and accessible alternative for high-resolution chemical characterization of semiconductor devices.

Fig. 1

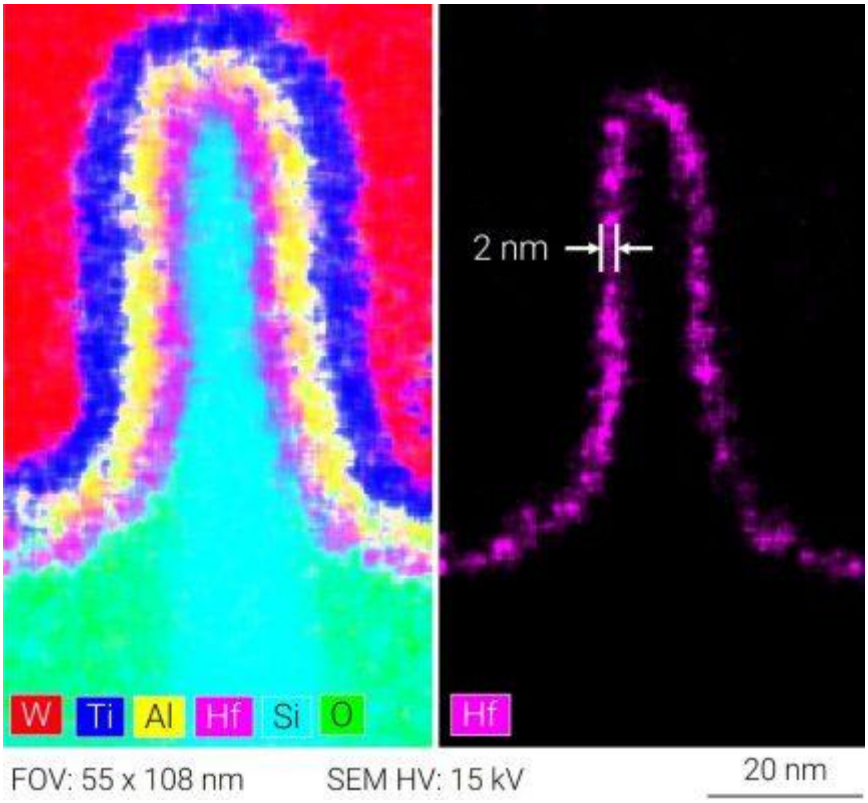
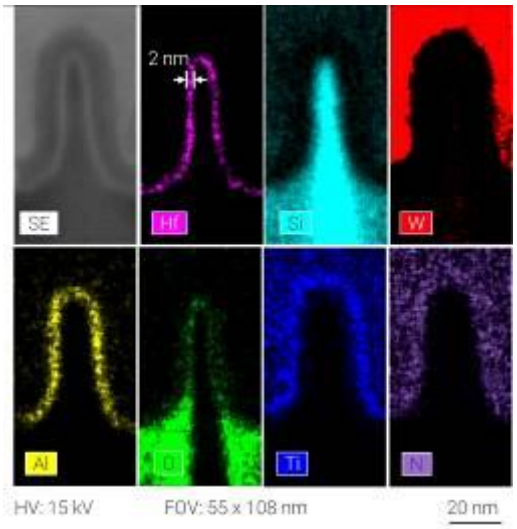

2 nm
W
Ti
Al
Hf
Si
O
Hf
FOV: 55 x 108 nm
SEM HV: 15 kV
20 nm

Fig. 2


2 nm
SE
Hf
Si
W
Al
O
Ti
N
HV: 15 kV
FOV: 55 x 108 nm
20 nm

IM2.P08
SEM-EDS analysis with cooling stage for beam sensitive materials

Y. Yamamoto[1], H. Onodera[1]

[1]JEOL Ltd., EP Application Dept. SEMG, Akishima, Japan

EDS combined with an SEM is an essential technique for elemental analysis of bulk materials. Recently, windowless EDS detectors with a large-area SDD have been developed to detect low-energy characteristic X-rays such as Li without absorption, enabling efficient detection of characteristic X-rays. This allows analysis under low acceleration voltage and small probe current conditions with minimal damage to the sample. However, in the analysis of alkali glass, attenuation of characteristic X-rays due to migration of alkali ions by electron irradiation has been reported[(1)(2)], and the similar phenomenon is confirmed in the analysis using windowless EDS under low acceleration voltage and small probe current conditions. On the other hand, it has been confirmed that cooling of the sample is effective for the analysis while maintaining the chemical state of materials that are easily changed by electron irradiation[(3)]. In this study, we attempted SEM-EDS analysis with a cooling stage to reduce attenuation of X-ray intensity.

We used Schottky FE-SEM, JSM-IT800 (JEOL), combined with the windowless EDS, DrySD™ Gather-X (JEOL) and cooling stage C1003 (Gatan, Inc.) to examine soda-lime glass. Area analysis of this specimen was performed continuously every 10 seconds for an area of approximately 2.5μm x 2μm at stage temperatures of room temperature (RT) and -120°C. The change over time of the Na Kα characteristic X-ray peak intensity of the obtained EDS spectra was traced.

The results of EDS area analysis at an accelerating voltage of 5 kV and a probe current of 300 pA, under RT are shown in Fig. 1. The peak intensity of the Na Kα characteristic X-ray changes as the total irradiation time elapses, indicating that the Na Kα peak intensity is attenuated by an increase in the total electron beam dose per unit area. Figure 2 shows the results of EDS area analysis performed under the same conditions as at RT while the specimen was cooled to -120°C. No significant change in the peak intensity of the Na Kα characteristic X-ray was observed in each measurement. Background processing was performed on the results obtained at RT and -120°C, and the integrated intensities of Na Kα characteristic X-ray peaks in the energy range from 0.97 keV to 1.10 keV were further calculated (Fig. 3). The results of RT show that the integrated intensity of Na Kα eventually decreased by about 59%, whereas at -120°C cooling, the integrated intensity hardly changed at all. In addition, comparing the integrated intensities at RT and at -120°C. during the irradiation time of 10 seconds, the integrated intensity at room temperature decreases, suggesting that the attenuation of the Na Kα characteristic X-ray peak intensity occurs immediately after the start of electron beam irradiation.

By cooling the sample to -120 °C using a cooling stage, the state of Na in the soda-lime glass was maintained and stable detection of Na Kα characteristic X-rays was achieved. This result leads the effectiveness of the SEM-EDS method with sample cooling for materials that are sensitive to state changes induced by electron irradiation. In this presentation, more examples of specimen cooling application for SEM-EDS analysis of materials whose state changes due to electron beam irradiation, will also be reported.

References: (1)J.L.Lineweaver, J. Appl.Phys.,34,1786(1963), (2)O. Gedeon et al., Microchimica Acta 132(2):505-510 (2000), (3)Y. Yamamoto et al., Microscopy Conference 2023, MS1.P01

Fig. 1

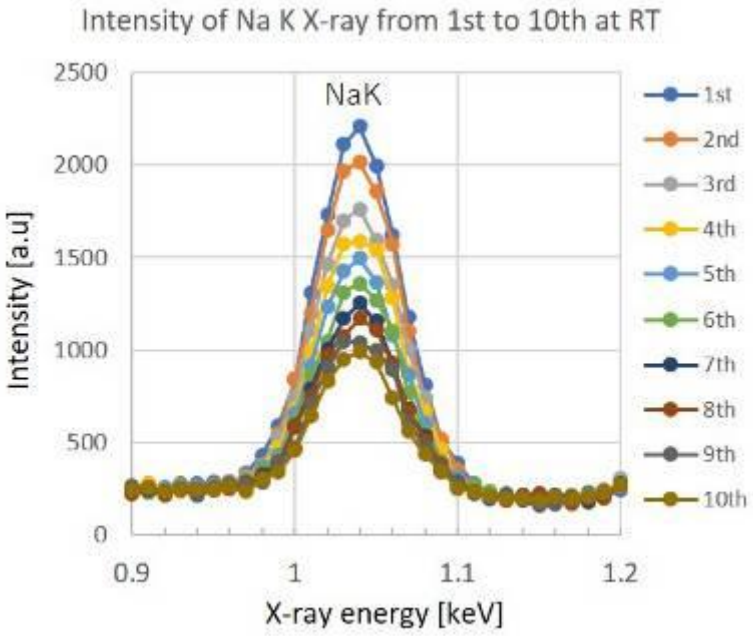

Intensity of Na K X-ray from 1st to 10th at RT
NaK
Intensity [a.u]
2500
2000
1500
1000
500
0
0.9
1
1.1
1.2
X-ray energy [keV]
1st
2nd
3rd
4th
5th
6th
7th
8th
9th
10th

Fig. 2

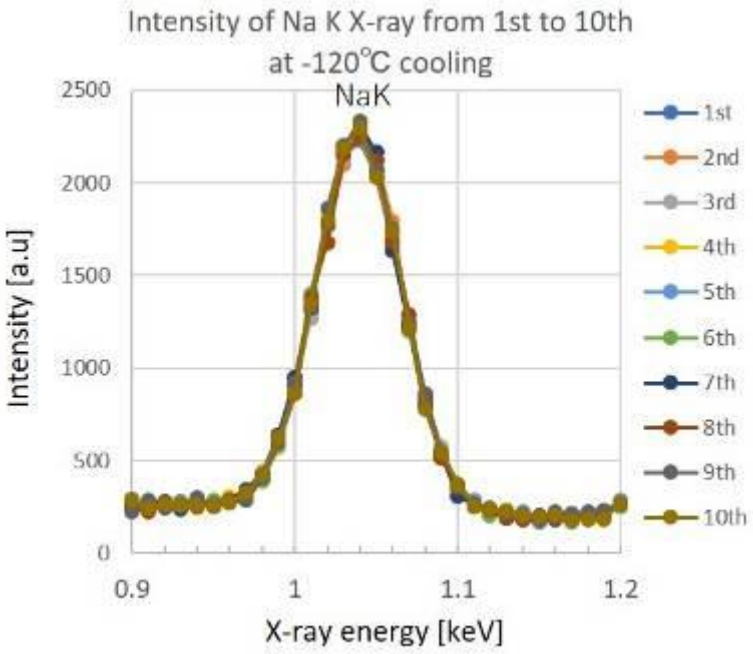
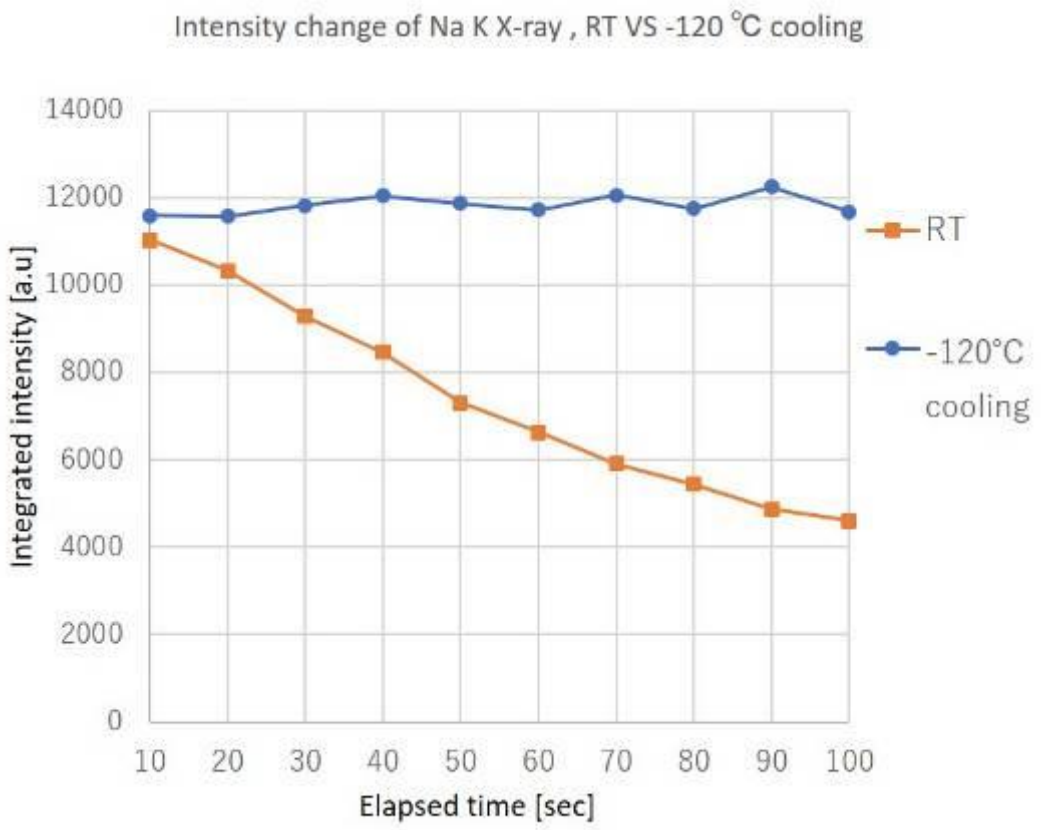

Intensity of Na K X-ray from 1st to 10th
at -120°C cooling
NaK
Intensity [a.u]
2500
2000
1500
1000
500
0
0.9
1
1.1
1.2
X-ray energy [keV]
1st
2nd
3rd
4th
5th
6th
7th
8th
9th
10th

Fig. 3


Intensity change of Na K X-ray , RT VS -120 ℃ cooling
Integrated intensity [a.u]
14000
12000
10000
8000
6000
4000
2000
0
10
20
30
40
50
60
70
80
90
100
Elapsed time [sec]
RT
-120°C cooling

IM2.P09
Cathodoluminescence excitation spectroscopy and the quest of suppressing transition radiation

A. Freilinger[1], Y. Auad[1], J. D. Blazit[1], X. Li[1], F. Castioni[1], M. Kociak[1], L. Tizei[1]

[1]Université Paris-Saclay, Laboratoire de Physique des Solides, Orsay, France

Introduction:

Cathodoluminescence excitation spectroscopy (CLE) in Scanning Transmission Electron Microscopy (STEM) is a technique that correlates electron excitation with subsequent photon emission events. These are measured via electron energy loss spectroscopy (EELS) and cathodoluminescence spectroscopy (CL) respectively and correlated via nano-second resolved coincidence detection using a Timepix3 detector for electrons and PMTs for CL. This aetup, currently installed on our Nion Hermes STEM, allows for the tracking of which excitation energy leads to a photon emission, crucial for dealing with the broadband nature of the electron-matter interaction. [3] We currently investigate single point defect emitters in nanomaterials like hexagonal Boron Nitride (hBN) and diamond nanoparticles.

Objectives:

CLE"s high sensitivity also picks up transition radiation (TR), which occurs in an energy range overlapping with in-gap excitations we aim to measure [2]. Filtering of TR can be temporal, spectral and spatial. We are currently working on a spatial approach, and plan to explore temporal filtering in the future. The emission angular distribution varies between TR and different excitations [4], allowing potentially not only to filter out TR background, but also to distinguish angular emission distributions of different signals. Complexity is added to the problem by the parabolic mirror used for CL light collection distorting the angular distribution [4].

Methods:

We are developing an optical system to be integrated in the CL light collection path. By imaging the Fourier plane of the parabolic mirror containing the emission angular distribution [4] and selectively placing a pinhole it will allow to select specific emission angles. In order to visualize the expected emission angular distributions, find optimal pinhole placements, and estimate possible gains in signal-to-background-ratios, we developed python code simulating the imaging of different excitations or their superpositions in an optical system with a parabolic mirror as in [4].

Results:

The code is implemented for diverse excitations and TR and their combinations. Work is ongoing on simulating TR emission patterns from electron incidence at an angle to the sample. The practical implementation of the optical system at our microscope is ongoing. By "blindly" placing a pinhole based on emission peaks optimization, we achieved a signal-to-background ratio enhancement of 2. Remaining challenges are that the parabolic mirror compresses a big part of the angular emission range into a relatively small portion of the resulting image, and so far rather poor image quality.

Conclusion:

Preliminary results inspire hope for the feasibility of using angular filtering to distinguish between TR and various other signals in CLE, possibly opening a path to the observation of in-gap excitations in CLE. However, simulations and initial tests highlight further technical challenges.

[1] N Varkentina et al, Science Advances 8 (2022) eabq4947

[2] R Bourellier et al, Nano Letters 16 (2016) p. 4317-4321

[3] Y Auad et al, Ultramicroscopy 239 (2022), 113539

[4] T Coenen, PhD thesis (2014)

Figure a) electron-photon coincidence detection for CLE.

Figure b) EELS spectrum and CLE spectrum of hBN, the latter showing TR. Reproduced from [1].

Figure c) Simulations of angular emission distributions of a Lambertian emitter and TR (left), and their transformation by our parabolic mirror (right).

Fig. 1

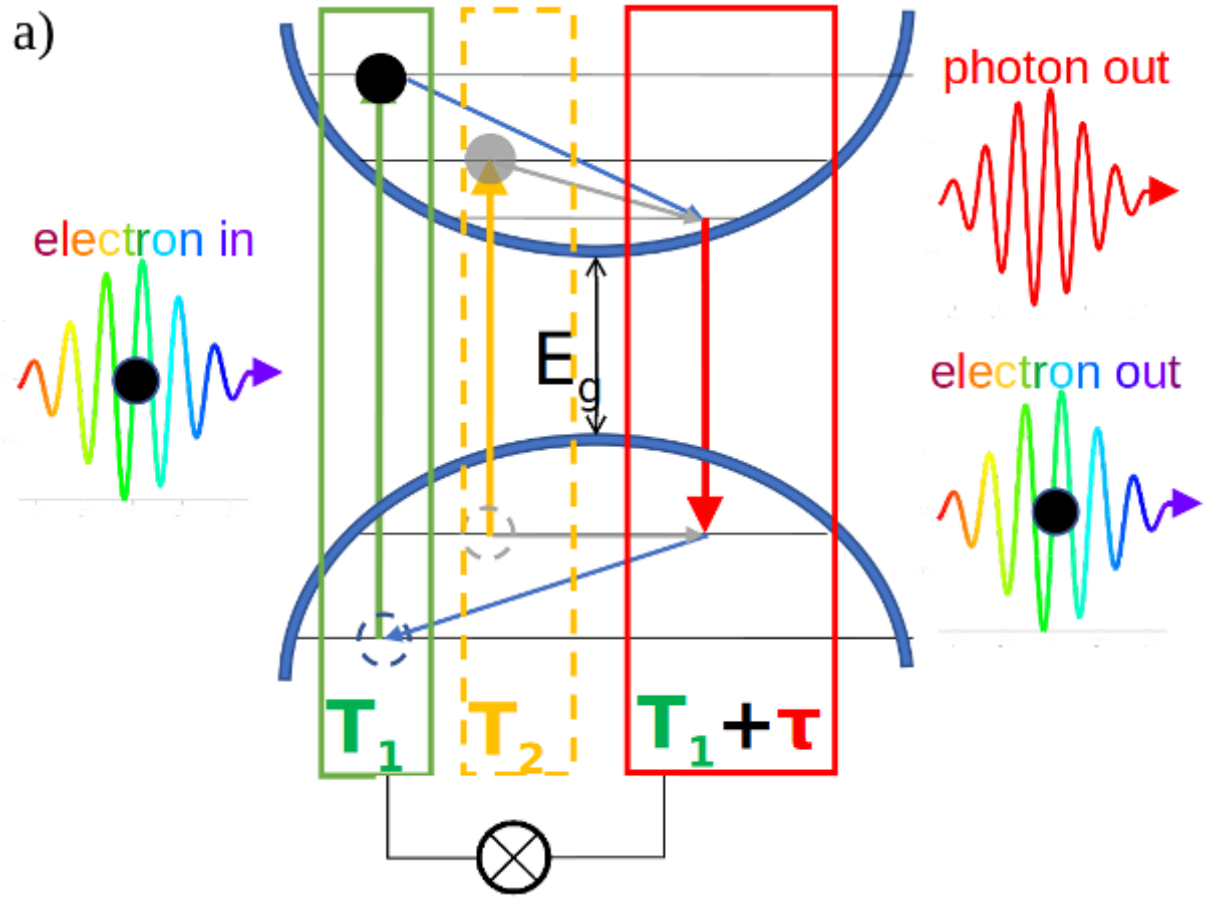


Fig. 2

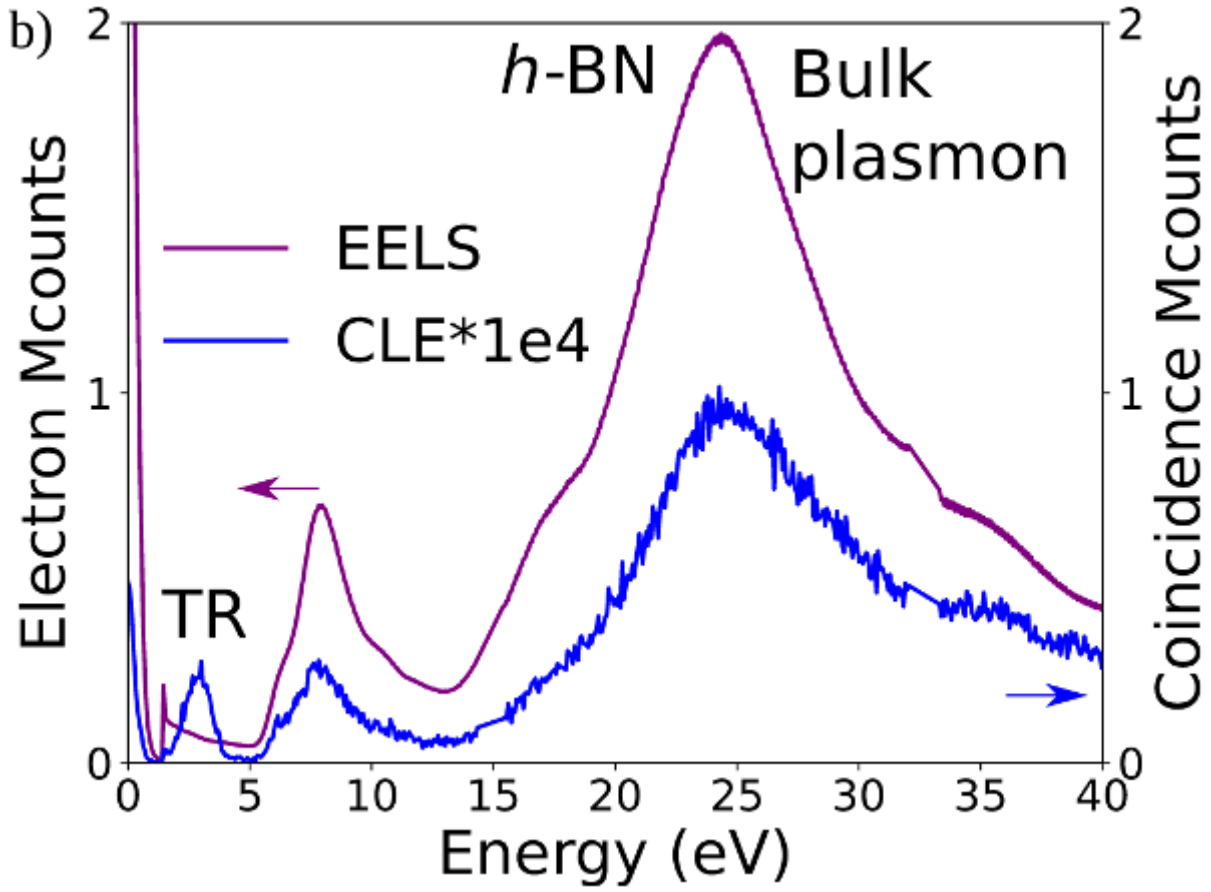
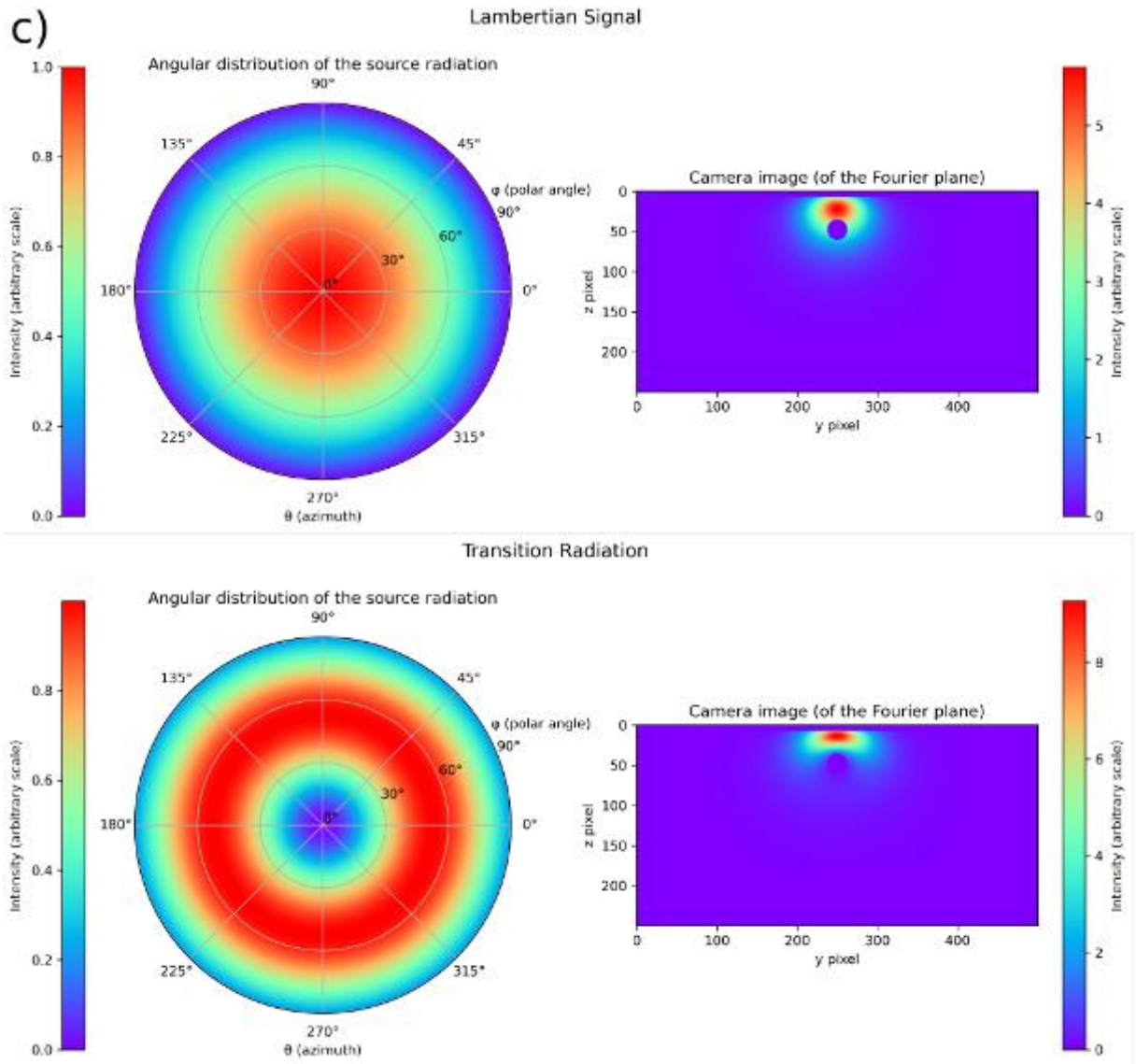

b)
h-BN
Bulk
plasmon
EELS
CLE*1e4
TR
Electron Mcounts
Coincidence Mcounts
Energy (eV)
0
1
2
0
5
10
15
20
25
30
35
40

Fig. 3


c)
Lambertian Signal
Angular distribution of the source radiation
Intensity (arbitrary scale)
φ (polar angle)
θ (azimuth)
Camera image (of the Fourier plane)
z pixel
y pixel
Transition Radiation
Angular distribution of the source radiation
Intensity (arbitrary scale)
φ (polar angle)
θ (azimuth)
Camera image (of the Fourier plane)
z pixel
y pixel

IM2.P10
Ferrimagnetic moment arrangement in the Ti-doped Barium hexaferrite revealed by EMCD

H. Makino[1], D. Singh Negi[2], J. Rusz[3], B. Rellinghaus[1], D. Pohl[1]

[1]DCN, TU Dresden, Physics, Dresden, Germany
[2]Indian Institute of Technology Jodhpur, Physic, Jodhpur, India
[3]Uppsala University, Physics and Astronomy, Uppsala, Sweden

Introduction

Barium hexaferrite ($BaFe_{12}O_{19}$) is one of the widely used ferri-magnets due to its great magnetic property such as high coercivity and high erosion resistance. However, there is still room to improve the temperature dependence of magnetic saturation. In such a circumstance, it has been discovered that high valence substitutional doping such as Ti^{4+} or Sb^{5+} can improve the Curie temperature [1,2]. It is important to understand the effect of oxidation state change by doping on the magnetic structure. Therefore, we decided to study this material from the point of view of transmission electron microscopy (TEM). Electron magnetic chiral dichroism (EMCD) is a TEM counterpart of X-ray magnetic circular dichroism proposed in 2003 and experimentally observed in 2006 [3,4]. This site-specific and oxidation-specific measurement method can elucidate the detailed mechanism on how the oxidation state change influence to the magnetic properties.

Objectives

In our study, barium hexaferrite samples with different Ti concentration are investigated by TEM. It is known that Fe^{3+} substitution with Ti^{4+} causes the oxidation state of the nearest neighbor Fe^{3+} to change to Fe^{2+}. Since these cations have chemical shifts on the Fe-$L_{2,3}$ spectrum, we can measure the magnetic structure change independently. Our goals are to experimentally determine the Fe magnetic moment arrangement of each site and oxidation state for each Ti concentration and to investigate the error behavior of the quantitative analysis.

Materials & methods

We prepared three single crystal barium hexaferrite lamellae with different Ti concentration ($BaFe_{12-\delta}Ti_{\delta}O_{19}$, δ=0, 0.6, 1) by focused ion beam. For later quantitative analysis, the EMCD signal must be of high quality. Therefore, we acquired a total of 8000 EEL spectra with an exposure time of 0.75 s using a parallel beam probe with a diameter of 200 nm to reduce beam damage during acquisition. After extracting the EMCD signal from the experimental data, the composition rate of Fe^{3+} and Fe^{2+} magnetic moment is calculated by applying a least square fit.

Results

The resulting EMCD signals and fitted reference spectra are shown in the figure. It can be seen, that with an increasing Ti-concentration, the absolute ratio of the Fe^{2+} EMCD signal is as well increased. However, the sign of the Fe^{2+} signal, corresponding to the magnetic moment orientation, is flipped in the δ=1.0 sample compared to the δ=0.6 sample. This suggests that the magnetic structure changes induced by the high Ti-doping. In addition, the fitting error behaviors such as random, systematic and energy shift error are thoroughly analyzed through a series of error investigations.

Conclusion

In this study, Fe magnetic moment arrangement changes in barium hexaferrite induced by Ti-doping are revealed using EMCD with a detailed error analyzes. Details of the atomistic moment rearrangement are under investigation.

Reference

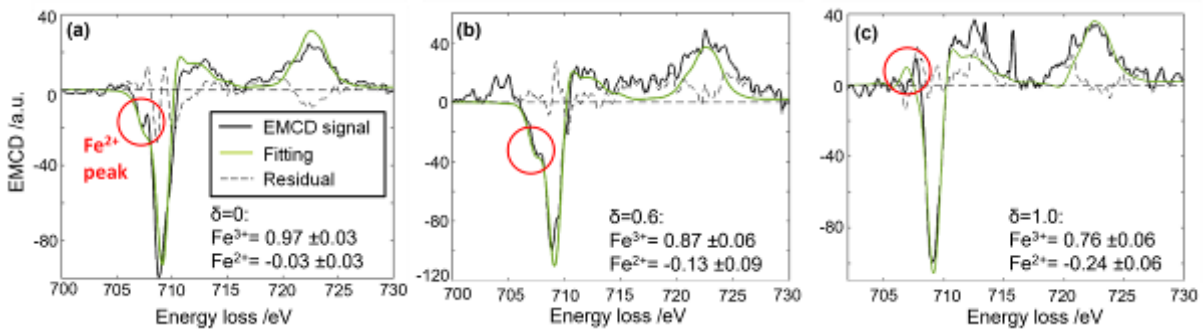
[1] V.A.M. Brabers, *et. al*, J. Magn. Magn. Mater. 196–197 (1999) 312–314.

[2] F.K. Lotgering, J. Phys. Chem. Solids 35 (1974) 1633–1639.

[3] C. Hébert, P. Schattschneider, Ultramicroscopy 96 (2003) 463–468.

[4] P. Schattschneider, *et.al*, Nature 441 (2006) 486–488.

Fig. 1



IM2.P11
Nanoscale spectroscopy on twisted bilayer 2D Moiré heterostructures

H. Zheng[1,2], X. Zhang[1,2], R. Jagadesh[1,2], H. Su[1,2], M. Bosman[1,2]

[1]National University of Singapore, Materials Science and Engineering, Singapore, Singapore
[2]Agency for Science Technology and Research, Institute of Materials Research and Engineering, Singapore, Singapore

Van der Waals heterostructures consist of vertically stacked two-dimensional (2D) materials bound by weak van der Waals forces. Introducing a small twist angle between layers creates a moiré superlattice, where atomic alignment or misalignment forms regular periodic patterns. This phenomenon can lead to unique electronic behavior, such as correlated insulating states [1], superconductivity [2], and ferromagnetism [3], particularly at specific "magic angles". In twisted bilayer graphene, for example, a "magic angle" of approximately 1.08° induces flat energy bands near the Fermi level, resulting in strong electron-electron correlations and correlated insulating states [2]. Besides graphene, transition metal dichalcogenides (TMDs) are another important type of 2D materials that are widely investigated for their applicability in microelectronics. In 2D TMDs, a transition metal layer (e.g., Mo or W) is sandwiched between two chalcogenide layers (e.g., S or Se). These atomically-thin layers exhibit unique properties, such as band structure tunability via dopant-vacancy complexes [4].

In this work, we demonstrate the use of electron energy-loss spectroscopy (EELS) to measure local band structure variations. Core-loss spectroscopy, as well as monochromated low-loss EELS spectroscopy on graphene and TMD twisted bilayers will be presented. With the help of electron ptychography, the alignment of the atoms between the top and bottom layer will be shown as a determining factor in the local variation of the low-loss EELS response.

References

[1] Scheurer Mathias S. et al. Spectroscopy of graphene with a magic twist. Nature 2019, 572 (7767), 40-41.

[2] Yuan Cao et al. Correlated Insulator Behavior at Half-Filling in Magic Angle Graphene Superlattices. Nature 2018, 556, 43.

[3] Aaron L. Sharpe et al. Emergent ferromagnetism near three-quarters filling in twisted bilayer graphene. Science 2019, 365 (6453), 605-608.

[4] Taposhree Dutta et al. Electronic properties of 2D materials and their junctions. Nano Materials Science 2024, 6 (1), 1-23.

Acknowledgements

The authors kindly acknowledge support from the Singapore Ministry of Education via the Academic Research Fund (project number MOE-T2EP50122-0016) and Singapore Land Women in Design and Engineering Fund – CDE Travel Fellowship Award.

IM2.P12
Free electrons quantum optics in phase-space

T. Fraysse[1], A. Lubk[2,3], M. Kociak[4], H. Florent[1], L. Hugo[1]

[1]CEMES-CNRS, Toulouse, France
[2]Leibniz Institute for Solid State and Materials Research Dresden, Dresden, Germany
[3]Technical University Dresden, Institute of Solid State and Materials Physics, Dresden, Germany
[4]Université Paris-Saclay, Laboratoire de Physique des Solides, Orsay, France

Photon Induced Near-field Electron Microscopy (PINEM) denotes the modulations of free electrons by a sample – typically an optical cavity – pumped by a laser source. This effect has been theoretically predicted and experimentally demonstrated in an ultrafast transmission electron microscope (UTEM) more than a decade ago [1,2]. Following these seminal developments, PINEM has been used to reconstruct the temporal dynamics of nano-optical systems with an attosecond temporal resolution [3].

Due to recent experimental developments in integrated photonics [4,5], the problem of PINEM in the low occupation regime – i.e. when the cavity is populated by a weak number of photons - has drawn an increasing theoretical interest. Indeed, in this situation, the classical description of the electromagnetic field falls short to describe the electron-cavity interaction, and a full quantum description becomes required. Several works have already pioneered this problem [6,7] and predicted strong quantum mechanical effects in PINEM. The goal of our work is to pursue this effort and provide an alternative and intuitive approach to this problem by using tools borrowed from the field of quantum optics.

The object of our study is thus the electron-cavity state before and after inelastic interaction. To accomplish this, the overall approach can be summarized in three points : first, we use common quantum optics states to describe light ; second, scattering theory allows us to calculate and understand the electron-light interaction ; and third, we use the Wigner function - roughly speaking, a probability distribution of the quantum state in the phase space (energy-time) - as a powerful visualization tool, as shown in figure 1.

In a first part, we will illustrate the influence of the quantum optical state of the cavity on the energetic and temporal structure of the electron beam during the PINEM interaction, and how we can visualize it with the Wigner function.

In a second part, we will show that a PINEM measurement in this regime is deeply connected to the standard quantum limit of the temporal resolution in a UTEM. Indeed, the Heisenberg uncertainty principle governs the inelastic interaction between the electron and the cavity, making impossible to know precisely the number of photons in the cavity, and the temporal dynamics at the same time.

In a third part, we will go deeper in the topic of the entanglement. More specifically, we will investigate in which circumstances the interaction would lead to entanglement, and its consequences on the electron"s dynamics. Again, employing the Wigner function will allow us to visualize the entanglement by treating the electron and electromagnetic field as a single object.

Figure 1. Electronic Wigner function after interaction with (a) a classical electromagnetic field and (b) a quantized electromagnetic field. The Wigner function (central panel) provides a direct visualization of the energy distribution (right panel) and the temporal modulation (top panel) of the electron.

[1] B. Barwick *et al.*, Nature 462, 902-906 (2006)

[2] A. Feist *et al.*, Nature 521, 200–203 (2015)

[3] J. H. Gaida *et al.*, Nature Photonics 18, 509–515 (2024)

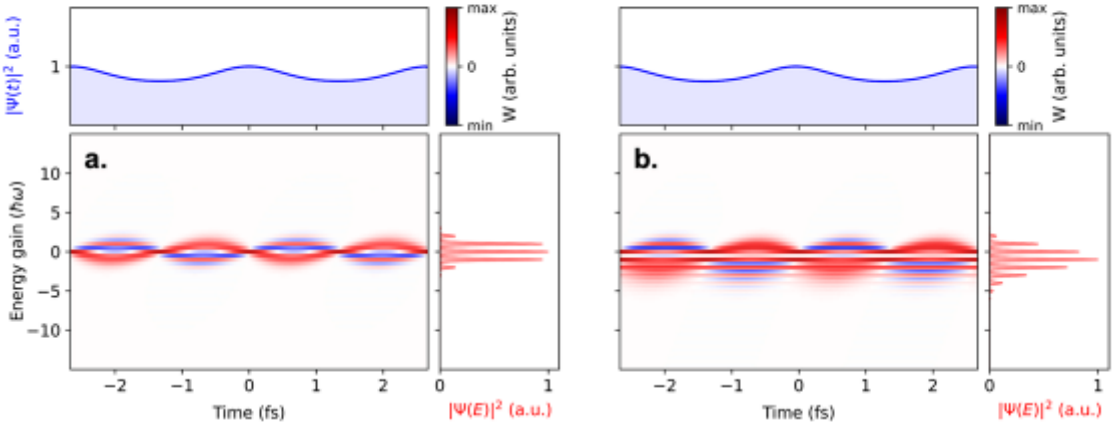
[4] J-W. Henke *et al.*, Nature 600, 653-658 (2021)

[5] A. Feist *et al.*, Science 377, 777-780 (2022)

[6] O. Kfir, Physical Review Letters 123, 103602 (2019)

[7] V. Di Giulio *et al.*, Optica 6 (12), 1524-1534 (2019)

Fig. 1



IM2.P13
Advancing high-resolution electron microscopy and spectroscopy – Integrating the CEOS rnergy-filtering and imaging device into the monochromated JEOL atomic-resolution multi-dimensional TEM at the Max Planck Institute for solid state research

T. Heil[1], H. Müller[2], S. Uhlemann[2], K. Elibol[1], P. Kükelhan[2], M. Linck[2], H. Wang[1], A. Nakamura[3], M. Mukai[3], P. A. van Aken[1]

[1]Max Planck Institute for Solid State Research, Stuttgart Center for Electron Microscopy, Stuttgart, Germany
[2]CEOS GmbH, Heidelberg, Germany
[3]JEOL Ltd., Tokyo, Japan

We present initial results from integrating the CEOS Energy-Filtering and Imaging Device (CEFID) with the monochromated JEOL Atomic-Resolution Multi-Dimensional Transmission Electron Microscope (ARMD-TEM) at the Max Planck Institute for Solid State Research. This state-of-the-art system enables unprecedented insights into materials" electronic and vibrational structures, achieving sub-Ångström spatial and meV energy resolution.

The CEFID, a post-column energy filter with outstanding energy-filtering capabilities, enhances ARMD-TEM"s analytical potential. Its minimal non-isochromaticity, large field of view, and exceptional long-term stability (<0.5 eV drift over 10 hours) ensure highly reliable data acquisition, advancing condensed matter physics and materials science [1,2].

The JEOL ARMD-TEM operates at 60 or 200 kV with a wide-gap objective lens pole piece, supporting in-situ and tomography studies. It integrates a Cs-probe corrector, bright-field/annular dark-field detectors, and an 8-segmented annular all-field (SAAF) detector, enabling sub-Ångström spatial resolution in scanning transmission electron microscopy (STEM) [3]. An advanced data acquisition system, including a Quantum Detectors MerlinEM direct electron detector, pre-/post-filter TVIPS XF416R CMOS cameras, and a post-filter Dectris ELA hybrid-pixel detector, facilitates sophisticated 4D STEM and electron energy-loss spectroscopy (EELS).

A key feature is the integrated double octopole-type Wien filter monochromator (MC), optimizing the trade-off between spatial and energy resolution [4]. Combined with CEFID, it enables high-resolution EELS with exceptional spectral precision. The current Schottky source achieves energy resolution below 30 meV, with 16 meV attainable under optimized conditions. A planned cold-field emission gun aims for sub-10 meV resolution, approaching 5 meV, significantly expanding low-energy excitation studies.

The synergy of ARMD-TEM and CEFID, supplemented by a dual energy-dispersive X-ray detector, allows comprehensive chemical and electronic structure mapping at unparalleled spatial and energy resolution. Additionally, a condenZero-developed liquid helium side-entry holder maintains temperatures below 10 K with ±2 mK stability, enabling extended cryo-TEM experiments exceeding 24 hours.

This integrated system enables localized, temperature-dependent studies of vibrational spectra and electronic states near the Fermi level, including magnons, multi-phonon excitations, and topological gap characterization. The sub-10 meV resolution provides direct access to phonons, charge-density waves, far-infrared surface plasmons, and potentially spin waves with unprecedented spatial precision.

Beyond conventional STEM-EELS, the post-filter Dectris ELA detector facilitates energy-filtered 4D STEM techniques such as center-of-mass analysis, parallax imaging, and electron ptychography, extending the frontiers of quantum materials and nanostructure research.

This presentation will highlight the MC-CEFID system"s performance and selected applications demonstrating its transformative capabilities [5].

References:

[1] Kahl F *et al.* Adv. Imaging Electron Phys. (2019) 212, 35-70.

[2] Caridad A R *et al.* Micron (2022) 160, 103331.

[3] Sagawa R *et al.* Ultramicroscopy (2022) 233, 113440.

[4] Mukai M *et al.* Ultramicroscopy (2014) 140, 37-43.

[5] PAvA acknowledges financial support from the Max Planck Society for funding the ARMD-TEM.

IM2.P14
Instrumental optimisation for high-loss STEM-EELS

G. Guzzinati[1], M. Watanabe[2,3], P. Kükelhan[1], M. Mukai[4], H. Sawada[2,3], V. Gerheim[1], M. Linck[1], H. Müller[1]

[1]CEOS GmbH, Heidelberg, Germany
[2]Lehigh University, Department of Materials Science and Engineering, Bethlehem, PA, United States
[3]Tohoku University, Institute for Materials Research, Sendai, Japan
[4]JEOL Ltd., Akishima, Japan

The recent years have seen a considerable development in the instrumentation available for electron energy loss spectroscopy (EELS). The availability of spectrometers and monochromators with improved performance and stability, as well as faster and more sensitive detectors and cameras, has unlocked a variety of new experimental possibilities.

One such example, is the possibility to greatly extend the field of application of *extended electron energy loss fine structure* (EXELFS). EXELFS, the electron counterpart of the extended X-ray absorption fine structure (EXAFS) routinely acquired at synchrotrons, allows to obtain chemically sensitive local structural information, even in amorphous samples. The ability to acquire this information with the angstrom resolutions available at TEMs, makes this an ideal method to study coordination chemistry [1]. In many cases however, its use was hampered by the experimental difficulty in acquiring spectra at the large energy losses of the edges of interest.

Here we show how current generation instrumentation, combined with the appropriate experimental design, can be used to reliably acquire edges with much larger onset energies than is currently common. First, the projective optics of the microscope have to be realigned, paying particular attention to the intermediate lens focus [2]. This is needed to ensure that the electrons in the energy range of interest can uniformly reach the spectrometer despite the large difference in energy. The spectrometer is also adapted. An energy selective beam-blocker is placed in the beam path to catch the intense ZLP and prevent the appearance of artifacts on the liner tube, and the multipole optics are set to a special large-range mode [3].

Despite the optimisations, the EELS signal at high losses remains weak, but can be reliably collected using a highly sensitive and robust hybrid-pixel detector.

Example data is also shown, including both spectra and maps acquired using a combination of a JEOL NEOARM microscope, a CEOS CEFID spectrometer [4], and Dectris ELA detector. In particular, we show that we can map the Ge K edge (11.1 KeV) with nanometer resolution, in a commercial Mag-I-Cal sample with SiGe layers.

Figure 1: Map (b) and spectra (c) from the Ge K edge in a commercial Mag*I*Cal sample (a). The spectra are obtained by integrating the signal collected over one Si or SiGe layer within the mapped area. The SiGe layers contain 19% Ge and 81% Si.

References:

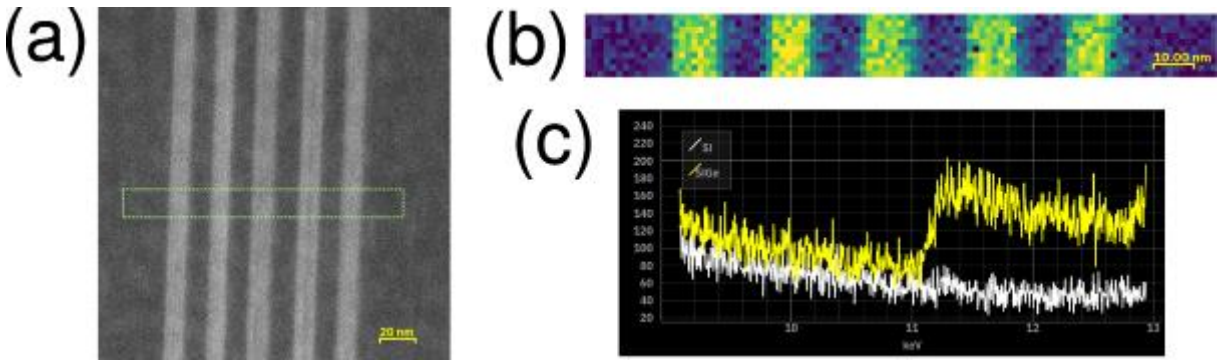
[1] R. F. Egerton, Electron Energy-Loss Spectroscopy in the Electron Microscope (Springer US, Boston, MA, 2011).

[2] A.J. Craven, et al, Ultramicrosc., 180, 66–80, (2017).

[3] M. Watanabe et. al, M&M, Volume 30, Supplement_1, ozae044.685 (2024)

[4] F. Kahl, et al, in Advances in Imaging and Electron Physics Including Proceedings CPO-10, Academic Press, pp. 35-71, (2019).

Fig. 1



IM2.P15
Vibrational dispersion of amorphous carbon from electron energy-loss spectroscopy

B. Haas[1], C. T. Koch[1], P. Rez[2]

[1]Humboldt University of Berlin, Institute of Physics & CSMB, Berlin, Germany
[2]Arizona State University, Department of Physics, Tempe, AZ, United States

Introduction

Despite their lack of long-range ordering, amorphous materials can have phonon-like dispersions. However, studies of the vibrational properties of amorphous materials are either purely computational [1] or measurements of just the density of states [2] (via neutron or X-ray scattering), not of the full dispersion (momentum-energy plots).

Nowadays, vibrations in amorphous materials are typically classified using the Allen-Feldman model as three different quasiparticles [3]. Propagons are similar to phonons in crystals and exist at rather low energies (typically a few meV). Diffusons exist at higher energies and have less-defined wave vectors. Locons are strongly localized in real space. As experiments with neutrons and X-rays are difficult, little is experimentally known about the vibrational dispersion of amorphous materials.

Objectives

To learn more about the vibronic quasiparticles in amorphous materials, momentum-resolved electron energy-loss spectroscopy (EELS) is applied to an amorphous carbon (a-C) film to study its dispersion.

Materials & methods

A Nion HERMES microscope equipped with the IRIS spectrometer and a Dectris ELA detector (operated at 60 kV) was utilized to investigate an a-C film from a lacey carbon covered copper grid (S166 from Plano GmbH, Wetzlar, Germany). A convergence semi-angle of 1 mrad was used together with a beam current of 3.5 pA (after monochromation). A slot-shaped aperture was placed in the entrance of the spectrometer to select a narrow momentum region across the direct beam. 300 dispersions of 2 s exposure time each were acquired and registered to account for slow drift. The zero-loss line of the integrated dispersion was digitally straightened.

Results

Fig. 1 a shows the vibrational dispersion of a-C and a diffraction pattern from the same sample position, which is indicated in the HAADF image in Fig. 1 b. The dispersion shows branches, whose peak around 200 meV (matching C-C vibration energies) coincides in momentum with the first C ring (2.1 Å) and terminating at the position of the second ring (1.2 Å). These branches are quite diffuse – and thus much harder to detect than for diamond [4] – and not limited by the energy resolution of about 10 meV or the momentum resolution. Given the low energy of propagons and the limited resolution of EELS so far, the visible branches should correspond to diffusons with the background intensity stemming mainly from locons.

The core-loss EELS data in Fig. 1 c shows that a significant amount of sp2 hybridization exists in the amorphous C, which we will use to realistically model the structure for validation of our results.

Conclusion

We have demonstrated the first momentum-resolved EELS of vibrations in an amorphous material. This approach opens new avenues to explore the roles of locons, diffusons and propagons.

Fig. 1. a Vibrational dispersion in juxtaposition with a diffraction pattern from the same region. **b** Overview image (HAADF) of the sample region. **c** Fine-structure of the Carbon K-edge in EELS from the same area.

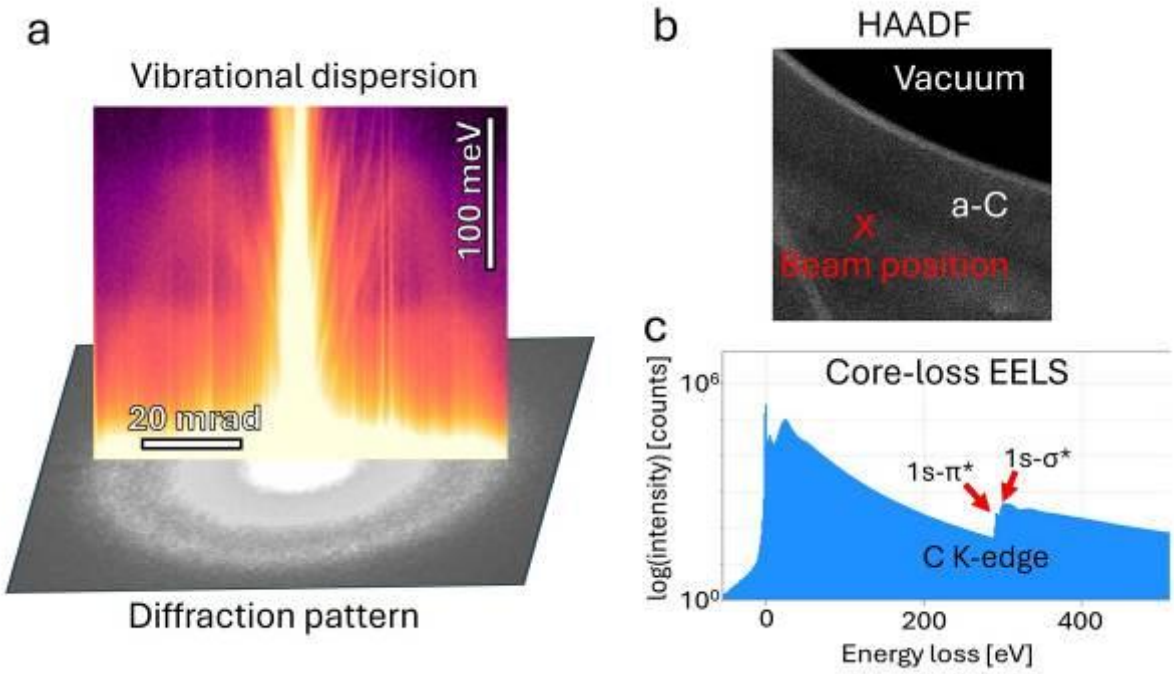
[1] Zhang Z *et al. npj Comput. Mater.* (2022), **8**, 96. https://doi.org/10.1038/s41524-022-00776-w

[2] Sette F *et al. Science* (1998), **280**, 1550-1555. https://doi.org/10.1126/science.280.5369.1550

[3] Allen PB *et al. Phil. Mag. B* (1999), **79**, 1715-1731. https://doi.org/10.1080/13642819908223054

[4] Haas B *et al. Microscopy Microanalysis* (2023), **29**, 356–357. https://doi.org/10.1093/micmic/ozad067.166

Fig. 1



IM2.P16
Nonlocal substrate effect on plasmon resonance of a supported silver nanoparticle

K. Oldenburg[1], K. H. Meiwes-Broer[1], I. Barke[1]

[1]University of Rostock, ELMI-MV, Department "Life, Light and Matter", and Institute of Physics, Rostock, Germany

Plasmonic excitations in metal nanoparticles and clusters are highly sensitive to subtle changes in their dielectric environment, forming the basis of numerous sensor applications. For supported nanostructures, substrates induce anisotropic effects on plasmon resonances, leading to mode splitting and inhomogeneous energy shifts.

Using electron energy loss spectroscopy (EELS) in a scanning transmission electron microscope (STEM), we investigate substrate effects on individual 11 nm silver nanoparticles deposited from the gas phase onto the narrow rim of a carbon substrate ("cliffhanger"), providing a cross-sectional view. The substrate's influence on the particle plasmon (Localized Surface Plasmon Resonance, LSPR) is generally considered local, weakening with distance [1]. However, contrary to this expectation, we find that the energy shift induced by the carbon substrate is strongest when the plasmon is excited farthest from the support.

This nonlocal substrate effect arises from the system's simplicity and size, as corroborated by boundary element method (BEM) simulations. BEM further enables the extraction of the full plasmon mode structure from experimental data. Spectral decomposition of the experimental maps based on BEM-derived results reveals the complete mode structure, emphasizing anisotropic environmental effects. These insights suggest that longstanding discrepancies in plasmon energy measurements for small spherical nanoparticles may stem from previously overlooked spectral effects of anisotropic environments [2].

[1] S. Mazzucco, et al., Nano Letters 12, 1288 (2012).

[2] H. Haberland, Nature (2013), 494 E1-E2

IM2.P17
Exploring different acquisition schemes for dual range EELS

P. Kükelhan[1], P. Stiegler[1], D. Lörks[1], G. Guzzinati[1], M. Linck[1], H. Müller[1]

[1]CEOS GmbH, Heidelberg, Germany

Dual range EELS has proven as a useful tool in analytical STEM [1, 2]. The basic idea is to acquire two EEL spectra per scan position with an energy shift in-between the spectra. To achieve this, careful synchronization of all involved hardware is necessary. The minimum hardware set requires a scan generator to control the position of the electron beam, a camera to acquire both spectra, and suitable electronics to enable the fast energy shift in-between the spectra. With a post-column spectrometer, this energy shift is typically realized by applying a bias voltage to the liner tube inside the magnetic prism. An additional optical element for fast re-focusing of the spectra can help to maintain optimal energy resolution for both spectra. Additionally, a fast blanker and a fast deflector can offer specific benefits depending on the acquisition scheme [1, 2, 3, 4].

Here, we consider two different acquisition schemes: both spectra can be acquired in the same camera image (single exposure) or both spectra can be acquired in separate camera images (dual exposure).

In acquisition schemes based on a single exposure (Figure 1a), the camera acquires one image during the dwell time of the scan generator. The energy-shift is performed during the exposure time of the camera. To avoid overlap of both spectra and to allow using the complete width of the camera, a fast deflector can shift one spectrum (or both) in non-dispersive direction [1]. A fast blanker can be used to avoid artifacts from the energy-shift by blanking the beam during the time it takes for the shift [2].

In acquisition schemes based on a dual exposure (Figure 1b), the camera acquires two images during the dwell time of the scan generator. Typically, these images have different exposure times with a shorter exposure time for the low loss spectrum and a longer exposure time for the core loss spectrum. Here, the fast deflector becomes obsolete by acquiring separate images for both spectra. Artifacts from the electrostatic energy-shift can be avoided by excluding the energy-shift latency from the acquisition of both spectra so that no fast blanker is necessary at all. The image acquisition scheme could easily be adapted to multi-range acquisition.

To enable the dual exposure acquisition scheme, the camera has to support externally triggered image acquisition (slave mode) which can be initiated (mastered) by either the scan generator or a dedicated synchronization device which we call "binary router". The solution that we present enables flexible synchronization between a wide range of cameras, scan generators and blanking signals for both acquisition schemes.

We demonstrate both acquisition schemes for dual range EELS with a CEOS Energy Filtering and Imaging Device (CEFID), binary router and different cameras and scan generators. The acquisition workflows are adapted according to the capabilities of different hardware combinations.

1. Tencé, M. et al. In Proc. IMC 16 Sapporo, Japan (2006) 824-825

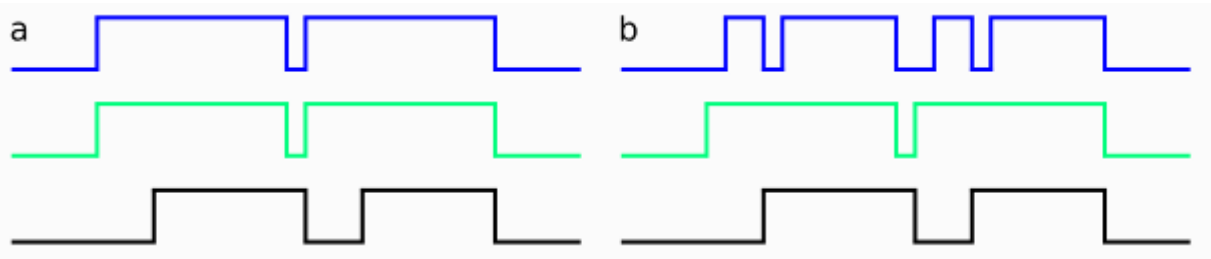
2. Scott, J. et al. Ultramicroscopy 108 (2008) 1586-1594

3.Tiemeijer, P. et al. In Proc. EMC 17 Copenhagen, Denmark (2024) 05015

4. Müller, H. et al, "Methods for Dynamic Re-Focussing of an Electron Energy-Loss Spectrum", this conference.

Figure 1: Schematic visualization of single and dual exposure acquisition schemes for dual range EELS. All devices are active when the signal is high.

Fig. 1



IM2.P18
Simulating momentum-resolved EELS STEM of Phonons in rutile TiO_2

M. Osmera[1], J. Alves Do Nascimento[2,3], S. Wang[4,5], J. Fawcett-Houghton[3], K. McKenna[3], P. Zeiger[1], Q. Ramasse[4,5,6], D. Kepaptsoglou[2,3,4], J. Rusz[1]

[1]Uppsala University, Physics and Astronomy, Uppsala, Sweden
[2]University of York, JEOL NanoCentre, Helsington, United Kingdom
[3]University of York, School of Physics, Engineering and Technology, Helsington, United Kingdom
[4]SciTech Daresbury Campus, SuperSTEM Laboratory, Daresbury, United Kingdom
[5]University of Leeds, School of Chemical and Process Engineering, Leeds, United Kingdom
[6]University of Leeds, School of Physics and Astronomy, Leeds, United Kingdom

Introduction

In the last decade the advancements in monochromator and spectrometer design enabled energy resolution below 10 meV in electron energy-loss spectroscopy (EELS) experiments performed in scanning transmission electron microscopes (STEM) [1-4]. This facilitated the direct observation of phonons with subatomic spatial resolution in STEM [3,4].

The transition amplitude in the electron-on-single-phonon scattering is directly proportional to the dot product of momentum transfer and the polarization vector of the atom in the vicinity of the electron beam [5]. By shifting the detector aperture off-axis it is possible to focus on phonons with specific polarization, (i.e. vibrations in a certain direction) [6,7]. The observation of a signal corresponding to such vibration can be understood as a direct evidence for the validity of the phonon model.

Rutile is a tetragonal phase of TiO_2 with screw axis symmetry ($P4_2/mnm$). Ti-O bonds in the base (*a-b* plane) of the unit cell are oriented in the [110] direction, whereas the analogous Ti-O bonds in the unit cell midsection are perpendicular to them oriented in the direction [110]. The O atoms within the bases are bound by three bonds in plane (110), whereas the two O atoms in the midsection plane are bound by bonds within the plane (110). We show on this system that the two sets of oxygen atoms (corresponding atomic columns) can be clearly distinguished in STEM low-loss EELS experiments.

Objectives

In this work we will present low-energy STEM EELS simulations with off-axis detectors for rutile. We will compare our results to experiment and show the possibility of bond-directionality analysis in crystals.

Materials & methods

The STEM-EELS signal is simulated using frequency resolved frozen phonon multislice (FRFPMS) [8] and time-autocorrelation of auxiliary wavefunctions (TACAW) [9]. For the FRFPMS method we used phonons obtained from the diagonalization of the dynamical matrix from density functional theory (DFT) calculations. TACAW is calculated from molecular dynamics (MD)-computed using Orb machine-learned potentials [10].

Results

We will present simulations of STEM EELS signal obtained within the methodology of FRFPMS and TACAW and compare them to experimental data. We will interpret the results and discuss the validity of used methods.

Conclusions

We confirm that the phonon-EELS signal can be resolved in polarization vector-direction at atomic scale. We will also demonstrate that O atomic columnsin rutile can be distinguished based on the directionality of their bonds with Ti.

References

[1] O. L. Krivanek et al., Nature 514, 209 (2014).

[2] O. L. Krivanek et al., Ultramic. 203, 60 (2019).

[3] M. J. Lagos et al., Microscopy 71, i174 (2022).

[4] N. Dellby et al., Microsc. Microanal. 28(S1), 2640 (2022).

[5] A. V. Martin et al., Phys. Rev. B 80, (2009).

[6] X. Yan et al., arXiv:2312.01694v1 (2023).

[7] E. R. Hoglund et al., Adv. Mater. 36 (33), 2402925 (2024).

[8] P. M. Zeiger and J. Rusz, Phys. Rev. Lett. 124, 025501 (2020).

[9] J. A. Castellanos-Reyes et al., Phys. Rev. Lett. 134, 036402 (2025).

[10] M. Neumann et al., arXiv:2410.22570v1 (2024).

IM2.P19
Breaking through EDS limitations – A study on using WDS for silicon wafer contaminant detection

S. Mu[1], J. Rafaelsen[1], D. Stowe[1], M. Schleifer[2]

[1]Gatan Inc., Pleasanton, CA, United States
[2]Ametek GmbH, Frankfurt a.M., Germany

EDS is widely used in Si wafer contaminant detection. Common elements found in contaminant particles include Sr, Y, W, and Ta. In bulk samples, EDS typically can resolve or deconvolve them from the Si K. However, under typical wafer inspection conditions, the e-beam penetrates through contaminants, generating a small signal from the contaminants and a much stronger Si K (1.740 keV) signal from the wafer itself. When measured with EDS, the Si K peak exhibits a FWHM of 80 eV but FWTM approaching 200 eV when taking the Si Kβ contribution into account (Fig 1a). The broad FWTM Si peak obscures the contaminant peaks including Sr and Y L, and W and Ta M lines (1.806, 1.922, 1.774, and 1.709 keV, respectively). WDS offers superior energy resolution and a better peak-to-background ratio (P/B), enabling the separation of the Si Kα and (weak) W Mα peak from the contaminant-on-silicon sample (Fig 1a). In this study, we explore the best practices for identifying contaminants on the surface of Si wafers by WDS.

To simulate a contaminant-on-silicon sample, a 3 nm thick W film was deposited on a Si wafer. WDS point analysis was performed using an EDAX Lambda Plus WDS (Gatan Inc.) in a FE-SEM. Accelerating voltages from 3, 5, 10, and 15 kV were tested. The beam current was maintained at 5 nA, consistent with the range typically used for wafer inspection with EDS. Rapid identification of contaminants is critical, so WDS reduced scans were designed around the W Mα using 6 background and 9 signal channels. A linear background was calculated from two background positions, and net counts were determined (Fig 1b). Dwell times of 0.5, 1, and 5s/channel and a 1 eV/channel step size were tested to determine the minimum time needed for W to be detected with statistical certainty.

Simulations [1] showed that from 3 to 15 kV, the electron penetration depth increased from 150 nm to 2 µm into the Si wafer, with a significantly reduced number of electrons exciting x-rays from the W film (Fig 2). Experimental results confirmed that the W Mα P/B decreased as the kV increased at all dwell times (Fig 3). Moreover, variations in the P/B at a given kV diminished with higher counting statistics at the increased kV. The statistical significance of the W Mα peak was confirmed at 3, 5, and 10 kV for all dwell times, with the highest P/B of 3.0 achieved at 3 kV with a 1s dwell. At a 0.5s dwell, a P/B of 2.7 was still achieved, with the scan time reduced from 15 to 7.5s. At 15 kV, the W Mα peak was not statistically significant due to limited electron interaction with the W film and consequently low W x-ray generation.

We have shown that WDS can identify sub 10 nm contaminants that are difficult to separate by EDS. W can be detected with statistical significance from 3 to 10 kV in 7.5s at 5 nA, in line with EDS conditions typically used for Si wafer inspection. Thus, simultaneous EDS-WDS is an excellent solution for Si wafer inspection under challenging conditions.

Fig 1. a) EDS (outline) and WDS (solid) spectra overlay of 3 nm W film on a Si wafer using 5 kV. b) WDS reduced scan spectrum of W Mα using 1s dwell.

Fig 2. Monte Carlo Simulation of e-beam and 3 nm W film on a Si wafer interaction at 3, 5, 10, and 15 kV (left to right): top) electron trajectory, the vertical scale is 2.5 µm for all, bottom) energy deposition. [1]

Fig 3. W Mα P/B vs. kV.

Reference:

1. Casino: Monte Carlo Simulation of Electron Trajectory in Solids,
https://casino.espaceweb.usherbrooke.ca

Fig. 1

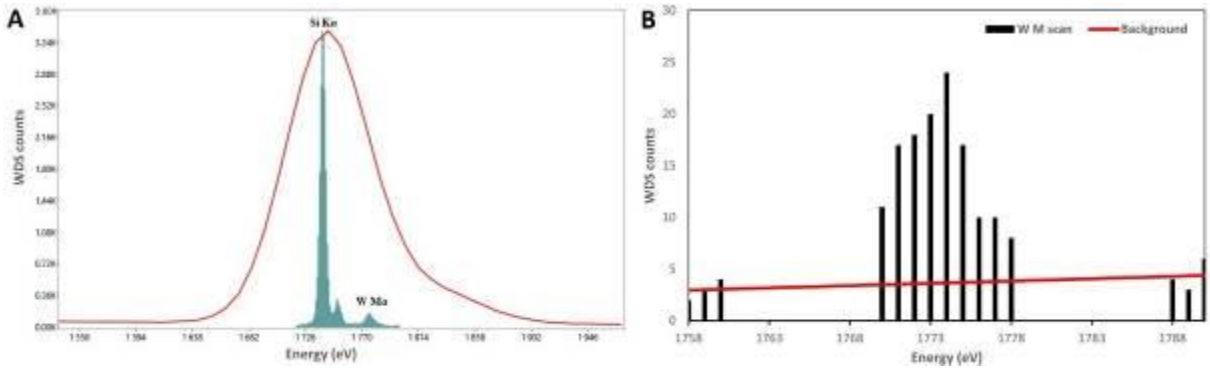


Fig. 2

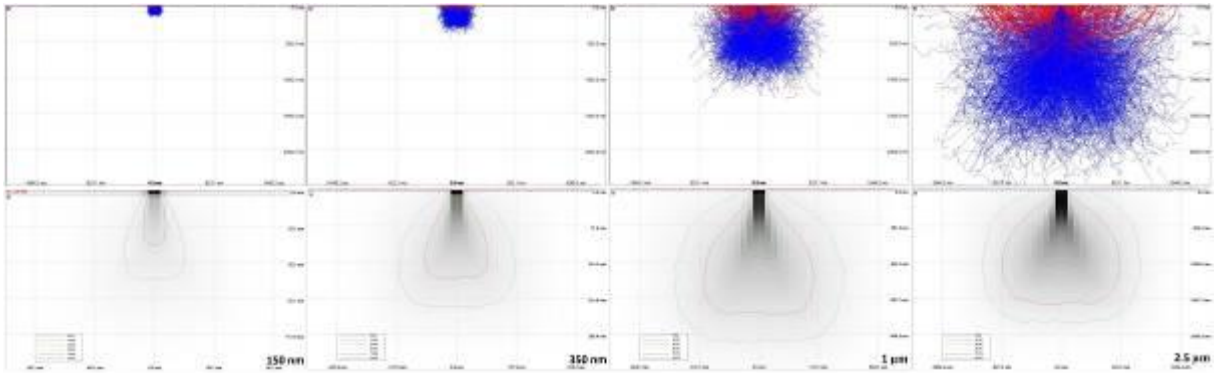
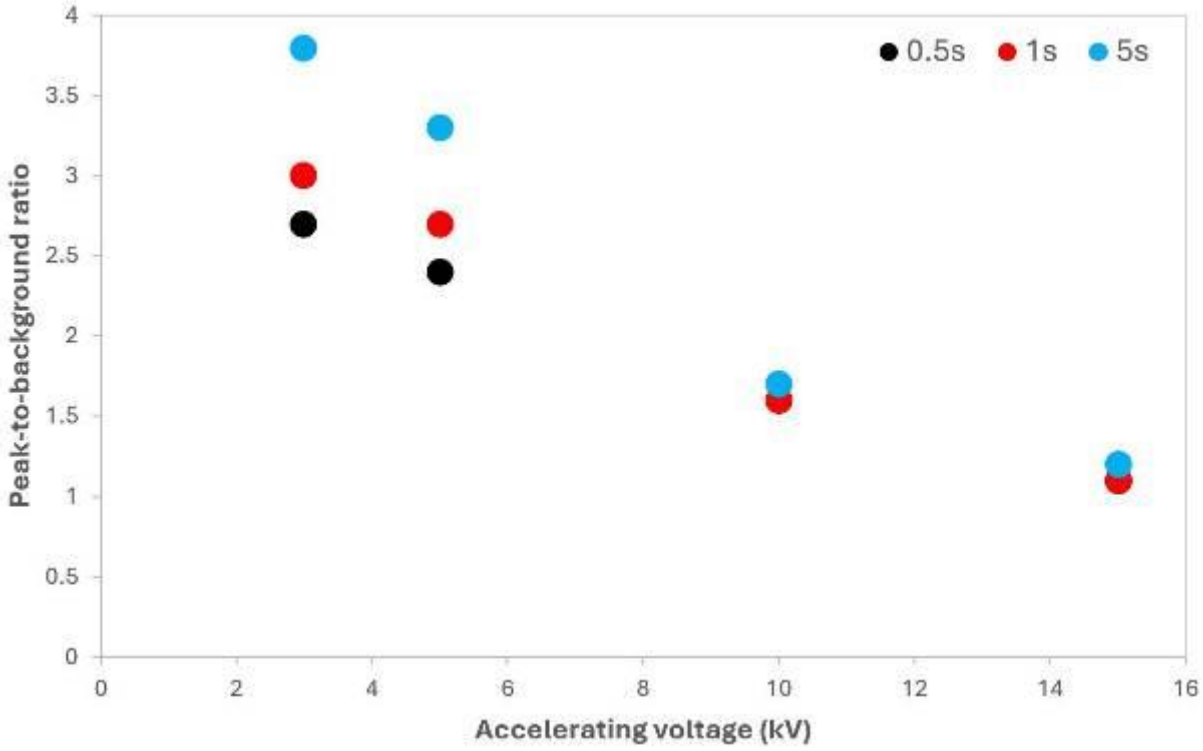


Fig. 3


0.5s
1s
5s
Peak-to-background ratio
Accelerating voltage (kV)
0
0.5
1
1.5
2
2.5
3
3.5
4
0
2
4
6
8
10
12
14
16

IM2.P20
In situ capabilities of X-ray microscopy for inspection and materials analysis

M. Kotrlý[1], J. Uher[2], J. Bohacova[2], J. Jakubek[3], I. Turková[1], P. Cejka[1]

[1]Institute of Criminalistics, Prague, Czech Republic
[2]Radalytica a.s., Prague, Czech Republic
[3]Advacam s.r.o., Prague, Czech Republic

The conduct of inspections, assessments, and forensic analyses of parts and components on-site is a common requirement when determining the causes of traffic or aviation incidents, industrial explosions, and a wide range of other forensic investigations. This includes imaging techniques, such as X-ray radiography and computed tomography (CT), as well as microanalytical methods like X-ray diffraction phase analysis/microanalysis (XRD/mXRD), microanalysis (EDS/XRF), and various other techniques. These procedures are employed across a broad spectrum of materials forensic analyses, material characterization, detection of internal defects, etc. Traditional methods often encounter challenges that may prevent the use of these techniques or allow only limited applicability, such as issues related to the size and accessibility of components, the need for disassembly, etc.

New robotic system enables the comprehensive characterisation and inspection of both 2D and 3D objects. The broad capabilities of X-ray imaging are complemented by X-ray fluorescence point analysis and mapping, multispectral imaging, and multispectral X-ray diffraction analysis. The standard configuration for X-ray imaging comprises two robotic stations. One robot carries an X-ray tube, and the other holds a photon-counting imaging, or any other detector. The system is capable of accurate geometrical calibrations that allow positioning of both robots precisely yet arbitrarily. Therefore, the robots can be moved to different locations during on-site inspections. Fig. 1 shows the system in a portable configuration.

The robotic arms are capable of movement in all directions within the X, Y, Z coordinate system, offering entirely new possibilities for radiographic imaging. This enables imaging techniques similar to those used in "classical" methods, as well as entirely new approaches that would not be feasible without robotic arms. The arms also provide enhanced capabilities for scanning irregular objects.

The spectral sensitivity of every pixel in an AdvaPIX TPX3 camera with a high-resolution Timepix3 chip enables a poly- chromatic X-ray beam to be used for EDXRD, resulting in a fast and compact system. This is possible because the X-ray tube teamed with a dual-stage collimator does not require monochromatizing and thus provides a high- intensity polychromatic X-ray beam. The high-resolution detector placed close to the sample and covering a large solid angle eliminates the need for mechanical angular scanning. The broad energy range (3–150 keV) allows analysis of even very absorbing samples (stainless steel, heavy metals and minerals).

The dual robot portable scanners represent a significant advancement in the field of non-destructive testing, particularly within aerospace and space applications. Its innovative design enables it to be transported to the object rather than requiring the object to be taken to a traditional CT machine, thereby expanding the scope and flexibility of inspections. The system represents a platform for other modalities as well, such as XRD, XRF, macrophotography, UV, IR and other.

Analytical methods were supported by projects of Ministry of the Interior VB01000046, VK01010153.

References:

Kotrlý M et al., J. Appl. Crystallogr., (2025), 58, 168–179.

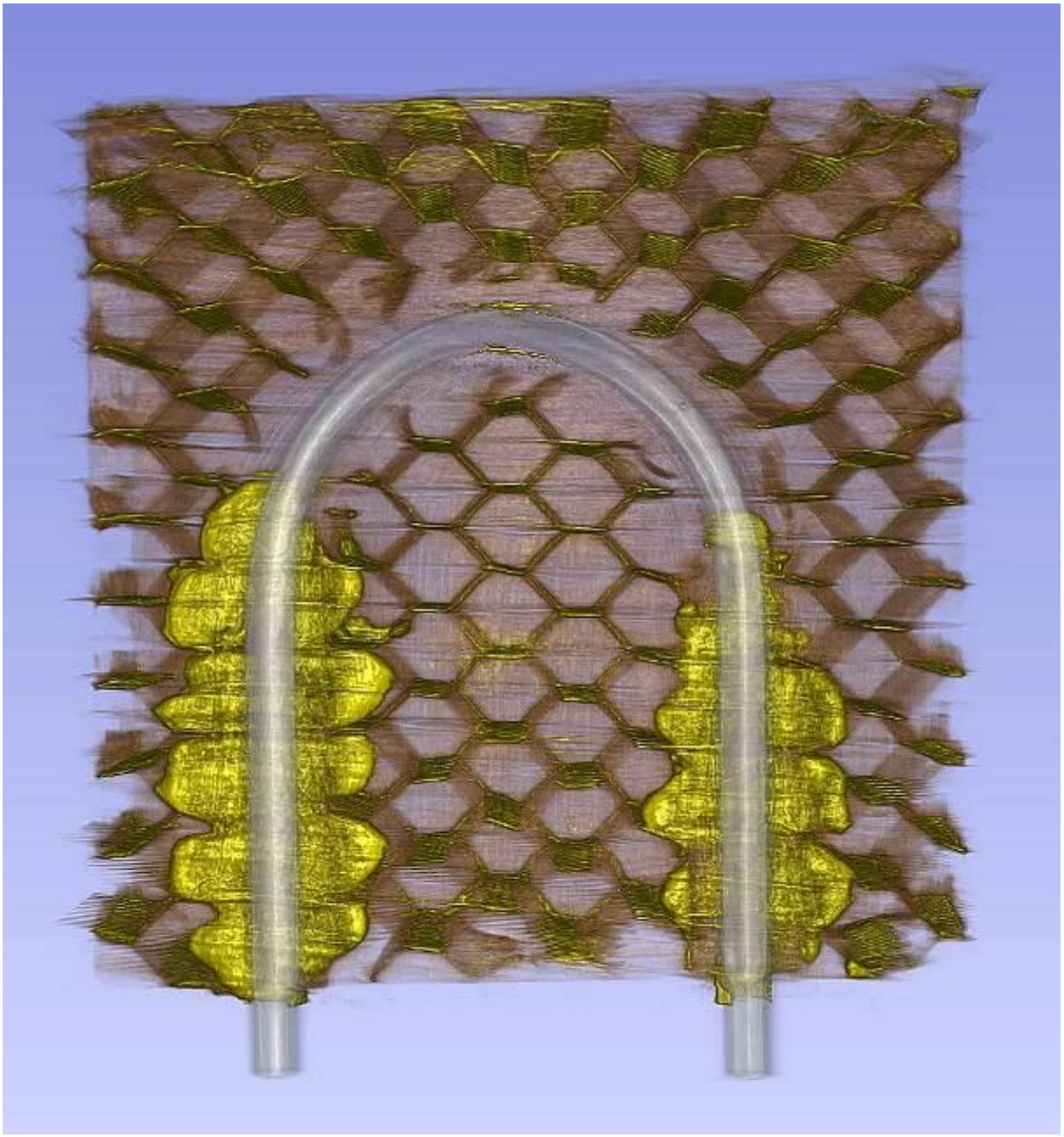
Fig. 1 Preparation of the mobile system for aircraft inspection, left robot 1, right robot 2.

Fig. 2 Examples of 3D visualizations of CT scans - the honeycomb sandwich panel.

Fig. 1



Fig. 2



IM2.P22
Valence band HOPG density of states by secondary electron emission spectroscopy in a low voltage scanning electron microscope

A. Kosari Mehr[1], M. Zaghloul[1], R. Tanwar[1], W. Cao[1], M. Khan[1], E. Afshar[1], S. M. Pietralunga[2], A. Khursheed[1], A. Tagliaferri[1]

[1]Politecnico di Milano, Physics, Milan, Italy
[2]CNR Istituto di Fotonica e Nanotecnologie, Milan, Italy

Introduction

Investigating the surface/near-surface Valence Band (VB) with nanoscale lateral resolution is critical for surface science and applications, though not available by conventional spectroscopic techniques. Scanning Electron Microscopy (SEM) offers nanoscale resolution that could be joined to secondary electron Emission spectroscopy (SEES, below 50 eV), with high yield and fast acquisition when it is excited in the low voltage excitation regime (<3 kV). The method enables fast nanoscale material mapping and Valence Band characterization [1]. Nonetheless, the data analysis in the low-kinetic energy range is challenging, as the information is hindered by the significant background associated with cascade SE generation. No model has been proposed so far that can comprehensively picture the entire secondary electron (SE) emission process, including its fine energy structure.

Objectives

This study establishes an experimental framework for Valence Band characterization of materials using SEMs equipped with a dedicated electron energy analyzer. The study discusses the scenarios behind the fine structure of the experimental spectra with the valence band's occupied and unoccupied quantum states. It also proposes an analytical model relating the valence-band Density of States (DOS) to the measured SE spectral function.

Materials & Methods

An ultra-high vacuum scanning Auger microscope (SAM) equipped with a Cylindrical Mirror Analyzer (CMA) is adapted for low-energy electron detection by designing dedicated entrance optics. Highly oriented pyrolytic graphite (HOPG) and several metallic samples are experimentally investigated at low primary beam energies (<3 kV). The beam-induced contamination at the sample surface was mitigated by operating in an Ultra-High Vacuum (UHV) environment and limiting the electron dose. The data are modeled using the Fermi Golden rule and perturbation theory fed by ab initio calculated DOS.

Results

The experimental signals show a high degree of reproducibility. By comparing the experimental spectra recorded at different Primary Electron (PEs) energies, the fine structure is coarsely preserved at different PE kinetic energies (Fig.1). The spectral features are found at SE kinetic energies in harmony with the model prediction, and their intensities show a promising similarity with the model as well.

Conclusion

We demonstrated the reproducibility and semi-quantitative modeling of SEES on HOPG, offering spectroscopic quantum state contrast in UHV, paving the way for the investigation of surface valence band DOS in bulky systems and devices.

References

[1] Han, W., et al. "Quantitative material analysis using secondary electron energy spectromicroscopy." Sci Rep 10, 22144 (2020).

Fig. 1

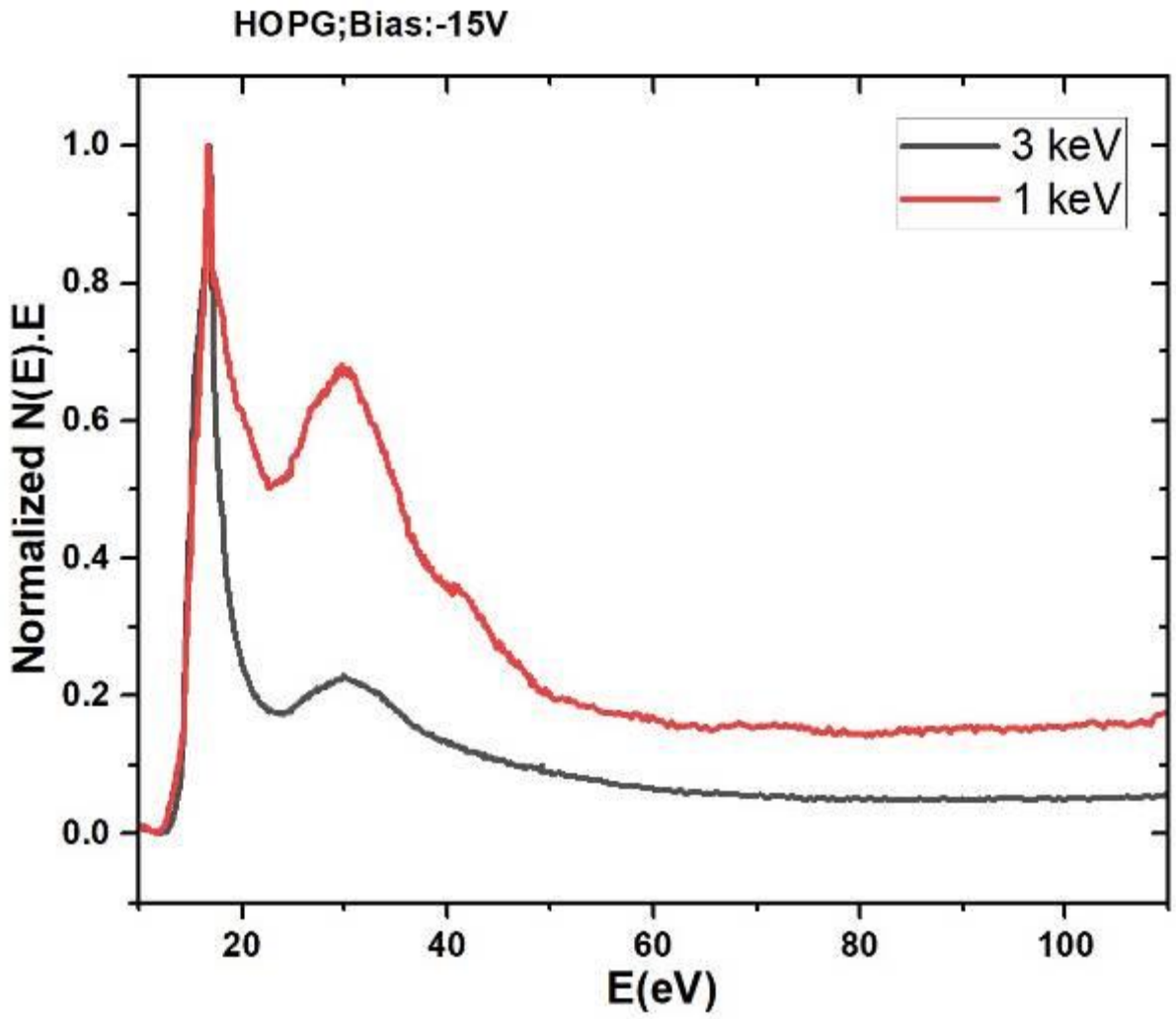


Fig.1 The spectral function of HOPG acquired at PEs of 1 keV (Red) and 3 keV (Black) while applying a negative bias of -15 V.

IM2.P23
Understanding of electronic structure by combination of soft x-ray spectrometer with electron energy loss spectrometer

C. Sun[1,2], A. Orekhov[2], M. G. Willinger[2]

[1]Tumint. Energy Research GmbH, Garching, Germany
[2]Technical University of Munich, Chemistry, Munich, Germany

The integration of soft X-ray emission spectrometer (SXES) with Scanning Electron Microscopy (SEM) significantly enhances the capabilities of elucidating the electronic structure of material [1]. SXES detects soft X-rays originating from electron transitions between the valence band and core levels, providing valuable insights into bonding energy states. In 2024, the installation of a new JEOL IT-800 SEM in Tumint-Energy Research GmbH, equipped with SXES, will support our efforts to characterize electronic structure of various materials. With an energy resolution 0.3 eV and its non-destructive nature, SXES holds potential for analyzing a wide range of energy materials.

While Electron Energy Loss Spectroscopy (EELS) is well-established for probing the density of states (DOS) in the conduction band, the combination of SXES and EELS provides a more comprehensive approach to analyzing the total electronic structure of materials. Our study aims to integrate these techniques for a deeper understanding of material properties.

We utilized two samples (Fig. 1) for the preliminary assessment of SXES determination. The red curve represents a standard Si wafer, showing three characteristic SXES peaks, marked by red bars. In contrast, the black curve, corresponding to SiO_2, clearly exhibits shifts in these peaks due to oxidation. Additionally, we observed increased self-absorption effects with higher electron beam energy (Fig. 2). The most distinct spectrum, acquired at 69.4 nA (Fig. 3), highlights the necessity of high beam currents in SXES experiments. Furthermore, variations in working distance resulted in peak shifts (Fig. 4), emphasizing the importance of standardized measurement conditions.

To further interpret SXES data, future work will focus on theoretical simulations. The combined application of SXES and EELS, alongside computational modeling, will facilitate a more comprehensive understanding of electronic structures across different material systems.

1. Zhou X, Qiao S, Yue N, et al. (2023) Soft X-ray emission spectroscopy finds plenty of room in exploring lithium-ion batteries, Materials Research Letters, 11:4, 239-249.
2. Terauchi M, Hatano T, Koike M, et al. (2022) Recent developments in soft X-ray emission spectroscopy microscopy. IOP Conference Series: Materials Science and Engineering, 891(1):012022.

Fig. 1 Soft X-ray emission spectra of (a) a Si wafer (Ted Pella) and (b) a Si wafer with a 285 nm SiO_2 layer and Au markers (Active Business Company).

Fig. 2 Variation in soft X-ray emission spectra of a Si wafer with changing electron beam energy.

Fig. 3 Variation in soft X-ray emission spectra of a Si wafer with changing electron beam current.

Fig. 4 Variation in soft X-ray emission spectra of a Si wafer with different working distances in SEM.

Fig. 1

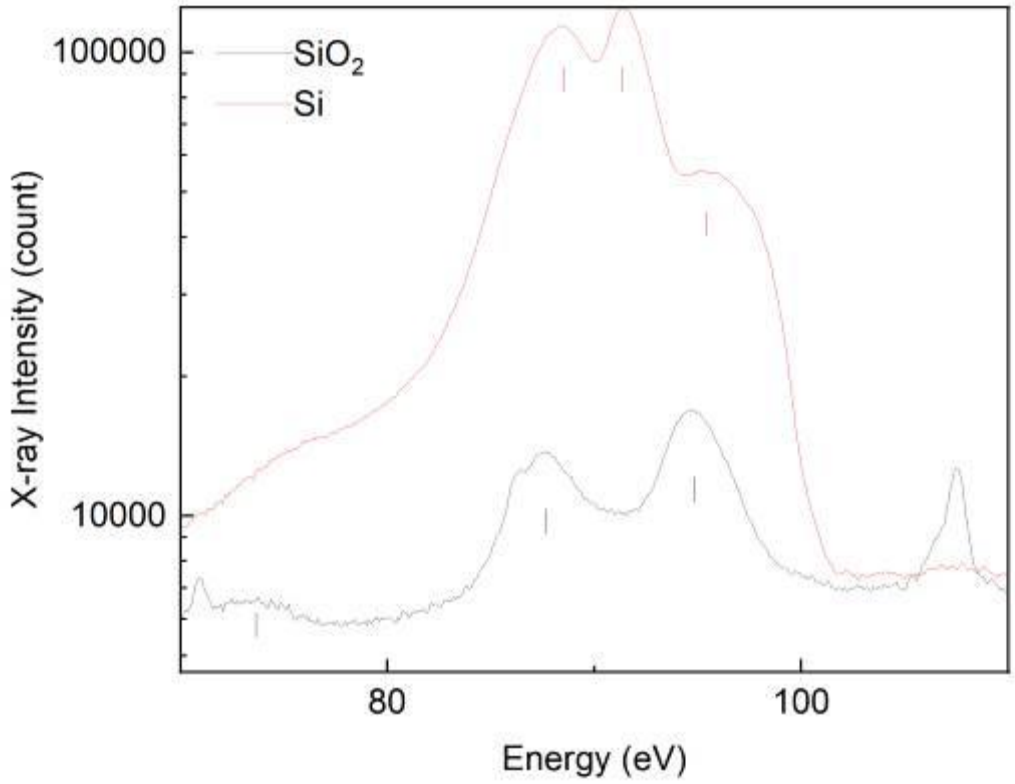


Fig. 2

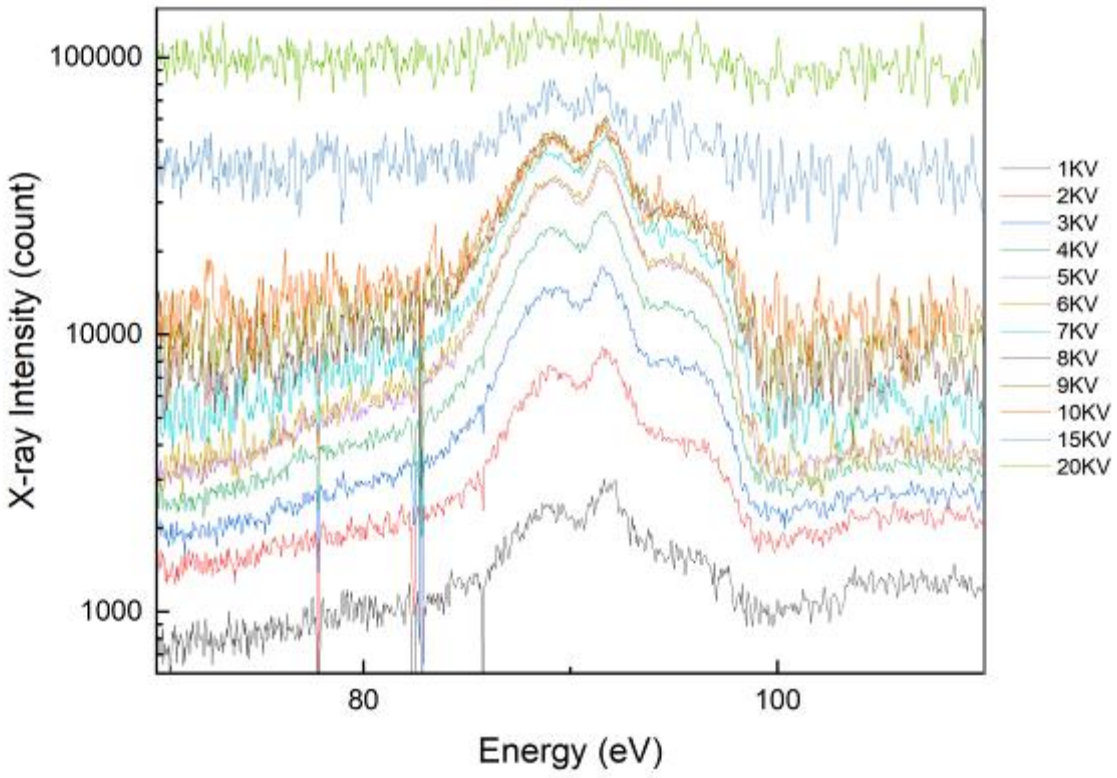

100000
10000
1000
X-ray Intensity (count)
80
100
Energy (eV)
1KV
2KV
3KV
4KV
5KV
6KV
7KV
8KV
9KV
10KV
15KV
20KV

Fig. 3

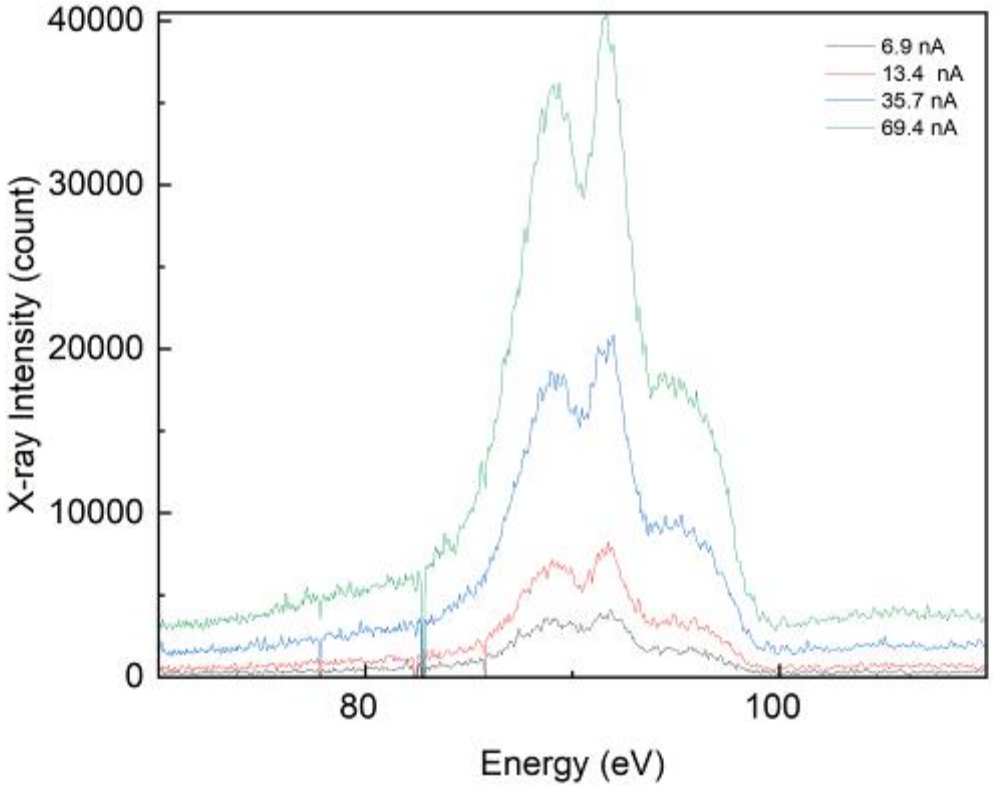
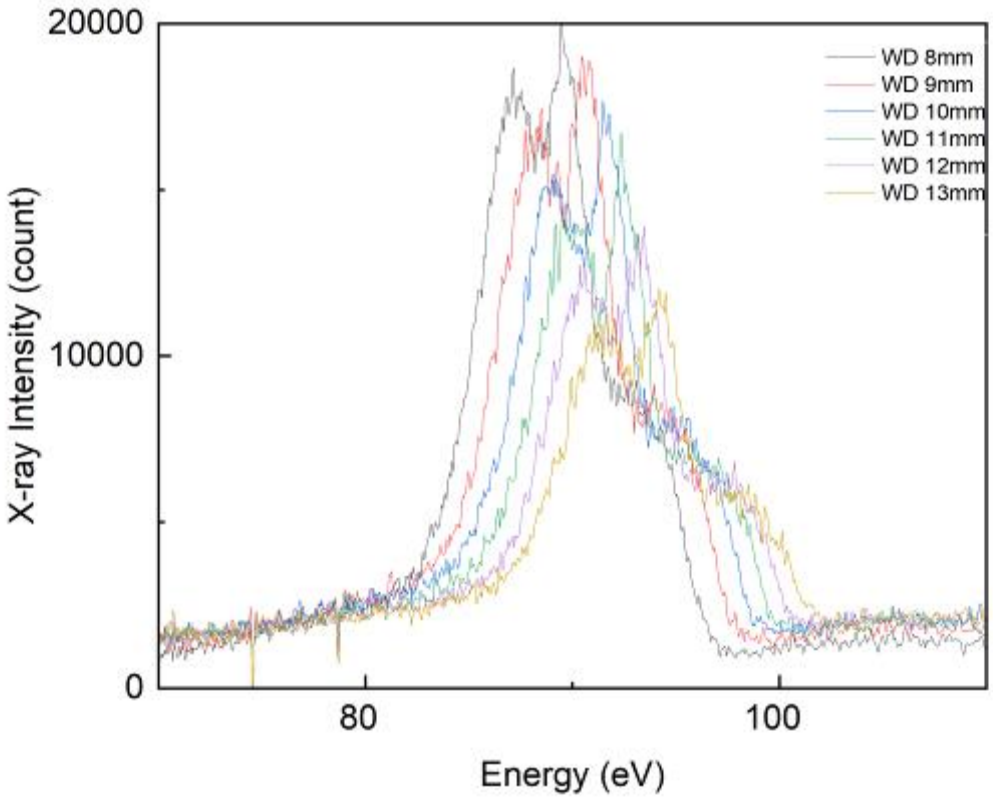

40000
30000
20000
10000
0
X-ray Intensity (count)
80
100
Energy (eV)
6.9 nA
13.4 nA
35.7 nA
69.4 nA

Fig. 4


20000
10000
0
X-ray Intensity (count)
80
100
Energy (eV)
WD 8mm
WD 9mm
WD 10mm
WD 11mm
WD 12mm
WD 13mm

IM2.P24
Dose-fractionated K-Edge ELNES for compositional and chemical state mapping in transition metals

S. Gorji[1], A. Thron[2], L. Spillane[2], R. Twesten[2]

[1]Ametek GmbH, Gatan + EDAX, Unterschleissheim, Germany
[2]Gatan Inc., Pleasanton, CA, United States

Introduction

The fine structure of transition metal (TM) K-edges in electron energy-loss spectroscopy (EELS) provides critical insight into local bonding and coordination environments [1]. Unlike $L_{2,3}$ edges, which probe unoccupied 3d states and are influenced by spin-orbit coupling, K-edges primarily involve transitions into 4p states, making them highly sensitive to bond lengths, angles, and oxidation state variations. However, their lower inelastic cross-section necessitates long acquisition times, increasing the risk of sample drift and beam damage.

Objectives

This study aims to enhance the detection and interpretation of TM K-edge fine structures by implementing dose-fractionated spectrum imaging (SI) and spatially resolved ELNES analysis. We investigate the Co K-edge in FeCoOx nanoparticles to assess how local Mn incorporation influences chemical state and bonding symmetry.

Materials & Methods

EELS SI was performed on FeCoOx nanoparticles using a JEOL F200 (cFEG, 200 kV, 1.9 nA) with a Continuum HR+Stela spectrometer. Data were acquired in DigitalMicrograph® using in-situ SI (<30 s per pass) and eaSI™ drift correction. Due to the small cross-sections of the transition metal K-edges the SI acquired took 70 mins. Since the SI is acquired in several passes using the in-situ SI acquisition, the total dose to the sample was fractioned out over the capture time. This enabled the monitoring of drift and ensured minimal effects of drift and enabling the observation of sufficient signal for weak Fe and Co K-edge ELNES analysis.

Results

Summing spectra across entire nanoparticles revealed Fe and Co as the primary elements (Figure 1a). However, the analysis of specific regions in the particles reveal the presence of the Mn K-edge signal, demonstrating the advantage of high spatial resolution for the detection of weak signals. Corresponding elemental maps (Figures 1b–1e) confirmed a homogeneous Fe and Co distribution, while Mn appears non-uniformly concentrated into clusters.

To further investigate electronic structure variations, non-linear least squares (NLLS) fitting was applied to the Co K-edge ELNES, analyzing the pre-peak and main peak features. Figure 1f shows an increase in the pre-peak intensity, in the Mn-rich regions, while Figure 1g indicates a higher-energy shift in the pre-peak position. The Co K pre-peak originates from a 1s → 3d non-dipole transition, which is sensitive to 3d band symmetry and electron occupancy. These spectral shifts suggest that Mn incorporation modifies the local bonding configuration, integrating into the FeCoOx lattice rather than forming a separate MnOx phase.

Conclusion

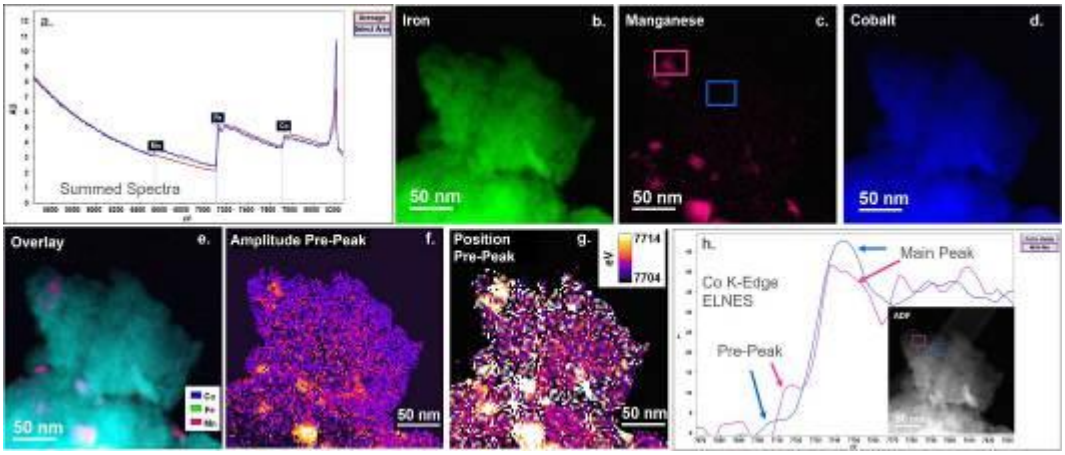
This study demonstrated how dose-fractionated SI and eaSI drift correction enable stable long-term EELS acquisitions, preserving sample integrity and improving signal detection. Using the Stela direct detection camera, we achieved high signal-to-noise ELNES mapping, correlating local composition with Co K-edge fine structure and showed that Mn incorporation alters the local bonding environment, integrating into the FeCoOx lattice. These findings underscore the value of advanced EELS strategies for detecting weak core-loss signals in TM systems.

Figure 1. (a) Summed EELS spectra from the entire nanoparticle (blue) and a selected region (red), revealing localized compositional variations. Elemental maps of (b) Mn, (c) Fe, (d) Co, and (e) their overlay illustrate elemental distribution. (f) Pre-peak intensity and (g) energy shift of the Co K-edge analyzed via NLLS Gaussian fitting. (h) Extracted Co K-edge spectra from selected regions in the inset ADF image, comparing areas with and without Mn, as indicated in (c).

Reference:

[1] Baker M.L., Mara M.W, Yan J.J., Hodgson K.O., Hedman B., Solomn E.I., *Coord. Chem Rev*, 345 (2017) 182–208

Fig. 1



IM2.P26
µRaman and scanning electron microscopy analysis of microplastic particles in environment and in human tissues

P. T. Miclea[1,2], H. U. Vaghasiya[2], M. Lelonek[3], J. Klehm[2], R. B. Wehrspohn[2]

[1]Fraunhofer Center for Silicon Photovoltaic, Halle (Saale), Germany
[2]Martin Luther University Halle-Wittenberg, Halle (Saale), Germany
[3]SmartMembranes GmbH, Halle (Saale), Germany

Introduction

Plastics are widely used due to their affordability, low density, and durability. However, these characteristics contribute to the accumulation of plastic waste. While environmental concerns regarding plastic disposal have existed for decades, recent attention has shifted to the fragmentation of large plastic objects into micro- and nano-sized particles. These pose an even greater threat to living organisms. Additionally, plastics are intentionally manufactured in micro sizes for specific applications. Researchers and environmental agencies actively monitor the levels and distribution of micro- and nanoplastics in the environment and assess their impact on ecosystems.

Objectives

The main objective of this research is to optimize automatic identification methods for microplastic particles using Micro-Raman spectroscopy, aiming to improve the efficiency and accuracy of polymer identification in environmental and tissue samples. Specifically, this study focuses on:

- Quantifying the similarity between Raman spectra of reference materials and environmental particles for automatic classification.
- Enhancing accuracy through machine learning, particularly using Convolutional Neural Networks (CNNs).
- Exploring the correlation between Scanning Electron Microscopy (SEM) and Raman spectroscopy to improve reliability.
- Optimizing the minimum peak size requirement and the Match value threshold.

Materials and Methods

Micro-Raman spectroscopy is used to identify polymer types in microparticles. The study involves calculating weighted correlations within selected Raman shift ranges to distinguish specific polymer particles from other materials. A minimum peak size requirement is applied to filter out weak spectra, which require manual analysis. Machine learning techniques, specifically Convolutional Neural Networks (CNNs), are employed to model Raman spectra and enhance classification performance. The bootstrap method is integrated with CNN-based spectral analysis to determine the optimal Match threshold. Additionally, SEM data is correlated with Raman spectra to validate the accuracy of the automatic identification system.

Results

Applying machine learning, particularly CNNs, to Raman spectra significantly improves the accuracy and efficiency of microplastic identification. The CNN model is trained to recognize distinct features of different polymer types, enhancing classification. The optimization of the minimum peak size requirement and Match threshold ensures that the system maintains a high true positive rate, reducing manual intervention. The correlation between SEM and Raman spectroscopy further validates the

reliability of the automatic identification process. The integrated approach enhances environmental monitoring and advances microplastic research.

Conclusion

This research demonstrates that automatic identification of microplastics using Micro-Raman spectroscopy, combined with machine learning techniques, improves speed and accuracy. Integrating SEM data and optimizing classification parameters further enhances reliability. This combined approach holds significant potential for advancing microplastic pollution studies and streamlining environmental monitoring efforts, offering a cost-effective solution for large-scale analysis.

IM 3: SEM and FIB developments

IM3.01(inv)
New opportunities in material contrast imaging and energy dispersive X-ray analysis in scanning electron microscopy

U. Golla-Schindler[1], D. Goll[1], V. Knoblauch[1], G. Schneider[1]

[1]Aalen University, Materials Research Institute Aalen (IMFAA), Aalen, Germany

In scanning electron microscopy, the detection of backscattered electrons (BSE) provides information about material contrast. The achievable spatial resolution improves with decreasing accelerating voltage due to the reduction of the interaction volume. Figure 1 a, b shows Monte Carlo simulations of the interaction volume for SmCo and primary energies (PE) of 20 keV (a) and 1 keV (b), where the size decreases by a factor of about one hundred. To push the spatial resolution to the limit, only the elastically reflected BSEs should be detected [1]. By using the in-lens energy-selective backscattered electron detector (EsB Zeiss) or the DELTA detector® of an aberration-corrected SEM, material contrast information in the nm range can be obtained [2]. Another possibility is the transmission mode in SEM (T-SEM), where the interaction volume is automatically reduced due to the lack of sample thickness. The absence of the edge effect further improves the spatial resolution compared to the top view image. Figure 1 shows cobalt ferrite nanoparticles on a lacey carbon film and the improved spatial resolution for the T-SEM mode. The next open question is the detection limit, where we have shown that atomic number differences of 0.03 can be visualised with the AsB (Zeiss) BSE chamber detector [3]. Insufficient electrical conductivity, radiation damage and contamination can significantly influence the image. Figure 2 a, b shows the image of Sm-rich precipitates, which appear bright or dark depending on the scanning speed (line time 256 ms; 52.5 ms). These charges are also referred to as potential contrast. This potential contrast can also be used positively to image differences in electrical conductivity Figure 2 c, d. When an image contains material contrast, the questions that automatically follow are: What is the chemical difference, can it be quantified, how reliable are the results? Energy dispersive X-ray analysis can provide initial answers. In order to prove the reliability of quantitative EDS analysis on Li-ion battery, we used alternative sample preparation methods and performed a round robin test. The subject was the stochiometric composition of the NiMnCo content of the cathode active material within a Li-ion battery. We obtained relative deviations between methods, institutions and preparation techniques of less than 10% for Ni and Co and less than 15% for Mn content. The next challenge is the detection of light elements in batteries, Li. There are new developments that are overcoming old limitations. In our laboratory we have the windowless Oxford Extreme EDS. There we can detect and, through the idea of element determination as difference, also quantitatively determine the Li content [4, 5].

[1] Böngeler R.; Golla U.; Kässens M.; Reimer L.; Schindler B.; Senkel R.; Spranck M. Scanning 15, (1993) p. 1-18

[2] Golla-Schindler, U.; Wacker, I.; Schindler, B.; Bernthaler, T.; Schneider, G.; Schröder, R. R.: In: *Microsc Microanal* 25 (S2) (2019), p. 448–449. DOI: 10.1017/S1431927619002976.

[3] Golla-Schindler, U.; Loeffler, R.; Groß, T.; Laukart, J.; Goll, D.; Schneider, G. In: *Microsc Microanal* 25 (S2), (2019) S. 2326–2327. DOI: 10.1017/S1431927619012364

[4] Golla-Schindler, U.; Barbosa Sa E.; Weisenberger, C.; Knoblauch, V; Schneider, G. In: Microsc Microanal 29 (S1) (2023), p. 117–118. DOI: 10.1093/micmic/ozad067.051.

[5] The authors gratefully acknowledge the German BMBF (FKZ:03XP0317A) and BMWK (FKZ:16BZF320C) for financial support.

Fig. 1

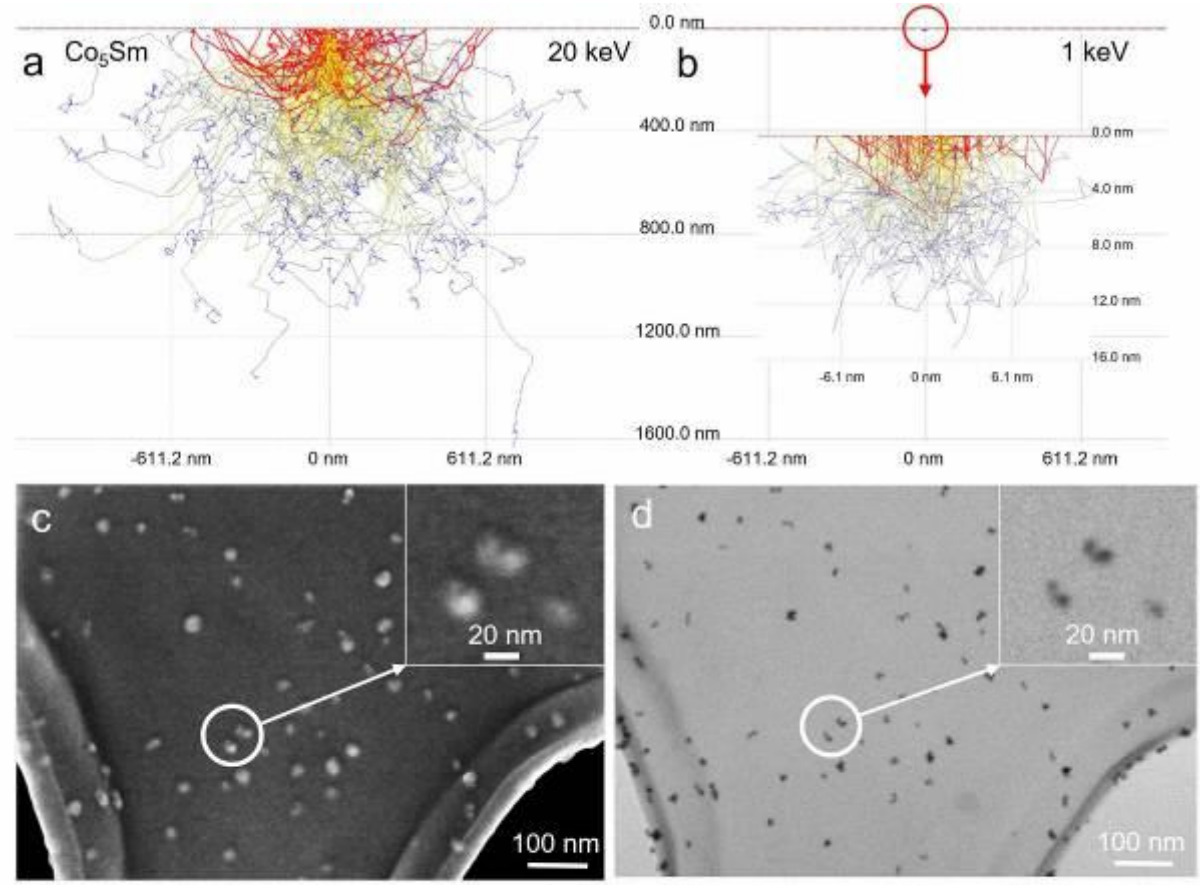


Figure 1 (a, b) Monte Carlo Simulations (http://www.lehigh.edu/~maw3/link/mssoft/mcsim.html) of CoSM for primary Energies of a) 20 keV and b) 1 keV. (c, d) Cobalt-Ferrite Nanoparticlles on a Lacey carbon film recorded with (c) the Inlens SE detector and (d) with a conversion detection system in the transmission mode.

Fig. 2

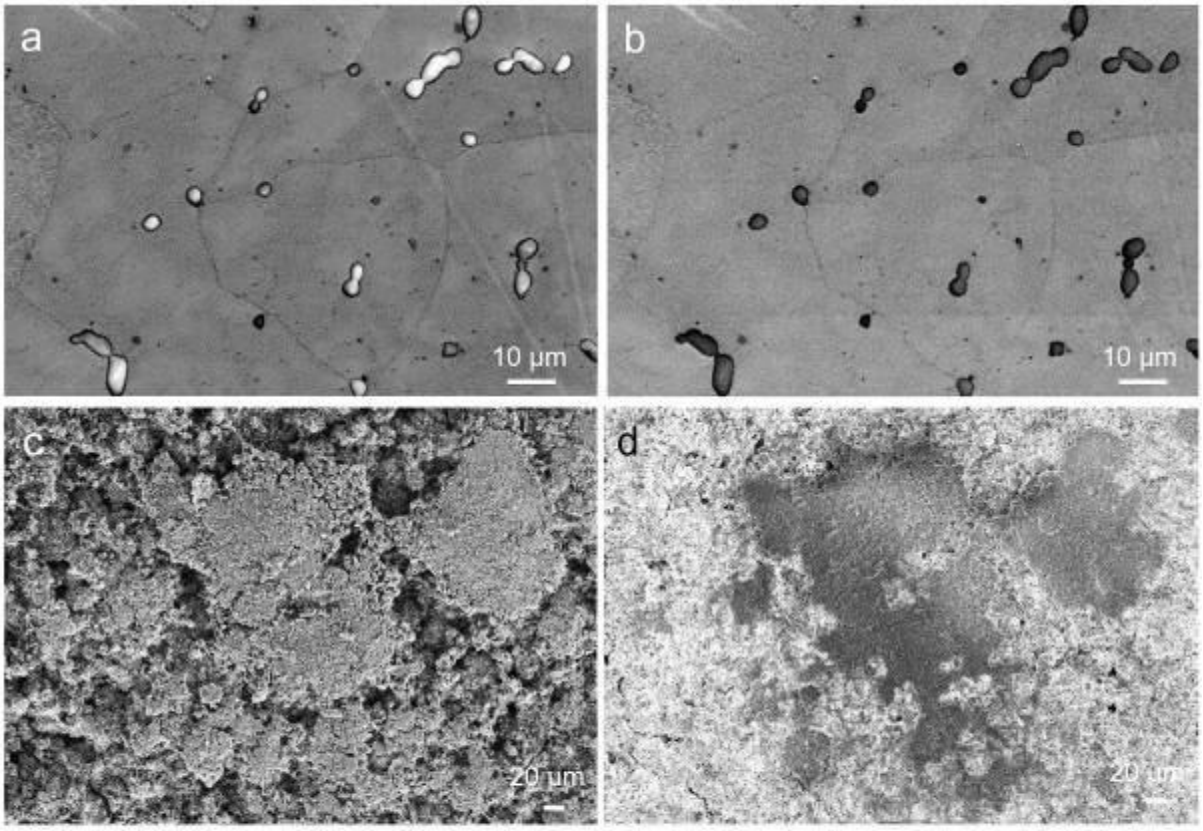


Figure 2 Potential contrast (a, b) SmCo magnets with Sm enriched precipitates (a) line time 256 ms, (b) line time 52,5ms. (c, d) top view image on Li-Ion battery anode (c) ETD (chamber SE detector), (d) inlens SE detector.

IM3.02
Backscattered electron energy loss spectroscopy – Analytical SEM imaging at sub-nanometer resolution

D. Ryklin[1], J. A. Kammerer[2], F. Feist[3], C. Barner-Kowollik[3,4], R. R. Schröder[1]

[1]Heidelberg University, BioQuant, Heidelberg, Germany
[2]Humboldt University of Berlin, Institute of Physics, Berlin, Germany
[3]Karlsruhe Institute of Technology, Institute of Nanotechnology, Karlsruhe, Germany
[4]Queensland University of Technology (QUT), Centre for Materials Science, Queensland, Australia

Analytical electron microscopy (EM) is well established in transmission mode ((S)TEM) to characterize material systems which otherwise do not yield sufficient bright or dark field contrast. However, TEM studies are limited by the necessity of thin samples, signal mixing due to projection, and – especially for organic and biological materials – also by beam damage.

Our goal is to establish Electron Energy Loss Spectroscopy (EELS) of the backscattered electrons (BSE) in an ultra-low voltage SEM, a technique we call backscattered EELS (bsEELS). bsEELS allows us to analytically study bulk samples with a high surface sensitivity, overcoming sample preparation and projection limitations of (S)TEM (Fig 1). In addition, the ultra-low primary electron energies (PE) (down to 10 eV) drastically reduce beam damage.

For bsEELS, we use a prototype of an electron-spectroscopic SEM, the Zeiss DELTA [1]. Sub-nanometer spatial resolution can be achieved in a wide PE range from a few keV down to ultra-low landing energies around 10 eV.

Fig 2 shows images of flat DNA origami platelets on silicon wafer at 80 eV (Fig 2b) and 10 eV (Fig 2c) PE. At 10 eV the signal is dominated by secondary electrons (SE) and contrast is inverted compared to the 80 eV BSE image. The strong contrast from only 40-50 atoms per nm^2 is unprecedented, demonstrating the high sensibility and resolution for organic materials at ultra-low PE. To test the spectroscopic sensitivity of bsEELS, we studied polymer microspheres with high chemical similarity [2]. Fig 3 a) shows the chemical structure of the two polymers studied – "eliminated" and "polyradical" spheres. They differ in only three H-atoms, requiring spectroscopic imaging to distinguish the two materials. As reference, the mono-chromated low-loss TEM spectra are given (Fig 3b). One advantage of SEM bsEELS is that we can also access the SE signal, providing information on surface potential. Since the polyradical spheres have a higher charge mobility than the eliminated spheres and the surrounding resin, they appear bright in the SE image (Fig 3c), enabling their identification. The conventional BSE image (Fig 3d) does not allow to distinguish the two materials. In the cumulative bsEEL spectrum recorded with the DELTA SEM (Fig 3e) a stronger signal is observed for the eliminated particles below 5 eV energy loss, while above 5 eV the polyradical particles show a stronger signal. This spectral information can be used to process the spectral images and generate contrast between the polyradical (brighter) and eliminated (darker) microspheres (Fig 3f).

These data demonstrate that – as for transmitted electrons – BSE carry material specific information from their elastic and inelastic interactions, which can be used for material characterization. Thus, bsEELS provides a new and powerful characterization tool especially for the direct visualization of beam sensitive, organic materials. By enabling the study of bulky samples and large areas, it adds important applications to the toolbox of analytical EM.

[1] RR Schröder et al., Microsc. Microanal. 24 (Suppl 1), 2018
[2] J Kammerer et al, Adv. Mater. 2023, 35, 2211074
[3] We thank M. Tran and K. Göpfrich (Heidelberg University) for DNA-origami samples and the DFG for funding via Excellence Cluster "3D Matter Made to Order" (EXC-2082). J.A.K. acknowledges

support by the DFG (500289223, 559314442). C.B.-K. additionally acknowledges funding by the Australian Research Council.

Fig. 1

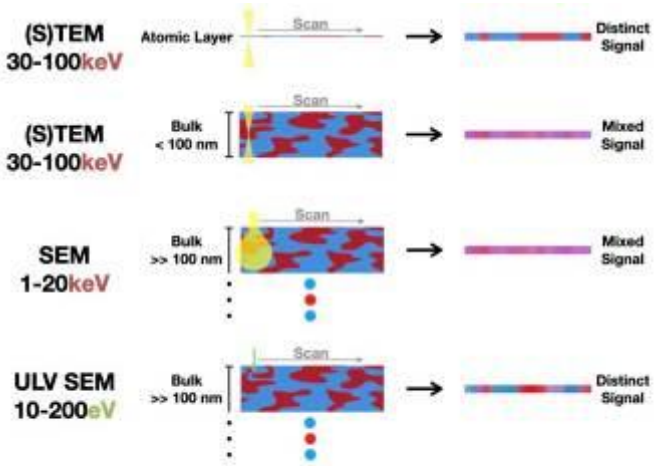


Figure 1: Schematic representation of signal generation in (S)TEM, SEM and ultra-low voltage SEM. (S)TEM is limited to thin(ned) samples and leads to signal mixture in nano-structured layers due to projection through the sample. With standard SEM the large interaction volume leads to signal mixing, but with ULV SEM the interaction volume decreases to nm-range allowing to measure distinct signal from bulk sample surfaces.

Fig. 2

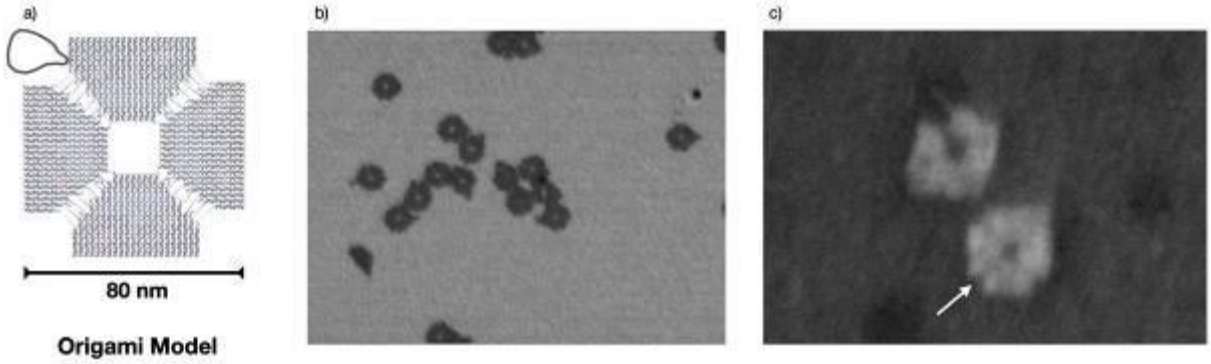


Figure 2: a) Model of the DNA-Origami with a central 20 nm Cavity and unfolded DNA at one corner. b) BSE images of recorded at 80 eV landing energy illustrate the strong contrast of the flat platelets (thickness 2 nm, 40-50 atoms within one pixel) on silicon wafer. c) Image of the DNA-Origami recorded at 10 eV landing energy with still remarkably high resolution allows visualization of the cavity and even the low-density gaps between the four distinct DNA areas (white arrow). At this energy a separation of BSE and SE is not possible. Note the contrast change to image b).

Fig. 3

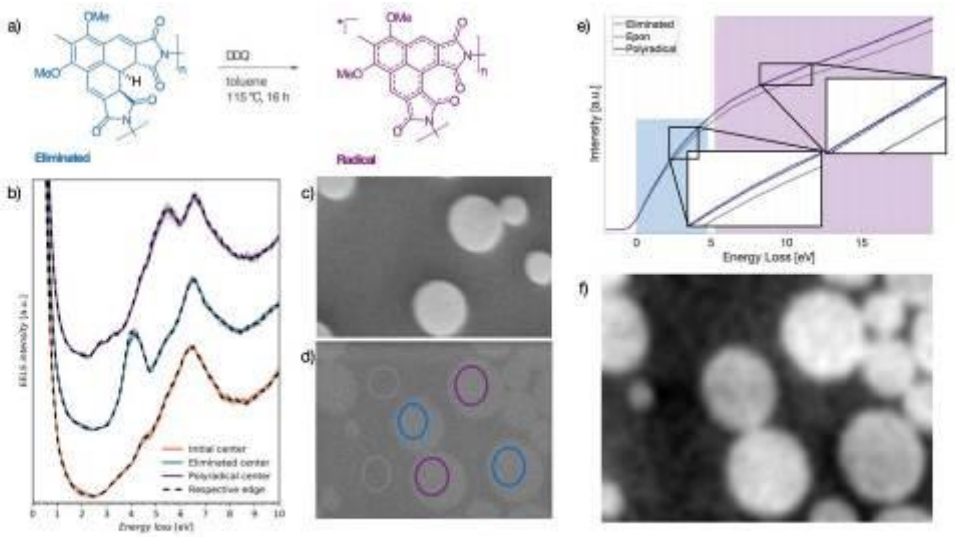


Figure 3: a) Chemical structure of the eliminated and polyradical polymers from [2] - note that the atomic structure differs only in three hydrogen atoms per monomer. b) TEM-EELS analysis, also from [2]. c) Surface potential map imaged with SE at 100 eV primary energy shows only the polyradical spheres - due to their increased charge mobility. d) BSE image at 100 eV primary energy of the same region visualizes both types of spheres. e) Cumulative bsEEL spectra recorded from the regions indicated by circles in d). f) Image generated by dividing the integrated signal under the purple area by the integrated signal under the blue area.

IM3.03
Enabling event-driven 4D-STEM in a multi-modal *in situ* environmental SEM

P. H. Lu[1], F. Perez Willard[2], B. Gamm[2], P. M. Anger[2], D. Byelov[3], W. van Bodegom[3], E. Hogenbirk[3], T. Schoenbeck[3], M. Heggen[1], R. E. Dunin-Borkowski[1]

[1]Forschungszentrum Jülich GmbH, Jülich, Germany
[2]Carl Zeiss Microscopy, Oberkochen, Germany
[3]Amsterdam Scientific Instruments, Amsterdam, Netherlands

Four-dimensional scanning transmission electron microscopy (4D-STEM) measures a series of 2D electron scattering pattern in reciprocal space while an electron probe scans over a 2D region of interest in real space. Such a high-dimensional dataset allows much richer sample information to be retrieved in a spatially-resolved way, ranging from crystallographic orientation and phase, strain, short and medium range ordering, to differential phase contrast and ptychographic imaging, as well as other new imaging modes. This was usually performed on a TEM instrument where a miniaturised sample is accommodated between a narrow objective lens pole piece. In recent years, there have been attempts to implement such a setup in an SEM instrument. This would bring a few unique opportunities. First of all, the large specimen stage and swift sample exchange would allow a high-throughput characterisation workflow, which becomes vital to the emerging AI-driven materials discovery. In addition, the large space and multiple available ports inside the chamber makes correlative and multi-modal imaging possible so that complementary information can be acquired simultaneously with 4D-STEM, which would assist 4D-STEM data analysis and give a complete picture to the investigated system. Last but not least, one can study the as-prepared specimen *in situ*, e.g., during growth in an environmental SEM (ESEM) or just after lift-out in a FIB-SEM dual beam instrument. This would avoid sample transfer and the associated contamination or degradation, especially for environment-sensitive specimens.

In view of this, we designed and built a 4D-STEM setup on a multi-modal *in situ* ESEM in cooperation with Zeiss and Amsterdam Scientific Instruments (ASI). Raman spectroscopy, AFM, EDS, EBSD, and 4D-STEM as well as the conventional SE and BSE imaging can be performed all in one station. Zeiss Gemini 460 optics were chosen because of its multiple condenser lenses and therefore independent control of convergence angle and beam current. Pre-mixed reactant gases can be introduced adjacent to the specimen via the local charge compensator device, followed by residue gas analysis using an attached mass spectrometer. The 4D-STEM detector is introduced to the chamber via a front upper port (Fig. 1a) and fixed to the SEM stage for its own manoeuvre (Fig. 1b). A 6 degree of freedom (DOF) SmarAct SMARPOD positioning stage is added on top of the original SEM stage (Fig. 1c) so that the specimen can be moved independently and oriented to the desired zone axis. A camera length up to 125 mm is accessible and potentially 200 mm would be possible with a bit of modifications.

The other highlight of this setup is the event-driven detection scheme powered by the new Timepix3 detector, CheeTah T3 Turbo, developed by ASI. CheeTah T3 Turbo is made of 2x2 Timepix3 chips, i.e. 512x512 pixels, with the maximally possible permitted event rate, 320 Mhit/s. This is 4 times as what single Timepix3 chip would allow and about one fourth of what the next generation Timepix4 chip would reach. Effectively MHz frame rate 4D-STEM measurement with more than 10 pA probe current would be possible using this detector. In comparison, frame-based detectors would only reach 1-10 kHz frame rate, while many other event-driven detectors would only allow very few pA probe current.

This work is funded by the ER-C 2.0 Project. A few preliminary application results will be presented in this contribution.

Fig. 1

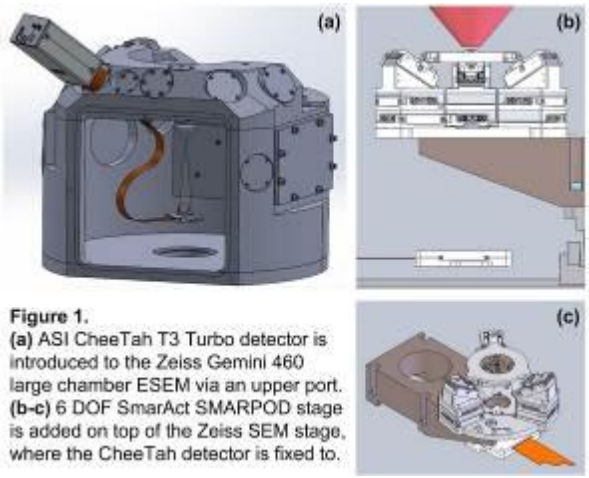


Figure 1.
(a) ASI CheeTah T3 Turbo detector is introduced to the Zeiss Gemini 460 large chamber ESEM via an upper port. **(b-c)** 6 DOF SmarAct SMARPOD stage is added on top of the Zeiss SEM stage, where the CheeTah detector is fixed to.

IM3.04(inv)
Automated SEM for large EBSD datasets: FS laser-FIB 3D volumes and *in situ* testing

J. Donoghue[1]

[1]University of Manchester, The Royce Institute, Manchester, United Kingdom

For over 30 years electron backscatter diffraction (EBSD) has been transforming our understanding of crystallographic materials. EBSD technologies have continuously evolved over this time to provide ever faster and more accurate indexing of orientation and phase. Two areas that greatly benefit from improvements in EBSD acquisition speeds are 3D studies (where improved speeds allow ever larger volumes to be investigated, or the same volume at greater volume resolution) and in-situ studies (where faster mapping allows events to be captured with ever greater experimental resolution). Simultaneous developments in both software and hardware on the SEM side, particularly with stability and the development of flexible application programming interfaces (APIs) has enabled the development of automated experiments to push these data collection rates even higher.

Presented here are two such systems. First, a Thermo Scientific (TS) femtosecond laser-PFIB that the University of Manchester (UoM) has worked with TS to develop workflows for 3D serial sectioning. The femtosecond laser material ablation rate is several orders of magnitude greater than traditional FIB technologies allowing larger volumes to be investigated. Particular attention is paid to optimising laser parameters to give a sample surface suitable for EBSD analysis, and where this is not achievable through laser parameters alone, how the automated runs can include an integrated FIB polishing step. Second, a system for the automated acquisition of EBSD (and other analyses) during in-situ experiments developed at UoM in collaboration with TESCAN and NewTec Scientific. The solution allows intricate straining/temperature experiments to run without intervention over several days, minimising user error and potentially tripling the data collected otherwise.

Several case studies are presented highlighting how such datasets are helping material scientists not only visualise microstructures on a whole new scale and interrogate physical phenomena at a higher resolution (both spatial, and temporal), but are also a valuable resource for simulation validation and as for inputs for modelling.

IM3.05
New methodology for FIB-SEM-SIMS data acquisition using alternative FIB scans

A. Miranda Martinez[1], O. de Castro[1], S. Sharma[1], O. Bouton[1], T. Wirtz[1], S. Eswara[1]

[1]Luxembourg Institute of Science and Technology, Belvaux, Luxembourg

Focused Ion Beam – Scanning Electron Microscopy (FIB-SEM) and Secondary Ion Mass Spectrometry (SIMS) are widely employed microscopical and analytical techniques for characterizing the structural and chemical composition of samples with high sensitivity and spatial resolution. Our group developed a magnetic sector SIMS that was incorporated into a FIB-SEM platform to combine both investigation modes, valuable for many applications [1].

The resolution in FIB-SEM-SIMS analysis is limited by beam damage and shot noise. Structural alterations are caused by beam damage, while shot noise influence in the signal-to-noise ratio (SNR), causing distortion in the image [2]. To overcome these distortions, new scanning protocols and techniques need to be explored.

To increase the functionalities of the instrument, and with the objective of reducing the dose radiated to the sample, it is necessary to implement a novel methodology. This methodology consists in controlling the FIB to scan over defined regions of the sample.

In this work we show the development of a methodology to implement alternative illumination and acquisition methods. The implementation was done in a high-vacuum FIB-SEM platform equipped with a SEM column, a Ga liquid metal ion source (LMIS)-based FIB column (Ga-FIB), and a magnetic sector SIMS system [1]. A custom-built acquisition system controlled by an acquisition card is used. The system manages the FIB control and data acquisition with a LabVIEW program. Furthermore, the system includes the use of python algorithms to determine the desired locations to be scanned.

To prove the new functionalities, different scanning patterns were used to form secondary electrons (SE) and SIMS images using a FeTi alloy as demonstration sample. Figure 1 shows SIMS images scanned using six different patterns. Also, an adaptive sampling method was implemented. This technique consists in performing a fast scan first with a low dwell time, followed by a second scan with a higher dwell time, but only in selected pixels of the image. A python algorithm makes the decision of the pixels of interest to be scanned after by using the first scan information. This method helps reducing the acquisition time and dose without severely affecting the resolution [3].

The developed methodology opens new possibilities in the implementation of sampling methods, achieving information acquisition with lower doses and increasing the acquisition speed, enhancing materials research. In this way, it will be possible to evaluate which acquisition technique, together with the respective data processing, allows to obtain a better image resolution.

The authors acknowledge funding from the European Union"s Horizon Europe research and innovation program under Grant Agreement No. 101104032 (OPINCHARGE).

Figure 1. Secondary Ions images obtained using different scan patterns.

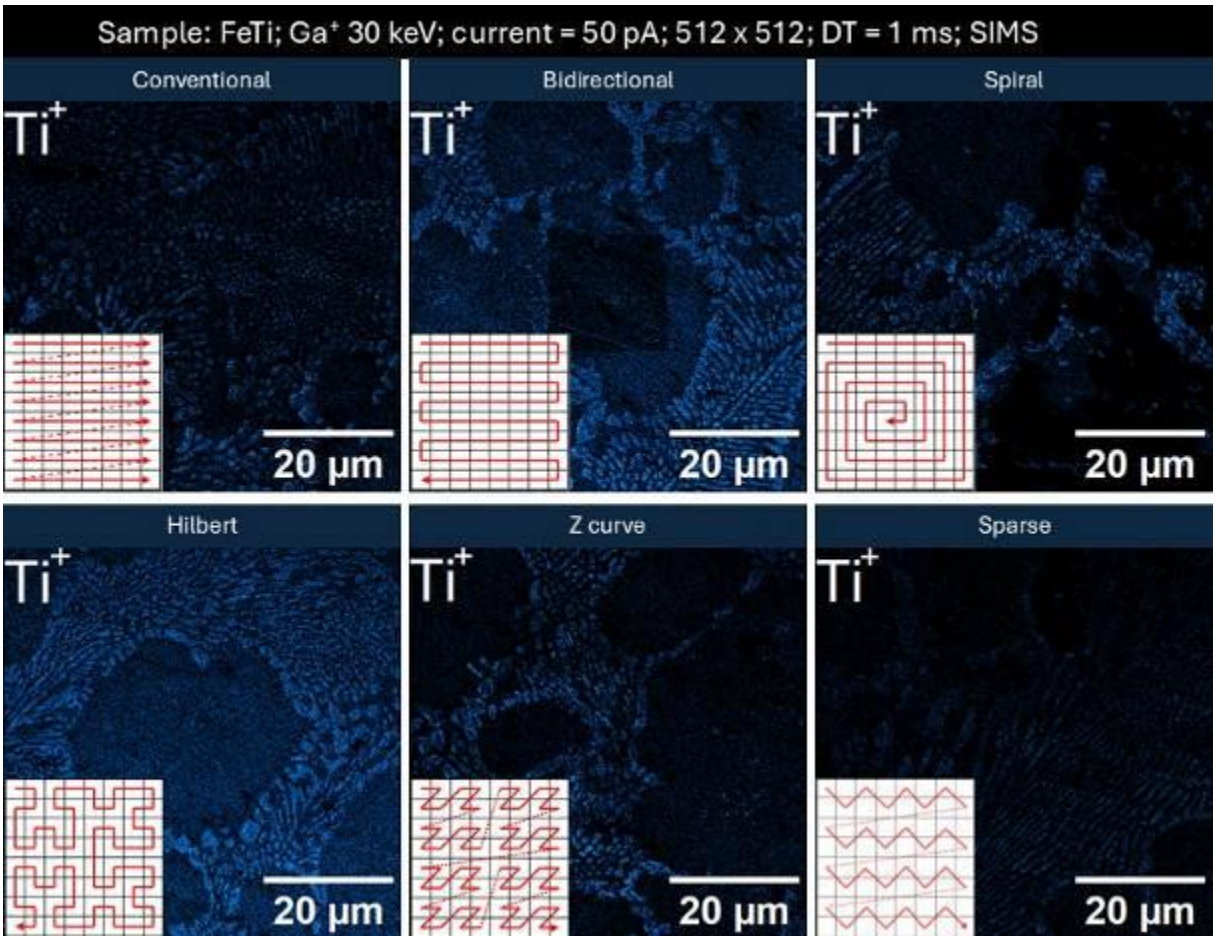
References

[1] De Castro, O., Audinot, J. N., Hoang, ... & Wirtz, T. (2022). Magnetic sector secondary ion mass spectrometry on FIB-SEM instruments for nanoscale chemical imaging. Analytical chemistry, 94(30), 10754-10763.

[2] Nicholls, D., Wells, J., Stevens, ... & Browning, N. D. (2022). Sub-sampled imaging for STEM: Maximising image speed, resolution and precision through reconstruction parameter refinement. Ultramicroscopy, 233, 113451

[3] Dahmen, T., & Trampert, P. (2019). Sparse and adaptive sampling in scanning electron microscopy. Microscopy and Microanalysis, 25(S1), 29-30.

Fig. 1



IM3.06
In situ Cryo-FIB/TKD validation of vitrified versus crystalline ice for Cryo-TEM and atom probe tomography applications

E. V. Woods[1], C. Wigge[2], T. M. Schwarz[1], B. Gault[1,3]

[1]Max-Planck-Institute for Sustainable Materials, MA, Düsseldorf, Germany
[2]Electron Imaging Solutions, Düsseldorf, Germany
[3]Imperial College London, Department of Materials, Royal School of Mines, London, United Kingdom

Introduction: One challenge for biological specimen preparation in cryo-transmission electron microscopy (cryo-TEM) and atom probe tomography (APT) is preserving vitreous (amorphous) ice on TEM grids and in APT specimens to avoid artifacts caused by ice crystallization (1–4). Historically, this preservation could only be verified in a TEM by screening initial lamellae before returning the specimens to the focused ion beam/scanning electron microscope (FIB/SEM) for further processing, as in-situ assessment of crystallinity within the FIB/SEM was unfeasible (3,4,5–9).

Objectives: This study aims to develop and validate an in-situ method for verifying the ice state using direct electron detector (DED)-based transmission Kikuchi diffraction (TKD) within the FIB/SEM. Specifically, we intend to:

Establish optimized, non-damaging TKD imaging parameters to avoid heating and crystallization. Integrate TKD into standard cryo-TEM lamella preparation workflows without compromising specimen integrity. Validate that TKD does not induce damage or crystallization on TEM grids or APT specimens, using subsequent cryo-TEM imaging and APT analysis. Assess the feasibility of applying TKD on fully sharpened APT specimens without causing bending or damage.

Materials and Methods: Experiments were conducted using a Thermo-Fisher FIB/SEM equipped with an EDAX DED EBSD/TKD detector and an Aquilos cryo-stage, alongside a Thermo-Fisher cryo-TEM system. Specimen handling utilized cryogenic vacuum transfer systems, including a glovebox and specialized shuttles. Vitrified biological specimens, such as sea urchin sperm, served as model systems. Beam parameters were carefully optimized to prevent any risk of inducing crystallinity while still providing reliable TKD signal detection across varying ice thicknesses.

Results: Our findings indicate that a lack of TKD signal reliably indicates amorphous ice. Optimized imaging parameters enabled clear differentiation between vitrified and recrystallized ice. APT analysis detected subtle structural differences between the two ice states, and cryo-TEM imaging of TKD-examined lamellae revealed no significant artifacts due to SEM beam exposure. However, performing TKD on fully sharpened APT specimens led to bending and localized damage, highlighting limitations when applying the technique at later stages of specimen preparation.

Conclusion: DED-TKD offers a promising in-situ approach for verifying ice state during cryo-preparation, potentially eliminating the need for separate TEM screening steps. Our combined APT and cryo-TEM analyses confirm that this method reliably distinguishes between amorphous and crystalline ice. When integrated into routine cryo-FIB workflows, TKD can enhance quality control and reproducibility in specimen preparation for both cryo-TEM and APT. Nonetheless, caution is warranted when applying TKD to fully processed APT specimens due to observed beam-induced deformation.

References

J. Dubochet, *Methods Cell Biol.* 7 (2007) 79.

J. Dubochet et al., *Q. Rev. Biophys.* 129 (1988) 21.

R.F. Thompson et al., *Methods* 3 (2016) 100.

B.A. Lucas, N. Grigorieff, *Proc. Natl. Acad. Sci. U.S.A.* e2301852120 (2023) 120.

E.V. Woods et al., arXiv:2404.12894 [physics.bio-ph] (2024).

E.V. Woods et al., *Microsc. Microanal.* 1172 (2024) 30.

E. Woods et al., *Microsc. Microanal.* 1992 (2023) 29.

B. Bammes, R. Bilhorn, *Microsc. Microanal.* 1186 (2020) 26.

A.J. Wilkinson et al., *Phys. Rev. Lett.* 065506 (2013) 111.

IM3.P01
Transmission diffraction and 4DSTEM in a SEM with pixelated detectors and custom sample stages – Development and applications

J. Müller[1], C. T. Koch[1]

[1]Humboldt University of Berlin, Berlin, Germany

Introduction

Four-dimensional scanning transmission electron microscopy (4DSTEM) provides structural information from thin electron-transparent sample areas on the Å to µm scale by recording a transmission diffraction pattern at each raster position [1]. Traditionally used in STEMs, 4DSTEM can also be employed in SEMs by placing a pixelated detector below the sample, similar to transmission Kikuchi diffraction (TKD) but with a larger camera length. 4DSTEM-in-SEM leverages the SEM's ease of operation, cost-effectiveness, large sample chamber, and wide field of view in the mm range while maintaining high spatial resolution in the nm and even sub-nm regime.

The required sample thickness for this method, using up to 30 keV electrons in SEMs, is in the range of a few tens of nm, which is accessible with common sample preparation techniques. Based on the inelastic mean free path (IMFP), the sample thickness should be approximately 4 times thinner when using 30 keV electrons compared to 200 keV electrons to acquire similar-looking diffraction patterns [2]. Additionally, due to stronger scattering at low electron energies, 4DSTEM-in-SEM is well-suited for investigating thin materials like 2D materials and low-density materials [3].

Objectives

Our goal is to demonstrate the feasibility of 4DSTEM-in-SEM for characterizing low-dimensional and thin bulk samples to expand the application range of SEMs while offering a wide range of customizability.

Materials & Methods

We developed 4DSTEM-in-SEM setups for our Zeiss GeminiSEM 500 using a fiber-coupled scintillator-based camera (Fig. 1) and a Timepix3 direct detector (Fig. 2) [3,4]. Both detectors can be used with a hexapod stage, allowing sample tilting and shifting relative to the electron beam (Fig. 1, 2), mimicking STEM double tilt holders. We also developed a sample stage mounted below the pole piece for only sample shifts (Fig. 2). These setups feature a variable camera length of up to 93 mm [3,4].

The pixelated detectors are hardware synchronized with the SEM and its electrostatic beam blanker using our in-house scan generator to maximize acquisition speeds and expose the sample only when detectors are recording. The scan generator also records the SEM detectors (e.g. SE signals) during the 4DSTEM-in-SEM dataset acquisition.

Results

We demonstrated 4DSTEM-in-SEM by mapping the in-plane orientation of an entire TEM grid covered with MoS_2 exfoliated by gold-mediation, using the SEM's large field of view to show its single crystallinity (Fig. 3). We also mapped the orientation and coverage of both constituents of a C60/MoS_2 van der Waals heterostructure (Fig. 3).

The Timepix3 detector enables dwell times below 2 µs at beam currents of approximately 8 pA, achieving acquisition speeds exceeding 500,000 frames per second and rivaling dedicated STEM detectors while recording diffraction patterns in a pixelated manner (Fig. 4).

Conclusion

4DSTEM-in-SEM expands the capabilities of SEMs with transmission diffraction, similar to TKD, enabling TEM grid screening, material characterization, and method development.

[1] C. Ophus. "Four-Dimensional Scanning Transmission Electron…". doi: 10.1017/S1431927619000497
[2] H. Shinotsuka, et al. "Calculations of Electron Inelastic Mean Free Paths…". doi: 10.1002/sia.5789
[3] J. Müller, et al. "Probing Crystallinity and Grain Structure…". doi: 10.1002/pssa.202300148
[4] J. Müller. "Transmission diffraction in a scanning electron...". doi: 10.18452/30820

Fig. 1

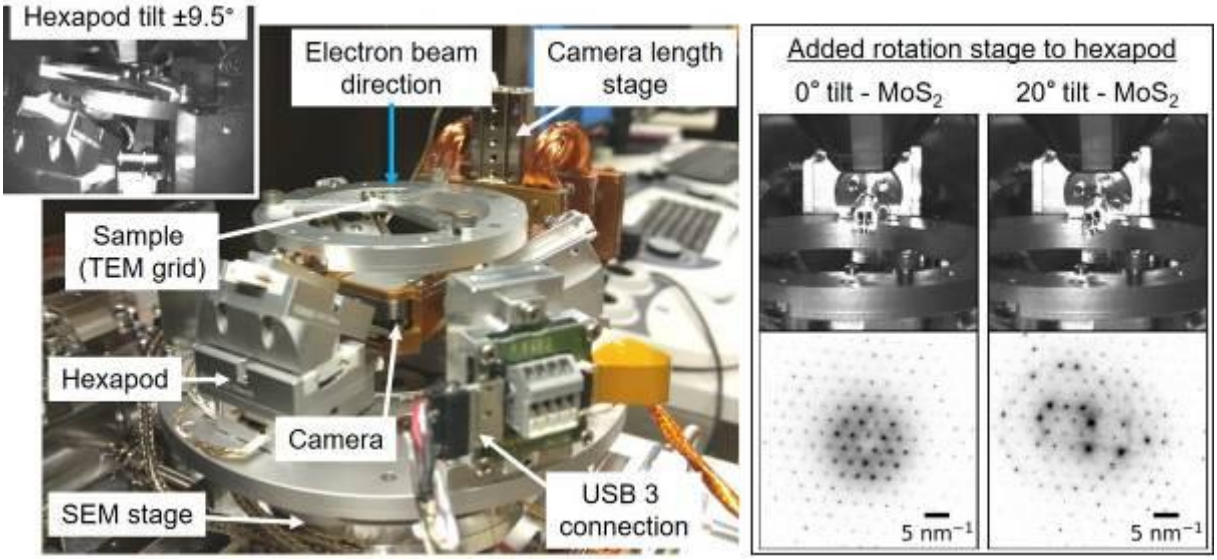


Fig. 2

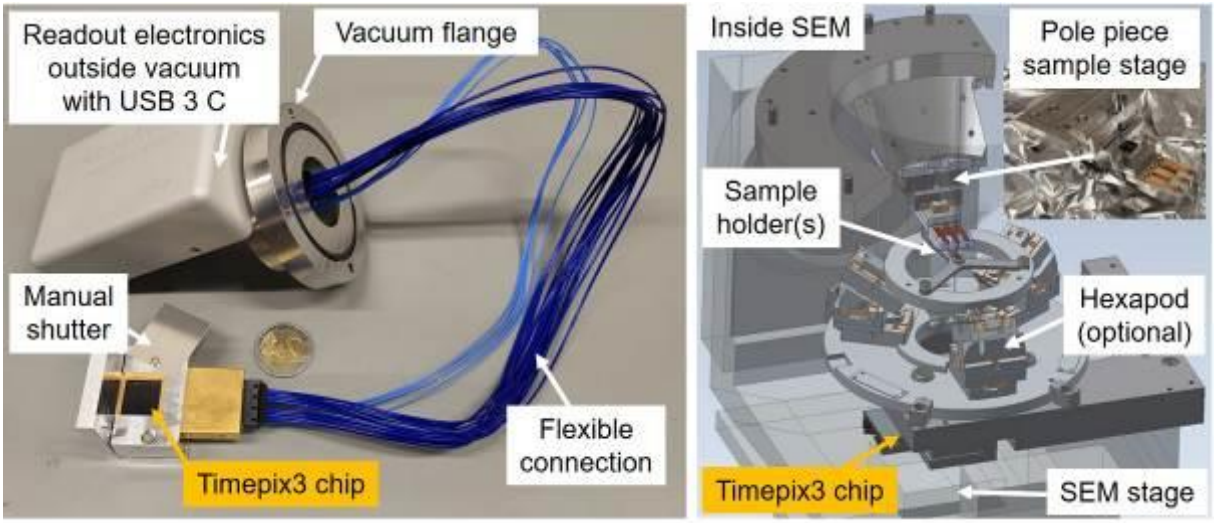


Fig. 3

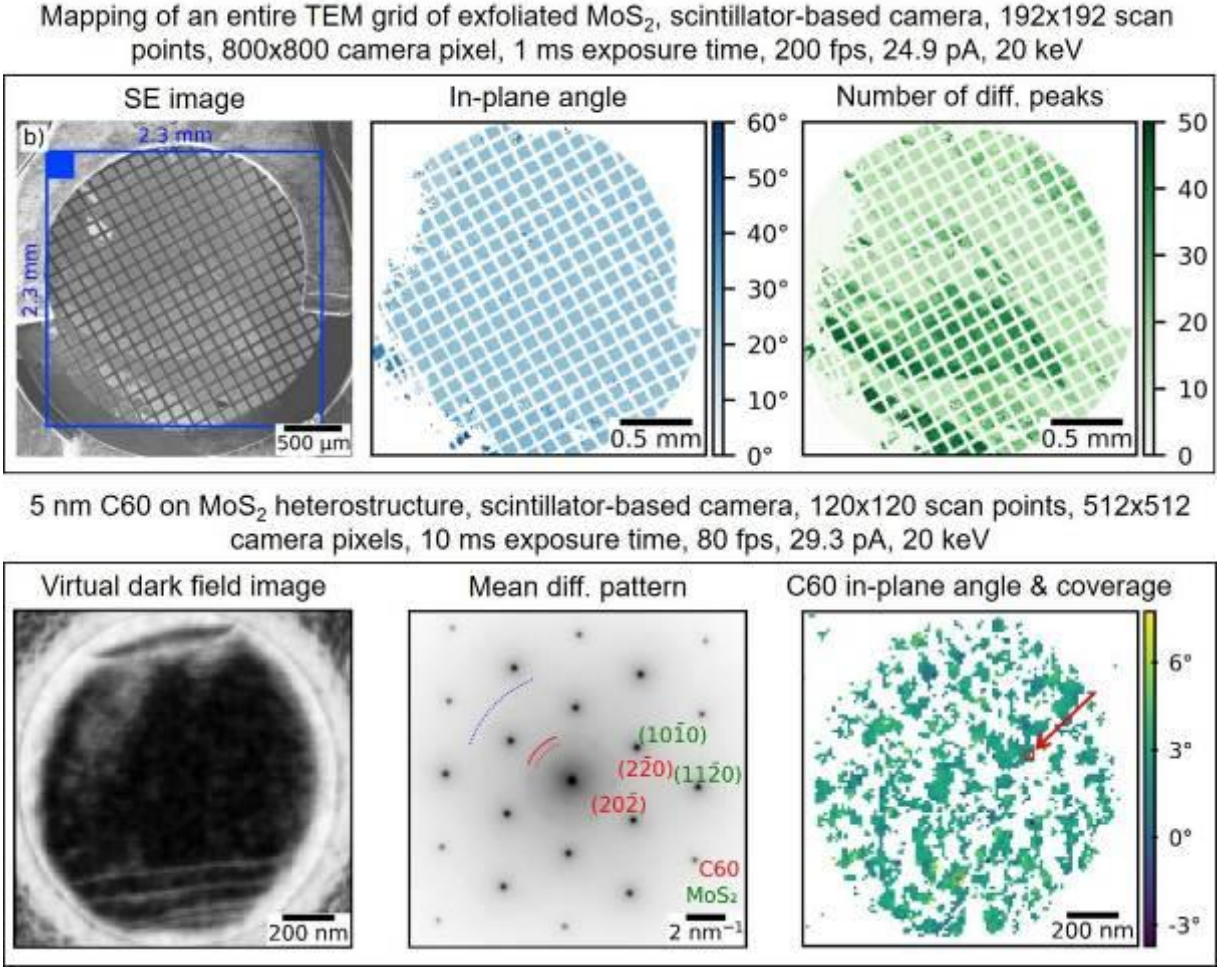
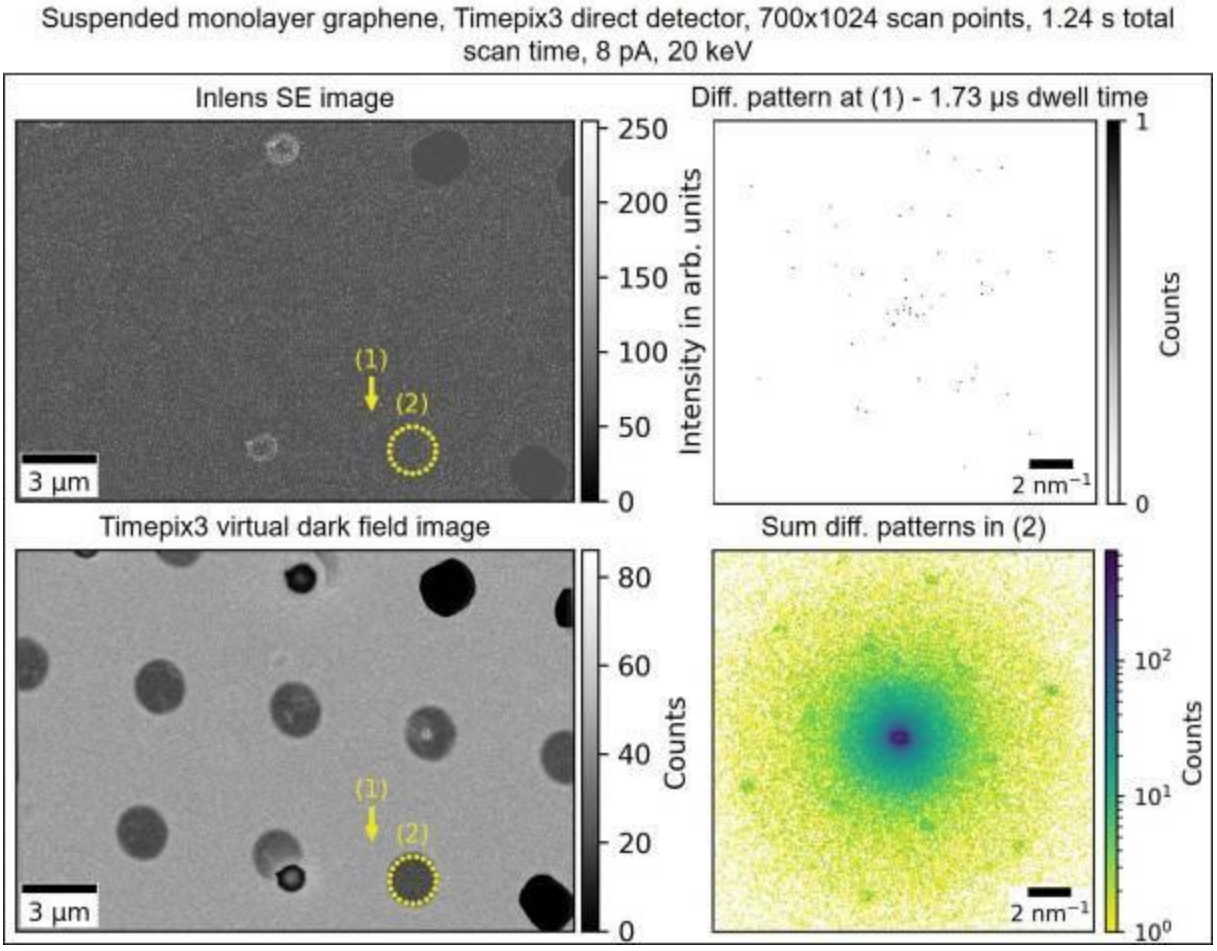

Mapping of an entire TEM grid of exfoliated MoS_2, scintillator-based camera, 192x192 scan points, 800x800 camera pixel, 1 ms exposure time, 200 fps, 24.9 pA, 20 keV
SE image
In-plane angle
Number of diff. peaks
b)
2.3 mm
2.3 mm
500 µm
0.5 mm
0.5 mm
60°
50°
40°
30°
20°
10°
0°
50
40
30
20
10
0
5 nm C60 on MoS_2 heterostructure, scintillator-based camera, 120x120 scan points, 512x512 camera pixels, 10 ms exposure time, 80 fps, 29.3 pA, 20 keV
Virtual dark field image
Mean diff. pattern
C60 in-plane angle & coverage
200 nm
$(10\bar{1}0)$
$(2\bar{2}0)$
$(11\bar{2}0)$
$(20\bar{2})$
C60
MoS_2
2 nm^{-1}
200 nm
6°
3°
0°
-3°

Fig. 4


Suspended monolayer graphene, Timepix3 direct detector, 700x1024 scan points, 1.24 s total scan time, 8 pA, 20 keV
Inlens SE image
Diff. pattern at (1) - 1.73 µs dwell time
Intensity in arb. units
Counts
Timepix3 virtual dark field image
Sum diff. patterns in (2)
(1)
(2)
3 µm
2 nm⁻¹

IM3.P02
Optimizing FIB-SEM serial sectioning tomography towards 24-Hour time-to-results

B. Winiarski[1], P. Barthelemy[2], C. Jiao[3], J. Giesebrecht[4]

[1]Thermo Fisher Scientific, Brno, Czech Republic
[2]Thermo Fisher Scientific, Lexington, KY, United States
[3]Thermo Fisher Scientific, Eindhoven, Netherlands
[4]ZIB, Berlin, Germany

The performance and durability of solid oxide fuel cell (SOFC) electrodes are closely tied to their porous microstructure and its evolution over the cell's lifetime. Comprehensive characterisation of three-dimensional (3D) microstructures is essential for optimising SOFC electrodes. FIB-SEM tomography has become a key technique for 3D reconstruction of SOFC microscopic structures with nanometric resolution (voxel size: ~20-40 nm³). However, Ga-based FIB-SEMs are limited to small material volumes, which may not be representative of the entire cell, especially in the latest designs of graded SOFCs. Plasma FIB-SEM (PFIB-SEM) microscopes, offering access to material volumes thousands of times larger than traditional FIB-SEMs, along with automated serial sectioning, multidetector SEM imaging techniques, and SEM auto-functions, provide an ideal platform for investigating SOFC microstructures and other porous materials.

The porous microstructure of SOFCs presents challenges during data collection and image processing, such as 'FIB curtaining artefacts' and the 'back-pore issue.' These are mitigated by pressure-filling pores with epoxy resins and using the rocking polish technique. However, small, disconnected pores can still cause electron charging effects and hinder accurate segmentation. Deep Learning (DL) U-Net-based segmentation methods have improved this, but electron charging can still obscure SEM images, potentially misleading the assessment of reaction site density. Once segmented, serial-sectioned SEM images are post-processed to create a 3D digital representation and determine gas and charge transport properties, e.g. tortuosity and triple-phase boundaries (TPBs).

This study presents a comprehensive characterisation workflow from 3D microstructure analysis using PFIB-SEM to thorough quantification, demonstrated through the examination of a freshly prepared SOFC. Using the PFIB-SEM platform and automated serial sectioning software (ASV5), we collected a large 3D volume of 180 × 150 × 30 µm³ with a voxel size of 32 × 32 × 50 nm³. The Xe+ PFIB serially sections specimens while SEM images are acquired using a through-lens detector for secondary electrons and a concentric backscattered electron detector. Optimised SEM imaging conditions maintain consistent imaging throughout the ASV run.

Automated Avizo recipes were developed for data processing and analysis, ensuring reliable data quantification, 3D visualisation and report generation. The image stack doublets were denoised and segmented into Ni, YSZ, and Voids using DL models, distinguishing percolated and non-percolated phases. The recipes calculate spatial parameters such as tortuosity, TPBs, phase volume fractions, and surface area/volume ratios. Recent advancements in SEM image post-processing and denoising using DL algorithms in Avizo software have reduced SEM imaging time by 50%, significantly decreasing total acquisition time.

This study describes a comprehensive characterisation workflow leveraging deep-learning predictions, covering the entire spectrum from 3D microstructure analysis using PFIB-SEM to thorough quantification. Advanced SEM imaging techniques and recent advancements in image processing streamline the characterisation process, significantly reducing overall workflow execution time, suggesting that a 24-hour turnaround is attainable.

IM3.P03
Advanced nanoscale analysis with ion microscopy and SIMS for life science and materials science applications

T. Richter[1], J. Stodolka[1], P. Gnauck[1], A. Ost[1]

[1]Raith Group, Dortmund, Germany

Gaining nanoscale insights into material composition and biological systems requires advanced characterization techniques with optimal spatial resolution and sensitivity [1,2]. The integration of Focused Ion Beam (FIB) systems with high-performance magnetic sector Secondary Ion Mass Spectrometry (SIMS) provides an advanced method for isotopic compositional analysis for depth profiling and high-resolution 2D and 3D chemical imaging.

A crucial innovation driving this capability is the Liquid Metal Alloy Ion Source (LMAIS) technology [3], particularly the GaBiLi source, which enables the simultaneous emission of multiple ion species. The downstream Wien filter allows rapid and precise switching between heavy ions (e.g., Bi^+) for efficient material sputtering and light ions (e.g., Li^+) for high-resolution imaging with minimal sample damage. By selecting the optimal and appropriate ion species for different materials, analytical performance is significantly enhanced. Smart workflows utilize lithium ion analysis for best spatial resolution, while Bi milling allows sputter efficiency, enabling fast and accurate 3D imaging [4].

The integrated magnetic sector SIMS unit includes a retractable secondary ion extraction and transfer optics, a magnetic sector for precise mass separation, and a focal plane detector, allowing for the simultaneous acquisition of complete mass spectra at each pixel within the rastered field of view (Figure 1). The combination of the smallest FIB probe size and an advanced detection system delivers unparalleled spatial SIMS image resolution below 20 nm with exceptional sensitivity.

Comprehensive sample information acquisition enables sophisticated data post-processing for correlative chemical and structural analysis. Additionally, a laser interferometer provides single-digit-nm precision for sample navigation and positioning, ensuring accurate targeting of regions of interest.

The powerful IONMASTER magSIMS platform unlocks new possibilities in life and materials science. In biological research, FIB-SIMS facilitates high-resolution chemical imaging in cell biology, allowing visualization of nanoscale distributions of nanoparticles and pharmaceuticals in tissues and cells. In materials science, this technology supports studies on critical compositional variations containing hydrogen and precise compositional mapping of functional materials, such as battery electrodes, and solid-state electrolytes.

This contribution presents the capabilities of this novel ion microscope and highlights applications demonstrating its outstanding resolution and sensitivity. The combination of FIB and magnetic sector SIMS represents a transformative tool for nanoscale analytics, advancing research in both life and materials sciences by expanding the frontiers of chemical imaging and structural characterization.

Fig. *1:* Schematic overview of the IONMASTER magSIMS system, consisting of a vertical FIB column equipped with a LMAIS and a compact SIMS unit with a magnetic sector for mass separation and a continuous focal plane detector

Fig. 2: SIMS images showing the Al-27 and Va-51 distributions of a biomedical implant obtained in positive SIMS mode.

Fig. 3: H distribution of the sample shown in (2) acquired in negative SIMS mode.

Fig. 4: Mouse gut cells with Al nanoparticles. Al nanoparticles (red) are clearly detected and resolved outside the cells showing the distribution around the cell body.

Fig. 1

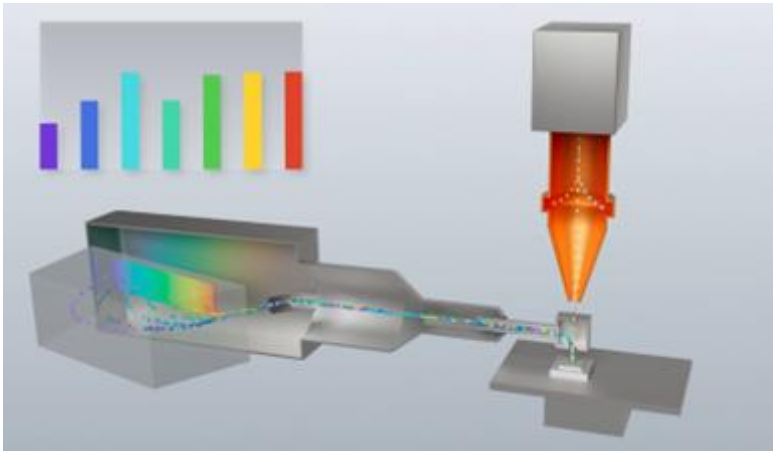


Fig. 2

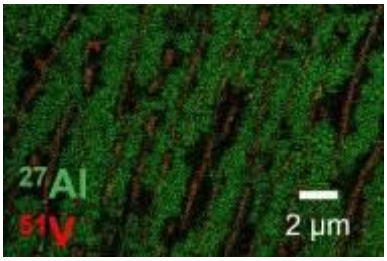


Fig. 3

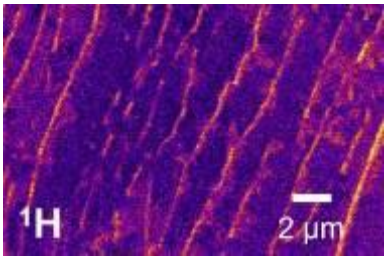
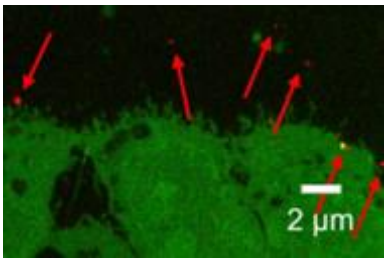


Fig. 4



IM3.P04
Enhancing cryogenic sample preparation to enable advanced battery studies in atom probe tomography

M. P. Singh[1], E. V. Woods[1], P. Yadav[1], B. Gault[1]

[1]Max-Planck-Institute for Sustainable Materials, Düsseldorf, Germany

Introduction

Atomic scale charcaterization of battery materials is challenging due to their senstivity to reactions and electron-beam irradiations, leading to inaccuracies in quantifying lithium (Li), carbon (C), and nitrogen (N). Atom probe tomography (APT) complements electron microscopy by enabling three-dimensional (3D) chemical mapping with equal sensitivity across all elements. And by employing cryogenic protocols, researchers can better preserve battery materials and gain more accurate atomic insights.

Objective

Our research aims to achieve high-precision understanding of LIBs using cryogenic APT. However, challenges include field-induced delithiation (deintercalation), premature sample failure due to weak grain boundaries, and the impact of porous structures. Preventing beam-induced damage during sample preparation is also critical. We address these challenges through innovative experimental designs and cryogenic focused ion beam (FIB) sample preparation techniques, gaining new insights into battery cathodes via APT. This presentation will cover encountered challenges, developed solutions, and obtained results.

Methods

We procured commercial NMC811 ($LiNi_{0.8}Co_{0.1}Mn_{0.1}O_2$) from Targray (Kirkland, Canada). Sample preparation utilized a Helios 5CX Ga dual-beam FIB instrument (Thermo-Fischer Scientific, Hillsboro, OR, USA). APT measurements were conducted using a local electrode atom probe (LEAP, Cameca Instruments Inc.), either a straight flight path (LEAP 5000XS) or a reflectron (LEAP 5000XR). Measurements were optimized as per the sample. Data reconstruction and analysis were carried out using AP Suite 6.1.

Results

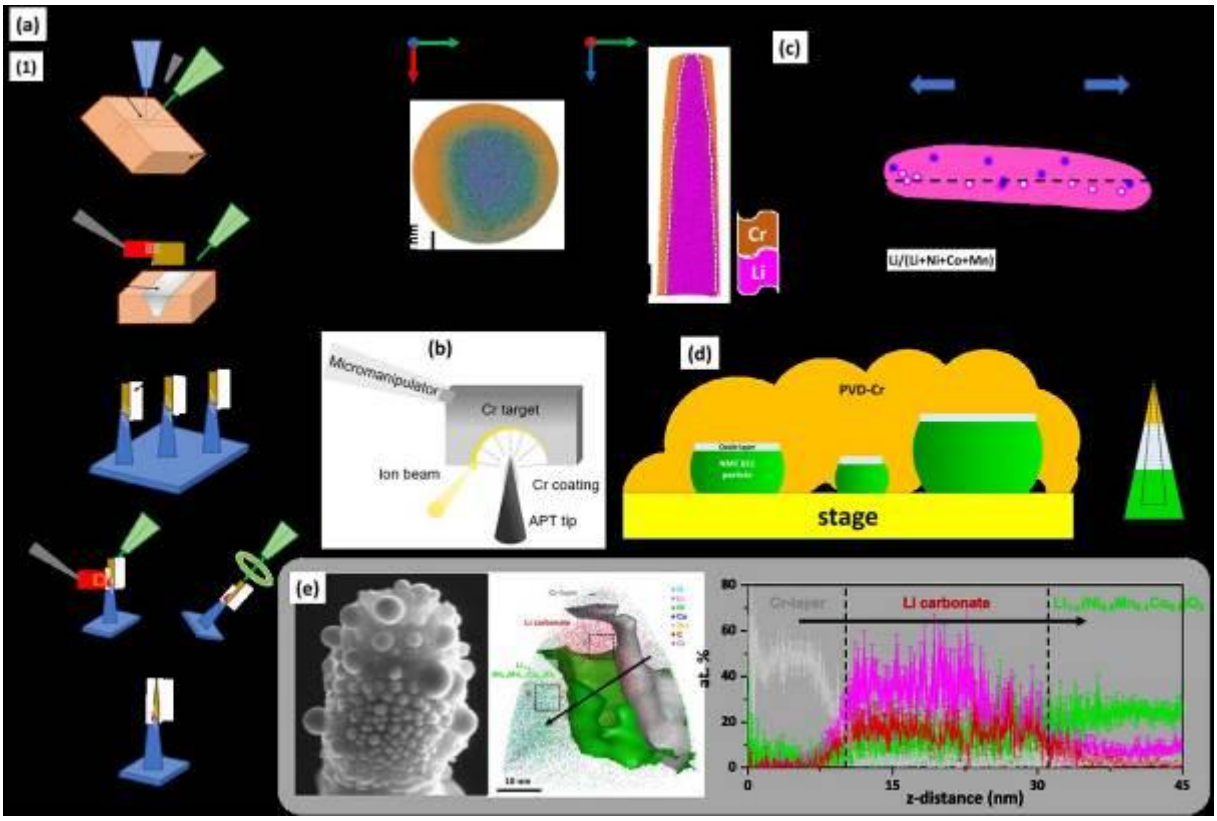
We have developed an innovative cryogenic specimen preparation technique for battery materials. This involves a novel "redeposition welding" method, which securely attaches APT specimens to Si micro-posts without requiring gas-injection system (GIS), see figure 1a [3]. We supplemented the technique with FIB-enabled, *in-situ* metal coating on the prepared APT specimens, see figure 1b [4]. These methods were applied successfully to study commercial materials like NMC811, LMO and cycled carbon fibers, with thin coatings proving effective in mitigating deintercalation, see figure 1c. This enabled the accurate Li quantification in battery materials using APT, serving as a valuable template for future battery investigation.

In the next study, we will explore how cryogenic APT workflows can easily study thin reactive layers formed on cathode particles exposed to ambient atmosphere, fig. 1d&e [5]. A similar approach can be applied to investigate thin secondary electrolyte (SEI) layers that forms on active materials in cycled batteries.

Conclusion

Facilitating battery studies using APT offer atomic scale understanding of Li segregation at defects, interfaces and the diffusional behavior of Li in the cycled LIBs. Cryo-preparation prevents beam damage, while metallic coating facilitates heat dissipation and provides mechanical support to the specimens against the Maxwell stresses generated by the applied field, a common cause of atom probe specimen failure. This approach provided high-yield, repetitive and precise compositional information across multiple samples. These procedures are further being used to study nanoscale compositional changes happening in the aged battery cathodes or anodes.

Fig. 1



IM3.P05
A novel adaptive carrier chip for *operando* Investigations of electronic devices

I. Häusler[1], T. Wagner[1], K. Elsner[1], S. Gaebel[2], J. Simke[3], H. Çelik[4], D. Berger[3], F. Hatami[1], M. Lehmann[4], C. T. Koch[1]

[1]Humboldt University of Berlin, Institute of Physics, Berlin, Germany
[2]Max-Born-Institut, B2: Imaging and Coherent X-rays, Berlin, Germany
[3]Technische Universität Berlin, Zentraleinrichtung Elektronenmikroskopie, Berlin, Germany
[4]Technische Universität Berlin, Institute of Optics and Atomic Physics, Berlin, Germany

Introduction

The availability of commercial in situ TEM holders has enabled new insights into externally switchable samples but has also introduced new challenges for sample preparation. In particular, the fabrication of electrically contacted TEM lamellae using FIB for in situ biasing experiments or operando investigations presents numerous obstacles. These include dramatically increased preparation times, geometric restrictions, electrical short circuits due to redeposition, and modifications of the electrical properties caused by ion implantation.

Objectives

This work introduces a novel carrier chip system that addresses the fundamental challenges of FIB-based sample preparation using adaptive freestanding electrodes in a vacuum (Fig. 1a), therefore enabling the rapid and reproducible fabrication of contacted TEM lamellae (Fig.1b). Specifically developed preparation routines for fabricating the carrier chips and streamlined, throughput-optimized FIB recipes are presented, offering the scientific community an accessible entry point into in situ electrical biasing TEM studies.

Materials & Methods

At the core of the self-designed carrier chip system is a freestanding gold short-circuit bridge, which can be precisely adapted to the geometric requirements of the sample or lamella using FIB milling. This approach produces freestanding electrodes in a vacuum (Fig.1a), enabling short-circuit-free preparation of a variety of device geometries, including planar, lateral, mesa, and VCSEL structures. To verify this concept, various nanodevices, such as an InGaP/GaP quantum dot LED in a mesa geometry, were prepared (Fig. 1b). Systematic investigations of the switching semiconductor nanodevices using off-axis electron holography (EH) and differential phase contrast (DPC), in combination with dedicated simulations and electrical characterizations, highlight the clear advantages of this novel system. These findings also underscore the remaining challenges in deriving quantifiable physical parameters from operando studies of electronic nanodevices, such as surface modifications and their correlated stray fields.

Results

The entire workflow for preparing contacted and reliably switching TEM samples was streamlined, reducing the preparation time to under five hours. Reconstructed phases and I-V characteristics of the

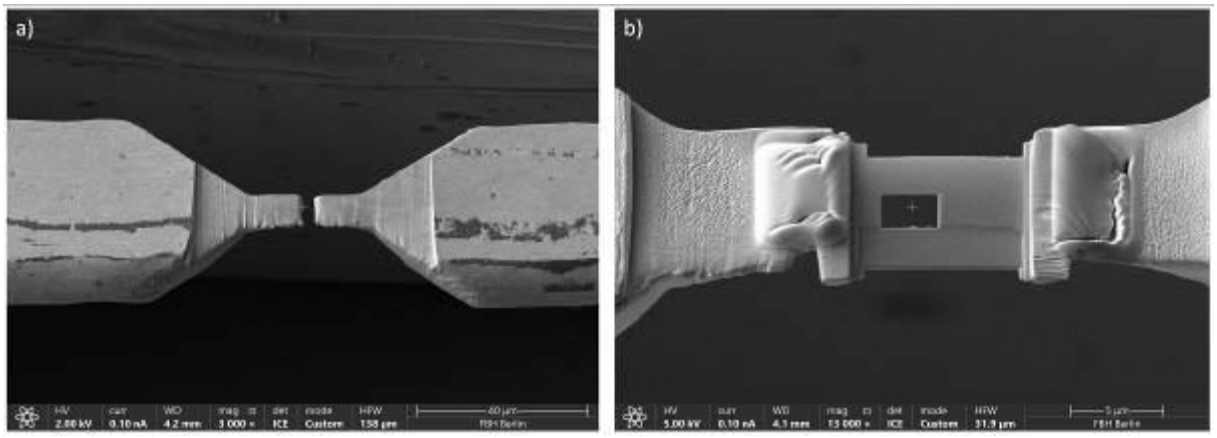
prepared lamella demonstrate the expected switching behavior of the quantum dot diode, proving the functionality of the developed system.

Conclusion

The adaptive carrier chip system introduced in this study represents a significant advancement in the preparation of contacted TEM lamellae for in situ electrical biasing experiments. Its efficient and reproducible workflow not only simplifies entry into operando TEM investigations but also broadens the range of possible applications, particularly for advanced device geometries. The demonstrated advantages of this system pave the way for more accessible, reliable, and high-throughput analyses of electronic nanodevices.

Fig. 1: FIB preparation of a contacted TEM lamella on the developed adaptive carrier chip. a) SEM image of the separated freestanding adaptive gold electrode of the developed carrier chip, modified via FIB ion milling to fit the dimensions of the extracted lamella. b) Contacted TEM lamella of an InGaP/GaP quantum dot LED device, featuring a reference window for improved EH accuracy.

Fig. 1



IM3.P06
4DSTEM in SEM measurements at low electron energy using a pixelated direct detector operated at room temperature

M. Huth[1], B. Eckert[1], A. Fram[1], P. Majewski[1], S. Aschauer[1], L. Strüder[2,3], H. Soltau[1]

[1]PNDetector GmbH, Munich, Germany
[2]University of Siegen, Physics, Siegen, Germany
[3]PNSensor GmbH, Munich, Germany

Four-dimensional scanning transmission electron microscopy (4D-STEM) imaging is a well-known technique in Transmission Electron Microscopy (TEM), increasingly applied to a wide range of materials. In a scanning electron microscope (SEM), detectors typically capture the emitted electrons from the sample surface. Using thin samples, scanning transmission measurements become possible using energies ranging from 30keV down to 0.5keV. Traditionally, single cell or multi-channel STEM diodes are used to collect STEM images at a fixed distance below the sample, with no optical lenses below the sample, measuring basic bright field (BF) or differential phase contrast (DPC) signatures.

To expand the applications and analytical capabilities of SEM we propose the conventional STEM diode are replaced with a pixelated detector. This approach mitigates the inherent alignment and positioning problems in lens less systems, as the spatially resolved images allow to determine the diffraction pattern geometry. The SEM, requiring high sensitivity and low noise and operation at room temperature, essential for rapid sample exchange and avoiding condensation, despite the challenge that higher temperatures typically increase readout noise.

We used our pixelated pnCCD (S)TEM camera [1] with 264x264 pixels to perform 4D STEM measurements in a SEM using up to 7500 frames per second. We present measurements taken at a temperature of stabilized +25°C in a Tescan Mira3 SEM.

To detect electron energies as low as a few keV, the readout noise needs to be very low and the detector entrance window has to be designed accordingly. To address the effects of the various insensitive layers on the detector, we present simulations showing the impact of the measurable signal for different electron energies.

The simulation results (Fig.1) show a strong dependence of the detector response on small variations of the insensitive layers on the detector entrance area versus the incident electron energy. From that a very precise mean detectable energy per electron can be extracted, a number which is key to determine the number of incidents electrons per pixel accurately.

Having spatially resolved diffraction patterns also allows full geometric reconstruction. The sensitivity to see single electron tracks even at low energies (Fig.2) is especially useful when working with sensitive samples and in the low dose regime. Additionally, employing flexible virtual apertures can create a variety of different contrasts to highlight certain characteristics.

The ambitious goal of transmission imaging in a SEM with low energy electrons at room temperature over a wide range of intensities can be achieved with pixelated direct detectors. Combining simulation results and measurements in varying illumination conditions can relate the observed detected signal to the precise number of incident electrons hitting the detector using smart counting algorithms.

[1] H. Ryll et al., "A pnCCD-based, fast direct single electron imaging camera for TEM and STEM" in Journal of Instrumentation, vol. 11, no. 04, P04006, Apr 2016, doi: 10.1088/1748-0221/11/04/P04006

Fig. 1 Detector collection efficiency (DCE) versus the electron energy for different entrance window geometries.

Fig. 2 Diffraction patterns measured in transmission at different locations on a Carbon nanotube sample at 5keV electron energy. The challenge is to image the complete intensity range from diffraction peaks to single electron traces.

Fig. 1

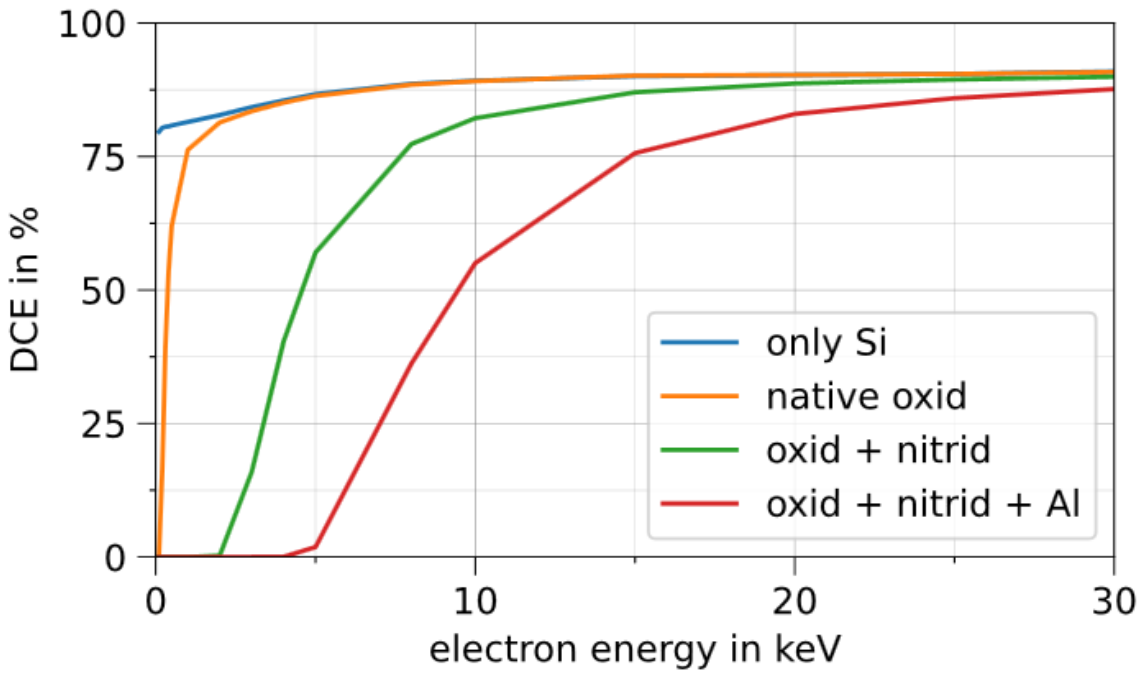
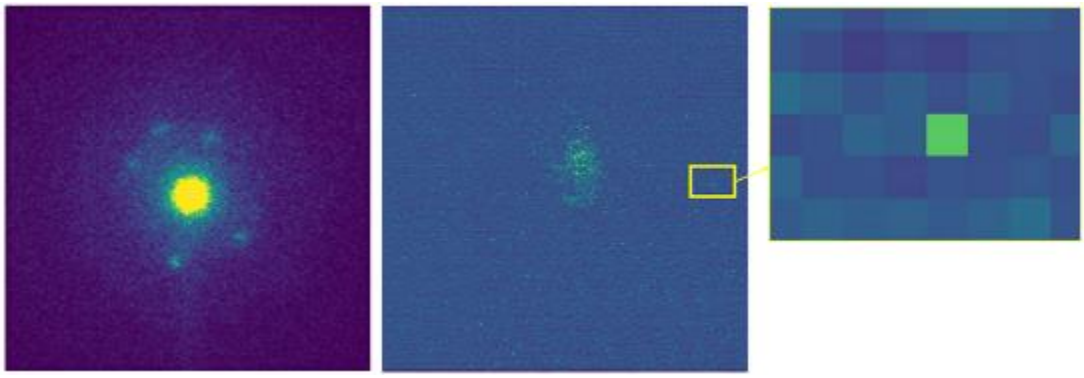


Fig. 2



IM3.P07
Electrostatic multipolar objective lens for plasma FIB

L. Berdou-Durrieu[1,2], J. B. Mellier[2], J. B. Fay[2], O. Salord[2], M. Reveillard[2], B. Warot-Fonrose[1], M. Viteau[2], F. Houdellier[1]

[1]CEMES-CNRS, Toulouse, France
[2]OrsayPhysics, Fuveau, France

Focused Ion Beam (FIB) columns are nowadays an indispensable high-precision milling tool used in different research fields such as the integrated circuits industry [1]. Thus a high current is a necessary quality to etch quicker the sample. For that, thanks to a higher sample current (up to 3µA), plasma sources are preferred to Gallium Liquid Metal Ion Sources (LMIS), the historical sources used for FIB columns (with a sample current up to 100nA). However, using plasma sources brings its own set of constraints. Indeed, the beam is larger and could fill the objective lens depending on the current requirements. Thus the contribution of the spherical aberration is important on the spot size.

A solution would be to increase the diameter aperture of the Einzel lens used for the objective lens. However, due to the Einzel lens's symmetry, this solution is technically complex to set up (high potentials are needed to maintain small working distances). We chose instead to investigate innovative optics based on multipole components, such as the solution proposed by Okayama-san *et al.* [2] [3].

We developed a new mechanical design for the objective lens, with a dedicated electronics and an associated software. We used homemade Python scripts to calculate the paraxial properties of our system (see Figure 1.a)) as well as the SIMION software to visualize real ions trajectories. First spots were obtained with this new column design (see Figure 1.b)).

This new design for an objective lens based on a quadrupoles solution for a FIB column presents some encouraging initial results, that we will present in more detail. We will discuss the spots we made and the issues we had to face with this first prototype.

Figure legends:

Figure 1: a) Marginal rays in sagittal and tangential directions for quadruplet quadrupoles (D: Defocus / F: Focus). b) Probe shape obtained with the new column design (30keV, 20s, D100µm, 619pA, FOV 7.75µm).

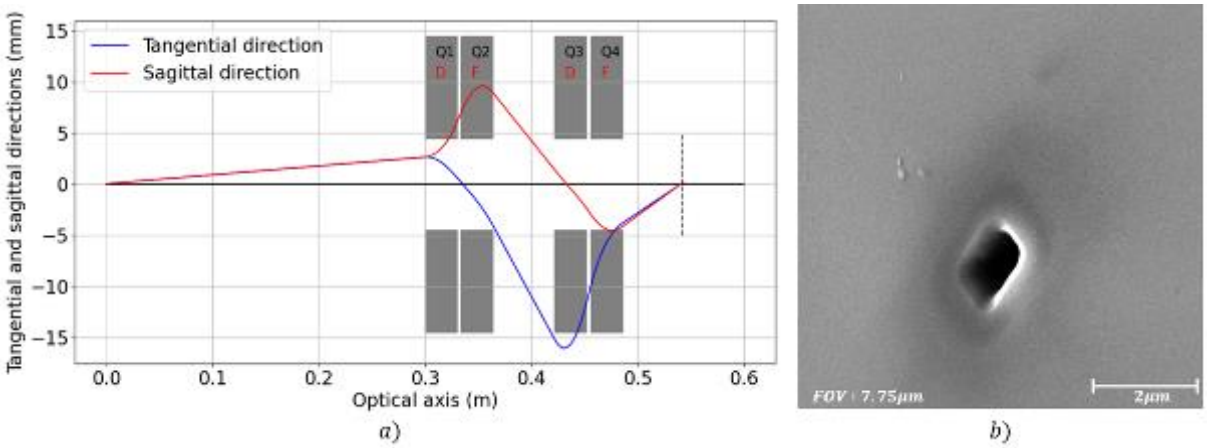
References:

[1] J. Orloff, ed., Handbook of charged particle optics. Boca Raton: CRC Press/Taylor & Francis, 2nd ed ed., 2009.

[2] S. Okayama and H. Kawakatsu, "A new correction lens," Journal of Physics E: Scientific Instruments, vol. 15, pp. 580–586, May 1982.

[3] S. Okayama and Y. Sugiyama, "High-Precision Quadrupole Correction Lens for Ion-Beam Focusing: Design and Test of Multistage Self-Aligned Quadrupole Correction-Lens System," Japanese Journal of Applied Physics, vol. 51, p. 026702, Feb. 2012.

Fig. 1


Tangential direction
Sagittal direction
Q1
D
Q2
F
Q3
D
Q4
F
Tangential and sagittal directions (mm)
15
10
5
0
−5
−10
−15
0.0
0.1
0.2
0.3
0.4
0.5
0.6
Optical axis (m)
FOV : 7.75μm
2μm

a) *b)*

IM3.P08
Upgrading an analytical SEM for metrology of nanostructures

S. Bauerdick[1], A. Peyyety[1], P. Weber[1], M. Chahid[2], Z. Benes[2]

[1]GenISys GmbH, Unterhaching, Germany
[2]Ecole Polytechnique Fédérale de Lausanne, Lausanne, Switzerland

Introduction

Scanning Electron Microscopes (SEM) are employed for a wide range of applications. Analytical material investigations and dimensional measurements are applied to raw materials, life science, and advanced material science. Another increasingly important area is lithography and nanofabrication, calling for SEM-based metrology. Optimization and monitoring of nano patterning processes require calibration and modeling using sophisticated test patterns for different materials, doses, densities, thicknesses, or critical dimensions (CD). Pattern transfer by different etching processes needs to be checked across chips and wafers. In nano scale research & development or device prototyping, analytical SEMs are used [1] instead of sophisticated and highly automated (but inflexible and costly) CD-SEMs in high-volume production [2]. While the versatility of a conventional SEM is important for covering various applications, it only provides manual and user-dependent measurements of CDs. The demand for analyzing large areas and large numbers of structures requires more advanced and automated SEM metrology. Finally, such capabilities would be beneficial for meta materials/ devices and 2D materials applications.

Objectives

We explored both SEM image analysis as well as add-on automation capabilities for different applications in nanofabrication. The target is to keep the versatility of the SEM tool and still enable it with automated metrology. Here, we investigate the scanning and measurements functionality with various use cases. Moreover, we analyze the corresponding limitations of a conventional SEM such as stage accuracy, drift, or focus correction and discuss approaches to overcome those.

Methods

We use an analytical Scanning Electron Microscope (SEM, ZEISS Gemini 550 L) and combine it with an add-on package for metrology (hardware for scanning and I/O"s, software for image scanning, analysis and metrology, GenISys InSPEC, Fig. 1). This setup enables navigation, image acquisition, shape detection, measurements, data processing, display, and export. The image scanning has advanced control over scan directions/ strategies and the analysis employs algorithm-based contour detection. Since the image acquisition is done in real-time via a direct hardware scan interface, image corrections and auto-focus are possible. Additionally, we implemented techniques to enhance positioning accuracy through image matching, reference points, and multiple automatic alignments.

Results & Conclusion

The proposed setup is applied to use cases in electron beam lithography, optical lithography, and plasma etching/ pattern-transfer steps. We present different examples for large area metrology with automated scanning and measurements showing the desired capabilities based on a conventional SEM. The results cover calibration patterns, test patterns, and routine checks for nanofabrication processes. Data are summarized in data tables or diagrams and extracted feature contours analyzed, e.g. in process variation plots (Fig. 2). This provides more automated data collection, improved data consistency, and higher SEM tool utilization. Strategies to compensate for SEM tool limitations are basically working but require more testing and improvements. Other next steps include extending the measured structures towards meta and 2D materials.

[1] J. A. Liddle, Nanoscale, 2011,3 , 2679

[2] T. Iwamatsu, J. Vac. Sci. Technol. B 19 (2001) 1264

Fig. 1

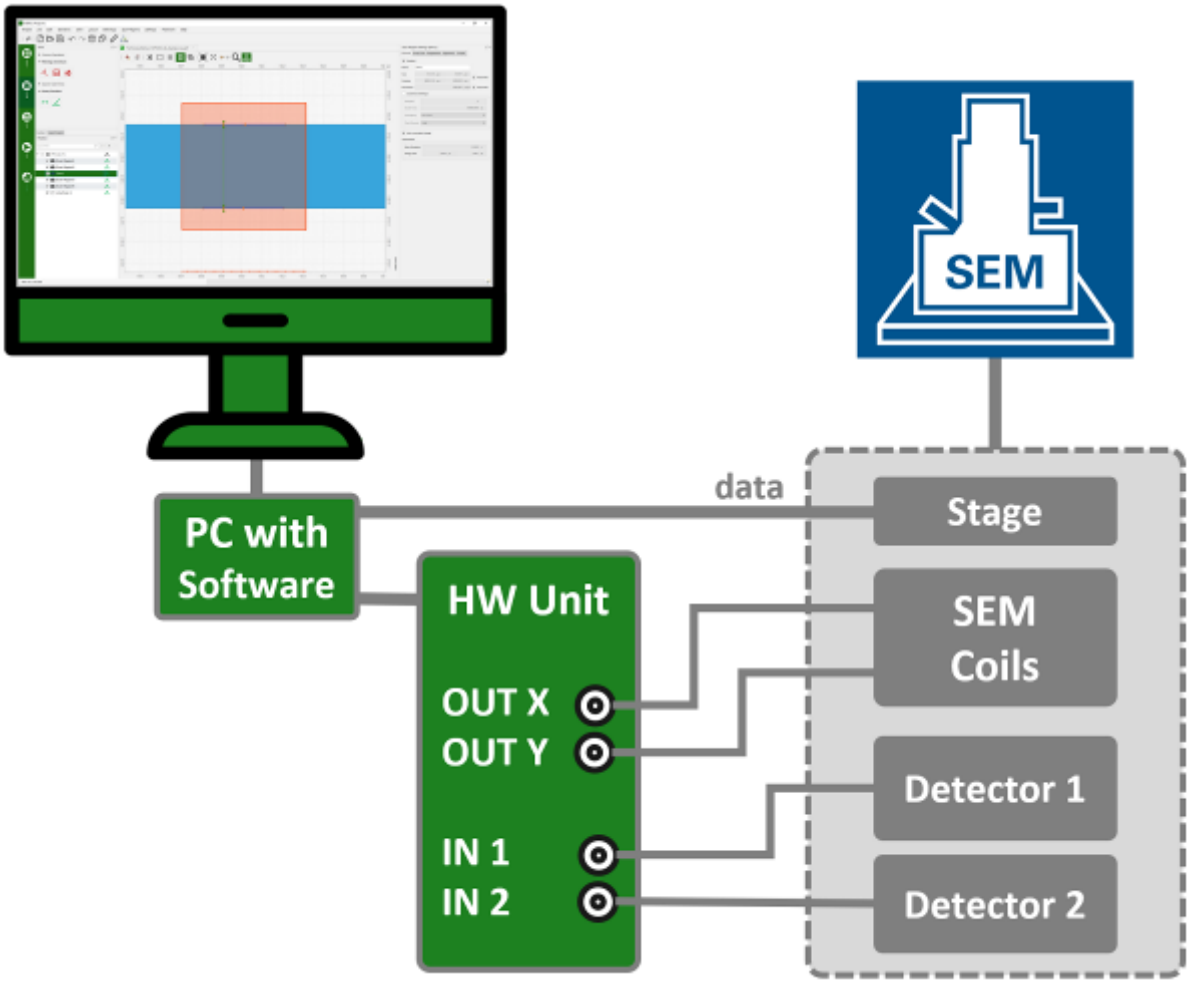
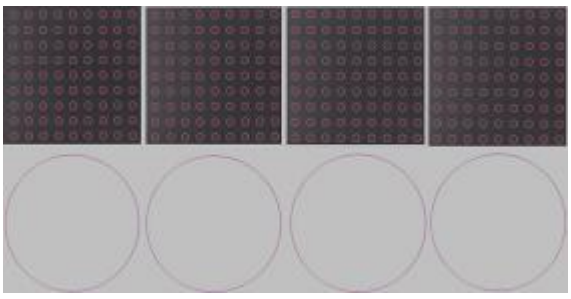


Fig. 2



IM3.P09
Probing the work function of catalytic platinum by energy band-pass filtered secondary electrons

E. Müller[1], A. Böttcher[2], Y. M. Eggeler[1,3,4]

[1]Karlsruhe Institute of Technology, Laboratory for Electron Microscopy, Karlsruhe, Germany
[2]Karlsruhe Institute of Technology, Institute of Physical Chemistry, Karlsruhe, Germany
[3]Karlsruhe Institute of Technology, 3DMM2O - Cluster of Excellence (EXC-2082/1 – 390761711), Karlsruhe, Germany
[4]Karlsruhe Institute of Technology, TrackAct (SFB1441, Project-ID 426888090), Karlsruhe, Germany

Work function (WF) is the energy needed to remove an electron from the material surface and is important in electrocatalysis [1]. The WF also determines the yield of secondary electrons (SE) which escape from irradiated samples. Different operational modes of the SE detectors allow to obtain the SE energy spectrum [2] and to draw conclusions related to the WF [3].

In this work we determine the WF for different oriented crystalline catalytic Pt by using the energy selective band of the SE detector and small voltage steps of sample biasing.

Thin Pt layers on Si/ SiO_2/graphene layers were dewetted at high temperature > 700 °C. The resulting Pt islands (Fig. 1a) were analyzed in a FEI DualBeam Helios G4 by SE imaging with the True-the-Lens detector (TLD). To collect the majority of the emitted SE, a 3 keV primary electron beam was used in the immersion mode of the objective lens at a working distance of 2 mm [4].

Sample biasing was applied to shift the SE peak through the detection band of the TLD. Fig. 1b shows the SE energy distribution calculated for a WF=5.5 eV for Pt and for different stage biases [3]. A negative stage bias places the SE peak above the detection band, while a positive bias shifts the peak out of the lower detection limit. For each 1 V step of the stage bias between -7 V and 7 V, the SE intensity was recorded by the TLD and is depicted in Fig. 2a. The shape of this curves reveals an upper limit of 7 eV and a lower one of 2 eV for the SE energy detection band of this experimental setup. Deconvolution of the integrating detection from the recorded intensity gave the energy distribution of the SE, as shown in Fig. 2b.

SE emission of Pt islands and the substrate shown in Fig. 1a was measured at different stage biases. The deconvoluted energy distribution of the SE"s is plotted in Fig. 2b and shows the relative shift of the corresponding peaks. The peak maximums indicate a lower WF for the substrate than for Pt.

Dewetting at 1000 °C of a thin Pt film on SiO_2 lead to the formation of Pt flakes consisting of different oriented grains, as shown in Fig. 3a. Band-pass filtering of the SE intensity of dark and bright Pt grains indicate a relative shift of ~100 meV of the peak positions of the SE energy spectra (Fig. 3b). This points out that the WF as well depends on the crystal orientation of the material.

In conclusion, band-pass filtering and sample biasing can be used to determine the energy distribution of SE emitted from materials scanned by an electron beam. The shape of the SE energy spectra is related to the WF of the corresponding material. By this method, orientational dependent differences of ~100 meV in the WF of crystalline Pt grains were detected.

[1] Z. Chen et al., Adv. Mater. 36 (2024)

[2] C. Rodenburg et al., J. Phys.: Conf. Ser. 241 (2010)

[3] M. S. Chung and T. E. Everhart, J. Appl. Phys. 45 (1974)

[4] I. Müllerova and I. Konvalina, Journal of Microscopy, 236 (2009)

[5] We acknowledge funding from 3DMM2O - Cluster of Excellence (EXC-2082/1 – 390761711) and from TrackAct (SFB1441, Project-ID 426888090)

Figure1: a) SE image of Pt on a SiO_2/graphene substrate, b) calculated SE energy distribution [3] for Pt at different stage bias.

Figure2: a) Band-pass detected SE and b) SE energy distribution as a function of stage bias.

Figure3: a) SE image of a dewetted Pt flake on SiO_2, showing grains with orientational contrast, b) SE energy distribution as a function of stage bias for different oriented Pt grains.

Fig. 1

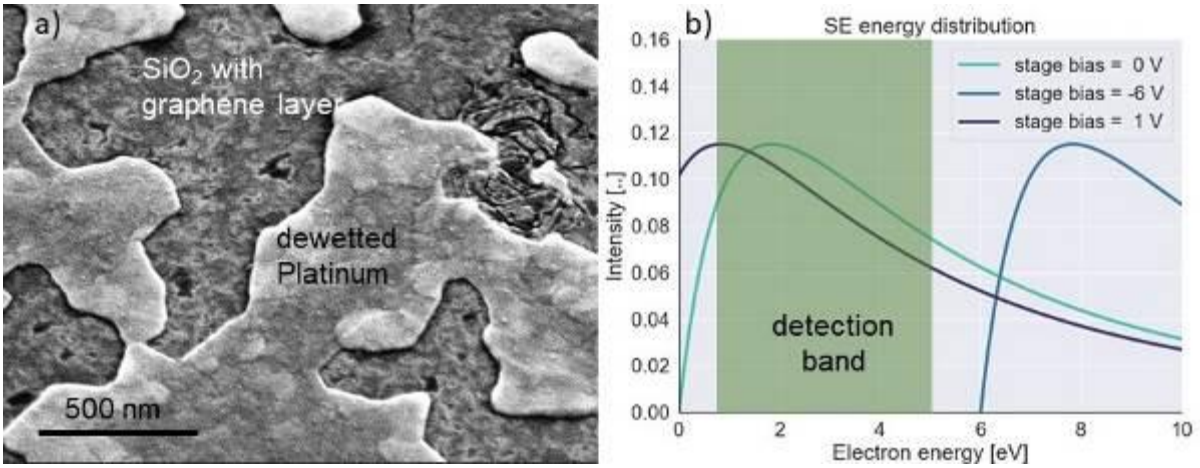


Fig. 2

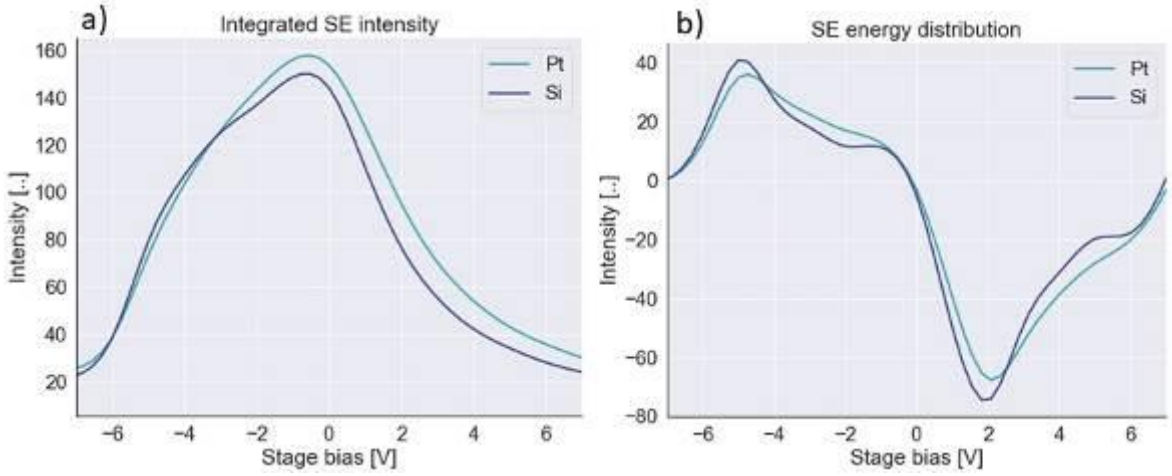
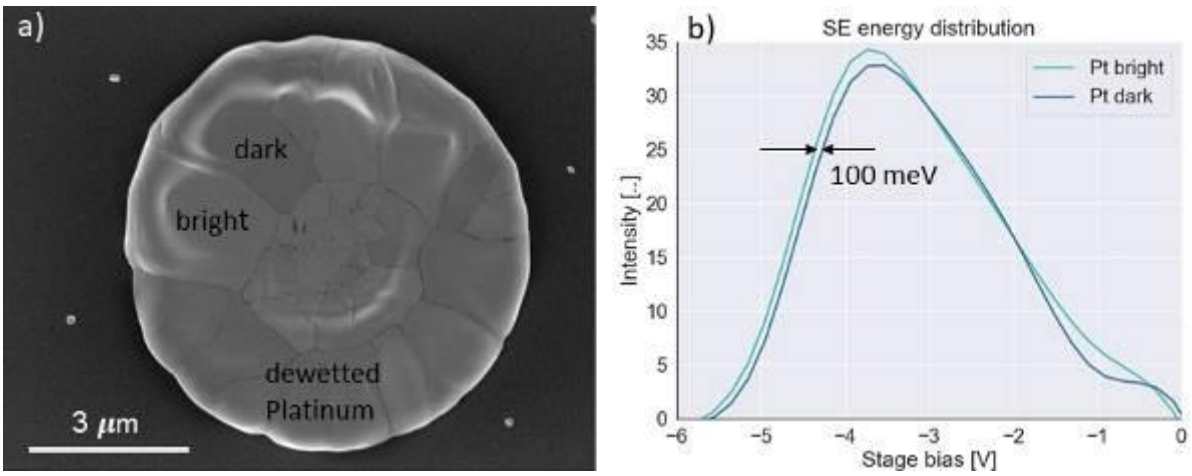


Fig. 3


a)
dark
bright
dewetted
Platinum
3 μm
b)
SE energy distribution
Pt bright
Pt dark
100 meV
Intensity [-]
Stage bias [V]
35
30
25
20
15
10
5
0
−6
−5
−4
−3
−2
−1
0

IM3.P10
Experimental and simulation insights on electron beam-induced heating during SEM experiments

A. Bastos da Silva Fanta[1], C. Koenig[1], J. R. Jinscheck[1]

[1]Technical University of Denmark, Nanolab - National Centre for Nano Fabrication and Characterization, Kongens Lyngby, Denmark

Given the extensive application of electron backscatter diffraction (EBSD) in materials research and the prolonged exposure of the samples to the electron beam during these experiments, it is noteworthy that electron beam-induced heating is often overlooked when interpreting structural phenomena under investigation. This very local sample heating effect can compromise the integrity of the sample in particular for temperature-sensitive materials and in in-situ heating experiments and, therefore, the reliability of data, as uncontrolled temperature fluctuations may cause unintended structural changes.

This study [1] investigates and quantifies electron beam-induced sample heating effects in SEM experiments. Using a MEMS-based heating device for in-situ real-time sample temperature monitoring, iron samples were analyzed to quantify the localized thermal effect under different SEM acquisition parameters. Our results indicate that the beam current is the main contributor to localized sample heating, with the temperature in the iron sample increasing up to 70 °C at high beam currents. Complementary finite element (FEM, COMSOL) and Monte Carlo (Casino) simulations were conducted to model the interaction between the electron beam and the sample, providing additional insight into the heat distribution within the sample and validating our experimental findings.

This study shows that beam-induced heating can significantly affect temperature-sensitive materials and alter local conditions in *in-situ* heating experiments, where precise thermal control and knowledge of temperature are required. Moreover, it highlights the importance of integrating active temperature feedback mechanisms into *in-situ* SEM heating setups to ensure the reliability of the experiments and minimize unintended thermal effects. Optimizing SEM parameters, such as reducing beam current or adjusting sample tilt, can help mitigate beam-induced heating and improve the accuracy of such microstructural analyses.

References:

1. Koenig *et al*., arXiv(2024), preprint: not peer reviewed, https://doi.org/10.48550/arXiv.2412.03361

IM3.P11
In situ cryo-transfer workflow with integrated TKD verification enabled by novel holders and jigs for Cryo-TEM and APT

E. V. Woods[1], C. Wigge[2], T. M. Schwarz[1], B. Gault[1,3]

[1]Max-Planck-Institute for Sustainable Materials, MA, Düsseldorf, Germany
[2]Electron Imaging Solutions, Düsseldorf, Germany
[3]Imperial College London, Department of Materials, Royal School of Mines, London, United Kingdom

Introduction: Developing reliable cryo-transmission electron microscopy (cryo-TEM) workflows has revolutionized biological imaging, yet specimen handling during transfer remains a critical challenge. Maintaining amorphous ice is essential for preserving native structures in biological samples. Similar issues affect air-sensitive materials, including lithium-ion batteries requiring continuous environmental protection. Existing commercial systems for frozen specimen preparation lack integrated verification of ice crystallinity, often necessitating multiple transfers and increasing risk of sample compromise. Here, we present an innovative cryogenic workflow integrating specimen transfer between liquid nitrogen temperatures (–190°C), inert gas environments, and ultra-high vacuum (UHV), facilitated by custom-designed holders and jigs ensuring universal compatibility with commercial cryo-transfer systems and incorporating in-situ transmission Kikuchi Diffraction (TKD) for quality control—to validate that samples are amorphous and check lamellas prior to cryo-TEM imaging.

Objectives: Our goal is to develop and validate an integrated workflow that streamlines specimen handling and maintains uninterrupted cryogenic conditions. Key objectives include:

(1) Designing novel specimen holders and transfer jigs providing robust, universal grid compatibility.

(2) Integrating in-situ TKD to verify ice crystallinity at critical workflow stages, eliminating extra transfers;

(3) Demonstrating system reliability for biological and air-sensitive materials, with hardware innovation as the central advancement.

Materials and Methods: A Ferrovac glovebox and UHV transfer modules were integrated with a Thermo-Fisher Focused Ion Beam/Scanning Electron Microscope (FIB/SEM) outfitted with an EDAX DED EBSD/TKD detector and Aquilos cryo-stage, alongside a Thermo-Fisher cryo-TEM. Custom-designed holders and jigs—engineered for universal compatibility with standard TEM grids, C-clipped Autogrids™, and FIB half-grids containing lamellas—enable continuous cryogenic handling. The integrated TKD module permits verification of ice state at key checkpoints, ensuring grids remain amorphous and lamellas maintain integrity before cryo-TEM analysis. Validation used sea urchin sperm for biological specimens and lithium-ion battery components for materials science.

Results: Initial validation confirms our holders and jigs reliably maintain cryogenic conditions throughout multiple transfer cycles. The integrated TKD system successfully verifies ice crystallinity at predetermined checkpoints on grids, with potential capability for lamella verification currently under development. Both conventional on-grid and cryogenic lift-out methods yielded specimens with maintained structural integrity as confirmed by cryo-TEM imaging. The workflow minimizes transfer steps and contamination risks, underscoring the system's advantages.

Conclusion: This innovative cryogenic workflow—anchored by universal specimen holders and transfer jigs and enhanced by in-situ TKD quality control—represents a significant advancement in specimen preparation for cryo-TEM and atom probe tomography (APT). By simplifying transfer processes while ensuring environmental control, the system reduces contamination risks and

streamlines multi-platform specimen handling. This approach opens new avenues for correlative microscopy studies in biological and materials science applications.

IM3.P12
Fabrication of nanoparticle from precursor material by irradiation with low-energy electrons

K. Weinel[1,2,3], M. B. Hahn[4], L. Agudo Jácome[3], A. Lubk[1,2]

[1]Technical University Dresden, Physics, Dresden, Germany
[2]Leibniz Institute for Solid State and Materials Research Dresden, Dresden, Germany
[3]Federal Institute for Material Research and Testing, Berlin, Germany
[4]University of Potsdam, Potsdam, Germany

Introduction: Nanoparticles (NPs) have garnered significant interest in various fields, including optics, chemistry, and medicine, due to their unique properties resulting from spatial confinement. Established fabrication techniques employ mechanical, physical, and chemical methods, such as condensation from gas or plasma phases, wet chemistry, and ion implantation. Methods featuring a relatively simple setup and limited amount of chemicals, like γ-ray and ion irradiation of precursors, are of particular interest owing to reduced material costs, applicability to wide range of materials and short processing times. Electron beams (e-beam) are widely used in characterization techniques such as electron microscopy, while e-beam irradiation serves as a fabrication tool in nanotechnology and manufacturing processes, such as e-beam lithography, e-beam welding, and e-beam-induced deposition. Objective: Here, we explore and study the use of low-energy electrons for decomposition of precursor materials into NPs. We exhibit the thermodynamics underlying the precursor deposition and reveal the role of inelastic scattering and thermal radiation, thereby laying the ground work for further application of the technique. Materials,Methods:Gold microparticles (MPs) deposited on thin SiO substrates are irradiated with e-beams of 5-30 kV in scanning electron microscopes (Fig. 1), varying the current between 5 and 45 nA. A detailed investigation of the e-beam – precursor interaction is performed utilizing Monte Carlo scattering simulations carried out with GEANTT 4, thereby computing the energy deposition due to inelastic electron scattering. Thermodynamic simulations considering the heating due to e-beam – sample interaction as well as cooling due to thermal radiation are employed to asses the temperature increase of the precursor MPs. Results: Utilizing an e-beam above the threshold of 8 nA leads to the synthesis of gold NPs whose sizes range from 100 nm close to the precursor location down to 2 nm further away. The synthesis mechanism, consisting of two steps, first a decomposition of the MP and second the deposition and growth of the NPs, is sketched in Figure 2. Irradiating a pristine gold crystal lattice (Fig. 2a) with an e-beam induces an energy transfer (Fig. 2b) due to inelastic scattering processes, which finally increases the temperature of the precursor resulting eventually in a decomposition of the MP (Fig. 2c). The scattering interaction between low-energy electrons and matter is tracked with a Monte Carlo scattering simulation exhibiting a huge amount of deposited energy, which induces a phase transition of the gold MP. The surrounding low pressure leads to a direct transition from solid into the gas phase. The deposited charge is negative and does not play a crucial role in this process. [1] Conclusion: Gold NPs could be fabricated from precursor MPs deposited on SiO substrate in vacuum irradiating them with low-energy electrons of 30 kV and a current above a threshold of 8 nA. The decomposition process of the MP is driven by thermal energy due to inelastic scattering processes, heating the MP beyond solid to gaseous phase transition. Figure 1: Sketch of the initial state of an gold precursor MP deposited on a thin substrate irradiated with an low-energy e-beam and the fabricated gold NPs. Figure 2: Synthesis steps at the atomic scale. Precursor decomposition: a) pristine gold, which is irradiated in b) with an e-beam depositing energy leading to heating and modifications. c) Vaporization at surface of precursor MP, shrinking the particle. The NP synthesis begins with d) the pristine SiO substrate that is subsequently covered e) by the gaseous gold atoms that f) finally grow together to form gold NPs. [1] K.Weinel, et al. arXiv:2408.02409 (2024)

Fig. 1

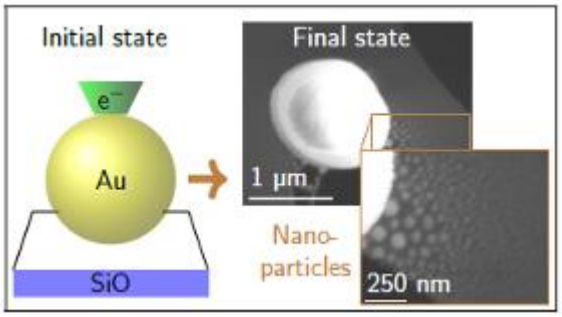
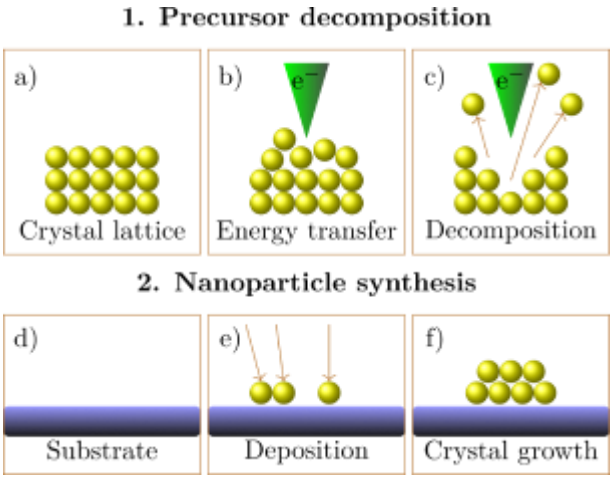

Initial state
Final state
e⁻
Au
SiO
1 µm
Nano-
particles
250 nm

Fig. 2


1. Precursor decomposition
a)
Crystal lattice
b)
e⁻
Energy transfer
c)
e⁻
Decomposition
2. Nanoparticle synthesis
d)
Substrate
e)
Deposition
f)
Crystal growth

IM3.P14
Challenges in FIB lamella preparation of 2D layered crystals

J. Deuschle[1], T. Heil[1], H. Wang[1], P. A. van Aken[1]

[1]Max Planck Institute for Solid State Research, Stuttgart Center for Electron Microscopy, Stuttgart, Germany

During focused ion beam (FIB) preparation of lamellae for transmission electron microscopy (TEM) analysis, bulk crystals of 2D layered materials, such as transition-metal diselenides, exhibit a very unusual and pronounced curtaining effect [1]. This curtaining effect leads to variations in the final thickness of the TEM lamella. Figure 1 shows a TEM image of such a lamella with periodically varying thickness.

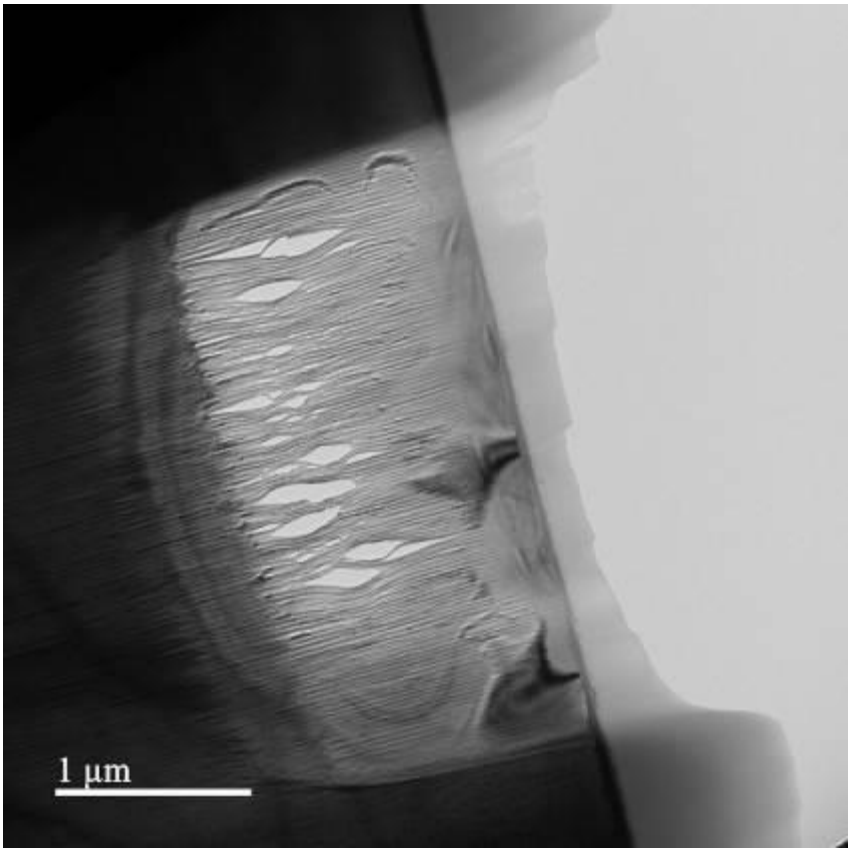
Since TEM investigations of such lamellae with thickness variations can be very challenging, our goal is to establish a FIB preparation routine that will minimize the curtaining effects and provide high-quality lamellae with constant thickness.

In this study, we investigate the influence of FIB milling parameters, milling geometry, and milling temperature on the occurrence of the curtains and the resulting lamella structure to gain a better understanding of the mechanisms behind the formation of the curtains and to develop strategies to avoid their formation.

Figure 1: TEM image of a lamella with periodical thickness variations.

[1] *Deuschle, J., T. Heil, H. Wang and P. A. van Aken,* FIB-induced nanorod formation in 2D layered crystals, BIO Web Conf. **129,** 22032 (2024). https://doi.org/10.1051/bioconf/202412922032

Fig. 1



IM3.P15
Development of a correlative MEMS-Based *in situ* SEM holder for heating, biasing, and microstructural characterization

Y. Pivak[1], C. Deen-van Rossum[1], M. Andersen[1], M. Pen[1], S. Basak[1,2], R. A. Eichel[2,3,4], H. Pérez Garza[1]

[1]DENSsolutions, Delft, Netherlands
[2]Forschungszentrum Jülich GmbH, Institute of Energy Technologies - Fundamental Electrochemistry (IET-1), Jülich, Germany
[3]RWTH Aachen University, Institute of Physical Chemistry, Aachen, Germany
[4]RWTH Aachen University, Faculty of Mechanical Engineering, Aachen, Germany

In situ scanning electron microscopy (SEM) is increasingly attracting interest, as it provides invaluable insights into the real-time evolution of materials under external stimuli like heating, electrical biasing, and mechanical stress. Such dynamic experiments bridge the gap between ex situ characterization and real-world applications for topics like pyrolysis [1], the microstructural evolution in steels during heat treatment [2], electrothermal responses of metals and semiconductors [2], additive manufacturing [3], and morphological studies of catalysts [4], among others. Additionally, in situ SEM serves as a powerful complementary technique to transmission electron microscopy (TEM). It enables studying microstructural changes and surface dynamics observed at lower magnifications in SEM, before being further examined in greater detail using TEM, thus providing multiscale insights into materials.

This work introduces a MEMS-based holder compatible with SEM and Dual Beam systems for in situ heating, biasing, and microstructural characterization. It leverages SEM"s flexible environment and diverse detectors for correlative studies using energy-dispersive X-ray spectroscopy (EDX), electron backscatter diffraction (EBSD), and transmission Kikuchi diffraction (TKD) [2]. The holder employs the same MEMS Nano-Chips as in situ TEM holders, facilitating cross-platform analysis. Furthermore, it can be integrated with atomic force microscopy (AFM) stages for advanced correlative microscopy.

To validate the system's performance, the MEMS-based holder was used to study thermal and electrical responses of various samples on Heating and/or Biasing Nano-Chips. Microstructural characterization during in situ heating was performed using on-axis and off-axis EBSD detectors. Experiments were conducted across multiple SEM/Dual Beam systems from different manufacturers, combined with an AFM stage for correlative analysis.

This versatile SEM stage enables real-time analysis of phase transformations, grain evolution, and defect dynamics under controlled thermal and electrical conditions, and grain evolution using EBSD and TKD, allowing for operando studies of material behavior at the microscale. Furthermore, it facilitates correlative microscopy studies by integrating SEM and AFM signals, while allowing seamless sample transfer to TEM without compromising microstructural integrity. Case studies on various materials reveal the system"s ability to capture fine-scale structural changes with high spatial and temporal resolution. Its cross-platform compatibility and correlative characterization capabilities bridge the gap between SEM, AFM, and TEM studies. This work paves the way for future research integrating multimodal in situ techniques, providing a more comprehensive understanding of dynamic material processes.

[1] Q. Sun et al, In Situ Pyrolysis of 3D Printed Building Blocks for Functional Nanoscale Metamaterials, Adv Func Mater 32 (2024), 2302358

[2] V. Bhatia et al, In-situ Heating and Biasing Transmission Kikuchi Diffraction, EMC2020 conference proceedings (2024), 10.22443/rms.emc2020.269

[3] A.B. da Silva et al, On the feasibility of using in-situ electron microscopy to investigate metal microstructures in additive manufacturing, 44th Risø International Symposium on Materials Science conference proceedings (2024).

[4] J. Cao et al, In situ observation of oscillatory redox dynamics of copper, Nat Com 11 (2020) 3554.

IM3.P16
Transfer and electrical contacting of nanomaterials for *in situ* TEM using FIB

S. Hettler[1,2,3], R. Arenal[2,3,4]

[1]Karlsruhe Institute of Technology, Laboratorium für Elektronenmikroskopie, Karlsruhe, Germany
[2]CSIC-Universidad de Zaragoza, Instituto de Nanociencia y Materiales de Aragon, Zaragoza, Spain
[3]CSIC-Universidad de Zaragoza, Laboratorio de Microscopias Avanzadas, Zaragoza, Spain
[4]Araid Foundation, Zaragoza, Spain

- Introduction

Electrical contacting without contaminating the specimen is crucial when aiming for *in-situ* TEM with electrical bias or current, especially if the material is a nanomaterial (NM) and cannot be cleaned after contacting and requires to be maintained in its pristine state. Therefore, the use of a carrier medium such as a carbon nanotube[1] was proposed. Here, we present a preparation technique that allows a clean and almost damage-free transfer exploiting a mechanically rigid support film.[2]

- Objectives

The objective was to obtain a clean and undamaged specimen for *in-situ* investigations where electrical currents are involved.

- Materials & Methods

Nanostructures of the misfit-layered compound (MLC) LaS-TaS_2 [3] were used to demonstrate the transfer process. A TFS Helios 650 was used for the scanning electron microscopy (SEM) and Ga^+ focused ion beam (FIB) work and two aberration-corrected TFS Titan microscopes with DENSsolutions Wildfire specimen holder for the *in-situ* TEM experiments. Holey silicon nitride (SiN) TEM grids from PELCO were used for the transfer process.

- Results

The process starts with a conventional preparation of the NM specimen on a holey SiN TEM grid. An individual NM is selected in a conventional TEM analysis, e.g., a nanotube and flake of the misfit-layered compound LaS-TaS_2 (Figure 1).[3] Using the dual-beam instrument, the NM with supporting membrane is then transferred to an *in-situ* chip using a microneedle and FIB induced deposition (FIBID) of Pt/C (Figures 2 and 3). The mechanical rigidity of the SiN guarantees the stability of the sustained NM and facilitates easy contacting of the membrane to the contact pads of the chip by FIBID. Finally, the membrane is removed in the central part to leave the NM as only conductive bridge.

Using this transfer technique, different NM devices were prepared and evaluated in detail regarding the transfer quality. Exemplary, Figure 4 shows a TEM image of the LaS-TaS_2 sample revealing no contamination or damage. The limitations of the method were explored with a WS_2 monolayer specimen, which revealed that Pt/C contamination during FIBID is kept well below a monolayer. Ga implantation can be kept to zero for 1D NMs, while a small amount of Ga is implanted at the edge of 2D NMs during the final step of removing the membrane in the central part. The method facilitated, e.g., *in-situ* TEM investigations on Pt nanoparticle synthesis and dynamics supported on carbon films.[4]

- Conclusion

The development of a support-based transfer and contacting procedure of individual NMs to chips used, e.g., for *in-situ* TEM investigations allows an almost artifact-free preparation of NM specimens. The resulting devices can be used to electrically characterize the NMs and to dynamically study the

effect of an electrical current on the sample, e.g., Joule heating, electromigration, electrical failure analysis or EBIC.[5]

References

[1] Gorji et al, *Ultramicroscopy* **219**, 113075, 2020.
[2] Hettler et al, *Small Methods* **8**, 2024.
[3] Hettler et al, *ACS Nano* **14**, 5445, 2020.
[4] Hettler, Arenal, *Carbon Trends* **15**, 100348, 2024.
[5] Funding from European Union, Spanish MICIU and Government of Aragón (DGA) is acknowledged.

Figure 1: SEM and inset TEM image of LaS-TaS_2 NM sustained by holey SiN membrane.
Figure 2: SEM image after take out of NM with sustaining membrane.
Figure 3: SEM image of the NM transferred to the *in-situ* chip.
Figure 4: TEM image of the flake and the nanotube after transfer.

Fig. 1

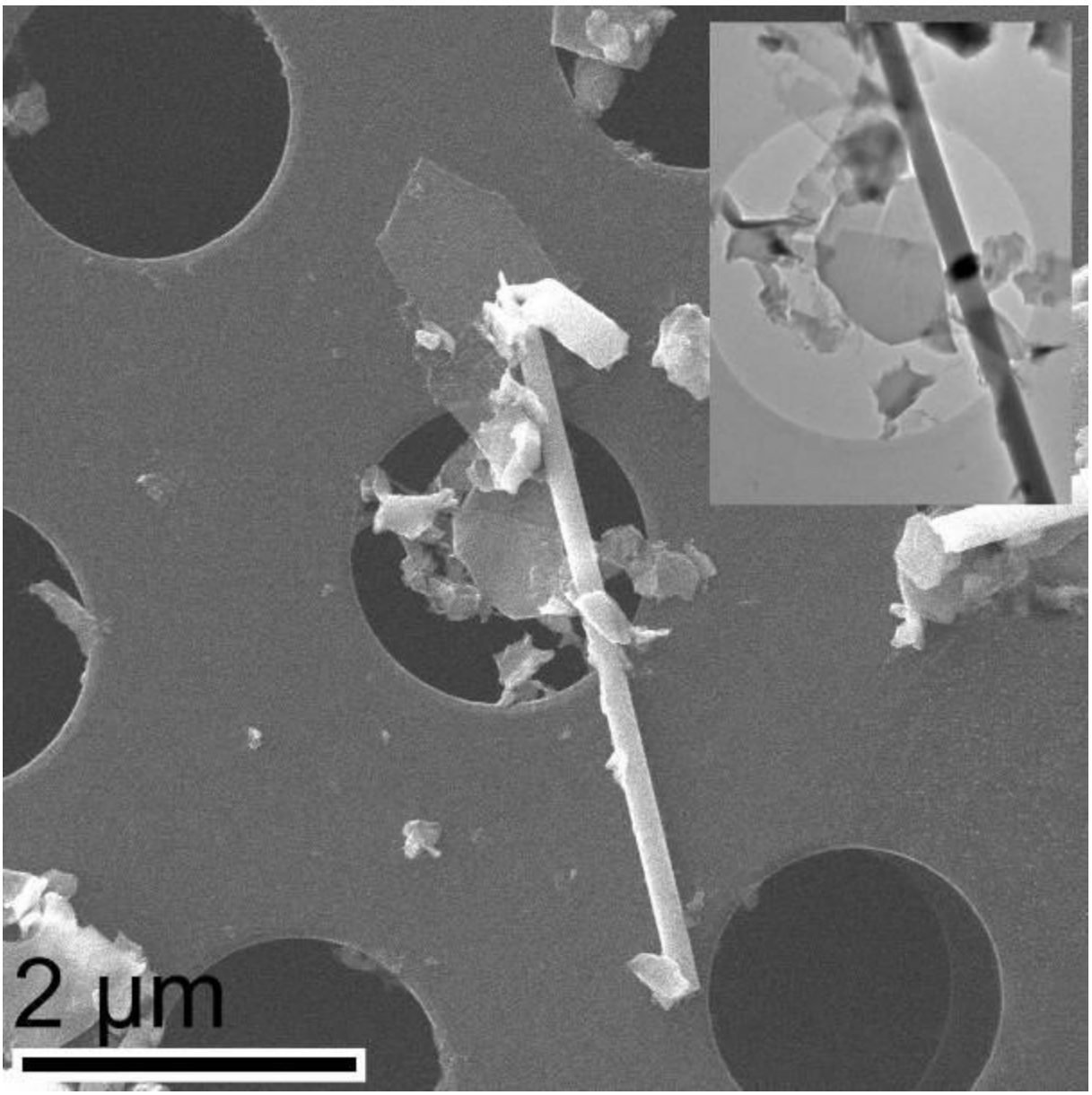


Fig. 2

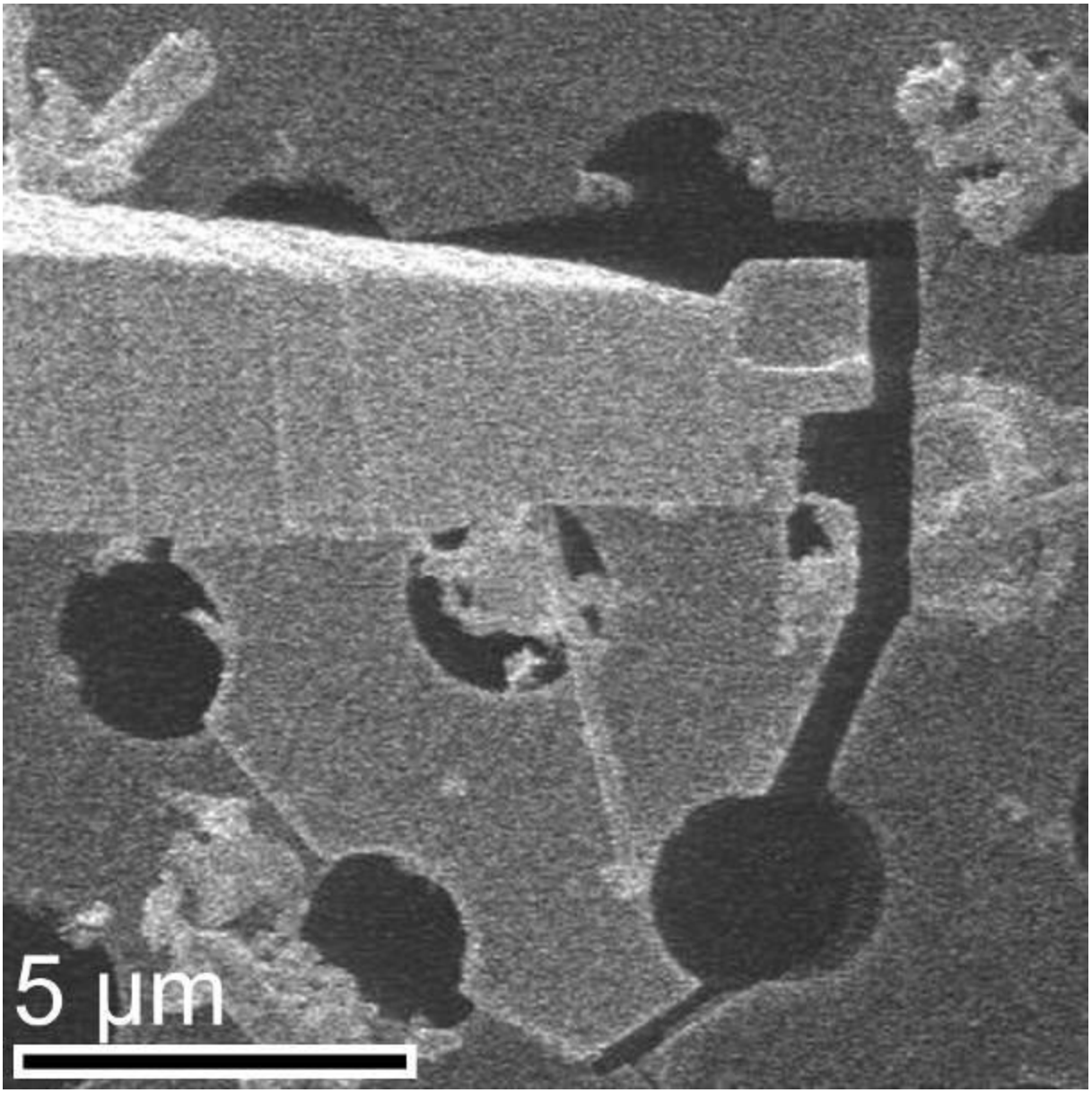

5 µm

Fig. 3

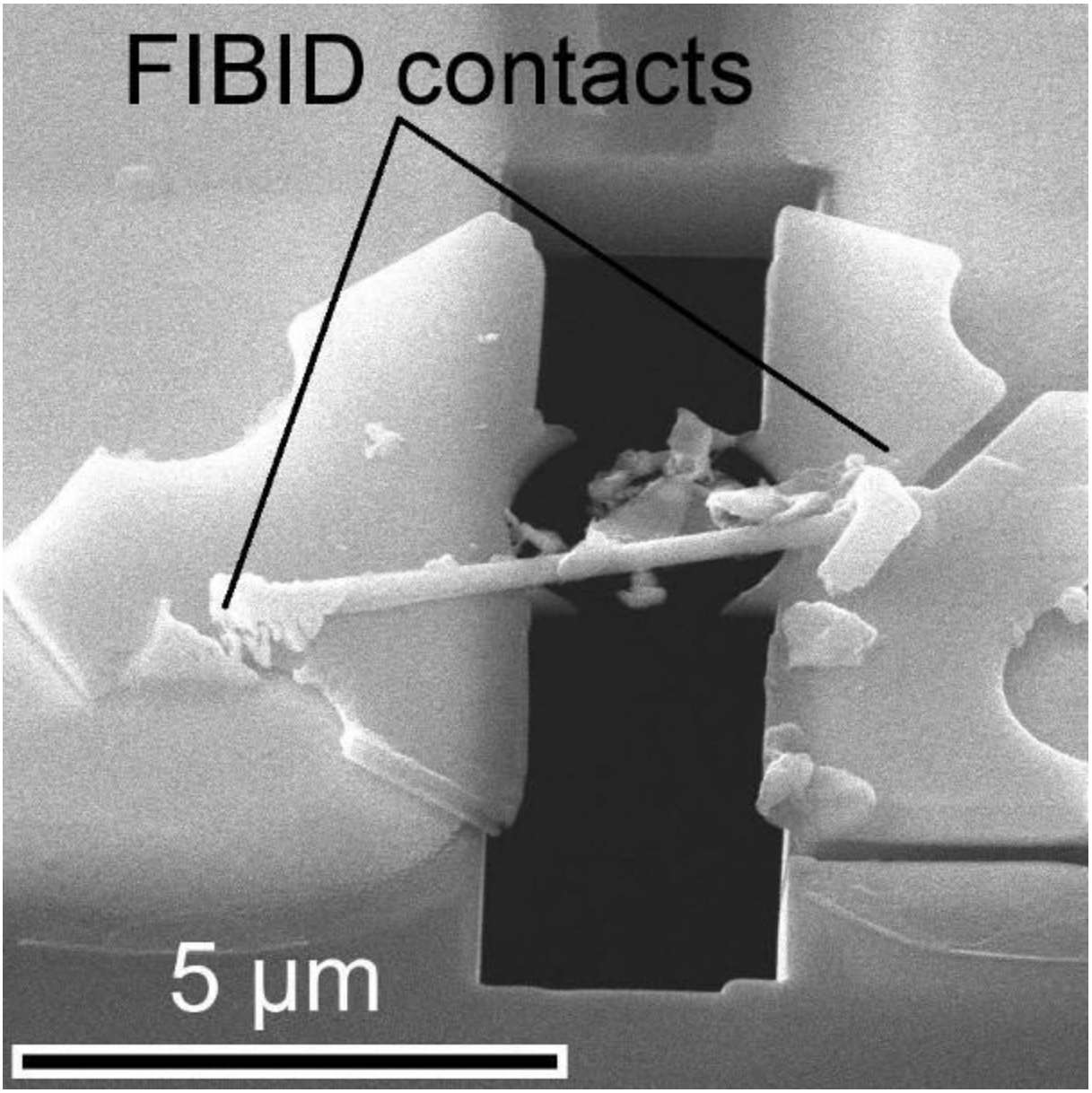
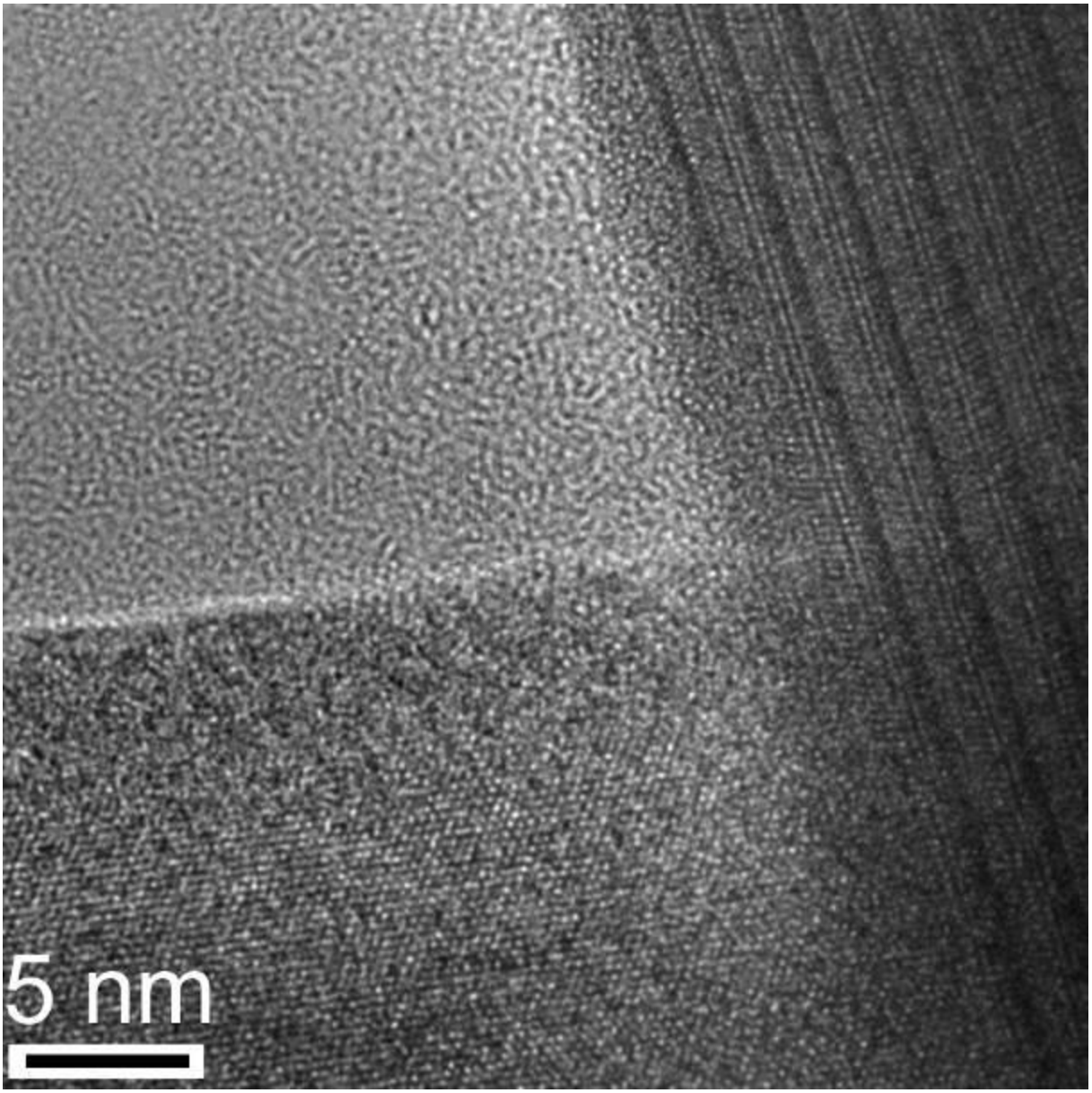


Fig. 4



IM3.P17
Influence of applied ion energy on low-damage (S)TEM sample preparation using different ion species and energies in FIB-SEM

M. Sláma[1], S. Basak[2], L. Giannuzzi[3], L. Ahrens[2], R. A. Eichel[2]

[1]TESCAN Group, Brno, Czech Republic
[2]Forschungszentrum Jülich GmbH, Jülich, Germany
[3]Tescan GmbH, Warrendale, PA, United States

This study aims to map and understand the formation of artifacts in TEM samples during the final low-keV polishing stage. Experiments were conducted using FIB-SEM systems equipped with a Ga+ liquid metal ion source, Xe+ plasma FIB-SEM, and a dedicated low-keV broad ion beam, each tested under various conditions. We examine how factors such as ion species, accelerating voltage, beam profiles, and process parameters affect the optimization of TEM sample preparation methods to minimize damage. Key damage mechanisms are analyzed, and different preparation techniques are systematically compared. Discussion includes optimized protocols that employ low-energy conditions down to 200 eV and polishing strategies adapted for specific ion sources and techniques. The study highlights the balance between milling efficiency and resolution, emphasizing the importance of selecting appropriate ion species and final ion energy settings based on material properties. The findings were established to create a solid framework for reducing ion-induced damage, ultimately improving the reliability of (S)TEM for high-resolution structural analysis and refining methodologies that consistently produce TEM samples with minimal artifacts.

IM3.P18
Nanoscale RRAM device fabrication via electron-beam deposition and Ga-Free multi-Ion plasma FIB Milling

A. W. Shakib[1], R. Winkler[1], A. Fakiner[1], D. Vasquez[1], L. Molina-Luna[1]

[1]Technical University of Darmstadt, AEM, Darmstadt, Germany

Introduction: Resistive Random Access Memory (RRAM) is a promising candidate for next-generation data storage, offering high scalability, low operating voltages, and rapid switching speeds. However, fabricating devices with lateral dimensions below 100 nm remains a key challenge. Optical lithography faces fundamental resolution limits at these scales[1]. Although electron-beam lithography can achieve features under 20 nm, recent multi-ion focused ion beam (FIB) systems provide an additional route for precise nanoscale fabrication[2].

Objective: We demonstrate two complementary strategies for producing pristine, sub-100 nm RRAM devices. First, electron-beam-induced Pt deposition is employed to form top electrodes on HfO_2 exactly at or away from TiN grain boundaries, enabling targeted studies of conductive filament (CF) formation. Second, non-metallic ion species (Ar^+, Xe^+) in a multi-ion plasma FIB are utilized to shrink existing micrometer-scale devices while preventing premature CF formation, thus preserving the pristine state for electrical characterization.

Materials and Methods: A TiN/HfO_2 Metal-Insulator-Metal (MIM) stack was grown on *c*-cut sapphire by reactive molecular beam epitaxy (RMBE). The top metal electrode was sputter coated after patterning the surface using optical lithography. A Thermo Fisher Helios 5 Hydra CX multi-ion plasma FIB (Xe^+, Ar^+, N^+, O^+) equipped with dual manipulators was used for both device fabrication and in situ electrical characterization via a Keithley 2450 Source Meter.

Results: Low-energy FIB milling parameters (≤2 kV/0.32 nA for Ar^+, ≤5 kV/0.1 nA for Xe^+) were found to prevent premature CF formation, effectively rendering the device usable for further testing in its pristine state (Figure 1). Second, electron-beam deposition of Pt electrodes at TiN grain boundaries highlighted the potential impact of local microstructure on the underlying mechanism for filament formation (Figure 2).

Conclusion: Both precisely controlled electron-beam-induced electrode deposition and low-energy, Ga-free multi-ion FIB milling provide a robust method of scaling RRAM devices to sub-100 nm dimensions while preserving their pristine state. Given that a single nanometer-scale conductive filament often governs RRAM behavior, this strategy could enable new possibilities for exploring how local structural features affect device performance.

References:

1 Lin, B. J. *Comptes Rendus Physique* 7, 858–874 (2006)

2 Utke, I. *et al. Journal of Vacuum Science & Technology B: Microelectronics and Nanometer Structures Processing, Measurement, and Phenomena* 26, 1197–1276 (2008)

The authors acknowledge funding from the ERC "HORIZON.1.1" Program under Grant No. 101088712-ELECTRON and Grant No. 101189511-BED-TEM and the research field matter and materials at TU Darmstadt under project No. 401 01 746.

Fig. 1. Fig. 1. A secondary electron (SEM) image of a TiN/HfO_2/Pt device that was electroformed and subsequently milled using a Xe^+ ion beam at 5 kV and 0.1 nA. Of the four newly created devices, only

the one at the lower right remains in a low-resistance state, as verified by the leakage current measurements shown in the inset. Scale bar is 10 µm.

Fig. 2. (a) SEM images demonstrating the patterning parameters and (b) the Pt-deposited device. Here, platinum was deposited onto the HfO_2 layer using an electron beam operated at 5 kV and 13 pA. The grain boundaries visible in the image arise from the TiN layer beneath. Scale bar is 100 nm.

Fig. 1

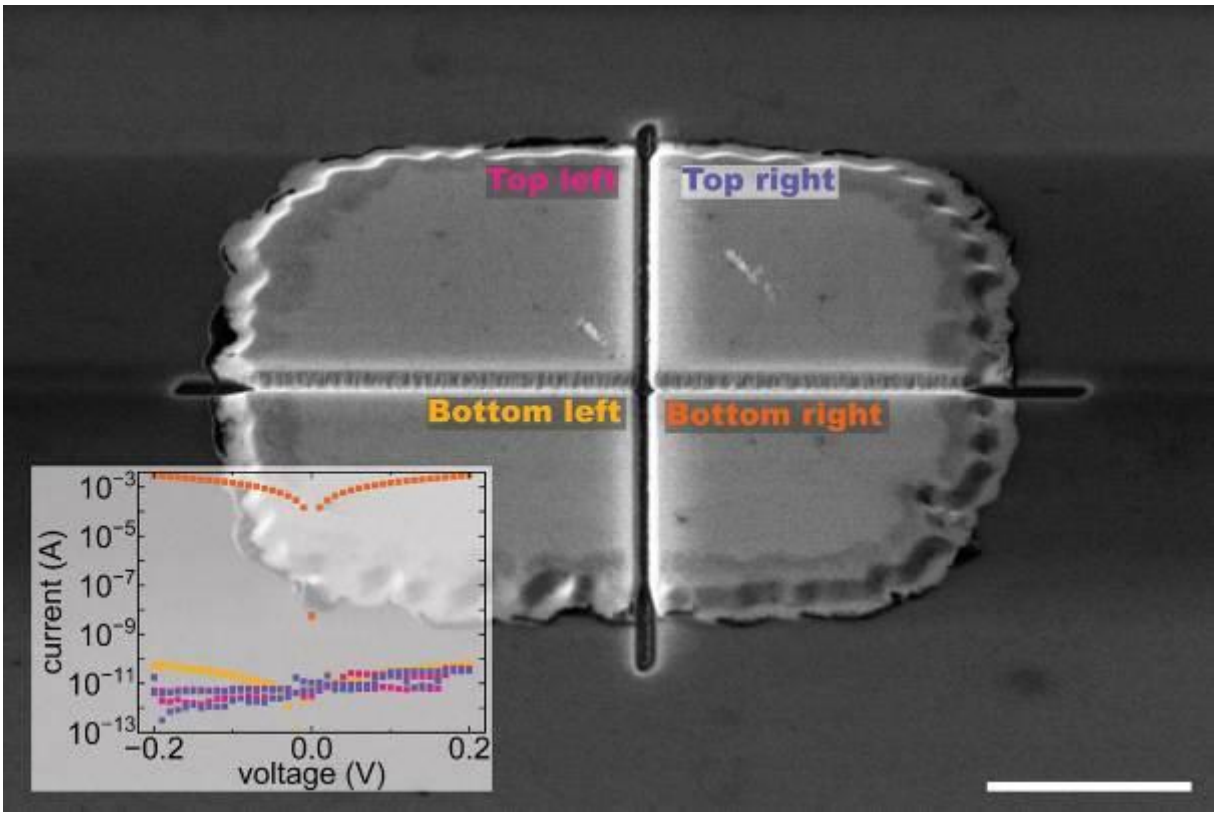
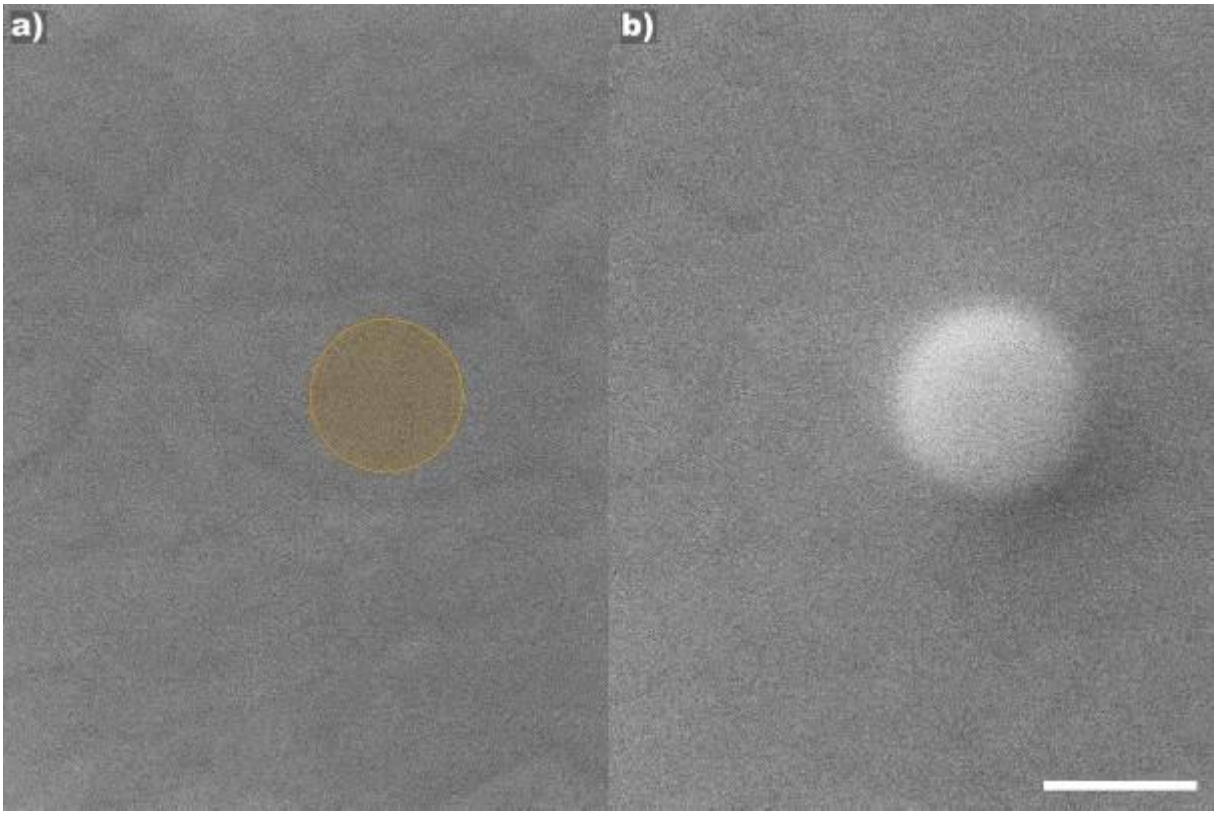


Fig. 2



IM3.P19
Exploring EBIC and SEEBIC in bulk and sross-sectional lamella devices through multi-ion PFIB preparation

D. Vasquez[1], R. Winkler[1], A. Fakiner[1], A. W. Shakib[1], L. Molina-Luna[1]

[1]Technical University of Darmstadt, AEM, Darmstadt, Germany

Introduction: Electron beam-induced current (EBIC) is a widely used technique for probing built-in electric fields in semiconductors, yielding insights into charge-carrier generation, transport, and recombination [1]. While EBIC often focuses on bulk specimens, applying this technique to thin-film or lamella devices offers higher spatial resolution near interfaces and grain boundaries. In reduced geometries, the volume for electron-hole pair generation is constrained, allowing surface phenomena to dominate. Secondary electron EBIC (SEEBIC), in particular, can overshadow genuine EBIC signals when lamella thickness decreases and surface irregularities (e.g., curtaining) become more pronounced [2,3].

Objective: We intend to establish a two-channel EBIC analysis strategy that reliably differentiates between genuine charge collection (EBIC) and surface-related effects (SEEBIC) by adjusting beam parameters and amplifier settings. Achieving this differentiation is key for accurately interpreting EBIC data in advanced materials research. We first verify this framework on plan-view Schottky barriers and later extend it to lamellar cross-sections. The objective is to determine the critical lamella thickness at which internal-field EBIC diminishes and SEEBIC dominates.

Materials and Methods: We performed all experiments in a dual-beam SEM-PFIB (Thermo Fisher Helios Hydra UX PFIB) equipped with an EBIC amplifier. The plan-view Schottky barriers were investigated at 1, 2, 5, and 10 kV and varied the current (10-11-10-9 A) to identify the conditions favoring SEEBIC or EBIC. We prepared lamella devices using a combined Xe+-Ar+ in situ lift-out procedure and placed them on membrane-free chip carriers to investigate the EBIC signal as a function of lamella thickness.

Results: Our experiments revealed distinct conditions under which EBIC and SEEBIC signals dominate. In plan-view Schottky barrier measurements, lowering the beam current and increasing the preamplifier gain suppressed bulk charge collection and revealed surface-driven SEEBIC contrast. Conversely, higher beam energies with moderate gains favored EBIC signals linked to the depletion region. Applying the method to lamella devices showed a clear thickness dependence: a thinner lamella device resulted in a weaker EBIC signal, while SEEBIC became more pronounced. This observation emphasizes the significance of calibrating lamella thickness and beam parameters to isolate true (SE)EBIC responses.

Conclusion: By tuning electron beam conditions and amplifier settings, we can pivot between EBIC-dominant and SEEBIC-dominant regimes. This flexibility is useful for investigating grain boundaries, heterojunctions, and other interfaces in emerging materials, where a small internal field may be masked by surface currents. The optimized multi-ion FIB lift-out protocol minimizes surface roughness and maintains consistent lamella thickness, reducing artifacts in EBIC or SEEBIC measurements.

References:

[1] H. J. Leamy, Journal of Applied Physics **53**, R51 (1982).

[2] D. Abou-Ras and T. Kirchartz, ACS Appl. Energy Mater. **2**, 6127 (2019).

[3] O. Dyck *et al.*, Microscopy and Microanalysis **28**, 1567 (2022).

The authors acknowledge funding from the ERC "HORIZON.1.1" Program under Grant Nos. 101088712-ELECTRON and 101189511-BED-TEM and funding from the research field "Matter and Materials" at TU Darmstadt under Project No. 40101746.

IM3.P20
Improved EBSD phase differentiation in fine-grained materials using spherical indexing

R. de Kloe[1], W. Lenthe[2], S. Wright[2], M. Nowell[2]

[1]EDAX-Gatan, Tilburg, Netherlands
[2]EDAX-Gatan, Pleasanton, CA, United States

Automatic phase differentiation during multiphase EBSD mapping is based on differences in the band geometry in the diffraction patterns. In conventional EBSD indexing, the location of the individual bands is detected by the Hough transformation after which the detected bands are matched against a reference structure. Such a reference structure contains a list of crystal lattice planes that are expected to produce strong bands in the EBSD pattern. For single phase materials or materials containing phases with different crystal structures this is an efficient method that allows consistent indexing and phase differentiation.

Difficulties arise when the crystal structure or band configurations of different phases are very similar. In such samples simultaneous collection of chemical information may be used for the discrimination of phases based on their composition [1]. However, EBSD patterns are generated in the top ~50 nm of a sample while EDS data may originate from up to 1000 nm depth and this restricts phase discrimination in structures with sub-micron grain sizes.

The development of spherical indexing using simulated EBSD (master) patterns [2] provides an alternative method for phase discrimination. Spherical indexing uses full pattern matching of the recorded experimental diffraction patterns with a dynamical simulation or with an experimental master pattern constructed using actual (verified) patterns from a specific phase [3,4]. The advantage of this method is that the entire pattern is used, including any small intensity variations and weaker bands that are normally not considered using Hough-based band detection and indexing.

In this study, the efficacy of spherical indexing for phase differentiation is verified by investigating of the orientation relationships of fine-grained multiphase aggregates with their host grains in a cast Al 6082 alloy. The aggregates are formed during casting and may affect the mechanical properties of the alloy. Phase discrimination by EBSD in the SEM is a challenge due to the sub-micron grain size and similarity in crystal structure of the main phases in the particles, Al, Si, Mg2Si.

Simultaneous EDS and EBSD mapping data including all EBSD patterns was recorded for off-line reprocessing. The effective resolution of the EDS mapping was unsuitable to locate the grain boundaries due to the large interaction volume (figure 1). During spherical indexing all patterns are matched against the dynamical and experimental master patterns for all phases and the solution with the highest correlation index is selected. This procedure allowed successful discrimination of all phases in the investigated particle aggregates (fig 2) such that the orientation relationship between the particles and the host grain could be determined (fig 3).

Figure 1: Simultaneously collected EDS map of Si and IPF map of Si particles as identified by spherical indexing

Figure 2: Phase distribution

Figure 3: Grain Reference Orientation Deviation map illustrating the misorientation of Al inside the aggregate with the host grain

References:

[1] M. M. Nowell and S. I. Wright (2004), Journal of Microscopy 213: 296-305

[2] Lenthe, W. C., Singh, S., & De Graef, M. (2019). Ultramicroscopy, 207, 112841

[3] Callahan, P. G., & De Graef, M. (2013). *Microscopy and Microanalysis*, *19*(5), 1255-1265

[4] Day, A. P. *Journal of microscopy* 230.3 (2008): 472-486

Fig. 1

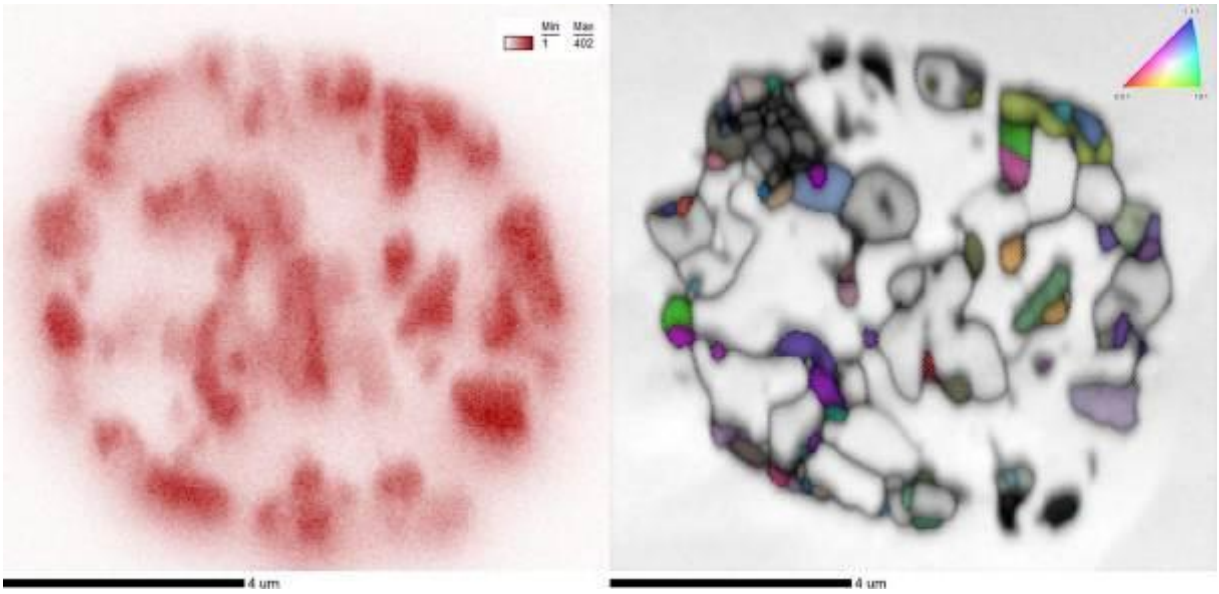


Fig. 2

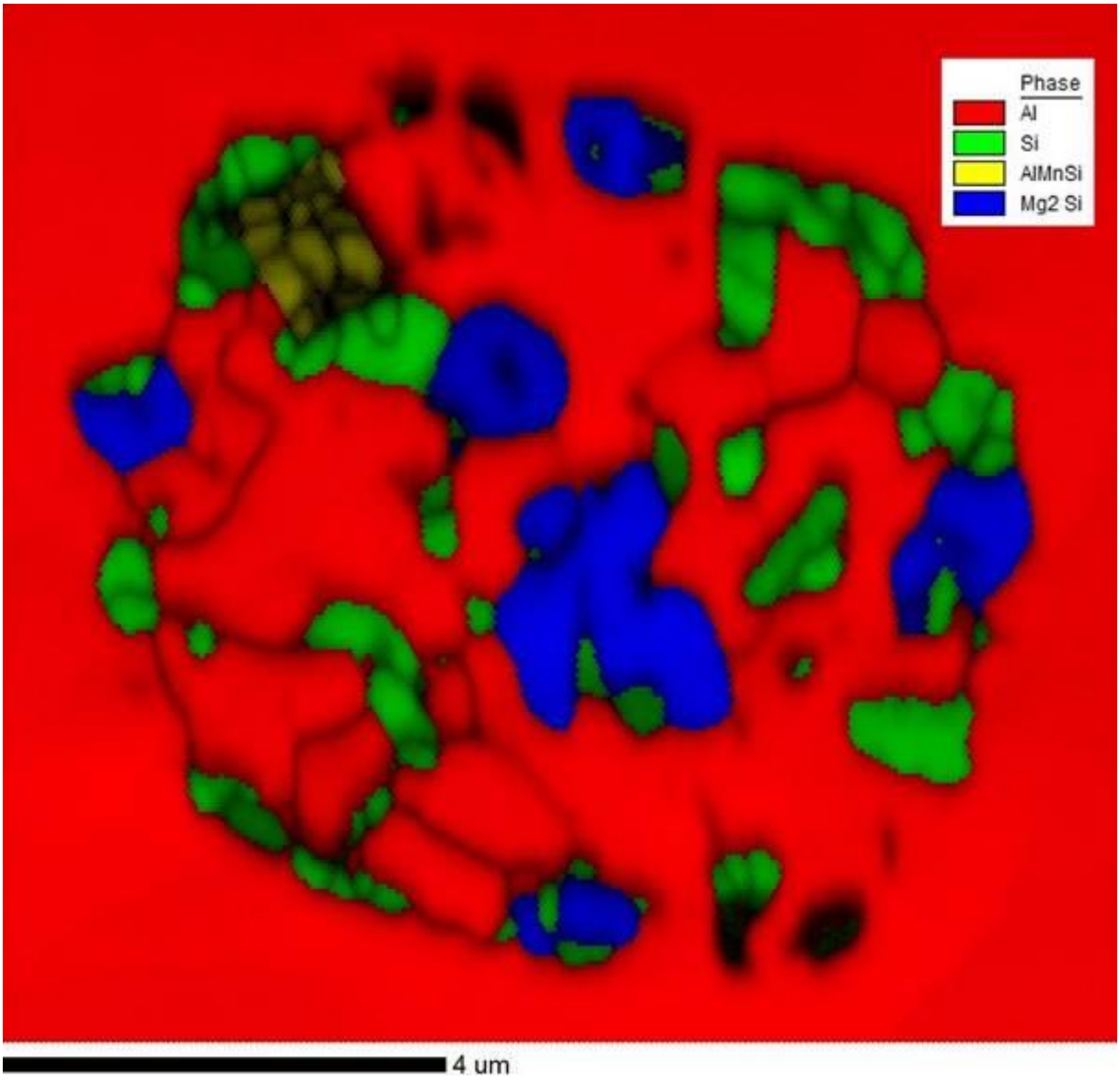
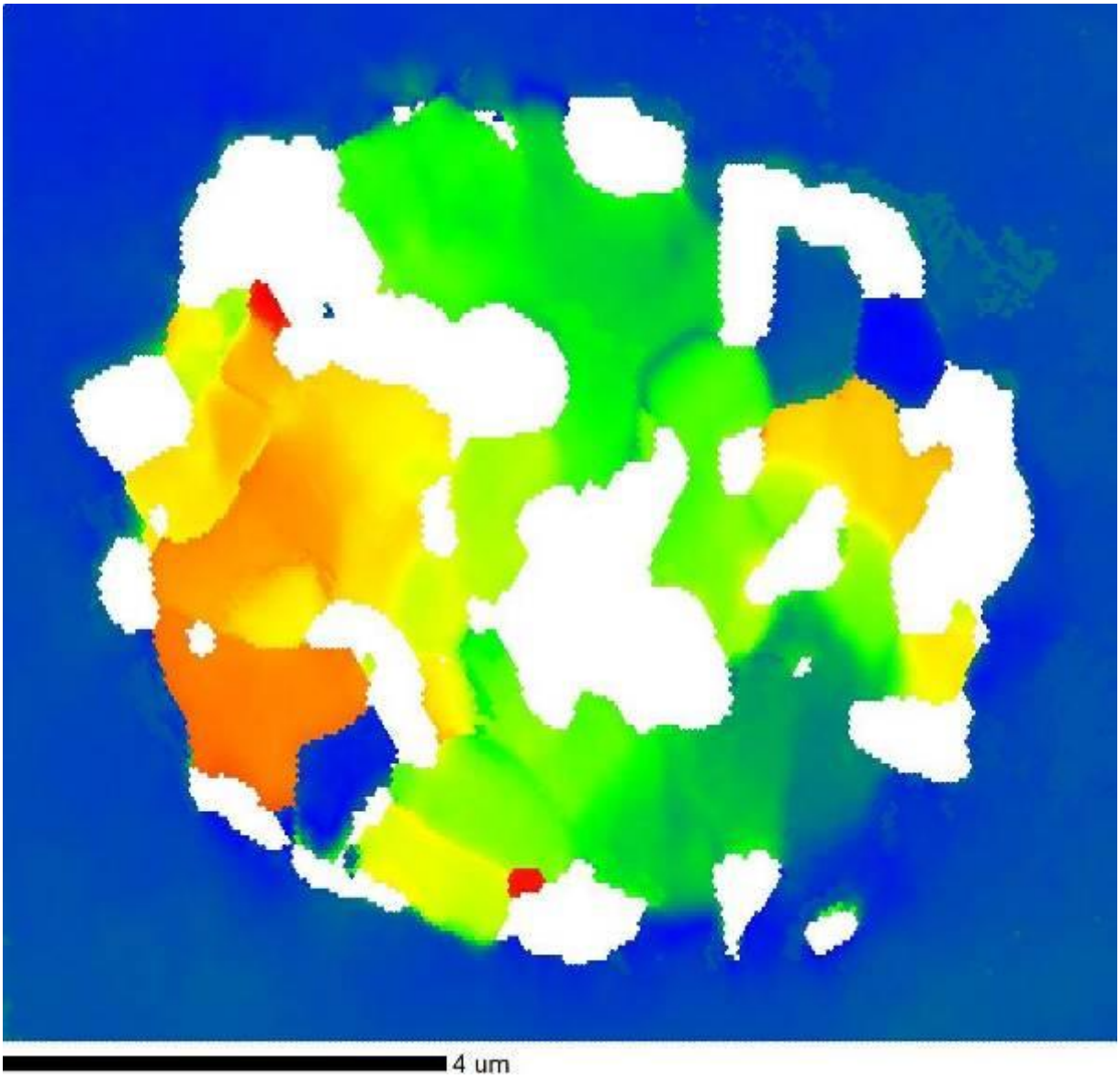


Fig. 3



IM3.P21
Application of photogrammetry in scanning electron microscopy for high-resolution 3D reconstruction of regions of interest

M. Hrabovsky[1], E. Modin[2], J. Dluhos[3], M. Jurasek[4]

[1]TESCAN Group, Product Marketing, Brno, Czech Republic
[2]CIC nanoGUNE, Electron Microscopy Laboratory, San Sebastian, Spain
[3]TESCAN Group, Product Management, Brno, Czech Republic
[4]TESCAN Group, Beam Lithography Department, Brno, Czech Republic

The integration of photogrammetry with Scanning Electron Microscopy (SEM) enables high-resolution three-dimensional (3D) reconstruction of regions of interest (ROI) at the micro- and nanoscale. This study presents an automated workflow that optimizes image acquisition, sample positioning, and computational processing for detailed 3D surface reconstruction. A **Python-based calibration and acquisition script** (Fig. 1) enhances the **FIB-SEM** system, automating stage tilting, detector adjustments, and multi-angle imaging (Fig. 2). A **systematic object movement strategy** (Fig. 3) ensures comprehensive sample coverage, capturing different perspectives for precise reconstruction.

Post-processing includes image alignment, feature detection, and multi-view stereo depth estimation, enhanced by **machine learning-based optimization**. The effectiveness of this approach is demonstrated through **high-fidelity 3D reconstructions**, as showcased in **Fig. 4**, which presents a micrograph of a seastar, highlighting the technique"s ability to resolve intricate surface details.

Compared to conventional stereoscopic SEM or focus variation methods, this automated **photogrammetry-enhanced SEM workflow** offers improved spatial accuracy, reduced computational overhead, and increased reproducibility. The technique has broad applications in **materials science, biological research, and nanotechnology**, where precise morphological characterization is crucial. This study highlights the advantages, challenges, and future potential of integrating photogrammetry with SEM for automated, high-precision 3D reconstructions.

Fig. 1

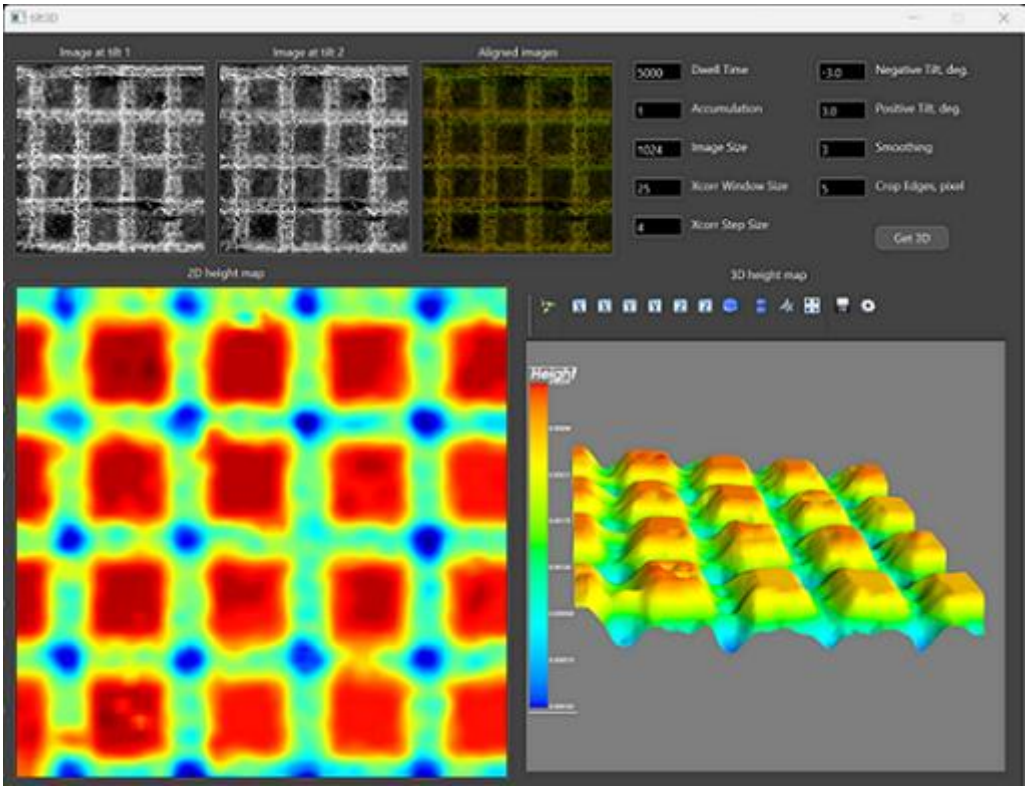

Image at tilt 1
Image at tilt 2
Aligned images
5000
Dwell Time
Accumulation
1024
Image Size
15
Xcorr Window Size
4
Xcorr Step Size
-3.0
Negative Tilt, deg
1.0
Positive Tilt, deg
3
Smoothing
5
Crop Edges, pixel
Get 3D
2D height map
3D height map
Height

Fig. 2

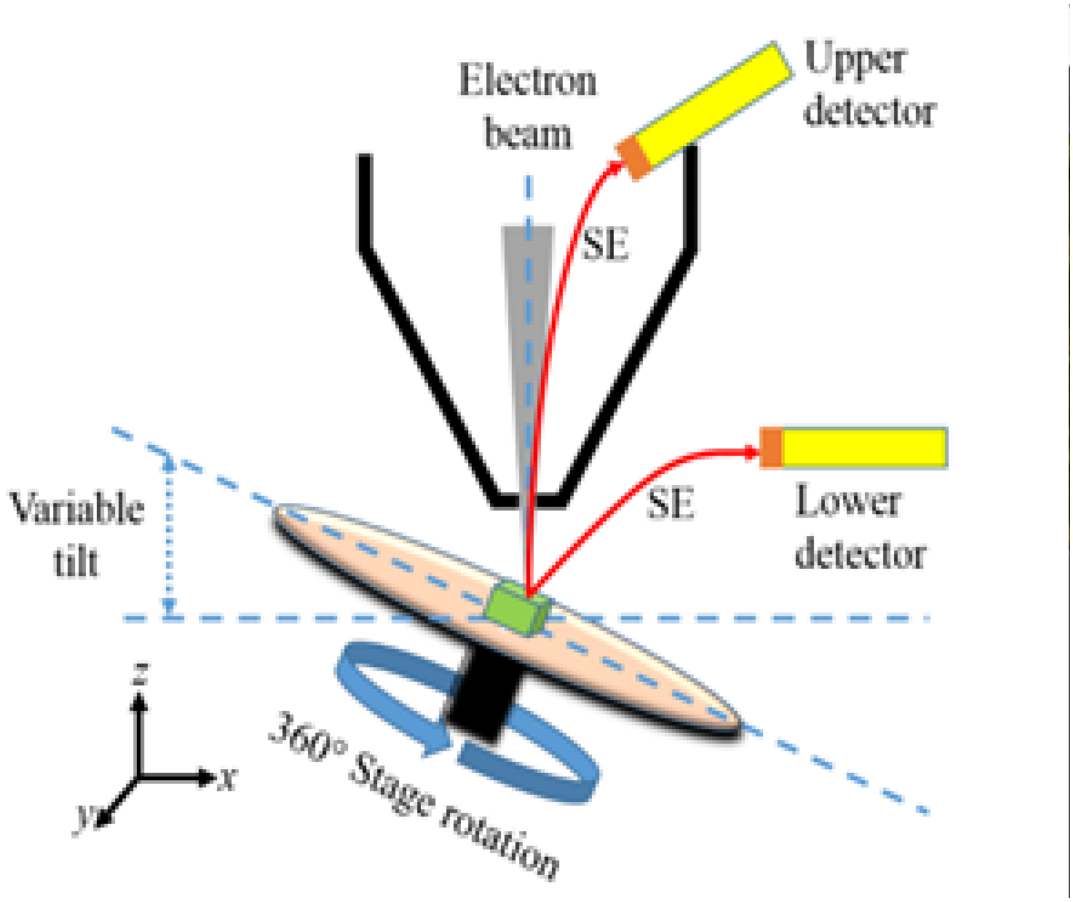

Electron beam
Upper detector
SE
SE
Lower detector
Variable tilt
z
x
y
360° Stage rotation

Fig. 3

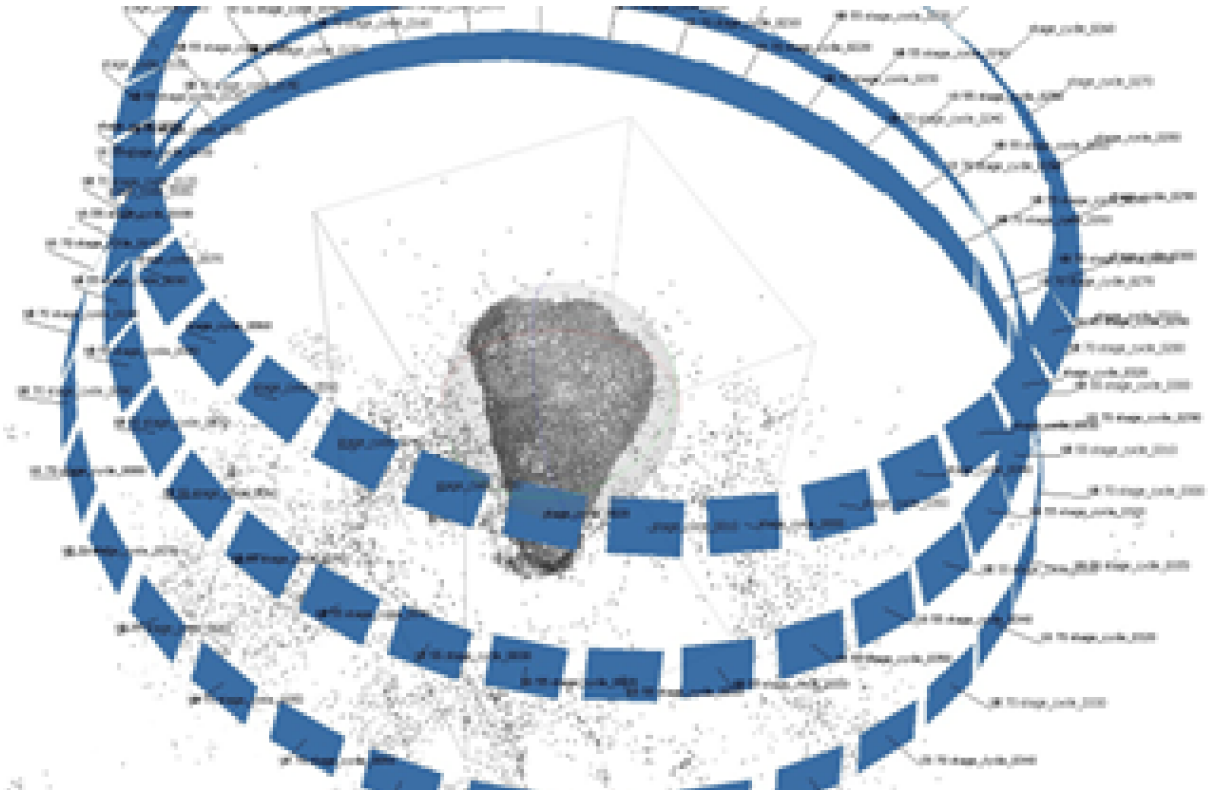
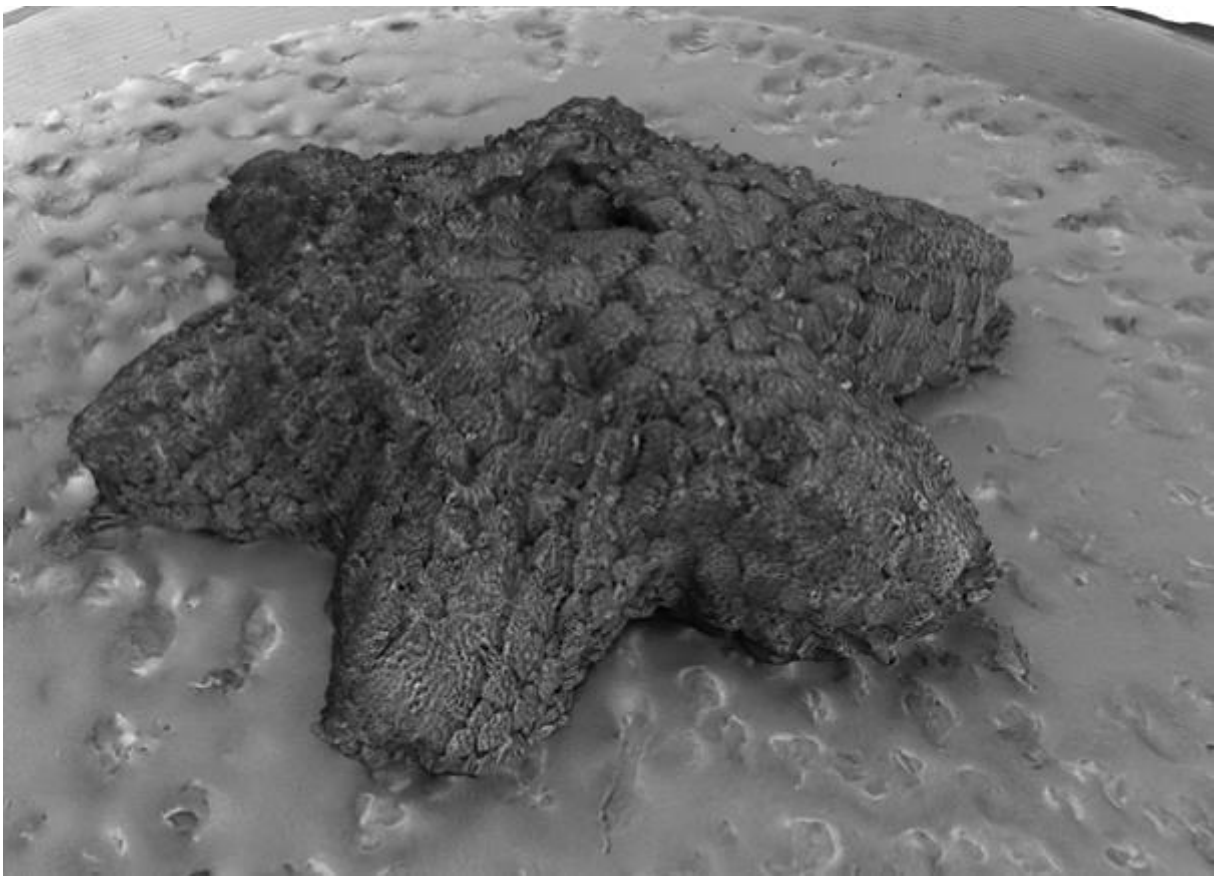


Fig. 4



IM3.P22
Development of chopped scan mode with lock-in amplification for electrical analysis of devices

R. Hammer[1], W. Joachimi[1], G. Moldovan[1]

[1]Point electronic GmbH, Halle (Saale), Germany

Electrical Analysis (EA) of devices and Integrated Circuits (ICs) in electron microscopy is a specialized and growing field, driven by the critical need for device characterization and IC failure analysis on ever-shrinking technology nodes. Popular techniques in this field are Electron Beam Induced Current (EBIC), Resistive Contrast Imaging (RCI) and Electron Beam Induced Resistance Change (EBIRCh). All these rely heavily on fast measurements and mapping of minute currents originating from the IC samples under electron beam irradiation. Practical limits in beam currents and beam damage often result in pA-level currents, that are extremely challenging to measure at the high speeds required for mapping [1,2]. A novel strategy of managing this challenge is presented here, combining an advanced chopped scan mode with lock-in amplification to achieve a step reduction in noise.

Lock-in amplification is an established method to manage noise in low-level measurements, whereby the electron beam is modulated on/off using a fast beam blanker, which results in a modulated EA signal from the IC. Lock-in amplification electronics are then used to "lock in" the modulated frequency, demodulate the signal and then measure without noise from adjacent frequencies. However, fast beam blankers are highly specialized devices missing from most electron columns, which prevents the practical application of this lock-in technique. A novel approach is proposed here, where the beam is blanked using the standard scan coils available on every electron column, as shown in Fig. 1. The beam is moved at high speed between a reference "blanking" position that produces no EA signal and the normal scan pixels. This results in modulated EA signal, similar with that of a fast beam blanker. Practical examples shown in Fig. 2,3 demonstrate a marked reduction of low-frequency noise in RCI, in particular for low ohmic devices. Further technical details will be presented on practical chopping frequency limits and the resulting lower noise in imaging, to illustrate the benefits of this novel approach.

Fig. 1. Schematic of chopped scan mode, showing how the electron beam is moved between a reference position and each beam position (image pixel). Time plots show the corresponding reference clock for beam chopping and lock-in amplification, output X and Y scan signals, and the modulated EA signal.

Fig. 2. Experimental RCI on a series of reference devices, demonstrating a marked reduction in noise.

Fig. 3. Comparison of electrical RCI data without and with chopped scan and lock-in amplification.

References

1. Vasco et al., Journal of Electronic materials (2024) 53 5850-5857
2. Rolf et al., ISTFA Conference proceedings (2017) 446-450

Acknowledgement

The authors acknowledge Imina Technologies SA for support with integrated nanoprobing

Fig. 1

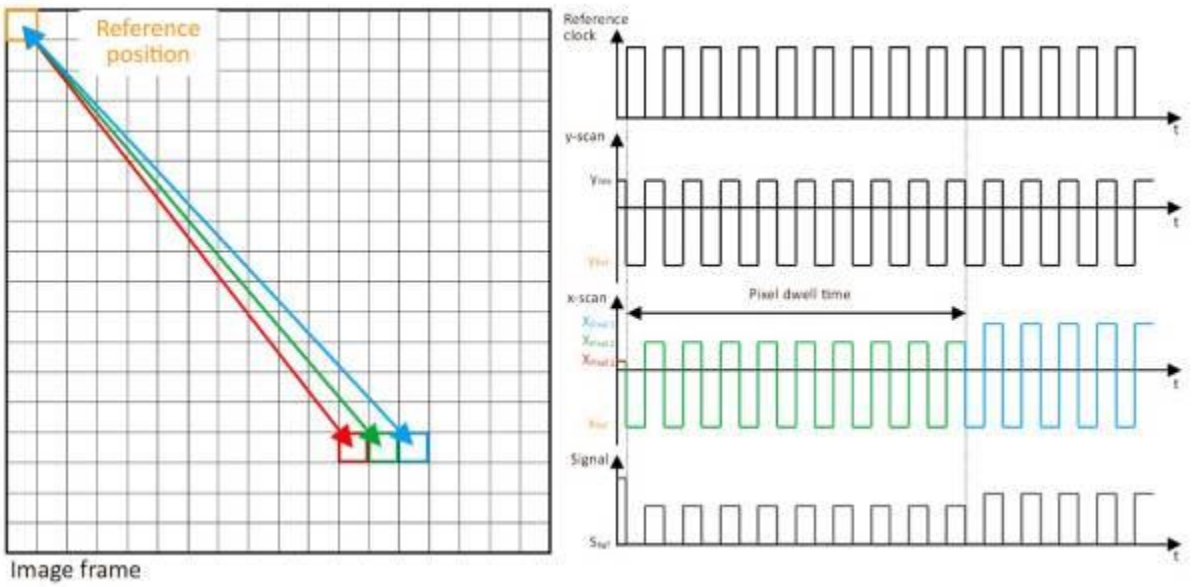

Reference position
Image frame
Reference clock
y-scan
x-scan
Pixel dwell time
Signal

Fig. 2

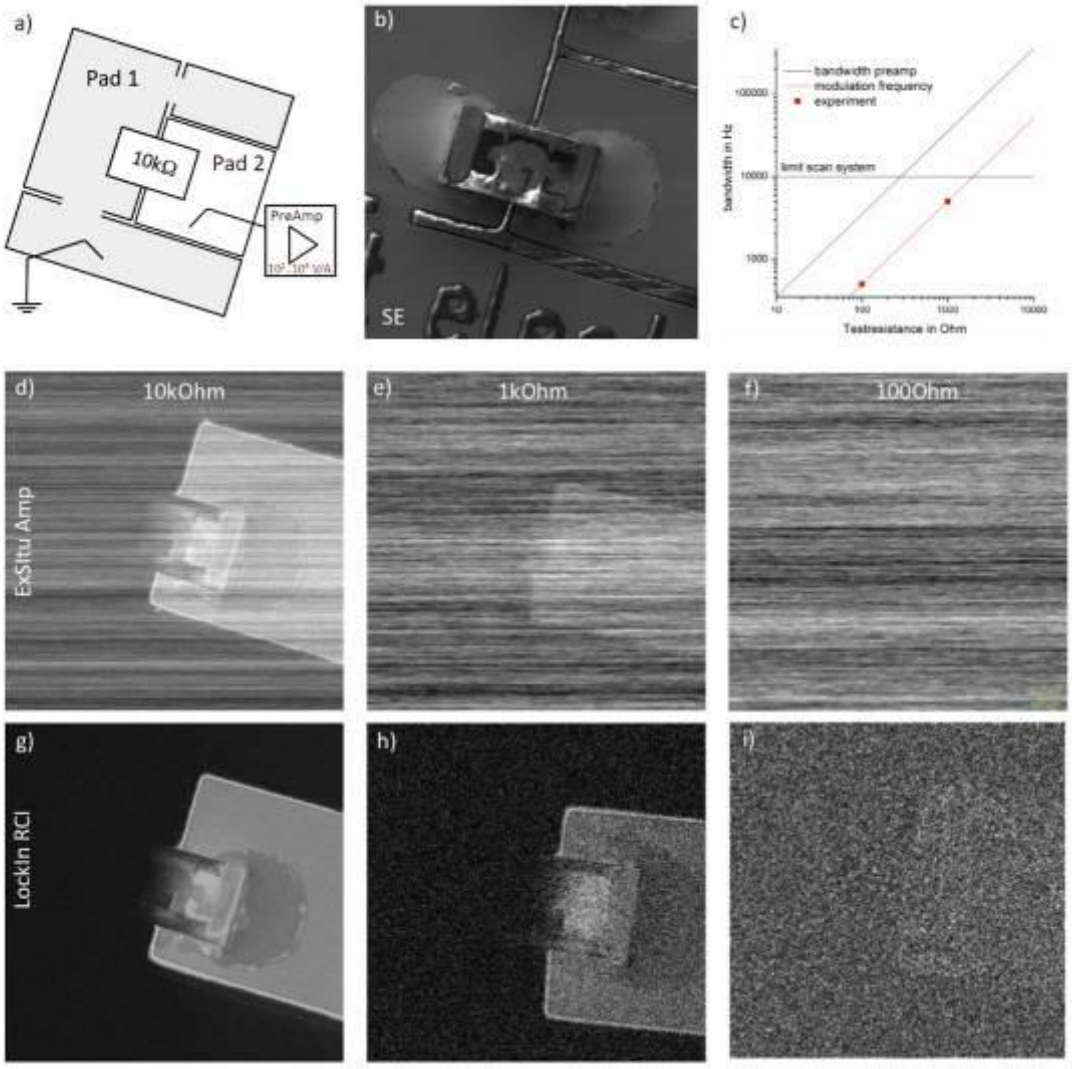
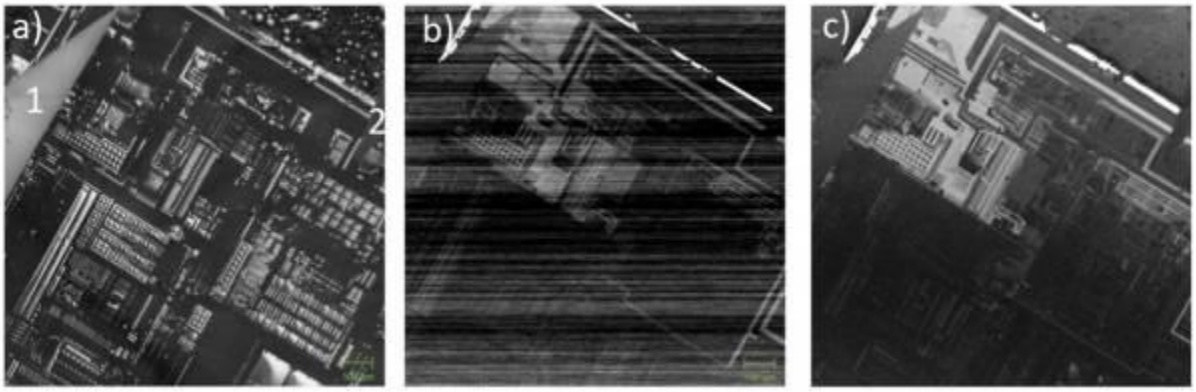

a)
Pad 1
10kΩ
Pad 2
PreAmp
b)
SE
c)
bandwidth preamp
modulation frequency
experiment
limit scan system
bandwidth in Hz
Testresistance in Ohm
d)
10kOhm
ExSitu Amp
e)
1kOhm
f)
100Ohm
g)
LockIn RCI
h)
i)

Fig. 3


a)
1
2
b)
c)

IM3.P23
The NanoMi open-source electron microscope – Electronics builds

D. Homeniuk[1], M. Malac[1,2], M. Schreiber[1,2], M. Salomons[1], S. Ruttiman[1,2], M. Kamal[3], S. Cockram[4], K. W. Kwan[4], O. Adkin-Kaya[3], J. A. Marin Calzada[2], X. Wang[5], P. Price[1], M. Cloutier[1], M. Hayashida[1], R. Egerton[2], K. Harada[6]

[1]National Research Council of Canada, Edmonton, Canada
[2]University of Alberta, Physics, Edmonton, Canada
[3]University of Alberta, Electrical and Computer Engineering, Edmonton, Canada
[4]University of British Columbia, Electrical Engineering, Vancouver, Canada
[5]University of Alberta, Computer Science, Edmonton, Canada
[6]RIKEN, Center for Emergent Matter Science, Hatoyama, Japan

Electron microscopes (EMs), either transmission (TEM), scanning (SEM), or scanning transmission (STEM), are useful tools in many fields of science. However, the high cost of commercial EMs can be prohibitive, limiting the usefulness of this valuable tool. Once an EM has been purchased, users may need to understand how an image is formed in order to properly use the instrument. With these factors in mind, we are leveraging the open-source concept to make EM more attainable to the community by suggesting users build their own to achieve a number of goals. Cost is minimized, setup is flexible so users can build any configuration they desire, users can design and build new components to suit their needs, interfaces are defined to allow for component sharing between builds, and through building the device users will learn how to take better images and improve the quality of science.

The project objective is to build a community of users sharing blueprints and schematics of components for a modular EM setup which we are calling NanoMi [1]. NanoMi can take on any form of electron microscopy based on placement of the lenses and deflectors, which are easily adjustable on a breadboard-like layout. All components aim to be low cost and high-vacuum compatible. Another publication [2] has presented the mechanical builds, so here we will showcase the electronics.

An EM requires control of deflectors for beam alignment, stigmators for beam shaping, mechanical motion for aperture and sample positioning, and optionally deflectors for scanning the beam in SEM/STEM modes. Control over lenses is also required but is not covered here. Custom printed circuit boards (PCBs) have been designed with free computer-aided design software, and then were built, assembled and tested for all of the above. The designs were made to be modular, flexible, and cost effective. Scanning electronics that we refer to as Scan-O-Mi were also created to synchronize the scan position of the beam to acquisition of data from the column at high speed.

Two prototypes of NanoMi have been completed, and validation of SEM and TEM is complete, with STEM mode in testing. PCBs for control of deflectors and stigmators are shown in Figure 1, a build to control a piezoelectric mover for mechanical motion is shown in Figure 2, and a Scan-O-Mi PCB is shown in Figure 3. Deflectors and stigmators operate on 70 Volts, while the piezoelectric mover operates on 400 Volts. Scan-O-Mi connects via USB to a computer, generates output X/Y scan signals in 16-bit resolution, allows simultaneous read-in of 8 14-bit resolution signals from the microscope, and has on-board RAM that stores image data until the computer is ready. Figure 4 shows early results of a Scan-O-Mi readout on the NanoMi user interface with the X output fed back into one of the image inputs as a means of calibration.

We are developing a public licence open-source electron microscopy platform called NanoMi. Our goal is for anyone to be able to build an electron microscope, train students and prototype new concepts. The NanoMi platform features modularity in its mechanical and electrical design for adaptability. Two microscopes have been built as a proof of concept.

Acknowledgment: Support for the project was provided by National Research Council (NRC) and by NSERC RGPIN-2021-02539

References:

[1] nanomi.org and https://github.com/NRC-NANOmi/NanoMi [2] M. Malac et. al, NanoMi: An open source electron microscope hardware and software platform, *Micron* **163** (2022) 103362.

Fig. 1

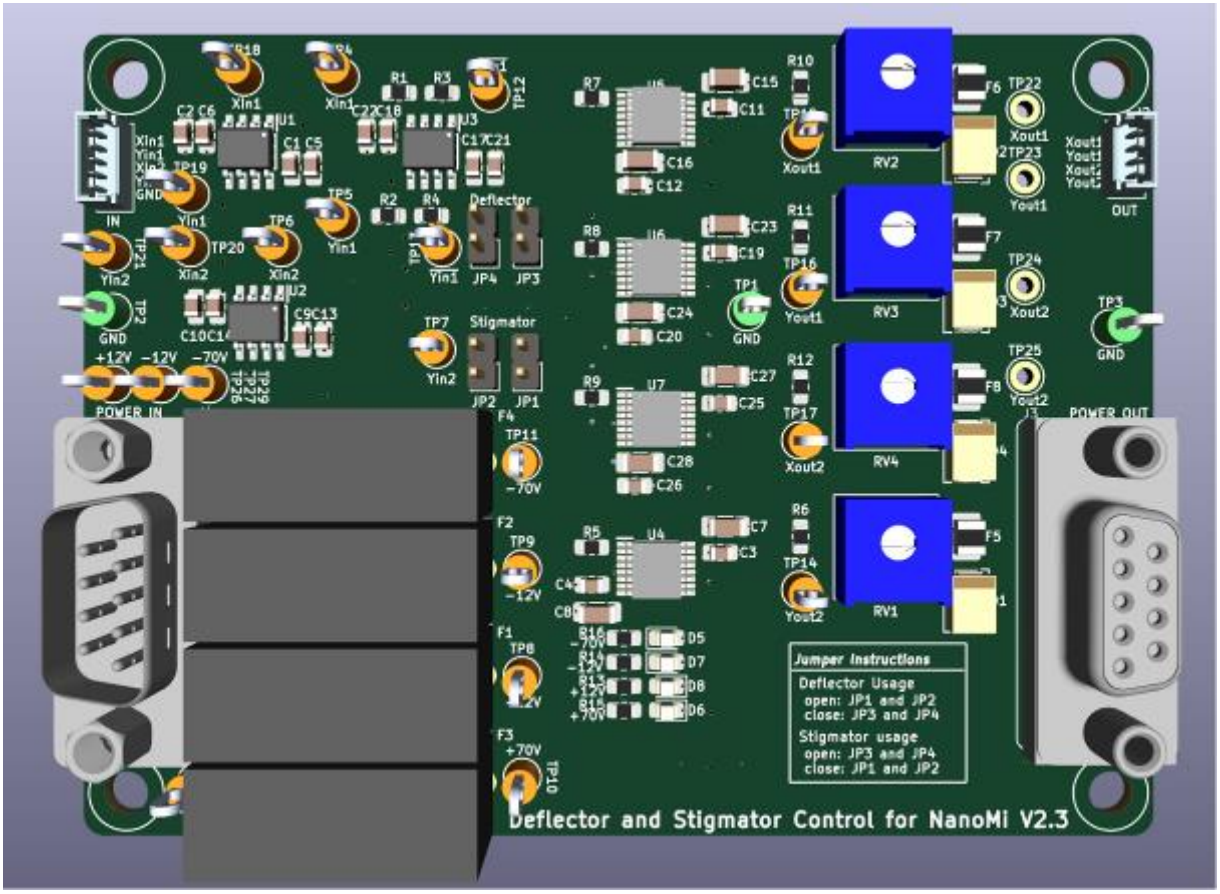


Fig. 2

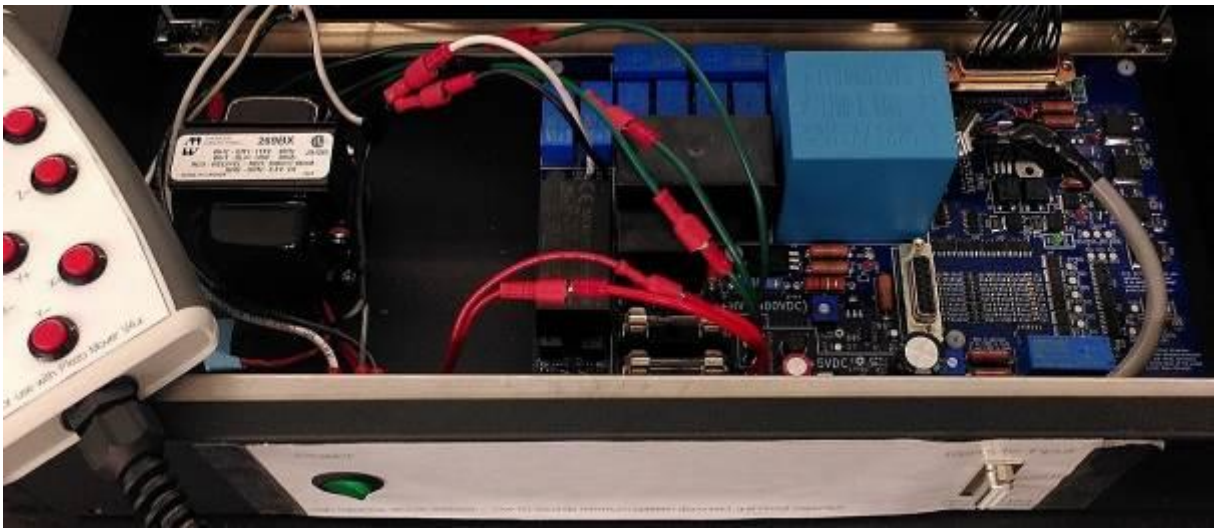


Fig. 3

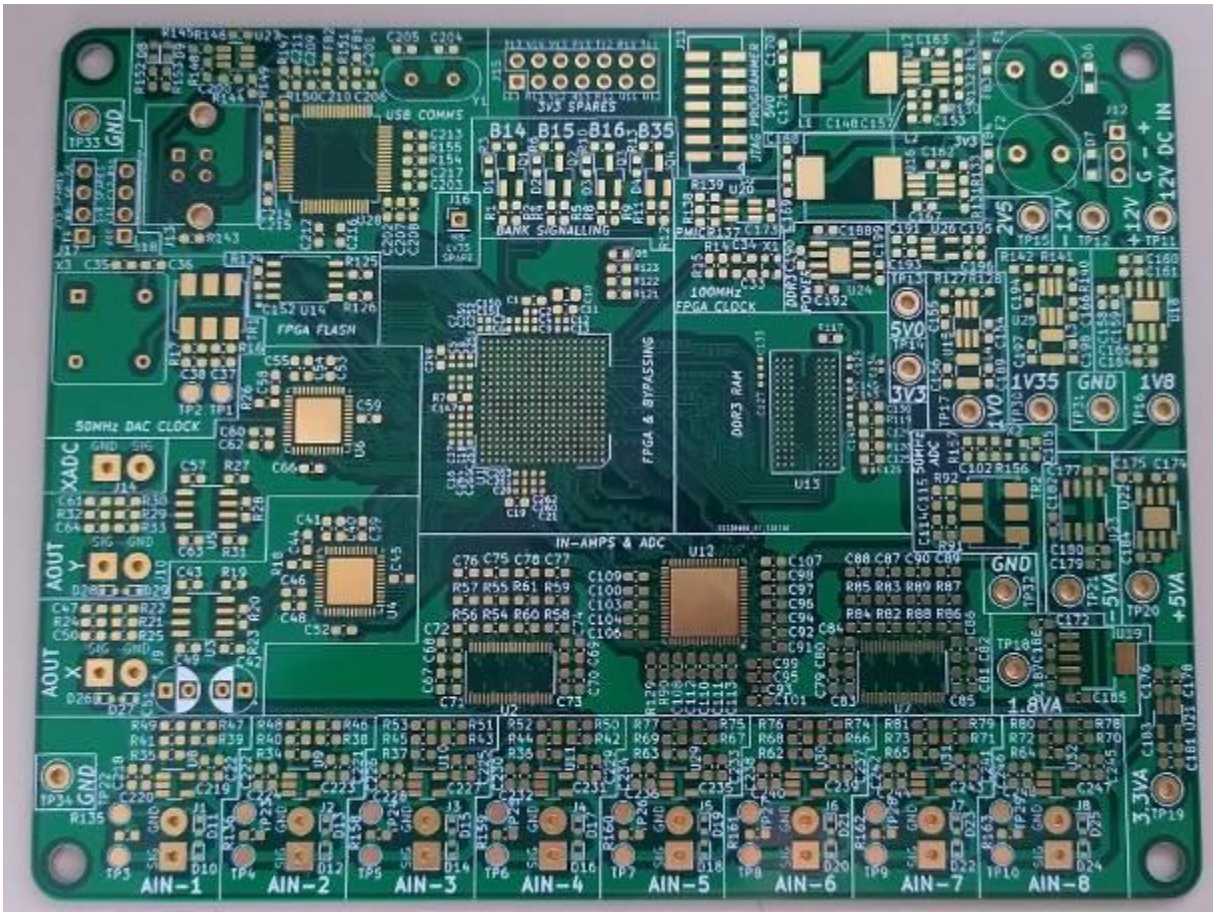
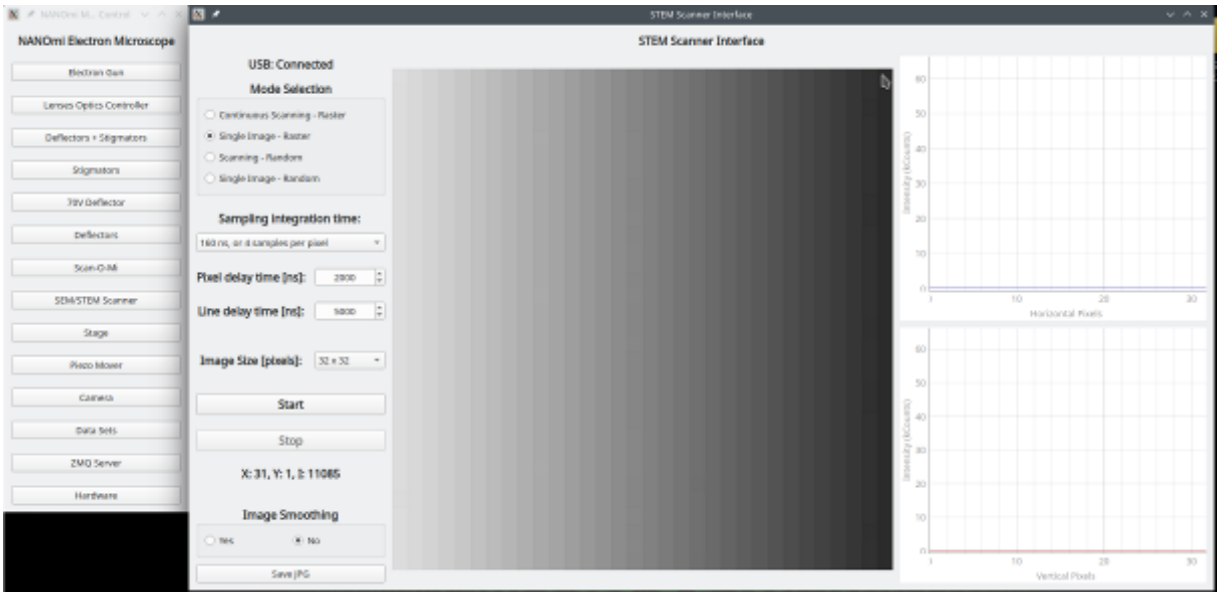

USB COMMS
SV3 SPARES
BANK SIGNALLING
FPGA FLASH
100MHz FPGA CLOCK
50MHz DAC CLOCK
FPGA & BYPASSING
DDR3 RAM
IN-AMPS & ADC
12V DC IN
+5VA
-5VA
1.8VA
3.3VA
AIN-1
AIN-2
AIN-3
AIN-4
AIN-5
AIN-6
AIN-7
AIN-8

Fig. 4


NANOmi Electron Microscope
STEM Scanner Interface
USB: Connected
Mode Selection
Sampling integration time:
Pixel delay time [ns]:
Line delay time [ns]:
Image Size [pixels]:
Start
Stop
Image Smoothing
Save JPG

IM3.P24
A multibeam SEM with >2700 beams for wafer defect inspection

A. Mangnus[1], E. Slot[2], E. Zolotarev[2], T. Fliervoet[1,2], M. Maassen[2], M. Wieland[1,2]

[1]ASML, Research, Veldhoven, Netherlands
[2]ASML, Development & Engineering, Delft, Netherlands

The semiconductor industry nowadays achieves with the production of electrical circuits on semiconductor wafers feature sizes of ~10 nm and feature densities of more than 100 million per mm^2. To check the functionality of all these features SEM imaging is regularly used for wafer defect inspection: its high resolution enables the detection of tiny pattern fidelity defects.

The objective for inline defect inspection during high-volume wafer production is to increase the throughput (scanned area per time) of the SEM. This would enable the inspection of sufficient wafer area for monitoring the production process and for capturing wafer defect fingerprints in high-volume production.

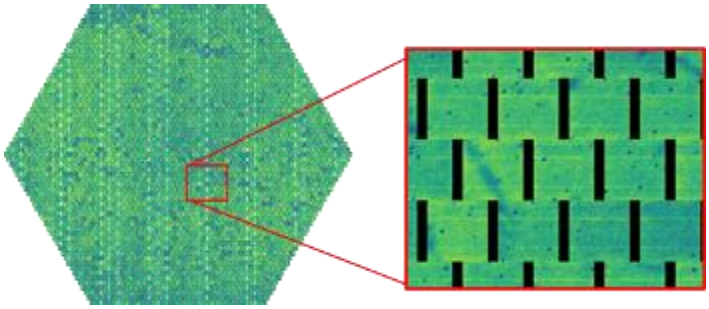
For this objective ASML is developing multibeam SEM systems. The first generation SEM multibeam system (eScan1100) with 25 beams has now been delivered to several customers. It yields a throughput improvement of about a factor 10 compared to single-beam inspection. The next step is the second generation multibeam (eScan2200) which will have >2700 beams, giving another throughput improvement of about a factor 10. This system has a new multibeam design based on MEMS technology which enables to scale down the pitch between beams and increase the number of beams. Each beam has an individual MEMS objective lens to do imaging with limited Coulomb Interaction effects. An in-lens detector enables individual detection for all beams.

Verification of the performance of the system technology is ongoing. All >2700 beams have shown to be functional and detector functionality and resolution performance have been demonstrated.

In conclusion, a new multibeam SEM system for wafer inspection with more than >2700 beams has been developed and is being tested. The system will increase the throughput of wafer inspection by about a factor of 100 compared to single-beam inspection, enabling monitoring of high-volume wafer production with electron beams.

Figure 1: verification of functionality of >2700 beams

Fig. 1



IM 4: Emerging techniques and applications in 4D-STEM

IM4.01(inv)
4D-STEM – From 3D crystal orientation mapping to atomic structure imaging

C. H. Liebscher[1]

[1]Ruhr University Bochum, Faculty of Physics and Astronomy, Bochum, Germany

Introduction

The emergence of pixelated electron detectors with fast readout speeds has enabled entirely novel imaging modalities, where full diffraction information is captured in each real space probe position in a scanning transmission electron microscope (STEM), termed 4D-STEM. By adjusting the probe semi-convergence angle it is possible to realize either nanobeam diffraction mapping for phase or crystal orientation mapping while an atomic resolution probe facilitates phase contrast imaging to determine local electric fields and image light elements in complex materials.

Objectives

The present talk showcases two examples where 4D-STEM is used to obtain 3D information on crystal orientations in a nanostructured metallic material and to image intricate oxygen octahedral tilting in $NaNbO_3$ thin films. In this first part of the talk, I will show the development of 4D scanning precession nanobeam electron diffraction (4D-SPED) tomography to determine 3D crystal orientations and the character of interfaces in a nanocrystalline Ni-W alloy.

I will then demonstrate atomic structure imaging of phase variants in $NaNbO_3$ thin films using an ultra-fast direct electron detector with a focus on modulations in oxygen sublattice arrangement. By capturing millions of diffraction patterns with pixel dwell times in the microsecond range, it is possible to reconstruct phase contrast images with a wide field of view for robust atomic resolution imaging while minimizing the influence of scan instabilities.

Materials & methods

The nanocrystalline Ni-14 at.% W alloy was electrodeposited on a Cu substrate obtained from Xtalic Corporation, USA. 4D-SPED tomography was performed using a scintillator coupled CMOS detector with pixel dwell times of 41 ms. Tomography data was acquired using an on-axis rotation tomography holder.

The $NaNbO_3$ thin films with a thickness of 100 nm were deposited on Nb:$SrTiO_3$ substrates. Atomic resolution 4D-STEM was performed with an ultra-fast hybrid pixel detector enabling to capture diffraction information down to ~10 µs pixel dwell times.

Results

We demonstrate that by using a multi-indexing automated crystal orientation mapping approach it is possible to account for overlapping crystals enabling to retrieve through thickness crystallographic information. Employing corresponding orientation-specific virtual apertures for each projection enables to form virtual dark-field images of individual crystals which are used for the tomographic

reconstruction. With this not only the 3D arrangement and morphology of the crystals becomes accessible, but also the full 3D crystallographic information.

Atomic resolution 4D-STEM using center-of-mass imaging reveals intricate oxygen octahedral tilting patterns within the $NaNbO_3$ thin films indicating the presence of different phase variants. The results from first moment measurements will be complemented by multislice electron ptychography to explore the potential of obtaining 3D information of domain formation within the sample along the electron beam direction.

Conclusions

We demonstrate that 4D-STEM is a versatile tool to obtain quantitative 3D information in nanocrystalline materials and at the same time reveal intricate structural modulations in simple, yet complex oxide materials at atomic resolution.

IM4.02(inv)
4D-STEM in Cryo-EM to study neurodegeneration

H. Stahlberg[1]

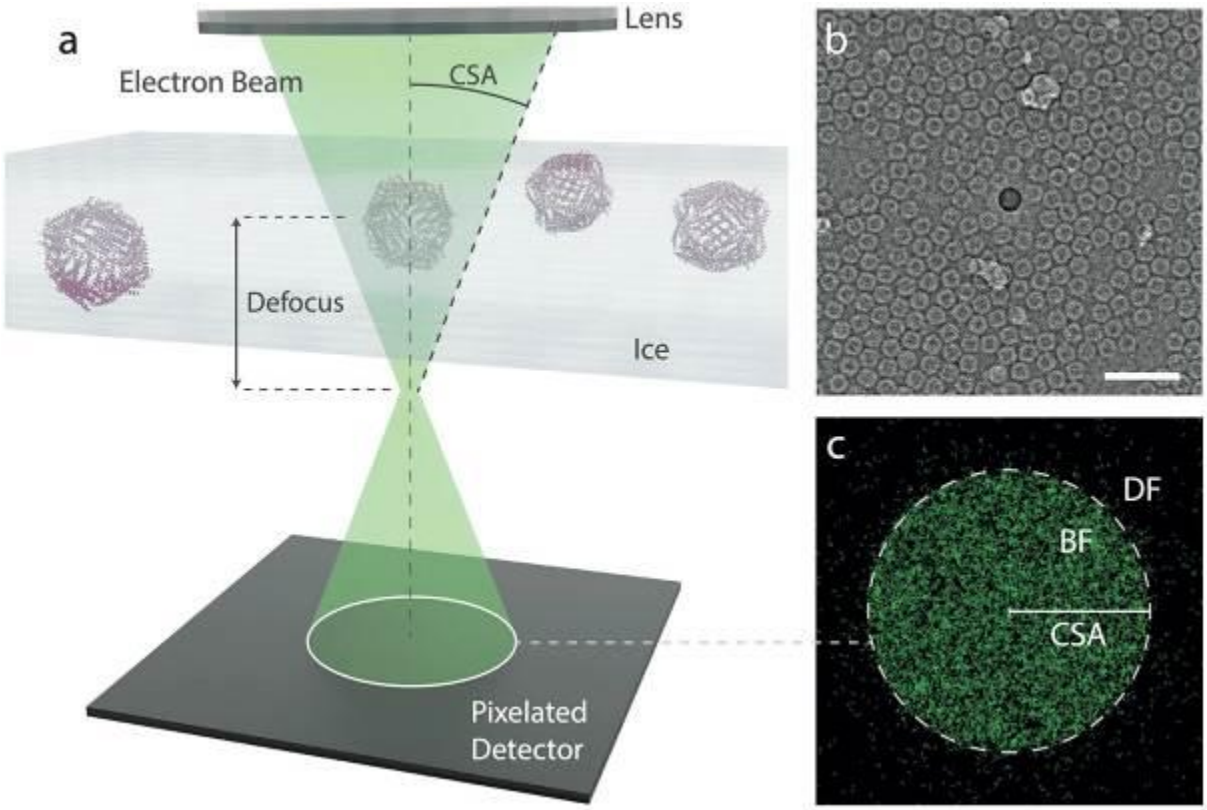
[1]Ecole Polytechnique Fédérale de Lausanne, Laboratory of Biological Electron Microscopy, Institute of Physics, Lausanne, Switzerland

Cryo-transmission electron microscopy (cryo-EM) or tomography (cryo-ET) of frozen hydrated specimens are efficient techniques for analyzing the structure of proteins or tissue sections. However, these methods face challenges due to their very low signal-to-noise ratio. Diffractive imaging, maximizing the recovery of signal from electrons interacting with the sample, promises improved phase contrast and resolution. We are using convergent beam electron diffraction with a probe aberration-corrected Titan Krios and an ultra-fast pixelated detector (4D-STEM), evaluating the data with ptychography and other data analysis methods, to maximize phase contrast signal recovery from a frozen hydrated cryo-EM specimen. This is applied to frozen hydrated human brain tissue and to vitrified single protein particles.

Küçükoğlu et al., Low-dose cryo-electron ptychography of proteins at sub-nanometer resolution. Nature Commun. 15, 8062 (2024).

https://doi.org/10.1038/s41467-024-52403-5

Fig. 1



IM4.03
Benchmarking analytical ptychography for the low-dose imaging of beam-sensitive materials

H. Lalandec Robert[1,2], A. Annys[1,2], T. Chennit[1,2], M. L. Leidl[3], K. Müller-Caspary[3], J. Verbeeck[1,2]

[1]University of Antwerp, Electron microscopy for materials science, Antwerp, Belgium
[2]University of Antwerp, NANOlight Center of Excellence, Antwerp, Belgium
[3]Ludwig-Maximilians University Munich, Chemistry and Centre for Nanoscience, Munich, Germany

Advances in scanning transmission electron microscopy (STEM), such as event-driven detectors (EDD) [1], have contributed in making it a viable solution for the high-resolution imaging of beam-sensitive specimens such as 2D materials, zeolites or viruses. The recovery of a far-field diffraction pattern at each scan position enabled using computational imaging approaches such as analytical ptychography. Those approaches, which are both direct and computationally efficient, include the Wigner distribution deconvolution (WDD) and side-band integration (SBI) methods. As they permit the measurement of the projected electrostatic potential with a high signal-to-noise ratio [2,3], their continued development is of high importance across materials science and biology.

This work aims at further exploring the capacity of analytical ptychography to measure the potential with low doses, i.e. below 10^3 $e^-/Å^2$ with atomic resolution, given realistic Poisson counting statistics an EDD [4]. This is done based on simulations, given a MoS_2 monolayer (see figure) and ice-embedded apoferritin. The dose-efficiency of both WDD and SBI, as well as of the integrated center of mass (iCoM) approach, are investigated and compared, for different numerical apertures and given a defocused illumination. General trends are thus evidenced, e.g. concerning the persistence of low- and high-frequency noise. The role of the contrast transfer function, and the assumption of weak scattering, are analyzed. Moreover, the scan-frequency partitioning algorithm (SFPA), a new memory-efficient and parallelizable solution to implement the methods, is demonstrated.

With the fundamental analysis of dose-efficiency and contrast transfer having been done, a new framework for live and event-driven analytical ptychography, based on discretized electron incidences, is introduced. This framework, referred to as guided progressive reconstructive imaging (GPRI), consists in the in-line treatment of a detection stream, provided by an EDD, and in a cumulative reconstruction process. Its theoretical foundation, implementation and very low computational complexity, are discussed. Experimental and simulated application cases are demonstrated.

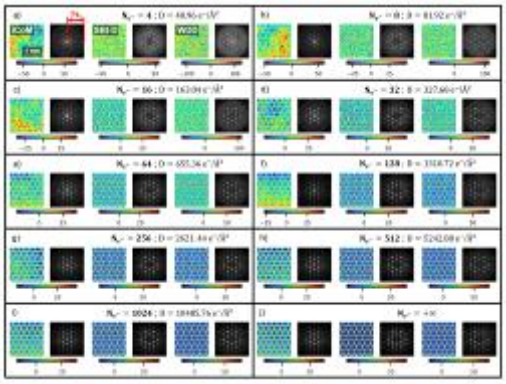
Overarchingly, this work illustrates the high interest of analytical ptychography for the low-dose imaging of beam-sensitive objects. This is due to a direct and relatively simple formulation, which ensures reproducibility as well as short processing times. In that respect, those methods are particularly appropriate for a generalized application to routine measurements, with low cost-of-access for users.

[1] D. Jannis et. al. ; Ultramicroscopy, 233, 113423 (2022) [2] C. O"Leary et. al. ; App. Phys. Lett., 116, 124101 (2020) [3] C. O"Leary et. al. ; Ultramicroscopy, 221, 113189 (2021) [4] H. L. Lalandec Robert et. al. ; submitted to Euro. Phys. Journ. App. Phys., arXiv:2501.08874v1

Funding was received from the Horizon 2020 research and innovation program (European Union), under grant agreement No 101017720 (FET-Proactive EBEAM).

Figure: results of analytical ptychography of monolayer MoS2, applied on a multislice STEM simulation (60 kV, 30 mrad). Calculations are done for a variety of dose D in e-/Å2. For each case, the measurement of the projected potential, in V·nm, is displayed with the square root of its FFT"s amplitude.

Fig. 1



IM4.04
Large-angle lorentz 4-dimensional scanning transmission electron microscopy for simultaneous local magnetization, strain and structure mapping

S. Kang[1,2,3], X. Mu[1], D. Wang[1,3], R. E. Dunin-Borkowski[4], J. McCord[5], C. Kübel[1,2,3]

[1]Karlsruhe Institute of Technology, Institute of Nanotechnology, Karlsruhe, Germany
[2]Technical University of Darmstadt, Department of Material- and Geosciences, Darmstadt, Germany
[3]Karlsruhe Institute of Technology, Karlsruhe Nano Micro Facility (KNMFi), Karlsruhe, Germany
[4]Forschungszentrum Jülich GmbH, Ernst Ruska-Centre for Microscopy and Spectroscopy with Electrons, Jülich, Germany
[5]Kiel University, Materials Science, Kiel, Germany

Small atomic adjustments can significantly influence magnetic properties. Strain, for example, modifies magnetic anisotropy and enables fine-tuning of the magnetic microstructure. However, its impact on nanoscale magnetism remains largely unexplored, and fluctuating strain makes directly linking structural changes to magnetic behavior challenging.

To address this, we developed LA-Ltz-4D-STEM, a technique for simultaneously mapping structural information, strain, and magnetic fields at the nanoscale. This method leverages reciprocal space data, providing detailed structural and magnetic insights. By customizing standard STEM optics, we optimized lens configurations to achieve large diffraction angles in Ltz-STEM mode, enabling high-precision mapping. The technique records both unscattered and diffracted electron beams, capturing phase shifts induced by local magnetic fields while preserving interatomic pair information.

We applied LA-Ltz-4D-STEM to a deformed amorphous ferromagnet with complex nanoscale strain variations [1-2]. The analysis revealed an anomalous magnetic configuration near shear bands, which exist in a magnetostatically high-energy state. Using pixel-to-pixel correlation across a large field of view, essential for studying industrial ferromagnetic materials, we classified magnetic moments into two groups: one influenced by magnetoelastic coupling and the other driven by magnetostatic energy competition. This approach provides a powerful tool for exploring the interplay between strain and magnetism, advancing our understanding of nanoscale ferromagnetic behavior.

Fig. 1: Schematic of LA-Ltz-4D-STEM and its optical setup. (a-c) Optical setups for nanobeam diffraction, conventional field-free Ltz-STEM, and LA-Ltz-4D-STEM. (d) Electron probe scanning in LA-Ltz-4D-STEM, collecting spatially-resolved diffraction patterns. (e) Example data: amorphous diffraction pattern (Fe-based alloy) and crystalline diffraction pattern (SmCo magnet). The direct beam shift reveals local magnetic fields via Lorentz force. Structural information is extracted from diffraction rings: atomic density from the 1st ring area, principal strains (ε1, ε2) from elliptical distortion, and S(q) via azimuthal integration. PDFs are obtained through Fourier sine transformation. (f) Visualization of magnetic field, strain, and relative density (Δρ) in a plastically deformed amorphous alloy.

References

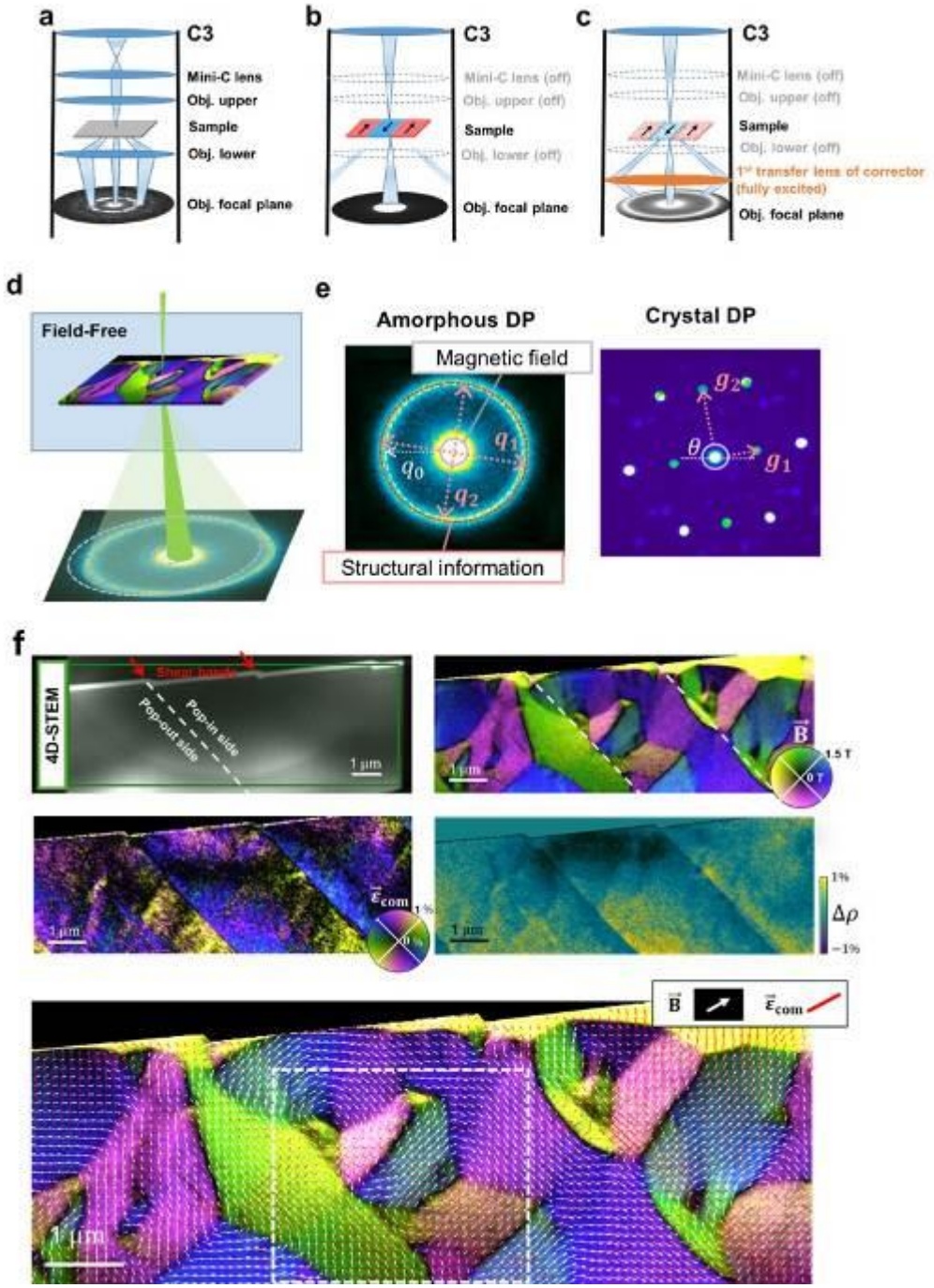
[1] Silveyra et al., Science 362, 418 (2018)

[2] Kang et al., Acta Materilla 119495 (2024)

[3] Kang et al., Advanced Materials 2212086 (2023)

[4] Kang et al., Nature Communications 16, 1305 (2025)

Fig. 1


a
C3
Mini-C lens
Obj. upper
Sample
Obj. lower
Obj. focal plane
b
C3
Mini-C lens (off)
Obj. upper (off)
Sample
Obj. lower (off)
Obj. focal plane
c
C3
Mini-C lens (off)
Obj. upper (off)
Sample
Obj. lower (off)
1st transfer lens of corrector (fully excited)
Obj. focal plane
d
Field-Free
e
Amorphous DP
Magnetic field
Structural information
Crystal DP
f
4D-STEM
Pop-in side
Pop-out side
1 μm
1.5 T
0 T
1%
Δρ
−1%

IM4.05
Harnessing strain relaxation in TEM lamellae – Composition and specimen geometry from Single 4D-STEM measurements

F. Otto[1], L. Niermann[1], T. Niermann[1], M. Lehmann[1]

[1]Technische Universität Berlin, Institut für Optik und Atomare Physik, Berlin, Germany

Modern electronics largely rely on nanoscale devices, many of which incorporate heterointerfaces of semiconductor alloys. These alloys are precisely engineered to optimize device performance. Accurately determining their composition is crucial for the development of such devices.

In contrast to X-ray-based analytical techniques, scanning transmission electron microscopy (STEM) provides the spatial resolution needed to measure alloy compositions directly from real devices at the nanoscale. For such investigations, STEM offers a wide range of compositional analysis tools, primarily based on diffraction or characteristic X-ray emission. Both approaches, however, have significant drawbacks: Characteristic X-ray analysis utilizes the inelastic interaction between the high-energy electron beam and the sample to identify elemental composition, requiring long acquisition times to achieve a sufficient signal-to-noise ratio. Additionally, correlating measured X-ray intensities with composition is often nontrivial, and, in thicker samples, the spatial convolution with the interaction volume must be considered, which degrades spatial resolution.

Diffraction techniques, inferring composition from the spacing of Bragg discs, lose precision in thicker samples, where the effects of dynamic diffraction become significant. Additionally, these strain-based techniques typically assume constant strain along electron beam direction. This assumption, however, does not hold for thin, electron-transparent TEM lamellae, where strain relaxes at the surfaces due to the absence of material, upholding the internal stress in the bulk wafer. This relaxation causes dynamic diffraction patterns to change across the strained interface. While this pattern variation is a parasitic effect in conventional strain evaluation via disc detection, it is also indicative of the initial stress at the interface.

Here, we directly infer the material composition from the variations in dynamic diffraction due to strain relaxation.Through the initial stress at the interface, impacting the magnitude of the relaxation, these variations depend on the lattice mismatch at a heterointerface. We access this information through the comparison of experimental 4D-STEM measurements, locally probing dynamic diffraction, with beam simulations, taking surface relaxation into account. These simulations utilize a forward-calculation in two steps: First we obtain the 3D-strain field of a relaxed lamella with a given composition and geometry from finite-element calculations. We incorporate this strain field into Dawin-Howie-Whelan (DHW) simulations of dynamic diffraction. Simulations are repeated over a range of compositions and geometries. We obtain the lamella thickness, quantum well width and alloy composition within the layer from a single 4D-STEM scan by finding the best match between experiment and simulation. Utilizing this technique, we accurately determine the composition of a series of QWs of the technologically significant AlN/GaN material system.

Our novel method of compositional analysis provides high accessibility, as it works over a wide range of specimen thicknesses and does not require any auxiliary equipment such as EDS detectors. Additionally, the ability to extract multiple specimen parameters, including composition, from a single scan makes the method suitable for beam-sensitive materials or those easily contaminating.

IM4.06
Automated tomographic 4D-STEM data acquisition workflow connected with ptychographic high-resolution 3D reconstruction

S. You[1], B. Zhu[2], X. Ye[2], P. Pelz[1]

[1]Fraunhofer Center for Silicon Photovoltaic, Department of Material Science, Erlangen, Germany
[2]Indiana University, Department of Chemistry, Bloomington, MN, United States

Manual tomographic 4D-STEM data acquisition requires continuous user intervention for alignment, and tilt adjustments, making it time-consuming and prone to errors. Additionally, prolonged exposure for focusing and manual tracking increases radiation dose, while delays between acquisitions introduce drift, degrading reconstructions. Additionally the 3D potential volume reconstruction using ptychographic tomography usually happens after the experiment session, inconsistent data acquisition will result in degradation of result quality, or even failure of reconstruction.

Here, we introduce an automated tomographic 4D-STEM data acquisition workflow for ptychographic tomography. It minimizes exposure time and ensures optimal imaging by controlling microscope parameters with pre-programmed workflows. This accelerates data acquisition, reduces radiation damage, and improves reproducibility. The 2D phase projection of each tilt angle is provided in real-time using multi-slice ptychography reconstruction to check the accuracy and consistency of data acquisition process.

The automated tomographic 4D-STEM data collection workflow is based on SerialEM [1] scripts and custom 4D-STEM camera plugin inspired by Seifer et al [2]. SerialEM is a program that include a variety of functions to control the microscope including tilting the sample, performing image shift, etc. The custom camera plugin connects with our external scan generator DISS6, which then controls the 4D-STEM ARINA camera. The camera plugin integrates the two main functions into one scan generator: image acquisition for general purposes, which is currently done using the HAADF channel, and 4D-STEM data acquisition, which is done using the ARINA detector.

The detailed workflow is described in Fig 1. The electron microscope is controlled by the microscope PC using SerialEM and custom scripts. The custom SerialEM scripts control the stage tilt and fine tracking of the target area using image shift and sub-window scan. A 2D phase projection of the current tilt angle is reconstructed using real-time multi-slice ptychography on high performance workstation, examples shown in Fig. 2a). End-to-end reconstruction [3] recovers the 3D potential volume of the sample, a preliminary result with Gd2O3Gd2O3 sample is shown in Fig. 2b), cross-section image in Fig. 2c).

By automating the workflow of tomographic 4D-STEM data collection, we minimize the human error and speed up the acquisition process. The real-time 2D phase projection reconstruction ensure the data quality and consistency. A 3D potential volume is reconstructed with near-isotropic resolution.

Fig. 1. The workflow of the automated tomographic 4D STEM data acquisition and 3D volume reconstruction. Custom scripts uses SerialEM commands to control the microscope performing the tilting and tracking tasks.

Fig. 2. a) 2D phase projections reconstructed using real-time multi-slice ptychography. b) 3D potential volume of a Gd2O3 sample using end-to-end reconstruction, the scale box is 1nm3. c) A cross-section image of the beam tilt direction, the scale bar is 1nm.

References:

1. Mastronarde DN. Journal of Structural Biology (2005) 152, 36–51.
2. Seifer S, Houben L, Elbaum M. Microscopy and Microanalysis (2021) 27, 1476–1487.
3. You S, Romanov A, Pelz PM. Physica Scripta (2024) 100, 015404.
4. The authors acknowledge funding from the EAM Starting Grant, the ERC Starting Grant HyperScaleEM, with grant number: 101164581

Fig. 1

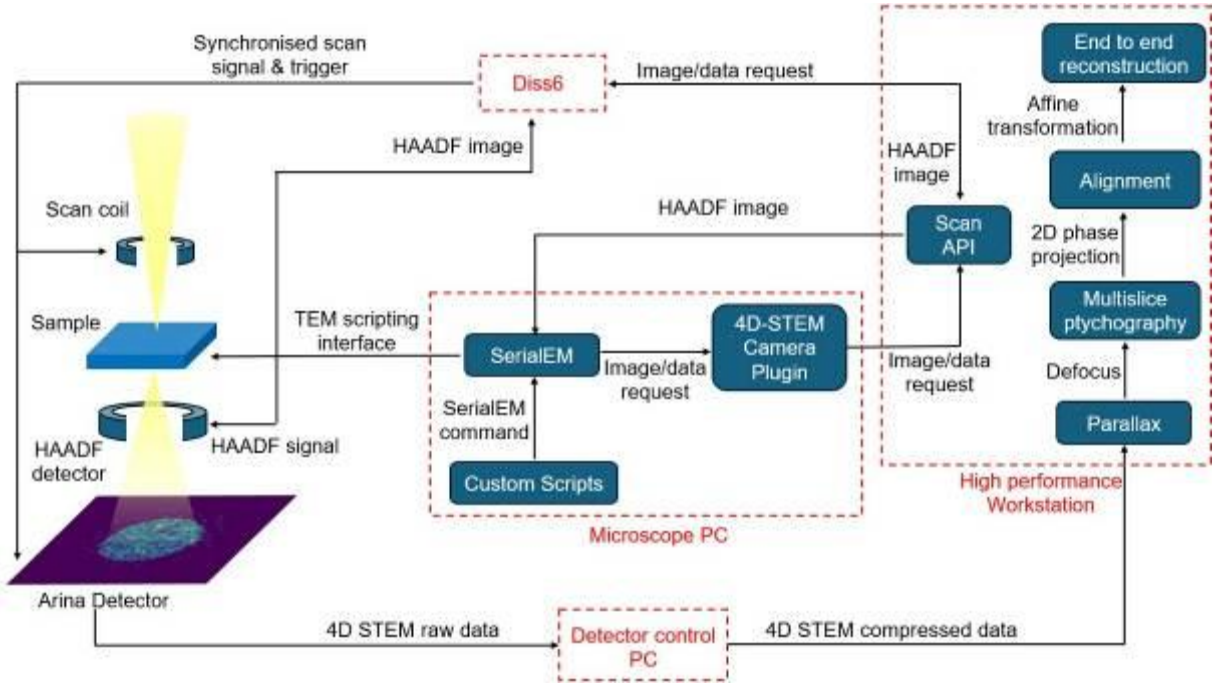
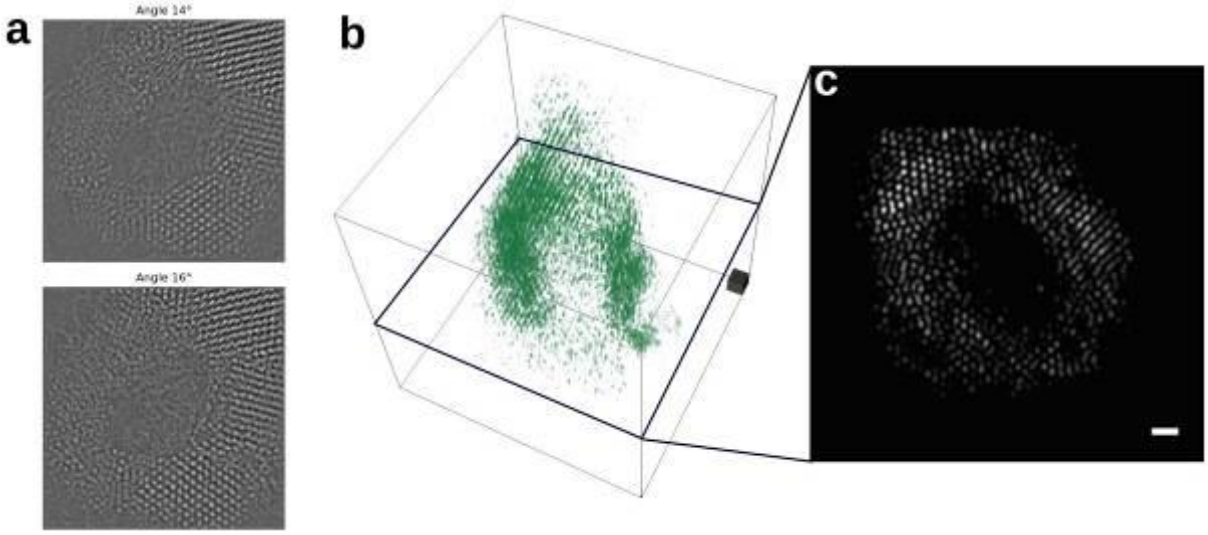


Fig. 2



IM4.P01
Investigating the effect of update strengths for atomic-resolution low-dose imaging in iterative ptychography

T. Chennit[1,2], S. Li[1,2], C. Hofer[1,2], N. J. Schrenker[1,2], A. Maiden[3,4], H. Lalandec Robert[1,2], S. Bals[1,2], T. Pennycook[1,2], J. Verbeeck[1,2]

[1]University of Antwerp, EMAT, Department of Physics, Antwerp, Belgium
[2]University of Antwerp, Nanolight, Center of excellence, Department of Physics, Antwerp, Belgium
[3]University of Sheffield, School of Electrical and Electronic Engineering, Sheffield, United Kingdom
[4]Diamond Light Source, Oxfordshire, United Kingdom

The adoption of aberration correction [1] has enabled atomic resolution imaging of crystalline materials, but beam damage presents challenges for high-resolution imaging [2]. While conventional transmission electron microscopy (CTEM) is widely used, scanning transmission electron microscopy (STEM) methods like ptychography show promise for low-dose imaging [3, 4]. Recently, electron ptychography has gained renewed interest with the advent of direct electron detectors [5, 6]. Iterative algorithms such as the extended ptychographic iterative engine (ePIE) [7] reconstruct the object and probe functions by iteratively refining an initial guess. However, finding the optimal update strength is tricky, as large updates can cause divergence, while small updates may lead to local minima. We find that for noisy data, smaller update strengths are needed for convergence.

Ptychographic reconstructions of ~2 nm thick formamidinium lead bromide ($FAPbBr_3$) from a simulated 4D dataset presented in figure 1, were performed with varying update strengths. At the highest dose (5000 $e^-/Å^2$), the reconstruction fails to correctly recover atomic site positions at $\alpha = \beta = 1$. At $\alpha = \beta = 10^{-1}$, 10^{-2}, and 10^{-3}, atomic positions are recovered but artefacts remain in the FFT, while artefact-free reconstructions occur with smaller update strengths. At 500 $e^-/Å^2$, the algorithm fails at $\alpha = \beta = 1$, and artefacts appear at $\alpha = \beta = 10^{-1}$, 10^{-2}, and 10^{-3}. Best results are achieved at $\alpha = \beta = 10^{-4}$ and 10^{-5}.

At the lowest dose (50 $e^-/Å^2$), the algorithm fails to converge at the three highest update coefficients, as shown in the FFT, but converges at lower values. This indicates that smaller update strengths are beneficial for convergence at low doses, though a balance must be struck between reconstruction quality and convergence speed.

To validate the arguments given above, a 4D dataset was experimentally obtained from a $FAPbBr_3$ sample using 200 kV and a 13 mrad semi-convergence angle, similar to the simulation parameters. The dataset was acquired with a Timepix3 camera [6] and 1 µs dwell time, with an electron dose below 50 $e^-/Å^2$. Figure 2 shows ePIE reconstructions for 100 iterations, with object and probe functions reconstructed at different update strengths. The optimal reconstruction was achieved at $\alpha = \beta = 10^{-3}$, with higher initial errors at lower update coefficients. This confirms the simulation results, where low update strengths are most effective at low doses. However, unlike simulations, the experimental dataset only successfully converged at $\alpha = \beta = 10^{-3}$, with lower values ($\alpha = \beta = 10^{-4}$) leading to noisier results and no recovery of higher frequencies.

In conclusion, optimizing update strengths in iterative ptychographic reconstructions is crucial for accurate convergence, especially at low electron doses. While lower update strengths improve reconstruction quality, they slow convergence and may lead to local minima. Experimental validation with a FAPbBr3 sample confirms that reduced update coefficients yield the best results, highlighting the trade-off between quality and convergence rate.

Fig. 1. ePIE phase reconstructions of ~2 nm $FAPbBr_3$ at various update strengths and electron doses from a simulated 4D dataset using 200 kV, 13 mrad, and a non-aberrated probe.

Fig. 2. ePIE phase retrieval results at different update strengths from an experimental 4D dataset. The reconstruction with $\alpha = \beta = 10^{-3}$ is averaged via template matching and shown at the bottom left.

Fig. 1

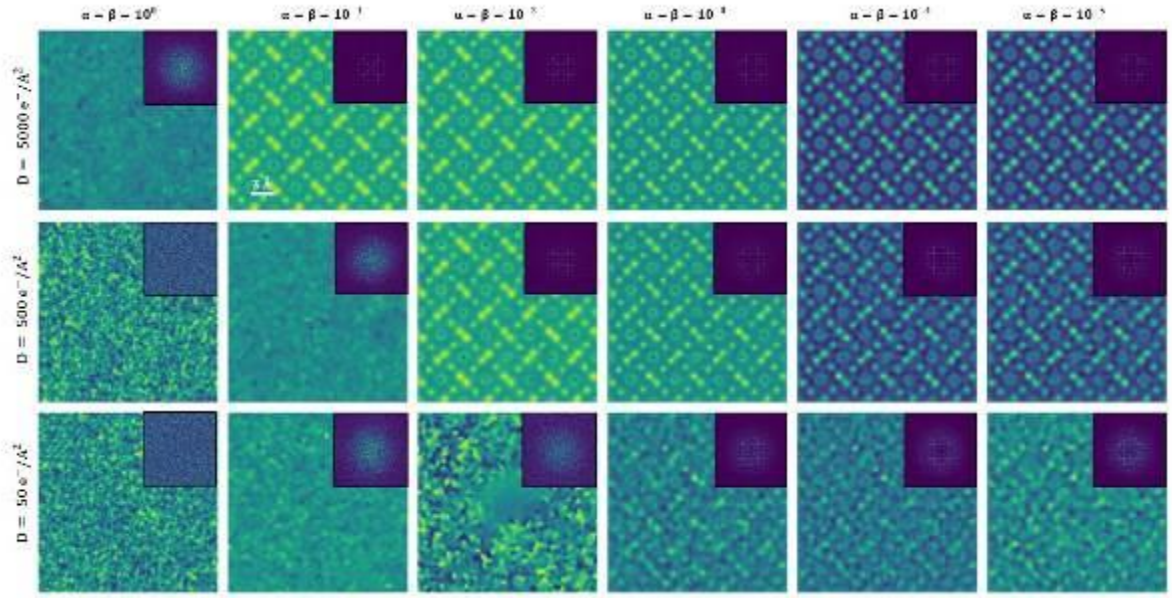
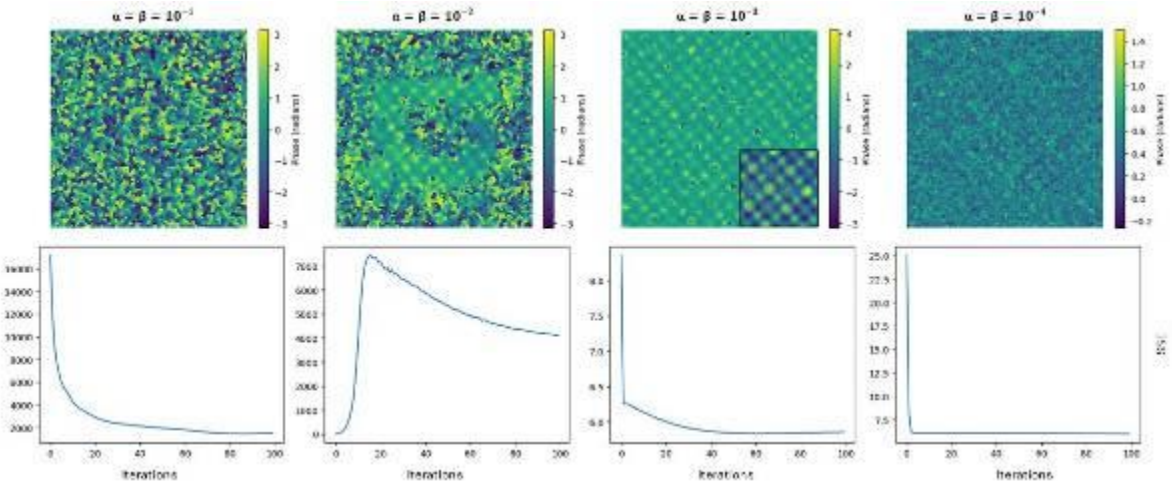


Fig. 2



IM4.P02
Cryo-STEM of biological macromolecules – Visualization by integrated differential phase contrast

A. Filopoulou[1], D. Mann[1], M. L. Leidl[2], I. Lazic[3], M. Wirix[3], K. Müller-Caspary[2], C. Sachse[1]

[1]Forschungszentrum Jülich GmbH, ER-C-3, Jülich, Germany
[2]Ludwig-Maximilians University Munich, Munich, Germany
[3]Thermo Fisher Scientific, Eindhoven, Netherlands

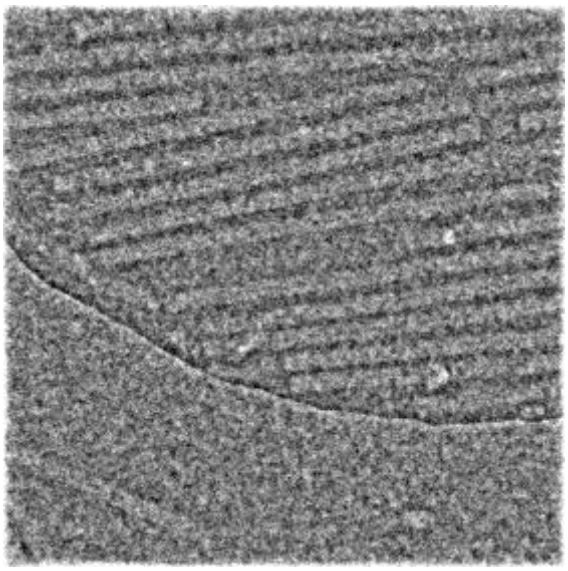
Scanning transmission electron microscopy (STEM) is a well-established method for the characterization of materials. However, it is not a widely used method for imaging biological samples in cryogenic conditions. Biological specimens are dose-sensitive, often have poor contrast against ice background and can therefore be challenging to visualize. Recently, we showed that integrated Differential Phase Contrast (iDPC)-STEM can be applied to vitrified biological specimens and near atomic resolution can be achieved (1). In STEM the resolution is dependent on the convergence semi-angle (CSA) of the focused beam. Using the iDPC-STEM approach, the maximum contrast of the image can be achieved in focus. In this work, tobacco mosaic virus (TMV) has been used as specimen at different CSAs (2.0, 4.0 mrad). In case of TMV near-atomic resolution results are demonstrated, in both types of data collection, micrographs and dose fractionated data. However, these challenges serve as a springboard for further research on the method in structural biology. Addressing the theoretical and experimental limitations can lead to methodological improvements and an expanded applicability of single-particle analysis to complex biological systems.

Fig. 1: TMV embedded in vitreous ice.

References:

(1) Lazić, I., Wirix, M., Leidl, M.L. *et al.* Single-particle cryo-EM structures from iDPC–STEM at near-atomic resolution. *Nat Methods* **19**, 1126–1136 (2022). https://doi.org/10.1038/s41592-022-01586-0

Fig. 1



IM4.P03
Simultaneous acquisition of 4D and EELS data by newly developed pixelated STEM detector

R. Sagawa[1], H. Hashiguchi[1], A. Nakamura[1], M. Huth[2], Y. Imari[2], V. Kroner[2], S. Aschauer[2], D. McGrouther[3]

[1]JEOL Ltd., R&D, Tokyo, Japan
[2]PNDetector GmbH, Munich, Germany
[3]JEOL Ltd., Welwyn Garden City, United Kingdom

In scanning transmission electron microscopy (STEM), efforts to obtain specimen information as much as possible have long been made and variety types of detectors have been developed. Pixelated STEM detector is one of these instruments for utilizing diffraction information that was otherwise partly lost in the conventional single-channel STEM detectors. Various types of applications have been introduced using the 4-dimensional (4D) dataset such as synthetic STEM image reconstruction, field map visualization and phase image reconstruction by ptychography, etc. [1,2]. Meanwhile, electron energy loss spectroscopy (EELS) is also an important means of obtaining information on the composition and even on the chemical bonding of a sample. Although simultaneous analysis using both instruments has been anticipated [3], making a center hole in the middle of a pixelated detector to let electron beam pass through into an EELS spectrometer was a manufacturing challenge. PNDetector is a company manufacturing high-speed pnCCD camera which can be operated at 7,500 frames per second for the 4D-STEM application. It recently manufactured a prototype pnCCD sensor with a center hole while keeping other specs the same, realizing the simultaneous acquisition of 4D and EELS data [4].

The prototype pnCCD camera was installed on a JEM-F200 (JEOL Ltd.) electron microscope with a cold field emission gun (Fig. 1). Below the camera, CEFID (CEOS GmbH) EELS spectrometer was mounted. Scan was triggered by an ELA (DECTRIS AG) camera mounted on the end of the CEFID. Then the microscope scanning system and the pnCCD camera readout were synchronized to it.

Fig. 2 shows the simultaneously obtained 4D-STEM and EELS data from a graphite sample. Fig. 2(a) shows an ADF image of the sample and Figs. 2(b) and 2(c) show synthetic STEM images created by simultaneously obtained 4D-STEM data. Since the sensor has a hole, there is a circular area at the center of the diffraction patterns where no electron signal was generated. Fig. 2(d) shows EELS spectra obtained from the areas indicated in Fig. 2(a). Figs. 2(e) and 2(f) are STEM images created using EELS intensity information at each peak in the spectra. Camera length of the microscope was set so as to let the transmitted electron beam pass through the hole while keeping the diffracted signals inside the field of view of the camera. By analyzing these data, we conclude that the 3D structure of this sample is a carbon graphite rolled up in a shell-like structure.

Fig. 1. Illustration of a simultaneous data acquisition of 4D-STEM and EELS with a pnCCD pixelated direct detector with a center hole in the middle.

Fig. 2. Simultaneously recorded 4D and EELS data. (a) ADF image. (b,c) STEM images created by extracting signals from the green areas in the diffraction patterns. Each pattern was obtained from the areas indicated in (a). (d) EELS spectra obtained from the same areas. (e,f) STEM images created using intensity information at each peak in the spectra (I_{π^*} and I_{σ^*}).

References:

[1] TJ Pennycook et al., *Ultramicroscopy*, 151 (2015) p. 160.
[2] R Sagawa et al., *Microsc. Microanal.*, 23 (2017) p. 52.
[3] B Song et al., *Physical Review Letters*, 121 (2018) p. 146106.
[4] M Huth et al., *Microscopy and Microanalysis*, 29 (2023) p. 401.

Fig. 1

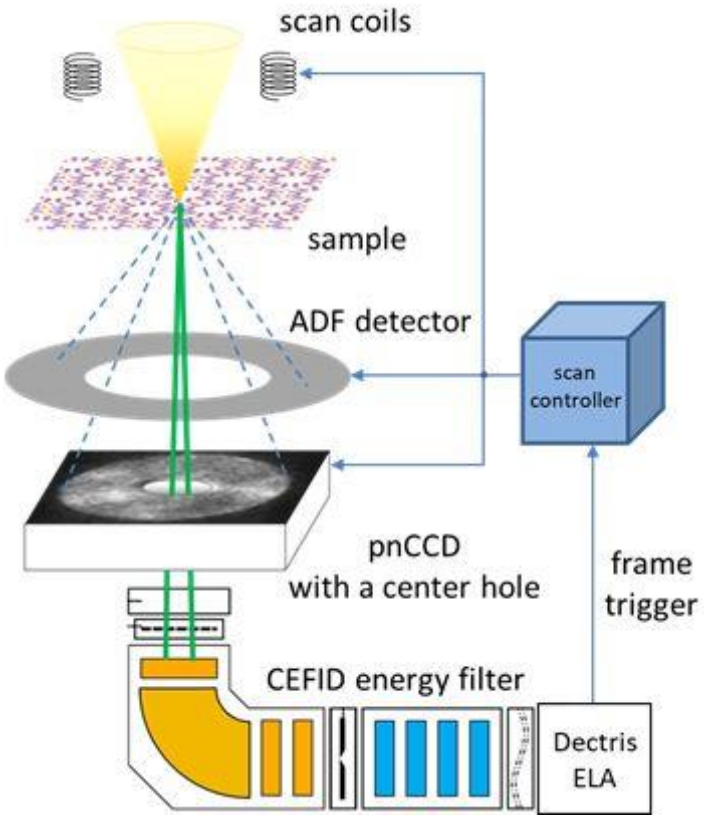
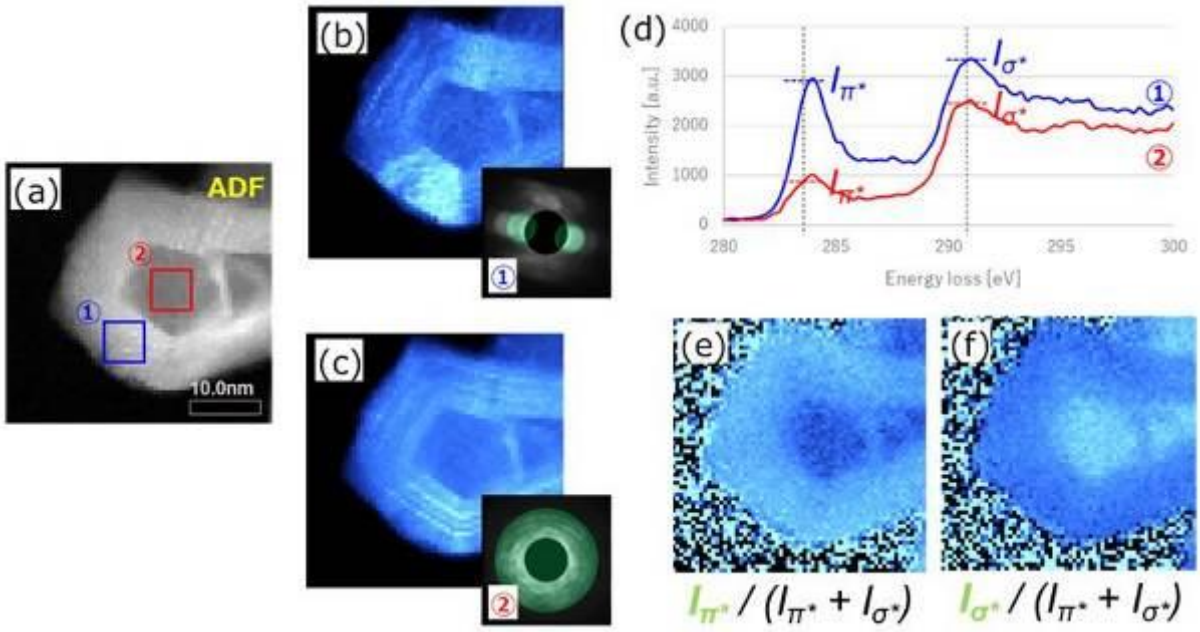

scan coils
sample
ADF detector
scan controller
pnCCD
with a center hole
frame
trigger
CEFID energy filter
Dectris
ELA

Fig. 2


(a)
ADF
10.0nm
(b)
(c)
(d)
Intensity [a.u.]
Energy loss [eV]
(e)
(f)

IM4.P04
From four t(w)o three – How 4D-STEM measurements of 2D materials lead to 3D information

C. Kofler[1,2], J. Kotakoski[1]

[1]University of Vienna, Faculty of Physics, Vienna, Austria
[2]University of Vienna, Vienna Doctoral School in Physics, Vienna, Austria

Scanning transmission electron microscopy (STEM) has been able to routinely resolve structures down to individual atoms for years. However, like all microscopy techniques, it is typically limited to 2D projections. While for bulk crystals there are well-established pathways to circumvent this projection problem, they cannot be easily adapted to thinner specimen. Despite their name, even two-dimensional (2D) materials such as graphene exhibit a three-dimensional (3D) structure that needs to be taken into account to fully understand their properties [1].
In this contribution, we present a number of promising methods for measuring the 3D structure of 2D materials, discuss their shortcomings and strengths, and aim to build upon these existing techniques to develop a more robust workflow for exploring structures beyond the 2D horizon.
Here we focus on twisted bilayer graphene (tBLG). Like all moiré materials, it exhibits a twist-angle-dependent moiré superstructure formed by rotational mismatch of the two graphene layers, which influences many material properties. Most widely discussed is the emergence of superconductivity at certain "magic angle" twists [2], but not only the electronic but also the 3D structure is altered by the moiré pattern. Calculations show, that the interlayer distance is modulated by the local stacking order and follows the moiré periodicity with an intensity depending on the twist-angle [3]. We discuss two methods to measure this variation that are both based on four-dimensional (4D)-STEM where the full convergent beam electron diffraction pattern is available at every scan position, therefore offering a significantly higher information content than "conventional" annular-dark-field STEM imaging.
The first approach, defocused Bragg interferometry shows promise for directly measuring the interlayer distance. Here, the intensity distribution in overlapping regions of diffraction disks originating from different material layers is analyzed to draw conclusions about the structure. The interference features in these regions are sensitive to out-of-plane modulations, and both their phase [4] and their rotation [5] have been used to determine average interlayer spacings of tBLG and similar structures.
The second method uses center of mass measurements to reconstruct images related to the projected electric field of the sample and exploits their sensitivity to the local stacking order and thickness variations in the sample to verify 3D structure models by comparing experimental data with simulations [6]. Both the methods and the studied system come with a host of challenges that have yet to be overcome to reliably and robustly study the interlayer distance. However, we hope that by understanding, adapting, and further developing these methods and combining them with simulations we can create a measurement technique that does not only provide average values but can also map the interlayer distance of tBLG as a function of the position in the moiré superstructure.

[1] Meyer et al., Nature 446, 60 (2007)
[2] Wang et al., Materials Today Physics 9, 100099 (2019)
[3] Uchida et al., Phys. Rev. B 90, 155451 (2014)
[4] Latychevskaia et al., Ultramicroscopy 219, 113020 (2020)
[5] Zachman et al., Small 17, 2100388 (2021)
[6] Argentero et al., Nano Lett. 17, 1409 (2017)

IM4.P05
Aberration correction in single side-band ptychography at low-dose imaging condition

S. Li[1,2], H. Lalandec Robert[1,2], C. Gao[3], C. Hofer[1,2], T. Pennycook[1,2], J. Verbeeck[1,2]

[1]University of Antwerp, NANOlight Center of Excellence, Antwerp, Belgium
[2]University of Antwerp, Electron Microscopy for Materials Science (EMAT), Antwerp, Belgium
[3]Nanjing University of Science and Technology, Center of Analytical Facilities, Nanjing, China

Electron ptychography is strongly valued for its high dose efficiency, ability to achieve resolution beyond the diffraction limit, and its ability to account for geometrical aberrations [1,2]. In particular, within the framework of the single side-band (SSB) ptychography [3], flattening the side-bands makes it feasible to eliminate the aberration effects. While this was successfully demonstrated in ref. [2], challenges were encountered when solving the aberration coefficients in low-dose conditions. In this work, we propose two approaches for optimizing the low-dose performance of aberration correction within the SSB framework. The first involves exclusively unwrapping phase within the side-band, and the second consists in an optimized selection strategy for the employed side-bands. We show how these improve our reconstructions based on simulated data.

Fig. 1 demonstrates the aberration correction process and compares the effectiveness of two phase unwrapping methods. Here, a simulated dataset of monolayer tungsten diselenide (WSe2) is used with an acceleration voltage of 60 keV, an aperture size of 25 mrad, a randomly aberrated probe, and an electron dose of 2000 e/A^2. Fig. 1(a) depicts the side-band structure before and after aberration correction. The aberration correction process is realized by flattening the aberrated side-band with parameterized aberration coefficients. For the selected side-band in Fig. 1(b), Fig. 1(c) involves unwrapping the entire image while setting values outside the side-band to zero, but discontinuities persist, leading to incomplete non-flat side-band. Fig. 1(d) unwraps the phase exclusively within the side-band, ensuring a well-unwrapped phase and resulting in the flat compensation. The effectiveness of these methods is evaluated through SSB reconstructions, as shown in Fig. 1(e) (uncorrected reconstruction), Fig. 1(f) (corrected by (c)), and Fig. 1(g) (corrected by (d)), respectively. These results highlight that the successful phase unwrapping is essential for accurate aberration correction, and demonstrate that the confined phase unwrapping process leads to more reliable reconstructions.

However, even with the most advanced phase unwrapping methods, a reduction of the dose below e.g. 1000 e/A^2 remains challenging for aberration correction. We thus propose a side-band selection strategy to complete the unwrapping method, where only those with the highest intensity are used. These high-intensity side-bands are expected to possess a higher SNR, making them more reliable for phase unwrapping. However, a lower noise level does not necessarily correspond to an easier unwrapping process. Fig. 2(a) shows unwrapping results for 12 side-bands using a reduced dose of 500 e/A^2. Using the first six highest magnitude frequencies to calculate the aberrations does not completely flatten the side-bands (Fig. 2(b)) and leads to a suboptimal reconstruction (Fig. 2(d)). In contrast, selecting only the well-unwrapped side-bands 5, 6 and 7 results in significantly flatter corrected side-bands (Fig. 2(c)) and a much clearer reconstruction (Fig. 2(e)). These results confirm that the optimized side-bands selection strategy enhances aberration correction in low-dose condition.

References:

1. Maiden A. & Rodenburg, J.M. *Ultramicroscopy.* **109**, 1256–1262 (2009).
2. Yang, H. et al. *Nat. Commun.* **7**,12532. (2016).
3. Rodenburg, J.M. et al. *Ultramicroscopy* **48**, 304-314 (1993).

Fig. 1

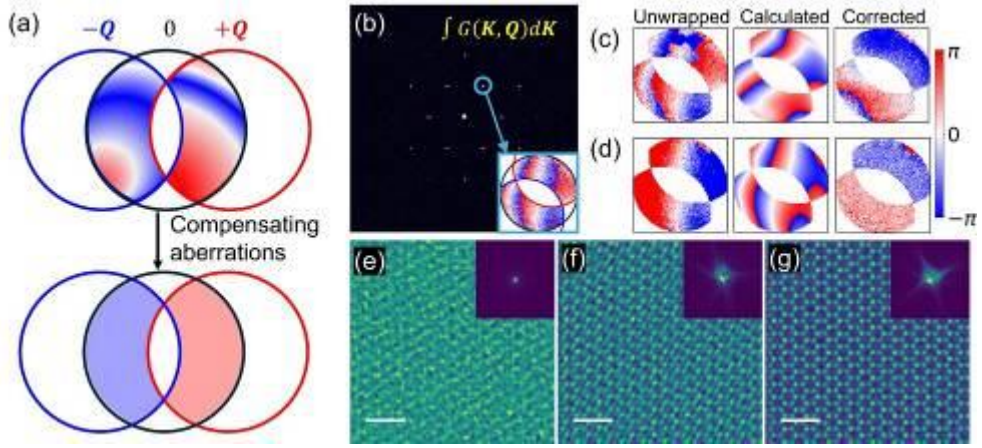
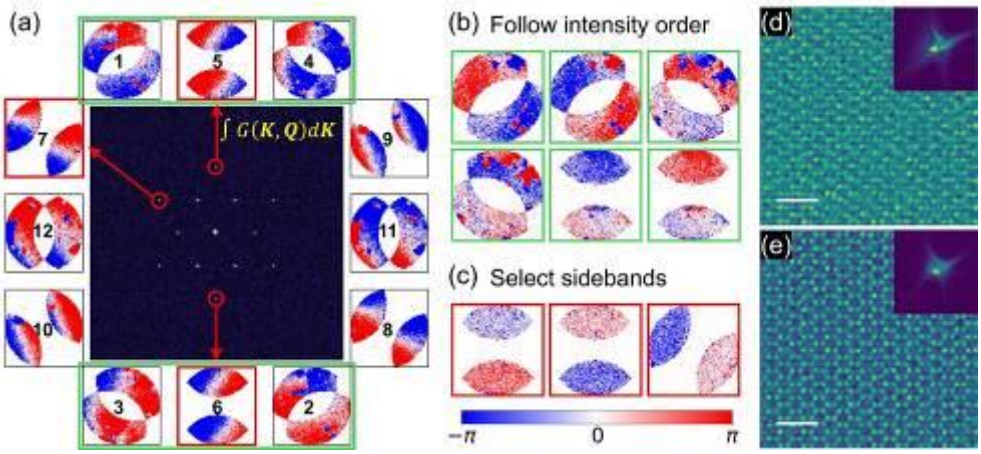

(a)
−Q
0
+Q
Compensating aberrations
(b)
∫ G(K,Q)dK
(c)
Unwrapped
Calculated
Corrected
(d)
π
0
−π
(e)
(f)
(g)

Fig. 2


(a)
1
5
4
7
9
12
11
10
8
3
6
2
∫ G(K,Q)dK
(b) Follow intensity order
(c) Select sidebands
−π
0
π
(d)
(e)

IM4.P06
3D, or not 3D? Strain is in question!

R. Specht[1], F. Otto[1], K. L. Jakob[1], L. Niermann[1], T. Niermann[1], M. Lehmann[1]

[1]Technische Universität Berlin, Berlin, Germany

Strain engineering plays a key role in the modern design of nanodevices, such as enhancing carrier mobilities at AlN/AlGaN interfaces.[1] Precise strain measurement is therefore a crucial feedback mechanism in device engineering. As device miniaturization continues to advance, strain measurement techniques must not only offer high precision but also exceptional spatial resolution.

Transmission electron microscopes can measure strain in the nanometer regime in both TEM and STEM modes. Examples of such methods include dark-field electron holography and nanobeam electron diffraction.[2,3] However, each technique has unique drawbacks and is typically effective only within specific measurement regimes, performing best for certain sample geometries or being limited to particular thicknesses. Dark-field off-axis electron holography, for example, requires a suitable reference region near the area of interest and uses non-standard instrumentation. Nanobeam electron diffraction, on the other hand, struggles with thicker samples where dynamic diffraction dominates. While a smaller convergence angle can improve precision in such cases, it comes at the expense of spatial resolution.

Additionally, all of the methods described above share one common assumption: they assume uniform strain along the electron beam direction. However, in thin, electron-transparent TEM lamellae, strain relaxes at heterointerfaces due to the absence of material at the surfaces - material that in the bulk wafer upholds internal stress. This results in a variation of strain along the electron beam direction, leaving a characteristic imprint on dynamic diffraction.[4] The resulting variations in dynamic diffraction patterns can be observed in CBED patterns at probe positions across the interface.[5] While precession electron diffraction aims to mitigate the influence of these pattern variations [6], the measured strain will be averaged along the beam direction.

Here, as an alternative, we infer the three-dimensional strain distribution from analyzing dynamic diffraction at an interface. Within reasonable error, this strain field can be obtained by comparing experimental diffraction data with beam simulations that use the 3D strain as input, seeking a close match. We measure the strain distribution over a series of strained quantum wells of varying dimensions and compare the 2D strain measured through various techniques with the in-plane component of our input 3D strain field averaged along the electron beam direction. Further, we discuss the limitations of 3D strain measurements using a comparative approach and explore potential future alternatives.

[1]: AlN/GaN/AlN High Electron Mobility Transistors, Springer International Publishing 10.1007, pp. 155-192 (2022).

[2]: Dark-field electron holography for the measurement of geometric phase, Ultramicroscopy 111, 1328 (2011).

[3]: Strain mapping of semiconductor specimens with nm-scale resolution in a transmission electron microscope, Micron 80, 145 (2016).

[4]: Dynamical diffraction effects on the geometric phase of inhomogeneous strain fields, Ultramicroscopy 10.1016, 112844 (2019).

[5]: Quantitative analysis of holz line splitting in cbed patterns of epitaxially strained layers, Ultramicroscopy 106, 951 (2006).

[6]: Improved strain precision with high spatial resolution using nanobeam precession electron diffraction, Appl. Phys. Lett. 103, 241913 (2013).

IM4.P07
Post-acquisition synchronization between a scanning and precessing convergent electron probe with unsynchronized cameras for strain mapping

M. Schowalter[1,2], F. F. Krause[1,2], A. Karg[1,2], C. Mahr[1,2], T. Grieb[1,2], T. Mehrtens[1,2], M. Eickhoff[1,2], A. Rosenauer[1,2]

[1]Institute of solid state physics, Bremen, Germany
[2]MAPEX center for materials and processes, Bremen, Germany

The emergence of ultra-fast cameras [1,2,3] paved the way for a new electron microscopical field known as 4D STEM. While the beam is scanning a 2-dimensional area, 2-dimensional diffraction patterns are recorded for each scan point yielding the name 4D STEM. From the variety of information that can be extracted from the diffraction pattern, we concentrate on strain in terms of nanobeam electron diffraction (NBED) in which the distance of reflections to the non-diffracting beam is measured. By increasing the convergence angle, the spatial resolution of NBED can be improved. The disadvantage is that the disks are unevenly illuminated due to dynamic diffraction, and the position of the disks is therefore more problematic. It has been shown that precession electron diffraction can reduce dynamical effects [4] and was later developed into a commercial product by NanoMEGAS. However, with this system the microscopes" viewing screen is filmed by an additional camera, whereby the camera characteristics are significantly worse than those of ultra-fast cameras. In this contribution we will use the NanoMEGAS system for scanning a precessing convergent electron probe, but record diffraction patterns using an EMPAD [2] or a Ceta camera (ThermoFisher) and analyse the diffraction patterns regarding strain.

As both cameras are not synchronized with the NanoMEGAS system, the scan was characterized in the following way: The microscope was switched to imaging mode and thus imaging the probe onto the camera (Fig. 1a)). Upon starting precession, the spot changed to a ring like structure (Fig. 1b)), which moved position when in addition the scan was started. By selecting the fastest frame time of the camera, the beam movement during the scan process could be observed with a high temporal resolution. Fig. 1c) and d) show the beam position as a function of frame number (time) over the whole scan or the scan of a line, respectively. It turned out that the beam precession and beam movements are faster than the fastest frame time of the cameras, but that there are significant pause times after and before scanning the lines, during which the beam control hardware is most likely waiting for a trigger from the viewing screen camera. We measured and parameterized these pause times and the actual dwell time as function of the software parameter "precessions per frame" and are thus able to assign the actual scan position/state to each frame (frames in pause times are discarded).

Figure 2 shows the result of strain measurements from κ-$(In_xGa_{1-x})_2O_3$/κ-Ga_2O_3/α-Al_2O_3 heterostructures with In concentrations of x=0.03 and x=0.18. The κ-$(In_xGa_{1-x})_2O_3$ layer in the first sample is fully strained, whereas it is fully relaxed in the second sample.

[1] K. Müller, H. Ryll, I. Ordavo, S. Ihle, L. Strüder, K. Volz, J. Zweck, H. Soltau, A. Rosenauer, Appl. Phys. Lett. 101 (2012), 212110.

[2] M. W. Tate, P.P., D. Chamberlain, K.X. Nguyen, R. Hovden, C.S. Chang, P. Deb, E. Turgut, J.T. Heron, D.G. Schlom, D.C. Ralph, G.D. Fuchs, K.S. Shanks, H.T. Philipp, D.A. Muller and S.M. Gruner; in Microscopy and Microanalysis 22, 237-249.

[3] A. Kobler, A. Kashiwar, H. Hahn and C. Kübel, Ultramicroscopy, 128 (2013), 68-81.

[4] R. Vincent and P.A. Midgley, Ultramicroscopy. 53 (1994), 271.

Fig. 1

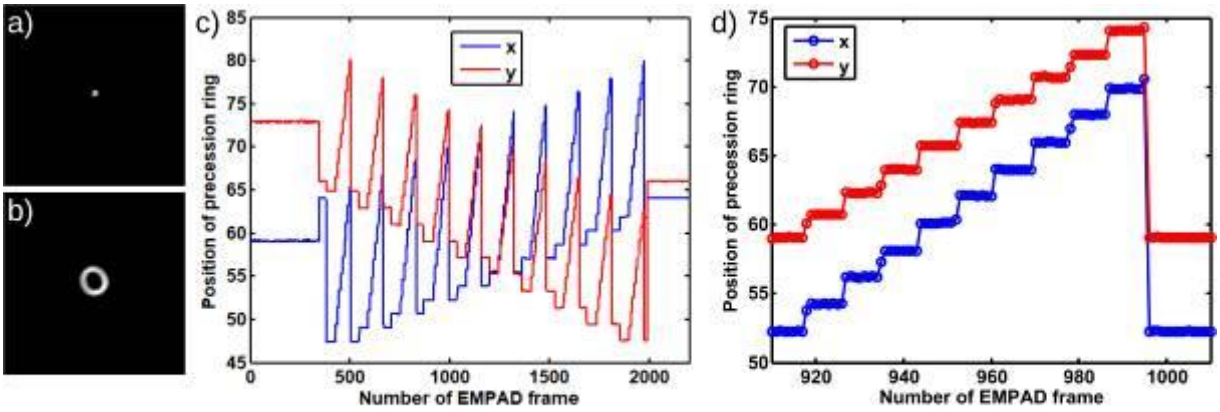


Fig. 1: a) Image of the static probe. b) Image of the precessing probe captured by the EMPAD camera with 1 ms frame time. c) Position of the probe during a full 2D scan. d) Position of the probe during the scan of a line.

Fig. 2

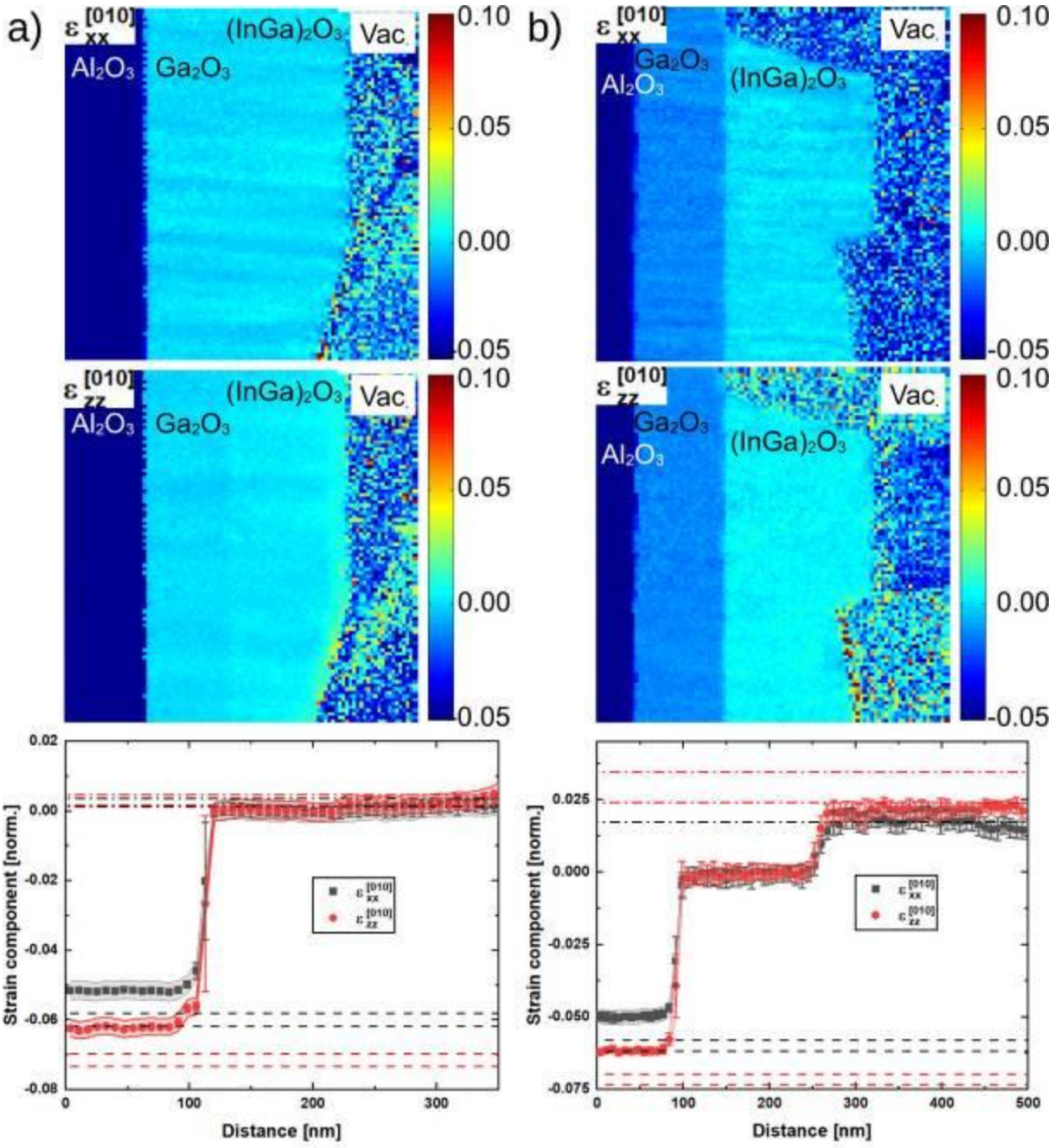


Fig. 2: Strain $\varepsilon_{xx}^{[010]}$ and $\varepsilon_{zz}^{[010]}$ maps and respective linescans for samples with In concentrations x=0.03 (a)) and x=0.18 (b)). Strain maps were measured in [010] zone axis orientation.

IM4.P08
Influence of the detector rotation on STEM-DPC investigation of atomic electric fields in WSe_2 with a segmented detector

M. Groll[1], J. Bürger[1], J. K. N. Lindner[1]

[1]Paderborn University, Physics, Paderborn, Germany

Quantitative imaging of the atomic electric field distribution using phase-retrieval methods such as STEM-DPC or 4D-STEM remains a challenging task due to the influence of the microscope and imaging parameters. Especially for segmented detectors, commonly used in DPC imaging, the influence of the detector geometry on the derived electric field distribution is of great importance. Due to the limited number of segments, these detectors exhibit a lower momentum space resolution compared to pixelated detectors. However, segmented detectors typically offer faster image acquisition times, preferable for beam-sensitive materials. The low momentum space resolution results in an anisotropic contrast transfer which depends on the arrangement and number of segments [1–4]. This anisotropy in the transfer of information introduces artefacts to the measured electric field distribution and hinders a correct conversion of DPC images into maps of atomic electric fields or charge densities. Thus, the influence of these artefacts is of importance for a proper interpretation of DPC images acquired with a segmented detector. In this study, a multislice image simulation of a 4D-STEM data set of a WSe_2 monolayer is used and evaluated using virtual detector segments to investigate the influence of the detector rotation on the derived electric field distribution.

It is found that the azimuthal orientation of CBED pattern and the detector significantly influences the electric field distribution even in DPC investigations of 2D materials with a specimen thickness of only a few atoms. To quantify this influence, the difference between the electric field distribution of a rotated and a non-rotated detector is calculated revealing strong variations, especially in between the atomic column positions. In addition, the difference in electric field distribution of a segmented detector is investigated with respect to a pixelated detector which exhibits an isotropic contrast transfer and a higher momentum space resolution. Comparing the electric field distributions of a (rotated) segmented detector and a pixelated detector shows pronounced changes in the vicinity of the atomic column positions. With relative changes in the electric field magnitude of up to 16 % for a WSe_2 monolayer, the detector rotation with respect to the CBED pattern is of great importance for investigations of charge redistribution and bonding effects using DPC with a segmented detector. Thus, this study highlights one of the challenges of using segmented detectors for quantitative measurements of atomic electric fields.

[1] S. Majert, H. Kohl, *Ultramicroscopy* **2015**, *148*, 81.

[2] H. Yang, T. J. Pennycook, P. D. Nellist, *Ultramicroscopy* **2015**, *151*, 232.

[3] K. Müller-Caspary, F. F. Krause, F. Winkler, A. Béché, J. Verbeeck, S. Van Aert, A. Rosenauer, *Ultramicroscopy* **2019**, *203*, 95.

[4] Z. Li, J. Biskupek, U. Kaiser, H. Rose, *Microscopy and Microanalysis* **2022**, *28*, 611.

IM4.P09
Correlated atomic vibrations unveiled by mixed-object electron ptychography

A. Gladyshev[1], B. Haas[1], C. T. Koch[1], T. Pekin[1,2]

[1]Humboldt University of Berlin, Institute of Physics, Berlin, Germany
[2]Carl Zeiss, Jena, Germany

Introduction

Far-field electron ptychography has emerged as a powerful phase retrieval technique, surpassing traditional resolution limits imposed by the instrumentation and capable of resolving specimen features as fine as the blurring due to the vibrations of atoms [1]. A rather simple model of coherent diffraction pattern formation standing behind conventional algorithms [1,2,3,4,5] does not allow to push the resolution beyond this limit.

Objectives & Methods

In order to overcome it, we utilize a mixed-object formalism initially proposed in 2013 for X-rays [3], but never applied to electron microscopy data without assuming explicit atom positions [4] or uncorrelated vibrations [5]. In contrast to conventional ptychography [1,2,3], which considers a single transmission function of a specimen, mixed-object ptychographic reconstruction introduces a sequence of superposed transmission functions, each producing a coherent diffraction pattern via a multislice simulation [1,2]. The total diffraction pattern is formed as an incoherent sum over the independent states [2,3,4,5].

Results

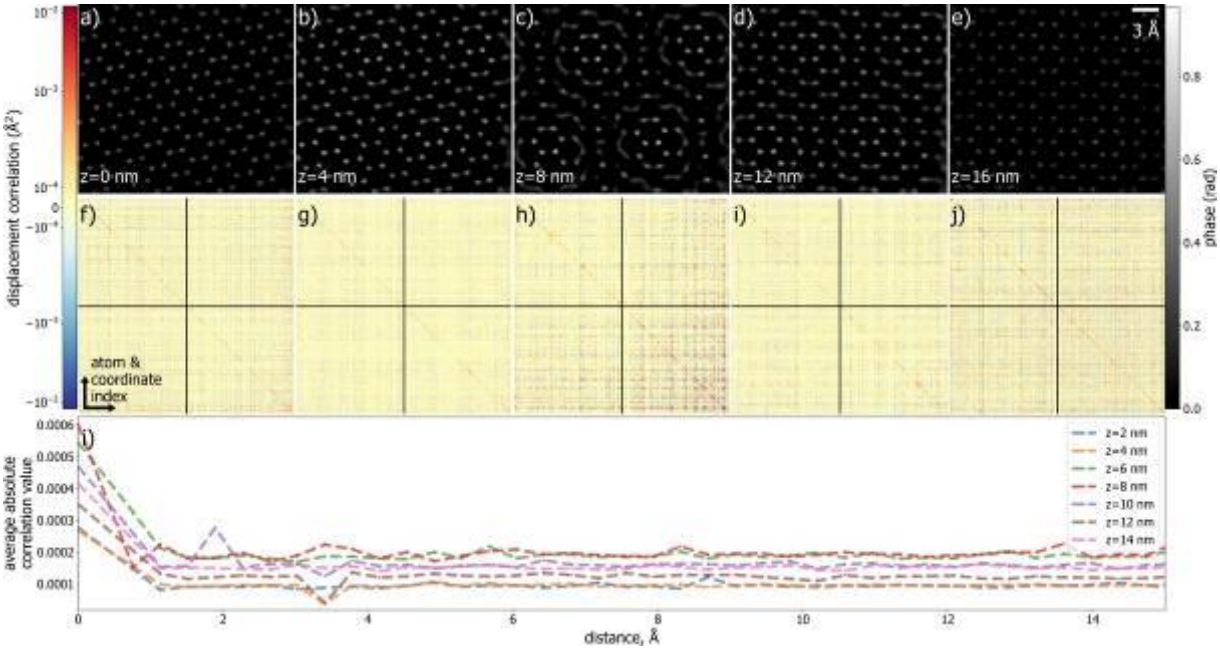
Using multislice and mixed-object formalisms, we recovered a transmission function of a 17 nm thick hBN sample in the [0001] zone axis, whose upper and lower halves were twisted by 11° relative to each other around the beam direction. The transmission function included 10 slices and 10 object states. We evaluate atomic vibrations using a center-of-mass measurement in a small region of the reconstruction around an equilibrium position of each atom and compute the lattice Green"s function coefficients as a second moment of the displacements [6]. The results are shown in Figure **1**.
Figure 1: Experimental ptychographic fit of approximately 17 nm thick hBN. The state-averages of the phase are shown for each second slice in panels **a-e**. The Green function coefficients are shown in panels **f-j**. The indices of these matrices correspond to x- or y-coordinate of atoms and the main diagonal represents an auto-correlation. The upper-left, lower-left, upper-right, and lower-right corners of the matrices show to **xx**, **xy**, **yx**, and **yy** correlations, respectively. The plot in panel **i** shows an average absolute correlation value vs. atomic distance for various slices. The highest correlation values can be observed around the interface between the two twisted halves of the crystal at z = 6 nm and z = 8 nm.

Conclusion

By treating the sample as an ensemble of multiple states, we can directly observe atomic vibrations and inter-atomic correlations. Our results reveal enhanced correlation of atomic vibrations in transition regions of a twisted hBN crystal, which is to be expected as atoms can move more freely in a less ordered structure. Differences in vibrations along the beam propagation direction validate our findings and rule out the possibility of influences from instrument instabilities. This study is a significant step forward in high-resolution electron microscopy, unlocking new possibilities for probing dynamic atomic-scale phenomena.

[1] Chen, Z., et al., doi: 10.1126/science.abg2533
[2] Gladyshev, A., et al., arXiv. doi:arXiv:2309.12017
[3] Thibault, P., & Menzel, A., doi:10.1038/nature11806
[4] Diederichs B. et al., doi: 10.1038/s41467-023-44268-x
[5] Herdegen, Z. et al., doi: 10.1103/PhysRevB.110.064102
[6] Kong, L., doi: 10.1016/j.cpc.2011.04.019.

Fig. 1



IM4.P10
Distribution of molecular chain orientations in fractured regions of high-density polyethylene visualized by nanodiffraction imaging

S. Kanomi[1,2], T. Miyata[1], H. Jinnai[1]

[1]Tohoku University, Institute of Multidisciplinary Research for Advanced Materials (IMRAM), Sendai, Japan
[2]Mitsubishi Chemical Corporation, Science & Innovation Center (SIC), Yokohama, Japan

Introduction Semicrystalline polymers are essential materials for producing fibers, films, and bottles due to their processability, thermal stability, and mechanical strength. Their hierarchical structure ranges from nanometers to over micrometers and comprises crystalline and amorphous regions (Fig. 1).

Fig. 1 Hierarchical structure of semicrystalline polymers.

During the stretching process of semicrystalline polymers, their internal structures change in various ways, including the rotation and fragmentation of crystals, the elongation of amorphous regions, and the formation of voids [1]. Although these deformation behaviors are closely related to the mechanical properties [2], the analysis of their relationship has proven difficult due to nanometer-scale heterogeneity. Nanodiffraction imaging (NDI) enables us to observe polymer crystals and map chain orientations by acquiring electron diffraction (ED) patterns with nanometer-scale spatial resolution [3]. In this study, a high-density polyethylene (HDPE) specimen with well-oriented molecular chains was prepared and then stretched inside an electron microscope to observe its deformation behavior. NDI was applied to the fractured regions to visualize HDPE crystals and the molecular chain orientations within the crystal.

Materials and Methods A 0.5 mm-thick HDPE film was stretched to a local strain of 8.3 at 80 °C. From this pre-stretched specimen, an ultrathin section with a thickness of 200 nm was prepared using cryo-microtome. The section was stretched parallel to the pre-stretched direction (the direction of molecular chain orientation) in the JEM-F200 (JEOL Ltd.), and transmission electron microscopy (TEM) images were acquired during the deformation process. NDI was performed at a strain of 5.1 by scanning a 1.4 nm-diameter electron beam in 5 nm steps.

Results The HDPE specimen was stretched parallel to the pre-stretched direction, generating many voids. The deformation mode changed from planar to uniaxial due to the elongation and rupture of the specimen. The TEM image of the deformed HDPE specimen at a strain of 5.1 (Fig. 2a) shows a fibrous area stretched until just before fracture. NDI was performed on this fibrous area, and *hk*0 spots of the PE crystal were observed in the ED patterns. A virtual dark-field (VDF) image was reconstructed from the spot intensity at each scanning position (Fig. 2b). Because bright pixels in the VDF image had relatively higher crystallinity than dark pixels, it was revealed that the fibrous area was composed of fibrils with high and low crystallinity. At the surface of the fibrous area, the high crystallinity fibrils were peeled off to form split-like structures (triangles in Fig. 2b). Fig. 2c shows a map of chain orientations, indicating that the molecular chains in the fibrous area are well oriented in the stretching direction, but nearly vertically oriented in the split-like structures.

The presentation will discuss the deformation mechanism of HDPE based on the time-series TEM images and NDI results from another field of view.

Fig. 2 (a) The TEM image of a HDPE specimen stretched parallel to the chain orientation at a strain of 5.1. (b) The VDF image of the fibrous area reconstructed by NDI. (c) The map of molecular chain orientations.

[1] Galeski, A. et al., *Macromolecules* **25**, 5705-5718 (1992). [2] H. Zhou & G. L. Wilkes, *J. Mater. Sci.* **33**, 287 (1998). [3] S. Kanomi, et al., *Nat. Commun.* **14**, 5531 (2023).

Fig. 1

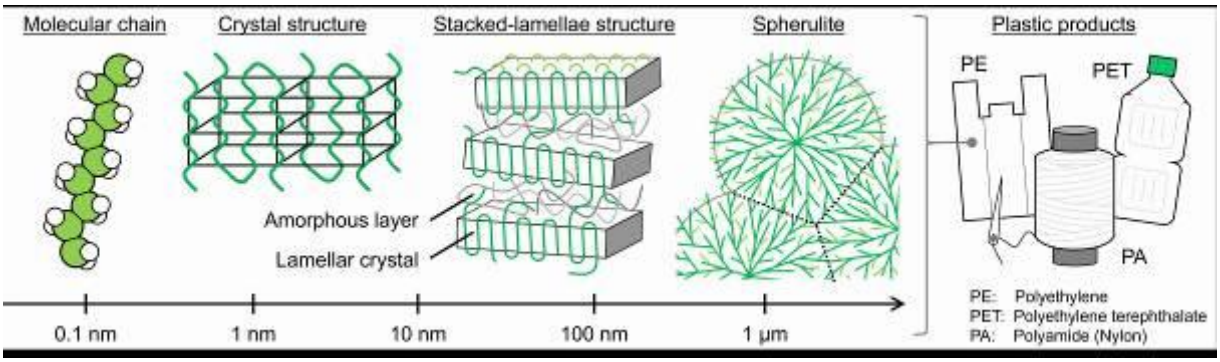
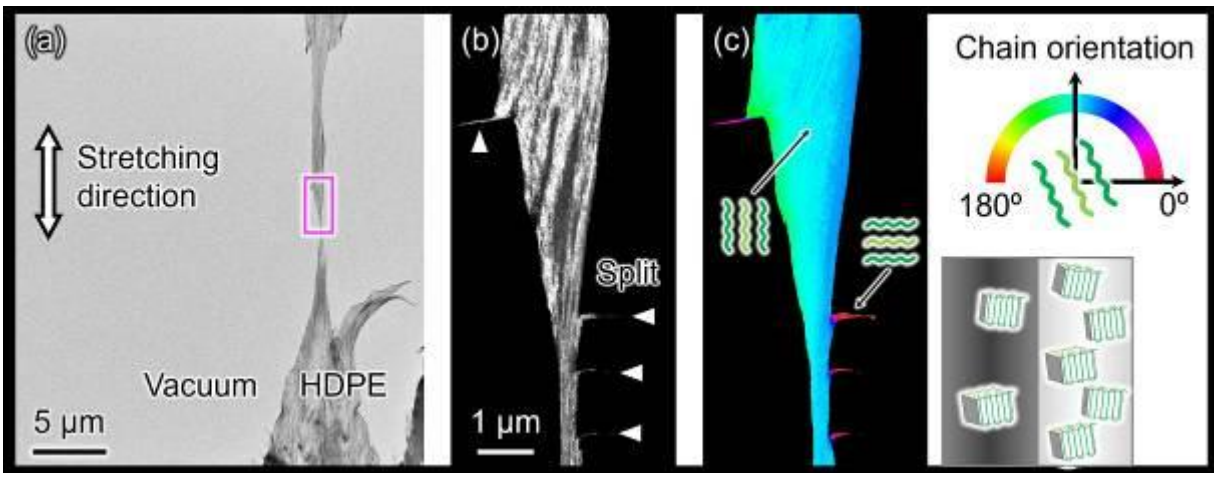


Fig. 2



IM4.P11
Analytical comparison of HRTEM and electron ptychography

F. Bennemann[1], A. Kirkland[1,2], P. D. Nellist[1]

[1]University of Oxford, Oxford, United Kingdom
[2]The Rosalind Franklin Institute, Didcot, United Kingdom

Introduction

Electron ptychography in the scanning transmission electron microscope (STEM) has been shown to be capable of providing low-noise phase images of beam sensitive materials at low dose [1]. For such materials, in particular biological samples, conventional high-resolution transmission electron (HRTEM) is the most widely used approach. The question then arises of whether ptychography or HRTEM offers the most dose-efficient imaging approach.

While resolution can be a useful measure for assess image quality, it is dependent on the electron dose. For some electron microscopy techniques, a phase contrast transfer function (PCTF) can be defined to quantify the technique"s performance with respect to spatial frequency. However, the PCTF also does not account for the dose used and is not uniquely defined for common electron ptychography techniques like the Wigner distribution deconvolution (WDD) method. The only attempt at a dose and sample independent comparison between the two techniques has so far been made by Dwyer and Paganin using information theory [2].

Objectives

In this work we introduce the detective quantum efficiency (DQE), applied to electron microscopy as a dose independent and sample independent measure of technique performance. The DQE is the squared ratio of the technique's signal to noise ratio to the squared ideal signal to noise ratio[3]. For a weak phase object, fully coherent Zernike phase contrast microscopy optimally coverts phase information to amplitude modulation. The DQE can be thought of as the fraction of incoming quanta contributing to the image.

Methods

In this work analytical expressions for the DQE of both Zernike phase contrast microscopy and single sideband ptychography were developed for weak phase objects. Different partial coherence and defocus conditions were studied. An expression for the DQE of an adaptation of single sideband ptychography that uses the triple overlap region was also developed.

Results

SSB ptychography reaches a maximum of around 20.5% for in-focus imaging. However, under defocus conditions the detective quantum efficiency tends to 100% at low spatial frequencies if the triple overlap region is optimally used. Meanwhile, HRTEM under ideal conditions can theoretically retain an efficiency of 100% for all spatial frequencies in-focus. When introducing partial coherence conditions HRTEM quickly loses high frequency information.

Conclusion

In this work we have successfully defined a dose and sample independent analytical framework in which HRTEM and electron ptychography can be compared against each other using the DQE. We showed that in the absence of partial incoherence, an HRTEM can achieve a DQE of 100% while electron ptychography has a maximum of around 20.5% for in-focus conditions. Under defocus, the

triple overlap region can be used to boost the DQE of electron ptychography towards 100% at low spatial frequencies.

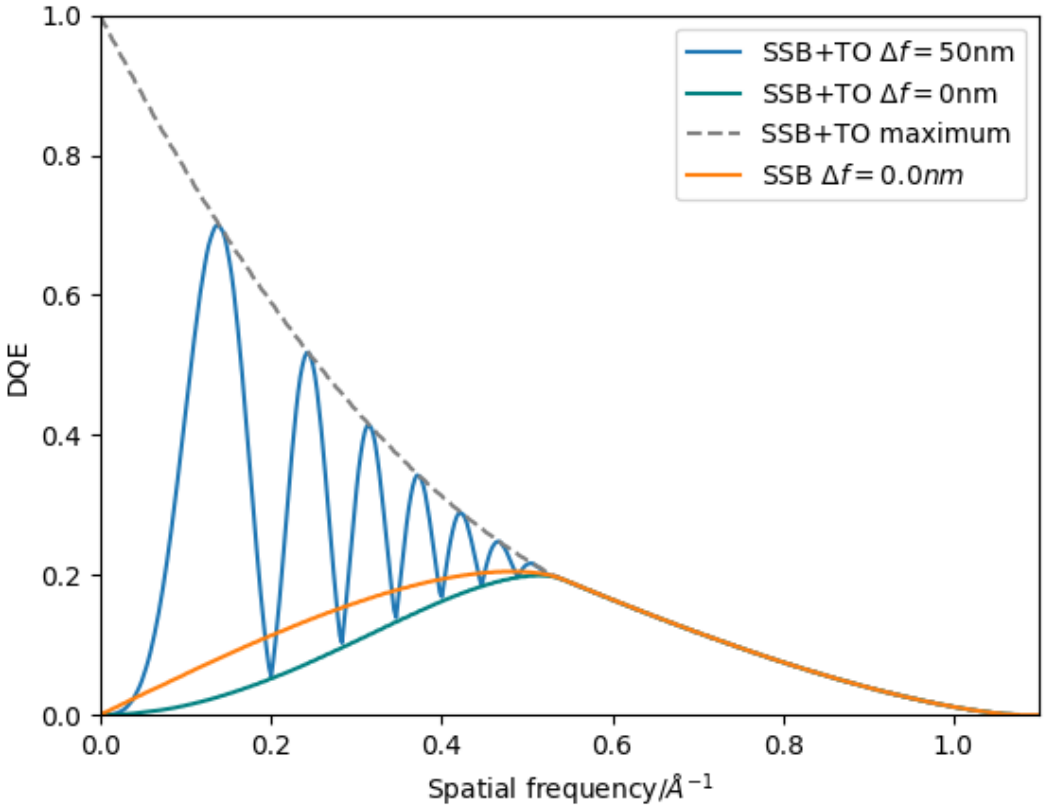
References

[1] Colum M. O"Leary, Gerardo T. Martinez, Emanuela Liberti, Martin J. Humphry, Angus I. Kirkland, & Peter D. Nellist (2021). Contrast transfer and noise considerations in focused-probe electron ptychography. Ultramicroscopy, 221, 113189.

[2] Dwyer, C., & Paganin, D. (2024). Quantum and classical Fisher information in four-dimensional scanning transmission electron microscopy. *Physical Review B, 110(2)*

[3] R. C. Jones. Advances in Electronics and Electron Physics XI (Academic Press. Inc., New York, 1959, p. 121.)

Fig. 1



IM4.P12
Using tomography to highlight low composition variations in GaAs/GaAsSb based nanowire

R. Zell[1], S. Sturm[1], H. Jeong[2], G. Koblmüller[2], K. Müller-Caspary[2]

[1]Ludwig-Maximilians University Munich, Chemistry and Pharmacy, Munich, Germany
[2]Technical University of Munich, Center for Nanotechnology and Nanomaterials, Munich, Germany

In the development of advanced nanophotonic and -electronic applications, group III/V semiconductors, especially nanowires (NWs), have risen in popularity over the past years due to their small footprint and high flexibility in material combinations. Owing to their well-tuned morphologies and precise 3D structures, creating finely tuned interfaces and band-gaps, GaAs-based NWs have become promising components for optoelectronic and photonic devices.[1] But the growth process of these NWs on the nanoscale has only been characterized for specific growth and manufacturing conditions, such that a comprehensive model has not been worked out.[2] As the incorporation of Sb in the GaAs crystal structure can be used as an indicator of the growth speed of the wire, mapping the areas of high incorporation throughout the wire gives insight in these growth dynamics.[3,4] Because the Sb composition variations of a few percent are comparably small, traditional HAADF-STEM tomography and STEM-EDX measurements are reaching their limitations in Z-contrast resolution, demanding for favorable measurement conditions and the inclusion of prior knowledge.

STEM-HAADF tilt series of GaAs(Sb)-NWs (Figure 1) were acquired with a tilt range of 76° to 74° employing a probe corrected FEI Titan Themis electron microscope operated at 300 kV. The series was reconstructed via weighted SIRT[5] with finite support correction after preprocessing, including Lambert-Beer correction and alignment. The iso-surface of the resulting tomographic structure is shown in Figure 2, consisting of six sidewall facets perpendicular to the main [111] growth direction and an imperfect flat capping layer.

Utilizing the tomographic reconstruction, the initially poor HAADF contrast can be enhanced visually (Figure 3). This reconstruction confirms the presence of Sb-enriched regions. Based on prior information about the growth characteristics, these enriched areas are expected to be of pyramidal structure, with a trigonal pyramidal base perpendicular to the NW axis. The base of these pyramids is expected to alternate for following pyramids with a 60° rotation along the NW axis. In order to further enhance the structure and contrast of the pyramidal geometry, the enforcement of a threefold symmetry has been implemented in an in-house developed WSIRT algorithm. This eliminates the impact of the missing wedge and recovers the pyramidal shape (Figure 4). Note that the pyramids still emerge naturally from the data rather than being direct consequence of the symmetry constraint.

The investigations demonstrate that even small variations in elemental composition in three dimensions, hardly visible in a single HAADF recording, can be enhanced using a tomographic reconstruction giving further insights into the underlying structure. Additionally, a 4D-STEM tilt series has been acquired, in which dedicated virtual detectors enhance compositional contrast, and, consequently, the pyramidal shape.

1. P. Schmiedeke, et al., Appl. Phys. Lett. 124, 071112 (2024).
2. Carina B. Maliakkal, Kimberly A. Dick, Nanoscale Adv., 3, 5928-5940 (2021).
3. A. Ajay, et al., *Appl. Phys. Lett.* 121, 072107 (2022).
4. H. W. Jeong, et al, Small 19, 2207531 (2023)
5. D. Wolf, et al., Ultramicroscopy, 136 (2014)

Fig. 1

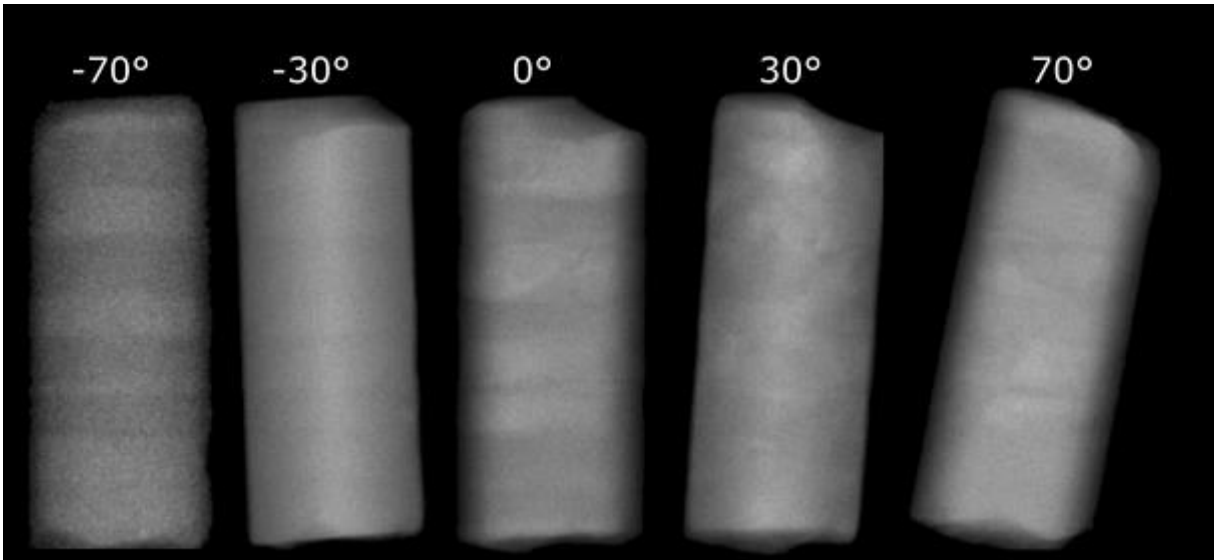


Fig. 1: Preprocessed STEM images at varying tilt angles, highlighting the low contrast of the Sb rich pyramidic structure.

Fig. 2



Fig. 2: Isosurface of the wire reconstruction showing the hexagonal structure and partially flat capping layer.

Fig. 3

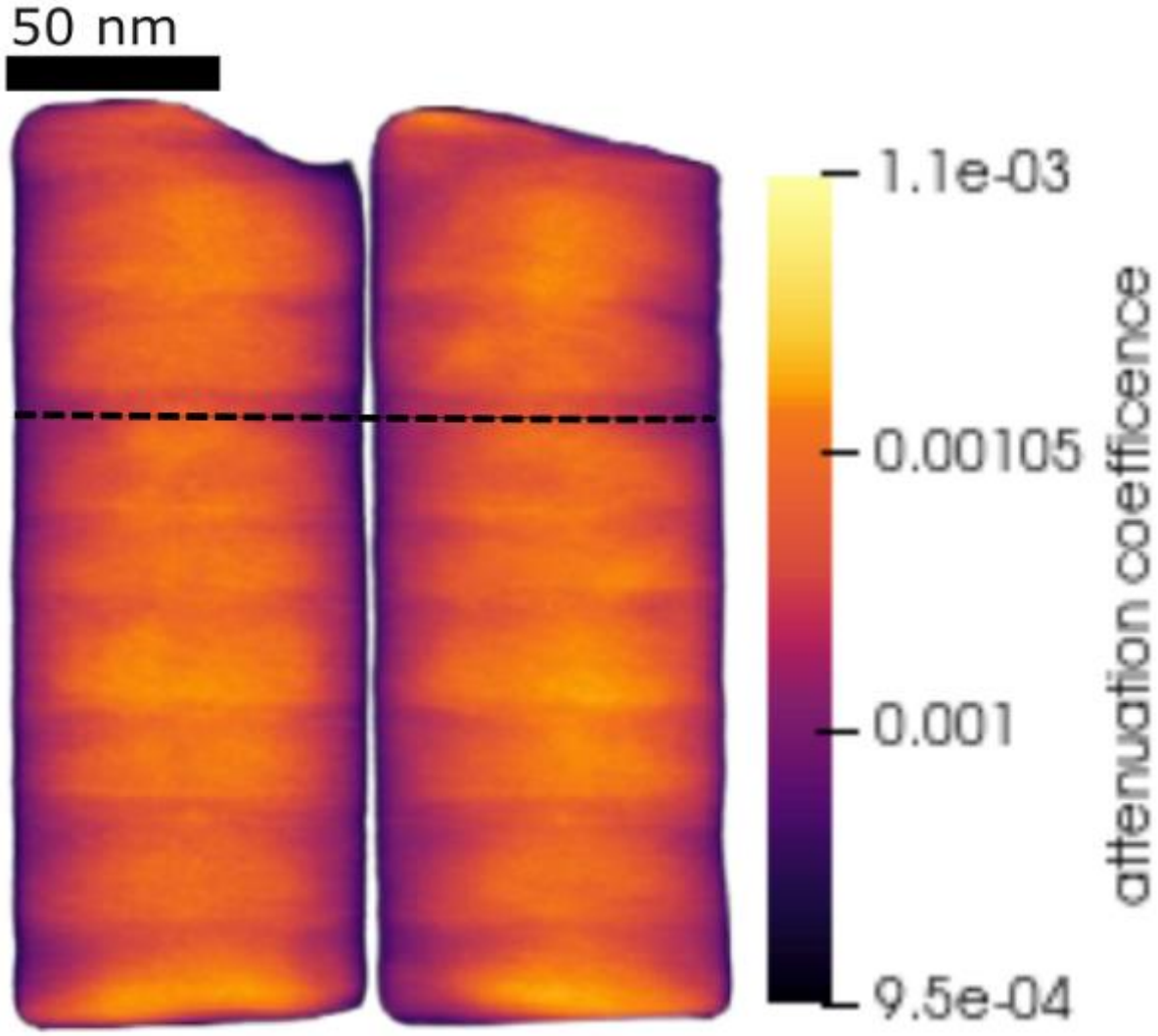


Fig. 3: Slices perpendicular to the [1-10] and [10-1]direction of the NW, highlighting the non-uniform pyramidal Sb concentration. The black dotted line indicates the position of the slice compared in Fig.4.

Fig. 4

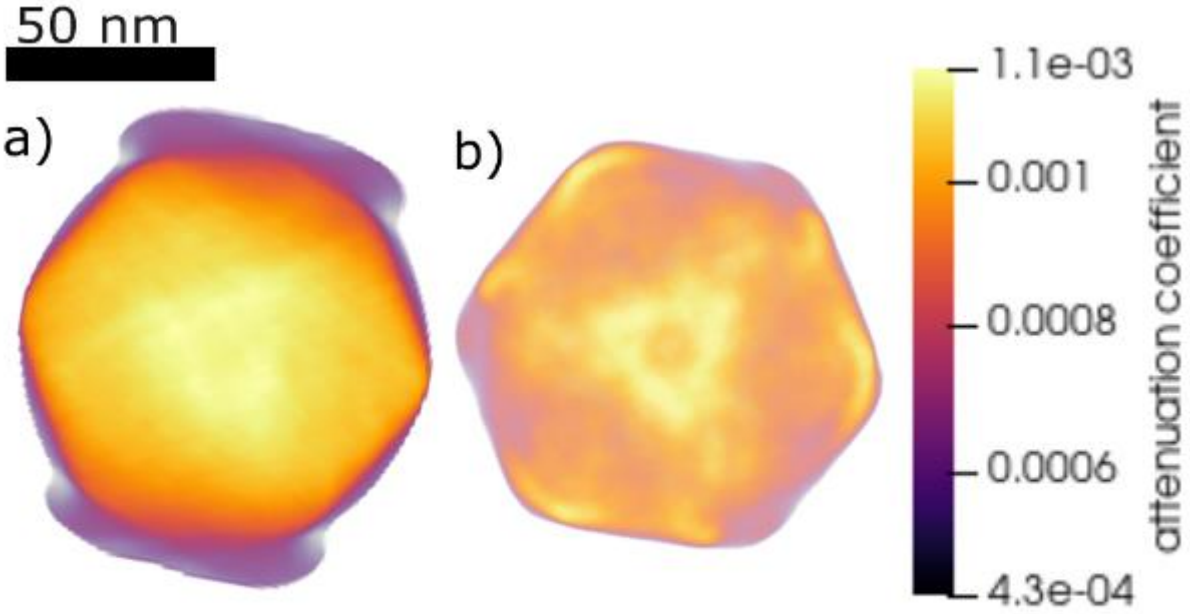


Fig. 4: Slices through a pyramid at the position indicated in (Fig.3) exhibiting the triagonal structure. a) classical WSIRT, b) 3-fold symmetry enforced WSIRT.

IM4.P13
Probing surface reconstruction of partially reduced nickelate films via 4D-STEM

C. Yang[1], R. Pons[1], W. Sigle[1], H. Wang[1], E. Benckiser[1], G. Logvenov[1], B. Keimer[1], P. A. van Aken[1]

[1]Max Planck Institute for Solid State Research, Stuttgart, Germany

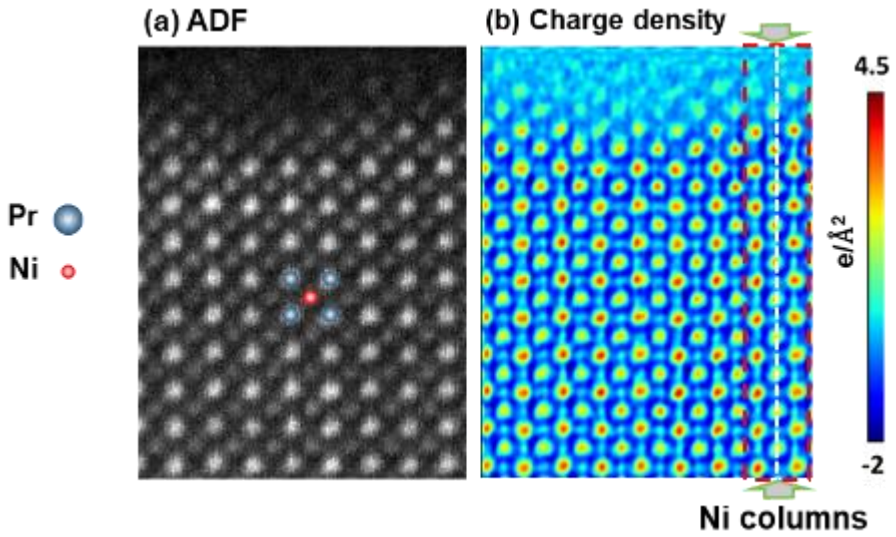
The polarity of a material's surface can have a significant impact on its fundamental properties via electronic and structural reconstruction. By exploring the atomic structure and electrostatic characteristics at the surface, we can gain a better understanding of how these properties are affected. In this study[1], we used annular bright-field imaging in scanning transmission electron microscopy (STEM) to investigate the oxygen distribution in a $Pr_{0.8}Sr_{0.2}NiO_{2+x}$ film. We observed a polar distortion coupled with octahedral rotations in the pristine $Pr_{0.8}Sr_{0.2}NiO_3$ sample, and an even stronger polar distortion in a partially reduced sample. The decay of polarization was limited to around three unit cells. Additionally, we employed four-dimensional STEM (4D-STEM) to directly image the local atomic electric field surrounding Ni atoms and discovered distinct valence variations of Ni atoms (See Figure 1), which were confirmed by atomic-resolution electron energy loss spectroscopy. Our findings suggest that the surface reconstruction in the reduced sample is related to oxygen vacancies resulting from topochemical reduction. These results provide valuable insights into the mechanisms and engineering of surface polarity at the atomic scale of these materials.

Reference

[1] C. Yang et al. Nat. Commun. 2024, 15, 378.

Figure 1 (a) ADF image and (b) charge density map reconstructed from the 4D-STEM dataset.

Fig. 1



IM4.P15
Field-free imaging and analysis for magnetic materials

R. Egoavil[1], M. Waaijer[2], E. van Cappellen[3], P. Tiemeijer[2], L. Keeney[4], M. Wirix[2], M. Meledina[2], M. Conroy[5], D. Jannis[2]

[1]Saarland University, Saarbrücken, Germany
[2]Thermo Fisher Scientific, Materials & Structural Analysis, Eindhoven, Netherlands
[3]Thermo Fisher Scientific, Materials & Structural Analysis, Hillsboro, OR, United States
[4]University College Cork, Tyndall National Institute, Cork, Ireland
[5]Imperial College London, Department of Materials, Royal School of Mines, London, United Kingdom

In the past, detailed study and chemical characterization of magnetic materials using scanning transmission electron microscopy (STEM) has been limited due to the need of unconventional optical setup to reduce the influence of objective field to the sample, which results in poor resolution and deficient analytical performance. In conventional STEM imaging and analysis, the sample placed inside the pole-pieces of the objective lens is subjected to strong magnetic fields, typically up to a few tesla. These magnetic fields can change, or even destroy, the magnetic structures of interest. Field-free imaging avoids this issue and preserves the sample's original state. Therefore, traditionally magnetic materials were observed in LM (low magnification) mode. The drawback of this approach is that spatial resolution is poor (several nanometers) and that there"s still a small residual magnetic field at the sample.

This work discusses a new Lorentz STEM mode, which when corrected for spherical aberration, can achieve a respectable resolution of 2.65 Å. At the other end of the magnification range, large field of view observations (~ 100µm) are made possible thanks to stable optics (aka steady pivot points). Besides being true field-free over a large volume (~ 100µm3), magnetization can be induced using the objective lens. In addition, feel free imaging together with Electron Energy Loss Spectroscopy (EELS) enables chemical characterization of magnetic materials granting access to the detailed electronic state of transitions metals which play a crucial role in understanding their magnetic behaviour. Measurements performed on a Themo Fisher Scientific ILIAD TEM platform demonstrate the spectral fingerprints of Ti-L_{23}, O-K, Mn-L_{23} and Fe-L_{23} of a $Bi_6Ti_xFe_yMn_zO_{18}$ multiferroic thin film [1]. Correlation between STEM iDPC and DPC maps is also considered. Additional examples on perovskite $La_{0.7}Sr_{0.3}MnO_3$-based heterostructures are discussed.

Atomic-scale magnetic field imaging and spectroscopy are critical for understanding and engineering materials used in quantum technology and next-generation semiconductor memory devices. These approaches provide insights into electronic and magnetic interactions at the nanoscale, which are foundational to developing high-performance devices with novel functionalities. Such advancements build on the progress in achieving high-resolution imaging to probe the intricate atomic and magnetic structures of materials [2].

Fig. 1. High resolution field-free iDPC and DPC maps of a $Bi_6Ti_xFe_yMn_zO_{18}$ multiferroic thin film. The inset shows the FFT with resolution performance of 2.65 Å.

Fig. 2. Electron Energy-Loss Near-Edge Structure (ELNES) spectra across the Bi6TixFeyMnzO18 multiferroic thin film measured at field free conditions. (Top) **Always in focus** as unique feature of the ILIAD EELS platform grants the measurement of electronic structure of Ti-L_{23}, O-K, Mn-L_{23} and Fe-L_{23} across the layer structure with high energy resolution. (Bottom) For clarity, the normalized average EELS signal is shown.

References:

1. Kalani Moore et al. *ACS Appl. Mater. Interfaces* (2022), **14**, 4, 5525–5536. https://doi.org/10.1021/acsami.1c17383

2. Juan Carlos Idrobo, *Nat Rev Mater* (2021), **6**, 100–102. https://doi.org/10.1038/s41578-020-00275-8
3. MC acknowledges funding from the Royal Society Tata University Research Fellowship (URF\R1\201318), EPSRC NAME Programme Grant EP/V001914/1 and Royal Society Enhancement Award RF\ERE\210200EM1 and ERC CoG DISCO grant. MC and LK acknowledge funding from the Irish Research Council 2023 Advanced Laureate Awards Programme.
4.

Fig. 1

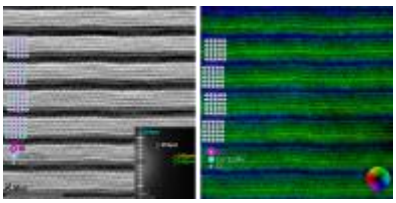
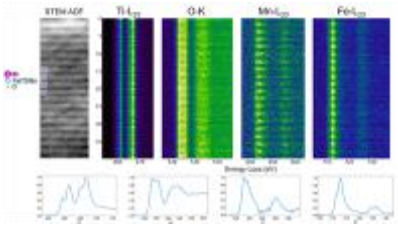


Fig. 2



IM4.P17
Novel automated & robust software for electric field & electron pair distribution function mapping from 4D-SPED

A. Galanis[1], A. Gomez-Perez[1], J. Portillo-Serra[1], E. Grivas[1], S. Nicolopoulos[1], M. Fransen[1], J. Gazquez-Alabart[2], R. Guzman[2], G. Herranz[2], M. Bibes[3], J. Guckelhorn[2], G. Singh[2], S. Plana-Ruiz[4], P. P. Das[1]

[1]NanoMEGAS, Brussels, Belgium
[2]Universitat Autònoma de Barcelona, ICMAB-CSIC, Barcelona, Spain
[3]Université Paris-Saclay, Laboratoire Albert Fert, CNRS, Thales, Palaiseau, France
[4]Universitat Rovira i Virgili, SRCIT, Tarragona, Spain

Introduction

Based on beam precession for enhancing electron diffraction data [1], Scanning Precession Electron Diffraction (4D-SPED) has been widely applied since the early 2000s as a robust technique [2]. Current work expands the applications of 4D-SPED to two modern characterizations: the mapping of electric field (EF) to probe the charge distribution in electronic, optical, and electromechanical materials, and electron pair distribution function (ePDF) mapping, to reveal atomic structures in nanocrystalline, amorphous and disordered materials [3].

Materials and Methods

EF studies: The use of beam precession for EF mapping is critical, towards reduction of the diffraction contrast inside the transmitted beam. A center of mass (COM) algorithm is used to detect the beam deflection caused by Coulomb forces. As a case study, the apparent EF at an interface of STO doped with 1% Ca and AlO is shown with and without the use of precession by employing an automated software through a COM algorithm. The uniformization of the transmitted beam intensity by precession, leads in more accurate analysis. [4].

ePDF Mapping: Data collection of multiple amorphous layers semiconductor material was performed using 4D-SPED. The data were analyzed by newly developed, fully automated software dedicated to ePDF mapping analysis. This software processes diffraction data by determining the center of each pattern, calculating 1D profiles, and computing the ePDF.

Results and Discussion

EF studies: The deflection of the central beam in the data series was calculated using a novel software employing a COM algorithm. The calculated beam deflection is presented as a color map related to the electric field direction. At the AlO-CaSrTiO interface, the emergence of a 2D electron gas can be directly and clearly identified in the precessed data, in contrast to the non-precessed.

Fig. 1: Electric Field maps by 4D-Scanning ED, without (left) and with Precession of 0.8^{o} (right). The colors are related to the direction of the EF based on the reference color wheel (middle up). Representative Diffraction pattern (bottom) without (left) and with precession (right).

ePDF Mapping: The ePDF"s were automatically computed for every pixel of the PED series. The obtained ePDF"s were used to determine the Pearson correlation function, enabling a rapid assessment of similarities and differences across the scanned area. Peak positions, widths, and heights of the ePDF profiles were analyzed to identify structural variations. Current study reveals two distinct layers: amorphous Si_3N_4 and SiO_2 layers.

Fig. 2: Color map showing the variation of peak positions (Å) in the scanned area, highlighting layers of Si_3N_4 and SiO_2 (left). Representative ePDF (blue curve) from these layers (right), with the first two peak positions and their numerical values—1.56 and 2.56 Å for the SiO_2 layer, and 1.65 and 2.95 Å for the Si_3N_4 layer.

Conclusions

We introduce two novel software tools for processing 4D-SPED data, enabling electric field and electron pair distribution mapping analysis in TEM. This work underscores the importance of incorporating precession in 4D-STEM experiments to enhance data quality and ensure reliable results.

References

[1] R. Vincent and P. Midgley, Ultramicroscopy **53** (1994) 271

[2] E.F. Rauch *et al*. Zeitschrift für Kristallographie **225** (2010) 103

[3] Y. Rakita et al. Acta Materialia, Volume **242** (2023) 118426

[4] V. S. Chejarla et al, Small Methods 2023, 2300453

Fig. 1

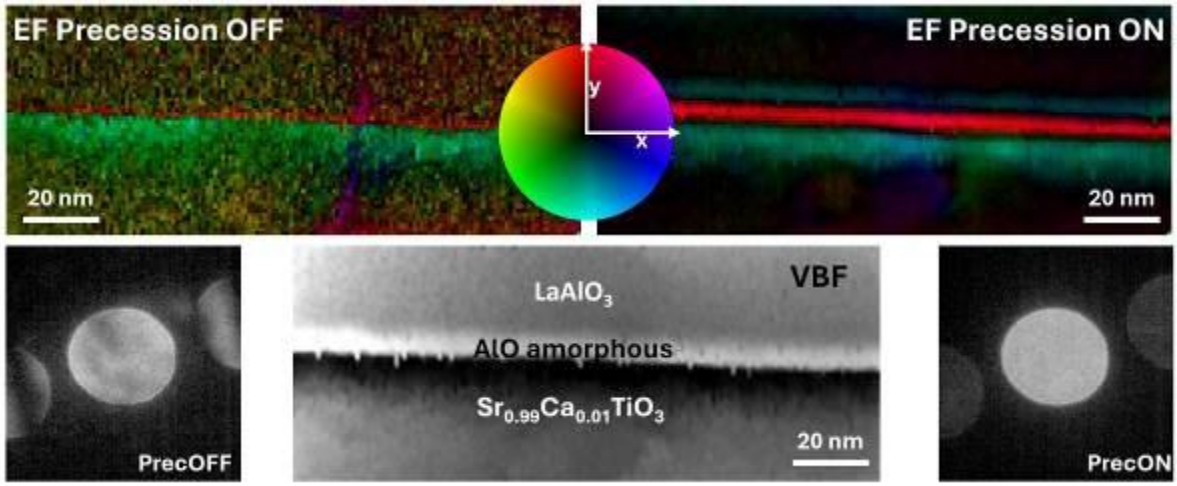
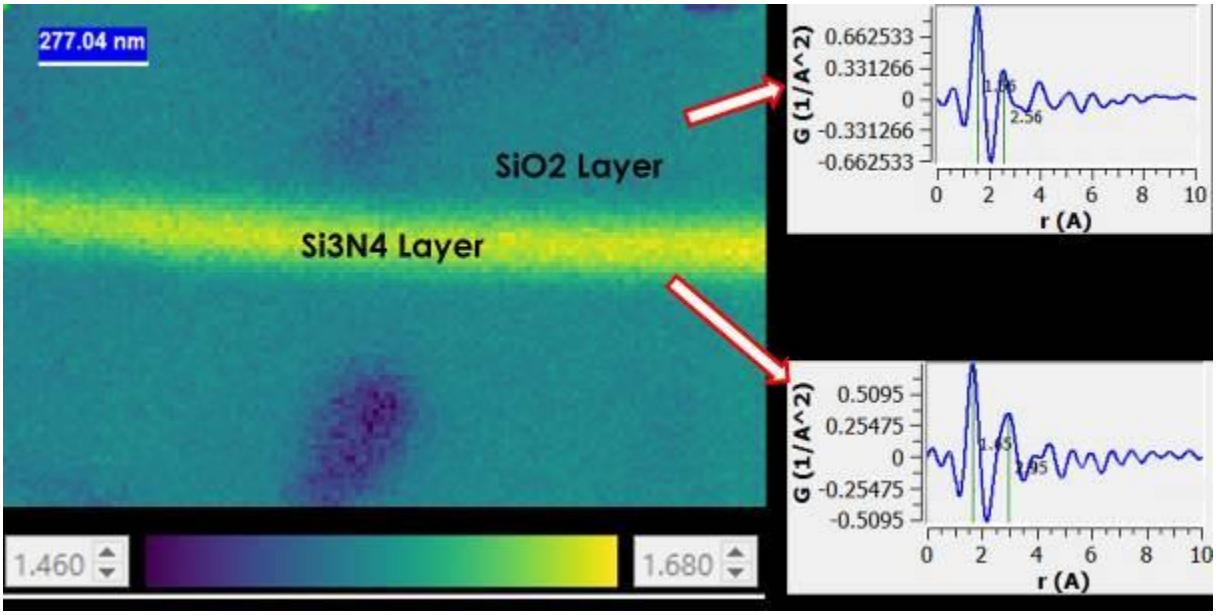


Fig. 2


277.04 nm
SiO2 Layer
Si3N4 Layer
1.460
1.680
G (1/A^2)
0.662533
0.331266
0
-0.331266
-0.662533
2.56
0 2 4 6 8 10
r (A)
G (1/A^2)
0.5095
0.25475
0
-0.25475
-0.5095
0 2 4 6 8 10
r (A)

IM4.P19
Towards flexible and reproducible 4D-STEM analysis – Exploring ASTAR and pyxem for orientation mapping

S. Koloffon Rosas[1], S. Selve[2], I. Häusler[3], T. Wagner[3], F. Otto[1], H. Çelik[1], M. Lehmann[1]

[1]Technische Universität Berlin, Institute of Optics and Atomic Physics, Berlin, Germany
[2]Technische Universität Berlin, Zentraleinrichtung Elektronenmikroskopie, Berlin, Germany
[3]Humboldt University of Berlin, Institute of Physics, Berlin, Germany

Introduction:

4D-STEM has become a key technique for nanoscale crystallographic analysis, enabling orientation mapping, strain mapping, and phase identification. The advancement of fast pixelated detectors has improved resolution and accessibility in orientation mapping. Commercial software packages like Nanomegas ASTAR provide well-integrated solutions [1] but come at high costs and limited flexibility. Open-source alternatives, such as pyxem, offer customisable workflows that enable reproducible analysis. This study explores the implementation of pyxem for orientation mapping and compares its performance to ASTAR, contributing to the development of flexible, open-source approaches for electron diffraction analysis.

Objectives:

This project explores the implementation of pyxem for orientation mapping and evaluates its performance against ASTAR. The study assesses pyxem's flexibility, reproducibility, and accuracy while identifying its limitations. By using 4D-STEM, it aims to extract crystallographic characteristics such as grain structure and orientation relationships. Additionally, the integration of EDX mappings will be explored to enhance phase differentiation and material characterisation.

Materials and Methods:

The study will utilise diverse samples, all with known FCC structures and varying grain sizes, to compare orientation mapping techniques. Orientation mappings are generated using pyxem, adapting existing methodologies [2]. Experiments are conducted using a JEOL JEM-ARM300F2 "GrandARM" S/TEM at 300kV, with a QD MerlinEM pixelated detector and a TVIPS Tietz universal scan generator. The results are benchmarked against ASTAR to evaluate pyxem's performance. EDX maps are also considered for phase identification and validation.

Results:

Orientation mappings obtained from pyxem enable the extraction of crystallographic information comparable to ASTAR, while offering greater flexibility through customisable workflows. Both methods rely on template matching for indexing diffraction patterns, generating orientation maps that reveal grain structures and phase distributions. ASTAR provides an integrated, streamlined workflow optimised for automated mapping, while pyxem supports adaptable indexing strategies and integration with other 4D-STEM techniques. As an open-source tool, pyxem enables modifications and tailored processing pipelines suited to various experimental needs. This study evaluates the accuracy and efficiency of pyxem-based orientation mapping and its potential for research applications.

Conclusion:

Pyxem is highlighted as a flexible, reproducible, and customisable alternative to commercial orientation mapping tools like ASTAR. By enabling the extraction of key sample characteristics such

as grain size and orientation relationships, pyxem enhances the understanding of material properties. These insights are valuable in metallurgy, semiconductors, and functional materials, where crystallographic information influences performance. The open-source nature of pyxem allows for adaptable workflows that integrate with modern 4D-STEM methodologies, promoting accessible and customisable electron diffraction analysis.

[1] D.Viladot et al., Journal of Microscopy 252 (1): 23–34 (2013).

[2] N. Cautaerts et al., Ultramicroscopy 237 (113517): 113517 (2022).

IM4.P20
Four-dimensional scanning transmission electron microscopy (4D-STEM) utilizing a CMOS camera

P. J. Lobpreis[1], C. O. Ogolla[1], B. Butz[1]

[1]University of Siegen, Micro- and Nanoanalytics, Siegen, Germany

Selected area electron diffraction (SAED) is a traditional electron microscopy technique used for phase analysis by isolating specific regions in a sample. The areas sampled by SAED are limited by the size of the SAED aperture, which limits the area that can be analyzed and limits the full capture of diffraction patterns at the nanoscale. In contrast, 4D-STEM involves simultaneous collection of 2D images of the sample (real space) and convergent beam electron diffraction (CBED) pattern (reciprocal space) at each probe position. This enables collection of information with a high resolution owing the small STEM probe size. [1] These advanced measurements rely on modern direct electron detector technologies, known for their high sensitivity and fast readout capabilities. 4D-STEM has therefore enabled a variety of advanced measurements, such as local phase, orientation and strain mapping. Furthermore, phase contrast imaging modes like ptychography, which provides high-resolution phase imaging and differential phase contrast (DPC) imaging for mapping electric and magnetic fields can be employed.

However, direct electron detectors are expensive and not readily available at many institutes. Herein the successful utilization of a standard installation scintillator-based Gatan Continuum CMOS camera for 4D-STEM data collection is demonstrated. The camera at hand features a 2048 × 2048 sensor format with 18-micron pixels, with a frame rate of 94.2 fps without binning. Scintillator-based cameras exhibit inherently slower readout speeds and generate larger data sets compared to state-of-the-art direct electron detectors. Given these challenges we established a workflow for handling the large datasets using py4DSTEM [2], a community-driven Python package for microscopy data analysis on a high-performance computer (HPC) here at the University of Siegen.

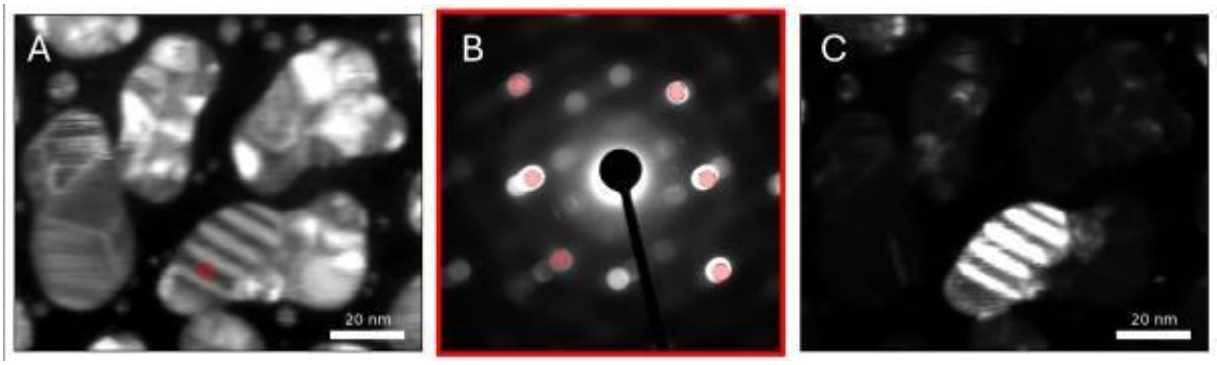
Figure 1: A) Virtual image of gold nanoparticles on carbon substrate **B)** virtual diffraction pattern derived from the mask in A) **C)** resulting virtual image with masks in B) acting as virtual objective apertures

Reference

[1] C. Ophus. Microscopy and Microanalysis 25, 563–582 (2019)

[2] C. Ophus, et al. Microscopy and Microanalysis 28, 390-403 (2022)

Fig. 1



IM4.P21
Analysis of organic semiconductor materials using 4D-STEM

M. N. Hussain[1], Y. Hao[1], T. Lorenzen[2], F. Malagreca[3], Y. Geerts[3], K. Müller-Caspary[2], S. van Aert[1]

[1]University of Antwerp, EMAT and NANOLIGHT center of excellence, Dept. of Physics, Antwerp, Belgium
[2]Ludwig-Maximilians University Munich, Chemistry, Munich, Germany
[3]Université Libre de Bruxelles, Laboratoire de Chimie des Polymères, Brussels, Belgium

INTRODUCTION

Organic semiconductors like Zinc Phthalocyanine (ZnPc) are used in phototransistors, biosensors and for 6G technology devices [1]. These molecules also serve as base molecules to develop other chiral molecules [2]. Since the molecular structure of ZnPc and its chiral derivatives is important for its optoelectronic properties, it needs to be imaged at an atomic scale. Scanning transmission electron microscopy (STEM) provides the advantage of better elucidating non-planar structures over other techniques like atomic force microscopy and scanning tunneling microscopy while also providing direct elemental information [3]. However, materials such as ZnPc pose significant challenges due to the high tendency of suffering beam damage. With the advent of four-dimensional STEM (4D-STEM) such materials can be better imaged as the dose requirement is much lower [4]. Additionally, unlike conventional high angle annular dark field STEM, 4D-STEM methods use pixelated detectors that record a full convergent beam electron diffraction pattern (CBED) for every scan position which makes them suitable for analyzing sensitive materials like zeolites [4].

METHODOLOGY

In this work, ZnPc nanocrystals are analyzed using 4D-STEM data and three different reconstruction methods (riCOM [4], AIRPI [5] and ptychography [5]) to obtain atomic resolution images of the crystals. riCOM (real time integrated center of mass) is a technique that reconstructs the projected potential from the center of mass of the CBED at each scan position, whereas AIRPI uses convolutional neural networks to reconstruct the complex electron wave function. Ptychography uses interferences in the diffraction discs in the CBED patterns for phase reconstruction. For analyzing the samples, a probe-corrected Titan Themis Z microscope is used (Thermo Fisher Scientific) equipped with an AdvaPIX TP3 camera at an acceleration voltage of 300 kV. The goal of this study is to evaluate the strengths and limitations of the reconstruction methods and parameters (such as electron dose and convergence angle) to optimize atomic-level imaging of ZnPc. This is the first time ZnPc will be studied using 4D-STEM.

RESULTS

Preliminary results suggest that 4D-STEM reconstruction using riCOM [4] yields a highly detailed, atomic scale image of ZnPc, allowing clear visualization of the molecular shape (see Figure 1). These findings will be further validated through simulations. This approach could also be extended to monolayers and chiral derivatives of ZnPc.

Figure 1 a) STEM versus b) 4D-STEM-riCOM. The latter image showing more details concerning the atomic structure. c) Overlay of ZnPc structure on the 4D-STEM-riCOM image.

ACKNOWLEDGEMENTS

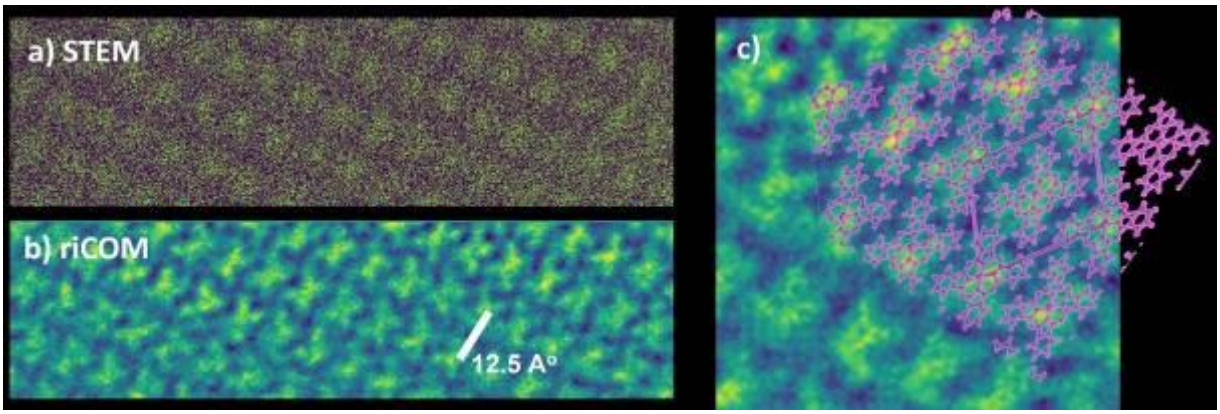
The authors acknowledge financial support from the Research Foundation Flanders (FWO, Belgium) and Fonds de la Recherche Scientifique (FNRS, Belgium) within the CHISUB network of the EOS (Excellence of Science) program (grant number 40007495).

References:

1. Qasrawi, A. F. and Daragme, R. B., *Phys Scr*, vol. 99 (2024), no. 5.
2. Gök, Y., Gök H. Z. and Karayiğit, İ. Ü., *J Organomet Chem*, vol. 873 (2018), pp. 43–49.
3. Kharel, P., Janicek, B. E., Bae, S. H., Loutris, A. L., Carmichael, P. T. and Huang, P. Y., *Nano Lett*, 2022.
4. Yu, C. P., Friedrich, T., Jannis, D., Van Aert, S., and Verbeeck, J., *Microscopy and Microanalysis*, vol. 28 (2022), no. 5, pp. 1526–1537.

5. Friedrich, T., Yu, C. P., Verbeeck, J., and Van Aert S., *Microscopy and Microanalysis*, vol. 29(2023), no. 1, pp. 395–407.

Fig. 1



IM4.P22
An alternative ptychography single slice algorithm for low and medium dose atomic resolution

M. Töllner[1], C. Kübel[1], X. Mu[2], O. Melnyk[3]

[1]Karlsruhe Institute of Technology, Institute of Nanotechnology, Karlsruhe, Germany
[2]Lanzhou University, School of Materials and Energy and Electron Microscopy Centre, Lanzhou, China
[3]Technische Universität Berlin, Berlin, Germany

High-resolution scanning transmission electron microscopy (HRSTEM) is a powerful technique for resolving the atomic structure of materials. However, it fails to retain the phase information of the exit wave. To address this limitation, advanced 4D-STEM techniques, such as electron ptychography[1], have been developed to retrieve phase information and enhance resolution. Conventional electron ptychography methods typically require high electron doses on the order of 1,000,000 e-/A² [2] to achieve reliable reconstructions with atomic resolution. Reducing the dose while maintaining the resolution power poses a fundamental challenge due to increased noise.

This study introduces a new approach to achieve high noise resistance in atomically resolved electron ptychography using the Alternating Amplitude Flow (AAF) method. We systematically studied parameters such as step size, convergence angle, maximum detector angle, dose, and sample thickness.

To demonstrate the effectiveness of our method, we applied it to $SrTiO_3$ (STO) and $PrScO_3$ (PSO). These samples were chosen for better comparability with other ptychography codes (STO) and due to the short atomic distances in PSO. Additionally, we have extended the applicability of electron ptychography to thicker samples up to 10 nm, without relying on multi-slice methods.In the reconstruction of a 10 nm STO sample, atomic resolution is preserved with only the Pb columns showing phase errors due to their high atomic weight. Our method enables high-resolution reconstructions at doses below 10,000 e^-/A^2 for single layers, as demonstrated in Figure 1. This figure shows the reconstruction of PSO at infinite dose, 10,000 e^-/A^2, and 1,000 e^-/A^2. By using a larger step size, as illustrated in Figure 2, where it is increased from 50 to 300 pm, the overlap area is reduced to around 25 %, allowing for effective phase retrieval at lower doses. Figure 3 shows the capablities for reconstructing the diffraction patterns at 1,000 e^-/A^2, where most of the noise can be removed and the reconstructed diffraction pattern looks very close to the infinite dose one

By providing a detailed analysis of the noise resistance and resolution capabilities of the AAF method, we aim to push the boundaries of low-dose high-resolution imaging. The ability to achieve high noise resistance with minimal dose rates opens up new possibilities for understanding the fundamental properties of materials and their applications in advanced technologies. This advancement not only enhances our ability to study materials at the atomic level but also paves the way for new discoveries in fields such as nanotechnology, materials science, and condensed matter physics.

[1] Nellist, P. D., McCallum, B. C., & Rodenburg, J. M. (1995). Resolution beyond the 'information limit' in transmission electron microscopy. *Nature*, 374(6523), 630-632. DOI: 10.1038/374630a0

[2] Zhen Chen et al., Electron ptychography achieves atomic-resolution limits set by lattice vibrations. Science 372, 826-831 (2021). DOI: 10.1126/science.abg2533

Figure 1: a) single layer PSO reconstructed from infinite dose, b) reconstructed at 10,000 e^-/A^2 and c) econstructed at 1,000 e^-/A^2

Figure 2: a) PSO reconstructed with a step size of 50 pm and b) PSO reconstructed with a step size of 300 pm

Figure 3: a) Diffraction pattern of PSO at infinite dose, b) Diffraction pattern of PSO at 1,000 e^-/A^2 and c) Reconstructed diffraction pattern of PSO at 1,000 e^-/A^2 using the AAF method

---

Fig. 1

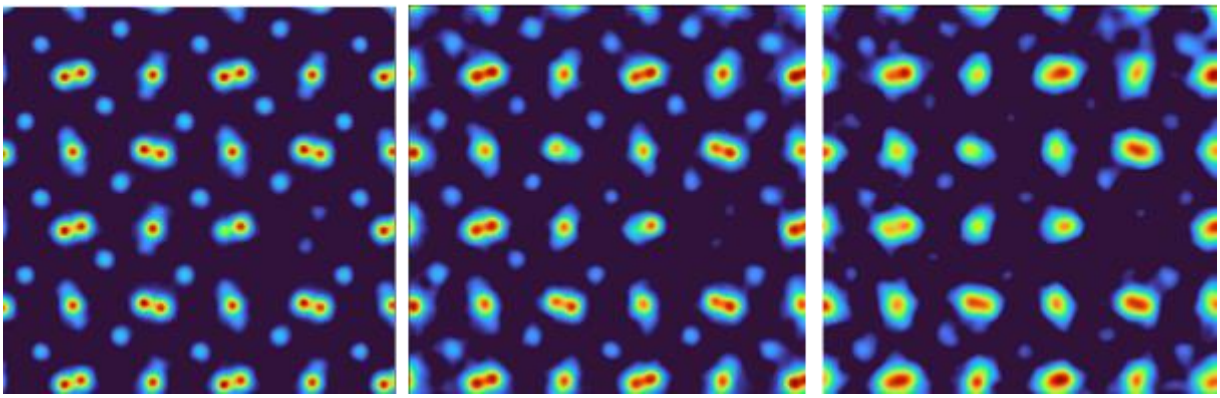


Fig. 2

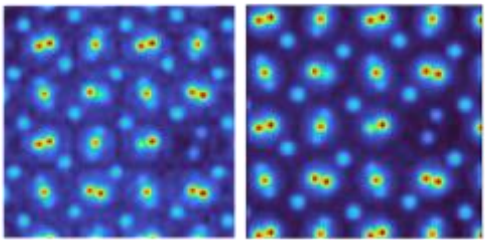
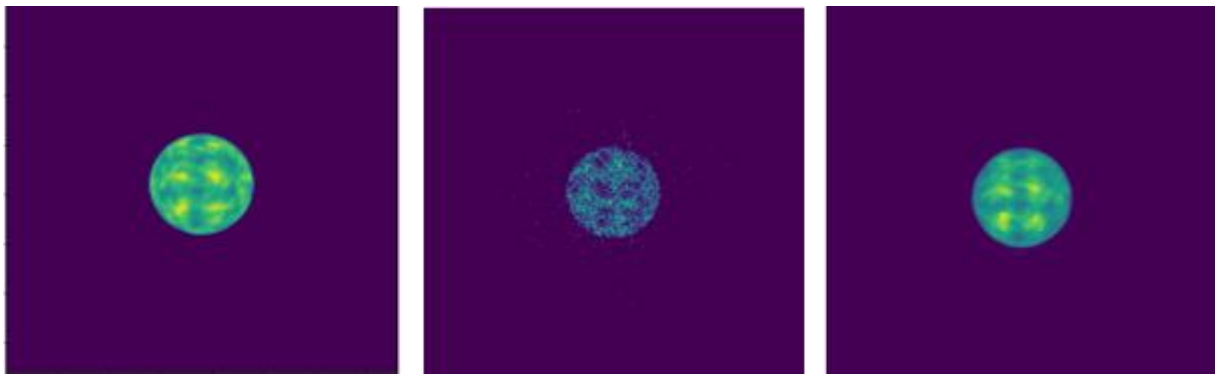


Fig. 3



IM4.P23
Optimizing electron ptychography experiments with *PtychoScopy*

E. Poghosyan[1], R. Skoupy[1], E. Müller[1], T. Pennycook[2], M. Guizar-Sicairos[3,4], E. Fabbri[5]

[1]Paul Scherrer Institute, CLS, Villigen, Switzerland
[2]University of Antwerp, Antwerp, Belgium
[3]Paul Scherrer Institute, CPS, Villigen, Switzerland
[4]Ecole Polytechnique Fédérale de Lausanne, Lausanne, Switzerland
[5]Paul Scherrer Institute, CEE, Villigen, Switzerland

Electron ptychography is a powerful computational diffractive imaging technique allowing, among other advantages, improved resolution, computational post-collection aberration correction and high dose efficiency. With the development of fast, efficient "noise-free" cameras and advanced computational phase retrieval algorithms, electron ptychography has gained momentum in the physical sciences and has also become a method of interest in the life sciences [1,2]. However, the complexity of the method - which involves the careful selection of various experimental parameters and processing algorithms - can be considered a bottleneck, limiting accessibility and appeal to newcomers in the field. With *PtychoScopy* [3], a Python-based tool developed in this work, we enhance the accessibility of electron ptychography to scientists across different disciplines. The tool displays various figures of merit which support the researcher selecting critical optical parameters, and which can be customized to individual microscope setups. It guides the researcher in determining optimal settings for successful ptychographic experiments and analysis.

We also demonstrate the importance of key parameters including convergence angle, defocus, and dose using both direct single side band and iterative phase retrieval algorithms [5,6] with experimental data of crystalline SmB_6 collected using the fast ARINA hybrid pixel detector from DECTRIS [4]. Additionally, we have investigated the effects of real and reciprocal space sampling, and balancing them to compromise between speed and quality. Providing guidance for such parameter selection, *PtychoScopy* substantially improves the accessibility of electron ptychography and paves the way for broader adoption of this versatile and highly promising imaging technique in various scientific fields.

References:

1. G. Li et al., *ACS Central Science* **8** (2022), https://doi.org/10.1021/acscentsci.2c01137

2. L. Zhou et al., *Nature Communications* **11**, 1 (2020), https://doi.org/10.1038/s41467-020-16391-6

3. Skoupy, R. et al. *Microsc. Microanal.* 30, 448, DOI: 10.1093/mam/ozae044.913 (2024)

4. Stroppa, D. G. et al. *Microsc. Today* 31,39810–14, DOI: 10.1093/mictod/qaad005 (2023)

5. C. M. O"Leary et al., *Ultramicroscopy* **221** (2021), https://doi.org/10.1016/j.ultramic.2020.113189

6. S. Gao et al., *Nature Communications* **8**, 163 (2017), https://doi.org/10.1038/s41467-017-00150-1

7. The authors acknowledge funding from the Swiss national science foundation (206021_177020) for co-financing the TEM ARM-200F and PSI Research Grant 2021 for financing this work (R.S.). We are very grateful to DECTRIS, especially to Daniel G. Stroppa and Matthias Meffert, for having the chance of using their detector and for their support with detector integration (ARINA) and experiments.

IM4.P25
Physical origin of giant enhancement vs. reduction of phase contrast in GaN doping structures

K. Ji[1], D. S. Rosenzweig[1], M. Schnedler[1], Q. Lan[1], J. F. Carlin[2], R. Butté[2], N. Grandjean[2], R. E. Dunin-Borkowski[1], P. Ebert[1]

[1]Forschungszentrum Jülich GmbH, Ernst Ruska-Center, Jülich, Germany
[2]Ecole Polytechnique Fédérale de Lausanne, Institute of Physics, Lausanne, Switzerland

Electron holography (EH) in a transmission electron microscope (TEM) developed into the method of choice for mapping and quantifying electrostatic potentials in semiconductor structures with high energy precision and nm resolution. Unfortunately, a quantitative analysis is not as straight forward as frequently suggested: For example, the electron optical phase contrast across a *p*-*n* junction is reported to be smaller, whereas across an, e.g., *n*-*n*$^+$ doping step, it is larger than expected. In addition, it has been shown that FIB-prepared TEM lamellas exhibit strong Fermi-level pinning near the surfaces.[1] Without an in-depth understanding of the physical origins, no quantitative values can be extracted from electron holography. Therefore, we present a comprehensive investigation of the electron optical phase changes in conjunctions with self-consistent semiconductor simulations, using GaN as model system.

The electron optical phase contrast at *n*-*n*$^+$ GaN doping steps is found to exhibit a giant enhancement, which is independent of the lamella thickness, in sharp contrast to *p*-*n* junctions, which are shown to have thickness-dependent phase change, reduced in magnitude. The physical origin of these observations can be understood in the framework of doping-dependent screening of surface Fermi-level pinning by FIB-induced defects. The pinning defects in *n*-type GaN can be traced to carbon on nitrogen sites. In addition, contacting-dependent electron beam induced charging and its effect on the phase change at *n*-*n*$^+$ and *p*-*n* junction is discussed. This work dissects the previously termed dead layers to identify the defect-rich crystalline inner shell and the screening of its Fermi-level pinning being solely relevant for electron optical phase differences, thereby providing a path towards a quantitative understanding of phase changes of semiconductor doping structures in EH.

[1] K. Ji et al., Ultramicroscopy 264, 114006 (2024)

IM4.P26
Quantification of interface magnetism in $La_{0.7}Sr_{0.3}MnO_3$ by off-axis electron holography

Q. Lan[1], M. Schnedler[1], P. Ebert[1], R. E. Dunin-Borkowski[1]

[1]Forschungszentrum Jülich GmbH, Ernst Ruska-Center, Jülich, Germany

Many intriguing magnetic phenomena arise at interfaces between layers with different magnetic orders, driven by discontinuities in chemical composition, crystal structure, and electronic band structure. This effect is particularly pronounced in manganese oxide heterostructures, where interfacial interactions play a critical role in determining magnetic properties. However, reliably measuring the interfacial magnetic field remains challenging due to several factors. TEM-based phase contrast techniques are widely employed to probe magnetic field distributions with high spatial resolution. However, a fundamental limitation of these techniques is the inherent overlap between magnetic and electrostatic potentials, which complicates the isolation of purely magnetic contributions. This coupling is particularly strong at interfaces, where significant electrostatic potentials arise from both the mean inner potential and charge-induced potential. Additionally, diffraction contrast at the interface is often dominant, further complicating phase interpretation. Furthermore, the interfacial magnetic signal in manganese oxide heterostructures is typically weak, often attributed to reduced magnetic moments (e.g. the formation of magnetic dead layers) or complex spin textures. The spatial resolution of the technique itself imposes further constraints on resolving subtle interfacial magnetic features.

Our previous work demonstrated that by integrating off-axis electron holography, electron spectroscopy, and self-consistent electrostatic potential simulations [1], it is possible to map the Curie temperature and magnetic field distributions at ferromagnetic/paramagnetic interfaces while simultaneously accounting for electrostatic potential effects [2,3]. In this study, we further investigate the artifacts and influencing factors that affect the measurement and interpretation of holography data, as well as strategies to mitigate these challenges. Using $La_{0.7}Sr_{0.3}MnO_3$ thin films grown on $SrTiO_3$ substrates as a model system, we conduct a detailed analysis of interfacial magnetic behavior. Through precise measurements and refined data interpretation, we successfully resolve magnetic signals within a 5 nm range of the interface, offering new insights into interfacial magnetism and demonstrating the potential of electron holography for probing nanoscale magnetic phenomena.

References:

1. Schnedler M., Dunin-Borkowski R. E., and Ebert Ph., Phys. Rev. B (2016) 93, 195444.
2. Lan Q., Wang C., Jin L., Schnedler M., Freter L., Fischer K., Caron J., Wei X.-K., Denneulin T., Kov ács A., Ebert Ph., Zhong X., and Dunin-Borkowski R. E., Phys. Rev. Lett. (2022)129, 057201.
3. Lan Q., Schnedler M., Freter L., Wang C., Fischer K., Ebert Ph., and Dunin-Borkowski R. E., Phys. Rev. B (2023)108, L180410.

IM4.P27
Toward quantitative measurement of polarization by precession 4D-STEM

P. Ranieri[1], V. Boureau[2], V. Tileli[1]

[1]Ecole Polytechnique Fédérale de Lausanne, Institute of Materials, Lausanne, Switzerland
[2]Ecole Polytechnique Fédérale de Lausanne, Interdisciplinary Center for Electron Microscopy, Lausanne, Switzerland

Mapping the local electric field of ferroelectric materials under biasing conditions can elucidate the mechanisms of domain switching, with implications in energy harvesting and computing applications [1]. 4-dimensional scanning transmission electron microscopy (4D-STEM) can provide electric field maps using the differential phase contrast (DPC) approach [2]. However, the measurements are affected by the mean inner potential (MIP), the thickness and most importantly by the diffraction contrasts of the sample. Thus, quantitative field measurement remains a challenge. Precession 4D-STEM has been shown to be promising for reliable field measurement [3], as will be investigated here for ferroelectric sample.

Our objective is to evaluate the accuracy of the technique measuring a ferroelectric BaTiO3 (BTO) wedge sample with a known thickness variation [4]. The cubic and tetragonal phases, respectively above and below the BTO Curie temperature (Tc=120°C), are measured with 4D-STEM and precession 4D-STEM.

The BTO wedge was prepared using a Xe plasma FIB (Helios G4 PFIB UXe) on a MEMS heating/biasing chip (DensSolutions), with a known wedge angle of 10.8°. Experiments were performed in a Thermo Fisher Scientific Titan Themis microscope operated at 300 kV, equipped with a MerlinEM detector and NanoMegas precession system.

Making use of the measurements above Tc help understanding the artefacts originating from the MIP and sample thickness variation, in absence of ferroelectric domains. Here the wedge geometry of the sample allows for measuring the MIP of BTO. 4D-STEM measurements lead to a quantitative evaluation of the MIP well above the theoretical value of 24 V. We show that precession-assisted experiment averages the contrasts originating from the dynamical diffraction and now provides a proper evaluation of the MIP.

The results demonstrate that combining precession with 4D-STEM reduces diffraction contrasts artefacts and we use the method to show improved electric field maps of the BTO wedge below Tc, as compared to standard 4D-STEM measurement.

This work was supported by the Swiss National Research Foundation (SNSF) under award number 200020_204240.

References

[1] R. Ignatans et al., Physical Review Letters 127.16 (2021)
[2] K. Moore et al., APL Materials, 9.2, (2021)
[3] L. Bruas et al., Journal of Applied Physics, 127 (2020)
[4] M. Wu et al., Ultramicroscopy, 176, (2017)

IM4.P28
Towards retrieving three-dimensional orientation of polycrystalline materials using 4D-STEM

C. Zhu[1], P. H. Lu[1], L. Jin[1], R. E. Dunin-Borkowski[1]

[1]Forschungszentrum Jülich GmbH, Jülich, Germany

Polycrystalline materials—consisting of numerous crystallites, or "grains," each with different orientations—form the backbone of structural alloys and many catalytic systems. Recovering their three-dimensional (3D) orientations, especially for nano-sized grains under transmission electron microscopy (TEM), is extremely challenging due to severe overlap along the beam direction and multiple diffraction events. The emergence of 4D-STEM techniques[1], however, provides new avenues for overcoming these difficulties and obtaining more detailed information about grain texture.

Here, we are trying to present an algorithm designed to determine grain orientations by leveraging a series of 4D-STEM datasets collected at various tilt angles with precession. Conceptually akin to tomographic reconstruction[2]—which seeks a consensus among real-space projections—this method instead requires achieving consistency in reciprocal space. By comparing multiple orientations inferred from different experimental conditions, the approach can more reliably disentangle overlapping diffraction signals.

Harnessing the power of 4D-STEM, our method first aligns virtual images precisely to create a volumetric representation of the specimen. Each voxel in this volume is assigned an initial orientation based on back-projection reconstruction using coarse 2D orientation mappings. We then construct parallel rays to link voxel orientations with diffraction patterns at each scan position. Forward diffractions are simulated on a ray-by-ray basis without factoring in peak intensities (mitigating the effects of multiple diffraction)[3,4], and the resulting discrepancies are measured against experimental data. By iteratively adjusting voxel orientations via a search over the symmetry-reduced spherical domain of SO(3), these discrepancies are progressively minimized. Ultimately, we expect that this tomography-like algorithm will converge on an optimal consensus across all datasets, yielding a high-fidelity 3D orientation map.

1. Ophus, C. Four-Dimensional Scanning Transmission Electron Microscopy (4D-STEM): From Scanning Nanodiffraction to Ptychography and Beyond. Microsc. Microanal. 25, 563–582 (2019).
2. (Classics in Applied Mathematics) Aninash C. Kak, Malcolm Slaney - Principles of Computerized Tomographic Imaging-Society for Industrial and Applied Mathematics (2001).pdf.
3. Cautaerts, N. et al. Free, flexible and fast: Orientation mapping using the multi-core and GPU-accelerated template matching capabilities in the Python-based open source 4D-STEM analysis toolbox Pyxem. Ultramicroscopy 237, 113517 (2022).
4. Ophus, C. et al. Automated Crystal Orientation Mapping in py4DSTEM using Sparse Correlation Matching. Microsc. Microanal. 28, 390–403 (2022).

IM4.P29
A 4DSTEM-based method for phase differentiation in phase change memory materials

X. Bai[1], J. Jo[1], R. E. Dunin-Borkowski[1]

[1]Forschungszentrum Jülich GmbH, Ernst Ruska-Centre for Microscopy and Spectroscopy with Electrons, Jülich, Germany

Introduction

With the rapid development of modern information technology, the novel approaches for storing and processing large volumes of data are being developed, from general concepts such as memory in computing, multi-level storage and neuromorphic computing to specific techniques such as new designs of circuits and storage devices. Different electronic devices are under development, such as magnetoresistive random access memory, resistive random access memory, phase change memory (PCM) and ferroelectric memory. PCMs that are based on chalcogenide materials are promising choices for data storage because phase transitions between amorphous and crystalline phases are quick and efficient. Such phase transitions result in changes between high and low resistance states, which correspond to "0" and "1" logic levels in data storage, respectively. However, the resistance of the amorphous phase in a PCM cell can drift over time, which reduces the reliability of PCM device. The resistance drift is likely attributed to the change in the amorphous phase in a PCM cell. Therefore, it is important to develop methods to differentiate between local crystalline and amorphous phases and characterize amorphous phases efficiently.

Objectives

In this project, we aim to develop a new methodology to identify the amorphous and crystalline phases at nm resolution in phase change materials using four-dimensional scanning transmission electron microscopy (4D STEM).

Materials & Methods

With the help of a fast pixelated detector (*e.g.* EMPAD), full 4D STEM datasets of diffraction patterns were collected from the PCM material, Ge2Sb2Te5(GST), as the electron beam was scanned across areas of interest. Approaches based on fluctuation electron microscopy (FEM) and radial Fourier analysis (RFA) were applied to create radial spectra as a function of momentum vector $\boldsymbol{k}$ from the diffraction patterns. Multivariate statistical analysis based on principal component analysis and non-negative matrix factorization was used to distinguish between different phases in the PCM materials, which visualizes the distribution of amorphous and crystalline phases.

Results

The approach was applied to study crystalline nanomaterials on amorphous layers to differentiate between different phases. First, optimal experimental parameters of scanning nanobeam diffraction were studied using test samples, such as cross-grating replica alignment specimen with amorphous carbon layer and Au nanocrystals on top of it. In general, it was found out that larger beam intensity, smaller convergence angle, and relatively larger camera length lead to the reliable phase separation. The developed method was then applied to the GST sample. Crystalline clusters in the amorphous GST layer could be distinguished using the method based on both FEM and RFA. The two methods were compared with each other. RFA was found to have better robustness to noise.

Conclusions

We have developed a method that can be used to differentiate between amorphous and crystalline phases in PCM materials by combining 4D STEM with FEM and RFA. Both FEM and RFA could distinguish successfully between amorphous and crystalline phases. However, RFA was more robust to noise than FEM. The two methods are complementary and can be used alongside each other to study unknown phase change materials, ultimately during switching.

IM4.P30
Atomic resolution DPC-STEM imaging of magnetic signal in antiferromagnets and beyond

J. Michalička[1], F. Křížek[2], J. Rusz[3], J. C. Idrobo[4], P. Wadley[5], T. Jungwirth[2,5]

[1]Brno University of Technology, Cryoelectron Microscopy and Tomography Core Facility, Brno, Czech Republic
[2]Czech Academy of Sciences, Institute of Physics of the Czech, Prague, Czech Republic
[3]Uppsala University, Physics and Astronomy, Uppsala, Sweden
[4]ORNL, Center for Nanophase Materials Sciences, Oak Ridge, TN, United States
[5]University of Nottingham, School of Physics and Astronomy, Nottingham, United Kingdom

Efficient manipulation of antiferromagnetic domains (AFD) and domain walls has opened up new avenues of research towards ultrafast, high-density spintronic devices [1,2]. AF domain structures are known to be sensitive to magnetoelastic effects, but the microscopic interplay of crystalline defects, strain, and magnetic ordering remained largely unknown. The previous study of antiferromagnetic CuMnAs epilayers by X-ray photoemission electron microscopy (XPEEM) imaging revealed that its AFD structure is dominated by nanoscale crystalline defects [3]. The results emphasized the crucial role of these defects in determining the AFDs and domain walls and provided a route to optimizing device performance in terms of scaling limits for the data density in the bulk of the antiferromagnet. However, even smaller magnetic objects were indirectly observed in the material, but they remained below the detection limits of XPEEM.

Here, atomic resolution imaging of abrupt AFD walls in CuMnAs epilayers is achieved by utilizing scanning transmission electron microscopy (STEM), differential phase contrast (DPC), and 4D-STEM techniques [4]. The identification of the magnetic domain DPC signal was based on the specific symmetry of the CuMnAs crystal, where the opposite magnetic Mn sublattices occupy crystallographically distinct noncentrosymmetric sites. With a focus on small field-of-view high-resolution imaging, the DPC-STEM signals could be associated with two types of abrupt Néel vector reversals: The first type occurs at a crystallographic antiphase boundary defect, while the second type forms in a part of the epilayer with no rystallographic perturbation detectable by STEM.

The DPC-STEM magnetic signal was reconstructed by calculating the centre of mass (COM) shifts of ronchigrams recorded with a pixelated or 4-segment detector. The signal intensities were plotted as a function of the integrated [001] component of the COM shifts corresponding to the direction of the Lorentz force due to sublattice magnetic Mn moments pointing in the (001) easy plane of antiferromagnetic CuMnAs aligned to the [100] zonal axis. This qualitative assessment of the magnetic order in Mn sublattices was paradoxically possible in substantially thick TEM lamellae, above 50 nm, and with small collection angles, below 10 mrad, since dynamical diffraction effects can be advantageous for magnetic imaging, as revealed by DFT Pauli multislice STEM-DPC simulations [4].

The observation of AFD walls in CuMnAs sheds light on the physics and engineering of spintronic devices with potential in neuromorphic and ultrafast optical applications. The novel application of STEM-DPC can play a crucial role in atomically resolved magnetic signal imaging in studies of other materials with similar symmetries, including α-MnTe, in which altermagnetism has recently been imaged by XPEEM [5]. Here, the applied DPC technique is additionally utilized to detect magnetic DPC signals from the collinear AF magnetic moments of Mn sublattices in the α-MnTe epilayer using the segmented DPC detector.

References:

[1] Jungwirth, T. et al., *Nature Nanotechnology*, 11(3), 231–241 (2016)
[2] Wadley, P. et al., *Science*, 351(6273), 587–590 (2016)
[3] Reimers, S. et al., *Nature Communications*, 13(1), 724 (2022)
[4] Křížek, F. et al., *Science Advances*, 8(13), eabn3535 (2022)
[5] Amin, O.J. et al. *Nature*, 636, pp. 348–353 (2024)

IM4.P31
Crystal Growth in 5D – *In situ* 4D STEM of gold particle crystallization in liquid

B. Miller[1], L. Spillane[1], E. Jensen[2], C. Czarnik[1], S. Gorji[3]

[1]Gatan Inc., Pleasanton, CA, United States
[2]Insight Chips ApS, Kongens Lyngby, Denmark
[3]Ametek GmbH, Gatan+EDAX, Unterschleissheim, Germany

Introduction Rapid advances in in-situ holder technology over the last decade have given access to diverse stimuli that can be applied with high precision. In parallel, 4D STEM has been widely adopted due to the wealth of material properties a single dataset yields at sub-nm resolution. Recent advances enabling continuous acquisition of 4D STEM data cubes continuously over time as the sample is modified, generate 5D datasets that provide valuable insights into material dynamics at the nanoscale.

Objectives This study aims to utilize continuously acquired in-situ 4D STEM to observe the growth of gold particles from solution using a unique liquid cell holder. The goal is to bypass the challenges posed by liquid cell TEM to achieving atomic resolution and instead access nano-scale atomic structural information through diffraction via 4D STEM.

Materials & Methods We recorded a 43-frame in-situ 4D STEM dataset with a temporal resolution of one frame every 9.6 seconds over a 672 x 624 nm field of view. The spatial resolution of the 4D data was 24 nm per pixel, while the STEM probe scanned faster during each camera frame, simultaneously producing higher resolution STEM images with 3 nm pixels, as seen in Figure 1. The liquid cell holder, produced by Insight Chips, features nanochannels of liquid with a nominal thickness of 40 nm. The K3® camera, combined with energy filtering, resulted in high-quality diffraction patterns. Visualization and processing of the in-situ 4D STEM data were performed using DigitalMicrograph® and a Python script [1,2].

Results The dataset revealed detailed information about crystallite size, orientation, and morphology during growth. The low dose rate resulted in slow beam-induced growth from the 0.5 mM $HAuCl_4$ solution, with an overall growth rate of approximately 0.3 nm/s. The particles were polycrystalline with varying crystallite sizes and growth rates, with minimal coalescence observed. Additionally, in-situ EELS data (Figure 2) were acquired from the same nanochannel chip during the same microscope session, confirming the composition of the particles and the presence and thickness of the liquid.

Conclusion In-situ 4D STEM is a powerful technique for elucidating material structures and dynamics. By combining a sensitive camera, unique holder, energy filtering, and advanced software, high-quality data can be obtained and analyzed. This study demonstrates the potential of in-situ 4D STEM to provide valuable insights into the growth mechanisms and dynamics of crystalline materials in liquid environments.

1. Gatan.com https://www.gatan.com/4d-stem-maximum-spot-mapping (accessed Feb 14, 2025)
2. Miller, B.*, et al. Microscopy and Microanalysis*, (2021) **27**, 2688–2690 https://doi.org/10.1017/S143192762100949

Figure 1: Screenshot from a video of the dataset being played back in DigitalMicrograph. A) The simultaneously acquired STEM image with 3 nm pixels. B) Virtual bright field image computed in real time from the in-situ 4D STEM dataset. C) The result of the maximum-spot-map python processing [1,2] applied to the 4D STEM dataset. D) The diffraction pattern from the small red ROI in B. (Full video available via the QR code in C)

Figure 2: EELS Data from a different part of the same sample. A-C show the initial state, with water and the SiNx chip. D-F show the final state with large Au particles A,D) Thickness maps. B,E)

Simultaneous ADF STEM scans. C,F) Low-Loss and High-Loss EELS Spectra. Data is a sum of 4 frames.

Fig. 1

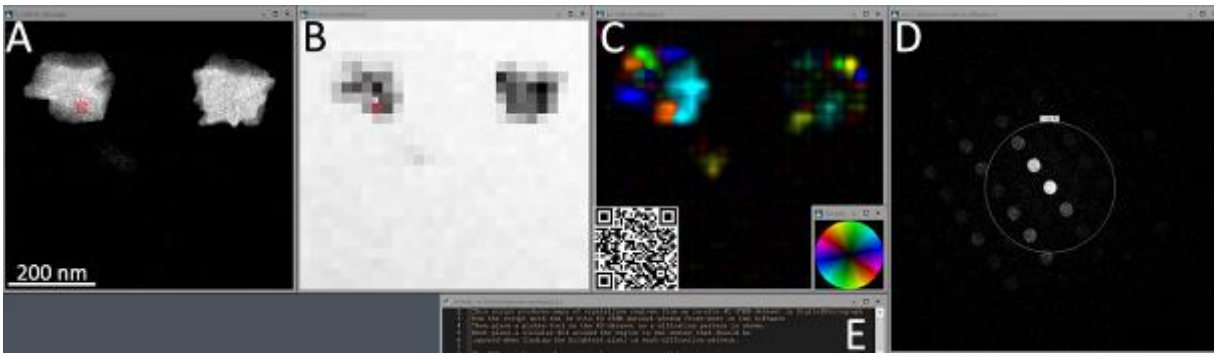
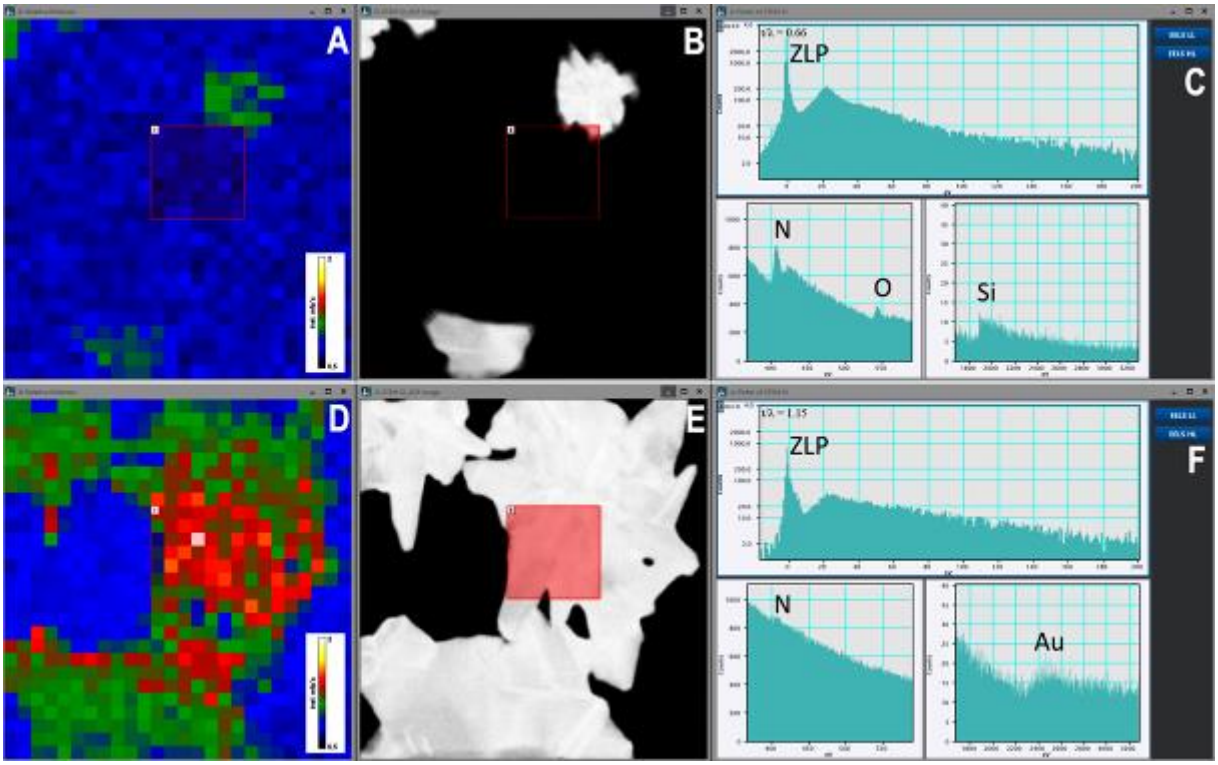


Fig. 2



IM4.P32
Post-acquisition mistilt mapping and correction via automated Laue-centre selection in 4D-STEM using thermal diffuse scattering

J. F. Dushimineza[1], K. Müller-Caspary[1]

[1]Ludwig-Maximilians University Munich, Chemistry, Munich, Germany

We present a post-acquisition tilt-correction methodology for 4D-STEM demonstrating position-wise tilt-estimation with sub-mrad precision and subsequent tilt-correction on crystalline matter using thermal diffuse scattering. A common issue in structure analysis is the global mistilt between probe and specimen, which can be removed by proper experiment alignment. Yet, local tilt variation across the probing area, e.g., due to crystal bending or across domain boundaries must still be accounted for. Fortunately, as per the principle of reciprocity between TEM and STEM [1], tilt-corrected TEM-images can be generated from 4D-STEM data by selection of the Laue-centre (LC) within the Ronchigram at each scan position (Fig. 1) which also corresponds to the Kikuchi-band crossing (KBC). Moreover, the estimated tilt is usable for other tilt-correcting methods such as ptychographic specimen reconstructions initialized with precise probe-tilt priors.

Here, the used tilt-estimation routine is carried out on $SrTiO_3$ evaluating CBEDs in analogy to Ref. [2]. The method proposed in Ref. [2] deduces the KBC by evaluating the azimuthal intensity profile of a CBED via geometrical relations. In contrast, an iterative gradient-descent model (GDM) is applied here, in which the KBC is modelled for each CBED. In particular, the crossing is initialized at the BF centre and iteratively fitted to the KBC (Fig. 2). Parameters such as scan rotation, the width and number of Kikuchi bands, the BF-disc halo emanating into the dark field can be included and automatically optimized for. Furthermore, the GDM incorporates a tilt-map for the whole scan region allowing for regularization. In this way, smooth tilt gradients can be enforced in bent specimens, whereas low or no regularization allows for abrupt tilt changes, e.g., at interfaces. The accuracy of the GDM is benchmarked using simulated data with normal-distributed random tilts at each probe position, achieving sub-mrad precision compared to set ground-truth, still allowing for tilt correction by LC selection (Fig. 3).

However, facing poor signal-to-noise ratio in experiment or elevated mistilts in general, especially when the KBC falls outside of the BF-disc, LC selection may not be applicable for tilt-correction. Surmounting, using the estimated tilt from GDM as probe-tilt initialization in a ptychographic reconstruction of 4D-STEM data of a bent specimen, a tilt-corrected specimen object is obtained (Fig. 4).

To conclude, the GDM enables efficient and robust tilt-estimation compared to numerically costly post-processing of multiple CBEDs under geometrical deduction of the KBC. Beyond tilt-estimation, the found tilt information can be beneficially used for advanced tilt-correction methodologies in conventional TEM and 4D-STEM ptychography.

References

[1]: *Krause, F., Rosenauer, A., 2017. Reciprocity relations in transmission electron microscopy: A rigorous derivation, Micron*

[2]: *Cattaneo, M., Dunin-Borkowski, R. E., et al, 2024. Automated detection and mapping of crystal tilt using thermal diffuse scattering in transmission electron microscopy, Ultramicroscopy*

Fig. 1

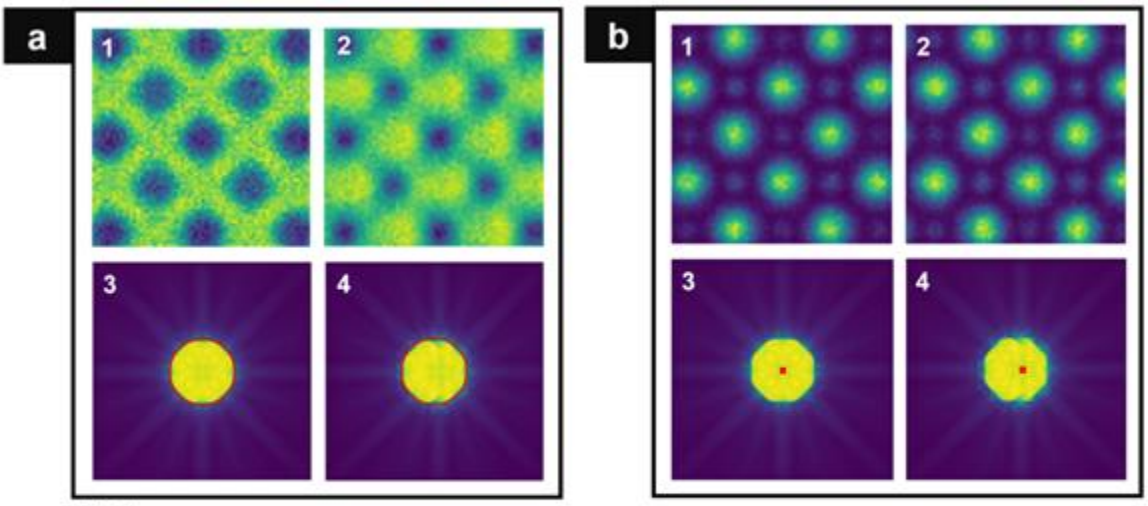


FIG 1:
a) BF image of 20nm thick $SrTiO_3$ with defocused (1) tilt-free and (2) tilted illumination. PACBED with red marked BF mask corresponding to (3) tilt-free and (4) tilted illumination.

b) Image generated via Laue-centre selection with (1) tilt-free and (2) tilted illumination. PACBED with red marked Laue-centre mask corresponding to (3) tilt-free and (4) tilted illumination.

Fig. 2

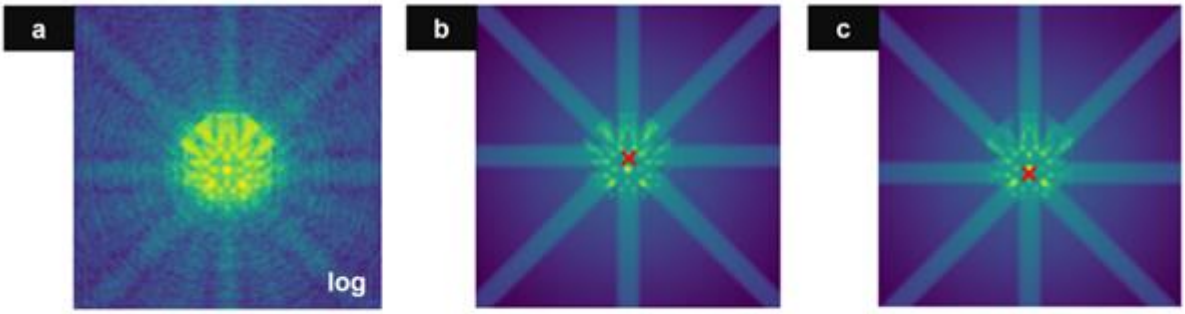


FIG 2:
a) CBED of tilted probe illumination at single scan position on 20nm thick $SrTiO_3$.
b) CBED and overlay of gradient-descent model initialised at BF centre.
c) CBED and overlay of gradient-descent model converged at Kikuchi-band crossing.

Fig. 3

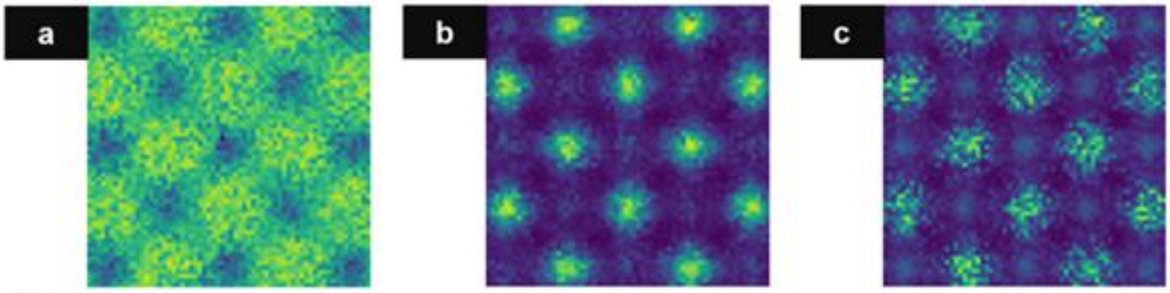


FIG 3:
a) Defocused BF image of 20nm thick $SrTiO_3$ with random probe tilt at each probe position (std = 4 mrad).
b) Image generated by Laue-centre selection at each probe position estimated by gradient-descent model.
c) Image generated by BF-centre selection at each probe position.

Fig. 4

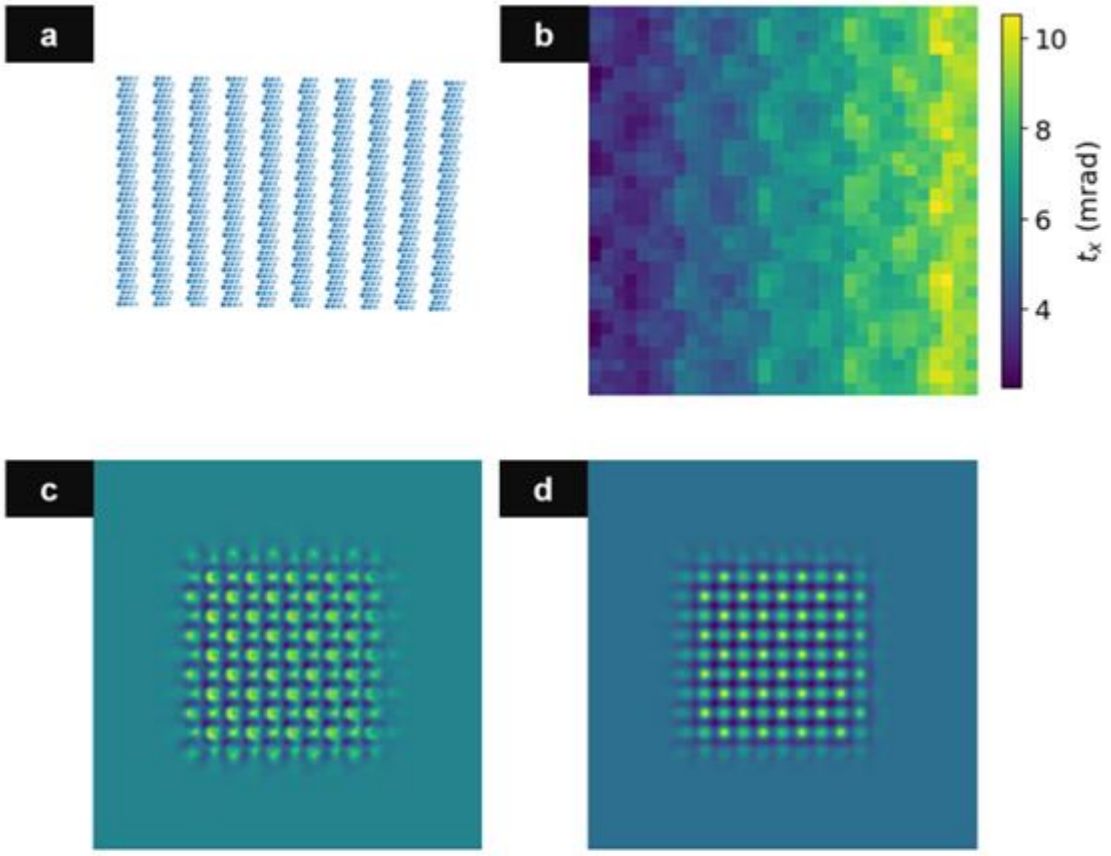


FIG 4:
a) 3D-model (selected planes, side view) of bent $SrTiO_3$ specimen used to create 4D data set with tilt-free probe.
b) Tiltmap estimated by gradient-descent model from 4D data set.
c) Ptychographic reconstruction using tilt-free probe.
d) Ptychographic reconstruction using probe initialised with tilt from tiltmap at each probe position.

IM4.P33
A cryo-electron ptychography workflow for single particle analysis

T. Lorenzen[1], J. Zivanov[1], M. L. Leidl[1], D. Mann[2], F. von Hammerstein[1], A. Schütz[1], H. Stahlberg[3], C. Sachse[2,4], K. Müller-Caspary[1]

[1]Ludwig-Maximilians University Munich, Chemistry, Munich, Germany
[2]Forschungszentrum Jülich GmbH, Ernst Ruska-Centre for Microscopy and Spectroscopy with Electrons, Jülich, Germany
[3]Ecole Polytechnique Fédérale de Lausanne, Laboratory of Biological Electron Microscopy, Lausanne, Switzerland
[4]Heinrich-Heine-Universität Düsseldorf, Biology, Düsseldorf, Germany

Ptychography is an advanced imaging technique that has revolutionized phase retrieval in scanning transmission electron microscopy (STEM) for material science specimen [1]. Recently ptychography has been applied to biologic specimen under cryogenic conditions reaching sub-nanometer resolution [2]. In this abstract we will describe a complete and automated workflow for the recording, reconstruction and evaluation of defocused 4D-STEM datasets in CryoEM single particle analysis.

First, the STEM data is recorded automatically using SerialEM [3], which controls stage motion and the beam. This limits the user interaction to the selection of parameters and grid holes. Using techniques based on the Ronchigram contrast transfer function [4] and the movement of the shadow image inside the ronchigram [5], we estimate the lower order aberrations and the parameters of the scan grid. This provides an initial overview over the data, and it enables the user to select of promising image grids (Figure 1).

An initial micrograph is then reconstructed using the extended ptychographic iterative engine (ePIE) [6]. Here, both the object transmission function and the illumination are updated. Scan points on strongly scattering support films are automatically removed, as proteins on this support will not be usable for single-particle analysis (Figure 2). At this point, cryosparc [7] is used to determine an initial single-particle 3D map from all successfully reconstructed micrographs.

Ptychographic reconstructions are then performed for all selected particles, using the positions and angles output by cryosparc. This is done under a Poisson loss [8] and including the effect of fringe-free imaging [9]. The probe aberrations are initialized by fitting axial aberrations to the pixelwise probes obtained from ePIE [10]. This allows the defoci to be corrected on a per-particle level, while the use of a Poisson loss function increases the performance at very low electron fluences [8].

The final performance of the workflow and the advantages of different algorithms will be compared using refined 3D models of real-world proteins such as tobacco mosaic virus and hepatitis virus particles.

Figure 1: Estimated defoci from a TEM session determined using the movement of the shadow image (left) and virtual bright field image of an exemplary dataset recorded of hepatitis virus particles.

Figure 2: Ptychographic reconstructions. Unfiltered object phases from ePIE reconstruction of tobacco mosaic virus (left), hepatitis shell particles (center) and the same reconstruction with a strong low-pass filter to highlight the particle positions (right). The real space scalebar equals 20 nm.

References:

[1] Science 372.6544 (2021): 826-831.

[2] Nature communications15.1 (2024): 8062.

[3] Microscopy and Microanalysis24.S1 (2018): 864-865.

[4] Ultramicroscopy 110.7 (2010): 891-898.

[5] Lupini, Andrew R. Scanning Transmission Electron Microscopy: Imaging and Analysis (2010): 117-161.

[6] Rodenburg. Ultramicroscopy 109.10 (2009): 1256-1262.

[7] Nature methods14.3 (2017): 290-296.

[8] Micron 185 (2024): 103688.

[9] Leidl, Max Leo, et al. Microscopy Conference (2025), submitted.

[10] Applied Physics Letters 126.8 (2025).

[11] T.L., J.Z., M.L.L., D.M., H.S., C.S. and K.M.-C. acknowledge funding from European Research Council under Grant Agreement 101118656 (ERC Synergy project 4D-BioSTEM)

Fig. 1

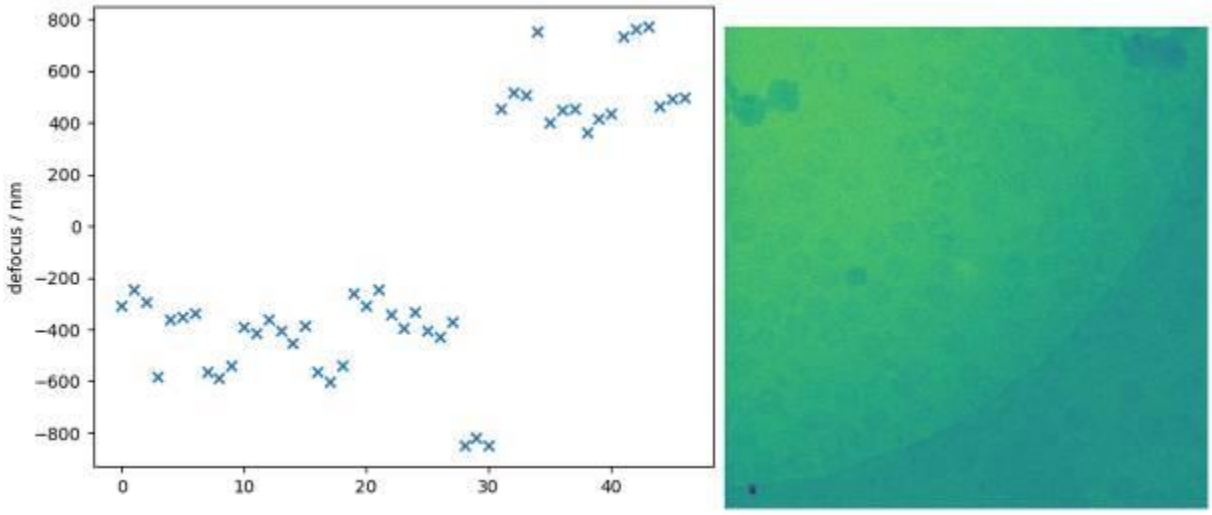
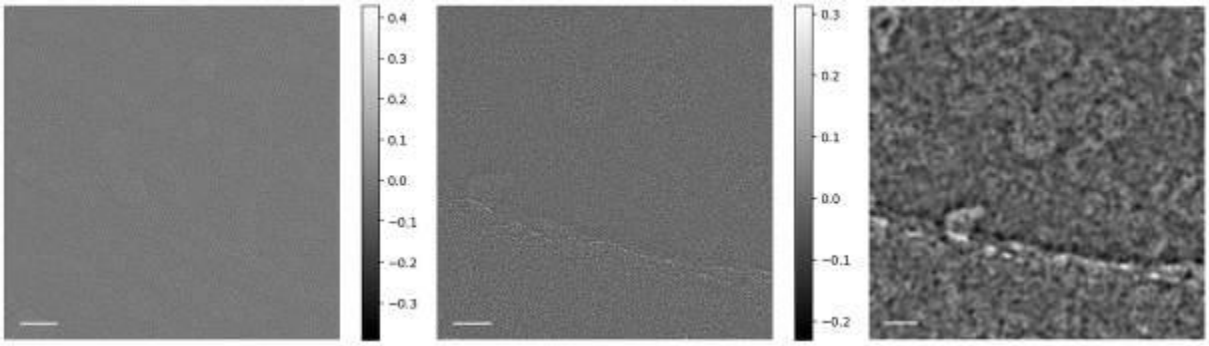


Fig. 2



IM4.P34
How quantitative is the EMCD analysis at sub-atomic scale in a 4D STEM approach

K. Leifer[1], S. K. Manjeshwar Sathyanath[1], V. Kapaklis[1], A. L. Ravensburg[1], B. Hjörvarsson[1], J. Rusz[1]

[1]Uppsala University, Uppsala, Sweden

Introduction and Objectives

X-ray and neutron-based analysis techniques, albeit their fantastic contributions to the field, cannot give the real space image of the magnetization at atomic scale. Until very recently, the atomic resolution analysis of magnetic interfaces has not been possible at all. Hitherto the TEM based techniques of holography and Lorentz microscopies have strongly contributed to our understanding of magnetism. These magnetic images at resolutions typically in the several nanometer scale could be explained by micromagnetic simulations or simulations including large number of atoms. By moving the spatial resolution in imaging of magnetic properties from the to the few Angstroms scale, we will be able to correlate our microscopic observations for the first time directly with ab-initio calculations. The first atomic resolution of single atomic lattice planes has been demonstrated using the techniques of electron energy loss magnetic circular dichroism (EMCD), electron holography and DPC [1].

In this work, we show that using the EMCD technique in STEM mode, quantitative magnetic information needed to compare to models, is achieved at atomic resolution and we demonstrate how it can be used to study details of magnetic excitations.

Materials and Methods

Fe films were grown on thin Al2MgO4 substrates by sputter deposition. The cross sectional and plan view samples were analysed using the EMCD technique in STEM mode. Spectra were acquired in a Titan/Themis TEM and a CEFID filter/direct electron camera ELA. One of the difficulties in acquisition of EMCD spectra consists in the fact that in the classical EMCD geometry, two STEM-EELS maps at the C+, C- positions have to be acquired. To lift related experimental ambiguities, we have introduced the apertured EELS technique that allows, by a 4D-STEM approach, to acquire the C+ and C- signals simultaneously [2], Figure 1.

Results

To approach atomic resolution conditions in a systematic way, we have studied the EMCD signal as a function of convergence angles corresponding to the electron probe sizes ranging from about 1 nm to 1 Å and optimized conditions to obtain the EMCD signal. For each convergence angle, we have acquired in the range of 10000 spectra as well as 4D STEM diffraction maps containing the orientation information. Thus, we could classify the local sample orientation in those EMCD maps based on the corresponding orientation maps. This not only enabled us to understand how the EMCD information evolves with convergence angle but also as a function of local orientation when the crystallites are slightly mistitled in the 0.01 ° range. In the next step, we have analysed, how the EMCD signal fluctuates with crystal orientation for the different convergence angles and discuss possible origins of the observations in this paper. Furthermore, we will discuss how our analysis of quantitative atomic plane EMCD and interfacial EMCD is used to understand magnetic properties at those scales.

Conclusion

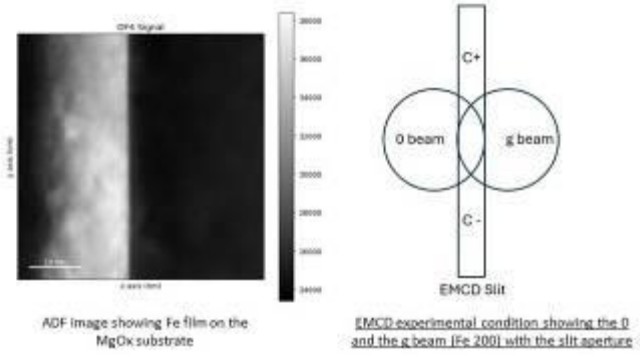
In summary we have carried atomic scale EMCD measurements on Fe and at the interface in a Fe/MgOx .

References:

[1] Wang,et.al. " Nat. Mat. 17 221.Tanigaki et al. Nat. 631, 2024,521. Shibata et al., Nat.Phys 8, 2012 611. Rusz et al., Nat. Comm 7, 2016,12672.

[2] Ali, et al., Sc. Rep.2021, 11:2180.

Fig. 1



ADF Image showing Fe film on the MgOx substrate

EMCD experimental condition showing the 0 and the g beam (Fe 200) with the slit aperture

IM 5: Beam shaping and analysis

IM5.01(inv)
Ponderomotive engineering of electron beams

M. C. Chirita Mihaila[1], N. Laštovičková Streshkova[1], M. Kozák[1]

[1]Charles University, Department of Chemical Physics and Optics, Prague, Czech Republic

The quest for enhanced resolution in electron microscopy has been a defining challenge for over a century. Remarkably, the core technology underpinning this field has remained largely unchanged since its inception. Today, as in the past, electron optics primarily relies on electrostatic and magnetostatic lenses. Despite incremental advancements and the introduction of multipole correctors [1], imperfections in the electron lenses continue to pose challenges.

The recent utilization of ponderomotive interaction between electrons and light represents a breakthrough in electron wave manipulation, particularly in shaping its longitudinal [2], and transverse components [3].

Building upon this foundation, we present in this study our progress in the field of aberration correction for electron lenses using light. Specifically, we show that spherical aberrations in the electron beam can be corrected by tailoring the optical intensity distribution to generate an inverse quartic or quartic ponderomotive potential, effectively compensating for electron phase distortions depending on the sign of the aberration [4]. Furthermore, we demonstrate that chromatic aberrations of the electron beams can be mitigated using a pulsed ponderomotive lens, where the time-dependent interaction, coupled with the electron temporal chirp and ponderomotive potential size, adjusts the focal position of electrons based on their energy [5].

This research not only presents a novel way to correct aberrations of electron optics but also paves the way for a paradigm shift in ultrafast electron microscopy. The prospect of replacing parts of the electron microscope with optical systems promises a significant enhancement in the resolution and contrast of electron images.

[1] M. Haider et al. "Current and future aberration correctors for the improvement of resolution in electron microscopy," Philosophical Transactions of the Royal Society A: Mathematical, Physical and Engineering Sciences, 367(1903):3665–3682 (2009).

[2] M. Kozák et al. "Ponderomotive Generation and Detection of Attosecond Free Electron Pulse Trains," Phys. Rev. Lett. 120, 103203 (2018).

[3] MCC Mihaila et al. "Transverse electron beam shaping with light," Phys. Rev. X 12, 031043 (2022).

[4] MCC Mihaila and Kozák M. "Design for light-based spherical aberration correction of ultrafast electron microscopes", Optics Express. 2025 Jan 7;33(1):758-75.

[5] MCC Mihaila et al. "Light-based Chromatic Aberration Correction of Ultrafast Electron Microscopes," arXiv preprint arXiv:2501.10210. 2025 Jan 17.

IM5.02
Prospects for correlative dynamic electron phase imaging of *Operando* Nanodevices

T. Wagner[1], H. Çelik[2], I. Häusler[1], S. Gaebel[3], D. Berger[4], D. Zhou[5], M. Lehmann[2], M. Albrecht[5], C. T. Koch[1]

[1]Humboldt University of Berlin, Institute of Physics, Berlin, Germany
[2]Technische Universität Berlin, Institute of Optics and Atomic Physics, Berlin, Germany
[3]Max-Born-Institut, B2: Imaging and Coherent X-rays, Berlin, Germany
[4]Technische Universität Berlin, Zentraleinrichtung Elektronenmikroskopie, Berlin, Germany
[5]Leibniz-Institut für Kristallzüchtung, Section Experimental Characterization, Berlin, Germany

Introduction

Understanding ultrafast dynamics in nanoscale electronic devices is critical for optimizing their functionality. However, capturing these transient processes remains a challenge due to limitations in time-resolved imaging techniques, particularly in transmission electron microscopy (TEM). While several approaches, such as the use of pulsed electron sources or fast detectors, have been proposed, none have yet proven effective for visualizing phase modulation at low spatial frequencies at picosecond and nanosecond time scales [1].

Objectives

This study presents the prospects and demonstrates the capabilities of correlative time-resolved electron holography (EH) with interference gating (iGate) [2] and dynamic differential phase contrast (D^2PC) for imaging dynamic projected electric potentials and fields [3] in electronic nanodevices under operando conditions. Approaching sub-nanosecond temporal resolution, both methods are used in a complementary manner to exploit their respective advantages. Specifically, DPC"s robustness against stray field effects and independence from a reference wave is combined with EH"s high sensitivity to minimal potential changes are leveraged in this correlative approach.

Materials & Methods

The instrumental implementation of both techniques in an image-corrected Titan 80-300 TEM, utilizing a custom self-developed RF aperture holder, a modified biasing holder, and a segmented detector with ultrafast read-out capability, is used to investigate electric transient effects in various semiconductor nanodevices. For example, a silicon diode, prepared into a contacted TEM lamella, dynamically switched between unbiased and reverse-biased states (0 V and -1 V, respectively) at 3 MHz, is examined (Fig. 1). Time-resolved holograms are acquired with a temporal resolution of 25 ns and a spatial resolution of approximately 30 nm. These results are complemented with HR static holography, DPC, and simulations to gain deeper insights into potential distributions and stray field effects.

Results

Correlative dynamic phase imaging reveals localized switching dynamics and preparation-induced effects, such as charge recombination at sample edges. These observations confirm excellent agreement with theoretical expectations and static phase data in core regions of the sample while

exhibiting a deviating behavior close to surfaces (Fig. 1). Challenges, including reduced signal-to-noise ratios in dynamic measurements and edge artifacts from ion implantation, are identified and addressed through adaptive measurement routines and targeted modeling approaches.

Conclusion

This work highlights iGate and D2PC as transformative techniques for spatiotemporal imaging of dynamic processes in operando nanodevices. By bridging gaps in temporal and spatial resolution, these methods offer a complementary toolkit for nanoscale real-time imaging.

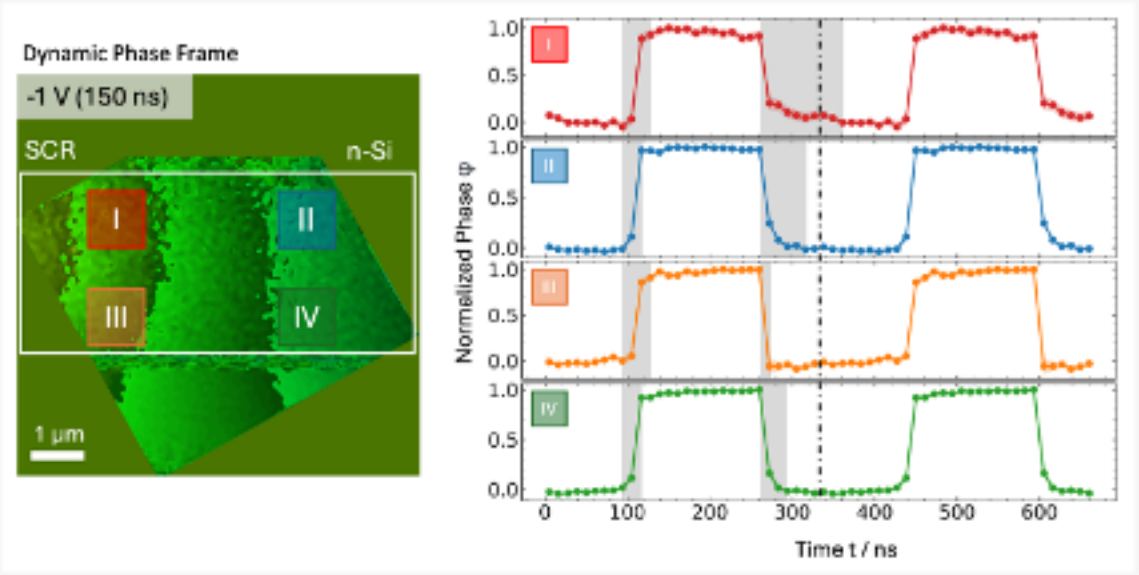
[1] F. Houdellier et al., Ultramicroscopy 202, 26 (2019).

[2] T. Wagner, H. Çelik et al., Electronics 14(1), 199 (2025).

[3] B. Haas et al., Ultramicroscopy 198, 58 (2019).

Fig. 1: Dynamic phase frame of the silicon diode at t = 150 ns (corresponding to 1 V reverse bias), depicting the SCR and its extension into the n-doped region, with the subregions (I–IV) marked for the analysis of the temporal phase progression, showing localized dynamic phase modulations. The gray-shaded areas indicate the captured transitions. For improved visibility, the period is repeated [2].

Fig. 1



IM5.03
Electron wavefront shaping with light in free space

M. Zanetti[1,2], T. Kraeft[1,2], L. A. Ixquiac Mendez[1,2], A. Pernisova[1,2], T. Juffmann[1,2]

[1]University of Vienna, Structural and Computational Biology, Vienna, Austria
[2]University of Vienna, Faculty of Physics, Vienna, Austria

INTRODUCTION

Electron Microscopes (EM) are fundamental tools in many research fields, as they can image samples with resolutions down to the nanometric scale. In EM a beam of accelerated electrons is directed to the sample through an array of electro-optical elements, then the scattered or transmitted electrons are detected to reconstruct an image. However, at least two effects are limiting EM power: Intrinsic aberrations of electron lenses, and sample damaging due to the intense electron flux, particularly affecting biological samples.

OBJECTIVE

The limits set by these effects can be overcome by shaping the electron wavefront of the electrons. Our goal is to show that it is possible to do it by exploiting direct electron-light interaction in free space, avoiding losses. To prove the wavefront shaping of the electrons, we prepare the electron wavefront in a manner similar to the classic double-slit experiment and we detect the resulting interference pattern (Fig.1).

METHODS

We use a 30keV Scanning EM which has been modified to work in transmission mode, and to be coupled to a high-power femtosecond pulsed laser. We split the laser into a UV branch that is directed to the electron source to trigger the electron pulses, and an IR branch that is prepared for the interaction with the electrons and directed to the EM chamber. The electron wavefront shaping takes place in the EM chamber. After the interaction we detect electrons with a self-made detector with micrometric resolution to measure their spatial distribution.

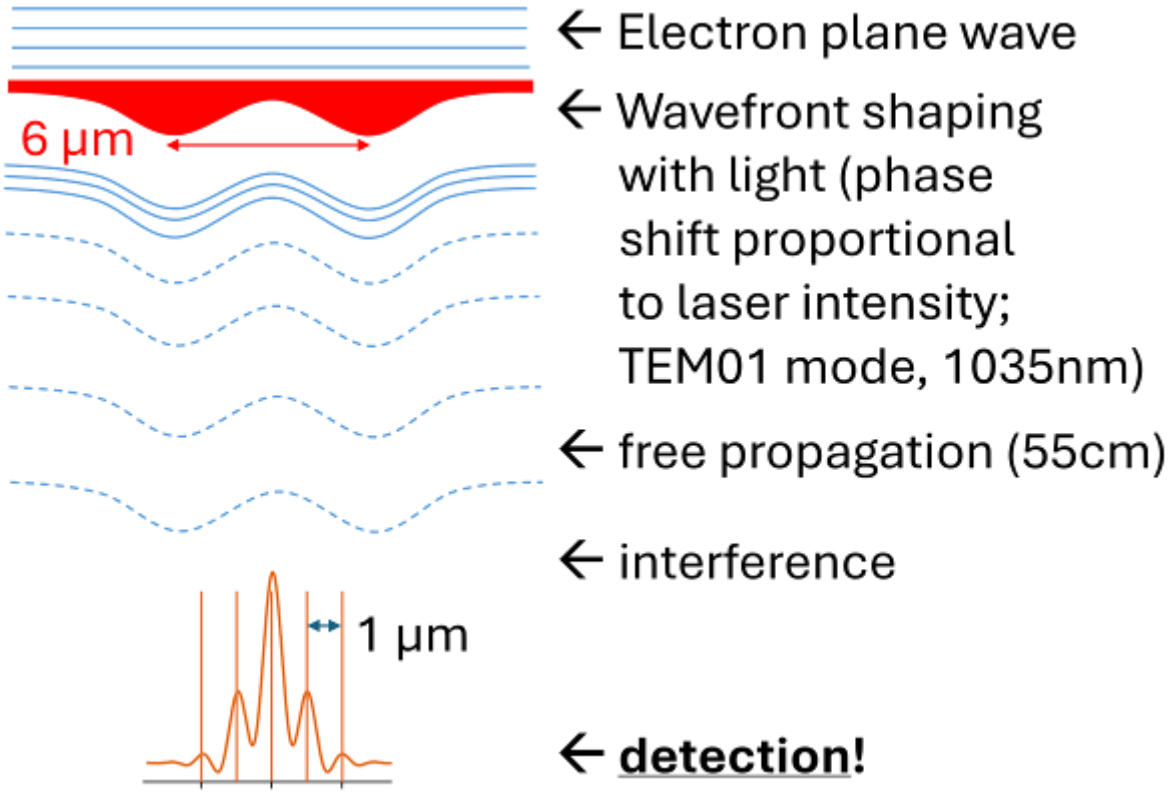
RESULTS

The need for high resolution measurements required to develop a single-electron detector which outperforms many commercially available ones in the 20-30 keV range, being at the same time more flexible and cheaper. We already achieved a resolution of 1.3µm, and we are still improving it. We successfully prapared the laser beam for the interaction; we compensate the electromagnetic fields and the vibrational noise at the level that should allow us to detect the interference pattern. We expect to be able to detect the interference pattern in the next few months.

CONCLUSION

In addition to aberration correction, our electron wavefront shaping in free space is a very flexible tool that will enable other EM techniques. For example, single-pixel imaging, phase contrast microscopy and electron-vorex beam generation. Moreover, the need for high resolution measurements led us to develop a single-electron detector which outperforms many commercially available ones in the 20-30 keV range, being at the same time more flexible and cheaper.

Fig. 1


6 µm
1 µm
← Electron plane wave
← Wavefront shaping with light (phase shift proportional to laser intensity; TEM01 mode, 1035nm)
← free propagation (55cm)
← interference
← detection!

IM5.04
Electron beam shaping using a tunable current-driven MEMS phase plate

P. Habibzadeh Kavkani[1], P. Rosi[2], V. Grillo[2], M. Beleggia[1]

[1]University of Modena and Reggio Emilia, Physics, Modena, Italy
[2]CNR Nano S3, Modena, Italy

Electron beam shaping is increasingly critical in advanced electron microscopy, supporting novel imaging, spectroscopy, and material characterization. Central to these developments are phase plates, electron-optical elements capable of precisely modulating both the phase and amplitude of the electron wavefunction [1]. By forming specific beam profiles, such as vortex beams, these devices boost nanoscale sensitivity to magnetic and structural properties and facilitate orbital angular momentum (OAM) measurements via dual-phase plate systems [2,3]. Such functionalities arise from interactions with carefully tailored electric or magnetic potentials, demonstrate that careful control of electron phase shifts can enhance resolution and enable advanced imaging techniques.

While electrostatic phase plates offer real-time tuning via voltage control, they remain limited by electrode configurations and biasing channels, complicating the generation of finely tuned or gradient-like fields. To address these challenges, we present an Current-Driven Phase Plate leveraging multi-material Micro-Electro-Mechanical Systems (MEMS) technology to establish a continuous, tunable potential gradient without relying on numerous discrete electrodes. Rooted in Maxwell"s equations, this approach supports advanced beam shaping scenarios—such as vortex beam generation and aberration correction—and provides real-time tunability for high-precision electron beam control.

We employed COMSOL Multiphysics (Electrocurrent module) to simulate and design the chip. Post-processing with Python scripts, including a multislice algorithm, determined the total phase shifts. Gradient-based optimization refined applied potentials and electrode geometries, ensuring alignment with analytically derived phase requirements for threefold astigmatism correction and vortex beam generation. The devices were then fabricated on silicon-on-insulator (SOI) wafers, fully compatible with electrically biased TEM holders. Simulation results confirm that the Current-Driven phase plate creates a continuous potential gradient while reducing the required number of electrodes, matching theoretical phase profiles for targeted beam shaping (Fig1 & 2).

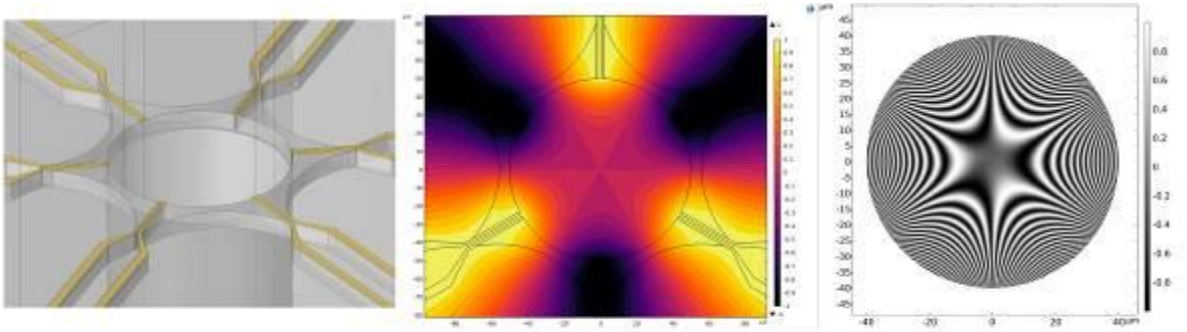
These findings highlight the significant promise of MEMS-based Current-Driven phase plates in overcoming electrostatic limitations by enabling tunable, continuous potential gradients. Ongoing experimental validations demonstrate robust performance in astigmatism correction, vortex beam generation, and advanced imaging. This versatile platform thus extends electron microscopy"s capabilities, opening new avenues in nanotechnology, materials science, and beyond.

[1] M. Malac et al., "Phase plates in the transmission electron microscope: operating principles and applications," J. Microsc., vol. 70, no. 1, pp. 75–112, 2021. doi:10.1093/jmicro/dfaa070.

[2] A. H. Tavabi et al., "Generation of electron vortex beams with over 1000 orbital angular momentum quanta using a tunable electrostatic spiral phase plate," Appl. Phys. Lett., vol. 121, no. 7, p. 073506, 2022. doi:10.1063/5.0093411.

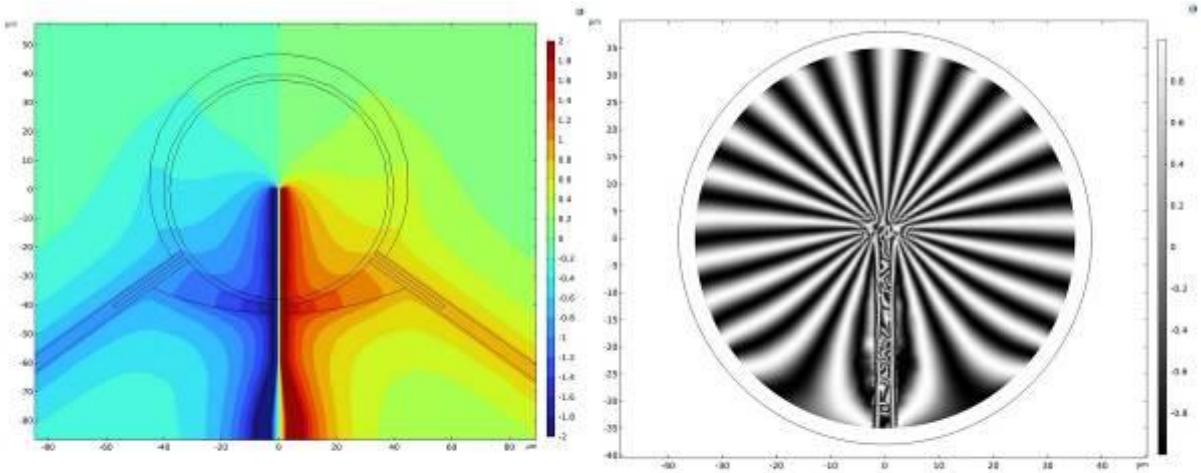
[3] G. Pozzi et al., "Design of electrostatic phase elements for sorting the orbital angular momentum of electrons," Ultramicroscopy, vol. 208, p. 112861, 2020. doi:10.1016/j.ultramic.2019.112861.

Fig. 1



Tunable Current-Driven Phase Plate for Three-Fold Astigmatism Correction: Gradient-Based Shape-Optimized Device (Left), Electric Potential Distribution (Middle), and Corresponding Phase Profile (Right).

Fig. 2



Tunable 4-Biased Current-Driven Phase Plate for the Generation of Electron Vortex Beams: Electric Potential Distribution (Left) and Corresponding Phase Profile (Right).

IM5.05(inv)
In situ biasing electron holography and dynamic automation – From dielectric and ferroelectric capacitors to charge dynamic studies

L. Zhang[1], K. Gruel[1], C. Dubourdieu[2,3], M. Hÿtch[1], C. Gatel[1,4]

[1]CNRS, CEMES, Toulouse, France
[2]Helmholtz-Zentrum Berlin, Materialien und Energie, Berlin, Germany
[3]Freie Universität Berlin, Physical and Theoretical Chemistry, Berlin, Germany
[4]University of Toulouse, CEMES, Toulouse, France

Electron holography is a powerful TEM technique for measuring local fields in materials and devices, from electric[1] and magnetic[2] to crystalline strain[3]. Most studies involving *in situ* biasing electron holography concern pn junction-type systems[4]. Here we have chosen to focus on purely capacitive systems based on dielectric and ferroelectric materials. These materials spur much fundamental and applied research over the years: the ability to measure polarisation locally and charge trapping in response to an applied electric field is essential to furthering understanding and to develop a new generation of microelectronic devices. In this presentation, we will show how the internal electric fields can be quantitatively mapped at the nanoscale within different dielectric and ferroelectric nanodevices using *in situ* electrical biasing and high-precision off-axis electron holography.For this purpose, we have implemented the dynamic automation on the I2TEM microscope (Hitachi HF-3300) equipped with a direct electron detection K3 camera. It is now possible to measure phase variations of a few mrad with a spatial resolution of 1 nm (*for an electrostatic potential, this corresponds to variations of a few mV*). Carrying out *in situ* experiments with electrical stimuli[5–7] also required the use of a dedicated instrumental chain including various protection systems against electrostatic discharges. For example, the capacity of a nanocapacitor with these dimensions does not exceed 1 fF (10-15 F).

We studied different capacitive systems, from multilayered HfO2- and Al2O3-based nanocapacitors[8] to a ferroelectric Hf0.5Zr0.5O2 (HZO) tunnel junction. Thanks to the high sensitivity to the phase shift of our holographic setup, the results highlight the presence of trapped charges at the different dielectric/dielectric and ferroelectric/dielectric interfaces with a strong effect on the distribution of the internal electric field. Particularly, we succeeded to map the polarisation switching of the HZO film (Figure 1) as the voltage gradually increases to the coercive voltage, observing that switching occurs via the nucleation and lateral growth of domains. This work also puts an end to the failed attempts made over many years to measure the local electric fields, and hence the charging, in ferroelectric materials by electron holography.

The next step is now to move from static experiments to time-resolved studies. We will show what strategies can be implemented in the instrumental chain for shaping the beam and the electrical excitations in order to study the charge dynamics in these nanocapacitors, and more generally the various electrical and magnetic properties.

Figure 1. High-resolution and phase image obtained on a HZO tunnel junction. The phase profile shows the internal electric fields.

[1] W. D. Rau *et al.*, *Phys. Rev. Lett.* **1999**, *82*, 2614.

[2] R. E. Dunin-Borkowski *et al.*, in *Springer Handbook of Microscopy* (Eds.: P. W. Hawkes, J. C. H. Spence), Springer International Publishing, Cham, **2019**, pp. 767–818.

[3] M. Hÿtch *et al.*, *Nature* **2008**, *453*, 1086.

[4] A. C. Twitchett *et al.*, *Phys. Rev. Lett.* **2002**, *88*, 238302.

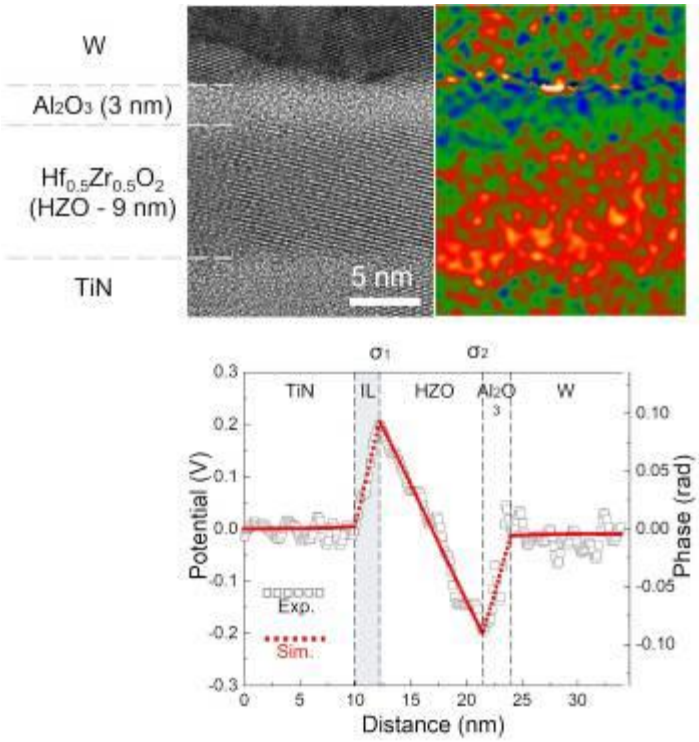
[5] C. Gatel *et al.*, *Phys. Rev. Lett.* **2022**, *129*, 137701.

[6] M. Brodovoi *et al.*, *Appl. Phys. Lett.* **2022**, *120*, 233501.

[7] L. Zhang *et al.*, *Nano Lett.* **2024**, *24*, 5913.

[8] L. Zhang *et al.*, *Advanced Materials* **2025**, *37*, 2413691.

Fig. 1



IM5.06
Nanoscale mapping of chiral magnetic textures in artificial double-helix nanowires

D. Wolf[1], N. Leo[2], O. Zaiets[1,3], A. Fernandez Pacheco[4], A. Lubk[1,3]

[1]IFW Dresden, TU Dresden, Dresden, Germany
[2]Loughborough University, Loughborough, United Kingdom
[3]Technical University Dresden, Dresden, Germany
[4]Technical University of Vienna, Vienna, Austria

Chiral magnetism requires either a restricted group of natural materials with proper crystal symmetry or synthetic systems that exploit interfacial effects. The latter can be achieved by modern nano-fabrication, such as focused electron beam induced deposition (FEBID) that enables imprinting of complex chiral spin states via three-dimensional geometric effects at the nanoscale. In particular, by balancing dipolar and exchange interactions in an artificial ferromagnetic double-helix nanostructure, magnetic domains and domain walls with a well-defined spin chirality, determined solely by the chiral geometry can be created [1]. Here, we demonstrate the ability to create and map 3D spin textures, e.g., Bloch points and topological defects by locally interfacing geometries of opposite chirality.

We used FEBID to fabricate free-standing magnetic Co nanowires (NWs) with ca. 100 nm in diameter at different geometries, i.e., double-helix structure including kinked (angle 5°-15°) tendril perversions at which the direction changes from left-handed to right-handed chirality. To investigate the remanent state of the NWs, we performed electron holography (EH) in combination with electron tomography (ET) [2]. EH allows to reconstruct the electro-magnetic Aharonov-Bohm phase shift of the electron wave after transmitting the NW sample due to its electrostatic potential and magnetic induction $\boldsymbol{B}$. By recording and reconstructing holographic tilt series, we retrieve both the mean inner potential (MIP) and the axial component of the $\boldsymbol{B}$-field of the NW in three dimensions. Finally, we visualize the magnetic configuration of the NWs and compare it with results computed by micromagnetic simulations.

The simultaneous 3D reconstruction of MIP distribution (Fig. 1a) and magnetic induction (Fig. 1b) allows to correlate the local material structure of the NW with the 3D magnetic configuration. The two NW parts with left-hand (LH) and right-hand (RH) chirality as well as the head-to-head domain configuration are obtained. The micromagnetic model with similar geometry as the experimental NW exhibits a very similar magnetic state as in the experiment, and suggests the presence of a Bloch point in the vicinity of the chiral switch (Fig. 1c). Although we reconstructed only one (axial) component of the vector-field $\boldsymbol{B}$, we could unambiguously deduce the 3D position of the BP in the experimental tomogram (Fig. 1b) by comparing projection data of simulation and experiment at different viewing directions.

This study shows how EH and ET applied on magnetic NWs with complex geometry together with the capabilities to apply *in-situ* magnetic fields in the TEM can be used to create, visualize and analyze magnetic spin configurations in 3D. In particular, we could reveal the existence of BP DWs in helical Co NWs with a resolution of a few nanometer.

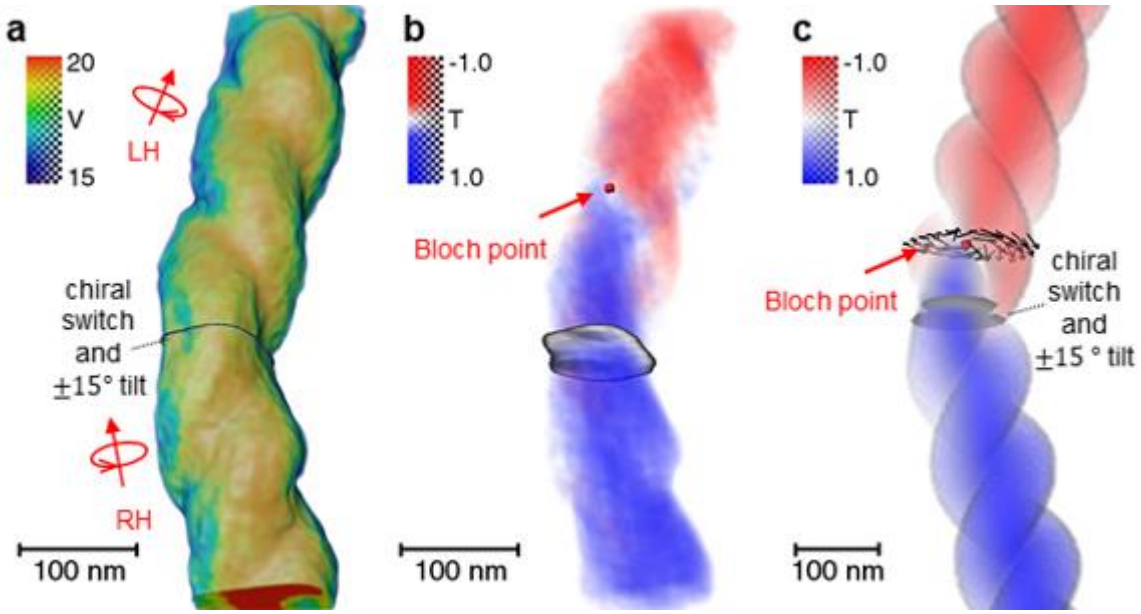
Figure 1. 3D magnetic field and electrostatic potential mapping of a Co nanowire (NW). (a) Volume rendering of the mean inner potential shows the helical morphology with opposite chirality top and bottom. (b) Reconstructed axial component of the magnetic induction **B** color-coded in blue-white-red reveals a head-to-head domain wall (DW) 140 nm away from the chiral switch. (c) Magnetization of a NW model displayed the same way as (b) unveils a head-to-head DW with a Bloch point (BP) 75 nm away from the chiral switch.

References

[1] D. Sanz-Hernández, *et al.* ACS Nano **14** (2020) 8084

[2] D. Wolf, *et al.* Commun. Phys. **2** (2019) 87

Fig. 1



IM5.07
Catastrophe charged particles optics

T. Fraysse[1], C. Robin[1], L. Hugo[1], H. Florent[1]

[1]CEMES-CNRS, Toulouse, France

The majority of physicists who uses charged particles optical devices, such as transmission electron microscopes (TEM), has seen caustics on their screen. These figures' geometric shapes are characterized by high electron density patterns. They are caused by the optical system's aberrations, and their geometry is determined by the symmetry of the electromagnetic lenses. The goal of our study is to better understand how these geometrical structures arise. While this might be accomplished using normal ray tracing methods, we choose to apply René Thom's catastrophe theory [1,2], which provides a relevant formalism to describe caustics shapes.

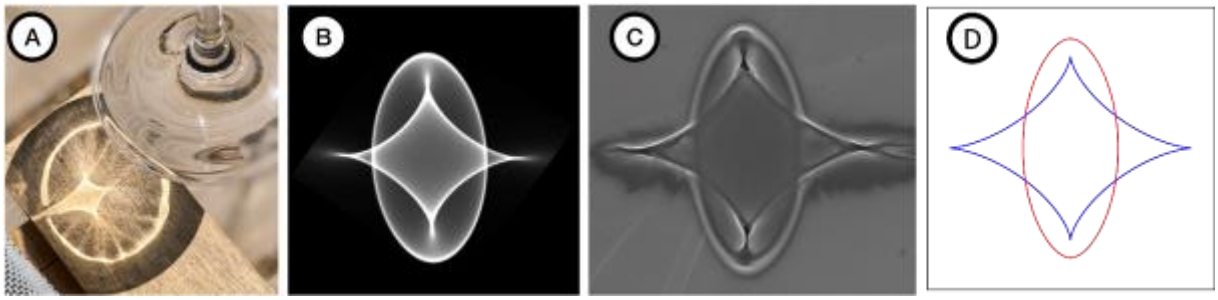
There is a large body of literature on the study of caustics for light optics [3,4,5]. These methods based on catastrophe theory are known as catastrophe optics. Catastrophe theory is a mathematical formalism aiming at describing singularities of characteristic functions that cause sudden changes in the behavior of a physical system, known as catastrophes. When we apply this approach to optics, the optical path is the relevant characteristic function, while the caustics represent the catastrophes. What makes this formalism efficient is that we do not need to know the entire system to anticipate the shape of the caustics, but only the symmetry of this function. The other way around, simply looking at the caustics should enable us to predict which aberrations are present in the optical system. This might lead to promising applications in aberration measurement for charged particle optical systems such as ion beam instruments.

In this talk we will first discuss catastrophe theory and its application to light optics. We will then demonstrate how this framework may be applied to charged particle optics. Finally, we will provide some examples of how we may extract information about aberrations from caustics images.

[1] R. Thom, Stabilité structurelle et morphogénèse : essai d"une théorie générale des modèles. Benjamin, 1972.
[2] V. I. Arnold, Catastrophe theory, 3rd ed. Springer.
[3] E. C. Zeeman, "Catastrophe theory," Scientific American, vol. 234, no. 4, pp. 65–83, 1976.
[4] M. Berry and C. Upstill, "IV catastrophe optics: Morphologies of caustics and their diffraction patterns," in Progress in Optics. Elsevier, vol. 18, pp. 257–346.
[5] J. F. Nye, "Symmetrical optical caustics," vol. 20, no. 7, p. 075612.

Figure 1. *Images of caustics (A) with a beam of light, (B) with an electron beam (in a TEM), (C) with an ion beam and, (D) simulated with catastrophe theory.*

Fig. 1



IM5.P01
Aberration limits for STEM – Single coefficient limits revisited

D. Azarkh[1], P. Hartel[1], M. Linck[1], H. Müller[1], S. Uhlemann[1]

[1]CEOS GmbH, Heidelberg, Germany

A well-corrected optical state is essential to obtain a sharp electron beam probe for STEM. This is crucial for advanced high-resolution STEM applications in materials science and nanotechnology. The presence of various aberrations directly impacts the image resolution hence the analytical precision. Therefore, it is important for the operator to precisely know how much aberrations are acceptable during the daily corrector tuning procedure and the subsequent data acquisition in the experiment.

Traditionally, limits for single aberration coefficients are derived from the pi/4 criterion [1], which is the individual aberration magnitude to reach a phase shift of pi/4 at the edge of the optical aperture in the wave aberration function. The pi/4 criterion is straightforward to calculate, offering simplicity in its application. However it is limited by its generalization as it imposes the same threshold on all aberration orders and multiplicities despite their actual impact on the probe shape.

Alternative criteria are e.g. intensity-based criteria (D-criteria) that quantify the size of the region in which a specified percentage of the total beam current is contained [2]. As a prominent example, the D59 contains 59% of the total beam intensity which equals to the radius of Airy disc's first zero. D-criteria provide a practical and intuitive way to assess the impact of aberrations on probe quality and STEM image resolution. Through the necessary probe simulations, it becomes especially sensitive to higher-order aberrations and offers a flexible, quantifiable metric for comparing different system configurations.

This study explores how single aberrations influence probe shape criteria by a simulation-based comparison of two commonly used criteria: the phase-based (pi/4) criterion and a set of D-criteria (D59, D50, D30). The dependence of each criterion on aberration type ranging from defous to complex higher-order aberrations, such as six-fold astigmatism – is thoroughly analyzed and compared to the ideal probe shape. The corresponding probe simulations account for beam energy, geometric source size and chromatic aberration. Special emphasis is placed on actual experimental conditions, i.e. using the optimum aperture semi-angle for the given chromatic blur [3].

It turns out that D-criteria are generally less strict by a factor of the order of 2...3 compared to the simple pi/4 criterion. This is an important aspect for the daily tuning of the aberration corrector of the electron microscope in order to maximize instrument time for experiments AND instrument performance i.e. STEM resolution. The pi/4 criterion remains essential for phase-sensitive applications but can be considered inappropriate (too strict) for general STEM applications.

[1] Uhlemann et al.: Residual wave aberrations in the first spherical aberration corrected transmission electron microscope, Ultramicroscopy 72 (1998), 109-119.

[2] M. Haider et al.: Upper limits for the residual aberrations of a high-resolution aberration-corrected STEM. Ultramicroscopy, 81 (2000), 163–175.

[3] R. Sagawa et al.: Exploiting the full potential of the advance two-hexapole corrector for STEM exemplified at 60kV, Ultramicroscopy, 233 (2022), 113440.

IM5.P02
Advanced 3-dimensional electrostatic potential reconstruction with electron holographic tomography

K. L. Jakob[1], L. Niermann[1], T. Niermann[1], F. Otto[1], H. Esmaielpour[2], G. Koblmüller[2], M. Lehmann[1]

[1]Technische Universität Berlin, Institute of Optics and Atomic Physics, Berlin, Germany
[2]Technical University of Munich, Walter Schottky Institute, Garching, Germany

Understanding the 3-dimensional distribution of electrostatic potentials at the nanoscale is crucial for advancing semiconductor nanostructures, e.g. InGaAs nanowires used in optoelectronic applications [1]. Electron tomography is capable of resolving the 3-dimensional structure, while off-axis electron holography directly measures electrostatic potentials. By combining these complementary techniques, we can gain deeper insights into the 3-dimensional potential landscape within such nanowires [2].

We aim to reconstruct the 3-dimensional electrostatic potential distribution in InGaAs nanowires containing an axial pn-junction using electron holographic tomography (EHT). A key focus is to evaluate the 3-dimensional uniformity of the electrostatic potential along the nanowire and to investigate the homogeneity of the electrostatic potential from the inner core to the outer surface of the nanowires.

The investigated InGaAs nanowires are grown by molecular-beam epitaxy (MBE) [3]. Off-axis electron holography is conducted in a FEI Titan 80-300 transmission electron microscope equipped with a electrostatic biprism, allowing phase shift measurements sensitive to local electrostatic potentials. Electron tomography is performed by acquiring a series of holograms over a wide angular range of specimen tilting for tomographic reconstruction. All holograms are first reconstructed individually using a Fast Fourier Transform and phase unwrapping. Additionally, the phases are aligned via cross-correlation and the 3-dimensional distribution is reconstructed with weighted back-projection.

This study demonstrates the feasibility of combining electron holography and tomography for quantitative 3-dimensional electrostatic potential mapping of pn-junctions in InGaAs nanowires. In this way we have investigated variations of the potential inside the nanowire and analyzed surface-related phenomena. The results emphasize the importance of integrating complementary techniques to assess the 3-dimensional electrostatic potential. These findings contribute to the fundamental understanding of semiconductor nanostructures, with implications for the design and optimization of next-generation optoelectronic devices [1] and energy devices, such as solar cells [4,5].

Keywords:

InGaAs, Tomography, Holography, Nanowires, Electrostatic Potential

Reference:

[1] Chen, R., Tran, TT., Ng, K. *et al.* "Nanolasers grown on silicon" *Nat. Photonics* **5**, 170-175 (2011).

[2] Wolf, D., Lubk, A., Röder, F., Lichte, H., "Electron holographic tomography" *Curr. Opin. Solid State Mater. Sci.*, **17** (3), 126-134 (2013)

[3] Koblmüller, G. and Abstreiter, G., "Growth and properties of InGaAs nanowires on silicon." *Phys. Status Solidi RRL*, **8** (1), 11-30 (2014)

[4] Otnes, G., Borgström, M. T., "Towards high efficiency nanowire solar cells" *Nano Today,* **12**, 31-45 (2017).

[5] Li, Z., Tan, H. H., Jagadish, C., Fu, L., "III–V Semiconductor Single Nanowire Solar Cells: A Review" *Adv. Mater. Technol.,* **3** (9), 31-45 (2018).

IM5.P03
Development of an RF aperture holder for time-resolved electron holography

T. Wagner[1], S. Siewert[2], H. Çelik[2], S. Gaebel[3], C. T. Koch[1], M. Lehmann[2]

[1]Humboldt University of Berlin, Institute of Physics, Berlin, Germany
[2]Technische Universität Berlin, Institute of Optics and Atomic Physics, Berlin, Germany
[3]Max-Born-Institut, B2: Imaging and Coherent X-rays, Berlin, Germany

Introduction

Time-resolved investigations in transmission electron microscopy (TEM) have gained increasing importance in recent years, as they deepen TEM's insight into the nanocosm by adding a new dimension: time. When being sensitive to the phase of the transmitted electrons, this allows for a more profound understanding of dynamic physical processes inside and at the surface of materials, such as charge carrier dynamics, correlated stray fields, or other transient behaviors. Common approaches that enable high temporal resolution in TEM often rely on pulsed illumination driven by photoemission or ultrafast detectors. However, these techniques involve significant costs and extensive instrumental modifications with corresponding downtimes of the instrument, posing a high barrier for widespread adoption.

Objectives

The recently developed interference gating (iGate) method addresses these limitations by enabling time-resolved electron holography (EH) of periodic processes [1]. This provides access to the phase progression of a reconstructed electron wave and consequently the projected potential of the sample with minimal technical and instrumental effort. The basic idea of iGate involves the synchronized destruction of the interference pattern, allowing it to form only during short intervals, referred to as the "gate". By synchronizing this gating mechanism with a periodic process in the sample, the interval for the formation of the interference pattern can be shifted in time (similar to lock-in detection or pump-probe techniques), enabling sampling across the entire period. However, as the destruction of the interference pattern relies on introducing synchronized dynamic phase shifts, a specialized electron optical element is required.

Materials & Methods / Results / Conclusion

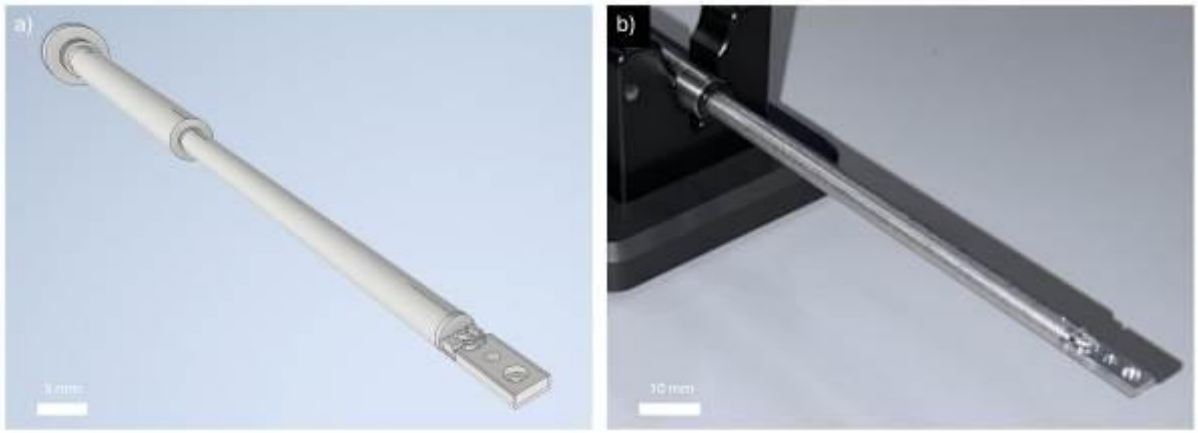
Here, we present the development, implementation, and testing of a novel RF aperture holder integrating an electron biprism and an RF phase-shifting element into a single device (Fig.1). This innovation reduces the barrier of entry for dynamic TEM investigations by transforming iGate into a plug-and-play solution, retrofittable to most standard instruments. Additionally, only a signal generator (i.e. a common arbitrary wave generator) with two synchronized channels and an electrical biasing TEM holder are needed in order to generate and apply the respective control signals to the RF aperture holder and the sample. This design enables dynamic imaging with nm spatial, ns temporal, and mrad phase resolution, paving the way for more accessible studies of fast processes in nanostructured electronic devices and materials [2].

[1] T. Niermann, M. Lehmann, and T. Wagner, Ultramicroscopy **182**, 54 (2017).

[2] T. Wagner, H. Çelik et al., Electronics **14**(1), 199 (2025).

Fig. 1: Development process of the RF aperture holder. a) 3D CAD model of the RF aperture holder showing the tip region, containing the special electron optics. b) Image of the manufactured RF aperture holder right before insertion into the SA aperture plane of the FEI 80-300 Titan Berlin Holography Special TEM.

Fig. 1



IM5.P04
Numerical study on beam splitting and local vortex centres of electron vortex beams inside crystalline material

C. Bick[1], D. Hüser[1]

[1]Physikalisch-Technische Bundesanstalt (PTB), Braunschweig, Germany

Introduction
Electron vortex beams (EVB) have been of interest for many applications in the scanning transmission electron microscope, such as electron magnetic circular dichroism (EMCD), nanoparticle manipulation as well as for their channelling properties.

Objectives
We want to improve the understanding of EVB behaviour inside crystals with regard to beam splitting and the formation of local vortex centres.

Materials & methods

Our study utilises the commonly used multislice algorithm to propagate the beam inside the crystal. We used vector analysis to follow the behaviour of local vortex centres inside crystalline material along with a software package for vortex tracking.

Results

We present an in-depth study on the propagation of electron vortex beams inside various crystalline materials of interest. We track the full dynamics of the probability density current to automatically identify local vortex centres and channelling.

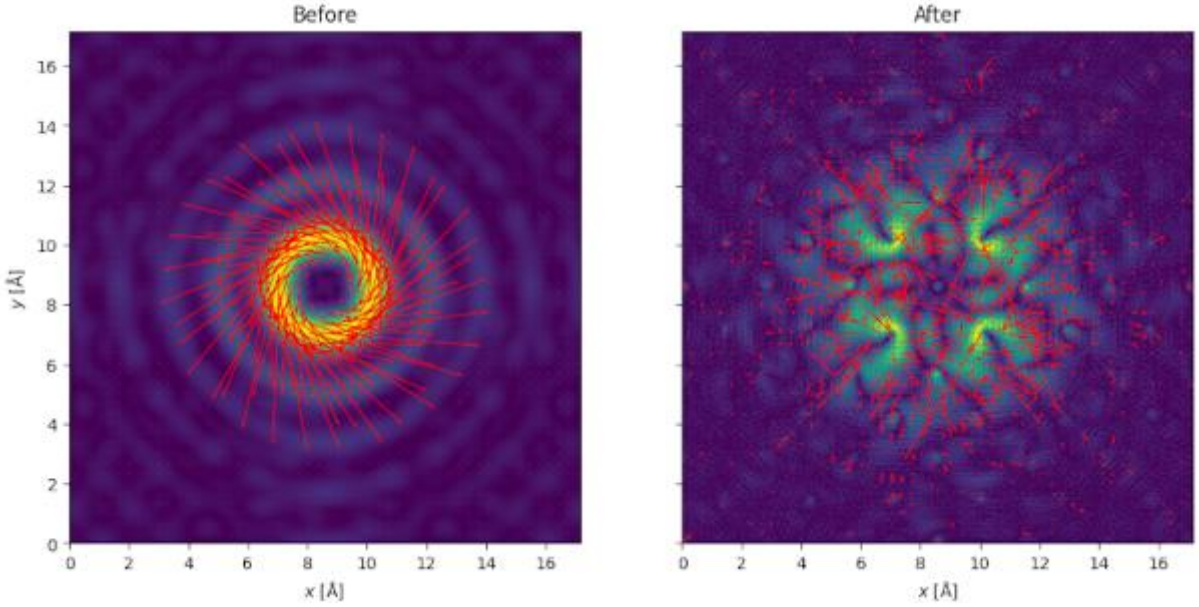
Conclusion

Our method is capable to predict the behaviour of elastically scattered electron vortex beams inside crystals and can help finding optimised beam parameters for experimental setups via simulations.

Fig 1:

he intensity of an electron vortex beam with m = 4, 200 kV acceleration voltage and a convergence semi-angle of 16 mrad, overlaid with its probability current density before and after being propagated through 200 Å of bcc iron.

Fig. 1



IM5.P05
Design and characterization of magnetic planar micro-optics for ultrafast *in situ* measurements in the TEM

M. Herzog[1], J. Schultz[1], A. Lubk[1,2]

[1]Leibniz Institute for Solid State and Materials Research Dresden, Dresden, Germany
[2]Institute of Solid State and Materials Physics of TU Dresden, Dresden, Germany

Introduction

The goal of miniaturizing magnetic electron optics is pursued for more than a decade now [1, 2], because smaller electron optics not only require less material and are easier to build, but also result in other favorable scaling effects. Firstly, the small pole distances allow for magnetic flux densities comparable to those of conventional electron optics with approx. two orders of magnitude smaller current and hence lower overall complexity regarding vacuum and cooling. Secondly, the small size translates to a low inductance, which in turn enables switching of the optics on sub-nanosecond (sub-ns) time scales/with radio frequencies (RF) up to several GHz.

Objectives

The aim of this work is to utilize those favorable scaling effects by building magnetic planar micro-optics that are capable of manipulating a fast electron beam like in TEMs on sub-ns timescales/with GHz frequencies. These could enable stroboscopic, sub-ns time resolved TEM measurements, e.g., to resolve magnetodynamics at high spatial resolution.

Materials & Methods

The micro-optics are produced using lithography/sputtering techniques on Si wafers. The first layer consists of conducting copper paths with a thickness of several hundred nm, while the second layer consists of soft magnetic permalloy pole pieces with a thickness of 800 nm. The current applied to the copper paths produces a magnetic field that is shaped and magnified by the pole pieces to manipulate the electron beam. Using this approach, many different geometries, e.g., dipole deflectors, quadrupoles, and higher order multipoles can be produced in an easily scalable way.

In order to supply the optics with RF current, a custom TEM holder was engineered. The holder carries a small circuit board on which the optics are mounted and that allows for impedance matching which is crucial for proper RF signal transmission. To characterize the spatial distribution of the electromagnetic fields, differential phase contrast (DPC) measurements were conducted. The RF capabilities of the dipole optics were evaluated in Lorentz diffraction mode by measuring the amplitude of the oscillation of the diffraction disc.

Results

The optics show deflections up to the tens of µrad at 300 kV acceleration voltage and no major drop off in deflection up to an excitation frequency of 2 GHz. This optical power corresponds to focusing quadrupole optics with a focal length of 30 cm at an acceleration voltage of 300 kV.

Conclusion

Magnetic planar micro-optics can be produced, which show enough optical power in the GHz regime to bring novel applications like stroboscopic, time resolved TEM measurements on sub nanosecond time scales, e.g., of transient states of magnetic domain walls, within reach. Furthermore, the miniaturization of more complex setups like the condenser system of a SEM might become possible in the future.

Reference:

[1] Rong Rong, Ho Seob Kim, et al. "Novel Magnetic Microstigmator for Electron Beam Astigmatism Correction in the Electron Beam Microcolumn System". In: Journal of Vacuum Science & Technology B 25.6 (Dec. 2007)

[2] Huber, F. Kern, et al. "Tailoring Electron Beams with High-Frequency Self-Assembled Magnetic Charged Particle Micro Optics". In: Nature Communications 13.1 (June 2022)

IM 6: Big data and AI techniques

IM6.01(inv)
Managing research data with NOMAD OASIS – Examples for materials characterization and microstructure evolution modeling

M. Kühbach[1,2], S. Shabih[1,2], L. Pielsticker[1,3], R. Mozumder[1], S. Brockhauser[1], M. Scheidgen[1], L. Himanen[1], A. Fekete[1], J. F. Rudzinski[1], J. A. Márquez Prieto[1], H. Weber[1,4], C. T. Koch[1,2], C. Draxl[1,2]

[1]Humboldt University of Berlin, Institute of Physics & CSMB, Berlin, Germany
[2]Humboldt University of Berlin, Department of Physics, Berlin, Germany
[3]Max-Planck-Institute for Chemical Energy Conversion, Mülheim a.d. Ruhr, Germany
[4]FAU Erlangen-Nürnberg, Institute of Condensed Matter Physics, Erlangen, Germany

Introduction
Interoperable knowledge representation for experiments and computer simulations [1-4] is the key motivation behind the implementation of software tools for FAIR research data management. This includes the condensed matter physics and materials engineering research communities. Writing documentation that is more complete and agreeing with colleagues on defining and using standardized knowledge representations are two effective strategies that improve the interoperability of materials research. We have analyzed the status quo and landscape of public research data management systems with a focus on electron microscopy, specifically for functionalities offered and dataset shared [5, 6]. These examples substantiate that working towards further standardization is useful.

Objectives
We will report an update on our data modeling activities towards extending NeXus [7] for electron microscopy with definitions covering domain- and several examples of method-specific data and metadata. Furthermore, we will provide an update on our software development activities towards parsing and normalizing electron microscopy using NeXus and how sharing of this content can be achieved exemplarily using the NOMAD research data management system [8-10] that is being developed by the FAIRmat consortium within the German National Research Data Infrastructure.

Materials & methods
The extension for NeXus towards electron microscopy [12, 13] covers classes to compose a technical design perspective of electron microscopes, i.e. their function to deliver controlled electron and optional ion beams, the metadata about their components, software and utility hardware used, and classes for describing conventions of frames of reference or computational details of specific processing steps. EBSD, EDS, and generic imaging are provided as examples. Furthermore, classes for documenting reconstructions of microstructures were developed. The software development covers pynxtools-em [14] and its integration as a default plugin into NOMAD. Parsing of data is achieved with pynxtools with examples provided from various technology partners of the electron microscopy community to NeXus. NOMAD as an open-source framework offers electronic lab notebook, file format parsing, cloud computing, and information retrieval services that can support individuals and research groups with documenting their research more explicitly.

Results
The functioning of these tools as a product was assessed by processing a corpus of several thousand electron microscopy datasets with a focus on materials science use cases mapping to NeXus and subsequently to NOMAD. Specific functionalities provided are support for beyond three-dimensional data visualization for contour plotting, method-specific visualizations that use RGB plots for quantification and segmentation. Examples include inverse pole figure for orientation mapping and orientation distribution functions for texture analysis serving as examples for diffraction and reporting

of directionally dependent properties at the single material point level, histograms of cross-sectional area for crystals, and documentation of the geometric primitives discretizing crystals and their delineating interface network.

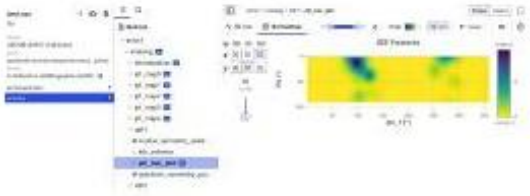
Fig. 1. Example how a dataset from a post-processed SEM/EBSD measurement with computed orientation distribution functions gets displayed in NOMAD. Interactive visualization and programmatic querying via NOMAD's RESTful API is offered. Content is mapped into searchable quantities via an automated mapping from NeXus to NOMAD's internal Metainfo data model [11].

Conclusion

Developed software tools in combination with the extension of NeXus as one standardized data model for electron microscopy that covers scanning, focused-ion beam, transmission, and scanning transmission use cases, provides not only standardized data for fostering further research within artificial intelligence and machine learning methods but also a platform for stimulating further exchange across electron microscopists on how to collaborate within their field and beyond. These solutions can be used out-of-the-box in NOMAD, as libraries in other software tools, or customized.

1 M. D. Wilkinson et al., (2016), https://doi.org/10.1038/s41524-017-0048-5
2 A. Jacobsen et al., (2020), https://doi.org/10.1162/dint_r_00024
3 M. Barker et al., (2022), https://doi.org/10.1038/s41597-022-01710-x
4 S. R. Wilkinson et al., (2025), https://doi.org/10.1038/s41597-025-04451-9
5 https://www.re3data.org
6 https://explore.openaire.eu
7 M. Könnecke et al., (2015), https://doi.org/10.1107/S1600576714027575
8 M. Scheidgen et al., (2023), https://doi.org/10.21105/joss.05388
9 https://gitlab.mpcdf.mpg.de/nomad-lab/nomad-FAIR
10 M. Scheffler et al., (2022), https://doi.org/10.1038/s41586-022-04501-x
11 L. Ghiringhelli et al., (2017), https://doi.org/10.1038/s41524-017-0048-5
12 https://github.com/nexusformat/definitions
13 https://github.com/nexusformat/definitions/pull/1423
14 https://github.com/FAIRmat-NFDI

Fig. 1



IM6.02(inv)
Feature enhancement during dictionary learning reconstructions of scanning transmission electron microscope images

R. Jinschek[1], J. Wells[2], A. W. Robinson[2], D. Nichols[2], M. Gianni[3], Y. C. Shen[1], N. D. Browning[2,4]

[1]University of Liverpool, Electrical Engineering and Electronics, Liverpool, United Kingdom
[2]SenseAI, Liverpool, United Kingdom
[3]University of Liverpool, Computer Science, Liverpool, United Kingdom
[4]University of Liverpool, Mechanical Engineering, Liverpool, United Kingdom

A main challenge in high-resolution STEM/TEM imaging is minimizing beam-induced damage, which can be mitigated through faster data acquisition methods to reduce the overall beam exposure time during acquisition. Sub-sampling is one of the solutions to this challenge, which allows scans that sample only a portion of the available pixels which is then paired with a Bayesian dictionary learning algorithm based on Beta Process Factor Analysis (BPFA) for a reconstruction of a full image [1]. This increases the speed of data acquisition while outputting less data, and the approach has been shown to work in live imaging mode for four-dimensional STEM [2], electron energy loss spectroscopy (EELS) [3], as well as high angular annular dark field (HAADF) and bright field (BF) STEM [4].

A limitation of sub-sampling and inpainting for high-resolution imaging is the presence of noise, which can limit the visibility of features and reduce analytical precision. Here we propose a novel method to improve the output of dictionary learning algorithms by enhancing features within the sub-sampled data prior to inpainting, as well as the re-ordering and combination of dictionary elements. These methods aid with the precision of the reconstruction by first re-ordering the dictionary elements and grouping them by the frequency of their signal (as seen in Fig. 1.), then partially selecting these groupings in order to accentuate certain features within a sample, such as different lattice orientations of atoms within a particle (as seen in the left image of Fig. 2.). This approach, which is similar in goal to the weighted back projection method for improved tomographic reconstructions, has yielded significant increases in reconstruction resolution (as seen in the Fourier transform of Fig. 2.), which suggests we are able to extract richer frequency content with these methods. It is also possible to enhance the features that are acquired sub-sampled prior to training the dictionary. The contrast of the input can be manipulated on a patch-by-patch basis, which makes it easier for the dictionary components to be learned and ultimately the reconstruction to have higher resolution. This improves the visibility of some features, such as the individual gold atoms that are observed on the carbon support in between the gold nanoparticles shown in Fig. 3.

In this presentation, we will show how these proposed methods aid with the precision of inpainted reconstructions for precise quantitative analysis of sub-sampled SEM/STEM data.

Fig. 1. Reconstructions of gold particles sampled at 25% and separated into different layers using dictionary re-ordering and grouping, with their respective FFT below.

Fig. 2. Recombination of reconstruction from selective layers from Fig.1. displaying defined lattice fringes of gold atoms.

Fig. 3. Figure A shows the 25% subsampled image with enhanced features and the resulting FFT to the right. Figure B shows the reconstruction, showing individual gold atoms between the larger nanoparticles, along with the resulting FFT to the right.

References:

1. A. W. Robinson, et al., *Journal of microscopy*290.1 (2023): pp. 53-66, doi: 10.1111/jmi.13177.

2. A. W. Robinson, et al. *Chinese Physics B*33.11 (2024): 116804. doi: 10.1088/1674-1056/ad8a4a.
3. A. W. Robinson, et al. *BIO Web of Conferences*. Vol. 129. EDP Sciences, 2024. doi: 10.1051/bioconf/202412906020.
4. D. Nicholls *et al*., *ICASSP (2022),* 2022, pp. 1586-1590, doi: 10.1109/ICASSP43922.2022.9746478.

Fig. 1

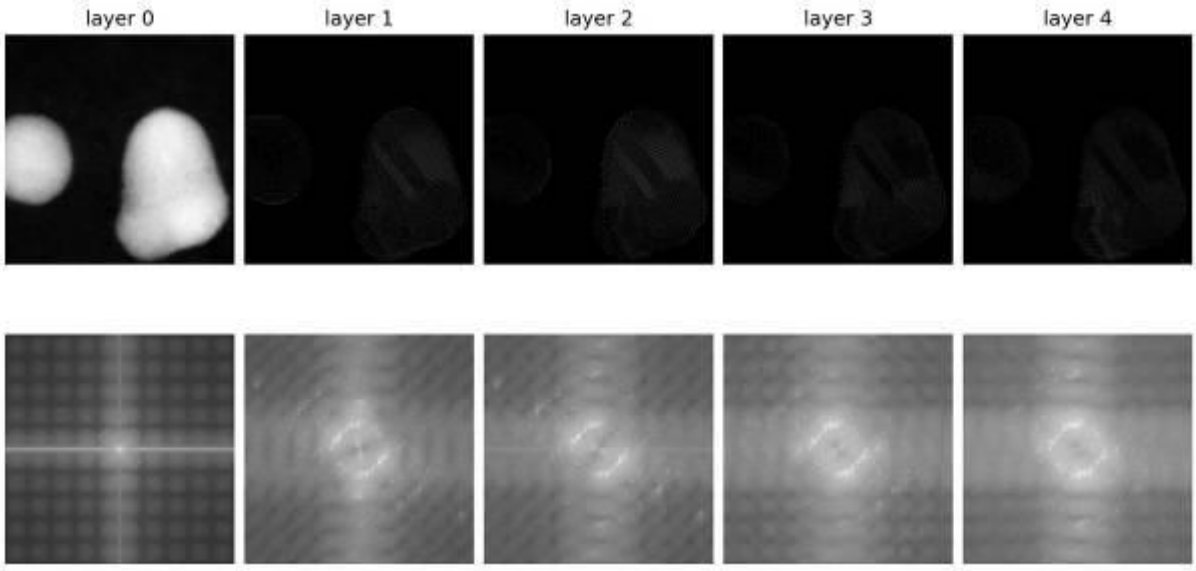


Fig. 2

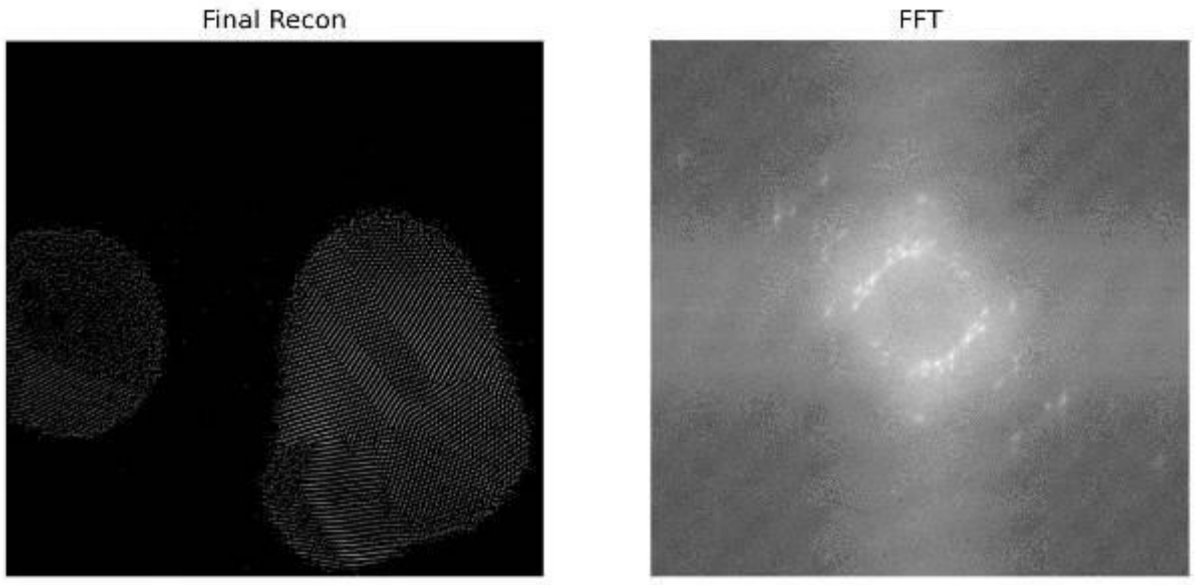
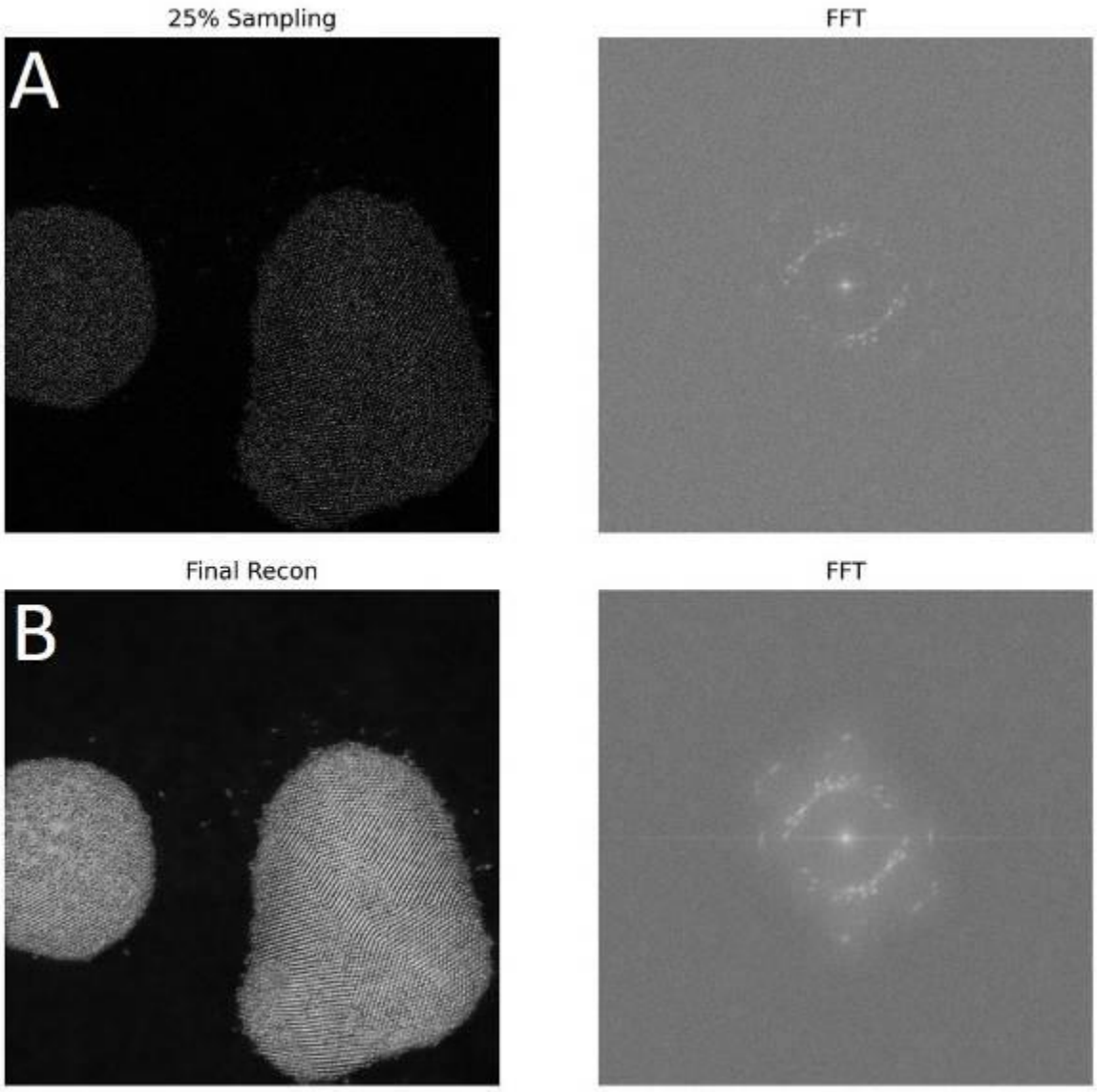


Fig. 3



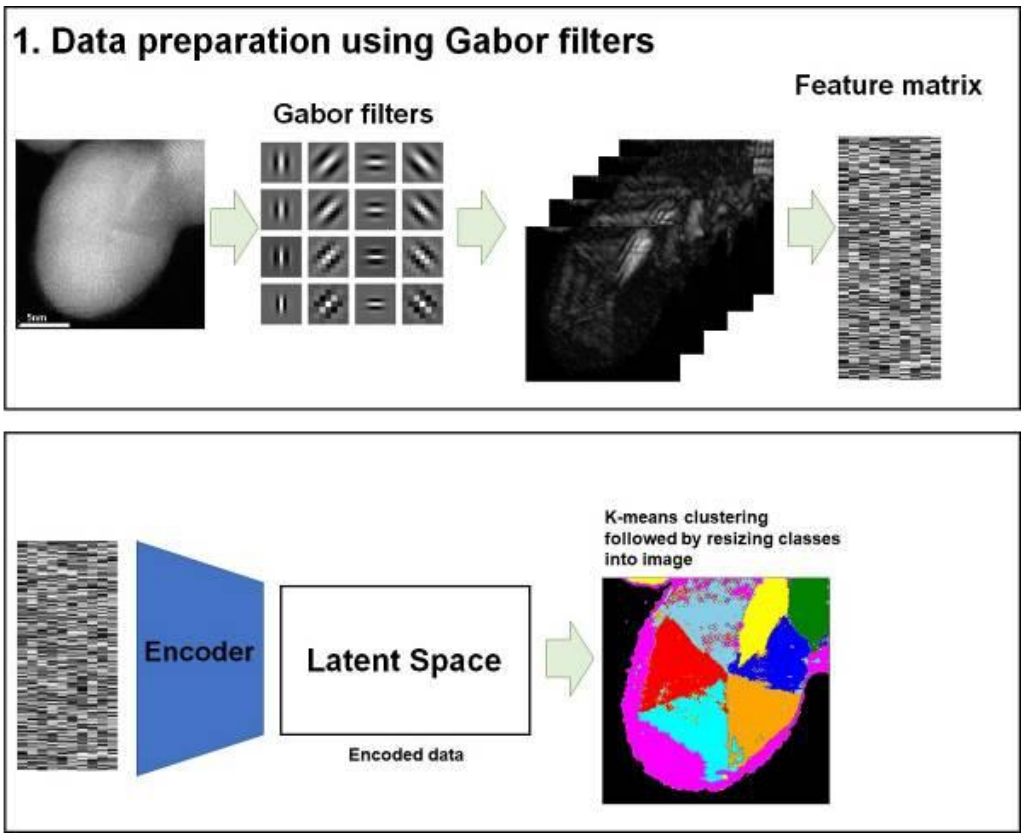
IM6.03
Leveraging unsupervised deep learning approach for segmentation of nanocrystals

W. Sohn[1], T. Kim[1], H. Baik[1]

[1]Korean Basic Science Institute, Seoul, South Korea

Nanocrystals play a crucial role in defining the structural, electronic, and optical properties of advanced materials. Their characterization via STEM or HRTEM images is essential for understanding and optimizing material performance. However, conventional segmentation methods often struggle with the complex and subtle patterns within these images, frequently relying on linear dimensionality reduction techniques (e.g., NMF) and human expertise. In this study, we present an unsupervised deep learning approach using a Variational Autoencoder (VAE) to map Gabor-filtered image features into a nonlinear latent space, followed by k-means clustering of the latent space, leading to segmentation of polycrystalline nanoparticles. As shown in Figure 1, a number of gabor filters with different angles and wavelengths are used and filtered images are reconstructed into a feature matrix. Next, VAE is applied to the feature matrix for dimension reduction and we carried out the k-means clustering for image segmentation. Our VAE-based framework provides improved robustness and finer segmentation granularity, overcoming the limitation of the NMF based dimension reduction. By optimizing pixel size of the STEM images, not only segmentation of grains but also finding additional features such as surface area and areas which are not research of interest is successful. Furthermore, segmentation results are similar even the dimensionality of the latent space is reduced, demonstrating that cluster structure of the feature matrix is distinct. This approach not only reduces subjective biases but also enhances scalability, providing a pathway towards more comprehensive and automated nanocrystal characterization.

Fig. 1



IM6.04
Catalyst nanoparticle size-prediction with generative AI and big data

H. Eliasson[1], R. Erni[1]

[1]EMPA - Swiss Federal Laboratories for Materials Science and Technology, Electron Microscopy Center, Dübendorf, Switzerland

Simulating multislice images is computationally heavy and limits the curation of large enough datasets to train accurate and robust machine learning networks for nanoparticle size estimation from HAADF-STEM images. The objective of this study is to teach a machine learning model to predict the multislice image of a given atomic model to drastically speed-up dataset generation after a small initial multislice set has been generated. Furthermore, we want to explore how beneficial a large dataset is for the nanoparticle size-estimation task.

We use a small initial dataset of 5000 multislice images with corresponding atomic models of Pt nanoparticles on CeO2. We voxelize the models into dense 128 x 128 x 256 representations and train a modified 3D U-Net to predict the multislice image from the model. This model performs well and is 100x faster than pyhsical multislice simulations, or 1000x faster if you ignore the time it takes to generate the atomic structure which has to be done for both approaches. We generate 100.000 synthetic multislice images and map all the simulated images to the "experimental domain" by a cycle-consistent generative adversarial network trained previously [1], ensuring generalization to experimental data. With this data we study different size-estimator architectures (U-Net, ResNet18, ResNet50) and see how well they perform as a function of training set size.

Our multislice surrogate model generates realistic multislice images that are nearly indistinguishable from the ground truth images, as seen in figure 1. We find that the subsequent size-estimator network only gets better with more synthetic data, and by using all the 100.000 synthetic multislice images, we drastically increase performance and the median absolute percentage error drops from 10.64% to 5.26%. We also find that it generalizes better to experimental data and achieves better predictions across all investigated particle sizes (figure 2)

We conclude that generating a large amount of high quality synthetic data is resource efficient compared to generating more real multislice data, and it is very beneficial for model accuracy and generalization [2].

Figure 1: Ground truth multislice images, 3D U-Net predictions, and absolute difference between the two.

Figure 2: (left) Size predictions for a couple of experimentally observed particles with example structures fitting the predictions. (right) The mean absolute percentage error of size predictions in different particle size ranges by our new model trained with synthetic data (red) compared to a previous model trained without (blue).

[1] Precise Size Determination of Supported Catalyst Nanoparticles via Generative AI and Scanning Transmission Electron Microscopy.

H. Eliasson, A. Lothian, I. Surin, S. Mitchell, J. Pérez-Ramírez, R. Erni

Small Methods 2024, 2401108.

[2] Improving Nanoparticle Size Estimation from Scanning Transmission Electron Micrographs with a Multislice Surrogate Model.

H. Eliasson and R. Erni

Nano Letters 2025, Article ASAP.

Fig. 1

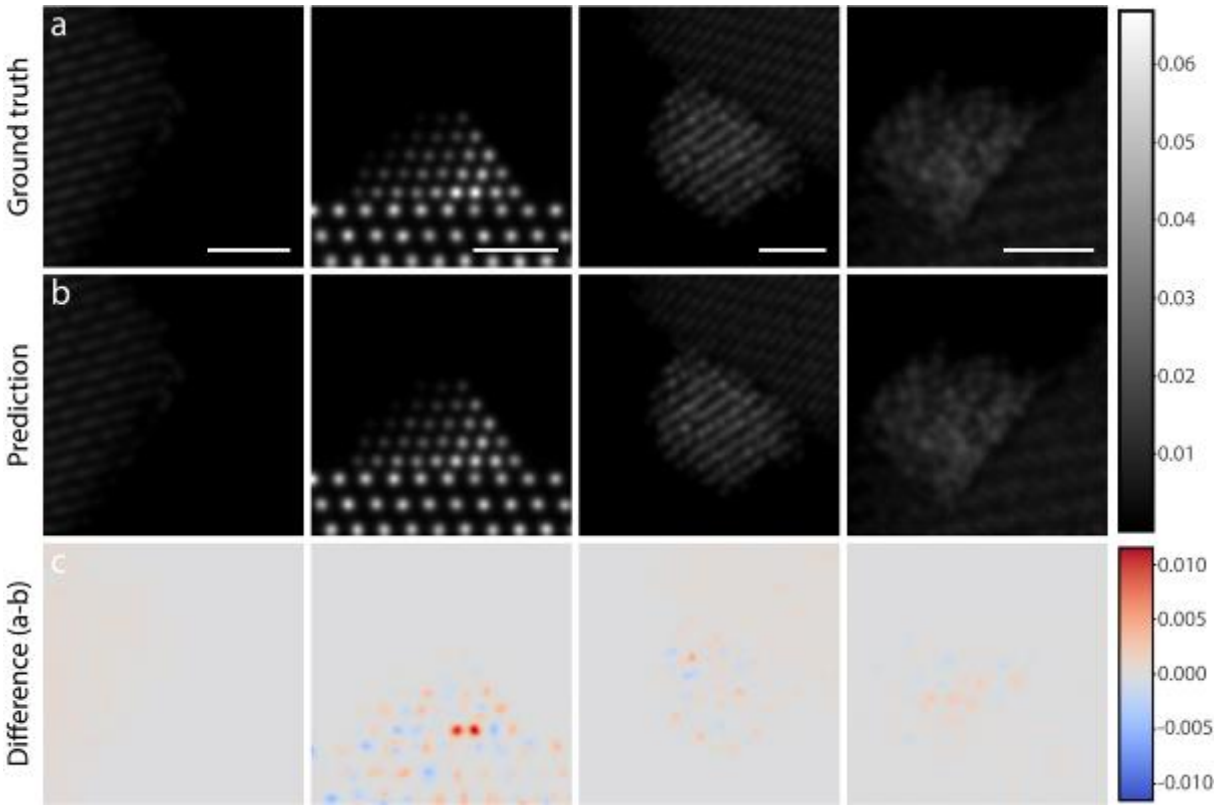
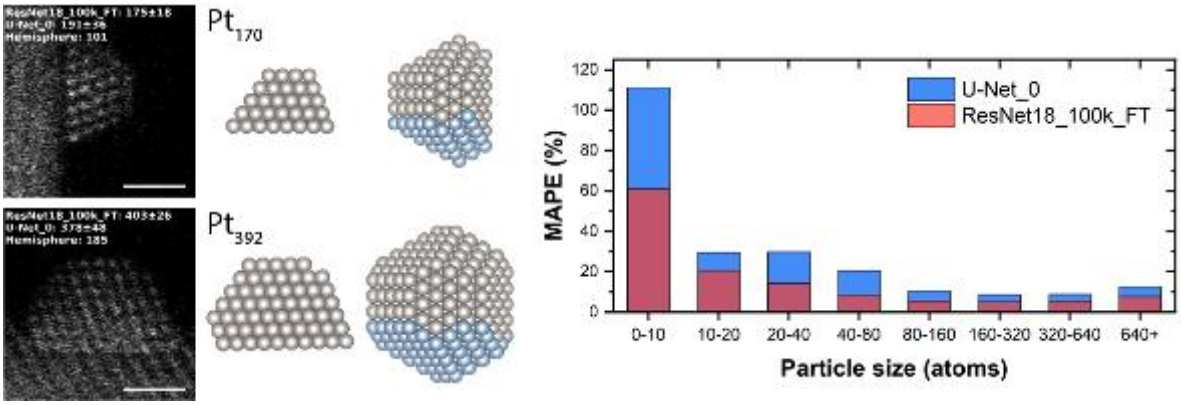


Fig. 2



IM6.05
A LLM-powered chatbot assisting complex data analysis workflows

M. Zhao[1], A. Gladyshev[1], S. Shabih[1], M. Schloz[1], C. T. Koch[1]

[1]Humboldt University of Berlin, Institute of Physics, Berlin, Germany

Introduction

The volume and complexity of data acquired from at the (S)TEM by various techniques, such as EELS or 4D-STEM, have significantly increased, requiring complex and specialized workflows for analysis. Data analysis workflows for processing such data are being developed by different research groups around the world, with distinct notations and software dependencies and, in many cases, only little documentation, making them difficult to be adopted, even when being open-source. Furthermore, many of these workflows lack user-friendly GUIs, necessitating some level of programming expertise to operate effectively. Even when GUIs are available, they tend to be highly complex and demand a certain level of prior knowledge/training from the user. This complexity creates a significant barrier for many microscopists, who are not skilled in programming. They might seek collaboration with experts, but this collaborative process, while necessary, often leads to inefficiencies due to communication gaps or misunderstandings, resulting in considerable time delays. Conversely, algorithm developers often find themselves spending a lot of time troubleshooting and offering training, which detracts from their primary focus on developing new methods. Moreover, when an update is required, both sides must invest considerable effort in new documentation, a task that does not seem highest priority.

Objectives

To address these challenges, we developed a chatbot powered by LLM for streamlining complex data analysis workflows in microscopy. This innovative tool offers several key advantages:

- It enables users to interact with the system through natural language, eliminating the need for the user to know a programming knowledge.

- The LLM inherently possesses the capability to explain many generic concepts and, supplemented by Retrieval-Augmented Generation, can provide accurate guidance to users on specific aspects of the software.

- The chatbot interface is integrated into the microscope's operating software and can autonomously access (GPU) compute servers, allowing for immediate data processing as soon as the data is acquired.

- It enforces a standardized code format, greatly simplifying code migration and enhancing interoperability.

Results

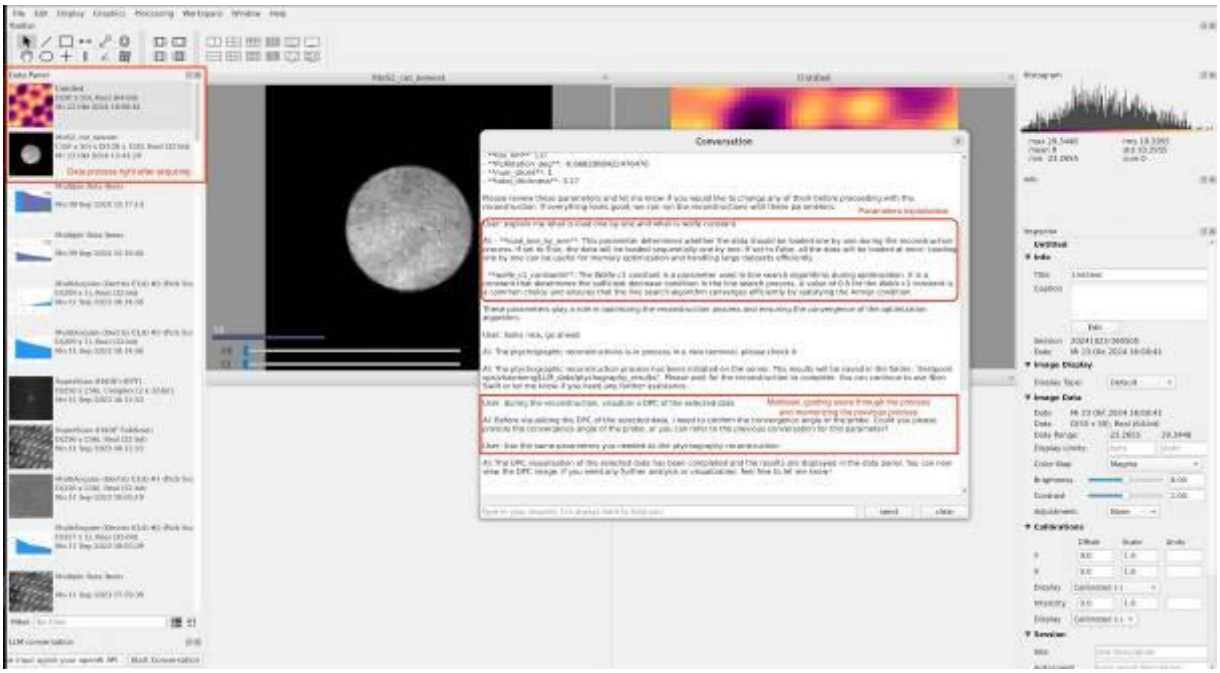
Realizing the above objectives we developed a chatbot plug-in for the Nion Swift software, which enables ptychographic reconstructions using our in-house code Pypty (see Fig. 1). This plug-in enables experimentalists, regardless of their previous experience with coding or ptychography, to smoothly obtain (3D) high-resolution phase images with z contrast immediately after data acquisition. Furthermore, this process enables the identification and correction of errors or misunderstandings during the experimental process.

Conclusion

In conclusion, our work demonstrates an efficient workflow in the field of microscopy, particularly addressing the challenge posed by workflows developed by individual developers that lack user-friendly interfaces. By leveraging the capabilities of LLMs, we highlight their potential to support routine experimental development and operation.

Fig. 1: Screenshot of the chatbot plugin to Nion-Swift in action, here performing a ptychographic reconstruction in the background, and computing an integrated COM reconstruction while waiting for the ptychography result. The reconstruction workflow includes also some GUI interactions, like selecting the desired experimental data set.

Fig. 1



IM6.06
Towards autonomous STEM – AI auto tilt for central beam and zone axis detection

D. Jannis[1], P. Potocek[1,2], E. Arslan Irmak[1], R. Egoavil[1], A. Chaddou[1], B. Groen[1], M. Peemen[1]

[1]Thermo Fisher Scientific, Eindhoven, Netherlands
[2]Saarland University, Saarbrücken, Germany

Background

While transmission electron microscopes enable atomic-scale imaging, they are complex to operate and require a skilled operator to achieve atomic resolution, limiting potential throughput. A particularly critical and time-consuming step in the alignment process involves tilting the crystal to align with a major zone axis relative to the electron beam. In recent years, a user-interactive method has been developed that requires input on both the central beam and zone axis to achieve the correct tilt. This approach significantly enhances throughput but still lacks the automation needed for self-driving microscopes

Methods

To tackle this issue, a novel algorithm emphasizing robustness has been developed to identify both the central beam and the major zone-axis position in a diffraction pattern. Although these points are easily identifiable by a trained human, traditional algorithms face difficulties due to the complexity and variety of parameters, including thickness, material type, and acceleration voltage. Consequently, supervised machine learning is employed to learn the critical features and accurately determine both the central beam and zone axis from the electron diffraction pattern.

Results

This work showcases the method's applicability across different crystallographic systems and parameters, such as thickness and convergence angle, and discusses the parameter space where the method yields reliable results. Figures 1(a) and 1(b) illustrate detection on silicon samples of varying thicknesses. Furthermore, this capability facilitates the automation of microscope operations, enhancing workflows and increasing throughput, particularly in nanoparticle characterization. Figure 1(c) presents an example involving a gold nanoparticle, with the head and tail indicating the central beam and zone axis, respectively.

Conclusion

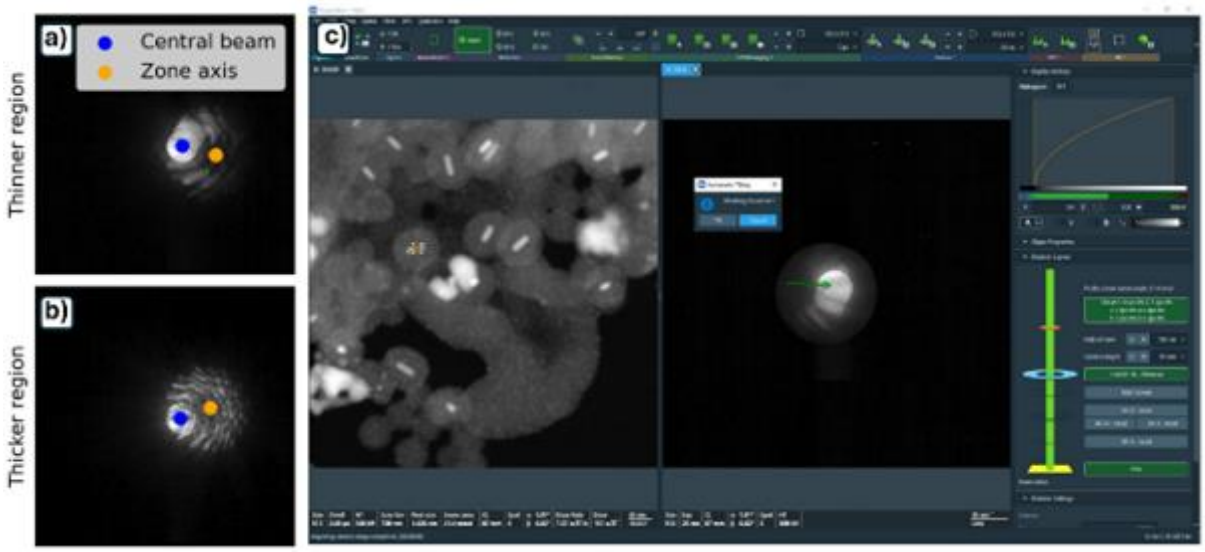
In conclusion, although transmission electron microscopes provide atomic-scale imaging, their complexity and the requirement for skilled operators restrict their throughput. By utilizing supervised machine learning, a new algorithm has been designed to reliably identify the central beam and zone axis in diffraction patterns. This advancement paves the way for increased automation and throughput in electron microscopy.

Figure 1: (a,b) The position of the central beam (blue) and zone-axis (orange) on a thin (a) and thicker (b) part of silicon. (c) An example of the diffraction pattern from a gold nanoparticle where the arrow indicates the tilt which needs to be applied to the particle to put it into zone-axis in the Velox application software.

References:

1. Huang *et al*. *Microscopy and Microanalysis* (2023) **29**, 728-729. https://doi.org/10.1093/micmic/ozad067.359
2. Cattaneo and Müller-Caspary *et al*. *Ultramicroscopy* (2024) **267**, 114050. https://doi.org/10.1016/j.ultramic.2024.114050

Fig. 1



IM6.P01
Large scale calculations of molecular poses and AI-aided analyses for cryo-EM structure-based drug design in a near-atomic resolution regime

Q. X. Jiang[1]

[1]Laoshan Laboratory and SUNY-Buffalo, Blue Life Science and Marine Strategic Biomedicine, Qingdao, China

Introduction:

With massive production of cryo-EM structures of near-atomic resolutions in the recent decade, many new structures were expected suitable for structure-based drug design (SBDD). However, such a promise has not materialized, partially because most near-atomic resolution cryo-EM structures are in a resolution regime of 2.1 - 4.5 Å, where conventional strategies for crystal SBDD perform poorly. New strategies are thus desired. We proposed a new strategy made of three steps: 1) to calculate a huge number of molecular poses in its binding site; 2) to refine top-ranked molecular poses against a cryo-EM structure of ~3.1 Å in resolution; and 3) to design molecular derivatives for better potency. We implemented this strategy in the design of an MTA-synergic inhibitor of a broad-spectrum anti-cancer target, protein arginine methyltransferase 5 (PRMT5). Our results suggest that this new strategy works well, even better than the popular AI-based strategy, and has the potential for more general applications.

Objectives:

Test the feasibility of using large-scale calculation of molecular pose to enable cryo-EM SBDD for structures of ~3.1Å resolutions and compare results with AI-aided ligand analysis and design.

Materials and methods:

1. Prepare PRMT5/MEP50 complex from sf9 cells and analyze its functions by biochemical and cell-based assays.
2. Synthesize and characterize of 11-2F, which shows an affinity of ~900 nM.
3. Calculate and compare 20 million poses of 11-2F and refine the top poses against the cryo-EM structure.
4. Generate derivatives of 11-2F based on its optimal binding configuration and compare their binding energy.
5. Test 11-9F for its enhanced potency and MTA-synergy
6. Use an AI-based strategy to redesign and evaluate 11-2F analogs

Results:

1. Establish PRMT5 and a micromolar-affinity, MTA-synergic inhibitor (11-2F) as a test system. The PRMT5/MEP50 complex is functional. 11-2F has a new chemical backbone but is limited in its potency.
2. Calculate and rank tens of millions poses of 11-2F in the substrate-binding pocket of PRMT5. Energetic comparison yielded ten top poses.
3. Refine top poses of 11-2F against its cryo-EM map to obtain an optimal binding configuration. Computational comparison of ~50 derivatives generated from this optimal pose led to three different molecules that are 5 to 50-fold higher in binding affinity.
4. One of the designed inhibitors, 11-9F, was synthesized. Biochemical studies confirmed its predicted 5-fold enhancement in PRMT5 binding and its high MTA-synergy in cell-based assays of symmetrical dimethylation of arginine.

5. Compare AI-based strategy with the large-scale calculation of molecular poses for cryo-EM SBDD. The AI-based ligand configuration search, affinity evaluation and derivatization work as well as the computational analysis of ligand poses when the ligand affinity changes by more than 10 folds.

Conclusion:

Large scale calculation and comparison of molecular poses in a compound binding pocket and an AI-based method make it feasible to use cryo-structures of ~3.0Å resolutions for SBDD, which will likely have broader applications in development of molecular therapeutics.

IM6.P02
Python-based data processing for quantitative analysis of focused Ion Beam (FIB) tomography

J. Park[1], T. Mehlkoph[1], J. P. Poc[1,2], P. K. Chakraborty[1,2], A. Karl[1], E. Jodat[1], S. Basak[1], R. A. Eichel[1,2,3]

[1]Forschungszentrum Jülich GmbH, IET-1, Jülich, Germany
[2]RWTH Aachen University, Institute of Physical Chemistry, Aachen, Germany
[3]RWTH Aachen University, Faculty of Mechanical Engineering, Aachen, Germany

Understanding the structure and properties of materials is crucial in various fields such as batteries, fuel cells and water electrolysis. Three-dimensional (3D) tomography is a powerful imaging technique that allows for the visualization of internal structures and their relationships to neighboring structures. Focused ion beam (FIB) tomography is a type of 3D tomography that is particularly suitable for analyzing cutting-edge materials with nm to µm sized features, like microporous structures in catalyst layer for energy applications.

However, handling FIB tomography datasets can be challenging due to their large size, typically consisting of hundreds of images. Additionally, FIB tomography datasets often contain artifacts such as image drifting caused by long acquisition times and curtaining effects resulting from ion beam damage. Furthermore, extracting quantitative information such as material composition and porosity requires advanced data processing techniques like segmentation.

To address these challenges, we have developed a Python-based data processing procedure for quantitative analysis of FIB tomography. Our procedure is designed to be versatile and applicable to most FIB tomography datasets with minimal modification. The procedure consists of three main steps: 1) pre-processing to organize and reshape the dataset, 2) segmentation to distinguish and label featured areas, and 3) data reconstruction to calculate and visualize quantitative information. We will present our Python-based data processing procedure using two energy-related applications: proton exchange membrane water electrolyzer and solid oxide fuel cell.

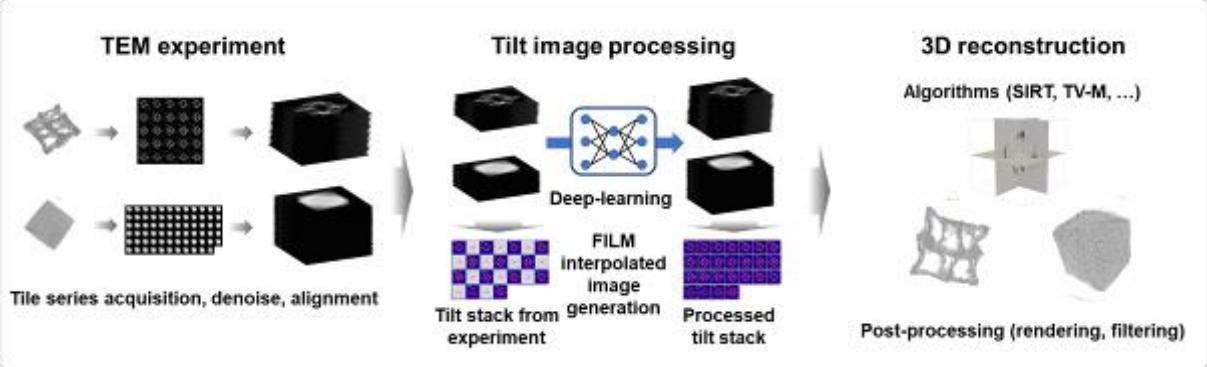
IM6.P03
Enhancing 3D nanoparticle reconstruction using generative Interpolation in STEM tomography

T. Kim[1], D. Lee[2], W. Sohn[1], T. Epicier[3], H. Baik[1]

[1]Korean Basic Science Institute, Seoul, South Korea
[2]Technology Innovation Institute, Abu Dhabi, United Arab Emirates
[3]IRCELYON CNRS, Lyon, France

Transmission electron microscopy (TEM) provides atomic-scale resolution, making it a vital tool for nanomaterial analysis. However, its inherently two-dimensional (2D) imaging nature limits its ability to fully capture three-dimensional (3D) structures. To overcome this limitation, electron tomography (ET) has been developed, reconstructing 3D morphologies from 2D tilt series. Despite its advantages, ET is constrained by beam sensitivity, leading to structural damage and imaging artifacts, particularly in electron beam-sensitive materials. Reducing the density of the tilt series can mitigate beam damage but often results in reduced reconstruction accuracy. In this study, we introduce the Frame Interpolation for Large Image Motion (FILM) method, which enhances image interpolation between tilt series to improve the quality of 3D reconstruction in scanning transmission electron microscopy (STEM) tomography. The effectiveness of FILM was evaluated for three types of nanoparticles—nanooctahedron, hollow nanotube, and nanoframe—with different tilt step sizes. The results demonstrate that FILM enables more precise image interpolation compared to conventional methods, particularly for complex nanostructures, leading to improved 3D reconstruction fidelity. Furthermore, FILM proves to be highly effective in reducing tilt series density while maintaining structural integrity and accuracy. The reconstructed 3D images exhibit reduced noise, enhanced clarity, and improved feature resolution. These findings highlight the potential of FILM as a powerful tool for minimizing electron beam exposure while preserving high-quality 3D reconstructions, offering significant advantages for electron tomography applications, particularly in the analysis of beam-sensitive and structurally intricate nanomaterials.

Fig. 1



IM6.P04
Automatic detection and analysis of micro/ nanoplastic in soil samples using SEM/EDX combined with a novel machine learning approach

A. Foetisch[1], K. Stricker[1], T. Scherer[2], M. Bigalke[1]

[1]Technical University of Darmstadt, Soil mineralogy and chemistry, Darmstadt, Germany
[2]Karlsruhe Institute of Technology, Institute of Nanotechnology, Karlsruhe, Germany

Numerous studies have shown the potential risk that nanoplastics (NP) represent for the living organisms in the different ecosystems. Yet NP remain one of the most challenging environmental plastic fraction to study and monitor. Only few studies have tried to quantify and characterise environmental NP. To the best of our knowledge, none could yet provide a single particle NP characterisation over the full nanoscale range combined with a high sample throughput.

The present work focuses on the challenge of NP full characterisation in soil using scanning electron microscopy coupled with energy dispersive X-ray spectroscopy (SEM-EDS). The data collected from nanoparticles 2D images (morphology/texture), EDS spectra and particle sensitivity to electron beam radiation are used to efficiently differentiate NP from remaining soil organic matter (SOM) particles. While morphological/textural features and EDS spectra have already been applied to plastic identification (1), only one study used Particle Deformation Behaviour (PDB) for MP identification (2). Automated EDS and PDB data acquisition remain to be developed and tested for NP. Finally, the collected data can be used to train a machine learning algorithm for NP automatic identification.

Homemade cryogrinded nanoparticles of polyethylene terephthalate (PET), polyethylene (PE), polypropylene (PP), polyamide (PA) and polyvinyl chloride (PVC) are deposited on silicon substrates and analysed by SEM-EDS to determine the elemental composition of the particles. Subsequently particles in a size range between 1 -0.1 µm are exposed to the electron beam for 40 seconds and images are recorded at T0s and T40s. The NP PDB is characterised and quantified by digital image correlation and compared to SOM behaviour when exposed to the same radiations. In this aim, humic horizon of forest soil and agricultural soils are extracted and analysed as described above.

The results are analysed to assess the suitability of the PDB to help differentiate NP from other nanoparticles present on the substrates after soil extraction. In this aim, the PDB measured on each polymer and SOM is quantified and characterized on a size range of 0.1-1 um and a wide range of NP shapes with varying circularity and convexity. The PDB is finally compared between polymers and SOM to evaluate the capacity of the developed method to differentiate plastic from SOM.

In case of success, the PDB of the materials could help providing a full characterization of environmental NP with a high sample throughput. In addition to the morphological/textural and elemental data provided by SEM-EDS, PDB could significantly improve the automatic detection of NP in environmental matrices when combined with machine learning (ML) algorithms for particle classification. This methods combination could then provide a more accurate assessment of the NP pollution in the environment.

References

1. Gniadek M, Dąbrowska A. The marine nano- and microplastics characterisation by SEM-EDX: The potential of the method in comparison with various physical and chemical approaches. Marine Pollution Bulletin. 2019 Nov;148:210–6.
2. Stine JS, Aziere N, Harper BJ, Harper SL. A novel approach for identifying nanoplastics by assessing deformation behavior with scanning electron microscopy. Micromachines. 2023 Oct 5;14(10):1903.

IM6.P05
Deep learning segmentation method for electron diffraction patterns in transmission spot-kikuchi diffraction in scanning electron microscope

Y. Zhang[1], J. Schiøtz[2], H. Wiik Ånes[3], A. Bastos da Silva Fanta[1]

[1]Technical University of Denmark, DTU Nanolab, Kongens Lyngby, Denmark
[2]Technical University of Denmark, DTU Physics, Kongens Lyngby, Denmark
[3]Xnovo Technology ApS, Køge, Denmark

Abstract

15 years have passed since the introduction of Transmission Kikuchi diffraction (TKD) in a scanning electron microscope (SEM) [1], allowing orientation mapping of thin nanocrystalline materials to be pushed towards sub-10 nm spatial resolution in on-axis TKD configuration [2]. However, the patterns obtained in an on-axis TKD experiment depend heavily on the atomic number and thickness of the sample as well as the beam energy. Moreover, diffraction spot and Kikuchi patterns can appear simultaneously [3], and we term such acquisition technique as transmission spot-Kikuchi diffraction (TSKD).

Being able to acquire spot and Kikuchi pattern simultaneously has its advantages and disadvantages. On one hand, indexing TSKD patterns individually via technique such as dictionary indexing in KikuchiPy [4] for Kikuchi patterns and template matching in Py4DSTEM [5] for spot patterns allows us to apply the on-axis transmission technique over a much wider range of samples compared to using only Kikuchi or spots indexing. On the other hand, the overlapping spot and Kikuchi patterns cause the existing template matching methods to fail since the traditional matching algorithm performs pixel-wise comparison without the ability to distinguish whether a pixel belongs to a spot or a Kikuchi pattern, thus erroneously indexing the pattern.

Therefore, segmenting and isolating the spot and Kikuchi patterns is crucial for successful indexing in TSKD. Research has shown that traditional segmentation attempts such as probe-template-matching are drastically out-performed by deep learning methods [6], and we have attempted to improve the traditional method by performing various image treatment [7] and concluded the method to be limited.

In this work, we explore deep learning segmentation methods for TSKD patterns obtained from samples of varying composition and thickness, and discuss the accuracy and performance of the employed methods.

Reference

[1]: R.H. Geiss, R.R. Keller, D.T. Read, **Transmission electron diffraction from nanoparticles, nanowires and thin films in a SEM with conventional EBSD equipment**, *microscopy and microanalysis*, **16** S2 (2010), pp. 1742-1743.

[2]: N. Brodusch, H. Demers, R.Gauvin, **Nanometres-resolution Kikuchi patterns from materials science specimens with transmission electron forward scatter diffraction in the scanning electron microscope**, *J. Microscopy*, 250 (2013), pp. 1-14.

[3]: E. Brodu, E. Bouzy, J-J. Fundenberger, **Diffraction contrast dependence on sample thickness and incident energy in on-axis Transmission Kikuchi Diffraction in SEM**, ultramicroscopy, **181** (2017), pp.123-133.

[4]: H.W. Ånes, L.A.H. Lervik, O. Natlandsmyr, T. Bergh, *et al*., **pyxem/kikuchipy: kikuchipy 0.11.1.post0 (v0.11.1.post0)**, (2024) Zenodo.

[5]: B.H. Savitzky, S.E. Zeltmann, L.A. Hughes, *et al*., **py4DSTEM: A software package for four-dimensional scanning transmission electron microscopy data analysis**, *Microscopy and Microanalysis*, 27-4 (2021), pp. 712–743.

[6]: J. Munshi, A. Rakowski, B.H. Savitzky, *et al.,* **Disentangling multiple scattering with deep learning: application to strain mapping from electron diffraction patterns**, *npj Comput Mater* **8**, 254 (2022).

[7]: Y. Zhang, J. Schiøtz, A.B.S. Fanta, **Simultaneous Indexing of Spot and Kikuchi Patterns in the Scanning Electron Microscopy (SEM)**, Abstract from European Microscopy Congress 2024, Copenhagen, Denmark.

IM6.P06
A documentation strategy for TEM / FIB experiments using Kadi4Mat as ELN

D. V. Szabó[1], S. Schlabach[1]

[1]Karlsruhe Institute of Technology, Eggenstein-Leopoldshafen, Germany

In order to facilitate Findable - Accessible - Interoperable - Reusable (FAIR) research data we developed a strategy to document the complex processes in an Electron Microscopy Laboratory. We present our approach of using Kadi4Mat, the Karlsruhe Data Infrastructure for Materials Science [1] as a web-based application and its functionality as an Electronic Lab Notebook (ELN). We therefore developed a set of templates related to TEM/FIB/SEM investigations, data evaluation, and also sample preparation tasks [2].

The idea behind the templates for the different steps in the TEM/FIB/SEM/or sample preparation environment is to create workflows by dividing the processes into "simple units"" and combining those steps in manifold ways. As prerequisite, all necessary process steps were analyzed and grouped into the categories "Sample Preparation" with diverse sub-steps, "Sample Investigation" with diverse investigation methods belonging to the respective technologies, and finally "Data Evaluation" with relevant sub-steps. Especially for the manual processes of classical TEM-sample or metallographic sample preparation, flexible but reliable documentation is important. Most of the instruments (like the saws, the polishing and grinding instruments) are "manually"-controlled, meaning that they generate no metadata by itself. For sample tracking, a sample questionnaire template was developed. In this way the templates are acting as a kind of construction kit.

The templates can be combined easily and have been designed to be user-friendly, but at the same time requesting the relevant metadata in a structured and standardized way. They ensure a consistent acquisition of metadata securing a minimum and comparable description of tasks. Additionally, by using templates a consistent labeling of inquiry fields ensures easier search abilities. Pre-defined permissions granting, e.g. a group of administrators, ensures long time data accessibility.

The use of templates makes it possible to specify a glossary for recording metadata. This means that they are well-defined from the outset and easier to search later on. Regarding FAIR principles, this is of importance. The developed templates can be exported in JSON-format and might be used as models for other experimental methods.

To document the whole experimental process in Kadi4Mat we are comprising one central record for the material/sample to be investigated, a record for the sample preparation, a record for the investigation/experiment, and a record for the data evaluation. The records can be grouped in collections, linked together, and also linked with the existing instrument records. These linked records can be graphically represented as knowledge graphs.

Research value is expected in the long run, as research data will be documented in a structured and FAIR way. Our approach may serve as a model for other researchers on how to apply an ELN. In the future, a direct connection of the high-end instruments to an ELN with direct transfer of instrument metadata is desirable. This would reduce the workload of scientists and also increase the acceptance of ELNs.

References

1. Brandt, N, et al., 2021. Kadi4Mat: A Research Data Infrastructure for Materials Science. Data Science Journal, 20 (8), 1-14

2. Schlabach, S, et al., 2024. Using ELN Functionality of Kadi4Mat (KadiWeb) in a Materials Science Case Study of a User Facility. Data Science Journal, 19 (50), 1-16

IM6.P07
Using convolutional neural networks for the characterization of metal-oxide nanoparticle hetero-aggregates by STEM – 3D-Reconstruction and 2D-Projection

F. F. Krause[1], C. Mahr[1], X. Wang[2], L. Völkl[3], J. Stahl[2], M. Schowalter[1], T. Grieb[1], N. Barsan[3], L. Mädler[2], A. Rosenauer[1]

[1]University of Bremen, Institut für Festkörperphysik, Bremen, Germany
[2]Leibniz Institut für Werkstofforientierte Technologien, Bremen, Germany
[3]University of Tübingen, Institut für Physikalische und Theoretische Chemie, Tübingen, Germany

Functional properties of nanomaterials strongly depend on the underlying structure and chemical composition. One example are hetero-aggregates in which nanoparticles of two different metal-oxides are mixed. Examples are hetero-aggregate systems of TiO_2/WO_3 or Co_3O_4/SnO_2 nanoparticles, which show enhanced functionality over the pure oxides. The performance of these aggregate systems depends on the mixing and composition. The hetero-aggregate structures investigated in this study are generated in a double-flame spray pyrolysis setup.

Consequently, any design or improvement of functional properties requires a characterisation of structure and mixing. In conventional STEM, 2D-projection images of the samples are acquired, information about the third dimension is lost. This drawback can be overcome by STEM tomography, where the 3D-structure is reconstructed from a series of projection images acquired using various projections. However, 3D-measurements are expensive with respect to acquisition and evaluation time. Hence, the measurement of 3D-reconstruction can only be done for a limited number of hetero-aggregates. To obtain statistically relevant results, information on many hetero-aggregates has to be gathered. Positions of many nanoparticles have to be determined in 2D- and 3D-data. This can be challenging especially in crowded regions in 2D-projection data. In recent years, it was demonstrated that the application of convolutional neural networks (CNNs) outperforms a manual measurement or classical object detection algorithms.

The application of CNNs requires a training of the network first. To this end, many training images are required. In the present contribution, we simulate realistic 2D-projection and 3D-reconstruction data of computer-generated virtual hetero-aggregates, in which particle positions and material types are known. In material systems that show weak contrast between the two materials, EDX-signals need to be included into the data, which by nature are much weaker and noisier than STEM-images. This is also simulated and used as another input channel to the CNNs. For evaluations of 2D-projection data we train a Mask R-CNN [1], for evaluation of 3D-reconstructions we train a StarDist-3D network [2]. An example experimental evaluation is shown in the figure.

We evaluate the trained CNNs using simulated data that has not been used during the training process and apply the networks to experimental 2D-projection and 3D-reconstruction data. Amongst the evaluated characteristics are the number of particles per aggregate, the material mass fractions, particle sizes, the fractal dimension as well as total and heterogeneous coordination numbers. It is demonstrated that for the measurement of some quantities, the evaluation of less expensive 2D-projection data is sufficient, whereas for a quantification of others a 3D-reconstruction is required [3].

When more sophisticated hetero-aggregate hetero-structures are created by flame spray pyrolysis, a plain statistical analysis of a set of randomly chosen aggregates does not suffice anymore. In this case a full preparation of the structure by focussed ion becomes necessary, complicated by the weak cohesion between the aggregates and the very porous nature of the deposition.

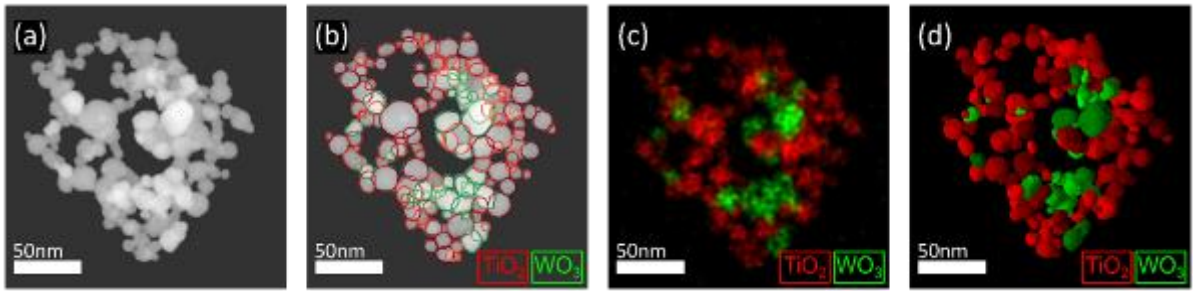
[1] He et al., IEEE ICCV 2017 (2017), 2980

[2] Weigert et al., IEEE WACV 2020 (2020), 3655

[3] Mahr et. al, Ultramicroscopy 265 (2024), 114020

(a): STEM image of a TiO2-WO3 hetero-aggregate. (b): particles detected by the Mask R-CNN. (c): EDX map. (d): particles as detected by the StarDist-3D network in the STEM tomography reconstruction.

Fig. 1



IM6.P08
3D MC-DIP – 3D multi-channel deep image prior approach for limited-angle spectroscopic electron tomography

S. Brosset[1], D. del Pozo Bueno[1], G. Navarro[1], P. Ciuciu[2,3], Z. Saghi[1]

[1]CEA, LETI, Grenoble, France
[2]CEA, NeuroSpin, Gif-sur-Yvette, France
[3]INRIA, MIND, Palaiseau, France

Electron tomography (ET) using electron energy loss spectroscopy (EELS) and energy dispersive x-ray spectrometry (EDX) has become a valuable technique for the 3D chemical analysis of nanomaterials. Although spectroscopic ET has been successfully applied to needle-shaped samples [1,2], its extension to slab-like specimen geometries and thick sample holders (e.g. for *in situ* measurements) is still a challenge as it requires the development of sophisticated algorithms for accurate reconstructions from severely limited tilt ranges.

Recently, we have shown that the Deep Image Prior (DIP) approach is very promising for limited-angle HAADF-STEM tomography [3]. As shown in Fig. 1, DIP outperforms classical simultaneous iterative reconstruction technique (SIRT) when the data covers a very restricted angular range ([-30°:+30°]). DIP produces more accurate reconstructions than SIRT, with reduced blurring and distortion, as reflected by the PSNR and SSIM values and the shape of the reconstructed particles.

In this work, we extend the DIP method to spectroscopic ET and add a multi-channel approach to optimize the quality of the reconstructions. The proposed 3D MC-DIP method is applied to the 3D chemical analysis of a phase-change memory device using STEM-EDX tomography. A thin lamella was prepared by focused ion beam (FIB) (Fig. 2(a)) and STEM-EDX datacubes were acquired in a Cold-FEG Jeol F200 equipped with a large SDD EDX detector. Acquisition was limited to [-30°:+30°] with 4° increment due to sample geometry constraints. Hyperspy was used to extract the tilt series corresponding to Ge, Te, Sb, Ti. After alignment, 3D MC-DIP was applied to the four elemental datasets simultaneously. Fig. 2(b) shows the 3D volume rendering of the device and the orthogonal cross-sections through the SIRT and 3D MC-DIP reconstructions. Compared with the SIRT reconstructions (Fig. 2(c,e,g)), 3D MC-DIP (Fig. 2(d,f,h)) produces high-quality elemental volumes, with a rectangular cross-section of the phase change material, a reliable chemical distribution of the different elements, and an expected depletion of Ge in the active region above the TiN heater.

Application of 3D MC-DIP to STEM-EELS tomography and the incorporation of the HAADF-STEM signal as a mean of further improving the reconstruction will also be presented.

[1] Rossouw, D. *et al.* (2016), Acta Materialia, 107, 229-238.

[2] Einsle, J.F. *et al.* (2018), PNAS, 115(49), E11436.

[3] Brosset, S. *et al.* (2025), Nanoscale Advances (to be submitted).

Acknowledgments: This work, carried out on the Platform for Nanocharacterisation (PFNC), was supported by the "Recherche Technologique de Base" program of the French ministry of research. The authors acknowledge the French National Research Agency through the PEPR DIADEM, and thank R. Ravelle-Chapuis for assistance with data acquisition.

Fig. 1. SIRT and DIP reconstruction of simulated nanoparticles, from projections acquired between -30° to +30°, with a 2° increment. (a) Reference image; (b) SIRT reconstruction and (c) DIP reconstruction. SSIM and PSNR are computed using (a) as a reference.

Fig. 2. Comparison of SIRT and 3D MC-DIP for limited-angle STEM-EDX tomography. (a) HAADF-STEM image of the sample, and in yellow: the region of interest for STEM-EDX tomography acquisition; (b) 3D volume rendering of the 3D-MC DIP reconstruction; (c,d) xy, (e,f) xz and (g,h) orthogonal views through the SIRT and 3D MC-DIP volumes. The missing wedge is in the y direction.

Fig. 1

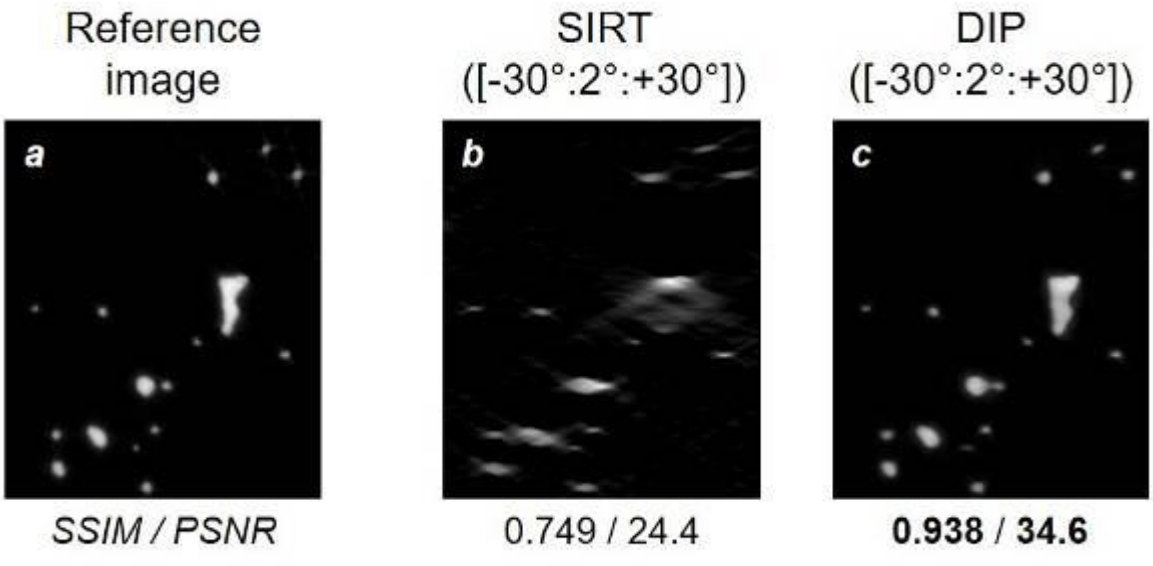
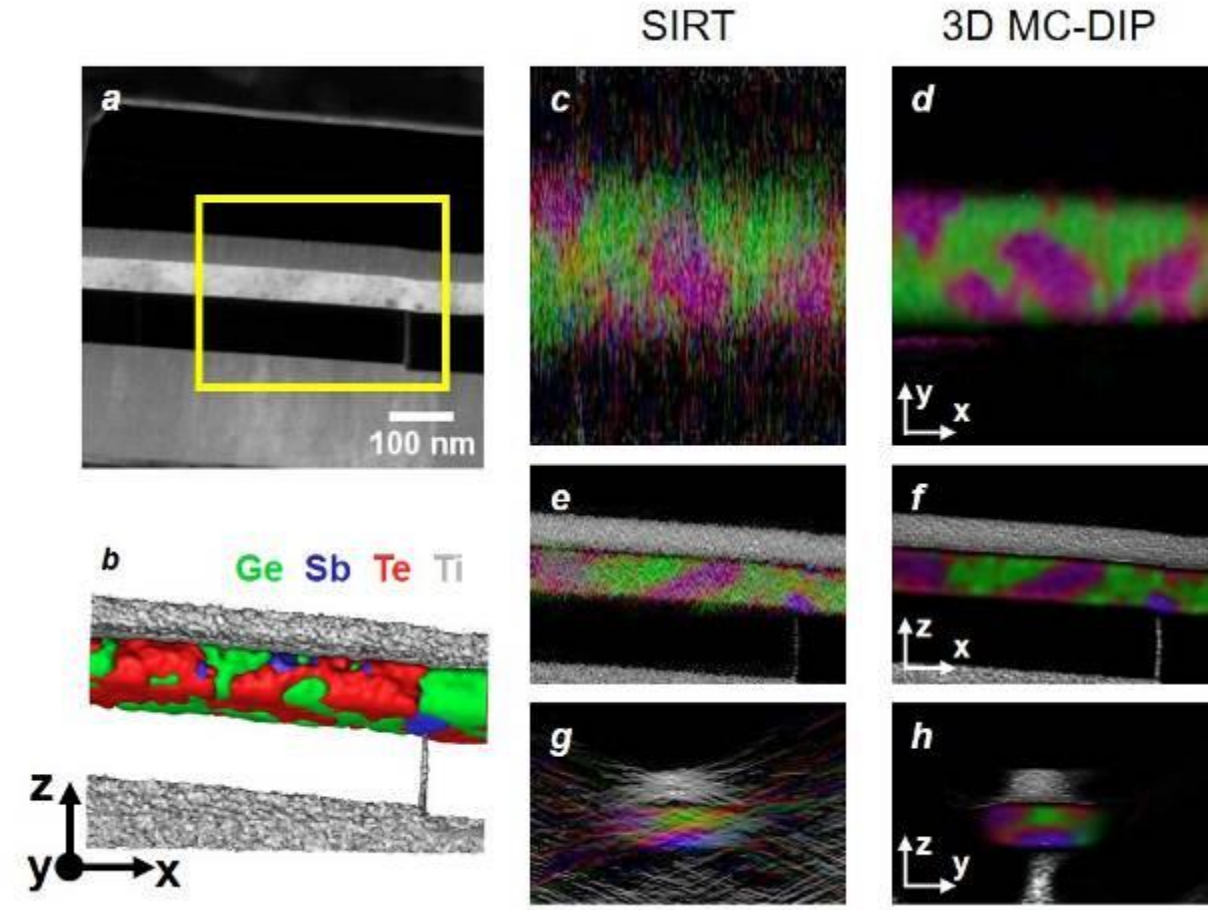


Fig. 2



IM6.P09
Workflow for near real-time processing of large 4D STEM experimental datasets

D. Stroppa[1], C. Dwyer[1], L. Leroy[1], C. Buhl Larsen[1], R. dos Reis[2,3]

[1]DECTRIS Ltd., Baden-Dättwil, Switzerland
[2]Northwestern University, Department of Materials Science and Engineering, Evanston, IL, United States
[3]Northwestern University, NUANCE Center, Evanston, IL, United States

Four-dimensional Scanning Transmission Electron Microscopy (4D STEM) experiments are becoming increasingly popular for high resolution imaging of a vast range of materials, including applications belonging to the materials sciences [1] and life sciences [2]. Recent advances in electron detection technology [3] allow fast frame rates, up to 120 kHz, and extended dynamic range, and thus enable high-throughput experiments with substantial information content and data bandwidth.

A current challenge in fast 4D STEM experiments lies in managing the massive datasets that are generated. Particular solutions to this challenge include the real-time visualization of preprocessed experimental data, e.g., using custom virtual STEM masks, and a simple, effective way to transfer data to high-performance computing environments for more advanced data processing, such as ptychographic reconstructions.

This contribution presents workflows designed to support fast 4D STEM experiments, including live image visualization with the NOVENA Acquire software, and near real-time data transfer and processing through the DECTRIS Cloud solution. These workflows enable live processing up to the maximum frame / data rates supported by current electron detectors with flexible virtual masks, and indicate sub-second data transfer latency for cloud-based, near real-time data processing using a pre-set environment.

These implementations in data handling and real-time, or near real-time, processing constitute significant progress in removing the "data bottleneck" in 4D STEM experiments. Crucially, this enables the experimentalist to perform rapid results interpretation in order to further optimize the experimental setup, indicating the next instrumental challenges to be addressed to aid 4D STEM wide adoption in different application areas [4].

1. M. Wu *et al.*, J. Phys. Mater. 6 (2023) 045008. DOI: 10.1088/2515-7639/acf524
2. S. Seifer *et al.*, Microsc. Microanal. (2024) 30(3):476-488. doi: 10.1093/mam/ozae050.
3. P. Zambon *et al.*, Front. Phys. (2023) 11:1308321. DOI: 10.3389/fphy.2023.1308321
4. This work made use of the EPIC facility of Northwestern University"s NUANCE Center, which has received support from the SHyNE Resource (NSF ECCS-2025633), the IIN, and Northwestern's MRSEC program (NSF DMR-2308691). This research was supported in part through the computational resources and staff contributions provided for the Quest high-performance computing facility at Northwestern University which is jointly supported by the Office of the Provost, the Office for Research, and Northwestern University Information Technology.

IM6.P10
The EM glossary – A community resource providing harmonised terminology in electron microscopy

V. Hofmann[1], R. R. Schröder[2], C. Pauly[3], A. Azócar-Guzmán[1], Ö. Özkan[4], M. R. Sedeqi[4], S. Brockhauser[5], R. Aversa[6], C. Hébert[7], M. Kühbach[5], P. Konijnenberg[1], O. Brendike-Mannix[4], S. Sandfeld[1]

[1]Forschungszentrum Jülich GmbH, Institute for Advanced Simulation - Materials Data Science and Informatics (IAS-9), Aachen, Germany
[2]Heidelberg University, BioQuant, Heidelberg, Germany
[3]Saarland University, Functional Materials, Saarbrücken, Germany
[4]Helmholtz Center Berlin for Materials and Energy, Berlin, Germany
[5]Humboldt University of Berlin, Institute of Physics & CSMB, Berlin, Germany
[6]Karlsruhe Institute of Technology, Scientific Computing Center, Karlsruhe, Germany
[7]Ecole Polytechnique Fédérale de Lausanne, Institute of Physics, Lausanne, Switzerland

With the EM glossary initiative, our goal is to harmonize terminology in the field of electron and ion microscopy so humans, devices and algorithms can exchange data easily and collaborate more efficiently and effectively.

We achieve this through the following measures:

1. moderation of a community collaboratively harmonising terminology,
2. provision of a machine-readable OWL artifact, [1]
3. provision of a human-readable web app - the EM Glossary explorer; [2]
4. support and counselling for application-level adoption of the resource.

The Helmholtz Metadata Collaboration (HMC) [3] is coordinating the EM glossary initiative. This includes a group of volunteers, with scientists from more than 23 institutions across Switzerland, Austria, and Germany, as well as representatives of the FAIRmat [4] and the NFDI-MatWerk [5] consortia, who meet every two weeks to discuss and achieve consensus on the definitions of terms commonly used in electron and ion microscopy. Our goal is to produce concise, unpacked definitions with rich annotations in accordance with semantic best practices. The initiative remains open to new contributors, fostering a collaborative and interdisciplinary approach to standardizing terminology in the field.

Up to now, there are more than 65 harmonized definitions forrelevant terms. These are provided as a machine accessible resource [1] in the web ontology language (OWL). The artifact offers stable domain-level semantics and is regularly updated based on progress in our community group. By aligning with, or adopting the artifact in application-level metadata, intra- and inter-disciplinary interoperability is improved.

Terminology adopters include the NFDI consortia FAIRmat and NFDI-MatWerk, the NFFA-Europe Pilot (NEP) [6], the Joint Lab "Integrated Model and Data-driven Materials Characterization" (JL-MDMC) [7], and the research data management platform NOMAD [8]. New adopters are encouraged and welcomed. To encourage new contributions we provide detailed support and counselling for potential adopters.

In addition to technical adoption there is scientific value in the glossary itself: easy browsing of the glossary is provided by the EM Glossary Explorer [2] to facilitate the use of the resource for technical writing or for teaching purposes.

In conclusion, through a consensus-based process we have produced a resource for the entire electron and ion microscopy community. Application-level semantics can be aligned with its machine-

readable implementation which acts as a semantic glue within the field. In addition, the human-readable resource reduces ambiguity in communication within the field.

Interested in getting involved? Send an email to hmc-matter@helmholtz-berlin.de or hmc@fz-juelich.de to get in touch!

References:

[1] EM Glossary OWL artifact base URI: https://purls.helmholtz-metadaten.de/emg/

[2] EM Glossary Web Explorer: https://emglossary.helmholtz-metadaten.de/

[3] Helmholtz Metadata Collaboration: https://helmholtz-metadaten.de/en

[4] FAIRmat project: https://www.fairmat-nfdi.eu/

[5] NFDI-Matwerk: https://nfdi-matwerk.de

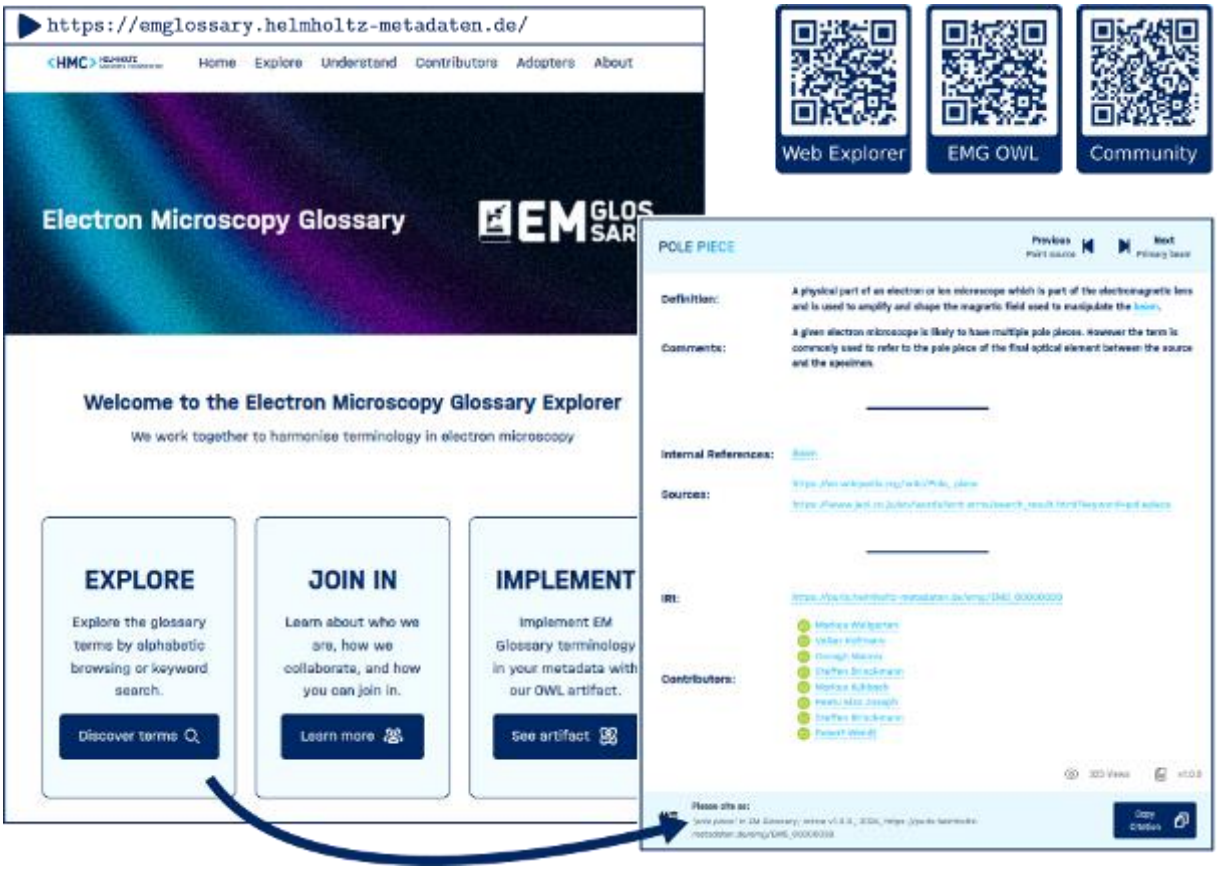
[6] NFFA-Europe Pilot : https://nffa.eu

[7] JL-MDMC : https://jl-mdmc-helmholtz.de

[8] NOMAD research data management platform: https://nomad-lab.eu/

Figure:
Screenshot of the EM Glossary Web Explorer landing page (large) and an example details page for the term "pole piece" (insert). QR codes link to (1) the EM Glossary Web Explorer, (2) the semantic artifact and (3) the co

Fig. 1


https://emglossary.helmholtz-metadaten.de/
Home
Explore
Understand
Contributors
Adopters
About
Electron Microscopy Glossary
Welcome to the Electron Microscopy Glossary Explorer
We work together to harmonise terminology in electron microscopy
EXPLORE
Explore the glossary terms by alphabetic browsing or keyword search.
Discover terms
JOIN IN
Learn about who we are, how we collaborate, and how you can join in.
Learn more
IMPLEMENT
Implement EM Glossary terminology in your metadata with our OWL artifact.
See artifact
Web Explorer
EMG OWL
Community
POLE PIECE
Definition:
Comments:
Internal References:
Sources:
IRI:
Contributors:

IM6.P11
Robust analysis tool for position averaged convergent beam electron diffraction patterns using a foundation model

D. Park[1,2], M. Nabawi[1], J. Guckel[1,2], T. Klein[1], J. Flügge[1], H. Bosse[1,2]

[1]Physikalisch-Technische Bundesanstalt (PTB), Braunschweig, Germany
[2]Laboratory for Emerging Nanometrology, Braunschweig, Germany

Position averaged convergent beam electron diffraction (PACBED) patterns provide precise local thickness and tilt information about the specimen investigated using scanning transmission electron microscopy (STEM) [1]. The analysis of PACBED can be performed by finding the best match between experimental and calculated PACBED patterns based on quantum mechanical theories. This matching can be done by manual inspection or using image quality metrics, like root mean square error (RMSE). While convolutional neural network (CNN)s with pre-trained models on the ImageNet dataset were suggested to enhance this visual inspection process [2], the vision transformer (ViT)-based contrastive language-image pre-training (CLIP) foundation model (Fig. 1 (a)) has emerged as the state-of-the-art computer vision system, showing superior performance and accuracy in various tasks. Therefore, we developed a robust software package based on advanced machine learning models to analyze numerous experimental PACBED patterns.

We employed the pre-trained ViT-B/16 model on the DataComp-1B dataset implemented in the Pytorch machine learning library within a Python environment [2]. The training process involves fine-tuning the last 2-3 layers and the multi-head self-attention head (MHSA)s with the regression layer to reliably predict the local thickness, tilt angle, and azimuth angle of the specimen (Fig. 1(b)). These modifications optimize the pre-trained model for our analysis. Some augmentation techniques were applied to increase the diversity of training data. The Wing loss function is used as a loss function to improve training capability for small and medium range errors [3]. For our local training, we used only the PACBED patterns calculated using MuSTEM based on the multislice algorithm [4]. The PACBED patterns of $SrTiO_3$ (STO), Si, and GaN were calculated with a maximum specimen thickness of about 200 nm in steps of 1 unit cell of the crystal structures. The convergent angle was fixed to 6.7 mrad at 200 kV. The specimen tilt varied from 0 to 10 mrad with an azimuth angle variation from 0 to π/2 rad in steps of π/20 rad. Over 100,000 calculated images with a size of 341 x 341 px^2 were used for the training and about 15,000 calculated PACBED patterns were tested for their evaluation.

Our novel analysis software reliably predicted local thickness and tilt of experimental PACBED patterns of STO, Si, and GaN. Our test results demonstrated high accuracy in analyzing the calculated PACBED patterns, which are randomly selected for STO and Si (Fig. 2(a)). An experimental PACBED pattern of STO along the [100] direction was acquired using a double-aberration corrected JEOL NeoARM 200F with a Gatan Oneview camera and analyzed using our novel analysis software package (Fig. 2(b)). The estimated thickness was 18.6 nm with no tilt and azimuth angle. The RMSE analysis result between experimental and calculated PACBED patterns confirmed this result.

This study presents a novel framework for PACBED analysis using ViT-based architectures with specialized loss functions and data augmentation strategies, significantly enhancing the accuracy and reliability of PACBED pattern matching.

[1] J. LeBeau et. al., Physical review Letters, 100, (2008)
[2] A. Radford et. al., https://arxiv.org/abs/2103.00020, (2021)
[3] Z. Feng et. al., https://arxiv.org/abs/1711.06753, (2017)
[4] L.J. Allen et. al., Ultramicroscopy 151, (2015)

Fig. 1

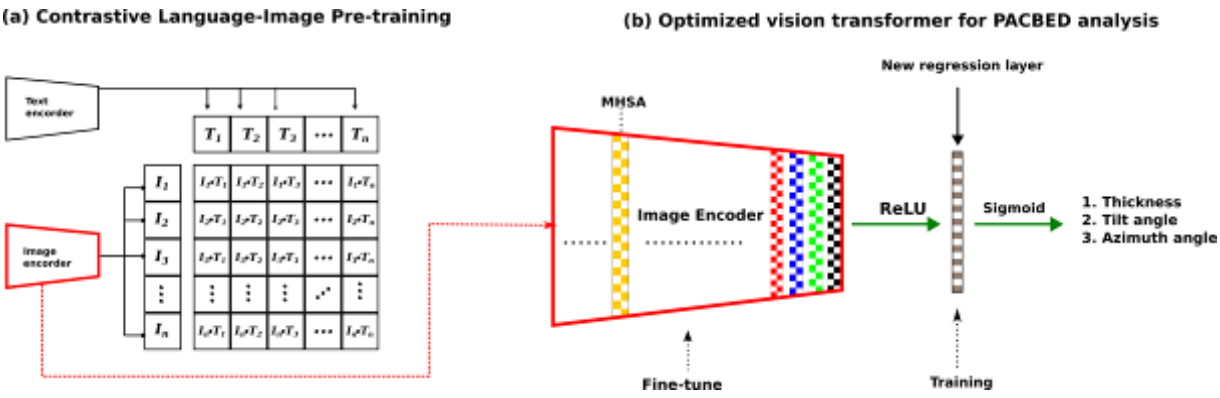
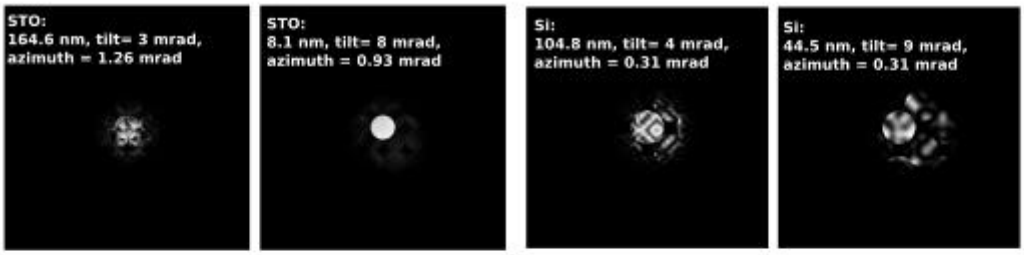
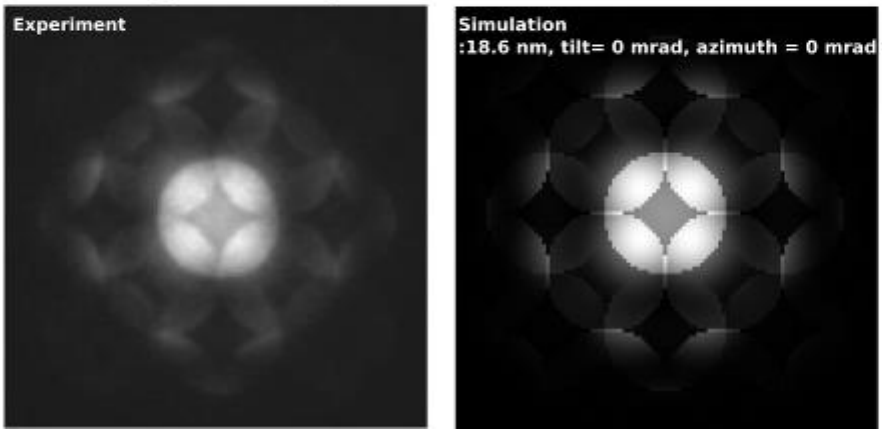


Fig. 2

(a) Evaluation test for randomly selected PACBED patterns of STO and Si calculated by MuSTEM



(b) Evaluation test for the experimental PACBED pattern of STO along the [100] direction using a robust analysis tool using a foundation model



IM6.P12
Multimodal data fusion for absorption correction in EDXS – Integrating EELS and HAADF for enhanced quantification

S. Cozma[1], P. Torruella[1], D. T. L. Alexander[1], C. Hébert[1]

[1]Ecole Polytechnique Fédérale de Lausanne, SB IPHYS, Lausanne, Switzerland

Introduction

The accurate quantification of elemental composition in energy-dispersive X-ray spectroscopy (EDXS) is hindered by absorption effects. The ESpM-NMF decomposition algorithm[1], a non-negative matrix factorisation (NMF) technique, that incorporates a physical modelling of the spectrum and Bremsstrahlung shows improved ability to perform accurate data decomposition reflecting the real compositional features of the sample. However, its effectiveness can be enhanced by incorporating complementary datasets.

Multimodal data integration in scanning transmission electron microscopy (STEM) improves chemical quantification accuracy. EDXS benefits from low-loss electron energy loss spectroscopy (EELS) data, which e.g. provides thickness information for absorption correction. When EELS is unavailable, incoherent high-angle annular dark-field (HAADF) images might offer an alternative for thickness estimation[2].

Objectives

This work develops a spatial registration framework for EDXS and EELS datasets acquired separately under optimal conditions. The thickness information is then used for improved absorption correction. Additionally, this study lays the groundwork for integrating 4D-STEM crystallographic phase maps to improve phase localisation and identification, contributing to more robust multimodal data fusion.

Materials & Methods

STEM experiments were performed on a Thermo Fisher Scientific Titan Themis at 300 kV. EDXS data were collected using a ChemiSTEM Super-X SDD detector, while EELS spectra were acquired using a Gatan Continuum K3 spectrometer. Advanced spatial registration methods aligned EDXS and EELS datasets, ensuring precise pixel mapping while addressing contrast differences, intensity variations, pixel spacing, drift, and distortions. Depending on the chosen dataset, fusion with EDXS data is handled differently. The EELS low-loss data computes the absolute thickness for each pixel, while HAADF data is used alongside initial EDXS chemical maps to incorporate mass-thickness information before running a subsequent ESpM-NMF decomposition. This approach significantly improved EDXS quantification accuracy.

Results

Figure 1. *(a)* ADF image acquired simultaneously with the EDXS dataset; *(b)* EELS LL dataset summed over the energy loss axis; Overlap of the summed LL dataset and the ADF image *(c)* before and *(d)* after applying the spatial registration algorithm and *(e)* Quantification results with and without absorption correction for one of the chemical phases present in the dataset.

Conclusion

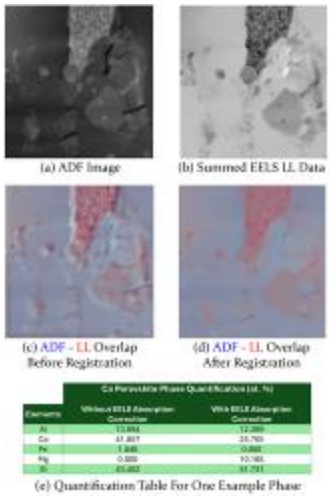
This study demonstrates the benefits of multimodal data fusion for absorption correction in EDXS. The proposed spatial registration framework ensures accurate dataset alignment, enabling improved chemical quantification through thickness-based corrections.

References

[1] Adrien Teurtrie et. al., Mach. Learn.: Sci. Technol. 5 045050, 2024, https:// doi.org/10.1088/2632-2153/ad9192.

[2] Jason Manassa et. al., Comp. Art., El. Micr., MSA, 2024, https://doi.org/10.69761/MXVR4353.

Fig. 1



(a) ADF Image (b) Summed EELS LL Data

(c) ADF - LL Overlap Before Registration (d) ADF - LL Overlap After Registration

(e) Quantification Table For One Example Phase

IM6.P13
Utilizing AI for advanced TEM script writing – Benefits and challenges using Microsoft Copilot

B. Miller[1], C. Czarnik[1], S. Gorji[2]

[1]Gatan Inc., Pleasanton, CA, United States
[2]Ametek GmbH, Gatan+EDAX, Unterschleissheim, Germany

Introduction

Widely available AI tools have proliferated in the past 5 years, enabling users to generate impressively detailed and human-like text, code, and visual content. The benefits of this technology to various fields are still being explored, and are expected to increase as AI models are refined and scientists learn to use these newly available tools more effectively.

Objectives

This work focuses on the value AI can bring to writing scripts for microscopy data collection, processing, analysis, and visualization in DigitalMicrograph®. For decades it has been possible to write DM scripts, which are C++ based, and more recently Gatan added Python scripting to DigitalMicrograph, but it can still be challenging for a user unfamiliar with the details of the DM script object structure and terminology to write scripts to move their research forward. We aim to demonstrate how Microsoft Copilot can facilitate script writing.

Materials and Methods

We utilized Microsoft Copilot, which is based on the GPT-4 architecture by OpenAI, in two contexts: the general Copilot chat included with Microsoft 365 [1], and the free Copilot chat on the GitHub website while browsing specific repositories containing existing Python scripts for DigitalMicrograph.

Results

We will demonstrate how Copilot can be used to write simple scripts by providing it with the scripting documentation PDFs included with every copy of DigitalMicrograph. We will also provide examples of the summaries Copilot can generate from existing publicly available scripts. One such summary is provided in Figure 1. These summaries are extremely useful for users who wish to modify an existing script written by another researcher, or to recall the structure of complex scripts written years ago. Finally, we will show how Copilot can be employed to modify existing scripts to alter their data processing/analysis routines.

The quality of the output from Copilot varies significantly. In some instances, Copilot produced perfectly written scripts. Other times, hallucinations led to scripts with non-existent functions or errors when executed in DigitalMicrograph. We will report on both the successful applications of Copilot to scripting for TEM experiments, and the failures, providing insights into prompt engineering for this niche application of AI.

Conclusions

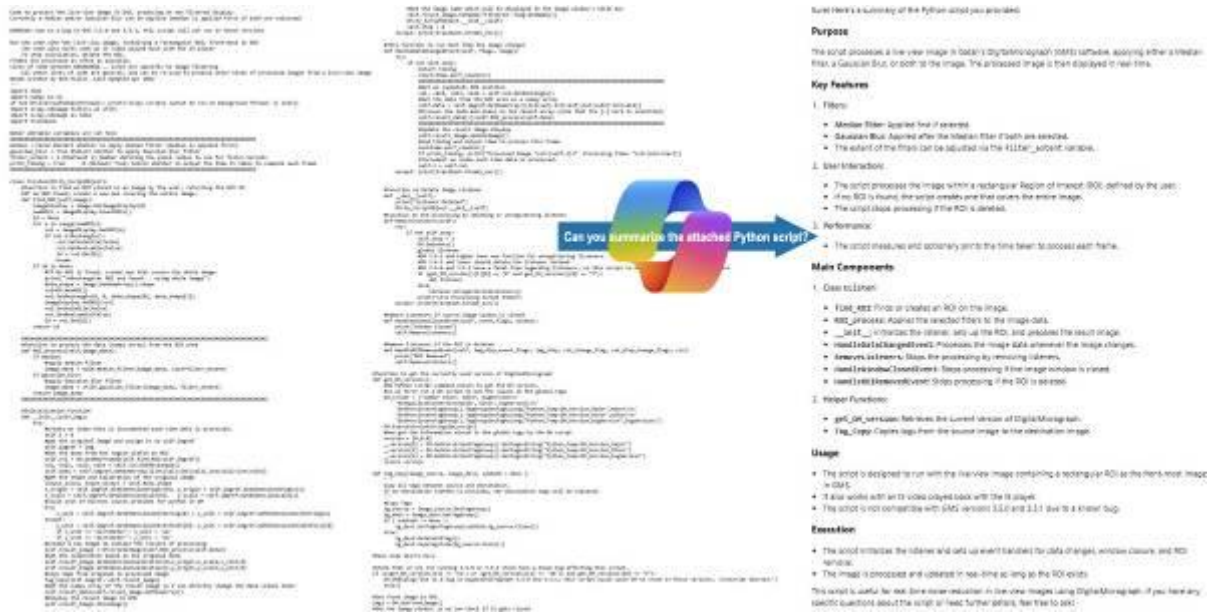
AI tools like Copilot are valuable for producing scripts that operate within DigitalMicrograph, whether by generating simple scripts, modifying existing ones, or outlining the functionality of existing code. While results are currently mixed, best practices can increase success rates, and future updates to AI tools will likely improve their output further.

References

1. Copilot https://copilot.cloud.microsoft (accessed March 4, 2025)
2. Gatan.com https://www.gatan.com/live-noise-reduction (accessed March 4, 2025)

Figure 1. A simple prompt, "Can you summarize the attached Python script?" can produce a readable and useful summary of the functionality of an existing python script. Here the script is a publicly available script from the Gatan website [2].

Fig. 1



IM 7: Electron crystallography

IM7.01(inv)
Novel algorithms for dynamical diffraction simulations

B. Mendis[1]

[1]Durham University, Dept of Physics, Durham, United Kingdom

Quantitative measurements in 4D STEM and electron crystallography require the Bragg diffracted intensities to be simulated dynamically. In a reasonably thick specimen, diffuse scattering due to phonons and plasmons is also present. For example, even for a 10 nm thick silicon sample the plasmon intensity is ~10% the elastic scattered intensity at 200 kV beam voltage. The theory of dynamical elastic diffraction is well established, and the simulation of Bragg beam intensities is implemented using either Bloch wave or multislice methods. There are pros and cons to each method. Bloch wave simulations are independent of specimen thickness, but are computationally expensive for large unit cell materials. It can only model thermal diffuse scattering phenomenologically using complex crystal potentials, which causes an unrealistic loss in intensity as the electron beam propagates through the specimen. Multislice on the other hand is suitable for any unit cell, but the computing time increases with specimen thickness. Thermal diffuse scattering can be accurately modelled using frozen phonons, although it can also be computationally expensive due to the number of phonon configurations that must be sampled.

Dynamical diffraction simulations for 4D STEM and electron crystallography are inherently computationally demanding. For example, in 4D STEM the electron exit wave must be simulated at each scan position, while in rotational electron diffraction the Bragg beam intensities are calculated at multiple specimen tilts. I will present two new algorithms for faster dynamical diffraction simulation. The first applies the physical optics principles of multislice to Bloch waves [1]. Specifically, the multislice phase grating and propagator functions are expressed in matrix form using elements of the Bloch wave structure matrix. The specimen is divided into thin slices and the electron wavefunction calculated by matrix multiplication iteratively within each slice. In this manner, the unique benefits of multislice can be realised with Bloch waves as well. The second method, called the "phase scrambling algorithm" (PSA), is applicable when Bragg beam intensities from different scattering pathways must be incoherently summed, such as in multislice frozen phonon. In PSA all scattering pathways are calculated simultaneously, with a random phase added to preserve incoherence between the different scattering events [2].

Finally, I will also present Monte-Carlo methods for phonon and plasmon diffuse scattering, which can be implemented in either a Bloch wave or multislice framework [3-4]. Unlike the phenomenological Bloch wave model there is no loss in electron intensity due to inelastic scattering, and the diffuse scattered background, such as Kikuchi bands, plasmon halos around Bragg beams, can also be accurately reproduced. The impact of inelastic scattering on the Bragg beam intensities has been experimentally measured for Si and SrTiO3 using energy filtered diffraction. The experimental results will be compared with theoretical simulations.

[1] B.G.Mendis, *Acta Cryst. A* (DOI: 10.1107/S2053273325000142).

[2] B.G. Mendis, *Microsc. Microanal.* **29** (2023) 1111.

[3] B.G. Mendis, *Acta Cryst. A* **80** (2024) 178.

[4] B.G. Mendis, *Ultramicroscopy* **206** (2019) 112816.

IM7.02(inv)
Serial precession electron diffraction – An improved flavour of a serial crystallography experiment in a TEM

S. Plana-Ruiz[1], P. H. Lu[2], G. Ummethala[2], R. E. Dunin-Borkowski[2,3]

[1]Universitat Rovira i Virgili, Servei de Recursos Científics i Tècnics, Tarragona, Spain
[2]Forschungszentrum Jülich GmbH, Ernst Ruska-Centre for Microscopy and Spectroscopy with Electrons, Jülich, Germany
[3]RWTH Aachen University, Aachen, Germany

The success of precession electron diffraction (PED) in the field of electron crystallography can be measured by how its use has led to major breakthroughs in different techniques in order to obtain better crystallographic characterizations. For instance, its use on zone-axis electron diffraction patterns for crystal structure determination [1], which later was extended to the initial 3D electron diffraction data acquisition protocol [2], or for 4D-STEM applications such as phase, orientation and strain mapping [3, 4]. This work intends to show how PED can also be used as an advantageous tool in a serial crystallography experiment for improved crystal structure analyses.

Figure 1. Representative sets of off-zone axis / randomly oriented electron diffraction patterns of barite nanocrystals with (precessed) and without (static) precession. The uniformization of reflection intensities and the disappearance of Kikuchi lines interference on the reflections is directly visible.

During last years, serial electron crystallography has gained attention for the structure determination of crystalline compounds that are sensitive to the irradiation of the electron beam [5,6]. By recording a single electron diffraction pattern per crystal, indexing hundreds or even thousands of measured particles, and merging the reflection intensities of the successfully indexed patterns, one can retrieve crystal structure models with strongly mitigated beam damage contributions [7]. However, one of the technique"s bottlenecks is the need to collect that many diffraction patterns, which done in an automated way results in a high number of patterns that are useless or not successfully indexed. This work shows how to lower this requirement by performing the serial crystallography experiment following a semi-automated routine with a precessed electron beam (SerialPED). The precession movement increases the number of reflections present in the diffraction patterns and dynamical effects related to specific orientations of the crystals with respect to the electron beam are smoothed out. This leads to more uniform reflection intensities across the serial dataset and a smaller number of patterns are required to merge the reflection intensities for good structural statistics (See Figure 1). Furthermore, structure refinements based on the dynamical diffraction theory becomes accessible, providing a novel heuristic approach for more accurate structure models. In this way, SerialPED is presented as a new technique for reliable and precise crystal structure characterization.

Materials and Instrumentation

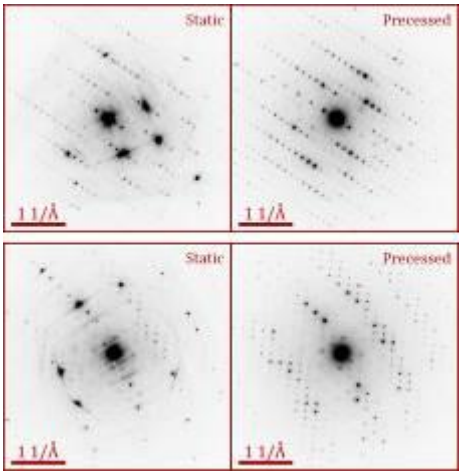
Barite ($BaSO_4$) nanocrystals are used as a test sample to prove the benefits of SerialPED with respect to SerialED. A JEOL F200 ColdFEG operated at 200kV and a TESCAN Tensor Schottky FEG operated at 100kV were used to collect Serial(P)ED data in a quasi-parallel STEM mode. A Gatan OneView camera and a Dectris Quadro detector were used in each respective microscope. Finally, a vacuum-sensitive and hydrated MOF was structurally characterized from SerialPED data.

References

1. Weirich et al., Ultramicroscopy 106 (2006) 164-175.
2. Mugnaioli et al., Ultramicroscopy 109 (2009) 758-765.

3. Viladoe et al., Journal of Microscopy 252 (2013) 23-34.
4. Cooper et al., Nano Lett. 15 (2015) 5289-5294.
5. R. Bücker et al., Nature Communications 11 (2020) 996.
6. P. Hogan-Lamarre et al., IUCrJ 11 (2024), 62-72.
7. J. C. H. Spence, IUCrJ 4 (2017), 322-339.

Fig. 1



IM7.03
Iterative phase retrieval methods in electron crystallography

T. Latychevskaia[1], T. E. Gorelik[2]

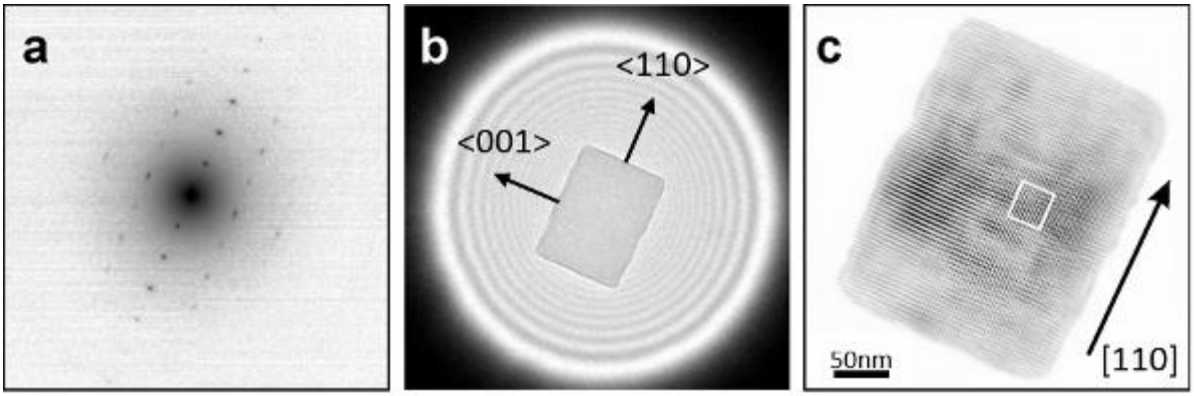
[1]Paul Scherrer Institute, Villigen, Switzerland
[2]Forschungszentrum Jülich GmbH, Jülich, Germany

Iterative phase retrieval methods are used to recover missing phase information in the detector plane and, consequently, to reconstruct the sample structure. We demonstrate the application of these methods for high-resolution structure reconstruction of nanocrystals and discuss the necessary experimental conditions.

The principles of iterative phase retrieval and related algorithms will be introduced, and the limitations of the method will be discussed. We show how an iterative phase retrieval method can be used to reconstruct a nanocrystal"s structure from two diffraction measurements—one in the near field and one in the far field—using a metal-organic framework (MOF) nanocrystal as an example. The crystal shape is directly reconstructed from the low-resolution diffraction pattern of the nanocrystal. High-resolution information is retrieved from the distribution of Bragg peaks and diffuse scattering. The obtained disordered lattice image reflects structural irregularities in the nanocrystal (Fig. 1).

Figure 1. Reconstruction images of DUT-8(Ni) MOF nanocrystals: (a) experimental electron diffraction pattern, (b) HRTEM images of the nanocrystal, (c) reconstruction. The crystal is oriented with [10] along the incident electron beam. The arrow in the reconstructions indicates the [110] crystallographic direction, corresponding to the stacking direction of Ni-dabco containing rows.

Fig. 1



IM7.04
Determination of magnetic symmetries by convergent beam electron diffraction

O. Zaiets[1,2], C. Timm[3,4], J. Rusz[5], J. Á. Castellanos-Reyes[5], S. Subakti[2], A. Lubk[4,1,2]

[1]Technical University Dresden, Institute of Solid State and Materials Physics, Dresden, Germany
[2]Leibniz Institute for Solid State and Materials Research Dresden, Dresden, Germany
[3]Technical University Dresden, Institute of Theoretical Physics, Dresden, Germany
[4]Technical University Dresden, Würzburg–Dresden Cluster of Excellence ct.qmat, Dresden, Germany
[5]Uppsala University, Physics and Astronomy, Uppsala, Sweden

Introduction

Convergent-beam electron diffraction (CBED) is a well-established probe for spatial symmetries of crystalline samples, mainly exploiting the well-defined mapping between the diffraction groups (symmetry groups of CBED patterns) and the point-group symmetries of the crystalline sample [1]. As much as this is true for scattering on electric potential, experimental results suggest that the same method can be applied for magnetic potential and symmetries [2,3].

Objectives

In this work, we extend CBED to determine magnetic point groups. We construct all magnetic CBED groups and provide the complete mapping between magnetic point groups and corresponding magnetic CBED groups. In order to verify the group-theoretical considerations, we conduct electron-scattering simulations on antiferromagnetic crystals and provide guidelines for the experimental realization.

Materials & methods

As an example of application for our method, we performed CBED multislice simulations for two antiferromagnetic materials: LaMnAsO and NiO. Unlike LaMnAsO, NiO has a magnetic unit cell twice as large as the structural one. As a result, in the case of NiO material, purely magnetic Bragg disks appear separately from structural ones. For LaMnAsO magnetic signal superimposes on structural Bragg discs.

Results

We constructed the full mapping between all 125 magnetic CBED groups and all 122 magnetic point groups for all unique crystal orientations. Simulation results for antiferromagnetic NiO and LaMnAsO are consistent with theoretical predictions. Additional calculations of signal to noise ratios and simulations of thermal diffuse background and mistilts, provide additional leverage for experimental feasibility. Also, we provide guidelines for experimental realization of this method for different types of magnetic materials (ferromagnets, antiferromagnets, etc.) and states (e.g. spin-flop).

Conclusions

Based on its feasibility using existing technology, as well as on its accuracy, high spatial resolution, and small required sample size, magnetic CBED promises to become a valuable alternative method for magnetic structure determination [4].

We gratefully acknowledge financial support by the Deutsche Forschungsgemeinschaft through Collaborative Research Center SFB 1143, projects A04 and C04, project id 247310070, and the Würzburg–Dresden Cluster of Excellence ct.qmat, EXC 2147, project id 390858490.

[1] B. F. Buxton, J. A. Eades, J. W. Steeds, G. M. Rackham, and F. C. Frank, The symmetry of electron diffraction zone axis patterns, Philos. Trans. R. Soc. London, Ser. A 281, 171 (1976).

[2] J. C. Loudon, Antiferromagnetism in NiO observed by transmission electron diffraction, Phys. Rev. Lett. 109, 267204 (2012).

[3] Y. Shen and D. E. Laughlin, Magnetic effects on the symmetry of CBED patterns of ferromagnetic PrCo5, Philos. Mag. Lett. 62, 187 (1990).

[4] O. Zaiets, C. Timm, J. Rusz, J.-Á. Castellanos-Reyes, S. Subakti, A. Lubk, Determination of Magnetic Symmetries by Convergent Beam Electron Diffraction, https://arxiv.org/abs/2410.12518 (2024)

IM7.05
Crystallographic analysis with LVEM – Exploring the diffraction potential of low-voltage TEM

J. Bačovský[1], V. Hrabalová[1], P. Štěpán[1], E. Coufalová[1], M. Klinger[2]

[1]Delong Instruments, Brno, Czech Republic
[2]Czech Academy of Sciences, Institute of Physics, Prague, Czech Republic

Low-voltage transmission electron microscopes (LVEMs), designed and developed by Delong Instruments (Brno, Czech Republic), are well known for their excellent imaging properties for samples composed of light elements. Compared to conventional TEMs, LVEMs provide exceptionally high image contrast, making them particularly useful for light materials applications in both life sciences (histology sections, proteins) and material sciences (e.g., carbon-based materials). The strong interaction between the low-voltage electron beam and the specimen guarantees high contrast, even for materials challenging for conventional TEMs.

To explore diffraction potential of LVEMs we used both recent models: LVEM5 and LVEM25E. LVEM5 is a benchtop system operating at 5 kV, ideal for routine imaging and basic characterizations of nanomaterials. LVEM25E (10–25 keV) is a versatile device combining capabilities of TEM, STEM, SEM, electron diffraction, dark field imaging, and EDS elemental analysis, allowing for comprehensive sample analysis.

Although LVEMs are better known for their imaging capabilities rather than crystallographic analysis, we explored their potential for diffraction-based studies of crystalline specimens. Since diffraction pattern analysis typically requires a higher level of expertise, we performed the analysis with the CrysTBox (Crystallographic Tool Box) software to enhance accessibility. Developed at the Institute of Physics of the Czech Academy of Sciences, CrysTBox [RM1] is a novel advanced toolkit using AI and computer vision for highly accurate, automated analysis and interactive visualization of TEM diffraction patterns. With sub-pixel precision and a high degree of automation, it simplifies routine crystallographic analyses for non-experts while offering advanced functionalities for experienced researchers.

This approach expands the accessibility of diffraction analysis to a broader user base. LVEM diffraction modes operate at significantly lower energies than conventional TEM diffraction regimes and with a slightly convergent beam carrying additional information, providing potential for more advanced analysis. The benefits of diffraction at low energy have not been comprehensively investigated, but Piazza has reported its potential [1,2]. They investigated ultrathin crystalline materials (graphene, diamane, diamanoïds) using diffraction at 5keV. Their research shows how the reduced Ewald sphere radius at lower electron energies alters diffraction patterns producing the same spot positions but with varying intensities. This phenomenon allows to distinguishing between single-layer domains with AA or AB stacking, as well as twisted bilayer graphene (2LG). In contrast, conventional TEM, typically operating around 100 keV, has an Ewald sphere that can be approximated as a plane, limiting its ability to reveal such stacking variations.

In this study, we examine how low-voltage electron diffraction can effectively be applied to samples benefiting from LVEM technology and show the advantages of combining LVEMs with CrysTBox for efficient and comprehensive crystallographic analysis, result interpretation, and visualization.

[1] PIAZZA, F., et al. Towards a better understanding of the structure of diamanoïds and diamanoïd/graphene hybrids. Carbon, 2020, 156, 234-241 DOI:10.1016/j.carbon.2019.09.057

[2] PIAZZA, F., et al.Progress on Diamane and Diamanoid Thin Film Pressureless Synthesis. C, 2021, 7(1) DOI:10.3390/c7010009

Fig. 1

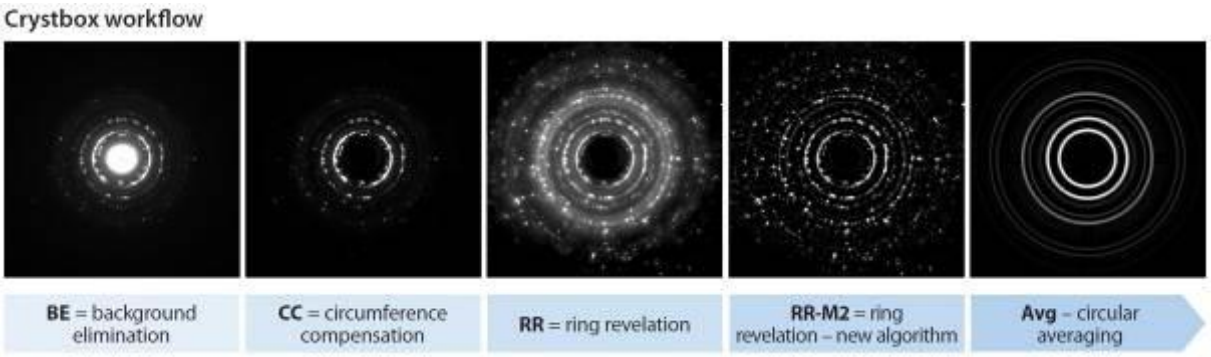
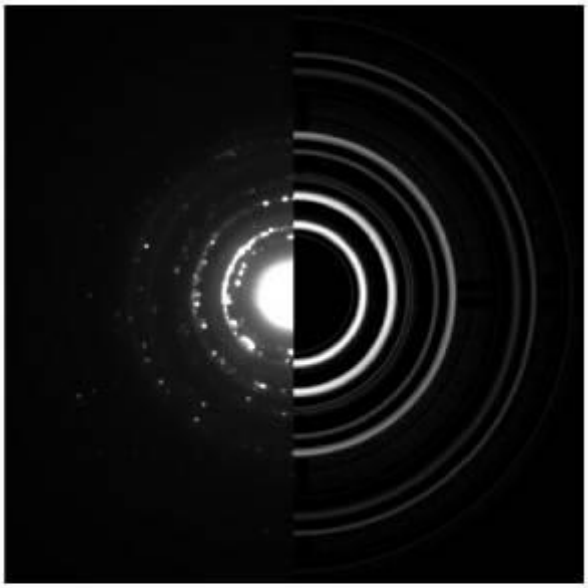
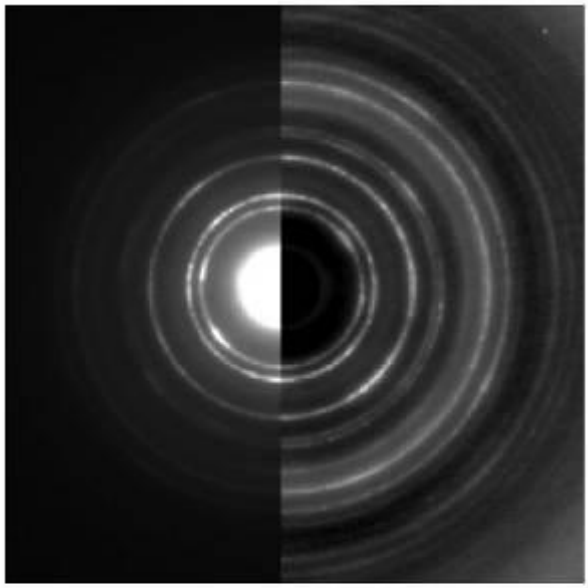


Fig. 2



Diffraction pattern of the snail shell processed by Crystbox



Diffraction pattern of the eggshell processed by Crystbox

IM7.06
3D electron diffraction expands the comprehensive TEM characterization of nanocrystalline organic semiconductors

I. Kraus[1], K. Dengel[1], M. Wu[1], J. Will[1], S. Rechberger[1], S. Maiti[2], A. Kuhlmann[3,4,5], M. Huck[3,4,5], M. Steinberger[6], L. Lüer[6,7], F. Bertram[8], H. G. Steinrück[3,4,5], T. Unruh[2], C. J. Brabec[6,7], E. Spiecker[1]

[1]FAU Erlangen-Nürnberg, Institute of Micro- and Nanostructure Research (IMN) and Center for Nanoanalysis and Electron Microscopy (CENEM), Erlangen, Germany
[2]FAU Erlangen-Nürnberg, Institute for Crystallography and Structural Physics, Erlangen, Germany
[3]Forschungszentrum Jülich GmbH, Institute for a Sustainable Hydrogen Economy (INW), Jülich, Germany
[4]RWTH Aachen University, Institute of Physical Chemistry, Aachen, Germany
[5]Paderborn University, Chemistry, Paderborn, Germany
[6]FAU Erlangen-Nürnberg, Institute Materials for Electronics and Energy Technology (iMEET), Erlangen, Germany
[7]Helmholtz Institute Erlangen-Nürnberg, Erlangen, Germany
[8]Deutsches Elektronen-Synchrotron DESY, Hamburg, Germany

Structural and nanomorphological characteristics of organic semiconductors are crucial for their properties and performance. This influence stems from the highly anisotropic optoelectronic band structures of the organic molecules, their local ordering, and the close interplay with nanoscale morphology. In bulk heterojunction (BHJ) thin films as active layers of organic solar cells (OSCs), these characteristics critically impact charge carrier transport and, ultimately, device performance. Modern TEM is a comprehensive and correlative characterization platform for such materials, granting access to nanomorphology through imaging, chemical composition via analytical methods, structure and phase through diffraction, and local crystallinity via diffraction imaging. However, 3D molecular ordering in BHJ thin films, including features such as texture and mosaicity, is currently mainly analysed using Grazing Incidence Wide Angle X-ray Scattering (GIWAXS). This method offers information averaged over large sample areas (mm^2 range) and enables in situ studies under various conditions. Yet, it lacks the comprehensive methods available within a single TEM instrument. Here, we demonstrate that 3D electron diffraction (3D ED) – a family of experimental and computational methods established for single crystal structure determination[1] – can fill this gap, enabling full structural and nanomorphological insights into radiation-sensitive and complex-structured OSCs within TEM (**Fig.1**).

We employ two model material systems for proof of principle: the fullerene acceptor $PC_{71}BM$ with the small molecule DRCN5T or the polymer P3HT as donor. STEM-EELS or EFTEM offer nanomorphology and chemical information. Energy-filtered selected area electron diffraction (EF-SAED) provides structural data with a high signal-to-noise ratio by suppressing inelastic scattering, which is especially pronounced at small scattering angles relevant for organic materials with nm-sized unit cells. SAED enables structural analysis averaged over a defined sample area. To minimize beam damage, we kept exposures below the critical dose and systematically shifted the sample for each diffraction pattern, leveraging the presumed in-plane isotropic structure of BHJs. Tilt series were acquired over approximately ±75°. Using custom-developed code, we reconstructed the 3D reciprocal space and extracted data for direct comparison with GIWAXS (**Fig.2**).

The qualitative and quantitative comparison of 3D ED and GIWAXS demonstrates excellent agreement, depicted for the DRCN5T system in **Fig.3**. The q_{rz} maps reveal matching diffraction rings and reflections. DRCN5T crystallites show a preferred edge-on and face-on orientation, with a mosaicity of ~6° from (002) and (10-1) peaks, and ~22.5° from in-plane π-stacking. A correlation between the crystal coherence lengths (~5 nm edge-on, ~20 nm face-on) and the 79x33 nm leaf-like domains observed by STEM-EELS suggests multiple crystallites within one domain, indicating grain boundaries as noted in literature.[2]

In conclusion, we validate 3D ED as a powerful tool for analysing texture and mosaicity in beam-sensitive organic thin films through comparison to GIWAXS. Integrating this method into a

comprehensive TEM workflow enables detailed characterization of polycrystalline films in general, offering distinct advantages for highly beam-sensitive organic materials.

1: M. Gemmi et al., ACS Cent. Sci. 2019, 5, 1315-1329; 2: C. Harreiß et al., Sol. RRL 2022, 2200127

Fig. 1

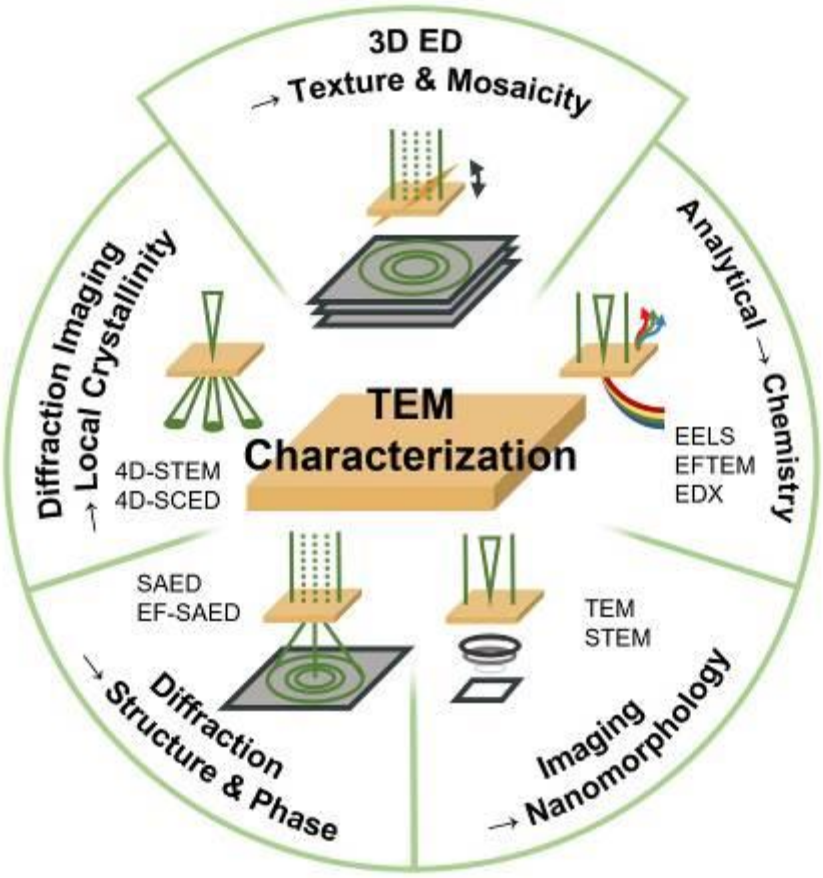


Fig.1: 3D ED adding information on 3D characteristics of molecular ordering to correlative and comprehensive TEM characterization platform for polycrystalline films.

Fig. 2



Fig.2: Processing of 3D ED datasets. I. starting from the acquired tilt series to II. the reconstruction of the reciprocal space volume and III. azimuthal integration around the q_z axis for q_{rz} map comparison to GIWAXS (Fig.3).

Fig. 3

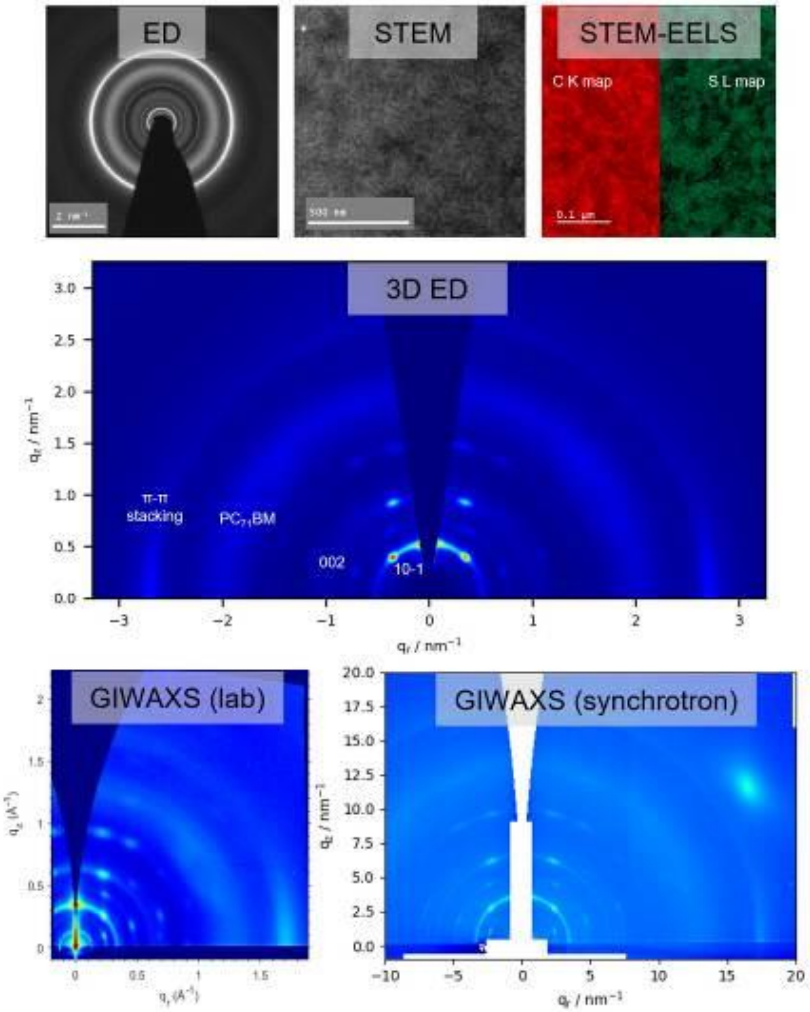


Fig.3: Results of the TEM and GIWAXS characterization of the solvent vapor annealed DRCN5T:$PC_{71}BM$ material system. The computed 3D ED q_{rz} reciprocal space map shows excellent agreement with GIWAXS (lab and synchrotron). Combination with ED, STEM and STEM-EELS enables comprehensive and correlative characterization of organic semiconductors within TEM.

IM7.P01
Indexing of zone axis spot patterns of cubic lattices with a DigitalMicrograph® script RAPID

T. E. Weirich[1], V. A. Maroufidis[1]

[1]RWTH Aachen University, Central Facility for Electron Microscopy (GFE), Aachen, Germany

Relatively small unit cell phases with cubic or pseudo-cubic symmetry still dominate most transmission electron microscopy (TEM) studies of metallic alloy systems, ceramics and semiconductors. Therefore, reliable information on the crystallographic orientation of the sample is often required on site to set up a specific experiment correctly. A standard method for aligning a zone axis (ZA) of a crystal parallel to the incident electron beam is selected area electron diffraction (SAED), which involves tilting the sample in the TEM along the goniometer axes until a symmetrical spot diffraction pattern (DP) is obtained.

While some methods have been shown to work well for post-evaluation of SAED patterns they are often less suitable for on-site crystallographic analysis in the TEM laboratory or cannot be applied for unknowns. Therefore, we have translated and adopted a previously developed code[1] for DigitalMicrograph®, which allows TEM users with GATAN® cameras to quickly index the ZA electron DPs of cubic lattices via the R_n ratio principle[1] without installing any additional software.

The program is easy to use and requires only the definition of three lines, which correspond to the three pairs of diffraction spots that are closest to the center of the SAED pattern, and specify the base geometry of the electron DP under investigation. In the next steps, the program asks the user to input the following parameters that control the calculations: number of reflections for each drawn line (calculates the average reciprocal vector length), the maximum considered value for h, k, l (default value of 2), the allowed ratio and angle errors (default values 2% and 2° respectively), the Bravais lattice type (P, I or F) that should be tested, the sign of the *uvw* ZA values and finally the limiting range for the allowed unit cell size.

The program works with both calibrated and non-calibrated ZA patterns and allows the user to quickly assess whether the material is cubic, pseudo-cubic, or neither. For calibrated patterns, the program provides the lattice parameter, which can be used to verify the material, determine the camera constant, or for phase identification in combination with a structural database.

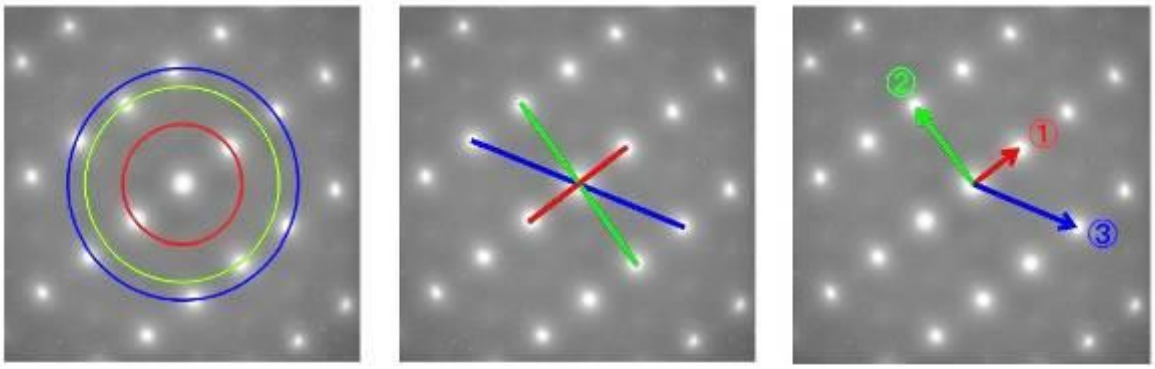
As examples, the script was used for the identification and orientation of: (i) γ-phase austenitic chrome-nickel-molybdenum steel, (ii) $D8_4$ type precipitates in austenitic chrome-nickel-molybdenum steel, and (iii) the Kikuchi pattern of an $AlZn_5Mg$ alloy. For the first case, RAPID found matches only for a cubic F-cell with ⟨011⟩ orientation and a = 3.596 Å for the γ-phase. As for the second case, all found ZA were variants of the unambiguous ⟨011⟩ orientation and the estimated lattice parameter for the identified F-lattice was a = 10.757 Å. Finally, for the test case of an uncalibrated Kikuchi pattern, the correct zone axis <114> was readily identified.

The developed program can be used for orientation determination of cubic structures, or to index Kikuchi patterns/FFTs of HR(S)TEM images. It has proven a valuable tool for on-site crystallographic analysis in the authors' TEM laboratory, where cubic materials are frequently studied and GATAN´s DigitalMicrograph® is used as the main platform for recording and analyzing electron DPs.

This work was funded by the BMBF-Germany in the project NEUROTEC (Project No.16ME0399, 16ME0398K, and 16ME0400) and DFG-German Research Foundation, Project-ID 278868966.

[1] Weirich, T. E., doi: 10.1107/S1600576724010215

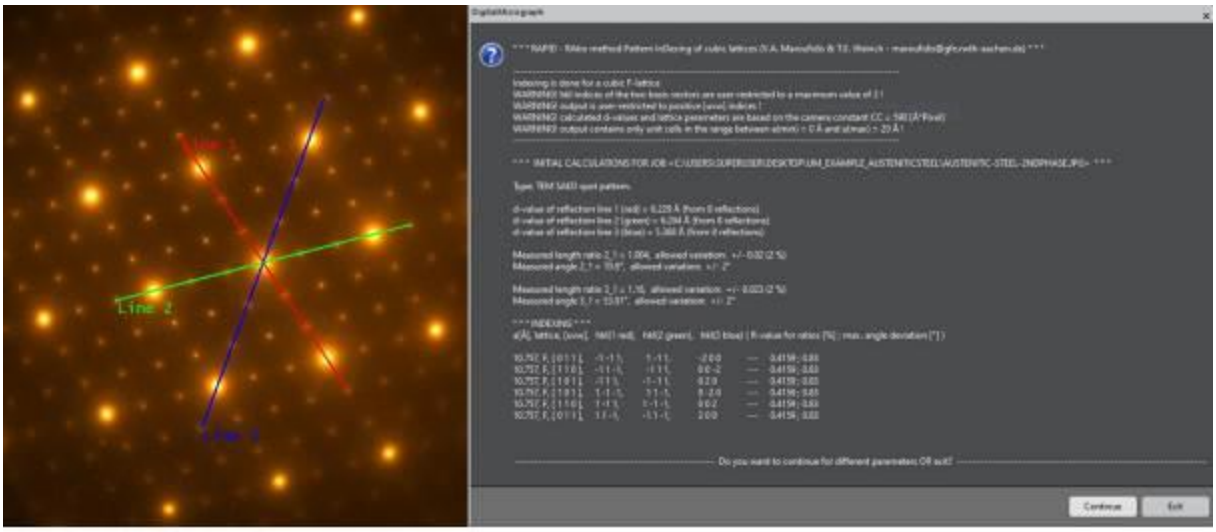
Fig. 1



(a) **(b)** **(c)**

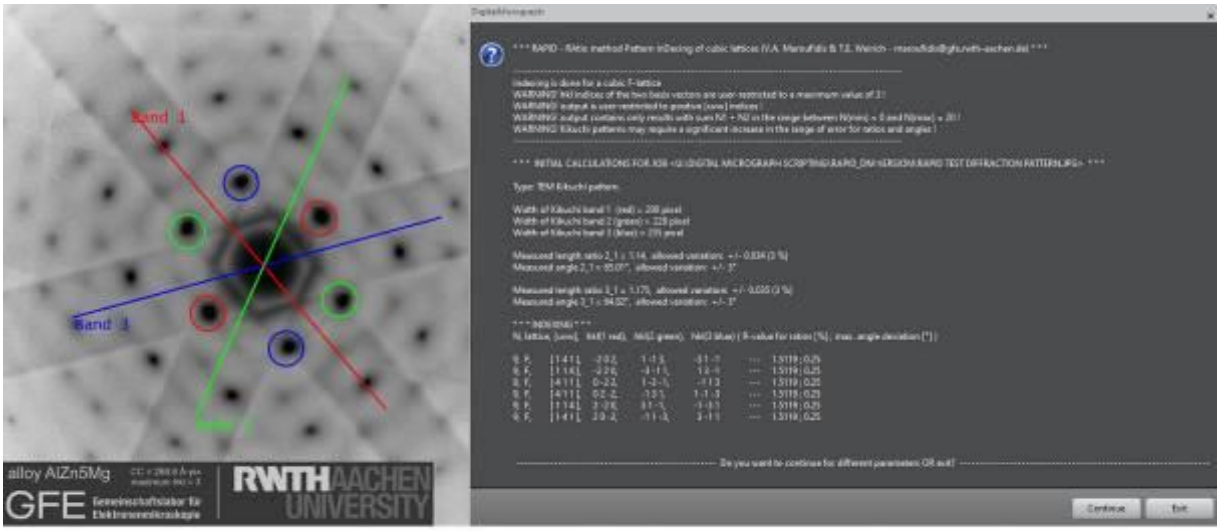
(a) The three sets of diffraction spots closest to the center of the shown SAED pattern on the left are indicated by red, green and blue rings, respectively. **(b)** For indexing with RAPID, lines must be drawn between the opposite reflections in each set in the order red 1st, green 2nd, blue 3rd as shown in the image (see text for more details). **(c)** The indexing for the corresponding base vectors obtained with RAPID refer always in the same sequence.

Fig. 2



(Left) Definition of the three lines for the identification and orientation relationship of $D8_4$ type precipitates in austenitic chrome-nickel-molybdenum steel with RAPID. **(Right)** The corresponding screen-log of the successful run for the cubic F-lattice.

Fig. 3



(Left) Definition of three Kikuchi bands for an $AlZn_5Mg$ alloy using RAPID. **(Right)** The corresponding screen-log of the successful run for the cubic F-lattice showcasing a ⟨114⟩ zone axis.

IM7.P03
Single-shot STEM imaging and electron diffraction using single bunched electron beam

K. Yamagishi[1], M. Kuwahara[1,2]

[1]Nagoya University, Energy Engineering, Nagoya, Japan
[2]Nagoya University, Institute of Material and Systems for Sustainability (IMaSS), Nagoya, Japan

Introduction

Transmission electron microscopy (TEM) is a powerful tool for advancing research in materials science, magnetic devices, macromolecule chemistry, catalysis, geology, medicine, and structural biology due to its high spatial resolution and versatile analytical capabilities. R. Bücker et al. developed Serial Nanobeam Electron Diffraction (Serial-NED), which determines protein and material structures by acquiring nanobeam diffraction (NBD) patterns while scanning an electron beam [1]. This method has demonstrated resolutions comparable to or exceeding those of X-ray free-electron lasers. However, proteins are susceptible to damage from electron beams, primarily through knock-on damage and ionization. Minimizing electron beam damage is crucial for accurate observation [2].

Objectives

To enable damage-less observation of electron beam-sensitive samples, we aimed to adapt the single-shot method, which irradiates each scanning position with a single electron pulse. This study focused on developing a synchronization system for single-shot Serial-NED.

Methods

We employed a 100-keV time-resolved TEM developed in our research group [3] and applied an optical system from our previous study on single-shot TEM imaging [4]. As shown in Fig. 1, a trigger signal for pulsed electron beam incorporation was obtained from a scanning signal system (DigiScan II, Gatan Inc.) and synchronized for single-shot imaging in STEM mode.

Results

We synchronized the optical system for single-shot operation and successfully performed single-shot STEM imaging. By using the scanning signal as a trigger and monitoring pulsed electron beam generation with an oscilloscope, we confirmed single-pulse generation. We conducted single-shot STEM imaging with a pixel time of 20 µs. Given that the acquisition limit for electron diffraction patterns with the Acousto-Optic Modulator (AOM) is ~25 ns, we performed imaging in the range of 20 ns to 10 µs. STEM-BF images were successfully acquired within this range (Fig. 2). Due to insufficient signal intensity for DF images, the imaging time was extended to 500 ns, leading to successful acquisition of STEM-ADF images (Fig. 3). Furthermore, using a Bis(dimethylglyoximato) platinum(II) thin film, we obtained single-shot diffraction patterns in STEM mode with pulse widths of 10 ms to 500 µs and an exposure time of 0.4 s (Fig. 4).

Conclusion

To achieve single-shot measurements on macromolecular materials, a higher electron dose is required for sufficient contrast and structural information. Further investigation is needed to assess sample damage due to specimen and membrane heating. We found that short-duration single electron pulses, shorter than the thermalization relaxation time, help extract damage-free information. Our future goal is to acquire diffraction patterns with even shorter pulse durations in Serial-NED conditions.

Reference

[1] R. Bücker et al., Nature Communications Vol.11, page No.996 (2020).

[2] K. Ohta, Kenbikyo, 57, 1, page 13-17(2022)

[3] M. Kuwahara et al., Appl. Phys. Lett. 121, 143503(2022)

[4] K. Nakakura., Nagoya University Master Paper(2021)

Fig 1 Developed optical system for single-shot experiment in the 100-keV TRTEM.

Fig 2 Single-shot STEM-BF image of 1-μs pulse duration in 20-μs pixel time

Fig 3 Single-shot STEM-ADF image of 500-ns pulse duration in 20-μs pixel time

Fig 4 Single-shot diffraction pattern of 500-μs pulse duration in 0.4-s exposure time

Fig. 1

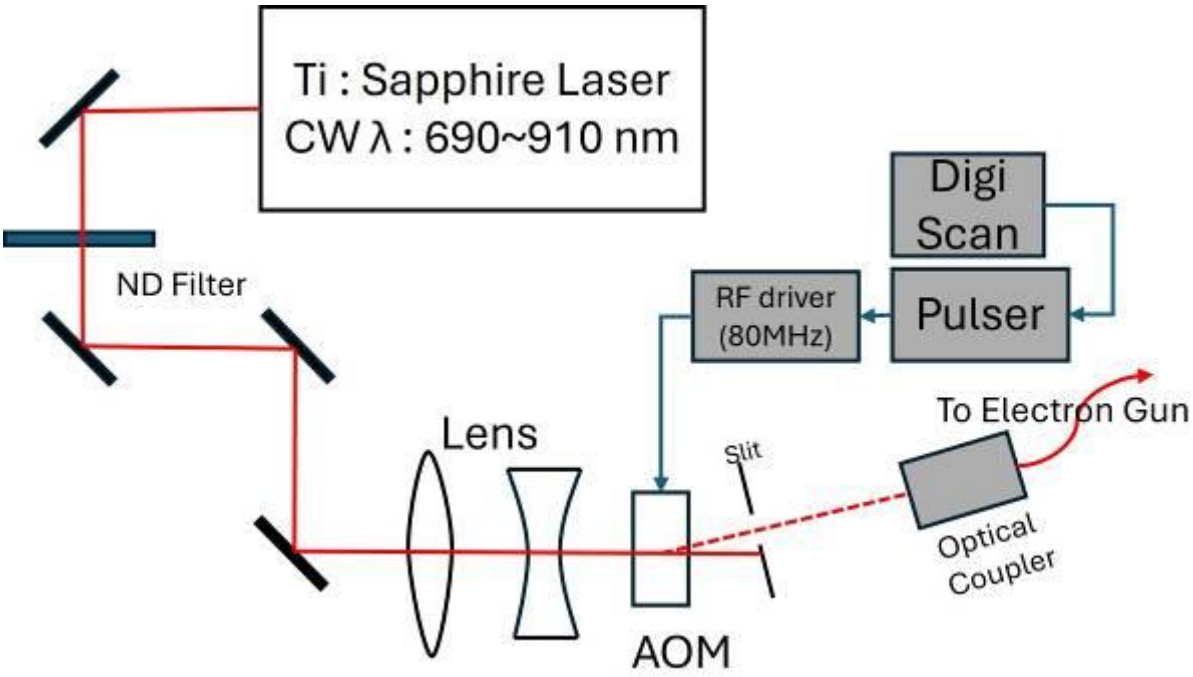


Fig. 2

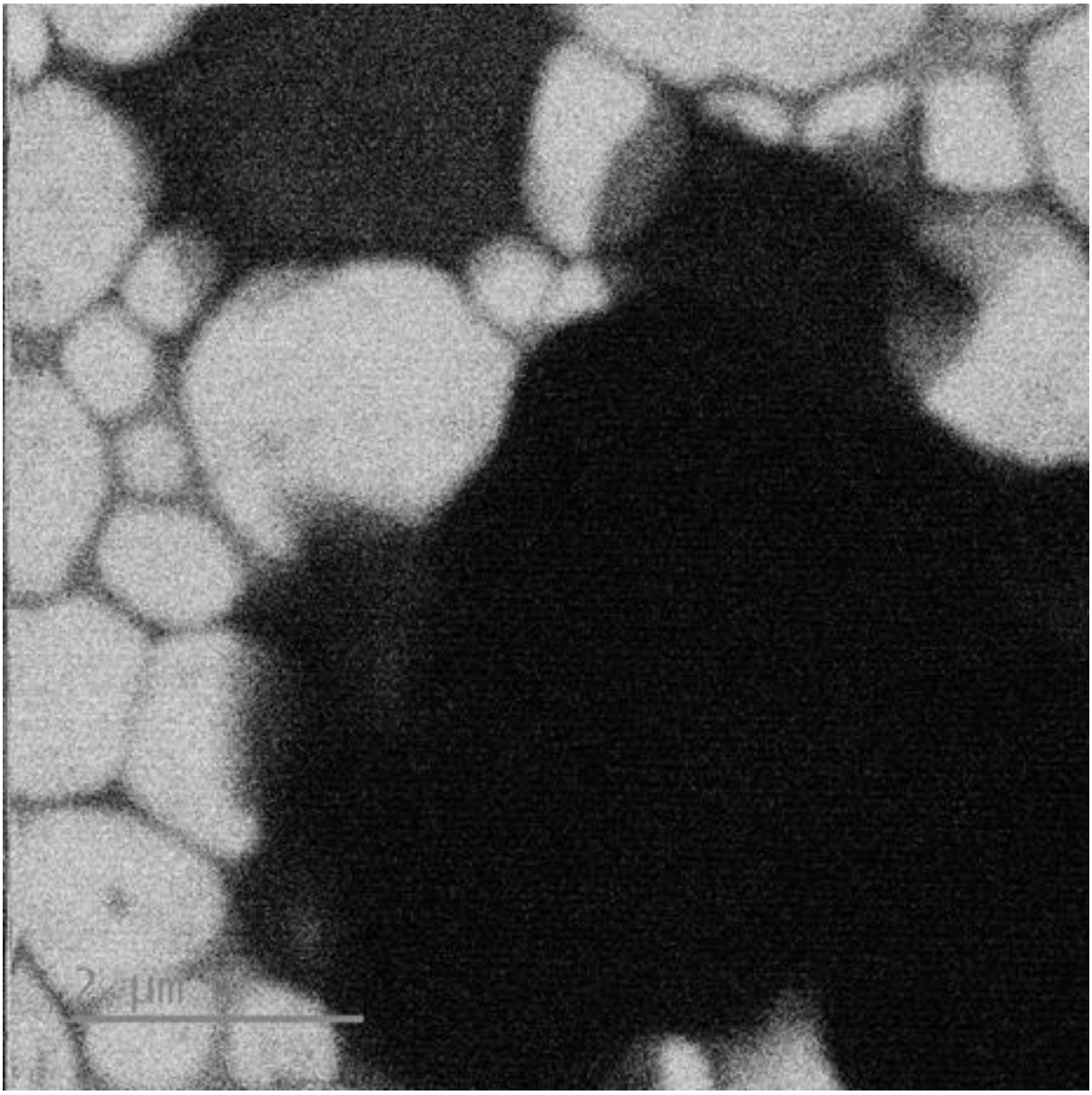


Fig. 3

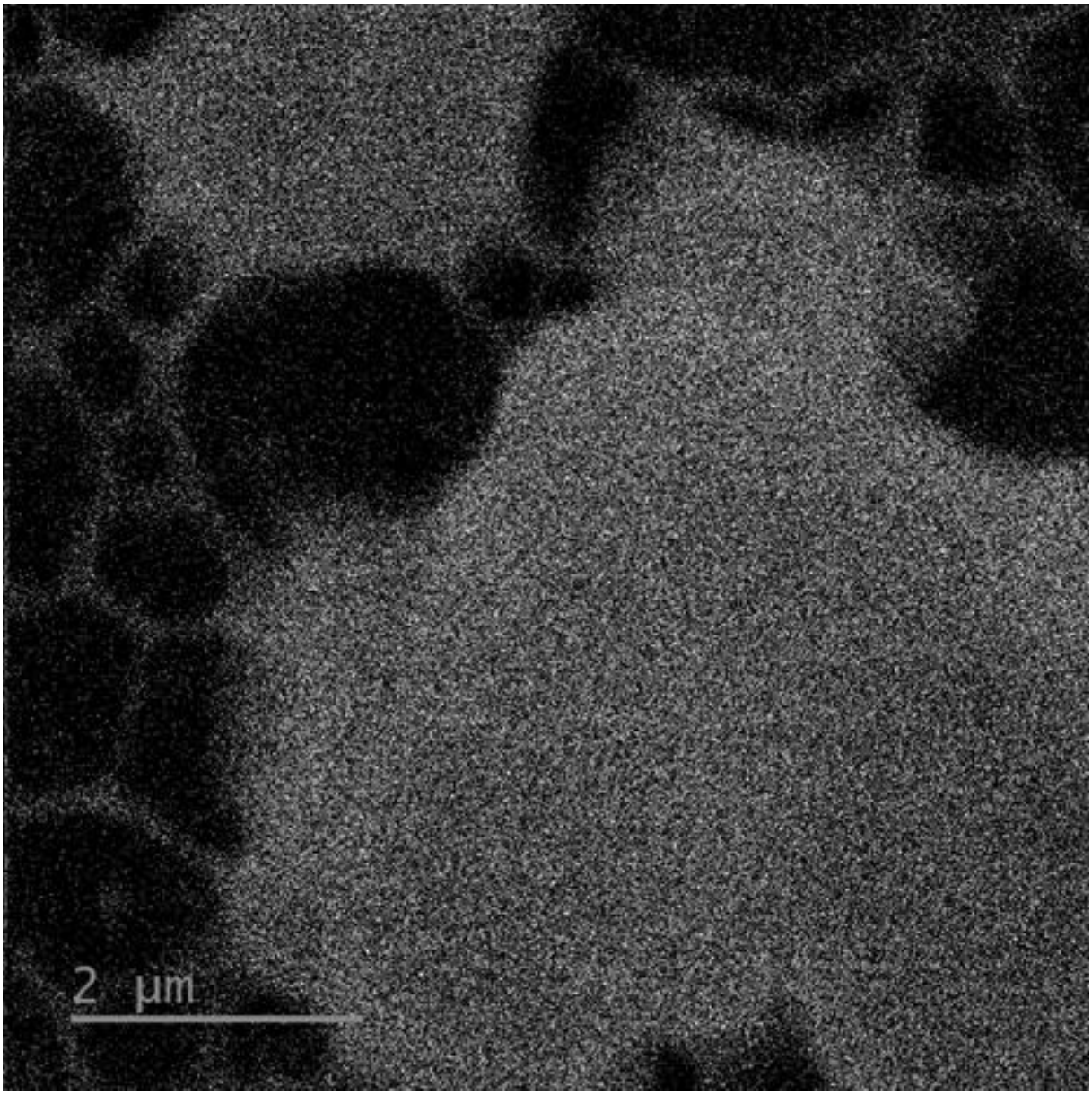
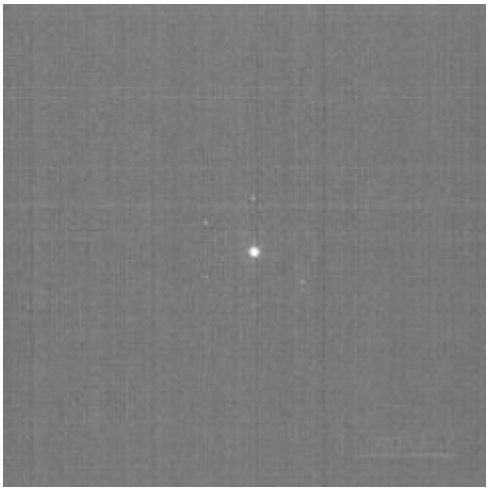


Fig. 4



IM7.P04
Can ePDF detect water in silicon nitride liquid cells?

T. E. Gorelik[1], G. Ummethala[1], A. Tavabi[1], R. E. Dunin-Borkowski[1], S. Basak[2], R. A. Eichel[2]

[1]Forschungszentrum Jülich GmbH, ER-C-1, Jülich, Germany
[2]Forschungszentrum Jülich GmbH, Institute of Energy Technologies - Fundamental Electrochemistry (IET-1), Jülich, Germany

Recent developments in in situ and environmental TEM have significantly advanced our ability to study dynamic processes at the nanoscale. Innovations in liquid and gas cell TEM have enabled real-time imaging of chemical reactions, material transformations, and biological processes under realistic conditions. Many of these processes are inherently heterogeneous and involve precipitation or crystallization. The most straightforward method for detecting early crystallization states in a liquid phase is the analysis of the electron Pair Distribution Function (ePDF).

Amorphous silicon nitride is one of the most widely used materials for in situ TEM liquid cells. As a result, the contribution of the membrane signal is inevitably present in the diffraction data of the sample. It is therefore crucial to analyse and understand the contributions of both the Si3N4 membrane and water as a solvent to accurately assign evolving structural features and distinguish them from the signal of the reaction species.

Detecting water in the presence of Si3N4 is not a trivial task, as most interatomic distances in their respective Pair Distribution Functions overlap. Consequently, rather than tracing the appearance of additional peaks, we must analyse the distribution of intensities, which are generally less reliable in ePDF due to multiple scattering.

Here, we present our results on the ePDF analysis of water-filled Si3N4 chips, demonstrating the information that can be extracted from ePDF data and discussing the limitations of the procedure.

IM7.P05
Expanding the crystallographic potential of low voltage transmission electron microscopes – Dark-field imaging capabilities of LVEM25E

V. Hrabalová[1], J. Bačovský[1], P. Štěpán[1], E. Coufalová[1]

[1]Delong Instruments, Brno, Czech Republic

The Low Voltage Electron Microscopes: LVEM25E, developed and manufactured by Delong Instruments (Brno, Czech Republic), is well-known for its exceptional performance in life science imaging, where low-energy electrons provide high image contrast for samples composed of light elements. Its primary applications include biological sections and particle-like life science samples, such as proteins, which benefit from reduced or even completely eliminated staining during sample preparation while still achieving results comparable to those of conventional TEMs that require post-staining protocols.

The latest version of the LVEM25 series, the All-in-One Electron Microscope LVEM 25E, introduces a technological advancement—dark-field imaging in both TEM and STEM modes. This new capability significantly enhances the microscope's multimodal functionality, which now includes TEM with electron diffraction at 25 keV, STEM at 10 and 15 keV, SEM with backscattered electron detection at 15 keV, and EDS for elemental analysis[RM1] . Despite the well-known strengths of this instrument in imaging biological sections, its multimodality opens new doors to comprehensive sample analysis using techniques that were previously exclusive to conventional high-voltage TEMs. These upgrades position LVEM25E as a versatile tool for advanced sample characterization.

Especially samples composed of light elements, such as graphene and other carbon materials, can také the advantage of LVEMs. Using low beam energy increases elastic scattering, thereby enhancing the image contrast in bright field imaging and increasing the signal in dark field modes [1].

This study focuses on the newly integrated dark-field imaging mode, exploring its potential for analyzing crystalline materials. In TEM dark-field mode, electrostatic deflectors shift the selected diffraction maximum onto the optical axis, guaranteeing optimal optical settings and thereby minimizing aberration effects.

In STEM dark-field mode, a specific diffraction maximum is selected using an objective aperture, enabling precise structural analysis.

We evaluated dark-field imaging across a diverse range of samples from both life sciences and materials science. Notably, metallographic samples, typically analyzed using high-voltage TEMs, produced remarkably interesting results under low-voltage conditions. These results revealed the potential of dark-field imaging in low-voltage electron microscopy expanding the analytical capabilities of LVEM25E beyond its conventional applications.

[1] R.F., Egerton, 2015. Opportunities for Low-Voltage TEM/STEM. Online. *Microscopy and Microanalysis*. Vol. 21, S3, pp. 349-350. ISSN 1431-9276. https://doi.org/10.1017/S1431927615002548.

Fig. 1: Aluminium TEM and STEM bright field and dark field imaging.

Fig. 2: β-phase in Al-Mg-Si alloy. Sample courtesy of prof. Kenji Matsuda, University of Toyama, Japan.

Fig. 1

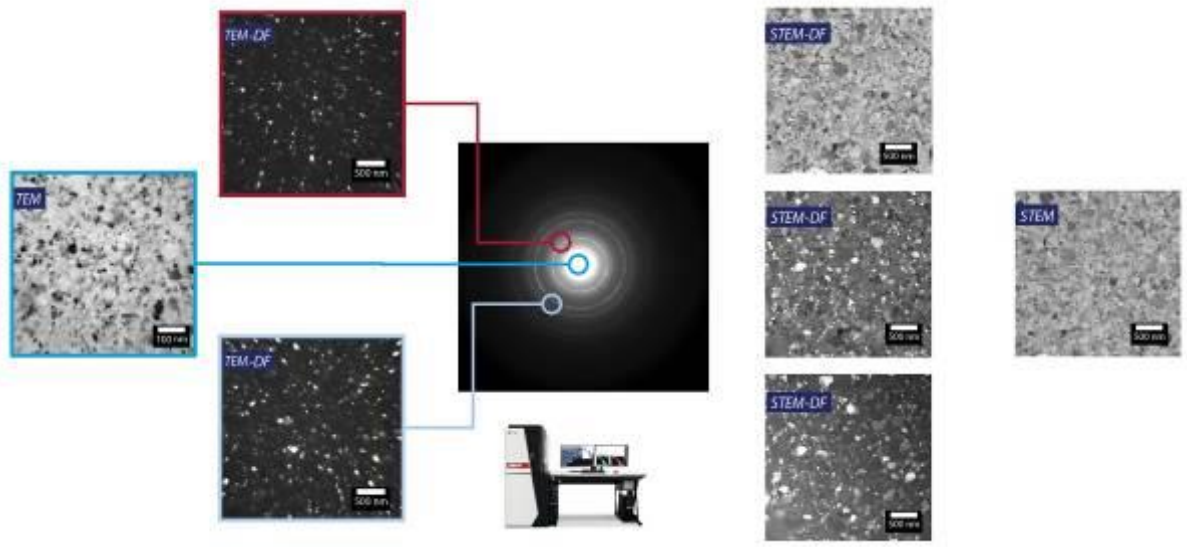
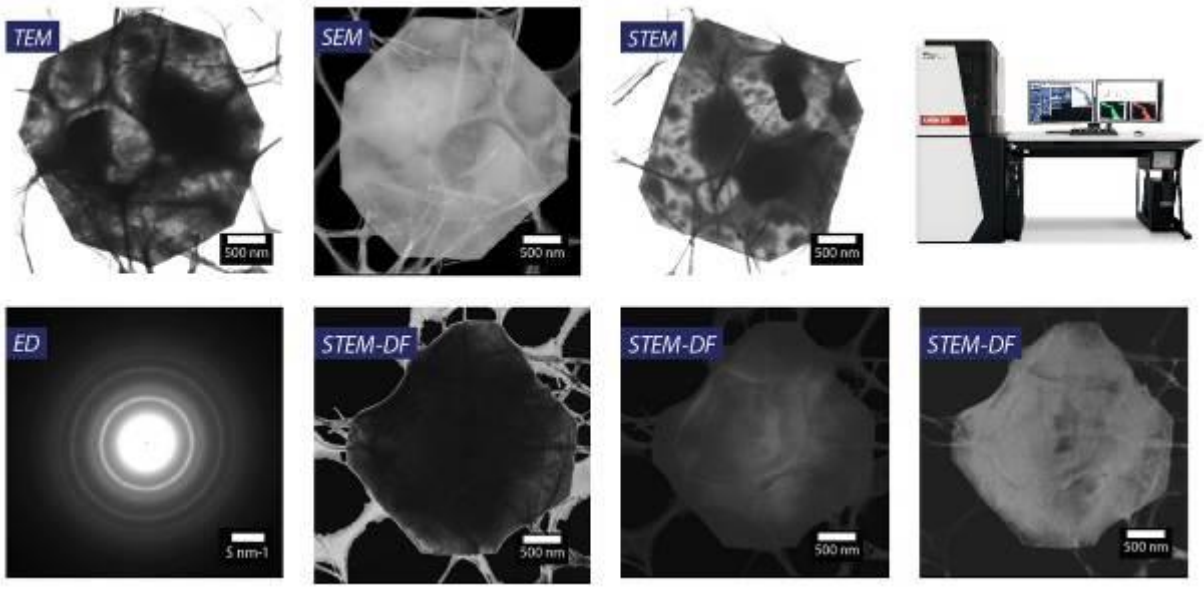

TEM-DF
TEM
TEM-DF
STEM-DF
STEM-DF
STEM-DF
STEM

Fig. 2


TEM
500 nm
SEM
500 nm
STEM
500 nm
ED
5 nm-1
STEM-DF
500 nm
STEM-DF
500 nm
STEM-DF
500 nm

Late Breaking Abstracts

MSLB.P01
Visualization of phase behavior of poly[(ε-caprolactone)-*b*-poly(L-lactide)] multiblock copolymer blends with poly(D-lactide)

Y. Pieper[1], A. Mandlule[1], Y. Liu[1], F. M. Toma[1], A. T. Neffe[1,2]

[1]Helmholtz-Zentrum Hereon, Institute of Functional Materials for Sustainability, Teltow, Germany
[2]Brandenburg University of Technology, Institute of Materials Chemistry, Senftenberg, Germany

Introduction In terms of promoting sustainable polymers, in addition to develop materials derived from renewable resources that are environmentally degradable, understanding of their structure-property-relationships is essential. Blends of poly[(ε-caprolactone)-*b*-(L-lactide)] multiblock copolymers (MBCs) with poly(D-lactide) (PDLA) are a modular material system that can be tuned in properties via their block lengths and mixing ratios.

Objective Understanding the structure-property relationships of phase-separating multiblock copolymers is challenging. Key aspects in this respect are the visualization of phases and the assignment of phases to chemical structures. The aim of this study was to study the influence of the composition of blends of P(PCL-*b*-PLLA)n MBCs and PDLA as well as their block lengths on the formation of different crystalline phases, including PLA stereocomplexes (SCs) and homocrystallites (HCs).

Materials and Methods The MBCs were synthesized by a block extension by means of a polycondensation reaction. For characterization, films were produced by mixing solutions of the MBC with PDLA in predetermined weight percentages and subsequent evaporation of the solvent. We show the formation of crystallite types and their sizes by correlative studies with Transmission Electron Microscopy (TEM), Polarized Optical Microscopy (POM) and Atomic Force Microscopy (AFM).

Results The phase structures of the films with different compositions were investigated by POM and AFM and were assigned to the different components in heating experiments. Mixtures in which no SC formation occurred showed large spherulitic structures of PLA HC, while samples with SCs revealed a clear phase separation and smaller SC crystallites. An increase in PCL content led to a decrease in PLA HC crystallite size, indicating inhibition of crystallization by PCL. The radial spherulitic structures consist of many small, needle-shaped crystals radiating from a central nucleation point. The agglomerates of crystallites are up to 100 µm in size and protruded from the surface, reaching heights of up to 250 nm (AFM). SCs likely acted as nucleating agents for PLA HCs, leading to large spherulites of PDLA on top.

Thenano-andmicrophase-separatedmorphologiesoftheblendswereinvestigatedby TEMandcorrelatedwiththeAFMatthesamesites. With increasing MBC content, the PLA phase domains get significantly smaller from around 100 nm to 10 nm. The visualization supports the conclusion that SCs act furthermore as nucleation points for PCL, which is supported by the covalent linkage by of PCL to the PLLA part of the SC´s. The correlationmoreover enabled assignment of thecrystallinedomains topolymercomponents.

Conclusion The correlative study of the MBCs and their mixtures with made it possible to decipher the phase morphology. The study has provided a better understanding of the parameters influencing the phase morphology and thus the relationship between structure and properties. SC formation is favored when PCL acts as a nucleating agent and is suppressed when the proportion of PDLA is too small. The work was able to show that systematic changes in the molecular structure have a significant influence on crystallinity and thus on the properties of MBCs. In the future, this may

contribute to the targeted production of design blends with defined properties and their application-oriented use.

MSLB.P03
Microstructure of Ag-Cu alloy nanotwinned film on SiC chips for thick Cu wire bonding on Ag sintered cladding of Cu stress buffer layers

T. H. Chuang[1], Y. T. Chen[2], Y. H. Chen[2]

[1]Wire Technology Inc. (WT), Taichung City, Taiwan
[2]National Taiwan University, Institute of Materials Science and Engineering, Taipei, Taiwan

Instruction-For an EV power module, reliable interconnection between chip and substrate to enable signal and power transmission is necessary. Thick copper (Cu) wire or ribbon is increasingly adopting as the bonding material, which offers high strength, excellent electrical conductivity, and improved reliability. Nevertheless, the high hardness of Cu can cause cracks and damage to the packaging die during the ultrasonic bonding process, especially for the SiC die due to its brittle nature. To solve this problem, an innovative method, called "die top metallization" has been proposed, that a Cu foil is cladded on the SiC chips via an Ag sintering method to buffer the external load during Cu wire or ribbon ultrasonic bonding.

Objectives-It is known that the a nanotwinned (nt-) film has high density of (111)- orientation and the diffusion on (111) plane is 3 to 5 orders of magnitude higher than that of (100) or (110) orientation. The merits of nt- films on direct die bonding for 3D-IC packages and Ag sintered die bonding for power modules. A concept is proposed in this study using the advantages of nt- films to reduce the porosity and enhance the bonding strength for the Ag sintered cladding of Cu stress buffer layers on SiC chips for the ultrasonic bonding of power modules using Cu thick wires and ribbons.

Material&method-The SiC chips were sputtered with Ag-Cu alloy nanotwinned film. Cu foils served as the stress buffer layer and were cladded on SiC with alloy nanotwinned film using pre-formed Ag sintered sheet. Cu thick wire and Cu ribbon were employed for the ultrasonic bonding on SiC chips and DBC substrates.

Results-Cross-sectional image of the Ag-8.2Cu alloy nanotwinned film sputtered on Ti pre-coated SiC chips contains columnar grains with a large amount of parallel aligned twins with an average twin spacing about 20 nm. High-resolution transmission electron microscopy images indicated that the atomic distance can be measured to be 0.239 nm. The Ag (111) and Cu (111) interplanar spacings are 0.235 nm and 0.208 nm, respectively. Therefore, the twin structure of this Ag-8.2 Cu alloy film is close to the interplanar spacing of Ag, and the cross-section is stacked along the deposition direction with the (111) plane. It was found that the selected area diffraction pattern corresponds to the Ag lattice constant, and the diffraction point has a high match with the Ag lattice constant. The employment of this Ag-8.2Cu nanotwinned film for the Ag sintered cladding on Cu foils resulted in very low porosities (1.3 to 2.1 %) and high cladding strengths (26.1 to 48.3 MPa) for various thicknesses of Cu foils. Through the ultrasonic bonding of Cu thick wires on the SiC chips sintered cladded with nanotwinned Cu stress buffer layers, satisfactory joints were obtained as evidenced. Non-destructive inspection using both scanning ultrasonic microscopy (SAM) and X ray tester indicated that no cracks can be found in the SiC dies after ultrasonic bonding. In addition, sufficient bond foot length and width with sound shear strengths of 5.8 Kgf and 6.3 Kgf were achieved at the interface of Cu wire/SiC chip and Cu wire/DBC substrate, respectively.

Conclusion-The merits of porosity reduction and strength increase for the Ag sintering of Cu foils on SiC chips through alloy nanotwinned film were verified. Ultrasonic bonding resulted in sound bonding strengths at the interface of Cu wire/SiC chip and Cu wire/DBC substrate, respectively.

Fig. 1

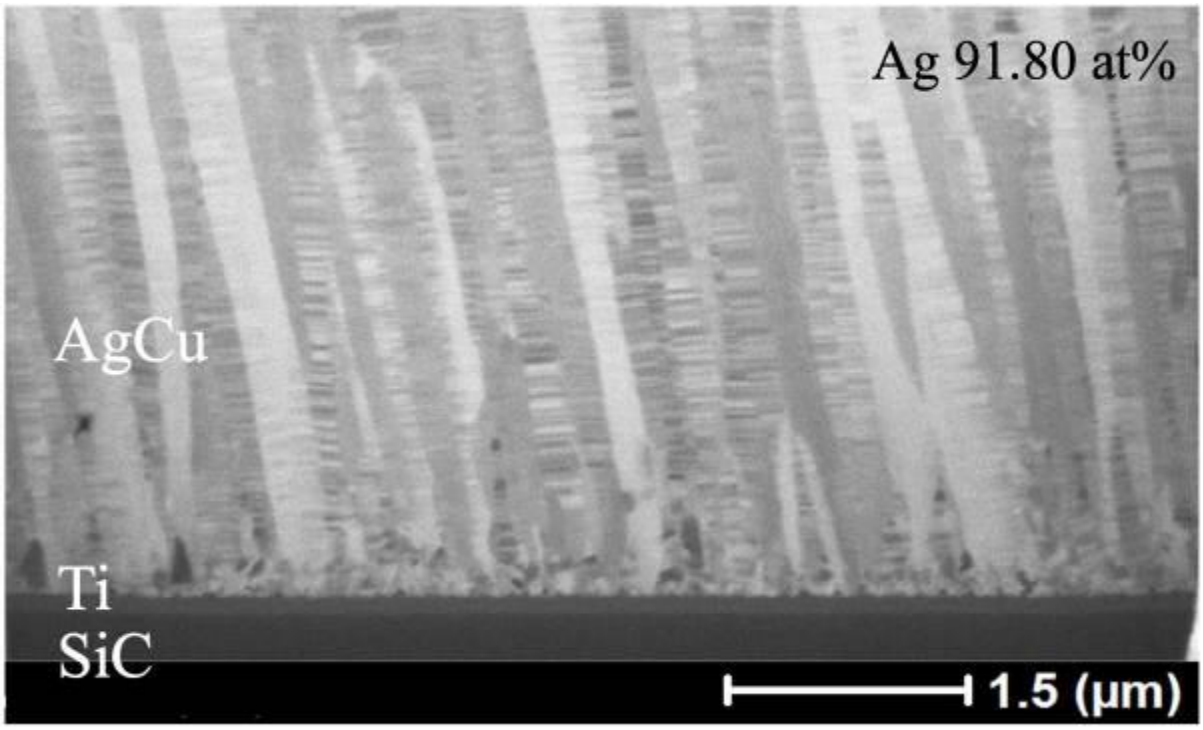

Ag 91.80 at%
AgCu
Ti
SiC
1.5 (μm)

Fig. 2

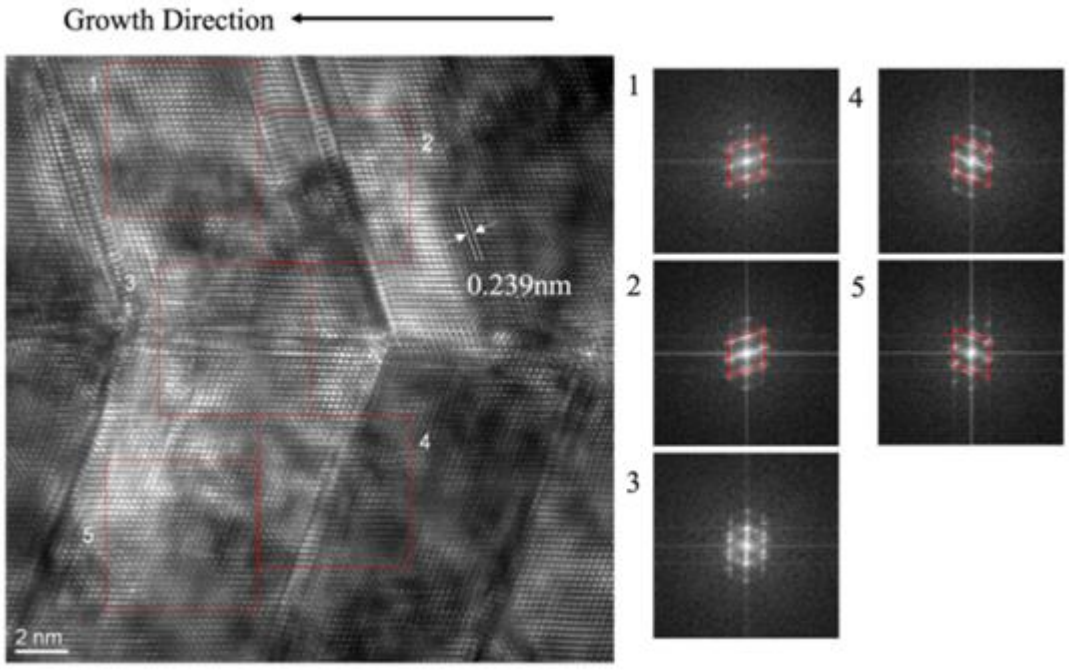

Growth Direction
1
2
3
4
5
0.239nm
2 nm

Fig. 3

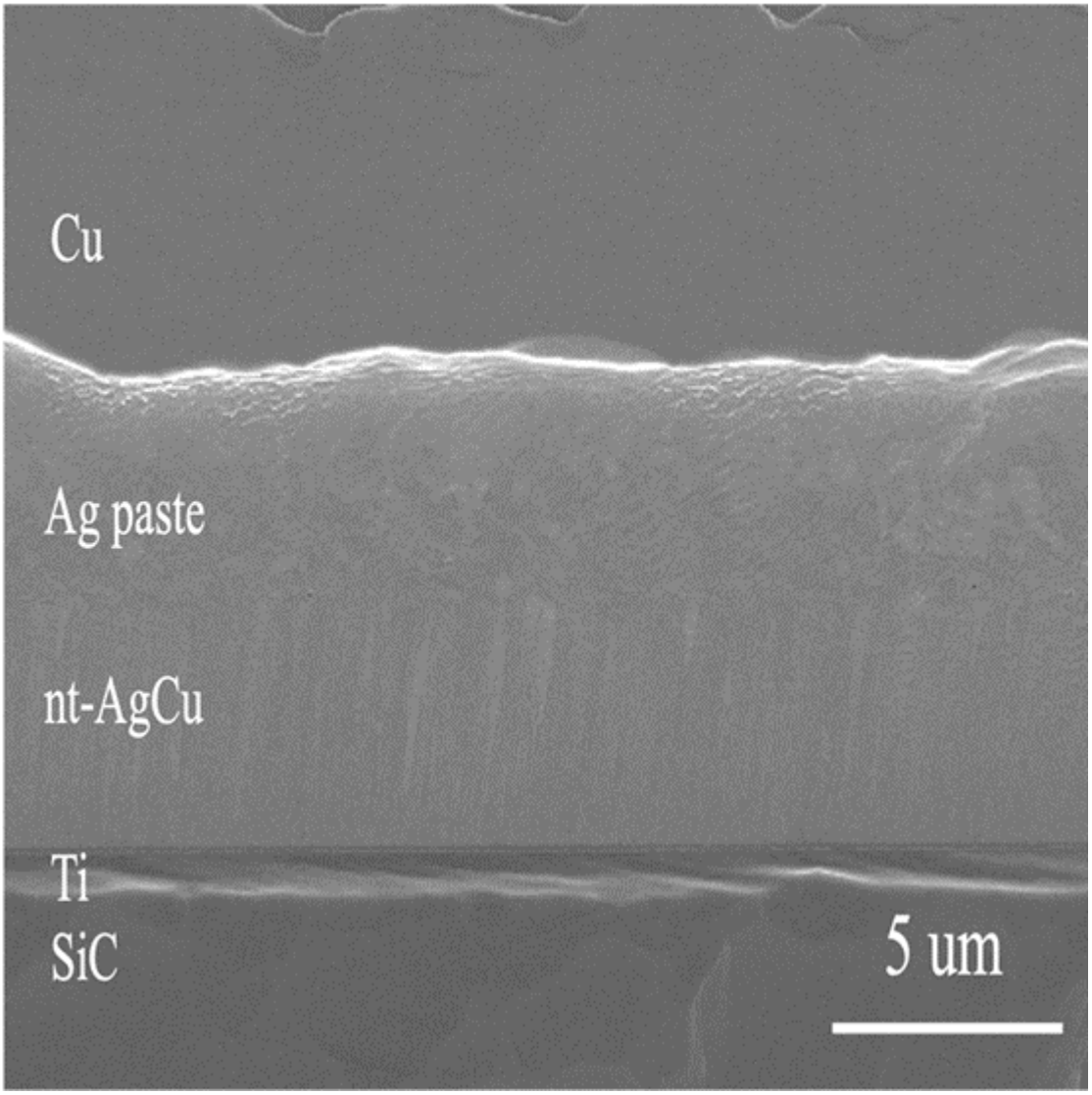
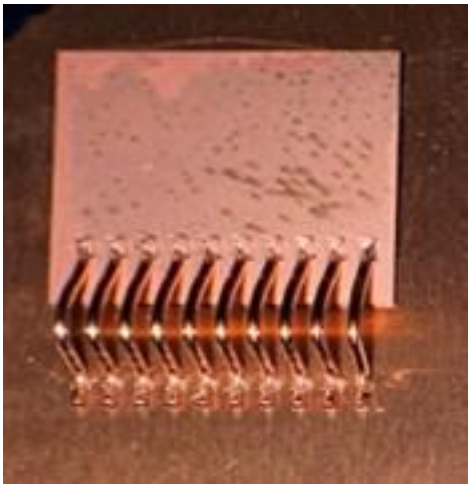


Fig. 4



MSLB.P04
Ecofriendly synthesis of cellulose-silver nanocomposite and the evaluation of their antibacterial activity

I. Charti[1]

[1]laboratoire physico-chimie des matériaux appliqués, Mohammedia, Morocco

Researchers are actively working on the development of innovative materials sourced from renewable and environmentally sustainable resources to generate valuable products. Over the past few decades, materials based on polysaccharides have emerged as highly promising options due to their abundant availability and ecological viability. Furthermore, their utilization across diverse fields has witnessed [1,2].

In this work, we report on a facile and environment-friendly microwave method to prepare cellulose/Ag nanocomposites using palm date wood extract as an effective reductant for silver ion onto surface of cellulose. In order to obtain cellulose microfiber (MFC) from date palm wood fibers, a succession of specific chemical treatments including alkalization and whitening treatment have been developed.

Cellulose obtained have been characterized by different techniques. FTIR spectra confirmed the removal of non-cellulosic components after chemical treatments and XRD confirmed the presence of cellulose pics.

Experimental results indicated that the palm date wood extract was an effective reductant for silver ions favoring the formation of silver with higher crystallinity and mass content in the nanocomposites.

Silver nanoparticles were identified within the cellulose matrix through Scanning Electron Microscopic (SEM). The FTIR characterization studies demonstrated the existence of silver in the cellulose nanocomposites. Additionally, the XRD analysis confirmed the formation of silver peaks within these composites.

Qualitative antibacterial tests towards gram negative (Escherichia coli) and gram positive (Micrococcus luteus) bacteria are carried out and the results demonstrated that the Ag-MFCs inhibit the bacteria growth, with 9–13 mm of inhibition zone for the both bacteria. These results demonstrated that the Ag-MFC possess suitable and promising antibacterial behavior and could be used for industrial and technological application.

Keywords : Silver nanoparticles; cellulose-silver nanocomposite; Antimicrobial activity

[1] Salama, A., et al., Cellulose–silver composites materials: Preparation and applications. Biomolecules,
2021. 11(11): p. 1684.

[2] Khenblouche, A., et al., Extraction and characterization of cellulose microfibers from Retama raetam
stems. Polímeros, 2019.

MSLB.P05
Electron microscopy analysis of organic thin-film transistors on the device level

S. Hettler[1], M. Peterlechner[1], U. Zschieschang[2], H. Klauk[2], Y. M. Eggeler[1]

[1]Karlsruhe Institute of Technology, Laboratorium für Elektronenmikroskopie, Karlsruhe, Germany
[2]Max Planck Institute for Solid State Research, Stuttgart, Germany

Introduction

In organic thin-film transistors (TFTs), the semiconductor is a thin layer of conjugated organic molecules. The performance of organic TFTs is strongly influenced by the carrier mobility in the semiconductor layer.[1-2] The crystal structure of the organic-semiconductor layer has a critical impact on this mobility, and a precise knowledge of the microstructure in dependence of the film-deposition parameters is required to be able to optimize the TFT fabrication process. In this work, we apply transmission electron microscopy (TEM) to study the microstructure of thin films and functional TFTs based on several different state-of-the-art organic semiconductors.[1-3]

Objectives

The TEM analyses of OTFT devices aim at resolving the relation between the microstructure of the organic-semiconductor layer and the performance of the TFTs.

Materials & Methods

Organic-semiconductor layers were fabricated by thermal vacuum sublimation of the molecules, including pentacene and DPh-DNTT.[3] Figure 1 shows a sketch of the DPh-DNTT crystal structure, where the long axis of the molecule agrees with the [001] crystal axis. The layers were deposited directly onto ultrathin amorphous carbon film TEM grids and onto the actual gate dielectric employed in the TFTs (Si substrate, Al gate electrode, AlOx gate dielectric, Au source/drain contacts). TEM cross-section lamellae of the TFTs were prepared by focused ion beam (FIB). TEM measurements including selected-area electron diffraction (SAED) were performed in a Titan^3 (TFS) operated at 300 keV and using electron doses below 2 $e^{-}A^{-2}s^{-1}$.

Results

SAED analyses performed on the organic semiconductor make it possible to identify their crystal structure. Figure 2 shows an SAED pattern of a 50-nm-thick pentacene film with the principal reflections indicated. The pattern reveals that the pentacene crystallized in its "bulk" phase (COD #4109834). The logarithmic scale reveals the presence of a weak forbidden [100] reflection, which is attributed to double diffraction in the relatively thick film (50 nm). Most of the films investigated here are found to grow in "standing" configuration, meaning that the long axis of the molecules ([001] in the crystal) agrees with the normal of the substrate. Only for DPh-DNTT, considerable portions are found in "lying" configurations, as indicated by the presence of [001] reflections in corresponding power spectra (Figure 3), suggesting a different growth mechanism. Figure 4 shows a TEM image of a cross-section prepared from a DPh-DNTT TFT, revealing the expected layers. Periodic lines are visible in the DPh-DNTT and the line periodicity (2.4 nm) corresponds to the [001] interplanar distance, confirming that the first layer of the active material grows with the molecules standing approximately upright on the surface, which is the preferred molecular orientation for lateral field-effect transistors.

Conclusion

The performed EM experiments make it possible to analyze the crystalline microstructure of the organic molecules both on a larger scale using plan-view TEM specimens and on the local scale of

devices using cross-section lamellae prepared by FIB. This information is used to understand the performances of the specific organic molecules as semiconductors in TFTs.[4]

[1]Hendrich et al, *Adv Synth Catalysis*, **363**, 549-557, 2021.
[2]Hendrich et al, *Adv Synth Catalysis*, **363**, 1401-1407, 2021.
[3]Kraft et al, *Organic Electronics* **35**, 33-40, 2016.
[4]Funded by DFG: CRC1249, 281029004.

Fig. 1

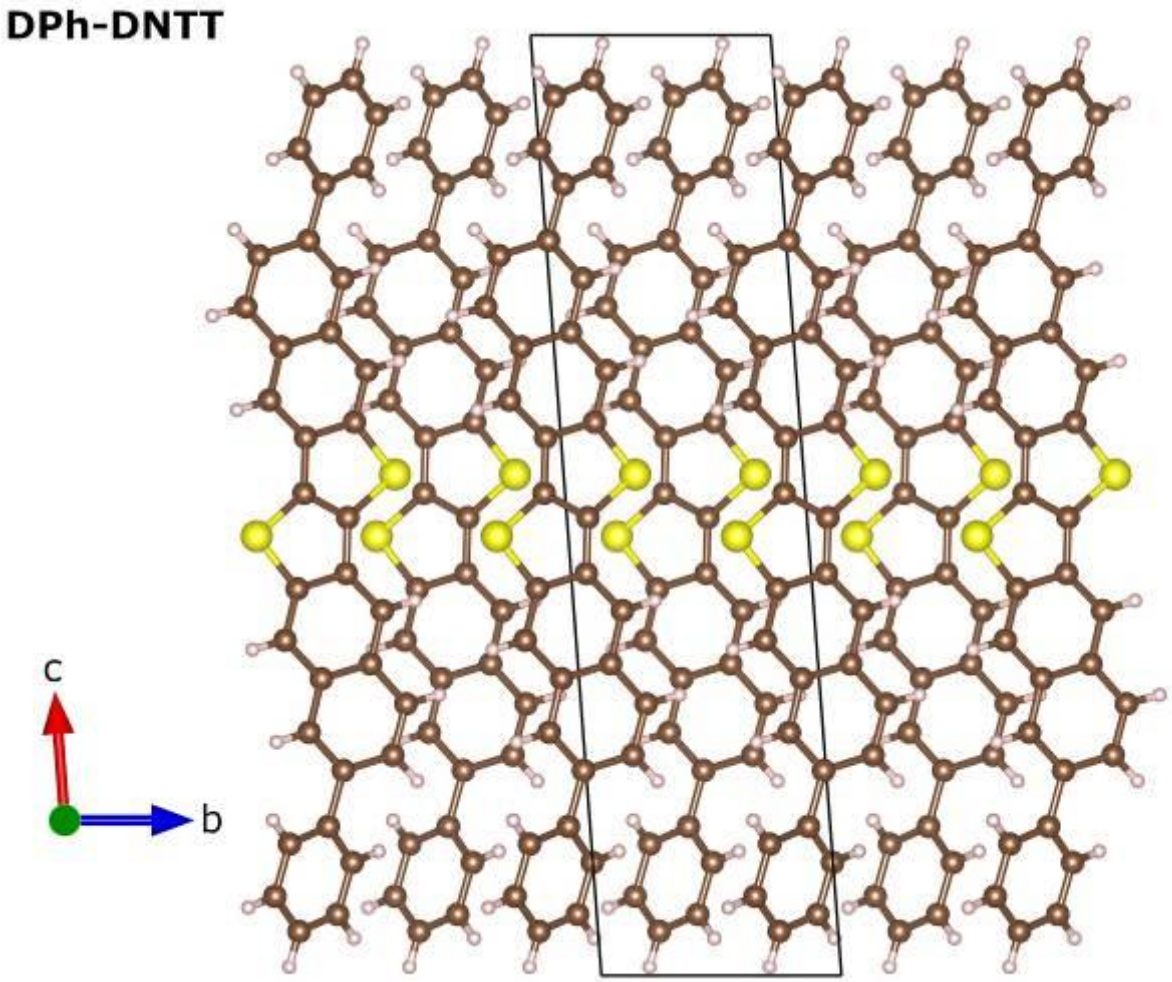


Figure 1: Sketch of the DPh-DNTT organic crystal with the crystal axes indicated.

Fig. 2

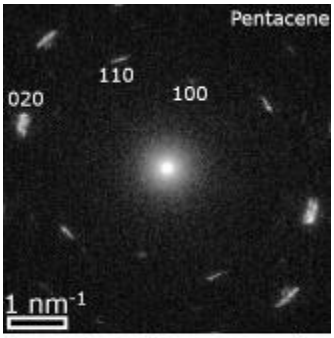


Figure 2: SAED pattern of a pentacene thin film with the major reflections indicated. The absence of [00l] reflections indicates a 'standing' configuration.

Fig. 3

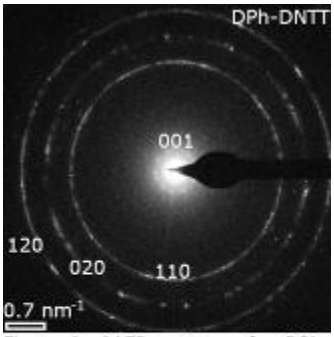


Figure 3: SAED pattern of a DPh-DNTT thin film. Both [001] reflections and [*hk*0] reflections are visible, revealing that for this crystal both 'standing' and 'lying' configurations are present in the thin film.

Fig. 4

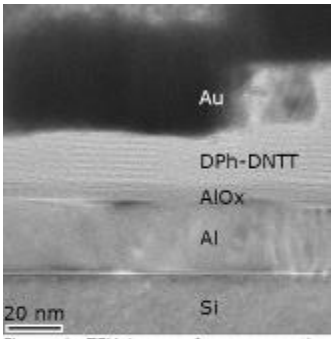


Figure 4: TEM image of a cross-section lamella prepared from a TFT device with DPh-DNTT as active layer. The different layers are named and the active layer reveals fringes with a periodicity of 2.4 nm, which agrees with the [001] lattice parameter. The image thus confirms that the first molecular layer is 'standing' on the gate dielectric.

MSLB.P06
High-temperature damage mechanisms in additively manufactured nickel-based superalloy IN939

M. Gálíková[1], I. Kuběna[1], I. Šulák[1], T. Babinský[2], S. Guth[3]

[1]Institute of Physics of Materials, CAS, Brno, Czech Republic
[2]Paul Scherrer Institute, Villigen, Switzerland
[3]Karlsruhe Institute of Technology, Karlsruhe, Germany

Inconel 939 (IN939) is a nickel-based superalloy renowned for its exceptional high-temperature mechanical properties, creep resistance, and oxidation resistance, making it ideal for demanding applications in aerospace industries. However, conventional casting of IN939 often results in large casting defects (up to 300 µm), which negatively impact fatigue performance. Additive manufacturing, specifically laser powder bed fusion (PBF-LB/M), offers a promising alternative by producing components with reduced defects. Although IN9399 was initially considered unsuitable for PBF-L, optimisation of printing parameters has made it possible to produce defect-free bulk material of IN939 with fine microstructure and minimal defects. This study investigates the high-temperature damage mechanisms in additively manufactured IN939, focusing on the influence of building orientation and loading conditions on fatigue performance.

The primary objectives of this study are to: (1) characterize the thermomechanical fatigue behaviour of PBF-LB/M IN939 using electron microscopy to identify damage mechanisms; (2) compare structural changes under different TMF loading amplitudes; and (3) evaluate the impact of vertical (V) and horizontal (H) building directions on fatigue performance.

IN939 was manufactured using an EOS M400 printer with EOS NickelAlloy IN939 powder (particle size 20–55 µm) under an argon atmosphere. A three-step heat treatment (solution annealing at 1175°C for 45 min, followed by precipitation hardening at 1000°C for 6 h and 800°C for 4 h) was applied to homogenise the microstructure and promote gamma prime (γ') precipitation. The microstructure featured elongated grains with a preferential (Fig. 1) orientation and bimodal γ' precipitates (Fig. 2). To understand the behaviour of PBF-L IN939 under high-temperature low-cycle fatigue, thermomechanical loading tests were conducted in both in-phase and out-of-phase conditions, ranging from 400°C to 800°C. The methods of electron microscopy were used to observe changes in microstructure.

The PBF-LB/M IN939 microstructure exhibited elongated grains with a orientation parallel to the building direction and coherent γ" precipitates post-heat treatment. TMF tests revealed that in-phase (IP) loading was more damaging than out-of-phase (OP) loading. Vertically built samples outperformed horizontally built ones, with longer fatigue lifetimes, particularly at higher strain amplitudes. Creep was the dominant damage mechanism at higher amplitudes, while oxidation prevailed at lower amplitudes. Fatigue crack initiation consistently occurred on specimen surfaces, with persistent slip bands along the {111} axis and stacking faults observed via STEM. Compared to isothermal low-cycle fatigue (ILCF), TMF tests showed shorter lifetimes, underscoring the need for TMF testing to ensure safe design.

This study demonstrates that PBF-LB/M IN939 exhibits complex thermomechanical fatigue behaviour influenced by building orientation and loading conditions. The vertically built samples showed superior fatigue performance compared to horizontal ones, highlighting the importance of build direction in optimising AM IN939. Creep and oxidation were identified as key damage mechanisms. These findings emphasise the necessity of TMF testing for AM superalloys and provide critical insights for improving the design and performance of PBF-LB/M IN939 in high-temperature applications.

Fig. 1

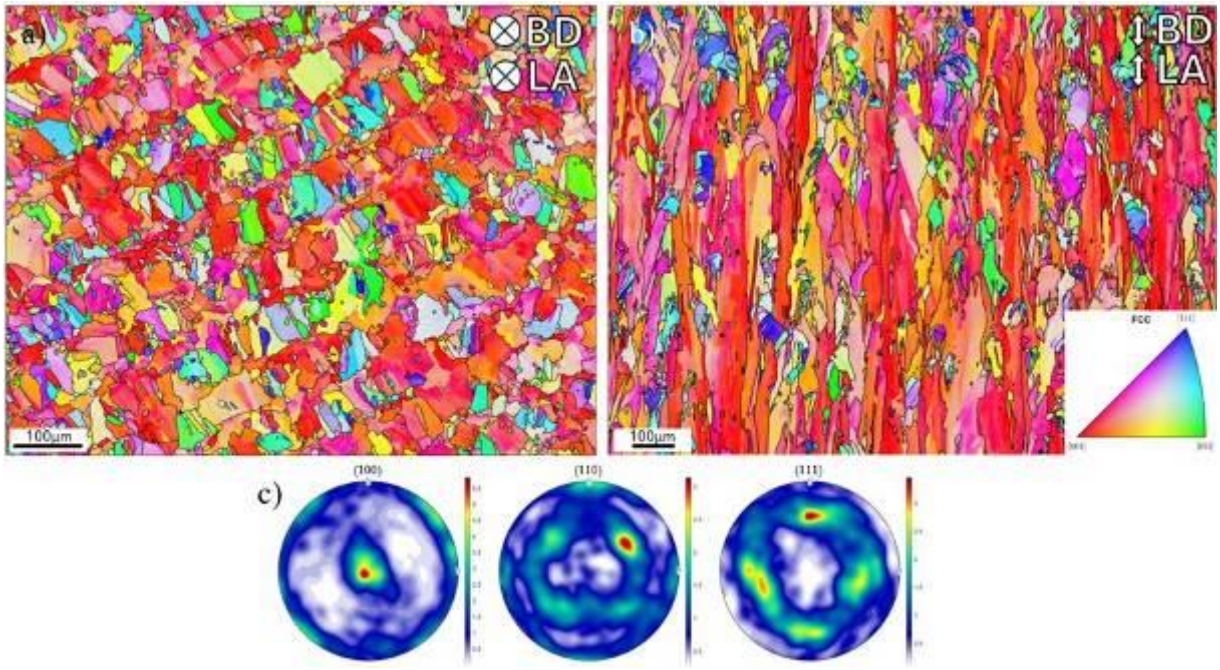
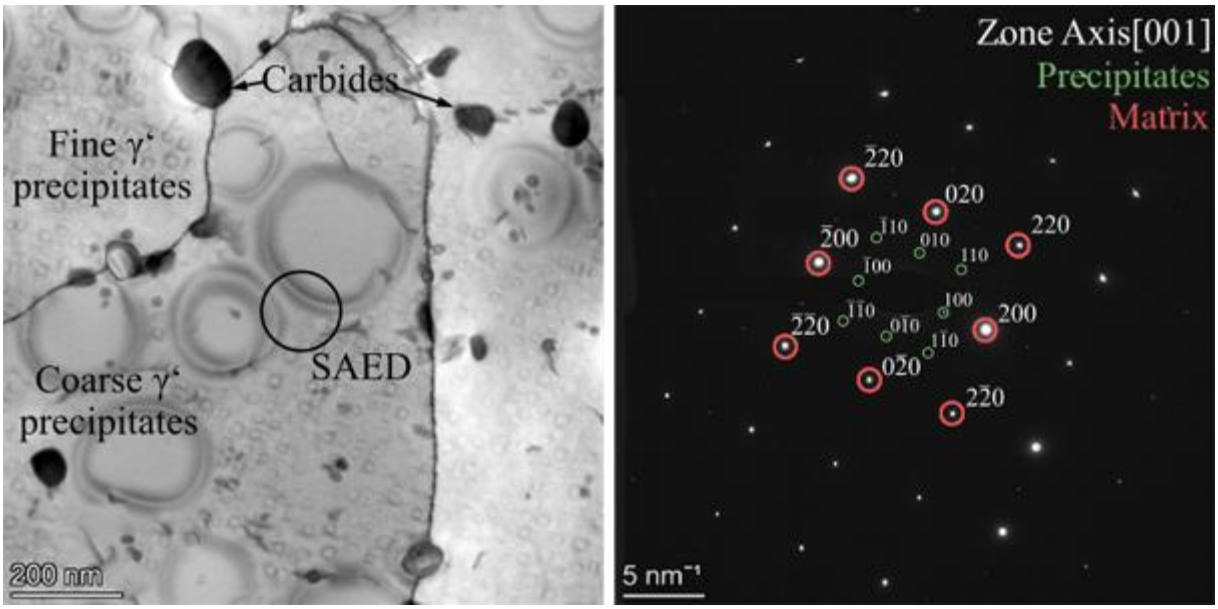

a)
BD
LA
100µm
b)
BD
LA
100µm
c)
(100)
(110)
(111)

Fig. 2


Carbides
Fine γ' precipitates
SAED
Coarse γ' precipitates
200 nm
Zone Axis[001]
Precipitates
Matrix
220
020
200
110
010
100
5 nm⁻¹

MSLB.P07
The influence of solution annealing on tensile properties of IN939 analysed by EBSD and KAM

I. Kuběna[1], M. Gálíková[1], I. Šulák[1]

[1]Institute of Physics of Materials, Brno, Czech Republic

Additive manufacturing (AM) is a rapidly evolving technology for producing structural components, offering several advantages over traditional methods such as casting or forging. It enables the direct fabrication of parts in their final shape, often with controlled surface quality [1], reducing or eliminating the need for post-processing. In many cases, this may lead to substantial cost savings. One of the most widely used AM techniques is Laser Powder Bed Fusion (L-PBF) [2]. Fundamentally, the L-PBF process is similar to welding, making weldability a key consideration. Consequently, typical welding-related defects, such as hot cracking, lack of fusion, and porosity, can appear in the resulting microstructure.

Nickel-based superalloys are critical materials for manufacturing components operating under high-temperature conditions, such as those in aircraft engines or gas turbines [3]. Their exceptional mechanical performance at elevated temperatures is primarily attributed to γ" strengthening precipitates formed through multistep heat treatment [4]. The AM processing window was recently revealed to prepare nickel-based superalloy IN939 by L-PBF. The AM process significantly reduces detrimental casting defects, frequent in IN939.

The IN939 produced by L-PBF with chemical composition (in wt.%) was: 22.5 Cr, 19.1 Co, 3.7 Ti, 2.0 W, 2.0 Al, 1.4 Ta, 1.0 Nb, with Ni as balance. The as-built microstructure was analysed by electron microscopy. Subsequently, the various solution annealing treatments were applied in a temperature range from 1175 °C to 1225 °C for different times. Specimens after a particular heat treatment were exposed to tensile loading at 800 °C, and the influence of heat treatment on the as-built microstructure was determined by the electron backscattered difraction (EBSD) and Kernel Average Misorientation (KAM) analysis.

The tensile data measured at 800 °C showed that the increasing annealing time decreases both the ultimate tensile strength and the elongation of the IN939. The EBSD analysis did not show a significant difference in the grain size in terms of high angle boundaries. Therefore, KAM analysis was adopted to show the distribution and frequency of low-angle boundaries and subsequently the changes in the geometrically necessary dislocations (GND). The solution annealing, even at 1225 °C, did not destroy the specific microstructure of the IN939 prepared by AM; texture and high-angle boundaries were not affected. The differences in the tensile response of particular specimens were attributed to the changes in the low-angle boundaries and dislocation distribution.

[1]D. Xin, X. Yao, J. Zhang, X. Chen, , J. Mater. Res. Technol. 23 (2023) 4135–4147.

[2]Z. Liu, D. Zhao, P. Wang, M. Yan, C. Yang, Z. Chen, J. Lu, Z. Lu, A, J. Mater. Sci. Technol. 100 (2022) 224–236.

[3]R.C. Reed, The Superalloys, Cambridge University Press, 2008.

[4] T. Murakumo, T. Kobayashi, Y. Koizumi, H. Harada, Acta Mater. 52 (2004) 3737–3744.

This publication was supported by the project "Mechanical Engineering of Biological and Bio-inspired Systems", funded as project No. CZ.02.01.01/00/22_008/0004634 by Programme Johannes Amos Commenius, call Excellent Research and grant No. 23-06167S of the Czech Science Foundation (GACR).

MSLB.P08
Investigating degradation in electrocatalysts with identical location 4D-STEM

F. Ruiz-Zepeda[1], A. R. Kamšek[1], L. Bijelić[1], A. Hrnjić[1], M. Bele[1], M. Smiljanić[1], P. Jovanovič[1], G. Dražić[1], N. Hodnik[1]

[1]National Institute of Chemistry, Department of Materials Chemistry, Ljubljana, Slovenia

Many efforts are currently underway to reduce the carbon footprint caused by the high energy consumption of modern society. As the effects of climate change become more apparent, the need for more sustainable energy technologies is becoming a topic of growing concern. Among the most promising and emerging solutions to this issue is the use of hydrogen fuel cells. However, one of the challenges surrounding catalytic nanoparticles inside a fuel cell is their degradation due to fluctuations in the applied potential and the harsh environment typically encountered during activation protocols or regular workload cycles. Nanocatalysts, which are usually composed of precious metal-based nanoparticles (e.g., Pt-M) deposited on a conductive support (such as carbon), face dissolution, dealloying, and other related phenomena that degrade their performance. This degradation affects both activity and stability, indirectly hindering their development as more suitable power sources. Therefore, studying degradation in nanoparticles and their support by tracking changes occurring after an electrochemical process can provide valuable insights into the structure-stability relationship. Identical-location scanning transmission electron microscopy (IL-STEM) is an effective method for monitoring these changes, not only in terms of morphology but also structurally. Furthermore, by incorporating 4D-STEM, it is possible to reveal even more information from the processed diffraction data set, specifically for certain regions. The data is collected from the same spot of the material before and after a preplanned electrochemical protocol, and then the two stages are compared. The changes observed are of particular interest, as their analysis can help in understanding degradation by providing important structural feedback. In this work, we describe how we have used identical-location techniques on electrocatalytic nanoparticles that have undergone different electrochemical cycling processes, either analyzed after an activation protocol or a degradation mechanism. The structural characteristics are investigated and compared at both stages. Additionally key factors that are used as descriptors are discussed. The findings show that it is possible to identify regions that have undergone slight or heavy modifications and correlate these with degradation or catalytic activity. These observations can lead to a more comprehensive understanding of the stability and durability of electrocatalytic materials.

Acknowledgements

Authors would like to thank the European Research Council (ERC) Starting Grant 123STABLE (Grant agreement ID: 852208) and the project J7-4637.

MSLB.P09
Revealing short range order in CeO_2 by electron energy loss spectroscopy

J. Bürger[1], E. Willinger[2], S. Gorji[3], A. Thron[4], M. G. Willinger[2]

[1]JEOL (Germany) GmbH, Application, Freising, Germany
[2]Technical University of Munich, Garching, Germany
[3]Ametek GmbH, EMT (Gatan + EDAX), Unterschleissheim, Germany
[4]Gatan, Inc., Pleasanton, CA, United States

Electron energy-loss Spectroscopy (EELS) is a powerful tool for nanoscale chemical analysis and bonding characterization with a scanning transmission electron microscope ((S)TEM). While conventional applications such as elemental mapping primarily utilize energy losses between ~50 eV and 2 keV, the analysis of energy losses above 3 keV is increasingly attracting attention, especially in connection with the extended range energy-loss fine structure (EXELFS) analysis. Like extended x-ray absorption fine structure (EXAFS), subtle oscillatory EXELFS features beyond the ionization edge of the EELS spectrum contain information about the element specific radial distribution function (RDF) of materials. EXELFS is therefore a promising candidate for precise short-range order analysis of amorphous metallic glasses and catalytically active nanoparticles [1]. Due to low ionization cross-sections above 3 keV, long acquisition times are needed for sufficient SNR in EXELFS, which raises the risk of beam-induced changes in delicate materials. In certain cases, beam-induced alterations can be mitigated by lowering the dose rate [2], a strategy that necessitates the use of sensitive direct electron detection cameras.

In this study, the EXELFS performance of JEOL's TEMs partnered with state-of-the-art energy filter and direct electron detection camera technology is demonstrated by characterizing the EXELFS signal of the Ce L_3 edge (~5.7 keV), acquired from CeO_2 nanoparticles, which are known to be sensitive to radiolysis depending on the dose rate [2].

STEM spectrum images (SI) are acquired using a JEOL JEM-F200 equipped with a Gatan GIF Continuum energy filter and STELA and K3 cameras. STEM-SI measurements were performed with multiple energy ranges, each for a selected CeO_2 particle covering the zero-loss region, the Ce $M_{5,4}$ and Ce $L_{3,2,1}$ edge. To minimize beam-induced reduction of Ce^{4+} to Ce^{3+}, the dose rate was kept under $3.1*10^5$ e/Å^2/s and dose distributing scan protocols were applied. Dedicated lens settings were used for the Ce L-edges generating an ideal coupling between the TEM and the GIF [3]. The EXELFS short-range order analysis is performed using Athena [4].

Fig. 1a) shows an EELS spectrum at the Ce L_3 edge with clear EXELFS features which are in good agreement with the EXAFS data. The short-range order analysis (Fig. 1b)) reveals robust signals corresponding to first- and second-shell Ce–O and Ce–Ce coordination which are consistent with known fluorite-type CeO_2 structures [5]. Notably, since the does rate was kept under $3.1*10^5$ e/Å^2/s, the Ce oxidation state was maintained, as can also be deduced from the presence of satellite peaks of the Ce L_3 edge.

This study highlights how EXELFS can be applied to beam-sensitive nanomaterials using optimized STEM acquisition protocols and state-of-the-art direct electron detection camera technology. The successful acquisition of Ce L_3 fine structure and short-range order analysis demonstrates EXELFS's value in catalyst research, where conventional synchrotron EXAFS may lack spatial resolution.

Fig. 1: a) EELS and XAS spectra at Ce L_3 edge. b) RDFs calculated from the spectra in a).

[1] F. M. Alamgir, et al., *Micron* 34.8 (2003), 433-439.

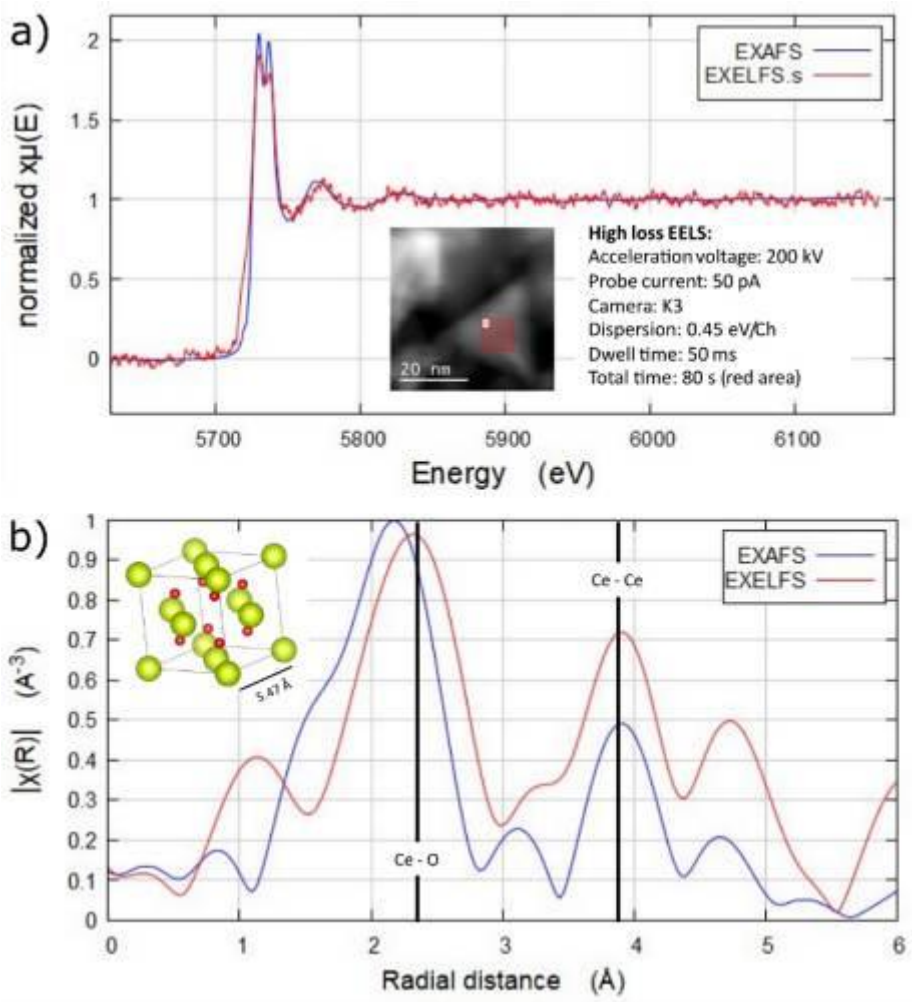
[2] A.C. Johnston-Peck, et al., *Ultramicroscopy* 170 (2016), 1-9.

[3] A. J. Craven, et al., *Ultramicroscopy* 180 (2017), 66-80.

[4] B. Ravel and M. Newville, *J. of Synchrotron Radiat.* 12 (2005), 537–541.

[5] E. Fonda, et al., *Synchrotron Radiat.* 6.1 (1999), 34-42.

Fig. 1



MSLB.P10
Atomic-scale investigation of solid oxide cell interfaces using an LSM/YSZ model system

X. Q. Tran[1,2], P. König[2], H. Ali[2,3], A. Hammud[2], V. Roddatis[4], A. Kaus[3], H. Türk[2], V. Vibhu[3], E. Stotz[2], Z. Gheisari[2], D. Abou-Ras[5], F. P. Schmidt[2], G. Koch[2], T. Götsch[2], F. Gunkel[3], T. Frömling[3], R. A. Eichel[3], K. Reuter[2], C. Scheurer[2], A. Knop-Gericke[2], T. Lunkenbein[2]

[1]Karlsruhe Institute of Technology, Institute of Nanotechnology, Eggenstein-Leopoldshafen, Germany
[2]Fritz Haber Institute of the Max Planck Society, Berlin, Germany
[3]Forschungszentrum Jülich GmbH, Jülich, Germany
[4]GFZ German Research Centre for Geosciences, Potsdam, Germany
[5]Helmholtz-Zentrum Berlin für Materialien und Energie GmbH, Berlin, Germany

Solid oxide cells (SOCs) are highly efficient electrochemical systems that convert electrical energy into chemical fuels, offering a promising solution for energy storage and addressing the intermittency of renewable energy sources in modern power grids. Operating at high temperatures—typically exceeding 600 °C—SOCs benefit from favourable thermodynamic and kinetic performance. However, such conditions can also induce structural changes that may either improve or degrade their catalytic behavior[1-3].

In this study, we examine the atomic-scale structure of a model SOC system composed of lanthanum-strontium manganite (LSM) thin films, epitaxially grown on yttria-stabilized zirconia (YSZ) substrates via pulsed laser deposition (PLD). Through a combination of advanced electron microscopy and first-principles calculations, we reveal a range of atomic-scale structural features that may influence electronic and ionic transport at the LSM/YSZ interface. These include a localized suppression of the MnO_6 octahedral rotation, an accumulation of oxygen vacancies (V_o??) accompanied by a reduced Mn^{2+} oxidation state (Fig. 1), and an increased disturbance of cation lattice.

Furthermore, we present a proof-of-concept investigation using identical-location electron microscopy within a quasi in-situ setup (Fig. 2). This approach enables the preparation of well-defined, electron transparent lamellae—configured as half-cell anode/cathode assemblies—mounted on MEMS chips and exposed to electrochemical and thermal stimuli in ambient air, thereby mimicking realistic SOC electrolysis conditions. Notably, near the interface of the operated sample, the LSM region displays an increased Mn^{2+} content relative to its non-operated counterpart, suggesting operation-induced interfacial modifications.

Collectively, these findings provide deeper atomistic insights into the structure-function relationships governing SOC performance and offer a basis for the rational design of more efficient and durable electrochemical cells.

1. H. Türk, X. Q. Tran et al., Adv. Energy Mater. 15 (2025) 2405599.
2. H. Türk, T. Götsch, F.-P. Schmidt et al., ChemCatChem 14 (2022) e202200300.
3. H. Türk, F.-P. Schmidt, T. Götsch et al., Adv. Mater. Interfaces 8 (2021) 2100967.

Fig. 1 (a) HAADF-STEM image of the LSM/YSZ interface. (b) and (c) Sequential EELS spectra showing the Mn $L_{3,2}$-edge and the corresponding calculated Mn L_3/L_2 ratio, respectively. A shift in peak position and an elevated Mn L_3/L_2 ratio indicate an increased Mn^{2+} concentration at the interface. (d) High-resolution ABF-STEM image highlighting V_o?? enrichment at the same interface.

Fig. 2 (a) Commercial experimental setup from DENSsolutions. (b) Our custom-built gas reactor, shown both as a computer-aided design (CAD) rendering and in a laboratory environment. (c) MEMS chip (DENSsolutions 2B4H heating/biasing) mounted inside the reactor. (d) Magnified view of the printed electrodes on the MEMS chip used for heating and biasing. (e) SEM image of a TEM lamella spanning the two biasing electrodes shown in (d). (f) Schematic representation of the lamella in (e), detailing the layered structure: Pt-Ga mixture||Pt (100 nm)||LSM (200 nm)||YSZ.

Fig. 1

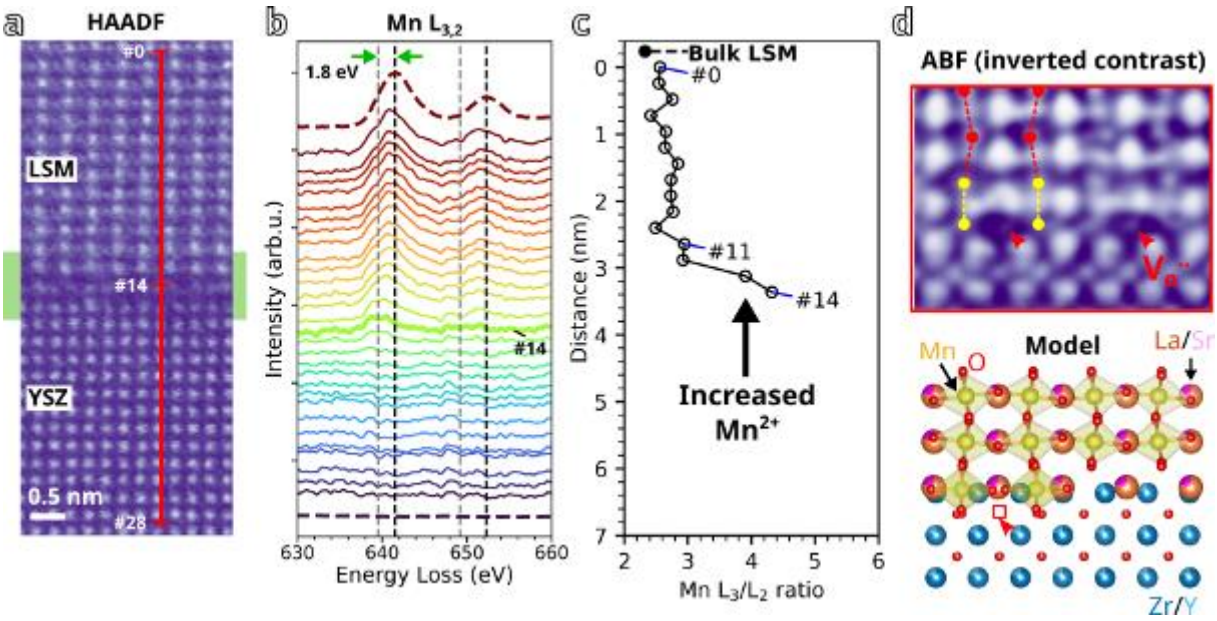
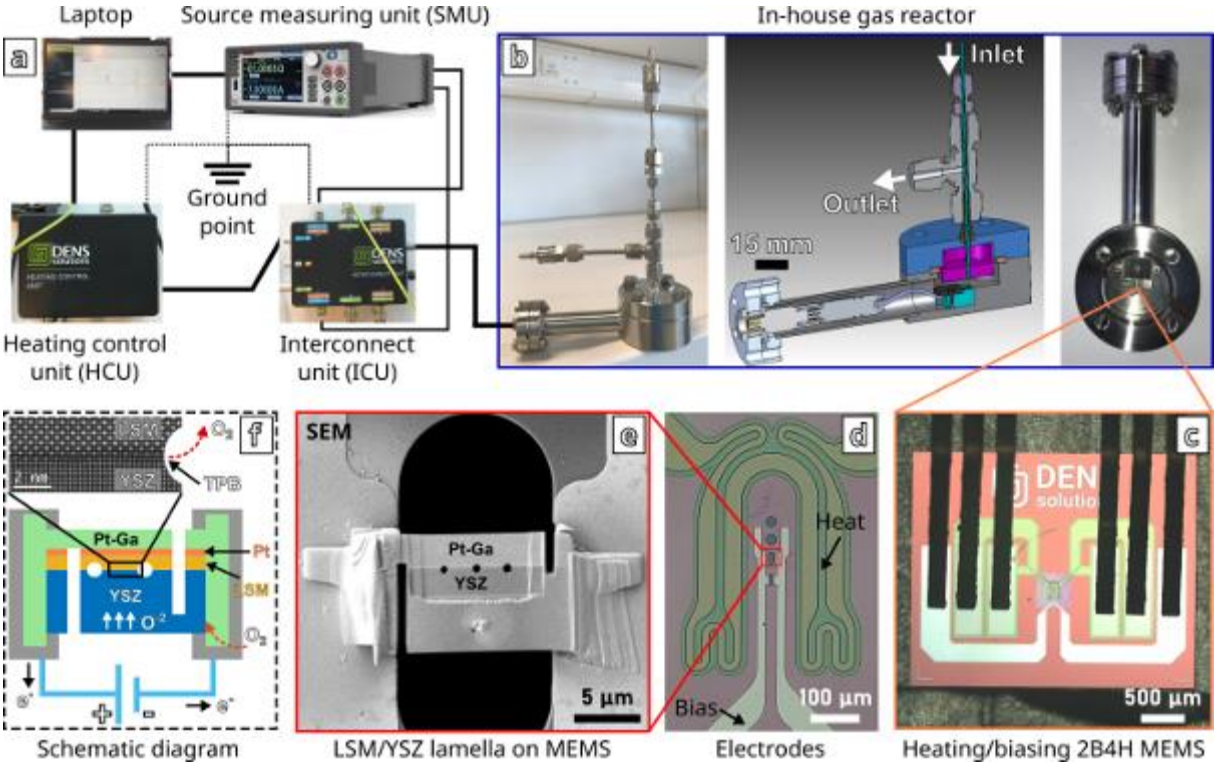

a
HAADF
#0
LSM
#14
YSZ
0.5 nm
#28
b
Mn L3,2
1.8 eV
Intensity (arb.u.)
#14
630
640
650
660
Energy Loss (eV)
c
Bulk LSM
#0
#11
#14
Increased
Mn2+
Distance (nm)
0
1
2
3
4
5
6
7
2
3
4
5
6
Mn L3/L2 ratio
d
ABF (inverted contrast)
Model
Mn
O
La/Sr
Zr/Y

Fig. 2


Laptop
Source measuring unit (SMU)
In-house gas reactor
a
Ground
point
Heating control
unit (HCU)
Interconnect
unit (ICU)
b
Inlet
Outlet
15 mm
f
LSM
YSZ
TPB
Pt-Ga
Pt
LSM
YSZ
e
SEM
Pt-Ga
YSZ
5 µm
d
Heat
Bias
100 µm
c
500 µm
Schematic diagram
LSM/YSZ lamella on MEMS
Electrodes
Heating/biasing 2B4H MEMS

MSLB.P11
In situ atomic-scale mechanical-thermal-electrical coupling testing system for transmission electron microcopy

Z. Li[1], H. Li[1], J. Cai[1], J. Zhang[2], S. Mao[2], X. Han[2]

[1]Bestron (Beijing) Science and Technology Co., Ltd, Beijing, China
[2]Beijing University of Technology, Beijing, China

Introduction

Understanding atomic-scale structure-property relationships under multifield coupling conditions is critical for advancing materials in extreme environments. However, real-time atomic-resolution characterization of materials exposed to simultaneous thermal, mechanical, and electrical stimuli remains challenging due to limitations in existing in situ transmission electron microscopy (TEM) technologies.

Objectives

For this reason, our group has dedicated to the development of an in-situ atomic-scale straining, heating and biasing system for TEM and has successfully applied the platform to study the atomic-scale response of various materials and revealing the mechanisms underneath.

Materials and methods

The multi-functional in situ TEM testing platform was developed mainly based on micro piezoelectric ceramic actuator and dedicated designs of MEMS chips with various heating and/or biasing functionalities. With a unique truss-like design, the heating chip can heat the sample from room temperature to 1200℃ with an accuracy of ±1℃ while allowing straining of the sample at any given temperature. The miniature straining actuator can apply a GPa-level stress, over 4 microns actuation displacement and an actuation resolution of up to 0.1 nm. The in-situ biasing chip can achieve precise application of electrical signals and pA and μV level measurement. The MEMS chips for heating and biasing and the miniature actuator for straining are fixated onto a rigid frame. A flexible printed circuit (FPC) connects the electrodes on the MEMS chips and the actuator to an outside control unit for the application and measurement of subtle signals. The rigid frame and the FPC comprises a functional cartridge, which can be conveniently connected to a specially designed double-tilt TEM holder.Various kinds of thermal/electrical/mechanical loading of samples can be carried out inside a TEM column. Throughout the entire loading process, the sample can be tilted freely around two orthogonal axes for ±15°. This capability is essential for achieving atomic-scale resolution, which requires precise alignment of the electron beam to a low-index zone axis of the sample during in-situ testing.

Results

With this in-situ platform, we conducted an in situ atomic-resolution study on the sliding-dominant deformation at general tilt grain boundary (GB) in platinum bicrystals. Both atomic-scale sliding along the GB and sliding with atom transfer across the boundary plane were observed directly in real-time. And for the first time, we uncovered that tungsten fractures at 700℃ in a ductile manner via a strain-induced multi-step body-centered cubic (BCC)-to-face-centered cubic (FCC) transformation and dislocation activities within the strain-induced FCC phase. Using this technique, researchers has also uncovered the atomic-scale process of GB dislocation climb in nanostructured Au during in situ straining.

Conclusion

Based on highly integrated MEMS chips and unique double-tilt system, we have developed an in-situ TEM testing platform that allows real-time observation of micro-structure evolution at atomic scale under flexible coupling of mechanical, thermal and electrical fields. Researches on revealing the atomic scale mechanisms of GB plasticity and Brittle-to-ductile transition of various metallic materials.

Fig. 1

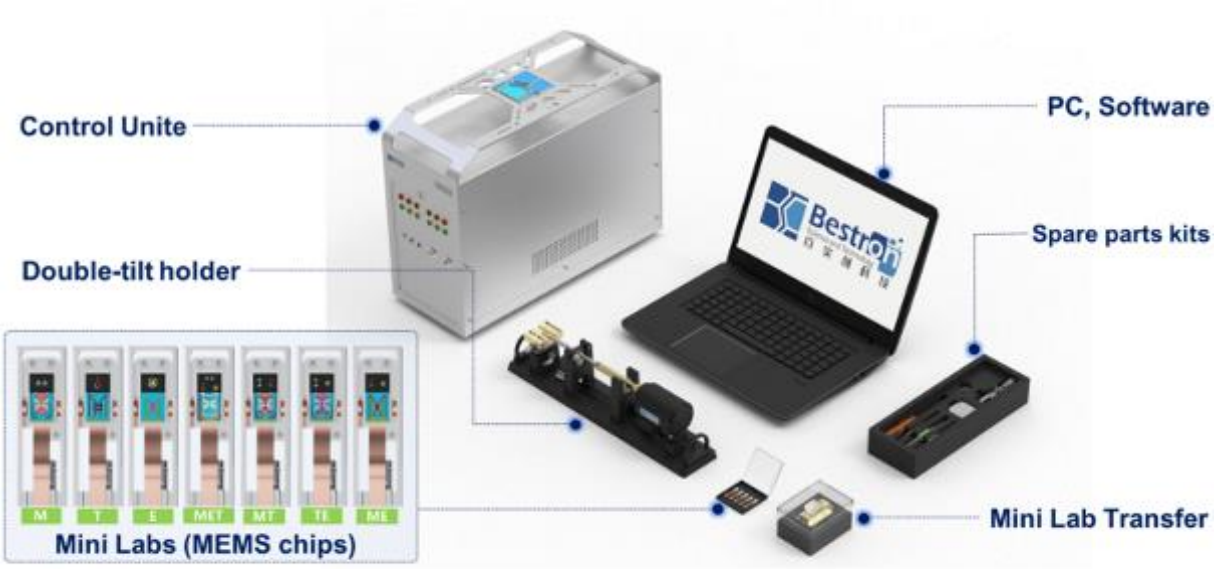


Fig. 2

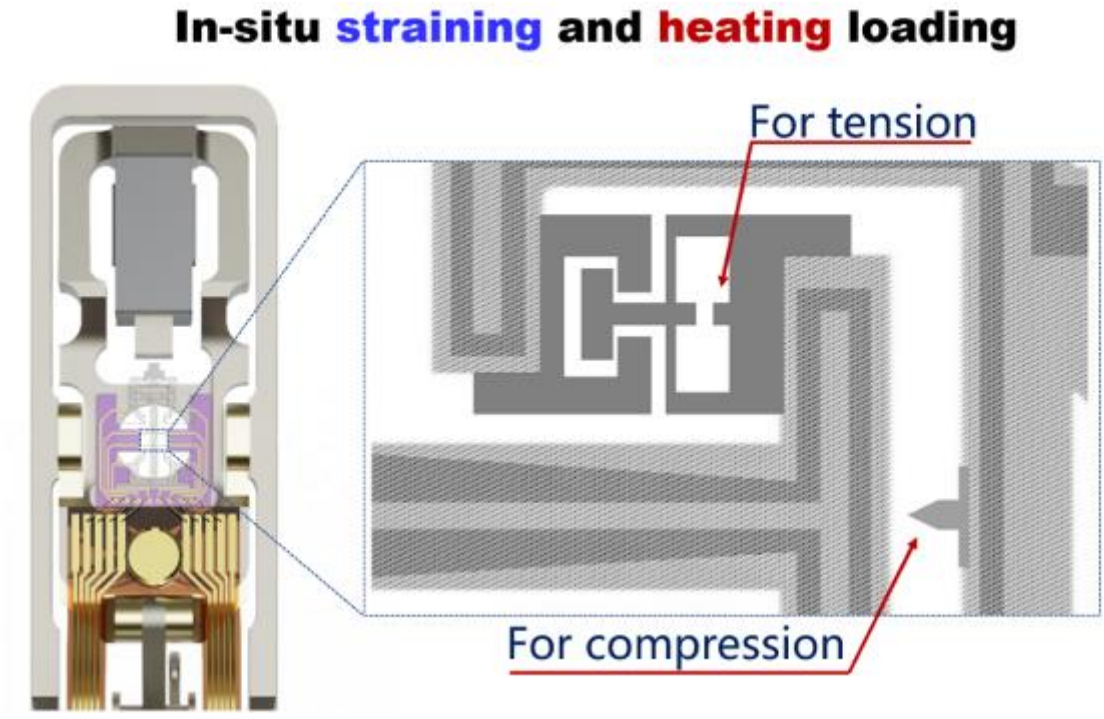


Fig. 3

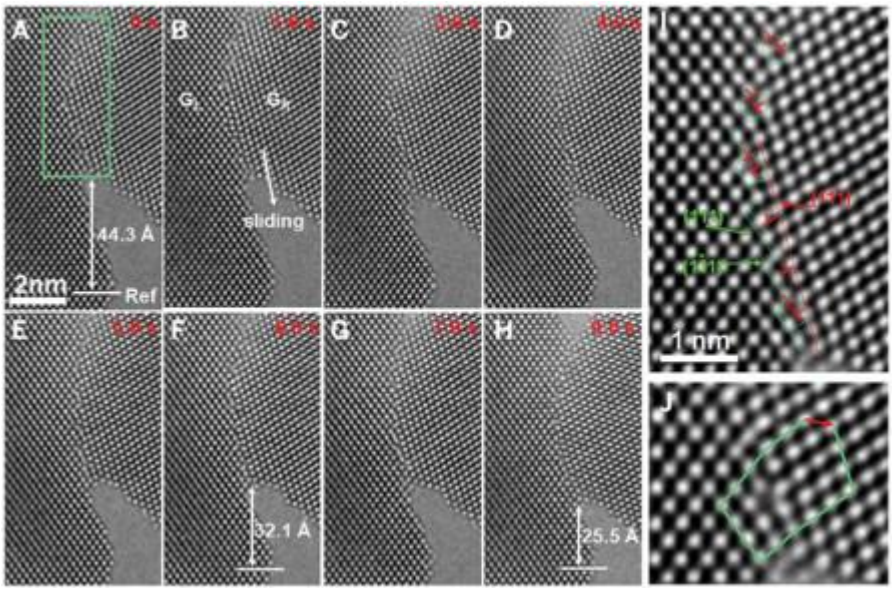
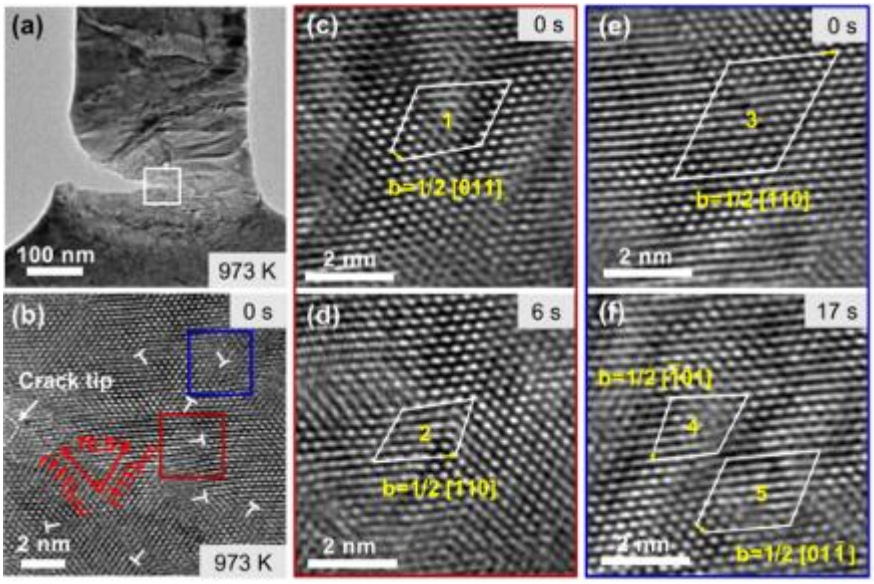

A
B
C
D
E
F
G
H
I
J
44.3 Å
Ref
2nm
sliding
32.1 Å
25.5 Å
1 nm

Fig. 4


(a)
100 nm
973 K
(b)
0 s
Crack tip
2 nm
973 K
(c)
0 s
1
b=1/2 [011]
2 nm
(d)
6 s
2
b=1/2 [110]
2 nm
(e)
0 s
3
b=1/2 [110]
2 nm
(f)
17 s
b=1/2 [10-1]
4
5
b=1/2 [011]
2 nm

MSLB.P12
Defect-engineered perovskites – Atomic scale nature of a-site vacancy-stabilized catalytically active phase

R. Talei Jeid[1], A. Mohammadi[2], T. F. Winterstein[2], G. Schmitz[1], S. Penner[2], N. Bonmassar[1]

[1]Stuttgart University, Institute for Materials Science, Material Physics, Stuttgart, Germany
[2]University of Innsbruck, Innsbruck, Austria

A-site-deficient perovskites offer a sustainable alternative to noble-metal catalysts, leveraging tunable defect structures to enhance catalytic performance in reactions such as NO reduction by CO. In this study, we investigate the atomic-scale structure and catalytic function of $La_{0.7}Fe_{0.7}Mn_{0.3}O_3$ ($La_{0.7}FM$), a model A-site-deficient perovskite, to elucidate the role of defects in its superior activity compared to its stoichiometric counterpart, $LaFe_{0.7}Mn_{0.3}O_3$ (LFM). Using aberration-corrected scanning transmission electron microscopy (STEM) and high-resolution energy-dispersive X-ray spectroscopy (EDXS), we uncover a heterogeneous defect landscape featuring a thin (2–3 unit cells) A-site-deficient $La_{0.7-x}Fe_{0.7}Mn_{0.3}O_3$ layer at particle surfaces and grain boundaries, transitioning to stoichiometric bulk. These defect-rich layers stabilize FeO_x nanoparticles (1–several nm) at the surface, identified as the catalytically active sites for NO reduction via a Mars–van Krevelen mechanism. In situ diffuse reflectance infrared Fourier transform (DRIFT) spectroscopy reveals the evolution of surface species, with $La_{0.7}FM$ exhibiting enhanced reducibility, marked by Fe^{2+} regeneration and CO adsorption on reduced Fe sites at elevated temperatures. Catalytic measurements demonstrate a significant reduction in NO reduction onset temperature (120 °C for $La_{0.7}FM$ vs. 180 °C for LFM), underscoring the promoting effect of A-site deficiency. Quantitative strain analysis via geometric phase analysis (GPA) and X-ray diffraction (XRD) confirms minimal lattice distortion despite significant La depletion (down to ~50 at.%), with strain confined to grain boundaries. Our findings establish a direct structure–property relationship, revealing that heterogeneously distributed A-site deficiencies create redox-active "hotspots" that enhance catalytic performance. This work highlights defect engineering as a powerful strategy for designing efficient, noble-metal-free perovskite catalysts for exhaust gas purification and other redox-driven applications.

MSLB.P13
Nanoscale investigation of the metal-insulator transition in free-standing VO_2 single crystals through *in situ* strain and temperature control in the S/TEM

A. Arteaga[1,2], C. Flathmann[3,4], L. Tian[5], P. C. Canfield[6,7], Y. Zhu[8], T. Meyer[5], C. H. Liebscher[3,4,9], B. H. Goodge[1]

[1]Max Planck Institute for Chemical Physics of Solids, Dresden, Germany
[2]University of British Columbia, Department of Physics and Astronomy, Vancouver, Canada
[3]Ruhr University Bochum, Faculty of Physics and Astronomy, Bochum, Germany
[4]Ruhr University Bochum, Research Center Future Energy Materials and Systems, Bochum, Germany
[5]University of Göttingen, Institute of Materials Physics, Göttingen, Germany
[6]U.S. Department of Energy, Ames Laboratory, Ames, United States
[7]Iowa State University, Department of Physics and Astronomy, Ames, United States
[8]North Carolina State University, Department of Mechanical and Aerospace Engineering, Raleigh, United States
[9]Max-Planck-Institute for Sustainable Materials, Düsseldorf, Germany

Vanadium dioxide (VO_2) is a correlated electron material that manifests a sharp metal-insulator transition (MIT) near 340 K in bulk single crystal form, accompanied by a first-order structural phase transition from a monoclinic (M1) to a rutile (R) phase [1,2]. While previous research has explored tuning the MIT temperature via biaxial strain in epitaxial thin films and uniaxial pressure along the c_R-axis in nanowires, the impact of strain along other crystallographic directions remains relatively unexplored [2-6].

In this contribution, we utilize a microelectromechanical system (MEMS)-based device to apply *in situ* uniaxial tension and heating to VO_2, enabling dynamic imaging of the structural phase transition at the nanoscale via scanning transmission electron microscopy (STEM).

Low-strain bulk single crystals of VO_2 were grown out of a V_2O_5-rich binary melt using solution growth techniques [5]. Electron-transparent lamellae were extracted from these crystals and mounted on the MEMS device using focused ion beam (FIB). Mechanical actuation is driven by an electrostatic comb drive, here designed for compatibility with a DENSsolutions 6-pin Lightning heating and biasing holder [7]. High-resolution TEM (HRTEM), STEM, 4D-STEM nano-diffraction, electron energy loss spectroscopy (EELS), and selected area electron diffraction (SAED) were conducted on the Titan 80–300 E-TEM at Georg-August-Universität Göttingen.

Sample heating through the MEMS device successfully reproduces the reversible MIT phase transition in VO_2 lamellae, confirmed by characteristic changes in SAED patterns and tracked by bright-field STEM imaging across the M1–R structural transition (Figure 1). Uniaxial tensile stress applied along the c_{M1} crystallographic direction results in the formation of elastic twin domains (Figure 2). Combined stress and heating experiments reveal a significant reduction in the MIT temperature under strain, further illustrating tunability of the MIT.

These experiments demonstrate the potential for *in situ* strain and temperature control in the S/TEM for tuning quantum materials while observing local structural and electronic response at the nanoscale. VO_2 serves as a model system to explore uncharacterized strain directions, expanding the understanding of structural and electronic coupling across the phase diagram. Future work will examine the effect of tensile stress along other crystallographic directions, as well as shear and complex strain states to investigate transitions between M1, M2, and R phases.

[1] F.J. Morin, Phys. Rev. Lett. 3, 34 (1959)

[2] Liu et al. Materials Today 21:8 (2018)

[3] J.P. Pouget et al., Phys. Rev. Lett. 35, 873 (1975)

[4] Park et al. Nature 500, 431-434 (2013)

[5] Liu et al. Physical Review B 91, 245155 (2015)

[6] Birkhölzer YA, Nanoscale strain control of oxide thin films. PhD Thesis: University of Twente, 2022.

[7] Zhu and Espinosa, Proc. Nat. Acad. Sci. 102:41, 14503-14508 (2005)

Figure 1. (a) Bright Field STEM images of VO_2 below (left) and above (right) the MIT. At high temperature, the corners of the lamella remain in the M1 phase while the center is fully R; arrows mark the R–M1 boundary. (b) Corresponding SAED patterns show loss of extra M1 peaks after transition. Primary peaks are labeled by crystal structure; arrows indicate the strain direction.

Figure 2. Dark Field TEM image of VO_2 under uniaxial pressure along c_{M1}. Strain induces elastic twin domains nucleating at lamella corners.

Fig. 1

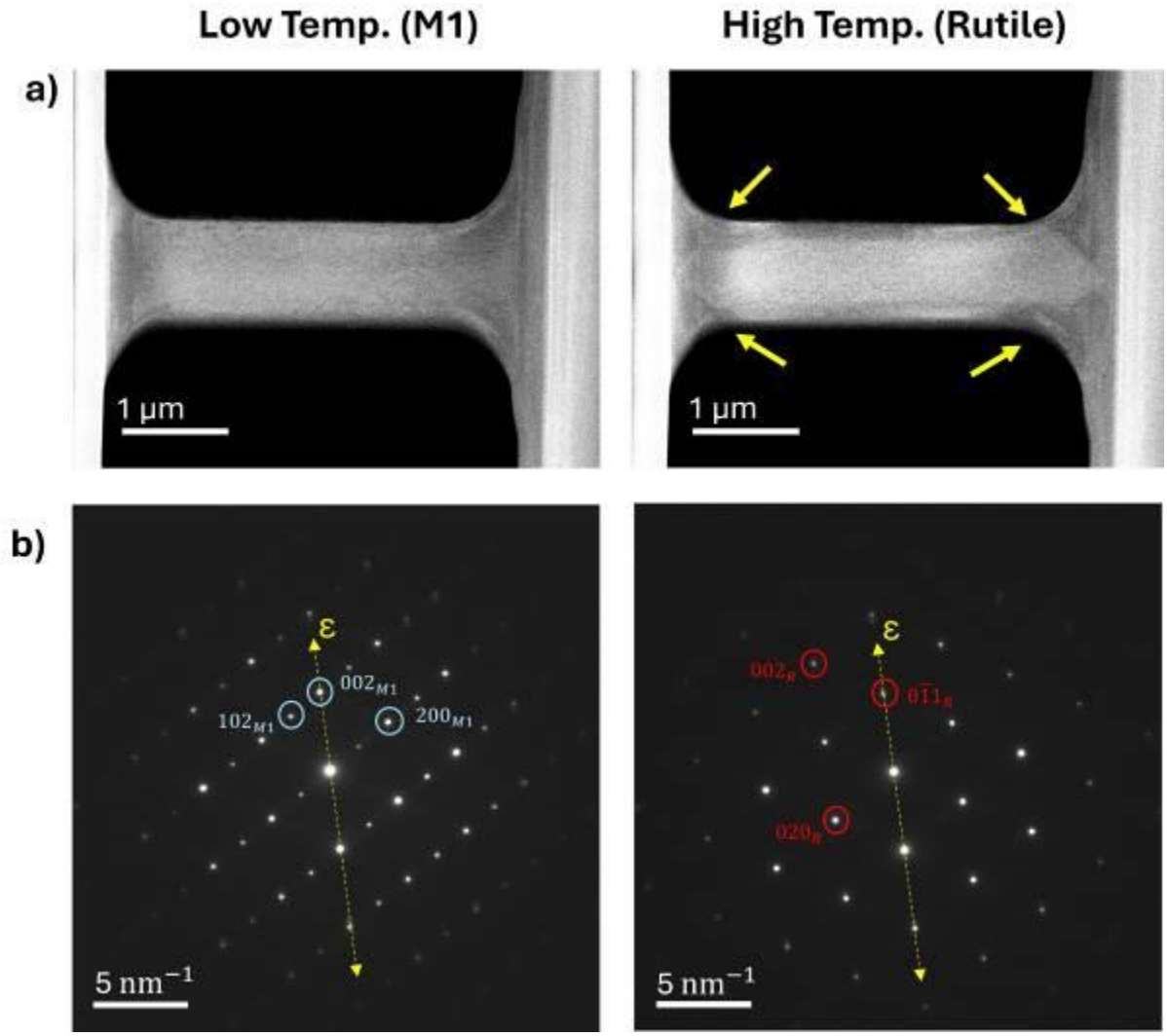
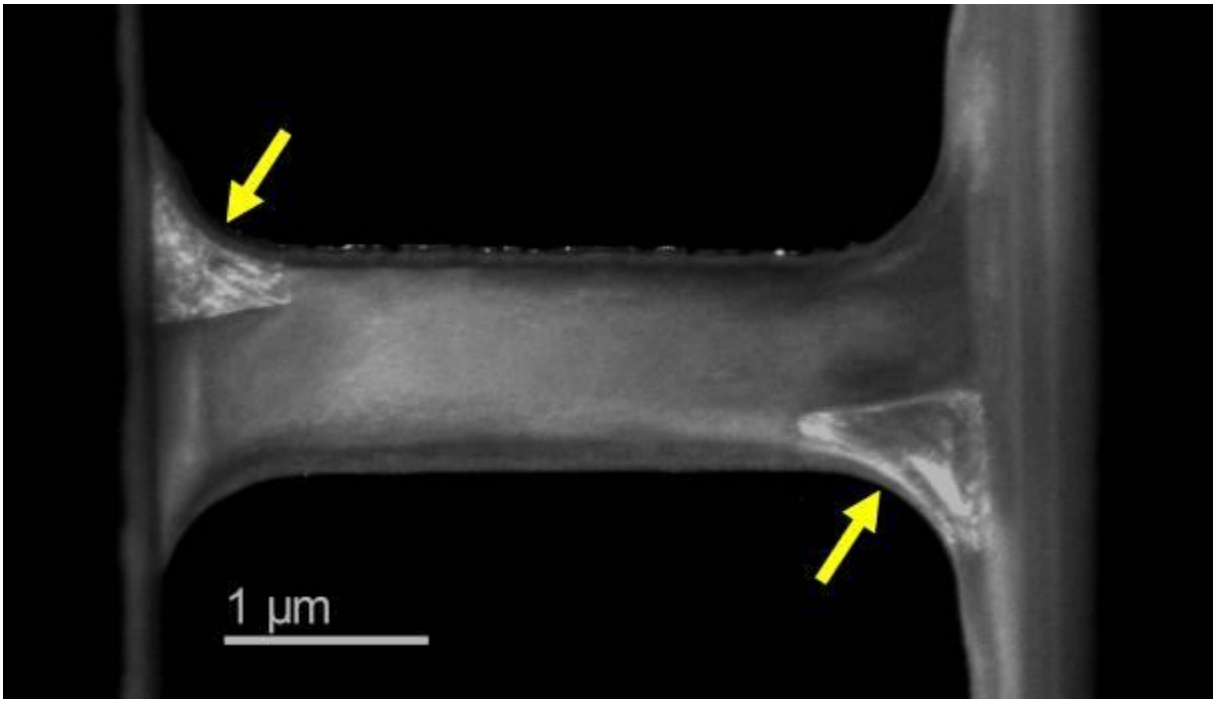


Fig. 2



MSLB.P14
A scale-bridging preparation routine for characterizing porous silica substrates infused with gallium and platinum

C. Rubach[1], S. Carl[1], J. Will[1], T. Przybilla[1], M. Landes[1], A. Görling[1], E. Spiecker[1]

[1]FAU Erlangen-Nürnberg, Institute of Micro- and Nanostructure Research, Erlangen, Germany

Introduction

Supported catalytically active liquid metal solutions (SCALMS) are composed of a small quantity of a catalytically active metal (such as Pd, Pt) dissolved in liquid metal droplets (typically Ga) which are distributed over a porous support (typically silica). They are highly dynamic catalysts that have displayed high activity, selectivity and long-term stability in propane dehydrogenation (PDH) [1-3]. The remarkable properties of SCALMS systems are credited to the highly dynamic liquid metal surface, which facilitates single atom catalysis.

Objectives

We infiltrated commercially available, millimeter sized porous silica particles with gallium and platinum. Our goal was to establish a preparation workflow which enabled a scale-bridging investigation of the infused particles ranging from millimeter down to the atomic scale before and after propane dehydrogenation.

Material & Methods

The loaded CARiACT particles were therefore embedded in epoxy resin (EpoThin2, Buehler) and polished to unveil the cross section of the particle. An EDX line scan was performed on the exposed surface over the radius of the support particle to show the penetration depth of gallium and platinum into the particle and to confirm a homogeneous deposition across the entire diameter (mm). For TEM characterization of the porous network within the particle, cross section lamellas were extracted from corresponding regions of particles before and after PDH using a FEI Helios Nano Lab 660 Dual Beam SEM/FIB. A probe-corrected Thermo Fisher Spectra 200 C-FEG was used to record high-angle annular dark-field scanning transmission electron microscopy (HAADF-STEM) overview images to monitor the local state of decoration of the porous network with Ga and Pt species on a micron scale. Those measurement were complemented by i) low and high resolution EDX maps revealing the presence and composition of both Ga and Pt species and ii) high-resolution HAADF-STEM images down to the atomic scale revealing Pt in different environments dispersed down to the single atom.

Results and Conclusion

We developed a preparation routine for millimeter-sized porous silica particles infiltrated with gallium and platinum which allows us to monitor the presence and distribution of the infused particles on scales ranging from millimeters to atomic levels, both before and after dehydrogenation. Furthermore we can analyze their morphology and composition, revealing how propane dehydrogenation modifies the Ga and Pt dispersion, and species.

[1] Taccardi N., Grabau M., Debuschewitz J., Distaso M., Brandl M., Hock R., Maier F., Papp C., Erhard J., Neiss C. (2017): Gallium-rich Pd–Ga Phases as Supported Liquid Metal Catalysts. *Nature Chemistry 9* (9), 862-867.

[2] Sebastian O., Al-Shaibani A., Taccardi N., Sultan U., Inayat A., Vogel N., Haumann M., Wasserscheid P. (2023): Ga–Pt Supported Catalytically Active Liquid Metal Solutions (SCALMS) Prepared by Ultrasonication – Influence of Synthesis Conditions on n-Heptane Dehydrogenation Performance. *Catalysis Science & Technology 13 (15)*, 4435-4450.

[3] Carl S., Will J., Madubuko N., Götz A., Przybilla T. Wu M., Raman N., Wirth J., Taccardi N., Apeleo Zubiri B., Haumann M., Wasserscheid P., Spiecker E. (2024): Structural Evolution of GaOx-Shell and Intermetallic Phases in Ga-Pt Supported Catalytically Active Liquid Metal Solutions. *The Journal of Physical Chemistry Letters 15 (17)*, 4711-4720.

MSLB.P15
Contrast enhancement in pd-decorated globular graphite by Al_2O_3 functionalization *via* atomic layer deposition

C. Hedrich[1], T. Krekeler[1], C. Roller[2], R. Zierold[3], R. H. Blick[3], B. Fiedler[2], M. Ritter[1]

[1]Hamburg University of Technology, Electron Microscopy Unit (BeEM), Hamburg, Germany
[2]Hamburg University of Technology, Institute of Polymers and Composites, Hamburg, Germany
[3]University of Hamburg, Center for Hybrid Nanostructures (CHyN), Hamburg, Germany

Abstract

STEM tomography of carbon-based porous materials such as globular graphite[1] is of great interest for characterizing the 3D structure, pore geometry and distribution, and carbon thickness. However, the low contrast in HAADF images associated with the carbon material is challenging for processing the images, namely by reconstructing the tilt series and segmenting the volume reconstruction, to generate 3D models. This gets even more pronounced when the carbon structure is decorated with noble metal nanoparticles based on the large contrast difference between C and the noble metal. To improve the contrast, we conformally functionalized the material with a thin Al_2O_3 layer by atomic layer deposition (ALD). ALD is a gas phase deposition technique based on sequential self-limiting reactions between gaseous precursors and solid substrate surfaces.[2] The self-limiting nature results in conformal coating of the entire substrate surface and a precise thickness control in the sub-nanometer range. Thus, ALD is ideally suited for conformal material deposition on porous structures.

In this work, we demonstrate how an ALD coating improves the contrast of a carbon-based porous material. Globular graphite decorated with Pd nanoparticles (Pd-GG) is characterized by STEM tomography at 200 kV and tilting angles between ± 68°. One measurement series investigates the as-prepared Pd-GG structure. The other measurement series is acquired after functionalizing the Pd-GG structure with about 2 nm Al_2O_3 by ALD. The contrast of the carbon structure is enhanced when it is functionalized with Al_2O_3 as shown in Figure 1 due to the higher atomic number compared to carbon. The contrast enhancement considerably facilitates the tilt series processing, especially the segmentation to generate a 3D model of the Pd-GG structure. Moreover, the STEM images verify the high conformality of the ALD-deposited Al_2O_3 coating.

In the future, conformal functionalization with thin films by ALD could be expanded to further carbon-based structures to enhance the contrast in TEM studies. According to the large variety of available ALD processes,[2] materials with higher atomic numbers could be deposited onto the carbon-based structures by ALD to further increase the contrast.

Figure 1. STEM images of Pd nanoparticle-decorated globular graphite structures as-prepared (left) and functionalized with 2 nm Al_2O_3 by ALD (right). The gray value profiles along the arrows demonstrate an increase of the carbon structure signal after Al2O3 functionalization.

References

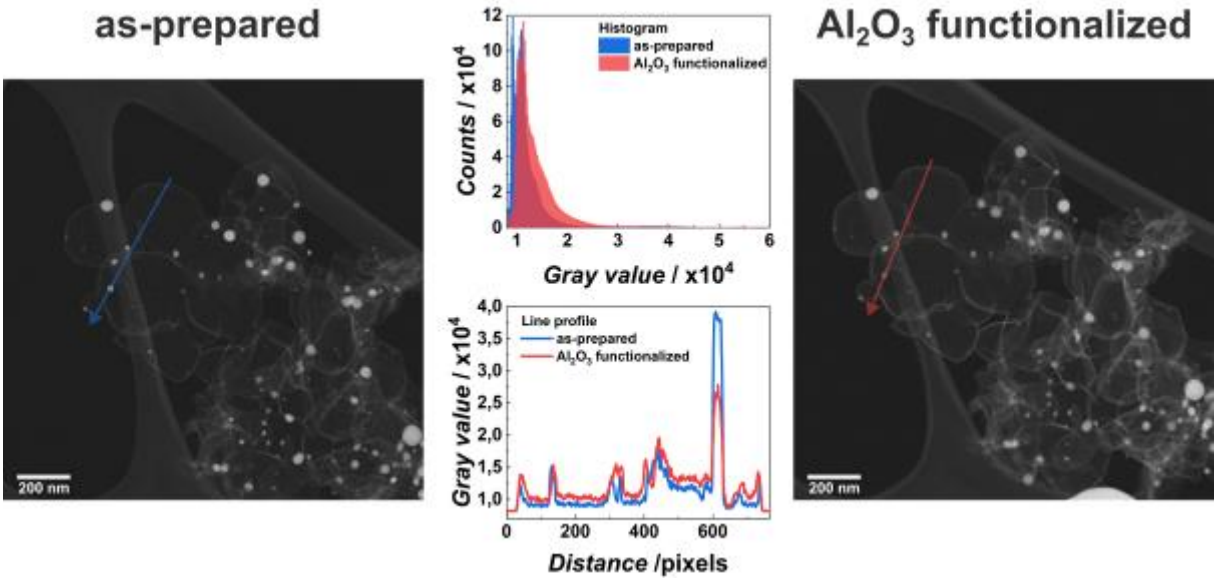
[1] J. Marx *et al.*, *Vac.* 155, 490-495 (2018), 10.1016/j.vacuum.2018.06.052.

[2] V. Miikkulainen *et al.*, *J. Appl. Phys.* 113, (2013), 10.1063/1.4757907.

Acknowledgements

The authors acknowledge funding by the German Research Foundation DFG via the SFB 1615 "SMART Reactors for Future Process Engineering" (project number 503850735).

Fig. 1



MSLB.P16
In situ trapping of nanoparticles in a monolithic nanochannel liquid cell for TEM Characterisation

M. Ramadan[1], N. Bottauscio[1], E. Jensen[1]

[1]Insight Chips, Kongens Lyngby, Denmark

Liquid-phase transmission electron microscopy (TEM) enables real-time observation of dynamic processes at the nanoscale, but traditional liquid cells often suffer from assembly complexities and limited control over sample confinement. Here, we introduce a novel monolithic liquid cell, termed the Nanochannel chip, which eliminates manual assembly and incorporates an integrated physical trap via a height step reduction in the channel. This design allows unrestricted liquid flow while selectively immobilizing suspended nanoparticles, facilitating high-resolution imaging in thin liquid layers.

The Nanochannel chip features a primary channel height of 125 nm, tapering to approximately 10 nm at the trap region. In our experiments, we utilized this chip to trap silica (SiO2) nanoparticles with an average diameter of 50 nm. The nanoparticle suspension was introduced simply by applying pressure from a syringe, enabling controlled flow through the cell. Real-time TEM imaging captured the trapping process, demonstrating efficient immobilization of particles at the height step without obstructing liquid passage.

Our results highlight the chip's capability for live imaging of nanoparticle dynamics in confined environments, with potential applications in studying colloidal assembly, catalysis, and biomolecular interactions. This monolithic approach enhances reproducibility and simplifies workflows for in situ TEM studies.

MSLB.P17
The study of the impact of internal pressure on the formation of pure sp3 bonded carbon phase

S. Rubanov[1]

[1]University of Melbourne, Bio21 Institute, Melbourne, Australia

The synthesis of sp3 bonded amorphous carbon remains scientifically and technologically challenging. However, this carbon phase could be fabricated through novel two steps process using ion implantation and annealing. This study investigates the impact of the ion implantation induced internal pressure on the fabrication of sp3 bonded amorphous carbon phase.

A number of trenches, served as apertures, were FIB milled into the surface of diamond (Fig.1a). 1 MeV He+ ion implantation with fluence 2.5×1017 ions/cm2 created implanted layer and disordered carbon channels below apertures. The FIB cuts were fabricated on both sides of some channels after ion implantation. This allowed to release internal pressure in selected channels through volume extension. The annealing was conducted in vacuum at 950 oC. TEM lamellas prepared after annealing contained cross-sections of implanted channels with released and unreleased pressure (Fig.1.c).

Fig.1 SEM images of a) diamond surface with apertures; b) after He implantation and milling additional FIB cuts; c) TEM lamella with visible apertures and implanted layer.

Fig.2 a) Cross-sectional TEM image of diamond with continuous implanted layer and implanted channels; diffraction pattern from implanted layer b) before and c) after annealing; from implanted channel d) before and e) after annealing.

TEM image in Fig.2a shows a continuous implanted layer with channels of disordered carbon below the apertures. Diffraction pattern confirm amorphous structure of implanted channels before and after annealing.

The EELS carbon K-edge shows the π* peak at 285 eV indicating the presence of sp2 bonded carbon in the implanted layer and in the channels after ion implantation (Fig.3a). After annealing continuous implanted layer became graphitic while the channels remained amorphous (Fig. 2c,e). EELS of carbon K-edge revealed the absence of peak at 285 eV in the channels (Fig.3b). The disappearance of π* peak indicates the complete conversion of sp2 bonds back to sp3 and formation of 100 % sp3 bonded amorphous carbon.

Fig.3. EELS of carbon K-edge in implanted channel after a) ion implantation and b) thermal annealing

The low loss EELS spectra are shown in Fig.4. Plasmon energy was variated with depth in continues implanted layer and was measured in range 25-27 eV (1.9 – 2.22 g/cm3, 0-22 % sp3). In channels the plasmon energy was measured to be 31 eV and calculated density 2.92 g/cm3(~73 % sp3). Volume

extension in channels was restricted by rigid properties of surrounded diamond lattice and resulted in high internal pressure (~60 GPa). Plasmon energy in channels after annealing was measured to be 32.6 eV and corresponding density ~3.27 g/cm3 which was lower than diamond but was consistent with a random distribution of sp3 sites. TEM and EELS studies showed no difference in structure, chemical bonding and mass density in channels with released and unreleased internal pressure.

Fig.4. Low loss EELS in a) amorphous diamond channel and b) bulk diamond

High internal pressure in channels during ion implantation results in suppressions of sp3 to sp2 transition and formation of amorphous carbon network with high sp3 fraction (~73%) which remains the same after pressure relies through FIB cuts. Annealing increases the mobility of the C atoms and allows this sp3 reach carbon network to overcome energy barriers to structural rearrangement and bonding changes to form 100% of sp3 bonded amorphous carbon.

Fig. 1

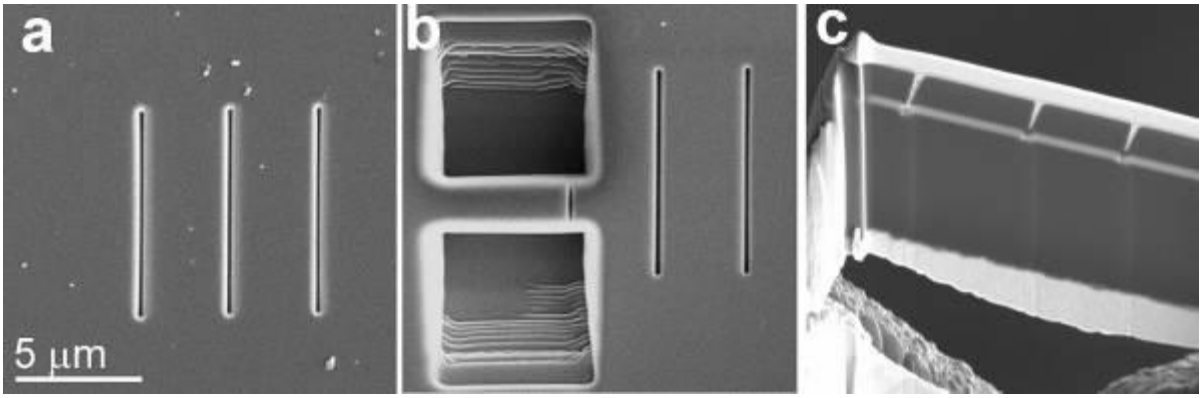


Fig. 2

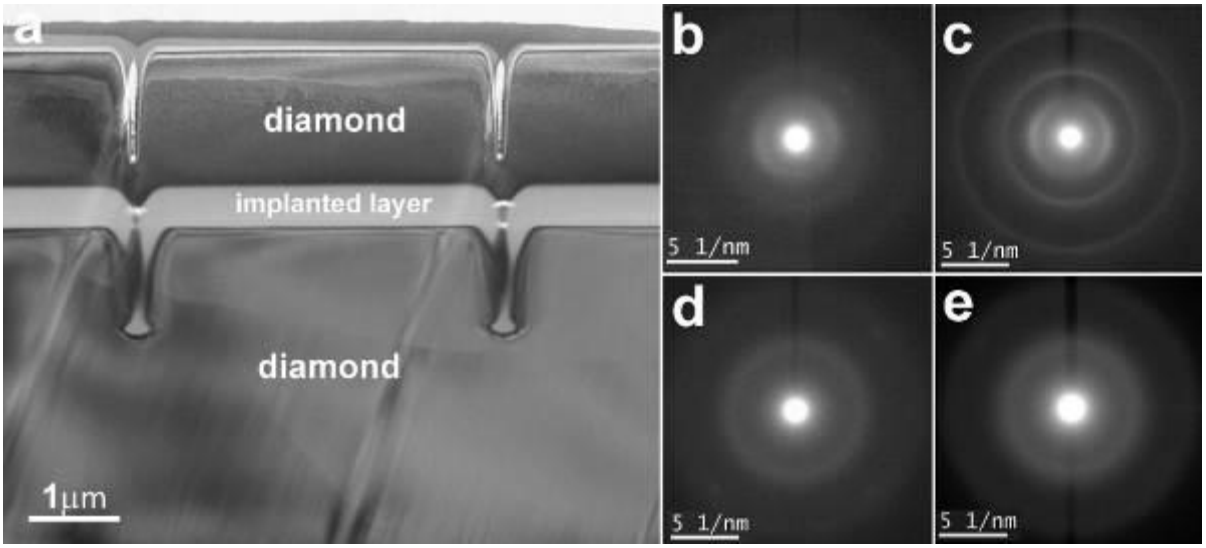


Fig. 3

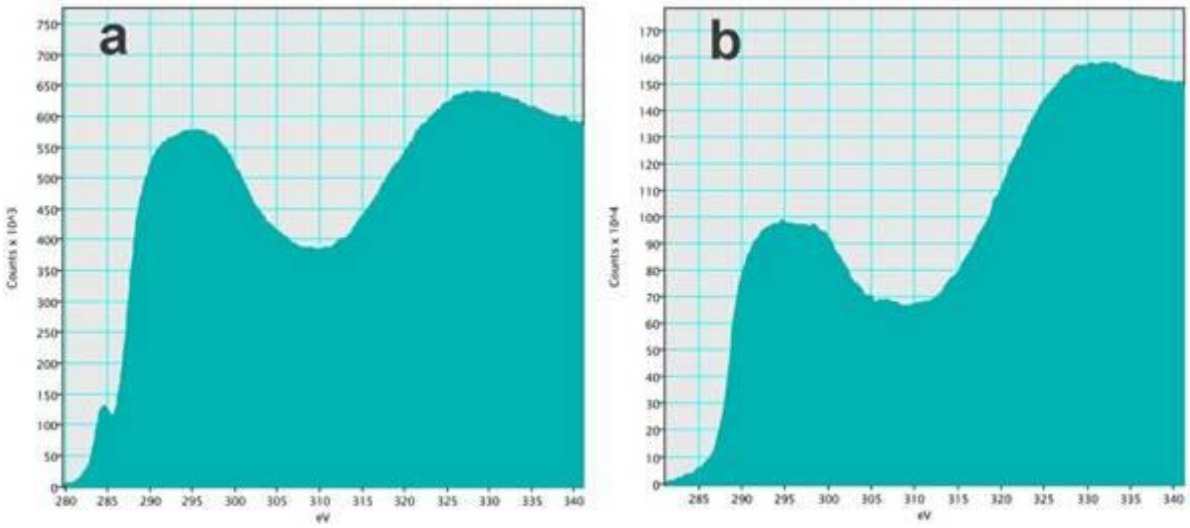
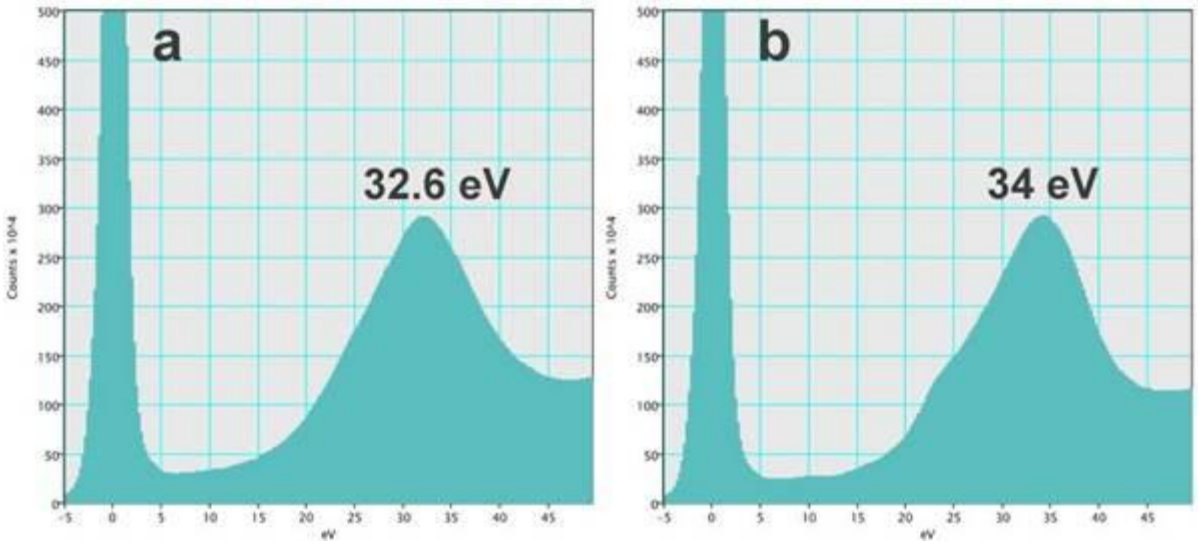


Fig. 4



MSLB.P18
Effects of Si/Al Molar Ratio on the microstructure of Metakaolin-Based Geopolymers

J. Lohmann[1,2], T. Krekeler[2], M. Ritter[2], F. Schmidt-Döhl[1]

[1]Hamburg University of Technology, Institute of Building Materials, Physics and Chemistry of Buildings, Hamburg, Germany
[2]Hamburg University of Technology, Electron Microscopy Unit (BeEM), Hamburg, Germany

Geopolymers are considered a promising alternative for enhancing sustainability in the construction sector. Their performance is closely linked to their microstructure—particularly pore type and distribution, crystallinity, and chemical composition. When metakaolin (MK) reacts with alkaline activators, an X-ray amorphous aluminosilicate gel matrix forms, accompanied by hydrate phases, including crystalline, zeolite-like structures as well as amorphous sodium and calcium aluminosilicate hydrates. The degree of cross-linking between –[Si-O-Si]– and –[Si-O-Al]– chains in the gel network depends, among other factors, on the Si/Al molar ratio of the raw materials.

This study investigates the fundamental relationship between the Si/Al ratio in alkali-activated MK and their resulting microstructure. Geopolymers based on kaolin were synthesized, and the Si/Al ratio was systematically modified by partial substitution with silica fume. The samples were characterized using scanning electron microscopy with energy-dispersive X-ray spectroscopy (SEM/EDX), porosity measurements, compressive strength tests, thermal analysis, and X-ray diffraction to assess crystallinity.

A key condition for the formation of an amorphous gel structure is the dissolution of the reactive precursors. Sodium cations in the solution serve to balance the charge within the gel network. It was found that a Si/Al ratio of 2 results in the highest compressive strength. Unreacted particles were embedded in a dense gel matrix composed of granular aluminosilicate particles at the nanometer scale. Increasing the Si/Al ratio to 4 resulted in an 88% decrease in strength, along with higher pore volume and lower density. Additionally, large regions of dense alkali-silica gel were observed, often with characteristic cracking and large voids. Thermogravimetric analysis revealed that denser structures are associated with lower water content. Moreover, as the Si/Al ratio increased, the temperature at which maximum reaction conversion occurred decreased, suggesting weaker chemical bonds within the network.

Rather than promoting stronger [-Si-O-Si-] bonds, a higher Si/Al ratio led to the formation of expansive alkali-silica (ASR) gels. This, in turn, negatively impacts the development of a robust aluminosilicate network. The dominance of silica polymerization in strength development leads to a slower reaction rate [3, 4]. Additionally, a higher concentration of soluble silica reduces the concentration of free OH^- [1], which, while impacting the dissolution process of metakaolin, is crucial for the formation of the geopolymer network. The resulting porosity was further enhanced by the presence of unreacted particles [2] and the reaction of silica with sodium hydroxide [5]. Conversely, at lower Si/Al ratios, granular N-A-S-H phases formed, which contributed to higher water incorporation.

Fig. 1: Homogeneous geopolymer structure with quartz grains.

Fig. 2: Unreacted clay particles (blue) in granular matrix (green).

Fig. 3: ASR gels (red) and voids.

Fig. 4: ASR gel with crack structure.

References

[1] Bernal, S. A. et al. 2012. Waste Biomass Valor 3, 1, 99–108.

[2] Duxson, P. et al. 2007. J Mater Sci 42, 9, 2917–2933.

[3] Duxson, P. et al. 2005. Colloids and Surfaces A: Physicochemical and Engineering Aspects 269, 1-3, 47–58.

[4] He, P. et al. 2016. Ceramics International 42, 13, 14416–14422.

[5] Zhang, M.-H. et al. 2000. ACI Materials Journal 97, 5, 576–586.

Fig. 1

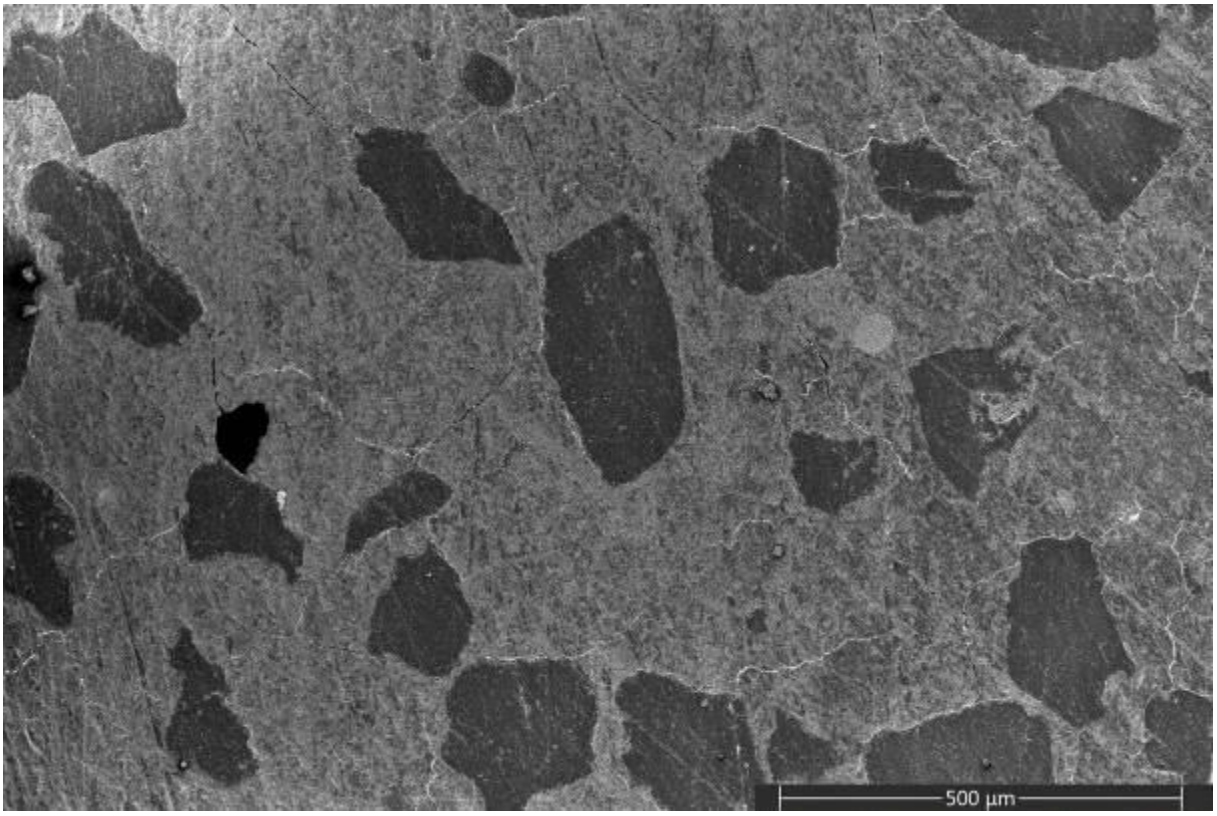


Fig. 2

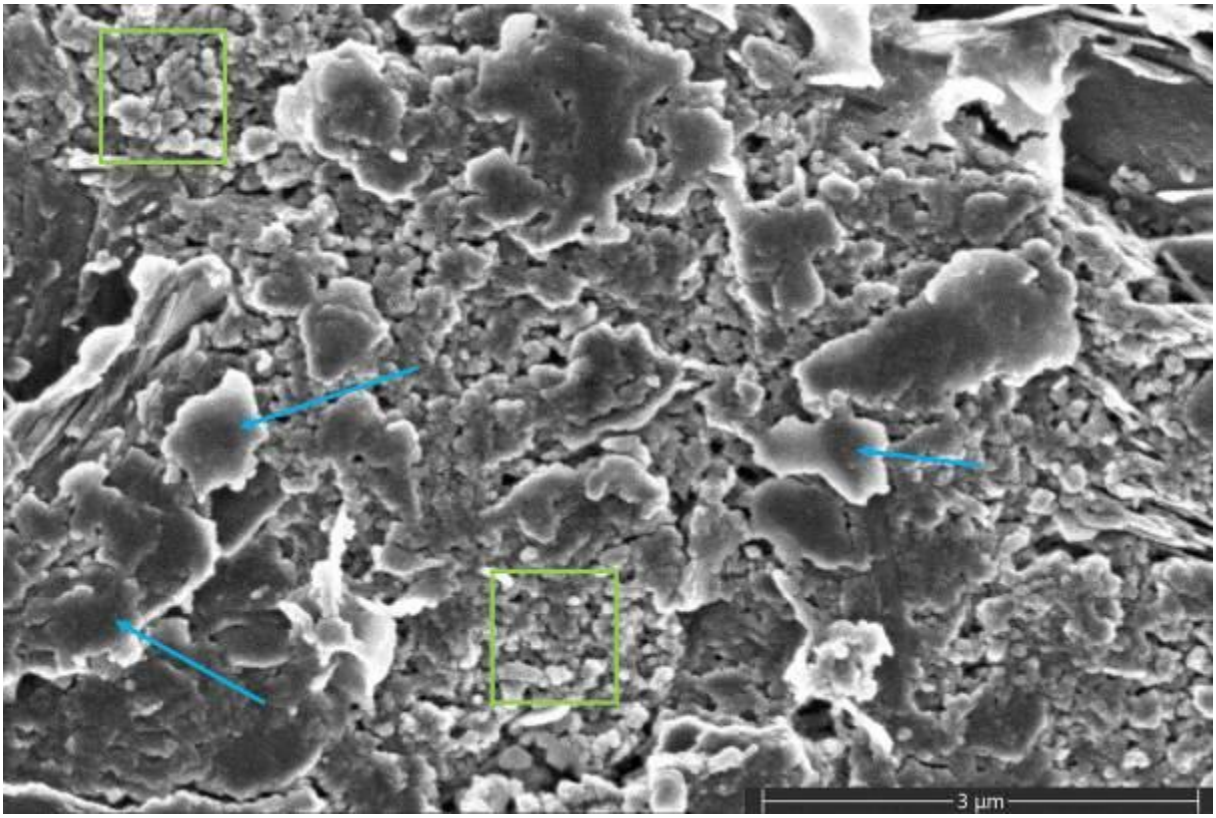


Fig. 3

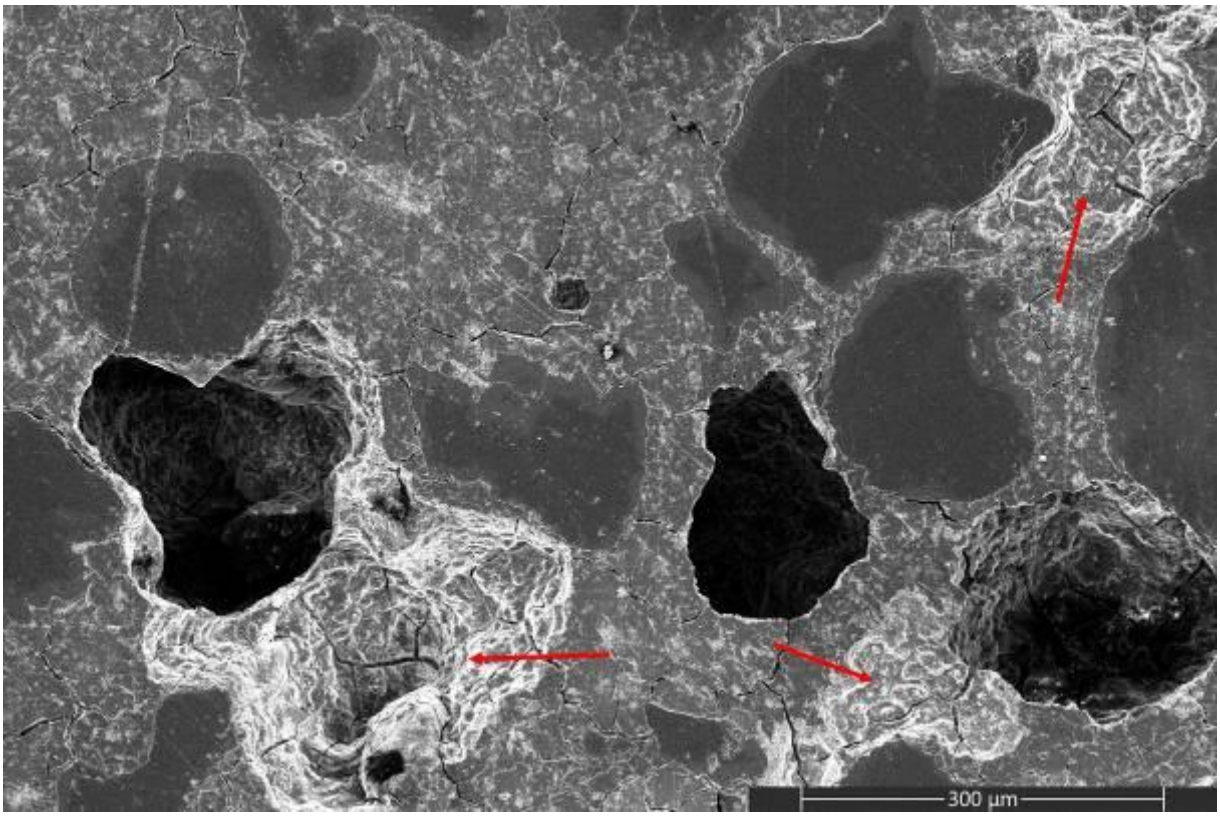
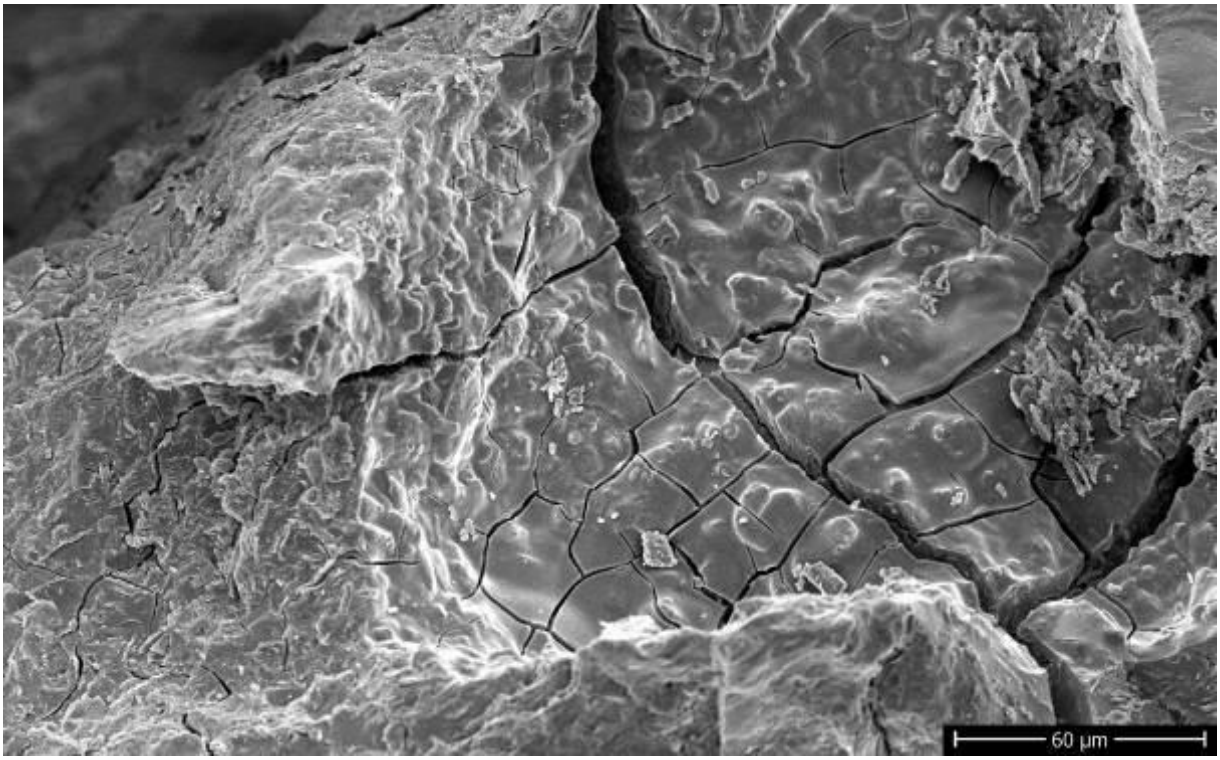


Fig. 4



MSLB.P19
Micro/Nano Patterning using laser-assisted carbonization and its applications of skin patches for small muscle sensing

Y. C. Chung[1], J. Y. Chan[1]

[1]National University of Kaohsiung, Chemical and Materials Engineering, Kaohsiung, Taiwan

Introduction

Flexible electrodes for wearable biomedical applications have gained significant attention due to their potential for continuous physiological monitoring. Traditional electromyography (EMG) systems face challenges including poor signal stability, difficulty in isolating specific muscle activity, and limited conformability to curved skin surfaces. Laser-assisted carbonization has emerged as a promising technique for fabricating conductive carbon-based materials with tunable electrical properties through rapid, cost-effective photothermal conversion. This approach enables precise micro/nano patterning of polyimide surfaces to produce functional electrodes without requiring high-temperature processing or complex transfer procedures, making it ideal for developing next-generation wearable sensors.

Objectives

This study aimed to develop a novel fabrication method using laser-assisted carbonization for creating highly sensitive skin electrode patches capable of detecting small muscle group activity. The primary objectives included: optimizing UV nanosecond laser parameters for carbonizing polyimide films into conductive electrodes, creating superhydrophobic surfaces to prevent water interference, and demonstrating practical applications for monitoring both small muscle groups like the levator veli palatini muscle and large muscle groups including fingers and wrists.

Materials & Methods

UV nanosecond laser carbonization was performed using optimized parameters to convert PI into conductive carbon electrodes with wrinkled microstructures. Characterization techniques included scanning electron microscopy (SEM), atomic force microscopy (AFM), four-point probe sheet resistance measurements, micro-Raman spectroscopy, and water contact angle analysis. Biocompatibility was assessed using MTT assays with L-929 fibroblasts.

Results

The laser-carbonized patch surfaces could be accessibly fabricated for their ruled micropatterns and nanoporous structures, largely increasing sensitivity of deformation with resistance changes. The microelectrodes can be produced to exhibit excellent electrical properties with a sheet resistance of 15.45 Ω/sq and demonstrated high sensitivity across the entire human skin strain range (0.5-15%). The wrinkled electrode structure achieved exceptional linearity (R^2 = 0.99) and a gauge factor of 10. Biocompatibility testing showed >90% cell viability, confirming safety for skin contact applications. The patches demonstrated remarkable durability, maintaining stable performance over 1000 mechanical cycles with only 0.8% signal degradation. The superhydrophobic surface effectively prevented water interference during operation. Practical applications successfully demonstrated detection of small muscle contractions in the levator veli palatini muscle as well as large muscle group movements in fingers and wrists, with response times of approximately 0.28 seconds.

Conclusion

This work presents a breakthrough approach for fabricating highly sensitive, biocompatible skin electrode patches through laser-assisted carbonization. The technique offers significant advantages including rapid single-step fabrication, excellent sensitivity to minute muscle contractions, and robust performance under various environmental conditions. This research opens new possibilities for personalized healthcare monitoring and human-machine interface applications.

Fig. 1

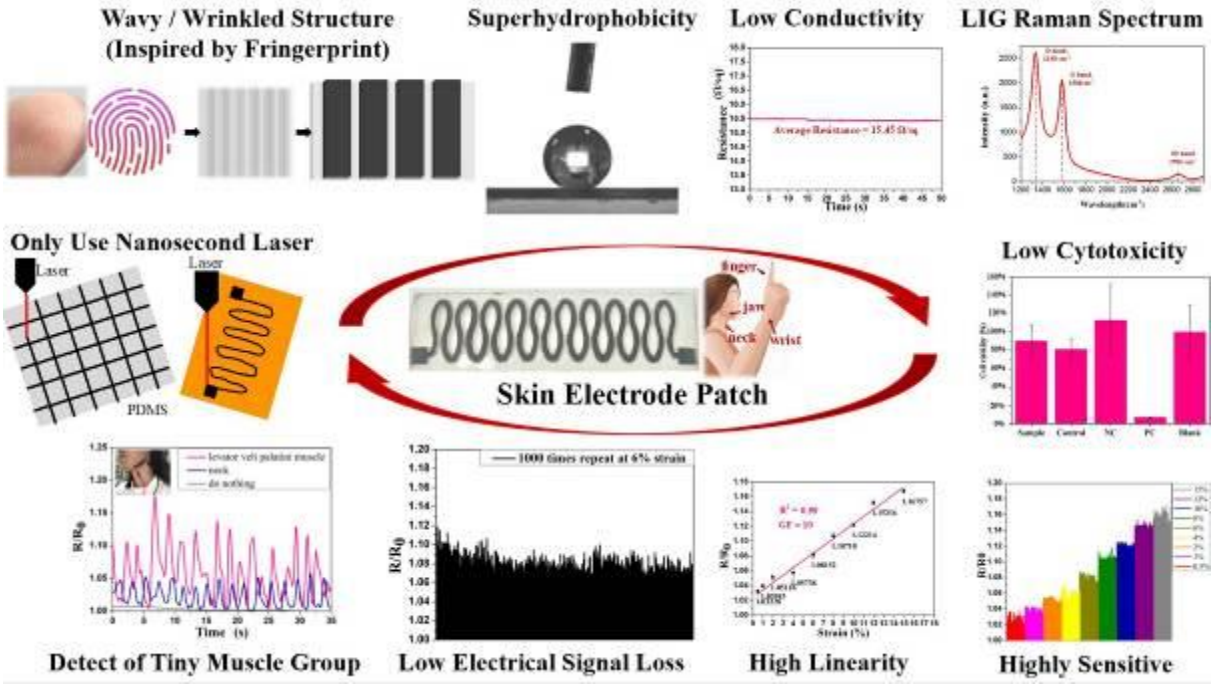


Fig. 2

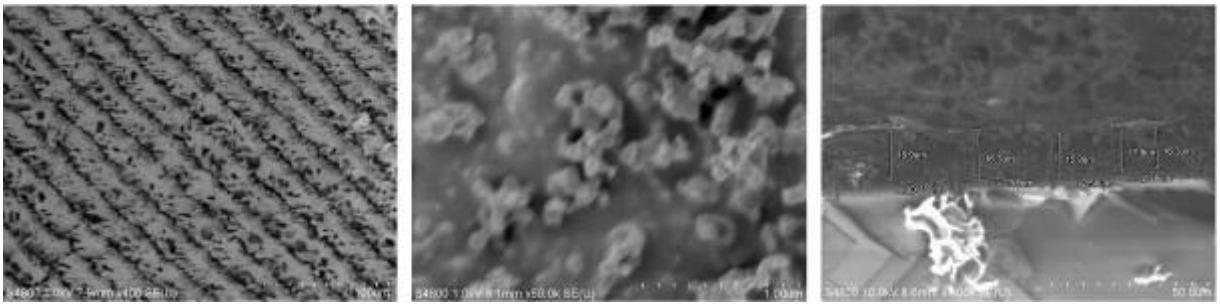


Fig. 3

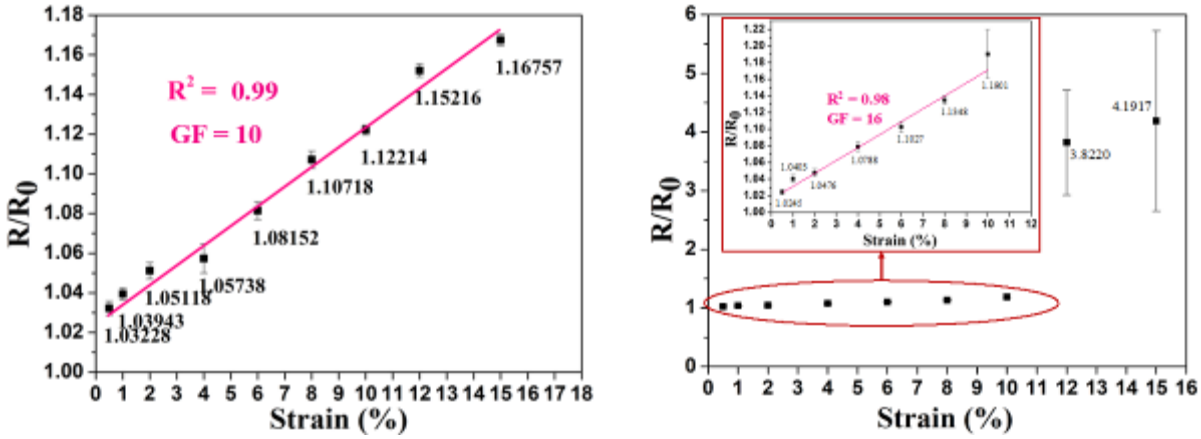
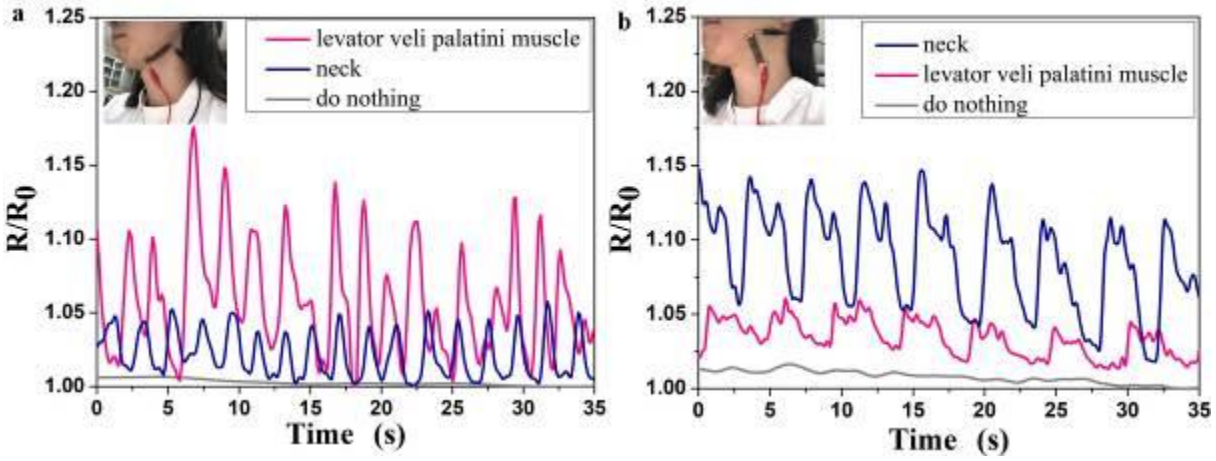

R² = 0.99
GF = 10
1.03228
1.03943
1.05118
1.05738
1.08152
1.10718
1.12214
1.15216
1.16757
R/R0
Strain (%)
R² = 0.98
GF = 16
3.8220
4.1917

Fig. 4


a
levator veli palatini muscle
neck
do nothing
R/R0
Time (s)
b
neck
levator veli palatini muscle
do nothing
R/R0
Time (s)

MSLB.P20
Revealing rapid nanoscale dynamics in copper catalysts during hydrogen oxidation reaction

G. Melinte[1], A. Genovese[1]

[1]King Abdullah University of Science and Technology (KAUST), KAUST Core Labs, Thuwal, Saudi Arabia

During their operations, catalysts undergo fast and localized structural and chemical transformations that drive them from thermodynamic stable states to non-equilibrium states. Studying these highly dynamical transformations induced by energy absorption and/or environmental conditions, will allow a more precise structure-environment-property correlation. However, as the catalyst-environment interactions happen away from the thermodynamic equilibrium within timescales inferior to 10-3 s and involve structural changes that nucleate and propagate at the nanoscale, only a limited understanding of them exist. Aberration-corrected TEM coupled with *in-situ* thermal gas-phase setups have an important contribution to the field of heterogenous catalysis owing to its ability to describe morphological and structural changes, phase transitions, and to probe the reversibility of these changes. Of special interest, is its ability to reveal aspects of the non-equilibrium dynamics, as changes in the environmental conditions (e.g., temperature, gas components partial pressure) induce continuous changes in the catalyst surface shape, composition, or structure [1].

Using the hydrogen oxidation reaction (HOR) on copper nanoparticles as model systems, this study focuses on revealing in real-time the dynamic phase-transitions of copper and their nanoscale propagation. Reversible transitions during the catalytic activation, from the inactive Cu0 to active Cu2O, the phase coexistence and their fast transformations at optimal performance, or the surface faceting evolution with the changes in the local chemical potential, will be investigated using a comprehensive in-situ gas phase TEM methodology. By ramping the reaction stimuli, e.g. temperature or O2 partial pressure, delivered by the Climate in-situ gas holder (DENS™), the aim will be to maximize the spatial resolution while maintaining a temporal resolution in the 10-3 s range. For this, the study will make use of the direct electron detection Gatan™ K3 and hybrid-pixel Gatan™ Stela cameras focusing on electron diffraction and EELS spectroscopy data.

Reference

[1] G. Melinte, et al., ACS Catalysis 7, 2017

LSLB.P01
Ultrastructural analysis of lamellar bodies in the human lung

D. Vanhecke[1], J. R. Nyengaard[2], B. Haenni[3], J. Schipke[4], M. Ochs[5]

[1]University of Fribourg, Adolphe Merkle Institute, Fribourg, Switzerland
[2]Aarhus University, Department of Clinical Medicine, Aarhus, Denmark
[3]University of Bern, Institute of Anatomy, Bern, Switzerland
[4]Hannover Medical School, Institute of Functional and Applied Anatomy, Hannover, Germany
[5]Charité - Universitätsmedizin Berlin, Institute of Functional Anatomy, Berlin, Germany

Pulmonary surfactant, which is critical for reducing alveolar surface tension, is produced by type II alveolar epithelial cells (AEC2). It is stored in lamellar bodies (LBs) before being secreted. Once triggered - e.g. when sighing - its release must be near-immediate and in large enough amounts.

The question of how such adequate amounts of surfactant are released to the alveolar space was raised. It was hypothesised that, in addition to the intraalveolar and the intracellular surfactant stores, a third, hitherto disregarded, pool of surfactant must be considered: the intermediate surfactant pool, defined as the surfactant stored in ready to launch intracellular LBs inside AEC2.

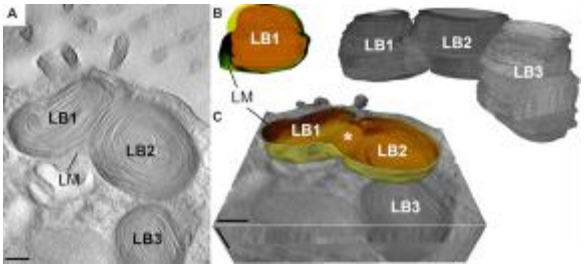
This study employs quantitative and ultrastructural methodologies to characterise number and organization of AEC2 and their LBs in human lungs, with an emphasis on locating this intermediate surfactant pool. The techniques employed in this study encompassed transmission electron microscopy, serial section electron tomography, and stereology.

A comprehensive analysis of five human lungs was conducted, yielding an average of 24 billion AEC2 per lung. It was further observed that the mean AEC2 was found to be 650 μm^3. The mean LB volume per lung was approximately 1.9 mL, and this was closely correlated with overall lung volume. Each AEC2s contained in average 324 LBs, resulting in a total volume of 74 μm^3 of LBs, with each individual LBs exhibiting an average volume of 0.24 μm^3.

The study also identified three distinct LB subtypes: The first category, the vast majority, is characterised by isolated LBs (approximately 300 per AEC2). The second category is distinguished by LBs connected to each other via small pores (in average 23 LBs per AEC2, see Figure A - tomogram, and B - rendering). The third category is defined by LBs connected to the plasma membrane via a fusion pore (approximately 1 per AEC2). An increase in LB size was observed across these categories, possibly indicating a progression towards secretion. Approximately 14% of the total LB volume of an AEC2 was found in connected LBs. These data, especially the existence of the second category of LBs, support the hypothesis of the existence of an intermediate surfactant pool involved in surfactant trafficking.

In summary, the present study provides fundamental data on the number, size and organisation of LBs in human AEC2. Furthermore, it offers morphological and quantitative evidence for the existence of an intermediate surfactant pool. This intermediate surfactant pool of LBs in AEC2 is not only directly connected to the plasma membrane via inter-LB connections, but also indirectly.

Fig. 1



LSLB.P02
TMPRSS2 and glycan receptors synergistically facilitate coronavirus entry

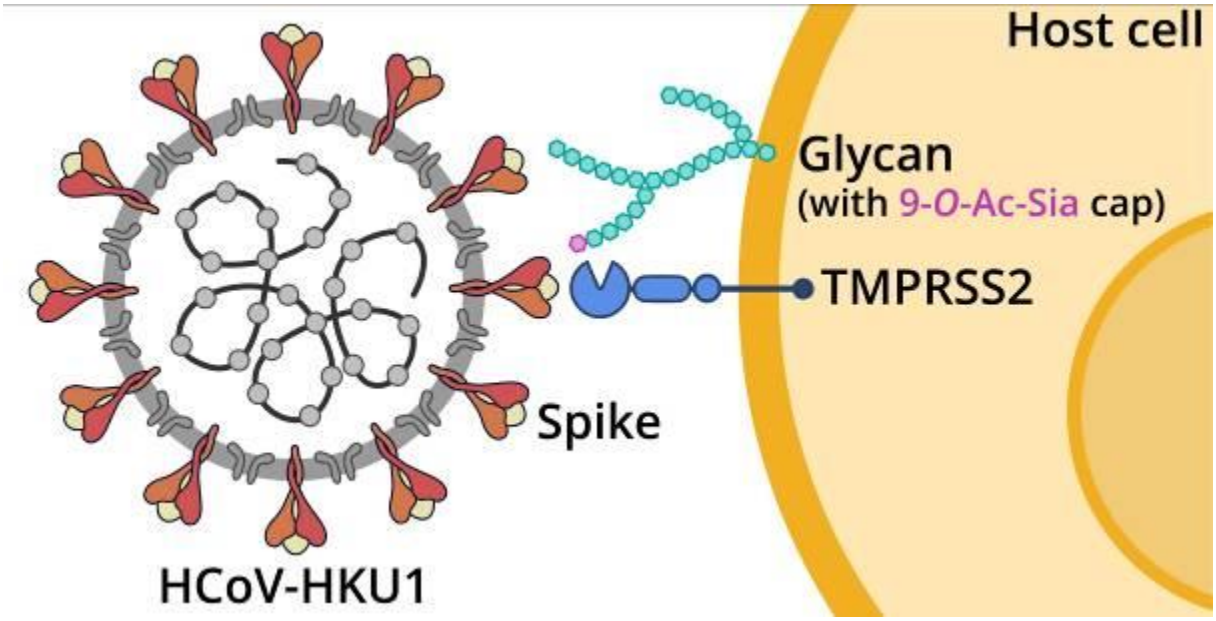
Y. Lu[1]

[1]ShanghaiTech University, Shanghai Institute for Advanced Immunochemical Studies (SIAIS), Shanghai, China

The entry of coronaviruses is initiated by spike recognition of host cellular receptors, involving proteinaceous and/or glycan receptors. Recently, TMPRSS2 was identified as the proteinaceous receptor for HCoV-HKU1 alongside sialoglycan as a glycan receptor. However, the underlying mechanisms for viral entry remain unknown. Here, we investigated the HCoV-HKU1C spike in the inactive, glycan-activated, and functionally anchored states, revealing that sialoglycan binding induces a conformational change of the NTD and promotes the neighboring RBD of the spike to open for TMPRSS2 recognition, exhibiting a synergistic mechanism for the entry of HCoV-HKU1. The RBD of HCoV-HKU1 features an insertion subdomain that recognizes TMPRSS2 through three previously undiscovered interfaces. Furthermore, structural investigation of HCoV-HKU1A in combination with mutagenesis and binding assays confirms a conserved receptor recognition pattern adopted by HCoV-HKU1. These studies advance our understanding of the complex viral-host interactions during entry, laying the groundwork for developing new therapeutics against coronavirus-associated diseases.

Figure 1. Illustration of HCoV-HKU1 recognition of host receptors.

Fig. 1



LSLB.P03
Behavioral states of *C. elegans* dauer larvae are supported by distinct structural and functional modifications of the GABAergic system

S. Stöckl[1], X. Dünninger[1], N. Alsheimer[1], E. Bencurova[2], F. Fink[3], T. Dandekar[2], P. Kollmannsberger[3], C. Stigloher[1]

[1]University of Würzburg, Imaging Core Facility, Würzburg, Germany
[2]University of Würzburg, Chair of Bioinformatics, Würzburg, Germany
[3]Heinrich-Heine-Universität Düsseldorf, Biomedical Physics, Düsseldorf, Germany

Harsh environmental conditions suppress the reproductive cycle in the nematode *Caenorhabditis elegans* (*C. elegans*) and favor an alternative life cycle, called dauer stage. Characteristic of dauer larvae are specific adaptations such as prolonged survival without solid food intake, protection from desiccation by cuticular changes, or a sealed mouth. The harshness of environmental conditions also poses specific demands on the nervous system to enable dauer-specific behaviors. For example, some sensory neurons undergo dendritic arborization or axon remodeling during dauer development, and in some cases the synaptic circuitry is altered. In contrast to the sensory system, specific changes and developmental plasticity in the motoric system have barely been analyzed in the dauer stage, although this is critically important for their survival. Therefore, we directly compare the dauer larva and its developmentally parallel reproductive stage L3 in this regard using light and electron microscopy as well as behavioral analysis.

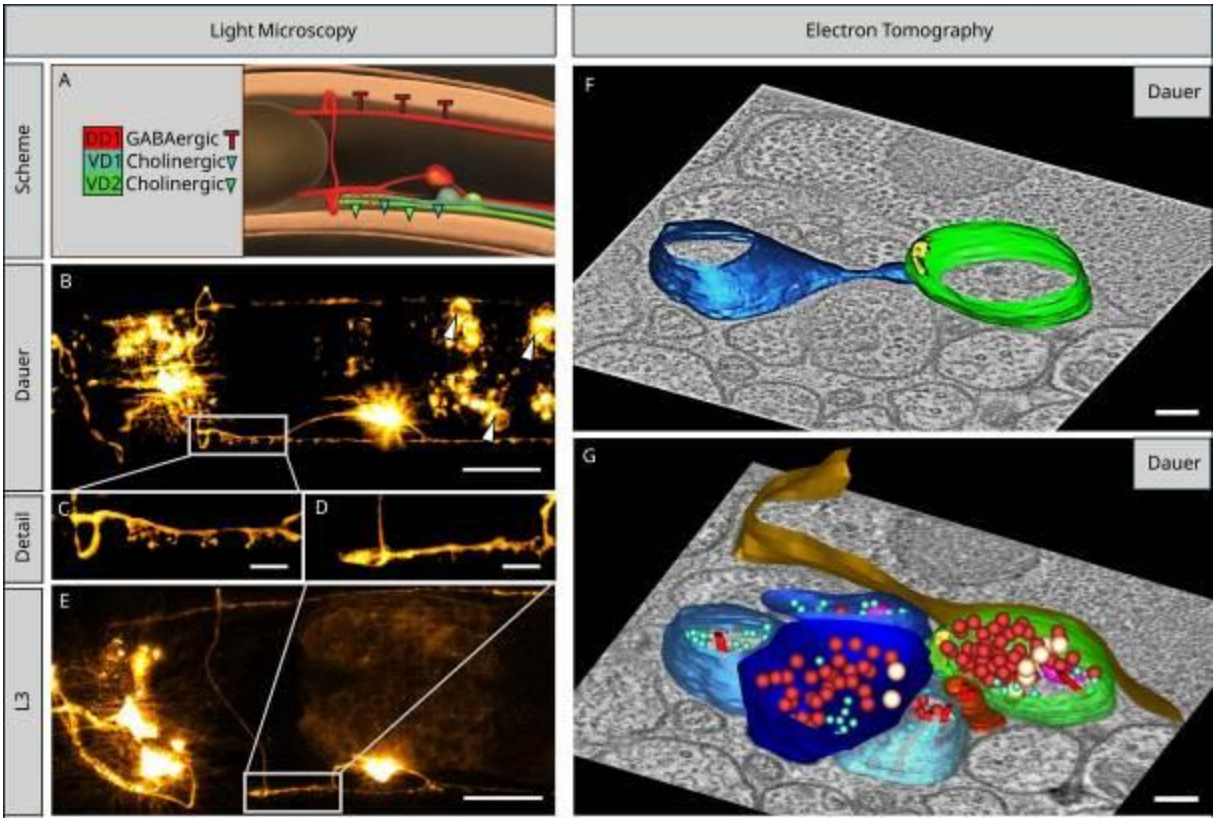
To assess underlying motor behavior of structural and functional developmental plasticity, we focused on high-energy depleting swimming, called thrashing, and compared dauer larvae to the L3 larval stage of the reproductive life cycle. We utilized focused ion beam - scanning electron microscopy (FIB-SEM) to perform volumetric reconstructions of the retrovesicular ganglion (RVG), a neuronal cluster at the transition from the head to the mid-body that integrates sensory input and regulates locomotion. To investigate functional plasticity, we applied light microscopy and global optogenetic silencing of the GABAergic nervous system.

Thrashing behavior analyses revealed that dauers exhibit a dual behavioral repertoire predominantly displaying locomotor lethargy, but also the capability to initiate strong bursts of exploratory dispersal by thrashing. In contrast, L3 larvae demonstrated also local dwelling or body bending and an elevated baseline activity. These behavioral differences were correlated with changes in our FIB-SEM data of the RVG, which revealed substantial neuronal plasticity between the two developmental stages and reorganization of motor circuits particularly regarding the inhibitory system. Furthermore, dauer larvae showed a diminished behavioral responsiveness to global optogenetic silencing of GABAergic neurons suggesting a diminished GABAergic system. Light microscopy also indicated a reduced or downregulated GABAergic system in dauer larvae relative to L3, yet revealed a more pronounced network of activity-dependent postsynaptic GABAergic dendritic spines (Figure 1).

Our findings suggest that dauer larvae undergo both structural and functional modifications in the motor system that enable distinct, adaptive behavioral outputs. The increased presence of postsynaptic GABAergic protrusions may enable flexible locomotion despite a globally reduced inhibitory system, facilitating a baseline energy-conserving lethargy while maintaining the capacity for environment-dependent exploratory dispersal.

Figure 1. Dauer larvae exhibit more extensive GABAergic dendritic spines compared to L3 larvae. A-E: Illustration of motoric feedback loop within the retrovesicular ganglion (RVG) (strain XMN46(*bggIs6*): Oppermann and Grill, Neural Dev. 2014); scale bars = 10 µm (B,E) / 2 µm (C,D). **F,G:** Tomographic reconstruction of a dendritic spine (blue) located postsynaptically to motor neuron (green); scale bar = 100 nm.

Fig. 1


Light Microscopy
Electron Tomography
Scheme
Dauer
Detail
L3
A
DD1 GABAergic
VD1 Cholinergic
VD2 Cholinergic
B
C
D
E
F
Dauer
G
Dauer

LSLB.P05
Postnatal development of the spine apparatus in the murine hippocampus: A multimodal imaging study

J. Hallenberger[1], E. Niggetiedt[1], C. Martin[1], M. Anstötz[1]

[1]Heinrich Heine Universität Düsseldorf, Vorklinik UKD, Anatomie 2, Düsseldorf, Germany

During postnatal brain development, excitatory synapses undergo extensive structural remodelling to support emerging connectivity and synaptic function. Often, dendritic spines on neuronal dendrites serve as primary sites for excitatory input. A key substructure in many spines is the so-called spine apparatus (SA) - a smooth endoplasmic reticulum-derived organelle involved in calcium regulation and synaptic plasticity. While its function is increasingly understood, the developmental emergence and maturation of the SA, particularly in the hippocampus, remain unclear. This study investigates the postnatal development, morphology, and localization of the SA in dentate gyrus granule cells of the murine hippocampus.

A multimodal imaging approach was used to assess dendritic spines and the SA across three developmental stages (juvenile, adolescent, mature). Golgi-Cox staining quantified changes in spine density and morphology. Immunohistochemistry combined with bright-field and confocal microscopy enabled localization of SA markers. In addition, 3D Focused Ion Beam-Scanning Electron Microscopy (FIB-SEM) provided ultrastructural insights into intracellular membrane organization.

Golgi-Cox staining revealed a progressive increase in spine density and morphological complexity, followed by a decline at later stages, suggesting dynamic synaptic maturation and pruning. FIB-SEM analysis indicated corresponding changes in subcellular membrane structures consistent with SA emergence and synapse maturation.

This study integrates complementary imaging techniques to track the developmental trajectory of the spine apparatus. Our findings contribute to a better understanding of synaptic refinement in the hippocampus and may inform research into neurodevelopmental disorders involving synaptic dysfunction.

LSLB.P06
Nanoscale grid writing modes and on-grid mixing of proteins before vitrification

J. Sedzicki[1], A. Lorca Mouliaá[1], D. E. Schneider[1], T. Braun[1], A. Engel[1]

[1]cryoWrite AG, Basel, Switzerland

One Mio projections suffice for determining the structure of a protein. This corresponds typically to <1 pg of pure protein. Dispensing 1 nL sample with a concentration of 1 mg/mL corresponds to 1 ng. The cryoWriter writes 1 nL as a 1 mm circular layer by moving a glass pipette across the grid, reproducibly yielding 20 suitable grid squares. This makes the placement of multiple samples or multiple sample layers on the same grid possible. The cryoWriter purifies proteins from µL cell lysates using magnetic beads providing enough sample to prepare more than 10 grids. On-grid mixing of multiple samples some milliseconds prior to vitrification allows conformational changes to be studied. In summary, the cryoWriter opens new possibilities for sample handling and grid writing.

Fig. 1

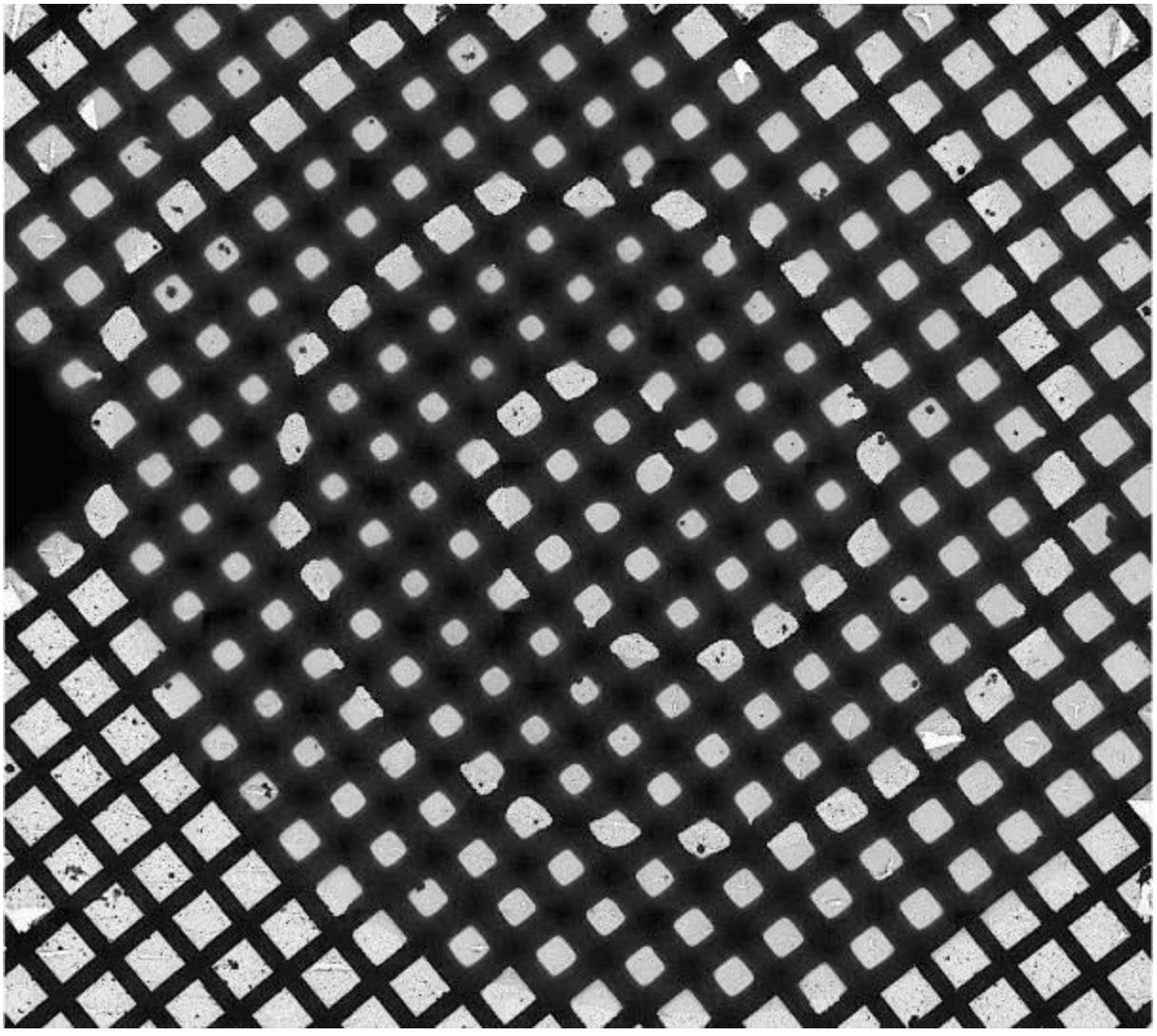


Fig. 2

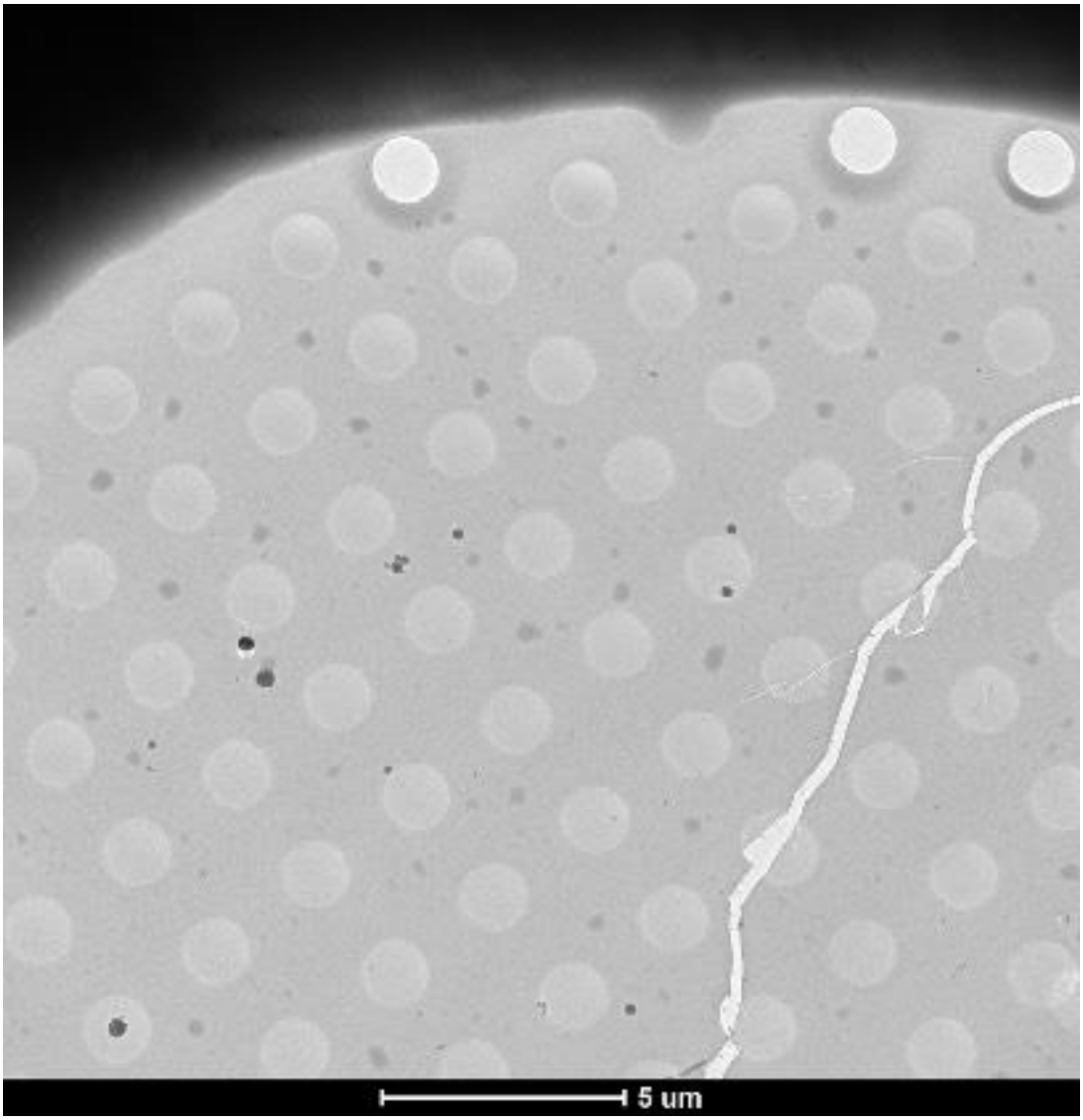
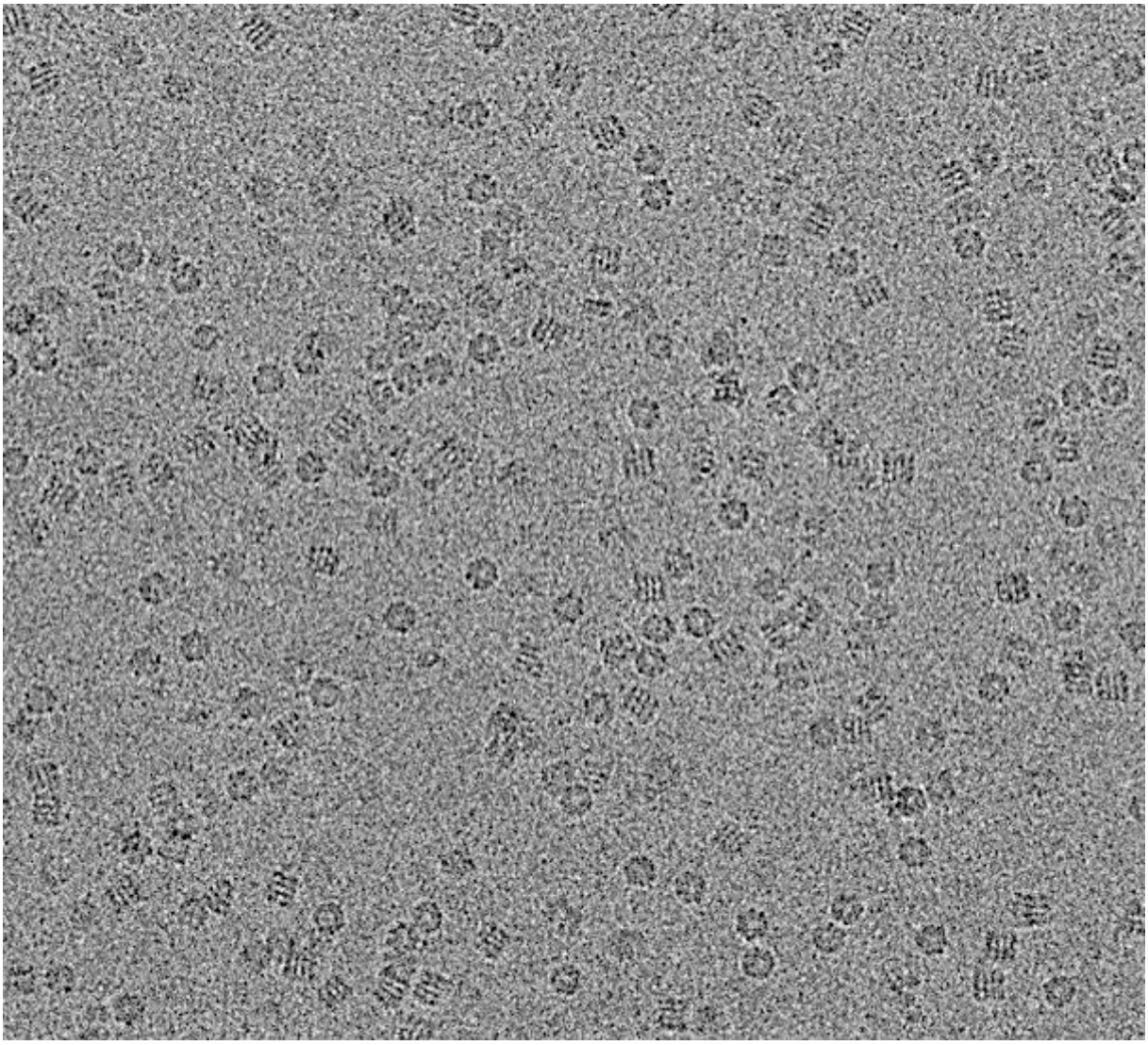


Fig. 3



LSLB.P07
Fast Focused Ion Beam Scanning Electron Microscopy (FIB-SEM) tomography of human brain tissue

L. Grünewald[1,2], C. Galanis[1], J. Straehle[3,4], M. H. Ulbrich[1], J. Beck[3,4,5], A. Vlachos[1,2,4,5]

[1]University of Freiburg, Institute of Anatomy and Cell Biology, Department of Neuroanatomy, Freiburg i. Br., Germany
[2]University of Freiburg, Center BrainLinks-BrainTools, Freiburg i. Br., Germany
[3]University of Freiburg, Medical Center and Faculty of Medicine, Department of Neurosurgery, Freiburg i. Br., Germany
[4]University of Freiburg, Medical Center and Faculty of Medicine, Center for Advanced Surgical Tissue Analysis (CAST), Freiburg i. Br., Germany
[5]University of Freiburg, Medical Center and Faculty of Medicine, Center for Basics in Neuromodulation (NeuroModulBasics), Freiburg i. Br., Germany

Introduction

Volume electron microscopy (vEM) provides ultrastructural insights into the neural tissue[1], thereby contributing to our understanding of brain function and pathology. FIB-SEM tomography (FST) enables isotropic high-resolution 3D reconstructions for quantitative ultrastructural analysis but suffers from limited throughput mostly due to slow SEM imaging[1]. Recent advances in deep learning–based denoising, such as content-aware image restoration (CARE)[2,3], offer a promising solution to this bottleneck.

Objectives

We aim to enhance FST throughput by combining fast SEM acquisition with CARE-based denoising[2]. CARE uses paired low- and high signal-to-noise ratio (SNR) images to train a network (Fig. 1). Low-SNR images are rapidly acquired using short dwell time per pixel, while every *n*th image is additionally recorded with high SNR (long dwell time) to serve as ground-truth. Post-acquisition, CARE denoises the low-SNR image series, enabling efficient analysis of human brain morphology, including responses to transcranial magnetic stimulation (TMS)[4].

Materials & Methods

Human cortical tissue obtained during neurosurgical procedures[5] was processed using standard EM protocols (chemically fixed, heavy-metal stained, dried, resin embedded). FST was performed on a Thermo Scientific Helios 5 CX Ga^+-ion FIB-SEM system using backscattered electron (BSE) detection at 2 keV with the in-column detector.

Results

Initial results focused on optimized SEM acquisition parameters (Fig. 2a) and preparing training datasets for CARE. High-SNR images reliably resolved key ultrastructural features (e.g., synaptic vesicles; Fig. 2b,c), which were poorly visible in low-SNR scans. Speed-related scan distortions were evident as image shifts and spectral artifacts (Fig. 2b,d). Image alignment using scale-invariant feature transform (SIFT) and the bUnwarpJ plugin[6] in Fiji corrected these distortions (Fig. 2e, blue arrowheads), allowing accurate pairing for CARE training. First denoising results (Fig. 3, $n = 10$) demonstrate improved image quality suitable for further processing (e.g., segmentation), although the low SNR images here were too noisy to recover the synaptic vesicles.

Conclusion

CARE-enhanced FST enables faster vEM imaging without substantially compromising image quality, significantly improving throughput. Remaining limitations relate to physical FIB slicing rate. The

approach is broadly applicable beyond neuroscience, including materials sciences and other fields requiring vEM.

References

1. Kievits et al., *J Microsc* **287**, 114–137 (2022)
2. Weigert et al., *Nat Methods* **15**, 1090–1097 (2018)
3. Buchholz et al., *Method Cell Biol*, **152**, 277–289 (2019)
4. Vlachos et al., *J Neurosci* **32**, 17514–17523 (2012)
5. Straehle et al., *Acta Neurochir* **165**, 1461–1471 (2023)
6. Arganda-Carreras et al., *Lect Notes Comput Sc*, **4241/2006**, 85-95 (2006)

Figure Captions

Fig. 1: CARE-based FIB-SEM tomography (FST) workflow. Fast scanning is used during FST run and additional slow-scan images are acquired every *n*th slice. Images are then denoised post acquisition with CARE.

Fig. 2: (a) Exemplary high SNR image from human brain tissue with zoom-in of (b) high and (c) low SNR image regions. Features are shifted in the low SNR image and (d) high-frequency scan artefacts are visible in the power spectra. (e) Registered image ready for CARE training with ground truth in (b).

Fig. 3: Comparison of high SNR, CARE, and block-matching and 3D filtering (BM3D) denoised images.

Fig. 1

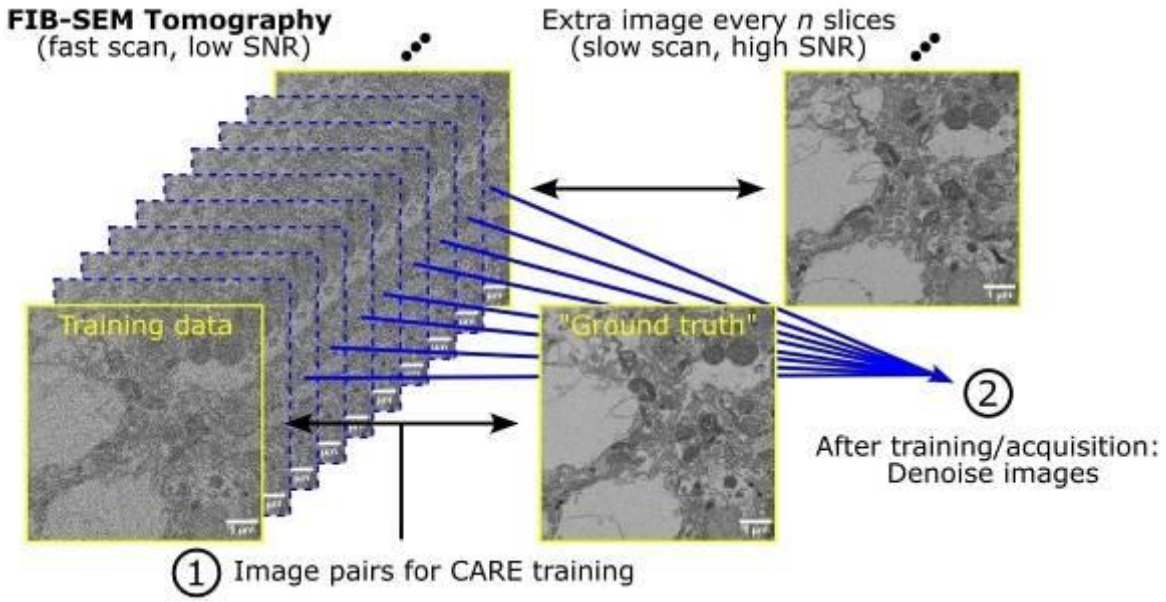


Fig. 2

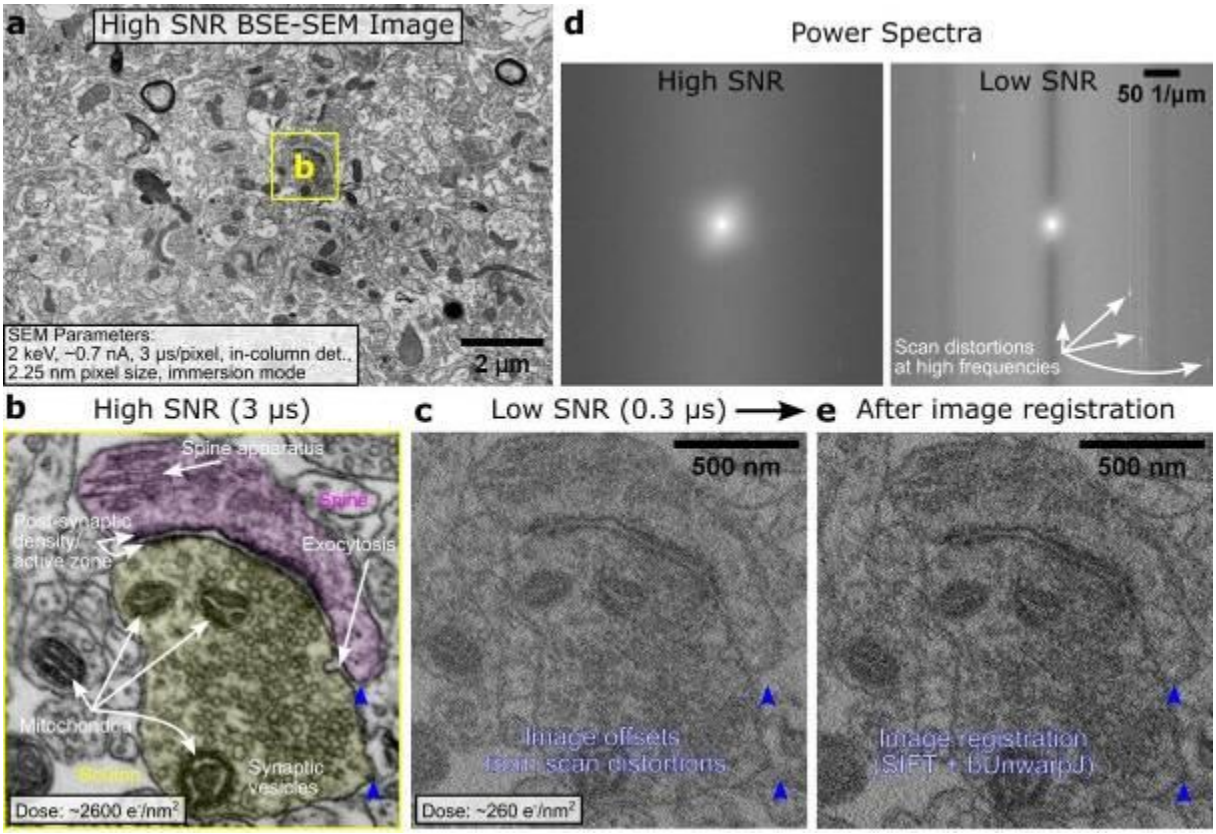
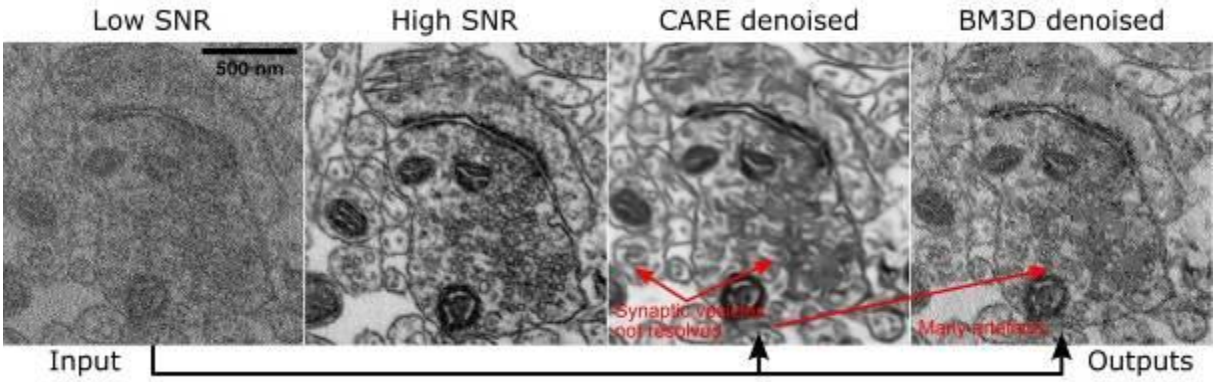

a
High SNR BSE-SEM Image
b
SEM Parameters:
2 keV, ~0.7 nA, 3 µs/pixel, in-column det.,
2.25 nm pixel size, immersion mode
2 µm
d
Power Spectra
High SNR
Low SNR
50 1/µm
Scan distortions
at high frequencies
b
High SNR (3 µs)
Spine apparatus
Spine
Post-synaptic
density,
active zone
Exocytosis
Mitochondria
Synaptic
vesicles
Dose: ~2600 e⁻/nm²
c
Low SNR (0.3 µs)
500 nm
Image offsets
from scan distortions
Dose: ~260 e⁻/nm²
e
After image registration
500 nm
Image registration
(SIFT + bUnwarpJ)

Fig. 3


Low SNR
High SNR
CARE denoised
BM3D denoised
500 nm
Synaptic vesicles
not resolved
Many artifacts
Input
Outputs

IMLB.P01
Optimising a modern high performance FE-SEM for multimodal vEM

E. Venter[1], S. Gürster[2], D. Gosselin[3]

[1]JEOL UK (Ltd), Application, Hertfordshire, United Kingdom
[2]JEOL (Germany) GmbH, Application, Freising, Germany
[3]JEOL USA, Inc., Application, Peabody, United States

The increasing popularity of Volume Electron Microscopy (vEM) in recent years is underscored by significant investments (such as those from the Chan Zuckerberg Initiative) and growing support from community-run platforms. This surge in interest has created a wealth of resources that allow vEM users to select optimal workflows and methodologies, enhancing experimental approaches and promoting collaborative learning. vEM techniques, particularly in Scanning Electron Microscopy (SEM), are now more accessible and versatile than ever, offering detailed imaging and 3D reconstruction of samples. This talk will focus on two main techniques within SEM: Array Tomography (AT) and Serial Block-Face SEM (SBF-SEM), discussing their unique advantages and limitations in terms of sample preparation, resolution, and material reuse.

Historically, hardware limitations often confined vEM users to a single technique or instrument. However, recent advancements in hardware and software now enable flexibility in workflow choices, including the ability to perform both AT and SBF-SEM within a single system. JEOL"s innovations in microscopy allow for tailored vEM solutions to meet the diverse needs of scientific inquiries. Key hardware developments include a Schottky Plus FEG electron gun, advanced column optics, and a new back-scattered electron detector optimized for low kV imaging. These improvements enable faster, high-resolution imaging, crucial for efficient vEM sample preparation.

The transition between imaging modes, such as switching from normal SEM to SBF-SEM, has also been simplified through collaboration with ConnectomX. This process, which involves mounting a Katana microtome, is quick and user-friendly. Moreover, JEOL's SEM Supporter software streamlines both the setup and execution of AT and SBF-SEM experiments, ensuring automated and seamless data acquisition. This software also facilitates easy transitions between workflows, reducing the complexity traditionally associated with vEM experiments.

Recent software advancements further enhance the post-acquisition process, offering solutions for image alignment, rendering, and segmentation, thereby completing the vEM workflow from data collection to analysis. With these integrated hardware and software solutions, JEOL provides researchers, regardless of their experience level, with an efficient and intuitive platform to conduct high-quality vEM studies.

In conclusion, JEOL"s innovations in both hardware and software provide a comprehensive, user-friendly platform for performing advanced vEM. This approach allows researchers to explore complex biological structures with unprecedented detail, while also simplifying the overall workflow, making vEM accessible to a broader audience.

Fig. 1

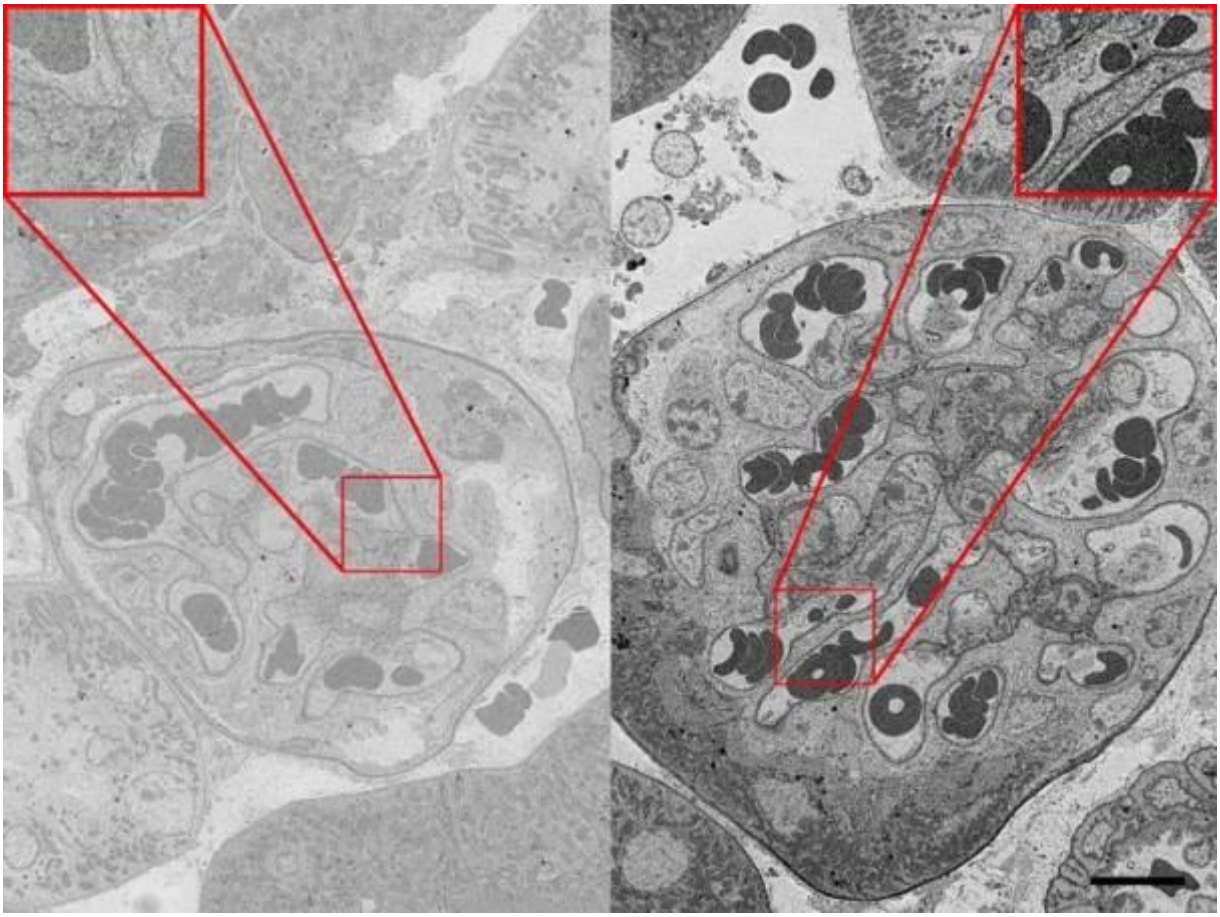


Fig. 2

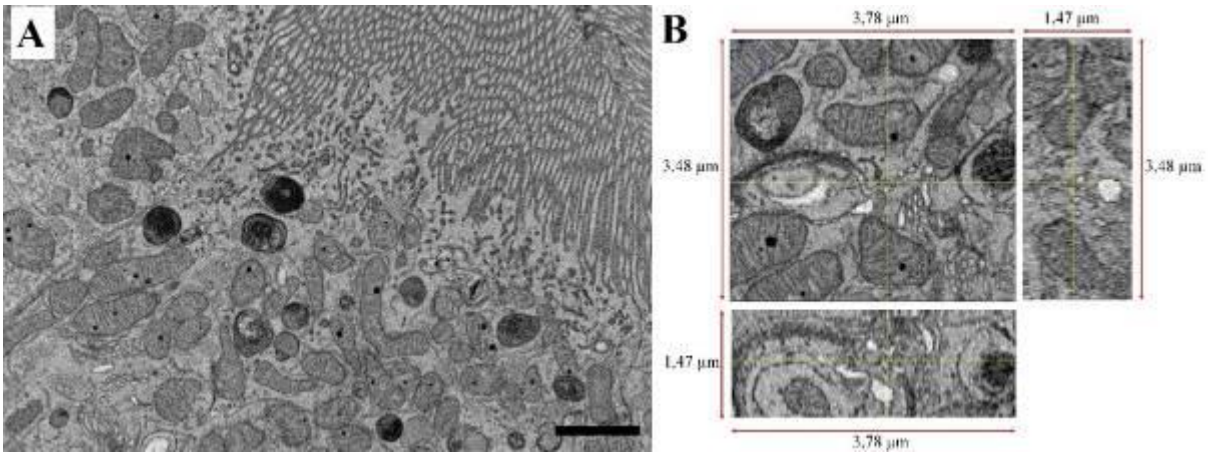
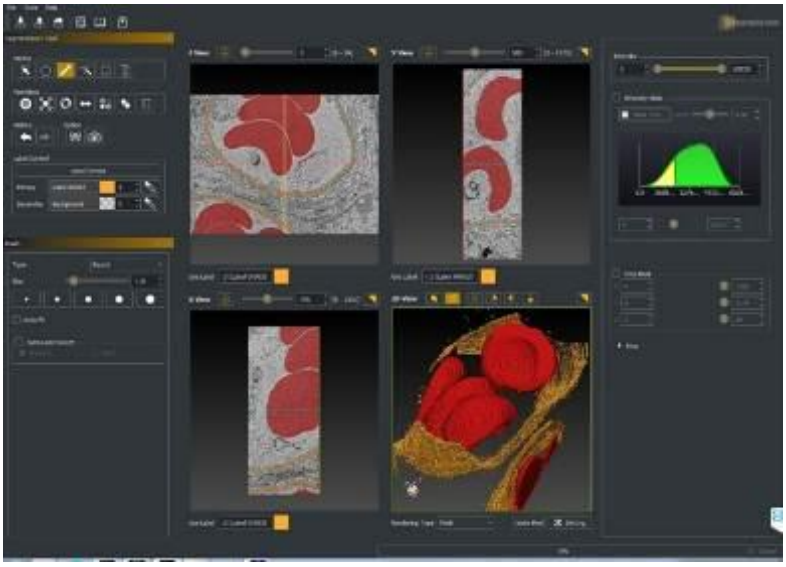


Fig. 3



IMLB.P02
JEOLs new high-end focused ion beam system JIB-PS500i for safe and smooth preparation of lamella for high-end TEM imaging

T. Harzer[1], E. Katzmann[1]

[1]JEOL (Germany) GmbH, Application, Freising, Germany

Focused ion beam (FIB) systems are typically known to be complex, requiring advanced skills for safe and productive operation.

JEOL took up the challenge and designed the all-new JIB-PS500i FIB preparation system to facilitate the fabrication, high-resolution imaging and analysis of thin TEM lamellae and cross sections. The AVERT engine provides users with a 3D model of the chamber, detectors, and sample holder at all times for maximum chamber overview and safety. Photos of the samples will be visible in this virtual chamber representation using an integrated light-optical system. The EDS system has been fully integrated into the FIB software. Even advanced analytical tasks such as quantification or phase analysis can now be performed and exported directly along with all other data. The new STEMPLING2 lamella preparation system is designed for high throughput and ease of use: Together with the fully integrated probing tool, multiple lamellae can be produced automatically and sequentially.

The large, easily accessible sample chamber is designed to accommodate very large samples and wafers and allows samples to be tilted more than 90°. As a result, TEM samples can be easily prepared, imaged, and analyzed directly in STEM mode. Both the objective lens and detectors have been further developed for high-end imaging and simultaneous analysis.

A high beam current gallium source (up to 100nA) for maximum ablation rates and the proven in-lens Schottky FEG (up to 500nA) for large area, fast elemental analyses are also available for fast workflows.

Owners of a JEOL TEM also benefit from the new "TEM Linkage" system: A double-tilt retainer can be attached to both the FIB-SEM holder and a TEM holder. Not only can lamellae be imaged in transmission mode in both microscopes, but they can also be transferred between systems without touching the TEM grid.

Figure 1. Specimen transfer workflow between FIB and TEM using a double-tilt retainer system.

Fig. 1



IMLB.P03
Nanoimaging of electrically- and laser-driven charge-density wave phase transformations

T. Domröse[1], N. Fernandez[2], C. Eckel[2], K. Rossnagel[3,4], R. T. Weitz[2], C. Ropers[1,5]

[1]Max Planck Institute for Multidisciplinary Sciences, Department of Ultrafast Dynamics, Göttingen, Germany
[2]University of Göttingen, 1st Institute of Physics, Göttingen, Germany
[3]Deutsches Elektronen-Synchrotron DESY, Ruprecht Haensel Laboratory, Hamburg, Germany
[4]Kiel University, Institute of Experimental and Applied Physics, Kiel, Germany
[5]University of Göttingen, 4th Physical Institute – Solids and Nanostructures, Göttingen, Germany

Introduction

The abrupt changes of a material's macroscopic properties across a structural transition are of profound technological relevance. Particularly fast switching at low energy consumption is found in charge-density wave systems, featuring sub-Angstrom periodic lattice distortions (PLDs) [1]. In the past, both electrical and optical excitation have been shown to drive transformations between such superperiodicities [2-4]. Yet, the influence of the material's microstructure on the switching behavior, and thus the macroscopic device performance, is far less understood.

Objectives

Here, we demonstrate nanoimaging of PLD phase transformations in the quantum material 1*T*-TaS_2 as driven by both optical [5] and electrical excitation [6]. We follow the nucleation and growth of the emergent high-temperature phase domain, characterizing the influence of structural heterogeneity on the propagation of the interphase boundary and the thermal hysteresis of the first-order transition.

Materials & methods

In electron diffractograms, PLD formation brings about additional diffraction spots - a direct measure of the PLD amplitude (Fig. 1B,D). Our nanoimaging approach utilizes tailored dark-field (DF) imaging based on these low-intensity features. The DF mask consists of 72 individual apertures arranged to filter out electrons scattered by the room-temperature PLD periodicities (Fig. 1C). Thereby, we obtain enhanced contrast to the phase switch at a spatial resolution of 5 nm across a micrometer field-of-view, as the structural transition leads to a pronounced intensity suppression in DF imaging.

Results

We follow the laser-induced high-temperature phase nucleation and the subsequent domain growth in thermal equilibrium (Fig. 1E) [5]. Therein, the interphase boundary displays characteristic 120° angles, a fingerprint of the trigonal host crystal structure, and we observe PLD phase pinning at defect sites.

In a second set of measurements, the transition is induced by local Joule heating upon applying a bias to the investigated two-terminal devices [6]. For a 1*T*-TaS_2 thin film of enhanced structural heterogeneity, the phase nucleation unfolds in a region of high dislocation density, which, additionally, also suppresses the thermal hysteresis. The subsequent domain growth is governed by pinning and sudden jumps of the interphase boundary (Fig. 2A-E), and this discontinuous behavior is mirrored in the macroscopic resistance extracted from accompanying electrical measurements. In contrast, we recover a more homogeneous switching and hysteretic behavior in a second device featuring controlled domain seeding and a lower defect density (Fig. 2F-J).

Conclusion

All in all, charge-density wave phase imaging resolves the influence of heterogeneity and microstructure on structural transformations and the associated macroscopic device properties. Our results underline the merit of nanoimaging approaches for characterizing functional devices based on quantum materials and informing their design for future technology.

References

[1] K. Rossnagel, J. Condens. Matter Phys. **23(21)** 213001 (2011)

[2] J. L. Hart, *et al.*, Nat. Commun. **14(1)** 8202 (2023)

[3] M. Eichberger, *et al*. Nature **468** 799-802 (2010)

[4] T. Domröse, *et al.*, Nat. Mater. **22(11)** 1345-1351 (2023)

[5] Th. Danz, T. Domröse, C. Ropers, Science **371(6527)** 371-374 (2021)

[6] T. Domröse, *et al.*, Nano Letters **24(40)** 12476-12485 (2024)

Fig. 1

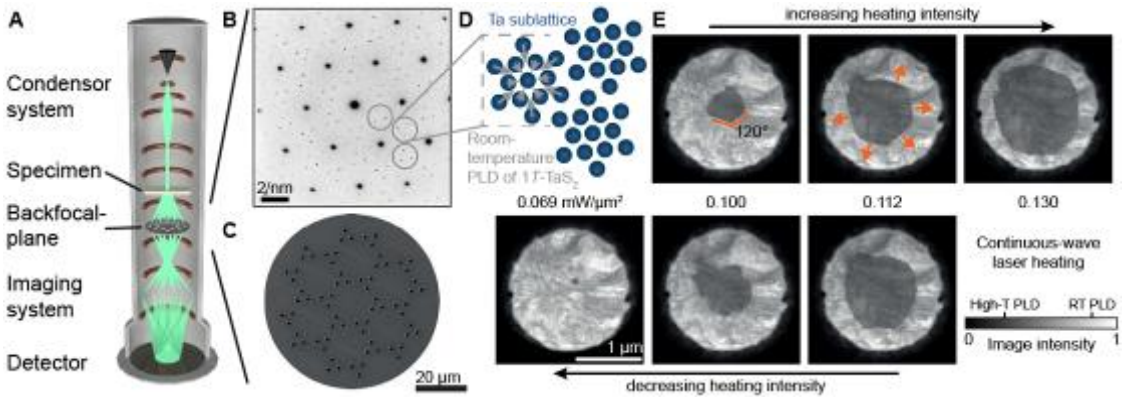
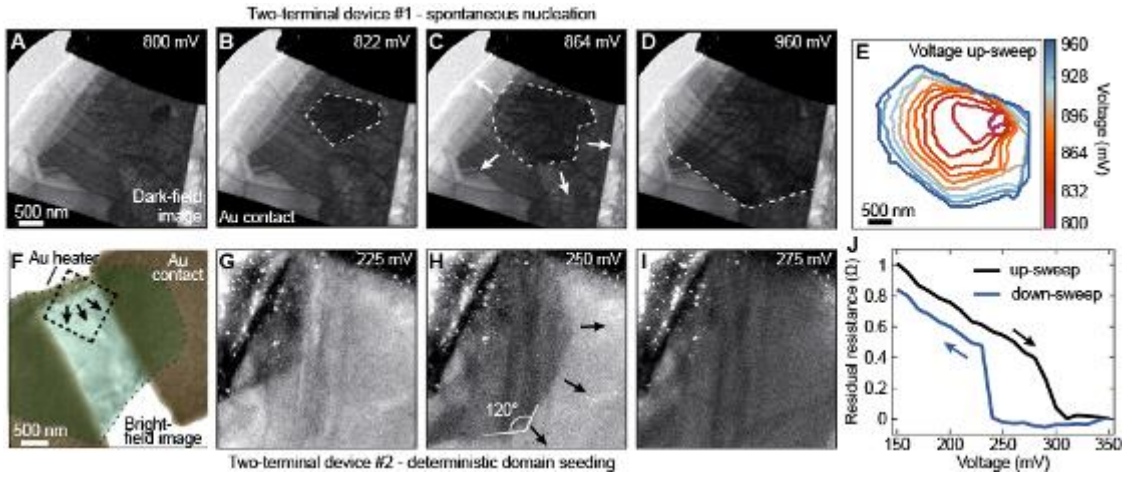


Fig. 2



IMLB.P04
Quantum entanglement between free electrons & photons demonstrated in an electron microscope

J. W. Henke[1,2], H. Jeng[1,2], M. Sivis[1,2], C. Ropers[1,2]

[1]Max Planck Institute for Multidisciplinary Sciences, Department of Ultrafast Dynamics, Göttingen, Germany
[2]University of Göttingen, 4th Physical Institute, Göttingen, Germany

Introduction

Quantum entanglement is the foundation of emerging quantum technologies including communication, computing and sensing. Transferring such entanglement-based techniques already employed in optical quantum sensing to electron microscopy could significantly enhance the sensitivity. While the quantum coherent scattering between free electrons and photons is expected to produce entangled states [1,2], verifying this entanglement is an outstanding challenge [3-5].

Objectives, Methods & Results

Here, we demonstrate such entanglement between photons and free electrons [6]. To this end, we prepare a coherent superposition of two electron beams by means of an amplitude grating placed in the condenser plane of our transmission electron microscope (TEM). Passing these beams by the two edges of a sub-micron sized, metal-coated glass prism, the electrons can spontaneously emit photons with polarization tied to the electron path. We first analyze the polarization state of the photons generated by a single electron beam, collecting them via an optical fiber and recording maps of the photon count rate for different wave-plate settings. Switching to the dual-beam scenario, we observe the interference between the recombined electron beams in coincidence with measurements of the photon polarization in different bases. This way, we implement quantum state tomography in our quantum eraser-type setup [4]. Based on the coincidence-filtered interference patterns, we reconstruct the full electron-photon quantum state, and find a violation of the Peres-Horodecki separability criterion by more than 7 standard deviations.

Conclusion

This observation of free-electron-photon entanglement will be central for future developments in free-electron quantum optics - from tailored quantum states of light as a resource for various applications to quantum-enhanced sensing in electron microscopy. Meanwhile, the use of dual-beam electron probes can facilitate the investigation of correlations in materials

References:
[1] O. Kfir, Phys. Rev. Lett. 123, 103602 (2019)
[2] A. Konecńa, F. Iyikanat, and F. J. García de Abajo, Sci. Adv. 8, eabo7853 (2022)
[3] E. Kazakevich, H. Aharon & O. Kfir, Phys. Rev. Res. 6, 043033 (2024)
[4] J.-W. Henke, H. Jeng & C. Ropers, Phys. Rev. A 111, 012610 (2025)
[5] P. Rembold et al., arXiv:2501.19536 (2025)
[6] J.-W. Henke, H. Jeng, M. Sivis & C. Ropers, arXiv:2504.13047 (2025)

IMLB.P05
Applications of Helium Ion Microscopy (HIM)

D. Exner[1], E. Okotete[1], S. Lee[1], S. Mück[1], R. Mönig[1], D. Kramer[1], C. Kirchlechner[1]

[1]Karlsruhe Institute of Technology, IAM-MMI, Karlsruhe, Germany

The Helium Ion Microscope (HIM) has become a versatile tool for nanoscale imaging of surfaces and their modification. In particular the use of the noble-gas ions and their weak chemical interaction with almost all materials makes HIM advantageous compared to the conventional Gallium-based FIB. HIM is attractive for applications requiring the combination of high-resolution imaging and nanoscale milling in one instrument. An ion beam of He or Ne with sub-nanometer size (0.35 nm edge resolution) is produced and scanned across the sample. Depending on the beam current and ion species, the beam can be used for imaging (e.g. via the generated electrons) and modification (milling) of the sample surface with a resolution in below 5 nm. For the milling of larger features of several micrometers our system features a Gallium beam (FIB). Compared to SEM, HIM is advantageous for uncoated insulating (e.g. biological) samples or for structuring materials with noble gas ions at a feature size in the low 100 nm regime. On the poster three different applications are presented:

We first show the imaging capabilities of HIM through high-resolution images of diverse samples, including biofilms, a nanostructured carbon film, and hydrated magnesia cubes, highlighting the technique"s versatility across biological and materials science applications. Second, we introduce applications in sodium batteries where we image Solid-Electrolyte-Interphase (SEI) layers formed on hard carbon and copper electrodes in Na-ion cells. Finally, the milling capabilities will be illustrated using Ne^+ ions as a Ga-free alternative for preparing notches in micro-cantilever fracture experiments.

IMLB.P06
3D strain field reconstruction by inversion of dynamical diffraction

L. Niermann[1], T. Niermann[1], C. Song[2], C. Ophus[3]

[1]Technische Universität Berlin, Institut für Physik und Astronomie, Berlin, Germany
[2]Lawrence Berkeley National Laboratory, Berkely, CA, United States
[3]Stanford University, Stanford, CA, United States

The strain field within a material has a large influence on its electronic, optical and catalytic properties. Consequently, the performance of many modern materials and devices is the result of finely engineered 3D strain fields. Prominent examples range from strain-enhanced carrier mobility in virtually every contemporary CMOS-based field effect transistor to precisely tuned strain fields in semiconductor quantum dots, which reduce fine structure splitting and enable the emission of entangled photons required for quantum technologies.

Despite its importance, measuring the 3D strain field, particularly variations along the electron beam direction, has remained a major challenge for S/TEM. State-of-the-art techniques can measure lateral strain variations in the directions perpendicular to the beam with the highest precision; however, they require a constant strain in the beam direction. Furthermore, the common assumption that the measured strain is a mere projection of the 3D strain along this direction, only holds for very thin specimens that are often not representative of the bulk structure due to significant surface relaxation effects. For most realistic, thicker specimens (>20 nm), where dynamical diffraction effects become dominant, this assumption even breaks down. In such cases, the measured signal exhibits a highly non-linear, often periodic, dependence on the depth of the strain inhomogeneity, rendering simple projection-based interpretations invalid.

This complex depth-dependent behavior represents a challenge for measurements with a parallel incident beam. However, in a 4D-STEM dataset obtained with a convergent electron beam, the dynamical diffraction effects contain the very information needed to determine the depth of strain inhomogeneities.

We present a newly developed method that reconstructs the 3D strain field by directly inverting these dynamical diffraction effects from a single 4D-STEM dataset. The core idea is to treat the 3D strain field as an unknown quantity and iteratively solve the inverse problem: finding the strain field that, when used in a simulation, best reproduces the experimentally measured dataset. The forward simulation is based on the computationally efficient numerical propagation of the Darwin-Howie-Whelan equations, which can be performed directly on the continuum strain field.

We first demonstrate the application of the method by reconstructing the variations of the displacement field from a simulated dataset of a 95 nm thick GaAs specimen containing a buried $In_{0.4}Ga_{0.6}As$ spherical quantum dot. Here, the method successfully reconstructed key features of the strain field, including the correct depth.

In a second application, we apply our method to reconstruct strain variations from experimental 4D-STEM data obtained from a 5.0 nm wide, pseudomorphically grown $Al_{0.47}Ga_{0.53}N$ layer, which is embedded in a 52.5 nm thick GaN specimen. Here, the method directly reconstructs the compressive strain of this layer and its inclined orientation within the specimen.

The presented technique overcomes a primary limitation of existing S/TEM strain mapping techniques by directly reconstructing the strain variations in beam direction from the information encoded in dynamical diffraction. We will further discuss symmetry aspects occurring within the reconstructions and strategies to overcome them.

IMLB.P07
High-precision chemical quantification of contaminated or geometrically unsuitable samples using in situ FIB-SEM preparation with coupled EDS and WDS

F. Kreps[1], K. Kelm[1]

[1]German Aerospace Center (DLR), Cologne, Germany

In quantitative measurements with SEM coupled EDS and WDS, homogeneity, contamination and, above all, the geometry of the sample have a significant influence on the quantification results with EDS or WDS. Especially for WDS the quality of the sample surface is very important to achieve an accuracy better 1%. For this reason, WDS was used in this study to verify the new approaches.

Many materials are susceptible to surface oxidation (Fig. 1b) or carbon contamination decreasing the quality of WDS and EDS measurements. The same counts for non-planar samples like particles.

The use of FIB allows the preparation of smooth cross-sections with high planarity (Fig.1, left). Using an EDS/WDS coupled FIB-SEM, an in-situ, site specific preparation followed by analysis without breaking vacuum is feasible. This enables a contamination- and oxidation-free preparation and analysis on a planar and even surface, significantly improving the quality of the measurement.

Cross-sections prepared with the FIB are usually not perpendicular to the electron beam, which is a pre-requisite for a proper quantitative EDS or WDS analysis. In this study, a new procedure is presented allowing an accurate quantification with EDS and WDS by using different tilt angles for the preparation and analysis.

Initially, the cross-section of a sample is prepared at a tilt of -10° producing a flat angle between sample and Ion beam on a system including an angle of 52° between electron and ion column. By tilting the sample to +28° afterwards, the cross-section is orientated perpendicular to the electron-beam enabling a quantification with EDS and WDS (Fig: 2).

The quantification results for the oxidized sample sum up to a total weight of 100.23% indicating a reliable combined EDS/WDS measurement compared to the metallographic prepared, oxidized surface with a total elemental sum of 92.23 wt.%. (Tab. 1). The quantification results for the unprepared particle show strong deviations from 84.17 wt.% to 107.16 wt.% (Tab. 2). Additionally, the surface is oxidized and the oxygen amount differs depending on the measured position. The quantification of the FIB prepared particle results in a total of 100.99 wt.% without traces of oxygen. These results indicate that this procedure significantly improves the quality of EDS and WDS quantitative results for originally geometrically nonsuited samples.

"Figure 1_FIB prepared and unprepared samples"

Fig. 1: FIB prepared surface of a thermoelectric MgAgSb oxidized sample (a) and the metallographically prepared oxidized surface of the same sample (b). Image (c) shows a small Ti64 particle intended for additive manufacturing with a diameter of 5µm and the same particle after FIB preparation (d)

"Table1_FIB prepared and metallographic prepared surface"

Tab. 1: Quantification of MgAgSb in a FIB prepared cross-section with corrected tilt and quantification with WDS of the same sample, but on its surface prepared by conventional metallography procedures. Mg was measured by WDS, AG and Sb by EDS

"Figure 2_Setup for FIB preparation"

Fig. 2: Left: Cross-Section with -10° stage tilt resulting in a -28° tilt compared to the sample surface; Right: Stage tilt of +28° to achieve the geometry necessary for WDS quantification

"Table2_FIB prepared and unprepared particle"

Tab. 2: Comparison between the quantification of a FIB prepared flattened surface of a particle and two different positions of an unprepared particle in its original form and surface.

Fig. 1

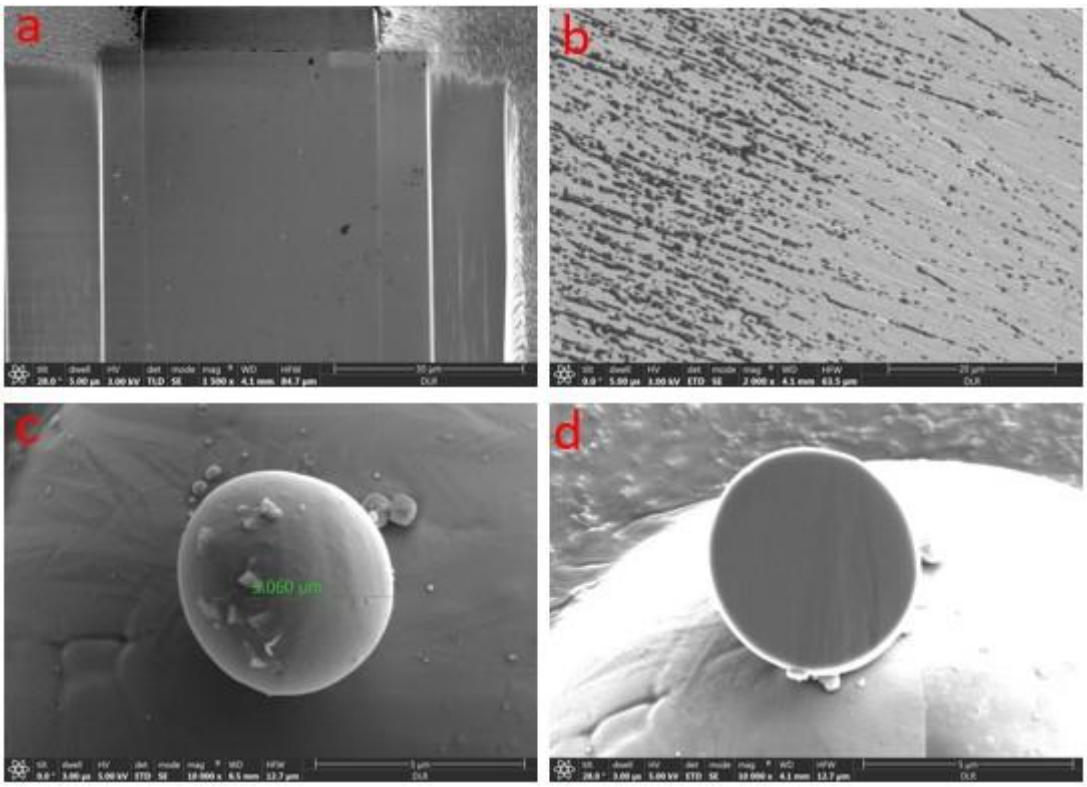


Fig. 2

	FIB Prepared		Metallographic Preparation	
Element	Wt [%]	At [%]	Wt [%]	At [%]
Mg+	8.82	31.28	8.74	33.14
Ag	40.74	32.65	37.53	32.06
Sb	50.67	35.97	45.96	34.79
Total	100.23	100.00	92.23	100.00

Fig. 3

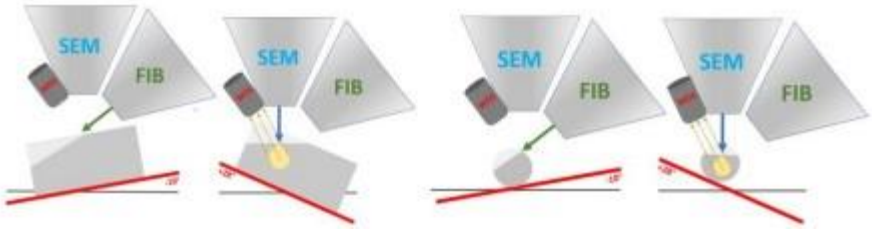


Fig. 4

	FIB Prepared		Unprepared 1		Unprepared 2	
Element	Wt [%]	At [%]	Wt [%]	At [%]	Wt [%]	At [%]
O	0.00	0.00	2.50	8.34	12.32	27.14
Al	5.83	9.83	1.15	2.27	5.96	7.78
Ti	89.67	85.25	74.53	83.11	82.25	60.50
V	5.50	4.91	5.99	6.28	6.64	4.59
Total	100.99	100.00	84.17	100.00	107.16	100.00

IMLB.P08
Multi-modal correlative microscopy – Simultaneous and colocalised Raman & SEM imaging

J. Diniz[1], G. Mabilleau[2], D. Boorman[1], J. Ferguson[1], T. Smith[1], D. Premužić[3]

[1]Renishaw plc, Wotton-under-Edge, United Kingdom
[2]University Angers / Nantes Université, ONIRIS, Angers, France
[3]Renishaw GmbH, Pliezhausen, Germany

Multi-modal sample analysis is essential to thoroughly characterise and understand our samples and materials and ultimately conduct cutting edge science.

Here we focus on 4 different modalities: Raman spectroscopy, optical imaging, SEM (scanning electron microscopy) imaging and EDS (energy dispersive X-ray spectroscopy). These techniques allow us to determine chemical composition, molecular and crystalline structure (Raman spectroscopy), collect optical images, image samples at high resolution (SEM imaging) and determine elemental composition (EDS). When combined, these techniques provide an excellent toolbox for sample characterisation.

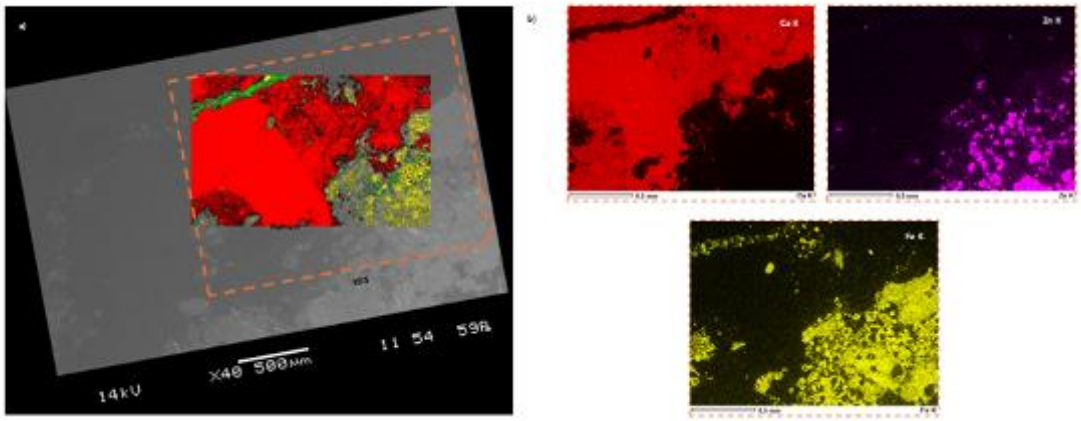
Measurements were conducted using an inLux™ SEM Raman interface attached directly to the SEM microscope. This enabled colocalised and simultaneous SEM, Raman, and optical imaging inside the SEM chamber, making correlation between the three techniques trivial, without ever moving the sample.

Figure 1 illustrates SEM, EDS and Raman images taken from a mineral section, demonstrating a clear and accurate overlay between minerals found with three techniques. Additionally, the complementary potential of the multi-modal analysis showed species detected only with Raman (anatase) or EDS (Zn, sphalerite). The presence of anatase also shows that Raman spectroscopy is sensitive to the many polymorphs of TiO2.

The application potential of correlative SEM and Raman imaging will also be demonstrated on batteries, polymeric and biological samples. With these examples, we illustrate how Raman and SEM can increase understanding of materials, and the power and ease of use when the techniques are combined inside a SEM.

Figure 1. a) BSE image of a mineral section with overlayed Raman image illustrating the distribution of calcite (red), pyrite (yellow), and anatase (green); b) complementary EDS information agrees with the Raman data, and in addition highlights Zn due to the presence of sphalerite.

Fig. 1



IMLB.P10
Phonon dynamics studied *in situ* by laser stimulated vibrational electron energy-gain spectroscopy

M. McCauley[1,2], J. Martis[3], O. Krivanek[3], B. Plotkin-Swing[3], T. Wagner[1,2], H. Çelik[1,4], K. Coogan[1,2], M. Zhao[1,2], G. Radtke[5], T. Lovejoy[3], C. T. Koch[1,2], B. Haas[1,2]

[1]Humboldt University of Berlin, Institute of Physics & CSMB, Berlin, Germany
[2]Humboldt University of Berlin, Center for the Science of Materials, Berlin, Germany
[3]Bruker AXS LLC, Kirkland, WA
[4]Technische Universität Berlin, Institute for Physics and Astronomy, Berlin, Germany
[5]Sorbonne University, CNRS UMR 7590, MNHN, IMPMC, Paris

Phonons play an important role in thermal transport and dynamics at the nanoscale and can be directly observed using electron energy loss spectroscopy (EELS) in a scanning transmission electron microscope (STEM) due to the high spatial and energy resolution of modern instruments. Phonons can be stimulated optically, either by resonant excitation or localised heating. By integrating a fibre-based laser into a STEM, we enable the investigation of in-situ phonon dynamics using monochromated EELS with variable laser powers and wavelengths.

The objective of this work is to study phonon transport and dynamics in different materials and across interfaces by means of focused laser stimulation, probed by electron energy gain and loss spectroscopy (EEGS/EELS).

Light from a 637 nm Thorlabs fibre laser diode was injected into a Nion HERMES microscope in a co-developed system [1] which focuses the laser to a spot size of around 20 µm at the sample from a shallow angle of about 20°. Monochromated electron energy gain and loss spectra were acquired using a DECTRIS ELA direct electron detector and a high tension of the microscope of 60 kV. We acquired spectra for different laser powers and at varied distances from the focused laser spot to study heat dissipation. We study phonon transport through materials by laser exciting in one position and probing with the electron beam at a defined distance. We are currently developing synchronisation between the laser excitation and the detector to facilitate pump-probe type experiments with nanosecond temporal resolution to study dissipation dynamics.

The local temperature was determined from analysis of the relative intensities of gain and loss peaks in monochromated EELS spectra [2,3], which are related to transitions between states with temperature dependant occupations. The ratio of loss, $P(\Delta q, \Delta E)$, to gain, $P(-\Delta q,-\Delta E)$, intensities in an energy range, ΔE, follows the principle of detailed balance described by

Eq.(1)

where k_B is the Boltzman constant and T is the local temperature. After background subtraction, the loss/gain peak intensities were used to calculate local temperatures at different positions and laser powers. These measurements enable mapping of temperature gradients induced by the focused laser beam.

By measuring the local phonon excitations we also gain information about the transport of different phonon modes across different materials. The goal is to study the influence of structural and morphological changes on phonon coupling. Momentum-resolved EELS will shed additional light on phonon transport in materials.

We demonstrate measurements of local phonon excitation and heating using in-situ laser stimulated EELS and EEGS within a STEM. These results provide a basis for future studies of phonon dynamics

at nanostructures which will also involve pump-probe type experiments using synchronised detection with laser pulses.

[1] Martis, J. *et al.* (2024), *Microsc. Microanal.*, 30(Supplement_1), 2182-2184.

[2] Lagos, M.J. and Batson, P.E. (2018), *Nano Lett.*, 18(7), 4556–4563.

[3] Idrobo, J.C. *et al.* (2018), *Phys. Rev. Lett.*, 120(9), 095901.

The authors thank George Corbin (formerly at Nion Co.) for help in developing the laser injection hardware and Petr Hrncirik (Bruker AXS LLC) for hardware support. Funding of the PuMMAVi project (number 530143441) by the Deutsche Forschungsgemeinschaft (DFG, German Research Foundation) is gratefully acknowledged.

Fig. 1

$$\frac{P(\Delta q,\Delta E)}{P(-\Delta q,-\Delta E)} = exp\left(\frac{\Delta E}{k_B T}\right),$$

IMLB.P11
Examination of the thermal decomposition of Ag_2CO_3 using ESEM and mass spectrometry

T. Krekeler[1], M. Ritter[1]

[1]Hamburg University of Technology, Electron Microscopy Unit, Hamburg, Germany

Environmental scanning electron microscopy (ESEM) is a well-established technique to image specimen of life- and/or material-science under low vacuum or near-ambient conditions [1]. The wide range of possible gases and pressures makes the environmental scanning electron microscope in combination with a heating stage a valuable tool for many important topics of material science like sintering, phase changes and catalysis. The addition of a mass spectrometer enhances the analytic capabilities of an ESEM by enabling correlations between visible structural changes and composition or changes of the sample environment.

In this work, we examine the microstructural changes during the thermal decomposition of Ag_2CO_3 to Ag_2O and Ag in an inert gas atmosphere. The instrument used is a Thermo Scientific Quattro S ESEM equipped with a Hiden HPR-30 gas analyzer connected to the differential pumping system of the ESEM. A small amount of Ag_2CO_3 (ca. 50 mg) was dispersed as a fine powder on a Pt-coated alumina crucible and heated with a rate of 10 K min^{-1} from 80 to 500 °C in a N_2 atmosphere of 1.7 mbar. During the heating experiment images and mass spectra where recorded with an interval of 8 seconds.

The first phase of the decomposition can be observed as early as 150 °C, where smaller Ag_2CO_3 particles develop pores or ridges at the surface (see marks in Fig. 1). After the CO_2 development is completed at 300 °C, the sample consists of rounded irregular polyhedrons. While the initial microstructure of the sample is still recognizable, the size of the individual particles was reduced significantly (see Fig 2).

The second phase of the decomposition starts at temperatures of 370 °C with a shrinking of the particles. At the maximum of oxygen development around 390 °C the microstructure coarsens rapidly resulting in large rounded ligaments (see Fig. 3). This second phase can be characterized by an induction period followed by a fast decomposition which can be explained with the autocatalytic character of the Ag_2O decomposition [2]. No structural changes have been observed in the temperature interval between 400 and 500 °C.

The observed temperatures for the gas development (see Fig. 4) are in good accordance to literature values for the decomposition of Ag_2CO_3 and Ag_2O acquired from TGA [3]. Although the sample amount is quite small, the gas development is well observable proving the great potential of mass spectrometry in ESEM.

Figure 1: SEM image of specimen at start of CO_2 release (T = 150 °C).

Figure 2: SEM Image of same location after complete CO_2 release (T = 330 °C).

Figure 3: SEM image of specimen after O_2 release (T = 500 °C).

Figure 4: Partial pressures of CO_2 and O_2 and temperature plot.

References

[1] G. D. Danilatos *Advances in Electronics and Electron Physics.* 71, 109–250, (1988).

[2] G. C. Hood *et al. J. Chem. Educ.* 26, 3, 169, (1949).

[3] W. A. Parkhurst *et al. J. Electrochem. Soc.* 131, 1739, (1984).

Fig. 1

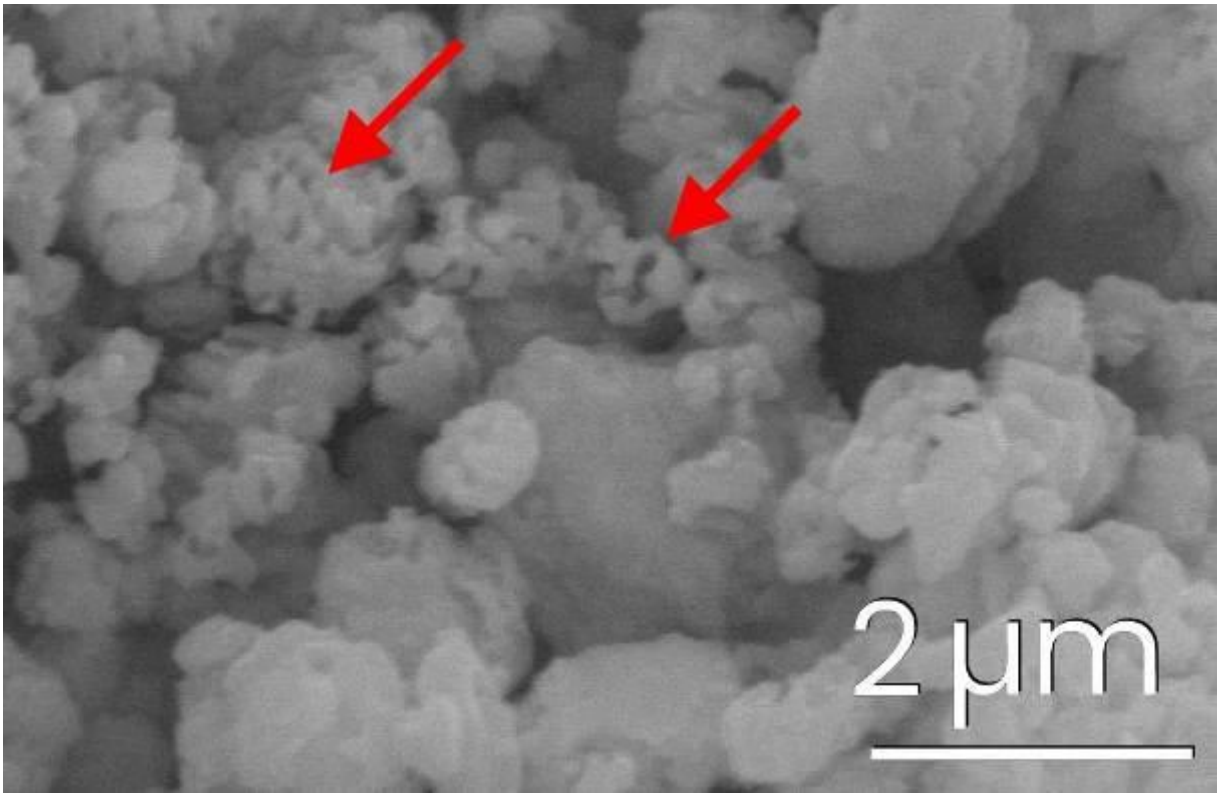


Fig. 2

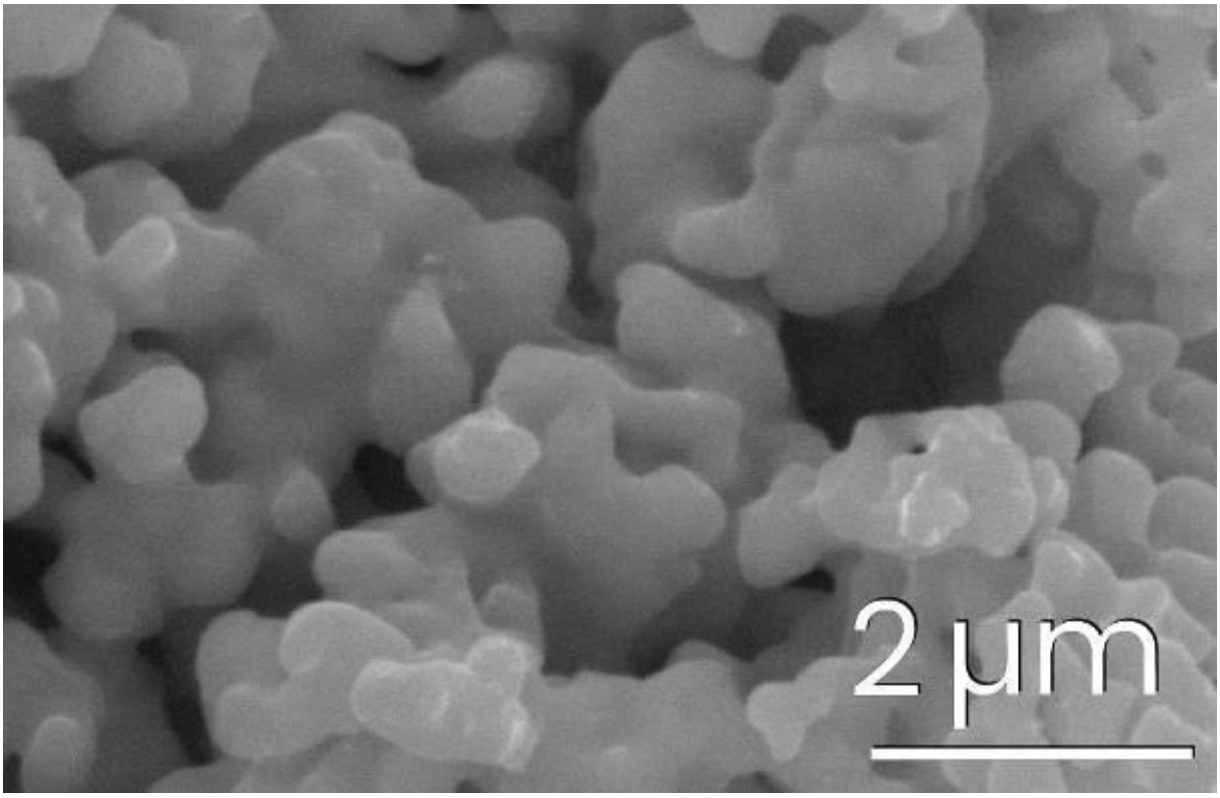


Fig. 3

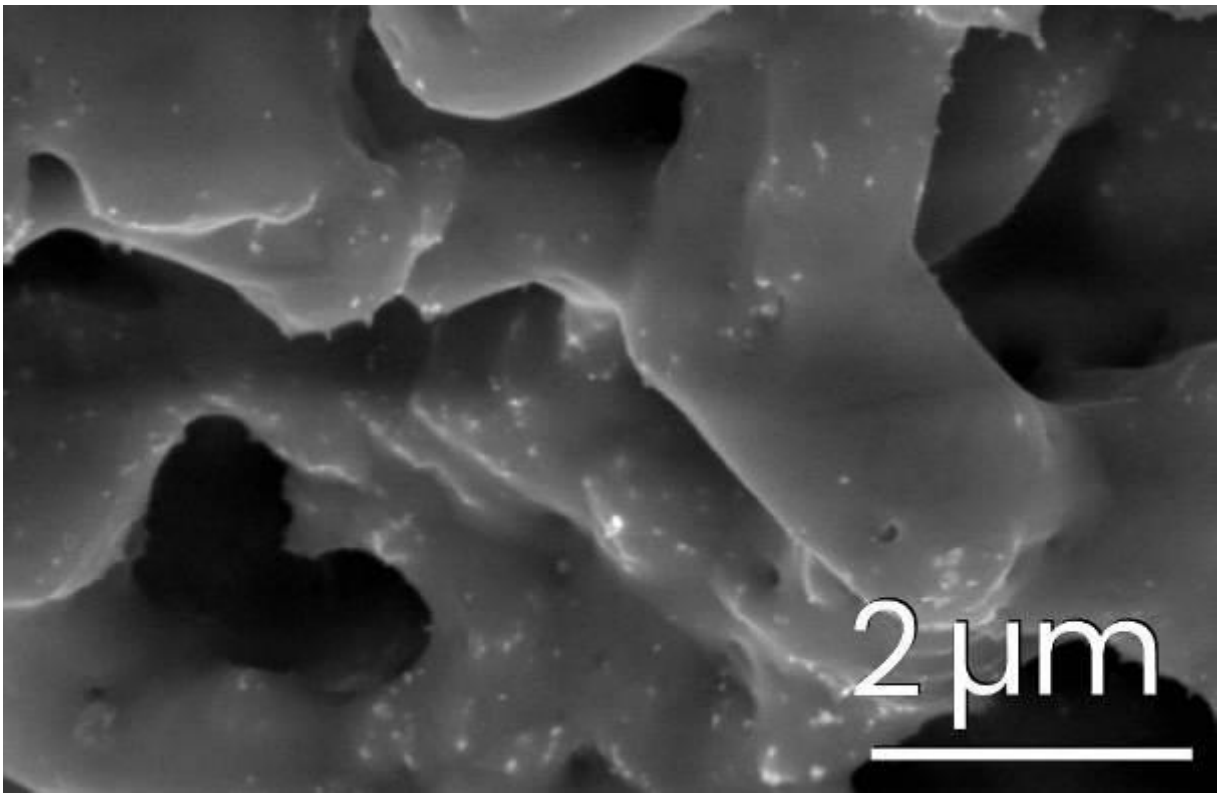
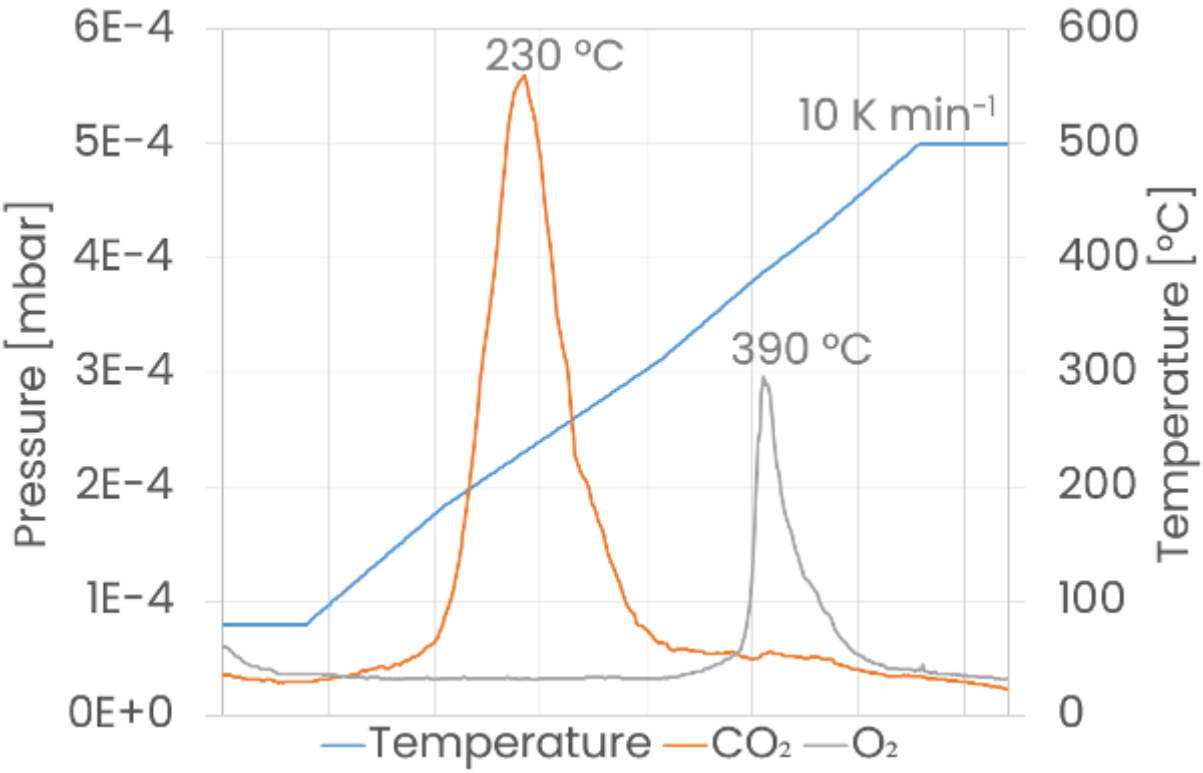


Fig. 4


6E-4
5E-4
4E-4
3E-4
2E-4
1E-4
0E+0
Pressure [mbar]
600
500
400
300
200
100
0
Temperature [°C]
230 °C
390 °C
10 K min⁻¹
Temperature
CO₂
O₂

IMLB.P12
Inelastic electron-light interaction probed by holographic scanning transmission electron microscopy

T. Dauwe[1,2], N. Bach[1,2], M. Sivis[1,2], C. Ropers[1,2]

[1]Max Planck Institute for Multidisciplinary Sciences, Ultrafast Dynamics, Göttingen, Germany
[2]University of Göttingen, 4th Physical Institute, Göttingen, Germany

Ultrafast Transmission Electron Microscopy (UTEM) is a unique tool to study inelastic electron-light scattering (IELS). Harnessing these capabilities, Photon-Induced Near-Field Electron Microscopy (PINEM) can now routinely image the amplitude and shape of optical fields at laser-excited nanostructures. Phase-resolved imaging is enabled by sequential interactions, and dispersive propagation yields attosecond electron pulses, both of which offer a pathway to sub-optical-cycle temporal resolution [1,2,3]. However, these techniques require an elaborate geometry with multiple optical interactions, rendering flexible imaging of nanostructures challenging.

In this work, we combine IELS with a STEM holography approach. To achieve this, we place an amplitude grating in the condenser aperture of our UTEM. This enables the creation of multiple coherent, focused electron probes in the sample plane [4,5]. Two beams are selected with an aperture, accessing the inelastic interaction at spatially displaced sample positions. A 2D camera, positioned behind an energy filter, records the far-field interference pattern of these probes in energy-dispersive mode. This provides us with simultaneous, direct access to the amplitude and relative phase of the inelastic interactions as well as elastic phase shifts, which we use to characterize the optical nearfield at a nanostructure quantitatively. Furthermore, this technique enables tailoring the electron-light interaction of each probe through sample design and laser illumination, thereby providing control over the final electron state. The interference pattern contains the coherent superposition of the individual probe states as a function of their relative phase. We showcase the resulting electron spectra, which display distinct features such as asymmetries that cannot be achieved using a single interaction.

Our approach enables the direct measurement of phase shifts induced by inelastic electron-light scattering. It may be extended to give access to material dynamics through phase-resolved diffraction. Besides, the superposition of multiple probes undergoing different IELS interactions can be used to synthesize tailored electron states, which could, for example, be optimized for temporal bunching as theoretically predicted [6].

[1] K.E. Priebe et al., Nature Photon 11, 793–797 (2017)
[2] D. Nabben et al., Nature 619, 63–67 (2023)
[3] J.H. Gaida et al., Nat. Photon. 18, 509–515 (2024)
[4] F.S. Yasin et al., Microscopy and Microanalysis. 2016;22(S3):506-507
[5] F.S. Yasin et al., J. Phys. D: Appl. Phys. 51 205104 (2018)
[6] F.J. Garcia de Abajo, Phys. Rev. Lett. 130, 246901 (2023)



© kanpisut, SimpLine – Stock.Adobe.com

25 YEARS conventus CONGRESSMANAGEMENT

first edition | only online | 8/2025 | ISBN - 978-3-948023-55-3

MC 2025 Karlsruhe